Green Energy and Technology

Lalita Ledwani
Jitendra S. Sangwai *Editors*

Nanotechnology for Energy and Environmental Engineering

Springer

Green Energy and Technology

Climate change, environmental impact and the limited natural resources urge scientific research and novel technical solutions. The monograph series Green Energy and Technology serves as a publishing platform for scientific and technological approaches to "green"—i.e. environmentally friendly and sustainable—technologies. While a focus lies on energy and power supply, it also covers "green" solutions in industrial engineering and engineering design. Green Energy and Technology addresses researchers, advanced students, technical consultants as well as decision makers in industries and politics. Hence, the level of presentation spans from instructional to highly technical.

Indexed in Scopus.

More information about this series at http://www.springer.com/series/8059

Lalita Ledwani · Jitendra S. Sangwai
Editors

Nanotechnology for Energy and Environmental Engineering

Springer

Editors
Lalita Ledwani
Manipal University Jaipur
Jaipur, Rajasthan, India

Jitendra S. Sangwai
Indian Institute of Technology Madras
Chennai, Tamil Nadu, India

ISSN 1865-3529 ISSN 1865-3537 (electronic)
Green Energy and Technology
ISBN 978-3-030-33773-5 ISBN 978-3-030-33774-2 (eBook)
https://doi.org/10.1007/978-3-030-33774-2

This Springer imprint is published by the registered company Springer Nature Switzerland AG
The registered company address is: Gewerbestrasse 11, 6330 Cham, Switzerland

Preface

Nanotechnology is one of the fastest growing fields in the scientific and industrial applications. It has applications in various domains from process development and intensification to energy and environmental sector. This book covers the potential applications of nanoscience and nanotechnology to promote eco-friendly processes and techniques for energy and environment sustainability. The goal of this book is to promote eco-friendly processes and techniques by covering various aspects of both the synthesis and applications of nanoparticles and nanofluids for energy and environmental engineering. The book highlights the development of reliable, economic, eco-friendly processes through advanced nanoscience and technological research and innovations. It not only covers detail of advanced nanotechnology research in energy and environment sectors but also bridge the gap between existing nanotechnology innovations and requirement of industries.

With an objective to benefit larger scientific community, the intended audience of the book consists of academicians and researchers working in the field of nanotechnology or nanomaterials, especially as applied to energy and/or environmental sustainability engineering. Graduate students in the same areas will also find it a valuable resource.

The book comprise of 25 contributed chapters with prime focus toward the scope and challenges with nanomaterials synthesis and applications considering energy and environment issues in the current scenario.

Chapter "Synthesis and Characterization of Nanofluids: Thermal Conductivity, Electrical Conductivity and Particle Size Distribution" is focused toward synthesis and characterization of a new type of fluid, called nanofluid. The properties of the nanofluid such as thermal conductivity, electrical conductivity, etc. have been discussed and summarized. The several factors that are responsible for the alteration of the properties of nanofluids along with its distinctive applications in various engineering fields are reviewed and discussed.

Chapter "Synthesis, Characterization, and Application of Biogenic Nanomaterials: An Overview" provides a review on current potential applications of nanotechnology into the bio-environmental systems and its correlation with the synthesis of biogenic nanoparticles. Green nanotechnology is implementation of green chemistry and green

engineering principles in the field of nanotechnology to influence the size of nanoparticles within a nanoscale range to make biogenic nanoparticles which can be useful in solving serious environmental problems in the area of wastewater treatment, pollutant removal, fatal diseases, climate change, and solar energy conversion.

Chapter "Thermal Plasma Processes and Nanomaterial Preparation" describes the basics of plasmas, types of plasma and nanoscience, and use of plasma in material processing, especially in preparation of nanomaterials. Plasma here refers to the fourth state of matter which has wide-ranging applications, ranging from industrial to biomedical. Primarily, the energy content in a plasma state is orders of magnitude higher than the energy content of the other three states of matter.

Chapter "Peptide Nanotubes: A Crystallographic Approach" focuses on peptide self-assembly formed by non-coded amino acids and formation of different nanostructures using crystallographic approach. Molecular self-assembly has led to a breakthrough in the field of nanomaterials. This has also resulted in myriad of potential applications in biology and chemistry. Peptides have proven to be the most promising platforms owing to their biocompatibility and diversity. They are also most studied among the other classes of organic building blocks due to their uncanny resemblance with the proteins.

Chapter "Halloysite Nanotubes: An 'Aluminosilicate Nanosupport' for Energy and Environmental Applications" highlights the usage of environment-friendly nanomaterial Halloysite Nanotube (HNT) as nanosupport systems to immobilize various types of guest molecules. These materials, which are naturally available, are clay-based aluminosilicate nanomaterial, which has attracted attention of many environmental researchers in recent times. Further, the use of such 'guest molecule-HNT' based nanosupport systems for the remediation of environmental pollutants, as well as for energy applications has been discussed. In recent years, emergence of nanotechnology-based materials has proved to be a helping hand in many applications in various sectors. However, the use of eco-friendly nanomaterials provides an upper hand over other nanomaterials for such applications.

Chapter "A Review on Contemporary Hole Transport Materials for Perovskite Solar Cells" presents a review focused on different types of hole-transporting materials (HTM) under research over the past few years in the perovskite-based solar cell (PSC) in achieving the goal of higher power conversion efficiency (PCE) and operational stability. HTMs are an indispensable part of PSC which affects both efficiency and stability. An overview of different types of HTMs (organic, inorganic, and polymeric) are presented detailing its structure, electrochemical, and physical properties, while highlighting several considerations for making a choice for a new HTM for PSC.

Chapter "Conjugation of Nanomaterials and Bioanodes for Energy Production in Microbial Fuel Cell" deals with the basic idea of microbial fuel cell (MFC) and its limitation. The use of nanoparticles as a solution for power enhancement in an MFC reactor is also elaborated in the chapter. The MFC reactors can be the added as one major area for application of nanoparticles. The use of surface enhancement property of nanomaterials can be applied in the field of biotic energy generation and simultaneous waste treatment technology. The two goals are targeted under MFC technology.

Chapter "A Model for Electro-osmotic Flow of Pseudoplastic Nanofluids in Presence of Peristaltic Pumping: An Application to Smart Pumping in Energy Systems" reveals the formulation of the model that can be useful in the experimental designs of smart nano-electro-peristaltic pumps; in addition, it can also be extended to nanotechnological applications, smart drug delivery systems, and various transport phenomena of environmental systems. The model presented in this chapter assumes that the movement of the fluids can be controlled by electroosmotic force generated as a result of an external electric field. A pseudoplastic fluid model is assumed as appropriate to compute the non-Newtonian effects. Nonlinear formulation present in the model is simplified with the help of lubrication theory and Hückel–Debye approximations. Modeled governing equations are solved to determine the flow, temperature, and electric potential fields. The flow behavior and thermal characteristics are simulated as a function of physical parameters.

Chapter "Synthesis of Nanomaterials for Energy Generation and Storage Applications" highlights the detail of polymer electrolyte membrane (PEM) fuel cell. It is a device in which an electrochemical reaction occurs between fuel and oxidant producing electricity, and water is the only by-product with zero emission. Different supported catalysts have been proposed to improve electrochemical stability of nanoparticles in PEM fuel cells and supercapacitor. Usually, Pt nanoparticles prepared on carbon support used for oxidation and reduction reaction in PEM fuel cells. The encapsulation of carbon with polyaniline (PANI)-supported Pt enhances the electrode stability in fuel cells by enhancing the active surface area (EASA), chemical resistance, and electron conductivity.

Chapter "Interaction of Heavy Crude Oil and Nanoparticles for Heavy Oil Upgrading" discusses the role of nanomaterials in the development of heavy oil recovery. Different types of mechanisms which explain the effects of nanoparticles and their interaction with oil and its constituents are highlighted. The effects coupled with the use of various thermal treatment schemes have been explained. Scope of applicability in the field of flow assurance has been discussed. The use of nanoparticles in improving the existing EOR applications and devising new ways to achieve production of heavy fractions has been highlighted.

Chapter "Application of Nanoparticles-Based Technologies in the Oil and Gas Industry" addresses the role of nanotechnology in different jobs played in the oil and gas industry such as exploration industry, drilling and production, refining, and processing and in enhanced oil recovery. Besides different types of nanoparticles, nanoemulsions, nanosensors, and nanofluids available for these applications have been discussed. Moreover, the mechanisms which reflect the activity of these nanomaterials have been explained individually. The chapter discusses how nanotechnology-based technologies can achieve more efficient, effective, and potential impact in the oil and gas industry.

Chapter "Effect of Nanoparticles on the Performance of Drilling Fluids" elaborates the application of various types of nanoparticles/nanocomposites to enhance the rheological and filtration properties of the drilling mud. Due to the extinction of conventional reservoirs, it is imperative for engineers to find the unconventional oil

and gas resources. Drilling an unconventional field requires engineered drilling fluids because an efficient drilling operation purely depends upon the performance of drilling fluid. Drilling fluid which is a combination of solids and fluids performs many functions such as cooling the drill bit, cleaning the wellbore, maintaining the wellbore pressure, and development of a filter cake to prevent the invasion of fluid into the formation.

Chapter "Interaction of Nanoparticles with Reservoir Fluids and Rocks for Enhanced Oil Recovery" details the types of NPs, preparation, and their characterization with the application of various nanoparticles in chemical enhanced oil recovery (CEOR). Limitation of NPs application in chemical enhanced oil recovery area is spelled out clearly with the recommendation at the end. The chapter focuses on work carried out by the researchers on chemical and rarely on thermal, gas injection, and biological EOR methods using NPs and their impact on the viscosity, interfacial tension (IFT), and wettability the major influencing factors for EOR. The authors intend to make the reader understand the pore-scale mechanism behind the enhanced oil recovery.

Chapter "Versatile 1-D Nanostructures for Green Energy Conversion and Storage Devices" reveals the updated literature survey on green synthesis of 1-D nanostructures applied in photovoltaic solar cells (PSC) and energy storage systems (ESS). Increasing population and living standards demands high energy provisions; but considering pollution issues and depleting fossil fuel reservoirs, the fulfillment of the energy demands through eco-friendly/green renewable energy technologies have become an urgent need. Among all renewable energy systems, photovoltaic solar cells (PSC) with energy storage systems (ESS) such as batteries or supercapacitors have attracted great attention as the next generation of energy suppliers.

Chapter "Nanoporous Polymeric Membranes for Hydrogen Separation" summarizes detail of H_2 gas separation based on the different membranes and approaches to prepare hydrogen-selective membranes. Among all renewable energy sources, hydrogen has been found more attractive energy carrier due to high efficiency and cost-effective, sustainable energy source. For practical use of H_2 as an energy source, it should be separated from a mixture of gases by using hydrogen-selective membranes.

Chapter "Functionalized Nano-porous Silicon Surfaces for Energy Storage Application" highlights the importance of electrochemically prepared porous silicon where the physical properties, e.g., pore diameter, porosity, and pore length that can be controlled by etching parameter and the functionalized nanostructured surfaces of porous silicon, might be the key material to develop high energy storage electrodes. Storing power from several intermittent sources has been a great interest of scientific community and grows as the renewable energy industry begins to generate a larger fraction of overall energy consumption.

Chapter "Optimization of $MAPbI_3$ Film Using Response Surface Methodology for Enhancement in Photovoltaic Performance" details the optimization of process parameters for the deposition of methylamine lead iodide ($CH_3NH_3PbI_3$ or $MAPbI_3$) film using parametric study and response surface methodology (RSM). The independent parameters to be optimized are PbI_2:CH_3NH_3I ratio (1:2–1:4), spin

speed (2000–3000 rpm), and annealing temperature (60–100°C). The dependent parameter considered in this study is power conversion efficiency (PCE) of perovskite solar cell (PSC) fabricated using $MAPbI_3$ layer.

Chapter "Application of Nanotechnology in Diagnosis and Therapeutics" emphasizes on the evolution of nanoparticles to meet the challenges relevant to healthcare system. In terms of human healthcare and therapy, nanoparticles are expected to contribute in drug delivery and regenerative medicine with its ability to target the source of disease with increased efficiency and minimal side effects. Nanomedicine offers several advantages, such as protection of the payload from degradation in both *in vitro* and *in vivo* milieu, facilitation of controlled release of entrapped drugs, prolonged therapeutic effect, and enhancement of targeted delivery along with diminished side effects. Nanotechnology has proved to address some of the problems related to diagnostics, therapeutics, and biomedical aspects.

Chapter "Designing Novel Photocatalysts for Disinfection of Multidrug-Resistant Waterborne Bacteria" reveals the detail of photocatalysis, a subsidiary of advanced oxidation processes for water decontamination. The already existing photocatalysts like titanium dioxide and zinc oxide are being depleted to their core. So, newer and novel photocatalysts need to be developed with a more proficient, eco-friendly, and bio-compatible approach. The detail in the chapter aims to have a closer look at the existing disinfection techniques and the emerging players in the field of photocatalysis.

Chapter "Magnetic Nanoparticles: Green and Environment Friendly Catalyst for Organic Transformations" highlights the detail of magnetic nanoparticles or magnetic core–shell nanoparticles that have gained a significant place due to their paramagnetic nature facilitates the separation of catalyst through the use of an external magnet which makes the recovery of catalyst easier and prevents loss of catalyst associated with conventional filtration or centrifugation methods. Additionally, the possibility of reusability and milder reaction conditions further enhance the potential of nanoparticle catalyzed organic transformations.

Chapter "A Comprehensive Characterization of Stress Relaxed ZnO Thin Film at Wafer Level" explores the impact of sputtering parameters on structural, optical, and mechanical properties of reactive magnetron sputtered ZnO thin film. Stress relaxed and room temperature deposited ZnO film is highly desirable from fabrication aspects. Theoretical model has been proposed to understand the consequences of oxygen-induced stress in ZnO thin films. It is established that nearly stress-free, single-phase, and highly c-axis oriented ZnO thin film can be deposited using a unique combination of sputter parameters.

Chapter "Microstructurally Engineered Ceramics for Environmental Applications" focusses on use of microstructurally engineered ceramics for environmental applications, e.g., in the development of materials that can be used for treatment of industrial wastewater. It is well known that industrial wastewater contains toxic ions and dyes. When such contents cross the permissible limit, it may become an issue of major environmental concern. The presented work demonstrates the use of microstructurally designed, phase pure $Mg(OH)_2$ nanoplatelets 99.99% adsorption of the toxic Cu (II) ion.

Chapter "Eco-friendly Surface Modification and Nanofinishing of Textile Polymers to Enhance Functionalisation" gives brief information about the application of non-thermal atmospheric pressure plasma and nanotechnology in the fields of textiles. The chapter reviews the recent studies involving modification and characterisation of textile highlighting plasma and nano pretreatment. This chapter also attempts to give an overview of the literature on treatment of textiles categorizing them on the basis of different functional properties like antimicrobial, UV resistance, easy care, dye adsorption, and flame-retardant finishes that could be achieved by the application of metal and metal oxide nanoparticles and enhanced by plasma pretreatment.

Chapter "Removal of Ni(II) and Zn(II) from Aqueous Media Using Algae-Sodium Bentonite Nanocomposite" enlightens the utilization composite, made by mixing dead *Spirogyra* algal biomass with nano-bentonite clay, to study the adsorption of Ni(II) and Zn(II) as a function of pH, contact time, adsorbent dosage, and initial ion concentration. An average crystal size of the composite synthesized was found to be 34.11 nm. Langmuir adsorption isotherm and pseudo-second-order models were found to be the best fit for equilibrium data, highlighting the potential of algae bentonite composite as possible feedstock for adsorption of heavy metals from aqueous media.

Chapter "Nucleic Acid Based Nanoconstructs for Environmental Analysis in Atypical Contexts" highlights the use of biomolecules toward environmental analysis that provides impressive advantages in terms of selectivity and efficiency. A proof-of-concept of nucleic acid based nanoconstructs as a reusable adsorbing agent is presented in the chapter. Immobilization of the nucleic acid architectures on magnetic nanoparticles enables their reuse across samples. Inherent sophistication of biomolecules in general and nucleic acid based constructs in particular supports their deployment in specialized applications at a smaller scale pertinent to individual human activity. The perspective presented in this chapter is expected to encourage environmental engineering in distinctive and atypical contexts.

We would wish to convey our gratitude to all authors for their significant contribution in the form of chapters for this book. We also acknowledge the support provided by Neeraj Gaur and our doctoral students (Gomathi, Umasankar, Rohan, Shruti, Mona, Mumal, and Priyanka) during the process. The support provided by family members is immense without which the book could not have seen the light of the day. Our special thanks to Springer Publication team especially Renette Francis Irine and Charlotte Cross for their constant cooperation.

Jaipur, India — Dr. Lalita Ledwani
Chennai, India — Dr. Jitendra S. Sangwai

Contents

Contributors

Akhil Agrawal Energy and Environment Research Laboratory, Department of Microbiology, School of Life Sciences, Central University of Rajasthan, Ajmer, India

Jamil Akhtar Smart Sensors Area, CSIR-Central Electronics Engineering Research Institute, Pilani, Rajasthan, India

K. Anand Kishore Department of Chemical Engineering, National Institute of Technology, Warangal, Telangana, India

Ambika Arkatkar Department of Chemical Engineering, Sardar Vallabhbhai National Institute of Technology, Surat, India;
Department of Biotechnology, Veer Narmad South Gujarat University, Surat, India

Kamlendra Awasthi Department of Physics, Malaviya National Institute of Technology, Jaipur, Rajasthan, India

Waris Baba Department of Chemical Engineering, National Institute of Technology Srinagar, Srinagar, Jammu & Kashmir, India

Ashima Bagaria Department of Physics, School of Basic Sciences, Manipal University Jaipur, Rajasthan, India

C. Balasubramanian Atmospheric Plasma Division, Institute for Plasma Research, Gandhinagar, India

Divya P. Barai Chemical Engineering Department, Laxminarayan Institute of Technology, Rashtrasant Tukadoji Maharaj Nagpur University, Nagpur, MS, India

Aradhana Basu School of Biotechnology, Kalinga Institute of Industrial Technology (KIIT), Bhubaneswar, India

Uma Sankar Behera Gas Hydrate and Flow Assurance Laboratory, Petroleum Engineering Program, Department of Ocean Engineering, Indian Institute of Technology Madras, Chennai, India

Bharat A. Bhanvase Chemical Engineering Department, Laxminarayan Institute of Technology, Rashtrasant Tukadoji Maharaj Nagpur University, Nagpur, MS, India

Shivani S. Chawhan Chemical Engineering Department, Laxminarayan Institute of Technology, Rashtrasant Tukadoji Maharaj Nagpur University, Nagpur, MS, India

Kalyani K. Chichghare Chemical Engineering Department, Laxminarayan Institute of Technology, Rashtrasant Tukadoji Maharaj Nagpur University, Nagpur, MS, India

Pradip Sekhar Das Advanced Mechanical and Materials Characterization Division (AMMCD), CSIR-Central Glass and Ceramic Research Institute, Kolkata, India;
Fuel Cell and Battery Division, CSIR-Central Glass and Ceramic Research Institute, Kolkata, India

Sourav Das School of Chemical Technology, Kalinga Institute of Industrial Technology (KIIT), Bhubaneswar, India;
School of Biotechnology, Kalinga Institute of Industrial Technology (KIIT), Bhubaneswar, India

Bhaskar Datta Department of Biological Engineering, Indian Institute of Technology Gandhinagar, Gandhinagar, Gujarat, India;
Department of Chemistry, Indian Institute of Technology Gandhinagar, Gandhinagar, Gujarat, India

R. R. Deshmukh Department of Physics, Institute of Chemical Technology, Matunga, Mumbai, India

Ankit Dodla Department of Biological Engineering, Indian Institute of Technology Gandhinagar, Gandhinagar, Gujarat, India

Jignasa V. Gohel Department of Chemical Engineering, Sardar Vallabhbhai National Institute of Technology, Surat, Gujarat, India

Ritu Goswami Department of Biotechnology, School of Life Sciences, Central University of Rajasthan, Ajmer, Rajasthan, India

A. P. Habeeb Rahman School of Chemical Technology, Kalinga Institute of Industrial Technology (KIIT), Bhubaneswar, India;
School of Biotechnology, Kalinga Institute of Industrial Technology (KIIT), Bhubaneswar, India

Bhupendra Harjani F H Medical College, Etmadpur, UP, India

Rohan M. Jadhav Department of Chemical Engineering, AC Tech Anna University, Chennai, India

Shikha Jain Department of Chemistry, School of Basic Sciences, Manipal University Jaipur, Rajasthan, India

V. K. Jain College of Engineering and Technology, Mody University, Lakshmangarh, Rajasthan, India

Priyanka Joshi Smart Sensors Area, CSIR-Central Electronics Engineering Research Institute, Pilani, Rajasthan, India;
College of Engineering and Technology, Mody University, Lakshmangarh, Rajasthan, India

Shruti Kakkar Department of Chemistry, Faculty of Science, School of Basic Sciences, Manipal University Jaipur, Rajasthan, India

A. S. Kalekar Department of Physics, Institute of Chemical Technology, Matunga, Mumbai, India

Kamakshi Department of Physics, Banasthali Vidyapith, Vanasthali, India

Kriti Kapil Department of Chemistry, Indian Institute of Technology Gandhinagar, Gandhinagar, Gujarat, India

S. R. Khaladkar Department of Physics, Institute of Chemical Technology, Matunga, Mumbai, India

Manoj Kumar Department of Physics, Malaviya National Institute of Technology, Jaipur, Rajasthan, India

Pushpendra Kumar Department of Physics, School of Basic Sciences, Manipal University Jaipur, Rajasthan, India

Rajesh Kumar Department of Physics, Malaviya National Institute of Technology, Jaipur, Rajasthan, India

Sanjay Kumar Department of Biological Engineering, Indian Institute of Technology Gandhinagar, Gandhinagar, Gujarat, India

Nitu Kumari Department of Chemical Engineering, Sardar Vallabhbhai National Institute of Technology, Surat, Gujarat, India

Lalita Ledwani Department of Chemistry, School of Basic Sciences, Manipal University Jaipur, Rajasthan, India

Naresh Ledwani Bhagwan Mahaveer Cancer Hospital and Research Centre, Jaipur, Rajasthan, India

Cecilia Stålsby Lundborg Department of Public Health Sciences, Karolinska Institute, Stockholm, Sweden

R. Mankamna Kumari Department of Biotechnology, School of Life Sciences, Central University of Rajasthan, Ajmer, Rajasthan, India

O. C. Maurya Department of Physics, Institute of Chemical Technology, Matunga, Mumbai, India

Amrita Mishra School of Biotechnology, Kalinga Institute of Industrial Technology (KIIT), Bhubaneswar, India

Ananyo Jyoti Misra School of Chemical Technology, Kalinga Institute of Industrial Technology (KIIT), Bhubaneswar, India;
School of Biotechnology, Kalinga Institute of Industrial Technology (KIIT), Bhubaneswar, India

Anoop Kumar Mukhopadhyay Advanced Mechanical and Materials Characterization Division (AMMCD), CSIR-Central Glass and Ceramic Research Institute, Kolkata, India;
Department of Physics, Faculty of Science, School of Basic Sciences, Manipal University Jaipur, Jaipur, Rajasthan, India

Arvind Kumar Mungray Department of Chemical Engineering, Sardar Vallabhabhai National Institute of Technology, Surat, India

Saikumar Nair Department of Chemical Engineering, Sardar Vallabhbhai National Institute of Technology, Surat, Gujarat, India

P. Narsimha Department of Chemical Engineering, National Institute of Technology, Warangal, Telangana, India

Surendra Nimesh Department of Biotechnology, School of Life Sciences, Central University of Rajasthan, Ajmer, Rajasthan, India

Gaurav Pandey Institute of Research and Development, Gujarat Forensic Sciences University, Gandhinagar, Gujarat, India

Sanjaykumar R. Patel Department of Chemical Engineering, Sardar Vallabhbhai National Institute of Technology, Surat, Gujarat, India

J. Prakash Department of Mathematics, Avvaiyar Government College for Women, Karaikal, Puducherry-U.T., India

K. Raghu Raja Pandiyan Department of Chemical Engineering, National Institute of Technology, Warangal, Telangana, India

P. Rajesh Kumar Department of Chemical Engineering, National Institute of Technology, Tadepalligudem, Andhra Pradesh, India

Suryanarayanarao Ramakumar Department of Physics, Indian Institute of Science, Bengaluru, India

Tanveer Rasool Department of Chemical Engineering, National Institute of Technology Srinagar, Srinagar, Jammu & Kashmir, India

Deepak Rawtani Institute of Research and Development, Gujarat Forensic Sciences University, Gandhinagar, Gujarat, India

M. Gnaneswara Reddy Department of Mathematics, Acharya Nagarjuna University Campus, Ongole, India

Rellegadla Sandeep Energy and Environment Research Laboratory, Department of Microbiology, School of Life Sciences, Central University of Rajasthan, Ajmer, India

Jitendra S. Sangwai Gas Hydrate and Flow Assurance Laboratory, Petroleum Engineering Program, Department of Ocean Engineering, Indian Institute of Technology Madras, Chennai, India

G. R. Seetharaman Gas Hydrate and Flow Assurance Laboratory, Petroleum Engineering Program, Department of Ocean Engineering, Indian Institute of Technology Madras, Chennai, India

Preeti Sharma Department of Biotechnology, Veer Narmad South Gujarat University, Surat, India

Rahul Shrivastava Department of Chemistry, School of Basic Sciences, Manipal University Jaipur, Rajasthan, India

Jitendra Singh Smart Sensors Area, CSIR-Central Electronics Engineering Research Institute, Pilani, Rajasthan, India

Mumal Singh Department of Chemistry, School of Basic Sciences, Manipal University Jaipur, Rajasthan, India

Aditi Singhal Department of Biological Engineering, Indian Institute of Technology Gandhinagar, Gandhinagar, Gujarat, India;
Manipal University Jaipur, Jaipur, India

Shirish H. Sonawane Department of Chemical Engineering, National Institute of Technology, Warangal, Telangana, India

Prashant L. Suryawanshi R & D Center, Hindustan Petroleum Corporation Ltd., Bangalore, India

Suman Swami Department of Chemistry, Manipal University Jaipur, Jaipur, Rajasthan, India

Ashok J. Tamhankar School of Biotechnology, Kalinga Institute of Industrial Technology (KIIT), Bhubaneswar, India;
Department of Public Health Sciences, Karolinska Institute, Stockholm, Sweden

Maithri Tharmavaram Institute of Research and Development, Gujarat Forensic Sciences University, Gandhinagar, Gujarat, India

Abhishek Kumar Tiwari Motilal Nehru National Institute of Technology Allahabad, Prayagraj, Uttar Pradesh, India

D. Tripathi Department of Mathematics, National Institute of Technology, Uttarakhand, India

Suraj K. Tripathy School of Chemical Technology, Kalinga Institute of Industrial Technology (KIIT), Bhubaneswar, India;
School of Biotechnology, Kalinga Institute of Industrial Technology (KIIT), Bhubaneswar, India

Mona Vajpayee Department of Chemistry, School of Basic Sciences, Manipal University Jaipur, Rajasthan, India

Ramsagar Vooradi Department of Chemical Engineering, National Institute of Technology, Warangal, Telangana, India

Synthesis and Characterization of Nanofluids: Thermal Conductivity, Electrical Conductivity and Particle Size Distribution

Divya P. Barai, Kalyani K. Chichghare, Shivani S. Chawhan and Bharat A. Bhanvase

Abstract A new type of fluid, called nanofluid, has found numerous applications in engineering sector due to its outstanding properties. These are known as suspensions of nano-sized particles in fluids called basefluids. The suspension of these nanoparticles in the basefluid shows significant influence on its physical properties. In view of this, in the present book chapter, the properties of the nanofluid like its thermal conductivity, electrical conductivity and so on have been discussed and the notable studies carried out in the past have been summarized. Several factors that are responsible for the alteration of the properties of nanofluids at varying degrees are identified and discussed in this chapter. Further, these properties contribute to the distinctive applications of nanofluids in various engineering fields, which are reviewed and discussed in this chapter.

Keywords Nanofluids · Thermal conductivity · Electrical conductivity · Particle size distribution (PSD) · Basefluid

1 Introduction

Owing to the ever-increasing need for heat management at micro level, such as computer chips, and macro-level, such as car engines, cooling and heat transfer has gained a lot of importance in domestic as well as industrial systems and technologies. It is a general truth about solids that they possess higher thermal conductivity than liquids. The great scientist James Clerk Maxwell (1881) developed the fact that solids dispersed in liquids enhance the thermal conductivity of those liquids, and that is when studies for enhancement of thermal properties of conventional heat transfer liquids gained an impetus. Millimetre or micrometre-sized particles were used to conduct these studies. But, the major issue coming in the way of using these particles was that they settle very rapidly in liquids and may also cause abrasion, clogging and additional pressure drop (Das et al. 2006). These issues limit the use of conventional

D. P. Barai · K. K. Chichghare · S. S. Chawhan · B. A. Bhanvase (✉)
Chemical Engineering Department, Laxminarayan Institute of Technology, Rashtrasant Tukadoji Maharaj Nagpur University, Nagpur, MS, India
e-mail: ba.bhanvase@nagpuruniversity.nic.in

L. Ledwani and J. S. Sangwai (eds.), *Nanotechnology for Energy and Environmental Engineering*, Green Energy and Technology,
https://doi.org/10.1007/978-3-030-33774-2_1

solid–liquid suspensions as practical heat transfer fluids. The rise of nanotechnology has created the possibility of producing nanoparticles which are characterized by the particle sizes below 100 nm. Nanofluids, a new group of heat transfer fluids, acquired by dispersing and suspending nanoparticles with typical dimensions of the order of 1–100 nm were found by Choi (1995). The main objective behind using nanofluids is to attain higher thermal properties and uniform and stable dispersions of nanoparticles. In order to achieve this objective, it becomes essential to understand how nanoparticles intensify energy transport in liquids. Since Choi (1995) formulated this new concept of nanofluids, many scientists expeditiously developed nanofluids and found scientific facts not only on enhanced thermal properties of nanofluids, but signifying new mechanisms that play major role in enhancing the thermal properties of nanofluids and expanding new mathematical models for the nanofluids. The type of nanoparticle, its size, shape and distribution are dominant properties that cannot be effortlessly measured but affect the thermal transport properties of the nanofluids. Other important factors include type of basefluids used, the method for the preparation of nanofluid, usage of surfactants and dispersing additives, pH, temperature, viscosity and other physical properties. Two nanofluid samples with different type of nanoparticles and amount of surfactants and/or pH adjusters while keeping all other parameters constant may result in different thermo-physical properties.

Many researchers have studied nanofluids containing Al_2O_3 nanoparticles (Heyhat et al. 2013; Sokhansefat et al. 2014; Usri et al. 2015), Cu nanoparticles (Eastman et al. 2001; Yu et al. 2010) or carbon nanotubes (CNTs) (Jiang et al. 2015; Leong et al. 2016) and found remarkable increase in thermal conductivities. Hence, nanofluids have gained attention in various heat transfer applications. There are various possible applications of nanofluids, which include transportation (engine cooling/vehicle thermal management) (Azimi and Ommi 2013; Sidik et al. 2017), electronics cooling (Khaleduzzaman et al. 2015; Roberts and Walker 2010), nuclear systems cooling (Mahmud et al. 2016), heat exchangers (Bozorgan and Shafahi 2017; Li et al. 2018), fuel cell (Islam et al. 2015; Zakaria et al. 2016), solar water heating (Kasaeian et al. 2015), chillers (Liu et al. 2011), lubricants (Mao et al. 2014), thermal storage (Harikrishnana et al. 2013); (Chieruzzi et al. 2013) and many others.

As the thermal transport properties have been largely studied, researchers then turned towards finding and analysing the electrical conducting properties of the nanofluids. Maxwell's model (Maxwell 1881) is found to be the pioneer in determining the electrical conductivity of the nanofluids theoretically based on the physical properties of the nano-sized particles and basefluid. These properties of the nanofluids are affected by many factors, one of which is the particle size distribution of the nano-sized particles in the nanofluids. Particle size distribution gives the amount of particles according to their sizes present in the nanofluid. It is basically the degree to which the sizes of the particles vary throughout the nanofluid. In a nanofluid, the dispersed nanoparticles are never of equal size and so its size distribution characterizes the nanofluid better than any exact value of size of the nanoparticles. This property is affected by many factors and affects other properties which are also discussed in this chapter. Several studies on nanofluids depicting the values of thermal conductivity, electrical conductivity as well as particle size are given in Table 1.

Table 1 A summary of studies on nanofluids done by various researchers

Nanofluid	Synthesis method of nanofluid	Concentration of nanofluid (vol.%)	Particle size (nm)	Thermal conductivity (W/mK)	Electrical conductivity (μS/cm)	Temperature (°C)	pH	Ref.
Aluminium oxide/water	Two-step	0.01	20	–	2.9	25	5.5	Timofeeva et al. (2007)
Aluminium oxide/water	Two-step	8.47	–	0.6812	314	21	–	Wong and Kurma (2008)
Aluminium oxide/water	Two-step	0.03	–	–	351	45	–	Ganguly et al. (2009)
Magnesium oxide/ethylene glycol	Two-step	5.0	20	0.354	–	30	–	Xie et al. (2010)
f-TEG (functionalized-thermally exfoliated graphene oxide)/water	Two-step	0.056 and 0.03	–	0.684 for 0.056 vol.%	60 for 0.03 vol.%	25	–	Baby and Ramaprabhu (2010)
f-TEG (functionalized-thermally exfoliated graphene oxide)/ethylene glycol	Two-step	0.05 and 0.03	–	0.258 for 0.05 vol.%	3.2 for 0.03 vol.%	25	–	Baby and Ramaprabhu (2010)
Titanium dioxide/water	Two-step	0.5–3	–	–	79.4–275	24–45	–	Sikadar et al. (2011)
Aluminium oxide/water	Two-step	1–4	–	–	4210 at 4% and 70C	25–70	–	Minea and Luciu (2012)

(continued)

Table 1 (continued)

Nanofluid	Synthesis method of nanofluid	Concentration of nanofluid (vol.%)	Particle size (nm)	Thermal conductivity (W/mK)	Electrical conductivity (μS/cm)	Temperature (°C)	pH	Ref.
Graphene nanosheets-ethylene glycol/distilled water	Two-step	0.041–0.395	–	0.30–0.347	1–87.2	10–70	–	Kole and Dey (2013)
Magnesium oxide/ethylene glycol	Two-step	5.0	60	0.328	–	25	–	Esfe et al. (2014)
Magnesium oxide/ethylene glycol	Two-step	0.1–3	20	–	3.01–14.05	25	9.66–10.84	Adio et al. (2015a)
Aluminium oxide/glycerol	Two-step	2	20–30	–	0.15	30	4.21	Adio et al. (2015b)
Graphene oxide/deionized water/ethylene glycol	Two-step	0.01–0.1	–	0.426–0.484	22.21718–238.3417	25–45	–	Ijam et al. (2015)
Palladium/water	Two-step	0–1	5.63	–	5.49–114.54	25–50	–	Goharshadi et al. (2015)
Magnetite/water	Two-step	0.5	–	–	19	60	–	Bagheli et al. (2015)
Aluminium oxide/water	Two-step	0.2	–	–	2370	25.9	–	Zawrah et al. (2016)
Aluminium nitride/ethylene glycol	Two-step	0.018–0.079	–	0.2496–0.2969	131.55–528.81	25.15	–	Zyla and Fal (2016)
Aluminium oxide/bio-glycol	Two-step	0-0.5	13	–	53–154	30–80	–	Khdher et al. (2016)

(continued)

Table 1 (continued)

Nanofluid	Synthesis method of nanofluid	Concentration of nanofluid (vol.%)	Particle size (nm)	Thermal conductivity (W/mK)	Electrical conductivity (μS/cm)	Temperature (°C)	pH	Ref.
Silicon dioxide/ethylene glycol	Two-step	0-0.026	–	0.2445–0.2526	0.85–1.33	25.15	–	Zyla and Fal (2017)
Maghemite/water	Two-step	2.50	–	–	14650	60	–	Nurdin and Satriananda (2017)
Silicon oxide /ethylene glycol/water mixture	Two-step	0.3	30	0.587–0.249	49.2–4.44	25–45	–	Guo et al. (2018)
Copper oxide/water	Two-step	0.004–0.028	12	–	–	25.15–75.15	–	Coelho et al. (2019)

2 Synthesis Techniques of Nanofluids

Preparation of nanofluid is the technique of evenly and uniformly dispersing the nanoparticles in the basefluid. This may seem to be simple and not so important, but this process largely affects several properties of the nanofluid. Also, the lab-scale preparation of nanofluids may possibly determine the complexity of preparing and using nanofluids in large-scale applications. There are two methods of nanofluid preparation: the two-step and one-step methods.

2.1 Two-Step Method

Two-step method is the most common and has been extensively used for preparing nanofluids. As the name indicates, there are two steps that are carried out in this method during preparation of nanofluids. In the first step, dry powder is produced as nanoparticles, nanofibres or nanotubes. Then in the second processing step, nanomaterial is directly distributed in the basefluid with the use of dispersing devices like magnetic stirrer (Duangthongsuk and Wongwises 2009; Kavitha et al. 2012; Liu et al. 2005), homogenizer (Liu et al. 2005; Wen and Ding 2005) or by using ultrasound devices like probe or bath (Duangthongsuk and Wongwises 2009; Hwang et al. 2007; Manimaran et al. 2014). Mostly, ultrasound device or a higher shear homogenizer is commonly used to stir nanopowders with the basefluids. As this method permits a gap between the synthesis and dispersion steps, many researchers have used readily-available nano-sized particles for the preparation of nanofluids in various basefluids (Xuan and Li 2000). It is a common observation that the two-step process is highly used for preparing metal oxide nanoparticles-based nanofluids than the metallic nanoparticles-based nanofluids (Eastman et al. 2001). In the two-step method, drying the nanoparticles, their transportation and storage are further process steps that cannot be neglected. The main advantage of this method is that it is easily scalable. However, the major disadvantage is the formation of agglomerates because of the attraction between the particles due to their high surface energy (Mohammed et al. 2011). Two-step method is favourable to almost every kind of fluids (Wang and Mujumdar 2007). The illustration of two-step method is given in Fig. 1.

2.2 One-Step Method

In one-step method, the process takes place in single step in accordance to its name. This process is composed of both, the production of the nanoparticles and the synthesis of nanofluids. Numerous single-step processes have been developed for the

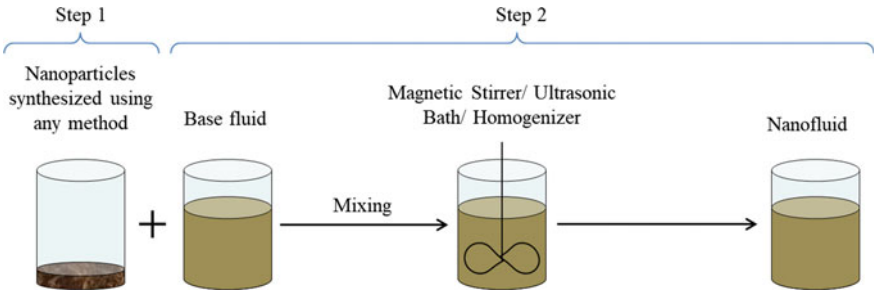

Fig. 1 Two-step method for nanofluid synthesis

production of nanofluid (Akoh et al. 1978; Eastman et al. 1997). Direct vapourization–condensation process that provided remarkable control over the size of nanoparticles produced a stable nanofluid without the addition of additive (Choi et al. 2001). Preparation of nanofluid by a novel process was introduced by Lo et al. (2005) using submerged arc nanoparticle synthesis system (SANSS) technique where a pure metal rod is heated by a submerged arc. SANSS is a constructive technique for avoiding nanoparticles agglomeration and also benefits in producing even dispersion of nanoparticles in deionized water.

In the one-step method, the costs for drying and dispersion of the nanoparticles in the basefluid can be avoided. The main disadvantages of this method are that it is not easily scalable because of its high cost of manufacture and that it is only applicable for the basefluids having low vapour pressure (Prakash et al. 2016; Wang and Mujumdar 2007). Zhu and Yin (2004) worked on a single-step chemical process for the synthesis of Cu nanofluids by reducing $CuSO_4 \cdot 5H_2O$ using $NaH_2PO_2 \cdot H_2O$ in ethylene glycol using microwave irradiation. This method is more efficiently proved to prepare mineral oil-based silver nanofluids. A vacuum-based submerged arc nanoparticle synthesis was studied by Lo et al. (2005) for the preparation of CuO, Cu_2O and Cu-based nanofluids using different dielectric liquids. The nanofluids were prepared by using the vapourized metal which is condensed and then dispersed in deionized water. The illustration for one-step method is given in Fig. 2.

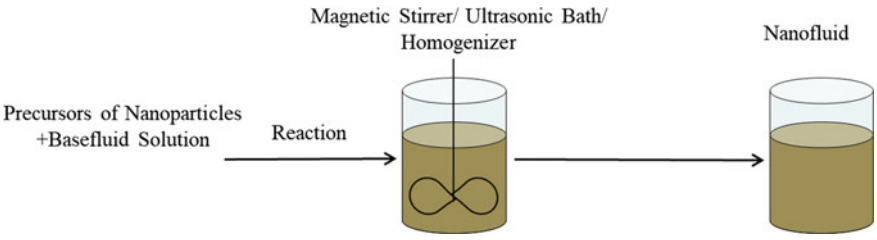

Fig. 2 One-step method for nanofluid synthesis

3 Thermal Conductivity of Nanofluids

Thermal conductivity is the ability of the nanofluids to transfer heat through them. There have been several studies to identify and study the thermal conductivity of fluids by incorporating various kinds of nanoparticles in them and to find out the enhancement in the thermal properties and the mechanism behind it.

3.1 Reason Behind Improved Thermal Performance of Nanofluids

Nanofluids as discussed earlier are suspensions of nanoparticles in a particular basefluid. We already know that the solids, due to the collision of their vibrating molecules, propagating phonons and diffused-free electrons transfer heat through them efficiently. This does not seem to happen in liquids and gases, because of their loosely packed molecules. On the other hand, the molecules of a solid are tightly packed, which makes it a good conductor of thermal energy. These solids, if incorporated into liquids affect the thermal properties as explained by Maxwell (1881). The solids act as "heat boats" that carry the thermal energy through the liquid and also as "stirrers" that generate convection currents, thus providing chances of collisions of molecules and augmentation of the thermal conductivity (Yang and Han 2006). Nanofluid can be called as a pseudo-homogenous suspension of solids into specific liquids, because of the very small size of the solid particles that are distributed throughout the base liquid called as the basefluid. They impart homogeneity to the mixture due to their size, which is between 1 and 100 nm.

There are many reasons which elevate the thermal properties of the basefluid when nanoparticles are contained in it. One of the reasons is the higher surface area of the nano-sized particles that is available to gain and distribute heat throughout their body. Major reasons include the Brownian motion of the nanoparticles in the fluid and the interfacial layer around the nanoparticles (Jang and Choi 2004). The Brownian motion is the movement that naturally occurs due to the movement of molecules of fluid around the particle. It gives rise to micro-mixing of the nanofluid, thus producing localized convection throughout the fluid. The thermal conductivity of the nanofluid is looked upon as a combined effect of the static and dynamic mechanisms which involve the thermal properties and interfacial layer phenomena and the Brownian motion phenomena, respectively (Sohel Murshed and Nieto de Castro 2011).

Another phenomenon that contributes to the enhanced thermal properties is the interfacial layer of liquid around the particle at the solid–liquid interface. The layer of liquid formed is an ordered molecule layer whose thickness plays a significant role in transportation of heat from solid surface to the bulk liquid (Yu and Choi 2003). It has been known that this interfacial layer has higher thermal conductivity than the bulk basefluid (Kotia et al. 2017). It has been found out by Yu and Choi (2003)

that the thermal conductivity of the interfacial layer is ten times more than the bulk fluid. A correlation as given in Eq. (1) has been proposed by Leong et al. (2006) for determining the thermal conductivity of the interfacial layer where k_l is the interfacial layer thermal conductivity, C is a constant specific for a type of nanoparticle, t is the interfacial layer thickness, r_p is the radius of the nano-sized particle and k_f is the thermal conductivity of the basefluid.

$$k_l = C\frac{t}{r_p}k_f \tag{1}$$

The authors observed that the thermal conductivity of the layer is 2–3 times greater than that of the basefluid.

3.2 Measurement of Thermal Conductivity of the Nanofluids

Owing to the fact that there can be a lot of improvement in the thermal transport properties of the fluids, there has been a lot of increase in the investigation of thermal conductivity of the nanofluids. For this purpose, many techniques have been used by researchers which include the steady-state coaxial cylinder method (Glory et al. 2008), transient hot wire (THW) method (Garg et al. 2008; Lee et al. 2008; Rusconi et al. 2007), IR thermometry method (Gharagozloo and Goodson 2008) and so on. The newest technique for determining the thermal conductivity of nanofluids that has been used by numerous researchers lately is the instrument known as KD2 Pro thermal property analyser, developed by Decagon Devices Inc., USA. A simple arrangement of the KD2 Pro thermal conductivity analyser for thermal conductivity measurement of nanofluids is given in Fig. 3. This instrument follows the working principle of transient hot wire method. It comprises a KS-1 needle which is 60 mm long and has a diameter of 1.3 mm. This needle is immersed in the nanofluid which is maintained at a certain temperature. After 2 min, the instrument directly displays the value of thermal conductivity as measured by it. Owing to such simple and fast

Fig. 3 Arrangement of KD2 Pro thermal conductivity analyser for thermal conductivity measurement of nanofluids (Zakaria et al. 2015)

operation of the instrument, it gained a lot of attention and utilization by researchers working in the field of nanofluid (Esfe et al. 2015a; Leong et al. 2018; Zadkhast et al. 2017). The transient hot wire method involves the use of dynamic technique that measures the rise in temperature in a specific distance from a linear source of heat, that is, a hot wire immersed in the test material. Thus, if the heat source has constant heat output along the test material, the thermal conductivity is known directly from the effect of change in temperature over a period of time. An instrument that uses this method consists of a heating wire along with a temperature sensor together making up the probe that electrically insulates the probe from the test material.

3.3 Factors Affecting Thermal Conductivity of Nanofluids

Thermal conductivity of the nanofluid, being a characteristic of thermo-physical property of its components, is bound to vary with a lot of conditions. It includes nature of the nanoparticle and the basefluid, composition of the nanoparticle, concentration of the nanofluid, that is, its volume fraction in the nanofluid, temperature and pH. Following are the various factors explained along with some findings in the literature.

3.3.1 Nature of Nanoparticle and Basefluid

The nanofluid comprises two basic components, that is, the nanoparticle and basefluid, the properties of which shall definitely affect the properties of the prepared nanofluid. In fact, the nature of both these components has a big impact on the behaviour of the nanofluid. First of all, we know that the thermal conductivities of different nanomaterials vary over a wide range, right from polymeric materials having very low thermal conductivities to some carbon allotropes having very high thermal conductivities. Few of the thermal conductivity data found for different nanoparticles dispersed in water have been plotted in Fig. 4 (Ahammed et al. 2016; Minea and Manca 2017; Sundar et al. 2013).

Nanoparticles of different materials can be of different sizes and shapes. Chopkar et al. (2008) found that the relative thermal conductivity of the nanofluid increases nonlinearly with decrease in diameter of the nanoparticles dispersed in it. Similar outcome was obtained by Esfe et al. (2015a) for metal-based nanofluid and by Teng et al. (2010) for metal oxide-based nanofluid. For silica-ethanol nanofluid, it was found by Darvanjooghi and Esfahany (2016) that there are –OH groups on the surface of silica nanoparticles and that the hydrophilicity of the surface of nanoparticles and restricted movement of molecules of basefluid at the interface increases the intramolecular force field, thus enhancing the heat conductance through the interface. Increase in the nanoparticle size increases the amount of –OH groups on its surface and ultimately increasing the thermal conductivity of the nanofluid. At nanofluid concentration of 0.15 vol.%, the value of relative thermal conductivity was found to

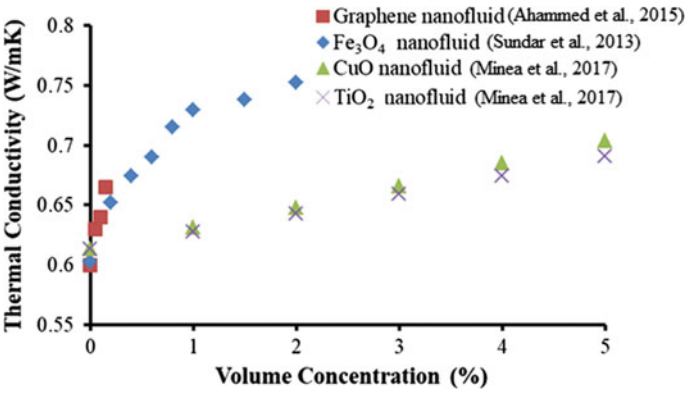

Fig. 4 Influence of type of nanoparticle on thermal conductivity of water-based nanofluids

be 1.02 and 1.1 for nanoparticle size of 20 and 63 nm, respectively, at temperature of 25 °C.

Along with size, it is well established that the shape of nanoparticles affects its thermal properties (Alawi et al. 2018). Ghosh et al. (2012) investigated the influence of particle shape on the heat transfer characteristics of its nanofluid. It has been reported that the heat transfer of a nanoparticle of high aspect ratio is greater than nanoparticle of low aspect ratio. They studied a cylindrical-shaped Cu nanoparticle with aspect ratio (length to diameter) of 4 using molecular dynamics simulation and found out that a spherical-shaped Cu nanoparticle of same volume transfers heat lesser than that transferred by the cylindrical-shaped Cu nanoparticle. This is reported to be happening due to the high heat transfer caused by the increased contact area with increasing aspect ratio. Jeong et al. (2013) investigated the influence of spherical-shaped and rectangular-shaped ZnO nanoparticles based on nanofluid and found 16 and 19.8% thermal conductivity improvement, respectively, for 5 vol.% nanofluid concentration.

Zhu et al. (2018) found that the CuO nanowires have better thermal performance than the CuO nanospheres, which is due to the efficient thermal transport happening in 1-D nanostructure of the nanowires than the 0-D nanostructure of the nanospheres. They have found a 6.98% and a surprisingly high enhancement in thermal conductivity of 60.78% for CuO nanospheres and CuO nanowires, respectively. This is reported to be occurring because of the high aspect ratio and transport of heat in one controllable direction.

The basefluid used for the synthesis of nanofluid makes up most of the nanofluid quantity and governs the flow properties and thermal transport properties of the nanofluid. Even though nanoparticles alter the flow and thermal properties of the nanofluid, these properties are bound by the limits of the basefluid. For example, the thermal conductivity of a nanofluid made using a basefluid having inherently high thermal conductivity will be higher than the nanofluid made using a basefluid having inherently low thermal conductivity with the same nanoparticles. Also, the

viscosity of the basefluid will determine the rheology of the nanofluid. Even though nanoparticles tend to alter the rheological behaviour of the nanofluid, the inherent flow property of the basefluid will rule the major part of the nanofluids' rheology. The effect of basefluid on the thermal properties of the nanofluid is well studied by Syam Sundar et al. (2017). They have prepared graphene oxide/Co_3O_4 nanocomposite-based nanofluid and used water, ethylene glycol and mixtures of both in the ratios of EG/water as 20:80, 40:60 and 60:40 as basefluids. Although there is enhancement in thermal conductivity of all the nanofluids, the thermal conductivity of water being higher than that of ethylene glycol, the thermal conductivity of the nanofluid also shows the same trend. Also, in the mixtures of ethylene glycol and water, the thermal conductivity is found to be 0.619, 0.496 and 0.402 for EG/water mixture basefluid having ratios as 20:80, 40:60 and 60:40, respectively. The thermal conductivity of the nanofluid is bound by the thermal conductivity of the mixture of the two fluids. This shows how the basefluid composition alters the thermal conductivity of the nanofluid to a larger extent.

Agglomeration of nanoparticles has been a common observation as well as a serious problem in dealing with nanofluids and must be avoided so as to obtain a stable nanofluid. Nanoparticles do agglomerate and form aggregates that try to settle down, thus degrading the thermal properties of a nanofluid. The method of dispersion does affect the agglomerating property of the nanofluid but there is a limit after which the nanoparticles do not stay uniformly dispersed in the nanofluid. Use of surfactants or some dispersing agents is the most common method which is used to decrease agglomeration of nanoparticles in the fluids (Xuan et al. 2013). They are amphiphilic compounds having a tail and polar head group which are hydrophobic and hydrophilic, respectively (Schramm et al. 2003). This hydrophobic tail gets attached to the nanoparticles which are hydrophobic in nature. And the hydrophilic group interacts with the surrounding fluid. Thus, the wettability of the nanoparticle is improved by the surfactant. This reduces the surface tension and assists fluid continuity. On the other hand, it has also been found out by Xuan et al. (2013) that the use of surfactants in the nanofluids affects the thermal properties of the nanofluid and deteriorates heat transfer. They studied the effect of sodium dodecyl benzoic sulphate (SDBS) as surfactant on nanofluid and found out that the heat transfer coefficient offered by 0.34 vol.% Cu nanofluid decreases from 21,000 to 20,000 W/m^2K as the amount of SDBS increases from 0.05 to 0.1 wt% in the nanofluid. Although this is the case for using surfactants, proper selection of surfactant must be done in order to control its effect over the crucial properties of a nanofluid. Xia et al. (2014) have studied the effect of two different surfactants on Al_2O_3/water nanofluids. They found out that polyvinylpyrrolidone (PVP), being a non-ionic surfactant has positive effects on the thermal conductivity of the nanofluid than sodium dodecyl sulphate (SDS) which is an anionic surfactant.

3.3.2 Composition of Nanoparticle

It has been already known that the nanoparticle nature influences the thermal conductivity of the nanofluid. Nanoparticles contained in a nanofluid may also be a composite of two or more nano-sized materials, which is known as nanocomposite. The components of a nanocomposite may have different properties and thus may impart their individual properties to the whole nanoparticle. So, there are chances that the amount of these components will determine the properties variation of a nanocomposite. Trinh et al. (2016) investigated the thermal conductivity of Cu/graphene nanocomposite-based nanofluid by changing the nanocomposite ratio using ethylene glycol as basefluid. They synthesized nanofluids containing Cu/graphene nanocomposite having graphene/Cu ratio of 7:1, 5:1, 3:1 and 1:1 by weight and found out that the thermal conductivity of Cu/graphene-based nanofluid is higher than that compared to graphene-based nanofluid. The thermal conductivity of Cu/graphene-based nanofluids containing nanoparticles of graphene/Cu ratio as 7:1 and 5:1 is 0.48 and 0.5 W/mK, respectively, at 60 °C. This is because of the combined effect of graphene sheets and Cu particles decorated over them, both having higher thermal conductivity. The decoration of graphene sheet with Cu particles decreases stacking of graphene sheets, thus elevating thermal properties of the nanofluid. Further, the nanofluid containing Cu/graphene nanoparticles having graphene/Cu ratio of 3:1 and 1:1 shows a decreasing trend of thermal conductivity values, that is, 0.42 and 0.415 W/mK, respectively. This is reported to be happening due to the formation of clusters of Cu particles as their amount is greater than that required to get attached to the functional groups over the graphene sheet. This is how the composition of nanoparticles plays an important role in altering the thermal conductivity of the nanofluid.

3.3.3 Volume Fraction of Nanoparticles in the Nanofluid

The increase in the thermal conductivity of a basefluid due to addition of nanoparticles is well known. But increasing the amount of nanoparticles in the basefluid also affects the thermal conductivity, as shown by many researchers (Alawi et al. 2018; Gupta et al. 2011; Khedkar et al. 2012; Kumar et al. 2018; Tijani and Sudirman 2018). The values of thermal conductivity for different ranges of volume fractions of nanoparticles in different nanofluids recorded in the past can be seen in Table 1. The nanoparticles acting as heat boats carry the heat through the nanofluid. Increasing the number of these heat boats ultimately leads to the increase in transport of the heat energy, thus augmenting the thermal conductivity of the nanofluid. This is due to the intensification of Brownian motion as the number of particles is high. Thermal conductivity of the nanofluid is reported to be having linear relationship with the concentration of the nanoparticles in it (Ali et al. 2010). Figure 5 depicts a trend of thermal conductivity of Al_2O_3/ethylene glycol nanofluids as a function of volume fraction at various temperatures as studied by Esfe et al. (2015a).

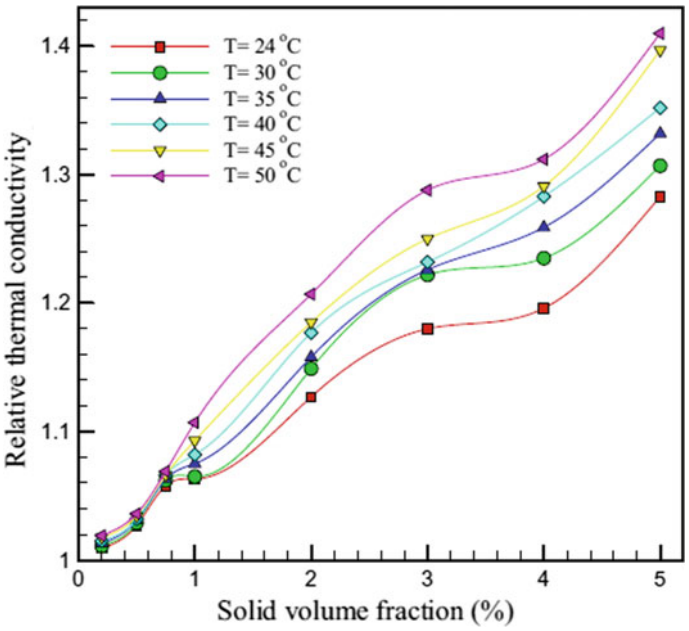

Fig. 5 Effect of volume fraction of Al_2O_3 nanoparticles in Al_2O_3–ethylene glycol nanofluids on relative thermal conductivity of the nanofluids (Esfe et al. 2015a)

3.3.4 Temperature

Temperature is found to be greatly influencing the thermal conductivity of a nanofluid which is studied by several researchers. Mintsa et al. (2009) investigated the thermal conductivity of Al_2O_3 and CuO-based nanofluids as a function of temperature and reported an increase in thermal conductivity with rise in temperature for different size of nanoparticles and concentrations of nanofluids. Increase in temperature increases the nanoparticles' surface energy leading to reduced agglomeration. Graphene, having attained most of the attention of the researchers, and its nanofluids have also found to show an increase in thermal conductivity with temperature, which is reported by Ahammed et al. (2016) at various concentrations of the nanofluid as shown in Fig. 6. It was clear that the factors like vibration of phonons and free electrons and molecular collision and molecular diffusion jointly affect the thermal conductivity of the graphene-based nanofluids.

One more reason behind the enhancement in the thermal conductivity with temperature is the increase in Brownian motion of the nanoparticles. Two factors responsible for this are the reduction of agglomeration of nanoparticles due to high surface energy at high temperatures and the reduction in viscosity of the basefluid which again facilitates swift Brownian motion of the nanoparticles (Yu-Hua et al. 2008).

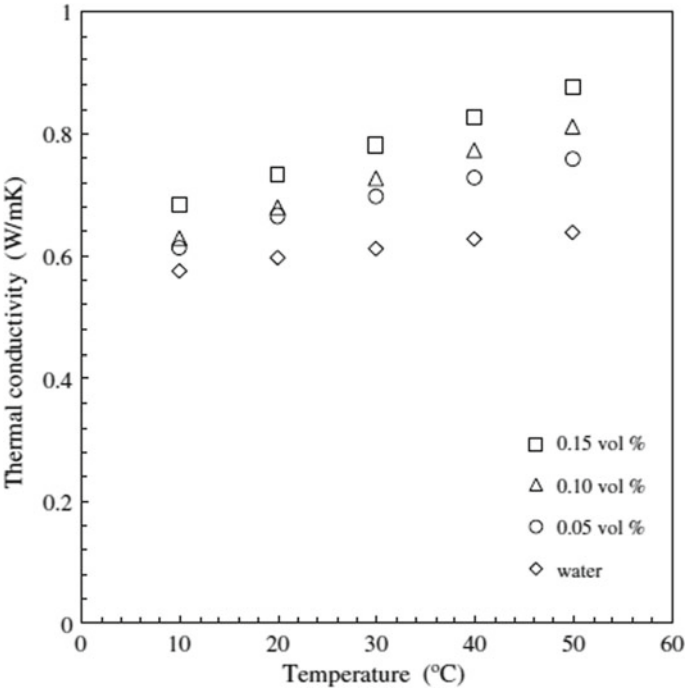

Fig. 6 Effect of temperature on thermal conductivity of graphene–water nanofluids (Ahammed et al. 2016)

It was also found that the solvent molecules get adhered and form layers of ordered arrangement of molecules to the hydrophilic colloidal particles, that is, nanoparticles added to it (Lee 2008). This layer possesses higher thermal conductivity and aids in increasing the heat transfer induced due to the nanoparticles (Keblinski et al. 2002). It is also well established by Suganthi et al. (2013) for ZnO-propylene glycol nanofluids that the thickness of this layer is high at lower temperatures where Brownian motion fails to be occurring due to higher viscosities of the basefluid. Thus, it was found that at a temperature of 10 °C, the liquid layer enhances the thermal conductivity of the nanofluid and attains a maximum, which further decreases as the temperature increases to 30 °C. This unusual but true mechanism of decrease in thermal conductivity with increase in temperature is also found out for ZnO-ethylene glycol nanofluids (Suganthi et al. 2014), as shown in Fig. 7.

3.3.5 pH

Nanofluid is a suspension of nano-sized material in some basefluid. Its uniform dispersion in a typical basefluid shall definitely depend upon the charges on its surface. The surface charges will affect the degree of agglomeration, which ultimately

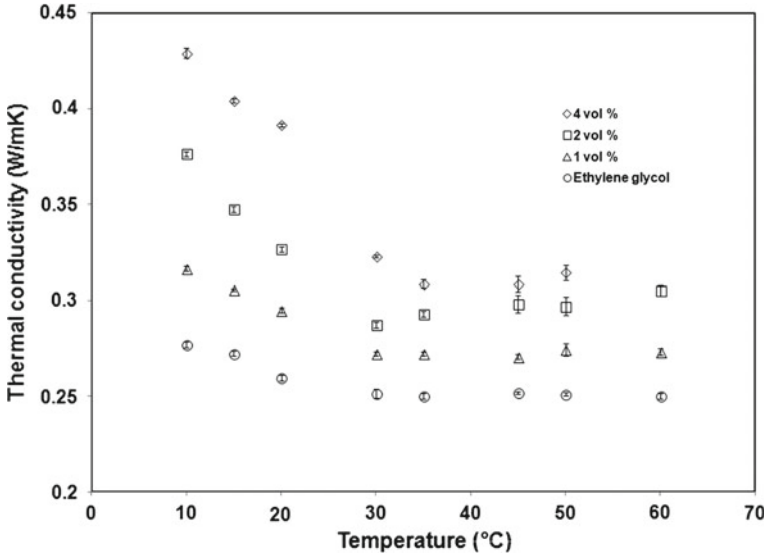

Fig. 7 Effect of temperature on thermal conductivity of ZnO–ethylene glycol nanofluids (Suganthi et al. 2014)

influences the thermal properties of the nanofluid. pH of a nanofluid affects these surface charges and this is well defined by Wang and Zhu (2009) in their investigation of thermal conductivity of Al_2O_3 and Cu-based nanofluids, which is shown in Fig. 8. An increase in pH alters the charges on the surface of nanoparticles which raises the electrostatic forces of repulsion between two nanoparticles. This leads to reduction in agglomerative tendency of the nanoparticles in the nanofluid. Thus, the pH is found

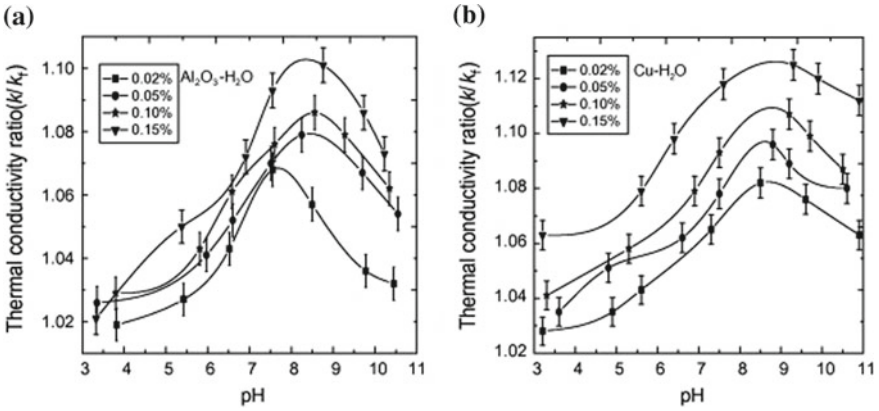

Fig. 8 Effect of pH of Al_2O_3 and Cu-based nanofluids on their thermal conductivity (Wang and Zhu 2009)

to be in direct relation with the electrical properties of the nanofluid, which will also be discussed later in this chapter.

3.4 Models for Thermal Conductivity Prediction

Thermal conductivity has been of great interest in the convective heat transfer study of nanofluids on which theoretical and experimental studies have been done. Mechanism of heat conduction has been proposed, which is found to be dependent on the Brownian motion of nanoparticles, interfacial liquid layer of nanofluid (effect of nanolayer), nanoparticle clustering and nature of heat transport of the nanoparticles in the nanofluid. Many researchers have strived to derive models that can exactly predict the thermal behaviour of the nanofluid. It was Maxwell (1881), who was the first to develop the effective thermal conductivity model as given in Eq. (2). The equation can predict the effective thermal conductivity of the solid–liquid suspensions (k_{eff}), where k_p is the thermal conductivity of the dispersed particles, k_l is the thermal conductivity of the basefluid (continuous phase of liquid) and $\emptyset$ is the volume concentration of the nanoparticles in the suspension.

$$k_{\text{eff}} = k_f \frac{k_p + 2k_l + 2\emptyset(k_p - k_l)}{k_p + 2k_l - \emptyset(k_p - k_l)} \tag{2}$$

Maxwell's model (Maxwell 1881) assumes the thermal conductivity improvement due to the presence of nanolayer at the surface of the solid in a solid–liquid suspension. It has been expected that the thermal conductivity of the nanolayer on the surface of the nanoparticle is higher than that of the basefluid. Further, this model was modified by Maxwell (1881) so as to form a modified Maxwell model as given in Eq. (3), where β is the ratio of thickness of nanolayer (h) to the radius of the nanoparticle (r) and is given as $\beta = h/r$. This equation is found to be valid for dispersion of spherical-shaped particles in the basefluid.

$$k_{\text{eff}} = \frac{k_p + 2k_l + 2\big(k_p - k_l\big)(1+\beta)^3\emptyset}{k_p + 2k_l - \big(k_p - k_l\big)(1+\beta)^3\emptyset} k_l \tag{3}$$

Further, Hamilton and Crosser (1962) introduced a model for a solid–liquid suspension as given in Eq. (4), where k_p is the thermal conductivity of particles, k_f is the thermal conductivity of basefluid, $\emptyset$ is the volume fraction of particles, n is the empirical shape factor defined as $n = \frac{3}{\psi}$ and ψ is the sphericity which is explained as the ratio of the surface area of a sphere having the same volume as that particle to the surface area of that particle. It is applicable for spherical and cylindrical particles.

$$\frac{k_{\text{eff}}}{k_f} = \frac{k_p + (n-1)k_f - (n-1)\emptyset\big(k_p - k_f\big)}{k_p + (n-1)k_f + \emptyset\big(k_p - k_f\big)} \tag{4}$$

Thermal conductivity model for randomly distributed spherical particles in a base-fluid using the thermal conductivity of the particles and basefluid has been reported by Bruggeman (1935a), as given in Eq. (5).

$$\emptyset\left(\frac{k_p - k_{eff}}{k_p + 2k_{eff}}\right) + (1-\emptyset)\left(\frac{k_f - k_{eff}}{k_f - 2k_{eff}}\right) = 0 \tag{5}$$

In this equation, the effective thermal conductivity k_{eff} is determined as given in Eq. (6).

$$k_{\text{eff}} = \frac{k_f}{4}\left[(3\emptyset - 1)\frac{k_p}{k_f} + (2 - 3\emptyset) + \frac{k_f}{4}\sqrt{\Delta}\right] \tag{6}$$

where the factor of Δ is calculated by using Eq. (7)

$$\Delta = \left[(3\emptyset - 1)^2\left(\frac{k_p}{k_f}\right) + (2 - 3\emptyset)^2 + 2\left(2 + 9\emptyset - 9\emptyset^2\right)\left(\frac{k_p}{k_f}\right)\right] \tag{7}$$

Xue (2005) reported a model as given in Eq. (8) to calculate the thermal conductivity of carbon nanotube (CNT)-based nanofluid, which is explained as follows:

$$k_{\text{eff}} = k_f\left[\frac{1 - \emptyset + 2\emptyset\frac{k_p}{k_p - k_f}\text{lnln}\frac{k_p + k_f}{2k_f}}{1 - \emptyset + 2\emptyset\frac{k_f}{k_p - k_f}\text{lnln}\frac{k_p + k_f}{2k_f}}\right] \tag{8}$$

Xuan et al. (2003) developed a model as given in Eq. (9) that considered the effect of Brownian motion and nanoparticles clustering, where R_d is the apparent radius of the nanoparticle clusters and K_B is Boltzmann constant.

$$k_{\text{eff}} = k_f\frac{k_p + 2k_f + 2\emptyset\left(k_p - k_f\right)}{k_p + 2k_f - \emptyset\left(k_p - k_f\right)} + \frac{1}{2}\rho_p C_p \emptyset\sqrt{\frac{K_B T}{3\pi\mu_f R_d}} \tag{9}$$

Later, Timofeeva et al. (2007) expressed a model, which is based on the effective medium theory as given in Eq. (10).

$$k_{\text{eff}} = k_f(1 + 3\emptyset) \tag{10}$$

Prasher et al. (2005) stated that there is occurrence of convection-induced Brownian motion called as nanoconvection and developed a model as given in Eq. (11), where $k_m = k_f(1 + 0.25Re_B Pr)$ is the matrix conductivity, $Re_B = \frac{1}{\upsilon}\sqrt{\frac{18K_B T}{\pi\rho_p d_p}}$ is the Brownian Re number, m = 2.5%± 15% is a regression constant, $\alpha_B = \frac{2R_b k_m}{d_p}$ is the particle Biot number and R_b is the interfacial thermal resistance existing between nanoparticle and liquid.

$$k_{\text{eff}} = k_f \frac{k_p(1+2\alpha_B) + 2k_m + 2\emptyset\left[k_p(1-\alpha_B) - k_m\right]}{k_p(1+2\alpha_B) + 2k_m - \emptyset\left[k_p(1-\alpha_B) - k_m\right]} \left(1 + A_{\text{eco}} Re_B^{M_{\text{eco}}} Pr_f^{0.33} \emptyset\right) \tag{11}$$

Later, Koo and Kleinstreuer suggested a model (Koo and Kleinstreuer 2004, 2005) as given in Eq. (12), which is a combined thermal conductivity model considering the Brownian motion and the volume fraction of the liquid with nanoparticles, where θ is the fraction of the liquid volume which travels with a particle.

$$k_{\text{eff}} = k_f \frac{k_p + 2k_f + 2\emptyset\left(k_p - k_f\right)}{k_p + 2k_f - \emptyset\left(k_p - k_f\right)} + 5 \times 10^4 \theta \rho_f C_{pf} \emptyset f(T, \emptyset) \sqrt{\frac{K_B T}{\rho_f d_p}} \tag{12}$$

However, the difficulty of this model is that θ and f are hard to obtain, and so they are to be expressed differently for different kinds of nanofluids. For example, for CuO nanofluid, the expression in Eq. (12) becomes the expression given in Eq. (13).

$$f(T, \emptyset) = (-6.04\emptyset + 0.4705)T + 1722.3\emptyset - 134.63) \tag{13}$$

Yu and Choi (2003) proposed a renewed Maxwell model as given in Eq. (14) considering the solid–liquid interfacial layer on nanoparticles in the nanofluid.

$$k_{\text{eff}} = k_p \frac{k_{\text{pe}} + 2k_f + 2\emptyset\left(k_{\text{pe}} - k_f\right)\beta_1^3}{k_{\text{pe}} + 2k_f - \emptyset\left(k_{\text{pe}} - k_f\right)\beta_1^3} \tag{14}$$

Feng et al. (2007) reported a model as given in Eq. (15) to enhance the Yu and Choi (2003) model by presenting an equivalent thermal conductivity of the nanoparticles. They also investigated the influence of presence of the interfacial layer between nanoparticles and liquid.

$$k_{\text{pe}} = k_p \frac{2(1-\gamma_1)\gamma_1 + \beta^3(1+2\gamma_1)\gamma_1}{-(1-\gamma_1) + \beta^3(1+2\gamma_1)} \tag{15}$$

Here, $\beta = 1 + \frac{t}{R, \text{ and } k_{\text{pe}}}$ is equal to the equivalent thermal conductivity of the nanoparticles and γ_1 is the thermal conductivity ratio of interfacial layer to particles.

Further, Pak and Choi (1998) presented a new model as given in Eq. (16) considering that the thermal conductivity enhancement of the nanofluids is caused due to the dispersion of the suspended nanoparticles.

$$\frac{k_{\text{eff}}}{k_f} = 1 + 7.47\emptyset \tag{16}$$

Jang and Choi (2007) established a model as given in Eq. (17) based on the influence of Brownian motion of nanoparticles. This thermal conductivity model is based on various four factors, like the collision of basefluid molecules, collision of

nanoparticles driven by Brownian motion, thermal diffusion in nano-sized particle and fluids, and the thermal interaction of particle with fluid molecules, where $Re_d = \frac{C_{\mathrm{RM}} d_p}{\upsilon}$ in which $C_{\mathrm{RM}} = \frac{K_B T}{3\pi \mu_f d_p l_f}$, d_f is the equivalent diameter of particle and l_f mean free path.

$$k_{\mathrm{eff}} = k_f(1 - \emptyset) + 0.01 k_p \emptyset + \left(18 \times 10^6\right) \frac{d_f}{d_p} k_f Re_d^2 Pr_f \emptyset \tag{17}$$

3.5 Applications Based on Thermal Properties of the Nanofluids

As it has been well known that the nanofluids possess extraordinary thermal properties, compared with conventional fluids, there has also been a tremendous increase in the studies for different applications of the nanofluids in numerous heat transfer systems. Several researchers have investigated the heat transfer intensification of nanofluids by using different geometries of lab-scale heat exchanger setups and have proposed a possible and feasible application of nanofluids as an alternative to conventional heat transfer fluids. Heyhat et al. (2013) studied the convective heat transfer performance of Al_2O_3 nanofluids with water as basefluid flowing in a horizontal tube at constant wall temperature and laminar flow conditions. An increase in the heat transfer coefficient was reported for the nanofluid compared to that of basefluid and that it was further noticeable at higher Reynolds numbers. At fully developed flow region, the improvement in heat transfer coefficient was reported to be 32% for 2 vol.% of Al_2O_3 nanofluid. Convective heat transfer performance of TiO_2/water nanofluid in a helical coiled tube heat exchanger has been studied by Kahani et al. (2014). A thermal performance factor of 3.72 was achieved for 2 vol.% TiO_2 nanofluid flowing at Reynolds number of 1750. A heat transfer coefficient enhancement of 105% has been found by Bhanvase et al. (2014) for TiO_2-based nanofluid using ethylene glycol/water mixture as basefluid flowing in a straight tube heat exchanger suggesting a great alternative for applications in heat transfer equipments. Huang et al. (2015) investigated the convective heat transfer and pressure drop of Al_2O_3-based and multi-walled carbon nanotubes-based (MWCNT) nanofluid. A higher heat transfer was achieved by using the nanofluids; however, increasing concentrations of the nanofluids increased the pressure drop. But, this was only found to be happening at higher concentrations of nanofluid due to increased viscosity, whereas viscosities of nanofluids with low concentrations did not seem to affect the pressure drop due to negligible increase in viscosity as compared to the basefluid. Convective heat transfer coefficient of Fe_3O_4/graphene nanocomposite-based nanofluid was found to enhance by 14.5% compared to the basefluid in a straight tube heat exchanger by Askari et al. (2017). Bhanvase et al. (2018) investigated the boost in heat transfer of polyaniline-based (PANI) nanofluids using water as a basefluid.

They found a 69.62% enhancement in heat transfer coefficient for 0.5 vol.% PANI nanofluid.

Applications of nanofluid as car radiator coolant have also been found by many researchers. Naraki et al. (2013) experimentally examined the heat transfer coefficient of CuO/water nanofluids in a car radiator coolant under laminar flow conditions. It has been reported that there is 8% increase in the heat transfer coefficient of the CuO nanofluids compared to water. However, it has been further pointed out that even though there is an increase in the thermal performance of the car radiator with application of the nanofluid, the factors like sedimentation and stability should also be considered before their application. Studies on thermo-physical properties comprising thermal conductivity, density, viscosity and specific heat of Al_2O_3-based nanofluids as car radiator coolants have been conducted by Elias et al. (2014). Similarly, Al_2O_3-based nanofluids using ethylene glycol as a basefluid have been studied for car radiator application by Goudarzi and Jamali (2017). For this purpose, the authors used a radiator with wire coil inserts and reported that the thermal performance of the radiator can be enhanced up to 14% by the use of Al_2O_3/ethylene glycol nanofluids. Ali et al. (2015) investigated the application of ZnO nanofluids as car radiator coolants and found an enhancement in heat transfer of 46% for a nanofluid of concentration 0.2 vol.%.

Nanofluids for cooling applications in electronic systems have also been studied widely. Selvakumar and Suresh (2012) studied the application of CuO/water nanofluid in a thin-channelled copper heat sink. A highest value of convective heat transfer coefficient of 29.63% was reported for the water block by using 0.2 vol.% CuO nanofluid compared to deionized water. Similar study has been presented by Sohel et al. (2014) using Al_2O_3/water nanofluids in an electronic heat sink that helped them achieve 18% improvement in the heat transfer coefficient compared to distilled water. They compared their study with the one previously made by Selvakumar and Suresh (2012) and found that the Al_2O_3/water nanofluid reduces the heat sink base temperature more than that reduced using the CuO/water nanofluid, even though the heat input is thrice the heat input for study using CuO/water nanofluid. Khaleduzzaman et al. (2015) studied the compatibility of Al_2O_3/water nanofluid to be used in a heat sink by investigating its stability. They studied Al_2O_3/water nanofluids in the volume concentration range of 0.1–0.25 vol.% and found that they are satisfactorily stable and that there is no sedimentation and clogging occurring using these nanofluids. Khatak et al. (2015) studied the effect of ZnO nanofluid in spray cooling of electronic devices. They observed that a 0.05 vol.% ZnO nanofluid was successful in decreasing the specimen surface temperature by 15% at a heat input and nanofluid flowrate of 180 W and 20 ml/min, respectively.

Nanofluids have also found applications in effective extraction of the solar energy. Efficiency of a solar collector has been studied by applying Al_2O_3/water nanofluid as an absorbing medium by Yousefi et al. (2012). For the study, they used a flat plate solar collector and passed the nanofluid to study the effect of nanofluid flowrate, concentration of nanoparticles in the nanofluid and use of surfactant. 28.3% increase in the thermal efficiency of the solar collector has been reported when 0.2 wt% Al_2O_3/water nanofluid was passed through the collector. Gupta et al. (2015) also

studied the Al_2O_3/water nanofluid in a direct absorber solar collector (DASC) of tube-in-plate type. The reported increase in the collector efficiency was 8.1% when 0.005 vol.% Al_2O_3/water nanofluid was passed through the DASC at a flowrate of 1.5 l/min. Sokhansefat et al. (2014) investigated the simulation of performance of Al_2O_3 nanofluid using synthetic oil as a basefluid in a parabolic trough collector tube and suggested a possible and beneficial application of it in the solar thermal energy collection in a parabolic trough geometry. Experimental study of CuO/water nanofluid application in a direct absorption concentrating parabolic solar collector (DAPSC) was reported to exhibit an increase in the thermal efficiency of 52% for CuO/water nanofluid with volume concentration of 0.008 vol.% (Menbari et al. 2016).

Nanofluids have also found to have gained pace in applications in refrigeration systems. Kumaresan et al. (2012) experimentally investigated convective heat transfer using MWCNT-based nanofluid as a secondary refrigerant using water/ethylene glycol mixture as basefluid in a tubular heat exchanger. An enhancement of nearly 160% was found to be occurring by the use of 0.45 vol.% of the MWCNT-based nanofluids, which was reportedly happening due to the higher thermal conductivity, larger aspect ratio of the nanoparticles, particles rearrangement and delayed development of boundary layer. Similar study using single-walled carbon nanotubes-based (SWCNT) nanofluid has been conducted by Vasconcelos et al. (2017). Influence of shape of ZnO-based nanorefrigerant on the heat transfer using the refrigerant R-134a as a basefluid is studied by Maheshwary et al. (2018). Spherical-shaped ZnO nanoparticles in the R-134a refrigerant found to exhibit a thermal conductivity enhancement of the refrigerant by 25.26%. Thus, the thermal properties of the nanofluids have been exploited in a numerous ways to make heat transfer processes more efficient with an augmentation in the thermal transport caused by the presence of nanoparticles in the nanofluid.

4 Electrical Conductivity of Nanofluids

Nanofluids are well known in the field of heat transfer as numerous researchers have already studied its heat transfer characteristics and have reported several applications of the nanofluids in thermal transport system as seen earlier in this chapter. But there are several other properties of nanofluids that cannot be ignored. One of them is the electrical conductivity of the nanofluids. As known already, the electrical conductivity is the ability to transport or conduct electric current. Awareness about the fact that the nanofluid may have superior electrical conductivity values than other materials makes one to analyse it and apply a certain nanofluid in a typical system which require fluids that conduct electrical energy. As the nanofluids possess higher thermal conductivity, it is possible for them to also possess higher electrical conductance.

Maxwell (1881) has very well defined that the electrical conductivity is affected by the physical properties of the nanoparticles and the basefluid. But many researchers

have found that it is not only affected by the properties of the components of the nanofluid but also their interaction with each other (Ganguly et al. 2009; Minea and Luciu 2012; Shen et al. 2012). Chakraborty and Padhy (2008) found that the agglomeration of the nanoparticles leads to efficient electrical conductivity due to the nanoparticles making physical contact with each other. But in contrast to that, they have stated that the agglomeration of the nanoparticles also leads to larger particle size having larger mass that may reduce the electrophoretic mobility due to increased viscosity of the nanofluid.

The DLVO theory developed for explaining the stability of colloids in suspension states that there is a formation of a charged layer on a colloidal particle in the nanofluid. This layer is composed of ions that are charged opposite to the particle surface and so form a charged diffuse layer over the particles. These ionic charges are found to be forming due to the adsorption and desorption of ions present in the solution on the particle surface (Cruz et al. 2005). These charged particles can then transfer the charge and behave as charge carriers. In a nanofluid, the nanoparticles act as carriers of electrical charge. The electrical double layer (EDL) has also found to be one of the mechanisms responsible for the electrical transport properties of the nanofluids by many researchers (Chakraborty and Padhy 2008; Ganguly et al. 2009; Minea and Luciu 2012).

4.1 Measurement of Electrical Conductivity of the Nanofluids

Electrical conductivity of nanofluids has mostly been measured by researchers all around the world by using electrical conductivity metre consisting of a probe, whose electrical circuit with the circular electrode that makes up the working principle of the electrical conductivity metre is shown in Fig. 9a. The one shown in Fig. 9b is a typical electrical conductivity measuring device known as a four-cell conductivity electrode metre (CyberScan CON 11) made by Eutech Instruments Pte Ltd in Singapore having in-built automatic temperature compensation (ATC). This metre gives instant value of electrical conductivity and temperature.

4.2 Factors Affecting the Electrical Conductivity of the Nanofluids

Electrical conductivity being the property dependent on the components of the nanofluid can be affected by many factors. As discussed earlier, the electrical conductivity of the nanofluids is dependent on the charge over the particles. They can also be dependent on the amount and size of these charge carriers, that is, the nanoparticles. These charges on the nanoparticles are dependent on the pH (Sigmund et al. 2000).

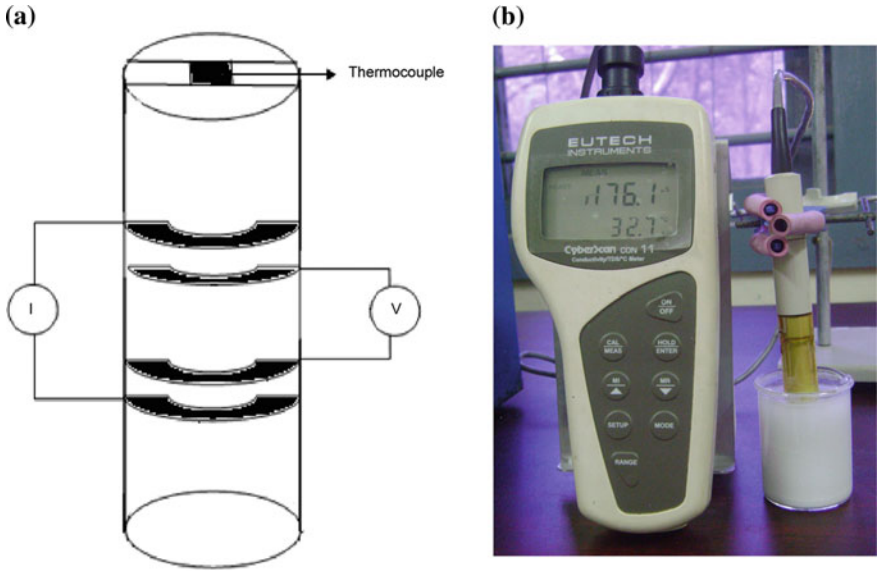

Fig. 9 Setup for electrical conductivity measurement. **a** Electrical circuit with electrode and **b** Electrical conductivity metre setup (Sarojini et al. 2013)

Also, other nanofluid environment factors like temperature may prove to be affecting the electrical conductivity similar to its governing effect on the thermal conductivity.

4.2.1 Concentration of Nanoparticles

It has been already known that the electrical conductivity is due to the electrical double layer formed over the nanoparticles, making them the electric charge carriers. Many researchers studied the effect of amount of these carriers, that is, nanoparticles dispersed in various kinds of basefluids on their respective nanofluid electrical conductivity (Baby and Ramaprabhu 2010; Glory et al. 2008; White et al. 2011). Increasing the nanoparticle concentration increases the interaction between the nanoparticles resulting in increase in electrical conductivity (Shoghl et al. 2016). Liu et al. (2004) investigated the electrical conductivity of the multi-walled carbon nanotube (MCNT) dispersed in chloroform and toluene and reported that the electrical conductivity of the nanofluids intensifies with increase in the concentration of the nanofluids. Lisunova et al. (2006) also studied the electrical conductivity of MCNTs nanofluid using water as a basefluid and Trixton X-305 as a dispersant. It has been reported that augmentation in the electrical conductivity is more pronounced as the volume fraction of the nanofluid exceeds 0.01, which happens reportedly due to the aggregation and percolation behaviour of the nanotubes. The concentration where this phenomenon occurs is known as the percolation threshold. The nanotubes having a high aspect ratio form networks and behave as electro-conductive clusters at higher

concentrations, which ultimately lead to a high electrical conductivity. However, Glover et al. (2008) reported that there is no percolation threshold for SWNT-based aqueous nanofluids and that there is a linear relationship between the electrical conductivity and the concentration depicting ionic conduction behaviour. The electrical conductivity of the water-based single-walled carbon nanotube (SWNT) nanofluids reported to be increased from 0.12×10^{-3} to 1.6×10^{-3} S/m when nanofluid concentration increases from 0 to 0.5 wt%, which was around 13 times more. It was shown for alumina nanofluids that the electrical conductivity also linearly increases with increase in the concentration of the nanofluid by Ganguly et al. (2009) and it was recorded to be 258 μS/cm for nanofluid volume fraction of 0.03 at room temperature. An enhancement of electrical conductivity exhibited by graphene-based nanofluids using mixture of water and ethylene glycol as basefluids was studied by Baby and Ramaprabhu (2010). They found that a 0.03% concentrated graphene nanofluid shows an electrical conductivity enhancement of almost 1400% at 25 °C. A 973 times higher electrical conductivity was recorded by Shen et al. (2012) by adding ZnO nanoparticles to insulating oil at a concentration of 0.75 vol.%. An outstanding enhancement of 25678% in electrical conductivity was recorded by Hadadian et al. (2014) for water-based graphene oxide nanofluid at a very low graphene oxide mass fraction of 0.0006. Electrical conductivity of nitrogen-doped graphene-based nanofluids was studied by Mehrali et al. (2015) and they found a maximum electrical conductivity enhancement of 1814.96% for a 0.06 wt% nanofluid. Adio et al. (2015a) investigated the effect of volume fraction on the electrical conductivity of MgO-based nanofluids using ethylene glycol as basefluids. For the MgO nanofluid concentrations of 0.1, 0.5, 1, 2 and 3 vol.%, the electrical conductivity was found to be 3.01, 6.68, 8.73, 11.74 and 14.05 μS/cm, respectively. Al_2O_3 nanofluids prepared using bio-glycol/water mixtures as basefluid were studied by Abdolbaqi et al. (2016) and they found a decrease in electrical conductivity with an increase in the concentration of the nanofluid. A nanofluid prepared using bio-glycol/water mixture in the ratio of 40:60 by volume showed a decrease in electrical conductivity from 620 to 472 μS/cm when the concentration of Al_2O_3 nanoparticles increased from 0 to 2 vol.%. It has been found that the effect of nanoparticle concentration is more pronounced than that of temperature on the electrical conductivity of the nanofluids (Heyhat and Irannezhad 2018).

4.2.2 Size of Nanoparticles

Sarojini et al. (2013) studied that for alumina nanoparticles, the reduction in particle size leads to an increment in the electrical conductivity of the nanofluids in which they are dispersed. This is found to be happening due to the higher electrophoretic mobility of the smaller-sized particles compared to the larger-sized particles. A 1 vol.% alumina nanofluid prepared using water as a basefluid show electrical conductivity of nearly 95, 240 and 300 μS/cm for dispersed nanoparticles of size 150, 80 and between 20 and 30 nm, respectively.

Different types of nanofluids were prepared by Konakanchi et al. (2011) to study the effect of different parameters affecting the electrical conductivity of the nanofluids. A decrease in the electrical conductivity has been reported with an increase in the particle size of Al_2O_3 nanoparticles. 1% Al_2O_3 nanofluid showed electrical conductivity of 165, 80 and 15 μS/cm when 10, 20 and 45 nm-sized Al_2O_3 nanoparticles were dispersed in propylene glycol and water mixture at 60:40 mass ratio, respectively, at around 40 °C. Further, 1% ZnO nanofluid showed electrical conductivity of 36 and 24 μS/cm, when 36 and 70 nm-sized Al_2O_3 nanoparticles were dispersed in the same basefluid, respectively, at around 40 °C. ZnO nanofluids containing different sizes of ZnO nanoparticles prepared using propylene glycol as basefluid have been studied by White et al. (2011). Also, a decrease in the electrical conductivity from 9.6 to 1.2 μS/cm with an increase in the ZnO nanoparticle size from 20 to 60 nm in 7 vol.% concentrated nanofluid has been reported. The effect of increasing the size of the nanoparticles is opposite to the effect of increasing volume fraction of the nanoparticles in the nanofluids, leading to a decrease in the electrical conductivity of the nanofluids.

Azimi and Taheri (2015) investigated the effect of particle size of CuO nanoparticles dispersed in water on the electrical conductivity of the water-based nanofluids. An optimum particle size of the CuO nanoparticles, which is 95 nm, has been determined that exhibits maximum electrical conductivity of 0.108 μS/cm for 0.18 g/l concentration of CuO nanofluid at 25 °C. A decrease of diameter below 95 nm or increase beyond 95 nm of the CuO nanoparticles in the nanofluid leads to a decrease in the electrical conductivity of their nanofluid.

4.2.3 Temperature

The electrical conductivity of nanofluids relies on the efficiency of electron transfer through the nanofluids due to the nanoparticles. With an increase in temperature, the electrons can transfer through the energy barriers very easily as found out by Liu et al. (2004) or multi-walled carbon nanotube nanofluids. Several researchers have reported an increase in electrical conductivity with an increase in temperature (Hadadian et al. 2014; Konakanchi et al. 2011; Shen et al. 2012). However, it has also been known that the influence of temperature on electrical conductivity is lesser than that of the concentration (Mehrali et al. 2015, Goharshadi and Azizi-Toupkanloo 2013). The increase in electrical conductivity of nanofluids becomes more pronounced at higher temperatures (Adio et al. 2015a; Heyhat and Irannezhad 2018). Also, the mechanism for an enhancement in the electrical conductivity of nanofluids is different from the mechanism of enhancement of their thermal conductivity (Sarojini et al. 2013). Ganguly et al. (2009) found an increase of electrical conductivity of 0.03 volume fraction of alumina/water nanofluids from 258 to 351 μS/cm for an increase in temperature from 24 °C to 45 °C. Baby and Ramaprabhu (2010) also studied the effect of temperature on the graphene-based nanofluids using water as well as ethylene glycol as basefluids and reported an increase in electrical conductivity if the temperature of the nanofluid was increased. Konakanchi et al. (2011) also showed almost a linear

relationship for electrical conductivity and temperature of Al_2O_3 and SiO_2 nanofluids prepared using mixture of propylene glycol and water as a basefluid. On the other hand, electrical conductivity of water-based Al_2O_3 nanofluids was found to remain constant with respect to temperature by Minea and Luciu (2012). Dong et al. (2013) showed that for aluminium nitride-transformer oil-based nanofluids, the electrical conductivity shows a decreasing trend from 25 °C to 40 °C, but it became stable after 40 °C. Higher temperature of nanofluids is found to promote aggregation and thus formation of transport paths for conduction of electric charge leads to enhancement in electrical conductivity of the nanofluids (Bagheli et al. 2015). Naddaf and Heris (2018) studied the electrical conductivity of MWCNT-based nanofluids using diesel oil as a basefluid and oleic acid as a surfactant and recorded the electrical conductivities as 0.18, 135.2, 299.9 and 444.9 μS/cm for MWCNT-based nanofluids of concentrations 0.05, 0.1, 0.2 and 0.5 wt%, respectively, at a temperature of 20 °C.

4.3 Role of Zeta Potential

When nanoparticles are dispersed in the basefluid, there is a certain layer of the basefluid surrounding it. The thin layer of the liquid formed on the particle in a nanofluid is called as the Stern layer. There is also a layer known as diffuse layer that comprises the loosely associated ions at the outer surface of the Stern layer. Both of these layers are responsible for the formation of the electrical double layer. The loosely associated ions in the diffuse layer shear with the ions in the bulk fluid when the particle undergoes a motion, most commonly the Brownian motion. Zeta potential is the electric potential at this shear surface. Schematic of zeta potential is shown in Fig. 10. The zeta potential is known by measuring the velocity of the particle moving towards the electrode in the presence of an electric field externally maintained across the nanofluid sample. A value of zeta potential of ± 30 mV is considered as a value exhibited by a stable nanofluid and that exhibiting a value above or below this value is known as stable nanofluid or unstable nanofluid, respectively. Zeta potential is measured by determining the electrophoretic mobility of the particles.

4.4 Relation of Stability and Electrical Conductivity of Nanofluids

Stability is the degree of uniform dispersion of the nanoparticles in the basefluid and also one of the factors considered in electrical conductivity of the nanofluids (Shoghl et al. 2016). Nanofluids contain nanoparticles that are susceptible to surface charges. These surface charges that have major role in electrical conductivity also have a major role in the stability of the nanofluid (White et al. 2011). The surface charge on a nanoparticle is due to the protonation and de-protonation of functional groups on its

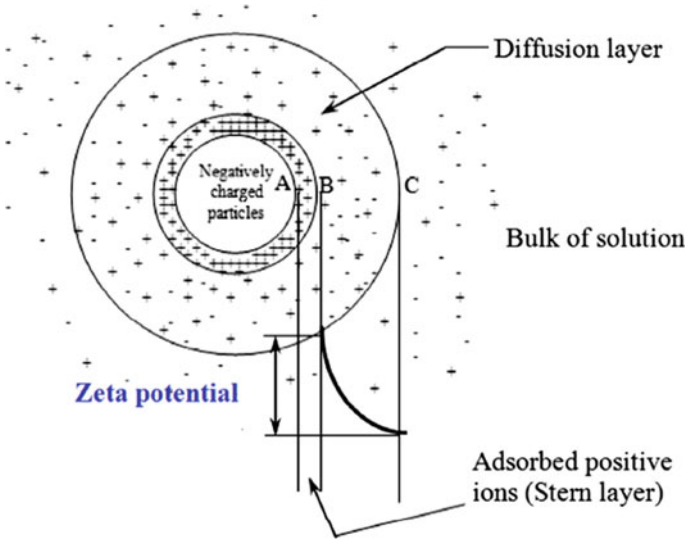

Fig. 10 Schematic of zeta potential (Chakraborty 2019)

surface (Lee et al. 2006), which causes the formation of electrical double layer (EDL) at the surface of the particles. For example, the stability of graphene oxide nanofluids is attributed to the charge developed on its surface due to the de-protonation of acidic groups on its surface (Hadadian et al. 2014). Use of dispersant or surfactants affect the ionic charges on the nanoparticles. They alter the pH of a nanofluid, and so, ultimately, the stability of the nanofluid is affected (Sarojini et al. 2013). The purpose of changing the pH is to deviate the charge of the nanoparticles from their isoelectric point (IEP), so as to decrease the agglomeration (Zawrah et al. 2016). IEP is the point when there is zero charge on the nanoparticles and which causes maximum aggregation of the nanoparticles due to maximum van der Waals forces of attraction. An increase in the pH will increase the ionic strength causing a decrease in the van der Waals forces and ultimately reduction in the aggregation (Younes et al. 2012). As we have seen that aggregation and de-aggregation is important as far as electrical conductivity of the nanofluid is concerned, the change in pH and stability is related to the electrical properties of the nanofluid. The study of electrical conductivity in relation to stability of the nanofluid has been done by some researchers (Cruz et al. 2005; Ganguly et al. 2009). In fact, the electrical conductivity helps determining the stability of the nanofluid (Shoghl et al. 2016).

4.5 Models for Electrical Conductivity Prediction

Models present an additional insight to the variations of certain parameter with respect to changes in other parameter and provide a prediction of the experimental results for the same. Similar to thermal conductivity, there are model equations which are derived for predicting the electrical conductivity as well. A classical model developed by Maxwell (1881) for conductivity in heterogeneous media as given in Eq. (18) is being used since long ago for the prediction of electrical conductivity of nanofluids. This equation gives the relation between the effective conductivity of the nanofluid (λ_{eff}) and conductivity of the basefluid (λ_{bf}) as a function of conductivity ratio of the two phases (α) and volume fraction of the nanoparticles in the nanofluid (ϕ). This correlation given by Maxwell is valid for spherical particles which are randomly distributed in the dispersions. Also, it assumes that there is no formation of aggregates and the distances between two particles is greater than their diameters.

$$\frac{\lambda_{\text{eff}}}{\lambda_{\text{bf}}} = 1 + \frac{3(\alpha - 1)}{(\alpha + 2) - (\alpha - 1)\phi} \tag{18}$$

Here, 'α' as given in Eq. (19) is the ratio of conductivity of the nanoparticles (λ_p) to the conductivity of the basefluid (λ_{bf}).

$$\alpha = \frac{\lambda_p}{\lambda_{\text{bf}}} \tag{19}$$

Certain approximations made by Cruz et al. (2005) to simplify the Maxwell's equation, are presented in Table 2. Maxwell's model only considers the properties of the individual components of the solid–liquid mixture and not their interaction.

Several researchers have tested this model for electrical conductivity of diverse nanofluids so as to verify whether it can predict their experimental results, but have reached a conclusion that it fails to predict the behaviour of nanofluid and do not comply with the practical findings (Ganguly et al. 2009; Lisunova et al. 2006). Lisunova et al. (2006) stated that the classical Maxwell model fails to predict the electrical conductivity of MWCNT-based nanofluids due to the elongated shape and high aspect ratio of the nanotubes that is not valid for usage of the Maxwell

Table 2 Approximations made by Cruz et al. (2005) to the Maxwell model (1881)

Condition	Simplified form of Maxwell's equation
If the dispersed phase, that is, nanoparticles are of insulating type ($\lambda_p \ll \lambda_{\text{bf}}$)	$\frac{\lambda_{\text{eff}}}{\lambda_{\text{bf}}} = 1 - \frac{3}{2}\phi$
If the dispersed phase, that is, nanoparticles have same conductivity as that of the basefluid ($\lambda_p = \lambda_{\text{bf}}$)	$\frac{\lambda_{\text{eff}}}{\lambda_{\text{bf}}} = 1$
If the dispersed phase, that is, nanoparticles are of conducting type ($\lambda_p \gg \lambda_{\text{bf}}$)	$\frac{\lambda_{\text{eff}}}{\lambda_{\text{bf}}} = 1 + 3\phi$

model. A higher electrical conductivity of the suspension for the concentration higher than 0.01 volume fraction was found, which was reportedly happening due to the aggregation and networking of the MWCNTs which form electroconductive clusters that behave as a pathway for electrical conductance. But this is not true for every kind of nanoparticles as proposed by Chakraborty and Padhy (2008) as the reduction in the density of particles due to their agglomeration shall reduce the electrical conductivity or if the particles are naturally non-conductive. Ganguly et al. (2009) also suggested that the Maxwell's model cannot predict the electrical conductivity. They have reported that the Maxwell model underpredicts the electrical conductivity of water-based Al_2O_3 nanofluids when compared to the experimental values. This was due to the dependence of electrical conductivity of the Al_2O_3 nanofluids on some additional factors rather than only the physical properties of the fluid and particles. Therefore, they presented a new correlation, as given in Eq. (20), to predict the electrical conductivity of the nanofluids.

$$\frac{(\lambda_{\text{eff}} - \lambda_{\text{bf}})}{\lambda_{\text{bf}}} = 3679.049\phi + 1.085799T - 43.6384 \tag{20}$$

Further, Konakanchi et al. (2011) studied the electrical conductivity of three types of nanofluids, namely Al_2O_3, SiO_2 and ZnO nanofluids, using propylene glycol/water mixture as the basefluid. They developed a correlation given in Eq. (21) for prediction of electrical conductivity of the Al_2O_3 nanofluids (λ_{nf}) with respect to temperature (T) which has correlation coefficient of 0.9923.

$$\lambda_{\text{nf}} = 1.3732T - 355.39; \qquad 273\,\text{K} \leq T \leq 363\,\text{K} \tag{21}$$

Also, for electrical conductivity of the SiO_2 nanofluids (λ_{nf}), they have confirmed the agreement of the experimental data with respect to temperature (T) with correlation given in Eq. (22) which has correlation coefficient of 0.99.

$$\lambda_{\text{nf}} = 2.5241T - 641.04;\ 273\,\text{K} \leq T \leq 363\,\text{K} \tag{22}$$

Similarly, for electrical conductivity of ZnO nanofluids (λ_{nf}), a correlation was developed. But, unlike the equation for Al_2O_3 nanofluid and SiO_2 nanofluid electrical conductivity, the equation for ZnO nanofluid electrical conductivity was a second-order polynomial equation as given in Eq. (23) which has correlation coefficient of 0.99.

$$\lambda_{\text{nf}} = -0.0012T^2 + 1.0844T - 202.61;\ 273\,\text{K} \leq T \leq 363\,\text{K} \tag{23}$$

Similarly, for the modelling of electrical conductivity of Al_2O_3 nanofluid (λ_{nf}) in relation with the percentage volumetric concentration of the nanofluid (ϕ) the authors present a polynomial equation, as given in Eq. (24), having correlation coefficient of 0.9994.

$$\lambda_{nf} = -0.2996\phi^2 + 12.242\phi + 3.5475;\ 1\% \le \phi \le 10\% \tag{24}$$

Further, they also developed correlations for electrical conductivity (λ_{nf}) in relation with the average particle size (d) for Al_2O_3, SiO_2 and ZnO nanofluids as given in Eqs. (25), (26) and (27), respectively.

$$\frac{\lambda_{nf}}{\lambda_{bf}} = \left[-1772.883\phi^2 + 1128.208\phi + 14.425\right] \times \left[-2.069\left(\frac{T}{T_0}\right)^2 + 4.578\left(\frac{T}{T_0}\right) - 2.204\right] \times \left[11.456\left(\frac{d_0}{d}\right) - 16.256\right] \tag{25}$$

$$\frac{\lambda_{nf}}{\lambda_{bf}} = \left[2928.485\phi^2 + 23095.615\phi + 419.136\right] \times \left[-3.373\left(\frac{T}{T_0}\right)^2 + 7.3092\left(\frac{T}{T_0}\right) - 3.3397\right] \tag{26}$$

$$\frac{\lambda_{nf}}{\lambda_{bf}} = \left[-8177.324\phi^2 + 1413.054\phi + 2.2848\right] \times \left[-2.719\left(\frac{T}{T_0}\right)^2 + 5.594\left(\frac{T}{T_0}\right) - 2.584\right] \times \left[11.681\left(\frac{d_0}{d}\right) - 8.383\right] \tag{27}$$

Ohshima (2003) investigated the electrokinetic phenomena of a dilute colloidal suspension consisting spherical particles in a salt-free medium that contains counter-ions. Further derivation for electrophoretic mobility of the suspended particles has been presented and expression for determining the electrical conductivity of the suspensions has been obtained. Further two types of cases have been stated for the model depending upon the relation between the actual charge, that is, amount of nanoparticles and its critical value. The first case states that if the charge is lower than the critical charge value, then there is a linear increase in the electrical conductivity and electrophoretic mobility occurring due to counter-ions with the increase in the charge. The second case states that if the charge is higher than the critical charge value, then the electrical conductivity and electrophoretic mobility become constant and are independent of the charge, that is, amount of nanoparticles due to counter-ion condensation effects. White et al. (2011) studied the electrical conductivity of ZnO-based nanofluids prepared using propylene glycol as a basefluid. They have used the model developed by Ohshima and clearly found that their experimental values are consistent with those given by the model. At lower volume fractions, the first case of the model is found to be satisfactorily predicting the electrical conductivity values arising due to the counter-ions and gives a linear fit. This model departs from a certain critical concentration proving the counter-ion condensation occurring at concentrations higher than the critical value. So they have also stated that this condition of the nanofluid is due to the elongated geometry which is different from that assumed by the model and that the optimization of the counter-ion condensation effects can increase their applicability. Minea and Luciu (2012) studied the Maxwell

model along with the Bruggeman model (1935a, b) as given in Eq. (28) for Al_2O_3 nanofluids prepared in water, but both the models could not predict the experimental data.

$$1 - \phi = \frac{k_p - k_{\text{eff}}}{k_p - k_{\text{bf}}} \left(\frac{k_p}{k_{\text{eff}}} \right)^{1/3} \tag{28}$$

So, they presented a new model, by performing a regression analysis, having a correlation coefficient of 0.9975 which is given in Eq. (29) relating the thermal conductivity of the Al_2O_3/water nanofluids (λ) with temperature (T) and volume fraction (ϕ).

$$\begin{aligned} \lambda = {} & 176.69 + 588.41\phi - 13.64T - 86.31\phi^2 + 0.36T^2 + 1.07T\phi \\ & + 11.06\phi^3 - 0.003T^3 + 0.18T^2\phi - 1.01T\phi^2 \end{aligned} \tag{29}$$

Again, as found out by Shen et al. (2012) for ZnO nanofluids prepared using insulated oil as a basefluid, the Maxwell model underpredicts the electrical conductivity of the nanofluid. They concluded that the electrical conductivity of the nanofluid depend on two additional factors along with Maxwell electrical conductivity (λ_M). Those two factors are the electrical conductivity due to electrophoresis (λ_E) and due to the Brownian motion (λ_B). The equation thus derived by them to predict the electrical conductivity of the ZnO-insulated oil nanofluid is as given in Eq. (30) where λ_{bf} is the electrical conductivity of the basefluid, ϕ is the volume fraction of the nanoparticles in the nanofluid, ε_r is the relatively dielectric constant of the nanofluid, ε_0 is the dielectric constant of the vacuum, U_0 is the zeta potential of the nanoparticles relative to the basefluid, r is the radius of the spherical nanoparticle, R is the thermodynamic constant, t is the temperature, L is the Avagadro's constant, λ is the viscosity index of the fluid, T_0 is the temperature of the nanofluid at which the viscosity is measured, ρ is the nanofluid density and ν is the nanofluid kinematic viscosity. This equation is valid for particles with higher electrical conductivity than the basefluid as the first term, that is the term for Maxwell conductivity, is approximated for such solid–liquid systems.

$$\begin{aligned} \lambda = \lambda_M + \lambda_B + \lambda_E = {} & \lambda_{bf}(1 + 3\phi) \\ & + \frac{3\phi\varepsilon_r\varepsilon_0 U_0}{r^{3/2}} \left(\frac{RT}{L} \varepsilon \frac{e^{\lambda(T-T_0)}}{3\Pi\rho\nu(1 + 25\phi + 625\phi^2)} \right)^{1/2} + \frac{2\phi\varepsilon_r^2\varepsilon_0^2 U_0^2}{\rho\nu(1 + 25\phi + 625\phi^2 r^2)} e^{\lambda(T-T_0)} \end{aligned} \tag{30}$$

Similar study was done by Dong et al. (2013) for transformer oil-based aluminium nitride (AlN) nanofluids in which they reported that the experimental electrical conductivity is in good agreement with the one predicted using the model given in Eq. (31), which is similar to the previous one by Shen et al. (2012) ignoring the effect of Brownian motion.

$$\lambda = \lambda_M + \lambda_E = \frac{\lambda_p + 2\lambda_{bf} - 2\phi(\lambda_{bf} - \lambda_p)}{\lambda_p + 2\lambda b_f - \phi(\lambda_{bf} - \lambda_p)} + \frac{2\phi\varepsilon_r^2\varepsilon_0^2 U_0^2}{\rho\nu(1 + 25\phi + 625\phi^2 r^2)} e^{\lambda(T-T_0)} \tag{31}$$

The Shen's model (2012) has been used by Bagheli et al. (2015) to predict electrical conductivity of Fe_3O_4 nanofluid and found that it can satisfactorily predict the electrical conductivity at lower volume fraction. However, at higher concentrations the Shen's model fails to predict the electrical conductivity of Fe_3O_4 nanofluid which is reportedly due to the agglomeration effects which are not considered in the model.

Sarojini et al. (2013) found that the Maxwell model fits well for conducting particles like Cu but not for non-conducting particles like Al_2O_3 and CuO dispersed in polar solvents. In fact, the Maxwell model underestimates the electrical conductivity of Al_2O_3 and CuO nanofluids. Same has been found by Zakaria et al. (2015) for water/ethylene glycol mixture-based Al_2O_3 nanofluids with ethylene glycol concentration in the basefluid above 40%. At higher ethylene glycol concentration, that is, above 80%, there is negligible error between the experimental value and the predicted value by the Maxwell model. Hadadian et al. (2014) studied the electrical conductivity of graphene oxide-based nanofluids and found out an equation for predicting electrical conductivity for the sheet-like material dispersed in water. They developed an equation for a range of temperature amongst which at 25 °C, the empirical relationship is as given in Eq. (32) having a correlation coefficient of 0.9998, where f_m is the mass fraction of the graphene oxide sheets in the nanofluid.

$$\lambda = 32.32 + 333228.571 f_m \tag{32}$$

Water-based nitrogen-doped graphene nanofluids using Trixton X-100 as a surfactant for dispersion were prepared by Mehrali et al. (2015) and similar equation was found out for determining the electrical conductivity of the nanofluid in relation with the weight percentage (wt%) at 25 °C having a correlation coefficient of 0.999 as given in Eq. (33).

$$\lambda = 5.7471 + 1517.8 \times (wt.\%) \tag{33}$$

The electrical conductivity of MgO/ethylene glycol nanofluids is also incorrectly predicted by the Maxwell as well as the Ohshima's model as per the study of Adio et al. (2015). Also, for Al_2O_3 nanofluids prepared using bio-glycol/water mixtures as basefluid, the Maxwell's model shows similar characteristics to those obtained by experiment but underpredicts the experimental data as found out by Abdolbaqi et al. (2016). Shoghl et al. (2016) studied a wide range of water-based nanofluids, namely Al_2O_3 nanofluid, carbon nanotube (CNT) nanofluid, CuO nanofluid, MgO nanofluid, TiO_2 nanofluid and ZnO nanofluid and found that the electrical conductivity of all these nanofluids cannot be satisfactorily predicted by the Maxwell model. So, they proposed new models for electrical conductivity (λ) of each nanofluid as given in Eqs. (34), (35), (36), (37), (38) and (39), each with a correlation coefficient of 0.999,

0.962, 0.998, 0.998, 0.999 and 0.976, respectively, as a function of volume percent of the nanofluid (ϕ).

$$\lambda = 20182.365 - 0.0236\ln(\phi) - \frac{177.905}{\ln(\phi)} - 20193.232e^{-\phi};\ 0 < \phi < 0.5 \tag{34}$$

$$\lambda = 59.9851\ln(\phi) + 626.2985;\ 0 < \phi < 0.5 \tag{35}$$

$$\lambda = 5.7234 + 1565\phi^2 - 3.835 \times 10^9\phi^3 - 24.397\phi^{0.5}\ln(\phi);\ 0 < \phi < 0.3 \tag{36}$$

$$\lambda = 94.07 - 597560.2\phi^2\ln(\phi) - 434.468\phi^{0.5}\ln(\phi) - 0.00018(\ln(\phi))^2;\ 0 < \phi < 0.55 \tag{37}$$

$$\lambda = 5.685 - 100847.89\phi - 14519.151\phi\ln(\phi) - \frac{209917.22\phi}{\ln(\phi)} - \frac{17.459}{\ln(\phi)};\ 0 < \phi < 0.52 \tag{38}$$

$$\lambda = 1950427497.325\phi^3 - 10130820.427\phi^2 + 16263.712\phi + 45.856;\ 0 < \phi < 0.35 \tag{39}$$

Nurdin and Satriananda (2017) reported that the electrical conductivity of maghemite (γ-Fe_2O_3)/water nanofluids also cannot be predicted by the Maxwell and Bruggeman model. Modern modelling techniques like the use of artificial neural network (ANN) have equipped researchers with newer methods to predict the electrical conductivities of nanofluids as studied by Aghayari et al. (2018). They found that the ANN can well predict the electrical conductivity of CuO/glycerol nanofluids. Cruz et al. (2005) have stated that the electric double layer (EDL) plays a major role in determining whether the nature of the suspended particles is insulating or conducting and also that this nature can be altered which is bound to affect the stability of the nanofluid.

4.6 Applications Based on Electrical Conductivity of Nanofluid

Applications of nanofluids particularly exploiting their electrical conductivity have not been yet discovered. It has been only studied by Zakaria et al. (2015) that the electrical conductivity of nanofluid applied for thermal application shall affect its thermal conductivity. It is reported that the Al_2O_3/water/ethylene glycol nanofluid in the role of coolant in the proton exchange membrane fuel cell (PEMFC) receives ions due to the contamination of the bipolar plate of the cell and also because of

the oxidation of ethylene glycol which is a component of the nanofluid's basefluid due to its degradation during the process (Dill 2005; Zhang and Kandlikar 2012). Also, it has been known that the electrical conductivity of the coolant can cause the occurrence of shunt current and electrolysis of the coolant on the electrical appliance (Elhamid et al. 2004; Gershun et al. 2009). Such occurrence of shunt current leads to the decrease in the efficiency of the appliance and can prove harmful to the user. They have analysed the thermo-electrical conductivity (TEC) ratio of the nanofluid which is advantageous at a higher value for its nanofluid application in fuel cell. Thus, this shows that the significance of electrical conductivity is in determining the feasibility of the application of a nanofluid for thermal applications in an electrically active environment.

5 Particle Size Distribution of Nanofluids

Particle size distribution (PSD) as specified earlier is the amount of particles present in the nanofluid classified according to their sizes. It gives the estimate of the variance of the sizes of the particles dispersed in the nanofluid. Nanofluids containing particles of a same size are called as monodisperse nanofluids and that containing particles of different sizes are called as polydisperse nanofluids. A monodisperse nanofluid exhibits a narrow particle size distribution, whereas a polydisperse nanofluid exhibits a wide particle size distribution, as shown in Fig. 11. As we already know that the various thermal, optical, electrical, mechanical and physical properties of the nanoparticles rely on their size (Dhamoon et al. 2018), so the study of the size distribution of these nanoparticles in the nanofluid is of great importance. It is to be first made clear that the size of the particle and the particle size distribution are two

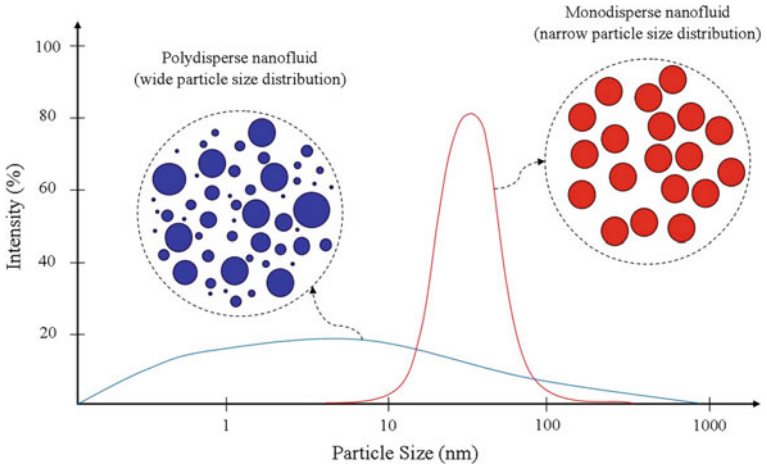

Fig. 11 Schematic of types of particle size distribution curves

different terminologies even though the latter is dependent on the earlier. There are many factors that affect the particle size of the nanoparticles in the nanofluid and so they indirectly affect the particle size distribution.

5.1 Characterization Techniques Used for Particle Size Distribution

There are several methods that can be used for determining the particles size of the nanoparticles dispersed in the nanofluid and characterize its particle size distribution (Lin et al. 2014). Dynamic light scattering is the method in which the intensities at which the laser beam is scattered by the nanoparticles are measured, which depends on their Brownian motion in the nanofluid. So, the hydrodynamic diameter (D_h) as a measure of particle size can thus be known by using the Stokes–Einstein relation given in Eq. (40) where k_b is the Boltzmann's constant, T is the thermodynamic temperature, n is the viscosity and D_t is the translational diffusion coefficient.

$$D_h = \frac{k_b T}{3\Pi n D_t} \tag{40}$$

In DLS, the hydrodynamic diameter is considered, which is equivalent to the diameter of a spherical particle that would have same translational diffusion coefficient. The Raman scattering technique is another technique that uses the differences in frequencies of the photons scattered after they are incident on a material and interact with the dipoles of its molecules. It gives the indirect measure of the size distribution of the nanoparticles.

There are electron microscopy techniques, like SEM and TEM, which examine the nanofluid stability and thus give an estimate of the particles size distribution. These methods use high-resolution microscopic techniques to capture images using electron beam. Both the methods include the evaporation of the basefluid and then capturing the image of the particles remaining on the grid of the microscopes. A direct determination of the size of all the particles seen in the image can give a size distribution of the nanofluid. Another method for determination of the size distribution of the nanoparticles, known as atomic force microscopy (AFM), uses a cantilever machined at micro-size having a sharp tip to detect its deflection caused by the repulsion forces and thus generate an image of the material. Another method is the UV–visible spectrophotometry that makes use of the amount of light absorbed by the nanoparticles to classify them into different sizes. Nanomaterials of different sizes absorb light at different wavelengths. The absorbance of light by a nanofluid is a function of size of the nanoparticles present in it and so their size can be indirectly known from the UV–visible spectra of the nanofluid.

5.2 *Factors Affecting Size Distribution of Particles or Aggregation in Nanofluids*

The distribution of particles throughout the nanofluid can be definitely a function of the nanomaterial synthesis method as well as nanofluid synthesis method. But there are several other factors that completely alter the distribution of the sizes of the particles when dispersed in the nanofluid. Some of them are discussed here.

5.2.1 Time of Sonication During Synthesis of Nanofluid

As we have already seen in previous sections of this chapter, there are basically two types of nanofluid synthesis methods. Amongst them, the two-step method involves drying of nanoparticles and then re-dispersing them before application using either mechanical means or ultrasonication, the latter being used at most of the times. But this method also gives scope for the nanoparticles to form clusters and aggregates and form a polydisperse nanofluid due to inefficient dispersion due to insufficient ultrasonication (Mahbubul et al. 2015). Ma and Banerjee (2017) have specified that there are four steps involved in the formation of particles, namely thermal decomposition, nucleation, diffusion growth and particle coagulation. Under the assumption that there is no coagulation of the nanoparticles, they have observed that the nanofluid shows almost monodisperse characteristics of size distribution and that the particle size increases as the reaction is proceeding. Also, the coagulation of the particles at the end of reaction happening due to Brownian motion-induced collisions produces a polydisperse nanofluid.

Suganthi and Rajan (2012) studied the effect of ultrasonication time on the particle size distribution of ZnO-based nanofluids prepared using water as a basefluid. They have clearly mentioned that the hydrodynamic size of the nanoparticles reduces as the ultrasonication time for dispersion increases. An optimum particle size distribution that gives a minimum hydrodynamic size of the nanoparticles has been found out as 3 h for 0.5 vol.% ZnO-based nanofluid. A further increase in ultrasonication time leads to agglomeration of the nanoparticles resulting in a higher particle size. Silambarasan et al. (2012) prepared TiO_2 particles using the stirred bead milling approach and then dispersed it in water to produce nanofluid using ultrasonication method. They found a wide size distribution of the particles produced by the stirred bead milling method ranging from 40 to 900 nm. They found that sonication of 6 and 7 h almost de-agglomerates the larger-sized particles and narrows down the particle size distribution of the TiO_2 nanoparticles between the sizes of 35 and 300 nm. Sonication time of 7 h increases the percentage of smaller-sized particles even more.

5.2.2 Concentration of Nanoparticles in Nanofluid

The concentration of the nanoparticles affects the particle size distribution of the nanoparticles in the nanofluid in a way that a large quantity of nanoparticles may form larger agglomerates and broaden the particle size distribution. Colla et al. (2014) prepared ZnO nanofluids and studied the effect of concentration on the intensity of size distribution of the particles in the nanofluid. They found that the intensity of particles in the narrow range increases as the ZnO nanofluid concentration increases from 1 to 5%. But the intensity again decreases as the nanofluid concentration further increases to 10% which can be due to the agglomeration of the some particles and formation of larger size particles, thus broadening the size distribution curve. Juneja and Gangacharyulu (2017) studied the effect of concentration of particle size distribution of Al_2O_3-based nanofluid prepared using distilled water, ethylene glycol and mixture of water/ethylene glycol (in the ratio 75:25). They prepared Al_2O_3 nanofluids in the volume fraction range of 0.1–1%. For water-based Al_2O_3 nanofluids, the mean diameter of the nanoparticles first increased till a volume concentration of 0.25 vol.% and then showed a decreasing trend till 1% nanofluid concentration. The one prepared using ethylene glycol as a basefluid showed a straight decrease in the mean diameter of Al_2O_3 nanoparticles, while the nanofluid prepared in water/ethylene glycol mixture as a basefluid exhibited no change in the mean diameter after increasing the nanofluid concentration above 0.5 vol.%.

5.2.3 Addition of Surfactants

Surfactants in the nanofluids play an important role in the dispersion of the nanoparticles and in preventing formation of agglomerates. Wang et al. (2009) studied the effect of addition of sodium dodecylbenzene sulfonate (SDBS) surfactant on the particle size distribution of Al_2O_3 and Cu nanoparticle in water-based nanofluids. They found that the presence of SDBS shifts the whole size distribution curve of both the nanofluids prepared at 0.05 wt% concentration to lower particle size range. In a similar study, Das et al. (2016) found that the TiO_2–water nanofluids can be well stabilized using acetic acid and cetyl trimethylammonium bromide (CTAB) as dispersants. They purchased 21 nm-sized TiO_2 nanoparticles, but their dispersion in water produced nanofluid containing average particle diameter of 147.6 and 207.7 nm with surfactants acetic acid and CTAB, respectively, at respective nanofluid concentrations of 1.5 and 1 vol.%. The higher size of the particles detected in the nanofluid occurred due to thermodynamically stable TiO_2 nanoparticle cluster formed in the nanofluid.

Saterlie et al. (2011) conducted a comparative study of the effect of two types of surfactants, namely cetyl trimethylammonium bromide (CTAB) and oleic acid, on the particle size distribution of Cu nanoparticles in water-based nanofluids at 0.55 and 1 vol.% concentrations of the nanoparticles. They observed that oleic acid and CTAB are able to produce Cu nanofluids with particle size distribution at lower ranges having an average particle size of nearly 120 and 80 nm, respectively, at a

nanofluid concentration of 0.55 vol.%. A similar size distribution is also obtained by using CTAB in 1 vol.% Cu nanofluid. But when oleic acid is used for dispersing same concentration of Cu nanoparticles in water, a substantial increase in the size of the particles is observed and the size distribution shifted to higher ranges exhibiting an average particle size of 800 nm. This was reported to be happening due to the heavy agglomeration of the nanoparticles due to inefficiency of oleic acid to keep them de-agglomerated and its failure in producing stable nanofluid.

5.2.4 Temperature

The temperatures, as known earlier, tend to affect the surface charges of the particles, which may affect their tendency to agglomerate. Also, the Brownian motion of the particles is greatly affected by temperature, which may have an indirect effect on the particle size. It was found by Suganthi and Rajan (2012) for ZnO-based nanofluids that the average particle hydrodynamic size increases with increase in temperature of the nanofluid. This was found to be happening due to the increase in Brownian motion of the particles. They prepared water-based ZnO nanofluids using sodium hexametaphosphate (SHMP) as a stabilizing agent. The adsorption of PO^{3-} ions generated due to dissociation of SHMP when dissolved in water on the surface of the ZnO nanoparticles reduces their agglomeration. This chemisorption of the PO^{3-} ions over the surface of the particles is a function of temperature and so an increase in the temperature resulted in the shift of the equilibrium of this exothermic adsorption towards desorption which is favourable at higher temperatures. Ultimately, this process leads to production of vacant sites on the surface of the ZnO nanoparticles, facilitating particle–particle interaction and thus agglomeration of the nanoparticles. Being dependent on the equilibrium of the adsorption of the PO^{3-} ions, this process is reversible and so restoration of the PO^{3-} ions took place as the temperature of the nanofluid was decreased and the difference between the particle size during the heating and cooling cycle was 2 nm at 25 °C.

5.3 Influence of Particle Size Distribution on Properties of Nanofluids

Particle size distribution of nanofluids determines whether the nanofluid is monodisperse or polydisperse. Size of the particles dispersed in the nanofluid impacts a lot of thermo-physical properties of the nanofluid. Below is given how the particle size distribution affects the thermal and optical properties of nanofluids.

5.3.1 Thermal Properties

Polydispersity of the nanofluids has a significant impact on the nanofluid thermal conductivity (Karthikeyan et al. 2008). It has been found out by Feng et al. (2008) that the thermal conductivity of the nanofluids is better when they exhibit uniform size distribution and that it is less when the size distribution is non-uniform.

Zhou and Wu (2014) developed a model of thermal conductivity as a function of PSD considering the clustering of the nanoparticles in tightly packed aggregates, as given in Eq. (41), where k_{nf} is the thermal conductivity of nanofluid containing primary particles as well as clusters, k_{bf} is the thermal conductivity of basefluid, k_{pm} is the thermal conductivity containing primary particles, k_p is the thermal conductivity of the particles, ξ is the shape factor defined as $\xi = 3/\psi$ (ψ is the sphericity of the nanoparticle clusters), ϕ_c is the volume fraction of clusters in the nanofluid and is the product of volume fraction of nanoparticle clusters in the nanofluid, ϕ_{cs}, and volume fraction of nanoparticles in the spherical clusters, ϕ_{ins}.

$$\frac{k_{\mathrm{nf}}}{k_{\mathrm{bf}}} = \frac{k_p + (\xi - 1)k_{pm} - (\xi - 1)\phi_c\left(k_{pm} - k_p\right)}{k_p + (\xi - 1)k_{pm} + \phi_c\left(k_{pm} - k_p\right)} \tag{41}$$

5.3.2 Optical Properties

Most of the times while characterizing the nanofluid we take into consideration its optical properties, a monodisperse system is assumed, even though practically, the particles are always dispersed in a polydisperse manner to some degree (Qin and Lee 2018). This is due to the fact that the larger-sized particles enhance the scattering of long wavelengths, unlike the small-sized particles that absorb only short wavelengths (Du and Tang 2015). Thus, the absorption of wavelengths by the nanofluid depends on the various sizes of nanoparticles dispersed in it, that is, on the size distribution of the nanoparticles. Agglomeration in such case plays a very important role. Agglomerates of nanoparticles shift the wavelength of absorption of the nanofluid. Agglomeration leads to conversion of a nearly monodisperse nanofluid into polydisperse nanofluid that distorts its absorption spectra. Optical properties of nanofluids play a major role in the solar thermal applications of nanofluids and so the particle size distribution of the nanofluids gains importance (Crisostomo et al. 2017; Hjerrild et al. 2016).

6 Summary

The field of nanotechnology has given rise to nanofluids that are proved to be having superior properties than conventional fluids. The two preparation methods of

nanofluids are discussed in this chapter along with few properties. The main properties of nanofluids are their thermal, electrical and optical properties which are very important as far as the various applications of nanofluids are concerned. Accordingly, there are some factors that affect these properties. There is certain mechanism which is responsible for the extraordinary behaviour of nanofluids.

Enhanced thermal properties of the nanofluids are an outcome of the high surface area provided by the nanoparticles in the nanofluid, their Brownian motion in the nanofluid and the interfacial layer of the basefluid that surrounds the nanoparticles and possesses higher thermal conductivity than the rest of the fluid in bulk. These are helpful in various heat transfer enhancement processes as studied by various researchers. Also, the formation of EDL on the surface of the nanoparticles is responsible for electrical conductivity of the nanofluids. There are model relationships that are useful in predicting the thermal conductivity as well as electrical conductivity of the nanofluids, as found out by various researchers. The role of zeta potential in the electrical properties of the nanofluids is also a factor to be considered. Researchers have used several methods to measure the thermal and electrical conductivities of the nanofluids, amongst which few have become very famous. There are several applications based on the thermal properties of the nanofluids but very few are based on the electrical properties of the nanofluids. Particle size distribution is yet another property that has importance as far as thermal and optical properties of the nanofluids are concerned. There are several factors that affect the particle size distribution. Agglomeration is one basic property that must be considered while determining the polydispersity of the nanofluids.

References

Abdolbaqi MKh, Azmi WH, Mamat R, Sharma KV, Najafi G (2016) Experimental investigation of thermal conductivity and electrical conductivity of bioglycol-water mixture based Al_2O_3 nanofluid. Appl Therm Eng 102:932–941

Adio SA, Sharifpur M, Meyer JP (2015a) Factors affecting the pH and electrical conductivity of MgO-ethylene glycol nanofluids. Bull Mater Sci 38:1345–1357

Adio SA, Sharifpur M, Meyer JP (2015b) Investigation into effective viscosity, electrical conductivity, and pH of γ-Al_2O_3-glycerol nanofluids in Einstein concentration regime. Heat Trans Eng 38:1241–1251

Aghayari R, Maddah H, Ahmadi MH, Yan W, Ghasemi N (2018) Measurement and artificial neural network modeling of electrical conductivity of CuO/glycerol nanofluids at various thermal and concentration conditions. Energies 11:1190

Ahammed N, Asirvatham LG, Titus J, Bose JR, Wongwises S (2016) Measurement of thermal conductivity of graphene–water nanofluid at below and above ambient temperatures. Int Commun Heat Mass 70:66–74

Akoh H, Tsukasaki Y, Yatsuya S, Tasaki A (1978) Magnetic properties of ferromagnetic ultrafine particles prepared by vacuum evaporation on running oil substrate. J Crystal Growth 45:495–500

Alawi OA, Sidik NAC, Xian HW, Kean TH, Kazi SN (2018) Thermal conductivity and viscosity models of metallic oxides nanofluids. Int J Heat Mass Transf 116:1314–1325

Ali FM, Yunus MM, Moksin MM, Talib ZA (2010) The effect of volume fraction concentration on the thermal conductivity and thermal diffusivity of nanofluids: numerical and experimental. Rev Sci Instrum 81:074901

Ali HM, Ali H, Liaquat H, Maqsood HTB, Nadir MA (2015) Experimental investigation of convective heat transfer augmentation for car radiator using ZnO-water nanofluids. Energy 84:317–324

Askari S, Koolivand H, Pourkhalil M, Lotfi R, Rashidi A (2017) Investigation of Fe_3O_4/Graphene nanohybrid heat transfer properties: experimental approach. Int Commun Heat Mass 87:30–39

Azimi M, Ommi F (2013) Using nanofluid for heat transfer enhancement in engine cooling process. J Nano Energy Power Res 2:1–3

Azimi HR, Taheri R (2015) Electrical conductivity of CuO nanofluids. Int J Nano Dimens 6:77–81

Baby TT, Ramaprabhu S (2010) Investigation of thermal and electrical conductivity of graphene based nanofluids. J Appl Phys 108:124308

Bagheli S, Fadafan HK, Orimi RL, Ghaemi M (2015) Synthesis and experimental investigation of the electrical conductivity of water based magnetite nanofluids. Powder Technol 274:426–430

Bhanvase BA, Sarode MR, Putterwar LA, Abdullah KA, Deosarkar MP, Sonawane SH (2014) Intensification of convective heat transfer in water/ethylene glycol based nanofluids containing TiO_2 nanoparticles. Chem Eng Process 82:123–131

Bhanvase BA, Sayankar SD, Kapre A, Fule PJ, Sonawane SH (2018) Experimental investigation on intensified convective heat transfer coefficient of water based PANI nanofluid in vertical helical coiled heat exchanger. Appl Therm Eng 128:134–140

Bozorgan N, Shafahi M (2017) Analysis of gasketed-plate heat exchanger performance using nanofluid. J Heat Mass Trans Res 4:65–72

Bruggeman DAG (1935a) Berechnung verschiedener physikalischer Konstanten von heterogenen Substanzen. Ann Phys (Leipzig) 24:636

Bruggeman DAG (1935b) Dielectric constant and conductivity of mixtures of isotropic materials. Ann Phys (Leipzig) 24:636–679

Chakraborty S (2019) An investigation on the long-term stability of TiO_2 nanofluid. Mater Today Proc 11:714–718

Chakraborty S, Padhy S (2008) Anomalous electrical conductivity of nanoscale colloidal suspensions. ACS Nano 2:2029–2036

Chieruzzi M, Cerritelli GF, Miliozzi A, Kenny JM (2013) Effect of nanoprticles on heat capacity of nanofluids based on molten salts as PCM for thermal energy storage. Nanoscale Res Lett 8:448

Choi SUS (1995) Enhancing thermal conductivity of fluids with nanoparticles. ASME Publications FED-vol. 231/MD 66:99–105

Choi SUS, Yu W, Hull JR, Zhang ZG, Lockwood FE (2001) Nanofluids for vehicle thermal management. In: Proceedings of the 2001 vehicle thermal management systems conference, society of automotive engineers

Chopkar M, Sudarshan S, Das PK, Manna I (2008) Effect of particle size on thermal conductivity of nanofluid. Metall. Mater. Trans Metall Mater Trans A 39A:1535–1542

Coelho MF, Rivas MA, Vilao G, Nogueira EM, Iglesias TP (2019) Permittivity and electrical conductivity of copper oxide nanofluid (12 nm) in water at different temperatures. J Chem Thermodyn 132:164–173

Colla L, Marinelli L, Fedele L, Bobbo S, Manca O (2014) Characterization and simulation of the heat transfer behavior of water-based ZnO nanofluids. J Nanosci Nanotechnol 14:1–11

Crisostomo F, Hjerrild N, Mesgari S, Li Q, Taylor RA (2017) A hybrid PV/T collector using spectrally selective absorbing nanofluids. Appl Energy 193:1–14

Cruz RCD, Reinshagen J, Oberacker R, Segadães AM, Hoffmann MJ (2005) Electrical conductivity and stability of concentrated aqueous alumina suspensions. J Colloid Interface Sci 286:579–588

Darvanjooghi MHK, Esfahany MN (2016) Experimental investigation of the effect of nanoparticle size on thermal conductivity of *in-situ* prepared silica–ethanol nanofluid. Int Commun Heat Mass 7:148–154

Das SK, Choi SUS, Patel HE (2006) Heat transfer in nanofluids—a review. Heat Transf Eng 27:3–19

Das PK, Mallik AK, Ganguly R, Santra AK (2016) Synthesis and characterization of TiO_2–water nanofluids with different surfactants. Int Commun Heat Mass Transf 75:341–348
Dhamoon RK, Popli H, Aggarwal G, Gupta M (2018) Particle size characterization techniques, factors and quality-by-design approach. Int J Drug Deliv 10:1–11
Dill NJ (2005) Fuel cell stack coolant conductivity monitoring circuit, ed: US Patent 6, 838, 201
Dong M, Shen LP, Wang H, Wang HB, Miao J (2013) Investigation on the electrical conductivity of transformer oil-based AlN nanofluid. J Nanomater 2013; 7 pages
Du M, Tang GH (2015) Optical property of nanofluids with particle agglomeration. Sol Energy 122:864–872
Duangthongsuk W, Wongwises S (2009) Measurement of temperature-dependent thermal conductivity and viscosity of TiO_2-water nanofluids. Exp Therm Fluid Sci 33:706–714
Eastman JA, Choi US, Li S, Thompson LJ, Lee S (1997) Enhanced thermal conductivity through the development of nanofluids. In: Materials research society symposium proceedings. Materials research society, vol 4576. Pittsburgh, PA, USA, Boston, MA, USA, pp 3–11
Eastman JA, Choi SUS, Li S, Yu W, Thompson LJ (2001) Anomalously increased effective thermal conductivities of ethylene glycol-based nanofluids containing copper nanoparticles. Appl Phys Lett 78:718–720
Elhamid MHA, Mikhail YM, Blunk RH, Lisi DJ (2004) Inexpensive dielectric coolant for fuel cell stacks, ed: Google Patents
Elias MM, Mahbubul IM, Saidur MR, Shahrul IM, Khaleduzzaman SS, Sadeghipour S (2014) Experimental investigation on the thermo-physical properties of Al_2O_3 nanoparticles suspended in car radiator coolant. Int Commun Heat Mass 54:48–53
Esfe MH, Saedodin S, Bahiraei M, Toghraie D, Mahian O, Wongwises S (2014) Thermal conductivity modeling of MgO/EG nanofluids using experimental data and artificial neural network. J Therm Anal Calorim 118:287–294
Esfe MH, Karimipour A, Yan W, Akbari M, Safaei MR, Dahari M (2015a) Experimental study on thermal conductivity of ethylene glycol based nanofluids containing Al_2O_3 nanoparticles. Int J Heat Mass Transf 88:728–734
Esfe MH, Saedodin S, Wongwises S, Toghraie D (2015b) An experimental study on the effect of diameter on thermal conductivity and dynamic viscosity of Fe/water nanofluids. J Therm Anal Calorim 119:1817–1824
Esfe MH, Yan WM, Akbari M, Karimipour A, Hassani M (2015c) Experimental study on thermal conductivity of DWCNT-ZnO/water-EG nanofluids. Int Commun Heat Mass Transf 68:248–251
Feng Y, Xu P, Zou M, Yu B (2007) The effective thermal conductivity of nanofluids based on the nanolayer and the aggregation of nanoparticles. J Phys D Appl Phys 40:3164
Feng Y, Yu B, Feng K, Xu P, Zou M (2008) Thermal conductivity of nanofluids and size distribution of nanoparticles by Monte Carlo simulations. J Nanopart Res 10:1319–1328
Ganguly S, Sikdar S, Basu S (2009) Experimental investigation of the effective electrical conductivity of aluminium oxide nanofluids. Powder Technol 196:326–330
Garg J, Poudel B, Chiesa M, Gordon JB, Ma JJ, Wang JJ, Wang JB, Ren ZF, Kang YT, Ohtani H, Nanda J, McKinley GH, Chen G (2008) Enhanced thermal conductivity and viscosity of copper nanoparticles in ethylene glycol nanofluid. J Appl Phys 103:074301
Gershun AV, Jeffcoate CS, Marinho FJ, Woyciesjes PM (2009) Heat transfer compositions with high electrical resistance for fuel cell assemblies, ed: Google Patents
Gharagozloo PE, Goodson KE (2008) Diffusion, aggregation and the thermal conductivity of nanofluids. Appl Phys Lett 93:103110
Ghosh MM, Ghosh S, Pabi SK (2012) Effects of particle shape and fluid temperature on heat-transfer characteristics of nanofluids. J Mater Eng Perform 22:1525–1529
Glory J, Bonetti M, Helezen M, Hermite ML, Reynaud C (2008) Thermal and electrical conductivities of water-based nanofluids prepared with long multiwalled carbon nanotubes. J Appl Phys 103:094309
Glover B, Whites KW, Hong H, Mukherjee A, Billups WE (2008) Effective electrical conductivity of functional single-wall carbon nanotubes in aqueous fluids. Synth Met 158:506–508

Goharshadi EK, Azizi-Toupkanloo H (2013) Silver colloid nanoparticles: Ultrasound-assisted synthesis, electrical and rheological properties. Powder Technol 237:97–101
Goharshadi EK, Toupkanloo HA, Karimi M (2015) Electrical conductivity of water-based palladium nanofluids. Microfluid Nanofluidics 18:667–672
Goudarzi K, Jamali H (2017) Heat transfer enhancement of Al_2O_3-EG nanofluid in a car radiator with wire coil inserts. Appl Therm Eng 118:510–517
Guo Y, Zhang T, Zhang D, Wang Q (2018) Experimental investigation of thermal and electrical conductivity of silicon oxide nanofluids in ethylene glycol/water mixture. Int J Heat Mass Trans 117:280–286
Gupta SS, Siva VM, Krishnan S, Sreeprasad TS, Singh PK (2011) Thermal conductivity enhancement of nanofluids containing graphene nanosheets. J Appl Phys 110:084302
Gupta HK, Agrawal GD, Mathur J (2015) Investigations for effect of Al_2O_3-H_2O nanofluid flow rate on the efficiency of direct absorption solar collector. Case Stud Thermal Eng 5:70–78
Hadadian M, Goharshadi EK, Youssefi A (2014) Electrical conductivity, thermal conductivity, and rheological properties of graphene oxide-based nanofluids. J Nanopart Res 16:2788
Hamilton RL, Crosser OK (1962) Thermal conductivity of heterogeneous two-component system. Ind Eng Chem Fundam 1:187–191
Harikrishnan S, Magesh S, Kalaiselvam S (2013) Preparation and thermal energy storage behaviour of stearic acid-TiO_2 nanfluid as a phase change material for solar heating system. Thermochima Acta 565:137–145
Heyhat MM, Irannezhad A (2018) Experimental investigation on the competition between enhancement of electrical and thermal conductivities in water-based nanofluids. J Mol Liq 268:169–175
Heyhat MM, Kowsary F, Rashidi AM, Momenpour MH, Amrollahi A (2013) Experimental investigation of laminar convective heat transfer and pressure drop of water–based Al_2O_3 nanofluids in fully developed flow regime. Exp Therm Fluid Sci 44:483–489
Hjerrild NE, Mesgari S, Crisostomo F, Scott JA, Amal R, Taylor RA (2016) Hybrid PV/T enhancement using selectively absorbing Ag–SiO_2/carbon nanofluids. Sol Energy Mater Sol Cells 147:281–287
Huang D, Wu Z, Sunden B (2015) Pressure drop and convective heat transfer of Al_2O_3/water and MWCNT/water nanofluids in a chevron plate heat exchanger. Int J Heat Mass Transf 89:620–626
Hwang Y, Lee JK, Lee CH, Jung YM, Cheong SI, Lee CG, Ku BC, Jang SP (2007) Stability and thermal conductivity characteristics of nanofluids. Thermochim Acta 455:70–74
Ijam A, Saidur R, Ganesan P, Golsheikh AM (2015) Stability, thermo-physical properties, and electrical conductivity of graphene oxide-deionized water/ ethylene glycol based nanofluid. Int J Heat Mass Trans 87:92–103
Islam MR, Shabani B, Rosengarten G, Andrews J (2015) The potential of using nanofluids in PEM fuel cell cooling systems: a review. Renew Sust Energy Rev 48:523–539
Jang SP, Choi SUS (2004) Role of Brownian motion in the enhanced thermal conductivity of nanofluids. Appl Phys Lett 84:4316–4318
Jang P, Choi SUS (2007) Effect of various parameters on nanofluid thermal conductivity. J Heat Trans 129:617–623
Jeong J, Li C, Kwon Y, Lee J, Kim SH, Yun R (2013) Particle shape effect on the viscosity and thermal conductivity of ZnO nanofluids. Int J Refrig 36:2233–2241
Jiang H, Zhang Q, Shi L (2015) Effective thermal conductivity of carbon nanotube – based nanofluid. J Taiwan Inst Chem Eng 55:76–81
Juneja M, Gangacharyulu D (2017) Effect of volume fraction on particle size distribution in aumina based nanofluids. J Thermal Energy Syst 2:27–32
Kahani M, Heris SZ, Mousavi SM (2014) Experimental investigation of TiO_2/water nanofluid laminar forced convective heat transfer through helical coiled tube. Heat Mass Transf 50:1563–1573
Karthikeyan NR, Philip J, Raj B (2008) Effect of clustering on the thermal conductivity of nanofluids. Mater Chem Phys 109:50–55

Kasaeian A, Eshghi AT, Sameti M (2015) A review on the applications of nanofluids in solar energy systems. Renew Sust Energy Rev 43:584–598
Kavitha T, Rajendran A, Durairajan A (2012) Synthesis, characterization of TiO_2 nano powder and water based nanofluids using two step method. Eur J Appl Eng Sci Res 1:235–240
Keblinski P, Phillpot SR, Choi SUS, Eastman JA (2002) Mechanisms of heat flow in suspensions of nano-sized particles (nanofluids). Int J Heat Mass Transf 45:855–863
Khaleduzzaman SS, Sohel MR, Saidur R, Selvaraj J (2015) Stability of Al_2O_3–water nanofluid for electronic cooling system. Procedia Eng 105:406–411
Khaleduzzaman SS, Sohel MR, Saidur R, Selvaraj J (2015) Stability of Al_2O_3-water nanofluid for electronics cooling system. Procedia Eng 105:406–411
Khatak P, Jakhar R, Kumar M (2015). Enhancement in cooling of electronic components by nanofluids. J Inst Eng India Ser C 96:245–251
Khdher AIM, Sidik NAC, Hamzah WAW, Mamat R (2016) An experimental determination of thermal conductivity and electrical conductivity of bio glycol based Al_2O_3 nanofluids and development of new correlation. Int Commun Heat Mass Transf 73:75–83
Khedkar RS, Sonawane SS, Wasewar KL (2012) Influence of CuO nanoparticles in enhancing the thermal conductivity of water and monoethylene glycol based nanofluids. Int Commun Heat Mass 39:665–669
Kole M, Dey TK (2013) Investigation of thermal conductivity, viscosity and electrical conductivity of graphene based nanofluids. J Appl Phys 113:084307
Konakanchi H, Vajjha R, Misra D, Das D (2011) Electrical conductivity measurements of nanofluids and development of new correlations. J Nanosci Nanotechnol 11:1–8
Koo J, Kleinstreuer C (2004) A new thermal conductivity model for nanofluids. J Nanopart Res 6:577–588
Koo J, Kleinstreuer C (2005) Impact analysis of nanoparticle motion mechanism on the thermal conductivity of nanofluids. Int Commun Heat Mass Trans 32:1111–1118
Kotia A, Borkakoti S, Deval P, Ghosh SK (2017) Review of interfacial layer's effect on thermal conductivity in nanofluid. Heat Mass Transf 53:2199–2209
Kumar N, Sonawane SS, Sonawane SH (2018) Experimental study of thermal conductivity, heat transfer and friction factor of Al_2O_3 based nanofluid. Int Commun Heat Mass 90:1–10
Kumaresan V, Velraj R, Das SK (2012) Convective heat transfer characteristics of secondary refrigerant based CNT nanofluids in a tubular heat exchanger. Int J Refrig 35:2287–2296
Lee YS (2008) Self-assembly and nanotechnology: a force balance approach. Wiley, New York
Lee D, Jae-Won K, Kim BG (2006) A new parameter to control heat transport in nanofluids: surface charge state of the particle in suspension. J Phys Chem B 110:4323–4328
Lee JH, Hwang KS, Jang SP, Lee BH, Kim JH, Choi SUS, Choi CJ (2008) Effective viscosities and thermal conductivities of aqueous nanofluids containing low volume concentrations of Al_2O_3 nanoparticles. Int J Heat Mass Transf 51:2651–2656
Leong KC, Yang C, Murshed SMS (2006) A model for the thermal conductivity of nanofluids—the effect of interfacial layer. J Nanopart Res 8:245–254
Leong KY, Ibrahim IC, Amer NH, Risby MS (2016) Thermal conductivity of carbon based nanofluids as heat transfer fluids. Appl Mech Mater 819:29–33
Leong KY, Razali I, Ahmad KZK, Amer NH, Akmal HN (2018) Thermal conductivity characteristic of titanium dioxide water based nanofluids subjected to various types of surfactant. J Eng Sci Technol 13:1677–1689
Li Z, Sheikholeslami M, Jafaryar M, Shafee A, Chamkha AJ (2018) Investigation of nanofluid entropy generation in a heat exchanger with helical twisted tapes. J Mol Liq 266:797–805
Lin P, Lin S, Wang PC, Sridhar R (2014) Techniques for physicochemical characterization of nanomaterials. Biotechnol Adv 32:711–726
Lisunova MO, Lebovka NI, Melezhyk OV, Boiko YP (2006) Stability of the aqueous suspensions of nanotubes in the presence of nonionic surfactant. J Colloid Interface Sci 299:740–746
Liu L, Yang Y, Zhang Y (2004) A study on the electrical conductivity of multi-walled carbon nanotube aqueous solution. Physica E 24:343–348

Liu MS, Lin MCC, Huang IT, Wang CC (2005) Enhancement of thermal conductivity with carbon nano-tube for nanofluids. Int Commun Heat Mass 32:1202–1210

Liu MS, Lin MCC, Wang C (2011) Enhancement of thermal condutivities with Cu, CuO, and carbon nanotube nanofluids and application of MWNT/water nanofluid on a water chiller system. Nanoscale Res Lett 6:297

Lo CH, Tsung TT, Chen LC, Su CH, Lin HM (2005) Fabrication of copper oxide nanofluid using submerged arc nanoparticle synthesis system (SANSS). J Nanopart Res 7:313–320

Ma B, Banerjee D (2017) Predicting particle size distribution in nanofluid synthesis. In: Proceedings of the ASME 2017 Heat Transfer Summer Conference HT2017, USA

Mahbubul IM, Shahrul IM, Khaleduzzaman SS, Saidur R, Amalina MA, Turgut A (2015) Experimental investigation on effect of ultrasonication duration on colloidal dispersion and thermophysical properties of alumina–water nanofluid. Int J Heat Mass Transf 88:73–81

Maheshwary PB, Handa CC, Nemade KR (2018) Effect of shape on thermophysical and heat transfer properties of ZnO/R-134a nanorefrigerant. Mater Today ProcMater Today: Proc 5:1635–1639

Mahmud KM, Yudistiram SA, Ramadhan AI (2016) Analytical study of forced convection in fluid cooling use nanofluid Al_2O_3- water on nuclear reactor core based fuel cylinder with hexagonal sub channel. Int J Energy Eng 6:8–15

Manimaran R, Palaniradja K, Alagumurthi N, Sendhilnathan S, Hussain J (2014) Preparation and characterization of copper oxide nanofluid for heat transfer applications. Appl Nanosci 4:163–167

Mao C, Huang Y, Zhou X, Gan H, Zhang J, Zhou Z (2014) The tribological properties of nanofluid used in minimum quantity lubrication grinding. Int J Adv Manuf Technol 71:1221–1228

Maxwell JC (1881) A treatise on electricity and magnetism, 2nd edn. Clarendon Press, Oxford, p 1881

Mehrali M, Sadeghinezhad E, Rashidi MM, Akhiani AR, Latibari ST, Mehrali M, Metselaar HSC (2015) Experimental and numerical investigation of the effective electrical conductivity of nitrogen-doped graphene nanofluids. J Nanopart Res 17:267

Menbari A, Alemrajabi AA, Razaei A (2016) Heat transfer analysis and the effect of CuO/Water nanofluid on direct absorption concentrating solar collector. Appl Therm Eng 104:176–183

Minea AA, Luciu RS (2012) Investigations on electrical conductivity of stabilized water based Al_2O_3 nanofluids. Microfluid Nanofluidics 13:977–985

Minea AA, Manca O (2017) Field-synergy and figure of merit analysis of two oxide water based nanofluid flow in heated tubes. Heat Transfer Eng 38:909–918

Mintsa HA, Roy G, Nguyen CT, Doucet D (2009) New temperature dependent thermal conductivity data for water-based nanofluids. Int J Thermal Sci 48:363–371

Mohammed HA, Al-aswadi AA, Shuaib NH, Saidur R (2011) Convective heat transfer and fluid flow study over a step using nanofluids: a review. Renew Sust Energy Rev 15:2921–2939

Naddaf A, Heris SZ (2018) Experimental study on thermal conductivity and electrical conductivity of diesel oil-based nanofluids of graphene nanoplatelets and carbon nanotubes. Int Commun Heat Mass Transf 95:116–122

Naraki M, Peyghambarzadeh SM, Hashemabadi SH, Vermahmoudi Y (2013) Parametric study of overall heat transfer coefficient of CuO/water nanofluids in a car radiator. Int J Therm Sci 66:82–90

Natarajan E, Sathish R (2009) Role of nanofluid in solar water heater. Int J Adv Manuf Technol 8:1–5

Nurdin I, Satriananda (2017) Investigation on electrical conductivity enhancement of water based maghemite (γ-Fe_2O_3) nanofluids. Int J Mater Sci Appl 6:32–36

Ohshima H (2003) Electrokinetic phenomena in a dilute suspension of spherical colloidal particles in a salt-free medium. Colloids Surf Physicochem Eng Asp 222:207–211

Pak BC, Choi YI (1998) Hydraulic Hydrodynamic and heat transfer study of dispersed fluids with submicron metallic oxide particles. Exp Heat Trans 11:151–170

Prakash SB, Kotin KN, Kumar PM (2016) Preparation and characterization of nanofluid (CuO/Water, TiO_2/Water). Int J Sci Eng 1:14–20

Prasher R, Bhattacharya P, Phelan PE (2005) Brownian-motion-based convective–conductive model for the effective thermal conductivity of nanofluids. J Heat Trans 128:588–595
Qin C, Lee BJ (2018) Effect of particle size distribution on optical property of nanofluids and DASC performance. Korean Soc Mech Eng 4:392–393
Roberts NA, Walker DG (2010) Convective performance of nanofluids in commercial electronics cooling systems. Appl Therm Eng 30:2499–2504
Rusconi R, Williams WC, Buongiorno J, Piazza R, Hu LW (2007) Numerical analysis of convective instabilities in a transient short-hot-wire setup for measurement of liquid thermal conductivity. Int J Thermophys 28:1131–1146
Sarojini KGK, Manoj SV, Singh PK, Pradeep T, Das SK (2013) Electrical conductivity of ceramic and metallic nanofluids. Colloids Surf Physicochem Eng Asp 417:39–46
Saterlie M, Sahin H, Kavlicoglu B, Liu Y, Graeve O (2011) Particle size effects in the thermal conductivity enhancement of copper-based nanofluids. Nanoscale Res Lett 6:217
Schramm LL, Stasiuk EN, Marangoni DG (2003) Surfactants and their applications. Ann Rep Program Chem Sect 99:3–48
Selvakumar P, Suresh S (2012) Convective performance of CuO/water nanofluid in an electronic heat sink. Exp Therm Fluid Sci 40:57–63
Shen LP, Wang H, Dong M, Ma ZC, Wang HB (2012) Solvothermal synthesis and electrical conductivity model for the zinc oxide-insulated oil nanofluid. Phys Lett A 376:1053–1057
Shoghl SN, Jamali J, Moraveji MK (2016) Electrical conductivity, viscosity, and density of different nanofluids: an experimental study. Exp Therm Fluid Sci 74:339–346
Sidik NAC, Yazid MNAWM, Mamat R (2017) Recent advancement of nanofluids in engine cooling system. Renew Sust Energy Rev 75:137–144
Sigmund WM, Bell NS, Bergstrom (2000) Novel powder-processing methods for advanced ceramics. J Am Ceram Soc 83:1557–1574
Sikadar S, Basu S, Ganguly S (2011) Investigation of electrical conductivity of titanium dioxide nanofluids. Int J Nanoparticles 4: 336–349
Silambarasan M, Manikandan S, Rajan KS (2012) Viscosity and thermal conductivity of dispersions of sub-micron TiO_2 particles in water prepared by stirred bead milling and ultrasonication. Int J Heat Mass Transf 55:7991–8002
Sohel Murshed SM, Nieto de Castro CA (2011) Contribution of Brownian motion in thermal conductivity of nanofluids. In: Proceedings of the world congress on engineering, vol III. London, UK
Sohel MR, Khaleduzzaman SS, Saidur R, Hepbasli A, Sabri MFM, Mahbubul IM (2014) An experimental investigation of heat transfer enhancement of a minichannel heat sink using Al_2O_3–H_2O nanofluid. Int J Heat Mass Transf 74:164–172
Sokhansefat T, Kasaeian AB, Kowsary F (2014) Heat transfer enhancement in parabolic trough collector tube using Al_2O_3/synthetic oil nanofluid. Renew Sust Energy Rev 33:636–644
Suganthi KS, Rajan KS (2012) Temperature induced changes in ZnO-water nanofluid: zeta potential, size distribution and viscosity profiles. Int J Heat Mass Trasnf 55:7969–7980
Suganthi KS, Parthasarathy M, Rajan KS (2013) Liquid-layering induced, temperature-dependent thermal conductivity enhancement in ZnO–propylene glycol nanofluids. Chem Phys Lett 561–562:120–124
Suganthi KS, Leela Vinodhan V, Rajan KS (2014) Heat transfer performance and transport properties of ZnO-ethylene glycol and ZnO–ethylene glycol–water nanofluid coolants. Appl Energy 135:548–559
Sundar LS, Singh MK, Sousa ACM (2013) Investigation of thermal conductivity and viscosity of Fe_3O_4 nanofluid for heat transfer applications. Int Commun Heat Mass 44:7–14
Syam Sumdar L, Singh MK, Ferro MC, Sousa ACM (2017) Experimental investigation of the thermal transport properties of graphene oxide/Co_3O_4 hybrid nanofluids. Int Commun Heat Mass 84:1–10
Teng T, Hung Y, Teng T, Mo H, Hsu H (2010) The effect of alumina/water nanofluid particle size on thermal conductivity. Appl Therm Eng 30:2213–2218

Tijani AS, Sudirman ASB (2018) Thermos-physical properties and heat transfer characteristics of water/anti-freezing and Al_2O_3/CuO based nanofluid as a coolant for car radiator. Int J Heat Mass Transf 118:48–57

Timofeeva EY, Gavriloy AN, McCloskey JM, Tolmachey YV, Sprunt S, Lopatina LM, Selinger JV (2007) Thermal conductivity and particle agglomeration in alumina nanofluids: experiment and theory. Phys Rev E 76:061203

Trinh PV, Anh NN, Quang LD, Thang BH, Hong PN, Hong NT, Khoi PH, Minh PN (2016) Thermal conductivity of ethylene glycol based copper nanoparticle decorated graphene nanofluids. Commun Phys 26:351–360

Usri NA, Azmi WH, Mamat R, Hamid KA, Najafi G (2015) Thermal conductivity enhancement of Al_2O_3 nanofluid in ethylene glycol and water mixture. Energy Procedia 79:397–402

Vasconcelos AA, Gomez AOC, Filho EPB, Parise JAR (2017) Experimental evaluation of SWCNT-water nanofluid as a secondary fluid in a refrigeration system. Appl Therm Eng 111:1487–1492

Wang XQ, Mujumdar AS (2007) Heat transfer characteristics of nanofluids: a review. Int J Therm Sci 46:1–19

Wang XJ, Zhu DS (2009) Investigation of pH and SDBS on enhancement of thermal conductivity in nanofluids. Chem Phys Lett 470:107–111

Wang X, Zhu D, Yang S (2009) Investigation of pH and SDBS on enhancement of thermal conductivity in nanofluids. Chem Phys Lett 470:107–111

Wen D, Ding Y (2005) Experimental investigation into the pool boiling heat transfer of aqueous based γ-alumina nanofluids. J Nanopart Res 7:265–274

White SB, Shih AJ, Pipe KP (2011) Investigation of the electrical conductivity of propylene glycol-based ZnO nanofluids. Nanoscale Res Lett 6:346

Wong KFV, Kurma T (2008) Transport properties of alumina nanofluids. Nanotechnology 19:345702

Xia G, Jiang H, Liu R, Zhai Y (2014) Effects of surfactant on the stability and thermal conductivity of Al_2O_3/de-ionized water nanofluids. Int J Therm Sci 84:118–124

Xie H, Yu W, Chen W (2010) MgO nanofluids: higher thermal conductivity and lower viscosity among ethylene glycol-based nanofluids containing oxide nanoparticles. J Exp Nano Sci 5:463–472

Xuan Y, Li Q (2000) Heat transfer enhancement of nanofluids. Int J Heat Fluid Flow 21:58–64

Xuan Y, Li Q, Hu W (2003) Aggregation structure and thermal conductivity of nanofluids. AIChE J 49:1038–1043

Xuan Y, Li Q, Tie P (2013) The effect of surfactants on heat transfer feature of nanofluids. Exp Therm Fluid Sci 46:259–262

Xue QZ (2005) Model for thermal conductivity of mixture of carbon-nanotube based composites. Physisca B Condens Matter 368:302–307

Yang B, Han ZH (2006) Temperature-dependent thermal conductivity of nanorod-based nanofluids. Appl Phys Lett 89:083111

Younes H, Christensen G, Luan X, Hong H, Smith P (2012) Effects of alignment, pH, surfactant, and solvent on heat transfer nanofluids containing Fe_2O_3 and CuO nanoparticles. J Appl Phys 111:064308

Yousefi T, Veysi F, Shojaeizadeh E, Zinadini S (2012) An experimental investigation on the effect of Al_2O_3-H_2O nanofluid on the efficiency of flat-plate solar collectors. Renew Energ 39:293–298

Yu W, Choi SUS (2003) The role of interfacial layers in the enhanced thermal conductivity of nanofluids: a renovated Maxwell model. J Nanopart Res 5:167–171

Yu W, Xie H, Chen L, Li Y (2010) Investigation on the thermal transport properties of ethylene glycol-based nanofluids containing copper nanoparticles. Powder Technol 197:218–221

Yu-Hua L, Wei Q, Jian-Chao F (2008) Temperature dependence of thermal conductivity of nanofluids. Chin Phys Lett 25:3319–3322

Zadkhast M, Toghraie D, Karimipour A (2017) Developing a new correlation to estimate the thermal conductivity of MWCNT-CuO/water hybrid nanofluid via an experimental investigation. J Therm Anal Calorim 129:859–867

Zakaria I, Azmi WH, Mohamed WANW, Mamat R, Najafi G (2015) Experimental investigation of thermal conductivity and electrical conductivity of Al_2O_3 nanofluid in water-ethylene glycol mixture for proton exchange membrane fuel cell application. Int Commun Heat Mass 61:61–68

Zakaria I, Azmi WH, Mamat AMI, Mamat R, Saidur R, Talib SFA, Mohamed WANW (2016) Thermal analysis of Al_2O_3-water ethylene glycol mixture nanofluid for single PEM fuel cell cooling plate: an experimental study. Int J Hydrogen Energy 41:5096–5112

Zawrah MF, Khattab RM, Girgis LG, Daidamony HEl, Aziz REA (2016) Stability and electrical conductivity of water-base Al_2O_3 nanofluids for different applications. HBRC J 12:227–234

Zhang G, Kandlikar SG (2012) A critical review of cooling techniques in proton exchange membrane fuel cell stacks. Int J Hydrog Energy 37:2412–2429

Zhou D, Wu H (2014) A thermal conductivity model of nanofluids based on particle size distribution analysis. Appl Phys Lett 105:083117

Zhu HT, Yin YS (2004) A novel one-step chemical method preparation of copper nanofluids. J Colloid Inter Sci 227:100–130

Zhu D, Wang L, Yu W, Xie H (2018) Intriguingly high thermal conductivity increment for CuO nanowires contained nanofluids with low viscosity. Sci Rep Sci Rep 8:5282

Zyla G, Fal J (2016) Experimental studies on viscosity, thermal and electrical conductivity of aluminium nitride-ethylene glycol (AlN-EG) nanofluids. Themochim Acta 637:11–16

Zyla G, Fal J (2017) Viscosity, thermal and electrical conductivity of silicon dioxide-ethylene glycol transparent nanofluids: an experimental studies. Thermochima Acta 650:106–113

Synthesis, Characterization, and Application of Biogenic Nanomaterials: An Overview

Shruti Kakkar, Bhupendra Harjani, Naresh Ledwani and Lalita Ledwani

Abstract Nanotechnology is the most promising and interdisciplinary field of research that has been growing rapidly worldwide in different fields. Nanotechnology commits a sustainable development through its continuous growth toward green chemistry to develop "green nanotechnology". Green nanotechnology is implementation of green chemistry and green engineering principles in the field of nanotechnology to influence the size of nanoparticles within a nanoscale range to make biogenic nanoparticles. These biogenic nanomaterials can help in solving serious environmental challenges in the area of wastewater treatment, pollutant removal, fatal diseases, climate change, and solar energy conversion. This review provides a brief idea about the current potential applications of nanotechnology into the bio-environmental systems and how this technology can help in the synthesis of biogenic nanoparticle. Biogenic synthesis of nanoparticles is an environmentally friendly approach; it reduces environmental pollutants and conserves natural resources without creating any environmental damages.

Keywords Nanotechnology · Green nanotechnology · Nanomaterials · Biogenic · Bio-environment

S. Kakkar · L. Ledwani (✉)
Department of Chemistry, Manipal University Jaipur, Rajasthan, India
e-mail: lalita.ledwani@jaipur.manipal.edu

B. Harjani
F H Medical College, Etmadpur, UP, India

N. Ledwani
Bhagwan Mahaveer Cancer Hospital and Research Centre, Jaipur, Rajasthan, India

L. Ledwani and J. S. Sangwai (eds.), *Nanotechnology for Energy and Environmental Engineering*, Green Energy and Technology,
https://doi.org/10.1007/978-3-030-33774-2_2

1 Introduction

1.1 Nanotechnology

Nanotechnology has recently become the most important area of research which deals with the manufacturing of new materials; it creates new processes and new applications (Ibrahim et al. 2016). Nanoparticles are synthesized by numerous physical, chemical, and biological methods. A biological method includes microbes, fishes, plants, and so on, for manufacturing of biogenic nanoparticles. This biological process does not involve any harmful chemicals and solvent. This method of nanoparticle synthesis is termed as "green synthesis".

It combines knowledge from diverse dimensions of science and found a major contribution to the field of physics, chemistry, biology, and medicine. It is one of the most rapidly growing fields of technology that has raised variety of new frontiers of research. Recently, nanotechnology focused on developing "clean" and "green" technologies which have various significant environmental benefits and has become a brand known as "green technology".

Nanotechnology is also formed in conjugation with biotechnology and engineering technologies, for synthesis of environment-friendly biogenic nanoparticles. The nanoparticles made from green innovations are eco-friendly, energy-efficient, reduce waste, and diminish greenhouse gas emissions. These nanoparticles have several advantages because of uniform size and shape. They remove harmful chemicals and pollutants from environment by counteracting them or through alteration in various synthesis conditions. These synthesized nanoparticles do not disturb earth's ecosystem and also conserves its natural resources (Ali Mansoori et al. 2008; Bhavani et al. 2014).

1.2 Green Technology and Green Nanotechnology

Green technology is an environment-friendly and innovative technology which conserves natural resources in order to make a sustainable development. The major goals of this technology are to reduce non-renewable resource, reduce energy usage, and increase the human quality in life without damaging natural resources on earth. This includes environment sustainability, source reduction, energy, green building, and green chemistry.

Green nanotechnology is the branch of green technology, with green energy system, green information technology, that uses green chemistry and green engineering principles. The principles of this technology are to produce safer and sustainable nanoparticles. For sustainable development of these nanoparticles, the biogenic process is required nowadays because they are eco-friendly, cost-effective, and consume less energy; it does not impart any hazardous effect on the environment and produces safer products and by-products (Patra and Baek 2014; Rani and Sridevi 2017).

2 Approaches for the Synthesis of Nanoparticles

Nanoparticles (NPs) are a group of substances where at least one dimension is lesser than the 100 nm. A nanoparticle shows various properties, such as enhanced reactivity, sensitivity, surface area, and stability. Nanoparticles are mainly divided into two parts: organic and inorganic nanoparticles. Natural or organic nanoparticles include carbon nanoparticles such as fullerenes, and inorganic nanoparticles include magnetic nanoparticles, steel nanoparticles (like silver and gold), and semiconductor nanoparticles (like titanium dioxide, magnesium, and zinc oxide). Various methods are used to increase the properties of nanoparticles and reduce the production costs. The processing conditions of nanoparticles are needed to be controlled for identical shape, identical size, and identical chemical composition of the particles (Ali Mansoori et al. 2008).

According to Siegel, nanomaterials are differentiated by 0-dimensional, 1-dimensional, 2-dimensional, and 3-dimensional (Lusvardi et al. 2017). The nanomaterials exist in different forms, such as single, fused, and aggregated with spherical, tubular, and irregular shapes. Nanoparticles are synthesized by two approaches: top-down and bottom-up (Mom et al. 2007).

The top-down approach includes the breaking of larger materials into smaller nanoparticles. It refers to slicing and breaking of large material to get nano-sized particles. And the bottom-up approach or constructive method refers to building up of the material from the bottom: atom by atom, molecule by molecule, which means a build-up of material from atom to clusters to nanoparticles (Chen et al. 2014; Marchiol 2012; Shukla et al. 2017). Top-down approach is mainly used in microfabrication methods. Attrition and milling for making nanoparticles are examples of top-down processes. The bottom-up approach is mainly used in the concept of molecular self-assembly. Synthesis of biogenic nanoparticles with the help of microorganism and plants by bottom-up approach is a very prominent, easy, and cost-effective method to synthesize green nanoparticles. The synthesis of nanoparticles by top-down and bottom-up approaches is shown in Fig. 1.

2.1 Synthesis of Nanoparticles

Various conventional techniques and several methods are used for manufacturing of nanoparticles (NPs). A couple of processes like physical, chemical, and biological are used for the synthesis of nanoparticle. Physical methods include plasma arcing, ball milling, thermal evaporate, pyrolysis, laser deposition, and so on. The chemical methods include colloids, colloids solution, and sol–gel method for nanoparticles synthesis. But these methods are costly and affect human health by causing certain environmental risks on the atmosphere and the survival of all organisms. The non-toxic and eco-friendly methods for manufacturing of nanoparticles are biological methods. The biogenic synthesis of nanoparticles with exact dimension and shapes

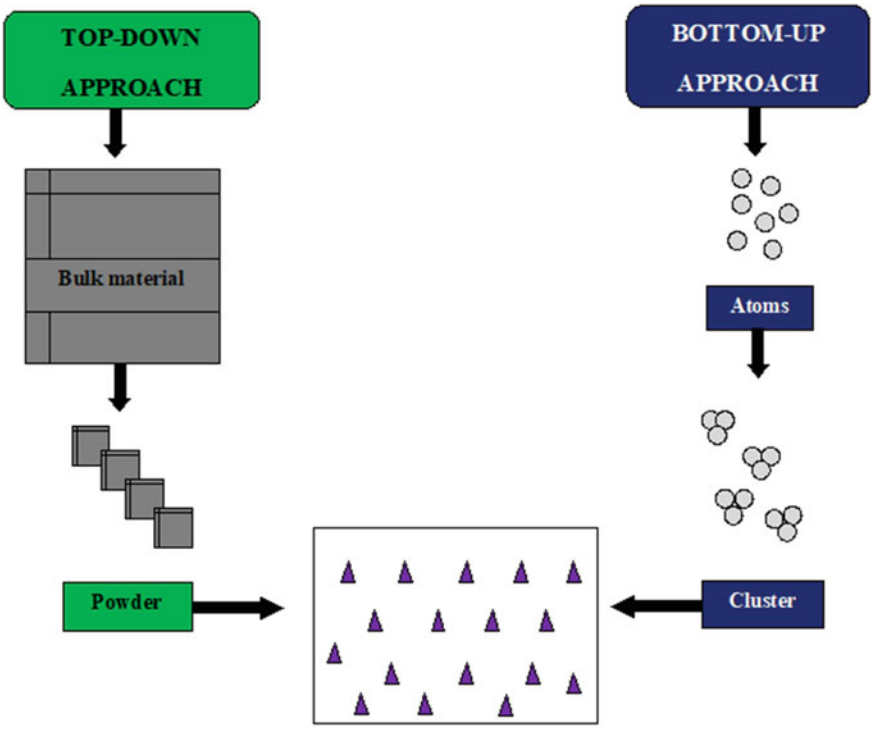

Fig. 1 Approaches for the synthesis of nanoparticles

is considered as cost-effective and novel method in biomaterial science. The synthesis of nanoparticles from biogenic methods is now most commonly used for medical, agriculture, and environmental purposes. A symmetric representation of different methods used for the manufacturing of these nanoparticles is shown in Fig. 2.

Biogenic synthesis includes the use of naturally present microorganism for the synthesis of nanoparticles. Microorganisms and pathogen cells are interacting with metals and form nanoparticles. The most commonly used microorganisms are fungi bacteria and algae. Except bacteria and fungi, on the other hand, plants are also used for the synthesis of nanoparticles in the past few years. Several parts of plants have also been used for the synthesis of nanoparticles, such as leaves, stems, shoots roots, flowers, and barks. In the biological method, the yield of nanoparticles is very high as compared to other conventional methods of synthesis and they do not cause any environmental problems. These biogenic nanoparticles are non-toxic in nature, biodegradable, and environment-friendly. The synthesis of biogenic nanoparticles is shown in Fig. 3.

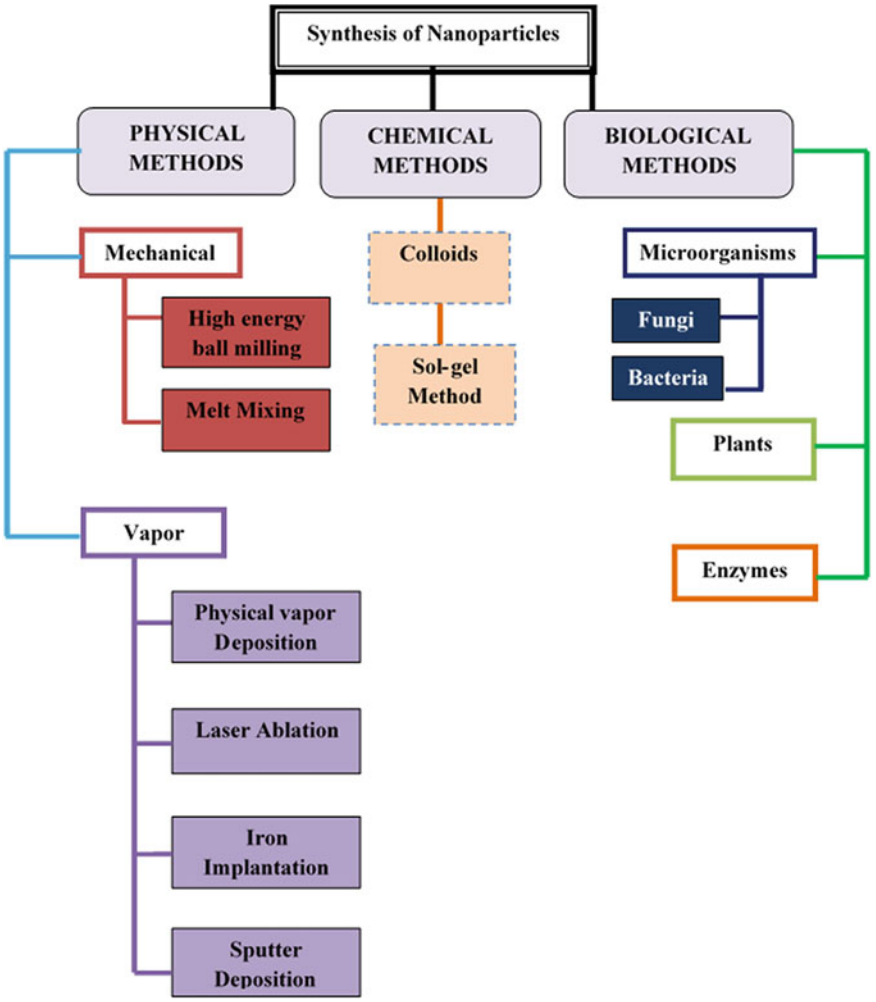

Fig. 2 Methods for the synthesis of nanoparticles

2.2 Types of Nanoparticles

2.2.1 Metal Nanoparticles

Metal nanoparticles are a type of nanoparticle mainly synthesized by biological methods. They help to protect the system against toxic effects of metal ion concentration. Different microorganisms and plants show tolerance to metal ions through this system. The most commonly used microorganism for the synthesis of metal nanoparticles is bacteria and fungi. The mainly synthesized metal nanoparticles through biological system are silver and gold nanoparticles.

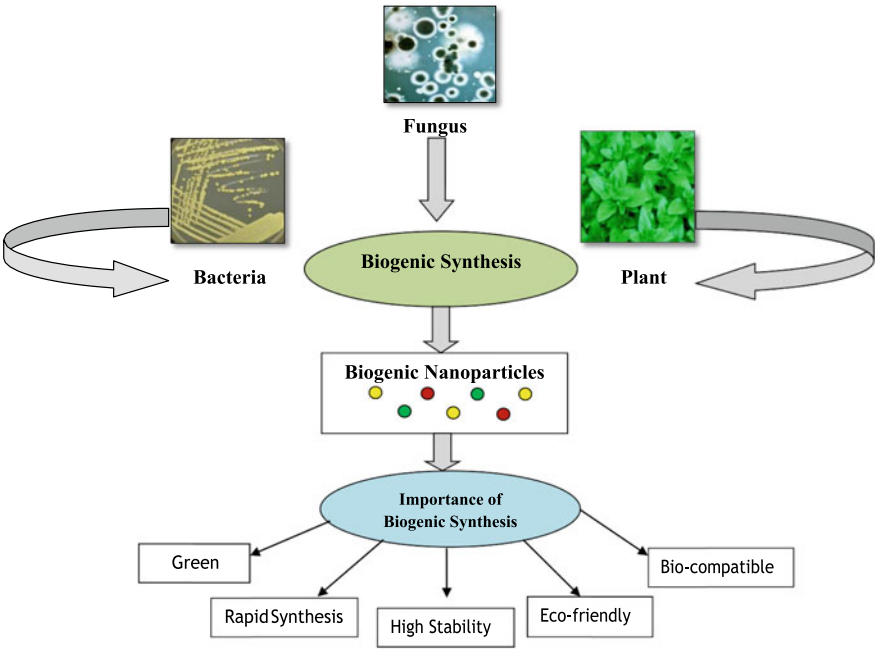

Fig. 3 Biogenic synthesis of nanoparticles

(a) Silver nanoparticles (Ag-NPs)

Silver is one of the fundamental elements that make up our planet (Mom et al. 2007). Conventionally, the silver NPs are synthesized by various chemical methods. Silver NPs are ultrafine particles of silver. They are 10–100 nm large and differ from the bulk silver as they have different color, such as yellow, as opposed to the silver (Carlson et al. 2008; Chaloupka et al. 2010; Morones et al. 2005). The two most conventional methods for synthesizing silver nanoparticles (Ag-NPs) via chemical reduction are Turkevich method (1951), where silver is reduced by trisodium citrate, and Brust method (1994), where silver is reduced by sodium borohydride. For biomedical applications, mainly bacteria, fungi, and plants are used. They produce very large amount of silver nanoparticles which show high antibacterial and antimicrobial activities against known pathogens.

The most commonly used biochemical methods for production of silver NPs are silver nitrate and plant extracts. In the biochemical reactions, $AgNO_3$ reacts with plant extracts and form Ag-NPs. There are several advantages of biogenic synthesis over the chemical synthesis of silver nanoparticles: the low cost, eco-friendly nature, and antimicrobial properties of silver show considerable attention in bio-environment system (Chen and Schluesener 2008). Because of higher antimicrobial properties the silver nanoparticles are widely used in various pharmaceuticals and biomedical treatments (Chugh et al. 2018; Natsuki et al. 2015; Sotiriou and Pratsinis 2011).

Nowadays, silver NPs also show a wide range of applications in wastewater treatments, laundry detergents, and other cleaning stuffs (He et al. 2018; Rai et al. 2012). Various properties of silver and silver nanoparticles are shown in Fig. 4.

(b) **Gold nanoparticles (Au-NPs)**

Gold nanoparticles (Au-NPs) are most commonly used in biotechnology and biomedical areas because of their large surface area and high electron conductivity. Gold nanoparticle is used as in assemblies of oligonucleotides, antibodies, and proteins to form bioconjugates. These bioconjugates show various applications in biomedical and biomaterials fields (Katas et al. 2018; Kefayat et al. 2019; Khan and Rizvi 2014; Khan et al. 2014; Lee et al. 2007; Vu et al. 2019). Au-NPs are emerging as a promising agent for cancer therapy and also proved to be the safest and much less toxic agents for drug delivery. Gold nanoparticles occur as a cluster of gold atoms up to 100 nm in diameter. The conventional methods for synthesizing gold nanoparticles (Au-NPs) via chemical reduction are the Turkevich method, Brust method, and Martin method. The biogenic synthesis of gold nanoparticles is also done by various microorganisms like bacteria and fungi. For the synthesis of biogenic gold NPs, the most commonly used microorganisms are *Pseudomonas aeruginosa* and *Rhodopseudomonas* (Singh et al. 2014, 2015). Schematic representations of gold nanoparticles used in biomedical practices are shown in Fig. 5.

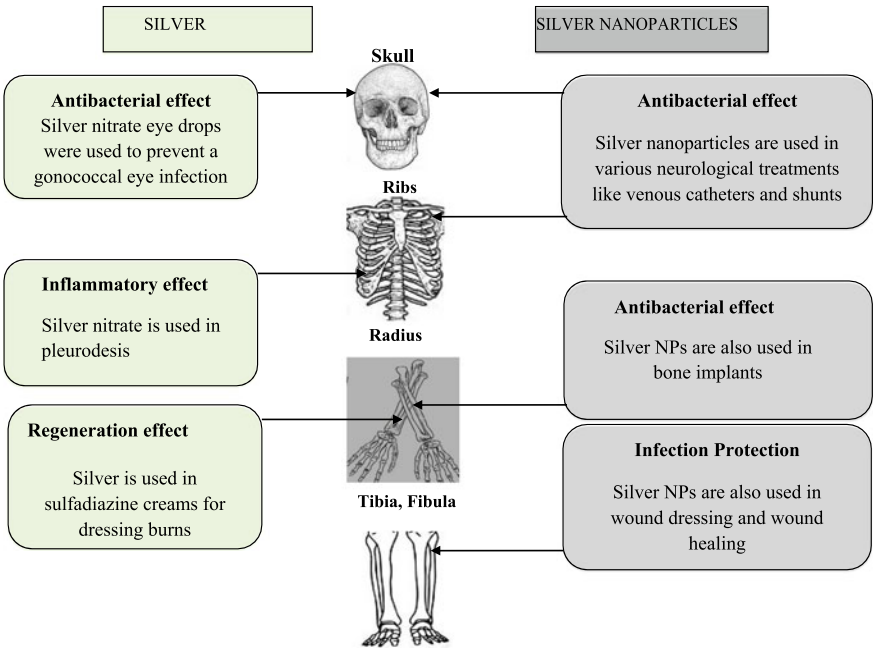

Fig. 4 Properties of silver nanoparticles

Fig. 5 Properties of gold nanoparticles

(c) **Zinc oxide nanoparticles (ZnO)**

Zinc is one of the most essential microelements. Owing to nano-dimension, the zinc particle ZnO acquires specific physical and chemical characteristics which are different from known metal compounds (Bogutska et al. 2013). Nanoscale zinc particles are typically 20–40 nm in size and are also available in 100 nm ranges. The ability of ZnO nanoparticles is to absorb a wide spectrum of radiation (ultraviolet, microwave, infrared, and at radio frequencies) that can be used for manufacturing cosmetic creams, ointments, and so on, which protect the organism from ultraviolet radiation. ZnO nanoparticles of 20–30 nm in size display antibacterial properties which are now used in the textile industry for producing fabrics for clothes. The formation of nanoparticles was monitored by SEM and FTIR spectroscopy.

(d) **Copper nanoparticles (Cu-NPs)**

Copper is a ductile metal, which has very high thermal and electrical conductivity. Cu-NPs show widespread applications because of their special properties like antibacterial activities, strong affinity, and strong catalysts activity. Cu-NPs have specific ligand binding activity with other nanoparticles because of their high surface area and volume ratio. Copper nanoparticles are round in shape and they appear as a brown to black powder and have various potential applications in the treatment of wastewater and radioactive waste by photochemical reactions.

(e) **Titanium dioxide nanoparticles (TiO_2 NPs)**

Recently, titanium dioxide nanoparticles are manufactured in large quantities because of its photostability properties. TiO_2 nanoparticles have the ability to block the ultraviolet radiation exposed by sun. Nowadays, TiO_2 nanoparticles are widely used in sunscreens to protect human skin by photo damage. They are widely used because of their high photocatalytic and photostability properties. In the medicinal field, TiO_2 nanoparticles play an important role in manufacturing of nanomedicine. TiO_2 NPs can also be used in the treatment of wastewaters, like clinical wastewater and hazardous industrial wastewater (Lusvardi et al. 2017). Recently, the biogenic titanium dioxide nanoparticles are most commonly used in advanced imaging and nanotherapeutics.

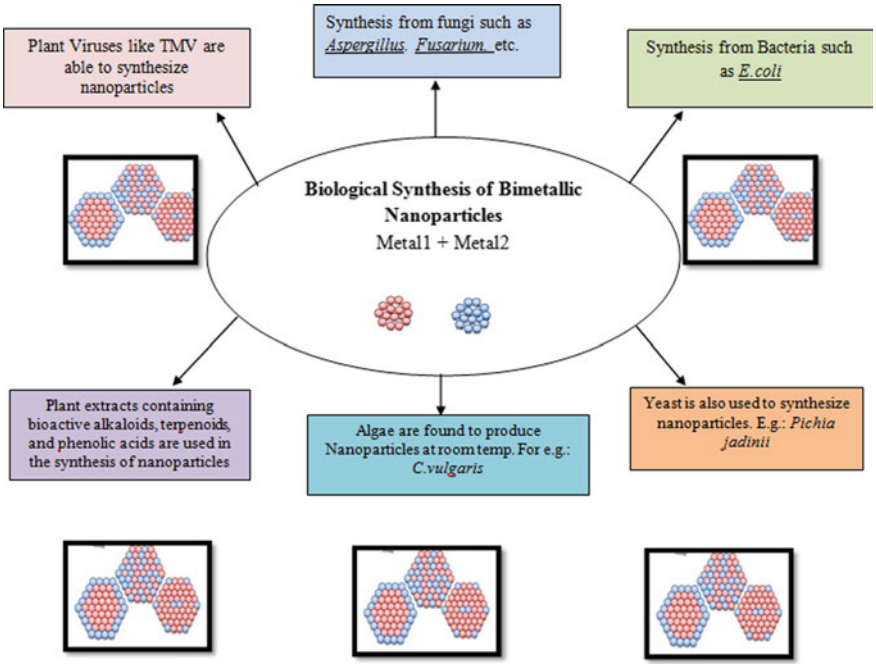

Fig. 6 Synthesis of bimetallic nanoparticles

2.2.2 Bimetallic Nanoparticles (BMNPs)

Syntheses of nanoparticles by a combination of two metal nanoparticles are termed as "bimetallic nanoparticles" (BMNPs) (Mazhar et al. 2017). In this type of nanoparticle, two metal nanoparticles have separate function to carry out overall reaction. Bimetallic nanoparticles have specific catalytic and selective activity than monometallic nanoparticles. Syntheses of bimetallic nanoparticles from different microorganisms were shown in Fig. 6.

There are several methods for the synthesis of bimetallic nanoparticles. The most commonly used methods are synchronous complexing method, sequential complex method, and partial substitution method. In synchronous method, two different metal ions are mixed with polymers to make bimetallic nanoparticles. The most commonly used bimetallic nanoparticles are shown in Fig. 7.

2.3 Factors Influencing the Synthesis of Nanoparticles

Various factors, such as temperature, pressure, pH, time, particle size, shape, and the concentration of the extracts, affect the synthesis and characterization of

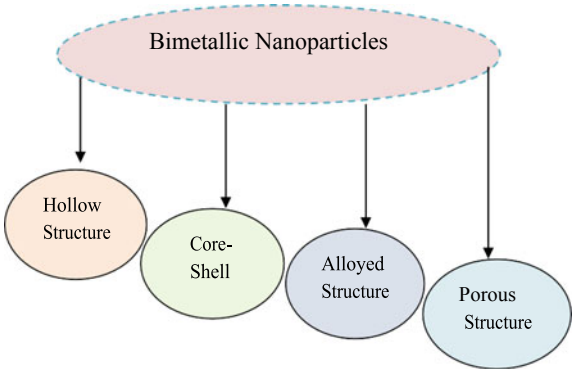

Fig. 7 Types of bimetallic nanoparticles

nanoparticles. Factors that influence the synthesis of nanoparticles are shown in Fig. 8.

1. **Mode of synthesis**: The synthesis of nanoparticles by physical and chemical methods includes mechanical protocols and various chemicals (organic and inorganic). The biological protocols involve natural products, respectively. The chemical and physical methods are very costly and their synthesized nanoparticles show several harmful effects on the environment. The biological modes of synthesis of nanoparticles are used widely because this mode of synthesis of nanoparticles is non-toxic and environmentally friendly in nature (Marchiol 2012; Patra and Baek 2014).
2. **pH**: pH is the most important and prominent factor for the synthesis of nanoparticles. It influences the size, texture, mode of synthesis of nanoparticles by alteration in the consistency of the media, or by altering the pH of the solution media.

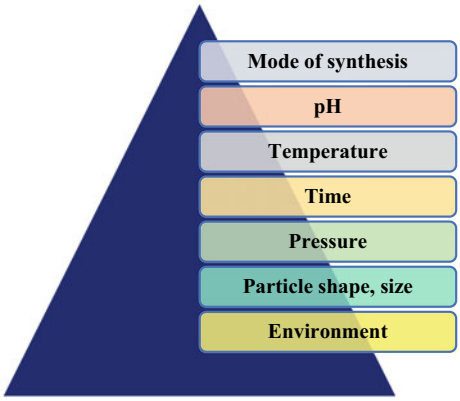

Fig. 8 Factors that influence the synthesis of nanoparticles

3. **Temperature**: Temperature is another influencing factor that affects the synthesis of nanoparticles. All three methods—physical, chemical, and biological—require the highest temperature for the synthesis of nanoparticles. The physical method requires at least 350 °C temperature and the chemical method requires less than 350 °C temperature. The synthesis of nanoparticles through biological system requires less than 100 °C temperature.
4. **Time**: Time influences properties and the characteristics of synthesized nanoparticles is the most important factor which influences the characteristics of nanoparticles. Variations in time affect the growth of nanoparticles, storage, and shelf life of the nanoparticles. The nanoparticles synthesized by biogenic approach are mainly influenced by incubation time.
5. **Pressure**: Pressure which is used for the reaction medium directly affects the size and shape of the nanoparticles.
6. **Particle Shape and Size**: Particle shape and size also play important role in the synthesis of nanoparticles. Properties of nanoparticles are based on accurate size and shape. Shape and size mainly affects the chemical properties of the nanoparticles.
7. **Environment**: Favorable environmental conditions determined the nature of the nanoparticles. Environment affects the physical and chemical properties of nanoparticles (Grillo et al. 2014; Hua et al. 2012; Ibrahim et al. 2016).

3 Characterization of Nanoparticles

Characterization means analysis of the materials, structure, composition, and physical–chemical properties. Characterization of nanoparticles is done by two most common methods: microscopy and spectroscopy.

Microscopy

1. Scanning electron microscopy (SEM)
2. Transmission electron microscopy (TEM)
3. Field emission scanning electron microscopy (FESEM)

Spectroscopy:

1. X-ray diffraction (XRD)
2. Ultraviolet spectroscopy (UV–Vis)
3. Fourier transform infrared spectroscopy (FTIR)

Characterization of nanoparticles is done by various techniques, like; SEM, TEM, FTIR, AFM, XRD, UV–Vis spectroscopy. These characterization techniques are most commonly used to determine the size, shape, structure, and surface area of the synthesized nanoparticles. Morphology and size of the nanoparticles are determined by TEM, SEM, and AFM (Choi et al. 2007). Summary of the experimental techniques that are used for nanoparticle characterization is shown in Table 1.

Table 1 Characterization techniques for nanoparticles

Techniques	Utility
Scanning electron microscopy (SEM)	Morphology/topology/imaging
Transmission electron microscopy (TEM)	Detect shape, size and localize NPs in matrices
UV–Vis spectroscopy (UV–Vis)	Optical properties, size, concentration
X-ray diffraction (XRD)	Crystal structure, composition
Fourier transform infrared spectroscopy (FTIR)	Surface composition, ligand binding
Field emission scanning electron microscopy (FESEM)	Topological information

(a) **Scanning electron microscopy (SEM)**

The basic principle of SEM is when the beam of electrons scattered on the surface of the specimen, they will interact with the atoms present in the samples. After the interaction SEM shows signals by generating backscattered electron or secondary electrons. The results were shown in the form of X-rays that gives the morphological and topological information of the samples.

Advantages	Disadvantages
Bulk samples can be observed	Samples must have surface electrical conductivity
Generates photo-like images	Time-consuming
Very high-resolution images	–

(b) **Transmission electron microscopy (TEM)**

TEM is another microscopy technique in which the beam of electrons passed through a thin specimen interacts with the samples. After the interaction of transmitted electrons and samples the result is shown by generating an image. These images are seen using CCD cameras or fluorescent screens.

Advantages	Disadvantages
Powerful magnification and resolution	Very expensive
Applied in various educational and scientific systems	Laborious sample preparation
Gives information of the elements and its structures	Require special trainings
Images are high-quality and detailed	Require special housing and maintenance

(c) **Field emission electron microscopy (FESEM)**

FESEM is a microscopic technique in which the microscope is used along with electrons. In this, the electrons are generated by field emission source and the specimen is scanned by electrons. After the interaction the results were shown in a zigzag pattern.

Advantages	Disadvantages
High-quality and low-voltage images	Very expensive
No need to add coatings on the materials	–

(d) **UV–visible spectroscopy (UV–Vis)**

It is a spectroscopic technique which absorbs both ultraviolet and visible lights. It follows Beer-Lambert law. It means when a beam of monochromatic light passed through a sample, the rate of radiation intensity and the thickness of the sample are directly proportional to the concentration of the sample.

Advantages	Disadvantages
Give extremely accurate readings	Spectra are not highly specific for particular molecules
Easy and simple to operate and inexpensive	Operation and analysis require special training

(e) **X-ray diffraction (XRD)**

X-ray diffraction is a method that determines the crystalline structures of the compounds. It is preliminarily used for crystalline materials. Analysis of the samples is done by X-rays. These X-rays are generated by cathode ray tubes present inside the XRD system.

XRD is an exclusive method in determination of crystallinity of a compound. It is mainly used for crystalline material. It differentiates amorphous and crystalline material. The analysis of XRD is based on constructive interference of

monochromatic X-rays and a crystalline sample. The X-rays are generated in XRD analysis by cathode ray tube.

Advantages	Disadvantages
Least expensive	Size limitations
Best method to determine crystal structure	Low in sensitivity

(f) **Fourier transform infrared spectroscopy (FTIR)**

FTIR is another spectroscopy technique that determines the organic and inorganic components of the unknown mixture of the samples. The main purpose of FTIR analysis is to identify the chemical bonds present inside the samples.

Advantages	Disadvantages
Short measurement time	More expensive
Measures entire wavelength range	Cannot detect atoms or monoatomic ions
Better sensitivity	–

4 Applications of Nanoparticles

Nanotechnology is nowadays used as a most powerful tool in various fields. It rapidly gains importance toward the wide range of biomedical, industrial, and environmental applications. Latest applications of nanotechnology are shown in biogenic synthesis of nanoparticles. These biogenic nanoparticles show their advantages in biomedicinal to drug delivery systems and early disease detections, agriculture to crop protections, safe environment, safe water purifications, and solar energy systems. The synthesis of nanoparticles through biological methods will play a major role in many technologies because of its cost-effective, rapid synthesis, reasonable, and eco-friendly nature.

Today, the products manufactured by these biogenic nanomaterials have specific applications in the treatment of cancer, early disease detection, and diagnosis. There are another several widespread applications of these biogenic nanoparticles in wastewater purifications, pharmaceuticals, agriculture, and food products, which were shown in Fig. 9.

4.1 Biomedical Application of Biogenic Nanoparticles

(a) **Anticancer and drug delivery**

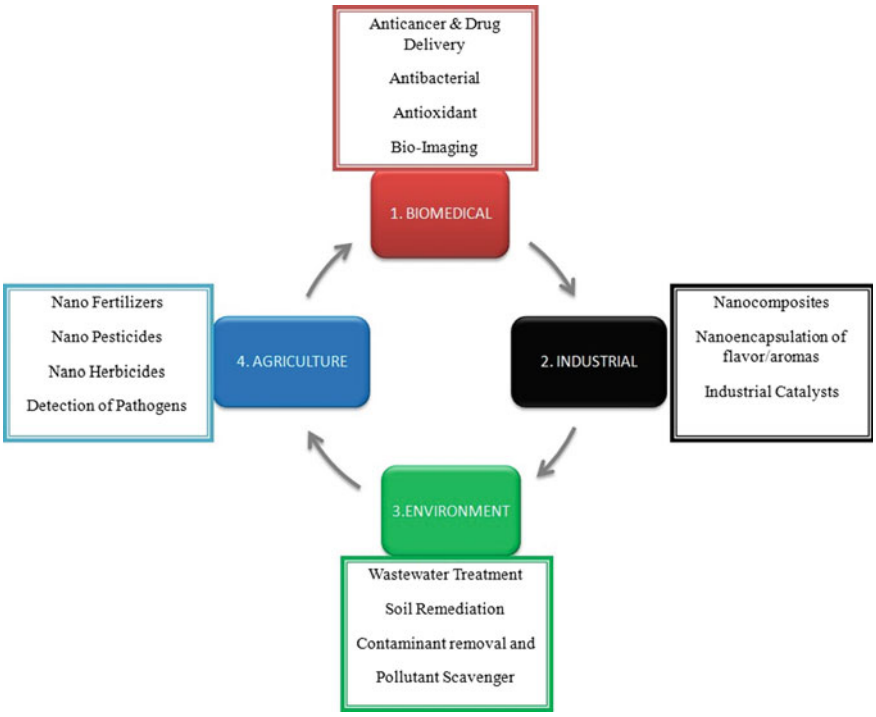

Fig. 9 Applications of nanotechnology in different fields

Biogenic nanoparticles are recently used in drug delivery and anticancer treatment because of their advantageous properties (Hong et al. 2006). The biogenic nanoparticles are designed as small so that they can be easily used as oral drug and for nanoencapsulations (Pandey and Khuller 2007). Gold and silver nanoparticles are the most commonly used nanoparticles in biomedical applications. Both gold and silver nanoparticles are capable of detecting and diagnosing the cancer.

Nanoparticles synthesized by physical and chemical methods are toxic in nature. These nanoparticles show various toxic side effects on human body. So there is a need to produce biogenic nanoparticles because of their cost-effective and eco-friendly in nature. Biogenic synthesis of metal nanoparticles provides cost-effective and safe therapeutics drugs for the treatment of cancer (Campbell et al. 2019; Chaloupka et al. 2010; Pandey and Khuller 2007). Nanoparticles like TiO_2, silica, and Au are used nowadays in the treatment of breast cancers. These nanoparticles have some specific ligand-binding characteristics that are capable in detecting the tumors in breast cancer images (Mu et al. 2017; Peng et al. 2014).

(b) **Antibacterial activities**

The biogenic synthesis of nanoparticles from microbial sources, like plants, bacteria, fungi, and so on, has become an emerging field due to simple, fast, eco-friendly,

energy-efficient, and less toxic nature. The most commonly used microorganisms are fungi and bacteria that have higher potential antimicrobial activity against known pathogens. Silver nanoparticles are mainly used against the pathogenic bacteria because silver have specific biocidal activity. Nanoparticles synthesize endophytic fungus, *Pestalotia sp*, and the bacteria *S. aureus and S. typhi*. *Pseudomonas stutzeri AG259* was the first bacterial strain synthesized by nanoparticles (Chugh et al. 2018).

(c) **Bio-imaging and disease diagnosis**

Nanoparticle technology offers the possibility for characterization and imaging of tissues, lesion, and cells. Recently, in early disease detection, nanoparticles are used as a "biomarker". The biogenic synthesis of these biomarkers includes the synthesis of small peptides. These peptide biomarkers are sent into the cells at a particular location and after that they indicate the signals whether a disease is present or not (Campbell et al. 2019). These peptide biomarkers are also used in protein analysis, early disease detection, and tissue imaging (Cai et al. 2011; Vu et al. 2019).

4.2 Industrial Application of Biogenic Nanoparticles

a. **Nanocomposites**

Nanocomposites are a type of nanoparticles in which the nanoparticles are incorporated into a matrix to improve the properties of nanoparticles. These matrix-incorporated nanoparticles are termed as "nanocomposites". The carbon nanotubes are specific matrix materials which enhance the properties of nanoparticles (Katas et al. 2018). Some examples of nanocomposites are:

1. **Nanoshells**: Nanoshells are a type of nanocomposites that absorb the heat from infrared light and help in destroying the tumor cells.
2. **Nanotubes**: Nanotubes are a scaffold of polymer composites which helps in bone and joint replacement and repairing the structures of bones.
3. **Use of graphene to manufacture composites**: Addition of graphene (Campbell et al. 2019) to the composites is used to make the strong nanoparticle composites. These manufactured composites and its components have the higher strength-to-weight ratios.

b. **Nanoencapsulation of flavor and aromas**

Bio-nanocomposite or nanoencapsulation shows various applications in food and food-packaging materials. Use of flavors and aromas in food helps in preserving the food materials. Nanoencapsulation is an attractive and emerging technology that is recently used in food industries. Nanoencapsulation technique provides specific protection to the food compounds by essential oils, such as glycerol, phenol, and triglycerides (Mousavi and Rezaei 2011).

4.3 Environmental Application of Biogenic Nanoparticles

After meeting the major challenges in environment development and sustainability, the biogenic nanomaterials can help in solving serious environmental challenges in the area of wastewater treatment, pollutant removal, fatal diseases, climate change, and solar energy conversion. Nanoparticles are considered a good source for removal of many organic compounds due to their chemical stability, high oxidation efficiency, cheap, and are environmentally friendly (Ali Mansoori 2008; Bhavani et al. 2014; Cai et al. 2011; Hasan et al. 2016).

Some of the environment applications (Chaloupka et al. 2010; Chen and Schluesener 2008; Chen et al. 2014; Choi et al. 2007) of nanoparticles are:

a. **Biosensors**: Various nanoparticles, biogenic and non-biogenic, like oxide, metals are used in constructing of biosensors, and these nanoparticles play a major role in detecting and sensing systems (Sotiriou and Pratsinis 2011).
b. **Wastewater treatment**: Nanotechnology shows three types of advantages in the treatment of wastewater; majorly like treatment and remediation, sensing and detection, and pollution control. Cleaning of wastewater streams, contaminants that are toxic in nature, or those that are difficult-to-treat promised treatment of wastewater because these technologies are rapid, specific, and worthwhile solutions for the treatment of contaminants. Significant concerns also focused on soil remediation and groundwater sedimentation. Some latest examples of biogenic treatment of wastewater are nanocoagulants to extract water contaminants from wastewater streams. In this the Actinia-like biomimetic micellar nanocoagulant is recently used to treat groundwater. The major use of this technology is to remove contaminants from water and produce high-quality water (Liu et al. 2019).
c. **Nanomaterials for wastewater clean-up**: The titanate nanofibers are used as an absorbent for the removal of heavy metals or several radioactive ions from the wastewater. These types of nanoparticles are mostly used in the treatment of radioactive wastewater (Hua et al. 2012).
d. **Nanotechnology for battery recycling**: Batteries are yet containing different types of chemicals and hazardous heavy metals, like mercury, lead, copper, nickel, cadmium and so on, which defile the environment and cause several risks to human health when they are improperly disposed off. Recently, pure zinc oxide nanoparticles are used to form recyclable batteries. The Zn-MnO_2 alkaline batteries are used nowadays to save the environment (Bogutska et al. 2013).
e. **Hydrogen production from sunlight-artificial photosynthesis**: Hydrogen production from sunlight-artificial photosynthesis is green glow, ecological, and biodegradable technology that proves to be beneficial for our planet. In this system, the solar energy is used to break hydrogen and oxygen from water through artificial photosynthesis which can offer a clean and green advantageous root for energy supply from the sunlight (Melis 2012).

4.4 Agriculture Application of Biogenic Nanoparticles

Nanotechnology is a highly probable technology that will help to recast agricultural operations (Mousavi SR, Rezaei 2011; Pérez-de-Luque and Rubiales 2009; Prasad et al. 2017; Sekhon 2014; Singh et al. 2015). In agriculture, it will show highly fruitful results in controlling fertilizers, nutrient suppliers, and also for sustainable development (Gruère 2012; He et al. 2018). The implication of the nanotechnology research in the agricultural sector is becoming to be necessary, and is even a key factor for sustainable development. Abiogenic nanoparticles, like titanium, zinc, are proved as good in resource management of agricultural field, drug-delivery mechanisms in plants, and help to maintain the fertility of the soil. Mainly, zinc oxide nanoparticles are used to enhance the growth of fertilizers and food crops by making zinc oxide colloidal solutions.

a. **Nanofertilizers**

Nanofertilizers are nutrient-rich fertilizers that supply nutrients to the soil and plants to revive the fertility of the soil. The nanofertilizers are freely available in the market in the last few years. They will help to maintain the plant growth and sustainability of soil. The main advantage of nanofertilizers is that they can be used in very small amount for the growth of plants (Wang et al. 2016).

b. **Nanopesticides**

Nanoparticles also play a major role in the control of pests and insecticides. Nanoencapsulation method is used to make nanopesticides. These nanopesticides have special properties, like soil solubility, specificity, and permeability (Bhattacharyya et al. 2016). These nanoencapsulated pesticides are used most commonly because of their slow releasing properties in the soil which make them suitable and sustainable for environment. The advantage of these nanopesticides is to develop non-toxic pesticide to enhance the growth of plants.

c. **Nanoherbicides**

Economic losses in crop yields and sustainability by weeds cause a serious problem in agriculture. Because of this serious problem, it is necessary to eliminate weeds from environment. Nanoherbicides are eco-friendly and cost-effective approach to protect the environment from wild weeds (Pérez-de-Luque and Rubiales 2009). Nanoherbicides are mixed with groundwater because of their high surface to volume ratio which provides a strong interaction with soil. Grillo obtained (Grillo et al. 2014) chitosan/tripolyphosphate nanoparticles and used as a carrier system to remove herbicides from the environment.

d. **Agriculture: Crop protection and livestock productivity**

In agricultural activities, nanotechnology shows a significant concern because their nano-sized particles help in increasing the crop productivity and in enhancing live stock quality. Nanotechnology in agriculture is a most efficient and sustainable application that will help to protect the plant growth from toxic chemicals and detect the

plant diseases. It is also used to enhance the food production and quality of food (Sekhon 2014).

References

Ali Mansoori G, Bastami TR, Ahmadpour A, Eshaghi Z (2008) Environmental application of nanotechnology. Ann Rev Nano Res 2(3):439–493

Bhattacharyya A, Duraisamy P, Govindarajan M, Buhroo AA, Prasad R (2016) Nano-biofungicides: emerging trend in insect pest control. Advances and applications through fungal nanobiotechnology. Springer, Cham, pp 307–319

Bhavani P, Sujatha ANU, Guntur ANU (2014) Impact of toxic metals leading to environmental pollution. J Chem Pharm Sci 3:70–72

Bogutska KI, Sklyarov YP, Prylutskyy YI (2013) Zinc and zinc nanoparticles: biological role and application in biomedicine. Ukr Bioorg Acta 1:9–16

Cai Z, Ye Z, Yang X, Chang Y, Wang H, Liu Y, Cao A (2011) Encapsulated enhanced green fluorescence protein in silica nanoparticle for cellular imaging. Nanoscale 3(5):1974–1976

Campbell E, Hasan MT, Pho C, Callaghan K, Akkaraju GR, Naumov AV (2019) Graphene oxide as a multifunctional platform for intracellular delivery, imaging, and cancer sensing. Sci Rep 9(1):416

Carlson C, Hussain SM, Schrand AMK, Braydich-Stolle L, Hess KL, Jones RL, Schlager JJ (2008) Unique cellular interaction of silver nanoparticles: size-dependent generation of reactive oxygen species. J Phys Chem B 112(43):13608–13619

Chaloupka K, Malam Y, Seifalian AM (2010) Nanosilver as a new generation of na**n**oproduct in biomedical applications. Trends Biotechnol 28(11):580–588

Chen X, Schluesener HJ (2008) Nanosilver: a nanoproduct in medical application. Toxicol Lett 176(1):1–12

Chen G, Qiu H, Prasad PN, Chen X (2014) Upconversion nanoparticles: design, nanochemistry, and applications in theranostics. Chem Rev 114(10):5161–5214

Choi Y, Ho NH, Tung CH (2007) Sensing phosphatase activity by using gold nanoparticles. Angew Chem Int Ed 46(5):707–709

Chugh H, Sood D, Chandra I, Tomar V, Dhawan G, Chandra R (2018) Role of gold and silver nanoparticles in cancer nano-medicine. Artif Cells Nanomed Biotechnol 46(sup1):1210–1220

Grillo R, Pereira AE, Nishisaka CS, de Lima R, Oehlke K, Greiner R, Fraceto LF (2014) Chitosan/tripolyphosphate nanoparticles loaded with paraquat herbicide: an environmentally safer alternative for weed control. J Hazard Mater 278:163–171

Gruère GP (2012) Implications of nanotechnology growth in food and agriculture in OECD countries. Food Policy 37(2):191–198

Hasan MM, Uddin F, Islam MM, Hasan M, Banik K, Islam MA, Hashid HA (2016) Nanotechnology drug delivery system: tools in advance pharmaceutical and human health care. Int J Biopharm 7(2):90–99

He X, Deng H, Hwang HM (2018) The current application of nanotechnology in food and agriculture. J Food Drug Anal 27:1–21

Hong R, Han G, Fernández JM, Kim BJ, Forbes NS, Rotello VM (2006) Glutathione-mediated delivery and release using monolayer protected nanoparticle carriers. J Am Chem Soc 128(4):1078–1079

Hua M, Zhang S, Pan B, Zhang W, Lv L, Zhang Q (2012) Heavy metal removal from water/wastewater by nanosized metal oxides: a review. J Hazard Mater 211:317–331

Ibrahim RK, Hayyan M, AlSaadi MA, Hayyan A, Ibrahim S (2016) Environmental application of nanotechnology: air, soil, and water. Environ Sci Pollut Res 23(14):13754–13788

Katas H, Moden NZ, Lim CS, Celesistinus T, Chan JY, Ganasan P, Suleman Ismail Abdalla S (2018) Biosynthesis and potential applications of silver and gold nanoparticles and their chitosan-based nanocomposites in nanomedicine. J Nanotechnol 1–13

Kefayat A, Ghahremani F, Motaghi H, Mehrgardi MA (2019) Investigation of different targeting decorations effect on the radiosensitizing efficacy of albumin-stabilized gold nanoparticles for breast cancer radiation therapy. Eur J Pharm Sci 130:225–233

Khan MR, Rizvi TF (2014) Nanotechnology: scope and application in plant disease management. Plant Pathol J 13(3):214–231

Khan AK, Rashid R, Murtaza G, Zahra A (2014) Gold nanoparticles: synthesis and applications in drug delivery. Trop J Pharm Res 13(7):1169–1177

Lee SY, Kim HJ, Patel R, Im SJ, Kim JH, Min BR (2007) Silver nanoparticles immobilized on thin film composite polyamide membrane: characterization, nanofiltration, antifouling properties. Polym Adv Technol 18(7):562–568

Liu J, Cheng S, Cao N, Geng C, He C, Shi Q, Xu C, Ni J, DuChanois RM, Elimelech M, Zhao H (2019) Actinia-like multifunctional nanocoagulant for single- step removal of water contaminants. Nat Nanotechnol 14(1):64

Lusvardi G, Barani C, Giubertoni F, Paganelli G (2017) The synthesis and characterization of TiO2 nanoparticles for the reduction of water pollutants. Materials 10(10):1208

Marchiol L (2012) Synthesis of metal nanoparticles in living plants. Ital J Agron 7(3):e37

Mazhar T, Shrivastava V, Tomar RS (2017) Green synthesis of bimetallic nanoparticles and its applications: a review. J Pharm Sci Res 9(2):102

Melis A (2012) Photosynthesis-to-fuels: from sunlight to hydrogen, isoprene, and botryococcene production. Energy Environ Sci 5(2):5531–5539

Mom TJ, Van Den Bosch FA, Volberda HW (2007) Investigating managers' exploration and exploitation activities: The influence of top-down, bottom-up, and horizontal knowledge inflows. J Manag Stud 44(6):910–931

Morones JR, Elechiguerra JL, Camacho A, Holt K, Kouri JB, Ramírez JT, Yacaman MJ (2005) The bactericidal effect of silver nanoparticles. Nanotechnology 16(10):2346

Mousavi SR, Rezaei M (2011) Nanotechnology in agriculture and food production. J Appl Environ Biol Sci 1(10):414–419

Mu Q, Wang H, Zhang M (2017) Nanoparticles for imaging and treatment of metastatic breast cancer. Expert Opin Drug Deliv 14(1):123–136

Natsuki J, Natsuki T, Hashimoto Y (2015) A review of silver nanoparticles: synthesis methods, properties and applications. Int J Mater Sci Appl 4(5):325–332

Pandey R, Khuller GK (2007) Nanoparticle-based oral drug delivery system for an injectable antibiotic–streptomycin. Chemotherapy 53(6):437–441

Patra JK, Baek KH (2014) Green nanobiotechnology: factors affecting synthesis and characterization techniques. J Nanomater 2014:219

Peng F, Setyawati MI, Tee JK, Ding X, Wang J, Nga ME, Ho HK, Leong DT (2019) Nanoparticles promote in vivo breast cancer cell intravasation and extravasation by inducing endothelial leakiness. Nat Nanotechnol 14(3):279

Pérez-de-Luque A, Rubiales D (2009) Nanotechnology for parasitic plant control. Pest Manag Sci: Former Pestic Sci 65(5):540–545

Prasad R, Bhattacharyya A, Nguyen QD (2017) Nanotechnology in sustainable agriculture: recent developments, challenges, and perspectives. Frontiers Microbiol 8:1014

Rai MK, Deshmukh SD, Ingle AP, Gade AK (2012) Silver nanoparticles: the powerful nanoweapon against multidrug-resistant bacteria. J Appl Microbiol 112(5):841–852

Rani K, Sridevi V (2017) An overview on role of nanotechnology in green and clean technology. Austin Environ Sci 2(3):1026

Sekhon BS (2014) Nanotechnology in agri-food production: an overview. Nanotechnol Sci Appl 7:31

Shukla G, Dixit R, Kumar A, Singh R, Rani A, Kumar P (2017) Nanotechnology: an innovative approach for waste water treatment. In: Applications of Nanotechnology an introduction. Horizon Books 1, p 89

Singh M, Kundu S, Sreekanth V, Motiani RK, Sengupta S, Srivastava A, Bajaj A (2014) Injectable small molecule hydrogel as a potential nanocarrier for localized and sustained in vivo delivery of doxorubicin. Nanoscale 6(21):12849–12855

Singh S, Singh BK, Yadav SM, Gupta AK (2015) Applications of nanotechnology in agricultural and their role in disease management. Res J Nanosci Nanotechnol 5(1):1–5

Sotiriou GA, Pratsinis SE (2011) Engineering nanosilver as an antibacterial, biosensor and bioimaging material. Current Opin Chem Eng 1(1):3–10

Vu VP, Gifford GB, Chen F, Benasutti H, Wang G, Groman EV, Scheinman R, Saba L, Moghimi SM, Simberg D (2019) Immunoglobulin deposition on biomolecule corona determines complement opsonization efficiency of preclinical and clinical nanoparticles. Nat Nanotechnol 14(1):1

Wang P, Lombi E, Zhao FJ, Kopittke PM (2016) Nanotechnology: a new opportunity in plant sciences. Trends Plant Sci 21(8):699–712

Yeh YC, Creran B, Rotello VM (2012) Gold nanoparticles: preparation, properties, and applications in bionanotechnology. Nanoscale 4(6):1871–1880

Thermal Plasma Processes and Nanomaterial Preparation

C. Balasubramanian

Abstract Plasma here refers to the fourth state of matter which has wide-ranging applications—right from industrial to biomedical. A word of caution: The term "plasma" should not be mixed up with the blood "plasma"—which is entirely different from the fourth state of matter—the subject area of this chapter. The interaction of this plasma—fourth state of matter—with the first (and to some extent the second state as well) state of matter is an area that brings about vast application potential. Primarily the energy content in a plasma state is orders of magnitude higher than the energy content of the other three states of matter. This large energy content is what is used for various applications mentioned above. This chapter contains in brief the basics of plasmas, types of plasma and nanoscience, and then describes in detail how plasmas can be used for various material processing—especially preparation of nanomaterials. Care has been taken to provide more experimental details in a simple flowing language. Images (mostly related to the author's own work) have been included for better clarity and easy understanding.

1 Nanoscience and Nanomaterials

This relatively new branch of science, though predicted by Richard Feynman towards the fag end of 1950s, actually started evolving only in 1980s after the invention of the scanning tunnelling microscope (STM)—a powerful probe microscope with which atomic scale features could be studied.

Nanoscience is the science of behaviour of materials when its size is reduced to a scale of within few tens of nanometres. It is observed that the behaviour and properties of materials change drastically from its bulk counterpart when the material is reduced in size. For example, materials like gold which is inert in its bulk form become highly reactive when reduced to nanometre size; materials like iron which are stable at bulk form become explosive when reduced to nanosize. The branch of nanoscience deals with the understanding of these drastic changes. The drastic

C. Balasubramanian (✉)
Atmospheric Plasma Division, Institute for Plasma Research, Gandhinagar, India
e-mail: balac@ipr.res.in

L. Ledwani and J. S. Sangwai (eds.), *Nanotechnology for Energy and Environmental Engineering*, Green Energy and Technology,
https://doi.org/10.1007/978-3-030-33774-2_3

change in properties of a material just by reducing its size has generated a large interest among the scientific community, not only to understand the basic phenomenon but also to explore the potential applications it holds. These applications are wide ranging right from biomedical (Salata 2004) to optoelectronics to day-to-day consumer products. In fact, it would not be an exaggeration if it is suggested that the far-reaching potential applications are actually driving the research and development of varied nanomaterials. Already nanomaterials, like zinc oxide, titanium dioxide, iron oxide and so on, have found industrial uses, and industrial houses are looking at ways to produce them in bulk quantities.

A range of methods are available for synthesis of various nanomaterials. Sol–gel and chemical vapour deposition (CVD) are the most commonly used techniques, especially at laboratory scale. A review of various liquid-phase syntheses of inorganic nanoparticles is discussed by Cushing et al. (2004). Apart from this liquid-phase synthesis, a range of gas-phase synthesis techniques are also available, like laser ablation, inert gas phase condensation and so on. When talking in terms of large industrial-scale production, both the commonly used techniques of sol–gel and CVD have certain limitations, like difficulty in scaling up; multistep processes; long time scales and so on, that restrict its production capacity.

Nanomaterials can also be produced by plasma, which is a high-temperature physical process. This process, though not so common, has distinct advantages for commercial-scale generation of various nanostructures. The various advantages of this process are given in Sect. 4.3. This chapter elucidates on the various aspects of the plasma process, methodologies, control parameters, advantages, disadvantages and so on. It also describes in detail the various nanomaterials that have been prepared using this process. Prior to this, it would be helpful to understand what is "*Plasma*".

2 Plasma

Plasma is the fourth state of matter. The other three states—solid, liquid and gas—are well-known and well-studied even in the school curricula. Almost all the natural terrestrial matters come under one of these states of solid or liquid or gas. However, terrestrial natural plasma state is not so common other than in lightening and ionosphere—this, probably, is the reason for plasma state not being taught in schools. However, more than 97% of the universe exists in plasma state!

So what exactly is plasma state? It is a state in which matter exists in ionised form—where the constituents are either negatively charged or positively charged. The properties of a plasma state, as expected, differ widely with respect to the other states of matter. Unlike gaseous state which is electrically neutral, plasma state, in which the constituents are charged particles, is the best conductor of electricity. It also responds to magnetic fields. The energy content of plasma state is much higher than that of the gaseous state. The most common example that is used to explain the four states of matter is the transformation of ice (solid state) to water (liquid state) and then to water vapour (gaseous state). Stretching it further, the water vapour with

sustained heating leads to the separation of H_2O molecule to its constituent atoms of H and O. These atoms on further heating lead to the removal of electrons from H and O atoms, resulting in the generation of negatively charged electrons (e^-) and positively charged O^+ and H^+ atoms. This collection of positive and negative charges is defined as plasma state. As can be seen, as one move from solid state to plasma state the temperature (thermal energy) increases steadily with plasma state having the highest enthalpy.

Since opposite charges attract each other and gets annihilated, one needs to pump in energy to maintain the charge separation and sustain the plasma state. There are a few prerequisites for a group of negatively and positively charged particles to be certified as plasma state—which are not part of this chapter.

2.1 Plasma and Material Processing

The interaction of the fourth state (plasma) with the first state (solid) has wide-ranging common industrial as well as societal applications (Fauchais et al. 2008): plasma cutting/welding, plasma pyrolysis (Huang and Tang 2007), plasma smelting and so on. It also has bio-medical applications in the fields of dentistry, integumentary system and so on. Modifications like etching, grafting of various surfaces are also used to impart functionalities, like hydrophobicity, hydrophylicity and so on, to the surface.

Based solely on the heat content/temperature, plasmas can be broadly classified into two categories: high temperature/thermal plasmas and low temperature/cold plasmas. The thermal energy content of high-temperature plasmas can go from hundreds of degree centigrade to tens of thousands of degree centigrade. All stars (including sun) consist of thermal plasmas. On the other hand, interstellar space plasmas, plasmas found in fluorescent bulbs are all examples of low-temperature plasmas.

Plasmas can also be classified depending on the process by which it is generated. For example, creation of plasma using microwave source is microwave plasma, inductively heated source leads to inductively coupled plasma, dielectric barrier discharge plasma and so on. Here in this chapter we would only discuss the properties and applications of plasmas classified on the basis of heat content; that is thermal and non-thermal plasmas.

The heat content in plasma is decided by the ambient pressure: Low pressure (few mbar or lower) plasma results in non-thermal/cold plasmas, whereas high pressure (few hundred mbar or more) would result in high temperature thermal plasmas. In the high pressure scenario, the particle (both charged as well as neutral) density would be higher resulting in higher collision between particles and consequent rise in temperature. On the other hand, in a low pressure system the particles would be able to move without much or significantly reduced number of collisions, and thereby having a higher kinetic energy rather than having heat energy.

As can be deduced, thermal plasma is used for heat-intense applications, like welding, cutting, pyrolysis, smelting and so on and non-thermal plasmas are used

for surface modifications, bio-medical applications and so on. The heat generated in thermal plasma can reach thousands of Kelvin depending on the plasma current applied. The high heat energy not only helps in melting, evaporation and so on, but also promotes higher chemical reactions. Nanoparticle synthesis which involves evaporation, nucleation and growth also employs high temperature plasma. Plasma torch and arc plasma are used for synthesis of nanoparticles. A detailed report on the use of various plasmas for synthesis of nanostructures is given by Siegmann et al. (2008).

Low-temperature plasma, on the other hand, is used extensively in surface modifications of various materials, including polymers, textiles and so on. It is also used to grow nanocrystalline films or 2-D nanostructures as well as nanocomposites (Tsai et al. 2009). It is also used to make nanopatterns on substrates. Plasma-enhanced chemical vapour deposition (PECVD), magnetron sputtering processes are all examples of low-temperature plasma, which are used effectively for nanostructure formations. Basically, the high kinetic energy of the charged particles in plasma is used to knock out surface atoms or atom clusters to impart changes to the surface roughness leading to changes in the surface properties and surface chemistry. The kinetic energy of the charged particles can also be used to break chemical bonds and then graft it with atoms of other elements, thereby imparting different functionality to the original surface.

In this chapter the focus would be exclusively on the properties, types and applications of thermal plasmas—with particular emphasis on nanomaterial synthesis.

2.2 Thermal Plasma Processes

2.2.1 Transferred and Non-transferred Plasma

Nanoparticles by thermal plasma can be prepared by two methods: either by transferred arc torch method or by non-transferred arc torch method.

In the non-transferred torch (as shown in Fig. 1) method, an electric arc is struck between the central cathode rod (typically water cooled tungsten) and the coaxially placed anode (typically water-cooled copper). This arc is extended outside of the nozzle by a strong gas draft (also known as plasma forming gas). The length of the extended arc (plume) can reach up to tens of centimetres long, depending on the gas flow rate and the voltage applied between the electrodes. The material of interest (whose nanostructure is to be formed) is either placed in a crucible at the plume end or it can be introduced in powder form between the electrodes along with the plasma-forming gas jet.

If it is placed in a crucible, the heat from the plume would evaporate the material which subsequently leads to nucleation, growth and condensation. If, on the other hand, the material is introduced in powder form, the powder comes directly in contact with the core of the plasma (which has a significantly higher temperature than at the

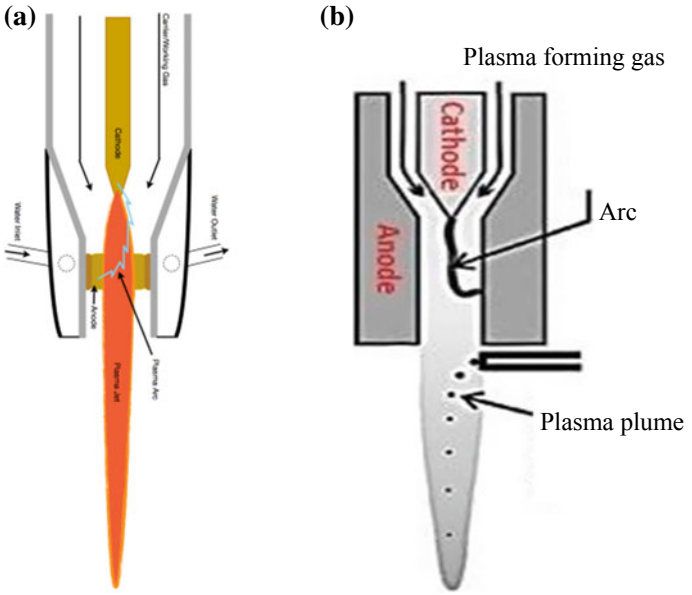

Fig. 1 Schematic of a (**a**) typical non-transferred plasma arc torch (**b**) with powder injection into the plasma plume

plume end) resulting in evaporation, and as it moves down axially, with decreasing temperature, forms clusters of nanostructures.

In the transferred arc plasma (as shown in Fig. 2) type, the job (material of interest) is placed in a crucible, and positive potential of the electric power supply is connected to it. A refractory material (typically tungsten or graphite) is used as a cathode. To strike an arc and create plasma between the electrodes, two options are available: (i) the electrodes are brought closer and made to touch each other, thereby "shorting" the circuit, and once the current starts flowing, the electrodes are moved apart slowly

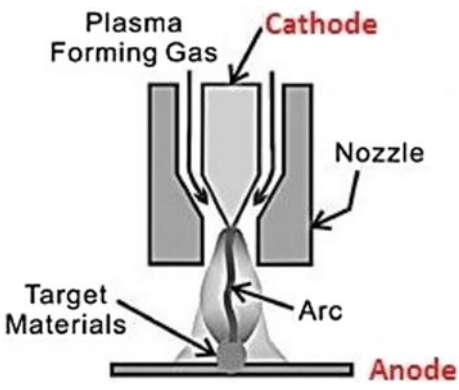

Fig. 2 Schematic of transferred arc plasma

and an arc column is created between the electrodes. For this to be done, either both the electrodes or at least one of the electrodes has to be movable. (ii) The electrodes need not be made to touch each other, if there is provision for a high-frequency starter in the power supply—it would be sufficient to bring the electrodes closer to initiate the arc followed by the plasma plume. The second option is helpful in cases where the arcing need to be created between two soft metal electrodes.

The power supply that is generally used for plasma torch (transferred as well as non-transferred) is a constant current DC power source. The power supply ratings are chosen, taking into consideration the materials to be evaporated—higher current for high melting point materials. Typically, the current could vary from few tens of amperes to hundreds of amperes. The load voltage could be few tens of volts. A large current is required as the material evaporation from the anode depends on the resistive heating given by I^2R, where I is the current and R is the resistance. A larger voltage would, on the other hand, support a long arc column.

The non-transferred arc assumes its name as the "job" material is not part of the electrical circuitry. So even if the material of interest is insulating in nature, it can be used for making nanostructures. On the other hand, in a transferred arc plasma, the material of interest is very much a part of the electrical circuitry and is, as described above, the anode itself. Both transferred and non-transferred arc plasmas have advantages and disadvantages: A non-transferred can be used both for conducting and insulating materials, whereas the transferred can be used only for electrically conducting materials. On the other hand for a transferred arc, the efficiency of the electrical power applied versus the power that is effectively used in evaporating the material is more than 90%, whereas the best efficiency that can be obtained from a non-transferred torch would not exceed 75% (more likely around 65%).

3 Synthesis of Nanomaterials

For synthesis of nanomaterials, both non-transferred as well as transferred arc plasma/torch can be used. In the following sections both the techniques would be discussed. However, more emphasis and details would be related to transferred arc plasma route of nanomaterial synthesis.

3.1 Non-transferred Plasma Process for Synthesis of Nanostructures

There are numerous published literatures on the synthesis of nanomaterials, using either of the plasma types. In a non-transferred type, as briefly mentioned earlier in Sect. 4.1, two possible mechanisms exist.

In the first type, the material of interest is directly placed on an anode crucible (could be made of graphite or any electrically conducting material). The heat content of the plasma plume would melt and evaporate it. The vapourised material, as it moves away from the plasma zone, would nucleate and form clusters of atoms/molecules.

In the second type, micron-sized powder of the material of interest is fed into plasma plume either at the gap between the two electrodes or where the plume exits the anode region. The introduced powder, due to the high heat content, will evaporate or melt and as it moves down will form small clusters of atoms/molecules.

3.2 Transferred Arc Plasma Process for Synthesis of Nanostructures

In transferred arc plasma process (as shown in Fig. 2), an electric arc is struck between the cathode and anode wherein the anode itself will melt and evaporate due to the plasma created between the two electrodes. The element of the material of interest is placed in a crucible (graphite or any conducting material), and positive potential of the electric power supply is connected to it. A refractory material (typically tungsten or graphite) is used as a cathode.

Once the arc is struck and plasma created, the high enthalpy from the plasma would evaporate the anode material turning it into charged particles within the plasma column which, as it moves away from the plasma zone, becomes neutral atoms followed by reaction with the surrounding gas ambient and then onto nucleation and growth of clusters, finally to condensation. A schematic of the arc plasma synthesis of nanoparticles is shown in Fig. 3.

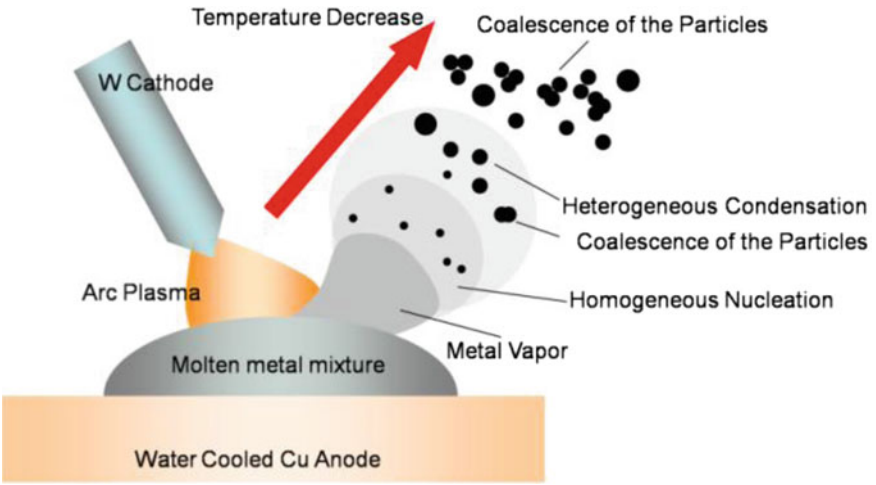

Fig. 3 Schematic of the nanomaterial generation using a transferred arc plasma process

3.3 Advantages of Plasma Process for Nanomaterial Synthesis

The major advantages of the plasma process for synthesis of nanomaterials are that

(i) the process is easily scalable;
(ii) faster time scales of synthesis and
(iii) single step process with significant control over impurities.

For commercial/industrial-scale production of nanomaterials, these three points are a game changer. Apart from the above, other advantages are:

(iv) The plasma process operates under atmospheric pressure and hence, unlike CVD process, does not require the cumbersome and time-consuming vacuum creation and so on.
(v) The high temperature of the plasma zone can evaporate all materials and hence nanostructures of most materials can be prepared using the same apparatus and setup.
(vi) The high temperature of plasma also promotes high rates of chemical reactivity and the products are generally highly crystalline. Additionally, it is also possible to produce metastable crystalline phases which are not normally formed in a low temperature process.
(vii) Plasma process also yields a range of morphological features with minor changes in the operational parameters.

Plasma process can also be used to prepare varied types of nanomaterials—metals, metal oxides, metal nitrides, metal carbides and so on. The gas ambient in the synthesis chamber dictates the product formation. If the anode material is evaporated in an inert ambient (argon or helium gas), then metal nanoparticles can be obtained. If the ambient is air or oxygen, one can obtain metal oxide nanoparticles. For nitrides, a high concentration of nitrogen ambient is sufficient to get the desired results. For carbides one can mix graphite/carbon powder along with the anode material in an inert atmosphere.

The sole disadvantage of the plasma process of nanomaterial synthesis is the wide size distribution of the nanostructures formed. Though this is unavoidable, it can be minimised. The reason for the large size distribution is: The steep temperature gradient (thousands of degree centigrade per centimetre) combined with high velocities (thousands of metres per second) of the evaporated material leads to very fast time scales of nucleation and growth of the nanostructures. Depending on the flight path of the evaporated atom/molecule clusters, the thermal history and condensation rates vary and hence the size of the nanoclusters also varies.

In the following sections, details of the different types of nanomaterials that have been synthesised as well as the morphological and other variations that can be obtained by varying certain plasma parameters will be provided.

3.4 Transferred Arc Plasma and Nonmaterial Preparation—System Details

As described in Sect. 4.3 plasma is created between cathode and anode, wherein anode is the material of interest—for example, for producing nanoparticles of aluminium or aluminium compounds (aluminium oxide, aluminium nitride etc.), elemental aluminium metal is used as anode; for preparing zinc or zinc compound nanomaterials, elemental zinc is used as anode and so on. The elemental metal (in any form: blocks, powder, pellets, scraps etc.) is placed in a graphite or copper crucible and connected to the anode potential of the power supply. The entire electrode assembly is housed inside a double-walled stainless steel chamber with multiple ports for electrode housing, powder collection, visual monitoring of the process and other necessary functions.

3.4.1 Nanomaterial Synthesis System

Inside the plasma zone both the evaporated material as well as the ambient gas/air would be in ionised state. As shown in Fig. 3 these charged particles/metal vapour move away from the plasma zone forming neutral atoms and then onto molecules and clusters. Depending on the heat energy available at the clustering zone, the cluster size could increase from few atoms/molecules to tens of thousands of atoms/molecules resulting in the formation of either small nanoclusters of few nanometres or bigger clusters of tens or hundreds of nanometres. The higher the temperature, the larger is the cluster size. So to obtain nanometre size small clusters, it is essential to reduce the ambient temperature inside the production chamber to a minimum. This is achieved by the water circulation between the two walls of the synthesis chamber.

As shown in the figure, the nucleation and growth of the atoms/molecules (cluster formation) occurs in the gas phase itself—homogeneous nucleation process—followed by agglomeration of the various clusters. These nanosized clusters (nanoparticles) deposit itself on the inner surface of the synthesis chamber walls.

In short, the single-step process consists of evaporating a material from its solid state and then recondensing it into small nanosize clusters. For evaporating the material, thermal plasma which has high enthalpy is used; and for an accelerated recondensation the chamber ambient is maintained at a low temperature. Higher chamber ambient temperature would lead to continued growth of clusters into micron size. The high temperature within the central plasma zone and low temperatures outside of it create a sharp temperature gradient that is at the crux of the nanomaterial synthesis.

The process and the apparatus can be used to produce varied nanomaterials. A schematic of a typical nanomaterial synthesis chamber is shown in Fig. 4. When the entire process of evaporation, nucleation and growth is done in air or oxygen medium, the metal vapours react with them to form metal oxide nanostructures. If, on the other hand, the air in the synthesis chamber is evacuated and filled with argon or helium

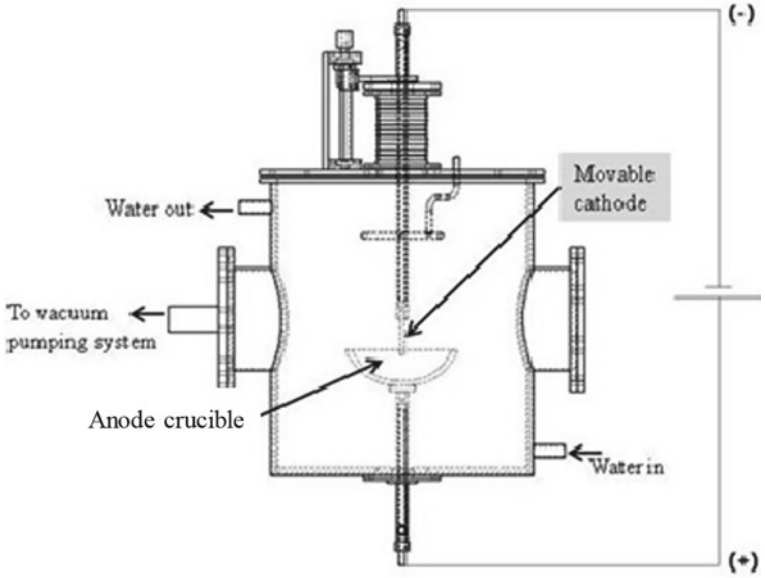

Fig. 4 Schematic of a typical plasma chamber for synthesis of various nanomaterials

gas, one can obtain metal nanostructures. Similarly, evacuating the chamber of air and filling it with nitrogen leads to nitride formation.

3.4.2 Power Supply

The heat required for melting and evaporation of the metal solid is generated by the electric power supply and as such it is a main component of the entire process. The heating of the anode metal raw material is done by "*joule heating*" or "*resistive heating*", wherein the power of heating P is given by the equation:

$$P = I^2 R$$

where I is the current passing through the resistor material (anode material in this case) and R is the resistance of the material. As one can observe, the heating depends on the square of the current applied. Application of higher current will lead to more heat generation and consequently melting/evaporation of materials whose melting or evaporation temperature is higher.

A constant current DC (direct current) power supply is used with ratings of few tens of kilowatts. Typicall, for evaporating low melting point materials like zinc, tellurium and so on, a plasma current of 10–15 A is sufficient. However, for materials like iron, titanium and so on, it would be necessary to pass a current of ~100 A or so. Carbon nanotubes, which can also be formed by this process, typically requires

100 A or more. It would be safe to assume a minimum requirement of 150 A current source DC power supply. The load voltage—which incidentally varies depending on the distance between the electrodes as well as the ambient gas and the electrode material—could be typically 50–100 V.

3.4.3 Water Chiller

As detailed earlier, it is imperative that the synthesis chamber is maintained at around room temperature in order to obtain nanosized particles. Due to high heat of the plasma, the ambient temperature inside the synthesis chamber increases steadily. This will result in the growth of the clusters to bigger size. Cooling the synthesis chamber ensures the walls of the chamber are at low temperature resulting in sharp temperature gradients and consequent arrest of the nanocluster growth. For this, a steady stream of water is allowed to flow between the two walls of the chamber, thereby maintaining the temperature of the chamber walls at ambient room temperature (or lower—as required). So it is essential to have a water chiller of appropriate capacity to maintain the temperature of production chamber. If the various flanges are sealed with neoprene or viton "O" rings, then the flanges also need to be water cooled, lest the heat damages the "O" rings.

4 Preparation of Various Nanostructures by Plasma Process

4.1 Preparation of Oxide Nanostructures

For metal oxide nanoparticles the synthesis chamber can be done in ambient air. At high temperatures, as that in plasma zone, the chemical reactivity is high and the metal vapours form oxides easily. These then can be collected for analysis/application. In the following sections, a brief of various metal oxides (both low as well as high melting point materials) that have been synthesised, and their synthesis parameters and properties of the obtained nanostructures are described in detail. Metal oxide nanomaterials that are to be covered are: iron oxide and cobalt oxide (magnetic), titanium dioxide (refractory) and zinc oxide (wide bandgap semiconductor).

4.2 Titanium Dioxide Nanoparticles

Titanium dioxide or titania (TiO_2) has wide application potential—especially in the daily-use consumer products. They are used in cosmetics (as UV protection agent), as pigments in paints, inks and so on (as an opacifier agent). Titania in nanosize is

also a good photocatalytic agent under UV light—helping in stain removal as well as antibacterial. There are three crystallographic forms of titania, viz. rutile (tetragonal), anatase (tetragonal; however, anatase has a steeper pyramid with a larger angle over the polar edge as compared to rutile phase) and brookite (orthorhombic).

Thermal plasma has proven to be an ideal process for production of these nanomaterials. Titanium metal block/pellets kept in graphite crucible are used as anode and tungsten or titanium was used as cathode. A current of 80–110 A was applied (depending on the anode dimensions) between the electrodes in an air ambient. The titanium metal vapours close to the plasma zone reacted with oxygen in the air to form titanium dioxide followed by nucleation and growth of clusters. The chamber wall temperature was maintained at 25 °C by way of water circulation between the two layers of the chamber wall. The process was run for duration of 5–10 min and then the plasma extinguished. After allowing a few hours time duration for the fine particles to settle down, the chamber was opened and the product removed for analysis.

High-resolution transmission electron microscopy was used to analyse the morphological features and X-ray diffraction technique to study the crystalline features. Figure 5 shows the TEM images.

The image on the left clearly shows the particles to be spherical in shape with fairly uniform size of ~40 nm. The image on the right is a magnified image of a single particle of size ~25 nm. One can clearly observe the highly crystalline structure from the well-defined atomic planes.

The formation of TiO_2 and its crystalline phase was confirmed by X-ray diffraction technique, as shown in Fig. 6. Both anatase and rutile phases are seen to be present in the sample. Multiphase formation is quite common in plasma processes.

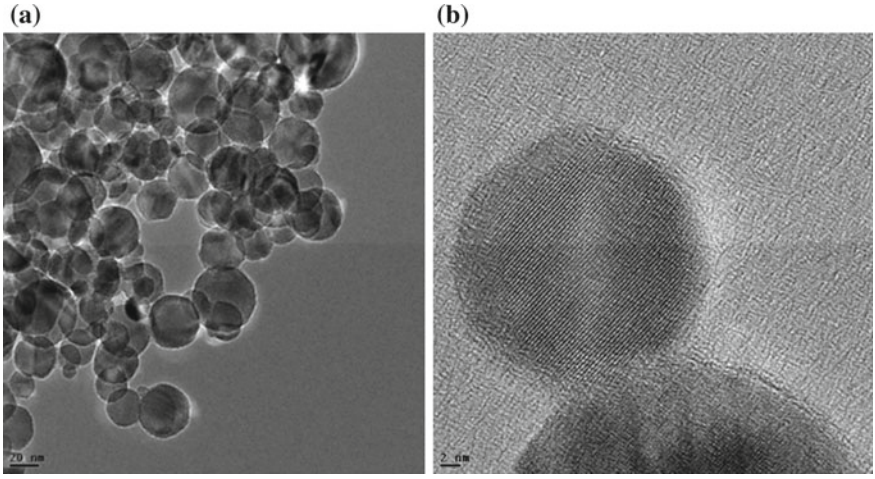

Fig. 5 Titanium dioxide nanoparticles, (**a**) larger area indicating a typical size range of 30–40 nm (scale bar: 20 nm) and (**b**) highly crystalline small particle of size ~25 nm (scale bar: 2 nm)

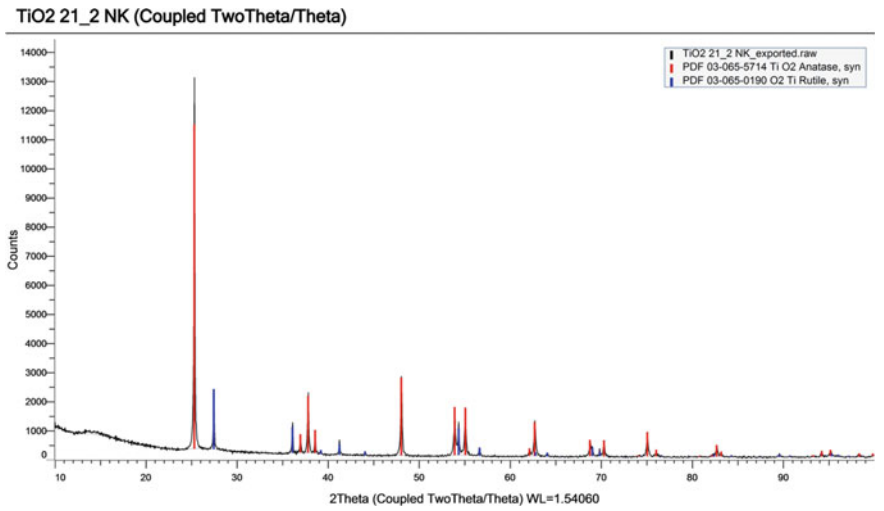

Fig. 6 XRD spectra of titanium dioxide nanoparticles showing the presence of anatase as well as rutile phase. The anatase phase is more predominant than rutile

Another important feature of high temperature plasma process is the possibility of pure metastable phase formation. This will be shown at a later subsection under aluminium nitride nanostructure.

4.3 Preparation of Carbide Nanostructures

For carbide nanostructure preparation, a mixture of carbon/graphite powder along with the metal elemental raw material has proven to yield the desired results. The selection of ambient gas during the preparation was expected to have a great control over the compositional stoichiometry and also on morphological features. Towards this end, studies were carried out on silicon carbide preparation under various plasma parameters including the ambient gas types. The outcome of the study is given in the following section.

4.4 Silicon Carbide Nanostructures

Silicon carbide (SiC) is a widely used ceramic material due to its unique properties such as good physical and mechanical properties, including high thermal conductivity as well as thermal stability, low thermal expansion coefficient, high mechanical strength, high refractive index, wide (tunable) bandgap and large chemical inertness. The nanostructures of SiC have applications in bio-medicine, gas sensing and as

hydrogen storage material. These 1-D nanostructures of SiC are excellent candidates for reinforcement composites with better nanomechanical properties. Field emitting properties of various types of SiC nanostructures (both doped and undoped) have also been widely studied and reported.

Silicon carbide nanostructures were prepared by placing in the anode crucible, a mixture of micron-sized graphite powder with high purity (99%) and silicon powder in the ratio of 1:1 by volume and to this was added a small quantity (0.5 wt%) of iron powder purity >99% as catalyst.

Two sets of experiments were performed under two different oxygen partial pressures: In the first set the synthesis chamber was evacuated to 10^{-5} mbar and then filled with helium gas till 1 atmosphere, and in the second set the chamber was evacuated to 10^{-3} mbar and then filled with helium gas till 1 atmosphere. Once the helium gas was filled, an electric arc was struck (in both sets separately) between a graphite cathode and the crucible containing the mixture of silicon, carbon and iron powder (anode). The arc current was maintained at 150 A. The high heat of the arc plasma facilitated the evaporation and gas-phase formation of the SiC product. The deposited SiC powder was then collected and analysed.

It was interesting to note that even variations in partial pressure of certain gases could lead to vastly different morphological nanostructures. The samples prepared under higher oxygen partial pressure (base vacuum 10^{-3} mbar) resulted in the formation of long (microns length) nanowires of SiC with average diameter of 30 nm. The edges of the wires showed the presence of SiO and an elemental mapping of the sample showed the absence of any Fe catalyst (Fig. 7).

On the other hand, the samples prepared under low oxygen partial pressure resulted in the formation of SiC nanotubes, as shown in Fig. 8. These tubes were typically 15–20 nm in diameter and lengths of few hundred nanometres—dimensions vastly

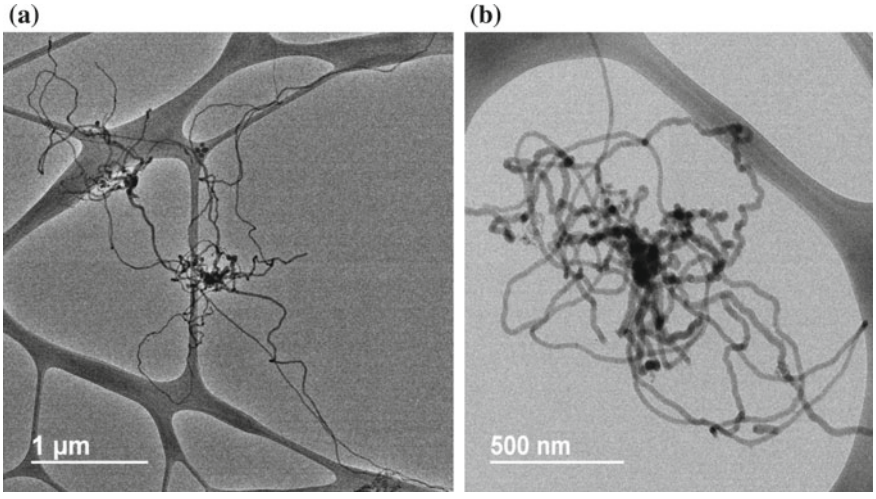

Fig. 7 Silicon carbide nanowires, (**a**) larger area image and (**b**) magnified image of the same

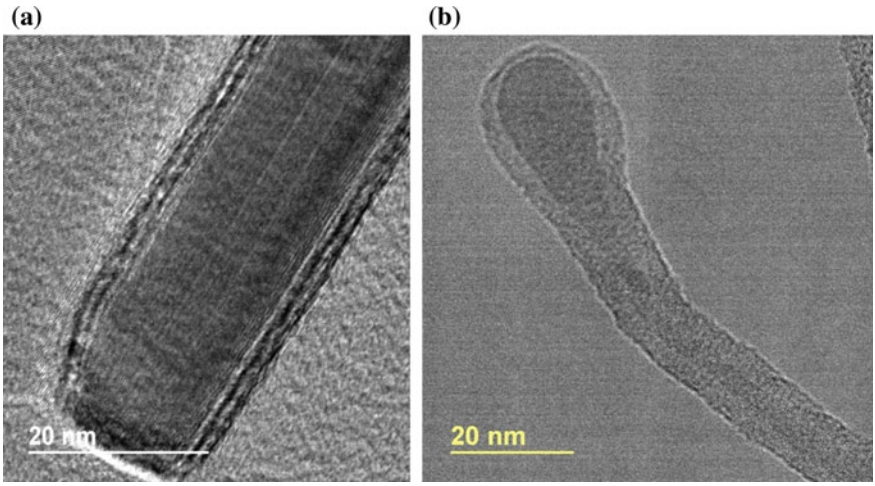

Fig. 8 Silicon carbide nanotubes

different from nanowire samples. From the elemental mapping, it was confirmed that the tips of the tubes contained the Fe catalyst. The conclusion is that small changes in the experimental parameters of the plasma process leads to drastic changes in the product morphology and other properties. The XRD spectra shown in Fig. 9

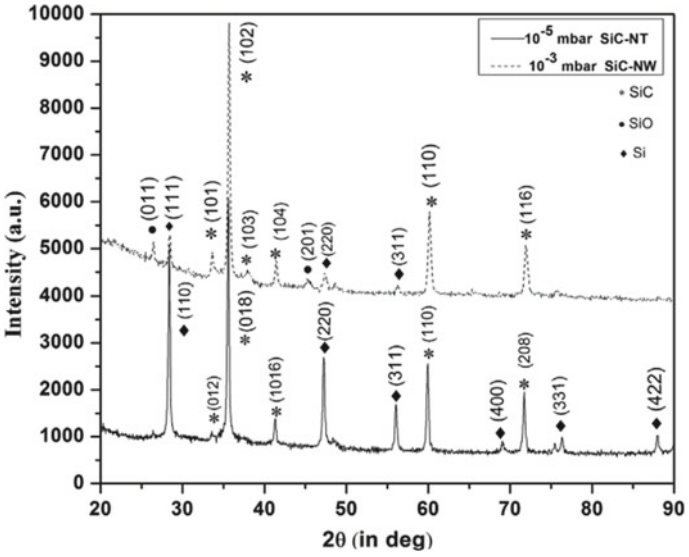

Fig. 9 XRD spectra of SiC nanotubes (SiC-NT) and SiC nanowires (SiC-NW) prepared under slightly varying parameters

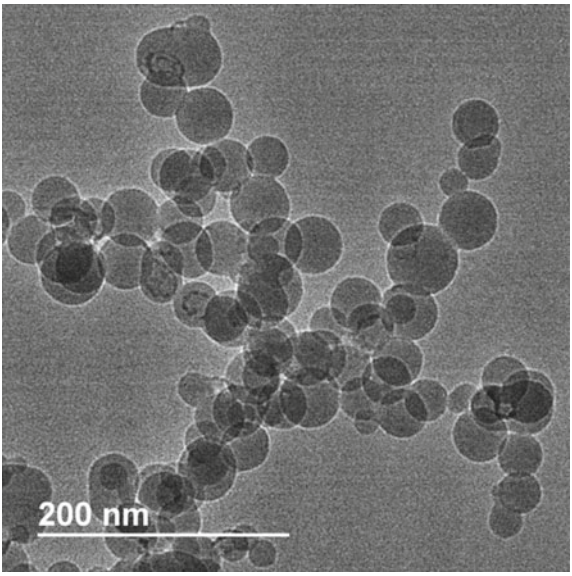

Fig. 10 Silicon carbide nanoparticles

clearly demarcate the composition and phase of these two structures—nanowires and nanotubes.

Under lower arc currents (<150 A) and high oxygen partial pressure, nanoparticles of SiC was also observed to be formed. These were highly spherical in shape with average diameter of ~25 nm. This is also shown in Fig. 10.

4.5 Preparation of Nitride Nanostructures

4.5.1 Aluminium Nitride Nanostructures

Aluminium nitride (AlN) is a wide bandgap semiconductor with very high thermal conductivity and electrically insulating. Its piezoelectric properties have been useful in the making of ultrasound transducers. It is also used as dielectric layer in optical storage media.

For AlN nanostructure preparation, pure aluminium discs were placed in a copper crucible which served as the anode and tungsten rod which served as the cathode. The synthesis chamber was evacuated to a pressure of 5×10^{-6} Torr and then flushed with a gas mixture of nitrogen and argon to atmospheric pressure. Here, the arc currents were varied from 50 to 150 A and the effect of this variation on the formation of AlN nanostructure was studied. Interesting results on crystalline phase formation as well as morphology were observed.

Figure 11 shows the overlaid XRD spectra recorded for three different AlN samples obtained from arc currents of 50, 100 and 150 A. The samples obtained from

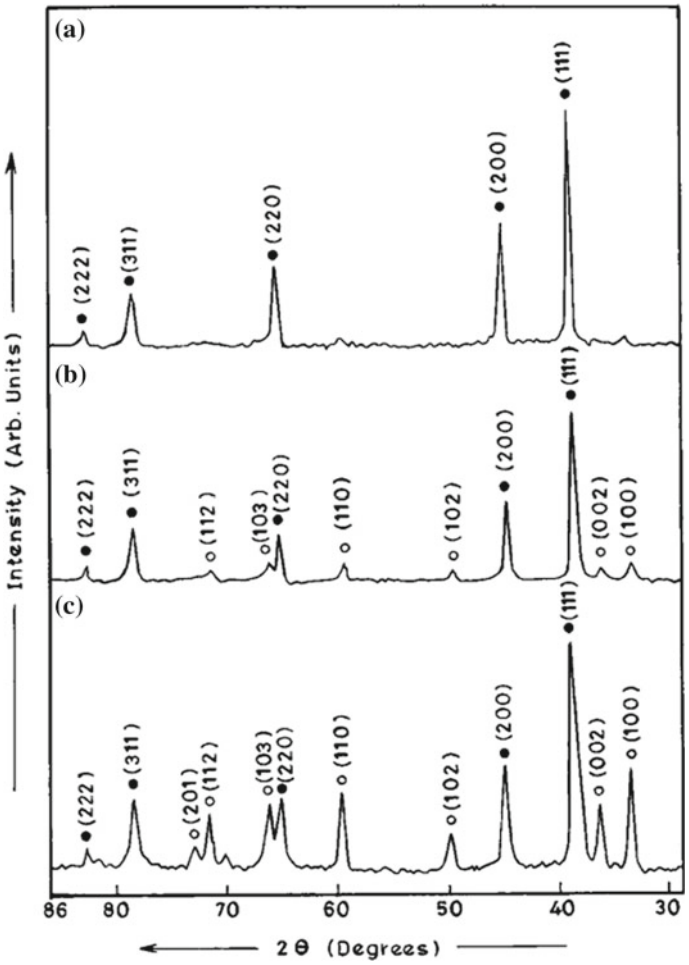

Fig. 11 XRD spectra of AlN nanostructure prepared under three different arc currents of **a** 50 A, **b** 100 A and **c** 150 A. The filled circles denote cubic phase AlN and the open circles denote hexagonal phase of AlN

50 A arc current (indicated by (a) in the spectra below) had five diffraction peaks—all matching with cubic phase of AlN. No other phases were detected. It is to be noted that cubic phase of AlN is a metastable crystalline phase in the bulk form. In the second sample (prepared under 100 A arc current—(b) in the spectra below) apart from the five peaks of 50 A sample, small, additional peaks were detected and they were found to be that of hexagonal crystal structure of AlN. The intensity of these hexagonal structure increased with increase in arc current to 150 A.

Morphological analyses of these samples brought out the significant changes in the nanostructure formation. The 50 A arc current samples consisted of nanowires and nanocoils, whereas the 150 A arc current samples consisted of nanoparticles.

4.6 *Preparation of Metal Nanoparticles*

4.6.1 Tellurium Nanoparticles

As stated in the introduction part, metal nanoparticles can also be prepared by the plasma process. Herein, preparation and analysis of tellurium nanoparticles is given in detail. For metal nanoparticle preparation, it is essential the base vacuum of the synthesis chamber is good. Though the operating pressure of the thermal plasma synthesis route is atmospheric pressure, to avoid oxidation reaction, it is essential to remove air/oxygen in the chamber and then fill with inert gases like argon or helium. The level of base vacuum required is decided by the reactivity of the metal with oxygen—especially at elevated temperatures. Higher the possibility of oxidation reaction, the base vacuum required would be 10^{-5} or 10^{-6} mbar range.

For the Te nanoparticle synthesis, Te powder of micron size was placed in the graphite crucible (which served as the anode) and with graphite rod as the cathode. The chamber was evacuated to 10–4 mbar range vacuum and then filled with helium gas till the pressure inside the chamber reaches 1 atmosphere. An arc current of 50 A was applied between the electrodes and synthesis done. The TEM analyses of the samples indicated formation of pure Te nanoparticles with larger size of approximately 100 nm. X-ray diffraction analysis (shown in Fig. 12) of the samples indicated the formation of highly crystalline tellurium structures.

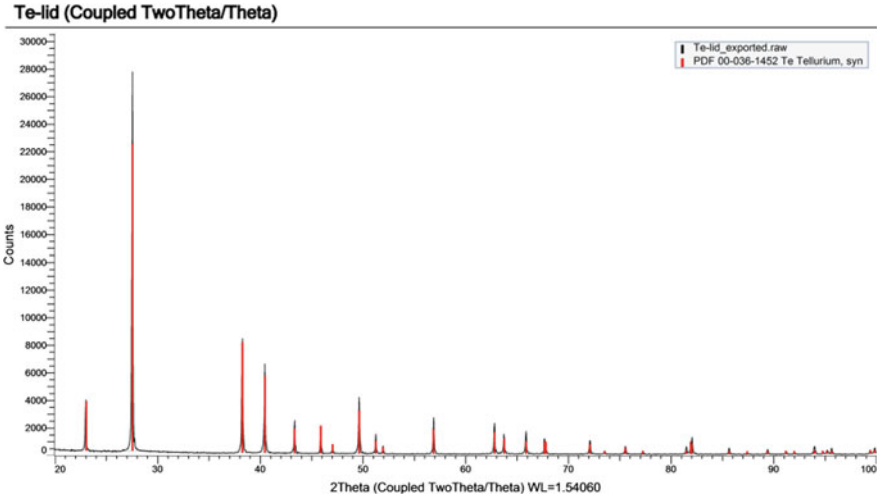

Fig. 12 XRD spectra of tellurium nanoparticles

5 Conclusion

Nanomaterials have wide-ranging applications and some of these nanomaterials have already found applications in our day-to-day customer products. The ever-increasing demand for these materials has driven the industries to explore the various ways of preparing/producing these which are economically viable. Thermal plasma process of making these nanomaterials holds a promise that is simpler, cost-efficient and wide types of materials under its reach. To reiterate this, it was shown in this chapter how the process as well as the equipment could be used to prepare a wide range of materials—metal oxides, metal nitrides, metal carbides and metal nanoparticles. It was also shown how small changes in the plasma operating parameters could lead to vastly varied crystalline structure and shape. What was covered was only a part of the possibilities—gas phase synthesis of nanostructures using thermal plasma. However, more possibilities exist when the same plasma process is used in a liquid medium—instead of in air/gas ambient. The growth dynamics are different and the morphologies would be vastly different from what is obtained from the gas-phase synthesis.

A large amount of literature is available with regard to the plasma process of making nanomaterials—both gas-phase as well as liquid-phase synthesis.

References

Balasubramanian C et al (2004) Synthesis of nanowires and nanoparticles of cubic aluminium nitride. Nanotechnology 15:370–373

Balasubramanian C, Bellucci S, Castrucci P, De Crescenzi M, Bhoraskar SV (2004) Scanning tunneling microscopy observation of coiled aluminum nitride nanotubes. Chem Phys Lett 383:188–191

Balasubramanian C et al (2016) Defective iron-oxide nanoparticles synthesised by high temperature plasma processing: a magnetic characterisation versus temperature. Nanotechnology 27:445701

Banerjee I et al (2006) Preparation of c-Fe_2O_3 nanoparticles using DC thermal arc-plasma route, their characterization and magnetic properties. Scr Mater 54:1235–1240

Bhave TM et al (2005) Oriented growth of nanocrystalline gamma ferric oxide in electrophoretically deposited films. Hyperfine Interact 160:199–209

Castrucci P et al (2006) Silicon nanotubes: synthesis and characterization. Thin Solid Films 508:226–230

Cushing BL, Kolesnichenko VL, O'Connor CJ (2004) Recent advances in the liquid-phase syntheses of inorganic nanoparticles. Chem Rev 104:3893–3946

De Crescenzi M et al (2005) Experimental imaging of silicon nanotubes. Appl Phys Lett 86:231901

Dokhale PA, Sali ND, Kumar PM, Bhoraskar SV, Rohatgi VK, Bhoraskar VN, Badrinarayanan S, Date SK (1997) Mater Sci Eng B 49:18

Fauchais P et al (2008) Thermal plasma applications. High Temp Mater Process 12:165–203

Huang H, Tang L (2007) Treatment of organic waste using thermal plasma pyrolysis technology. Energy Convers Manag 48:1331–1337

Koushika EM, Shanmugavelayutham G, Saravanan P, Balasubramanian C (2018) Rapid synthesis of nano-magnetite by thermal plasma route and its magnetic properties. Mater Manuf Process 33:1701–1707

Kumar PM, Borse P, Rohatgi VK, Bhoraskar SV, Singh P, Sastry M (1994) Mater Chem Phys 36:354
Kumar V et al (2008) Gas-phase, bulk production of metal oxide nanowires and nanoparticles using a microwave plasma jet reactor. J Phys Chem C 112:17750
Lee C-H, Rai P, Moon S-Y, Yu Y-T (2016) Thermal plasma synthesis of Si/SiC nanoparticles from silicon and activated carbon powders. Ceram Int 42:16469–16473
Madhu Kumar P, Balasubramanian C, Sali ND, Bhoraskar SV, Rohatgi VK, Badrinarayanan S (1999) Nanophase alumina synthesis in thermal arc plasma and characterization: correlation to gas-phase studies. Mater Sci Eng, B 63:215–227
Meng H, Zhao F, Zhang Z (2012) Preparation of cobalt nanoparticles by direct current arc plasma evaporation method. Int J Refract Met Hard Mater 31:224
Orpe PB, Balasubramanian C, Mukherjee S (2017) Influence of DC arc current on the formation of cobalt-based nanostructures. Pramana J Phys 89:20
Patel J, Balasubramanian C, Sasmal C, Satyaprasad A (2018) Preparation of SiC nanowires and nanotubes by thermal arc plasma and study of parameters controlling its growth. Phys E 103:377–382
Raut SA et al (2018) Single step, phase controlled, large scale synthesis of ferrimagnetic iron oxide polymorph nanoparticles by thermal plasma route and their rheological properties. J Mag Mag Mater 449:232–242
Salata OV (2004) Applications of nanoparticles in biology and medicine. J Nanobiotech 2:3
Sergiienko R et al (2007) Formation and characterization of graphite-encapsulated cobalt nanoparticles synthesized by electric discharge in an ultrasonic cavitation field of liquid ethanol. Acta Mater 55:3671
Shigeta M, Watanabe T (2007) Growth mechanism of silicon-based functional nanoparticles fabricated by inductively coupled thermal plasmas. J Phys D Appl Phys 40:2407–2419
Siegmann S, Girshick S, Szépvölgyi J, Leparoux M, Shin J-W, Schreuders C, Rohr L, Ishigaki T, Jurewicz JW, Habib M, Baroud G, Gitzhofer F, Kambara M, Diaz JMA, Yoshida T (2008) Nano powder synthesis by plasmas. Report of the session held at the international round table on thermal plasma fundamentals and applications: Sharm el Sheikh, Egypt, Jan. 14–18, 2007, High Temp. Mater. Processes, 12:205–254
Tondare VN, Balasubramanian C, Shende SV, Joag DS, Godbole VP, Bhoraskar SV (2002) Field emission from open ended aluminum nitride nanotubes. Appl Phys Lett 80:4813–4815
Tsai P-C, Chen W-J, Chen J-H, Chang C-L (2009) Deposition and characterization of TiBCN films by cathodic arc plasma evaporation. Thin Solid Films 517:5044–5049
Wan X, Fan Y, Ma W, Li S, Huang X, Yu J (2018) One-step synthesis of nano-silicon/graphene composites using thermal plasma approach. Mater Lett 220:144–147

Peptide Nanotubes: A Crystallographic Approach

Ashima Bagaria and Suryanarayanarao Ramakumar

Abstract Molecular self-assembly has led to a breakthrough in the field of nanomaterials. This has also resulted in a myriad of potential applications in biology and chemistry. Peptides have proven to be the most promising platforms owing to their biocompatibility and diversity. They are also most studied amongst the other classes of organic building blocks due to their uncanny resemblance to the proteins. There is a wide spectrum of literature available wherein the self-assembly of peptides has been constructed using several amino acids and sequences. The wide range of potential applications of such structures has been explored in drug delivery, surfactants, tissue engineering, etc. This chapter focuses on peptide self-assembly formed by non-coded amino acids, and formation of different nanostructures, using a crystallographic approach.

1 Introduction

Molecular self-assembly is an attractive tool by which, designing and fabrication of advanced nanomaterials can be done. In molecular self-assembly, well-defined higher order structures result from the spontaneous association of the components mainly via head-to-tail hydrogen bonding, π-π stacking, electrostatic and van der Waals interactions. Supramolecular chemistry has opened new channels for the chemists with new possibilities to synthesize a variety of molecular structures and materials held together by relatively weak, non-covalent interactions.

It has been eons of molecular selection and evolution that nature has gone through to create chemically harmonizing and structurally attuned constituents for molecular self-assembly. Molecular self-assembly can be defined as the spontaneous organization of individual components into an ordered structure without human intervention. The challenge lies in fabricating basic structural molecular building blocks that can

A. Bagaria (✉)
Department of Physics, Manipal University Jaipur, Jaipur, India
e-mail: ashima.bagaria@jaipur.manipal.edu

S. Ramakumar
Department of Physics, Indian Institute of Science, Bengaluru, India

L. Ledwani and J. S. Sangwai (eds.), *Nanotechnology for Energy and Environmental Engineering*, Green Energy and Technology,
https://doi.org/10.1007/978-3-030-33774-2_4

undergo spontaneous organization into a stable macroscopic structure using non-covalent interactions (Lehn 1993; Whitesides and Grzybowski 2002). The interactions typically include H-bonds, water-mediated H-bonds, ionic bonds, hydrophobic and Vander Waals interactions (Pauling 1939). These forces alone may not suffice for the overall organization of the defined structures; the cooperation of interactions can yield highly stable and robust structures.

Supramolecular assemblies of small biomolecules have generated a lot of interest, as the chemical modifications can offer large variations. Numerous reports of tubular assemblies of carbon (Ajayan and Ebbesen 1997; Iijima 1991) boron nitrite (Chopra et al. 1995), zeolites (Dessau et al. 1990; Meier and Olson 1988) and carbohydrate-based nanotubes (Harada et al. 1993) have catapulted the research in this vast area of material science research. Parang et al. suggested that the designed cyclic D, L-α-peptides could potentially self-assemble in bacterial membranes, increasing the membrane permeability and thus exhibiting antibacterial activity.

The peptide-based nanostructures of interest as they offer many opportunities for chemical variations, and hence control, in designing molecular assemblies, which have been successfully demonstrated to be good models for ion channels and membrane pores (Engels et al. 1995; Ghadiri et al. 1994; Granja and Ghadiri 1994; Hauser and Zhang 2010; Kim et al. 1998). The crystal structure of many hydrophobic dipeptides have pores filled with the crystallizing solvent molecules. This has opened avenues for the use of such structure as biosensors, biocatalysts and specific molecular recognition platforms (Akazome et al. 2000; Gazit 2007; Gorbitz 2001, 2002a, b, 2003, 2006; Gorbitz et al. 2005; Mahler 2006; Reches and Gazit 2003). To exemplify, hollow tubular structures act as conduits of chemical information in the form of transmembrane ion channels (Nonner and Eisenberg 1998) and provide closed reaction chambers as demonstrated by protein folding chaperonins (Xu and Sigler 1998) and protein degradation enzymes (Voges et al. 1999; Zwickl et al. 1999). Attempts to generate synthetic water channels that mimic the aquaporin channel have met with some success (Liu et al. 2005; Sidhu et al. 2004; Videnova-Adrabiska 2002). A zwitterionic helical tube of nanodimensions that mimics aquaporin with water incorporated inside the channel has been studied by solid-state ^{2}HNMR spectroscopy and X-ray crystallography (Fei et al. 2005; Middleton et al. 2013).

Pioneering work on tube-like structures, invariably formed by the stacking of cyclic molecules through intermolecular hydrogen bonds between functional groups in the peptide backbones, has been carried out by Ghadiri and co-workers for cyclic peptides with 8–12 residues (Engels et al. 1995; Ghadiri et al. 1993, 1994; Kim et al. 1998; Sidhu et al. 2004). Several short peptides have a pronounced tendency to form long needles or fibres when being crystallized from aqueous or non-aqueous solution. A well-ordered and discrete peptide nanotubes formed by the self-assembly of the diphenylalanine as core recognition motif of Alzheimer's β-amyloid polypeptide (Abromovic et al. 2006; Reches and Gazit 2003), has further to the use of peptide-based nanostructures for the design of folded and self-organized modules (Gorbitz 2006). However, the stability check of the peptide-based structures under different physical, chemical and biochemical conditions needs to be established before utilizing them as biomolecular entities.

The potential use of self-assembled peptide nanostructures as novel materials has been demonstrated in the field of biomaterials and use for carrier-mediated drug delivery, tissue engineering, antimicrobial agents, imaging tools, energy storage, biomineralization. The self-assembled peptides have been exploited for generating bio-inspired nanostructures, including nanotubes, nanofibers, nanospheres, nanobelts, and hydrogels.

While there have been many studies of protein-coded amino acids engaged in molecular self-assembly, not much work has been done on molecular self-assembly formation utilizing non-coded amino acids. The incorporation of non-coded amino acids in the molecular self-assembly of a dipeptide motif may offer an added advantage in terms of variety and stability.

2 Back Bone Conformation Constraining Amino Acids

There are varieties of non-coded, conformation constraining amino acids and many of them occur in natural proteins and peptides from microbial sources. α, β-Dehydroamino acids (Δa.a), α,α-disubstituted amino acids constitute the class of conformation constraining amino acids. The ability of these amino acids to dictate the folding of the polypeptide chains has been well established (Balaram 1999; DeGrado 1988; Jain and Chauhan 1996; Karle 1992; Mathur et al. 2004; Venkatraman 2001). Furthermore, the development of a biosynthetic method for site-specific incorporation of unnatural amino acids into proteins (Liu and Schultz 1999; Mendel 1995; Noren et al. 1989) is promising to promote a great interest in using these amino acids in protein design.

Among the conformation constraining amino acids, α, β-dehydrophenylalanine (ΔPhe) a member of α, β-dehydroamino acid group is being extensively used in the modular approach to synthetic protein design. ***Herein, the possibility of incorporating α, β-dehydrophenylalanine (ΔPhe) residue in the peptide sequences for studies in molecular self-assembly has been explored***.

2.1 α, β-dehydroamino Acids

These are the derivatives of protein amino acids (saturated amino acids) with a double bond between C^{α} and C^{β} atoms (Fig. 1) and are represented by a prefix symbol 'Δ'. They are also referred as α, β-unsaturated amino acids and are frequently found in natural peptides of microbial, fungal metabolite sources (Aubry et al. 1985; Gross and Morell 1967; Jung 1991), and in some proteins, e.g. histidine ammonia-lyase from bacterial and mammalian, and phenylalanine ammonia-lyase from plants (Noda et al. 1983). Peptides containing these amino acids are synthesized in the ribosome via a precursor protein followed by enzymatic modifications (Allgaier et al. 1986). Polycyclic peptide antibiotics called lantibiotics such as nisin, subtilin, epidermin, and

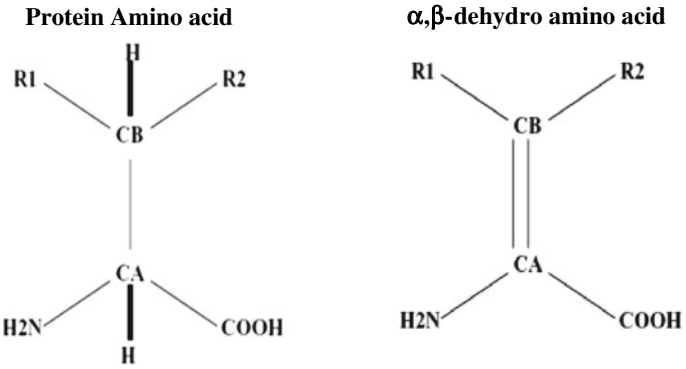

Fig. 1 General chemical structure of protein amino and α, β-dehydro ammo acid. The main difference between α, β-dehydroamino acid and protein amino acids is the double bond between C^{α} and C^{β} atoms. In this figure, C^{α} is represented as CA, C^{β} as CB and so on

ancovenin are composed of α, β-dehydroamino acids (Jung 1991). While nisin, subtilin contain dehydroalanine (ΔAla) and dehydroaminobutyric acid (ΔAbu), epiderm in and ancovenin have ΔAbu and ΔAla, respectively (Jung 1991). Other dehydro residues such as dehydroleucine (ΔLeu) and dehydrophenylalanine are present in albonoursin (Komatsubara et al. 1977), dehydrotryptophan (ΔTrp) in neochinulins (growth inhibitor) (Dossena et al. 1974), dehydroVal (ΔVal) in penicillin (Shimohigashi et al. 1982). Dehydroalanine (ΔAla) which forms a part of the active site in histidine ammonia-lyase, plays an important role in the catalytic activity of the enzyme and lack of ΔAla residue results in disease (Langer et al. 1995).

The presence of dehydroamino acids in bioactive peptides has shown to result in an increase in resistance to enzymatic degradation (English and Stammer 1978) **and confers altered bioactivity** (Shimohigashi et al. 1981). While dehydroamino acids are already occurring in natural bioactive peptides as mentioned above, these residues have also been incorporated in certain bioactive peptides with the intention to obtain highly active agonist and antagonist analogues (Iijima 1991; Nitz et al. 1986; Salvadori et al. 1986a, b; Shimohigashi et al. 1981, 1982, 1983a, b, 1984, 1987). Dehydro-angiotensin (Hallinan and Mazur 1979; Wong and Goldberg 1984), dehydrobradkynin (Fisher et al. 1981), dehydro-dermorphin (Morelli et al. 1989; Noren et al. 1989; Pieroni et al. 1986; Salvadori 1986), dehydro-somatostatin (Brady et al. 1984), dehydrosubstance P fragments (Jain and Chauhan 1996), dehydro-enkephalin (Shimohigashi et al. 1984, 1982, 1983a, 1983b), dehydro-gramicindin S (Shimohigashi et al. 1987) are some of α, β-dehydroamino acid analogues of some peptide hormones, that have been synthesized and their biological activity has been reported. In some cases, insertion of dehydroamino acids into peptide sequences makes them more effective in metal binding (Brasun et al. 2004).

Thus the double bond between C^{α} and C^{β} atoms in dehydroamino acids (a simple modification to protein amino acids), induces apparent changes to conformational and biochemical properties of peptides containing dehydroresidues. This double bond

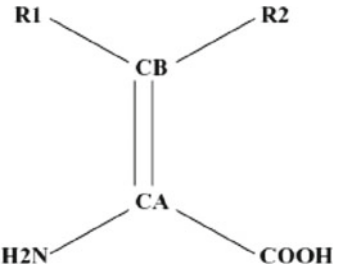

R1 = H	R2 = H	ΔAla
R1 = CH3	R2 = H	Δ^{Z} Abu
R1 = CH3	R2 = CH3	ΔVal
R1 = $CH(CH_3)_2$	R2 = H	ΔLeu
R1 = C6H5	R2 = H	Δ^{Z} Phe

Fig. 2 The chemical structures of some of dehydroamino acids

introduces certain geometric alterations in dehydroresidues and restricts the conformational flexibility of dehydropeptide backbone and side chains of dehydroresidue. These special features have influenced the use of α, β-dehydroamino acids in the design of model peptides (Jain and Chauhan 1996; Mathur et al. 2004; Narula et al. 1998; Singh and Kaur 1996).

Dehydroalanine (ΔAla), dehydrovaline (ΔVal), dehydroleucine (ΔVal), dehydroaminobutyric acid (ΔAbu), dehydroisoleucine (ΔIle), dehydroproline (ΔPro) and dehydrophenylalanine (ΔPhe) are some of the dehydroamino acids used in the design of model peptides. However, dehydrophenylalanine is used in most of the studies mainly because of its convenient chemical synthesis and interesting conformational restricting properties (Jain and Chauhan 1996; Mathur et al. 2004; Singh and Kaur 1996). The chemical structures of some of these dehydroamino acids are shown in Fig. 2.

2.1.1 α, β-dehydrophenylalanine (ΔPhe) Residue

As mentioned earlier in the definition, it is an analogue of phenylalanine residue, with a double bond between C^{α} and C^{β} atoms. It can exist in two isomeric forms, Z-isomer (Δ^{Z}Phe) and the E-isomer (Δ^{E}Phe) (Noda et al. 1983) (Fig. 3). In the Z-isomer the C=O group is in *trans* position with respect to the phenyl ring, while in the E-isomer it is in *cis* position. Among these isomers, the conformational studies are extensively done on Z-isomer due to the fact that most synthetic processes result in Z-isomer (Δ^{Z}Phe) and the E-isomer is sensitive to the chemical environment of the synthetic procedure. However, recently E-isomer has been reportedly incorporated in model peptide (Broda et al. 2005). The peptide work presented discussed here is exclusively on Z-isomer (Δ^{Z}Phe) and here afterwards we represent it by ΔPhe or ΔF.

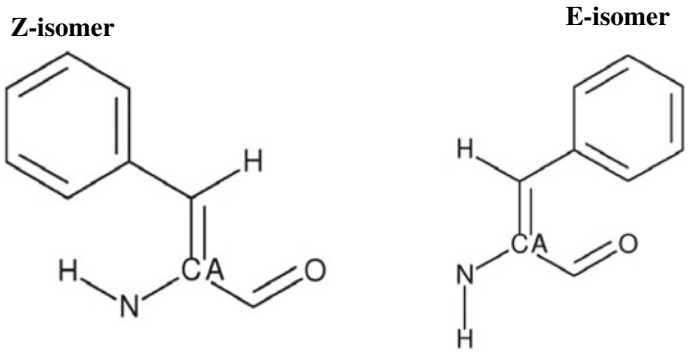

Fig. 3 Isomers of dehydrophenlalanine residue Z-isomer (ΔPhe^{Z}) and E-isomer (ΔPhe^{E})

2.1.2 Geometric Features of ΔPhe

ΔPhe is an achiral molecule and its interesting conformational features enable the design of structural elements of proteins. The backbone conformation constraining property to the ΔPhe is imparted due to the double between C^{α} and C^{β} atoms. The double bond is the consequence of dehydrogenation of saturated amino acid phenylalanine at C^{α} and C^{β} atoms, which involve the conversion of the sp^3 hybridization states of C^{α} and C^{β} atoms into sp^2 states (Fig. 4). This results in certain changes in geometrical features of ΔPhe. There is an extended conjugation of the ΔPhe ring electrons with sp^2 hybridized C^{α} and C^{β} atoms. This renders the ΔPhe residue a

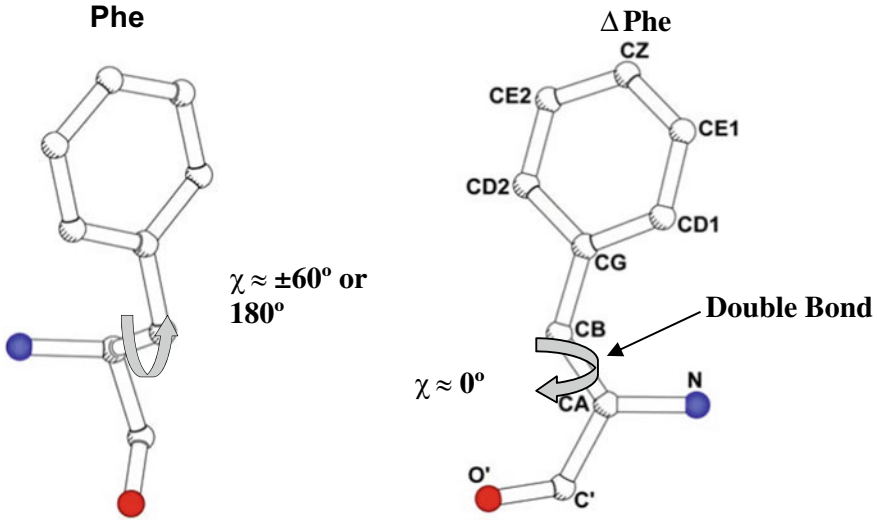

Fig. 4 The coded and the non-coded amino acid Phenylalanine (Phe) and α, β-dehydrophenylalanine (ΔPhe)

planar residue as a whole. The shorter C^{α} and C^{β} bond (~1.33 Å, an ideal C=C double bond), increased planarity and the conjugation effects produce certain unfavorable steric interactions within the residue. This includes specifically, the steric clash between CD1–H and N–H groups, which results in opening up of the bond angles $C^{\alpha}=C^{\beta}–C^{\gamma}$ and $N–C^{\alpha}=C^{\beta}$. These bond angles usually assume values of approximately 130° and 125°, respectively, in ΔPhe containing peptides, indeed deviating significantly from ideal trigonal value of 120° (Jain and Chauhan 1996; Mathur et al. 2004; Singh and Kaur 1996). Steric clash is released, in part by rotation around $N–C^{\alpha}$ bond (φ) by approximately ±60° and in part by a slight deviation of the planarity of the residue (non-zero values of χ^1 torsion angle). Besides, there is additional compensation for steric hindrance paid by the slight deviation in bond angles of $N–C^{\alpha}–C'$ and $C^{\beta}=C^{\alpha}–C'$. There are shortening of $N–C^{\alpha}$, $C^{\alpha}–C'$, and $C^{\beta}–C^{\gamma}$ single bond lengths and elongation of C′=O double bond maybe due to partial conjugation of the $C^{\alpha}=C^{\beta}$ bond and the peptide bond (Jain and Chauhan 1996; Mathur et al. 2004; Singh and Kaur 1996). Thus the double bond between C^{α} and C^{β} introduces strong steric effects in a dehydro residue resulting in a significant geometrical alteration.

2.1.3 Conformational Features of ΔPhe

As mentioned earlier, the steric clash in ΔPhe residue is released in part by the rotation of $\varphi \approx +60°$ or $-60°$. When $\varphi \approx +60°$, the allowed values of ψ can approximately be +30° or +150° after removing the steric clashes. Similarly when $\varphi \approx -60°$, ψ can be approximately −30° or −150°. Thus from the simple model building studies it has been inferred that the most favourable conformation for ΔPhe residues is (φ, ψ) ≈ (60°, 30°), (60°, −30°), (60°, 150°), (−60°, −150°). The theoretical conformational studies have suggested that there are six energy minima possible for ΔPhe residue (Ajo et al. 1982). However, experimentally observed conformations are approximately close to a few of these minima. To date, approximately 50 crystal structures of peptides containing ΔPhe residues have been reported. The analyses of these structures suggest that ΔPhe residue can assume conformations (φ, ψ) ~ (−60°, −30°), (−60°, 150°), (−80°, 0) or their enantiomers (Mathur et al. 2004; Singh et al. 1990; Singh and Kaur 1996). Figure 5 shows the Ramachandran map for ΔPhe containing peptides, in which the observed (φ, ψ) values are plotted. It is clear that a majority of the observed (φ, ψ) values are in helical regions in the Ramachandran map. As a consequence, the experimental results from X-ray crystallography match with the model building observations and partially with the theoretical conformational analyses, though the helical region is highly preferred.

This work highlights the inclusion of a non-coded, achiral, conformation constraining α, β-dehydrophenylalanine (ΔPhe) residue in the dipeptide, to probe the process of molecular self-assembly. Incorporation of dehydroamino acids provides the peptide with unique properties: rigidity, increased hydrophobicity, electrophilic reactivity, the restricted orientation of β-substituents and resistance to enzymatic degradation. The conformational flexibility of both, the dehydro peptide backbone as well as the specific side chain of the dehydro residue, is expected to be

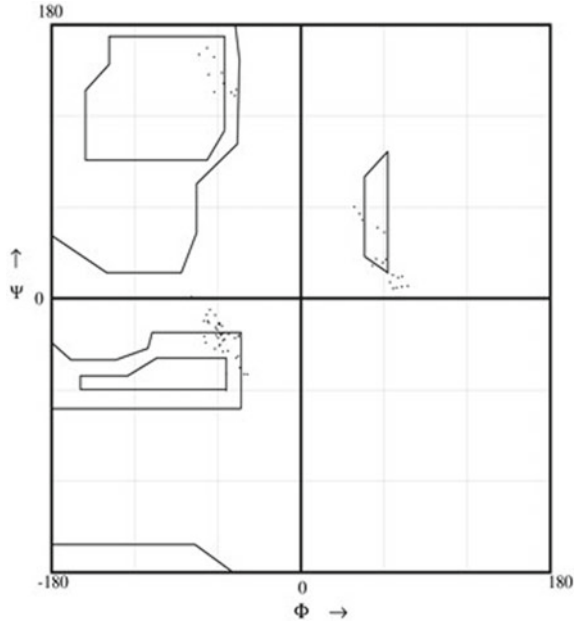

Fig. 5 The observed φ, ψ values for the ΔPhe containing peptides

restricted on account of a double bond between C^{α} and C^{β} atoms. Dipeptides were synthesized by Boc chemistry using solution-phase peptide synthesis. The crystal structures of the following designed dipeptides are reported here. All the peptides were found to be in the zwitterionic conformation.

I. **$^{+}H_3N$-Phe-ΔPhe-COO^{-}, (FΔF)**
II. **$^{+}H_3N$-Val-ΔPhe-COO^{-}, (VΔF)**
III. **$^{+}H_3N$-Ala-ΔPhe-COO^{-}, (AΔF)**

Apart from the crystallographic study, the peptides FΔF and AΔF were also studied using Transmission Electron microscopy, Scanning Electron Microscopy, Environmental Scanning Electron Microscopy, Congo red staining and birefringence, Dynamic Light Scattering and Differential Interference Contrast Microscopy.

Although biological scaffolds, including short peptides, offer a myriad of potential applications to nanotechnology, their relative instability may be a major concern in realizing their potential application. **The main aim of this work is to explore the possibility of self-assembly formation using non-coded amino acids**.

3 Characterization of Dipeptides

3.1 Characterization of Dipeptide I (F ΔF)

3.1.1 Crystallization and Data Collection

The crystals of peptide I were grown by slow evaporation of peptide solution in acetic acid and water mixture. The suitable crystal was mounted on the glass fibre and X-ray diffraction data were collected on a Bruker AXS SMART APEX CCD diffractometer equipped with Mo K_α radiation. Unit cell parameters and orientation matrix were determined initially by collecting three sets of data collected at three different settings (set1 $\varphi = 0°$, $2\theta = -28°$, $\omega = -28°$; set2 $\varphi = 90°$, $2\theta = -28°$, $\omega = -28°$; set3 $\varphi = 0°$, $2\theta = 28°$, $\omega = 28°$), each data set consists of 50 frames with ω-scan width of 0.3°. The diffraction data were acquired over a hemisphere of reciprocal lattice space by three different settings of φ ($\varphi = 0°, 90°, 180°$) and keeping detector at an angle of $2\theta = -25°$, with detector to crystal distance of 6.07 cm. For each setting of φ, 606 diffraction image frames with ω-width of 0.3° and exposure time of 20 s per fame were obtained. The data processing was done by reducing the image frames to obtain the integrated intensities for each reflection and intensities were corrected for Lorentz and polarization factors. The data processing was done using the software SAINTV6.1 (Bruker 1998). The data sets were corrected for the absorption effect by using software SADABS (Sheldrick 1996). Finally, the corrected intensity data were used for the structure solution and refinement.

3.1.2 Structure Determination and Refinement

The structure solution was obtained using direct methods employed in SHELXS97 software (Sheldrick 1997). All the non-hydrogen atoms were located in the E-map of the best solution with a combined figure of merit (CFOM) value 0.0405. After assigning each peak to the corresponding element, isotropic refinement was carried out using the computer program SHELXL97 (Sheldrick 1997). The acetic acid molecule was located in the electron density map. Anisotropic refinement was carried out for all non-hydrogen atoms after the convergence of isotropic refinement. All hydrogen atoms were fixed using stereochemical criteria and during the refinement, they were allowed to ride on their parent atoms. Refinement converged at the agreement factor of 3.92%, shown in Table 1.

3.1.3 Molecular Dimensions

Figure 6 shows the conformation of dipeptide I (FΔF) with residue labelling. The molecular parameters of all non-hydrogen atoms are given in Appendix C. In general, the bond lengths and bond angles of the coded amino acid [Phe] are in agreement

Table 1 Crystal, diffraction and refinement parameters for peptide I (FΔF)

Empirical formula	C_{18} H_{17} N_2 O_3. $1CH_3COOH$
Molecular weight	309.3
Crystal system	Monoclinic
Space group	P 2_1
Cell parameters	a = 5.5776(6) Å, b = 13.0942(14) Å, c = 12.8239(14) Å, α = γ = 90°, β = 92.64°
Cell volume	935.59(2) $Å^3$
Z	2
Density calculated	1.10 gm cm^{-3}
Absorption coefficient	0.076 mm^{-1}
Radiation used	Mo (λ = 0.71073 Å)
Resolution	0.87 Å
Unique reflections	1969
Observed reflections	1678 (|Fo| > 4 σ (|Fo|))
Structure Solution	Shells
Refinement procedure	Full-matrix least-square refinement on $\|Fo\|^2$ using Shelxl (97–2)
No: of parameters refined	247
Data/parameter	6.8
R-factor	3.92%
wR2	8.97%
GooF (s)	1.117
Residual electron density	Max. = +0.14 e/$Å^3$, Min. = − 0.12 e/$Å^3$

with the previously observed values for the geometry of peptide groups (Benedetti 1977). In addition, all the geometric parameters [CA=CB; N–CA; CA–C′; CB–CG; CA=CB–CG; N–CA=CB; N–CA–C′; CB=CA–C′] of the ΔPhe residues in the peptide molecule are in agreement with the previously reported values for ΔPhe residues in the literature (Jain and Chauhan 1996; Mathur et al. 2004; Singh and Kaur 1996).

3.1.4 Molecular Conformation

Molecular conformation of dipeptide I with non-hydrogen atoms labelled is shown in Fig. 7. It shows the thermal ellipsoidal representation (Johnson 1976). Table 2 shows important torsion angles for FΔF which are compared with the corresponding values for the saturated analogue FF (Gorbitz 2001).

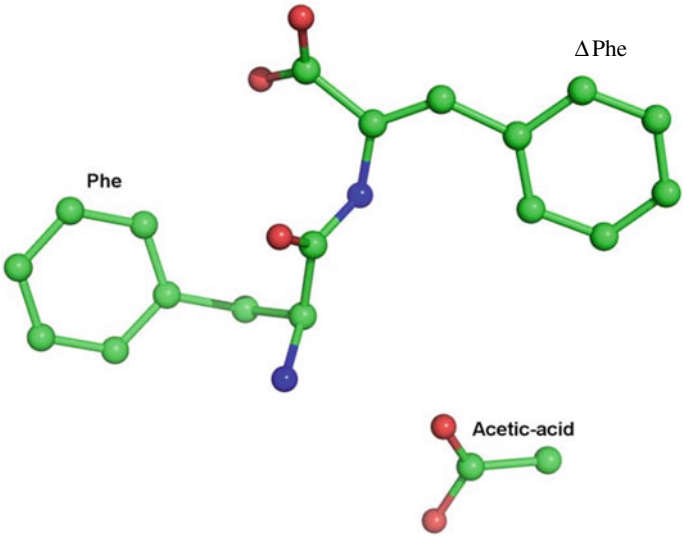

Fig. 6 Conformation of debited I (FΔF) with residue labelling

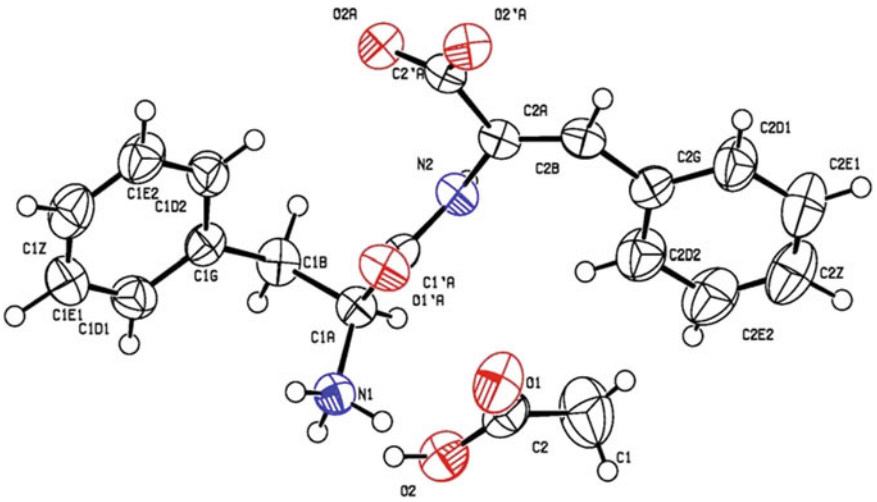

Fig. 7 The asymmetric unit of FΔF with the atomic numbering scheme. Displacement ellipsoids are shown at the 50% probability level. H atoms are shown as spheres of arbitrary size

3.1.5 Crystal Packing

FΔF exists as a monomer in the crystal asymmetric unit. The tubular structure is formed by the aggregation of four dipeptide molecule (Fig. 8) **in contrast to Phe-Phe that exhibits channels formed by the self-assembly of six dipeptide**

Table 2 Backbone Torsion angles (°) for $_{L}$-Phenyalanyl-α, β-dehydrophenylalanine, dipeptide I (FΔF) and $_{L}$-Phenyalanyl-$_{L}$-phenylalanine (FF)

Torsion angle	FΔF	FF
$\psi_1 = N_1–C_1^{\alpha}–C_1'–N_2$	150.57 (20)	157.82 (4)
$\omega 1 = C_1^{\alpha}–C_1'–N_2'C_2^{\alpha}$	177.96 (20)	−179.10 (4)
$\phi 2 = C_1'–N_2–C_2^{\alpha}–C_2'$	−66.84 (28)	55.40 (5)
$\Psi T1 = N_2–C_2^{\alpha}–C_2'–OT1$	−29.3 (3)	43.8 (5)
$\Psi T2 = N_2–C_2^{\alpha}–C_2'$-OT2	154.1 (2)	−139.8 (4)
$\theta = C_1^{\beta}–C_1^{\alpha}L\ C_2^{\alpha}–C_2^{\beta}$	149.70	40.21

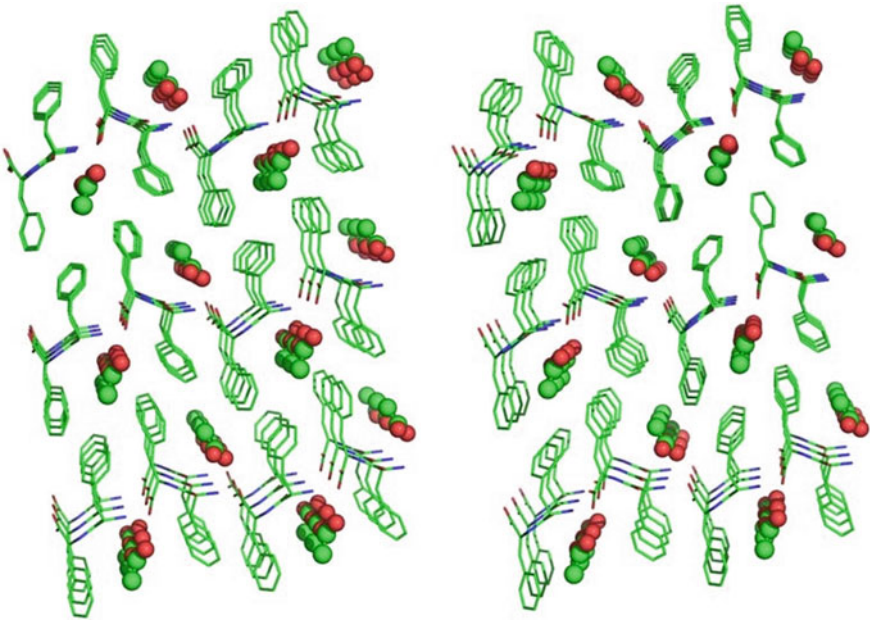

Fig. 8 Stereo view of the crystal packing is shown here. It reveals a tubular structure formed by the assembly of four dipeptide molecules of $^{+}H_3N$–Phe–ΔPhe–COO^{-}

molecules (Gorbitz 2001). Phe-ΔPhe (FΔF) has side chains on either side of the peptide bond plane, imparting an amphipathic nature to the channel. **The resulting tubular structure thus formed has a rectangular channel having Vander Waals dimension of** 6.0 × 4.5 Å. **The acetic acid molecules trapped in the channel formed by Phe–ΔPhe is crystallographically detected**. A similar feature has been previously reported in the self-assembly of the dipeptide (R)-Phenylglycine-(R)-Phenylglycine, where the dimensions of the self-assembled structure were shown to be modulated by the nature of the solvate sulphoxide. Interestingly, in those structures, different sulphoxide molecules modulate the overall conformation of the self-assembled structure (Akazome et al. 2000).

Various hydrogen bonds and the parameters for the Phe-ΔPhe molecule are tabulated in Table 3. The crystal structure of the Phe–ΔPhe dipeptide shows a C(8) pattern (Etter et al. 1990) of head-to-tail hydrogen bonding meaning that eight atoms are encountered in traversing the shortest pathway from the hydrogen atom of one hydrogen bond to the acceptor atom of the next (Fig. 9). A similar pattern of hydrogen bonding has been previously reported in the crystal structure of hydrophobic

Table 3 The intermolecular and intramolecular hydrogen bonds observed in the structure of dipeptide I (FΔF)

D (donor)	A (acceptor)	DLA (Å)	HLA (Å)	D-HLA (°)	Symmetry code
C1A	O1	3.245	2.65	120	x, y, z
C1A	O1′A	3.228	2.53	129	x − 1, +y, +z
C1D2	O2A	3.379	2.46	169	x, y, z
C2D2	N2	3.073	2.46	123	x, y, z
C1B	O2′A	3.666	2.90	137	x − 1, +y, +z
C1E2	O2	3.645	2.97	131	−x − 1, +y + 1/2, -z + 1
C2E1	O1	3.771	2.83	171	−x − 1, +y + 1/2, −z
N1	O2	3.041	2.33	137	x + 1, +y, +z
N1	O2′A	2.851	2.09	142	−x, +y − 1/2, −z + 1
N1	O2A	2.779	1.93	159	−x − 1, +y − 1/2, −z + 1
N2	O2′A	2.819	2.03	152	x − 1, +y, +z
O2	O2A	2.585	–	–	−x − 1, +y − 1/2, − z + 1
O2	O1′A	3.074	–	–	x − 1, +y, +z

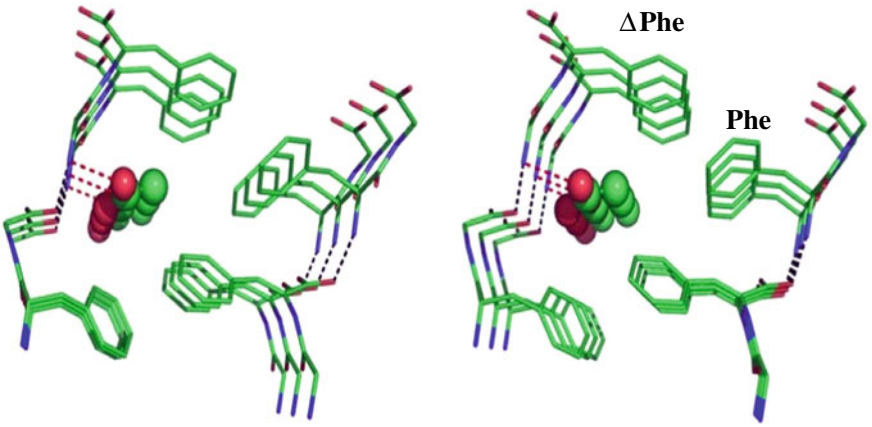

Fig. 9 Zoomed stereo view of the tubular structure formed by the aggregation of four dipeptide molecules of FΔF with the acetic acid molecule being trapped inside the tube. The figure also shows the head-to-tail hydrogen bonding seen in the dipeptide molecule. *(The side chains not involved in the channel core formation have been omitted for clarity)

dipeptides (Gorbitz 2001). **The stacked aromatic rings in the dehydrodipeptide are held by intermolecular C–H · π interactions, contributing to the overall stability of the assembled structure**. The centroid of the dehydrophenylalanine ring acts as the acceptor and the C1E1 acts as the donor. The donor to acceptor distance is 3.942 Å, the hydrogen to acceptor distance is 3.07 Å while the angle D-HLA (where D is donor and A is acceptor) is 156° (Brandl et al. 2001).

3.1.6 Discussions About Dipeptide I (FΔF)

Self-assembly has recently become a major thrust for material scientists. This process of self-assembly ultimately would give us the potential to create artificial molecules whose architecture and function is not limited by the paradigms found in nature but only by the creativity of the chemist. In this context, small peptides like dipeptides have gained much attention in displaying a myriad of structures and their potential applications. Recent work by Reches and Gazit (2003) showing the supramolecular assembly in a Phe-Phe dipeptide motif and the crystallographic detail realized by Gorbitz (2001), earlier, has led us to investigate the potential of conformation constraining residue ΔPhe in the dipeptide motif.

The tubular structure is formed by the aggregation of four dipeptide molecules (Figs. 8 and 9) **resulting in a rectangular channel having van der Waals dimension of** 6.0 × 4.5 Å. In contrast, the saturated analogue, Phe–Phe, exhibits nearly circular channels formed by the assembly of 6 peptide molecules (Gorbitz 2001), with a diameter of 24 Å. **Further differences in the two structures, Phe–Phe and Phe–ΔPhe, are seen in their molecular conformations**. A simplified description of a dipeptide can be made by calculating a torsion angle θ = C_1^{β}–C_1^{α} … C_2^{α}–C_2^{β}, proposed by Gorbitz (2001). It defines the relative position of the two side chains with respect to the peptide plane. Gorbitz et al. have shown that for zwitterionic $_{L}$-Xaa-$_{L}$-Xaa dipeptides (Xaa is neither Gly nor Pro), the side chains usually point in the almost opposite direction with |θ| usually being >135. **According to this torsion angle description, Phe–Phe occurs in the most unusual conformation with θ being 40.2°. The side chains are thus located on the same side of the peptide bond plane and appear to emanate out from the channel core. However, for Phe–ΔPhe this torsion angle |θ| has a value of 149.70° suggesting the side chains being present on both sides of the peptide bond plane, imparting an amphipathic nature to the channel**. The acetic acid molecules trapped in the channel formed by Phe–ΔPhe is crystallographically detected (Gupta et al. 2007).

Self-assembly of the dehydrodipeptide was investigated under acidic, neutral and basic conditions by varying the pH of the medium used, and it was interesting to note that the morphology of the fundamental tubular unit remains unchanged (27–30 nm) over the range of pH used. The characteristic lateral association of the tubes observed under different pH conditions might arise due to contributions from hydrophobic interactions. This lateral association was absent in Phe–Phe dipeptide with both the side chains located at the same side of the plane defined by the peptide bond.

3.2 Characterization of Dipeptide II (VΔF)

3.2.1 Crystallization and Data Collection

The crystals of peptide II were grown by slow evaporation of peptide solution in methanol and water mixture. Rod-shaped crystals suitable for x-ray diffraction, appeared within 4–5 days. The suitable crystal was mounted on the glass fibre and X-ray diffraction data were collected on a Bruker AXS SMART APEX CCD diffractometer equipped with Mo K_α radiation. Unit cell parameters and orientation matrix were determined initially by collecting three sets of data collected at three different settings (set1 $\varphi = 0°$, $2\theta = -28°$, $\omega = -28°$; set2 $\varphi = 90°$, $2\theta = -28°$, $\omega = -28°$; set3 $\varphi = 0°$, $2\theta = 28°$, $\omega = 28°$), each data set consists of 50 frames with ω-scan width of 0.3°. The diffraction data were acquired over a hemisphere of reciprocal lattice space by three different settings of φ ($\varphi = 0°$, 90°, 180°) and keeping detector at an angle of $2\theta = -25°$, with detector to crystal distance of 6.07 cm. For each setting of φ, 606 diffraction image frames with ω-width of 0.3° and exposure time of 15 s per fame were obtained. The data processing was done by reducing the image frames to obtain the integrated intensities for each reflection and intensities were corrected for Lorentz and polarization factors. The data processing was done using the software SAINTV6.1 (Bruker 1998). The data sets were corrected for the absorption effect by using software SADABS (Sheldrick 1996). Finally, the corrected intensity data were used for the structure solution and refinement.

3.2.2 Structure Determination and Refinement

The structure solution was obtained by using direct methods employed in SHELXS97 software (Sheldrick 1997). All the non-hydrogen atoms were located in the E-map of the best solution with a combined figure of merit (CFOM) value 0.061. After assigning each peak to the corresponding element, isotropic refinement was carried out using the computer program SHELXL97 (Sheldrick 1997). Two water molecules were located in the electron density map. Anisotropic refinement was carried out for non-hydrogen atoms after the convergence of isotropic refinement. All hydrogen atoms were fixed using stereochemical criteria and during the refinement, they were allowed to ride on their parent atoms. The refinement converged at the agreement factor of 4.63% shown in Table 4.

3.2.3 Molecular Dimensions

Figure 10 shows the conformation of dipeptide II (VΔF) with residue labelling. The molecular parameters of all non-hydrogen atoms are given in Appendix C. In general, the bond lengths and bond angles of the coded amino acid [Val] are in agreement with the previously observed values for the geometry of peptide groups

Table 4 Crystallographic details of dipeptide II (VΔF)

Empirical formula	(C14 H17 N2 O3)2. 2H2O
Molecular weight	262.308
Crystal system	Monoclinic
Space group	C 2
Cell parameters	a = 31.0101(62) Å, b = 5.5658(11) Å, c = 18.8130(38) Å, β = 115.43(30)°
Cell volume	2932.57(463) $Å^3$
Z	8
Density calculated	1.18 gm cm^{-3}
Absorption coefficient	0.084 mm^{-1}
Radiation used	Mo (λ = 0.71073 Å)
Resolution	0.9 Å
Unique reflections	3085
Observed reflections	2949 (|Fo| > 4 σ (|Fo|))
Structure solution	Shelxs
Refinement procedure	Full-matrix least-square refinement on $\|Fo\|^2$ using Shelxl (972)
No: of parameters refined	360
Data/parameter	8.2
R-factor	4.63%
wR2	13.16%
GooF (s)	1.044
Residual electron density	Max. = 0.49e/$Å^3$, Min. = −0.18 e/$Å^3$

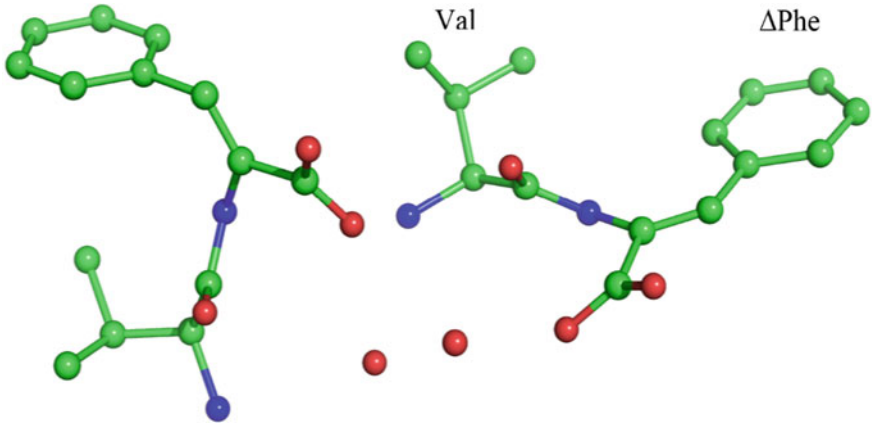

Fig. 10 Conformation of peptide II (VΔF) with residue labelling

(Benedetti 1977). In addition, all the geometric parameters [CA=CB; N–CA; CA–C′; CB–CG; CA=CB–CG; N–CA=CB; N–CA–C′; CB=CA–C′] of the ΔPhe residues in the peptide molecule are in agreement with the previously reported values for ΔPhe residues in the literature (Jain and Chauhan 1996; Mathur et al. 2004; Singh and Kaur 1996).

3.2.4 Molecular Conformation

Molecular conformation of dipeptide II with non-hydrogen atoms labelled is shown in Fig. 11. It shows the thermal ellipsoidal representation ORTEP, (Johnson 1976). Table 5 shows important torsion angles for the peptide.

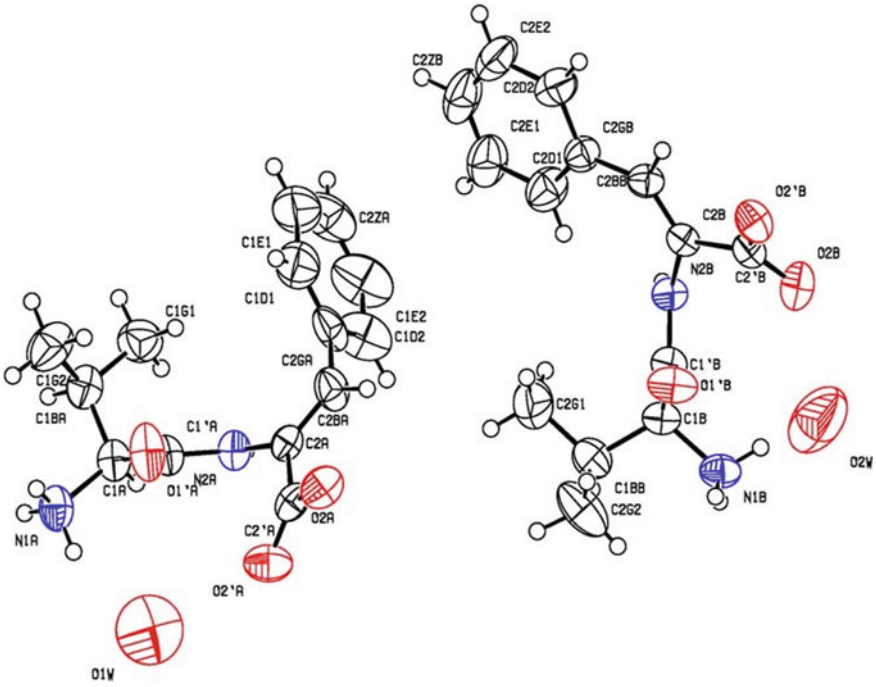

Fig. 11 The asymmetric unit of V ΔF with the atomic numbering scheme. Displacement ellipsoids are shown at the 50% probability level. H atoms are shown as spheres of arbitrary size

Table 5 Backbone Torsion angles (°) for two conformers A and B of L-Valyl-α, βdehydrophenylalanine (VΔF) and for L-Valyl-L-phenylalanine

Torsion angle	$(V\Delta F)_A$	$(V\Delta F)_B$	VF (Form 1)
ψ1 = N1–C1α–C1′-N2	145.95 (31)	127.36 (30)	151.35 (11)
ω1 = C1α–C1′–N2′C2α	178.75 (29)	−174.01 (27)	172.31 (11)
ϕ2 = C1′–N2–C2α–C2′	58.36 (41)	53.41 (39)	48.55 (16)
ΨT1 = N2–C2α–C2′–OT1	23.26 (50)	25.84 (48)	48.4 (10)
ΨT2 = N2–C2α-C2′-OT2	−158.48 (34)	−157.17 (33)	−136.3 (14)
θ = C1β–C1αL C2α–C2β	22.2	40.4	19.97

3.2.5 Crystal Packing

The dipeptide VΔF (Fig. 12) was crystallized by controlled slow evaporation in methanol–water mixture. **There are two crystallographically independent conformers in the asymmetric unit. The two conformers of VΔF, have** $|\theta| = C_1^{\beta}$–$C_1^{\alpha}LC_2^{\alpha}$–$C_2^{\beta} = 22.23°$ **and 40.4°** (Table 5) **respectively, thereby exhibiting conformation with both side chains located on the same side of the plane defined by the peptide bond**.

In VΔF, four peptide molecules constitute the circumference of the rectangular channel. The crystal packing can be seen in Fig. 12. **The interior of this channel is hydrophilic due to the presence of CONH moieties and** NH_3**+ and −OOC groups, while the exterior is hydrophobic as it is occupied by the side**

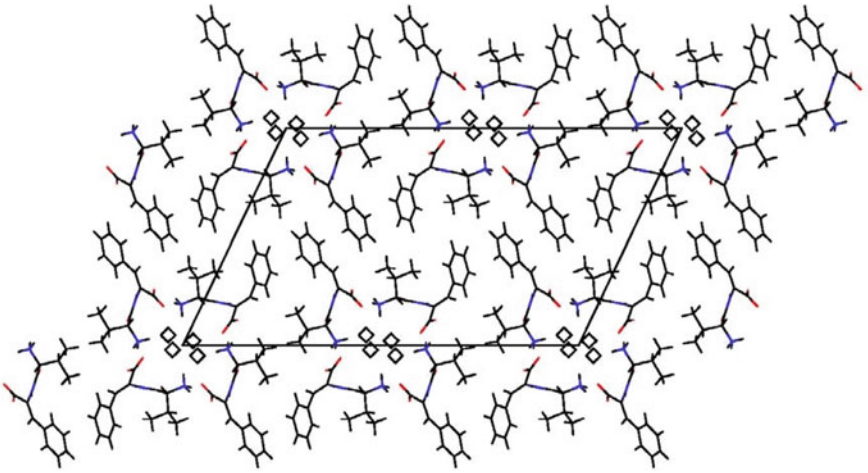

Fig. 12 The crystal packing of the dipeptide II as seen down the b axis, It can be seen that four dipeptide molecules aggregate to form a rectangular channel with water molecules (◊) trapped inside

chains of Val and ΔF. The crystal structure further revealed that the individual peptide columns are regularly aligned via intermolecular hydrogen bonds (Table 6) and other non-covalent interactions to form higher ordered supramolecular arrays along the crystallographic basis (Fig. 12). The interior of the channel is hydrophilic and water molecules are crystallographically detected inside the channel. The channel formed by VΔF is shown in Fig. 13. All side chains appear to emanate from the channel core filled with water molecules. The structure can thus be visualized as close packing of the hydrophobic tubes with the interior lined by many polar atoms. This channel has van der Waals dimension of 4.0 × 5.0 Å.

These water molecules exhibit N–HLO hydrogen bonding with the NH_3^+ group. **The VΔF molecules depict a direct head-to-tail hydrogen-bond pattern similar to that seen in other dipeptides consisting of coded amino acids**. The pattern was analysed on the graph set theory (Etter et al. 1990) (Fig. 14). The centroid of the dehydrophenylalanine ring acts as the acceptor and the C1G1 acts as the donor in a C-HLπ interaction (Brandl et al. 2001). The donor to acceptor distance is 3.929 Å,

Table 6 Hydrogen–bond parameters for L-Valyl-α, β-dehydrophenylalanine (VΔF)

D (donor)	A(acceptor)	DL.A (Å)	HLA (Å)	D-HLA (°)	Symmetry Code
N1A	O2B	3.413	2.56	161	−x, +y − 1, −z
N1A	O2′B	2.827	2.06	143	−x, +y − 1, −z
N1A	O1W	3.087	2.25	156	−x, +y, −z
N1A	O2B	2.824	2.00	135	−x, +y, −z
N2A	O2A	2.822	2.08	145	x, +y − 1, +z
N1B	O1W	3.045	2.33	138	x, +y − 1, +z
N1B	O2W	2.927	2.39	120	x, +y − 1, +z
N1B	O2′A	3.377	2.52	161	x, +y − 1, +z
N1B	O2A	2.802	2.05	142	x, +y − 1, +z
N1B	O2′A	2.808	2.09	138	x, y, z
N2B	O2′B	2.807	2.08	142	x, +y − 1, +z
C1A	O1′A	3.220	2.48	132	x, +y − 1, +z
C2D1	N2B	3.096	2.47	125	x, y, z
C1B	O1′B	3.225	2.45	135	x, +y − 1, +z
C2G2	O1'B	3.072	2.44	123	x, y, z

D (donor)	A(acceptor)	D …. A (Å)	H … A (Å)	D-H … A (°)	Symmetry Code
O1W	O2W	3.430	–	–	x, +y − 1, +z
O1W	O2W	3.114	–	–	−x, +y − 1, −z
O1W	O2W	3.070	–	–	−x, +y, −z
O1W	O2′A	2.733	–	–	−x, +y, −z
O2W	O2W	2.809	–	–	−x, +y, −z
O1W	O1′A	3.347	–	–	−x, +y, −z

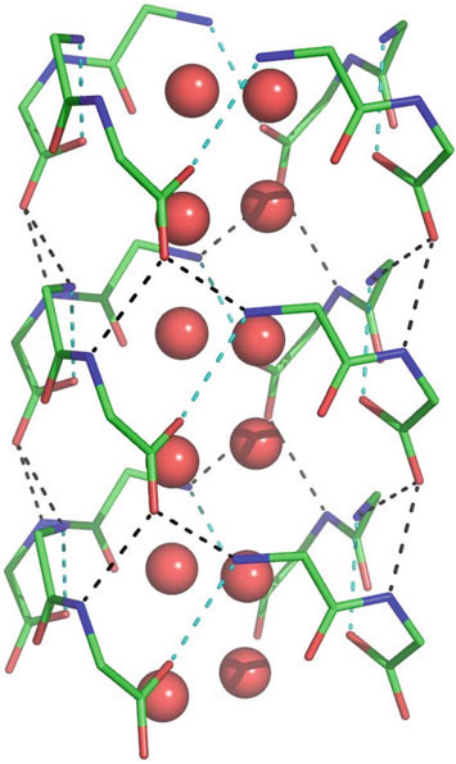

Fig. 13 View of the tubular structure formed by the aggregation of four dipeptide molecules of VΔF with the water molecule being trapped inside the tube. The water molecules are shown as spheres. Cyan color dashes show head-to-tail hydrogen bonds and black dashes show hydrogen bonds with the water molecule trapped inside the channel. The side chains have been omitted for clarity

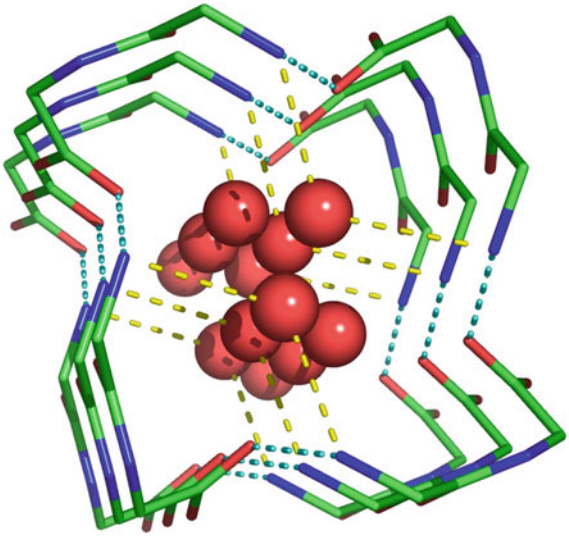

Fig. 14 The figure shows the head-to-tail hydrogen bonding seen in the VΔF molecule. The side chains not involved in interactions have been omitted for clarity

the hydrogen to acceptor distance is 3.11 Å while the angle D-HLA (where D is the donor and A is the acceptor) is 145°.

3.2.6 Discussions About Dipeptide II (VΔF)

In VΔF, four peptide molecules constitute the circumference of the rectangular channel of dimension 5.0 × 4.0 Å. The interior of this channel is hydrophilic due to the presence of CONH moieties and NH_3+ and −OOC groups, while the exterior is hydrophobic as it is occupied by the side chains of Val and ΔF.

The crystal structure of the dipeptide $_L$-Valyl-$_L$-Phenylalanyl (VF) was solved by Gorbitz (2002a, b). VF does not reveal the presence of channel structures. The crystal packing of VF in one of the crystal form depicts a hydrogen-bond cage formation around the hydrophobic groups by co-crystallized water molecules.

3.3 Characterization of Dipeptide III (AΔF)

3.3.1 Crystallization and Data Collection

Crystals of peptide III were grown by slow evaporation of peptide solution in methanol and toluene mixture (1:1 v/v). Rod-shaped crystals suitable for x-ray diffraction, appeared within 4–5 days. The suitable crystal was mounted on the glass fibre and X-ray diffraction data were collected on a Bruker AXS SMART APEX CCD diffractometer equipped with Mo K_α radiation. Unit cell parameters and orientation matrix were determined initially by collecting three sets of data collected at three different settings (set1 $\varphi = 0°$, $2\theta = -28°$, $\omega = -28°$; set2 $\varphi = 90°$, $2\theta = -28°$, $\omega = -28°$; set3 $\varphi = 0°$, $2\theta = 28°$, $\omega = 28°$), each data set consists of 50 frames with ω-scan width of 0.3°. The diffraction data were acquired over a hemisphere of reciprocal lattice space by three different settings of φ ($\varphi = 0°$, 90°, 180°) and keeping detector at an angle of $2\theta = -25°$, with detector to crystal distance of 6.07 cm. For each setting of φ, 606 diffraction image frames with ω-width of 0.3° and exposure time of 20 s per fame were obtained. The data processing was done by reducing the image frames to obtain the integrated intensities for each reflection and intensities were corrected for Lorentz and polarization factors. The data processing was done using the software SAINTV6.1 (Bruker 1998). The data sets were corrected for absorption effect by using software SADABS (Sheldrick 1996). Finally, the corrected intensity data were used for the structure solution and refinement.

3.3.2 Structure Determination and Refinement

The structure solution was obtained by using direct methods employed in SHELXS97 software (Sheldrick 1997). All the non-hydrogen atoms were located in the E-map

Table 7 Crystallographic details of dipeptide III (AΔF)

Empirical formula	C12 H14 N_2 O_3. $2H_2O$
Molecular weight	234.3
Crystal system	Monoclinic
Space group	P 2_1
Cell parameters	a = 5.8106(11) Å, b = 7.9171(16) Å, c = 14.9073(29) Å, β = 93.77°
Cell volume	684.30(3) $Å^3$
Z	2
Density Calculated	1.14 gm cm^{-3}
Absorption Coefficient	0.083 mm^{-1}
Radiation Used	Mo (λ = 0.71073 Å)
Resolution	1.00 Å
Unique Reflections	1420
Observed Reflections	1310 (|Fo| > 4 σ (|Fo|))
Structure Solution	Shelxs
Refinement Procedure	Full-matrix least-square refinement on $\|Fo\|^2$ using Shelxl (972)
No: of Parameters Refined	174
Data/Parameter	7.5
R-Factor	4.24%
wR2	11.63%
GooF (s)	1.133
Residual Electron Density	Max. = 0.20 e/$Å^3$, Min. = −0.11 e/$Å^3$

of the best solution with a combined figure of merit (CFOM) value 0.041. After assigning each peak to the corresponding element, isotropic refinement was carried out using the computer program SHELXL97 (Sheldrick 1997). Water molecules were located in the electron density map. Anisotropic refinement was carried out for all non-hydrogen atoms after the convergence of isotropic refinement. All hydrogen atoms were fixed using stereochemical criteria and during the refinement, they were allowed to ride on their parent atoms. The structure was refined to an R-factor of 4.24% and the refinement converged at the agreement factor shown in Table 7.

3.3.3 Molecular Dimensions

Figure 15 shows the conformation of dipeptide III (AΔF) with residue labelling. The molecular parameters of all non-hydrogen atoms are given in Appendix C. In general, the bond lengths and bond angles of the coded amino acid [Ala] are in agreement with the previously observed values for the geometry of peptide groups (Benedetti 1977). In addition, all the geometric parameters [CA=CB; N–CA; CA–C′;

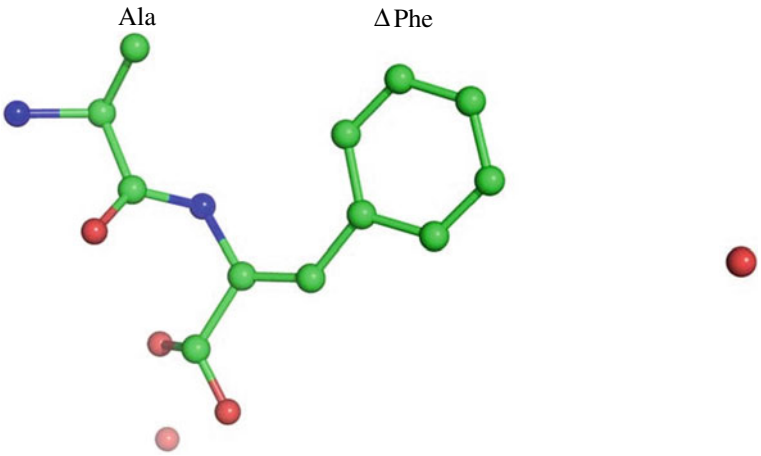

Fig. 15 Conformation of dipeptide III (AΔF)

CB–CG; CA=CB–CG; N–CA=CB; N–CA–C′; CB=CA–C′] of the ΔPhe residues in the peptide molecule are in agreement with the previously reported values for ΔPhe residues in the literature (Jain and Chauhan 1996; Mathur 2004, Singh and Kaur 1996).

3.3.4 Molecular Conformation

Molecular conformation of dipeptide III with non-hydrogen atoms labelled is shown in Fig. 16. It shows the thermal ellipsoidal representation Johnson (1976). Table 8 shows important torsion angles for the peptide.

3.3.5 Crystal Packing

The dipeptide AΔF (Fig. 16) was crystallized by controlled slow evaporation in methanol–toluene mixture. The structure was refined to an R-factor of 4.24%. **The dipeptide exists as a monomer in the asymmetric unit**. **AΔF was studied in order to find the effect of change in the molecular structure on the self-assembly**. Figure 17 shows the crystal packing of AΔF. It can be seen that the dipeptide forms an extended structure rather than a hydrophobic channel. The torsion angles for AΔF and its analog AF are listed in Table 8. **For AΔF the value of torsion angle** $|\theta| = 2.85°$, **showing that the dipeptide has conformation with both the side chains lying on the same side of the peptide bond plane**. **Two water molecules are crystallographically associated with the dipeptide**. Various hydrogen bond parameters for the dipeptide are shown in Table 9.

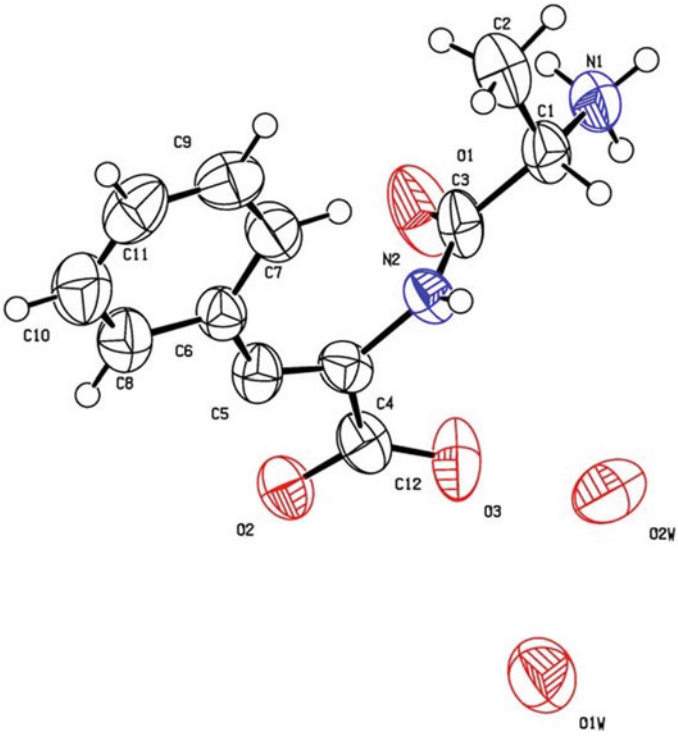

Fig. 16 The asymmetric unit of AΔF with the atomic numbering scheme. Displacement ellipsoids have shown 50% probability level. H atoms are shown as a sphere of arbitrary size

Table 8 Backbone Torsion angles (°) for of L-alanyl-α, β-dehydrophenylalanine (AΔF) and its analog L-alanyl-L phenylalanyl (AF)

TORSION ANGLE	AΔF	AF
ψ1 = N1-C1α-C1′-N2	161.73 (36)	159.8 (4)
ω1 = C1α-C1′-N2-C2α	177.27 (35)	171.4 (4)
ϕ2 = C1′-N2-C2α-C2′	64.25 (50)	−77.6 (5)
ΨT1 = N2-C2α-C2′-OT1	19.76 (54)	−32.0 (4)
ΨT2 = N2-C2α-C2'-OT2	−163.66 (35)	152.1 (5)
θ = C1β–C1αL C2α–C2β	−2.85	162

The peptide exhibits a C (8) pattern of hydrogen bond depicting a head-to-tail bonding (Fig. 18). **From the crystal packing diagram** (Fig. 17) **it is clear that the dipeptide is divided into a hydrophilic layer with peptide main chain and water molecules connected by the hydrogen bonds and hydrophobic layers** including peptide side chains.

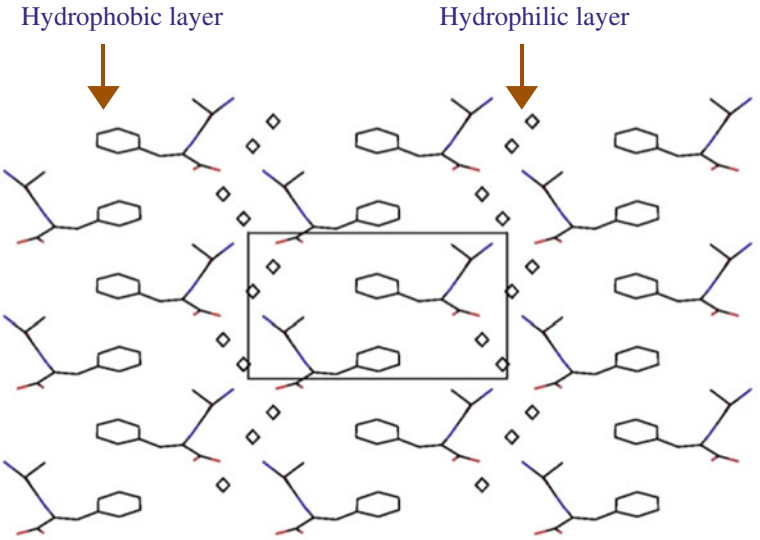

Fig. 17 The crystal of AΔF viewed along the c-axis shows the formation of alternate hydrophobic layer. Water molecules (Δ) are part of the hydrophilic layer

Table 9 Hydrogen-bond parameters for $_{L}$-Alanyl-α, β-dehydrophenylalanine (AΔF)

D (donor)	A(acceptor)	DLA (Å)	HLA (Å)	D-HLA (°)	Symmetry Code
C7	N2	3.091	2.48	124	x, y, z
N1	O2 W	2.780	2.05	137	−x + 1, +y + 1/2, −z + 1
C2	O1 W	3.652	2.91	135	x + 1, +y + 1, +z
N1	O1 W	3.071	2.33	141	−x + 1, +y + 1/2, −z
N1	O1 W	2.865	1.99	169	x + 1, +y + 1, +z
N1	O3	3.002	2.32	134	−x + 1, +y + 1/2, −z
C1	O2	3.396	2.66	132	x + 1, +y, +z
N2	O2	2.869	2.07	155	x + 1, +y, +z
C2	O1	3.121	2.51	122	x + 1, +y, +z
O1 W	O1	3.068	–	–	x, +y − 1, +z
O1 W	O1	3.142	–	–	−x + 1, +y − 1/2, −z
O1 W	O3	2.847	–	–	−x + 1, +y − 1/2, −z
O1 W	O2 W	3.221	–	–	x, +y − 1, +z − 1
O1 W	O2 W	3.354	–	–	−x, +y − 1/2, −z + 1
O1 W	O2 W	3.460	–	–	−x + 1, +y − 1/2, −z + 1
O2 W	O2	2.745	–	–	−x, +y + 1/2, −z + 1
O2 W	O3	2.783	–	–	−x + 1, +y + 1/2, −z + 1

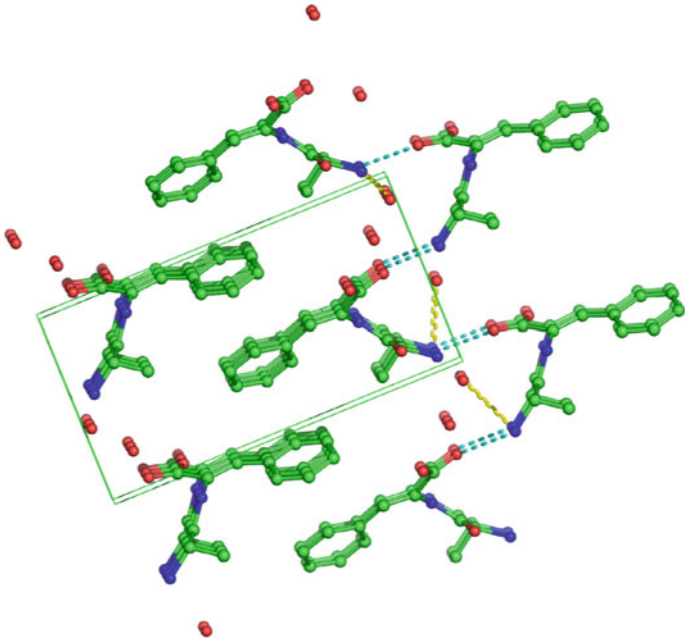

Fig. 18 The figure shows the head-to-tail hydrogen bonding seen in the AΔF molecule. The side chains not involved in interactions have been omitted for clarity

3.3.6 Discussions About Dipeptide III (AΔF)

The dipeptide III (AΔF) was characterized using various techniques apart from X-ray crystallography. No tubular assembly was suggested by these techniques as well. **The crystal packing reveals the division of the dipeptide assembly into two layers: hydrophilic and hydrophobic**. **The hydrophobic layers are formed by the peptide side chain while the hydrophilic layers are formed by the peptide main chain moieties and a water molecule**.

The molecular packing depicted by AΔF is similar to its counterpart $_{L}$-alanyl-$_{L}$phenylalanyl (AF) with a co-crystallized organic solvent molecule (Görbitz 1999). The peptide AΔF did not display any tubular structure as seen using different imaging techniques (at the concentration at which Phe-ΔPhe was investigated ~1 mg/ml).

4 Conclusion

Self-assembly has recently become a major thrust for material scientists. This process of self-assembly ultimately would give us the potential to create artificial molecules, whose architecture and function are not limited by the paradigms found in nature but

only by the creativity of the chemist. In this context, small peptides like dipeptides have gained much attention in displaying a myriad of structures and their potential applications. Recent work by Reches and Gazit (2003) showing the supramolecular assembly in a Phe–Phe dipeptide motif and the crystallographic detail solved by Gorbitz (2001), earlier, has led us to investigate the potential of conformation constraining residue ΔPhe in the dipeptide motif. In a minimalist approach towards examining the role of ΔPhe residue towards self-assembly, Phe–ΔPhe, Val-ΔPhe and AlaΔPhe dipeptides have been investigated.

The peptide $_{L}$-Phenylalanyl-α, β-dehydrophenylalanine (FΔF) forms self-assembly by the aggregation of four dipeptide molecules. The self-assembly has been depicted in all the methods by which the peptide was characterized. The rectangular channel thus formed is amphipathic in nature and holds an amphipathic, acetic acid molecule. The introduction of ΔPhe that introduces a restriction on account of a double bond between C_{α} and C_{β} atoms seem to provide order and directionality needed for the formation of well-ordered supramolecular structures and can be potentially utilized in fine-tuning the nature of other molecular assemblies.

The two dipeptides $_{L}$-Valyl-α, β-Dehydrophenylalanine (VΔF) and $_{L}$Alanyl-α, β-Dehydrophenylalanine (AΔF) show different packing arrangements and were studied together to investigate how the self-assembly behaves when the molecular structure is modified. Here we have used two different hydrophobic residues Ala and Val, Ala being less hydrophobic than Val. The conformations of both the peptides are almost similar. VΔF forms hydrophobic columns having a hydrophilic core while AΔF forms hydrophilic and hydrophobic layers with peptide main chain moieties and peptide side chains, respectively.

A systematic survey carried by Gorbitz 2004 (Helle et al. 2004) reveals that dipeptides constructed from two amino acid residues with large hydrophobic side chains may give porous structures with hydrophilic inner surfaces. This structural family is referred to as FF class after $_{L}$-Phe-$_{L}$-Phe and includes Leu-Leu, Leu-Phe, Ile-Phe, Ile-Leu. The absolute value of the torsion angle θ for this class is less than 90°, meaning thereby that both side chains lie on the same side of the peptide bond plane. In an attempt to understand the effect of change in molecular structures on self-assembly, we have compared the solid-state structures of VΔF and AΔF. VΔF falls under FF class fulfilling both the criteria and being more hydrophobic prefers channel formation tracing helicity. Albeit, for AΔF $|\theta| < 90°$, but it being less hydrophobic, prefers extended layer formation. It is clear that the introduction of the hydrophobicity parameter brings about changes in packing. Even though the confirmation of these two peptides is quite similar, both exhibit remarkably different packing arrangements. Thus we can say that changes in molecular structure by altering the hydrophobicity of the dipeptide in the dehydro peptides studied here alter the self-assembly.

π-stacking is considered as one of the major determinants in self-assembly process. **The present peptide structures however revealed that it is just not the π-stacking but also the overall hydrophobicity of the molecule that dictates self-assembly. Phe has a high hydrophobicity index than Ala. The absence of tubular assembly in Ala-ΔPhe as compared to Phe-ΔPhe substantiates the above**

Table 10 Summary of various parameters for the hydrophobic dipeptides in discussion

Dipeptide	Tube dimensions [Å]	θ [°]	Crystal packing
FΔF	6.0 × 4.5	150	Tubular assembly
VΔF	4.0 × 5.0	22, 40	Tubular assembly
AΔF	–	−3	Hydrophobic and hydrophilic layers

hypothesis. **A summary of various parameters for the dipeptides reported here is given in** Table 10.

The biological scaffolds like short peptides and motifs offer a wide range of applications in the field of nanotechnology. Because of this, the research has been upscaled in this field of novel biomaterials. But there are certain drawbacks that need to be finely addressed. The relative instability of such scaffolds is a major bottleneck in realizing their potential application. The **introduction of ΔPhe in the dipeptides as discussed in the chapter has affected the pattern of peptide assembly and also in the peptide structure itself**. **The tubes formed by the dehydrodipeptide are discrete structures, which are longer and thinner than previously reported peptide-based tubular structures** (Reches and Gazit 2003). **ΔPhe residue offers a high degree of resistance to a highly non-specific protease thereby making the bio-nanotubes suitable for applications in biological systems**. **The peptide structures discussed herein are easy to synthesize, cost-effective and open avenues for designing novel nanotubular scaffolds**.

References

Abromovich LA, Reches M, Sedan VL, Allen S, Tendler SJB, Gazit E (2006) Thermal and chemical stability of diphenylalanine peptide nanotubes: implications for nanotechnological applications. Langmuir 22:1313–1320

Ajayan PM, Ebbesen TW (1997) Nanometer size tubes of carbon. Rep Prog Phys 60:1025–1062

Ajo D, Casarin M, Granozzi G (1982) On the conformational flexibility of model compounds of β-substituted α, β-unsaturated peptides. J Mol Struct 86:297–300

Akazome M, Ueno Y, Ooiso H, Ogura K (2000) Enantioselective inclusion of methyl phenyl sulfoxides and benzyl methyl sulfoxides by (R)-phenylglycyl-(R)-phenylglycine and the crystal structures of the inclusion cavities. J Org Chem 65:68–76

Allgaier H, Jung G, Wener RG, Scheider U, Zahner H (1986) Eidermin: sequencing of a heterodetic tertracyclic 21-peptide amide antibiotic. Eur J Biochem 160:9–22

Aubry A, Allier F, Boussard G, Marraud M (1985) Crystal structure of a dehydromonopeptide, (Z)-N-Ac-ΔPhe-NHMe. Biopolymers 24:639–646

Balaram P (1999) De novo design: backbone conformational constraints in nucleating helices and beta-hairpins. J Pept Res 54:195–199

Benedetti E (1977) Structure and conformation of peptides: a critical analysis of crystallographic data. In: Goodman M, Meienhofer J (eds) Peptides proceedings of fifth american peptide symposium. Wiley, pp. 257–273

Brady SF, Cochran DW, Nutt RF, Holly FW, Bennett CD, Paleveda WJ, Curley PE, Arison BH, Saperstein R, Veber DF (1984) Synthesis and conformational study of a cyclic hexapeptide analog of somatostatin containing dehydrophenylalanine. Int J Peptide Protein Res 23:212–222

Brandl M, Weiss MS, Jabs A, Sühnel J, Hilgenfeld R (2001) C-h$\cdots\pi$-interactions in proteins. J Mol Biol 307(1):357–377

Brasun J, Makowski M, Oldziej S, Swiatek-Kozlowska J (2004) Coordination ability of pentapeptides with two dehydro-amino acid residues inserted into their sequences. J Inorg Biochem 98:1391–1398

Broda MA, Siodlak D, Rzeszotarska B (2005) Conformational investigation of alpha, beta-dehydropeptides. XV: N-acetyl-alpha, beta-dehydroamino acid N 'N' dimethylamides: conformational properties from infrared and theoretical studies. J Pept Sci 11:546–555

Bruker (1998) SMART, SAINT, XPREP and SHELXTL. Bruker AXS Inc., 5465 East Cheryl Parkway, Madison, WI, USA, pp 53711–5373

Chopra NG, Luyken RJ, Cherrey K, Crespi VH, Cohen ML, Louie SG, Zettl A (1995) Boron nitride nanotubes. Science 269:966–967

DeGrado WF (1988) Design of peptides and proteins. Adv Protein Chem 39:51–124

Dessau RM, Schlenker JL, Higgins JB (1990) Framework topology of aluminophosphate AlPO4-8: the first 14-ring molecular sieve. Zeolites 10:522–524

Dossena A, Marchelli R, Pochini A (1974) New metabolites of Aspergillus amstelodami related to the biogenesis of neoechinulin. J Chem Soc Chem Commun 771–772

Engels M, Bashford D, Ghadiri MR (1995) Structure and dynamics of self-assembling peptide nanotubes and the channel-mediated water organization and self-diffusion. a molecular dynamics study. J Am Chem Soc 117:9151–9158

English ML, Stammer CH (1978) D-Ala2, ΔzPhe4-methionine enkephalin amide, a dehydropeptide hormone. Biochem Biophys Res Commun 85(2):780–782

Etter MC, MacDonald JC, Bernstein J (1990) Graph-set analysis of hydrogen-bond patterns in organic crystals. Acta Crystallogr B 46:256–262

Fei Z, Zhao D, Geldbach TJ, Scopelitti R, Dyson PJ (2005) A synthetic zwitterionic water channel: characterisation in the solid state by X-ray crystallography and NMR spectroscopy. Angew Chem Int Ed 44:5720–5725

Fisher GH, Berryer P, Ryan JW, Chauhan VS, Stammer CH (1981) Dehydrophenylalanyl analogs of bradykinin: synthesis and biological activities. Arch Biochem Biophys 211:269–275

Gazit E (2007) Self-assembled peptide nanostructures: the design of molecular building blocks and their technological utilization. Chem Soc Rev 36:1263–1269

Ghadiri MR, Granja JR, Milligan RA, McRee DE, Khazanovich N (1993) Self-assembling organic nanotubes based on a cyclic peptide architecture. Nature 366:324–327

Ghadiri MR, Granja JR, Buehler LK (1994) Artificial transmembrane ion channels from self-assembling peptide nanotubes. Nature 369:301–304

Gorbitz CH (2001) Nanotube formation by hydrophobic dipeptides. Chem Eur J 7:5153–5159

Gorbitz CH (2002a) An exceptionally stable peptide nanotube system with flexible pores. Acta Crystallogr Sect B 58:849–854

Gorbitz CH (2002b) Beta turns, water cage formation and hydrogen bonding in the structures of L-valyl-L-phenylalanine. Acta Crystallogr B 58:512–518

Gorbitz CH (2003) Nanotubes from hydrophobic dipeptides: pore size regulation through side chain substitution. New J Chem 27:1789–1793

Gorbitz CH (2006) The structure of nanotubes formed by diphenylalanine, the core recognition motif of Alzheimer's beta-amyloid polypeptide. Chem Commun (Camb) 2332–2334

Görbitz CH (1999) Acta Crystallogr C Cryst Struct Commun 55(12):2171–2177

Gorbitz CH, Nilsen M, Szeto K, Tangen LW (2005) Microporous organic crystals: an unusual case for L-leucyl-L-serine. Chem Commun 14:4288–4290

Gross E, Morell JL (1967) The presence of dehydroalanine in the antibiotic nisin and its relationship to activity. J Am Chem Soc 89:2791–2792

Gupta M, Bagaria A, Mishra A, Mathur P, Basu A, Ramakumar S, Chauhan VS (2007) Self-assembly of a dipeptide-containing conformationally restricted dehydrophenylalanine residue to form ordered nanotubes. Adv Mater 19:858–861

Hallinan EA, Mazur RH (1979) In peptides: structure and biological function. Gross E, Meienhofer (eds) Pierce Chemical Co., Rochford, Illinois. pp. 475–477
Harada A, Li J, Kamachi M (1993) Synthesis of a tubular polymer from threaded cyclodextrins. Nature 364:516–518
Hauser CAE, Zhang SG (2010) Designer self-assembling peptide nanofiber biological materials. Chem Soc Rev 39:2780–2790
Helle IH, Løkken CV, Görbitz CH, Dalhus B (2004) Acta Crystallogr C Cryst Struct Commun 60(10):o771–o772
Horwich AL, Weber-Ban EU, Finley D (1999) Chaperone rings in protein folding and degradation. Proc Natl Acad Sci USA 96:11033–11040
Iijima S (1991) Helical microtubules of graphitic carbon. Nature 354:56–58
Jain RM, Chauhan VS (1996) Conformational characteristics of peptides containing α, β-dehydroamino acid residues. Biopolymers (Peptide Science) 40:105–119
Johnson CK (1976) ORTEP. A Fortran thermal-ellipsoid plot program for crystal structure illustrations. ORNL Report 5138. Oak Ridge National Laboratory, Tennessee, USA
Jung G (1991) Lantibiotics-Ribosomally synthesised biologically active polypeptides containing sulfide bridges and α, β-dehydroamino acids. Angew Chem Int Ed Engl 30:1051–1068
Karle IL (1992) Folding, aggregation and molecular recognition in peptides. Acta Crystallogr. B48:341–356
Kaur P, Patnaik GK, Raghubir R, Chauhan VS (1992) Synthesis and biological evaluation of dehydrophenylalanine containing substance P fragments. Bull Chem Soc Jpn 65:3412–3418
Kim HS, Hartgerink JD, Ghadiri MR (1998) Oriented self-assembly of cyclic peptide nanotubes in lipid membranes. J Am Chem Soc 120:4417–4424
Komatsubara S, Kisumi M, Chibata I, Gregorio MMV, Müller US, Crout DHG (1977) Stereochemistry of the conversions in vivo of L- and D-threonine into 2-oxobutanoic acid by the L-and D-threonine dehydratases of Serratia marcescens J Chem Soc Chem Commun 839–841
Langer M, Pauling A, Retey J (1995) The role of dehydroalanine in catalysis by histidine ammonia lyase. Angew Chem Int Ed Engl 34:1464
Lehn JM (1993) Supramolecular chemistry. Science 260:1762–1763
Liu DR, Schultz PG (1999) Progress toward the evolution of an organism with an expanded genetic code. Proc Natl Acad Sci USA 96:4780–4785
Liu K, Kozono D, Kato Y, Agre P, Hazama A, Yasui M (2005) Conversion of aquaporin 6 from an anion channel to a water-selective channel by a single amino acid substitution. Proc Natl Acad Sci USA 102:2192–2197
Mahler A, Reches M, Rechter M, Cohen S, Gazit E (2006) Rigid, self-assembled hydrogel composed of a modified aromatic dipeptide. Adv Mater 18(11):1365–1370
Mandal D, Shirazi NA, Parang K (2014) Self-assembly of peptides to nanostructures. Org Biomol Chem 12(22):3544–3561
Mathur P, Ramakumar S, Chauhan VS (2004) Peptide design using alpha, beta-dehydro amino acids: from beta-turns to helical hairpins. Biopolymers 76:150–161
Meier WM, Olson DH (1988) Atlas of zeolite structure types, Butterworths, London: Mendel D, Cornish VW, Schultz PG (1995) Site-directed mutagenesis with an expanded genetic code. Annu Rev Biophys Biomol Struct 24:435–462
Mendel D, Cornish VW, Schultz PG (1995) Site-directed mutagenesis with an expanded genetic code. Annu Rev Biophys Biomol Struct 24:435–462
Middleton DA, Madine J, Castelletto V, Hamley IW (2013) Insights into the molecular architecture of a peptide nanotube using FTIR and solid-state NMR spectroscopic measurements on an aligned sample. Angew Chem Int Ed 52:10537–10540
Morelli MAC, Saviano G, Temussi PA, Balboni G, Salvadori S, Tomatis R (1989) NMR studies of a series of dehydrodermorphins. Biopolymers 28:129–138
Narula P, Patel HC, Singh TP, Chauhan VS, Sharma AK (1988) Crystal structure and molecular conformation of N-boc-L-pro-dehydro-leu-OCH3. Biopolymers 27(10):1595–1606

Nitz TJ, Shimohigashi Y, Costa T, Chen H, Stammer CH (1986) Synthesis and receptor binding affinity of both E-and Z-dehydrophenylalanine enkephalins. Int J Peptide Protein Res 27:522–529
Noda K, Shimohigashi Y, Izumiya N (1983) α, β-dehydroamino acids and peptides. In: Gross E, Meienhofer J (eds) The peptides 5. Academic Press, NewYork, pp 285–339
Nonner W, Eisenberg B (1998) Ion permeation and glutamate residues linked by Poisson-Nernst-Planck theory in L-type calcium channels. Biophys J 75:1287–1305
Noren CJ, Anthony-Cahill SJ, Griffith MC, Schultz PG (1989) A general method for incorporation of unnatural amino acids into proteins. Science 244:182–188
Pauling L (1939) The nature of the chemical bond. Cornell University Press, Ithaka, NewYork
Pieroni O, Fissi A, Salvadori S, Balboni G, Tomatis R (1986) Dehydro-demorphins. Int J Peptide Protein Res 28:91–100
Reches M, Gazit E (2003) Casting metal nanowires within discrete self-assembled peptide nanotubes. Science 300:625–627
Salvadori S, Marastoni M, Balboni G, Marzola G, Tomatis R (1986a) Dehydro-demorphins. Int J Peptide Protein Res 28:254–261
Salvadori S, Marastoni M, Balboni G, Marzola G, Tomatis R (1986b) Dehydro-demorphins. Int J Peptide Protein Res 28:262–273
Sheldrick GM (1996) SADABS, Siemens area detector absorption software. Universitat Gottingen, Germany
Sheldrick GM (1997) SHELX-97 A program for automatic solution and refinement of crystal structures. University of Gottingen, Gottingen, Germany
Shimohigashi Y, Costa T, Stammer CH (1981) Dehydro-enkephalins: Receptor binding activity of unsaturated analogs of LeuS-Enkephalins. FEBS Lett 133:269–271
Shimohigashi Y, English ML, Stammer CH, Costa T (1982) Dehydro enkephalin. IV. Descriminative recognition of δ and μ opiate receptors by enkephalin analogs. Biochem Biophys Res Commun 104:583–590
Shimohigashi Y, Dunning JW, Kolar AJ Jr, Stammer CH (1983a) Dehydro-enkephalins. Int J Peptide Protein Res 21:202–208
Shimohigashi Y, Stammer CH, Costa T, Vonvoigtlander PF (1983b) Synthesis and biological activity of ΔPhe4-enkephalins. Int J Peptide Protein Res 22:489–494
Shimohigashi Y, Costa T, Nitz TJ, Chen H, Stammer CH (1984) Importance of the stereo-orientation of aromatic groups in enkephalins to opiate receptor recognition. Biochem Biophys Res Commun 121:966–972
Shimohigashi Y, Kodama H, Imazu S, Horimoto H, Sakaguchi K, Waki M, Uchida H, Kondo M, Kato T, Izumiya N (1987) [4,4′-(Z)-Dehydrophenylalanine]gramicidin S with stabilised bioactive conformation and strong antimicrobial activity. FEBS Lett 222:251–255
Sidhu PS, Udachin KA, Ripmeester JA (2004) Water and tris(5-acetyl-3-thienyl) methane (TATM) assemble into a one-dimensional channel compound. Chem Commun (Camb) 12:1358–1359
Singh TP, Kaur P (1996) Conformation and design of peptides with α, β-dehydro-amino acid residues. Prog Biophys Mol Biol 66:141–165
Singh TP, Narula P, Patel HC (1990) α,β-Dehydro residues in the design of peptide and protein structures. Acta Crystallogr B Struct Sci 46(4):539–545
Videnova-Adrabiska Veneta (2002) Ring templated nanochannel architecture of imidazolium phosphonoacetate. J Mater Chem 12:2931–2935
Venkatraman J, Shankaramma SC, Balaram P (2001) Design of folded peptides. Chem Rev 101:3131–3152
Voges D, Zwickl P, Baumeister W (1999) The 26S proteasome: a molecular machine designed for controlled proteolysis. Annu Rev Biochem 68:1015–1068
Whitesides GM, Grzybowski B (2002) Self-assembly at all scales. Science 295:24182421
Wong TW, Goldberg AR (1984) Kinetics and mechanism of angiotensin phosphorylation by the transforming gene product of Rous sarcoma virus. J Biol Chem 259:3127–3131
Xu Z, Sigler PB (1998) GroEL/GroES: structure and function of a two-stroke folding machine. J Struct Biol 124:129–141

Zwickl P, Voges D, Baumeister W (1999) The proteasome: a macromolecular assembly designed for controlled proteolysis. Philos Trans R Soc Lond B Biol Sci 354:1501–1511

Halloysite Nanotubes: An 'Aluminosilicate Nanosupport' for Energy and Environmental Applications

Gaurav Pandey, Maithri Tharmavaram and Deepak Rawtani

Abstract Environmental engineering focuses on the use of engineering principles for protecting the local, as well as global environment, from damaging effects caused either due to natural or human actions. One of the major tasks in this field is to develop efficient and economical systems, which can assist in reducing the environmental pollution, especially in air and water. Additionally, development of eco-friendly systems which can act as energy storage devices is also a key thrust area of research for environmental engineers and scientists. In recent years, emergence of nanotechnology-based materials has proved to be a helping hand in many applications in various sectors. However, the use of eco-friendly nanomaterials provide an upper hand over other nanomaterials for such applications. One such environment-friendly nanomaterial is Halloysite Nanotube (HNT). It is a naturally available, clay-based aluminosilicate nanomaterial, which has attracted attention of many environmental researchers in recent times. These nanotubes exhibit negative charge on the exterior surface, while the internal lumen (interior surface) exhibits a net positive charge. The current chapter highlights the usage of HNT as nano-support systems to immobilize various types of guest molecules. Further, the use of such 'guest molecule HNT'-based nano-support systems for the remediation of environmental pollutants, as well as for energy applications has been discussed.

Keywords Halloysite nanotubes · Environment · Energy · Pesticide · Pollution · Nanotechnology

1 Introduction

Population explosion and speedy industrialization have become a major cause for the increasing environmental pollution in recent years. Air, water and soil are getting polluted and adversely affected due to the development of civilization. Such polluted environment is becoming a serious threat for the survival and health of human beings,

G. Pandey · M. Tharmavaram · D. Rawtani (✉)
Institute of Research and Development, Gujarat Forensic Sciences University, Gandhinagar, Gujarat, India
e-mail: rawtanid@gmail.com

L. Ledwani and J. S. Sangwai (eds.), *Nanotechnology for Energy and Environmental Engineering*, Green Energy and Technology,
https://doi.org/10.1007/978-3-030-33774-2_5

as well as for the ecological safety (Wang et al. 2018). Developing countries witness around 14,000 deaths per day, majorly because of the consumption of contaminated water (Johnston et al. 2010; Rodríguez-Lado et al. 2013). Pollutants such as pesticides (Rawtani et al. 2018), nitrates (Tyagi et al. 2018) and metals (Khatri et al. 2017a, b) are severely depleting the quality of surface and groundwater (Khatri and Tyagi 2015; Khatri et al. 2016a). Apart from pollution, the need of energy has increased many folds in past years due to the huge population. Energy production through green routes and development of eco-friendly energy storage systems is becoming the need of the hour.

In the past decade, various technological and scientific works have been made by environmental engineers to tackle the problem of environmental pollution and depleting energy sources (Kamat 2007, 2008). Environmental engineering deals with the employment of principles of engineering in order to safeguard the environment of the earth and local surroundings from detrimental effects, which are produced due to natural or human activities. The thrust areas of research in this field mainly include the development of highly efficient, and at the same time economical solutions for the eve increasing pollution levels in the environment, mainly for the treatment of polluted air and water.

In recent years, nanotechnology has emerged as an efficient technological aid in order to tackle such kinds of energy and environmental issues. This recent technology deals with the fabrication of materials in the nanometer range by manipulating the atoms and molecules present in the bulk material (Pandey et al. 2016; Tharmavaram et al. 2017). Various kinds of nanomaterials, especially nanoparticles, nanotubes, nanowires, nanosheets and nanorods have proficiently proved their potential in different areas. In the field of environmental remediation, early determinations mainly concentrated in the development of photocatalytic nanomaterials for degrading toxic dyes from the industries (Akpan and Hameed 2009; Byrne et al. 2018). Using nanotechnology-based materials, some of the recent researchers have targeted the pharmaceutical effluents, products of personal care with endocrine disrupting compounds, since these types of contaminants do not get effectively removed during the wastewater treatment (Ebele et al. 2017; Fagan et al. 2016). However, a major concern regarding the toxicity of nanomaterials has arisen before the researchers, as far as environmental applications are concerned (Du et al. 2018). Moreover, the cost involved in the synthesis of various nanomaterials is also significantly high, which limits their bulk usage for energy storage or environmental remediation. Therefore, in the field of environmental engineering, an eco-friendly and non-toxic alternative for these nanomaterials can be a better choice for various applications such as the production of green energy, energy storage, water remediation and gas separation.

Halloysite Nanotubes (HNT), a naturally occurring clay-based nanomaterial can be the best alternative for the aforementioned purposes. This chapter initially sheds light on the HNT, its structure, properties and the types of guest molecules which can be immobilized on the nanotubes. Further, the use of such guest@HNT composite for the energy and environmental applications has also been discussed in detail.

2 Halloysite Nanotubes: Structure and Properties

Halloysite Nanotubes (HNT) are clay-based nanomaterials, which are having an alumina- and silica-rich composition (Rawtani and Agrawal 2012a). These are the nanotubular form of the Halloysite, a clay mineral formed because of the variations produced by hydrothermal activities in carbonate and volcanic rocks (Tharmavaram et al. 2018). Other non-dominant forms of Halloysite are plates and spheroidal (Yuan et al. 2015). The structure as well as properties of HNT are majorly based on its origin, i.e. the deposit from where HNT has been mined (Cavallaro et al. 2018; Makaremi et al. 2017). The chemical formula of HNT is $Al_2(OH)_4Si_2O_5 \cdot nH_2O$, and exhibit the 1:1 dioctahedral aluminosilicate structure, in either hydrated or dehydrated forms (Rawtani and Agrawal 2012b). The earlier notion of HNT being a solid nanotube like structure has reformed over the years to a layered structure of thin aluminosilicate sheet, having silica moieties rich external surface, and internal surface being rich in alumina moieties. The interlayer spaces in these nanotubes (hydrated form) are having rich content of water (Bates et al. 1950). The disparity between the minor gibbsite octahedral and major tetrahedral layers is responsible for the tubular structure of HNT (Yuan et al. 2015). The structure of HNT has been depicted in Fig. 1. The presence of alumina groups in the lumen of HNT, i.e. on the internal surface provides a positive charge, while the silica-rich external surface possesses negative charge. Such diversity of charge on the surface of HNT is responsible for the tunable surface chemistry of the nanotubes (Deepak and Agrawal 2012). The alumina and silica moieties assist in the functionalization of HNT's surface with various modification agents.

The slender and mesoporous lumen is in the range of nanometers, while the length varying from nano- to micrometers provide excellent property of adsorption to the nanotubes. The natural availability, non-toxicity, biocompatibility, cost-effectiveness are some of the merits associated with the use of HNT (Rawtani et al. 2018). The

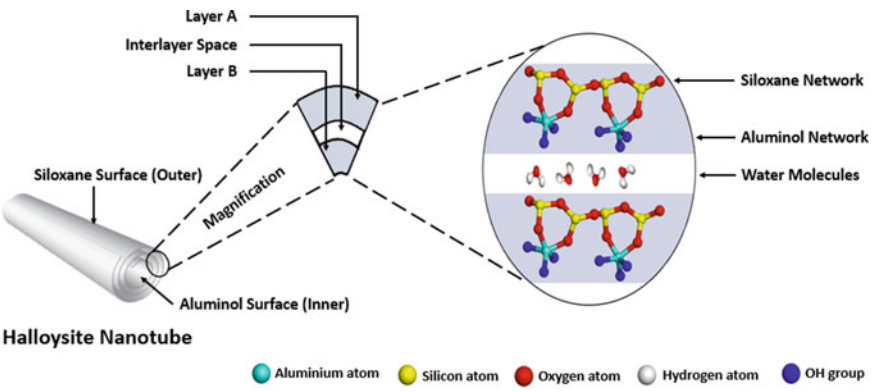

Fig. 1 Structure of Halloysite Nanotubes Reprinted with permission from Tharmavaram et al. (2018). Copyright (2018) Elsevier

outermost layer of the nanotubes becomes approachable for diverse kind of foreign molecules or agents for modification because of the existence of explicit surface area and large overall pore volume. However, the values of SSA and TPV show variations in HNTs, which come from different deposits (Joussein et al. 2005; Pasbakhsh et al. 2013). The nanotubes which come from Western Australia are known to be having the highest levels of purity. Nanotubes from this deposit have less than 2% impurities and exhibit high surface area when compared to nanotubes from other origins (Tharmavaram et al. 2018). HNT also exhibits excellent tensile strength as well as thermal stability. However, these properties vary with the structure of the nanotubes. Longer nanotubes are known to possess high degrees of thermal stability and tensile strength in comparison to the shorter nanotubes (Makaremi et al. 2017). The rotational dynamic behaviour is found to be of the highest degree in the HNT, which comes from the Dragon Mine. A noteworthy discrepancy is witnessed in the surface morphology of HNT acquired from unalike deposits (Cavallaro et al. 2018; Tharmavaram et al. 2018). Hence, the proper selection of the nanotubes becomes the utmost essential for any specific type of application.

The surface morphology and tubular lumen of the nanotubes can be studied using Transmission Electron Microscopy (TEM). The analysis shows that the internal diameter of the nanotube is in the range of 15–20 nm, while the external diameter is between 50 and 100 nm (Pandey et al. 2017a). The surface modification of the nanotubes can also be visualized using this characterization technique (Rawtani et al. 2017). Analysis of functional groups on HNTs surface can be performed through Fourier Transform Infrared Spectroscopy (FTIR) The analysis of functional groups present on the HNT is carried out by Fourier Transform Infrared Spectroscopy (FTIR). The analysis spectra reveal the characteristic vibrations of HNT at 905–910 cm^{-1} for Al-OH stretching, and at 1025–1035 cm^{-1} for Si-O-Si stretching (Rawtani et al. 2013). The X-ray Diffraction (XRD) analysis of HNT shows the crystalline behaviour of the nanotubes and is an excellent analysis for differentiating between hydrated and dehydrated forms of the nanotubes (De Silva et al. 2015). The stability of the nanotubes in a solution can be analyzed using Dynamic Light Scattering (DLS), by measuring the zeta potential. Pristine HNT is known to exhibit high zeta potential value in the negative range, possibly due to the presence of silica moieties on the external surface (Lazzara et al. 2018; Massaro et al. 2017). Such kinds of diversity in the properties of HNT allow them to be used for various applications in the field of biology, catalysis, environment (Tharmavaram et al. 2018) and forensics (Pandey et al. 2017b).

2.1 Halloysite Nanotubes as 'Nanosupport' for Different Guest Molecules

The tunable surface chemistry along with huge surface area plays a vital part in immobilizing different kinds of guest molecules on the exterior and interior surface

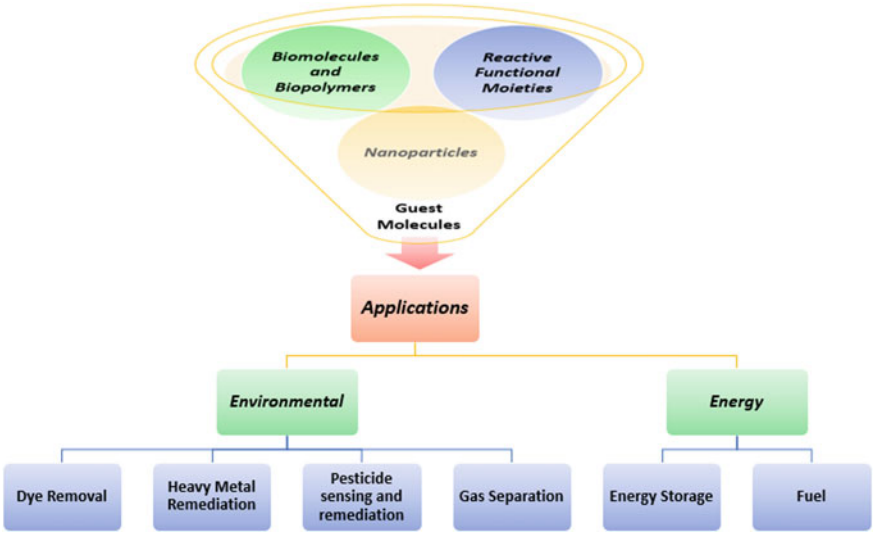

Fig. 2 Types of Guest Molecules on Halloysite Nanotubes for energy and environmental applications

of HNT. A 'guest molecule' can be defined as any foreign molecule or group that is not a part of pristine HNT, and has been immobilized or attached on HNT's layers via external agents. In the past, different researchers have immobilized myriad types of guests on HNT for diverse applications. Guests such as drugs, vaccines, antioxidants and corrosion inhibitors have been introduced on the surface of HNT (Lvov et al. 2016). Nanoparticles of silver (Rawtani et al. 2013) and gold (Rawtani and Agrawal 2012b, c) have been introduced on HNT's surface to study the interaction of such composite with DNA. Biological molecules such as enzymes (Pandey et al. 2017a) and hormones (Lvov et al. 2008) have also been immobilized as guests on HNT.

As far as energy and environmental applications are concerned, several commonly used guest molecules have been depicted in Fig. 2. These molecules mainly include reactive functional moieties, primarily from organosilanes (Zeng et al. 2016) and surfactants (Jinhua et al. 2010); biomolecules such as dopamine (Hebbar et al. 2016) and enzymes (Pandey et al. 2017a); biopolymers, mainly chitosan (Peng et al. 2015); and nanoparticles (Afzali and Fayazi 2016).

3 Energy and Environmental Applications of Halloysite Nanotubes

In Sect. 2.1, the different kinds of guest molecules that are immobilized on HNT have been discussed. The guest molecules provide versatile properties to HNT and thereby increase its applicability for energy and environmental applications. In this section,

the different energy and environmental applications of HNT are discussed, while giving special emphasis on the effect, the guest molecules have on the nanotube and thereby on its applicability. Table 1 depicts the different guest molecules, which are immobilized on HNTs for different kinds of energy and environmental applications.

3.1 Environmental Applications

Surplus pollutants present in water bodies require immediate treatment to prevent hazardous effects on nearby flora and fauna. In recent years, HNT has garnered worldwide attention through its use as a unique nano-support for the remediation of environmental pollutants. Their non-toxic and biocompatible nature further aides their applicability in such fields. Over the years, HNT have been utilized for the remediation of dyes such as auramine yellow and orange (Khatri et al. 2016b), heavy metals, drugs, pesticides and even nanoparticles such as silver (AgNP). HNT immobilized with various guest molecules have also been employed for such purposes. This section highlights the utilization of HNT immobilized with various guest molecules for environmental remediation.

3.1.1 Dye Remediation

Contamination of water bodies with dyes largely results from the runoff of synthetic dyes from industries of textile, cosmetics, plastic making or other manufacturing units. When the effluent discharge from such industries is not monitored properly, it results in release of copious amounts of toxic dyes, which pose a serious risk to life in the waterbody and its environment. Some of the dye components have also proven to be mutagenic or carcinogenic, and therefore, their remediation is highly essential. Over the years, waste water treatment methods such as primary and secondary treatments which involve techniques such as flocculation (Lee et al. 2014), catalytic degradation (Pirilä et al. 2015), and filtration (Li et al. 2017a, 2017b) have served the purpose. However, such treatments are economically difficult to implement, and come with additional difficulties such as high-operational cost and energy requirements.

HNT due to their tubular structure, biocompatibility and non-toxic nature along with high physical and chemical stability are exceedingly suitable to be used either as adsorbents in order to remove harmful dyes, or as support for immobilizing various guest molecules to impart catalytic properties to the nanotube. The guest molecules can also be selected in such a way that they enhance the adsorption property of the HNT as well. When HNT is used as an adsorbent, factors such as dosage of the adsorbent, pH and temperature of the solution, and contact time have to be contemplated (Anastopoulos et al. 2018). Based on such factors, the types of guest molecules that can be immobilized on the surface of HNT can be considered.

Table 1 Halloysite Nanotubes immobilized with different Guest molecules for energy and environmental applications

S. No.	Application	Guest molecule	Source	Target	References
1.	Dye Removal	Fe_3O_4 nanoparticles	$FeCl_3 \cdot 6H_2O$, $FeSO_4 \cdot 7H_2O$	Methyl Violet 2B	Bonetto et al. (2015)
		Fe_3O_4 nanoparticles	$FeCl_3 \cdot 6H_2O$, $FeSO_4 \cdot 7H_2O$	Methyl Violet	Duan et al. (2012)
		Fe_3O_4 nanoparticles	$FeCl_3$	Methylene Blue	Jiang et al. (2014)
		Fe_3O_4 nanoparticles	$FeCl_3 \cdot 6H_2O$, $FeSO_4 \cdot 7H_2O$	Methylene Blue, Neutral Red, Methyl Orange	Xie et al. (2011)
		Fe_3O_4 nanoparticles	$FeCl_3 \cdot 6H_2O$, $FeSO_4 \cdot 7H_2O$	Naphthol Green B	Riahi-Madvaar et al. (2017)
		Fe_3O_4 nanoparticles	$FeCl_3 \cdot 6H_2O$, $FeSO_4 \cdot 7H_2O$	Methyl Red, Methyl Orange	Liu et al. (2018)
		$-NH_2$ groups	APTES	Direct Red 28	Zeng et al. (2016)
		$-NH_2$ groups	Dopamine	Direct Red, Direct Yellow, Direct Blue	Zeng et al. (2017)
		Catechol and $-NH_2$ groups	Polydopamine	Methylene Blue	(Wan et al. 2017)
		$-NH_2$ groups	Chitosan	Methylene Blue, Malachite Green	Peng et al. (2015)
		TiO_2 nanoparticles	Titanium dioxide	Aniline	Szczepanik et al. (2016)
2.	Heavy metal removal	Quaternary Ammonium ions	HDTMA	Cr (VI)	Jinhua et al. (2010)
		$-NH_2$ groups	APTES and Polyethyleneimine	Cr (VI)	Tian et al. (2015)
		$-NH_2$ groups	3-AzPTMS	Pb (II)	Cataldo et al. (2018)
		Fe_3O_4 nanoparticles	$FeCl_3 \cdot 6H_2O$, $FeSO_4 \cdot 7H_2O$	Pb (II)	Afzali and Fayazi (2016)
		$-NH_2$ groups	APTES, N-2 Pyridylsuccinamic acid	Pb (II)	He et al. (2013)
		Catechol and $-NH_2$ groups	Polydopamine	Pb (II), Cd (II)	Hebbar et al. (2016)
3.	Pesticide	$-COOH$ groups and Fe_3O_4 nanoparticles	Succinic Anhydride, $Fe(acac)_3$	2,4,6,-Trichlorophenol	Pan et al. (2011)

(continued)

Table 1 (continued)

S. No.	Application	Guest molecule	Source	Target	References
		Cu^{2+} ions	$CuSO_4$	2,4,6,-Trichlorophenol	Zango et al. (2016)
		−OH, and NH_2 groups	NaOH, APTES	Diazinon, Parathion, Fenthion	Saraji et al. (2017)
		TiO_2 nanoparticles	Titanium Dioxide	Parathion	Saraji et al. (2016)
		Rose Bengal	Rose Bengal	n-nonylphenol	Bielska et al. (2015)
		Fe_3O_4 nanoparticles	Fe $(NO_3)_3 \cdot 9H_2O$	Pentachlorophenol	Tsoufis et al. (2017)
4.	Gas separation	$-NH_2$	APTES	CO_2	Ge et al.(2017)
		$-NH_2$	AEAPTMS	CO_2, CH_4	Hashemifard et al. (21)
5.	Energy storage	−SH groups, Ni_3S_2 nanoparticles, Carbon Nanoparticles	MPTS, Nickel Sulphide	Supercapacitor	Li et al. (2017a, 2017b)
		Graphene	Graphene aerogel	Electrothermal storage	Zhou et al. (2019)
		Catechol and -NH_2 groups	Dopamine	Vanadium Flow Battery	Yu et al. (2018)
6.	Fuels	NiO and CoO catalysts	Metal Chloride	Crude Oil Catalyst	Abbasov et al. (2016a, 2016b)
		PANI	Aniline	Oxygen Reduction Reaction Catalyst	Liu et al. (2018)
		$-HSO_3$ groups	CSPTMS, PhTES, MPTS	Biodiesel	Silva et al. (2015)

$FeCl_3 \cdot 6H_2O$: Ferric Chloride Hexahydrate; $FeSO_4 \cdot 7H_2O$: Ferrous Sulphate Heptahydrate; APTES: 3-aminopropyltriethoxysilane; $Fe(acac)_3$: Ferric triacetylacetonate; AzPTMS: Azidopropyltrimethoxysilane; HDTMA: Hexadecyltrimethylammonium bromide; AEAPTMS: Aminoethyl-aminopropyltrimethoxysilane; MPTS: Mercaptopropyltrimethoxysilane; PANI: Polyaniline; CSPTMS: 2-(4-chlorosulphonylphenyl)ethyltrimetoxysilane; PhTES: triethoxyphenylsilane

For instance, in a study, researchers had developed HNT-Fe_3O_4 nanocomposites for the adsorption of Methyl Violet 2B (MV2B) from aqueous solutions. Immobilization of magnetic nanoparticles on the surface of HNT imparts a magnetic property to the nanotube, thereby ensuring its easy separation from solutions. Immobilization of magnetic nanoparticles does not produce extra contaminants, thus making it suitable for dye removal. The nanoparticles also enhance the surface area and thereby increase the number of adsorption sites. The developed nanocomposite demonstrated a maximum adsorption capacity of 20.04 mg/g and showed high reusability when it retained its properties even after 4 cycles of adsorption–desorption (Bonetto et al.

2015). Duan et al. (2012) had also employed a similar HNT-Fe_3O_4 nanocomposite for the removal of Methyl Violet. This nanocomposite showed a higher adsorption capacity of 90.09 mg/g (Duan et al. 2012). The adsorption capacities of HNT-Fe_3O_4 nanocomposites can also be increased by incorporating it with carbon-based adsorbent. In a study, the magnetic nanocomposite was incorporated with glucose originated hydrothermal carbon. Hydrothermal carbon is known to have a high adsorption capacity due to its higher number of oxygen-containing groups, which serve as adsorption sites. This nanocomposite was further used for the adsorption of Methylene Blue (MB), and it showed an adsorption capacity of 88.42 mg/g through Langmuir Adsorption Isotherm (Jiang et al. 2014). HNT-Fe_3O_4 nanocomposite has also been employed to eliminate Neutral Red (NR), MB and Methyl Orange (MO). This study also showed that the developed magnetic HNT nanocomposite was capable of removing neutral (MB), cationic (NR) and anionic (MO) dyes (Xie et al. 2011). Similarly, HNT -Fe_3O_4 nanocomposites have been used in the removal of naphthol green B as well (Riahi-Madvaar et al. 2017). In addition to this, HNT-Fe_3O_4 nanocomposites have found their way for the recognition of azo dyes as well. These nanocomposites were used to construct a magnetic hemimicelle for Solid-Phase Extraction (SPE) adsorption of dyes. These hemimicelles offered multiple advantages such as detection and removal of azo dyes, enhanced extraction capacity, and simplified elution of analytes. The synthesized adsorbent demonstrated an adsorption capacity of 121.95 mg/g. The hemimicelle also showed excellent Limit of Detection (LOD) of 0.042 μg/L and 0.050 μg/L in samples spiked with Methyl Red (MR) and Methyl Orange (MO), respectively (Liu et al. 2018).

Other techniques of dye removal using guest@HNT complex include development of membranes for enhanced dye rejection and filtration. Nanofiltration films have nanosized pores and are easy to implement. HNT implemented nanofiltration membranes further allows enhanced hydrophilicity of the membrane because of the hydroxyl moieties existing on the surface of HNT. Several studies have incorporated HNT into the nanofiltration membranes and used such membranes for eliminating harmful dyes. For instance, amine groups had been grafted on the surface of HNT through 3-aminopropyltriethoxysilane (APTES). This composite was later incorporated in a PVDF nanofiltration membrane for the removal of Direct Red (DR). The membrane had showed a dye rejection rate up to 94.9%, which was very high in comparison to pure PVDF membranes. The membranes also demonstrated excellent rejection stability and high reusability after multiple tests (Zeng et al. 2016). In yet another approach of immobilizing amino groups on the surface of HNT for enhancing the adsorption and hydrophilicity of the membranes, HNT with immobilized Polydopamine (PDA) have been introduced in the PVDF membranes for removal of DR28, Direct Yellow (DY) and Direct Blue (DB) dyes. PDA contains catechol and amino groups, which when combined with amino groups upsurge the number of sites for adsorption on HNT. Therefore, the membrane showed a dye rejection rate of 96.5% for DR28, while for DY, it was 85%. The membrane showed a rejection rate of 93.7% for DB (Zeng et al. 2017).

Apart from films, several novel structures with HNT incorporated in them have been developed as well. For instance, Polydopamine (PDA) had been immobilized

on HNT in order to impart mussel-inspired properties to the nanotube to develop a novel core@double shelled structure, consisting of HNT modified with PDA and KH550, which is an organosilane that attaches amino groups on the surface, along with magnetite nanoparticles (Fe_3O_4). This core@double shell structure showed a high adsorption capacity by removing 714.23 mg/g of Methylene Blue (MB) from aqueous solutions at 318.15 K. Such a high adsorption capacity was contributed by the Fe_3O_4 nanoparticles as well, which enhanced the surface area of the structure. These nanoparticles also imparted magnetic property to the structure, thereby ensuring their easy separation from aqueous solutions. This structure also showed high reusability even after 5 cycles of adsorption and desorption of MB (Wan et al. 2017). Another study had reported the use of chitosan and HNT based hydrogel beads for the removal of MB and Malachite Green (MG). The incorporation of HNT into the beads formed a rough surface which in turn increased the number of adsorption sites. This along with the abundance of amine groups contributed by chitosan allowed adsorption of the dyes up to 92% for MB and up to 97% for MG (Peng et al. 2015).

In addition to adsorption, dyes have also been removed through photocatalytic degradation of HNT based nanocomposites. A study had reported photodegradation of Aniline by HNT that had been chemically activated by incorporating titanium dioxide (TiO_2). The chemical activation allowed the reduction of amorphous part of HNT, and an upsurge in the amount of Halloysite and Kaolinite. This catalyst showed a reaction rate constant of up to 0.431 ± 0.003 for concentrations of aniline kept at 0.04 mg/cm^3 (Szczepanik and Słomkiewicz 2016).

3.1.2 Heavy Metal Remediation

The chief reasons for pollution caused by heavy metals are industrial activities, agricultural runoffs, and traffic emission. Heavy metals are non-biodegradable and are present in the environment for longer periods of time. The persistent exposure of heavy metals may cause adverse effects on living beings. In recent years, the use of HNT-based nanocomposites for the removal of heavy metals such as chromium Cr(VI)) and lead (Pb(II)) has gained attention. The different ways of removal of heavy metals have been through adsorption, filtration, SPE and reduction (Gidlow 2015; Mason et al. 2014).

In another work, quaternary ammonium ions (NH_4^+) were grafted onto HNT's surface through treatment by Hexadecyltrimethylammonium bromide (HDTMA), which is a surfactant for the removal of Cr (VI) ions. The adsorbent showed high adsorption capacity by removing 90% of chromates within 5 min. Factors such as ionic strength and pH deemed to be a heavy influence on the adsorption by HNT, which was confirmed by the decrease observed in the rate of adsorption upon increasing the ionic strength and pH (Jinhua et al. 2010). The negatively charged chromate ions get attracted to the positively charged surface of HNT, thus resulting in enhanced adsorption of the metal ions. Apart from NH_4^+ ions, amine groups have been grafted on HNT's surface though treatment by Polyethyleneimine (PEI) for the removal of Cr (VI). These nanocomposites showed excellent adsorption rate, which was deemed to

be 64 times higher than pristine HNTs and showed a maximum adsorption capacity of 102.5 mg/g at 328 K. A sequential step for reduction of Cr(VI) to Cr(III) followed by adsorption on the positively charged surface had occurred, which enhanced the adsorption capacity (Tian et al. 2015).

Apart from the elimination of chromium ions, several researches have stated the removal of lead ions as well. In a study, amino groups were grafted on the surface of HNT through organosilanes treatment. This contributed a positive charge to the surface, which enhanced the adsorption rate and showed a maximum adsorption capacity of 12.18–46 mg/g. The wide range was obtained as a result of wide pH range from 3 to 6. The nanocomposite also showed high reusability (Cataldo et al. 2018). Similarly, HNT of magnetic nature were fabricated by grafting Fe_3O_4 nanoparticles on its surface, followed by further deposition by MnO_2 nanoparticles for the elimination of Pb (II) ions. This composite demonstrated a high adsorption capacity of 59.9 mg/g and the adsorption process were said to be spontaneous and endothermic. A major factor behind was touted to be the presence of MnO_2 nanoparticles, which have high affinity for many heavy metals along with increased surface area, porosity and particle size. The nanocomposite also showed high reusability even after 5 cycles of adsorption/desorption processes (Afzali et al. 2016). Interestingly, Pb (II) ions have also been removed through SPE techniques by employing HNT with N-2-Pyridylsuccinamic acid grafted on it. The developed adsorbent showed an enhancement in the adsorption rate by 67 times and the capacity of adsorption was found to be 23.58 mg/g (He et al. 2016).

Filtration has also been utilized as an alternate method for the eradication of heavy metals. For instance, in a study, polydopamine was attached on HNT's surface, and this composite was used to develop polyetherimide mixed matrix membranes for the elimination of heavy metals such as Pb (II) and cadmium Cd (II). The membranes showed a rejection rate of 34% and 27% for Pb (II) and Cd (II), respectively (Hebbar et al. 2016).

3.1.3 Pesticide Remediation and Sensing

Pesticides are chemicals that control and eliminate weeds and pests, and are widely used across the world. However, 90% of the pesticides reach water bodies due to agricultural runoffs and seepage (Khatri et al. 2017a, b; Khatri and Tyagi 2015). Chronic exposure to pesticides can seriously affect biodiversity, endangered species and destruction of habitat of birds. During the last decade, several approaches have been established for elimination of pesticides from aqueous environment. However, conventional techniques have the limitations of high-operational cost and need of technical expertise. In the past few years, several HNT-based nanocomposites have been used for the detection and removal of pesticides (Rawtani et al. 2018).

In a study, 2,4,6-trichlorophenol had been selectively recognized and removed through HNT-based nanocomposites using SPE. Molecularly Imprinted polymers (MMIP) were grafted and synthesized on the surface of HNTs with magnetic nanoparticles immobilized on them. The MMIPs served as sorbents for this purpose. The

developed nano-adsorbent showed a maximum adsorption capacity of 246.73 mg/g at 298 K. When applied to real spiked samples, the composite showed recovery rates of 83.3% ± 6.1% to 96.3% ± 2.7% (Pan et al. 2011). Apart from the detection and removal of 2,4,6-trichlorophenol, a study had reported its adsorption on HNT with Copper (Cu^+) ions immobilized on it. The nanocomposite was developed with different concentrations of Cu^+ on HNT. It was observed that there was a proportional increase in the adsorption of the pesticide with an increase in the concentration of Cu^+ on HNT's surface. Pristine nanotubes had shown a maximum adsorption capacity of 75.5 mg/g while 4.9 wt% Cu^+ on HNT showed 76.7 mg/g and 9 wt% Cu^+ on HNT showed 80.3 mg/g (Zango et al. 2016).

Chemically modified HNT-based nanocomposites have been successful as a fibre coating for Solid-Phase Microextraction (SPME). For instance, Saraji et al. (2017) had worked on the grafting of amine groups on HNT's surface that were acid etched and hydroxylated. APTES had been used to attach the amine groups on HNTs surface. The synthesized nanocomposite was used to detect organophosphorus insecticides in different spiked samples. The nanocomposite showed high extraction efficiency along with no significant change in its composition or structure (Saraji et al. 2017). Parathion, which is a type of organophosphate insecticide was successfully detected through a HNT-TiO_2 hybrid. This hybrid was used as a fibre coating for Solid Phase Microextraction (SPME). The nanocomposite showed very quick response time for the determination of parathion. In spiked samples, the LOD for celery, strawberry and apples were 0.3 μg/kg, 0.5 μg/kg and 0.3 μg/kg, respectively. The nanocomposite also showed excellent recovery for the analysis of the pesticide in the spiked samples (Saraji et al. 2016).

Rose Bengal (RB), which is a photosensitizer was immobilized on HNT for the degradation of n-nonylphenol, a dangerous pesticide. RB when in the presence of light release a singlet oxygen which oxidizes pesticides and thus degrades it. This particular nanocomposite served as an efficient photosensitizer even in the presence of small quantities of RB (0.412 mg/g) (Bielska et al. 2015). Similarly, magnetic HNT had also been used for the decomposition of pentacholorophenol, which is another commonly used insecticide with hazardous health effects. HNT provided thermal stability to the nanoparticles which enhanced its activity thus allowed enhanced decomposition of the pentachlorophenol which was shown by obtaining a 180% higher catalytic yield. The hybrid also showed high reusability and was shown to be reused even after multiple cycles (Tsoufis et al. 2017). Apart from this, oxidase enzymes such as laccase have also been immobilized on the surface of HNT in order to degrade pesticides. In a study, magnetic nanoparticles and -NH_2 groups through APTES were grafted on the surface of HNT. Then using glutaraldehyde as a crosslinker, laccase was further immobilized on it. The nanocomposite was later used to degrade pesticides (Kadam et al. 2017).

3.1.4 Gas Separation

Gas separation is often required in cases where multiple products or a single purified product is required. Over the years, methods using adsorbents (zeolites, activated charcoals) have been developed. However, the most commonly used and the most efficient method is through membranes. Mixed Matrix Membranes (MMM) are a polymeric hybrid system consisting of the adsorbents as fillers in a flexible polymeric base. Proper dispersion of such fillers can enhance the free volume in the membranes, thus bringing an increase in membrane permeability.

A couple of studies have incorporated HNTs as fillers in the development of MMM. By using HNT as a filler and by ensuring its proper dispersion in the membrane, high permeability and selectivity can be imparted to it. In a study, HNTs which had been surface etched through alkali had been further subjected to treatment by APTES in order to immobilize of amine groups. These HNTs were later used as a filler in a 6FDA-durene polyimide polymer. The presence of HNT had significantly increased the gas permeability and the presence of amine groups had a major effect on the selectivity of the membrane towards the gas (here, CO_2) by showing an adsorption capacity of 6.1 cm^3/g (STP) at a pressure of 120 kPa at 298 K (Ge et al. 2017). Similarly, N-[3-(Trimethoxysilyl)propyl]ethylenediamine (AEAPTMS) was used to treat HNT for the grafting of amine groups on its surface. The studies showed an enhancement in the adsorption capacity with increment in the amine groups. However, after a certain concentration of the amount of amine groups on HNT's surface, the adsorption had decreased. The reason behind this is touted to be the blocking of pores by the groups (Hashemifard et al. 2011).

3.2 Energy Applications

With rising depletion in natural non-renewable sources, finding an alternative source of energy or implementing 'greener' improvements in current techniques are necessary in order to improve life all over the world. Over the years, several techniques have been developed that can decrease the consumption of energy, increase its production or find alternative methods that can produce greener fuels such as biodiesel.

In the past few years, HNT has been utilized for energy storage and development of green fuels. In this section, the use of HNT in energy applications and the effect of immobilization of newer guest molecules on the surface of HNT for such applications has been discoursed.

3.2.1 Energy Storage

A common method of energy storage is through the use of supercapacitors due to their long cycling life, enhanced power delivery, increased power density and low

cost (Miller and Simon 2008; Simon et al. 2014). Some of the commonly used supercapacitors are carbon-based Electrochemical Double Layer Capacitor (SC-EDLC). However, a major limitation of such supercapacitors is that the charge is confined to the surface thus leading to an overall low-energy density. HNT due to their nanotubular structure are capable of storing surplus charge within its lumen. This storage can be enhanced by carefully selecting guest molecules that are capable of enhancing energy storage. For instance, in a study, HNT had been used as support to first introduce sulphydryl groups on the surface through treatment by mercaptotriethoxysilane (KH-90), followed by growing Nickel Sulphide (Ni_3S_2) nanoparticles on the surface. Further carbon nanoparticles were immobilized on the surface to ensure efficient charge dispersion. The synthesized supercapacitor showed excellent energy storage performance, by delivery a capacity of 450.4 C/g and a high charge retention of 82.6% even over 2000 cycles. This supercapacitor also showed a maximum energy density at 79.6 Wh/kg, thereby suggesting the potential use of such eco-friendly supercapacitors (Li et al. 2017a, b). Apart from this, HNT have also been used in the development of Phase Change Material (PCM) for energy storage. In this study, Graphene aerogels (GA) had been grafted on the surface of HNT, followed by their implementation in the preparation of polyurethane-based solid–solid PCMs. This structure showed enhanced light thermal and electrothermal energy conversion and storage ability. In case of light-thermal, η was 75.6%, while in case of electrothermal, η was 67.2%. The developed materials also showed enhanced thermal stability and reliability and therefore can be efficiently used in energy storage (Zhou et al. 2019).

Another method of energy storage is through the use of Vanadium Flow Batteries (VFB). Ion exchange membranes are highly crucial structures in such flow batteries, since they act as an efficient physical separation between the oppositely charged electrolytes. These structures also prevent the mixture of vanadium ions. Therefore, a proper selection of the membrane is highly crucial such that it has excellent ion selectivity, mechanical strength and chemical stability. Implementation of HNT with guest molecules immobilized on it in such membranes can fulfil these factors. In a study, PDA had been immobilized on HNT and incorporated in sulfonated poly(ether ether ketone) membranes. The presence of dopamine on the surface enhanced the proton conductivity, while the nanostructure of the tube acted as a crosslinker to form a strong mesh like membrane structure. This membrane showed excellent durability and high performance at 40–200 mA/cm^2. It also showed high energy efficiency of 75% and a robust coulombic efficiency at 99% (Yu et al. 2018).

3.2.2 Fuel

Apart from energy storage, finding alternative fuel sources or implementation of methods that can increase the yield of existing fuels is crucial. For instance, crude oil, which is the most widely used fuel across the world is catalytically hydrocracked in order to increase the yield of different products. Over the years, thermal and catalytic cracking are the commonly used techniques for increasing the yields. However, they

have disadvantages of having low yields for lighter fuels and therefore require high-quality feedstock. Such a process also consumes a high quantity of hydrogen, thus making it economically limited.

In the past decades, several studies have shown HNT to be used in increasing the yield output and decreasing the formation of coke during the cracking process (Abbasov et al. 2013, 2016a, b). In a recent study, NiO and CoO catalysts were deposited on HNT's surface for the cracking process. This catalyst allowed the hydrocracking process to occur at lower hydrogen pressure of 1 MPa as compared to the usual 10–20 MPa. The catalyst had also enhanced the total yield from 52 to 57% under increasing hydrogen pressure of up to 4 MPa (Abbasov et al. 2016a, b).

HNT have also been used as a template to fabricate cathode catalyst for applications in alkaline fuel cell, which is an alternative for existing fuel sources. Commonly used cathode catalysts are made from noble metals; however, they come with the limitation of high price and therefore cannot be put into mass production. In this study, HNT have been used as stencils for the fabrication of nitrogen-doped carbon nanotubes (N-CNT), which will serve Oxygen Reduction Reaction (ORR) electro catalysts. Aniline had been loaded on the surface of HNT, which was then oxidised to form Polyaniline-HNT hybrids. These hybrids were further pyrolyzed in order to obtain HNT with nitrogen-doped CNTs. These CNTs showed excellent electrocatalytic performance towards ORR (Liu et al. 2019).

Along with HNT used as a template and a catalyst, they have also been used in the production of biodiesel production from hybrid feedstocks. In a study, HSO_3 groups were grafted on the surface of HNT through different methods such as organosilylation, sulfonation, and 2 steps organosilylation and sulfonation. These HNTs were later used as catalyst for the esterification of fatty acids. The catalysts obtained through sulfonation showed the highest catalytic activity with a turnover frequency of 94 h^{-1} and a mass normalized activity of 0.08 $mol.g^{-1}h^{-1}$ (Silva et al. 2018).

4 Conclusion

Nanotechnology-based advancements have emerged as a helping hand for environmental engineers for solving various kinds of issues related to the environment. However, the toxicity of most of the nanomaterials in addition to the cost involved in their synthesis has always limited their bulk usage, especially for energy and environmental applications. HNT are naturally occurring aluminosilicate nano-supports with additional benefits such as being eco-friendly biocompatible and non-toxic, and these nanotubes have found that their way is an excellent alternative for applications in the fields of energy and environment.

The nanotube showcases excellent thermal and mechanical properties, along with an alterable surface chemistry. These properties in addition to the good adsorption behaviour make HNT a suitable nano-support for various guest molecules. In the field of environment, commonly used guest molecules include functional reactive moieties, biomolecules and biopolymers, and nanoparticles. HNT immobilized with

such kinds of guest molecules have been used for tackling environmental pollution by the detection and remediation of pesticides, removal of harmful dyes, heavy metals and gases from the environment. In addition to these, such guest immobilized HNT have also been used for energy storage and increasing the efficiency of various fuels. In future, with more technological advancements, HNT-based biosensors can be developed for rapid and on-site detection of different pollutants such as greenhouse gases and pesticides. With such diverse applications in this field, HNT can become a 'silver bullet' for environmental engineers for undertaking issues related to energy and environmental remediation.

References

Abbasov V, Mammadova T, Aliyeva N, Abbasov M, Movsumov N, Joshi A (2016a) Catalytic Cracking of Vegetable oil and vacuum gasoil with commercial high alumina zeolite and Halloysite Nanotubes for biofuel production. Fuel 181:55–63

Abbasov V, Mammadova T, Andrushenko N, Hasankhanova N, Lvov Y, Abdullayev E (2013) Halloysite-Y-zeolite blends as novel mesporous catalysts for the cracking of waste vegetable oils with vacuum gasoil. Fuel 117A:552–555

Abbasov VM, Ibrahimov HC, Mukhtarova GS, Abdullayev E (2016b) Acid treated Halloysite clay Nanotubes as catalyst supports for fuel production by catalytic hydrocracking of heavy crude oil. Fuel 184:555–558. https://doi.org/10.1016/j.fuel.2016.07.054

Afzali D, Fayazi M (2016) Deposition of MnO_2 nanoparticles on the magnetic Halloysite Nanotubes by hydrothermal method for lead(II) removal from aqueous solutions. J Taiwan Inst Chem Eng 63:421–429. https://doi.org/10.1016/j.jtice.2016.02.025

Akpan UG, Hameed BH (2009) Parameters affecting the photocatalytic degradation of dyes using TiO_2-based photocatalysts: a review. J Hazard Mater 170:520–529. https://doi.org/10.1016/j.jhazmat.2009.05.039

Anastopoulos I, Mittal A, Usman M, Mittal J, Yu G, Núñez-Delgado A, Kornaros M (2018) A review on Halloysite-based adsorbents to remove pollutants in water and wastewater. J Mol Liq 269:855–868. https://doi.org/10.1016/j.molliq.2018.08.104

Bates T, Hildebrand FA, Swineford A (1950) Morphology and structure of endellite and Halloysite. 35:463–484

Bielska D, Karewicz A, Lachowicz T, Berent K, Szczubiałka K, Nowakowska M (2015) Hybrid photosensitizer based on Halloysite Nanotubes for phenol-based pesticide photodegradation. Chem Eng J 262:125–132. https://doi.org/10.1016/j.cej.2014.09.081

Bonetto LR, Ferrarini F, de Marco C, Crespo JS, Guégan R, Giovanela M (2015) Removal of methyl violet 2B dye from aqueous solution using a magnetic composite as an adsorbent. J Water Process Eng 6:11–20. https://doi.org/10.1016/j.jwpe.2015.02.006

Byrne C, Subramanian G, Pillai SC (2018) Recent advances in photocatalysis for environmental applications. J Environ Chem Eng 6:3531–3555. https://doi.org/10.1016/j.jece.2017.07.080

Cataldo S, Lazzara G, Massaro M, Muratore N, Pettignano A, Riela S (2018) Functionalized Halloysite Nanotubes for enhanced removal of lead(II) ions from aqueous solutions. Appl Clay Sci 156:87–95. https://doi.org/10.1016/j.clay.2018.01.028

Cavallaro G, Chiappisi L, Pasbakhsh P, Gradzielski M, Lazzara G (2018) A structural comparison of Halloysite Nanotubes of different origin by Small-Angle Neutron Scattering (SANS) and Electric Birefringence. Appl Clay Sci 160:71–80. https://doi.org/10.1016/j.clay.2017.12.044

De Silva RT, Pasbakhsh P, Lee SM, Kit AY (2015) ZnO deposited/encapsulated Halloysite–poly (lactic acid) (PLA) nanocomposites for high performance packaging films with improved mechanical and antimicrobial properties. Appl Clay Sci 111:10–20. https://doi.org/10.1016/j.clay.2015.03.024

Deepak R, Agrawal YK (2012) Study of nanocomposites with emphasis to Halloysite Nanotubes. Rev Adv Mater Sci 32:149–157

Du J, Tang J, Xu S, Ge J, Dong Y, Li H, Jin M (2018) A review on silver nanoparticles-induced ecotoxicity and the underlying toxicity mechanisms. Regul Toxicol Pharmacol 98:231–239. https://doi.org/10.1016/j.yrtph.2018.08.003

Duan J, Liu R, Chen T, Zhang B, Liu J (2012) Halloysite Nanotube-Fe_3O_4 composite for removal of methyl violet from aqueous solutions. Desalination 293:46–52. https://doi.org/10.1016/j.desal.2012.02.022

Ebele AJ, Abou-Elwafa Abdallah M, Harrad S (2017) Pharmaceuticals and personal care products (PPCPs) in the freshwater aquatic environment. Emerg Contam 3:1–16. https://doi.org/10.1016/j.emcon.2016.12.004

Fagan R, McCormack DE, Dionysiou DD, Pillai SC (2016) A review of solar and visible light active TiO_2 photocatalysis for treating bacteria, cyanotoxins and contaminants of emerging concern. Mater Sci Semicond Process Mater Appl Water Treat Water Split 42:2–14. https://doi.org/10.1016/j.mssp.2015.07.052

Ge L, Lin R, Wang L, Rufford TE, Villacorta B, Liu S, Liu LX, Zhu Z (2017) Surface-etched Halloysite Nanotubes in mixed matrix membranes for efficient gas separation. Sep Purif Technol 173:63–71. https://doi.org/10.1016/j.seppur.2016.09.015

Gidlow DA (2015) Lead toxicity. Occup Med (Lond) 65:348–356. https://doi.org/10.1093/occmed/kqv018

Hashemifard SA, Ismail AF, Matsuura T (2011) Mixed matrix membrane incorporated with large pore size Halloysite Nanotubes (HNT) as filler for gas separation: experimental. J Colloid Interface Sci 359:359–370. https://doi.org/10.1016/j.jcis.2011.03.077

He Q, Yang D, Deng X, Wu Q, Li R, Zhai Y, Zhang L (2013) Preparation, characterization and application of N-2-pyridylsuccinamic acid-functionalized Halloysite Nanotubes for solid-phase extraction of Pb(II). Water Res 47:3976–3983. https://doi.org/10.1016/j.watres.2012.12.040

Hebbar RS, Isloor AM, Ananda K, Ismail AF (2016) Fabrication of polydopamine functionalized Halloysite Nanotube/polyetherimide membranes for heavy metal removal. J Mater Chem A 4:764–774. https://doi.org/10.1039/C5TA09281G

Jiang L, Zhang C, Wei J, Tjiu W, Pan J, Chen Y, Liu T (2014) Surface modifications of Halloysite Nanotubes with superparamagnetic Fe_3O_4 nanoparticles and carbonaceous layers for efficient adsorption of dyes in water treatment. Chem Res Chin Univ 30:971–977. https://doi.org/10.1007/s40242-014-4218-4

Jinhua W, Xiang Z, Bing Z, Yafei Z, Rui Z, Jindun L, Rongfeng C (2010) Rapid adsorption of Cr (VI) on modified Halloysite Nanotubes. Desalination 259:22–28. https://doi.org/10.1016/j.desal.2010.04.046

Johnston RB, Hanchett S, Khan MH (2010) The socio-economics of arsenic removal. Nat Geosci 3:2

Joussein E, Petit S, Churchman J, Theng B, Righi D, Delvaux B (2005) Halloysite clay minerals—a review. Clay Miner 40:383–426. https://doi.org/10.1180/0009855054040180

Kadam AA, Jang J, Lee DS (2017) Supermagnetically tuned Halloysite Nanotubes functionalized with aminosilane for covalent laccase immobilization [WWW Document]. https://doi.org/10.1021/acsami.7b02531

Kamat PV (2007) Meeting the clean energy demand: nanostructure architectures for solar energy conversion. J Phys Chem C 111:2834–2860. https://doi.org/10.1021/jp066952u

Kamat PV (2008) Quantum dot solar cells. semiconductor nanocrystals as light harvesters. J Phys Chem C 112:18737–18753. https://doi.org/10.1021/jp806791s

Khatri N, Tyagi S (2015) Influences of natural and anthropogenic factors on surface and groundwater quality in rural and urban areas. Front Life Sci 8:23–39. https://doi.org/10.1080/21553769.2014.933716

Khatri N, Tyagi S, Rawtani D (2017a) Rural environment study for water from different sources in cluster of villages in Mehsana district of Gujarat. Environ Monit Assess 190:10. https://doi.org/10.1007/s10661-017-6382-8

Khatri N, Tyagi S, Rawtani D (2017b) Recent strategies for the removal of iron from water: a review. J Water Process Eng 19:291–304. https://doi.org/10.1016/j.jwpe.2017.08.015

Khatri N, Tyagi S, Rawtani D (2016a) Assessment of Drinking Water Quality and its Health Effects in Rural Areas of Harij Taluka, Patan District of Northern Gujarat. Environ Claims J 28:223–246. https://doi.org/10.1080/10406026.2016.1190249

Khatri N, Tyagi S, Rawtani D (2016b) Removal of basic dyes auramine yellow and auramine O by Halloysite Nanotubes. Int J Environ Waste Manag 17:44. https://doi.org/10.1504/IJEWM.2016.076427

Lazzara G, Cavallaro G, Panchal A, Fakhrullin R, Stavitskaya A, Vinokurov V, Lvov Y (2018) An assembly of organic-inorganic composites using Halloysite clay Nanotubes. Curr Opin Colloid Interface Sci 35:42–50. https://doi.org/10.1016/j.cocis.2018.01.002

Lee CS, Robinson J, Chong MF (2014) A review on application of flocculants in wastewater treatment. Process Saf Environ Prot 92:489–508. https://doi.org/10.1016/j.psep.2014.04.010

Li Q, Li Y, Ma X, Du Q, Sui K, Wang D, Wang C, Li H, Xia Y (2017a) Filtration and adsorption properties of porous calcium alginate membrane for methylene blue removal from water. Chem Eng J 316:623–630. https://doi.org/10.1016/j.cej.2017.01.098

Li Y, Zhou J, Liu Y, Tang J, Tang W (2017b) Hierarchical nickel sulfide coated Halloysite Nanotubes for efficient energy storage. Electrochim Acta 245:51–58. https://doi.org/10.1016/j.electacta.2017.05.140

Liu W, Fizir M, Hu F, Li A, Hui X, Zha J, He H (2018) Mixed hemimicelle solid-phase extraction based on magnetic Halloysite Nanotubes and ionic liquids for the determination and extraction of azo dyes in environmental water samples. J Chromatogr A 1551:10–20. https://doi.org/10.1016/j.chroma.2018.03.051

Liu W, Ru Q, Zuo S, Yang S, Han J, Yao C (2019) Controllable synthesis of nitrogen-doped carbon nanotubes derived from Halloysite-templated polyaniline towards nonprecious ORR catalysts. Appl Surf Sci 469:269–275. https://doi.org/10.1016/j.apsusc.2018.10.225

Lvov Y, Wang W, Zhang L, Fakhrullin R (2016) Halloysite clay nanotubes for loading and sustained release of functional compounds. Adv Mater 28:1227–1250. https://doi.org/10.1002/adma.201502341

Lvov YM, Shchukin DG, Möhwald H, Price RR (2008) Halloysite clay Nanotubes for controlled release of protective agents. ACS Nano 2:814–820. https://doi.org/10.1021/nn800259q

Makaremi M, Pasbakhsh P, Cavallaro G, Lazzara G, Aw YK, Lee SM, Milioto S (2017) Effect of morphology and size of Halloysite Nanotubes on functional pectin bionanocomposites for food packaging applications. ACS Appl Mater Interfaces 9:17476–17488. https://doi.org/10.1021/acsami.7b04297

Mason LH, Harp JP, Han DY (2014) Pb neurotoxicity: neuropsychological effects of lead toxicity [WWW Document]. Biomed Res Int. https://doi.org/10.1155/2014/840547

Massaro M, Lazzara G, Milioto S, Noto R, Riela S (2017) Covalently modified Halloysite clay Nanotubes: synthesis, properties, biological and medical applications. J Mater Chem B 5:2867–2882. https://doi.org/10.1039/C7TB00316A

Miller J, Simon P (2008) Electrochemical capacitors for energy management. Science 321:651–652. https://doi.org/10.1126/science.1158736

Pan J, Yao H, Xu L, Ou H, Huo P, Li X, Yan Y (2011) Selective recognition of 2,4,6-trichlorophenol by molecularly imprinted polymers based on magnetic Halloysite Nanotubes composites. J Phys Chem C 115:5440–5449. https://doi.org/10.1021/jp111120x

Pandey G, Munguambe DM, Tharmavaram M, Rawtani D, Agrawal YK (2017a) Halloysite Nanotubes—An efficient 'nano-support' for the immobilization of α-amylase. Appl Clay Sci 136:184–191. https://doi.org/10.1016/j.clay.2016.11.034

Pandey G, Rawtani D, Agrawal YK (2017b) Future aspects of Halloysite Nanotubes in forensic investigations. J Nanomed Res 6. https://doi.org/10.15406/jnmr.2017.06.00153

Pandey G, Rawtani D, Agrawal YK (2016) Aspects of nanoelectronics in materials development. In: Kar A (ed) Nanoelectronics and materials development. InTech. https://doi.org/10.5772/64414

Pasbakhsh P, Churchman GJ, Keeling JL (2013) Characterisation of properties of various Halloysites relevant to their use as nanotubes and microfibre fillers. Appl Clay Sci Clays and clay Miner: Geol Prop Uses 74:47–57. https://doi.org/10.1016/j.clay.2012.06.014

Peng Q, Liu M, Zheng J, Zhou C (2015) Adsorption of dyes in aqueous solutions by chitosan–Halloysite Nanotubes composite hydrogel beads. Microporous Mesoporous Mater 201:190–201. https://doi.org/10.1016/j.micromeso.2014.09.003

Pirilä M, Saouabe M, Ojala S, Rathnayake B, Drault F, Valtanen A, Huuhtanen M, Brahmi R, Keiski RL (2015) Photocatalytic degradation of organic pollutants in wastewater. Top Catal 58:1085–1099. https://doi.org/10.1007/s11244-015-0477-7

Rawtani D, Agrawal YK (2013) A study of the behavior of HNT with DNA intercalator acridine orange. BioNanoScience 3:52–57. https://doi.org/10.1007/s12668-012-0066-1

Rawtani D, Agrawal YK (2012a) Multifarious applications of Halloysite Nanotubes: a review. Rev Adv Mater Sci 30:282–295

Rawtani D, Agrawal YK (2012b) Halloysite as support matrices: a review. Emerg Mater Res 1:212–220

Rawtani D, Agrawal YK (2012c) Study the interaction of DNA with Halloysite Nanotube-gold nanoparticle based composite. J Bionanosci 6:95–98. https://doi.org/10.1166/jbns.2012.1080

Rawtani D, Agrawal YK, Prajapati P (2013) Interaction behavior of DNA with Halloysite Nanotube-silver nanoparticle-based composite. BioNanoScience 3:73–78. https://doi.org/10.1007/s12668-012-0071-4

Rawtani D, Khatri N, Tyagi S, Pandey G (2018) Nanotechnology-based recent approaches for sensing and remediation of pesticides. J Environ Manag 206:749–762. https://doi.org/10.1016/j.jenvman.2017.11.037

Rawtani D, Pandey G, Tharmavaram M, Pathak P, Akkireddy S, Agrawal YK (2017) Development of a novel 'nanocarrier' system based on Halloysite Nanotubes to overcome the complexation of ciprofloxacin with iron: An in vitro approach. Appl Clay Sci 150:293–302. https://doi.org/10.1016/j.clay.2017.10.002

Riahi-Madvaar R, Taher MA, Fazelirad H (2017) Synthesis and characterization of magnetic Halloysite-iron oxide Nanocomposite and its application for naphthol green B removal. Appl Clay Sci 137:101–106. https://doi.org/10.1016/j.clay.2016.12.019

Rodríguez-Lado L, Sun G, Berg M, Zhang Q, Xue H, Zheng Q, Johnson CA (2013) Groundwater arsenic contamination throughout China. Science 341:866–868. https://doi.org/10.1126/science.1237484

Saraji M, Jafari MT, Mossaddegh M (2017) Chemically modified halloysite nanotubes as a solid–phase microextraction coating. Anal Chim Acta 964:85–95. https://doi.org/10.1016/j.aca.2017.02.018

Saraji M, Jafari MT, Mossaddegh M (2016) Halloysite nanotubes-titanium dioxide as a solid-phase microextraction coating combined with negative corona discharge-ion mobility spectrometry for the determination of parathion. Anal Chim Acta 926:55–62. https://doi.org/10.1016/j.aca.2016.04.034

Silva SM, Peixoto AF, Freire C (2018) HSO_3-functionalized halloysite nanotubes: New acid catalysts for esterification of free fatty acid mixture as hybrid feedstock model for biodiesel production. Appl Catal A: Gen 568:221–230. https://doi.org/10.1016/j.apcata.2018.10.008

Simon P, Gogotsi Y, Dunn B (2014) Where do batteries end and supercapacitors begin? | science. Science 343:1210–1211. https://doi.org/10.1126/science.1249625

Szczepanik B, Słomkiewicz P (2016) Photodegradation of aniline in water in the presence of chemically activated halloysite. Appl Clay Sci 124–125:31–38. https://doi.org/10.1016/j.clay.2016.01.045

Tharmavaram M, Pandey G, Rawtani D (2018) Surface modified halloysite nanotubes: a flexible interface for biological, environmental and catalytic applications. Adv Colloid Interface Sci 261:82–101. https://doi.org/10.1016/j.cis.2018.09.001

Tharmavaram M, Rawtani D, Pandey G (2017) Fabrication routes for one-dimensional nanostructures via block copolymers. Nano Converg 4:12

Tian X, Wang W, Wang Y, Komarneni S, Yang C (2015) Polyethylenimine functionalized halloysite nanotubes for efficient removal and fixation of Cr (VI). Microporous Mesoporous Mater 207:46–52. https://doi.org/10.1016/j.micromeso.2014.12.031

Tsoufis T, Katsaros F, Kooi BJ, Bletsa E, Papageorgiou S, Deligiannakis Y, Panagiotopoulos I (2017) Halloysite nanotube-magnetic iron oxide nanoparticle hybrids for the rapid catalytic decomposition of pentachlorophenol. Chem Eng J 313:466–474. https://doi.org/10.1016/j.cej.2016.12.056

Tyagi S, Rawtani D, Khatri N, Tharmavaram M (2018) Strategies for Nitrate removal from aqueous environment using Nanotechnology: a review. J Water Process Eng 21:84–95. https://doi.org/10.1016/j.jwpe.2017.12.005

Wan X, Zhan Y, Long Z, Zeng G, He Y (2017) Core@double-shell structured magnetic halloysite nanotube nano-hybrid as efficient recyclable adsorbent for methylene blue removal. Chem Eng J 330:491–504. https://doi.org/10.1016/j.cej.2017.07.178

Wang D, Pillai SC, Ho S-H, Zeng J, Li Y, Dionysiou DD (2018) Plasmonic-based nanomaterials for environmental remediation. Appl Catal B: Environ 237:721–741. https://doi.org/10.1016/j.apcatb.2018.05.094

Xie Y, Qian D, Wu D, Ma X (2011) Magnetic halloysite nanotubes/iron oxide composites for the adsorption of dyes. Chem Eng J 168:959–963. https://doi.org/10.1016/j.cej.2011.02.031

Yu L, Mu D, Liu L, Xi J (2018) Bifunctional effects of halloysite nanotubes in vanadium flow battery membrane. J Membr Sci 564:237–246. https://doi.org/10.1016/j.memsci.2018.07.033

Yuan P, Tan D, Annabi-Bergaya F (2015) Properties and applications of halloysite nanotubes: recent research advances and future prospects. Appl Clay Sci 112–113:75–93. https://doi.org/10.1016/j.clay.2015.05.001

Zango ZU, Garba ZN, Abu Bakar NHH, Tan WL, Abu Bakar M (2016) Adsorption studies of Cu2 + –Hal nanocomposites for the removal of 2,4,6-trichlorophenol. Appl Clay Sci 132–133:68–78. https://doi.org/10.1016/j.clay.2016.05.016

Zeng G, He Y, Zhan Y, Zhang L, Pan Y, Zhang C, Yu Z (2016) Novel polyvinylidene fluoride nanofiltration membrane blended with functionalized halloysite nanotubes for dye and heavy metal ions removal. J Hazard Mater 317:60–72. https://doi.org/10.1016/j.jhazmat.2016.05.049

Zeng G, Ye Z, He Y, Yang X, Ma J, Shi H, Feng Z (2017) Application of dopamine-modified halloysite nanotubes/PVDF blend membranes for direct dyes removal from wastewater. Chem Eng J 323:572–583. https://doi.org/10.1016/j.cej.2017.04.131

Zhou Y, Wang X, Liu X, Sheng D, Ji F, Dong L, Xu S, Wu H, Yang Y (2019) Polyurethane-based solid-solid phase change materials with halloysite nanotubes-hybrid graphene aerogels for efficient light- and electro-thermal conversion and storage. Carbon 142:558–566. https://doi.org/10.1016/j.carbon.2018.10.083

A Review on Contemporary Hole Transport Materials for Perovskite Solar Cells

Saikumar Nair and Jignasa V. Gohel

Abstract The present review article is focussed on different types of hole-transporting materials (HTMs) under research over the past few years in the perovskite-based solar cell (PSC) in achieving the goal of higher power conversion efficiency (PCE) and operational stability. There has been a growth spurt of efficiency from 3.8 to 22.1% in the last decade which has attracted researchers and the renewable industry. HTMs are an indispensable part of PSC which affects both efficiency and stability. An overview of different types of HTMs (organic, inorganic, and polymeric) is presented detailing its structure, electrochemical, and physical properties, while highlighting several considerations for making a choice for a new HTM for PSC. The recent progress is shown with PSC's device architecture, fabrication technique and their respective JV characteristics to help readers understand the challenges surrounding HTM and opportunities to make it highly efficient and stable.

Keywords Perovskite solar cells · Hole transport materials · Charge carriers · Methylammonium lead iodide

1 Introduction

In 2009, Miyasaka et al. in their seminal work found out that organometal halide perovskite can be used as a light-absorbing layer in a solar cell (Kojima et al. 2009). This particular solar cell had an efficiency of 3.8% which made a big paradigm shift onto a premise of a novel type of solar cell. The perovskite compound which was used as the visible light sensitizer has the chemical form of $CH_3NH_3PbX_3$ or $MAPbX_3$ where X is a halogen. This gave rise to a plethora of new research under solar cells which are collectively called "third-generation solar cell." At present, the efficiency

S. Nair · J. V. Gohel (✉)
Department of Chemical Engineering, Sardar Vallabhbhai National Institute of Technology, Surat 395007, Gujarat, India
e-mail: jignasa.narsinhbhai@gmail.com

S. Nair
e-mail: saikunair@gmail.com

L. Ledwani and J. S. Sangwai (eds.), *Nanotechnology for Energy and Environmental Engineering*, Green Energy and Technology,
https://doi.org/10.1007/978-3-030-33774-2_6

has surpassed to more than 20% with the advent of new measures to control stability and increase the power conversion efficiency of perovskite solar cells. Currently, the highest reported efficiency is at 22.7% (NREL 2018). This spurge in efficiency was in a matter of few years. Contrastingly, silicon-based solar cells took almost 60 years to achieve the same level of efficiency (NREL 2018; Economist 2018). Talks are also underway to bring the first commercial perovskite solar cells to the market in a year (Economist 2018).

This development in perovskite research is not free from pitfalls. It is still plagued with many problems surrounding stability of the different layers involved (HTM, Perovskite layer, and ETL).

To compete with the silicon-based solar cells which dominate the PV market, there are certain issues that are of paramount concerns. The stability of perovskite-based solar cells is very low compared to silicon-based cells. There have been countless research studies pertaining to the stability of the different layers involved in the perovskite cells, and there have also been many attempts to improve the efficiency of perovskite cells by using a tandem configuration with silicon.

The major instability issues for PSC can be attributed to moisture, temperature, oxygen, and UV Light (Conings et al. 2015; Misra et al. 2015; Aristidou et al. 2015; Han et al. 2015; Senocrate et al. 2018). HTM plays an important role in the long-term stability of the solar cells. It plays a vital role in transferring holes from the perovskite layer to the back contact metal electrode. Additionally, it acts as a barrier between perovskite and metal electrode; this in turn increases the device stability and effectively blocks the transfer of the electron from perovskite layer to the anode. Consequently, HTM should ensure higher stability and efficiency. HTM would also require higher thickness to avoid leakage currents and pinholes.

The most commonly used HTM is a solid-state HTM called Spiro-OMeTAD. It was discovered by Park and his co-workers (Kim et al. 2012) as an alternative to conventional liquid-based electrolyte HTM. This gave an efficiency of 9.7%. Since then, researchers have focussed on different types of HTM using organic, inorganic, and polymeric materials.

2 Organic-Based HTM

2.1 Spiro-Based HTM

After the first use of spiro-based HTM by Kim et al. (2012), there is a great progress in the use of spiro-based HTM using different dopants. The molecular configuration of Spiro-OMeTAD is such that it offers a good optical stability and proper thermal stability. Moreover, methoxy substituent located at the end of triphenylamine in the spiro configuration influences the optical and electrical properties. Consequently, many derivatives are synthesized by changing the location of the methoxy groups. The spiro structure (Fig. 1) suffers from poor hole mobility (~10^{-4} cm^2 V^{-1} s^{-1})

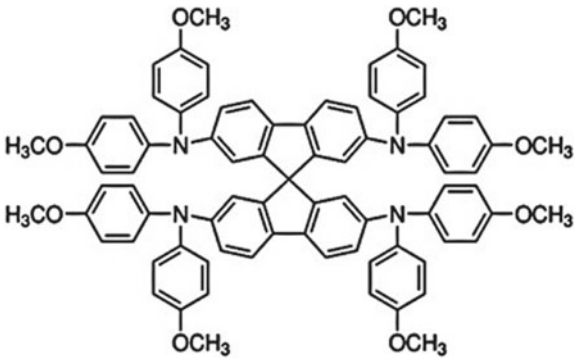

Fig. 1 Structure of Spiro-OMeTAD

and poor conductivity (~10^{-5}) in its original form. To counter this, it is usually blended with certain additives like TBP (4-tert-butylpyridine) and Li-TFSI (lithium bis(trifluoromethylsulfonyl)) to increase the conductivity for hole transport and collection and decrease recombination at the interface (Snaith and Grätzel 2006). But it is found that additives may lead to decrease in the long-term stability of the spiro structure.

Snaith and his co-workers used a low-cost method to develop a mesostructured PSC with an efficiency of 10.9% (Lee et al. 2012). This was done using mesoporous alumina scaffold, a mixed halide perovskite absorber, and Spiro-OMeTAD. Then, a sequential deposition method was proposed by Julian and Graetzel (2013) to deposit perovskite pigment to the porous metal oxide using Spiro-OMeTAD as a HTM (Fig. 2). A power conversion efficiency of about 15% was achieved using his method.

Spiro-OMeTAD has also been doped with p-type dopants like Li and Co to achieve an efficiency as high as 19.7% (Li et al. 2016; Kumari et al. 2019). Nam and Co-workers found out that just by changing the position of methoxy groups in a

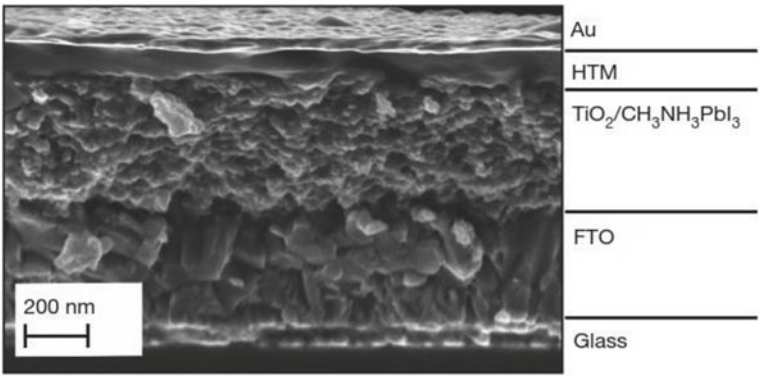

Fig. 2 Cross-sectional SEM image of a photovoltaic perovskite cell using Spiro-OMeTAD. Reprinted with permission from Burschka (2013) Copyright (2013) Nature

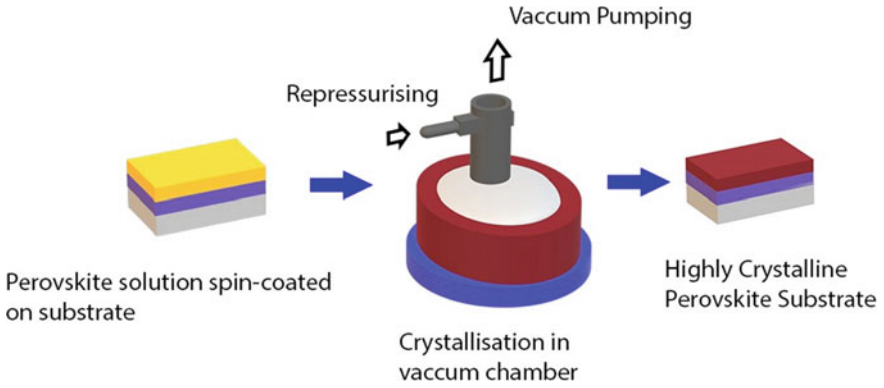

Fig. 3 Procedure for obtaining perovskite film from a vacuum flash-assisted solution processing (VASP) wherein substrate is kept under a vacuum chamber to get crystallized and then annealed to form a highly crystalline perovskite substrate

spiro configuration, the cell performance was drastically changed (Jeon et al. 2014). NMR and mass spectroscopy showed that spiro derivative of *o*-OMe substituent exhibited higher performance with PCE of 16.7% as compared to conventional *p*-OMe-substituted spiro derivative (Jeon et al. 2014).

Zhang et al. (2018) designed and characterized asymmetric methoxy substituents of Spiro-OMeTAD. The spiro derivative 2,4-Spiro-OMeTAD exhibited PCE of 17.2% and excellent stability (90% PCE after 504 h) than conventional spiro-OMeTAD under the same conditions (Zhang et al. 2018) (Fig. 3).

Vacuum flash solution processing method (VASP) was used by Li and Graetzel to prepare metal halide PSCs with Spiro-OMeTAD as a HTM using bis(trifluoromethylsulfonyl) imide (Li-TFSI) and tert-butylpyridine (t-BP) as an additive. A certified efficiency of 19.6% was obtained with no hysteresis effect (Li et al. 2016).

In spite of the high PCE obtained over the course of recent years, spiro-based HTMs suffer from poor conductivity and low hole mobility. Also, dopants like 4-tert-butylpyridine (TBP) and Li salts increase the hole conductivity with a decrease in stability due to their hygroscopic nature. This exacerbates the stability of HTM since Spiro-OMeTAD is more susceptible to humidity (Leijtens et al. 2012). Another major impediment is cost factor where Spiro-OMeTAD fares badly.

2.2 Triphenylamine Organic Hole Transport Material

Triphenylamine-based HTM has garnered the attention of many researchers because of their good hole mobility properties, lower cost, and easier synthesis methods. They are also considerably low cost compared to Spiro-OMeTAD. A study by Lv et al.

(2015) has found that triphenylamine-based HTM containing vinyl derivatives, 3,6-di (2-(4-(N,N-di(p-tolyl)amino)phenyl)vinyl)-9-ethylcarbazole (apv-EC) and 3,6-di (2-(4-(N,N-di(p-tolyl)amino)phenyl)vinyl)-2-thiophene (apv-T) had a PCE of about 12% without the use of any dopant material. Their overall efficiency was reported to be less than Spiro-OMeTAD. Triphenylamine has low solubility in organic solvents and low ionic potential which would be conducive to PSCs (Lv et al. 2015). It is found that devices with HTM with no dopant offered comparable efficiency as that of Spiro-OMeTAD but had lower stability. Also, the nonplanar TPA compound lead to lower hole mobility due to increased long intermolecular distance. To counter this effect, additives like lithium are added to increase hole mobility and stability.

Choi and Park synthesized triphenylamine-based two star-shaped HTM (FA-MeOPh) and TPA-MeOPh were by that had a fused triphenylamine and a triphenylamine core. FA-MeOPh showed a comparable efficiency of 11.86% to that of Spiro-OMeTAD-based cell (12.75%) (Choi et al. 2014). It also showed good relative stability of 250 h under the sun (Choi et al. 2014). It is easy to synthesize, and inexpensive materials would make it a good alternative to spiro-based HTM (Fig. 4).

Zhang and Graetzel reported a novel butterfly-shaped HTM (Z1011) based on triphenylamine. The PSC based on this configuration managed to get an efficiency of about 16.3% with no doping compared to an efficiency of 16.5% in p-doped Spiro-OMeTAD. Moreover, the stability of these materials was better than Spiro-OMeTAD with no encapsulation for about 1000 h (Zhang et al. 2016).

To improve the charge transfer, Park et al. prepared HTM based on three molecules triphenylamine (TPA) and [2,2]-paracyclophane. The three molecules varied in their number of TPA groups and thus named Di-TPA, Tri-TPA, and Tetra-TPA. It was found that with the increase in TPA groups, the efficiency, JV characteristics, and fill factor increased. Tetra-TPA had the highest PCE of 17.9% with V_{oc} of 1.05, J_{sc} of 22 $mAcm^{-2}$, and fill factor of 78. This enhanced photovoltaic performance is attributed to pronounced charged transport in the HTM film (Park et al. 2016) (Figs. 5 and 6).

2.3 Thiophene-Based Organic Hole Transport Material

Li and Co-workers first reported a thiophene-based heterocyclic molecule 3,4 ethylenedioxythiophene (H101) as a hole-transporting material (HTM) to achieve an efficiency of about 10.8% with no doping (Li et al. 2014a). This result was compared to H101 with varied dopings of 5% and 15% chemical FK102 and Spiro-OMeTAD with 15% doping. The results showed that H101 with 15% of doping achieved a PCE of about 13.8 compared to that of Spiro-OMeTAD's 13.7 (Li et al. 2014a). This gave a promising start for thiophene-based HTM.

Based on this study later on, Li synthesized two more molecules based on H101, H111, and H112 which had slightly better PCEs (14.7 and 14.9%). The *Tg* values for the new HTMs were high, which indicated that it had better stability and it was also reported that it had better HOMO levels, which consequently accounted for higher V_{oc} (Li et al. 2014b).

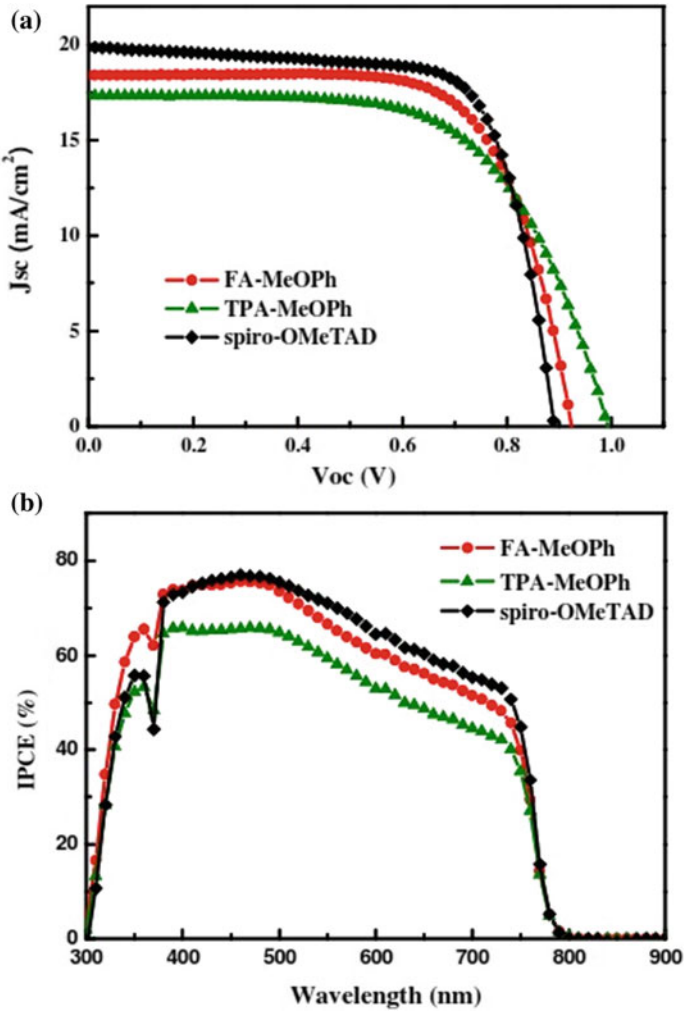

Fig. 4 JV characteristics of FA-MeOPh and TPA-MeOPh in comparison to Spiro-OMeTAD. Reprinted with permission from Ko (2014) Copyright (2014) Royal Society of Chemistry

2.4 Carbozole Hole Transport Material

Do Sung et al. (2014) were among the first to focus on carbozole molecule-based HTM. They managed to synthesize and characterize this molecule SGT-407, SGT-405, and SGT-404 based on two- and three-arm typed armed structures linked via phenylene amine derivative-based core. Among these three molecules, SGT-405 with three-armed structure exhibited highest PCE of 14.79% compared to that of Spiro-OMeTAD (15.23%) (Do Sung et al. 2014).

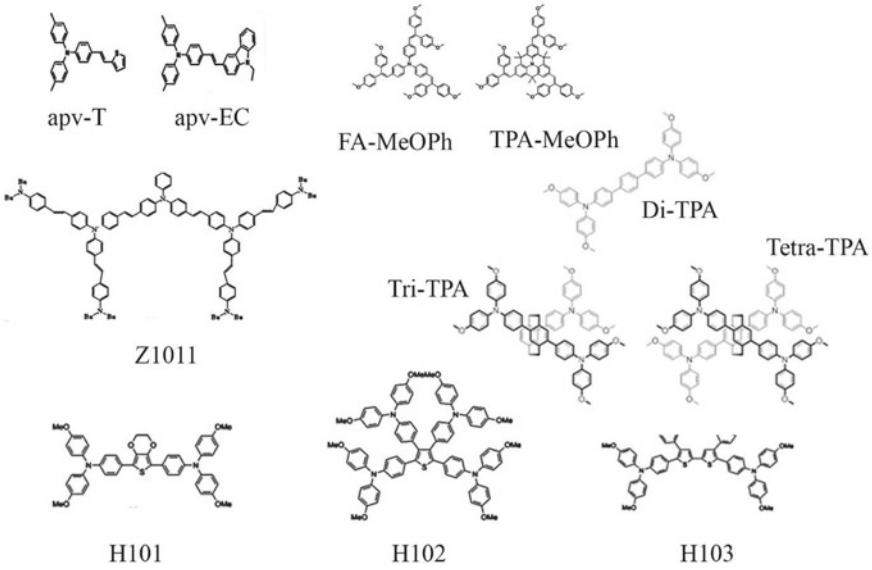

Fig. 5 Structures of organic hole transport layers

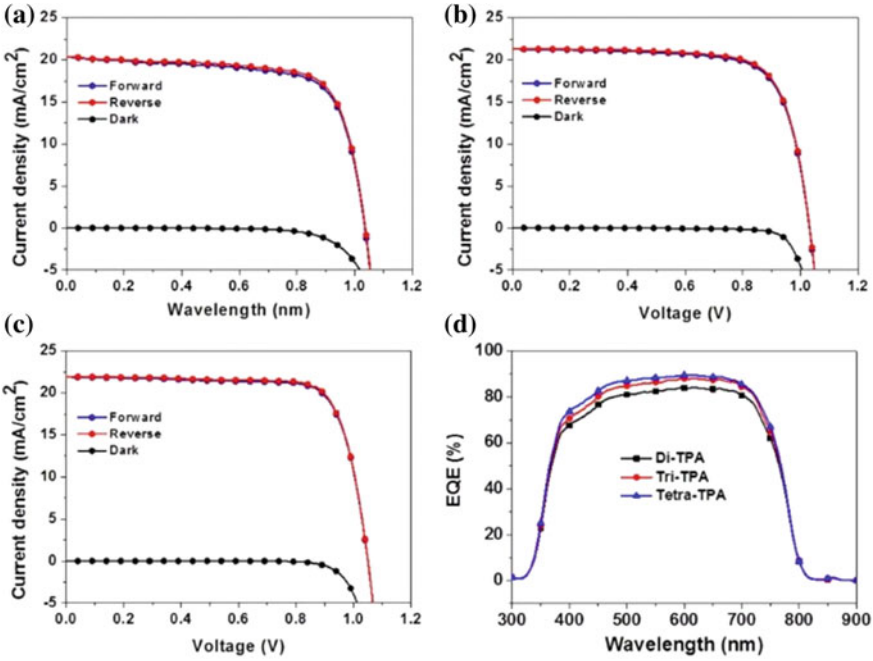

Fig. 6 JV characteristics of Di-TPA, Tri-TPA, and Tetra-TPA. Reprinted with permission from Park (2016) Copyright (2016) Royal Society of Chemistry (Open Access)

Fig. 7 Structure of V950

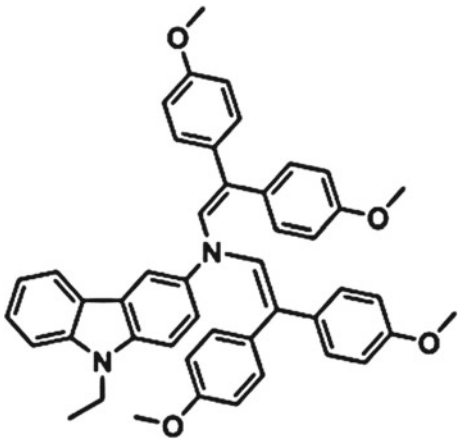

A new twin molecule V886 based on methoxydiphenylamine-substituted carbazole was synthesized by Gratia and his co-workers (2015). On using it as a HTM in CH3CH2NH3PbI3-based PSC, it offered a PCE close to 17% (compared to Spiro-OMeTAD) and high current density of (>21 $mAcm^{-2}$). *Tg* values were reportedly higher than that of Spiro-OMeTAD which shows higher thermal stability. Being fully amorphous V886 showed higher electrical conductivity than Spiro-OMeTAD under same conditions. Also, V886 had good film-forming and solubility properties to allow for high-quality thicker films (Gratia et al. 2015) (Fig. 7).

Daskeviciene et al. (2017) developed a method to synthesize a novel low-cost carbozole-based HTM for PSC. This carbozole-based HTM, namely, V950 (3 amino 9 ethylcarbazole and 2,2-bis(4-methoxyphenyl)acetaldehyde moieties) was synthesized using simple method like one-step synthesis from inexpensive commercial reagents and entailed no expensive catalysts. The material and chemical synthesis cost was far much lower for this HTM compared to Spiro-OMeTAD. It offered a PCE of about 17.8% and JV characteristics comparable to that of Spiro-OMeTAD (Daskeviciene et al. 2017).

2.5 Pyrene Derivatives

Due to high cost of conventional HTMs like Spiro-OMeTAD, smaller organic molecules made of pyrene have garnered interest among researchers. Jeon et al. (2013) successfully synthesized and characterized three pyrene arylamine derivatives, Py-A 1-(N,N-di-p-methoxyphenylamine)pyrene, Py-B (1,3,6-tris-(N,N-di-p-methoxyphenylamine)pyrene), and Py-C (1,3,6,8-tetrakis-(N,N-di-p-methoxyphenylamine)pyrene) with NMR spectroscopy, elemental analysis, and mass spectrometry (Fig. 8).

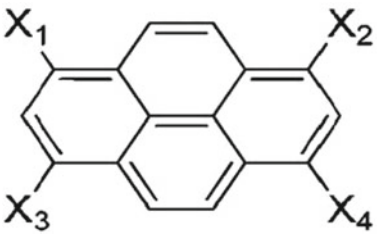

Fig. 8 Structure of Py-A, Py-B and Py-C. Py-A: X1 = X X2, X3 X4 = H, Py-B: X1, X2, X3 = X X4 = H, Py-C: X1, X2, X3 X4 = X

The efficiencies obtained for the three derivatives were 3.3, 12.3, and 12.4%. The PCE of Py-C was comparable to that of Spiro-OMeTAD (12.7%) but with a slightly lower V_{oc}. This could be due to recombination of the charge carriers (Jeon et al. 2013).

2.6 Triptycene Derivatives

Krishna et al. (2014) designed and synthesized their HTM based on three different molecules 2,6,14-Tri (N,N-bis(4-methoxyphenyl)amino) triptycene (T101) 2,6,14-Tri(N,N-bis(4-methoxyphenyl)aminophen-4-yl) triptycene (T102), 2,6,14-Tri(50-(N,N-bis(4-methoxyphenyl)aminophen-4-yl)thiophene-2-yl)-triptycene (T103) with a triptycene core. This type of structure allowed for a higher *Tg* value and good solubility in organic solvents. The two molecules (T102 and T103) showed a PCE of 12.24 and 12.38% comparable to that of spiro-OMeTAD (12.87%) (Krishna et al. 2014).

In fact, all the three molecules had a higher V_{oc} than spiro-OMeTAD. The fill factor of the two molecules (T102 and T103) was reported higher than that of Spiro-OMeTAD.

2.7 Triazine-Based Derivatives

Star-shaped HTMs based on 1,3,5-triazine core were prepared by Do Sung et al. (2014). Two triazine derivatives Triazine-Th-OMeTPA, (2,4,6-tris[N,N-bis (4-methoxyphenyl)amino-N-phenylthiophen-2-yl]-1,3,5-triazine) and Triazine-Ph-OMeTPA (2,4,6-tris[N,N-bis(4-methoxyphenyl)-amino-N-diphenyl]-1,3,5-triazine) were prepared and characterized. The photovoltaic performance was different owing to structure differences observed in both the molecules. The triazine derivative, Triazine-Th-OMeTPA, showed a comparable PCE of 12.51% with Spiro-OMeTAD (13.45%) (Do Sung et al. 2014).

The overall performance of both the triazine derivatives was low compared to that of Spiro- OMeTAD. Moreover, an appreciable stability of 250 h was obtained for Triazine-Th-OMeTPA (Do Sung et al. 2014) (Table 1).

3 Polymer-Based HTM

3.1 P3HT Poly(3-Hexylthiophene)

In the past few years, P3HT-based polymer HTMs have garnered popularity among the researches. Snaith et al. used PSC based on P3HT as the HTM. They used a fullerene C60SAM-based organic monolayer to induce electron transfer from the polymer HTM and the perovskite layer of $CH_3NH_3PbI_{3-x}Cl_xI$ (Abrusci et al. 2013). But it only gave an efficiency of about 6.7% as compared to the PCE of 11.7% for Spiro-OMeTAD. This paved the way for future research for P3HT as HTM.

The thickness of P3HT plays a good role in photovoltaic measurements of the PSC as demonstrated by Abbas et al. (2015). Their research entailed the use of P3HT with the three types of different HTM thicknesses. They found out that the thinnest layer (20 nm) of P3HT lead to loss of voltage and a very thick layer (45 nm) of P3HT lead to increase in shunt resistance, thus decreasing the overall performance of the cell. The intermediate thickness of 30 nm gave the highest PCE of 13.7%.

Dopants have also been extensively used in P3HT-based HTM. Xiao et al. (2015) have reportedly used a graphdiyne dopant in a P3HT HTM. The GD dopants have found to increase the scattering of light, which in turn increases the absorbance rate of the PSC. The dopants have found to influence the HOMO levels through interaction with P3HT. The HOMO level is decreased due to π−π stacking of dopant and P3HT. This decrease in HOMO level causes an ease in the movement of the charge carrier between perovskite and HTM. The PCE of these devices was found to be up to 14.58% (Conings et al. 2015).

Habisreutinger et al. (2014) focussed on the use of single-walled carbon nanotubes (SWNT) in P3HT to use as HTM. The intent was to tune the functionalizing polymer around SWNT into a selective p-type hole collection layer in PSC. The P3HT/SWNT-PMMA (poly(methylmethacrylate) showed no degradation even up to 96 h compared with other HTMs (Li-Spiro-OMeTAD, P3HT, PMMA, PTAA) under the same condition and resulted in an efficiency of 15.3%.

Recently, Kundu and Kelly (2018) synthesized P3HT nanowire and deposited it in a PMMA poly(methylmethacrylate) matrix to use it as an HTM layer. Different device HTMs of same configuration PMMA:P3HT 80:20, 85:15, 90:10, and 95:05 were prepared using P3HT and PMMA by varying their ratios. It was found that the device performance was heavily impacted by the ratios of PMMA:P3HT. The blended configuration of P3HT/PMMA gave an efficiency ranging from 5.6% (for PMMA:P3HT 95:05) to 9.1% (for PMMA:P3HT 90:10). Interestingly, P3HT-only

Table 1 Organic HTMs with their JV characteristics

Name	J_{sc} (mA/cm^2)	V_{oc} (V)	FF	PCE (%)	Perovskite	Dopants used	Reference
Spiro-OMeTAD	17.8	0.98	0.63	10.9	$MAPbI_2Cl_2I$	None	Lee et al. (2012)
Spiro-OMeTAD	21.1	1.01	0.65	15	$MAPbI_3$	Co(III), Li-TFSi, t-BP	Burschka et al. (2013)
Spiro-OMeTAD	20.4	1.00	0.737	15.2	$MAPbI_3$	Li-TFSi, t-BP	Jeon et al. (2014)
po-Spiro-OMeTAD	21.2	1.02	0.776	16.7	$MAPbI_3$	Li-TFSi, t-BP	Jeon et al. (2014)
2,4 Spiro-OMeTAD	25.6	0.956	0.701	17.2	$MAPbI_3$	Li-TFSi, t-BP	Zhang et al. (2018)
Spiro-OMeTAD	23.19	1.14	0.76	20.38	$FA_{0.81}MA_{0.15}PbI_{2.51}Br_{0.45}$	Li-TFSi, t-BP	Li et al. (2016)
apv-EC	18.4	0.932	0.7	12	$MAPbI_3$	None	Lv et al. (2015)
apv-T	15.4	0.932	0.63	9	$MAPbI_3$	None	Lv et al. (2015)
FA-MeoPh	18.4	0.92	0.698	11.9	$MAPbI_3$	Li-TFSi, t-BP	Choi et al. (2014)
TPA-MeOPh	17.3	0.99	0.627	10.8	$MAPbI_3$	Li-TFSi, t-BP	Choi et al. (2014)
Z1011	20.5	1.09	0.7	16.3	$MAPbI_3$	None	Zhang et al. (2016)
Di-TPA	20.5	1.03	0.733	15.3	$MAPbI_3$	Li-TFSi, t-BP	Park et al. (2016)
Tri-TPA	21.8	1.03	0.777	16.3	$MAPbI_3$	Li-TFSi, t-BP	Park et al. (2016)
Tetra-TPA	22	1.05	0.78	17.9	$MAPbI_3$	Li-TFSi, t-BP	Park et al. (2016)
H101	20.5	1.04	0.65	13.8	$MAPbI_3$	FK102, Li-TFSi, t-BP	Li et al. (2014a)
H111	19.8	1.08	0.72	15.4	$MAPbI_3$	Li-TFSi, t-BP	Li et al. (2014b)
H112	20	1.07	0.71	15.2	$MAPbI_3$	Li-TFSi, t-BP	Li et al. (2014b)
SGT-405	20.3	1.02	0.713	14.8	$MAPbI_3$	FK209, Li-TFSi, t-BP	Do et al. (2014)
SGT-404	19.8	0.96	0.698	13.3	$MAPbI_3$	FK209, Li-TFSi, t-BP	Do et al. (2014)
SGT-407	20.6	0.99	0.686	13.9	$MAPbI_3$	FK209, Li-TFSi, t-BP	Do et al. (2014)
V886	21.4	1.09	0.734	16.9	$MAPbI_3$	FK209, Li-TFSi, t-BP	Gratia et al. (2015)

(continued)

Table 1 (continued)

Name	J_{sc} (mA/cm^2)	V_{oc} (V)	FF	PCE (%)	Perovskite	Dopants used	Reference
V950	22.5	1.07	0.74	17.8	FAMA0.15Pb(IBr0.15)3	Ag-TFSI	Daskeviciene et al. (2017)
PyA	10.8	0.89	0.346	3.3	$MAPbI_3$	FK209, Li-TFSi, t-BP	Jeon et al. (2013)
PyB	20.4	0.95	0.637	12.3	$MAPbI_3$	FK209, Li-TFSi, t-BP	Jeon et al. (2013)
PyC	20.2	0.89	0.694	12.4	$MAPbI_3$	FK209, Li-TFSi, t-BP	Jeon et al. (2013)
T-101	13.5	1	0.626	8.4	$MAPbI_3$	FK102, Li-TFSi, t-BP	Krishna et al. (2014)
T-102	17.2	1.03	0.681	12.2	$MAPbI_3$	FK102, Li-TFSi, t-BP	Krishna et al. (2014)
T-103	20.3	0.99	0.619	12.4	$MAPbI_3$	FK102, Li-TFSi, t-BP	Krishna et al. (2014)
Triazine-Th-OMeTPA	19.1	0.93	0.61	10.9	$MAPbI_3$	FK102, Li-TFSi, t-BP	Do Sung et al. (2014)
Triazine-Ph-OMeTPA	20.7	0.92	0.66	12.5	$MAPbI_3$	FK102, Li-TFSi, t-BP	Do Sung et al. (2014)

devices gave an efficiency of 10.7% but degraded within 24 h and PMMA:P3HT (90:10) degraded slowly under rigorous condition (99% > RH).

3.2 PEDOT: PSS

PEDOT: PSS (poly (3,4-ethylenedioxythiophene):poly (styrenesulfonate) sulfonic acid) has been widely used as an HTM in inverted planar configurations. PEDOT:PSS has excellent photovoltaic properties compared to inorganic HTMs. The use of PEDOT:PSS was first reported by Chen et al., when they used PEDOT:PSS in PSC made of $CH_3NH_3PbI_3$ perovskite film. The configuration of the PSC was glass/indium titanium oxide ITO/PEDOT:PSS/$CH_3NH_3PbI_3$/fullerene(C60)/thin bathocuproine (BCP) aluminum/(Al). They obtained a modest PCE of 3.9% which was much lower than highest PCE obtained before (Jeng et al. 2013).

An inverted planar configuration was used by Heo et al. (2015) to fabricate a $MAPbI_3$ PSC with PEDOT:PSS as a HTM. A configuration of ITO/PEDOT:PSS/$MAPbI_3$/PCBM/Au was adopted by them to get an efficiency of 18%. This type of PSC exhibited better stability and efficiency than other conventional $MAPbI_3$ devices owing to addition of PCBM as an electron-extracting layer (Heo et al. 2015).

Recently, Chiang and co-workers used PEDOT:PSS as an HTM in an inverted planar in $CH_3NH_3PbI_3$ absorber cell. H_2O, as an additive in the PbI2/DMF precursor solution, and DMF vapor treatment were combined to prepare thick perovskite layer (500 nm) with smooth surface and large grain size. Two-step spin coating was used to prepare $CH_3NH_3PbI_3$ absorber layer. This combined synergistic effect of H_2O and DMP vapor treatment resulted in maximum PCE exceeding 20% and the PSC showed no hysteresis, either in ambient air or nitrogen glove box (Chiang et al. 2017).

3.3 PTAA

Heo et al. (2013) introduced a novel structure incorporating the use of polytriarylamine (PTAA) as the HTM in PSC. PTAA as an HTM was compared with other PSC containing polymeric HTM (P3HT poly-3-(hexylthiophene)), PCPDTBT (poly-[2,1,3-benzothiadiazole-4,7-diyl[4,4-bis(2-ethylhexyl)-4H-cyclopenta [2,1-b:3,4-b] dithiophene-2,6-diyl]]), PCDTBT (poly-[[9-(1-octylnonyl)-9H-carbazole-2,7-diyl]-2,5-thiophenediyl2,1,3-benzothiadiazole-4,7-diyl-2,5-thiophenediyl]), and PSCs with no HTM. The device configuration was FTO/TiO_2/mpTiO_2/$CH_3NH_3PbI_3$/HTM/Gold electrode (Heo et al. 2013). The PCE of PTAA was reportedly the highest (9%) with highest J_{sc} of 16.4 mA/cm^2. This could be attributed to PTAA's higher hole mobility than other polymeric HTMs which lead to better interaction with $CH_3NH_3PbI_3$. Interestingly, PSC with no HTM had the lowest efficiency and JV characteristics (Fig. 9).

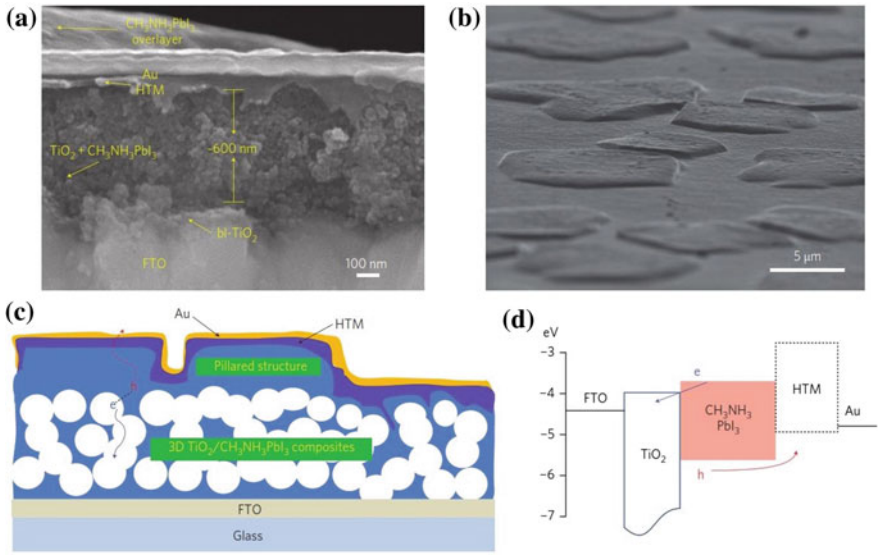

Fig. 9 **a** Cross-sectional SEM image of hybrid organic–inorganic heterojunction solar cell comprising of polymeric HTM, **b** SEM surface image of $MAPbI_3$-coated mesoporous TiO_2 film. **c** Illustration of device architecture. **d** Energy levels for TiO_2, $MAPbI_3$, and HTM. Reprinted with permission from Heo (2013) Copyright (2013) Nature Photonics

Bi et al. (2015) reported the use of larger grain size non-wetting PTAA to reduce charge carrier recombination in the PSC. This increased aspect ratio of HTM in PSC led to an efficiency of about 18.3% and a current density of around 20.8 $mAcm^{-2}$. It was found out through thermal admittance spectroscopy (TAS) measurements that the larger grain size influenced the PCE of the DSC (Table 2).

4 Inorganic Hole Transport Materials

The PSC based on organic and polymer HTMs suffer from humidity sensitiveness and a very high cost. The current price of high purity of Spiro-OMeTAD is almost 10 times the price of gold and silver. This is again necessitated by the fact that PSC should meet stringent conditions when deployed commercially. For this reason, p-type inorganic semiconductor is gaining popularity because of their chemical stability, higher mobility, and easier manufacturing process (Patel et al. 2018; Patel and Gohel 2018; Kumari et al. 2018).

Table 2 JV characteristics of polymeric HTM

Name	J_{sc} (mA/cm^2)	V_{oc} (V)	FF	PCE (%)	Perovskite	Dopants/Additives/Blends used	Reference
P3HT	14.9	0.68	0.55	6.7	$CH_3NH_3PbI_{3-X}Cl_x$	None	Abrusci et al. (2013)
P3HT	21.76	0.96	0.65	13.7	$MAPbI_3$	None	Abbas et al. (2015)
P3HT	21.7	0.941	0.713	14.58	$MAPbI_3$	GD	Xiao et al. (2015)
P3HT	22.71	1.02	0.66	15.3	$CH_3NH_3PbI_XCl_{3-x}$	SWNT(CG200)-PMMA	Habisreutinger et al. (2014)
P3HT/PMMA	16.7	0.99	0.64	10.7	$MAPbI_3$	Varied ratios of P3HT/PMMA blends	Kundu and Kelly (2018)
PEDOT:PSS	10.32	0.6	0.63	3.9	$MAPbI_3$	None	Jeng et al. (2013)
PEDOT:PSS	20.9	1.1	0.79	18.1	$MAPbI_3$	None	Heo et al. (2015)
PEDOT:PSS	23.51	1.03	0.83	20.1	$MAPbI_3$	H_2O	Chiang et al. (2017)
PTAA	16.4	0.9	0.61	9	$MAPbI_3$	None	Heo et al. (2013)
PTAA	20.8	0.88	0.99	18.3	$MAPbI_3$	None	Bi et al. (2015)

4.1 CuI (Copper Iodide)

CuI was the first inorganic HTM to be deployed by Christians et al. (2014). A PCE of 6% was achieved with good stability and higher electrical conductivity (J_{sc} = 17.8 mA/cm^2, V_{oc} = 0.55 V); this was comparable with results obtained with Spiro-OMeTAD (J_{sc} = 16.1 mA/cm^2, V_{oc} = 0.79 V, PCE = 7.9%). The lower efficiency was attributed to the lower value of V_{oc} using CuI. A gas–solid reaction method was used for the deposition of CuI film on perovskite which yielded a very high J_{sc} of 32.72 mA/cm^2 and an efficiency of 7.4% (Gharibzadeh et al. 2016). It was also reported in this study that there was low hysteresis observed due to high hole mobility of CuI. As observed in the previous study, this study also reported a lower value of V_{oc} (0.73 V) due to recombination effects at the CuI–perovskite interface. This solid–gas reaction was further used by Yu and co-workers to use CuI as a hole transport material. Yu et al. managed to achieve an efficiency of 14.7% with a J_{sc} of 20.9 mA/cm^2 and V_{oc} of 1.04 V (Wang et al. 2017). A low-temperature solution process method was adopted by Bian and co-workers to deposit CuI on perovskite layer. This led to an efficiency of 16.8%, the highest reported so far for CuI-based HTMs (Sun et al. 2016). It was observed by the authors that CuI had better air stability than polymer-based HTM like PEDOT:PSS under similar conditions.

Recently, CuI has also been used in conjunction with PEDOT:PSS as a double hole transport layer by Wang and co-workers (2018). The CuI acted as a buffer layer which greatly increased the stability of the device and hole extraction. The average exciton lifetime was significantly reduced to 2.7 ns. A PCE of 14.3% was achieved for this device.

4.2 CuSCN

Copper thiocyanate (CuSCN) is another p-type HTM that has gained popularity among researchers because of its high mobility of 0.01–0.1 cm^2 V^{-1}S^{-1}, high conductivity (10^{-2}–10^{-3} S cm^{-1}), and high chemical stability. There are different fabrication methods for the preparation of CuSCN like doctor blading technique, chemical bath deposition, electrochemical deposition, and ionic layer absorption reaction. Chavhan et al. (2014) investigated the first use of CuSCN as an inorganic hole transport material in a planar heterojunction-based glass/FTO/TiO_2/$CH_3NH_3Pb_{3-x}Cl_x$/CuSCN/Au with power efficiency of 6.4%. The devices were characterized, and it was found that the main limiting photovoltaic parameter was a low V_{oc} (0.727 V), which was attributed to low diffusion length. Qin et al. used a doctor blading technique for depositing CuSCN. The device structure had the configuration of FTO glass/ TiO_2/ $CH_3NH_3PbI_3$/CuSCN/Au (Qin et al. 2014). The presence of CuSCN gave a solar performance of PCE 12.4%. An inverted planar structure was used by Bian and co-workers (2015) by one-step deposition crystallization method to fabricate $CH_3NH_3PbI_3$ films on top of CuSCN. This PSC prepared

by one-step method reportedly had higher reproducibility and stability and the efficiency of the device reached up to 16.6%. The highest efficiency for a CuSCN-based HTM was reported by Lee and et al. (2017) with an efficiency of 17.10% using spray deposition technique and the use of no additives. It was noted that the conventional doctor blading technique damages the perovskite layer during the coating process of CuSCN. The authors reported that the use of this technique made no damage to the perovskite layer, and the fabricated PSC gave a remarkably long-term thermal stability with JV characteristics being J_{sc} of 23.1 mA/cm^2, V_{oc} of 1.013 V, and FF of 0.731. The lower V_{oc} can be attributed to the use of no additives. Therefore, the deposition method used in fabrication of HTM layers in PSC plays an important role in the overall performance of the cell.

4.3 NiO

NiO has been extensively used as an HTM in thin-film structures and mesostructured scaffold because of its good hole conductivity, deep valence band level −5.3 eV, and large energy gap (3.5–3.9 eV). The first high-performance PSC based on NiO as HTM was based on an inverted planar configuration (NiONC/$CH_3NH_3PbI_3$/PCBM/Al), and it was fabricated using sol–gel process by Zhu et al. (2014). It was recommended by the authors that the cells must have high-quality perovskite and sufficient thickness for NiO nanocrystalline film as a hole transport layer. The efficiency obtained in this study was 9.11% with J_{sc} 16.27 mA/cm^2, V_{oc} = 0.882 V, and FF = 0.635. The efficiency of PSCs using Ni-based HTM was further increased by Kim et al. to 15.4% by doping 5% Cu in HTM (Kim et al. 2015). The J_{sc} and V_{oc} values obtained were all higher than PEDOT:PSS and NiOx with no doping under similar conditions. Owing to higher Eg levels, it shows higher V_{oc} levels and appropriate alignment with high Eg levels found in perovskite. Jung et al. (2015) reported a low-temperature combustion process to prepare Cu-doped NiOx HTM for high performance. The films prepared from this method were better than high-temperature sol–gel methods with an efficiency of 17.7%.

He et al. (2018) recently focussed on post-treatment of NiO hole transport layer through surface modification by using a trifunctional molecule cysteine (Cys) to enhance the interfacial contact.

This type of protocol achieved the highest efficiency of 18.3%, gave V_{oc} of more than 1.12 V and suppressed the hysteresis to negligible.

PSC incorporating 5% Y (yttrium) doped in NiO HTM layer was demonstrated by Hu et al. 2018. The doping of Y led to lower recombination rate, proper charge carriers, and enhanced hole mobility. A PCE of 16.31% was achieved with current density J_{sc} of 23.82 mA/cm^2.

4.4 Graphene Oxide (GO)

Graphene and its derivates have been used both in electron transport layer (ETL) and hole transport layer (HTM). Graphene oxide (GO) is the most commonly used graphene derivative as HTM because of its high thermal conductivity (600 Wm^{-1} k^{-1}), appreciable valence band (5.2 eV), and high charge mobility. Wu and co-workers (2014) first time employed graphene oxide (GO) as a conductor. They found that perovskite films observed on graphene exhibited much better crystallization and efficient hole extraction. An efficiency of about 12.4% was observed. Moreover, GO was employed as a dual functional buffer layer by Li.et al. 2014 to address the issues with wettability of the HTM solution on perovskite surface and recombination of charge carriers. This led to an efficiency of about 15.1% with a high J_{sc} of 20.2 mA/cm^2, V_{oc} of 1.04 V, and a film factor of 0.73. The highest reported efficiency was 18.1% by Agresti et al. (2016) in which they used graphene in both ETL and HTM. Graphene oxide was used as a buffer layer between perovskite and HTM layer and doped graphene flakes in their mesoporous structure. This structure showed a good stability of 88% of PCE after 16 h under one sun illumination (Table 3).

5 Outlook

In this review, focus was given on recent research strides in hole transport materials (HTM) based on organic, inorganic, and polymer-based substances. As progress continues in the field of photovoltaics pertaining to perovskite, hole transport layers play an indispensable part in charge transportation. It is one of the three main layers constituting the perovskite cell and has a huge impact on efficiency and stability of the cell.

Whilst costly, Spiro-OMeTAD still dominates the role as an HTM for perovskite cells among researchers. With its costly synthetic production, researchers are developing and incorporating different alternatives using novel materials. Among the organic-based small molecules, triphenylamine, thiophene, carbazole, triptycene, and triazine have garnered interest among researchers. It has been found through literature that doped organic-based HTMs may lead to high efficiency but are more susceptible to degradation with time. A proper HTM must have good film-forming properties, must be chemically stable and should have higher mobility. A good HTM should also have a suitable HOMO energy level for efficient transport of holes from the perovskite to the hole-transporting layer. Also, HOMO energy level is not the only limiting factor in choosing an efficient HTM; it should also have proper recombination of charge carriers, because recombination of charge carriers in perovskite–HTM interface plays an important role in the efficiency and stability of the cell.

Small organic molecule-based HTM possess proper interface contact, good film-forming ability, and more processing solvent compared to polymeric HTM. Polymeric HTMs like P3HT and PTAA have tunable HOMO level, high conductivity, and

Table 3 JV characteristics of inorganic HTMs and buffer layer

HTM	J_{sc} (mA/cm^2)	V_{oc} (V)	FF	PCE (%)	Structure	Dopants/Additional HTM	Reference
CuI	17.8	0.55	0.61	6	FTO/TiO_2 blocking layer/CuI/	–	Christians et al. (2014)
CuI	32.72	0.73	0.31	7.4	$CH_3NH_3PbI_3/TiO_2$/CuI overlayer/Au FTO/$TiO_2/CH_3NH_3PbI_3$/CuI/Au	–	Gharibzadeh et al. (2016)
CuI	20.9	1.04	0.67	14.7	FTO/CuI/$CH_3NH_3PbI_3$/PCBM/polyethyleneimine (PEI)/Ag	–	Wang et al. (2017)
CuI	22.8	1.01	0.73	16.8	ITO/CuI/$CH_3NH_3PbI_3$/fullerene (C60)/bathocuproine (BCP)/Ag	–	Sun et al. (2016)
CuI	20.5	0.92	0.76	14.3	ITO/CuI/PEDOT:PSS/$CH_3NH_3PbI_3$/PC61BM/ZnO/Al	PEDOT:PSS	Hu et al. (2018)
CuSCN	14.4	0.72	0.61	6.4	Glass/FTO/$TiO_2/CH_3NH_3PbI_{3-x}Cl_x$/CuSCN/Au	–	Chavhan et al. (2014)
CuSCN	11.9	1.01	0.62	12.4	FTO glass/$TiO_2/CH_3NH_3PbI_3$/CuSCN/Au	–	Qin et al. (2014)
CuSCN	21.6	1	0.75	16.6	ITO/CuSCN/$CH_3NH_3PbI_3$/C60/BCP/Ag	–	Ye et al. (2015)
CuSCN	23.1	1.01	0.73	17.1	FTO/$TiO_2/CH_3NH_3PbI_3$/CuSCN/Au	–	Yang et al. (2017)
NiO	16.27	0.88	0.63	9.11	NiONC/$CH_3NH_3PbI_3$/PCBM/Al	–	Zhu et al. (2014)
NiO	18.75	1.11	0.72	15.4	ITO/Cu:NiOx/$CH_3NH_3PbI_3$/PC61BM/C60/Ag	Cu	Kim et al. (2015)
NiO	22.23	1.05	0.76	17.7	ITO/Cu:NiOx/$CH_3NH_3PbI_3$/C60/Bis-C60/Ag	Cu	Jung et al. (2015)

(continued)

Table 3 (continued)

HTM	J_{sc} (mA/cm^2)	V_{oc} (V)	FF	PCE (%)	Structure	Dopants/Additional HTM	Reference
NiO	23.6	1.11	0.7	18.3	ITO/Cu:NiOx/Cys/perovskite/PCBM/Bphen/Al	Cu, CyS	He et al. (2018)
NiO	23.82	1	0.68	16.31	FTO/Y:NiO/$CH_3NH_3PbI_3$/PCBM/Au	Y	Hu et al. (2018)
GO	17.46	1	0.71	12.4	ITO/GO/$CH_3NH_3PbI_{3-x}Cl_x$/PCBM/ZnO/A	–	Wu et al. (2014)
Spiro-OMeTAD - GO	20.2	1.04	0.73	15.1	FTO/TiO_2/$CH_3NH_3PbI_3$/GO/Spiro-OMeTAD/Au	Li-TFSI and TBP	Li et al. (2014)
Spiro-OMeTAD - GO	22.48	1.08	0.75	18.1	FTO/mTiO_2 + G/$CH_3NH_3PbI_3$/GO/Spiro-OMeTAD/Au	Li-TFSI and TBP	Agresti et al. (2016)

good solubility. PEDOT:PSS also showed appreciable efficiency range of stability and efficiency.

Inorganic HTMs like CuI and GO greatly improve stability when it acts like a buffer layer. In addition, NiO doped with other p-type inorganic materials showed better JV characteristics and suppressed hysteresis. Moreover, the p-type inorganic HTMs are chemically stable, have higher hole mobility, and are cheaper to manufacture.

Owing to different desirable factors in HTMs, it will be important to explore the characteristics of potential HTM (Interfacial properties, hole mobility, and charge carrier recombination) for enhanced device performance in perovskite-based solar cells. The varied photovoltaic performance among different HTMs is a characteristic of the interaction of the perovskite and HTM layers. The chemical mechanisms of such interactions have not been studied in deep at present. For a proper design of new HTM interfaces, these mechanisms have to be thoroughly investigated. In addition, the use of inorganic buffer layers to HTM interface needs to be realized for proper interface contact and stability.

References

Abbas HA, Kottokkaran R, Ganapathy B, et al (2015) High efficiency sequentially vapor grown n-i-p $CH_3NH_3PbI_3$ perovskite solar cells with undoped P3HT as p-type heterojunction layer. APL Mater 3. https://doi.org/10.1063/1.4905932

Abrusci A, Stranks SD, Docampo P et al (2013) High-performance perovskite-polymer hybrid solar cells via electronic coupling with fullerene monolayers. Nano Lett 13:3124–3128. https://doi.org/10.1021/nl401044q

Agresti A, Pescetelli S, Taheri B et al (2016) Graphene-perovskite solar cells exceed 18% efficiency: a stability study. Chemsuschem 9:2609–2619. https://doi.org/10.1002/cssc.201600942

Kojima Akihiro, Teshima K, Shirai Y, Miyasaka T (2009) Organometal Halide Perovskites as Visible- Light Sensitizers for Photovoltaic Cells. J Am Chem Soc 131:6050–6051. https://doi.org/10.1021/ja809598r

Aristidou N, Sanchez-Molina I, Chotchuangchutchaval T et al (2015) The role of oxygen in the degradation of methylammonium lead trihalide perovskite photoactive layers. Angew Chemie Int Ed 54:8208–8212. https://doi.org/10.1002/anie.201503153

Bi C, Wang Q, Shao Y et al (2015) Non-wetting surface-driven high-aspect-ratio crystalline grain growth for efficient hybrid perovskite solar cells. Nat Commun 6:1–7. https://doi.org/10.1038/ncomms8747

Burschka J, Pellet N, Moon SJ et al (2013) Sequential deposition as a route to high- performance perovskite-sensitized solar cells. Nature 499:316–319. https://doi.org/10.1038/nature12340

Chavhan S, Miguel O, Grande H-J et al (2014) Organo-metal halide perovskite-based solar cells with CuSCN as the inorganic hole selective contact. J Mater Chem A 2:12754–12760. https://doi.org/10.1039/C4TA01310G

Chiang C-H, Nazeeruddin MK, Grätzel M, Wu C-G (2017) The synergistic effect of H_2O and DMF towards stable and 20% efficiency inverted perovskite solar cells. Energy Environ Sci 10:808–817. https://doi.org/10.1039/C6EE03586H

Choi H, Park S, Paek S et al (2014) Efficient star-shaped hole transporting materials with diphenylethenyl side arms for an efficient perovskite solar cell. J Mater Chem A 2:19136–19140. https://doi.org/10.1039/C4TA04179H

Christians JA, Fung RCM, Kamat PV (2014) An inorganic hole conductor for Organo-lead halide perovskite solar cells. improved hole conductivity with copper iodide. J Am Chem Soc 136:758–764. https://doi.org/10.1021/ja411014k

Conings B, Drijkoningen J, Gauquelin N et al (2015) Intrinsic thermal instability of methylammonium lead trihalide perovskite. Adv Energy Mater 5:1–8. https://doi.org/10.1002/aenm.201500477

Daskeviciene M, Paek S, Wang Z et al (2017) Carbazole-based enamine: low-cost and efficient hole transporting material for perovskite solar cells. Nano Energy 32:551–557. https://doi.org/10.1016/j.nanoen.2017.01.015

Do Sung S, Kang MS, Choi IT et al (2014) 14.8% Perovskite solar cells employing carbazole derivatives as hole transporting materials. Chem Commun 50:14161–14163. https://doi.org/10.1039/C4CC06716A

Do K, Choi H, Lim K et al (2014) Star-shaped hole transporting materials with a triazine unit for efficient perovskite solar cells. Chem Commun 50:10971–10974. https://doi.org/10.1039/C4CC04550E

Economist T (2018) A new type of solar cell is coming to market. Economist. https://www.economist.com/news/science-and-technology/21736122-perovskites-have-potential-outshine-silicon-solar-panels-new-type. Accessed 30 Apr 2018

Gharibzadeh S, Nejand BA, Moshaii A et al (2016) Two-step physical deposition of a compact cui hole-transport layer and the formation of an interfacial species in perovskite solar cells. Chemsuschem 9:1929–1937. https://doi.org/10.1002/cssc.201600132

Gratia P, Magomedov A, Malinauskas T et al (2015) A Methoxydiphenylamine- substituted carbazole twin derivative: an efficient hole-transporting material for perovskite solar cells. Angew Chemie Int Ed 54:11409–11413. https://doi.org/10.1002/anie.201504666

Habisreutinger SN, Leijtens T, Eperon GE et al (2014) Carbon nanotube/polymer composites as a highly stable hole collection layer in perovskite solar cells. Nano Lett 14:5561–5568. https://doi.org/10.1021/nl501982b

Han Y, Meyer S, Dkhissi Y et al (2015) Degradation observations of encapsulated planar $CH_3NH_3PbI_3$ perovskite solar cells at high temperatures and humidity. J Mater Chem A 3:8139–8147. https://doi.org/10.1039/C5TA00358J

Heo JH, Im SH, Noh JH et al (2013) Efficient inorganic-organic hybrid heterojunction solar cells containing perovskite compound and polymeric hole conductors. Nat Photonics 7:486–491. https://doi.org/10.1038/nphoton.2013.80

Heo JH, Han HJ, Kim D et al (2015) Hysteresis-less inverted $CH_3NH_3PbI_3$ planar perovskite hybrid solar cells with 18.1% power conversion efficiency. Energy Environ Sci 8:1602–1608. https://doi.org/10.1039/C5EE00120J

He J, Xiang Y, Zhang F et al (2018) Improvement of red light harvesting ability and open circuit voltage of Cu:NiOx based p-i-n planar perovskite solar cells boosted by cysteine enhanced interface contact. Nano Energy 45:471–479. https://doi.org/10.1016/j.nanoen.2018.01.017

Hu WD, Dall'Agnesel C, Wang XF, et al (2018) Copper iodide-PEDOT:PSS double hole transport layers for improved efficiency and stability in perovskite solar cells. J Photochem Photobiol Chem 357:36–40. https://doi.org/10.1016/j.jphotochem.2018.02.018

Hu Z, Chen D, Yang P, et al (2018) Sol-gel-processed yttrium-doped NiO as hole transport layer in inverted perovskite solar cells for enhanced performance. Appl Surf Sci 441:258–264. https://doi.org/10.1016/j.apsusc.2018.01.236

Jeng JY, Chiang YF, Lee MH et al (2013) $CH_3NH_3PbI_3$ perovskite/fullerene planar- heterojunction hybrid solar cells. Adv Mater 25:3727–3732. https://doi.org/10.1002/adma.201301327

Jeon NJ, Lee J, Noh JH et al (2013) Efficient inorganic-organic hybrid perovskite solar cells based on pyrene arylamine derivatives as hole-transporting materials. J Am Chem Soc 135:19087–19090. https://doi.org/10.1021/ja410659k

Jeon NJ, Lee HG, Kim YC et al (2014) O-methoxy substituents in spiro-OMeTAD for efficient inorganic-organic hybrid perovskite solar cells. J Am Chem Soc 136:7837–7840. https://doi.org/10.1021/ja502824c

Jung JW, Chueh CC, Jen AKY (2015) A low-temperature, solution-processable, Cu- Doped Nickel Oxide hole-transporting layer via the combustion method for high- performance thin-film perovskite solar cells. Adv Mater 27:7874–7880. https://doi.org/10.1002/adma.201503298

Kim HS, Lee CR, Im JH et al (2012) Lead iodide perovskite sensitized all-solid-state submicron thin film mesoscopic solar cell with efficiency exceeding 9%. Sci Rep 2:1–7. https://doi.org/10.1038/srep00591

Kim JH, Liang PW, Williams ST et al (2015) High-performance and environmentally stable planar heterojunction perovskite solar cells based on a solution-processed copper- doped nickel oxide hole-transporting layer. Adv Mater 27:695–701. https://doi.org/10.1002/adma.201404189

Krishna A, Sabba D, Li H et al (2014) Novel hole transporting materials based on triptycene core for high efficiency mesoscopic perovskite solar cells. Chem Sci 5:2702–2709. https://doi.org/10.1039/C4SC00814F

Kumari N, Patel SR, Gohel JV (2018) Current progress and future prospective of perovskite solar cells: a comprehensive review. Rev Adv Mater Sci 53:161–186

Kumari N, Patel SR, Gohel JV (2019) Superior efficiency achievement for FAPbI3- perovskite thin film solar cell by optimization with response surface methodology technique and partial replacement of Pb by Sn. Optik (Stuttg) 176:262–277. https://doi.org/10.1016/j.ijleo.2018.09.066

Kundu S, Kelly TL (2018) Improving the moisture stability of perovskite solar cells by using PMMA/P3HT based hole-transport layers. Mater Chem Front 2:81–89. https://doi.org/10.1039/C7QM00396J

Lee MM, Teuscher J, Miyasaka T et al (2012) Efficient hybrid solar cells based on meso- superstructured organometal halide perovskites. Science 338:643–647. https://doi.org/10.1126/science.1228604

Leijtens T, Ding I-K, Giovenzana T et al (2012) Hole transport materials with low glass transition temperatures and high solubility for application in solid-state dye-sensitized solar cells. ACS Nano 6:1455–1462. https://doi.org/10.1021/nn204296b

Li H, Fu K, Hagfeldt A et al (2014a) A simple 3, 4-Ethylenedioxythiophene based hole-transporting material for perovskite solar cells. Angew Chemie Int Ed 53:4085–4088. https://doi.org/10.1002/anie.201310877

Li H, Fu K, Boix PP et al (2014b) Hole-transporting small molecules based on thiophene cores for high efficiency perovskite solar cells. Chemsuschem 7:3420–3425. https://doi.org/10.1002/cssc.201402587

Li W, Dong H, Guo X et al (2014) Graphene oxide as dual functional interface modifier for improving wettability and retarding recombination in hybrid perovskite solar cells. J Mater Chem A 2:20105–20111. https://doi.org/10.1039/C4TA05196C

Li X, Bi D, Yi C et al (2016) A vacuum flash assisted solution process for high-efficiency large-area perovskite solar cells. Science 80(8060):1–10. https://doi.org/10.1126/science.aaf8060

Lv S, Song Y, Xiao J et al (2015) Simple triphenylamine-based hole-transporting materials for perovskite solar cells. Electrochim Acta 182:733–741. https://doi.org/10.1016/j.electacta.2015.09.165

Misra RK, Aharon S, Li B et al (2015) Temperature- and component-dependent degradation of perovskite photovoltaic materials under concentrated sunlight. J Phys Chem Lett 6:326–330. https://doi.org/10.1021/jz502642b

NREL (2018) NREL efficiency chart for solar research cells. https://www.nrel.gov/pv/assets/images/efficiency-chart.png. Accessed 30 Apr 2018

Park S, Heo JH, Yun JH et al (2016) Effect of multi-armed triphenylamine-based hole transporting materials for high performance perovskite solar cells. Chem Sci 7:5517–5522. https://doi.org/10.1039/C6SC00876C

Patel SB, Gohel JV (2018) Enhanced solar cell performance by optimization of spray coated CZTS thin film using Taguchi and response surface method. J Mater Sci Mater Electron 29:5613–5623. https://doi.org/10.1007/s10854-018-8530-5

Patel SB, Patel AH, Gohel JV (2018) A novel and cost effective CZTS hole transport material applied in perovskite solar cells. CrystEngComm 20:7677–7687. https://doi.org/10.1039/c8ce01337c

Qin P, Tanaka S, Ito S et al (2014) Inorganic hole conductor-based lead halide perovskite solar cells with 12.4% conversion efficiency. Nat Commun 5:1–6. https://doi.org/10.1038/ncomms4834

Senocrate A, Yang TY, Gregori G et al (2018) Charge carrier chemistry in methylammonium lead iodide. Solid State Ionics 321:69–74. https://doi.org/10.1016/j.ssi.2018.03.029

Snaith HJ, Grätzel M (2006) Enhanced charge mobility in a molecular hole transporter via addition of redox inactive ionic dopant: Implication to dye-sensitized solar cells. Appl Phys Lett 89

Sun W, Ye S, Rao H et al (2016) Room-temperature and solution-processed copper iodide as the hole transport layer for inverted planar perovskite solar cells. Nanoscale 8:15954–15960. https://doi.org/10.1039/C6NR04288K

Wang H, Yu Z, Jiang X et al (2017) Efficient and stable inverted planar perovskite solar cells employing CuI as hole-transporting layer prepared by solid-gas transformation. Energy Technol 5:1836–1843. https://doi.org/10.1002/ente.201700422

Wu Z, Bai S, Xiang J et al (2014) Efficient planar heterojunction perovskite solar cells employing graphene oxide as hole conductor. Nanoscale 6:10505–10510. https://doi.org/10.1039/C4NR03181D

Xiao J, Shi J, Liu H, et al (2015) Efficient $CH_3NH_3PbI_3$ perovskite solar cells based on graphdiyne (GD)-modified P3HT Hole-transporting material. Adv Energy Mater 5:1–7. https://doi.org/10.1002/aenm.201401943

Yang IS, Sohn MR, Do Sung S et al (2017) Formation of pristine CuSCN layer by spray deposition method for efficient perovskite solar cell with extended stability. Nano Energy 32:414–421. https://doi.org/10.1016/j.nanoen.2016.12.059

Ye S, Sun W, Li Y et al (2015) CuSCN-based inverted planar perovskite solar cell with an average PCE of 15.6%. Nano Lett 15:3723–3728. https://doi.org/10.1021/acs.nanolett.5b00116

Zhang F, Yi C, Wei P et al (2016) A novel dopant-free triphenylamine based molecular "Butterfly" hole-transport material for highly efficient and stable perovskite solar cells. Adv Energy Mater 6:1–7. https://doi.org/10.1002/aenm.201600401

Zhang MD, Zhao DX, Chen L et al (2018) Structure-performance relationship on the asymmetric methoxy substituents of spiro-OMeTAD for perovskite solar cells. Sol Energy Mater Sol Cells 176:318–323. https://doi.org/10.1016/j.solmat.2017.10.014

Zhu Z, Bai Y, Zhang T et al (2014) High-performance hole-extraction layer of sol-gel- processed nio nanocrystals for inverted planar perovskite solar cells. Angew Chemie Int Ed 53:12571–12575. https://doi.org/10.1002/anie.201405176

Conjugation of Nanomaterials and Bioanodes for Energy Production in Microbial Fuel Cell

Ambika Arkatkar, Arvind Kumar Mungray and Preeti Sharma

Abstract The term nanotechnology is popularized for the study of small particles with unique properties. Nanoparticles are widely studied for their use in the medicinal field. The application of these tiny particles in the abiotic world of energy generation is also acceptable. The use of surface enhancement property of nanomaterials can be applied in the field of biotic energy generation and simultaneous waste treatment technology. The two goals are targeted under microbial fuel cell (MFC) technology. The MFC reactors can be added as one major area for application of nanoparticles. This chapter will deal with the basic idea of MFC and its limitation. We will further understand the use of nanoparticles as a solution for power enhancement in an MFC reactor.

Keywords Nanoparticles · Microbial fuel cell · Anode · Power enhancement

1 Introduction of MFC

The day by day depletion of nonrenewable source of energy has become a prime concern for the world economy. The renewable sources of energy are not abundantly available in all parts of the world throughout the year. The voluminous generation of waste is another parameter bothering the safe survival of animal and plant kingdom on earth. The scientific community has now shifted its focus toward developing a technology that can simultaneously target the two big issues as stated above.

Microbial fuel cell (MFC) technology is emerging as an alternative method for waste treatment and up to some extent a system that can generate power. The technology holds its roots in 1910–1911 (Bullen et al. 2006; Franks and Nevin 2010) when it was discovered that few microbes can give out electrons which can be captured to generate power. The research then again gained its momentum in the early twentieth

A. Arkatkar · A. K. Mungray (✉)
Department of Chemical Engineering, Sardar Vallabhbhai National Institute of Technology, Surat 395007, India
e-mail: amungray@yahoo.com

A. Arkatkar · P. Sharma
Department of Biotechnology, Veer Narmad South Gujarat University, Surat 395007, India

L. Ledwani and J. S. Sangwai (eds.), *Nanotechnology for Energy and Environmental Engineering*, Green Energy and Technology,
https://doi.org/10.1007/978-3-030-33774-2_7

century (Schröder 2012) when the research was initiated for development in nearly all aspects of MFC technology. In this reactor, the activity of oxidation and reduction of electrons was separated in two chambers. In one chamber substrate was oxidized by the microbes to generate electrons. These electrons were channelized to travel in the second chamber; in this chamber either they will reduce a chemical or react with air/oxygen. The chambers will be separated internally by means of a proton permeable membrane (PEM) that allows the passage of protons toward the adjacent chamber. The proton and electron combine with air/oxygen to form water (Logan 2008).

The different parts of MFC have their application in different fields. The anode chamber, where the waste substrate is degraded mostly serves as a treatment facility. The cathode chamber where the electrons and protons ultimately unite can be used as a recovery system for different metals, (Liang et al. 2011; Rikame et al. 2018; Song et al. 2016) as a biomass generation unit, (Gajda et al. 2015) as a hydrogen generation unit (Ogawa et al. 2018), etc. Based on its application MFC is often conjoined with other treatment facilities like septic tank, (Alzate-Gaviria et al. 2016) osmotic fuel cell, (Qin and He 2017; Qin et al. 2015), etc.

2 Limitations of MFC

The MFC reactor has proven to treat domestic wastewater up to the level of an activated sludge reactor (ASR) used in a wastewater treatment (WWT) plant (Asai et al. 2017). The major setback for the commercialization of this technology is its ability to produce limited power. The efficiency loss during scale-up process, higher cost of PEM and the internal resistances in a reactor are thought to be the hindering factors behind the marketing of this technology (Logan et al. 2006; Mathuriya et al. 2018). The various aspects taken into consideration for the reduction of these internal resistances are (a) Designs of reactors; (b) Membranes; (c) Biofilms, and (d) Electrodes.

The designs of reactors are majorly changing to reduce the internal resistance in the MFC reactors. The work has been extensively done by researchers at Penn State University (Logan et al. 2006) and Bristol Robotics Laboratory, West England University (Ieropoulos et al. 2005). The researchers are also shifting from the lab scale double chamber reactor to more feasible single chamber, air-cathode reactors because its small size offers easy handling and mass experimentation with it at the laboratory level. The different designs and structures are always casted as per the requirement of the end application of this technology. The next aspect "membranes" are the costliest part of the reactor. Membrane less reactors (Zhou et al. 2018; Zhu et al. 2011) and ceramic membranes (Ghadge et al. 2014; Ieropoulos et al. 2013; Winfield et al. 2016) are being studies for the replacement of costlier proton exchange membranes in the reactors. The working force behind the technology is biofilm (Arkatkar et al. 2019). The work on isolation of capable exoelectrogen is going on worldwide; the microbes like *Shewanella sp*., *Geobacter sp*., etc. are studied in depth for understanding the

mechanism of electron generation and transfer few studies are also carried out on bioengineered microbes (Choudhury et al. 2017). The focus of this chapter will be mainly on the anode electrode modification through the use of nanomaterials and its effect on biofilms on the electrode. The other topics can be studied in detailed elsewhere.

3 Bioanodes/Microbial Growth in MFC

The anode chamber in MFC reactor is the place where electron and proton are generated. This generation process completely depends on the microbes, also known as exoelectrogens. The major factors that affect the electron generation and its flow in the anode chamber are: (a) choice of substrate; (b) choice of exoelectrogens; (c) electrode material (i) large surface area (ii) biocompatible and electron conductive nature; and (d) conductivity of anolyte (Xie et al. 2015).

Theoretically magnitude of substrate degradation is directly proportional to the magnitude of the generation of electron and protons in a reactor (Logan 2008). The microorganism may have limitation for the degradation of a particular substrate (Zhang et al. 2011). Thus the choice of substrate and choice of exoelectrogens are interrelated issues (Pant et al. 2010). The electrode material should have a conductive, biocompatible nature with larger surface area (Choudhury et al. 2017; Logan et al. 2006). The biocompatible nature helps in the building of biofilm on the electrode surface. Larger the surface area better will be the space available for biofilm formation and capturing of electrons. The conductive nature of both electrode and electrolyte (anolyte) is important for the smooth flow of electrons (Du et al. 2015).

The generation of electrons will not be restricted to happen in the anode biofilm. In a mixed culture condition, it is possible that the degradation of substrate and release of electron may occur at some distance from the anode electrode. Under such conditions the conductive nature of electrolyte can be helpful for the flow of electrons toward the electrode. Once the electron is released from the outer membrane of the exoelectrogens, it has many paths to follow. As shown in Fig. 1 the electron may be consumed by another microbe; (Rotaru et al. 2014) it may directly travel to the anode (Arkatkar et al. 2019), or it may be channelized toward anode via a mediator

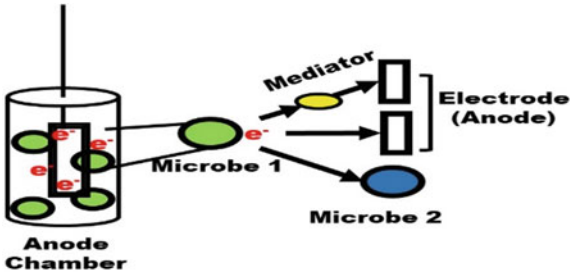

Fig. 1 Pictorial representation of path followed by an electron in the anode chamber

(artificial (Tharali et al. 2016) or natural (Bosire et al. 2016; Cao et al. 2019; Huang et al. 2018)).

The growth of microbial culture is always subjected to the environmental condition around it. A spontaneous drive of electron in the outer space will increase the rate of reaction inside the bacterial cell. Thus, it is important to increase the rate of electron consumption in the outside environment of an exoelectrogen. To increase the electron consumption in anode chamber the strategies like growth of exoelectrogenic biofilm on the anode surface, addition of mediators in the anolyte, and coating of electron acceptor on the anode surface can be implemented.

The growth of conductive biofilm helps the anode to capture electrons (Babauta et al. 2012). As explained through earlier studies the addition of a mediator from outside or a secretion of the microbial culture will boost the flow of electrons toward the anode. The electrode surface when coated with oxides of metals and other materials can serve as an improved electron receptor (Lv et al. 2012; Zhang et al. 2016).

4 Application of Nanomaterial/Nanoparticles in MFC

Nanotechnology is a branch of science that deals with the nanoscale particles. These particles have small size (in the range of 1–100 nm), and unique properties which are exhibited by their bulky counterparts. These tiny particles alter the role of the base substance in a reaction. The small size facilitates the rate of reaction in which these nanoparticles are involved. The nanoparticles are used for coating of the electrode surface in MFC. It has been very well proven that the coating of nanoparticles/nanomaterials enhance the power production in MFC (Jiang et al. 2014).

Mostly metal oxides having highelectron accepting capability are chosen for coating on an electrode. The method of preparation of nanoparticles and coating varies in each study (Table 1). The reduction in the size of metal oxide enhances the surface area for electron reaction and simultaneously increases the availability of oxides as electron acceptor. In an MFC reactor the electrode, anode, and cathode accept electrons; anode accepts it from microbes and cathode accepts it from anode via an external circuit. As the anode is always in contact with the microbial culture it is termed as bioanode. Thus, while coating of the nanoparticles on anode one should consider a few biological aspects. The compatibility and durability of coating are major parameters to given attention on.

5 Review of Research

The metal oxides like iron (Fe), (Mohamed et al. 2018a, b) manganese (Mn), (Kalathil et al. 2013) tin (Sn), palladium (Pd), (Xu et al. 2018) molebdenum (Mo) (Zeng et al. 2018a, b), and carbon nanotubes (Table 1) are frequently used metals for preparation

Table 1 Tabular information regarding nanomaterials used in MFC

Sr. no.	MFC design	Electrode material	Modified electrode	Nanomaterial used	Synthesis process	Power enhanced	References
1	H-Shaped MFC	Graphite felt	Both anode and cathode	Single-walled carbon nanotubes (SWCNTs), Graphitised carbon black (GCB), Carbon nanofibres (CNFs), and Graphitised carbon nanofibres (GCNFs)	Suspension was prepared by mixing readymade nanoparticles	Graphitised carbon nanofibres (GCNFs) 41 mV	Alharbi (2013)
2	Single-chamber MFCs with an air-cathode	Graphite felt	Anode	Nano polypyrrole (nano-PPy)	Electricpolymerization reaction using cyclic voltammetry (CV) with different cycle duration	PPy-2 Maximum power density was 430 mW/m^2, a 15% increase compared with that of the control	Chi (2013)
3	H-Shaped MFC	Carbon paper	Anode	CNT/MnO_2 nanocomposite	Fabrication of composite was done in laboratory	Modified anode—power density 120 mW/m^2	Kalathil et al. (2013)
4	H-Shaped MFC	The glassy carbon electrode	Anode	Multi-walled carbon nanotubes and tin oxide (MWCNTs/SnO_2)	Fabrication of composite was done in laboratory	Modified anode—maximum power densities 1421 mWm^{-2}	Mehdinia et al. (2014)
5	Single chamber MFC	Carbon felt	Anode	Carbon felt Supported nano-molybdenum carbide(Mo_2C)/carbon nanotubes (CNTs) composite	Microwave-assisted method	Modified anode—maximum power densities 1.05 mWm^{-2}	Wang et al. (2014)

(continued)

Table 1 (continued)

Sr. no.	MFC design	Electrode material	Modified electrode	Nanomaterial used	Synthesis process	Power enhanced	References
6	H-Shaped MFC	Carbon cloth	Anode	Nitrogen doped carbon nanoparticles (NDCN)	Chemical vapor deposition method	Modified anode—maximum power densities 298.0 mWm^{-2}	Yu et al. (2015)
7	Membrane less single cell Biofuel cell (BFC)	Teflon rods electrode cavity	Glucose oxidase enzyme + nanoparticles on anode and Laccase Enzyme on cathode	Graphene oxide (GO) and Graphene–platinum hybrid nanoparticles (Gr-Pt hybrid NPs)	Fabrication of composites was done in laboratory	Power and current densities as 2.40 $\mu W\ cm^{-2}$ and 211.90 $\mu A\ cm^{-2}$ for GO based BFC and 4.88 $\mu W\ cm^{-2}$ and 246.82 $\mu A\ cm^{-2}$, for Gr-Pt hybrid NPs based BFC	Tepeli and Anik (2015)

(continued)

Table 1 (continued)

Sr. no.	MFC design	Electrode material	Modified electrode	Nanomaterial used	Synthesis process	Power enhanced	References
8	Single air-cathode MFC	Carbon cloth (CC), Carbon paper (CP) Graphite (G) and Activated carbon (AC)	Anode	Nanoflakes of cobalt sheathed with cobalt oxide	Electrodeposition technique	Power generation significantly increased from 56.3, 78.4, 173.3, and 337 mWm^{-2} to 133.4,159.2, 473.1 and 576.3 mWm^{-2} by 103, 137, 173 and 71% for the CC, CP, G and AC electrodes, respectively	Mohamed et al. (2017)
9	Single chamber membrane less air-cathode MFC (SCMFC)	The graphite felt (GF)	Anode	Modified with 0.008 g/cc polypyrrole nanoparticles (Ppy-NPs) and 0.024 g/cc poly-thiophene nanoparticles (PTh-NPs)	Conventional dip-dry method	A maximum power density (1.22 W/m^2) was obtained for Ppy-NP modified GF than PTh-NP modified GF (0.8 W/m^2)	Sumisha and Haribabu (2018)
10	Single chambered MFC	Cell-aginate-graphite (CAG)	Anode	Cell suspension mixed with graphite powder and sodium alginate	Immobilization technique	Immobilization was achieved	Wahab et al. (2018)

(continued)

Table 1 (continued)

Sr. no.	MFC design	Electrode material	Modified electrode	Nanomaterial used	Synthesis process	Power enhanced	References
11	Single chambered MFC	Carbon paper	Anode	Iron chloride (CP-Fe) or Cobalt chloride (CP-Co)	Electrodeposition technique	Pure culture Pristine CP 57.6 mW/m^2 CP-Fe 87.2 CP-Co 138.4 Mixed culture Pristine CP 78.5 mW/m^2 CP-Fe 117.8 CP-Co 165.6	Mohamed et al. (2018a, b)
12	Single chambered MFC	Carbon felt (CF), Carbon cloth (CC), and Graphite (G)	Anode	Fe/Fe_2O_3 nanoparticle	Electrodeposition technique	Power generated in mW/m^2 Carbon Felt 200 Modified 970 Graphite 156 Modified 360 Carbon Cloth 74 Modified 200	Mohamed et al. (2018a, b)
13	Membrane-less vertical MFC, air purging cathodic chamber placed on the top	Stainless steel (SS) type 316 wire mesh	Both anode and cathode	Polypyrrole (PPy) and MnO_2 catalyst	Electrodeposition technique	Power density achieved 440 mW/m^{-2}	Phonsa et al. (2018)

(continued)

Table 1 (continued)

Sr. no.	MFC design	Electrode material	Modified electrode	Nanomaterial used	Synthesis process	Power enhanced	References
14	Dual-chamber MFC	Carbon cloth	Anode	Palladium nanoparticles (PdNPs)	*S. oneidensis* MR-1 was used as the bacteria to form PdNPs	The Pd1-MFC (1 mg Pd cm^{-2} anode) and Pd1-MFC (2 mg Pd cm^{-2} anode) generated a maximum power density of 499 ± 11 mWm^{-2} and 447 ± 15 mWm^{-2}, respectively	Quan et al. (2018)
15	Dual-chamber MFC	Carbon paper	Anode	Magnetic nanoparticle (MNP)	Chemically synthesized	Maximum power density of modified anode 4.9 ± 0.5 Wm^{-3}	Sarma et al. (2018)
16	H-shaped MFC	Stainless steel (SS) wire disk	Both anode and cathode	Carbon nanoparticles (CNPs) derived from candle soot	Simple deposition in laboratory	Maximum power density of modified anode 1650 ± 50 mW/m^2	Singh et al. (2018)
17	Dual-chamber MFC	Carbon cloth	Anode	Biogenic gold nanoparticles (BioAu) and nanohybrids of multi-walled carbon nanotubes blended with BioAu (BioAu/MWCNT)	*S. oneidensis* MR-1 was used as the bacteria to form Biogenic gold nanoparticles (BioAu)	Maximum power density of BioAu/MWCNT 178.34 ± 4.79 mW/m^2	Wu et al. (2018)

(continued)

Table 1 (continued)

Sr. no.	MFC design	Electrode material	Modified electrode	Nanomaterial used	Synthesis process	Power enhanced	References
18	Dual-chamber MFC	Carbon cloth	Anode	MnO_2, Pd, and Fe_3O_4 nanoparticles	Fe_3O_4 and MnO_2 were prepared chemically. Pd nanoparticles were prepared using *Shewanella oneidensis* MR-1 as the reducing bacteria	Maximum power density of Pd, MnO_2 and Fe_3O_4 824 ± 36, 782 ± 37 and 728 ± 33 mWm^{-2} respectively	Xu et al. (2018)
19	Air-cathode cylindrical MFCs	Waste cotton textiles	Anode	Molybdenum carbide nanoparticles	Chemical and dip coating technique	power density of 1.12 W/m^2	Zeng et al. (2018a, b)
20	Single-chamber MFC	Carbon Felt	Anode	polydopamine-modified Molybdenum carbide Mo_2C/MoO_2 nanoparticles (HD-Mo_2C/MoO_2)	Carbon thermal reduction	Maximum power density of HD-Mo_2C/MoO_2 1.64 ± 0.09 W/m^2	Zeng et al. (2018a, b)
21	Dual-chamber MFC	Graphene	Anode	Molybdenum carbide hybridized graphene nanocomposite	Facile soft template-assisted assembly and calcination procedure	Maximum power density of modified anode 1697 mWm^{-2}	Zou et al. (2019)
22	Single chamber, cubic-shaped MFC	Carbon fibers brush	Anode	Vertical carbon nanotubes/polypyrrole composites	Carbon nanotubes are vertically grown on the carbon fibers by the chemical vapor deposition method	Maximum power density of modified anode 876.62 mWm^{-2}	Zhao et al. (2019)

(continued)

Table 1 (continued)

Sr. no.	MFC design	Electrode material	Modified electrode	Nanomaterial used	Synthesis process	Power enhanced	References
23	Dual-chamber MFC	Carbon paper	Anode	Copper doped Iron oxide nanoparticles (Cu-doped FeO)	Nanopartcles synthesized using phyto-compounds of *A.blitum* plant. Coated by simple brush coating method	Maximum power density of coated anode 161.5 mW/m^2	Sekar et al. (2019)
24	Dual-chamber MFC	Carbon paper	Anode	Iron doped Zinc oxide (Fe-ZnO) nanoparticles	Nanopartcles synthesized using *A. Indica* leaf extract. Coated by simple brush coating method	Maximum power density of coated anode 134.7 mW/m^2	Muthukumar et al. (2019)

of nanoparticles to be applicable in MFC. These metals are chosen due to the ability of these metal oxides to accept electrons.

The metal oxide nanomaterials are generally mixed with polymer-like polytetrafluoroethylene (PTFE), (Rajesh et al. 2018) NAFION (mostly in case of air-cathode) (Yan et al. 2013), etc. to provide a holding matrix for nanoparticles and facilitating the growth of microbe. The coating of the composite on anode is done by various methods like chemical vapor deposition, dip coating, simple brush coating, doping, etc. out of which the latest method is electrodeposition where an external voltage is applied to the solution which affects the polarity of the desired electrode and leads to the deposition of oxide on the electrode.

The synthesis of nanoparticles is done chemically under high-temperature conditions. Few scientists are also exploring the green synthesis pathway of nanoparticles where the microorganism, *S. oneidensis* MR-1 is used as reducing bacteria which can synthesis the nanoparticles of palladium Pd by reducing Pd^{2+} to Pd^{0} on its cell walls and in its periplasmic spaces (Quan et al. 2018; Wu et al. 2018). The plant extract of *A.blitum* (Sekar et al. 2019) and *A. Indica* (Muthukumar et al. 2019) are also been used as reducing agents of the synthesis of nanoparticles. As depicted in Table 1 all the anode materials from graphite to carbon felt support the coating of nanoparticles. The table also summarizes that use of nanoparticles is not subjected to any specific design of MFC; it is used in both dual-chambered as well as single-chambered MFC design.

The primitive goal of power enhancement is achieved with the coating of nanoparticles but the second parameter of wastewater treatment is also not a neglected aspect. The researchers have achieved treatment of pharmaceutical, (Xu et al. 2018) dairy (Sekar et al. 2019) as well as domestic wastewater (Mohamed et al. 2018a, b) using these nanoparticles coated bioanodes. Thus, this approach is promising for both fronts.

6 Future Prospects

Most of the power enhancement has been achieved and studied in laboratory scale reactors. The research in this field has yet to be applied in field. In one such study of benthic microbial fuel cell (BMFC) coating of cerium (Ce) nanoparticles was applied which resulted in the enhancement of power density (Pushkar et al. 2018). The need to apply the nanoparticles directly in field condition may face challenges like loss of nanoparticles in the environment, durability and stability of coating, and biocompatibility of these particles. The synthesis of nanoparticles through green pathway is also under consideration. The potential of nanoparticles for the MFC reactors can fix the minimum use of materials, good growth of biofilm, and better surface area for electron reception.

7 Conclusion

The application of nanoparticles in the field of microbial fuel cell technology (MFC) is a recent approach in its preliminary phase. The application of nanoparticles on an electrode surface changes with respect to the chosen metal and microbe. Optimization of this metal-microbe combination will be a crucial aspect of this research. This sector can be divided under major areas like synthesis, deposition, its effect, and sustainability. The synthesis of metal oxide and their nanoparticles through green synthesis pathways holds its importance under both financial as well as environmental prospective. The deposition technique affects the sustainability of this dual technology. The effect of this technology needs an in-depth understanding regarding microbe-nanoparticle interactions. The laboratory-based research has opened a new avenue for the researches to club these two technologies and develop a hybrid technology which can be economically viable for field use.

References

Alharbi NS (2013) A microbial fuel cell modified with carbon nanomaterials for organic removal and denitrification. Math Probl Eng 9

Alzate-Gaviria L, García-Rodríguez O, Flota-Bañuelos M, Del Rio Jorge-Rivera F, Cámara-Chalé G, Domínguez-Maldonado J (2016) Stacked-mfc into a typical septic tank used in public housing. Biofuels 7:79–86

Arkatkar A, Sharma P, Mungray AK (2019) In: Tomar DAS, Mandaliya DVB (ed) Red biotechnology. Daya Publishing House® A Division of Astral International Pvt. Ltd, New Delhi, India, pp 1–42

Asai Y, Miyahara M, Kouzuma A, Watanabe K (2017) Comparative evaluation of wastewater-treatment microbial fuel cells in terms of organics removal, waste-sludge production, and electricity generation. Bioresour Bioprocess 4:30–30

Babauta J, Renslow R, Lewandowski Z, Beyenal H (2012) Electrochemically active biofilms: facts and fiction. A Rev Biofouling 28:789–812

Bosire EM, Blank LM, Rosenbaum MA (2016) Strain- and substrate-dependent redox mediator and electricity production by *Pseudomonas aeruginosa*. Appl Environ Microbiol 82:5026–5038

Bullen RA, Arnot TC, Lakeman JB, Walsh FC (2006) Biofuel cells and their development. Biosens Bioelectron 21:2015–2045

Cao Y, Mu H, Liu W, Zhang R, Guo J, Xian M, Liu H (2019) Electricigens in the anode of microbial fuel cells: pure cultures versus mixed communities. Microb Cell Fact 18:39

Chi M (2013) Graphite felt anode modified by electropolymerization of nano-polypyrrole to improve microbial fuel cell (MFC) production of bioelectricity. J Microb Biochem Technol 01:1–4

Choudhury P, Prasad Uday US, Bandyopadhyay TK, Ray RN, Bhunia B (2017) Performance improvement of microbial fuel cell (mfc) using suitable electrode and bioengineered organisms: A review. Bioengineered 8:471–487

Du YL, Feng YL, Teng Q, Li HR (2015) Effect of inorganic salt in the culture on microbial fuel cells performance. Int J Electrochem Sci 10:1316–1325

Franks AE, Nevin KP (2010) Microbial fuel cells, a current review. Energies 3:899–919

Gajda I, Greenman J, Melhuish C, Ieropoulos I (2015) Self-sustainable electricity production from algae grown in a microbial fuel cell system. Biomass Bioenergy 82:87–93

Ghadge AN, Sreemannarayana M, Duteanu N, Ghangrekar MM (2014) Influence of ceramic separator's characteristics on microbial fuel cell performance. Int J Electrochem Sci 4:315–326

Huang L, Tang J, Chen M, Liu X, Zhou S (2018) Two modes of riboflavin-mediated extracellular electron transfer in geobacter uraniireducens. Front Microbiol 9:2886

Ieropoulos I, Melhuish C, Greenman J, Horsfield I (2005) Ecobot-ii: AN artificial agent with a natural metabolism. Int J Adv Robot Syst 2:31

Ieropoulos IA, Ledezma P, Stinchcombe A, Papaharalabos G, Melhuish C, Greenman J (2013) Waste to real energy: the first mfc powered mobile phone. Phys Chem Chem Phys 15:15312–15316

Jiang X, Hu J, Lieber AM, Jackan CS, Biffinger JC, Fitzgerald LA, Ringeisen BR, Lieber CM (2014) Nanoparticle facilitated extracellular electron transfer in microbial fuel cells. Nano Lett 14:6737–6742

Kalathil S, Nguyen VH, Shim J-J, Khan MM, Lee J, Cho MH (2013) Enhanced performance of a microbial fuel cell using CNT/MnO_2 nanocomposite as a bioanode material. J Nanosci Nanaotechno 13:7712–7716

Liang M, Tao HC, Li SF, Li W, Zhang LJ, Ni JR (2011) Treatment of Cu^{2+} containing wastewater by microbial fuel cell with excess sludge as anodic substrate. J Environ Sci (China) 32:179–185

Logan BE (2008) Microbial fuel cells. Wiley, New Jersey

Logan BE, Hamelers B, Rozendal R, Schröder U, Keller J, Freguia S, Aelterman P, Verstraete W, Rabaey K (2006) Microbial fuel cells: methodology and technology. Environ Sci Technol 40:5181–5192

Lv Z, Xie D, Yue X, Feng C, Wei C (2012) Ruthenium oxide-coated carbon felt electrode: a highly active anode for microbial fuel cell applications. J Power Sources 210:26–31

Mathuriya AS, Jadhav DA, Ghangrekar MM (2018) Architectural adaptations of microbial fuel cells. Appl Microbiol Biotechnol 102:9419–9432

Mehdinia A, Ziaei E, Jabbari A (2014) Multi-walled carbon nanotube/SnO2 nanocomposite: a novel anode material for microbial fuel cells. Electrochim Acta 130:512–518

Mohamed HO, Abdelkareem MA, Obaid M, Chae S-H, Park M, Kim HY, Barakat NAM (2017) Cobalt oxides-sheathed cobalt nano flakes to improve surface properties of carbonaceous electrodes utilized in microbial fuel cells. Chem Eng J 326:497–506

Mohamed HO, Obaid M, Poo K-M, Ali Abdelkareem M, Talas SA, Fadali OA, Kim HY, Chae K-J (2018a) Fe/Fe_2O_3 nanoparticles as anode catalyst for exclusive power generation and degradation of organic compounds using microbial fuel cell. Chem Eng J 349:800–807

Mohamed HO, Sayed ET, Obaid M, Choi Y-J, Park S-G, Al-Qaradawi S, Chae K-J (2018b) Transition metal nanoparticles doped carbon paper as a cost-effective anode in a microbial fuel cell powered by pure and mixed biocatalyst cultures. Int J Hydrog Energy 43:21560–21571

Muthukumar H, Mohammed SN, Chandrasekaran N, Sekar AD, Pugazhendhi A, Matheswaran M (2019) Effect of iron doped zinc oxide nanoparticles coating in the anode on current generation in microbial electrochemical cells. Int J Hydrog Energy 44:2407–2416

Ogawa T, Takeuchi M, Kajikawa Y (2018) Analysis of trends and emerging technologies in water electrolysis research based on a computational method: a comparison with fuel cell research. Sustainability 10:478

Pant D, Van Bogaert G, Diels L, Vanbroekhoven K (2010) A review of the substrates used in microbial fuel cells (MFCs) for sustainable energy production. Bioresour Technol 101:1533–1543

Phonsa S, Sreearunothai P, Charojrochkul S, Sombatmankhong K (2018) Electrodeposition of mno_2 on polypyrrole-coated stainless steel to enhance electrochemical activities in microbial fuel cells. Solid State Ion 316:125–134

Pushkar P, Prakash O, Imran M, Mungray AA, Kailasa SK, Mungray AK (2018) Effect of cerium oxide nanoparticles coating on the electrodes of benthic microbial fuel cell. Sep Sci Technol 54:213–223

Qin M, He Z (2017) Resource recovery by osmotic bioelectrochemical systems towards sustainable wastewater treatment. Environ Sci Water Res Technol 3:583–592

Qin M, Ping Q, Lu Y, Abu-Reesh IM, He Z (2015) Understanding electricity generation in osmotic microbial fuel cells through integrated experimental investigation and mathematical modeling. Bioresour Technol 195:194–201

Quan X, Xu H, Sun B, Xiao Z (2018) Anode modification with palladium nanoparticles enhanced evans blue removal and power generation in microbial fuel cells. Int Biodeter Biodegr 132:94–101

Rajesh PP, Noori MT, Ghangrekar MM (2018) Graphene oxide/polytetrafluoroethylene composite anode and chaetoceros pre-treated anodic inoculum enhancing performance of microbial fuel cell. J Clean Energy Technol 6:236–241

Rikame SS, Mungray AA, Mungray AK (2018) Modification of anode electrode in microbial fuel cell for electrochemical recovery of energy and copper metal. Electrochim Acta 275:8–17

Rotaru AE, Shrestha PM, Liu F, Markovaite B, Chen S, Nevin KP, Lovley DR (2014) Direct interspecies electron transfer between geobacter metallireducens and methanosarcina barkeri. Appl Environ Microbiol 80:4599–4605

Sarma MK, Quadir MGA, Bhaduri R, Kaushik S, Goswami P (2018) Composite polymer coated magnetic nanoparticles based anode enhances dye degradation and power production in microbial fuel cells. Biosens Bioelectron 119:94–102

Schröder U (2012) Editorial: microbial fuel cells and microbial electrochemistry: into the next century! Chemsuschem 5:959–959

Sekar AD, Jayabalan T, Muthukumar H, Chandrasekaran NI, Mohamed SN, Matheswaran M (2019) Enhancing power generation and treatment of dairy waste water in microbial fuel cell using cu-doped iron oxide nanoparticles decorated anode. Energy 172:173–180

Singh S, Bairagi PK, Verma N (2018) Candle soot-derived carbon nanoparticles: an inexpensive and efficient electrode for microbial fuel cells. Electrochim Acta 264:119–127

Song T-S, Jin Y, Bao J, Kang D, Xie J (2016) Graphene/biofilm composites for enhancement of hexavalent chromium reduction and electricity production in a biocathode microbial fuel cell. J Hazard Mater 317:73–80

Sumisha A, Haribabu K (2018) Modification of graphite felt using nano polypyrrole and polythiophene for microbial fuel cell applications-a comparative study. Int J Hydrog Energy 43:3308–3316

Tepeli Y, Anik U (2015) Comparison of performances of bioanodes modified with graphene oxide and graphene–platinum hybrid nanoparticles. Electrochem Commun 57:31–34

Tharali AD, Sain N, Osborne WJ (2016) Microbial fuel cells in bioelectricity production. Front Life Sci 9:252–266

Wahab KAA, Nazri AAA, Azam AAM, Ghazali NF, Salleh EM, Mahmood NAN (2018) Development of immobilised bioanode for microbial fuel cell. Chem Eng Trans 63:607–612

Wang Y, Li B, Cui D, Xiang X, Li W (2014) Nano-molybdenum carbide/carbon nanotubes composite as bifunctional anode catalyst for high-performance escherichia coli-based microbial fuel cell. Biosens Bioelectron 51:349–355

Winfield J, Gajda I, Greenman J, Ieropoulos I (2016) A review into the use of ceramics in microbial fuel cells. Bioresour Technol 215:296–303

Wu X, Xiong X, Owens G, Brunetti G, Zhou J, Yong X, Xie X, Zhang L, Wei P, Jia H (2018) Anode modification by biogenic gold nanoparticles for the improved performance of microbial fuel cells and microbial community shift. Bioresour Technol 270:11–19

Xie X, Criddle C, Cui Y (2015) Design and fabrication of bioelectrodes for microbial bioelectrochemical systems. Energy Environ Sci 8:3418–3441

Xu H, Quan X, Xiao Z, Chen L (2018) Effect of anodes decoration with metal and metal oxides nanoparticles on pharmaceutically active compounds removal and power generation in microbial fuel cells. Chem Eng J 335:539–547

Yan ZH, Wang M, Huang BX, Liu RM, Zhao JS (2013) Graphene supported pt-co alloy nanoparticles as cathode catalyst for microbial fuel cells. Int J Electrochem Sci 8:149–158

Yu Y-Y, Guo CX, Yong Y-C, Li CM, Song H (2015) Nitrogen doped carbon nanoparticles enhanced extracellular electron transfer for high-performance microbial fuel cells anode. Chemosphere 140:26–33

Zeng L, Chen X, Li H, Xiong J, Hu M, Li X, Li W (2018a) Highly dispersed polydopamine-modified Mo_2C/MoO_2 nanoparticles as anode electrocatalyst for microbial fuel cells. Electrochim Acta 283:528–537

Zeng L, Zhao S, Zhang L, He M (2018b) A facile synthesis of molybdenum carbide nanoparticles-modified carbonized cotton textile as an anode material for high-performance microbial fuel cells. RSC Adv 8:40490–40497

Zhang Y, Min B, Huang L, Angelidaki I (2011) Electricity generation and microbial community response to substrate changes in microbial fuel cell. Bioresour Technol 102:1166–1173

Zhang C, Liang P, Yang X, Jiang Y, Bian Y, Chen C, Zhang X, Huang X (2016) Binder-free graphene and manganese oxide coated carbon felt anode for high-performance microbial fuel cell. Biosens Bioelectron 81:32–38

Zhao N, Ma Z, Song H, Xie Y, Zhang M (2019) Enhancement of bioelectricity generation by synergistic modification of vertical carbon nanotubes/polypyrrole for the carbon fibers anode in microbial fuel cell. Electrochim Acta 296:69–74

Zhou Y, Zhao S, Yin L, Zhang J, Bao Y, Shi H (2018) Development of a novel membrane-less microbial fuel cell (ml-mfc) with a sandwiched nitrifying chamber for efficient wastewater treatment. Electroanalysis 30:2145–2152

Zhu F, Wang W, Zhang X, Tao G (2011) Electricity generation in a membrane-less microbial fuel cell with down-flow feeding onto the cathode. Bioresour Technol 102:7324–7328

Zou L, Huang Y, Wu X, Long Z-E (2019) Synergistically promoting microbial biofilm growth and interfacial bioelectrocatalysis by molybdenum carbide nanoparticles functionalized graphene anode for bioelectricity production. J Power Sources 413:174–181

A Model for Electro-osmotic Flow of Pseudoplastic Nanofluids in Presence of Peristaltic Pumping: An Application to Smart Pumping in Energy Systems

J. Prakash, M. Gnaneswara Reddy, D. Tripathi and Abhishek Kumar Tiwari

Abstract Thermal enhancement in non-Newtonian nanofluids is a challenge which can be observed in energy systems. Recent developments in biomimetics identified that deformable conduit structure is beneficial for sustainable energy systems. Such recent developments in energy systems motivated the present study to discuss the mathematical modeling of electro-osmotic flow of non-Newtonian nanofluids through a microchannel in the presence of Joule heating and peristalsis. The model presented in this chapter assumes that the movement of the fluids can be controlled by electro-osmotic force generated as a result of an external electric field. A pseudoplastic fluid model is assumed as appropriate to compute the non-Newtonian effects. Nonlinear formulation present in the model is simplified with the help of lubrication theory and Hückel–Debye approximations. Modeled governing equations are solved to determine the flow, temperature, and electric potential fields. The flow behavior and thermal characteristics are simulated as a function of physical parameters. The results are represented graphically and correlated using physical phenomena. The significant features of pumping and trapping are also briefly addressed. The formulation of the model presented in this chapter can be useful in the experimental designs of smart nano-electro-peristaltic pumps, in addition, it can also be extended to nanotechnological applications, smart drug delivery systems, and various transport phenomena of environmental systems.

Keywords Non-Newtonian model · Joule heating · Peristaltic pumping · Electroosmosis · Zeta potential · Energy systems

J. Prakash
Department of Mathematics, Avvaiyar Government College for Women, Karaikal 609602, Puducherry-U.T., India

M. G. Reddy
Department of Mathematics, Acharya Nagarjuna University Campus, Ongole 523001, India

D. Tripathi (✉)
Department of Mathematics, National Institute of Technology, Uttarakhand 246174, India
e-mail: dtripathi@nituk.ac.in

A. K. Tiwari
Motilal Nehru National Institute of Technology Allahabad, Prayagraj 211004, Uttar Pradesh, India

L. Ledwani and J. S. Sangwai (eds.), *Nanotechnology for Energy and Environmental Engineering*, Green Energy and Technology,
https://doi.org/10.1007/978-3-030-33774-2_8

Nomenclature

$(a_1,\ a_2)$	dimensional (wave) amplitude of the left and right walls
$(a,\ b)$	dimensionless amplitude of the left and right walls
$(Bh_1,\ Bh_2)$	heat transfer Biot numbers at left and right walls
Br	local nanoparticle Grashof number
c	wave speed
c'	volumetric volume expansion coefficient
C	nanoparticle concentration,
C_0, C_1	nanoparticle concentration at the left and right walls, respectively
D_B	Brownian diffusion coefficient and
D_T	themophoretic diffusion coefficient
d	dimensionless width of the channel
d/dt	material time derivative,
$(d_1 + d_2)$	dimensional width of the left and right walls
e	fundamental charge
E_x	applied electrical field
F	dimensionless mean flows
f	body force
Gr	local temperature Grashof number
H_1, H_2	left and right wall boundaries of the micro-asymmetric channel
I	identity tensor
k_B	Boltzmann constant
k'	mean absorption coefficient
Nt	thermophoresis parameter
Nb	Brownian motion parameter
n_0	bulk concentration (number density)
Pr	Prandtl number
$(p,\ P)$	pressures in wave and fixed frame of references
Q_0	heat source/sink parameter
Q	dimensional volume flow rate in laboratory frame
R	Reynolds number
Rn	thermal radiation
S	extra stress tensor
S^{∇}	upper-convected derivative
t	dimensional time
T_0, T_1	temperature at the left and right walls, respectively
T	nanoparticle temperature,
T_n	absolute temperature
T_m	fluid mean temperature
$(U,\ V)$	velocity components in the wave frame $(X,\ Y)$
$(u,\ v)$	velocity components in the (x, y)-directions

Uhs	Helmholtz–Smoluchowski velocity
V	velocity vector
z	valence of ions

Greek Symbols

ϕ	phase difference
κ	thermal conductivity
Υ	Cauchy stress tensor
μ	dynamic viscosity
λ_1 and μ_1	relaxation times
$\bar{\Phi}$	electric potential
ε	dielectric permittivity of the medium
κ	Debye length
ρ_f	density of the nanofluid
g	acceleration due to gravity
β_t	thermal expansion coefficient
ρ_p	density of the nanoparticle
σ'	Stefan–Boltzmann constant
δ	wave number
β	Joule heating parameter
ξ	pseuoplastic fluid parameter
Θ	dimensionless time average flux
σ	dimensionless rescaled nanoparticle volume fraction
θ	dimensionless temperature
ψ	stream function

Recent trends in engineering design strongly gravitated toward energy-inspired designs. Energy systems have perfected many intricate mechanisms which can be applied to upgrade conventional engineering systems to a new level of performance and endurance. Nanofluids have been proven useful in this context.

1 Nanofluid Mechanics in Energy Management

Nanofluid mechanics is one of the modern mechanics of the energy systems where the thermal conductivity of the base fluids can easily be enhanced by using the nanoparticles. Nanofluids are the moderately new category of fluids in which nano-sized particles (1–100 nm) are suspended in the base fluid (like water, oil, ethylene-glycol, etc.). These particles can be found in the metals such as (Al, Cu), oxides (Al_2O_2),

carbides (SiC), nitrides (SiN), or nonmetals (graphite, carbon nanotubes, nanofibers, nanosheets, droplets). The resulting suspension achieves improved thermal conductivity and modified viscosity properties. The surface area per unit volume of nanoparticles is much larger (millions of times) than that of conventional microparticles. The number of surface atoms per unit of interior atoms of nanoparticles is very large. These characteristics can be exploited in many complex systems including medical engineering, energy engineering, and materials processing. Nanofluids have infiltrated into many areas of energy and also biomedical technology as they may be manipulated to yield more biologically friendly, sustainable, and durable products. The word "nanofluid" was given by Choi and Eastman (1995). He analyzed that nanofluids reduced pumping power as compared to pure liquid to reach equivalent heat transfer amplification and particle clogging as compared to conventional slurries, consequently promoting system miniaturization. Khanafer and Vafai (2018) presented a lucid summary of solar nanofluid device applications, emphasizing that efficiency of any solar thermal system is dictated by thermophysical properties (viscosity, density, thermal conductivity, and specific heat) of the operating fluid and the geometric characteristics. Critical features of nanofluids for improving solar collector and pump efficiency are types of the nanoparticles (metallic-based work best e.g., copper, silver, and titanium), nanoparticles volumetric concentration in the base fluid, and the nanofluid viscosity and conductivity. The inclusion of copper nanoparticles considerably elevates the heat gain capacity of a solar pump. Carbon nanotube nanofluids not only improve the efficiency of solar collectors but have the added advantage of decreasing CO_2 emissions. It should also be noted that there are a diverse range of mathematical models available for simulating nanofluid transport phenomena which have also been addressed in Khanafer and Vafai (2018). These include two-component model (Buongiorno 2006) which emphasizes thermophoretic forces and Brownian motion dynamics as the key contributors to thermal conductivity enhancement. The other popular model is of Tiwari and Das (2007) which simulates the nanoscale effect based on volume fraction (concentration) of the nanoparticles.

A smart pumping technology is being used in transporting the fluids in small and large scale. This technology is very popular nowadays for pumping the fluids with low energy loss and without any contamination. This mechanism was observed in natural physiological systems and it is largely implemented in the industry for pumping process. One of the applications of nanofluid mechanics is also in drug delivery system (Tripathi and Bég 2014). The thermal radiation effects on peristaltic pumping of nanofluids are also examined by Kothandapani and Prakash (2015a, b). They have discussed the applicability of their models to solar energy systems. In transport phenomena, thermal and velocity slip effects play an important role and considering the importance of slip effects. This model is also reported by Akbar et al. (2016). Another model for the drug delivery system to see the effects of thermophoresis and Brownian motion effects is developed by Ghasemi (2017). Most recently, some novel mathematical models (Mekheimer et al. 2018; Mosayebidorcheh and Hatami 2018a, b; Prakash et al. 2019) for peristaltic pumping of nanofluids evolved to analyze the

flow characteristics and thermal characteristics under the influences of various flow geometries, various fluid models, and various physical constraints.

2 Magnetohydrodynamic (MHD) Regulation of Fluid Motion

Magnetohydrodynamics (MHD) is a well-known mechanism to explore the effect of magnetic field on fluid flow behavior. MHD analysis explained that fluid velocity reduces with an increase in the magnitude of magnetic field (Hartmann number). Similarly, electrohydrodynamics (EHD) is another mechanism which explains that how external electric field controls the fluid velocity and the direction of fluid flow. Electroosmosis (electrohydrodynamics) which is an intricate phenomena of EHD is defined as the bulk displacement of the liquid analogues to a stationary surface contingent on the applied external electric field. This mechanism has wide range of applications in design and development of microfluidics devices with application to energy systems and biomedical technologies. The electroosmosis phenomenon as a charged induced flow, experimentally studied in porous clay was investigated by Reuss (1809). Later on, a mathematical theory for the electro-osmotic flow was presented by Wiedemann (1852). An experimental study on electro-osmotic flow in rectangular microchannel is reported by Sadr et al. (2004). It is concluded that the electroosmosis mechanism has a curial role in the regulation of fluid flow in the microfluidic channel. The influence of pressure on the axial velocity over the electro-osmotic flows has theoretically been analyzed by Santiago (2001). The electrical double layer effects on liquid flow via a rectangular microchannel have been studied by Yang and Li (1998). The rheological parameter effects on electrokinetic flow are computed by Das and Chakraborty (2006) in the presence of capillary motion through rectangular microchannel. Recently, some mathematical models (Bandyopadhyay and Chakraborty 2018; Ganguly et al. 2015; Shehzad et al. 2018; Zhao and Jian 2018; Zhao et al. 2016, 2019) on electro-osmotic flow of nanofluids in microchannel and capillary have been presented to investigate how electric field control the pressure-driven flow and heat transfer phenomenon.

3 Models of Electroosmosis-Driven Peristaltic Fluid Motion

The presence of electro-osmotic mechanism with peristaltic pumping develops a new domain in the area of nanofluid dynamics. The combined mechanism may be useful for bioinspired-micro-peristaltic pumps. Chakraborty (2006) established a mathematical model on peristaltic pumping in presence of thin electric double layer (EDL) where it is concluded that the combination of electrokinetic body force and pressure-driven force due to peristaltic pumping can significantly improve the time-averaged

flow rate. Thereafter, Bandopadhyay et al. (2016) improved the Chakraborty's model for thick EDL and unsteady peristaltic flow in the presence of electroosmosis. The authors explained the effects of EDL thickness and Helmholtz–Smoluchowski (HS) velocity on pumping characteristics and trapping phenomenon. The pumping mechanism can be smoothly controlled using the electroosmosis mechanism. In this direction, many more mathematical models (Goswami et al. 2016; Shit et al. 2016; Tripathi et al. 2017a, b) have been reported to investigate the effects of non-Newtonian parameters on the electroosmotically induced peristaltic pumping through capillary/microchannel. Furthermore, the effect of heat transfer analysis to understand the applications in bioenergy systems and bionanofluid dynamics, some mathematical models (Bhatti et al. 2017; Guo and Qi 2017; Prakash et al. 2018a, b; Ranjit and Shit 2017; Tripathi et al. 2018) are added in literature to analyze the thermal radiation effects, Joule heating, buoyancy effects, and entropy generation on peristaltic pumping in presence of electric field.

A depth literature review on the electroosmosis modulated peristaltic pumping enabled us to identify that there is hardly any modeling method on the pseudoplastic nanofluids flow in presence of electroosmosis. Motivated from the huge applications of nanofluid dynamics with electroosmosis and peristaltic pumping mechanisms in bioenergy systems and biotechnologies, this chapter attempts to give an idea on the development of a mathematical model to investigate the effects of Joule heating parameter and EDL thickness on flow characteristics, pumping characteristics, thermal characteristics, and trapping. The flow geometry is considered as a vertical asymmetric microchannel which is assumed to be a complex flow geometry. Assumptions such as Debye–Hückel linearization, low Reynolds number, and large wavelength are considered in the model. Numerical simulation of the model is using MATHEMATICA 9 symbolic software. The numerical results are also validated with the existing analytical results. The findings of this chapter may be extended to design the bioinspired-smart micro pumps for bioheat transfer and energy transport systems. The model may also be further developed as a benchmark to work experimentally in the field of microfluidics device design and development.

4 Mathematical Formulation of the Problem

4.1 Problem Definition

A two-dimensional peristaltic motion of pseudoplastic nanofluid subject to heat flux through a microfluidic channel with thickness $(d_1 + d_2)$ is considered. The movement is caused by the flow of the sinusoidal peristaltic motion with constant speed c *along* with different amplitudes and phase of the microfluidic asymmetric channel walls. We prefer a rectangular coordinate system for the microfluidic vessel with x along the centerline in the direction of wave propagation and y is taken normal to it. The potential electric field is enforced along the microfluidic asymmetric channel, which

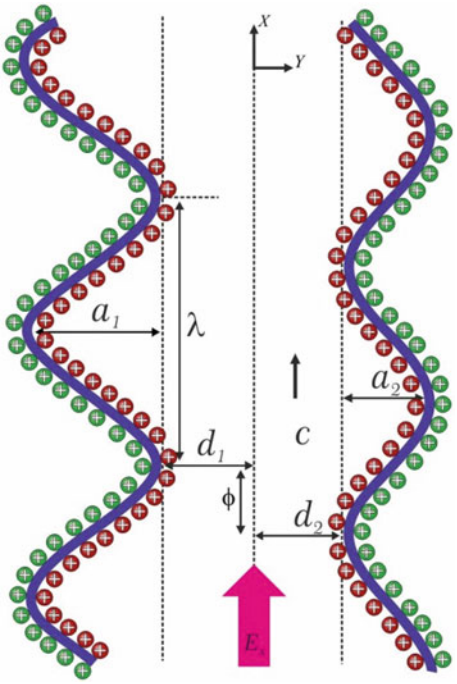

Fig. 1 The two-dimensional peristaltic motion of pseudoplastic nanofluid through a microfluidic asymmetric channel

induces the driving force for the electro-osmotic motion. The geometry of the problem is sketched in Fig. 1. The geometry of the wall surface is represented by the following equation:

$$H_2(x,t) = d_2 + a_2 \cos^2\left(\frac{\pi(x-ct)}{\lambda}\right), \tag{1a}$$

$$H_1(x,t) = -d_1 - a_1 \cos^2\left(\frac{\pi(x-ct)}{\lambda} + \phi\right). \tag{1b}$$

In the above expression $d_1 + d_2, a_1, a_2, t, \phi$ are the width of the vessel, wave amplitude of left and right walls, respectively, time and phase difference.

4.2 Governing Equations

The continuity, momentum, temperature, nanoparticle volume fraction, and magnetic force function for an incompressible pseudoplastic nanofluid are given as follows:

$$\nabla \cdot \mathrm{V} = 0\,, \tag{2}$$

$$\rho \frac{d\mathrm{V}}{dt} = div\, \Upsilon + f + \rho_e E_x, \tag{3}$$

$$(c'\rho)_f \frac{dT}{dt} = \alpha_m \nabla^2 T + (c'\rho)_p \left[D_B \nabla C \cdot \nabla T + \frac{D_T}{T_m} \nabla T \cdot \nabla T \right] - \nabla q_r, \tag{4}$$

$$\frac{dC}{dt'} = D_B \nabla^2 C + \frac{D_T}{T_m} \nabla^2 T, \tag{5}$$

in which V is the velocity vector, d/dt represents the material time derivative, f is the body force, c' is the volumetric volume expansion coefficient, E_x is the applied electrical field, α_m is the thermal conductivity, ρ_p is the density of the nanoparticle, p is the pressure, T_m is the fluid mean temperature, T is the nanoparticle temperature, C is the nanoparticle concentration, D_B is the Brownian diffusion coefficient and D_T is the themophoretic diffusion coefficient.

The expression of Cauchy stress tensor Υ is adapted from (Noreen et al. 2012)

$$\Upsilon = -pI + S, \tag{6}$$

$$\mathrm{S} + \lambda_1 \mathrm{S}^{\nabla} + \frac{1}{2}(\lambda_1 - \mu_1)(\mathrm{A_1 S} + \mathrm{S A_1}) = \mu \mathrm{A_1}, \tag{7}$$

$$\mathrm{S}^{\nabla} = \frac{d\mathrm{S}}{dt} - \mathrm{S L}^T - \mathrm{L\, S}, \tag{8}$$

$$\mathrm{L} = grad\ \mathrm{V}, \tag{9}$$

$$\rho_e = -\varepsilon\, \nabla^2 \bar{\Phi} \tag{10}$$

in which p, I, S, S^{∇}, μ, λ_1, μ_1,$\bar{\Phi}$, ε, respectively, denote the pressure, the identity tensor, the extra stress tensor, the upper-convected derivative, the dynamic viscosity, the relaxation times, the electric potential, and dielectric permittivity of the medium.

The electric charge density follows the Boltzmann distribution which is yielded by

$$\rho_e = -2n_0 ez \sinh\left(\frac{ez\bar{\Phi}}{k_B T_n}\right), \tag{11}$$

where n_0, e, z, k_B, and T_n represent the bulk concentration (number density), elementary charge valence, valence of ions, Boltzmann constant, and absolute temperature. Using Debye–Hückel linearization, the Poisson–Boltzmann equation can reduce to

$$\nabla^2 \bar{\Phi} = \kappa^2 \bar{\Phi}, \tag{12}$$

where $\kappa = d_2 ez\sqrt{\frac{2n_0}{\varepsilon k_B T}}$ represents the ratio of the characteristic transverse length to the Debye length; this indicates the penetration of the zeta potential at the surface into the bulk fluid.

For the problem under consideration, the velocity is defined as

$$\mathrm{V} = [u(x, y, t),\ v(x, y, t), 0] \tag{13}$$

To simplify the analysis, we lead the following changes in the position between fixed and wave frames

$$X = x - ct,\ Y = y,\ P(X, Y) = p(x, y, t),\ U = u - c \text{ and } V = v. \tag{14}$$

In the presence of electric field, thermal radiation and Joule heating, the equation for the mass and momentum conservation for pseudoplastic nanofluid Eqs. (2)–(10) are written in terms of the leading transformation yield as follows:

$$\frac{\partial U}{\partial X} + \frac{\partial V}{\partial Y} = 0, \tag{15}$$

$$\rho_f\left(U\frac{\partial U}{\partial X} + V\frac{\partial V}{\partial Y}\right) = -\frac{\partial P}{\partial X} + \frac{\partial S_{XX}}{\partial X} + \frac{\partial S_{XY}}{\partial Y} + \rho_e E_x + (1 - C_0)\rho_f g\beta_t(T - T_0) - \left(\rho_p - \rho_f\right)g(C - C_0), \tag{16}$$

$$\rho_f\left(U\frac{\partial V}{\partial X} + V\frac{\partial V}{\partial Y}\right) = -\frac{\partial P}{\partial Y} + \frac{\partial S_{XY}}{\partial X} + \frac{\partial S_{YY}}{\partial Y}, \tag{17}$$

$$\left(\rho c'\right)_f\left(U\frac{\partial T}{\partial X} + V\frac{\partial T}{\partial Y}\right) = \alpha_m\left[\frac{\partial^2 T}{\partial X^2} + \frac{\partial^2 T}{\partial Y^2}\right] - \frac{\partial q_r}{\partial Y} + \left(\rho c'\right)_p D_B\left[\frac{\partial C}{\partial X}\frac{\partial T}{\partial X} + \frac{\partial C}{\partial Y}\frac{\partial T}{\partial Y}\right] + \frac{\left(\rho c'\right)_p D_T}{T_m}\left[\left(\frac{\partial T}{\partial X}\right)^2 + \left(\frac{\partial T}{\partial Y}\right)^2\right] + Q_0(T - T_0), \tag{18}$$

$$U\frac{\partial C}{\partial X} + V\frac{\partial C}{\partial Y} = D_B\left[\frac{\partial^2 C}{\partial X^2} + \frac{\partial^2 C}{\partial Y^2}\right] + \frac{D_T}{T_m}\left[\frac{\partial^2 T}{\partial X^2} + \frac{\partial^2 T}{\partial Y^2}\right], \tag{19}$$

in which

$$2\mu\frac{\partial U}{\partial X} = S_{XX} + \lambda_1\left[U\frac{\partial S_{XX}}{\partial X} + V\frac{\partial S_{XX}}{\partial Y} - 2\frac{\partial U}{\partial X}S_{XX} - 2\frac{\partial U}{\partial Y}S_{XY}\right] + \frac{1}{2}(\lambda_1 - \mu_1)\left[4S_{XX}\frac{\partial U}{\partial X} + 2S_{XY}\left(\frac{\partial U}{\partial Y} + \frac{\partial V}{\partial X}\right)\right],$$

$$2\mu\frac{\partial V}{\partial Y} = S_{YY} + \lambda_1\left[U\frac{\partial S_{YY}}{\partial X} + v\frac{\partial S_{YY}}{\partial Y} - 2\frac{\partial V}{\partial Y}S_{YY} - 2\frac{\partial V}{\partial X}S_{XY}\right] + \frac{1}{2}(\lambda_1 - \mu_1)\left[4S_{YY}\frac{\partial V}{\partial Y} + 2S_{XY}\left(\frac{\partial U}{\partial Y} + \frac{\partial V}{\partial X}\right)\right],$$

$$\mu\left[\frac{\partial U}{\partial Y}+\frac{\partial V}{\partial X}\right]=S_{XY}+\lambda_1\left[U\frac{\partial S_{XY}}{\partial X}+V\frac{\partial S_{XY}}{\partial Y}+\frac{\partial V}{\partial X}S_{XX}-\frac{\partial U}{\partial Y}S_{YY}\right]$$
$$+\frac{1}{2}(\lambda_1-\mu_1)\left[(S_{XX}+S_{YY})\left(\frac{\partial U}{\partial Y}+\frac{\partial V}{\partial X}\right)\right],$$

where U and V are velocity components along X- and Y-directions, respectively, ρ_f is the density of the nanofluid, P is the pressure of the nanofluid, g is acceleration due to gravity, β_t is the thermal expansion coefficient and Q_0 is the heat source/sink parameter. The radiative heat flux in the X-direction is considered negligible as compared to Y-direction. Hence, by using Rossel and approximation for thermal radiation, the radiative heat flux q_r is given as follows:

$$q_r=-\frac{4\sigma'}{3k'}\frac{\partial T^4}{\partial Y}, \tag{20}$$

where σ' and k' are the Stefan–Boltzmann constant and the mean absorption coefficient, respectively. We assume that the temperature difference within the flow is sufficiently small such that the term T^4 in a Taylor series about a free stream temperature T_0 and neglecting higher order terms in the first order in $(T-T_0)$, we obtain

$$q_r=-\frac{16\sigma' T_0^3}{3k'}\frac{\partial T}{\partial Y}, \tag{21}$$

4.3 Nondimensional Analysis

The dimensionless variables are introduced as

$$\bar{x}=\frac{X}{\lambda},\bar{y}=\frac{Y}{d_2},\bar{u}=\frac{U}{c},\bar{v}=\frac{V}{c},h_1=\frac{H_1}{d_2},h_2=\frac{H_2}{d_2},\bar{p}=\frac{d_2^2P}{c\lambda\mu},\theta=\frac{T-T_0}{T_1-T_0},\xi\left(=\mu_1^2-\lambda_1^2\right),$$
$$\sigma=\frac{C-C_0}{C_1-C_0},a=\frac{a_1}{d_2},b=\frac{b_1}{d_2},d=\frac{d_1}{d_2},\delta=\frac{d_2}{\lambda},R=\frac{\rho_f c d_2}{\mu},\beta=\frac{\bar{Q}_0 d_2^2}{(T_1-T_0)\mu c_p},$$
$$Gr=\frac{(1-C_0)\rho_f^2 g\beta_t d_2^3(T_1-T_0)}{\mu^2},Br=\frac{(\rho_f-\rho_p)\rho_f g d_2^3(C_1-C_0)}{\mu^2},\mathrm{Pr}=\frac{\mu c'_f}{\alpha_m},\Phi=\frac{\bar{\Phi}}{\hat{\xi}},$$
$$Rn=\frac{16\sigma' T_0^3}{3k'\mu c'_f},Nb=\frac{(\rho c')_f D_B(C_1-C_0)}{\alpha_m},Nt=\frac{(\rho c')_p D_T(T_1-T_0)}{T_m\alpha_m},Uhs=-\frac{E_x\varepsilon\hat{\xi}}{\mu c}. \tag{22}$$

The continuity Eq. (15) is identically satisfied by using the stream function $u=\frac{\partial\psi}{\partial y}$, $v=-\delta\frac{\partial\psi}{\partial x}$ (dropping the bars) and then Eqs. (15–19) yield:

$$R\delta\left[\frac{\partial\psi}{\partial y}\frac{\partial^2\psi}{\partial x\partial y}-\frac{\partial\psi}{\partial x}\frac{\partial^2\psi}{\partial y^2}\right]=-\frac{\partial p}{\partial x}+\delta\frac{\partial S_{xx}}{\partial x}+\frac{\partial S_{xy}}{\partial y}+Uhs\left(\delta^2\frac{\partial^2\Phi}{\partial x^2}+\frac{\partial^2\Phi}{\partial y^2}\right)+Gr\theta+Br\sigma, \tag{23}$$

$$-R\delta^3\left[\frac{\partial^2\psi}{\partial t\partial x}+\frac{\partial\psi}{\partial y}\frac{\partial^2\psi}{\partial x^2}-\frac{\partial\psi}{\partial x}\frac{\partial^2\psi}{\partial y\partial x}\right]=-\frac{\partial p}{\partial y}+\delta^2\frac{\partial S_{xy}}{\partial x}+\delta\frac{\partial S_{yy}}{\partial y}, \tag{24}$$

$$\begin{aligned}R\delta\left[\frac{\partial\psi}{\partial y}\frac{\partial\theta}{\partial x}-\frac{\partial\psi}{\partial x}\frac{\partial\theta}{\partial y}\right]&=\frac{1}{\mathrm{Pr}}\left[\delta^2\frac{\partial^2\theta}{\partial x^2}+\frac{\partial^2\theta}{\partial y^2}\right]+Rn\frac{\partial^2\theta}{\partial y^2}\\&\quad+Nb\left[\delta^2\frac{\partial\sigma}{\partial x}\frac{\partial\theta}{\partial x}+\frac{\partial\sigma}{\partial y}\frac{\partial\theta}{\partial y}\right]\\&\quad+Nt\left[\delta^2\left(\frac{\partial\theta}{\partial x}\right)^2+\left(\frac{\partial\theta}{\partial y}\right)^2\right]+\beta\theta,\end{aligned} \tag{25}$$

$$R\,\delta\left[\frac{\partial\psi}{\partial y}\frac{\partial\sigma}{\partial x}-\frac{\partial\psi}{\partial x}\frac{\partial\sigma}{\partial y}\right]=\left[\delta^2\frac{\partial^2\sigma}{\partial x^2}+\frac{\partial^2\sigma}{\partial y^2}\right]+\frac{Nt}{Nb}\left[\delta^2\frac{\partial^2\theta}{\partial x^2}+\frac{\partial^2\theta}{\partial y^2}\right], \tag{26}$$

in which

$$\begin{aligned}2\delta\frac{\partial^2\psi}{\partial x\partial y}&=S_{xx}+\lambda_1\left[\delta\frac{\partial\psi}{\partial y}\frac{\partial S_{xx}}{\partial x}+\delta\frac{\partial\psi}{\partial x}\frac{\partial S_{xx}}{\partial y}-2\delta\frac{\partial^2\psi}{\partial x\partial y}S_{xx}-2\frac{\partial^2\psi}{\partial y^2}S_{xy}\right]\\&\quad+\frac{1}{2}(\lambda_1-\mu_1)\left[4\delta S_{xx}\frac{\partial^2\psi}{\partial x\partial y}+2S_{xy}\left(\frac{\partial^2\psi}{\partial y^2}-\delta^2\frac{\partial^2\psi}{\partial x^2}\right)\right],\end{aligned} \tag{27}$$

$$\begin{aligned}-2\delta\frac{\partial^2\psi}{\partial y\partial x}&=S_{yy}+\lambda_1\delta\left[\frac{\partial\psi}{\partial y}\frac{\partial S_{yy}}{\partial x}-\frac{\partial\psi}{\partial x}\frac{\partial S_{yy}}{\partial y}+2\frac{\partial^2\psi}{\partial y\partial x}S_{yy}+2\delta\frac{\partial^2\psi}{\partial x^2}S_{xy}\right]\\&\quad+\frac{1}{2}(\lambda_1-\mu_1)\left[-4\delta S_{yy}\frac{\partial^2\psi}{\partial y\partial x}+2S_{xy}\left(\frac{\partial^2\psi}{\partial y^2}-\delta^2\frac{\partial^2\psi}{\partial x^2}\right)\right],\end{aligned} \tag{28}$$

$$\begin{aligned}\frac{\partial^2\psi}{\partial y^2}-\delta^2\frac{\partial^2\psi}{\partial x^2}&=S_{xy}+\lambda_1\left[\delta\frac{\partial\psi}{\partial y}\frac{\partial S_{xy}}{\partial x}-\delta\frac{\partial\psi}{\partial x}\frac{\partial S_{xy}}{\partial y}+\delta^2\frac{\partial^2\psi}{\partial x^2}S_{xx}-\frac{\partial^2\psi}{\partial y^2}S_{yy}\right]\\&\quad+\frac{1}{2}(\lambda_1-\mu_1)\left(S_{xx}+S_{yy}\right)\left(\frac{\partial^2\psi}{\partial y^2}-\delta^2\frac{\partial^2\psi}{\partial x^2}\right),\end{aligned} \tag{29}$$

where δ, R, Uhs, Gr, Br, Pr, Rn, Nt, Nb, β, and ξ are the wave number, Reynolds number, Helmholtz–Smoluchowski velocity, local temperature Grashof number, local nanoparticle Grashof number, Prandtl number, thermal radiation, thermophoresis parameter, Brownian motion parameter, Joule heating parameter, pseuoplastic fluid parameter, and continuity equation is automatically satisfied.

Under the assumptions of long wavelength and low-Reynolds number and neglecting the terms of order δ and higher, Eqs. (23–29) become

$$\frac{\partial p}{\partial x}=\frac{\partial S_{xy}}{\partial y}+Uhs\frac{\partial^2\Phi}{\partial y^2}+Gr\theta+Br\sigma, \tag{30}$$

$$\frac{\partial p}{\partial y} = 0\,, \tag{31}$$

$$\left(\frac{1}{\mathrm{Pr}} + Rn\right)\frac{\partial^2\theta}{\partial y^2} + Nb\frac{\partial\sigma}{\partial y}\frac{\partial\theta}{\partial y} + Nt\left(\frac{\partial\theta}{\partial y}\right)^2 + \beta\theta = 0, \tag{32}$$

$$\frac{\partial^2\sigma}{\partial y^2} + \frac{Nt}{Nb}\frac{\partial^2\theta}{\partial y^2} = 0, \tag{33}$$

in which

$$S_{xx} = (\lambda_1 + \mu_1)\frac{\partial^2\psi}{\partial y^2}S_{xy},\ S_{yy} = (-\lambda_1 + \mu_1)\frac{\partial^2\psi}{\partial y^2}S_{xy},$$
$$S_{xy} = \frac{\partial^2\psi}{\partial y^2}\left(1 + \xi\left(\frac{\partial^2\psi}{\partial y^2}\right)^2\right)^{-1}, \tag{34}$$

Employing Eqs. (30) and (34), we have

$$\frac{\partial p}{\partial x} = \frac{\partial^3\psi}{\partial y^3} - \xi\frac{\partial}{\partial y}\left[\left(\frac{\partial^2\psi}{\partial y^2}\right)^3\right] + Uhs\frac{\partial^2\Phi}{\partial y^2} + Gr\theta + Br\sigma, \tag{35}$$

Equations (35) and (31) yield,

$$\frac{\partial^4\psi}{\partial y^4} - \xi\frac{\partial^2}{\partial y^2}\left[\left(\frac{\partial^2\psi}{\partial y^2}\right)^3\right] + Uhs\frac{\partial^3\Phi}{\partial y^3} + Gr\frac{\partial\theta}{\partial y} + Br\frac{\partial\sigma}{\partial y} = 0. \tag{36}$$

Employing Debye–Hückel linearization the nondimensional Poisson-Boltzmann equation can also be deduced in Eq. (13) as follows:

$$\frac{\partial^2\Phi}{\partial\eta^2} = \kappa^2\Phi. \tag{37}$$

The instantaneous volume flow rate in the fixed frame is given by

$$Q(X,t) = \int_{H_1(X,t)}^{H_2(X,t)} U(X,Y,t)dY. \tag{38}$$

The above expression in wave frame becomes,

$$F(x) = \int_{h_1(x)}^{h_2(x)} u\,(x,y)dy\,. \tag{39}$$

The coordinates and velocities in the two frames (laboratory and wave frames) are correlated as follows:

$$X = x - ct,\ Y = y,\ U = u - c \text{ and } V = v. \tag{40}$$

From Eqs. (38–40), we get

$$Q = F + h_2 - h_1. \tag{41}$$

The time-averaged flow rate ($\Theta = \int_0^1 Q(X,t)dt$) can be expressed as follows:

$$\Theta = F + 1 + d + \left(\frac{a+b}{2}\right). \tag{42}$$

The nondimensional boundary conditions (convective boundary conditions) are employed as (Kothandapani and Prakash 2016):

$$\psi = \frac{F}{2},\ \frac{\partial \psi}{\partial y} = -1,\ \frac{\partial \theta}{\partial y} = Bh_2(1-\theta),\ \sigma = 1 \text{ and } \Phi = 1 \text{ at } y = h_2, \tag{43a}$$

$$\psi = -\frac{F}{2},\ \frac{\partial \psi}{\partial y} = -1,\ \frac{\partial \theta}{\partial y} = Bh_1\,\theta,\ \sigma = 0 \text{ and } \Phi = 0 \text{ at } y = h_1. \tag{43b}$$

where Bh_1 and Bh_2 are Biot numbers at left and right walls, respectively.

5 Numerical Simulation and Physical Interpretation

In this chapter, the electro-osmotic flow of pseudoplastic nanofluids through an asymmetric microchannel is modeled under the influence of Joule heating and peristaltic pumping mechanisms. This enables us to find out the numerical calculations for various physical parameters such as velocity field, temperature field, nanoparticle concentration, and streamlines across the microfluidic asymmetric channel. NDsolve function built-in command of MATHEMATICA-9 is employed to simulate the results. The significant physical behavior of the pertinent parameters on the flow characteristics, thermal characteristics, nanoparticle volume fraction, and streamlines are clearly represented in the graphs. The present numerical results have very good agreement with the analytical results obtained by Bandopadhyay et al. (2016) which is a special case of the present model for $\xi = 0$, $d = 1$, $a = b$, $Br = 0$, $Gr = 0$.

5.1 Electro-osmostic Flow Characteristics

To analyze the electro-osmotic flow characteristics under the effects of various physical parameters such as Debye–Hückel parameter (κ), Helmholtz–Smoluchowski velocity (Uhs), thermal Grashof number (Gr), and Species Grashof number (Br), Figs. 2, 3, 4, and 5 are plotted between the axial velocity field transverse displacement. The impact of electro-osmotic parameter κ (Debye–Hückel parameter) on the velocity profile is scrutinized in Fig. 2. There is a progressive boost and reduction in axial velocity flow near the lower wall and the upper wall with increasing electro-osmotic parameter.

The impact of Helmholtz–Smoluchowski velocity (i.e., maximum electro-osmotic velocity) on dimensionless velocity function is manifested in Fig. 3. The behavior of the axial velocity function is similar or that of Debye–Hückel parameter. Since the electro-osmotic velocity enhances, the characteristic wave velocity diminishes which accelerates the axial velocity at the core part of the channel.

Figure 4 demonstrates the evolution in dimensionless axial velocity for different values of grashof number (Gr). It perceived that the axial velocity accelerates near the upper wall and diminishes near the lower wall with the strengthening of Gr.

The response in the axial velocity field to the variation in nanoparticle Grashof number (Br) through the asymmetric channel is exhibited in Fig. 5. It is explored that the fluid velocity function dwindles with enhancing values of Br near the lower wall and it reverses at the other side of the channel. It is important to notice that

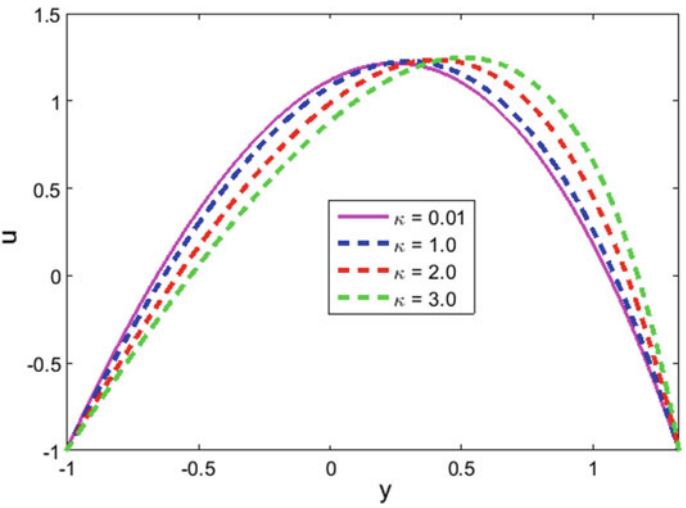

Fig. 2 Effect of κ on velocity with $a = 0.3$, $b = 0.5$, $d = 1$, $\phi = \pi/3$, $\Theta = 2$, $\xi = 0.01$, $Uhs = 1$, $Gr = 2$, $Br = 2$, $Pr = 0.7$, $Nb = 0.2$, $Nt = 0.2$, $Rn = 1$, $Bh_1 = 0.4$, $Bh_2 = 2$, and $\beta = 0.2$

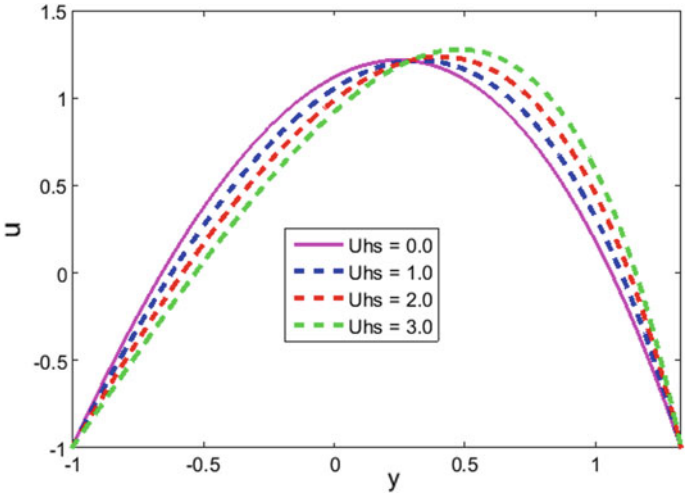

Fig. 3 Effect of Uhs on velocity with $a = 0.3$, $b = 0.5$, $d = 1$, $\phi = \pi/3$, $\Theta = 2$, $\xi = 0.01$, $\kappa = 1$, $Gr = 2$, $Br = 2$, $Pr = 0.7$, $Nb = 0.2$, $Nt = 0.2$, $Rn = 1$, $Bh_1 = 0.4$, $Bh_2 = 2$, and $\beta = 0.2$

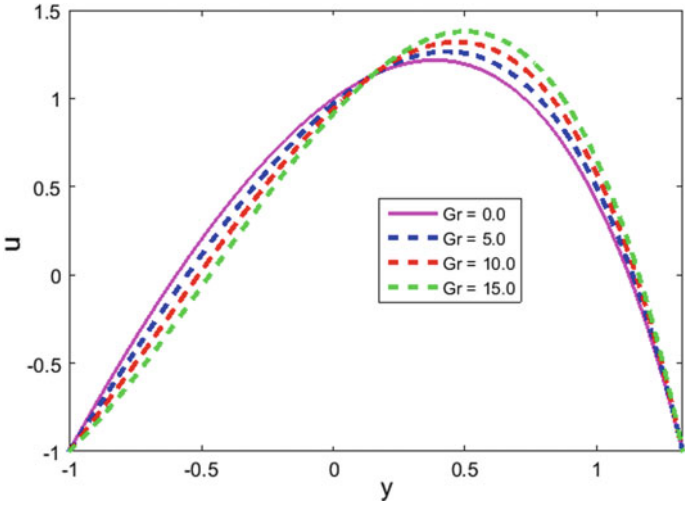

Fig. 4 Effect of Gr on velocity $a = 0.3$, $b = 0.5$, $d = 1$, $\phi = \pi/3$, $\Theta = 2$, $\xi = 0.01$, $Uhs = 1$, $\kappa = 1$, $Br = 2$, $Pr = 0.7$, $Nb = 0.2$,$Nt = 0.2$,$Rn = 1$, $Bh_1 = 0.4$, $Bh_2 = 2$, and $\beta = 0.2$

the impact of both thermal and nanoparticle Grashof numbers have alike behavior throughout the microchannel.

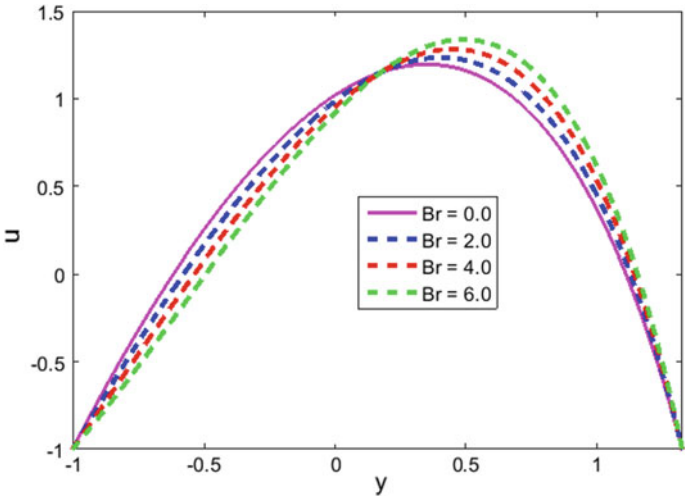

Fig. 5 Effect of Br on velocity with $a = 0.3$, $b = 0.5$, $d = 1$, $\phi = \pi/3$, $\Theta = 2$, $\xi = 0.01$, $Uhs = 1$, $\kappa = 1$, $Gr = 2$, $Pr = 0.7$, $Nb = 0.2$, $Nt = 0.2$, $Rn = 1$, $Bh_1 = 0.4$, $Bh_2 = 2$, and $\beta = 0.2$

5.2 *Electrothermal Characteristics*

To examine the electrothermal characteristics under the influences of the thermal radiation parameter (Rn), Prandtl number (Pr), heat source parameter (β), Brownian motion parameter (Nb), thermophoresis parameter (Nt) and Biot numbers (Bh_1, Bh_2) along the asymmetric microchannels, Figs. 6, 7, 8, 9, 10, 11, and 12 are illustrated between the dimensionless temperature and transverse (spanwise) coordinate. It can be observed from Fig. 6 that there is substantial decrease in response with boosting the radiation effects. It is clear that the mean absorption coefficient increases for the escalating in the radiation which indicates that the less energy is absorbed by the liquid. In addition, for the condition $Rn = 0$ in the analysis, we acquired a special case of non-radiative nanofluid flow phenomena.

Figure 7 depicts that fluid temperature declines with increasing the values of Prandtl number Pr. Figure 8 exhibits the impact of heat source parameter $\beta(\beta = 0.0, 0.5, 1.0, 1.5)$ on fluid temperature function along the channel. It is observable that the liquid temperature field enhances with the magnification in the heat source intensity. Also, the higher positive values of β give more energy as compared to the lower intensity heat source.

Figures 9 and 10 indicate that the nanofluid temperature θ grows for higher Nb and Nt. Thermophoresis and Brownian motion transfer less energy to the walls of the channel. Nanofluid temperature field within the liquid accelerates due to the random movement of nano-liquid particles. It is also noted that the impact of Nb and Nt on the energy distribution is alike behavior throughout the asymmetric microchannel.

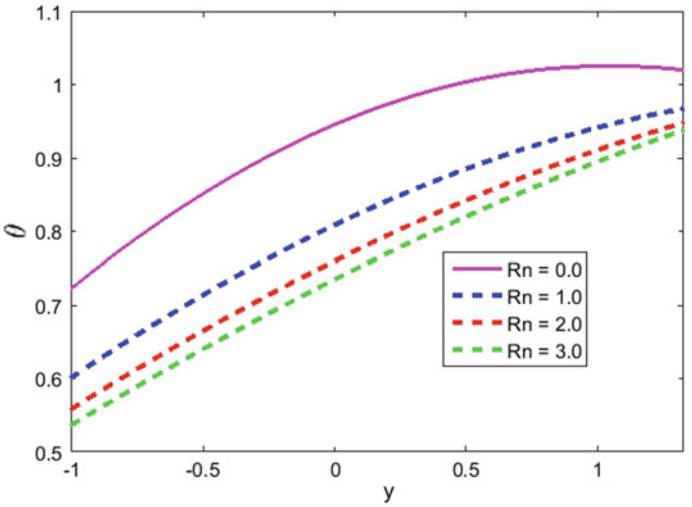

Fig. 6 Effect of Rn on temperature with $a = 0.3$, $b = 0.5$, $d = 1$, $\phi = \pi/3$, $\Theta = 2$, $\xi = 0.01$, $Uhs = 1$, $\kappa = 1$, $Gr = 2$, $Br = 2$, $Pr = 0.7$, $Nb = 0.2$, $Nt = 0.2$, $Bh_1 = 0.4$, $Bh_2 = 2$, and $\beta = 0.2$

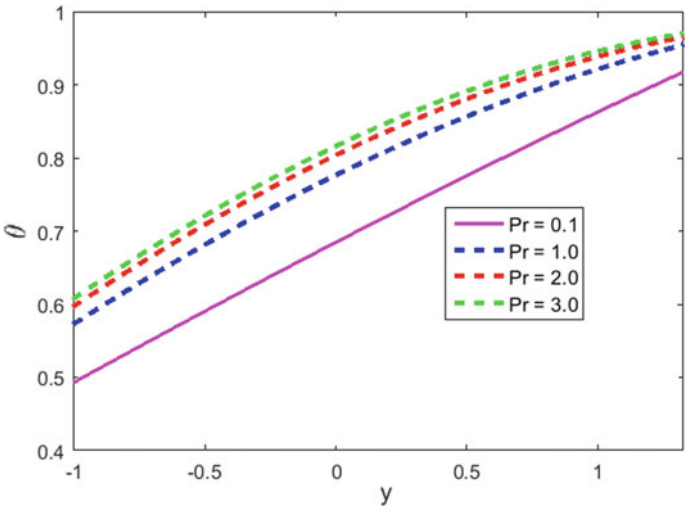

Fig. 7 Effect of Pr on temperature with $a = 0.3$, $b = 0.5$, $d = 1$, $\phi = \pi/3$, $\Theta = 2$, $\xi = 0.01$, $Uhs = 1$, $\kappa = 1$, $Gr = 2$, $Br = 2$, $Nb = 0.2$, $Nt = 0.2$, $Rn = 1$, $Bh_1 = 0.4$, $Bh_2 = 2$, and $\beta = 0.2$

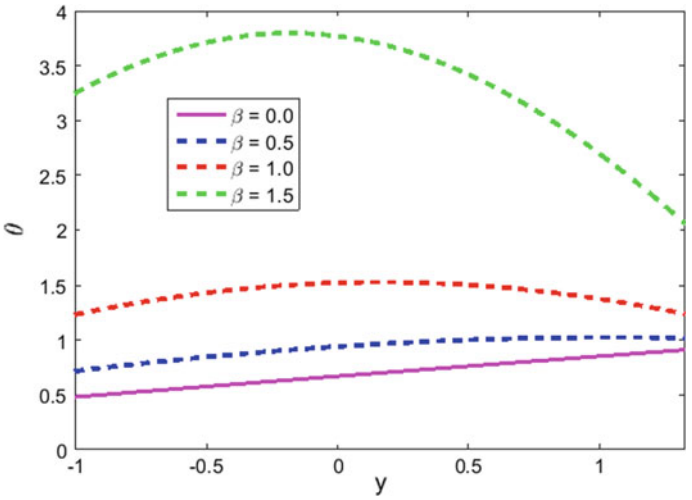

Fig. 8 Effect of β on temperature with $a = 0.3$, $b = 0.5$, $d = 1$, $\phi = \pi/3$, $\Theta = 2$, $\xi = 0.01$, $Uhs = 1$, $\kappa = 1$, $Gr = 2$, $Br = 2$, $Pr = 0.7$, $Nb = 0.2$, $Nt = 0.2$, $Rn = 1$, $Bh_1 = 0.4$, $Bh_2 = 2$

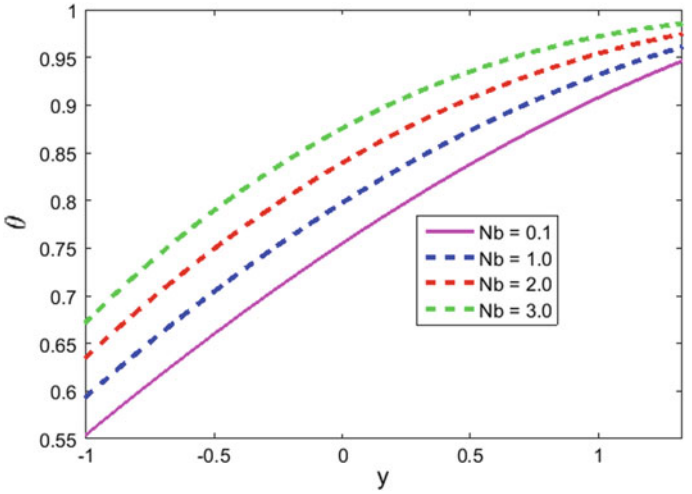

Fig. 9 Effect of Nb on temperature with $a = 0.3$, $b = 0.5$, $d = 1$, $\phi = \pi/3$, $\Theta = 2$, $\xi = 0.01$, $Uhs = 1$, $\kappa = 1$, $Gr = 2$, $Br = 2$, $Pr = 0.7$, $Nt = 0.2$, $Rn = 1$, $Bh_1 = 0.4$, $Bh_2 = 2$, and $\beta = 0.2$

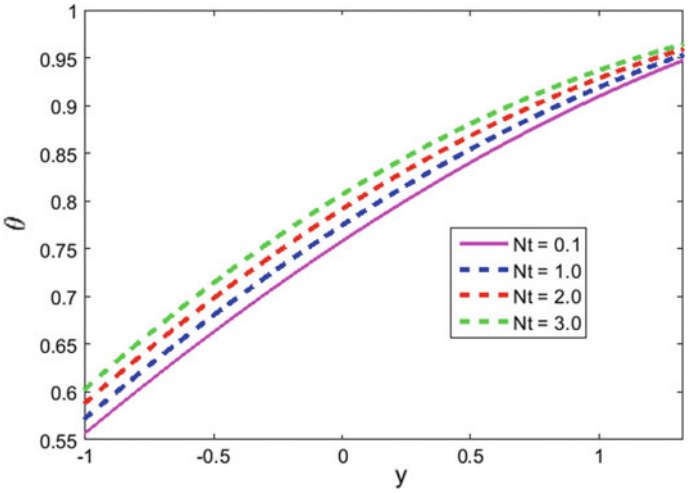

Fig. 10 Effect of Nt on temperature with $a = 0.3$, $b = 0.5$, $d = 1$, $\phi = \pi/3$, $\Theta = 2$, $\xi = 0.01$, $Uhs = 1$, $\kappa = 1$, $Gr = 2$, $Br = 2$, $Pr = 0.7$, $Nb = 0.2$, $Rn = 1$, $Bh_1 = 0.4$, $Bh_2 = 2$, and $\beta = 0.2$

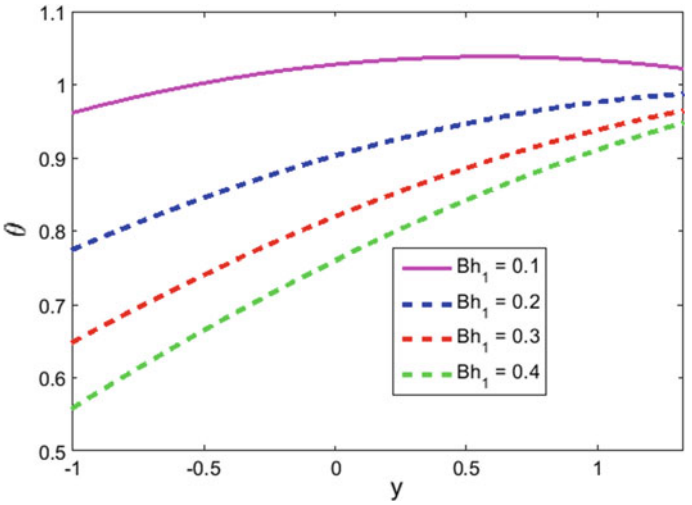

Fig. 11 Effect of Bh_1 on temperature with $a = 0.3$, $b = 0.5$, $d = 1$, $\phi = \pi/3$, $\Theta = 2$, $\xi = 0.01$, $Uhs = 1$, $\kappa = 1$, $Gr = 2$, $Br = 2$, $Pr = 0.7$, $Nb = 0.2$, $Nt = 0.2$, $Rn = 1$, $Bh_2 = 2$, and $\beta = 0.2$

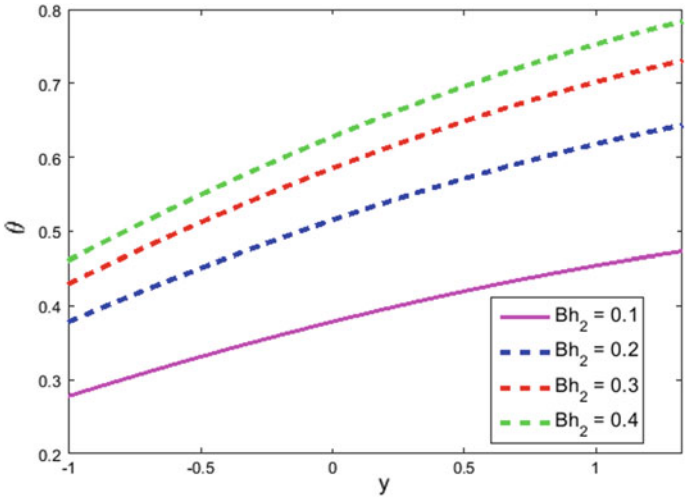

Fig. 12 Effect of Bh_2 on temperature with $a = 0.3$, $b = 0.5$, $d = 1$, $\phi = \pi/3$, $\Theta = 2$, $\xi = 0.01$, $Uhs = 1$, $\kappa = 1$, $Gr = 2$, $Br = 2$, $Pr = 0.7$, $Nb = 0.2$, $Nt = 0.2$, $Rn = 1$, $Bh_1 = 0.4$ and $\beta = 0.2$

Figures 11 and 12 show the response of temperature Biot numbers Bh_1 and Bh_2 on dimensionless nanofluid temperature. It is revealed that the temperature field strongly depends on the Biot numbers Bh_1 and Bh_2.

5.3 Nanoparticle Concentration in Presence of Electroosmosis

The evolution in dimensionless nanoparticle concentration function σ along the asymmetric channel with relevant variations in Brownian motion and thermophoresis is manifested in Figs. 13 and 14 respectively. An active motion of nanoparticles causes enhanced fluid density which repercussion in the enhancement of species flux. Therefore, an enhancement in the nanoparticle concentration is observed. But the opposite behavior is found for the thermophoresis parameter Nt with compared to the thermophoresis parameter Nb.

5.4 Trapping Phenomenon in the Presence of Electroosmosis

The trapping phenomenon (nanofluid bolus dynamics) distribution to the impact for the dimensionless flow variables (κ, Uhs, Gr, Br, ξ) are visualized in Figs. 15, 16, 17, 18, 19, 20, 21, 22, 23, and 24 respectively. Figures 15 and 16 simulate on

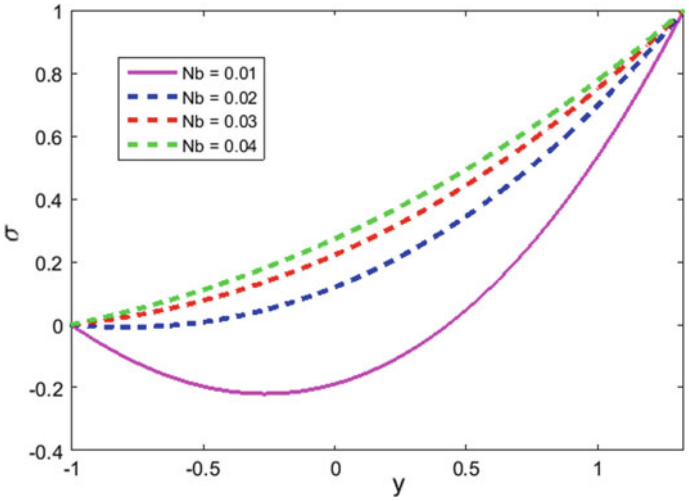

Fig. 13 Effect of Nb on concentration with $a = 0.3$, $b = 0.5$, $d = 1$, $\phi = \pi/3$, $\Theta = 2$, $\xi = 0.01$, $Uhs = 1$, $\kappa = 1$, $Gr = 2$, $Br = 2$, $Pr = 0.7$, $Nt = 0.2$, $Rn = 1$, $Bh_1 = 0.4$, $Bh_2 = 2$, and $\beta = 0.2$

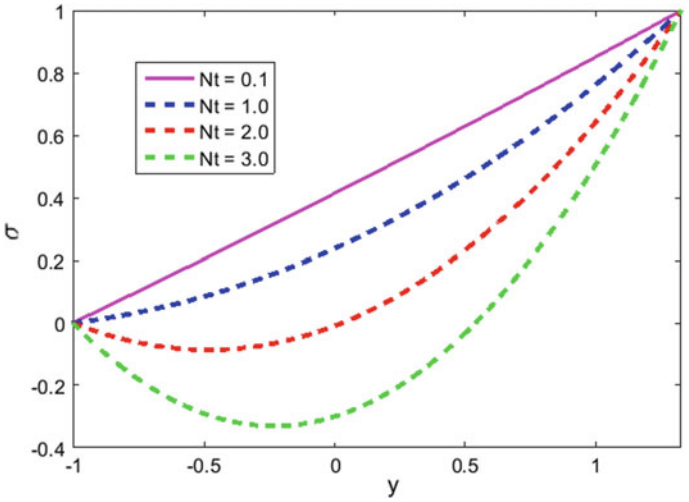

Fig. 14 Effect of Nt on concentration with $a = 0.3$, $b = 0.5$, $d = 1$, $\phi = \pi/3$, $\Theta = 2$, $\xi = 0.01$, $Uhs = 1$, $\kappa = 1$, $Gr = 2$, $Br = 2$, $Pr = 0.7$, $Nt = 0.2$, $Rn = 1$, $Bh_1 = 0.4$, $Bh_2 = 2$, and $\beta = 0.2$

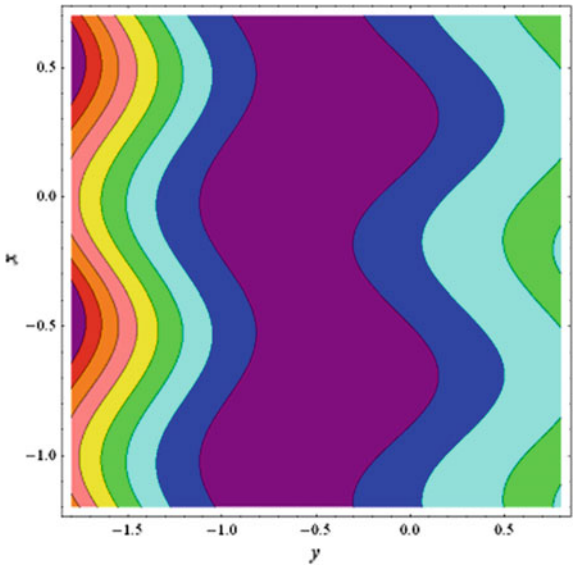

Fig. 15 Streamlines for $\kappa \to 0$ with $a = 0.3$, $b = 0.5$, $d = 1$, $\phi = \pi/3$, $\Theta = 2$, $\xi = 0.01$, $Uhs = 1$, $Gr = 2$, $Br = 2$, $Pr = 0.7$, $Nb = 0.2$, $Nt = 0.2$, $Rn = 1$, $Bh_1 = 0.4$, $Bh_2 = 2$, and $\beta = 0.2$

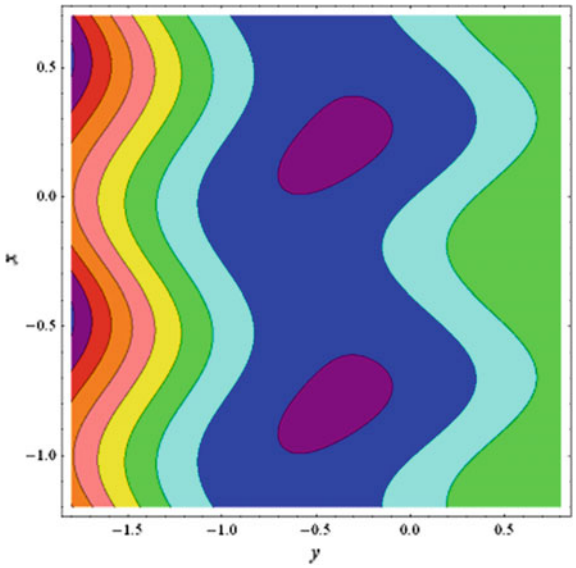

Fig. 16 Streamlines for $\kappa = 1$ with $a = 0.3$, $b = 0.5$, $d = 1$, $\phi = \pi/3$, $\Theta = 2$, $\xi = 0.01$, $Uhs = 1$, $Gr = 2$, $Br = 2$, $Pr = 0.7$, $Nb = 0.2$, $Nt = 0.2$, $Rn = 1$, $Bh_1 = 0.4$, $Bh_2 = 2$, and $\beta = 0.2$

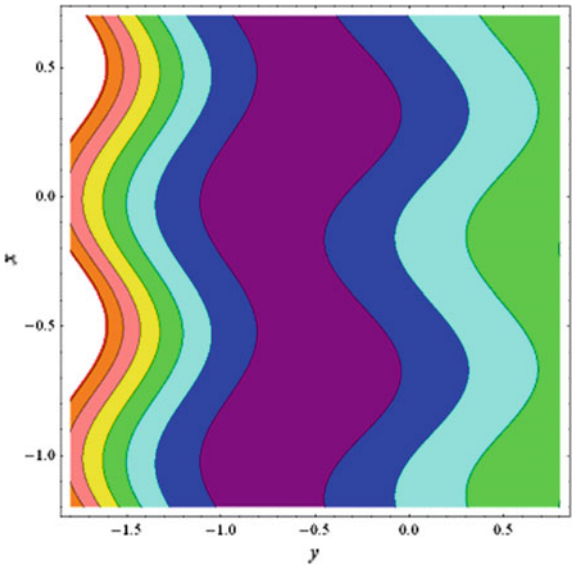

Fig. 17 Streamlines for $Uhs = -1$ with $a = 0.3$, $b = 0.5$, $d = 1$, $\phi = \pi/3$, $\Theta = 2$, $\xi = 0.01$, $\kappa = 1$, $Gr = 2$, $Br = 2$, $Pr = 0.7$, $Nb = 0.2$, $Nt = 0.2$, $Rn = 1$, $Bh_1 = 0.4$, $Bh_2 = 2$, and $\beta = 0.2$

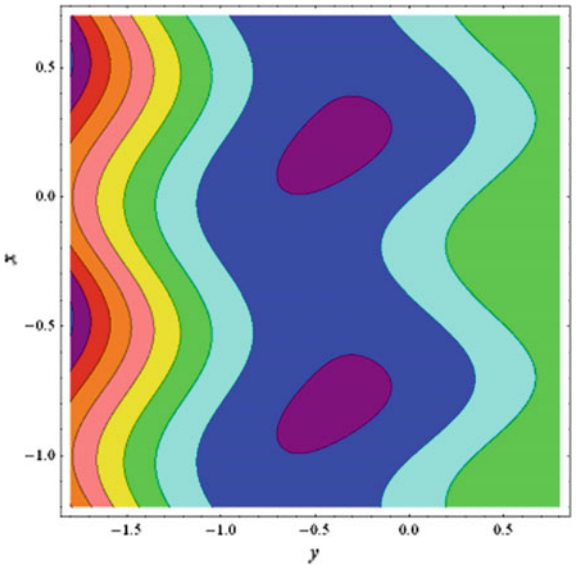

Fig. 18 Streamlines for $Uhs = 1$ with $a = 0.3$, $b = 0.5$, $d = 1$, $\phi = \pi/3$, $\Theta = 2$, $\xi = 0.01$, $\kappa = 1$, $Gr = 2$, $Br = 2$, $Pr = 0.7$, $Nb = 0.2$, $Nt = 0.2$, $Rn = 1$, $Bh_1 = 0.4$, $Bh_2 = 2$, and $\beta = 0.2$

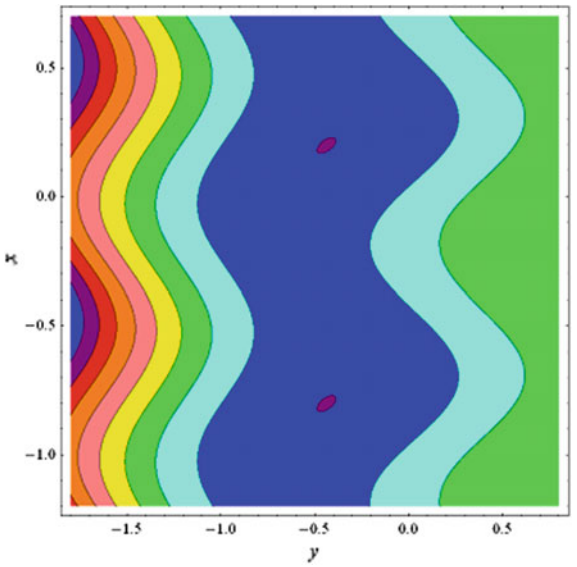

Fig. 19 Streamlines for $Gr = 0$ with $a = 0.3$, $b = 0.5$, $d = 1$, $\phi = \pi/3$, $\Theta = 2$, $\xi = 0.01$, $Uhs = 1$, $\kappa = 1$, $Br = 2$, $Pr = 0.7$, $Nb = 0.2$, $Nt = 0.2$, $Rn = 1$, $Bh_1 = 0.4$, $Bh_2 = 2$, and $\beta = 0.2$

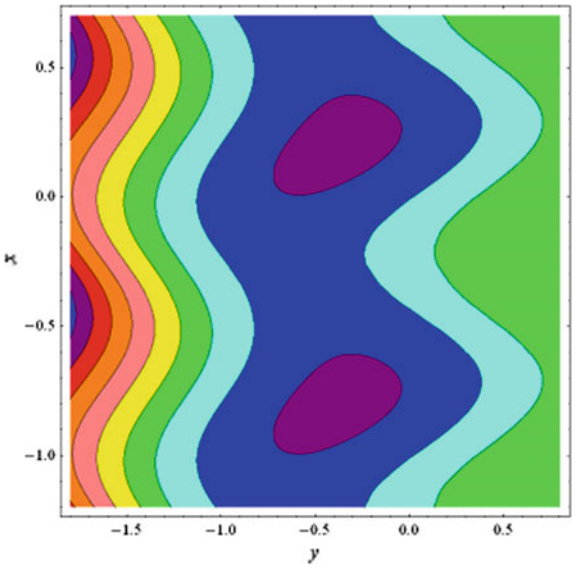

Fig. 20 Streamlines for $Gr = 2.0$ with $a = 0.3$, $b = 0.5$, $d = 1$, $\phi = \pi/3$, $\Theta = 2$, $\xi = 0.01$, $Uhs = 1$, $\kappa = 1$, $Br = 2$, $Pr = 0.7$, $Nb = 0.2$, $Nt = 0.2$, $Rn = 1$, $Bh_1 = 0.4$, $Bh_2 = 2$, and $\beta = 0.2$

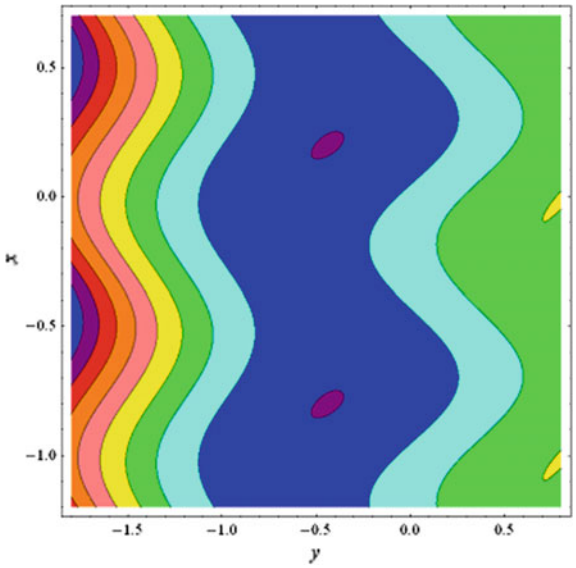

Fig. 21 Streamlines for $Br = 0$ with $a = 0.3$, $b = 0.5$, $d = 1$, $\phi = \pi/3$, $\Theta = 2$, $\xi = 0.01$, $Uhs = 1$, $\kappa = 1$, $Gr = 2$, $Pr = 0.7$, $Nb = 0.2$, $Nt = 0.2$, $Rn = 1$, $Bh_1 = 0.4$, $Bh_2 = 2$, and $\beta = 0.2$

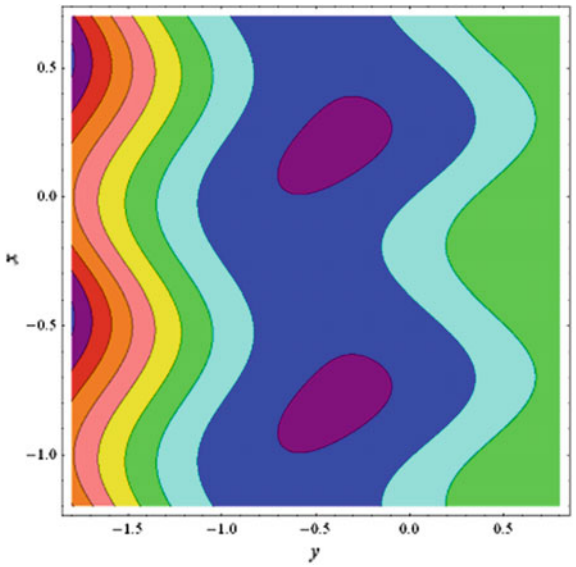

Fig. 22 Streamlines for $Br = 2.0$ with $a = 0.3$, $b = 0.5$, $d = 1$, $\phi = \pi/3$, $\Theta = 2$, $\xi = 0.01$, $Uhs = 1$, $\kappa = 1$, $Gr = 2$, $Pr = 0.7$, $Nb = 0.2$, $Nt = 0.2$, $Rn = 1$, $Bh_1 = 0.4$, $Bh_2 = 2$, and $\beta = 0.2$

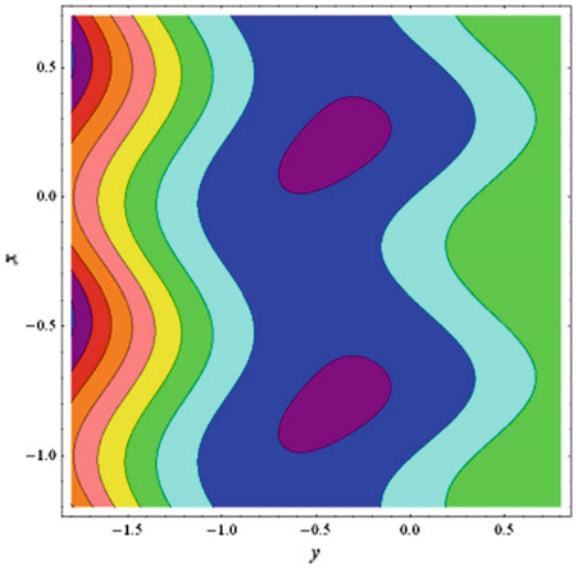

Fig. 23 Streamlines for $\xi = 0$ with $a = 0.3$, $b = 0.5$, $d = 1$, $\phi = \pi/3$, $\Theta = 2$, $Uhs = 1$, $\kappa = 1$, $Gr = 2$, $Br = 2$, $Pr = 0.7$, $Nb = 0.2$, $Nt = 0.2$, $Rn = 1$, $Bh_1 = 0.4$, $Bh_2 = 2$, and $\beta = 0.2$

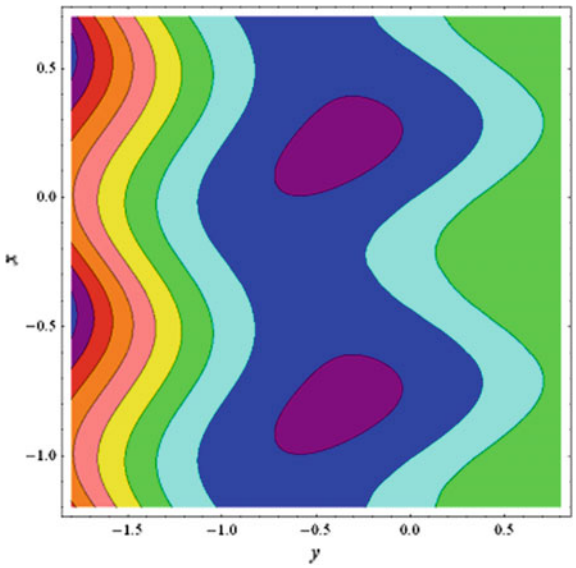

Fig. 24 Streamlines for $\xi = 0.01$ with $a = 0.3$, $b = 0.5$, $d = 1$, $\phi = \pi/3$, $\Theta = 2$, $Uhs = 1$, $\kappa = 1$, $Gr = 2$, $Br = 2$, $Pr = 0.7$, $Nb = 0.2$, $Nt = 0.2$, $Rn = 1$, $Bh_1 = 0.4$, $Bh_2 = 2$, and $\beta = 0.2$

the streamline distribution to the influence of enhance Debye–Hückel parameter (κ) from $\kappa \to 0$ to 1 with remaining dimensionless variables are kept fixed. From these two plots, it is noticed that the trapped bolus vanish when there is absence of Debye–Hückel parameter and there is progress in trapping bolus with enhancement in the value of κ. It is inspected that a boost in Debye–Hückel parameter increases the volume of the bolus grow and its circulation flattens.

The variation in the trapping bolus distribution for the Helmholtz–Smoluchowski velocity Uhs is exhibited in Figs. 17 and 18 with the contrast from -1 to 1. As Helmholtz–Smoluchowski velocity strengthens, there is an escalation in the expanse of the trapped bolus dynamics (a closer propinquity of the streamlines). This is due to a justification that a stimulation in the strength of the axial electrical field with the boost in Uhs.

The bolus phenomenon is scrutinized in Fig. 19 and 20 for escalating values of Gr. It is explored that the size and shape of the streamlines are enhanced to magnify in Gr. The similar conduct for the nanoparticle Grashof number Br (see Figs. 21 and 22). Eventually, Figs. 23 and 24 illustrate the impact of dimensionless pseudoplastic parameter (ξ varies from 0 to 0.01) on the streamline function along the channel. It is observed that the size of closed streamlines reduced with enhancing the pseudoplastic parameter.

6 Conclusion

This chapter presents a numerical model of peristaltic pumping of pseudoplastic nanofluid controlled by the electroosmosis mechanism. The effects of Grashof numbers (thermal and species) on the electro-osmotic flow characteristics and electrothermal characteristics have been discussed to examine the role of gravitational forces. The effects of thermal radiations and Joule heating on thermal characteristics are analyzed and explained. The impact of Biot numbers on the thermal characteristics is computed to analyze the nature of convective boundary conditions. Furthermore, the influences of various pertinent parameters on trapping phenomenon are simulated. It is observed that flow characteristics can be altered by the electroosmosis mechanism. It is also noted that the thermal temperature enlarges with increase in the Joule heating parameter and fluid temperature rise and with an increase in thermal radiation effects. It is further noticed that fluid temperature enhances with an increase in the heat transfer Biot number at the right wall and reversed nature is noted at the left wall. Finally, it is observed that the size and circulation of the trapped boluses increase with the increase in the Debye–Hückel parameter (inverse of EDL thickness/Debye length) and pseudoplastic parameter. The outcomes demonstrate a promising use of this model in analyzing the real-time behavior of bioinspired-micro-peristaltic pumps and energy-lab-on-chip devices which may also be exploited for thermal transport in energy systems and smart drug delivery systems, etc.

References

Akbar NS, Huda AB, Tripathi D (2016) Thermally developing MHD peristaltic transport of nanofluids with velocity and thermal slip effects. Eur Phys J Plus 131(9):332

Bandopadhyay A, Tripathi D, Chakraborty S (2016) Electroosmosis-modulated peristaltic transport in microfluidic channels. Phys Fluids 28(5):52002

Bandyopadhyay S, Chakraborty S (2018) Thermophoretically driven capillary transport of nanofluid in a microchannel. Adv Powder Technol 29(4):964–971

Bhatti M, Zeeshan A, Ellahi R, Ijaz N (2017) Heat and mass transfer of two-phase flow with Electric double layer effects induced due to peristaltic propulsion in the presence of transverse magnetic field. J Mol Liq 230:237–246

Buongiorno J (2006) Convective transport in nanofluids. J Heat Transf 128(3):240–250

Chakraborty S (2006) Augmentation of peristaltic microflows through electro-osmotic mechanisms. J Phys D Appl Phys 39(24):5356

Choi SU, Eastman JA (1995) Enhancing thermal conductivity of fluids with nanoparticles. Argonne National Lab, IL (United States)

Das S, Chakraborty S (2006) Analytical solutions for velocity, temperature and concentration distribution in electroosmotic microchannel flows of a non-Newtonian bio-fluid. Anal Chim Acta 559(1):15–24

Ganguly S, Sarkar S, Hota TK, Mishra M (2015) Thermally developing combined electroosmotic and pressure-driven flow of nanofluids in a microchannel under the effect of magnetic field. Chem Eng Sci 126:10–21

Ghasemi SE (2017) Thermophoresis and Brownian motion effects on peristaltic nanofluid flow for drug delivery applications. J Mol Liq 238:115–121

Goswami P, Chakraborty J, Bandopadhyay A, Chakraborty S (2016) Electrokinetically modulated peristaltic transport of power-law fluids. Microvasc Res 103:41–54

Guo X, Qi H (2017) Analytical solution of electro-osmotic peristalsis of fractional Jeffreys fluid in a micro-channel. Micromachines 8(12):341

Khanafer K, Vafai K (2018) A review on the applications of nanofluids in solar energy field. Renew Energy 123:398–406

Kothandapani M, Prakash J (2015) Effects of thermal radiation parameter and magnetic field on the peristaltic motion of Williamson nanofluids in a tapered asymmetric channel. Int J Heat Mass Transf 81:234–245

Kothandapani M, Prakash J (2015) Effect of radiation and magnetic field on peristaltic transport of nanofluids through a porous space in a tapered asymmetric channel. J Magn Magn Mater 378:152–163

Kothandapani M, Prakash J (2016) Convective boundary conditions effect on peristaltic flow of a MHD Jeffery nanofluid. Appl Nanosci 6(3):323–335

Mekheimer KS, Hasona W, Abo-Elkhair R, Zaher A (2018) Peristaltic blood flow with gold nanoparticles as a third grade nanofluid in catheter: Application of cancer therapy. Phys Lett A 382(2–3):85–93

Mosayebidorcheh S, Hatami M (2018) Analytical investigation of peristaltic nanofluid flow and heat transfer in an asymmetric wavy wall channel (Part I: Straight channel). Int J Heat Mass Transf 126:790–799

Mosayebidorcheh S, Hatami M (2018) Analytical investigation of peristaltic nanofluid flow and heat transfer in an asymmetric wavy wall channel (Part II: Divergent channel). Int J Heat Mass Transf 126:800–808

Noreen S, Alsaedi A, Hayat T (2012) Peristaltic flow of pseudoplastic fluid in an asymmetric channel. J Appl Mech 79(5):54501

Prakash J, Ramesh K, Tripathi D, Kumar R (2018) Numerical simulation of heat transfer in blood flow altered by electroosmosis through tapered micro-vessels. Microvasc Res 118:162–172

Prakash J, Sharma A, Tripathi D (2018) Thermal radiation effects on electroosmosis modulated peristaltic transport of ionic nanoliquids in biomicrofluidics channel. J Mol Liq 249:843–855

Prakash J, Siva E, Tripathi D, Kuharat S, Bég OA (2019) Peristaltic pumping of magnetic nanofluids with thermal radiation and temperature-dependent viscosity effects: Modelling a solar magneto-biomimetic nanopump. Renew Energy 133:1308–1326

Ranjit N, Shit G (2017) Entropy generation on electro-osmotic flow pumping by a uniform peristaltic wave under magnetic environment. Energy 128:649–660

Reuss F (1809) Charge-induced flow. Proc Imp Soc Nat Mosc: 327–344

Sadr R, Yoda M, Zheng Z, Conlisk A (2004) An experimental study of electro-osmotic flow in rectangular microchannels. J Fluid Mech 506:357–367

Santiago J (2001) Electroosmotic flows in microchannels with finite inertial and pressure forces. Anal Chem 73(10):2353–2365

Shehzad N, Zeeshan A, Ellahi R (2018) Electroosmotic flow of MHD power law Al2O3-PVC nanouid in a horizontal channel: couette-poiseuille flow model. Commun Theor Phys 69(6):655

Shit GC, Ranjit NK, Sinha A (2016) Electro-magnetohydrodynamic flow of biofluid induced by peristaltic wave: a non-Newtonian model. J Bionic Eng 13(3):436–448

Tiwari RK, Das MK (2007) Heat transfer augmentation in a two-sided lid-driven differentially heated square cavity utilizing nanofluids. Int J Heat Mass Transf 50(9–10):2002–2018

Tripathi D, Bég OA (2014) A study on peristaltic flow of nanofluids: application in drug delivery systems. Int J Heat Mass Transf 70:61–70

Tripathi D, Yadav A, Bég OA (2017) Electro-kinetically driven peristaltic transport of viscoelastic physiological fluids through a finite length capillary: mathematical modeling. Math Biosci 283:155–168

Tripathi D, Yadav A, Bég OA (2017) Electro-osmotic flow of couple stress fluids in a micro-channel propagated by peristalsis. Eur Phys J Plus 132(4):173

Tripathi D, Sharma A, Bég OA (2018) Joule heating and buoyancy effects in electro-osmotic peristaltic transport of aqueous nanofluids through a microchannel with complex wave propagation. Adv Powder Technol 29(3):639–653

Wiedemann G (1852) First Quantitative study of electrical endosmose. PoggendorfsAnnalen 87:321–323

Yang C, Li D (1998) Analysis of electrokinetic effects on the liquid flow in rectangular microchannels. Colloids Surf A 143(2–3):339–353

Zhao G, Jian Y (2018) Heat transfer of the nanofluid in soft nanochannels under the effects of the electric and magnetic field. Powder Technol 338:734–743

Zhao G, Jian Y, Li F (2016) Streaming potential and heat transfer of nanofluids in parallel plate microchannels. Colloids Surf A 498:239–247

Zhao G, Wang Z, Jian Y (2019) Heat transfer of the MHD nanofluid in porous microtubes under the electrokinetic effects. Int J Heat Mass Transf 130:821–830

Synthesis of Nanomaterials for Energy Generation and Storage Applications

P. Narsimha, P. Rajesh Kumar, K. Raghu Raja Pandiyan, Prashant L. Suryawanshi, Ramsagar Vooradi, K. Anand Kishore and Shirish H. Sonawane

Abstract A Polymer Electrolyte Membrane (PEM) fuel cell is a device in which an electrochemical reaction occurs between fuel and oxidant producing electricity and water is the only by-product with zero emission. Usually, Pt nanoparticles prepared on carbon support used as oxidation and reduction reaction in PEM fuel cells. Because, carbon-supported platinum shows better oxidation and reduction activity among all the pure metals. Alloying of Pt with another non-noble metal is a strategy to develop Pt-based electrocatalysts, which reduces the Pt loading in electrodes and alters the intrinsic properties such as active sites available on surface and binding strength and electronic effect of species. Carbon support loss its catalytic activity due to electrooxidation under fuel cell operating conditions for long-term operations. In particular, the encapsulation of carbon with polyaniline (PANI) supported Pt enhances the electrode stability in fuel cells by Enhancing the Active Surface Area (EASA), chemical resistance and electron conductivity. Different supported catalysts have been proposed to improve electrochemical stability of nanoparticles in PEM fuel cells and supercapacitor.

Keywords Pt-based nanomaterials · Ultrasound/microreactor assisted method · PEM fuel cell · Supercapcaitor · Cathode materials

1 Introduction

The projected energy demand is going more than hundred percentage by year two thousand fifty due to exponential increase in population. Most of energy demand is

P. Narsimha · K. Raghu Raja Pandiyan · R. Vooradi · K. Anand Kishore · S. H. Sonawane (✉)
Department of Chemical Engineering, National Institute of Technology, Warangal 506004, Telangana, India
e-mail: shirish@nitw.ac.in

P. L. Suryawanshi
R & D Center, Hindustan Petroleum Corporation Ltd., Bangalore, India

P. Rajesh Kumar
Department of Chemical Engineering, National Institute of Technology, Tadepalligudem, Andhra Pradesh 534102, India

L. Ledwani and J. S. Sangwai (eds.), *Nanotechnology for Energy and Environmental Engineering*, Green Energy and Technology,
https://doi.org/10.1007/978-3-030-33774-2_9

fulfilled by using fossil fuel. After the industrial revolution, an exponential increase in energy usage has been observed in sectors such as transportation, industrial, and residential. Choice of the energy source to meet the existing needs is based on the following factors: availability of energy resource, location of availability, technology adapted to tap the resource, and associated costs with an account environmental effects. The energy usage policies and economic status of the country influence the weightage of the above factors. The conventional sources such as coal, oil, natural gas, and wood. are still primary sources for energy generation, and these are the main contributors for CO_2 emission. To mitigate the CO_2 emissions, 195 signatory countries adopted the historic Paris agreement.

Harvesting energy from renewables is becoming a sustainable alternative as compared to the fossil energy. However, intermittent availability of renewable energy is a major drawback in replacing the fossil energy for baseload power supply. Hence, the extensive use of energy storage devices is essential to make the renewable energy as a sustainable option. In recent days, research is more focused on development of nanoparticulate technology for sustainable renewable energy conversion, utilization, and storage (Mao et al. 2012). Metal chalcogenide nanomaterials exhibit good optical and electrical properties and having widespread applications in batteries, photovoltaics, and display devices (Cho et al. 2014; Wu and Lee 2018). The nano-structuring semiconducting materials such as n-type, p-type, chalcogenide, and nitrides are being used for conversion to generate hydrogen energy (Alfaifi et al. 2018; Li and Wu 2015). Different metal nanoparticles such as ZnO, CuO, TiO_2, and Ag are used in the form of layers and tubes in dye-based solar cells (Lai et al. 2008; Mor et al. 2006; Sharma et al. 2015; Suliman et al. 2007).

Nano-structured systems such as nanotubes, hydrides, carbon/hydride nanocomposites, metal–organic frameworks, alanates, and polymer nanocomposites have been considered as potential candidates for solid-state hydrogen storage (Niemann et al. 2008). Applications of nanotechnology brought revolutionary changes in the area of solid oxide fuel cells (SOFC) by improving the following characteristics: operational temperature is reduced to range of 400–700 °C from 700 to 900 °C, reduced the internal resistance which has been a major problem at low operating temperature (Abdalla et al. 2018; Fan et al. 2018).

2 Role of Nanomaterial for Energy Generation and Storage

Nanomaterials play a vital role in energy sector where their applications can be broadly categorized to energy resources, energy transfer/change, energy distribution, energy storage, and energy usage. Examples of nanomaterial applications and development specifically to energy generation and storage are tabulated in Table 1.

3 Synthesis of Nanomaterials

The synthesis of nanoparticles depends on two major approaches: (i) Top-down method and (ii) Bottom-up method. In top-down approach, the macro bulk form of the precursor has been physically processed to break and bring down particle size to nano dimensions. In contrast, bottom-up method, the nanoparticles are synthesized by

Table 1 Role of nanomaterial for energy generation and storage

Nanomaterial for energy generation	*Specific energy generation system*	*Specific role*
	Photovolatic cells	Nano-optimized cells in the form of dots, thin films, refractive coatings, etc.
	Wind energy blades	Energy-efficient weight reduced structures made up of nanocomposites
	Geothermal energy, fossil fuels—oil explorations	Nano-coatings, structures for wear-resisting drilling equipment
	Hydro and tidal power	Corrosive protective coatings and structures using nanocomposites
	Biomass energy	Increased yield via farming based on nano-sensors in process control
	Nuclear energy	Nanocomposites for radiation shields, reactors/containers, personal protection equipments, etc.
	Turbines, combustion engines	Ceramic/intermetallic nano-coatings/structures for thermal &corrosion protective blades, structures
	Fuel cells	Nano-based proton exchange membranes
	Hydrogen generation	Nano-Catalysts and novel processes for H_2 generation
	Electrical motors	Super conducting nanocomposites components
Nanomaterial for energy storage	*Specific energy storage system*	*Specific role*
	Electrical energy	Batteries—Nano-structured electrodes and separators for batteries
		Supercapacitors—Nano-structured electrodes with high charge capacities

(continued)

Table 1 (continued)

	Chemical energy	Accumulators—Nano-structured electrodes and separators for recyclable batteries with cyclic reactions that convert chemical energy into useful energy
		Nano-structures/Fuel storage tanks—For storing liquid and gaseous fuels without hydrocarbon leakages
		Fuel reforming/refining—Novel nano-catalysts used for fuel production or refining such as petroleum refining and coal fuels
	Thermal Energy	Nano-Phase Change Material and Heat Transfer Nano Fluids—industrial heat transfer applications
		Nanoporous adsorption storage including metallo-organic cage-like structures for storing compressed and liquefied hydrogen, methane, natural gas

consolidating atoms/molecules/clusters through nucleation and growth process either via chemical or biological routes. The different methods for synthesis of nanoparticles are depicted in Fig. 1. The different synthesis methods for nanoparticles are well documented in the literature.

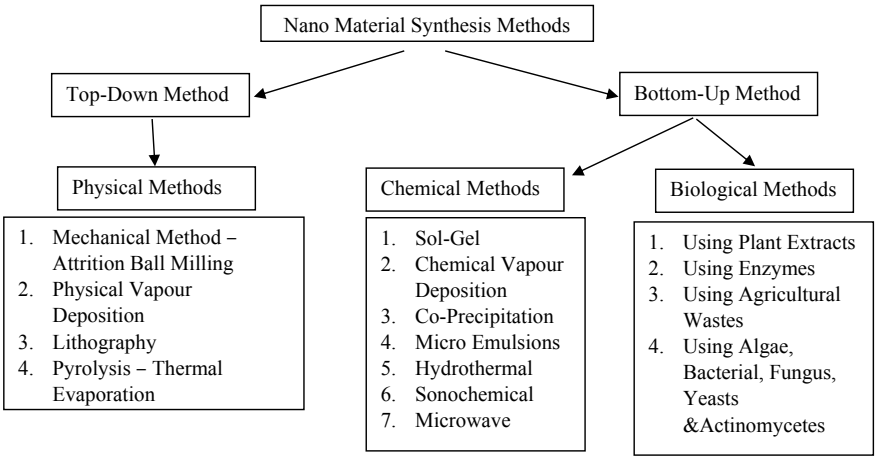

Fig. 1 Nanoparticles synthesis methods

4 Synthesis and Characterizations of Reduced Graphene-SnO_2-Polyaniline Nanocomposites Using Sonochemical Approach for Supercapacitor

4.1 Sonochemical Synthesis of Reduced Graphene-SnO_2-Polyaniline Composite

Using modified Hummers method, graphene oxide [GO] was prepared from graphite powder (Guo et al. 2015). Then, the prepared GO was used as a precursor for graphene. Sonochemical synthesis method was used for the preparation of reduced graphene-SnO_2-polyaniline. At first, the dispersion of GO in distilled water (8 gm/ml) was carried out using ultra-sonification for a period of 30 min to obtain an exfoliated yellow-brown GO suspension. Subsequently, 3 g of $SnCl_4.5H_2O$ was added into the GO suspension under sonication and stirring for 1 h to get a black GS solution. Then 0.5 mL aniline was slowly added. Further, the mixture was sonicated for 15 min and then, added with drops of 10 mL aqueous solution containing 2 g ammonium persulfate (APS). After the sonification process, the content was kept in ice bath for 1 h. Next, the Reduced graphene-SnO_2-polyaniline nanocomposite was filtrated and washed with ethanol and deionized water. Finally, the washed contents were dried at 60 °C in oven under vacuum conditions. The experimental setup and complete process flow are shown in Figs. 2 and 3, respectively.

The electrochemical performance of the supercapacitor was evaluated using a standard three-electrode setup that contains aqueous 1M H_2SO_4 electrolyte solution. Also, the Reduced graphene-SnO_2-polyaniline composite coated carbon paper was working as electrode, graphite plate and standard saturated calomel electrode (SCE) were working as counter electrode and reference electrode, respectively. The

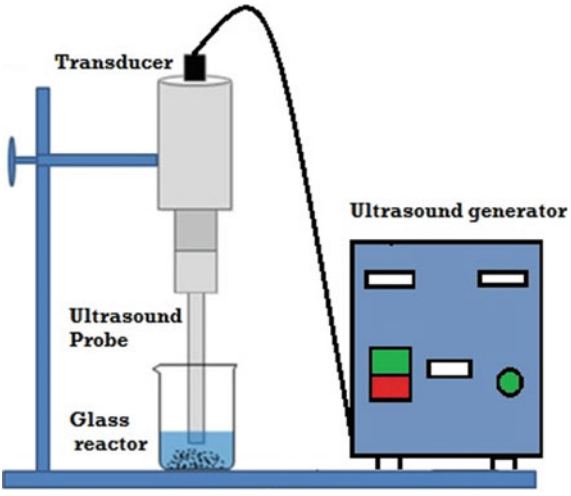

Fig. 2 Ultrasound set up for the synthesis of Reduced graphene-SnO_2-polyaniline composite

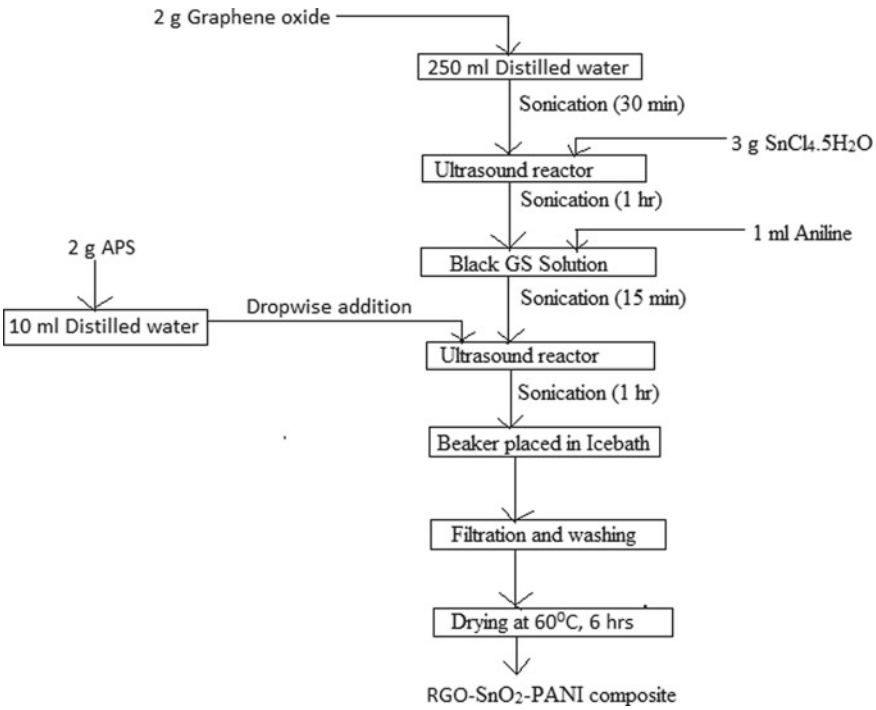

Fig. 3 Procedural flow of the synthesis of Reduced graphene-SnO_2-polyaniline composite

performance of supercapacitor was evaluated by Cyclic voltammetry (CV), galvanostatic charge–discharge (GCD) and electrochemical impedance spectroscopy (EIS) at room temperature by using A/g). Electrochemical impedance spectroscopy (EIS) measurements were carried out in the frequency range of 0.1–1,00,000 Hz at 5 mV open-circuit voltage.

The XRD patterns of Reduced graphene-SnO_2-polyaniline composites are shown in Fig. 4. There was no GO or graphite peak detected, which indicates that completely GO was reduced. Due to the amorphous polymer present in the composite, no polyaniline peak detected. The observed 2ϴ peaks at 26.73°, 34.57°, 51.90°, and 64.69° which associated with (110), (101), (211), and (301) planes of the SnO_2, which are consistent with the standard JCPDS values (JCPDS No. 41-1445). The Structural-parameters of as-synthesized Reduced graphene-SnO_2-polyaniline nanocomposite shown in Table 2. The crystallite size of the Reduced graphene-SnO_2-polyaniline composite evaluated using Scherrer Formula (Rajesh Kumar et al. 2018a).

$$L_p = \frac{0.94\lambda}{\beta_{1/2}\cos\theta} \tag{1}$$

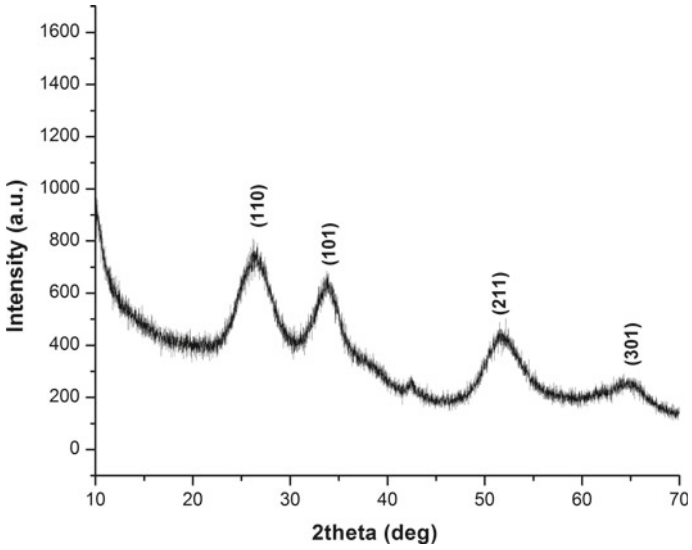

Fig. 4 X-ray diffraction pattern of Reduced graphene-SnO_2-polyaniline

Table 2 Structural parameters of synthesized Reduced graphene-SnO_2-polyaniline nanocomposite

S. no	2Θ (Degree)	(h k l)	d-Spacing (A^O)	FWHM	Crystallite size (nm)
1	26.73	(110)	3.33	0.62	13.55
2	34.57	(101)	2.59	0.75	11.50
3	51.90	(211)	1.76	0.50	18.32
4	64.69	(301)	1.44	0.32	30.27

where Lp = Crystallite size, β = Full width at half maximum of peaks (Line broadening), θ = Bragg reflection angle, λ = X-ray wavelength.

The morphological study of the Reduced graphene-SnO_2-polyaniline nanocomposite was carried out using transmission electron microscopy (TEM) analysis. The resulted TEM images of reduced graphene-SnO_2-polyaniline nanocomposite are shown in Fig. 5. The TEM image shows that the obtained nanoparticles are irregular in shape and those nanoparticles are agglomerated onto graphene sheets. The resultant average size of the composite is from 10 to 50 nm.

The electrochemical characteristics of prepared materials for supercapacitors were evaluated by different electrochemical analyses. The CV measurements of reduced graphene-SnO_2-polyaniline composite at different scan rates are shown in Fig. 6. It can be seen that curves at 80 and 160 mV/s are without any redox peak with rectangle. But two redox peaks at different scan rates, which indicate the EDLC behavior. Following equation is used to calculate capacitance (Mao et al. 2012):

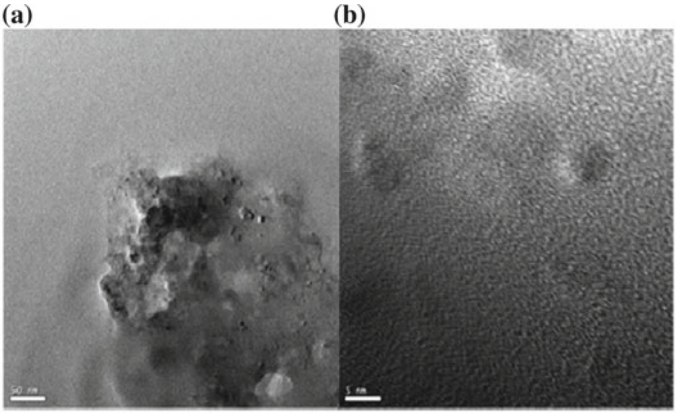

Fig. 5 Morphology of synthesized Reduced graphene-SnO_2-polyaniline composite **a** 50 nm and **b** 10 nm by ultrasound-assisted method

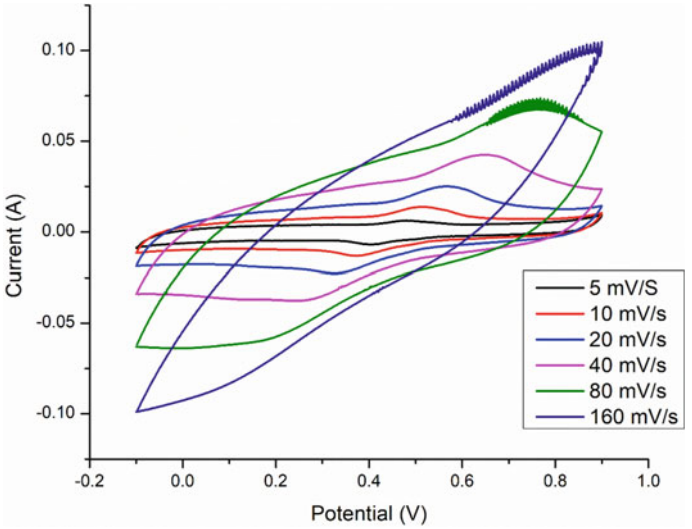

Fig. 6 CV curves for reduced graphene-SnO_2-polyaniline composite at different scan rates (5, 10, 20, 40, 80, and 160 mV/s)

$$C_s = \frac{\int i dV}{2V_s m \Delta V} (\text{F/g}) \tag{2}$$

where C_S = Specific Capacitance (F/g), i = Current in (A), V = Potential in CV Test (V), V_S = Scan rate (V/s), m = Mass of active Material (g) ΔV = Potential Window (V).

For the nanocomposite specific capacitance was calculated from the CV curves was 215 F/g at a scan rate of 5 mV/s, 191.10 and 174.5 F/g at 10 and 20 mV/s scan rates respectively. Results show that with increase in the scan rate, specific capacitance decreases which indicates that at lower scan rates specific capacitance values are more precise (as shown in Fig. 7).

The GCD curves of starch-PANI composites at different current densities of 0.5, 1 and 2 A/g are shown in Fig. 7. As shown in Fig. 7, nanocomposite shows 80, 63.50, and 57.10 F/g at 2, 1, and 0.5 A/g current densities, respectively. The specific capacitance (Cs) values can be evaluated by the following equation (Li et al. 2018):

$$C_s = \frac{I \times \Delta t}{m \times \Delta V} \tag{3}$$

where ΔV = Potential Window (V), I = Discharge Current in (A), Δt = Time for discharge in (s), m = Mass of active Material (g), C_S = Specific Capacitance (F/g).

To find the conductivity of the Reduced graphene-SnO_2-polyaniline composite electrodes, the electrochemical impedance measurements used to test the conductivity of the material, the experiments were conducted in the range from 0.01–1,00,000 Hz frequency. The Nyquist plot of the Reduced graphene-SnO_2-polyaniline composite has shown in Fig. 8. It can be observed that small half circle with linear line observed in low-frequency region. In general, at large frequency regions, a small semicircle can be observed which indicates that the resistance is being offered by

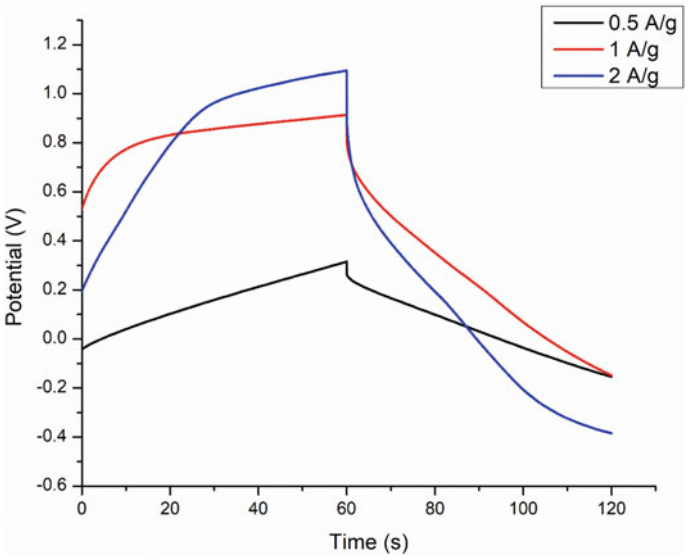

Fig. 7 Curves of charge-discharge cycle of reduced-SnO_2-PANI at different current densities (0.5, 1 and 2 A/g)

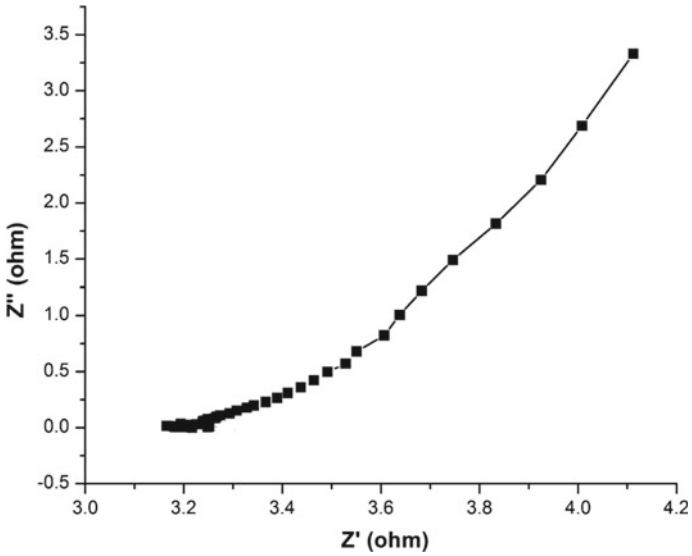

Fig. 8 EIS spectra of reduced graphene-SnO_2-polyaniline nanocomposite

internal pore diffusion, while linear line at low-frequency region indicates the fabricated Reduced graphene-SnO_2-polyaniline electrode material is an ideal capacitor property (Yang et al. 2017).

5 Nanomaterials for the PEM Fuel Cell Applications

Fuel cell is important device to obtain electrical energy from chemical reaction conversion. There are several issues with fuel cells to make into commercial scale, some of the important challenges are the cost of the fuel cell stack, catalyst cost, and the stability of the catalyst. Hence, in this chapter an attempt has been made to show how the platinum-based catalyst can be replaced by using non-noble metals, especially at cathode side. The exclusive study also been attempted to use the polyaniline as support conductive material along with the carbon in order to make more electrochemical transformations (Yaldagard et al. 2014).

Polyaniline (PANI) is one of the best-conducting polymers which can be used to prepare electrodes to convert into electrochemical energy. The addition of PANI with carbon increases the support surface which leads to raise active electrochemical area and increases the durability of electrocatalyst. The encapsulation of catalyst particles with PANI enhanced the electrochemical activity. It is well known that the metal nanoparticles are uniformly encapsulated by the conducting polymers such as polyaniline [PANI], and polypyrole [PPy], which can be easily coated onto gas diffusion layers. The sonochemical method is an effective method to synthesize the

monometallic electrocatalysts for fuel cell applications. In the literature numbers of attempts have been made to synthesize the Pt-based catalyst including the sol–gel method, reduction method. However, the wide distribution of particles is one of the challenges for the electrocatalyst to make uniform distribution onto the support materials. It is interesting to know that the sonochemical synthesis method makes the catalyst synthesis very small in size and with uniform distribution of the catalyst. In this work, an attempt was made to synthesize to make a functional electrocatalyst for better electrochemical conversion (Bang and Suslick 2010; Kaltsa et al. 2014; Valh et al. 2017).

5.1 Synthesis of the Support and Catalyst Preparation for PEM Fuel Cell

For the preparation of the support, additional aniline was polymerized using the oxidative polymerization system. The polymerization was carried out using ultrasound-assisted miniemulsion polymerization so that the uniform droplet size and uniform conductivity of the polymer particle will be maintained. Sonication was carried using the probe type ultrasound and it was conducted for less than 30 minutes. During the formation of the conducting polymer the ultrasound makes the deposit onto the conducting support. It is also carried out the synthesis of bimetallic nanoparticles such as Platinum–cobalt and Platinum–cobalt/C and Platinum–cobalt/PANI. During the synthesis K_2PtCl_6—and cobalt nitrate was used as precursors and it was reduced using the sodium borohydride. The Membrane electrolyte assembly was prepared using the commercial carbon black powder and using the PANI using the electrocatalyst (Rajesh Kumar et al. 2017, 2018a, b).

From the XRD analysis, it has been found that the Platinum–cobalt/C and Platinum–cobalt/C-PANI nanoparticles as 15.75, 9.61 nm with major peak at 39.89°. Further as shown in from TEM images the particle size of the C/PANI support is less than the conventional system. The size of the catalyst is below 20 nm (as shown in Fig. 9) while the size of Pt-Co—Cabon/PANI support is below 50 nm (Rajesh Kumar et al. 2017; Skorb and Andreeva 2013).

Cyclic voltammetry curve of the Platinum–cobalt/C-PANI cathode electrode is shown in Fig. 10. Electrochemical Scanning depicts the oxidation current increase in forward sweep while reduction current decreases in reverse sweep.

Characteristic peak corresponding to the PANI in the figure predicts that PANI conversion occurs to emeraldine phase during the forward sweep. The maximum current density was achieved by the Platinum–cobalt/C-PANI electrocatalysts was 2.32 mA/cm^2 at 1.00 V during the forward scan (Yaldagard et al. 2014; Zhou et al. 2010).

Cycle time of synthesized electrocatalyst was to check the stability using cyclic voltammetry (CV) analysis. It is sound that the synthesized catalyst Pt_{83}-Co_{17}/C has

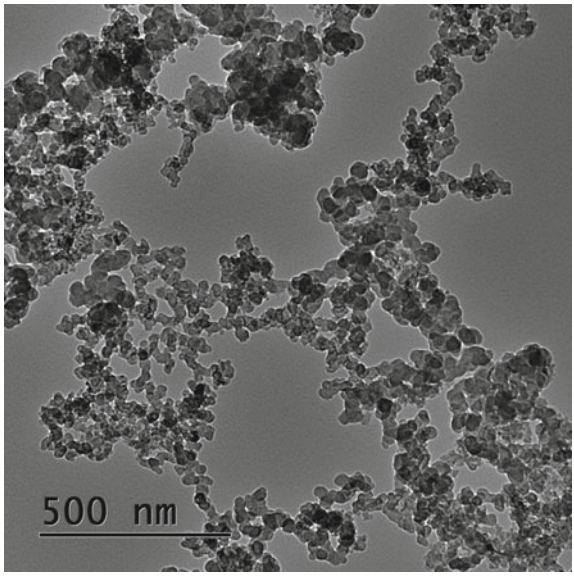

Fig. 9 TEM image of sonochemically synthesized platinum–cobalt/C-PANI nanoparticles

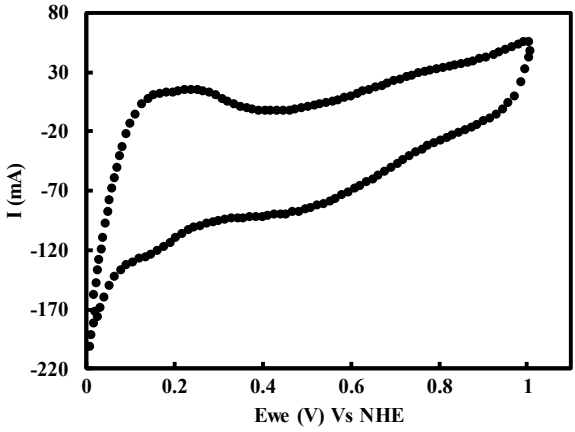

Fig. 10 Cyclic voltammetry (CV) of Platinum–cobalt/C-PANI cathode in a 0.5 M H_2SO_4 aqueous electrolyte at a scan rate of 50 mV/s (Rajesh Kumar et al. 2017) [with permission from Elsevier Chemical Engineering and Processing: Process Intensification 121, 2017, 50–56]

the stability more than 3000 h cycles in PEM fuel cell which do not contain the conductive support such as polyaniline (PANI) as shown in Fig. 11.

As shown in Table 3, There is an improvement in the current density with the addition of PANI. However, there is significant reduction in the electrochemical active area. Due to increase in the polymer chains length the particle size of the catalyst is increased. But it is interesting to know that the addition of the conducting polymer always leads to increase in the stability and durability of the electrode.

Figure 12 shows the PEM fuel cell performance using Platinum–cobalt/C-PANI electrocatalysts on cathode side, Platinum/C electrocatalysts on anode side and

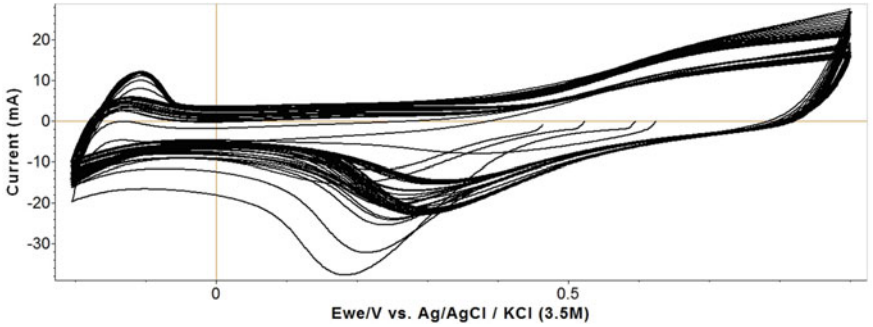

Fig. 11 CV Curve of Pt_{83}-Co_{17}/C measured against NHE in the H_2–N_2 atmosphere at a scan rate of 50 mV/s

Table 3 Synthesized Pt/C, platinum–cobalt/C and platinum–cobalt/C-PANI electrocatalysts using sonochemical method and electrochemical parameters

Parameter	Electrocatalyst		
	Pt/C	Platinum–cobalt/C	Platinum–cobalt/C-PANI
Crystal size (nm)	10.8	9.61	15.75
EASA (m^2/g)	7.88	8.7	5.98
OCP (V)	1	0.9	0.91
Power density (W/cm^2)	0.32	0.27	0.36

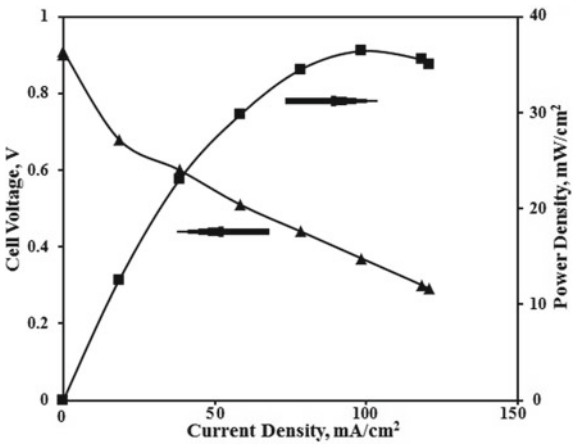

Fig. 12 Power density Vs current density curve of synthesized catalyst for cathode (Rajesh Kumar et al. 2017) [with permission from Elsevier Chemical Engineering and Processing: Process Intensification 121, 2017, 50–56]

Nafion membrane in between them operated at 50 °C. It is observed from the figure, as increasing in the current density, the power density increased and reached the maximum value. Further, there is a drop in power density due to the mass transfer resistances, which are increased in the ionic species. The peak power density was

achieved at 0.37 V and identified as 36.4 mW/cm^2 whereas the highest current density was achieved at 0.29 V and identified as 120.8 mA/cm^2. From figure, the density of current decreases with increase in the voltage because of saturation of active sites on the electrode (Wang et al. 2014; Xia et al. 2015).

6 Conclusion

It is found that ultrasound-assisted technique gives uniform particle size and particle size distribution. The particle size distribution plays important role in the preparation of the energy storage devices as supercapacitor and PEM fuel cell as energy generation device. From the capacity curves, it is found that small half circle at large frequency and followed by a linear line at low-frequency region. In general, at large frequency regions, a small half circle can be observed which indicates that pore diffusion resistance of the electrode material and it can see that straight line at low-frequency region indicates fabricated reduced graphene-SnO_2-polyaniline electrode material is an ideal capacitor property. The durability of the Platinum–cobalt/C cathode and performance curves in PEM fuel cell after different potential cycles operating at cell temperature of 40 °C. Polarization curves of PEM fuel cell with Platinum–cobalt/C cathodes exhibit a moderated degradation rate as the potential cycling number increased measured with the H_2–O_2 atmosphere. The open circle voltage (OCV) of the fuel cell is 0.98 V, which is lower than the commercial Pt/C cathode is about 1 V.

References

Abdalla AM, Hossain S, Azad AT, Petra PMI, Begum F, Eriksson SG, Azad AK (2018) Nanomaterials for solid oxide fuel cells: a review. Renew Sust Energy Rev 82:353–368

Alfaifi BY, Ullah H, Alfaifi S, Tahir AA, Mallick TK (2018) Photoelectrochemical solar water splitting: from basic principles to advanced devices. Veruscript Funct Nanomater 2:1–26

Bang JH, Suslick KS (2010) Applications of ultrasound to the synthesis of nanostructured materials. Adv Mater 22(10):1039–1059

Cho DH, Lee WJ, Park SW, Wi JH, Han WS, Kim J, Cho MH, Kim D, Chung YD (2014) Nontoxically enhanced sulfur reaction for formation of chalcogenide thin films using a thermal cracker. J Mater Chem A 2(35):14593–14599

Fan L, Zhu B, Su PC, He C (2018) Nanomaterials and technologies for low temperature solid oxide fuel cells: recent advances, challenges and opportunities. Nano Energy 45:148–176

Guo C, Lü Q-F, Zhao H-B (2015) SnO_2-decorated graphene/polyaniline nanocomposite for a high-performance supercapacitor electrode. J Mater Sci Technol 31:1101–1107

Kaltsa O, Gatsi I, Yanniotis S, Mandala I (2014) Influence of ultrasonication parameters on physical characteristics of olive oil model emulsions containing xanthan. Food Bioproc Tech 7(7):2038–2049

Lai WH, Su YH, Teoh LG, Hon MH (2008) Commercial and natural dyes as photosensitizers for a water-based dye-sensitized solar cell loaded with gold nanoparticles. J Photochem Photobiol A 195(2–3):307–313

Li J, Wu N (2015) Semiconductor-based photocatalysts and photoelectrochemical cells for solar fuel generation: a review. Catal Sci Technol 5(3):1360–1384

Li K, Liu X, Chen S, Pan W, Zhang J (2018) A flexible solid-state supercapacitor based on graphene/polyaniline paper electrodes. J Energy Chem 0:1–8

Mao SS, Shen S, Guo L (2012) Nanomaterials for renewable hydrogen production, storage and utilization. Proc Nat Sci Mater 22(6):522–534

Mor GK, Shankar K, Paulose M, Varghese OK, Grimes CA (2006) Use of highly-ordered TiO_2 nanotube arrays in dye-sensitized solar cells. Nano Lett 6(2):215–218

Niemann MU, Srinivasan SS, Phani AR, Kumar A, Goswami DY, Stefanakos EK (2008) Nanomaterials for hydrogen storage applications: a review. J Nanomater, Article ID 950967

Rajesh Kumar P, Suryawanshi PL, Gumfekar SP, Sonawane SH (2017) Ultrasound-assisted synthesis of conducting polymer-based electrocatalysts for fuel cell applications. Chem Eng Process 122:50–56

Rajesh Kumar P, Suryawanshi PL, Gumfekar SP, Sonawane SH, Ashokkumar M (2018a) Ultrasound-assisted synthesis of Platinum-cobalt/C bimetallic alloys for oxygen reduction in PEM fuel cells. Sustain Energy Fuels 2:1491–1499

Rajesh Kumar P, Suryawanshi PL, Gumfekar SP, Bhanvase BA, Sonawane SH (2018b) Sonochemical synthesis of platinum-cobalt/C electrocatalyst for PEM fuel cell applications. Surf Interfaces 12:116–123

Sharma JK, Akhtar MS, Ameen S, Srivastava P, Singh G (2015) Green synthesis of CuO nanoparticles with leaf extract of calotropis gigantea and its dye-sensitized solar cells applications. J Alloys Compd 632:321–325

Skorb EV, Andreeva DV (2013) Bio-inspired ultrasound assisted construction of synthetic sponges. J Mater Chem A 1(26):7547–7557

Suliman AE, Tang Y, Xu L (2007) Preparation of ZnO nanoparticles and nanosheets and their application to dye-sensitized solar cells. Sol Energy Mater Sol Cells 91(18):1658–1662

Valh JV, Vajnhandl S, Skodic L, Lobnik A, Turel M, Voncina B (2017) Effects of ultrasound irradiation on the preparation of ethyl cellulose nanocapsules containing spirooxazine dye. J Nanomater, Article ID 4864760

Wang XX, Tan ZH, Zeng M, Wang JN (2014) Carbon nanocages: a new support material for Pt catalyst with remarkably high durability. Sci Rep 4:4437

Wu JJ, Lee GJ (2018) Advanced nanomaterials for water splitting and hydrogen generation. In: Bhanvase BA, Vijay Pawade BA, Dhoble SJ, Hari Sonawane S, Ashok Kumar M (eds) Nanomaterials for green energy. Elsevier, pp. 145–167

Xia Z, Wang S, Jiang L, Sun H, Liu S, Fu X, Zhang B, Su DS, Wang J, Sun G (2015) Bio-inspired construction of advanced fuel cell cathode with Pt anchored in ordered hybrid polymer matrix. Sci Rep 5:16100

Yaldagard M, Seghatoleslami N, Jahanshahi M (2014) Preparation of Pt-Co nanoparticles by galvanostatic pulse electrochemical codeposition on in situ electrochemical reduced graphene nanoplates based carbon paper electrode for oxygen reduction reaction in proton exchange membrane fuel cell. Appl Surf Sci 315:222–234

Yang Y, Xi Y, Li J, Wei G, Klyui NI, Han W (2017) Flexible supercapacitors based on polyaniline arrays coated graphene aerogel electrodes. Nanoscale Res Lett 12:1–9

Zhou ZM, Shao ZG, Qin XP, Chen XG, Wei ZD, Yi BL (2010) Durability study of Pt-Pd/C as PEMFC cathode catalyst. Int J Hydrog Energy 35(4):1719–1726

Interaction of Heavy Crude Oil and Nanoparticles for Heavy Oil Upgrading

Rohan M. Jadhav and Jitendra S. Sangwai

Abstract The relevance of nanotechnology in the field of energy resources has been growing at a swift pace. The term 'catalyst' has a whole new outlook since the foundation of nanomaterials in process industries. Nanocatalysts, in general, play a vital role in the improvement of resource handling and process efficiency. New prospects to achieve sustainable processing have been made possible through the progress in nanotechnology. These developments of nanomaterials in the energy sector have also reached the parts of the oil and gas industry. In downstream processing of oil and gases, the use of nanocatalysts is commonplace. As the focus towards the production of heavy crude oil has seen an uprising, the use of nanomaterials has shown a promising scope in altering heavy oil properties to favour the oil recovery mechanisms. The majority of the reservoirs around the world have volumes of heavy crude oil with only a few effective ways to produce it. With the ever-growing energy demands it is of due importance that the focus has been shifted to implement nanotechnology in heavy oil production. This chapter discusses the role of nanomaterials in the development of heavy oil recovery. Different types of mechanisms that explain the effects of nanoparticles and their interaction with oil and its constituents are highlighted. The effects coupled with the use of various thermal treatment schemes have been explained. The scope of applicability in the field of flow assurance has been discussed. The use of nanoparticles in improving the existing EOR applications and devising new ways to achieve the production of heavy fractions.

Keywords Nanotechnology · Nanomaterials · Heavy oil · EOR · Thermal treatment

R. M. Jadhav
Department of Chemical Engineering, AC Tech Anna University, Chennai 600025, India

J. S. Sangwai (✉)
Gas Hydrate and Flow Assurance Laboratory, Petroleum Engineering Program, Department of Ocean Engineering, Indian Institute of Technology Madras, Chennai 600036, India
e-mail: jitendrasangwai@iitm.ac.in

L. Ledwani and J. S. Sangwai (eds.), *Nanotechnology for Energy and Environmental Engineering*, Green Energy and Technology,
https://doi.org/10.1007/978-3-030-33774-2_10

1 Introduction

Through the advent of nanotechnology at the turn of the century, nanomaterials have invariably become a part of our growing technology. Nanomaterials, especially due to their sizes are preferable over conventional materials for identical applications. The scope for development and the range of wide applicability makes nanotechnology suitable for a vast expanse of operations. Their use as catalysts has been duly appreciated in many areas of expertise. Industrial applications have also recognized the benefits of nanomaterials and have employed them for different purposes. Nanomaterials, for most of their part, have found generous use in the field of energy production. Worldwide energy generation processes (conventional and unconventional) use nanomaterials in some way or the other. This involvement of nanomaterials in the energy sector has been termed as nano-energy which is regarding the role of nanomaterials in harnessing energy from resources (Menéndez-Manjón et al. 2011).

When contemplating energy production it gives us a perspective of how abundantly we are dependent on non-renewable sources of energy. An ample amount of energy around the world is generated through the use of fossil fuels. The needs of power generation and fuel for transportation are only fulfilled through petroleum derivatives which makes the majority of the energy sector dedicated to the oil and gas industry. As such, the scene of economical energy has seen a shift due to the depletion of the worldwide oil and gas reserves. The existence and use of other renewable sources such as hydropower and solar energy to meet the global energy requirements will take a considerable amount of time due to limited accessibility. These situations have put the global energy scenario in a perilous situation. The majority of the oil reservoirs are facing depletion of light crude oil. Crude oil sitting at the bottom of the reservoirs is either void of the driving force or is relatively heavy. Also, the depletion of conventional oil and gas reservoirs has drawn the attention to produce heavy and extra-heavy oil from the unconventional reservoirs. The inherent properties such as viscosity and density of heavy oils make it difficult to extract them for further operations. Several enhanced oil recovery (EOR) processes have been employed to produce the oil deep down in the reservoirs. The emergence of nanotechnology has attracted the necessity to use nanomaterials in the production of heavy crude oil.

Nanomaterials are a broad classification of constituents whose range lies across the nanoscale (1–100 nm). These materials have numerous properties that are favourable for different kinds of applications. Nanomaterials can be used to enhance the attributes of other materials or to imbue them with new ones. Their main merit lies in the fact that the nature of their particle sizes makes them more efficient and effective in facilitating processes that would otherwise need a conventional material of larger dimensions. This chapter gives an overview of the properties of nanomaterials and their applications in the field of heavy oil recovery.

1.1 Need of Nanotechnology

Nanotechnology, in its entirety, focuses on using a minimal amount of resources to process large-scale operations. The reduction of the size of the particles itself is a profound way to utilize any material efficiently. The use of a few micrograms can do the same work that a few grams could do. This is a way to employ the conservation of resources sustainably. Everyday industrial processes generate a lot of unused substances. Nanomaterials, due to their dimensional advantages, minimize their specific amount required for any application which adds an edge to the whole operation regarding resource handling and usage. These properties make the use of nanoparticles an efficient way to achieve a stable groundwork between sustainability and effectiveness.

Nanotechnology and its facets have also shown potential in improving the effluent suppression and gas capture processes. Successful mitigation of greenhouse gases has been achieved in small scale processes involving nanomaterials. Materials such as nanoclay have been identified as a well-known and cheap alternative for CO_2 capture and have been an interesting area of research (Roth et al. 2013). In oil recovery, techniques such as CO_2 flooding using CO_2 foam have also been observed to provide better results with the addition of nanoparticles and improved sequestration of CO_2 (Aminzadeh-Goharrizi et al. 2012). Numerous applications can be found where nanomaterials are proven to be better alternatives in tackling these problems. A wide array of properties makes them versatile for some processes requiring high efficacy in energy production. This potential of nanomaterials makes them an attractive candidate in assisting environmental issues with smart solutions.

2 Properties of Heavy and Extra-Heavy Oils

Crude oil is a naturally occurring mixture of different fractions of carbon compounds. These fractions can be classified into groups of Saturates, Aromatics, Resins, and Asphaltenes (SARA) (Fig. 1). These together make the structure of oil and give it its various properties. The viscosity of oil is a vital property that affects its mobility in reservoirs. In the case of heavy and extra-heavy oils, viscosities up to 10,000 cp and higher have been observed. Tar sands being practically solid in nature pose extreme difficulty in extraction. The heavy oil which sits at the bottom of the reservoir creates a challenge as it is very difficult to displace. Owing to the depletion of lighter fractions, the processing of these heavier fractions has become important to sustain the fuel requirements. But what makes this a difficult task is the fact that the heavy and extra-heavy oils are unsusceptible to primary and secondary recovery treatments. Oils are characterized by their API (American Petroleum Institute) gravity. API gravity gives a comparison with respect to water of how heavy or light the oil is. Medium and heavy oils usually range from 25 to 15° API in comparison with light crudes

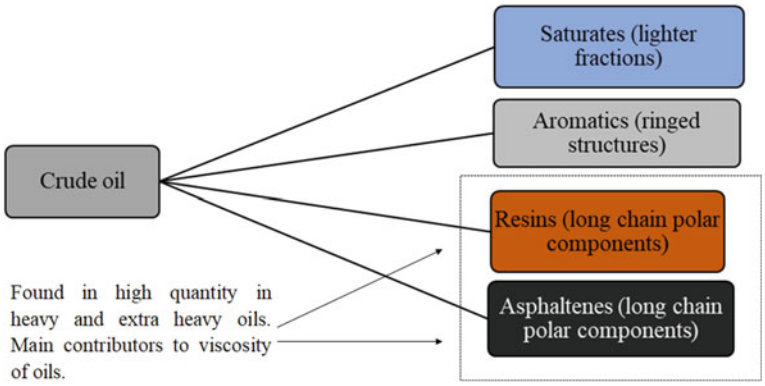

Fig. 1 Various fractions found in crude oil

which go above 30° API. Any hydrocarbon which goes below 15° API is considered extra-heavy.

Heavy oils are usually categorized by their inability to flow, highly viscous nature and difficulties posed by being inoperable by conventional techniques. The viscous nature of heavy oil is attributed to the presence of asphaltenes and resins which have a complex molecular structure with high molecular weight. This high viscous nature makes it difficult for further processing of light fractions. It mainly gets utilized in the production of asphalt, and upgrading processes like delayed coking and hydro-cracking. Asphaltene structures are high molecular weight polyaromatic chains containing heteroatoms (compounds containing nitrogen, oxygen, sulphur). They are present in the bulk oil as a suspension which influences the behaviour of the oil. Their deposition in the pipelines is a nuisance to flow assurance operations and require cumbersome treatments. Heavy crude oil treatment is basically how the heavy oil can be made accessible for further handling. The use of thermal treatments to mobilize heavy oil is an old practice. Understanding the interaction between heat and oil forms the basis of upgrading processes.

2.1 Heavy Oil Upgrading and Rheology

Upgrading of heavy oil in basic terms implies reducing the viscosity of heavy oil so it can be processed by downstream operations. Heavy and extra-heavy oils have viscosity several times higher than that of a conventional light crude oil. The reduction of the viscosity of such oils must be carried out through temperature intensive processes. The upgrading process to recover heavy oil from the reservoirs are as follows:

1. Cyclic Steam Stimulation/Steamflooding.
2. Fire flooding/In situ combustion.

3. Steam-assisted gravity drainage (SAGD).
4. Cold heavy oil production by sand (CHOPS).

The methods mentioned above are used, some more than others, and are important for the recovery of heavy and extra-heavy oils. Figure 2 gives the general operation of the steam flooding process. Inside the reservoir, the steam creates a heat front. This heat front comes in contact with the heavy oil, reduces its viscosity and pushes it towards the production well.

Steam-assisted gravity drainage is a relatively new technique that considerably increases recovery through effective steam usage. Two holes, one beneath the other are dug into the reservoir. The hole at the top injects steam into the reservoir. The heat from steam creates a chamber and reduces the viscosity of the oil, and it flows below under the influence of gravity. The bottom hole is then used for the production of oil. Figure 3 gives a representation of the process schematic of SAGD.

Cold heavy oil production with sand (CHOPS) is a non-thermal process that involves the production of sand. During completion stages, sand is calculatingly produced to improve the bottom oil recovery. Though this method allows the production of oil, it is mechanically exhaustive. CHOPS method has been only used in limited fields (namely Canada), thus it is crucial to have a well founded degree of understanding of the flow behaviour of oils. The flow behaviours are dependent on various factors that influence the rheological properties of heavy oils.

Understanding the rheology of heavy oils is of essential interest. The flow of oils in the reservoir is subject to the nature of the oil and its mobility in the reservoir. In comparison with lighter fractions, heavy oil proves to be a big inconvenience because of its characteristic flow properties. Better knowledge about the flow behaviours of these oils is important to figure out the appropriate method to extract them from the reservoirs. Heavy oil at ambient temperatures behaves as an extremely viscous fluid and, in some cases as a semi-solid. At higher temperatures, however, the oil matrix starts to break down and exhibits a Newtonian behaviour (smooth flow). The

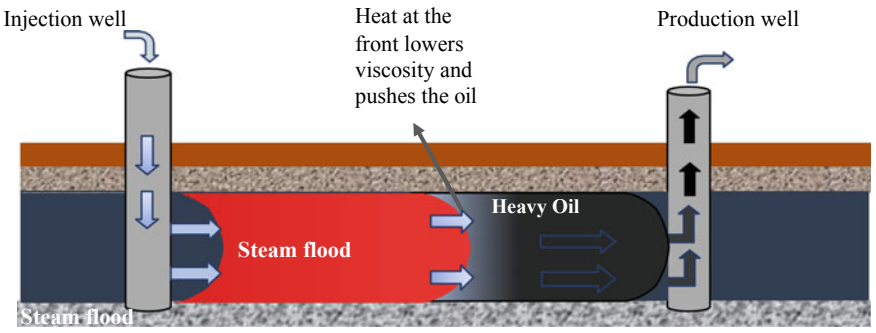

Fig. 2 An illustration of steam flooding

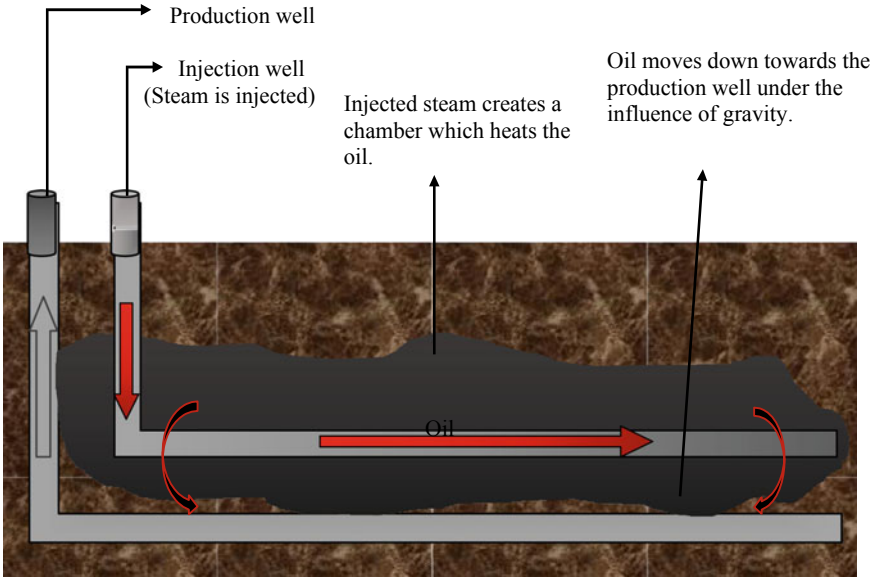

Fig. 3 Steam assisted gravity drainage (horizontal profile)

flow of these oils, at ambient temperatures is that of a Bingham plastic fluid which indicates that the semi-solid structure needs high shear to be broken down which can initiate flow in these oils (Ghaffari et al. 2017). Figure 4 shows the contrasting

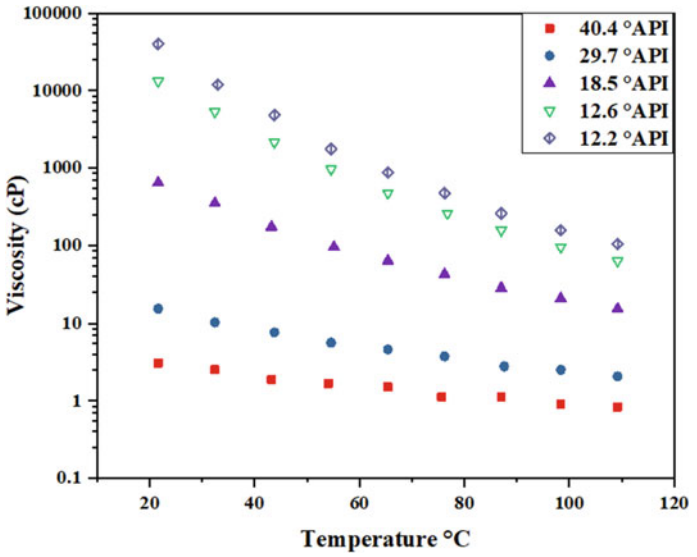

Fig. 4 Viscosity versus temperature of crude oils of various API gravities. Reprinted with permission from Ramírez-González (2016). Copyright (2016) American Chemical Society

viscosities of heavy oil and light oils (obtained from various fields in Mexico) at different temperatures (Ramírez-González 2016).

It is evident that the properties of heavy crudes differ by a large margin when compared with light crudes. This disparity between the two comes from the fact that the polar components dominate the oil matrix in heavy oils. The high molecular weight structure of asphaltenes and resins associate themselves with the oil which causes them to become viscous and dense in nature. In many instances at cracking temperatures, even heavy oils with lower asphaltene content can display asphaltene deposition whereas high asphaltene content oils exhibit a lower amount of deposition. This might happen due to the temperature affecting the asphaltene structure to a certain extent which allows deposition. Since these heavy oils are complex fluids, an accurate estimate of their behaviour is of questionable nature. These oils exhibit viscoelastic behaviour which is very deterministic of how they behave at high temperatures. Their viscoelastic behaviour can be quantified by observing how they work under a particular frequency of shear. These properties are characterized by loss and storage modulus (G″ and G′). These are of importance as they define the characteristics of the viscoelastic material which surfaces during deformations by shear. A more dominant loss modulus (G″) indicates a viscous flow indicating a liquid property of the fluid, whereas a prominent storage modulus (G′) is indicative of elastic nature which implies a solid property behaviour.

Figure 5 shows the dependency of loss (G″) and storage (G′) modulus on the

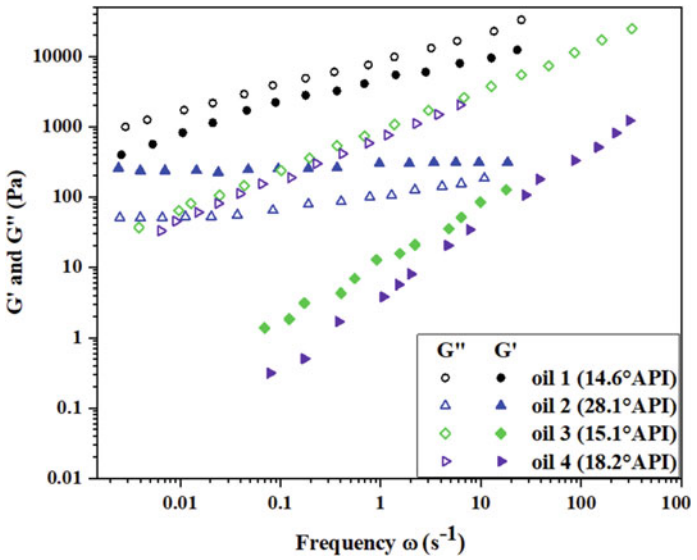

Fig. 5 Dependence of loss (open symbol) and storage (filled symbol) modulus (G″ and G′) with respect to deformation frequency of various oils (ranging from 14 to 28° API). Reprinted with permission from Ilyin and Strelets (2018). Copyright (2018), with permission from American Chemical Society

frequency of deformation for oils of different API gravity (ranging from light to heavy) obtained from different oilfields in Russia (Ilyin and Strelets 2018). It is evident that oils of different API gravities behave differently in the presence of different degrees of deformation (Fig. 5). Oil 1 with the lowest API gravity exhibits a narrow band between the loss and storage modulus. This indicates that heavy oils usually have a dominant solid behaviour at ambient temperatures hence the difficulty in mobilizing them. The deformation rates generate small cracks in the semi-solid structure of heavy oil. The oil matrix resists the changes in these deformations by rebounding back to the original structure, which brings forth the elastic nature. This corresponds to the solid behaviour of heavy oil. As the frequency and amplitude of shear changes, these small cracks can propagate into larger ones and initiate the flow of oil which points to the viscous behaviour of oil. These properties are of importance in understanding how the flow of these oils work and what can be done to improve it. This is relevant from transportation to processing of these oils. Their interaction with various chemicals and thermal treatments becomes the basis for understanding the recovery of these oils.

The processes to recover heavy oils are, however, sometimes too energy exhaustive and complex. Heavy oil recovery takes twice if not more time than the extraction of light crudes, which puts in perspective the difficulty of the entire process. The real challenge lies in the optimization of recovery processes. Since most of these methods utilise steam, the steam-to-oil ratio (SOR) determines the economic value of the said process. The SOR ratio shift can cause capital costs and requirements of the process to increase drastically making the process less feasible. Another aspect of using steam apart from providing heat to reduce viscosity is, it brings chemical changes in oil composition. Steam causes bond breakage and hydrolysis in oil structure (Clark and Hyne 1984). Usually, the first bond to break is sulphur–carbon as its dissociation energy is the lowest. The breaking of the sulphur bond helps in achieving low viscosity. This process is termed as aquathermolysis. Aquathermolysis is one of the main mechanisms in the upgrading of heavy oil. Methods to catalyze the aquathermolysis reactions draw attention towards nanoparticles and their abilities as catalysts.

3 Nanomaterials and Their Properties

Nanomaterials are classified as structures at the nanoscale level. They come in various shapes with different arrangements and properties. At such a small scale, their properties become rather profound. Small structural changes drastically affect the nature of the particles. The arrangement of the structures can be of various forms such as nanotubes, crystals, wires, rods and dendrites. They can also be identified based on their dimensional proportion, 1-dimensional, 2-dimensional, etc. A 1-dimensional particle will only have one of its sides in the nanoscale (i.e. a nanorod would only have its radius in nanoscale, and its length could be greater) as such goes for 2- and 3-dimensional particles (Tiwari et al. 2012). Figure 6 shows various structures (nanorod

Fig. 6 Various SEM and TEM images of **a** nanorod (Cao et al. 2017); **b** nanotube (Sandoval et al. 2017); **c** nanosheets (Wang et al. 2017). Reprinted with permission from Elsevier

(Cao et al. 2017), nanotubes (Sandoval et al. 2017), nanosheets (Wang et al. 2017)) of nanomaterials that can be fabricated. Specific shapes provide variable surfaces with different dimensional properties.

These specific characteristics define how the particles would behave in certain conditions and how they interact with their surroundings. Following are a few properties of nanomaterials:

1. **Surface Area to Volume Ratio**: The particles exhibit a very high surface area for a relatively small volume. This expansive area allows for an increase in surface activity. Since most reactions in chemical processes occur at the surface, this makes the surface activity of nanoparticles more suitable to facilitate reactions. This property has been seen to affect the flow behaviours of crude oil in many cases. The increase in surface action makes them excellent for adsorption mechanisms, by adsorbing materials on the active sites.
2. **Selectivity**: Nanoparticles show a highly selective nature. Specific types show an affinity towards only certain types of molecules. It has been specified in many cases that the active sites of nanoparticles influence the acidity–basic nature of the reactants and selectivity of the product formation when being considered as catalysts (Muraza and Galadima 2015).
   This selective nature allows certain catalyst particles to inhibit by-product formation and allow selective yield of product, which is a requirement for most chemical reactions.
3. **Structural Stability**: The nanomaterials possess superior structures compared to their conventional counterparts. The hardness of the material can be altered by introducing nanomaterials into a host material which imbues them with a more stable structure. An example would be the alteration of the hardness of magnesium done by adding silicon carbide nanoparticles to form composites with improved structural and mechanical properties (Lan et al. 2004). Graphene-based nanoparticles which are, in comparison, smaller than graphene sheets can be used to form composites to give extra mechanical stability and flexibility to other materials.
4. **Optical Properties**: The optical properties concerning the emission and scattering of light are important for many photochemical processes. The optical properties of nanoparticles are useful in characterization studies of other substances.

An example would be the use of optical properties of gold nanoparticles in the field of medicine for photothermal therapy (Huang and El-Sayed 2010).

5. **Magnetism**: Nanomaterials exhibit magnetism which can be utilized in a number of ways. These can be used for magnetically induced heating in nanofluid applications.

One of the fascinating aspects of nanoparticles and their properties is that they can be crafted to suit particular requirements. There are several methods to attain desirable properties (high surface area, selectivity) and shapes (clusters, nanowires, etc.) in these materials. There are namely two broad classifications of processes involved in nanoparticle production, top-down process and bottom-up process.

The top-down process can be visualized as breaking down of a particular material until nanoscale is reached. Top-down processes usually involve more mechanical input for achieving a reduction in size. Some examples are high energy milling, laser ablation process, nano-lithography, etc.

The bottom-up methodology is the technique which proceeds from individual molecules and atoms to nanoparticle formation. They are widely used because they give high-purity particles and are more preferred for the structural stability of nanoparticles. These processes also allow more control over the size distribution and structure manipulation. Some examples would include the sol-gel process, epitaxial growth processes (atomic, molecular liquid phase), vapor deposition techniques, etc. Figure 7 gives a visual understanding of the processes involved in the fabrication of nanomaterials from the two methods.

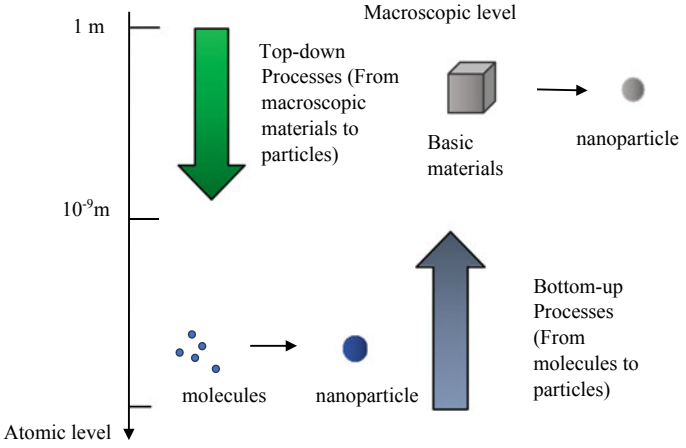

Fig. 7 Fabrication routes of nanomaterials

4 Role of Nanomaterials in Heavy Oil Recovery and its Operations

In oilfields, after the primary and secondary oil recovery is done, the reservoir is subjected to external stimulation to retrieve the oil which cannot be produced due to the absence of a driving mechanism. The methods applied at this stage are termed as Enhanced Oil Recovery. These methods can also be applied at the primary stage is the oil is not mobile, as in the case of heavy oil. Processes such as gas injection, polymer injection, steam flood, steam injection, etc., provides the heat to reduce viscosity and also driving force to mobilize the oil at the bottom of the reservoir to increase the production. This is achieved by injecting an external agent (liquids or gases) into the reservoir to push the oil towards the production wells. There are several strategies and methods to execute enhanced oil recovery techniques (thermal, chemical and microbial EOR). Heavy oils being extremely dense and viscous are indispensably subjected to heat treatment to unlock their movement. The interaction between oil and nanomaterials has been an area of interest and its use in oil recovery has seen quite a development. Especially, the treatment of heavy oil and heavy fractions has seen substantial growth in terms of nanotechnology applications.

4.1 Interaction with Nanoparticles and its Effects on Heavy Oil Properties

Involving nanotechnology in the field of heavy oil recovery is a way of exploring efficient ways to implement the same process but with improved results. A clear understanding of how these particles interact with the oil in reservoir conditions is an area of extensive research. Their effects on parameters such as rheology of heavy oil, compositional changes, etc., have been closely studied to obtain insight on how to improve the processing of these oils. Metal and metal oxide particles have shown considerable improvement in altering heavy oil properties. Heavy oil is a complex mixture with a myriad of properties that influence each and every aspect of its flow behavior. Heavy oils are laden with asphaltenes in the bulk which imparts them with their semi-solid structure. Breaking or more technically called ‘cracking’ of the asphaltene structure is the first step in making the oil more accessible to further treatment. Cracking also distributes the long-chain asphaltene into lighter fractions which increases the value of the oil.

4.1.1 Metallic Nanoparticles

Nanoparticles show intriguing behaviour when they are used for thermal treatments of these heavy oils. Their effects in catalyzing the breaking of bonds in heavy oil

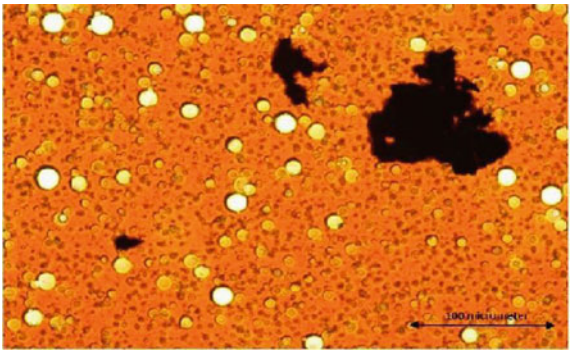

Fig. 8 Asphaltenes (black patch) forming clusters in the presence of nickel nanoparticles in heavy oil, observed after aquathermolysis (240 °C for 6 days) under a microscope. Reprinted with permission. Shokrlu and Babadagli (2014). Copyright (2014) From Elsevier

were first observed by Clark and Hyne in 1984. Further developments in identifying the catalyzing properties of metals were found in the subsequent years. Their effects on heavy oils were observed by Shokrlu and Babadagli (2014) in a series of aquathermolysis reactions. Asphaltenes were found forming clusters on the surface of nanoparticles (Cu, Fe and Ni) of different diameters. This effect has been supported by many literature stating that the surface properties play a key role in causing clustering. Figure 8 shows the microscopic image of the clustering of asphaltenes observed after aquathermolysis of heavy oil (14.7° API) in the presence of nanoparticles.

Asphaltene particles when present in the bulk oil show a charge distribution across the bulk. Along with resins, they are polar in nature. They exhibit positive charge in most cases but there have been instances in which they exhibit a negative charge across a mixture (Azari et al. 2018). The nature of the asphaltene chains and the presence of heteroatoms influence the charge distribution. Surface charges possessed by nanoparticles influence the adsorption of asphaltenes (Patel et al. 2018). The charge difference in the nanoparticles and asphaltenes causes the adsorption. When asphaltenes come in contact with nanoparticle surfaces, the aggregation process occurs. This aggregation lowers the charge on asphaltene aggregates thereby making them stable (Azari et al. 2018) and less prone to attach back to the bulk of the oil.

Figure 9 illustrates the surface activity and charge of nanoparticles attracting the asphaltenes. Metallic nanoparticles are also excellent heat conductors (Eastman et al. 2001) which when added to heavy oil can increase the heat flow in the oil, effectively reducing the viscosity. Heat conduction due to dispersed nanoparticles can facilitate faster reactions aiding in the reduction of viscosity and catalyzing the aquathermolysis process. Dispersed nanoparticles can be used as nanofluids with high thermal conductivity. The agglomeration removes the asphaltenes from the bulk of the oil which makes the oil less viscous. The cohesive forces between the asphaltene molecules progress the agglomeration. This effect has been observed even in heavier fractions such as bitumen and residual oils. Another approach by means of hydrogen donors has been looked into to upgrade these residual and heavy oils (Del Bianco et al. 1995). Upgrading by using hydrogen donors is an efficient way to improve the Hydrogen/Carbon (H/C) ratio (Hendraningrat et al. 2014; Wang et al. 2012). Hydrogen donors are additional agents which provide hydrogen to improve hydrogen ratio. Hydrogen donors can be solvents, hydrogen gas or hydrogen-producing bacteria which can involve hydrogen into a system. Solvents can be utilized as an effective means of providing hydrogen in heavy oil systems. Nanoparticles can make stable emulsions with solvent mixtures to provide better action with heavy oil (Kumar et al. 2018). Figure 10 shows the viscosity reduction of heavy crude oil (Venezuela fields) in the presence of carbon support nickel nanoparticles (Guo et al. 2017). They have utilized a highly conductive form of carbon black (Ketjenblack) as a support to boost the performance of nickel particles.

It is apparent from Fig. 10 that the viscosity reduction in the presence of hydrogen gas has the highest impact. Nickel particles having carbon nanostructures as support in the presence of hydrogen gas reduce oil viscosity by a greater margin.

Heavy and extra-heavy oils usually have a poor H/C ratio which makes them more likely to form coke at high temperatures. Coke formation takes place due to the reason that heavy oil undergoes a disproportionation reaction and produces an unusual amount of carbon with little or no hydrogen. When the cleavage of the C–S bond takes place during aquathermolysis, the removal of sulphur makes the molecules undergo polymerization to form a higher molecular weight structure to stabilize. By providing hydrogen, further polymerization remains in control and the

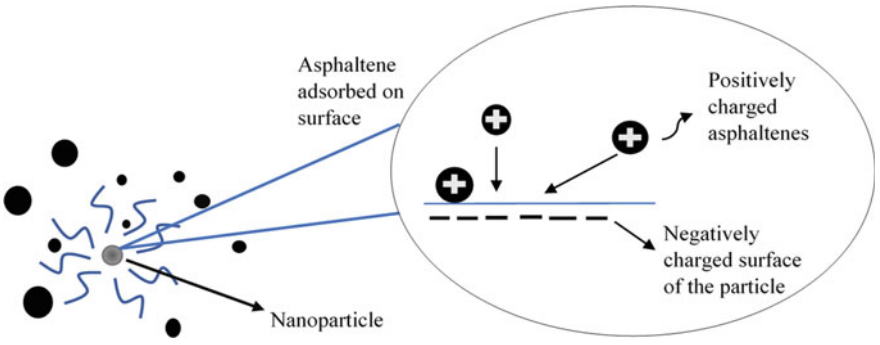

Fig. 9 Charge of nanoparticles affecting the asphaltene adsorption

formation of intermediate structures becomes stabilized. Desulphurization process is of importance because apart from the reduction of viscosity it reduces the sulphur content thereby upgrading the oil (Guo et al. 2018). Thiophene is an active compound found in the asphaltene structures and requires desulphurization to upgrade the oil. Figure 11 shows the thiophene (heterocyclic aromatic) catalytic conversion under the influence of cobalt and nickel nanoparticle of different sizes. The desulphurization was more successful with nickel nanoparticles of smaller size. Nickel usually exhibits a better catalytic activity due to being more electronegative in nature. The ability of transition metal compounds to alter their oxidation states is of importance in relevance with their catalytic activity. The common trend in the activity of transition elements is a direct correlation to the element's electronegativity playing a dominant part in their roles as catalysts. As they can donate and accept electrons readily, they serve as excellent catalysts for reactions. The surface and electrostatic properties of nanoparticles are the main contributors to viscosity alteration mechanisms.

It is apparent from Fig. 11 that the size and concentration of nanoparticles are a deciding factor in C–S bond breakage and the reduction of viscosity. Increase in the size of nanoparticles directly result in an increase of the particle volume. Since the reactions occur on the surface and not inside the bulk, the increased volume causes hindrance and the effectivity is decreased. When the concentration of nanoparticles in a fluid increases, the individual activity of attraction of particles comes into play (Rudyak 2013). The attraction between the particles can be attributed to van der Waals force of attraction. As the concentration of particles increases, the attraction between the nanoparticles become more prominent than the interaction of the particles and oil.

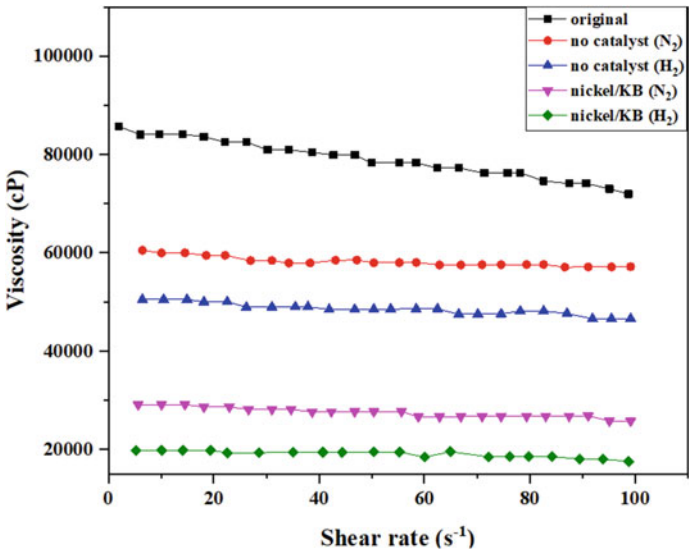

Fig. 10 Effects of nickel nanoparticles with ketjenblack carbon support in reducing viscosity of heavy crude oil. Reprinted with permission (Guo et al. 2017). Copyright (2017)

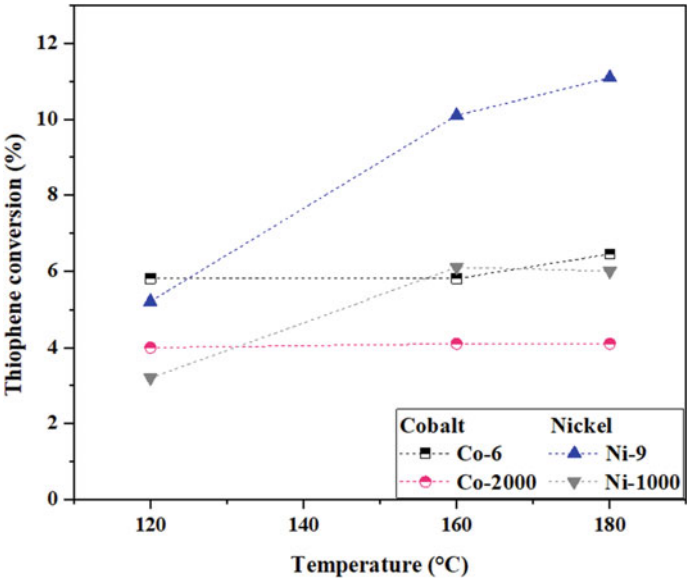

Fig. 11 Temperature versus thiophene conversion under the influence of nanoparticles (Co, Ni) of different sizes. Reprinted with permission (Guo et al. 2018). Copyright (2018)

As the oil viscosity reduces the entire oil molecule structure starts to slacken up. This causes the movement of nanoparticles to become more erratic and prone to collisions. There is a destabilization due to an increase in surface energy. At higher temperatures, the reduction of oil viscosity can cause metallic nanoparticles to coalesce together to form small aggregates (Hashemi et al. 2012). These aggregates can inversely affect the viscosity of oils by causing a surge in the viscosity of the oil.

Nonetheless, metallic particles can effectively catalyze aquathermolysis to cause a reduction in viscosity of oils. As the oil comes in contact with high-temperature steam, viscosity reduction of oil occurs. This action can be coupled with the viscosity reducing property of metallic nanoparticles in different injection schemes to further improve the process. These particles can be used in reservoirs at the end stages of the steam stimulation process to initiate more recovery of oil (Farooqui et al. 2015). As recovery decreases at the end stages, nanoparticles can be used as a final drive to recover the oil.

4.1.2 Metal Oxides

Other than metal particles, metal oxides are also effective in changing the property of heavy oils. Metal oxides nanoparticles are capable of causing asphaltene deposition on their surfaces. Metal oxides are rather easy to produce and can have better catalytic life. Their catalyst potency lies in their charge distribution. Asphaltene deposition

by the use of metallic oxides has been observed in many cases. Table 1 provides an overview of the various nanoparticles used in the studies.

It is evident that transition metals and metal oxides are excellent in improving the adsorption of asphaltene, reducing coke formation and increasing the catalytic efficiency of cracking reaction. Apart from being able to suppress asphaltene precipitation, metal and metal oxide nanoparticles are effectively able to break sulphur

Table 1 Literatures involving various metal oxides and their impact on asphaltene processing

S. no.	Nanoparticle	Experimentation	Results	Source
1.	Titanium oxide (TiO_2) in the presence of an electric charge	Upgrading of asphaltenes	Charged TiO_2 particles initiated the degradation of oil and achieved catalysis and breaking of heavy fractions	Lai et al. (2017)
2.	Oxides of Cerium, Cobalt and Manganese (CeO_2, Co_3O_4, MnO_2)	Catalytic cracking of residual oil by the aid of supercritical water and synthesized nanoparticles	Cerium oxide particles were the most stable during supercritical water cracking and had the ideal adsorption	Golmohammadi et al. (2016)
3.	Oxides of silicon, nickel and iron (SiO_2, NiO, Fe_2O_3)	Adsorption of asphaltenes in the presence of n-heptane	Silicon oxide was the most optimal in adsorption with a concentration of 2000 ppm followed by nickel and iron oxides	Kazemzadeh et al. (2015)
4.	Dispersed iron oxide (Fe_2O_3)	In-situ catalytic upgrading of heavy oil	A decrease in viscosity of the oil and an increase in API gravity and lighter fractions	Al-Marshed et al. (2015)
5.	Iron oxide (Fe_3O_4)	Catalytic oxidation and adsorption of thermally cracked asphaltenes	Drop in oxidation temperature (from 380 °C to 220 °C) and decrease in activation energy increasing the adsorption	Nassar et al. (2012)
6.	Oxides of cobalt, nickel and iron (Fe_2O_3, Co_3O_4, and NiO)	Steam cracking of asphaltenes for heavy oil upgrading	Catalytic activity is subject to adsorption effectiveness. Nickel oxide had the best adsorption	Nassar et al. (2011)

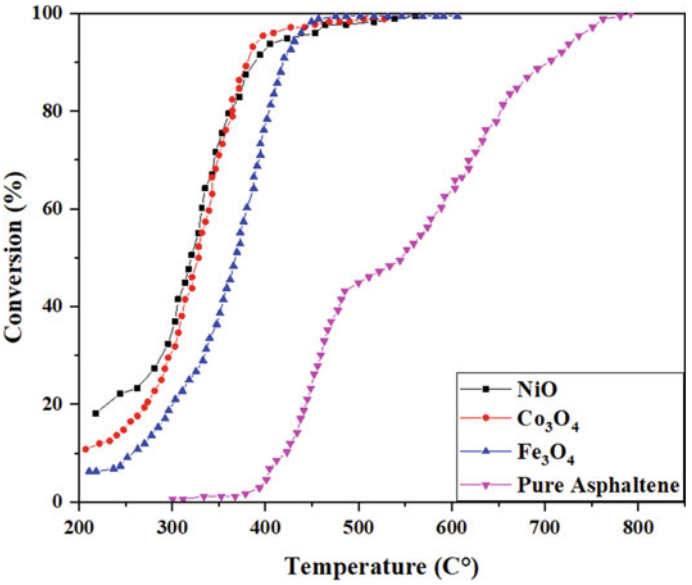

Fig. 12 Catalytic conversion of asphaltenes during steam cracking process under the influence of different nanoparticle oxides (nickel, cobalt, ferrous) used as catalysts. Reprinted with permission (Nassar et al. 2011). Copyright (2011)

linkages. As discussed earlier, the dissociation energy of sulphur–carbon bond is low and hence breaking of the bond can be achieved more rapidly by the addition of nanoparticle catalysts. Metal oxides, due to their ability to change their oxidation states more easily are an interesting candidate for asphaltene adsorption and cracking. Figure 12 shows the conversion of asphaltene during steam cracking reactions and how the presence of different nanoparticles effects the cracking temperatures (Nassar et al. 2011). The asphaltene was extracted from Athabasca bitumen and was subjected to adsorption and subsequent cracking process with nanoparticles.

It can be seen from Fig. 12 that the highest conversion effects were observed in the presence of Nickel oxide nanoparticles. In case of asphaltenes adsorbed on nanoparticles, the onset of cracking temperature was found to reduce with the highest reduction observed in cobalt and nickel oxide nanoparticles when compared to iron oxide nanoparticles and pure asphaltene. This is indicative of the fact that metal oxides can readily provide a better reduction in activation energy to initiate asphaltene cracking reactions.

4.2 *Effects of Dispersion on the Performance of Nanoparticles*

The means by which nanoparticles are introduced into heavy oil systems are also important in determining the reduction of viscosity and upgrading of heavy oil. The dispersion of particles in either the oil phase or water phase is crucial when it comes to the interaction of these particles with the oil matrix. As the particles get dispersed, the stability of the system increases which prevents the degradation of the catalytic activity of the particles. The dispersion of the particles can be achieved in both oil and water depending on the hydrophilic/hydrophobic or lipophilic/lipophobic nature of the particles.

Metals and their compounds such as nickel and even the likes of molybdenum can be dispersed using surfactants in water to be utilized for steam cracking processes (Mironenko et al. 2017). Salts and other composites of transition metals also possess the ability to catalyze upgrading operations. An example would be Keggin-structured (heteropoly acid structure) catalysts which can aid viscosity reduction in aquathermolysis reactions (Chen et al. 2009). The main advantages of these acids are that they are re-usable acid catalysts and can increase the catalyst life. Water-solubility of nanoparticles allows a simple dispersion. These particles can be directly utilized in aqueous applications by forming emulsions and stable mixtures for thermal methods. Water dispersed particles, though effective, can cause a hindrance when their effects are mediated in the presence of oils. In this case, oil-soluble catalysts can allow much better dispersion in the oil phase and be more effective that the water-soluble counterparts. Proper dispersion in the oil phase can improve the viscosity altering effects during in situ processes. Oil-soluble nickel and cobalt are ideal at producing catalyzing effects at low concentrations when used with hydrogen donors for aquathermolysis process.

Certain types of catalyst nanoparticles which can be dispersed in both oil and water called dispersed catalyst nanoparticles have shown remarkable performance in recovery operations. These catalysts can be dispersed with the help of surfactants or organic dispersants and have been found to be more effective than the usual oil-soluble and water-soluble catalysts. These catalysts can be in the form of organometals or suspensions of nanoparticles. Dispersed catalysts of nickel nanoparticles have been used for the upgrading of heavy oil (Alkhaldi and Husein 2014; Li et al. 2007). Effective aquathermolysis can be achieved in the presence of dispersed catalysts because they can be dispersed in both oil and water. Since the dispersion in oil and water is high, the contacting between these two can result in a better aquathermolysis process allowing better cracking. Silica nanoparticles are extremely versatile as far as dispersions are concerned. They can be dispersed quite efficiently in both oil and water (Gavrielatos et al. 2017). They have excellent prospective in development for heavy oil upgrading. They are a cheaper alternative to the metal and metal oxides and are utilized widely.

The dispersions can also be made up of combinations of metals. Multimetallic particles are something which is not common and these can be dispersed in heavy

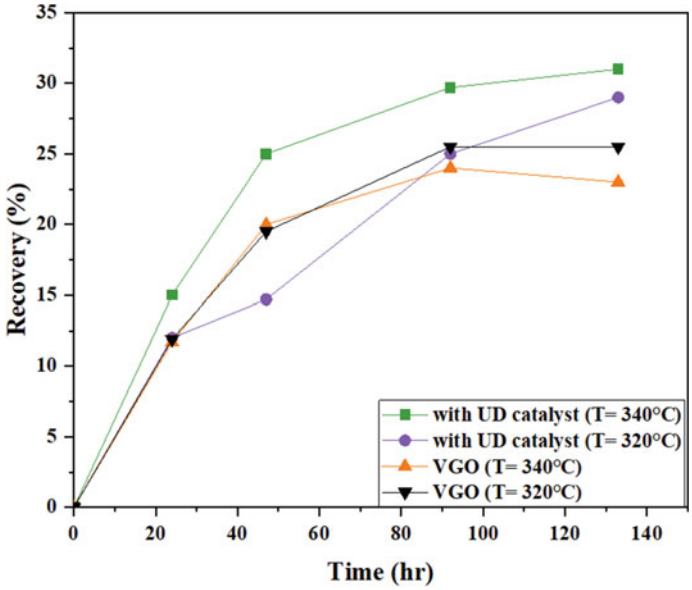

Fig. 13 Effects of ultra-dispersed catalyst (NiMoW) on recovery of vacuum gas oil at two temperatures (340 °C and 320 °C) with time from the sand pack experiment. Reprinted with permission (Hashemi et al. 2013). Copyright (2013)

fractions. Multimetallic particles are more focused on incorporating the individual properties of specific metals into a single particle. An example would be a mixture of asphaltene adsorption properties of nickel and better hydrodesulphurization properties of molybdenum and tungsten (Hashemi et al. 2013). Figure 13 shows the recovery plots in a fluid flooding process involving vacuum gas oil (Nexen, Alberta) in the case of ultradispersed (UD) trimetallic (NiWMo) colloidal nanoparticles.

It is evident from Fig. 13 that multimetallic nanoparticles are effective in colloidal dispersions to recover heavy fractions. As the temperature increases, the effectivity of the particles becomes more prominent in recovering the gas oil. At 340 °C the vacuum gas oil recovery sees a plateau which is in contrast with the increased recovery through the dispersed catalyst at the same temperature.

The effectiveness of dispersed catalysts stems from the fact that apart from being dispersive in both oil and water, they affect the interface and give a dynamic surface for the temperature and water to break down heavy oil structure. The effectiveness of individual nanoparticles can be increased by using them as emulsions and nanofluids. Nanoemulsions (nanoparticles forming colloidal suspensions in fluids) have shown prospective development in oil recovery experiments. They can be developed from many types of nanoparticles which can be used for the formation of suspensions. Other than thermal methods use of miscible injection coupled with thermal methods has also been shown to improve oil recovery. They produce changes in interfacial tension and altering the reservoir rock properties. Heat intensive processes are one of

the best ways to obtain high recovery of heavy oil. However, there are other methods that involve the use of injecting miscible gases and uses of solvents to treat heavy oil have also seen a rise in the production of heavy oil.

4.2.1 Nanoparticle Stabilized Miscible Flooding

Miscible flooding operations and their impact are entirely dependent on the changes in interfacial tension of the oil, reservoir rocks and the miscibility of the gas with oil. Miscible gases cause swelling of oil which helps the oil inside pores to flow more easily and allow better recovery. The arrangement of particles at the interface controls the strength of the interfacial tension (IFT). IFT reduction is crucial for processes such as miscible injections. The applicability of metal oxide nanoparticles has pronounced effects on the IFT in the CO_2 injection process for heavy oil and CO_2 upgrading systems. CO_2 injection is an effective mechanism to reduce IFT in heavy oil systems. CO_2 dissolution also helps in lowering the viscosity of heavy oils (Hu et al. 2015) and is usually employed in an alternating miscible scheme to recover oil. The only limitation being the precipitation of asphaltenes because of CO_2. They reported that the addition of metal oxide nanoparticles in tandem with CO_2 injection gave a significant reduction in IFT. Even at higher asphaltene contents, the reduction of IFT was appreciable. Figure 14 depicts the IFT reduction with increasing asphaltene content in the presence of nanoparticles with different oil samples (various API ranging from 16 to 26) obtained from various oil reservoirs in Iran (Kazemzadeh et al. 2018). Figure 14b depicts that nickel oxide particles exhibit a steady decrease in IFT as the asphaltene content increase. The charge distribution of nickel oxide is effective in attracting asphaltenes away from the interface, thereby reducing IFT. The deposition of asphaltenes on the surface of metal particles allows more room for IFT reduction which in turn allows more CO_2 to get miscible with the oil hence improving the sweep of oil.

Another strategy to use CO_2 is in the form of foam. The foam helps in increasing the sweep and reduce mobility ratio. Foam also acts as a gas blocking agent which further helps in the recovery of oil. Foam injection coupled with other EOR techniques can give very effective results in mobilising oil. Consequently, to improve the efficiency of CO_2 foams, nanoparticles can be used as stabilizers to maintain the foam structure inside the reservoirs. The stability of foams can be improved to achieve better effects in the distance up to which the foams can propagate in the reservoir. The hydrophilic/hydrophobic nature of nanoparticles helps in the stabilization of CO_2 foam. Occupancy of nanoparticles at the CO_2 interface provide thermal stability to the foam at reservoir temperatures (Espinosa et al. 2010). Nanoparticle-stabilized foams can provide a better sweep at a pore scale-level, which can result in the increased overall recovery of oil (Nguyen et al. 2014). The use of nanofluids in an alternating slug injection pattern coupled with CO_2 also results in inhibition of asphaltenes. Lu et al. (2016) observed that asphaltene precipitation can be inhibited by asphaltene adsorption on Al_2O_3 nanofluids. Using the nanofluids slug in

association with CO_2 flooding can increase the adsorption at high concentrations of nanofluid.

4.2.2 Applications in Areas of Flow Assurance

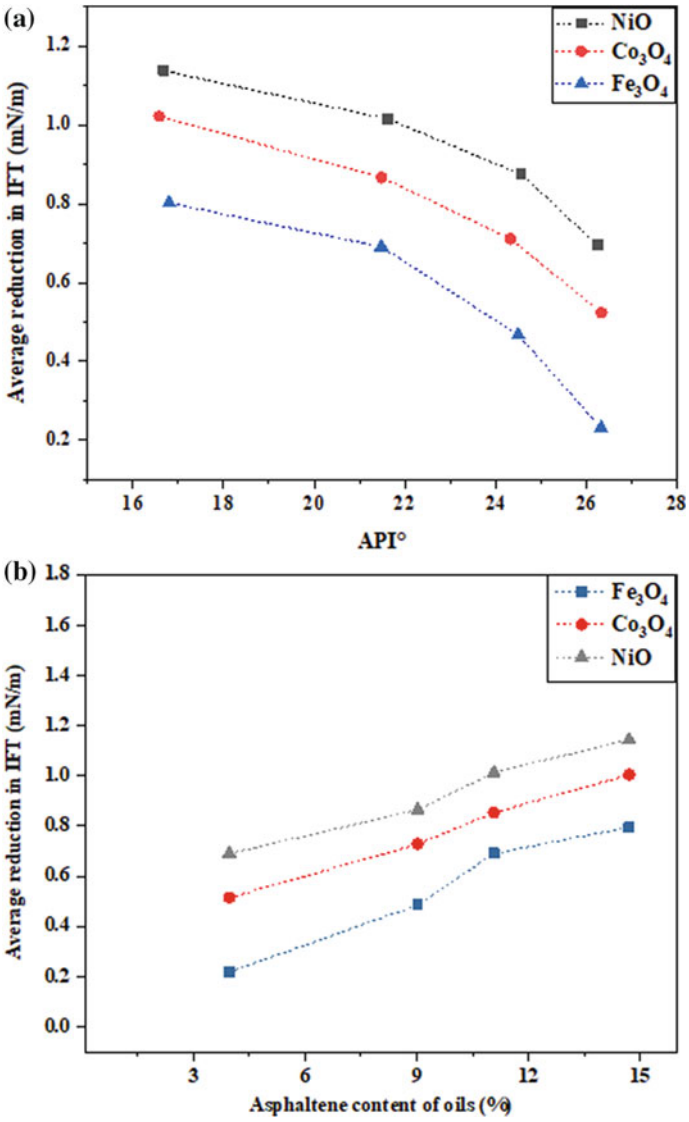

Fig. 14 Effect of nanoparticle dispersion: **a** Reduction in IFT of different API oils; **b** Reduction in IFT versus Asphaltene content (%) of the four oil samples. Reprinted with permission (Kazemzadeh et al. 2018)

Areas of flow assurance also face the disruption of processes caused by heavy oil transportation. Flow assurance deals with the efficient flow of recovered hydrocarbons from the reservoirs to the processing industries. Flow assurance has become an important term in the production process of oil transportation scenario owing to the need for ensuring the smooth working of the processing facilities. Difficulties in flow assurance operations (asphaltene deposition, hydrates, wax deposition, etc.) can cause major problems on a large scale. Problems in flow can cause processing delay which can lead to loss of capital. Heavy oils especially due to their viscous nature and asphaltene deposition cause flow stringencies. They get deposited on the inner surface of pipelines forming large blockages and restricting flow. Different mechanisms exist to counter the problems of asphaltene deposition such as solvent and asphaltene inhibition treatments but these techniques become troublesome at subsea levels.

Few applications have been sought out using nanoparticles and their properties to find a solution to these problems. Nanofluids can be used as asphaltene inhibitors to control the precipitation. Mohammadi et al. (2011) have tested the asphaltene inhibition qualities of silica-, zirconium- and titanium-based nanofluids and found that titanium oxide nanofluids were effective in controlling asphaltene precipitation at acidic conditions. Owing to the hydrogen bonding caused between the nanoparticles and asphaltenes, the precipitation is limited. The use of heating to keep the flow in check has also been explored through the use of paramagnetic nanoparticles for subsea pipelines (Mehta et al. 2014). It has been observed that nanoparticles exhibiting paramagnetic behaviour generate heat when under the influence of a magnetic field. These can be developed to provide temperature control over the flow of hydrocarbons inside the pipe. Such innovative solutions in the field of flow assurance have seen steady growth, allowing further optimal processing.

4.3 Challenges in the Application of Nanotechnology

Nanomaterials certainly have their advantages and potential in the field of heavy oil recovery. Excellent use as catalysts in enhancing the existing EOR techniques is significant merit. However, limitations can be found in the applications which can negatively impact the process economy. Fabrication processes of nanomaterials are quite expensive which makes them a priced commodity. It is evident that EOR operations require the injection of copious volumes of stimulants into the reservoir to extract oil. Injection of nanomaterial-based stimulants can affect the economy of the process. This heavily affects the application of nanomaterials on operational terms.

Introducing nanoparticles in the reservoir is a dicey gamble when it comes to the recovery of these particles. Obtaining these particles back from the reservoir can pose a major challenge as the particles, if once injected, may not be recovered completely. Applications involving the extraction of magnetic particles have been under development which can effectively recover a certain degree of particles. Extracting particles from recovered oil should also be a viable option to improve the recovery

of nanoparticles. Another challenge is the aspect of reusability. Reuse of particles should be an option that can guarantee a longer process life. The life of the particles should be high, as the time period for production can vary and the particles should be functional for a long time.

5 Conclusion

Nanotechnology is just beginning to find its applications in oil recovery operations, more so in heavy oil recovery. Tackling different problems of fields related to, production processes and reservoir geology is something which is being constantly improvised to find better solutions. Nevertheless, nanomaterials have shown potential in altering the properties like viscosity and sulphur content of heavy oils. Their extraction processes can certainly be optimized to ensure a better recovery and provide a new outlook at the production of heavy oil. Heavy oil is certainly the next step in catering to the increasing fuel requirements. Field applications of utilizing nanomaterials are on the run. Identifying new and efficient strategies can positively unlock reservoirs of heavy oil to harness and sustain the energy needs.

References

Alkhaldi S, Husein MM (2014) Hydrocracking of heavy oil by means of in situ prepared ultradispersed nickel nanocatalyst. Energy Fuels 28:643–649

Al-Marshed A, Hart A, Leeke G, Greaves M, Wood J (2015) Optimization of heavy oil upgrading using dispersed nanoparticulate iron oxide as a catalyst. Energy Fuels 29:6306–6316

Aminzadeh-Goharrizi B, DiCarlo DA, Chung DH, Kianinejad A, Bryant SL, Huh C (2012) Effect of nanoparticles on flow alteration during CO_2 injection. In: SPE annual technical conference and exhibition, San Antonio, Texas, USA, 8–10 October. SPE 160052

Azari V, Abolghasemi E, Hosseini A, Ayatollahi S, Dehghani F (2018) Electrokinetic properties of asphaltene colloidal particles: determining the electric charge using micro electrophoresis technique. Colloids Surf A 541:68–77

Cao T, Zhou Z, Chen Q, Li Z, Xu S, Wang J, Xu M, Bisson T, Xu Z (2017) Magnetically responsive catalytic sorbent for removal of Hg^0 and NO. Fuel Proc Technol 160:158–169

Chen Y, Wang Y, Lu J, Wu C (2009) The viscosity reduction of nano-keggin-K3PMo12O40 in catalytic aquathermolysis of heavy oil. Fuel 88:1426–1434

Clark PD, Hyne JB (1984) Steam-oil chemical reactions: mechanisms for the aquathermolysis of heavy oils. Aostra J Res 1:15–20

Del Bianco A, Garuti G, Pirovano C, Russo R (1995) Thermal cracking of petroleum residues: 3. technical and economic aspects of hydrogen donor visbreaking. Fuel 74:756–760

Eastman JA, Choi SUS, Li S, Yu W, Thompson LJ (2001) Anomalously increased effective thermal conductivities of ethylene glycol-based nanofluids containing copper nanoparticles. Appl Phys Lett 78:718–720

Espinosa D, Caldelas F, Johnston K, Bryant SL, Huh C (2010) Nanoparticle-stabilized supercritical CO_2 foams for potential mobility control applications. In: SPE improved oil recovery symposium, Tulsa, Oklahoma, USA, 24–28 April. SPE 129925

Farooqui J, Babadagli T, Li HA (2015) Improvement of the recovery factor using nano-metal Particles at the late stages of cyclic steam stimulation. In: SPE Canada heavy oil technical conference. Calgary, Alberta, Canada, 9–11 June. SPE-174478-MS

Gavrielatos I, Mohan R, Shoham O (2017) Effect of intermediate wettability nanoparticles on oil-water emulsion stability. J Petrol Sci Eng 152:664–674

Ghaffari A, Sharifi K, Ivakpour J (2017) An experimental study on the effects of temperature and asphaltene content on the rheological behavior of vacuum residues. Pet Sci Technol 35:768–774

Golmohammadi M, Ahmadi SJ, Towfighi J (2016) Catalytic cracking of heavy petroleum residue in supercritical water: study on the effect of different metal oxide nanoparticles. J Supercrit Fluids 113:136–143

Guo K, Zhang Y, Shi Q, Yu Z (2017) The effect of carbon-supported nickel nanoparticles in the reduction of carboxylic acids for in situ upgrading of heavy crude oil. Energy Fuels 31:6045–6055

Guo K, Hansen VF, Li H, Yu Z (2018) Monodispersed nickel and cobalt nanoparticles in desulfurization of thiophene for in-situ upgrading of heavy crude oil. Fuel 211:697–703

Hashemi R, Nassar NN, Pereira-Almao P (2012) Transport behavior of multimetallic ultradispersed nanoparticles in an oil-sands-packed bed column at a high temperature and pressure. Energy Fuels 26:1645–1655

Hashemi R, Nassar NN, Pereira Almao P (2013) Enhanced heavy oil recovery by in situ prepared ultradispersed multimetallic nanoparticles: a study of hot fluid flooding for Athabasca bitumen recovery. Energy Fuels 27:2194–2201

Hendraningrat L, Souraki Y, Torsater O (2014) Experimental investigation of decalin and metal nanoparticles-assisted bitumen upgrading during catalytic aquathermolysis. In: SPE/EAGE European unconventional resources conference and exhibition. Vienna, Austria, 25–27 February. SPE 167807

Huang X, El-Sayed MA (2010) Gold nanoparticles: optical properties and implementations in cancer diagnosis and photothermal therapy. J Adv Res 1:13–28

Hu R, Crawshaw JP, Trusler JPM, Boek ES (2015) Rheology of diluted heavy crude oil saturated with carbon dioxide. Energy Fuels 29:2785–2789

Ilyin SO, Strelets LA (2018) Basic fundamentals of petroleum rheology and their application for the investigation of crude oils of different natures. Energy Fuels 32:268–278

Kazemzadeh Y, Eshraghi SE, Kazemi K, Sourani S, Mehrabi M, Ahmadi Y (2015) Behavior of asphaltene adsorption onto the metal oxide nanoparticle surface and its effect on heavy oil recovery. Ind Eng Chem Res 54:233–239

Kazemzadeh Y, Eshraghi SE, Riazi M, Zendehboudi S (2018) How do metal oxide nanoparticles influence on interfacial tension of asphaltic oil-supercritical CO_2 systems? J Supercrit Fluids 135:1–7

Kumar G, Kakati A, Mani E, Sangwai JS (2018) Nanoparticle stabilized solvent-based emulsion for enhanced heavy oil recovery. In: SPE Canada heavy oil technical conference, Calgary, Alberta, Canada, 13–14 March. SPE-189774-MS

Lai YH, Zhou Z, Basheer C, Zare RN (2017) Upgrading asphaltenes by oil droplets striking a charged TiO_2-immobilized paper surface. Energy Fuels 31:12685–12690

Lan J, Yang Y, Li X (2004) Microstructure and microhardness of SiC nanoparticles reinforced magnesium composites fabricated by ultrasonic method. Mater Sci Eng A 386:284–290

Li W, Zhu JH, Qi JH (2007) Application of nano-nickel catalyst in the viscosity reduction of Liaohe extra-heavy oil by aqua-thermolysis. J Fuel Chem Technol 35:176–180

Lu T, Li Z, Fan W, Zhang X, Lv Q (2016) Nanoparticles for inhibition of asphaltenes deposition during CO_2 flooding. Ind Eng Chem Res 55:6723–6733

Mehta P, Huh C, Bryant SL (2014) Evaluation of superparamagnetic nanoparticle-based heating for flow assurance in subsea flowlines. In: International petroleum technology conference. Kuala Lumpur, Malaysia, 10–12 December. IPTC-18090-MS

Menéndez-Manjón A, Moldenhauer K, Wagener P, Barcikowski S (2011) Nano-energy research trends: bibliometrical analysis of nanotechnology research in the energy sector. J Nanopart Res 13:3911–3922

Mironenko OO, Sosnin GA, Eletskii PM, Gulyaeva YK, Bulavchenko OA, Stonkus OA, Rodina VO, Yakovlev VA (2017) Catalytic steam cracking of heavy crude oil with molybdenum and nickel nanodispersed catalysts. Catal Ind 9:221–229

Mohammadi M, Akbari M, Fakhroueian Z, Bahramian A, Azin R, Arya S (2011) Inhibition of asphaltene precipitation by TiO_2, SiO_2, and ZrO_2 nanofluids. Energy Fuels 25:3150–3156

Muraza O, Galadima A (2015) Aquathermolysis of heavy oil: a review and perspective on catalyst development. Fuel 157:219–231

Nassar NN, Hassan A, Pereira-Almao P (2011) Application of nanotechnology for heavy oil upgrading: catalytic steam gasification/cracking of asphaltenes. Energy Fuels 25:1566–1570

Nassar NN, Hassan A, Carbognani L, Lopez-Linares F, Pereira-Almao P (2012) Iron oxide nanoparticles for rapid adsorption and enhanced catalytic oxidation of thermally cracked asphaltenes. Fuel 95:257–262

Nguyen P, Fadaei H, Sinton D (2014) Pore-scale assessment of nanoparticle-stabilized CO_2 foam for enhanced oil recovery. Energy Fuels 28:6221–6227

Patel H, Shah S, Ahmed R, Ucan S (2018) Effects of nanoparticles and temperature on heavy oil viscosity. J Petrol Sci Eng 167:819–828

Ramírez-González PV (2016) Rheological behavior from light to heavy oils: construction of master curves. Energy Fuels 30:7094–7099

Roth EA, Agarwal S, Gupta RK (2013) Nanoclay-based solid sorbents for CO_2 capture. Energy Fuels 27:4129–4136

Rudyak V (2013) Viscosity of nanofluids. Why it is not described by the classical theories, Adv Nanopart 2:266–279

Sandoval A, Hernández-Ventura C, Klimova TE (2017) Titanate nanotubes for removal of methylene blue dye by combined adsorption and photocatalysis. Fuel 198:22–30

Shokrlu YH, Babadagli T (2014) Viscosity reduction of heavy oil/bitumen using micro- and nano-metal particles during aqueous and non-aqueous thermal applications. J Petrol Sci Eng 119:210–220

Tiwari JN, Tiwari RN, Kim KS (2012) Zero-dimensional, one-dimensional, two-dimensional and three-dimensional nanostructured materials for advanced electrochemical energy devices. Prog Mater Sci 57:724–803

Wang Q, Guo L, Wang Z, Mu B, Guo A, Liu H (2012) Hydrogen donor visbreaking of Venezuelan vacuum residue. J Fuel Chem Technol 40:1317–1322

Wang F, Zhang L, Xu L, Deng Z, Shi W (2017) Low temperature CO oxidation and CH_4 combustion over Co_3O_4 nanosheets. Fuel 203:419–429

Application of Nanoparticles-Based Technologies in the Oil and Gas Industry

Rellegadla Sandeep, Shikha Jain and Akhil Agrawal

Abstract The demand for energy is inclined toward staggering heights worldwide and is proportional to the requirements of crude oil for satisfying energy needs. Globally, pollution has created a menace in each and every portion of the society we look at. Therefore, much of the today's technology is focused on making the process much economical and sustainable, thereby lowering pressures on environment. Nanotechnology has provided options to enhance such possibilities by contributing to more economical, highly efficient and sustainable approaches with environmentally favored technologies than those conventionally available. This chapter addresses such roles of nanotechnology in different jobs played around the oil and gas industry, such as exploration industry, drilling and production, refining and processing, and in enhanced oil recovery. Besides, the different types of nanomaterials such as nanoparticles, nanoemulsions, nanosensors and nanofluids available for these applications have been discussed. Moreover, the mechanisms which reflect the activity of these nanomaterials have been explained individually. The chapter discusses how nanotechnology-based technologies can achieve more efficient, effective and potential impact in the oil and gas industry.

1 Introduction

Hydrocarbons are till date contributing toward fulfilling a larger segment of energy demands around the globe. Research for sustainable alternatives has not got its pace and the world still relies on fossil fuels for the energy needs. Hence, methods employing ways for efficient recovery of crude oil can help utilize these energy resources in a sustainable way. Emerging nanotechnologies, such as the development of nanoparticles and nanofluids, offer such a solution and have found its roots in the field of

R. Sandeep · A. Agrawal (✉)
Energy and Environment Research Laboratory, Department of Microbiology, School of Life Sciences, Central University of Rajasthan, Ajmer, India
e-mail: akhilagrawal@curaj.ac.in

S. Jain
Department of Chemistry, Manipal University Jaipur, Jaipur, India

L. Ledwani and J. S. Sangwai (eds.), *Nanotechnology for Energy and Environmental Engineering*, Green Energy and Technology,
https://doi.org/10.1007/978-3-030-33774-2_11

oil production. Today, there are different nanomaterials that have been developed for stimulating the increase in the recovery of the crude oil in a much efficient way, compared to available methods. Oil is recovered primarily by using the earth geological pressure, known as primary recovery (Rellegadla et al. 2017). With time the amount of oil recovered reduces with decreasing pressure. At this moment a variety of injected fluids like water is injected for enhancing the sweep efficiency of the displacing fluid. Although the recovery of crude oil increases till 35% of the original oil in place (OOIP), but with time it gradually decreases due to increased viscous fingering (Rellegadla et al. 2017). Tertiary methods known as enhanced oil recovery are later employed at this point for increasing the recovery of residual oil in place. A number of tertiary methods have been developed for increasing the recovery potential. Owing to the reservoir heterogeneity issues, different types of enhanced oil recovery methods are currently been used in the fields to recover crude oil.

The three major types of tertiary recovery methods used currently are (Alvarado and Manrique 2010; Ayatollahi and Zerafat 2012; Kong and Ohadi 2010; Silva et al. 2007; Viebahn et al. 2015):

Thermal Methods—Thermal methods involve introducing heat in the bottom-hole of the heavy oil reservoirs to promote crude oil mobility by affecting its physical properties (lowering of density and viscosity). There are different thermal methods such as cyclic steam simulation, steam assisted gravity drainage (SAGD) and steam flooding.

Chemical Methods—Chemical flooding involves altering the properties of the injected fluids. Secondary flooding results in increase of viscous fingering, thereby lowering the efficiency of the recovery potential. Henceforth, long chain polymers are added to the injection water to increase the viscosity of the drive fluid with improved sweep efficiency. Besides, surfactants are also added to the injection fluid to lower the interfacial tension (IFT) of the oil–rock interface and alter wettability of the rock surface toward water wet.

Gas Methods—Different gaseous hydrocarbons (such as methane, propane or natural gases) and non-hydrocarbons (N_2 or CO_2) are injected into the reservoir during gas flooding. These gases dissolve in the oil layer and further reduce their viscosity by expanding its volume leading to increased recovery.

But all the above-mentioned methods have their own limitations. Cost of application is a common issue for thermal and chemical methods. Besides, low thermal conductivity of reservoir rocks and fluids, an escape of heat in a two-stage process, that is, during flooding from heat generator to the reservoir and loss to undesired layers create an issue during steam flooding. Formation damage can be a big issue during chemical flooding due to incompatibility issues. The injected chemicals could have lower effect on IFT and wettability alteration, whereas during gas flooding fingering can occur at bottom-hole leading to early breakthrough. Besides, deposition of asphaltene has been reported during gas flooding. In brief, summarizing the effects of the above-mentioned processes includes many advantages, such as decreasing oil viscosity, improved mobility, lowering IFT, wettability alteration, oil expansion and

emulsification activities. However, there are many important challenges still faced by these methods.

Nanoparticles-enhanced oil recovery or NEOR is a novel technique, currently developed to overcome the limitations of such earlier applied methods. Different types of nanoparticles have been synthesized till date, and the process for their application in increasing the efficiency for oil recovery has started. The oil-producing companies today face peer pressure due to the reduced efficiency of available technologies to recover crude oil to meet the energy demands. Also, new geological discoveries are taking place and require more intricate technologies for the production of crude oil in order to maximize the recovery potential. Nanotechnology has the capability of increasing the potential of both the upstream and downstream processes of the oil industries. It provides a wide range of materials and processes to be applied in the oil fields. Such novel techniques employing the nanomaterials for different oil processes have been explored in laboratory simulated conditions, as well as been developed for the field processes.

Nanoparticles (NPs) are particles in the nanodimensions with size ranging from 1 to 100 nm. These particles offer many advantages in the field of oil recovery.

Nanodimensional Size: The major problem faced during enhanced oil recovery is the recovery of crude oil from thief zones. These areas are the small pores in the oil that are trapped and not mobilized in the continuum of drive fluid. Though it appears to be a smaller segment of the reservoir but as a whole it contributes to a larger part of residual oil in place (ROIP). Besides, such spaces are also held responsible for the trapping of injected chemicals, thereby leading to the damage of the formation by reducing formation permeability and increasing the economics of flooding (Ahmadi et al. 2011).

The nanoparticles used commonly for the application of EOR range in the dimensions of 10–100 nm (SiO_2, TiO_2, Al_2O_3, etc.), which is smaller compared to the pore throats or thief zones (Alomair et al. 2014). Hence, the NPs improve the flooding potential through the porous media without reducing permeability and increasing recovery from thief zones. Altogether, NPs can increase the microscopic sweep efficiency with increased area of contact.

Increased Area of Contact (High Surface to Volume Area): With reduced size, the NPs have a larger surface area and therefore have a larger area of contact in the swept zone. For the same volume and mass of the sample, the number of particles increases with reducing size, thereby increasing the overall surface area contributed by the particles. This increased surface area increases the proportion of atoms on the surface of NPs (Zhang and Liu 2001).

Lower Cost of Application with Reduced Pressure on Environment: A wide range of chemicals have been applied in the oilfields as a part of chemical enhanced oil recovery process. These injected fluids possess risk to the environment affecting the bottom-hole as well as in the produced water. Besides, the cost of application of such chemicals is higher, and therefore, it further raises the economics of the overall recovery. Application of NPs and nanofluids is cheaper and offers advantage to such

limitations (Sun et al. 2017). Also, NPs are environmental-friendly, such as silica nanoparticles that has been reported in many field trials. Silica is a component of sandstone and therefore the process is cheaper.

There are immense literatures about the applications of different types of nanoparticles in medical and biological applications. The use of nanoparticles is now advancing to different areas as well. The current trends show the nanoparticles are gaining applications in the oil field processes. But a lot of principles and techniques go into the oil field processes and require modification of existing nanotechnology suitable for unique nature of the reservoirs. Many different nanoparticles have been synthesized for these purposes with a large number of field trials as well. This chapter identifies such potentials of the nanoparticles as well as their characteristics responsible for EOR. Additionally, the use of nickel nanoparticle for increasing the recovery potential of polymer flooding has been mentioned as an example for novel EOR method.

2 Research on Nanotechnology Application in the Petroleum Industry

Nano-sized materials have revolutionized the petroleum industry in processes both upstream and downstream, starting from the exploration, drilling, and leading to the production of crude, and processes involved in improving the existing technologies, that is, EOR, as well as for the refinery processes.

2.1 Nanotechnology in Exploration Industry

The rising demands for energy have now raised the needs for exploration of hydrocarbons in more challenging reservoirs, and further development of new technologies for use has been proposed. Therefore, the use of techniques which are more economical and sustainable and employing methods that are more technically advanced than conventional approaches are highly encouraged. Nanotechnology provides a solution to such problems with the development of "nanosensors" which are in the pace of development for geo-exploration by seismic characterization, data interpretation and formations evaluations characterized by conditions prevailing in oil-bearing strata (Bera and Belhaj 2016).

When NPs are injected into the reservoir, few of them passes through the pores in the reservoir rocks, while others get adsorbed onto the surface. The information of the physical properties of the rock and 3D spatial arrangement of the formation can be derived from the analysis of these adsorbed NPs (Kapusta et al. 2011). Furthermore, the core and surface characteristics of NPs can be modified bringing about significant changes in the various properties of the NPs. These optical, magnetic and electrical

properties can be enhanced for making them suitable candidates as nanosensors or imaging materials (Bennetzen and Mogensen 2014).

A number of researchers have also found such novel applications of NPs as nanosensors. In 2007, Song et al. developed the use of hyperpolarized silicon NPs as nanosensors in oil and gas exploration (Song and Marcus 2007). These hyperpolarized NPs were tested and were found to be promising from the results in bio-medical engineering as alternative tracker particles for magnetic resonance imaging (MRI) (Cassidy et al. 2013; Schröder et al. 2006). Jahagirdar proposed the detection of oil microbes in the formations using nano-optical fibers based on the principle of Raman spectroscopy (Jahagirdar 2008). As microbes have characteristics specific to their environment, this method can be utilized to measure the reservoir properties such as pressure, temperature and salinity indirectly. Li et al. patented the technology for real-time monitoring of two-dimensional analysis for oil reservoir evaluation, using carbon nanostructure and surface sensors (Li and Meyyappan 2011). Besides, magnetic NPs have been applied for detecting flood front and oil–water interfaces (Al-Shehri et al. 2013). Similarly, Rahmani et al. applied superparamagnetic NP for tracking the drive fluid front using a magnetic sensing method (Rahmani et al. 2015).

Nanorobots have also made significant advancement and are most recently used for oil and gas exploration (He et al. 2016). Liu et al. had successfully used a nanodetection device which combined with a reservoir sensor and micro-signal transmission helps in detection of geological strata (He et al. 2016). All these studies demonstrate that NPs have the potential to be applied for characterization of the reservoirs and exploration of hydrocarbons.

2.2 Nanotechnology in Drilling and Production

With the decline in the oil production rates over the year throughout the globe, the oil and gas exploration and production industry have now increased the focus on technological advancements. Owing to higher challenges faced at operational depth, increased complexity of drilling projects, associated subsurface geo-hazards with increasing depths, complex wellbore profiles, length of horizontal and number of laterals departure to maximize production are a number of factors that limits the operations of current drilling and production technologies (Kong and Ohadi 2010).

Owing to recent advancements, nowadays oil and gas E&P industries are looking for alternatives that are smaller in dimension, chemically and thermally stable (withstand harsh reservoir conditions), biological in nature, environmentally friendly, polymer or other natural products that can be constituted as smart fluids for use in both drilling and production. As for the future production, Amanullah and Ashraf (2009) acknowledge the increase in number of recoveries from deep water reserves (40–50% of future oil recovery) compared to onshore reserves (Amanullah and Al-Tahini 2009). Such type of reserves requires different operating conditions than normal drilling and production projects. The drilling hazards are more due to complex reservoir nature as it involves shift from vertical to horizontal drilling, and increased

operational depth, the existing drilling and well stimulation fluids are not stable and perform poorly. Conventional drilling programs (macro- or micro-material-based) are partially successful in overcoming such limitations. Besides, drilling industries require new improved, stable, lightweight, rugged structural materials for a number of applications (reduced weight of offshore platforms, energy efficient vessels and better performing drilling parts) (Krishnamoorti 2006).

Currently, nano-based materials which can sustain its intrinsic properties at high temperatures and pressures, abrasions, corrosiveness and other harsh environmental conditions are been employed. The drilling mechanical parts, equipments and platforms are coated with such materials composed of NPs for improving their properties. These coatings provide resistance toward corrosion, wear and abrasions, shock proof, thermal conduciveness and reduced wetted state. Oil well cements in deep wells also require materials with good qualities and properties. Silica and Fe_2O_3-based NPs are especially used for this purpose and are widely applied in increasing the strength of portland and belite cements (Li 2004; Xu et al. 2003).

Besides, custom-made functional nanomaterials have revolutionized the applications of NPs in the field of oil and gas industries. These tailored NPs are manufactured with custom natures, ionic properties, physical shapes, sizes, charge densities for a variety of application in drilling and well stimulation-related functions. These fluids are also known as "*smart fluids*" which provide additional benefits, such as wettability alteration behavior, drag reduction and consolidated sand binders (Chaudhury 2003; Wasan and Nikolov 2003). These superfine powders and nano-sized particles improve the drilling process and lower the risk of damage to reservoir rocks. This further increases the recovery percentage of crude oil (Esmaeili 2011).

2.3 Nanotechnology in Refining and Processing

High sulfur content and increased CO_2 emissions are two of the major problems faced by the refining and processing industries today. Fuels that are cleaner and reduce pressure on environment are highly encouraged. Hence, refineries are under peer pressure to increase their yields while utilizing fewer resources (steel, energy and CO_2). Heavy organic components in the crude oil are yet another limitation. In order to reduce their energy footprints, the oil refineries are currently working on new technologies that can reduce the costs while meeting the new emissions standards laid by various environmental protection agencies.

From the past decade, nanotechnology has made significant contributions to the refining of crude and conversion of fossil fuels. Nanofilters are developed that significantly changed the downstream refining processes. Mesoporous catalyst (MCM-41) is one such example. These nano-sized filters and particles help adsorb and remove harmful toxic substances such as various oxides (nitrogen oxides, sulfur oxides) related acids, anhydrides and mercury from the soil and water (Kong and Ohadi 2010). Furthermore, nanomembranes are been developed that enhance separation of

the gas streams and oil impurities from the oil. Nanotechnology also contributes to the carbon capture and storage to long terms.

Upgradation of heavy oil and bitumen on-site is now possible due to applications of nanotechnology (Ying and Sun 1997). High density and viscosity makes it difficult for their transport for refining and are therefore converted with the help of nanocatalysts on-site, making the process simpler and friendlier. These nanocatalysts also increase the refining efficiency including for sour crude oils and extra heavy oils (Esmaeili 2011). Additionally, nanosensors are also been used for improved monitoring of the refining process.

2.4 Enhanced Oil Recovery

The worldwide demand for energy is tremendous and meeting the needs globally is the primary challenge of oil and gas industries. However, the number of oil-producing wells around the globe is declining that has left the E&P industry with two options: Either to promote discoveries of new oil fields or improve the oil-producing efficiencies of existing mature oil fields. Enhanced oil recovery (EOR) is highly addressed for solving this problem as conventional methods fail in recovering two-thirds of the crude oil left in many of the world's reservoirs. Three different categories have been formed with successful history of EOR: (1) Thermal recovery, involving injection of steam to reduce the viscosity of the heavy oil and improving the flow of the highly viscous oil, (2) Gas injection, involving injection of gases (CO_2, nitrogen) which expand bottom-hole in the wellbore region promoting recovery of residual oil, the gases also dissolve in the oil whereby reducing the viscosity and promoting flow, (3) Chemical EOR, involving injection of polymers to improve the sweep efficiency of drive fluid, and injection of surfactants which lowers interfacial tension and surface tension of the oil–water interface increasing the efficiency of the water flood (Rellegadla et al. 2017). Nanoparticles offer a broad range of mechanisms which can improve the crude oil recovery with a better efficiency. NPs can improve the geomechanics of the reservoir by lowering the surface tension of oil, altering wettability of reservoir rock surface. The injection fluid (water, CO_2, surfactant solution) viscosity can be improved with addition of NPs, thereby improving mobility, increasing oil recovery efficiency. Shah (2009) found that the viscosity of CO_2 increased to 140 times when 1% CuO NPs were added to it with small amount of dispersants (Shah 2009). Besides, NPs have also found their use in stabilizing emulsions. Emulsification helps increase recovery efficiency, and emulsions stabilized with NPs can withstand higher temperatures and harsh reservoir conditions for prolonged periods of time. There are a number of other mechanisms which the NPs use for enhancing the EOR processes. The oil and gas industries extract benefits from such mechanisms of the NPs which are discussed further in the preceding sections.

3 Role of Nanomaterials in EOR

There are different types of nano-assisted EOR materials that have been applied in oil fields for increasing the efficiency of the oil recovery processes. These can be used as nanofluids/nanoparticles, nanoemulsions and nanocatalysts. All these nano-sized materials have solved different purposes during the EOR recovery. A lot of different mechanisms go into the process during the recovery of crude oil.

3.1 Nanofluids/Nanoparticles

The key reason for the nanoparticles having a tremendous potential in the field of oil recovery is its size, which allows it to freely flow in the reservoir without getting retained/adsorbed due to straining (Ko and Huh 2018). They have been used for a wide variety of upstream and downstream oilfield applications with the synthesis in a wide variety of size ranges and tailored with different surface coatings. NPs have been employed as stabilizers, for improving the mobility of hydrocarbons, formation of emulsions for better recovery, CO_2 foams, constituting formulation of drilling fluids and altering rock surface wettability for improved oil recovery. Nanofluids, on the other hand, are base fluids (water, oil or gas) that are composed of NPs ranging in size below 100 nm in a colloidal suspension (El-Diasty and Ragab 2013; Sun et al. 2017). In general, these nanofluids are prepared in water or brine to improve the efficiency of secondary flooding. Both NPs and nanofluids have been studied widely and a number of mechanisms have been explained for their role in EOR.

3.1.1 Pore Throat Plugging

Plugging of the porous media channels occurs due to two different mechanisms, log-jamming and mechanical entrapment (Skauge et al. 2010). These mechanisms can prove beneficial to the NEOR application or can be a limiting process for the same. Mechanical entrapment occurs when the dimensions of the pore throats are smaller compared to the sizes of the injected EOR materials. However, the dimensions of NPs are usually in nanometers and smaller compared to the sizes of the pore throats that are in micrometers. Moreover, some of the NPs synthesized from metal ions are larger in size and can block the pore channels resulting in reduced efficiency of NEOR (Hashemi et al. 2013; Zamani et al. 2012). This issue can be avoided during the initial evaluation of NEOR fluid in laboratory studies in oil field simulating sandpacks or during core flooding studies.

Log-jamming, on the other hand, occurs during the flow of nanofluids and NPs when the sizes of the pore throats are smaller than the sizes of the NPs (Sun et al. 2017). It leads to accumulation of the NPs at these pore throats creating a bulk pressure difference with narrowing of the pore channels. This leads to the increase

in the velocity of NPs drive fluid. This further improves the efficiency of the drive fluid and the overall NEOR process. When there is a blockage of the pore throats it raises the pressure of the adjacent pore throats. This increased differential pressure pushes the oil trapped in the pore throats out in the continuum. As the trapped oil is mobilized, the pressure drops and the blockage of the NPs is released, thereby bringing the NPs back in the flow. Both these phenomena depend on the size and concentration of the NPs, flow rate and dimensions of the pore throats.

Also, few of the researchers have also used a combination of polymeric microspheres and nanospheres for reducing water cut and improving sweep efficiency (Cheraghian et al. 2013; Cheraghian and Hendraningrat 2016; Cheraghian and Tardasti 2012; Tian et al. 2012). When the combination of these two contacts, they get swelled up in the formation, which reduces the water permeability through the porous media and change the path of water flow. This results in the flow of water to bypass the area and enhance the oil displacing efficiency (Cheraghian and Hendraningrat 2016).

3.1.2 Lowering of the Interfacial Tension

A majority of the oil fields discovered till date are carbonate formations. The efficiency of water flooding in these reservoirs is lower due to the existence of the microscopic trapping and macroscopic bypassing (Sharma and Mohanty 2013; Sheng 2013; Souayeh et al. 2018). Interfacial tension determines the flow behavior and distribution in the porous media. The reduction of IFT enhances the oil recovery potential by lowering the capillary forces (Zhang et al. 2010). A number of nanoparticles have been found to lower the IFT, contributing as a major mechanism toward EOR. The IFT between the equilibrated oil and the NPs is measured using the pendant drop method in goniometry or with the help of spinning drop tensiometer (Cheraghian and Hendraningrat 2016). The value of IFT is measured by analyzing the surface of a drop from the thin capillary tube using a high-resolution camera and image analysis software. The dimensions of the oil drop help derive the IFT values using the Young–Laplace equation.

The decrease in IFT values between the crude oil and different types of NPs has been mentioned by a number of researchers. Hendraningrat et al. (2013) had measured the IFT using synthetic oil and NPs dispersed in the brine. They had reported a decrease in IFT (14.7–9.3 mN/m) which further reduced t from 9.3 to 5.2 mN/m with increasing concentration of NPs. Their results showed that an increasing concentration of NPs decreases the IFT showing sensitivity toward NPs concentration. Li and Parvazdavani found that the SiO_2 NPs have a more impact toward IFT reduction than alteration of surface wettability of reservoir rocks (Li et al. 2013; Parvazdavani et al. 2014). Recently, a number of studies were conducted evaluating the potential of metal nanoparticles (Al_2O_3, MgO, Fe_2O_3, TiO_2) (Cheraghian and Hendraningrat 2016). Alomair et al. had evaluated the efficiencies of different nanoparticles (Al_2O_3, NiO and SiO_2) and had found that NiO had reduced the IFT to lowest values while SiO_2 had the lowest IFT value. However, some of the researchers have found good results

with a combination of nanoparticles compared to using silica-based nanoparticles (Cheraghian and Hendraningrat 2016).

Few of the researchers have also studied the blends of nanoparticles and surfactants. Le et al. had studied such combination using SiO_2 NPs for EOR in high temperature reservoirs (Le et al. 2011). Resasco et al. had found more interesting results (Resasco et al. 2015). Their studies showed that when a mixture of nanoparticles and anionic surfactants is used for EOR, the reduction in IFT is 70% more compared to the sole use of surfactant. The increased adsorption of nanoparticles modifies the interfaces of oil and water, thereby reducing the IFT (Munshi et al. 2008; Ravera et al. 2006).

3.1.3 Wettability Alteration

The term wettability reflects the tendency of a liquid to adhere to a solid surface while competing with another immiscible liquid (Le Van and Chon 2016). In the context of oil fields, wettability alteration refers to the change of the reservoir rock surface toward water wet (Mohammed and Babadagli 2015). It is an important factor that affects the oil recovery process by influencing capillary pressure, relative permeability and fluid saturation (Sun et al. 2017). In general, the efficiency of crude oil recovery decreases when the surface of reservoir rock becomes more oil wet. Several different thermal and chemical EOR methods have been proposed that alter the wettability of rocks toward water wetness, although this ability depends upon the characteristics of rock mineralogy and that of brine and oil composition. Besides, because of reservoir heterogeneity, the potential of wettability alteration depends upon the crude oil interaction of the crude oil with the rock and brine that differs from reservoir to reservoir (Mohammed and Babadagli 2015).

Wettability alteration occurs by changing oil, brine and rock characteristics due to two different mechanisms: coating and cleaning (Giraldo et al. 2013). Coating results in the covering of the oil wet surfaces by a water wet layer such as that of surface active agents and NPs. For example, certain NPs are hydrophilic in nature, such as zirconium nanoparticles (Karimi et al. 2012). Cleaning occurs due to surface active agents such as cationic surfactants that wipe out the oil wet layers rendering the surface more water wet (Standnes and Austad 2000). A combined effect was also noticed when a mixture of anionic surfactant and alumina NPs was used (Giraldo et al. 2013).

A number of wettability alteration measurement techniques are used, such as contact angle measurement (CAG), spontaneous imbibition (SI), zeta potential measurement (ZPM) and surface imaging tests (atomic force microscopy, SEM, NMR). CAG is the measurement of the point at which oil and water interface meets at rock surface. It is used to monitor the altering wettability of the surface by measuring the shift of the affinity of rock surface toward one fluid than another in an advancing manner (Morrow 1990). Magzhi et al. had used CAG approach to monitor change in wettability of glass surfaces coated with SiO_2 nanofluid and oil with different

viscosities (Maghzi et al. 2012). They had reported that the wettability was altered toward water-wet state regardless of the viscosity of the oil on the surface.

SI monitors determine the ability of the wetting phase to displace the non-wetting phase (Mohammed and Babadagli 2015). ZPM monitors change surface charges; a shift from positive to negative potential reflects the altering wettability of the surface during treatments with anionic surfactants (Hirasaki and Zhang 2004). Imaging techniques help giving insights of the microscopic view of the surface to monitor change in wettability (Karimi et al. 2012; Schembre et al. 2006). For example, Karimi et al. had shown using SEM images and EDX (energy-dispersive X-ray) that NPs get adsorbed on the surface of calcite forming nano-textured surfaces (Karimi et al. 2012). Similarly, in order to visualize the surface of rock after treatment with NPs, Al-Anssari et al. used SEM–EDS and AFM measurements and observed the homogenous distribution of NPs after nanomodification of surface (Al-Anssari et al. 2016; Nikolov et al. 2010).

Amott test and core displacement tests are also used for the evaluation of the wettability alteration characteristics. Amott test involves the measurement of the volume of fluids that is spontaneously or forcibly imbibed by a rock sample. It is measured by calculating wettability index (I_w) as mentioned in the following equation:

$$I_w = \frac{V_{o1}}{V_{o1} + V_{o2}} - \frac{V_{w1}}{V_{w1} + V_{w2}}$$

where V_o and V_w denote the volume of oil imbibed and the volume of water drained during the process, respectively. The subscript "1" represents spontaneous process and "2" means forced displacement process. The values of I_w range from -1, representing as complete water-wet state, 1 as oil-wet to 0 as neutral wettability of the surface (Sun et al. 2017). Li et al. had performed Amott test to monitor the change in wettability of rock surface after treatment with SiO_2 NPs (Li et al. 2013, 2015). They had reported the change in wettability of sandstone surface from oil wet to neutral wet. Roustaei et al. had used SiO_2 NPs for altering wettability of carbonate cores and also found similar results (Roustaei and Bagherzadeh 2015). The results were consistent when Al-Anssari et al. had used SiO_2 nanofluids and found the wettability altered to a mixed wet state (Al-Anssari et al. 2016).

Core wettability also helps determine the wettability alteration by analyzing the changes the residual water saturation, oil relative permeability and the point where the oil and water relative permeability are equal (Sun et al. 2017).

3.1.4 Improving Sweep Efficiency

Craig in 1971 has suggested that the oil recovery efficiency depends upon volumetric sweep efficiency, which can be defined by the following equation (Craig 1971):

$$E_r = E_d \times E_v$$

where E_r is the recovery efficiency expressed as a fraction of the OOIP, E_d is the microscopic oil displacement which reflects the total volume of oil displaced by a unit segment of rock and E_v is the volumetric sweep efficiency which represents the total volume of the reservoir that is in contact with recovery fluid. Hence if the sweep efficiency gets lowered, it further reduced the amount of oil recovered (Rellegadla et al. 2017). Further, the poor sweep efficiency results from the difference of oil and aqueous phase mobilities. The water tends to move faster compared to oil and therefore results in the water reaching the production well faster than oil. The mobility ratio of oil and aqueous phase is expressed as:

$$M = \frac{(k_w \mu_o)}{(k_o \mu_w)}$$

where M is the mobility ratio, k_w is the relative permeability of aqueous phase (water) in the water flooded region, k_o is the relative permeability of the oil in oil-saturated region and μ_o and μ_w represent viscosity of oil and water, respectively. When the mobility ratio increases due to water channeling through the same pathways, time (viscous fingering) and again it leads to a decrease in the amount of area swept (Abidin et al. 2012). This causes a poor conformance and poor sweep efficiency and thus results in a lower recovery potential. However, when the mobility ratio is <1 it favors a higher recovery of oil with improved sweep efficiency by a uniform displacement of drive fluid (Rellegadla et al. 2017). NPs provide a solution to the above problem by increasing the effective viscosity of the drive fluid, thereby promoting favorable mobility ratios. Rellegadla et al. had found an increase in the viscosity of the xanthan solution when a mixture of xanthan and nickel NPs was used as injection fluids for EOR (Rellegadla et al. 2018). Shah et al. had found an increase in viscosity 140 times of CO_2 nanofluids (CuO NPs in CO_2 gas phase) compared to CO_2 flooding (Shah 2009). Similar results were also observed by Molnes et al. while preparing nanofluids by dispersing cellulose nanocrystals in deionized water (Molnes et al. 2016).

Also, viscosity of NPs solution or nanofluids is affected by a number of factors, which include temperature, salinity, shear stress/rate and NP types and concentration. Many researchers have evaluated such factors, for example, SiO_2 nanofluids viscosity increases at lower shear rates (Al-Anssari et al. 2016). Cellulose nanofluids behave in a distinct manner due to their structural arrangement. Their viscosity increases when shear rates are higher and decreases when shear rates are reduced, thereby showing shear thinning behavior in the latter case (Wei et al. 2016). Furthermore, SiO_2 nanofluids are more viscous compared to Al_2O_3 nanofluids at the same concentration (Salem Ragab and Hannora 2015; Tarek and El-Banbi 2015).

3.1.5 Disjoining Pressure

Sun et al. had explained the flow behavior of the nanofluids in the porous matrix due to which a wedge-shaped arrangement of the NPs takes place (Sun et al. 2017). This structural arrangement helps in removing the oil droplet from the rock surface.

This wedge-shaped film appears because of the structural disjoining pressure created by the osmotic pressure created during injection of the nanofluids (Mcelfresh et al. 2012). When the nanofluids are injected bottom-hole the injection pressure creates a uniform layer in a confined region ahead due to exerted pressure and the layer tends to arrange with more NPs in the flow. The entropy of this arrangement increases with increasing number of NPs and further results in an additional disjoining pressure exerted at the interface than that of the bulk liquid (Aveyard et al. 2003; Chengara et al. 2004). A higher concentration of NPs raises Brownian motion and electrostatic repulsions between the particles generating the disjoining pressure. The size of NPs, amount, composition of base fluid (salinity levels), rock characteristics all affects the disjoining pressure. For example, larger amount of NPs increases the force to 50,000 psi at the vertex (Aveyard et al. 2003).

3.1.6 Limiting Asphaltene Precipitation

Asphaltene precipitation is a major problem encountered during primary recovery and EOR methods leading to deposits in the porous media (Papadimitriou et al. 2007; Solaimany-Nazar and Zonnouri 2011). Whereas wettability alteration contributes toward higher EOR recovery potential, precipitation of asphaltene causes plugging of the reservoir, alteration of wettability from water-wet toward more oil-wet and lowering of the relative permeability of the oil (Nghiem et al. 1998; Pina et al. 2006). Many researchers have found NPs as a solution to this problem without leading to any environmental pressure. Tarboush et al. found that NiO NPs have a higher affinity toward asphaltene leading to the uptake of this particles and stabilizing precipitation (Tarboush and Husein 2012). Similarly, testing of SiO_2–Al_2O_3 NPs by Alomair revealed that as the concentration of NPs is increased, it delayed the precipitation further (Alomair et al. 2014). Kazemzadeh et al. additionally determined how SiO_2, NiO and Fe_3O_4 NPs were adsorbed on the surface of asphaltene molecules, which significantly reduced the flocculation in the porous media (Kazemzadeh et al. 2015).

3.2 Nanoemulsions

Nanoemulsions are emulsions stabilized by NPs with a droplet size ranging from 50 to 500 nm. The physicochemical properties of these micro-droplets (<100 nm) can help successfully enhance the EOR efficiency by recovering. These emulsions are much more stable than conventional emulsions which are stabilized by surfactants (Mandal et al. 2012). Also, these NPs stabilize the nanoemulsions by forming a kinetically controlled system which can withstand extreme conditions (higher temperature, salinity and increased pressures) by retaining their morphology even with change in oil volume fractions (Binks and Lumsdon 2000). The size of nanoemulsions can even help them to penetrate through the thief zones and pore throats with lower rates of adsorption (Zhang et al. 2010). Additionally, nanoemulsions have a

higher viscosity that can help improving the mobility ratio of the drive fluid. Hence, nanoemulsions prove an advantage over polymers, as polymers are retained due to adsorption on rock surface (Binks et al. 2005; Binks and Rodrigues 2005). These properties make its applications extended to large-scale field jobs.

A number of NPs have been developed to be used as nanoemulsions. Silica NPs have found wide use as nanoemulsions in many of the recent studies. The concentration of silanol groups in the silica NPs containing nanoemulsions plays an important role in many of its intrinsic characters, such as the wettability, hydrophilicity and hydrophobicity. Wettability character is controlled with the amount of silanol groups present on the surface (Mcelfresh et al. 2012). Hydrophilicity behavior of the nanoemulsion increases with increasing percentage (over 90%) of silanol groups on the surface. This helps in forming stable oil-in-water (o/w) emulsions. When the concentration is only 10% on the surface, the hydrophobic character yields water-in-oil (w/o) emulsions. This change helps control the formation of o/w emulsions and w/o emulsions, which further improves interaction with non-polar oils or polar oils, respectively (Aveyard et al. 2003).

The emulsification behavior has also been observed in some micro-model experiments earlier. The key reasons for such behavior of NPs on emulsion are also mentioned by some studies. Images viewed by an optical microscope also show the uniform size of the NPs generating a compact, well-structured unilayer at the aqueous/non-aqueous interface, thereby making the emulsions highly stable under extreme temperatures (Alomair et al. 2014).

3.3 Nanocatalysts

Nanocatalysts act as nanodimensional-sized metal particles with an increased surface area of contact that helps in better interaction of the surface of oil with nanocatalysts (Hashemi et al. 2013, 2014). These catalysts are therefore used for upgrading the properties of crude oil by reacting with bitumen in the crude oil to convert it into lighter products by some chemical reactions. Such type of reactions is referred as aquathermolysis. These occur while injection of nanocatalysts during steam injection into heavy oil reservoirs. The presence of nano-sized metal particles, such as nickel and iron, provides an increased surface area for catalyzing the breaking of carbon sulfur bonds within asphaltenes. This, therefore, increases the amount of saturates and aromatics present in the heavy oil (Hyne 1986).

The percentage of carbon monoxide produced during this reaction reacts with water to produce hydrogen (during thermal EOR process at 200–300 °C). These hydrogen molecules that have been produced later react with the unsaturated molecules of heavy oil, thereby producing lighter, saturated crude oil components by hydrogenolysis (Callaghan 2006).

Aquathermolysis also helps in decreasing the viscosity of the heavy oils. When metal NPs were used as catalysts they caused a greater reactivity compared to micron-sized particles. As noted by Shokrlu et al., nickel NPs were able to reduce oil viscosity

from 2700 to 1900 mPa at a concentration of 500 ppm of NPs (Shokrlu and Babadagli 2011). Same was observed during a number of experiments such as by Clarke et al. during the use of metal NPs during aquathermolysis process (Clark et al. 1990; Clark and Hyne 1990).

4 A Laboratory Evaluation of Nanoparticle-Assisted Polymer Flooding

Rellegadla et al. had demonstrated a new method of EOR with the help of a combination of nanoparticle and polymer flooding (Rellegadla et al. 2018). They had shown when a mixture of nickel nanoparticles along with the xanthan gum is injected in the sand packed columns the amount of additional oil recovered increases. They had calculated the amount of additional oil recovered in the effluents with the help of a spectrophotometric method explained below.

Initially, they had prepared the standards by mixing parent oil to dichloromethane (DCM) (1:10 ratio). Then a known volume of parent oil–DCM standard mix was poured into a separatory funnel containing 30 ml of deionized water. This oil–water mixture was then extracted with 5 ml volumes of DCM. The separatory funnel was vigorously shaken for few seconds and was then allowed to stand for few minutes to allow phase separation after which the oil was extracted. This extraction procedure was again followed using a total of three portions of DCM. Lastly, the final DCM volume for the whole extracts was made up to a total volume of 20 ml with DCM.

The authors had prepared standard dilutions from the stock solution by adding a known volume of DCM to parent oil. The absorbance for the standard solutions was measured and a standard curve was plotted. Later the amount of oil produced from the bioreactor during flooding experiment was measured by adding a known amount of DCM (VDCM) to the measured volume of water (V_{H2O}) and then the volume of oil (V_{oil}) was determined from the optical density at 600 nm (OD_{600}) of the oil–DCM phase to derive the concentration of oil (C_{oil}) in mg/ml; OD_{600} was determined using a spectrophotometer. V_{oil} was then calculated as ($V_{oil} = C_{oil} \times VDCM/\rho_{oil}$), where ρ_{oil} is the density of Ankleshwar oil.

Enhanced oil recovery efficiency of this injection mixture was evaluated in sand packed bioreactors with ~0.6 PV of residual oil in place (ROIP). Flooding results had shown the highest recovery of 5.98% of additional ROIP with xanthan–nickel nanoparticle mixture compared to 4.48 and 4.58% of ROIP during sole injection of xanthan and nanoparticles, respectively.

5 Overview and Future Prospects

There are a number of areas in petroleum industry in which nanotechnology has found its applications. These technologies are more efficient, more economical and environmental-friendly than conventional methods and a number of researchers have defined their future possibilities in a number of areas in the oil and gas industry itself.

(1) Improved polymers, binders for sand consolidation and other drilling composites critical to deep drilling under high temperature/pressure environments.
(2) Oil refining and petrochemicals technologies.
(3) New materials for anti-corrosive coatings for surface and subsurface facilities, drilling equipments.
(4) Improvement of EOR and gas recovery through reservoir property modification and improving drive fluid constituents for better sweeping efficiency.
(5) Improved nanofiltration for oil refining and waste management.
(6) Nano-based materials to enhance stability, strength and endurance for drilling equipments, mechanical and movable parts.
(7) Improve nanosensors facilitating improvement of geo-exploration, improved data gathering, recognition of dry holes and shallow hazards.
(8) New lightweight, abrasion proof rugged nanomaterials for transportation vessels, offshore platforms.

6 Conclusion

The present chapter presented an overview of the nanotechnology intervention in the oil and gas industry. The reviewed literature marks the progress in research made by the materials in the nanodimensions and the mechanisms behind their applications. The oil and gas industries are facing a number of technology-based challenges that has to be addressed with the use of new materials in both the upstream and downstream sectors. Nanotechnology offers solution to many such problems which are difficult by conventional approaches. A variety of nanotechniques, smart fluids, NPs, nanoemulsions, nanocatalysts, nanosensors, nanomembranes and other nanosized materials have been developed and have been extensively used by oil and gas industries. Besides, most of these nanomaterials have been tested in the laboratory setups, and they are finding their uses in the oil and gas industry with time. There are many innovations which are been improvised to field conditions. However, such innovations when applied to the field could bring about a technological breakthrough with benefits on both sides of the industry.

References

Abidin A, Puspasari T, Nugroho W (2012) Polymers for enhanced oil recovery technology. Proc Chem 4:11–16

Ahmadi M, Habibi A, Pourafshari P, Ayatollahi S (2011) Zeta potential investigation and mathematical modeling of nanoparticles deposited on the rock surface to reduce fine migration. In: SPE middle east oil and gas show and conference, Manama, Bahrain. 142633-MS, 25–28 September 2011. Society of Petroleum Engineers

Al-Anssari S, Barifcani A, Wang S, Maxim L, Iglauer S (2016) Wettability alteration of oil-wet carbonate by silica nanofluid. J Colloid Interface Sci 461:435–442

Al-Shehri AA, Ellis ES, Servin JMF, Kosynkin DV, Kanj MY, Schmidt HK (2013) Illuminating the reservoir: magnetic nanomappers. In: SPE middle east oil and gas show and conference, Manama, Bahrain. 164461-MS, 10–13 March 2013. Society of Petroleum Engineers

Alomair OA, Matar KM, Alsaeed YH (2014) Nanofluids application for heavy oil recovery. In: SPE Asia pacific oil & gas conference and exhibition, Adelaide, Australia. 171539-MS, 14–16 October 2014. Society of Petroleum Engineers

Alvarado V, Manrique E (2010) Enhanced oil recovery: an update review. Energies 3:1529–1575

Amanullah M, Al-Tahini AM (2009) Nano-technology-its significance in smart fluid development for oil and gas field application. In: SPE Saudi Arabia section technical symposium, Al-Khobar, Saudi Arabia. 126102-MS, 9–11 May 2009. Society of Petroleum Engineers

Aveyard R, Binks BP, Clint JH (2003) Emulsions stabilised solely by colloidal particles. Adv Colloid Interface Sci 100:503–546

Ayatollahi S, Zerafat MM (2012) Nanotechnology-assisted EOR techniques: new solutions to old challenges. In: SPE international oilfield nanotechnology conference and exhibition, Noordwijk, The Netherlands. 157094-MS, 12–14 June 2012. Society of Petroleum Engineers

Bennetzen MV, Mogensen K (2014) Novel applications of nanoparticles for future enhanced oil recovery. In: International petroleum technology conference, Kuala Lampur, Malaysia. IPTC-17857-MS, 10–12 December 2014

Bera A, Belhaj H (2016) Application of nanotechnology by means of nanoparticles and nanodispersions in oil recovery—a comprehensive review. J Nat Gas Sci Eng 34:1284–1309

Binks BP, Lumsdon S (2000) Influence of particle wettability on the type and stability of surfactant-free emulsions. Langmuir 16:8622–8631

Binks BP, Rodrigues JA (2005) Inversion of emulsions stabilized solely by ionizable nanoparticles. Angew Chem Int Ed 44:441–444

Binks BP, Philip J, Rodrigues JA (2005) Inversion of silica-stabilized emulsions induced by particle concentration. Langmuir 21:3296–3302

Callaghan CA (2006) Kinetics and catalysis of the water-gas-shift reaction: a microkinetic and graph theoretic approach. Doctoral thesis, Worcester Polytechnic Institute. https://digitalcommons.wpi.edu/etd-dissertations/255

Cassidy M, Chan H, Ross B, Bhattacharya P, Marcus CM (2013) In vivo magnetic resonance imaging of hyperpolarized silicon particles. Nat Nanotechnol 8:363

Chaudhury MK (2003) Complex fluids: spread the word about nanofluids. Nature 423:131

Chengara A, Nikolov AD, Wasan DT, Trokhymchuk A, Henderson D (2004) Spreading of nanofluids driven by the structural disjoining pressure gradient. J Colloid Interface Sci 280:192–201

Cheraghian G, Tardasti S (2012) Improved oil recovery by the efficiency of nano-particle in imbibition mechanism. In: 2nd EAGE international conference KazGeo

Cheraghian G, Hendraningrat L (2016) A review on applications of nanotechnology in the enhanced oil recovery part A: effects of nanoparticles on interfacial tension. Int Nano Lett 6:129–138

Cheraghian G, Hemmati M, Masihi M, Bazgir S (2013) An experimental investigation of the enhanced oil recovery and improved performance of drilling fluids using titanium dioxide and fumed silica nanoparticles. J Nanostruct Chem 3:78

Clark PD, Hyne JB (1990) Studies on the chemical reactions of heavy oils under steam stimulation condition. Aostra J Res 29:29–39

Clark PD, Clarke RA, Hyne JB, Lesage KL (1990) Studies on the effect of metal species on oil sands undergoing steam treatments. Aostra J Res 6:53–64

Craig FF (1971) The reservoir engineering aspects of waterflooding, vol 3. HL Doherty Memorial Fund of AIME, New York. Society of Petroleum Engineers. ISBN: 978-0-89520-202-4

El-Diasty AI, Ragab AMS (2013) Applications of nanotechnology in the oil & gas industry: latest trends worldwide & future challenges in Egypt. In: North Africa technical conference and exhibition, Cairo, Egypt. 164716-MS, 15–17 April 2013. Society of Petroleum Engineers

Esmaeili A (2011) Applications of nanotechnology in oil and gas industry. In: AIP conference proceedings, vol 1. AIP, pp 133–136

Giraldo J, Benjumea P, Lopera S, Cortés FB, Ruiz MA (2013) Wettability alteration of sandstone cores by alumina-based nanofluids. Energy Fuels 27:3659–3665

Hashemi R, Nassar NN, Pereira Almao P (2013) Enhanced heavy oil recovery by in situ prepared ultradispersed multimetallic nanoparticles: a study of hot fluid flooding for Athabasca bitumen recovery. Energy Fuels 27:2194–2201

Hashemi R, Nassar NN, Almao PP (2014) Nanoparticle technology for heavy oil in-situ upgrading and recovery enhancement: opportunities and challenges. Appl Energy 133:374–387

He L, Xu J, Bin D (2016) Application of nanotechnology in petroleum exploration and development. Pet Explor Dev 43:1107–1115

Hendraningrat L, Li S, Torsater O (2013) Effect of some parameters influencing enhanced oil recovery process using silica nanoparticles: an experimental investigation. In: SPE reservoir characterization and simulation conference and exhibition, Abu Dhabi, UAE. 165955-MS, 16–18 September 2013. Society of Petroleum Engineers

Hirasaki G, Zhang DL (2004) Surface chemistry of oil recovery from fractured, oil-wet, carbonate formations. SPE J 9:151–162. 88365-PA

Hyne J (1986) Aquathermolysis: a synopsis of work on the chemical reaction between water (Steam) and heavy oil sands during simulated steam stimulation. AOSTRA Library of Information Service, Canada, OSTI ID: 220464, Reference Number: SCA: 040401

Jahagirdar SR (2008) Oil-microbe detection tool using nano optical fibers. In: SPE western regional and pacific section AAPG joint meeting, Bakersfield, California, USA. 113357-MS, 29 March–4 April 2008. Society of Petroleum Engineers

Kapusta S, Balzano L, Te Riele PM (2011) Nanotechnology applications in oil and gas exploration and production. In: International petroleum technology conference, Bangkok, Thailand, International Petroleum Technology Conference. IPTC-15152-MS, 15–17 November 2011

Karimi A, Fakhroueian Z, Bahramian A, Pour Khiabani N, Darabad JB, Azin R, Arya S (2012) Wettability alteration in carbonates using zirconium oxide nanofluids: EOR implications. Energy Fuels 26:1028–1036

Kazemzadeh Y, Eshraghi SE, Kazemi K, Sourani S, Mehrabi M, Ahmadi Y (2015) Behavior of asphaltene adsorption onto the metal oxide nanoparticle surface and its effect on heavy oil recovery. Ind Eng Chem Res 54:233–239

Ko S, Huh C (2018) Use of nanoparticles for oil production applications. J Petrol Sci Eng 172:97–114

Kong X, Ohadi M (2010) Applications of micro and nano technologies in the oil and gas industry-overview of the recent progress. In: Abu Dhabi international petroleum exhibition and conference, Abu Dhabi, UAE. 138241-MS, 1–4 November 2010. Society of Petroleum Engineers

Krishnamoorti R (2006) Extracting the benefits of nanotechnology for the oil industry. J Petrol Technol 58:24–26

Le NYT, Pham DK, Le KH, Nguyen PT (2011) Design and screening of synergistic blends of SiO_2 nanoparticles and surfactants for enhanced oil recovery in high-temperature reservoirs. Adv Nat Sci: Nanosci Nanotechnol 2:035013

Le Van S, Chon BH (2016) Chemical flooding in heavy-oil reservoirs: from technical investigation to optimization using response surface methodology. Energies 9:711

Li G (2004) Properties of high-volume fly ash concrete incorporating nano-SiO_2. Cem Concr Res 34:1043–1049

Li J, Meyyappan M (2011) Real time oil reservoir evaluation using nanotechnology. US Patents 7,875,455

Li S, Genys M, Wang K, Torsæter O (2015) Experimental study of wettability alteration during nanofluid enhanced oil recovery process and its effect on oil recovery. In: SPE reservoir characterisation and simulation conference and exhibition, Abu Dhabi, UAE. 175610-MS, 14–16 September 2015. Society of Petroleum Engineers

Maghzi A, Mohammadi S, Ghazanfari MH, Kharrat R, Masihi M (2012) Monitoring wettability alteration by silica nanoparticles during water flooding to heavy oils in five-spot systems: a pore-level investigation. Exp Thermal Fluid Sci 40:168–176

Li S, Hendraningrat L, Torsaeter O (2013) Improved oil recovery by hydrophilic silica nanoparticles suspension: 2 phase flow experimental studies. In: IPTC 2013: international petroleum technology conference, European Association of Geoscientists & Engineers, Beijing, China, 26–28 March 2013

Mandal A, Bera A, Ojha K, Kumar T (2012) Characterization of surfactant stabilized nanoemulsion and its use in enhanced oil recovery. In: SPE international oilfield nanotechnology conference and exhibition, Noordwijk, The Netherlands. 155406-MS, 12–14 June 2012. Society of Petroleum Engineers

Mcelfresh PM, Olguin C, Ector D (2012) The application of nanoparticle dispersions to remove paraffin and polymer filter cake damage. In: SPE international symposium and exhibition on formation damage control, Lafayette, Louisiana, USA. 151848-MS, 15–17 February 2012. Society of Petroleum Engineers

Mohammed M, Babadagli T (2015) Wettability alteration: a comprehensive review of materials/methods and testing the selected ones on heavy-oil containing oil-wet systems. Adv Colloid Interface Sci 220:54–77

Molnes SN, Torrijos IP, Strand S, Paso KG, Syverud K (2016) Sandstone injectivity and salt stability of cellulose nanocrystals (CNC) dispersions—Premises for use of CNC in enhanced oil recovery. Ind Crops Prod 93:152–160

Morrow NR (1990) Wettability and its effect on oil recovery. J Pet Technol 42(1):476–471, 484

Munshi A, Singh V, Kumar M, Singh J (2008) Effect of nanoparticle size on sessile droplet contact angle. J Appl Phys 103:084315

Nghiem LX, Coombe DA, Ali S (1998) Compositional simulation of asphaltene deposition and plugging. In: SPE annual technical conference and exhibition, New Orleans, Louisiana. 48996-MS, 27–30 September 1998. Society of Petroleum Engineers

Nikolov A, Kondiparty K, Wasan D (2010) Nanoparticle self-structuring in a nanofluid film spreading on a solid surface. Langmuir 26:7665–7670

Papadimitriou N, Romanos G, Charalambopoulou GC, Kainourgiakis M, Katsaros F, Stubos A (2007) Experimental investigation of asphaltene deposition mechanism during oil flow in core samples. J Petrol Sci Eng 57:281–293

Parvazdavani M, Masihi M, Ghazanfari MH (2014) Monitoring the influence of dispersed nanoparticles on oil–water relative permeability hysteresis. J Petrol Sci Eng 124:222–231

Pina A, Mougin P, Béhar E (2006) Characterisation of asphaltenes and modelling of flocculation–state of the art. Oil Gas Sci Technol-Revue de l'IFP 61:319–343

Rahmani AR, Bryant S, Huh C, Athey A, Ahmadian M, Chen J, Wilt M (2015) Crosswell magnetic sensing of superparamagnetic nanoparticles for subsurface applications. SPE J 20(1):067–061, 082

Ravera F, Santini E, Loglio G, Ferrari M, Liggieri L (2006) Effect of nanoparticles on the interfacial properties of liquid/liquid and liquid/air surface layers. J Phys Chem B 110:19543–19551

Rellegadla S, Prajapat G, Agrawal A (2017) Polymers for enhanced oil recovery: fundamentals and selection criteria. Appl Microbiol Biotechnol 101:4387–4402

Rellegadla S, Bairwa HK, Kumari MR, Prajapat G, Nimesh S, Pareek N, Jain S, Agrawal A (2018) An effective approach for enhanced oil recovery using nickel nanoparticles assisted polymer flooding. Energy Fuels 32:11212–11221

Resasco DE, Drexler S, Harwell JH, Shiau BJ, Kadhum MJ, Faria J, Ruiz MP (2015) Method and foam composition for recovering hydrocarbons from a subterranean reservoir. US Patent Application 14/344,241, June 2015

Roustaei A, Bagherzadeh H (2015) Experimental investigation of SiO_2 nanoparticles on enhanced oil recovery of carbonate reservoirs. J Pet Explor Prod Technol 5:27–33

Salem Ragab AM, Hannora AE (2015) A comparative investigation of nano particle effects for improved oil recovery—experimental work. In: SPE Kuwait oil and gas show and conference, Mishref, Kuwait. 175395-MS, 11–14 October 2015. Society of Petroleum Engineers

Schembre JM, Tang G-Q, Kovscek AR (2006) Interrelationship of temperature and wettability on the relative permeability of heavy oil in diatomaceous rocks (includes associated discussion and reply). SPE Reserv Eval Eng 9:239–250

Schröder L, Lowery TJ, Hilty C, Wemmer DE, Pines A (2006) Molecular imaging using a targeted magnetic resonance hyperpolarized biosensor. Science 314:446–449

Shah RD (2009) Application of nanoparticle saturated injectant gases for EOR of heavy oils. In: SPE annual technical conference and exhibition, New Orleans, Louisiana. /29539-STU, 4–7 October 2009. Society of Petroleum Engineers

Sharma G, Mohanty K (2013) Wettability alteration in high-temperature and high-salinity carbonate reservoirs. SPE J 18:646–655

Sheng JJ (2013) Surfactant enhanced oil recovery in carbonate reservoirs. In: Enhanced oil recovery field case studies. Elsevier, Amsterdam, pp 281–299

Shokrlu YH, Babadagli T (2011) Transportation and interaction of nano and micro size metal particles injected to improve thermal recovery of heavy-oil. In: SPE annual technical conference and exhibition, Denver, Colorado, USA. 146661-MS, 30 October–2 November 2011. Society of Petroleum Engineers

Silva IG, de Melo MA, Luvizotto JM, Lucas EF (2007) Polymer flooding: a sustainable enhanced oil recovery in the current scenario. In: Latin American & caribbean petroleum engineering conference, Buenos Aires, Argentina. 107727-MS, 15–18 April 2007. Society of Petroleum Engineers

Skauge T, Spildo K, Skauge A (2010) Nano-sized particles for EOR. In: SPE improved oil recovery symposium, Tulsa, Oklahoma, USA. 129933-MS, 24–28 April 2010. Society of Petroleum Engineers

Solaimany-Nazar AR, Zonnouri A (2011) Modeling of asphaltene deposition in oil reservoirs during primary oil recovery. J Petrol Sci Eng 75:251–259

Song Y, Marcus C (2007) Hyperpolarized silicon nanoparticles: Reinventing oil exploration. In: International presentation presented at the Schlumberger seminar, Schlumberger, College Station, TX, USA

Souayeh M, Al-Maamari RS, Aoudia M, Karimi M, Hadji M (2018) Experimental investigation of wettability alteration of oil-wet carbonates by a non-ionic surfactant. Energy Fuels 32:11222–11233

Standnes DC, Austad T (2000) Wettability alteration in chalk: 2. Mechanism for wettability alteration from oil-wet to water-wet using surfactants. J Petrol Sci Eng 28:123–143

Sun X, Zhang Y, Chen G, Gai Z (2017) Application of nanoparticles in enhanced oil recovery: a critical review of recent progress. Energies 10:345

Tarboush BJA, Husein MM (2012) Adsorption of asphaltenes from heavy oil onto in situ prepared NiO nanoparticles. J Colloid Interface Sci 378:64–69

Tarek M, El-Banbi AH (2015) Comprehensive investigation of effects of nano-fluid mixtures to enhance oil recovery. In: SPE North Africa technical conference and exhibition, Cairo, Egypt. 175835-MS, 14–16 September 2015. Society of Petroleum Engineers

Tian QY, Wang L, Tang Y, Liu C, Ma C (2012) Wang T Research and application of nano polymer microspheres diversion technique of deep fluid. In: SPE international oilfield nanotechnology conference and exhibition. Society of Petroleum Engineers, Noordwijk, The Netherlands. 156999-MS, 12–14 June 2012

Viebahn P, Vallentin D, Höller S (2015) Integrated assessment of carbon capture and storage (CCS) in South Africa's power sector. Energies 8:14380–14406
Wasan DT, Nikolov AD (2003) Spreading of nanofluids on solids. Nature 423:156
Wei B, Li Q, Jin F, Li H, Wang C (2016) The potential of a novel nanofluid in enhancing oil recovery. Energy Fuels 30:2882–2891
Xu G, Zhang J, Song G (2003) Effect of complexation on the zeta potential of silica powder. Powder Technol 134:218–222
Ying JY, Sun T (1997) Research needs assessment on nanostructured catalysts. J Electroceram 1:219–238
Zamani A, Maini B, Pereira-Almao P (2012) Flow of nanodispersed catalyst particles through porous media: effect of permeability and temperature. Can J Chem Eng 90:304–314
Zhang L, Liu Y (2001) Preparation and application technology for ultrafine powder. J North China Inst Technol 22:32–43
Zhang H, Dong M, Zhao S (2010a) Which one is more important in chemical flooding for enhanced court heavy oil recovery, lowering interfacial tension or reducing water mobility? Energy Fuels 24:1829–1836
Zhang T, Davidson D, Bryant SL, Huh C (2010) Nanoparticle-stabilized emulsions for applications in enhanced oil recovery. In: SPE improved oil recovery symposium. Society of Petroleum Engineers, Tulsa, Oklahoma, USA. 129885-MS, 24–28 April 2010

Effect of Nanoparticles on the Performance of Drilling Fluids

Gomathi Rajalakshmi Seetharaman and Jitendra S. Sangwai

Abstract Owing to the extinction of conventional reservoirs, it is imperative for engineers to find the unconventional oil and gas resources. Drilling an unconventional field requires engineered drilling fluids because an efficient drilling operation purely depends upon the performance of drilling fluid. Drilling fluid which is a combination of solids and fluids performs many functions, such as cooling the drill bit, cleaning the wellbore, maintaining the wellbore pressure and development of a filter cake to prevent the invasion of fluid into the formation. The drilling fluid can be classified into oil-based mud (OBM), water-based mud (WBM) and pneumatic fluid (or) air-based fluid. Conventional drilling fluids which are in use lose their efficacy during drilling a complex reservoir, like high temperature high pressure (HTHP) and highly saline reservoir. Nanomaterials which are unique due to their distinctive properties, like high surface to volume ratio, thermal stability and conductivity, found their application in almost all fields of engineering. Many studies have been conducted to analyse the enhancement of drilling fluids through the application of nanoparticles. The studies resulted in enhancement in rheological, filtration, thermal properties of the drilling mud and also improved the wellbore stability. This chapter elaborately discusses about how the application of various types of nanoparticles/nanocomposites helps to enhance the rheological and filtration properties of the drilling mud.

Keywords Drilling fluids · Rheological properties · Nanoparticles · High temperature high pressure

G. R. Seetharaman · J. S. Sangwai (✉)
Gas Hydrate and Flow Assurance Laboratory, Petroleum Engineering Program, Department of Ocean Engineering, Indian Institute of Technology Madras, Chennai, India
e-mail: jitendrasangwai@iitm.ac.in

L. Ledwani and J. S. Sangwai (eds.), *Nanotechnology for Energy and Environmental Engineering*, Green Energy and Technology,
https://doi.org/10.1007/978-3-030-33774-2_12

1 Introduction

1.1 Drilling Fluids

A well-organized reservoir operation consists of many important stages, starting from finding the presence of crude oil to extracting the oil from the reservoir. An important parameter in-between these two stages that decides the fate of drilling is the drilling fluids. A successful drilling operation depends upon the effectiveness of the drilling fluid. Drilling a long hole from surface till deep inside the earth produces a huge amount of heat, which reduce the performance of drilling bit. A drilling fluid (or) mud, which is a combination of various chemicals, solids and liquids, is generally used to cool down the drilling bit. The drilling fluid also needs to perform other functions such as to carry the cuttings from the subsurface, minimize formation damage by producing a filter cake and to maintain the wellbore stability. The drilling fluids are classified into water-based drilling mud or fluids (WDM), oil-based drilling mud or fluids (OBM) and pneumatic drilling fluid. Since drilling fluids encounter high temperature high pressure (HPHT) environment, maintaining the viscosity of drilling fluid is the crucial part for effective functioning. Any deviation in the rheological, physical and chemical properties of the drilling fluids severely affects the performance. The flowchart in Fig. 1 briefs about the role of the properties and their functions in drilling fluids.

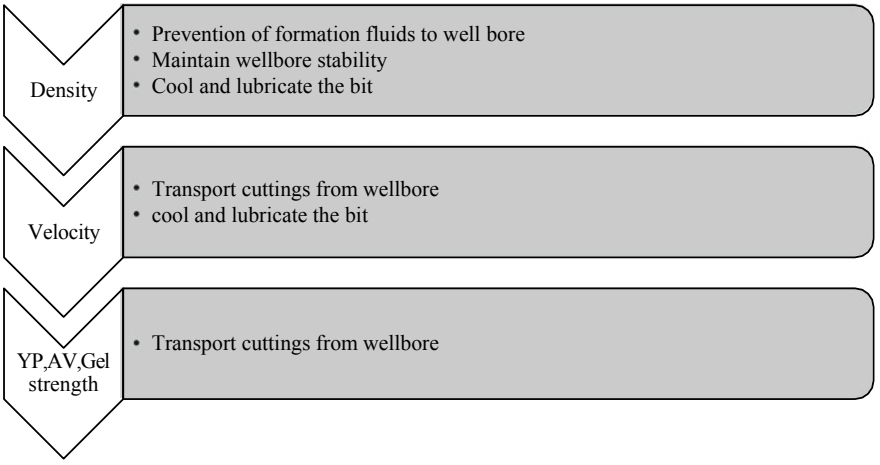

Fig. 1 Properties and functions of drilling fluid

1.2 Classification of drilling fluids

1.2.1 Water based drilling fluids

Water, brine or formate salt is used as the continuous phase in water-based mud. Since this mud is inexpensive and environmental-friendly, this is most commonly used in the industry. These are also referred to as water-based mud (WBM). Table 1 shows the various additives added to improve the properties of water-based drilling fluids.

1.2.2 Oil-Based Drilling Fluids (ODF)

The oil-based drilling fluid is also referred to as oil-based mud (OBM). The base fluid is mostly mineral oil, diesel, olefins or paraffin. Barite is used to increase the system density and bentonite clay is used as the viscosifier. Oil-based mud significantly retards the clay swelling and showed better performance in deviated well and provides a high degree of lubricity. Even though the performance of oil-based mud is superior to water-based mud (WBM) due to the toxic nature of the mud, it is strictly restricted at environmentally sensitive areas. OBM is also classified into invert emulsion method in which the water is emulsified in oil.

1.2.3 Pneumatic (or) Air-Based Drilling Fluids

Air or nitrogen is commonly used in pneumatic drilling fluid technique. The main advantage of air-based drilling fluid is it offers higher penetration rates, better hole cleaning efficiency and less formation damage, whereas air-based drilling fluid does not provide enough pressure for the prevention of inflow of the reservoir fluids.

Table 1 Additives for drilling fluids

S. No.	Additive	Property
1.	Clay	Viscosity control
2.	Barite, starch, organic colloid (sodium carboxy methyl cellulose), polyacrylates, lignosulphonates, polyanionic cellulose	To improve the rheological properties and control the density
3.	Polymers like xanthum gum, polyacrylamide and carboxymethyl cellulose	Viscosity control (HTHP affects the performance)

2 Nanotechnology and Nanomaterials

It was in 1959 when Richard Feynman coined the term "There is a plenty of room at the bottom" that leads to the invention of a new technology called nanotechnology. The materials involved in the revolution of nanotechnology are called nanomaterials which are of 10^{-9} m size. Owing to its exceptional property, like high surface to volume ratio, nanoparticle found its application in almost all fields of engineering and technology. The surface of nanoparticle offers greater area of chemical reactivity and alters the quantum effects that lead to changes in optical, magnetic, electrical and other substantial properties. Nanomaterials are extremely small in size, having dimension from 1 to 100 nm or even less. For example, the one-dimensional nanomaterial is surface film, two dimension is strands or fibres, three dimension is particles and the most common types of nanomaterials which found application in engineering and technology are nanotubes, dendrimers, quantum dots and fullerenes. There are several approaches to produce nanomaterial of various sizes; they are top-down and bottom-up approach. The nanomaterial should be dispersed in the base fluid and used as a nanofluid in drilling operation.

2.1 Importance of Nanoparticles in Drilling Muds

Owing to deterioration of conventional drilling mud at HTHP, the drilling muds failed to maintain the rheological properties. This results in loss of mud filtrate volume, which subsequently leads to failure in drilling operation. Nanoparticles, such as metal oxide, can support heat transfer from the drilling fluids by increasing the thermal conductivity. In addition, due to their extremely small size, nanoparticles plug the pores of formation and reduce the mud filtrate volume. Nanoparticles, because of their large free energy of adsorption, attach themselves to the interface between oil and water in an emulsion (Agarwal et al. 2011). The rheological properties of the drilling fluids are further enhanced due to the physiochemical, electrical and thermal properties of the nanoparticles. Hassani et al. (2016) showed that quantum effects of nanoparticles in drilling fluids make many physical changes without altering the bulk chemistry. Comparing the performance of bulk phase material, nanoparticle enhances the rheological properties, fluid loss control, wellbore and shale stabilization, wellbore strengthening, cuttings suspension and thermal properties.

3 Enhancement in Drilling Fluid Properties Due to Nanoparticles

Nanoparticles enhance the rheological properties of the drilling fluids using various mechanisms which mostly depends on the concentration, physical and chemical properties of nanoparticle and continuous phase of drilling fluids.

3.1 Effect of Nanoparticles on Rheology

Since drilling fluid is a combination of solids and fluids, controlling the rheological properties deep under the earth under high pressure and temperature is always a crucial part. Rheological properties are the basics for all analysis of wellbore hydraulics and to assess the functionality of the mud system. The rheological characteristics of drilling mud include apparent and plastic viscosity, yield point and gel strength. Researchers found that addition of various types of nanoparticles to the drilling mud modified or enhanced the rheological properties. Addition of nanoparticles to the drilling mud enhanced the plastic and apparent viscosity and maintained the yield point and gel strength.

The increment in rheological property of the bentonite-based mud by iron oxide nanoparticles was studied by Jung et al. (2011). Iron oxide nanoparticle of concentration 0.5–5 wt% increased the yield stress and viscosity of the mud. The observed enhancement in rheological properties is due to the fact that the nanoparticles got embedded in randomly distributed pore structure on the surface of clay particle in mud and confers a link between bentonite suspensions and promotes gelation of the mud. The increment in rheological properties is stable even at high temperature. At high temperature of 99 °C, the ferric oxide nanoparticle displaces the dissociated cations from clay and yields a different clay platelet microstructure and gives higher yield stress value (Mahmoud et al. 2016). Barry et al. (2015) showed that iron oxide clay hybrid and drilling fluid containing various concentration of iron oxide nanoparticle showed higher stresses at all shear rate compared to the bentonite-based drilling mud. The nanoparticles can improve the rheological properties of the drilling mud without the need of any rheological additives and this is also confirmed by Contreras et al. (2014). They used an oil-based drilling fluid prepared with iron oxide nanoparticle and graphite as a lost circulation material (LCM) rheological additive. The combination of both the nanoparticle and LCM reduced the yield point at high graphite concentration. Figure 2a shows the rheogram of bentonite and iron oxide-based drilling mud. Addition of iron oxide nanoparticle to the bentonite-based mud increased the shear stress with increase in temperature.

It is to be noted that higher temperature yielded higher yield stress of value 7.15 Pa at 60 °C because higher temperature create continuous gel strength in the bentonite suspension. The yield stress is calculated from the rheograms after extrapolating the graphs to zero shear rate and fitted in Herschel–Buckley (HB) model; $\tau =$

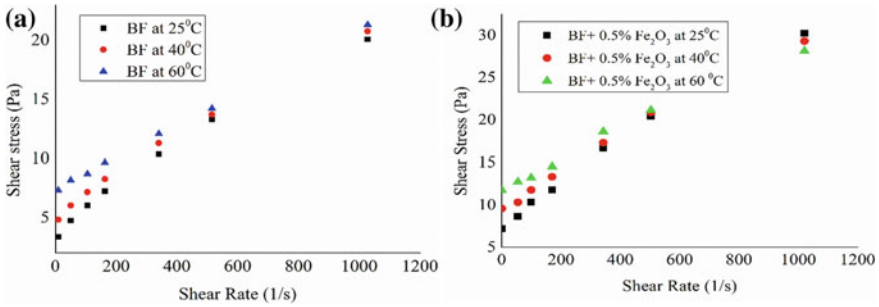

Fig. 2 **a** Rheogram of base fluid, BF, with 7 wt% bentonite at different temperature; **b** base fluid bentonite containing iron oxide nanoparticles at different temperature (Vryzas et al. 2018) (Reprinted and modified with permission from Elsevier copyright at 2018)

$\tau_{HB} + K(\gamma)^n$, where τ and γ are shear stress and shear rate, τ_{HB} is the yield stress and K is the flow consistency index which indicates suspension viscosity and n indicates flow behaviour index. $n < 1$ shows shear thinning and $n > 1$ shows shear thickening behaviour (Vryzas et al. 2018).

The dimension and concentration of the nanoparticle is also one of the decisive factors in altering the rheological properties of the drilling fluids. The silica nanoparticles dispersed in oil-based mud enhanced the viscosity of the drilling mud and remained stable at HTHP when the diameter is 20 nm (Anoop et al. 2014). But for low temperature and low pressure (LTLP) condition the dimension of the silica nanoparticle can be further reduced to 10 nm with concentration of 0.5 wt%, and it has enhanced the plastic viscosity and yield point at LTLP condition (Ghanbari et al. 2016; Hassani et al. 2016). The rheological properties of the drilling mud can be further enhanced by enhancing hydrogen bond in the drilling mud by making nanocomposite from nanoparticle mixed with polyacrylamide grafted/polyethylene glycol (Jain et al. 2015).

The enhancement in rheological properties by the addition of silica nanoparticle was also confirmed by various researchers (Mao et al. 2015a, b; Srivatsa and Ziaja 2012; Taraghikhah et al. 2015). Figure 3 shows the enhancement in apparent viscosity of the drilling mud. It is to be noted that the enhancement in viscosity is high for carbon nanotubes (CNT) and SiO_2 than ZnO nanoparticles.

Abdo and Haneef (2013) showed that when nano-palygorskite (PAL) added to the montmorillonite (Mt), which is an important constituent of bentonite-based mud, increased the gel strength by about 200% from 0.3 to 4.5. This behaviour confirms the superior performance on holding the drill cuttings under static condition. The Mt-based drilling fluid is subjected to flocculation at HPHT, while when the nano-PAL added as an additive in small quantity improves the quality of drilling mud at HPHT. Further, the rheological properties of Mt-based mud can be increased by preparing a nanocomposite of ZnO, Mt and PAL (Abdo et al. 2014). Because ZnO–clay nanocomposites impart stable colloidal mechanisms to clays as it highly discourages flocculation of clays in water, this renders significant stability to the

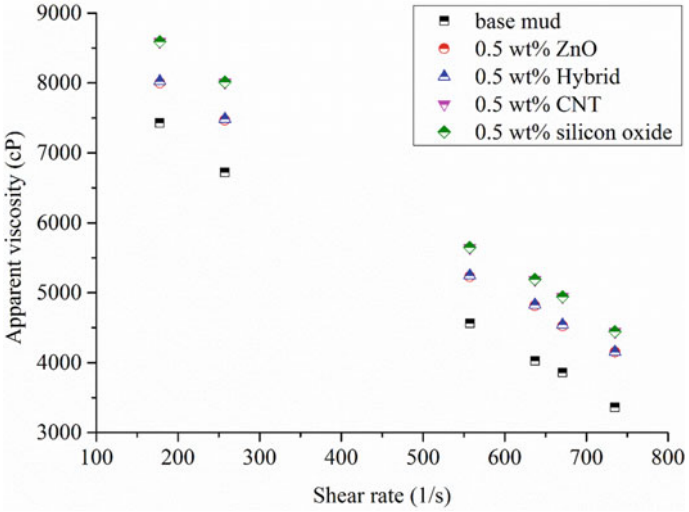

Fig. 3 The apparent viscosity versus shear rate for the water-based drilling mud in the presence of various nanoparticles (Hassani et al. 2016) (Reprinted and modified with permission from Elsevier Copyright 2016)

drilling fluids sepiolite which is an important class of clay when used in nanoform and improved rheological properties of water-based mud like plastic viscosity and yield point at both LTLP and HTHP conditions (Abdo et al. 2016; Needaa et al. 2016). Figure 4 shows the viscosity of graphene-oil nanofluid and hydrogenated oil at 30 °C by Ho et al. (2016). It is found that increase in graphene nanoparticle concentration increased the viscosity. At concentration 25 ppm and shear rate of 125 (1/s), a sharp increase in viscosity is observed due to jamming of nanoparticles at the bottom of apparatus. The shear thinning behaviour of graphene-oil-based nanofluid OBM was confirmed by decrease in viscosity with increase in shear rate. Further enhancement on rheological properties by various other nanoparticles is presented in Table 2.

3.2 Wellbore Stability and Strengthening

Wellbore instability is one of the serious issues in drilling operation. The main reasons for wellbore instability are sloughing (or) swelling and abnormal pressured formations. Owing to shale inhibition property of OBM, maintaining the wellbore for effective drilling operation is quite easy, but owing to high cost, environmental restriction and mud disposal difficulties, the application of OBM in field is restricted. For formation with low permeability (nanodarcy), the conventional drilling fluids cease to produce a filter cake. A reasonable way to overcome this problem is to prevent pressure increase at near wellbore. The nanoparticles employed in the drilling

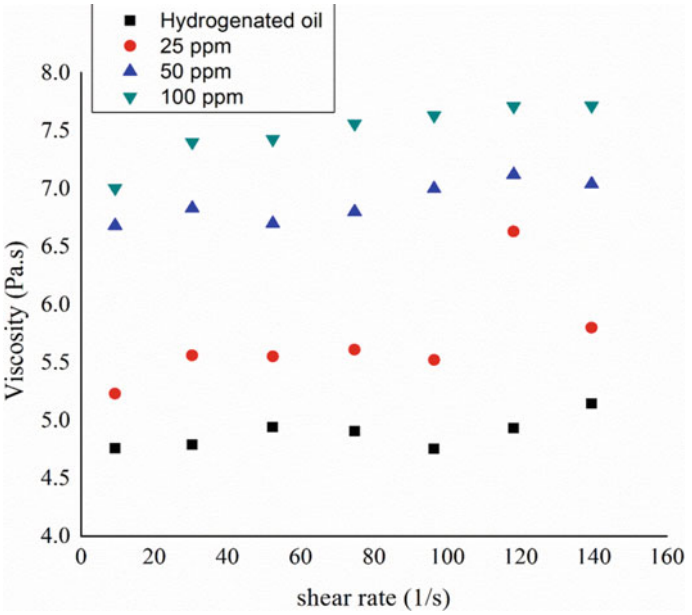

Fig. 4 Comparison of viscosity for 25, 50, 100 ppm of graphene-oil nanofluid and hydrogenated oil OBM at 30 °C (Ho et al. 2016) (Reprinted and modified with permission from Elsevier (Ho et al. 2016))

fluids penetrate through the pores of the shale and act as a bridging material and a wellbore strengthening material.

Akhtarmanesh et al. (2013) showed that silica nanoparticles reduced the fluid penetration into Grupi shale up to 68% in comparison with WBM, and the minimum concentration required to reduce the permeability and minimize the fluid invasion is 10 wt%. Nanoparticles with diameter of 35 nm showed better plugging efficiency than 50 nm sized nanoparticle due to the pore size in the formation. 1 wt% of nanosilica in WBM improved the shale stability by plugging the pores through physical pore plugging mechanism (Taraghikhah et al. 2015). Silica nanoparticles of 10–30 nm produced a lowest amount of fluid loss of 4 ml in an American Petroleum Institute (API) fluid loss test using a hydrophilic filter membrane with 100 nm pores (Hoelscher et al. 2012). Since biopolymers are stable at high temperature, xanthum gum combined with silica nanoparticles in a particle plugging apparatus at pressure of 1000 psi and a temperature of 93 °C (200 F) produced a minimum fluid loss of 7.9 ml and also very effective in plugging the pores (Srivatsa and Ziaja 2012). But the same silica nanoparticle with dimension of 10–20 nm in OBM produced higher filtration than the base mud and further increasing the concentration of nanoparticles, the cracks in the mud cake propagates, because of poor dispersion of silica nanoparticles in OBM (Kang et al. 2016).

Nwaoji et al. (2013) combined the lost circulation material (LCM) with nanoparticles to control the well instability problem. Iron (III) hydroxide nanoparticle when

Table 2 Application of nanoparticles on modification of rheological of properties drilling fluids

S. No.	Author	Types of NPs	Base fluid	Enhancement in rheological properties[a]
1	Agrawal et al. (2011)	Clay and silica	Oil	• Improved the viscosity and gel strength of invert emulsion at HTHP • A combination of 2 wt% of nanoclay and 1 wt% nanosilica showed enhanced rheological properties
2	Li et al. (2010)	Cellulose particle	Water	Improved PV, YP and gel strength at 0.5 wt% at HTHP
3	Song et al. (2016a, b)			Improved PV, YP and gel strength at 3.5 wt% at LTLP
4	Sadeghalvaad and Sabbaghi (2015)	TiO_2/PAM nanocomposite	Water	Increased PV and YP compared to nanoparticle
5	William et al. (2014)	CuO and ZnO	Water	Better rheological stability for nano-based WBM compared to base fluids at HTHP

[a]*PV* Plastic viscosity; *YP* Yield point

mixed with graphite (LCM) increased the fracture breakdown pressure by 70% over unblended water-based mud, and the increment in fracture breakdown pressure is 47% higher than OBM because WBM is primarily made of organophillic clay and water. It interacts strongly with nanoparticles, thereby stabilizing them. There are no electrostatic attractions or van der Waals forces between nanoparticles and the fluid constituents unlike OBM.

3.3 Enhancement in Thermal Property

Enormous amount of heat is produced due to drilling deep down the earth and the friction between drilling bit and the surface of rock added on the heat to the drilling bit which deteriorates the performance of the drilling fluid. The metal oxide nanoparticle in nature generally has high thermal conductivity, so the applicability of nanoparticles in drilling fluids improves the rate of heat transfer. The particle is in micrometre range and does not possess Brownian motion, leading to lower thermal conductivity. For example, a carbon nanoparticle with 0.2 wt% in WBM showed higher

thermal conductivity than 0.4 wt% due to increase in distance between particles (Ho et al. 2014). Increase in temperature increased the thermal conductivity of the nano-enhanced drilling fluid. Silver nanoparticles with diameter 5 nm dispersed in kerosene-based mud showed higher conductivity at 50 °C than at 25 °C because of the enhanced Brownian motion (Li et al. 2010). The increment in thermal conductivity of the drilling mud by the addition of nanoparticles made the mud to cool faster as it moves up the surface. The increase in nanoparticle concentration increased the thermal property of the drilling fluid. The enhancement in thermal conductivity was higher in the case of CuO than ZnO for a particle concentration of 0.1, 0.3 and 0.5 wt% (William et al. 2014). The enhancement in thermal conductivity for nano-sized particle was significant than with micro-sized particle. Nanoparticle concentration (0.5 wt%) promoted better thermal conductivity and the value of thermal conductivity will be lowered if the nanofluid was prepared in base fluid which are highly viscous in nature (PEG 600) because the nanoparticles may get entrapped in the microstructure of network forming aggregates (Ponmani et al. 2016). Figure 5 shows the comparison of thermal conductivity for various concentrations of ZnO nanoparticle. It is clear that increase in nanoparticle concentration increased the thermal conductivity.

Since multiwalled carbon nanotubes (MWCNTs) are hydrophobic in nature, dispersion in WBM remains a greater challenge. Modifying the surface with hydrophilic (nitric acid) group produced a stable dispersion in WBM, leading to enhancement in thermal conductivity by 23.2% for 1 vol% of functionalized MWCNTs (Sedaghatzadeh and Khodadadi 2012). CNTs which are functionalized by hydrophilic group through acid treatment increased the thermal conductivity by 31.8% at 50 °C and the increment in thermal conductivity is even higher for oil-based mud (Fazelabdolabadi et al. 2015).

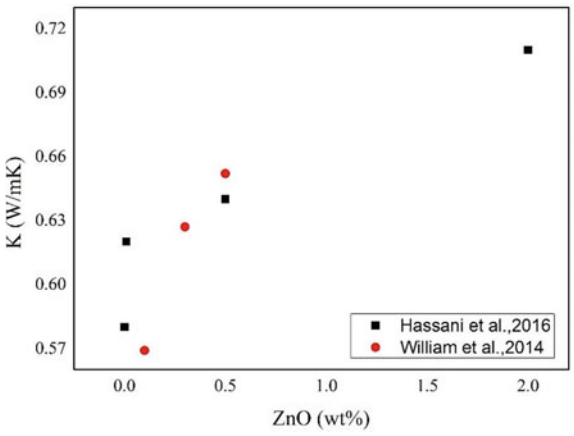

Fig. 5 Comparison of thermal conductivity for ZnO nanoparticle from Hassani et al. (2016) and William et al. (2014). Reprinted and modified with permission from Elsevier, copyright (Elsevier 2014, 2016)

Table 3 Application of nanoparticles on modification of rheological properties of drilling fluids

S. No.	Author	Drilling mud	NPs	Enhancement in lifting capacity
1	Boyou et al. (2019)	Water	Silica (0.5, 1, 1.5 ppb)	The SiO_2 nanoparticles increased the cutting transport efficiency for all inclination and increase in nanoparticle increased the efficiency
2	Gbadamosi et al. (2019)	Water	Silica (0.001–1.5 wt%)	Smaller the cutting particles, higher the efficiency Larger particles are least affected by buoyancy and viscous force
3	Samsuri and Hamzah (2011)	Water	MWCNTs (0.001–0.003 wt%)	Low concentration of MWCNTs has minimum impact on cuttings recovery

3.4 Enhancement in Lifting Capacity

The most important function of the drilling fluid is transporting the cuttings to the surface. There are many factors which affect the cutting capacity of the drilling mud, like flow rate of the mud, particle settling velocity, geometry, orientation and concentration of the particle. The cutting transport remains a major problem in vertical and inclined well due to gravitational force.

The nanoparticles added to the drilling mud increase the annular viscosity of the drilling mud which helps to increase the lifting capacity of the mud. Another phenomenon which is commonly encountered is by balancing the gravity force or overcoming the gravity force. The nanoparticles added to the drilling mud increased the drag force on the drilled cuttings which helps to overcome the gravity force by increasing the surface force. The enhancement in lift capacity for various nanoparticles is presented in Table 3.

3.5 Fluid Loss Control by Nanoparticles

One of the very important properties of drilling mud is filtration control. Drilling through the depleted, deep water and deviated reservoir result in regular huge loss of mud and results in fluid invasion. The reason behind the fluid loss is the differential

pressure that occurs between the formations and the wellbore. In the process of filtration, a solid cake (or) filtration cake is produced by the solids and chemicals present in the mud, to inhibit (or) stop the fluid invasion into the formation. Since the particles associated with the conventional drilling fluids are usually large in size than the pores of formation, it fails to inhibit the fluid loss. In this case, the filtration cake produced by the drilling mud is usually thick resulting in pipe sticking and inability to plug the pores. Loss circulation is another important issue in drilling fluid in which the drilling fluid is lost at any depth. The nanoparticles added to the drilling mud produces a filter cake of minimum thickness because volume of filtrate entering the formation is very less due to low permeability and low porosity. Moreover, due to the relatively small size of the nanoparticle it can enter the pores of the formation and inhibit the fluid invasion (Fig. 6).

Silica nanoparticles with concentration of 3% by volume and size ranges from 40 to 130 nm in WBM reduced the mud cake thickness up to 34% than the normal WBM (Javeri et al. 2011). While the same silica nanoparticle in bio-polymer and surfactant-based mud reduced the filtration loss up to 40% (Srivatsa and Ziaja 2012) and once the filter cake is produced by the polymer, the nanoparticles create a thin layer of deposit on the surface of the formation, which helps to prevent the polymer invasion into the formation. Mao et al. (2015) used silica-based drilling fluid with dimension of 12 nm and performed API fluid loss. The results revealed that the nano-based drilling mud reduced the fluid loss up to 80%. Mahmoud et al. (2016)

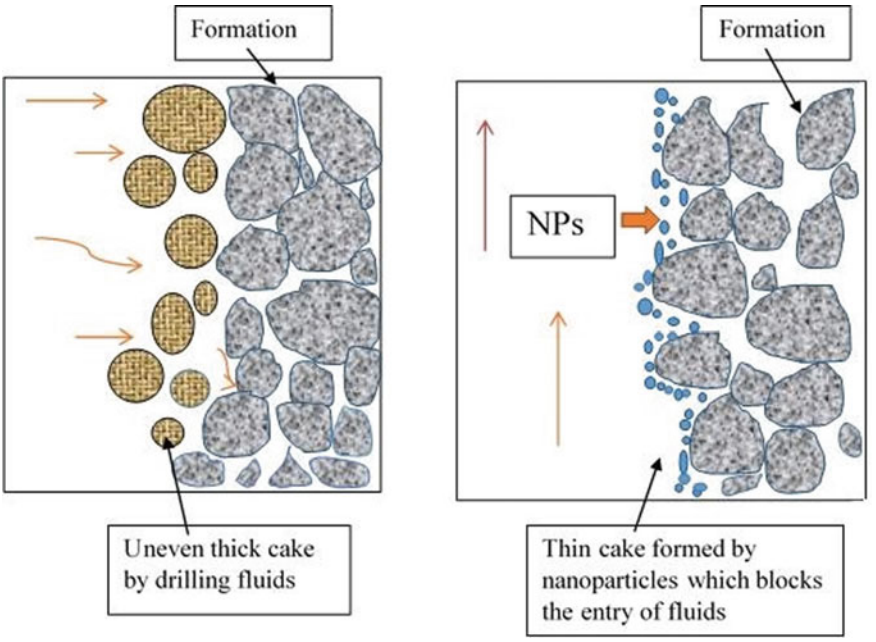

Fig. 6 Nanoparticles act as a barrier to prevent the inflow of mud into the formation

produced a minimum mud cake thickness of 1 mm for a silica nanoparticle of 0.7 wt%. Even though increase in nanoparticle concentration reduced the filtration due to agglomeration of particles, an increase in porosity and permeability was found in the mud cake. The particle size distribution of nanoparticles in the drilling mud is one of the decisive factors that decide the fate of filtration, because bentonite nanoparticles of 4–9 nm in WBM increased the filtration loss due to poor distribution or the fact that the nanoparticles are so small and they just pass through the filter cake (Abdo and Haneef 2013). So in order to attain the larger particle size distribution, the nanoparticles were mechanically prepared and the filter cake produced was also more compact in nature such that sealing pressure is tolerable (Akhtarmanesh et al. 2013). Nasser et al. (2013) observed the effect of pressure on fluid loss for nanographite-based mud and normal drilling mud. It is found that normal drilling fluid will lose its fluidity with increase in pressure, whereas for nano-based mud the observed loss is very minimum.

Figure 7 shows the filtration loss properties of ZnO in PEG and PVP-based drilling fluids (Ponmani et al. 2016). Though the trend of increase in fluid loss with time is the same for all the mud, the loss in quantity of fluid is decreased by the introduction of 0.1 wt% nano ZnO. Further increase in concentration of nanoparticles from 0.1 to 0.5 wt% showed considerable improvement in reducing the fluid loss. The obtained results in fluid loss for nano-based mud are also compared with micro-based mud and the results confirm that nano-based mud shows superior performance in reducing the fluid loss than micro- and polymer-based mud. Jung et al. (2011) compared the fluid filtration behaviour of bentonite mud and mud with bentonite and iron oxide nanoparticles. Compared to the raw bentonite-based mud, the mud with iron oxide nanoparticles reduced the filtrate volume. Perween et al. (2018) produced a thin filter cake with zinc titanate nanoparticles dispersed in bentonite-based mud consisting of various additives of viscosity, fluid loss and clay stabilizer. The API filtrate test

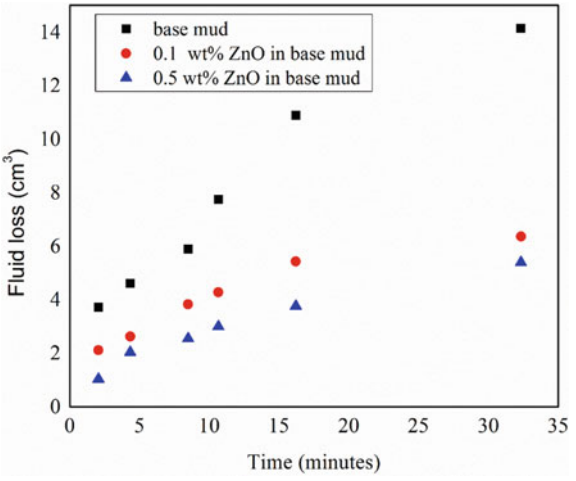

Fig. 7 Fluid loss during a period of 30 min for WBM and NWBM (ZnO) (Reprinted and adopted from SPE, (Ponmani et al. 2016))

Table 4 Thickness of mud cake produced by nano clay–silica (CS) composite with increase in temperature

Sample*	Thickness of mud cake (in.)	
	25 °C	90 °C
Base mud (WBM)	0.137	0.149
WBM + 0.1 wt% nano CS	0.066	0.068
WBM + 0.5 wt% nano CS	0.059	0.058
WBM + 1 wt% nano CS	0.052	0.053
WBM + 1.5 wt% nano CS	0.054	0.051
WBM + 0.1 wt% nano SiO_2	0.071	0.077
WBM + 0.5 wt% nano SiO_2	0.067	0.079
WBM + 1.0 wt% nano SiO_2	0.066	0.076
WBM + 1.5 wt% nano SiO_2	0.066	0.074

*WBM+nano CS or WBM+SiO_2

result shows that the action of $ZnTiO_3$ in drilling fluid produced mud cake of ~1 mm thickness.

Table 4 shows the thickness of the mud cake produced by Cheraghian et al. (2018) for nanocomposite of clay and silica and silica nanoparticles alone. It is found that increase in nanoparticle produced mud cake of minimum thickness. The mud cake produced by silica nanoparticles alone is off high in thickness whereas for nanocomposite consisting of silica and clay, the mud cake thickness is low. This is due to the fact that the synthesized nanocomposite is smaller in size than the silica nanoparticle and the effective plugging can also be easily achieved. There is a considerable reduction in fluid loss by nanocomposite of silica and clay than WBM and silica-based mud. A low concentration of nanocomposite is sufficient to reduce the fluid loss. Table 5 presents the work done by various researchers on fluid loss with various nanoparticles.

4 Field Application

Field test was conducted in horizontal wells in Canada. The calcium-based nanoparticle emulsion is produced via water–oil micro emulsion approach. The calcium nanoparticle was selected because of its good compatibility with invert emulsion, low toxicity and is inexpensive. The field application of calcium-based 0.5 wt% nanoparticle in invert emulsion-based mud was presented by Borisov et al. (2015). Table 6 shows the comparison of various properties of calcium-based drilling fluid at field and lab scale.

Addition of 10 vol% of carrier emulsion fluid did not affect the basic properties of OBM drilling fluids but the average filtrate volume is reduced to 20–30% of control wells. The filtrate volume remains unchanged once an optimum concentration

Table 5 Reduction of filtration loss of drilling fluids by nanoparticles

S. No.	Base fluid	NPs	Modification in filtration property	Author
1	Water	ZnO/polymer nanocomposite	Under HPHT condition 1.0 g of ZnO nanoparticle reduced the filtrate loss	Aftab et al. (2016)
2	Oil	1. Iron 2. Calcium	LCM (graphite) was used in minimum concentration with minimum Fe and Ca nanoparticles. Iron nanoparticle showed better performance than Ca	Contreras et al. (2014)
3	Water	Carbon nanotubes	0.8 wt% of CNT reduced the filtration loss under HPHT	Halali et al. (2016)
4	Water	Cellulose nanoparticle	Reduced fluid loss at an optimized concentration of 0.5 wt%	Li et al. (2015)
5	Water	Graphene	Reduced filtrate loss up to 30% in 10 ppg WBF	Taha and Lee (2015)
6	Water	1. CuO 2. ZnO	Fluid loss and filtrate cake thickness reduced significantly under LPLT and HPHT condition, ZnO nanoparticle showed a better result than CuO	William et al. (2014)
7	Synthetic	SiO_2	A quantity of 40 wt% of silica nanoparticles was needed to reduce the filtrate loss at HTHP condition	Yusof and Hanafi (2015)

of calcium nanoparticles in the circulating mud is attained. Taha and Lee (2015) presented a field data using nanographene blended in a surfactant for extremely hard formation in Myanmar with temperature up to 176 °C (349 °F). It was found that drilling fluid performance is directly proportional to nanoparticle concentration, and once the nanoparticle concentration reduced 2% by volume, the rate of penetration also reduced. In the field trail when the graphene nanoparticle concentration was

Table 6 Comparison between carrier emulsion samples having 5 wt% calcium nanoparticles prepared on an industrial scale

Properties	Field scale	Lab scale
MW (kg/m^3)	1045 ± 5	1049 ± 3
ES (mV)	582 ± 57	780 ± 20
PV (cP)	12 ± 2	12 ± 2
YP ($lb/100ft^2$)	5 ± 2	5 ± 2
GS 10 s (lb/ft^2)	4 ± 0.5	4 ± 0.5
GS 10 min (lb/ft^2)	5.0 ± 0.5	6.0 ± 0.5
OWR	83/17	83/17
Solids (vol%)	8.0 ± 0.5	8.0 ± 0.5

kept between 2 and 3%, it improved the rate of penetration up to 125% and improved bits lifespan by 75%. The improvement in drilling performance and bits' lifespan had reduced operator's operational time and cost.

5 Recommendations and Challenges of Nanofluids

Though a lot of studies and positive results were available on the applicability of nanoparticles in drilling muds, application of nanoparticles in a field study has a serious of challenges and issues. Stability of nanoparticle dispersion in drilling fluid is a major problem. Even after performing high shearing with ultrasonic baths, magnetic stirrers or homogenizers nanoparticle try to re-agglomerate due to strong van der Waals forces. Though introduction of surfactant in a drilling fluid effectively disperse the nanoparticles, surfactants are very expensive and can alter the rheological properties of the mud. Another major issue associated with the nanoparticle is sedimentation and flocculation. If flocculation and sedimentation is not controlled in drilling muds, it leads to plugging in drilling lines, mud pumps which yield poor rheological performance and shale inhibition. As suggested in the literature, instead of single sphere molecule, metal oxide and polymer composite reduced the problem of flocculation and sedimentation in drilling mud, but much results are not available in the area.

6 Conclusion

The overall studies on the application of nanoparticles in the drilling fluids showed a greater improvement in rheological properties, thermal stability, and reduction in fluid loss and wellbore stability. Addition of nanoparticles to the drilling mud increased the viscosity, and the shear thinning behaviour of the drilling fluids was also maintained at HTHP condition. Though the positive effect of increasing the

concentration of nanoparticles increased the viscosity, sometimes it leads to agglomeration which reduces the performance of drilling mud. Thus tuning the appropriate concentration of nanoparticles in a drilling fluid is an important step to remember. Further with the addition of nanoparticles, the nano-enhanced drilling mud exhibited continuous gel strength while maintaining the yield stress value. The enhancement in the drilling fluid properties by the addition of nanoparticles completely depends on the particle shape, size and concentration. The shale permeability of the formation can also be reduced by physical plugging of pores by nanoparticles. The filtrate cake which has been produced by the nanoparticles is of very minimum in thickness compared to conventional drilling mud. The API tests proved that nano-enhanced mud can reduce the filtrate volume up to 60%. Since nanoparticles are oxide in nature, addition of nanoparticles to the drilling mud increased the thermal conductivity, which allowed the mud to cool in a faster. Thus addition of nanoparticles to the drilling mud could be a better solution for drilling complex, depleted and deviated reservoir and HTHP environment.

References

Abdo J, Haneef MD (2013) Clay nanoparticles modified drilling fluids for drilling of deep hydrocarbon wells. Appl Clay Sci 86:76–82

Abdo J, Zaier R, Hassan E, AL-Sharji H, Al-Shabibi A (2014) ZnO–clay nanocomposites for enhance drilling at HTHP conditions. Surf Interface Anal 46:970–974

Abdo J, AL-Sharji H, Hassan E (2016) Effects of nano-sepiolite on rheological properties and filtration loss of water-based drilling fluids. Surf Interface Anal 48:522–526

Aftab A, Ismail AR, Khokhar S, Ibupoto ZH (2016) Novel zinc oxide nanoparticles deposited acrylamide composite used for enhancing the performance of water-based drilling fluids at elevated temperature conditions. J Petrol Sci Eng 146:1142–1157

Agarwal S, Tran P, Soong Y, Martello D, Gupta RK (2011) Flow behavior of nanoparticle stabilized drilling fluids and effect of high temperature aging. In: Presented in AADE national technical conference and exhibition, Houston, 12–14 April 2011, pp 12–14

Akhtarmanesh S, Shahrabi MA, Atashnezhad A (2013) Improvement of wellbore stability in shale using nanoparticles. J Petrol Sci Eng 112:290–295

Anoop K, Sadr R, Al-Jubouri M, Amani M (2014) Rheology of mineral oil-SiO2 nanofluids at high pressure and high temperatures. Int J Therm Sci 77:108–115

Barry MM, Jung Y, Lee JK, Phuoc TX, Chyu MK (2015) Fluid filtration and rheological properties of nanoparticle additive and intercalated clay hybrid bentonite drilling fluids. J Pet Sci Eng 127:338–346

Borisov AS, Husein M, Hareland G (2015) A field application of nanoparticle-based invert emulsion drilling fluids. J Nanoparticle Res 17:340

Boyou NV, Ismail I, Sulaiman WRW, Haddad AS, Husein N, Hui HT, Nadaraja K (2019) Experimental investigation of hole cleaning in directional drilling by using nano-enhanced water-based drilling fluids. J Petrol Sci Eng 176:220–231

Cheraghian G, Wu Q, Mostofi M, Li MC, Afrand M, Sangwai JS (2018) Effect of a novel clay/silica nanocomposite on water-based drilling fluids: Improvements in rheological and filtration properties. Colloids Surf A: Physicochem Eng Asp 555:339–350

Contreras O, Hareland G, Husein M, Nygaard R, Al-Saba M (2014) Application of in-house prepared nanoparticles as filtration control additive to reduce formation damage. In: Presented in SPE

international symposium and exhibition on formation damage control, Lafayette, Louisiana, USA, 26–28 February 2014. [SPE-168116-MS]
Fazelabdolabadi B, Khodadadi AA, Sedaghatzadeh M (2015) Thermal and rheological properties improvement of drilling fluids using functionalized carbon nanotubes. Appl Nanosci 5:651–659
Gbadamosi AO, Junin R, Abdalla Y, Agi A, Oseh JO (2019) Experimental investigation of the effects of silica nanoparticle on hole cleaning efficiency of water- based drilling mud. J Petrol Sci Eng 172:1226–1234
Ghanbari S, Kazemzadeh E, Soleymani M, Naderifar A (2016) A facile method for synthesis and dispersion of silica nanoparticles in water-based drilling fluid. Colloid Polym Sci 294:381–388
Halali MA, Ghotbi C, Tahmasbi K, Ghazanfari MH (2016) The role of carbon nanotubes in improving thermal stability of polymeric fluids: experimental and modeling. Ind Eng Chem Res 55:7514–7534
Hassani SS, Amrollahi A, Rashidi A, Soleymani M, Rayatdoost S (2016) The effect of nanoparticles on the heat transfer properties of drilling fluids. J Petrol Sci Eng 146:183–190
Ho CY, Yusup S, Soon CV (2014) Study on the effect of nanoparticle loadings in base fluids for improvement of drilling fluid properties. J Adv Chem Eng 4:115
Ho CY, Yusup S, Soon CV, Arpin MT (2016) Rheological behaviour of graphene nano-sheets in hydrogenated oil-based drilling fluid. Proc Eng 148:49–56
Hoelscher KP, De Stefano G, Riley M, Young S (2012) Application of nanotechnology in drilling fluids. In: Presented in SPE international nanotechnology conference, Noordwjik, The Netherlands, 12–14 June 2012. [SPE-157031-MS]
Jain R, Mahto V, Sharma VP (2015) Evaluation of polyacrylamide-grafted- polyethylene glycol/silica nanocomposite as potential additive in water based drilling mud for reactive shale formation. J Nat Gas Sci Eng 26:526–537
Javeri SM, Haindade ZMW, Jere CB (2011) Mitigating loss circulation and differential sticking problems using silicon nanoparticles. In: Presented at SPE/IADC middle east drilling technology conference and exhibition, Muscat, Oman, 24–26 October 2011. [SPE-145840-MS]
Jung Y, Barry M, Lee JK, Tran P, Soong Y, Martello D, Chyu M (2011) Effect of nanoparticle-additives on the rheological properties of clay-based fluids at high temperature and high pressure. In: Presented in AADE national technical conference and exhibition, Houston, 12–14 April 2011, pp 1–4
Kang Y, She J, Zhang H, You L, Song M (2016) Strengthening shale wellbore with silica nanoparticles drilling fluid. Petroleum 2:189–195
Li D, Hong B, Fang W, Guo Y, Lin R (2010) Preparation of well-dispersed silver nanoparticles for oil-based nanofluids. Ind Eng Chem Res 49:1697–1702
Mahmoud O, Nasr-El-Din HA, Vryzas Z, Kelessidis VC (2016) Nanoparticle-based drilling fluids for minimizing formation damage in HP/HT applications. In: Presented in SPE international conference and exhibition on formation damage control, Lafayette, Louisiana, USA, 24–26 February 2016. [SPE-178949-MS]
Mao H, Qiu Z, Shen Z, Huang W, Zhong H, Dai W (2015a) Novel hydrophobic associated polymer based nano-silica composite with core–shell structure for intelligent drilling fluid under ultra-high temperature and ultra-high pressure. Prog Nat Sci: Mater Int 25:90–93
Mao H, Qiu Z, Shen Z, Huang W (2015b) Hydrophobic associated polymer based silica nanoparticles composite with core–shell structure as a filtrate reducer for drilling fluid at ultra-high temperature. J Petrol Sci Eng 129:1–14
Nasser J, Jesil A, Mohiuddin T, Al Ruqeshi M, Devi G, Mohataram S (2013) Experimental investigation of drilling fluid performance as nanoparticles. World J Nano Sci Eng 3:57
Needaa AM, Pourafshary P, Hamoud AH, Jamil ABDO (2016) Controlling bentonite-based drilling mud properties using sepiolite nanoparticles. Pet Explor Dev 43:717–723
Nwaoji CO, Hareland G, Husein M, Nygaard R, Zakaria MF (2013) Wellbore strengthening- nanoparticle drilling fluid experimental design using hydraulic fracture apparatus. In: Presented at SPE/IADC drilling conference and exhibition, Amsterdam, Netherlands, 5–7 March 2013. [SPE-163434-MS]

Perween S, Beg M, Shankar R, Sharma S, Ranjan A (2018) Effect of zinc titanate nanoparticles on rheological and filtration properties of water based drilling fluids. J Petrol Sci Eng 170:844–857

Ponmani S, Nagarajan R, Sangwai JS (2016) Effect of nanofluids of CuO and ZnO in polyethylene glycol and polyvinylpyrrolidone on the thermal, electrical, and filtration- loss properties of water-based drilling fluids. SPE J 21:405–415

Sedaghatzadeh M, Khodadadi A (2012) An improvement in thermal and rheological properties of water-based drilling fluids using multiwall carbon nanotube (MWCNT). Iran J Oil Gas Sci Technol 1:55–65

Sadeghalvaad M, Sabbaghi S (2015) The effect of the TiO2/polyacrylamide nanocomposite on water-based drilling fluid properties. Powder Technol 272:113–119

Samsuri A, Hamzah A (2011) Water based mud lifting capacity improvement by multiwall carbon nanotubes additive. J Pet Gas Eng 5:99–107

Song K, Wu Q, Li M, Ren S, Dong L, Zhang X, Lei T, Kojima Y (2016a) Water- based bentonite drilling fluids modified by novel biopolymer for minimizing fluid loss and formation damage. Colloids Surf A: Physicochem Eng Asp 507:58–66

Song K, Wu Q, Li MC, Wojtanowicz AK, Dong L, Zhang X, Ren S, Lei T (2016b) Performance of low solid bentonite drilling fluids modified by cellulose nanoparticles. J Nat Gas Sci Eng 34:1403–1411

Srivatsa JT, Ziaja MB (2012) An experimental investigation on use of nanoparticles as fluid loss additives in a surfactant-polymer based drilling fluids. In: Presented in international petroleum technology conference, Bangkok, Thailand, 15–17 November 2012. [IPTC-14952-MS]

Taha NM, Lee S (2015) Nano graphene application improving drilling fluids performance. In: Presented at international petroleum technology conference, Doha, Qatar, 6–9 December 2015. [IPTC-18539-MS]

Taraghikhah S, Kalhor Mohammadi M, Tahmasbi Nowtaraki K (2015) Multifunctional nanoadditive in water based drilling fluid for improving shale stability. In: Presented in international petroleum technology conference, Doha, Qatar, 6–9 December 2015. [IPTC-18323-MS]

Vryzas Z, Zaspalis V, Nalbandian L, Terzidou A, Kelessidis VC (2018) Rheological and HP/HT fluid loss behavior of nano-based drilling fluids utilizing Fe3O4 nanoparticles. Mater Today: Proc 5:27387–27396

William JKM, Ponmani S, Samuel R, Nagarajan R, Sangwai JS (2014) Effect of CuO and ZnO nanofluids in xanthan gum on thermal, electrical and high pressure rheology of water-based drilling fluids. J Petrol Sci Eng 117:15–27

Yusof MAM, Hanafi NH (2015) Vital roles of nano silica in synthetic based mud for high temperature drilling operation. In: AIP conference proceedings, July 2015, vol 1669, no 1. AIP Publishing, p. 020029

Interaction of Nanoparticles with Reservoir Fluids and Rocks for Enhanced Oil Recovery

Uma Sankar Behera and Jitendra S. Sangwai

Abstract Nanotechnology is a common word used by academia which is referred to the applied nanoscience conducted at nanoscale (1–100 nm) for variety of industrial applications. Application of nanotechnology in various fields is increasing extensively resulting in an enormous amount of publications in the distinct field. Nanoparticles (NPs) possess unique properties due to their larger surface area which leads to prolong application in multifold. Researchers working in enhanced oil recovery (EOR) areas are trying to get rid of challenges faced by the oil and gas companies for crude oil production. This chapter, therefore, focuses on work carried out by the researchers on chemical and rarely on thermal, gas injection, and biological EOR methods using NPs. Chemical enhanced oil is recovery (CEOR) methods taken into consideration due to their popularity in oilfields than the other existing methods. Viscosity, interfacial tension (IFT), and wettability are the major influencing factors for EOR. The authors intend to make the reader understand the pore-scale mechanism behind the enhanced oil recovery in the presence of NPs. In the early stage of enhanced oil recovery, it is essential to understand the properties of various NPs. Literature review reveals that properties of NPs mostly depend on methods they are prepared. Hence, at the beginning of the chapter, the types of NPs, preparation, and their characterization are explained briefly with the application of various nanoparticles in CEOR. Limitation of NPs application in chemical EOR area is spelled out clearly with the recommendation at the end.

Keywords Enhance oil recovery · Interfacial tension · Nanoparticles · Nanotechnology · Wettability

U. S. Behera · J. S. Sangwai (✉)
Gas Hydrate and Flow Assurance Laboratory, Petroleum Engineering Program, Department of Ocean Engineering, Indian Institute of Technology Madras, Chennai, India
e-mail: jitendrasangwai@iitm.ac.in

L. Ledwani and J. S. Sangwai (eds.), *Nanotechnology for Energy and Environmental Engineering*, Green Energy and Technology,
https://doi.org/10.1007/978-3-030-33774-2_13

1 Introduction

The existence of natural resources indicates the strength of the country and the adoption of newer technologies in their production magnifies its economy. When we talk about natural resources, it includes minerals, hydrocarbon, soil, forest, well-connected rivers, etc. World energy consumption is increasing day by day. The main reason for the high utilization of energy is due to the increase in human population all over the world. Most of the developed and developing nation of the world utilizes more than 90% of the total energy produced in the world. Though there are various sources exist for the production of energy such as nuclear power, hydropower, geothermal power, solar power, and hydrocarbon fuel, the importance of the use of hydrocarbon fuel has grown due to its wide occurrences and ease of applications. In most cases, at least 50% (approximate) of energy requirement of a country is being fulfilled by hydrocarbon fuel (IEA report 2016). According to the BP world energy data, the petroleum reserves are limited (BP statistical review of world energy, June 2018). Hence more attention has been paid to recover crude oil from depleted or matured reservoirs. As the world reservoirs are growing older and older day by day, it is difficult to extract more hydrocarbons using conventional methods. The existing traditional methods in practice can lead to recovering maximum 10–15% original oil in place. This initial recovery is due to the internal pressure of the reservoir also known as a primary recovery method. Additional 15–20% original oil in place (OOIP) can be recovered by water or gas flooding which are known as secondary recovery methods (U.S. Department of energy 2011). Approximately more 15–20% of the OOIP can be recovered by proper, suitable technology at tertiary level, which are called as enhanced oil recovery (EOR) methods. Figure 1 shows various recovery processes adopted for oil production. Injection of an exotic substance into the reservoir to increase the output is called EOR. The classification of EOR by application is represented in Fig. 2.

Literature reviews disclose that the implant of nanotechnologies in the enhanced oil recovery process has the potential to accelerate oil production from the matured formation. Due to the nanosize, multiple shapes, and larger surface area make the

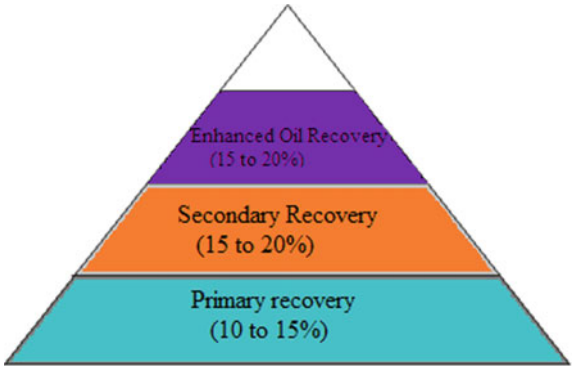

Fig. 1 Percentage of oil recovery by the various processes

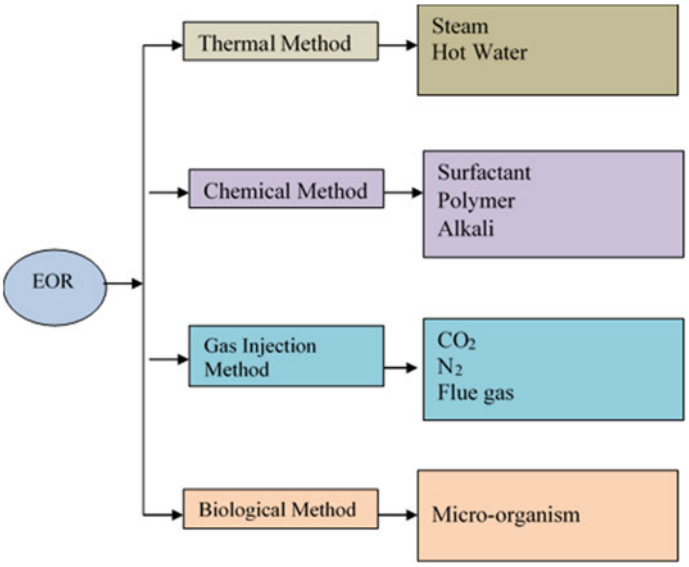

Fig. 2 Classification of various EOR methods

nanoparticles unique than the other micro-size particles. Nanoparticles can be prepared from various metal oxide as they are much stable than the native metal. Formation of nanofluid is quite simple in which NPs are added in different base fluids to obtain a stable suspension. Role of nanoparticles in enhanced oil recovery can be better understood only when we can able to analyze its properties. To figure out the features of nanoparticles, one should realize the formation method of nanoparticles as it plays a vital role in determining the properties of nanoparticles. Hence, here, few methods of preparation and properties of nanoparticles are included along with their characterization process.

2 Nanoparticles and Their Origin

The particulate matter with at least one dimension less than 100 nm is generally known as nanoparticles (Christian et al. 2008; Sarit et al. 2007). The size of the nanoparticles put them within the range of colloidal particles as shown in Fig. 3. Based on the scale, nano, and colloidal particles are defined and based on these different types of particles are observed in the environment. The examples of such system found in the atmosphere are dispersion (solid in liquid), emulsion (liquid in liquid), and aerosols (solid in gas). Formation of colloids is a natural phenomenon in the environment, and it might have taken millions of years to form.

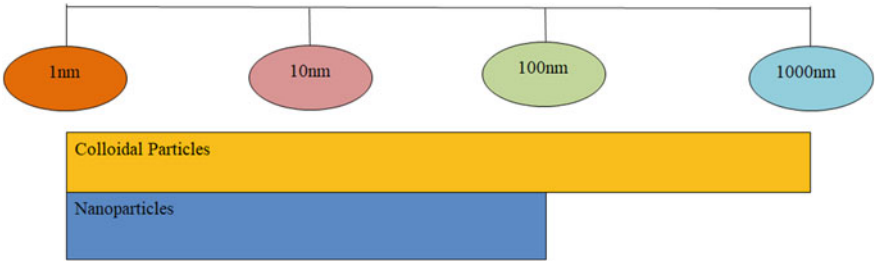

Fig. 3 Size comparison of nano (sub-colloidal) and colloidal particles

2.1 Uniqueness of Nanoparticles

Surface to volume ratio of the nanoparticles is comparatively higher than other particles which make nanoparticles unique. Mostly the physical, chemical, and optical properties of nanoparticles are due to its nanoscale size and shape. Nanoparticles are complex molecules and consist of following three layers.

Surface layer: This may be functionalized in the presence of tiny particles, metal ions, surfactants, and polymers.
Shell layer: This layer is a chemically different material from the core in all aspects.
Core layer: This is a central part of the nanoparticles (Shin et al. 2016).

2.2 Grouping of Nanoparticles

Nanoparticles are exclusive categories based on their size, morphology, and physicochemical properties. NPs synthesized from heavy metals such as lead, mercury and tin are reported as rigid and stable but their degradation is not readily achievable, which may lead to environmental toxicity (Ibrahim et al. 2017). Therefore, application of such types of nanoparticles is limited. Some of the nanoparticles used in many applications are discussed here briefly.

2.2.1 Carbon Nanoparticles

Carbon nanoparticles are mostly derivative of graphite, charcoal, activated carbon, and fullerene. They exhibit in crystalline form either a single layer or multiple layers. The diameter of carbon nanotube varies from 0.5 to 3 nm and length 20–1000 nm (Davis et al. 2008). These types of nanoparticles have excellent strength and good electrical properties developed within them (Ceriotti 2014). These are extensively used for fluid loss control in drilling fluid, enhanced oil recovery, gas adsorbent, filler in many commercial applications and as support medium for many organic and inorganic catalysts (Mabena et al. 2011).

2.2.2 Metal Nanoparticles

Metal nanoparticles are obtained by further dividing microscale particles of pure metal such as Au, Ag, Zn, and Fe, or their metal oxide, metal hydroxide, and a metal sulfide, etc. Nanoparticles of the alkali and noble metals, i.e., gold, zinc, and copper have a broad absorption band in the visible region of the electromagnetic solar spectrum. Due to their excellent optical properties, metal nanoparticles find applications in many research fields. Coating of gold nanoparticles is extensively used for making the sample ready for Scanning Electron Microscope (SEM) analysis, to enhance the electronic stream, which helps in obtaining high-quality SEM images. Magnetite (Fe_3O_4) is mostly used in the field of biomedical applications. To achieve the high-resolution images during Magnetic Resonance Imaging (MRI) test, magnetite is also utilized (Mody et al. 2010).

2.2.3 Ceramic Nanoparticles

These nanoparticles are nonmetallic inorganic solid substances synthesized through successive heating and cooling. They are an oxide, carbide, and phosphate of a metalloid. Ceramic nanoparticles are amorphous; hence, they have excellent porosity and can be sized as per requirement. Mostly ceramic nanoparticles are used in applications such as catalysis, photocatalysis, degradation of dye, and imaging application (Thomas et al. 2015).

2.2.4 Polymeric Nanoparticles

Polymeric nanoparticles are generally prepared by polymerization of a monomer such as an alkyl cyanoacrylate. They are mostly biodegradable, biocompatible, and hence their application in various fields is increasing. They prove themselves as an excellent carrier for control delivery of drugs. Polymeric nanoparticles also possess good surface modification character. They are mostly nanospheres or nanocapsules shaped (Ealias and Saravanakumar 2017). They are a suitable adsorbent for protein adsorbate.

2.2.5 Semiconductor Nanoparticles

A semiconductor nanoparticle behaves peculiarly due to the high energy gap between the valence band and the conduction band. A significant change in the properties of nanoparticles is observed with bandgap tuning, and hence they are considered as vital material for photocatalysis, photo-optics, and electronic devices. They are also used for making biosensor and metal sensor devices. These nanoparticles found exclusively in water splitting application due to suitable bandgap and band edge position (Hisatomi et al. 2014). These particles are usually charge stabilized.

2.3 Synthesis Process of Nanoparticles

Synthesis of nanoparticles involved various methods but all the synthesis methods associated with the formation of nanoparticles either from bigger particle to smaller (top-down) or from smaller to bigger one (bottom-up). If the preparation method derives from the larger molecule, then the preparation method is called as top-down process. Similarly, if the preparation method derives from molecular level to nanosize particle, it is called as bottom-down method. Pictorial representation for production of nanoparticles is given in Fig. 4.

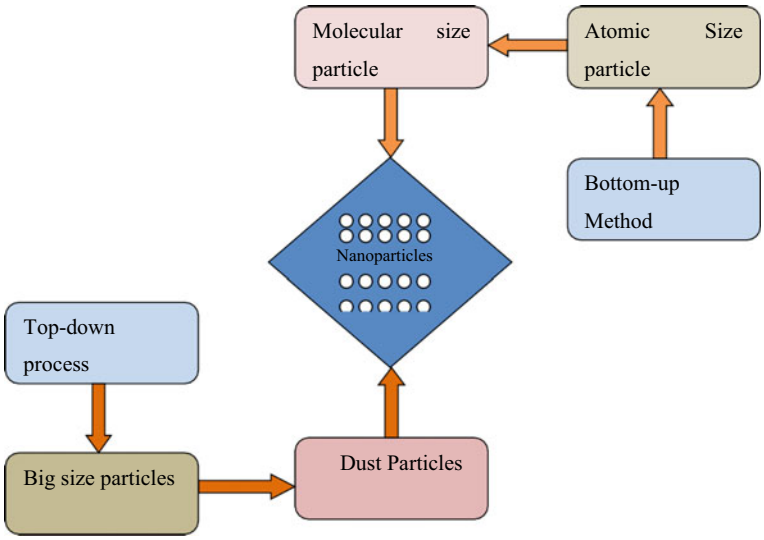

Fig. 4 Process involved for the production of nanoparticles

2.3.1 Top-Down Process

The process in which bigger size particles are sub-divided into nanoscale size particles by various processes such as thermal, mechanical, laser ablation, and arc discharge methods.

Thermal Decomposition

Thermal decomposition for synthesis of nanoparticles is an endothermic reaction in which the system is subjected to tremendous heat. In the presence of an enormous amount of heat, a chemical bond exists in the substance get decomposed. During decomposition of substance some secondary substance is produced, along with nanoparticles. A specific purification method can be adopted to separate nanoparticles from undesired secondary substances. The purification method is based on physical state of the substance from which nanoparticles are being formed.

Mechanical Milling

Mechanical milling is one of the most popular processes for the synthesis of nanoparticles. In this process, the material is subjected to a milling process in which the material is converted to nanoscale particles with application of strong shear stress. The different types of millers used are ball mill, shaker mill, attrition, etc. The most demerit of the process is the production of contaminated nanoparticles due to the ball present in the mill.

Laser Ablation

It is the technique in which laser beam is used to produce nanoparticles. In this process, the high laser beam is focused on the target in the solvent. The laser beam project short pulses of energy on the tiny part of the metal to vaporize it. The vapors later condensed to form nanoparticles in the solvent. This method applies for the generation of nanoparticles of noble metal. It is a reliable process for the production of nanoparticles and considered as an alternative to the chemical vapor decomposition method (Ealias and Saravanakumar 2017).

Arc Discharge

It is one of the oldest physical methods under top-down process for the production of nanoparticles. In the arc discharge process, two electrodes are dipped very close to each other in the solution and subjected to high voltage. Under the high potential difference, an electrical breakdown exists in the medium, resulting in arc discharge

which produces a strong thermal plasma discharge. The discharge process leads to raising the temperature of about thousand of degrees Celsius which vaporized the electrode surfaces in the solvent medium. The vaporized metal gets condensed giving nanoparticles.

Bottom-up Process

It is the process in which nanoparticles are formed from much smaller particles such as atoms and hence also known as building up approach. This process involved in producing the uniform size and required property of nanoparticles which is otherwise quite difficult to produce in mechanical milling process of the top-down approach. Chemical vapor decomposition (CVD), spinning, sol–gel, and biosynthesis are the most commonly used processes which come under the bottom-up approach.

Chemical Vapor Deposition

In chemical vapor deposition, a thin layer of vapor is accumulated on the surface of the solid substrate. The whole process of deposition is carried out inside the reactor at ambient temperature. Initiation of a chemical reaction is observed when a heated substrate comes in contact with the vapor. At the end of the reaction, a thin film of nanoparticles is deposited on the solid surface, then the nanoparticles are separated, which are found to be uniform, pure, hard and strong (Ealias and Saravanakumar 2017).

Spinning

In this process, synthesis of nanoparticles is done inside the reactor containing a spinning disc under the control of the affecting factor such a temperature. The reactor is packed with nonreacting gases like N_2 to avoid any reaction. The disc is rotated at a variable speed in the presence of precursor and water. The rotation causes the particle agglomerate and precipitate is formed. The precipitate is collected and dried (Mohammadi et al. 2014). Other parameters such as liquid flow rate, rpm of the disc, liquid precursor ratio, disc surface area, etc. determine the properties of nanoparticles. Electrospinning is a kind of method used to produce a thin sheet of polymer fiber.

Sol–Gel

Sol–gel is the old industrial process for the production of colloidal nanoparticles from the liquid phase. The sol–gel process is mostly used for generation of oxide nanoparticles and composite nonmaterial. It is the most preferred bottom-up approach to create nanoparticles due to its ease of operation. Sol is a colloidal solution of

suspended solids in the liquid. A gel is a solid macromolecule present in the liquid. The precursor is dispersed in the liquid by the help of sonicator, and later stage, the phase separation takes place to segregate nanoparticles.

Pyrolysis

It is the most widely used method for bulk production of nanoparticles in industries. It is carried out by burning a precursor with the help of flame. The precursor is either liquid or vapor that is fed into the furnace under high pressure through a small hole where it burns (Kammler et al. 2001). Combustion of precursor result production of certain undesired gases which are later separated to isolate the nanoparticles. A handful number of industries use plasma instead of flame to produce high temperature.

2.4 Characterization of Nanoparticles

There are different characterization methods that have been adopted for characterizing the physicochemical properties of nanoparticles. The characterization process determines the potential and application of nanoparticles. Some of the techniques are discussed in Table 1.

3 Enhanced Oil Recovery

There are potential numbers of improved oil recovery processes in practice employed by the oil and gas industries. Some of them have been described in the introduction section. However, single EOR method cannot be adopted for all kinds of formations, which is because of the variable characteristic of reservoir structure which may be due to the presence of different types of rocks in particular and distinct characteristics of the crude oil. Injection of surfactant for enhanced oil recovery is one of the common EOR methods which is observed by all the industries throughout the world. This process generally comes under chemical injection categories. Proper selection of surfactant based on the intense study of their interaction with rock mineralogy and crude oil can enhance the oil recovery, or else awful situations may develop leading to a decrease in oil recovery. Literature review suggests the following points to be considered for enhanced oil recovery.

- Reduction of interfacial tension between water and oil phase.
- Alteration of wettability, i.e., from oil-wet rock surface to water-wet.
- Reduction of the viscosity of crude oil system.
- Reduction in density of the oil phase.

Table 1 Various characterization methods of nanoparticles

S. No	Characteristics	Methods
1	**Size**: It is one of the crucial characterizations which determine the size and distribution of the particle. It also tells whether the particle falls under nanosize or micro-size	**Solid phase**: The image of the particle is measured by a scanning electron microscope (SEM) or transmission electron microscope (TEM) **Liquid phase**: Photon correlation spectroscopy and centrifugation **Gas phase**: Scanning mobility particle sizer (SMPS), it provides a fast and accurate measurement
2	**Surface area**: Surface area to volume ratio has a significant influence on the performance and properties of nanoparticles	**Solid phase**: It is measured by BET analysis. BET stands for Brunauer–Emmett–Teller analysis **Liquid phase**: Nuclear Magnetic Resonance Spectroscopy (NMR) is used to find out the surface area of nanoparticles in the liquid phase **Gaseous phase**: A modified SMPS and differential mobility analyzer (DMA) is used to determine the surface area of nanoparticles in the gas phase
3	**Composition**: The presence of unwanted substances along with nanoparticles may reduce the performance. Hence, the composition test is essential	**Solid phase**: Composition study is done with X-ray photoelectron spectroscopy (XPS) **Liquid phase**: Wet chemical analysis, i.e., mass spectrometry, atomic emission spectroscopy, ion chromatography **Gas phase**: Particle are collected by electro statistically and analyzed by wet chemical analysis
4	**Surface architecture**: It indicates the texture of the surface, i.e., construction of the surface with types of nanoparticles and their arrangement. Shape (spherical, cylindrical, tubular, conical, and irregular) of the nanoparticles plays an important role in deciding the properties of nanoparticles	**Solid phase**: SEM and TEM analysis **Liquid phase**: Electron microscopy, the analysis is done after collecting particle from the deposited surface **Gas phase**: Nanoparticles are collected by electrostatically and analyzed under advanced electronic microscope
5	**Surface charge**: Charge of the nanoparticles decide interaction of nanoparticles with the target and their stability in the disperse medium	**Solid phase**: Zeta potential is determined by dynamic light scattering (DLS) technique **Liquid phase**: Zeta potential is determine by dynamic light scattering (DLS) technique **Gas phase**: Differential mobility analyzer
6	**Crystallography**: Structure of nanoparticles	**Solid, liquid and gas phase**: Powder X-ray and neutron diffraction

Literature review exposes that reduction of interfacial tension in the presence of nanoparticles with the surfactant is more than the pure surfactant. The influence of nanoparticles in altering the various factors such as IFT, wettability, viscosity, and density are discussed in detail with a case study taken from multiple researchers.

3.1 Interfacial Tension

Interfacial tension is the force that observed between interphase of two fluids which hold the molecule of the interface tightly. The force is mostly measured by the unit of dyne/cm. This force is also affected by concentration of surfactant, alkali, and nanoparticles in the disperse medium. IFT of two fluid phases also depends on pressure and temperature of the systems. As the surfactant is added into the fluid phase during EOR in the reservoir, the surfactant molecule enters into the interphase and makes the force week which in turn decreases the capillary force in pores, which increases oil production. It has also been known that interfacial tension reduces the presence of surfactant and alkali. The process of reduction of interfacial tension of water–oil system in the presence of surfactant is called surfactant flooding. Similarly, in the presence of alkali, the EOR process is called as alkali flooding.

Figure 5 shows that due to the introduction of the exotic element (e.g., silicon dioxide nanoparticles) at the interphase of oil–water system, force of attraction between the molecules of two immiscible phases reduces. The reduction in attraction force among the molecules of the two phases reduces the IFT value of oil–water system.

Research indicates that interfacial tension is minimum when optimum salinity of water is achieved (Chou and Shah 1981). Beyond the cloud point temperature, IFT measurement became impossible as the surfactant solution becomes cloudy. Similarly, in the case of anionic surfactants, Kraft temperature exists below which

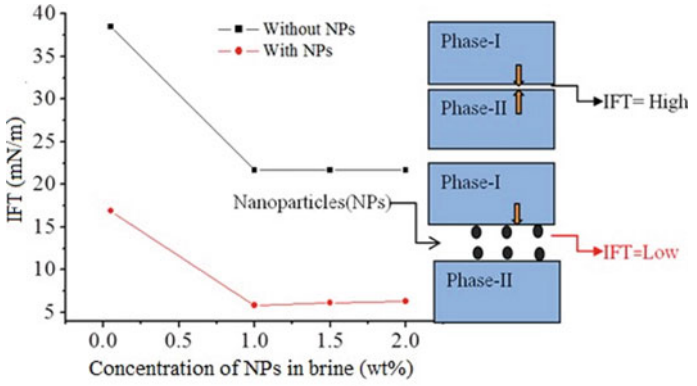

Fig. 5 Interfacial tensions (IFT) between two-phase fluid in the presence and absence of nanoparticles. Data were obtained from Kamal et al. 2017

surfactant became inactive and drops out from the solution (Negin et al. 2017). The concentration of surfactant must be more than the critical micelle concentration in the liquid phase to get the oil solubilized leading to higher production (Hirasaki et al. 2011). In the case of alkyl ethoxy carboxylated nonionic surfactant, ethoxy groups form a hydrogen bond with water resulting in the decrease in IFT. This indicates that the different types of surfactants have different effects on the IFT. Various cationic surfactants of the family belong to CnTAB (Trimethylammoniumbromide) had been taken to study the impact of IFT on the surfactants. The results were not the same for all cationic surfactants. It was minimum, i.e., 0.23 mN/m in the presence of C15TAB and maximum, i.e., 7.6 mN/m for C16TAB. This may be due to the structure of the surfactants (Kumar et al. 2016). Hence, it can be concluded that all surfactants have a different impact on the IFT of two fluid phases. This may depend on the nature, density, and architecture of the two immiscible fluids. IFT can be measured with the help of a device known as Tensiometer. Pendant drop and Wilhelmy plate method are the other popular methods carried out in the laboratory should be replaced by: most popular methods carried out in the laboratory for IFT measurement. A laboratory study with sodium silicates, sodium phosphates, sodium carbonate, and sodium hydroxide as additives in the presence of Petro-step petroleum sulfonate surfactant manufactured by Stepan Corporation reported that interfacial tension of injected fluid and oil decreases significantly. The effect of alkali on Petro-step 420 surfactant with NaOH of 0.02 and 0.1 wt% found very low IFT values, 0.023 and 0.008 dyne/cm, respectively (Krumrine et al. 1982).

3.1.1 Effect of Silica Nanoparticles

Silica nanoparticles (SiO_2) are the most widely used nanoparticles for investigation by the researchers due to its low cost. SiO_2 nanoparticles have high impact in the reduction of interfacial tension between formation fluids. It can be measured by various methods available. Suleimanov et al. (2011) state that to measure IFT, mostly by pendant drop method is adopted for its accuracy. IFT which was measured in the above said method between oil and brine was found to be 19mN/m. After the addition of varying concentrations of silicon dioxide (SiO_2) nanoparticles (10–30 nm) injected in brine, the significant reduction in IFT between oil and brine was observed, i.e., 8mN/m. This implies that nanoparticles have a good impact on IFT reduction and hence improve oil recovery. Hendraningrat et al. (2013) studied the effect of silicon dioxide nanoparticles on the reduction of IFT for oil–brine system. A significant reduction in IFT of oil–brine system in the presence of SiO_2 NPs (7 nm) was reported (Fig. 6a). Reduction in IFT of oil–brine system in the presence of nonuniform SiO_2 NPs (10–40 nm) was also investigated. It can be seen from Fig. 6b that there is a continuous reduction in IFT with increase in concentration of NPs (Kamal et al. 2017). Therefore, it can be concluded that SiO_2 NPs have good impact in reducing the IFT of oil–brine system.

It has also been observed that with the increase in the size of the particle, the recovery of oil may decrease due to pore plugging (Fig. 7a) (Almahfood and Bai 2018). On the other hand, the smaller size of nanoparticles (20–30 nm) can increase electrostatic repulsion force within nanoparticles, which causes higher disjoining

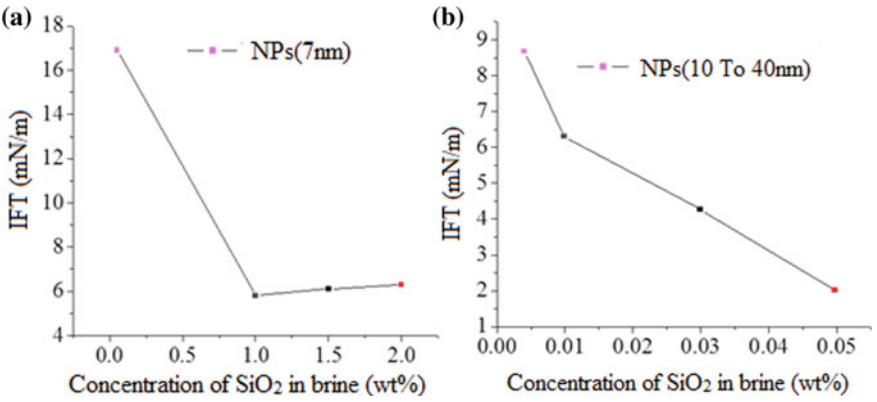

Fig. 6 Interfacial tension (IFT) measurements for crude oil against brine with various concentrations of NPs (SiO_2). **a** Brine with fixed size NPs. Data were obtained from Hendraningrat et al. (2013); **b** Brine with variable size NPs. Data were obtained from Kamal et al. (2017)

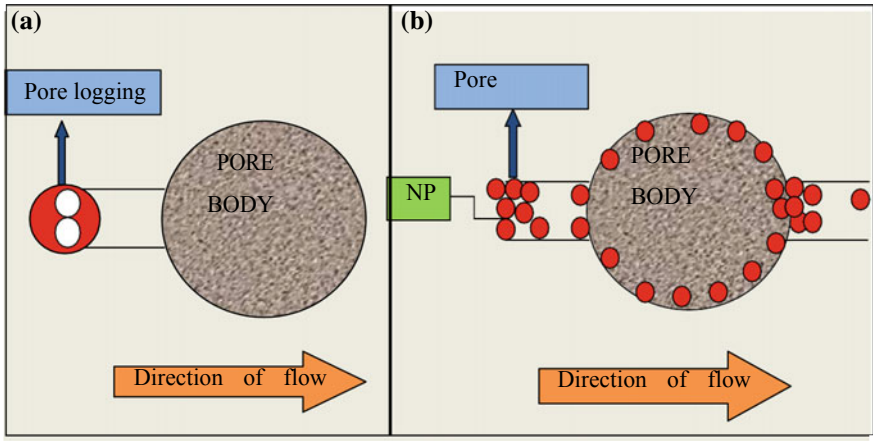

Fig. 7 **a** Mechanical entrapment mechanism; **b** Pore jamming mechanism

pressure. Disjoining pressure driven by the Brownian motion and electrostatic repulsion between molecules of two phases results in the reduction of IFT of two phases. It has also been observed that smaller size of nanoparticles (<10 nm) can cause log-jamming (Fig. 7b) (Almahfood and Bai 2018). This may result in a reduction in oil production. Figure 8 shows that with increase in the concentration of particular size nanoparticles, IFT of the oil–brine system decreases and hence increases the oil production. A similar study is conducted to see the stability of silica nanoparticles (5 nm) on oil–water emulsion in the presence of surfactant polyoxyethylene sorbitan mono palmitate. Performance of nanoparticles in reduction of IFT of oil–water system increases as it became hydrophobic in the presence of the surfactant. Adsorption

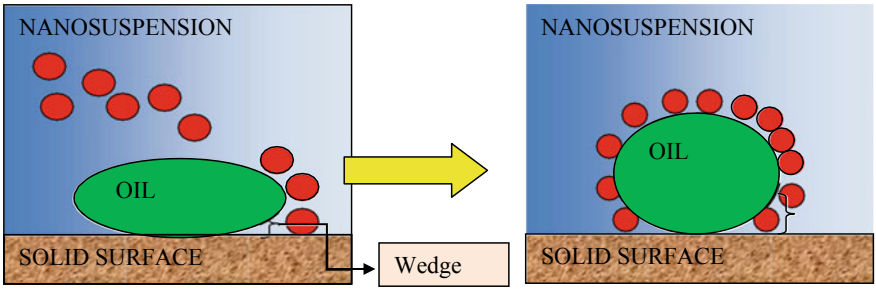

Fig. 8 Interaction of NPs with the liquid interface to induced disjoining pressure gradient

of surfactant in the interface of oil–water system is observed to be reduced in presence of nanoparticles (Sharma and Sangwai 2017). Due to hydrophobic nature, more nanoparticles occupy the area of interface of oil–water, leading to the reduction in IFT (Xu and Zhu 2016).

3.1.2 Effect of Alumina Nanoparticles

Aluminum dioxide (Al_2O_3) NPs with crystalline structure and various shapes were used by the researcher in EOR applications. A recent laboratory experiment reported that Al_2O_3 NPs (40 nm) have good stability at all temperatures (25–60 °C) with considerable reduction in IFT. The mechanism of IFT reduction has been shown diagrammatically for better understanding in Fig. 8. Observed reduction in IFT is due the presence of NPs at the interfacial layer. In low concentration of NPs, they attach on the surface of liquid layer due to adsorption phenomenon which lead to reduction in IFT. It was also observed that 92.8% of Al_2O_3 nanoparticles were recovered after excess flooding of deionized water but 8.2% remains unrecovered from the pores of the device. The experimental result reveals that maximum 65.7% of oil recovery was achieved at 60 °C temperature due to reduction in IFT of oil–water system (Ali et al. 2014). Kiani et al. (2016) have prepared gamma-alumina NPs from high-purity gibbsite (99.99%)/ammonium bicarbonate with weight ratio of about 25–45%, and deionized water of 3–5 mL. The mixture was mixed and placed in a 300 mL. Teflon-lined autoclave at 75–85 °C for 10 h then the solution is cooled at room temperature for about 30 min. Prepared gamma-alumina NPs with 0.1 weight percent in low salinity ranging from 2000, 20000, and 200000 ppm reduced adsorption of solvent on the sandstone surface and hence improve oil recovery. The experimental result reported that significant reduction in IFT value is due to the adsorption of Al_2O_3 NPs at the interface of oil–water system. The recovery percentage of oil for different salinity rage of 2000, 20000, and 200000 were observed as 56.9%, 64.8%, and 71.48%, respectively. It can be concluded from the above results that Al_2O_3 nanoparticles have significant effect on the reduction of IFT value of two fluid phases.

3.1.3 Effect of Titanium Dioxide Nanoparticles

Titanium dioxide (TiO_2) nanoparticles are crystalline in structure and have wide applications in different fields. The application of TiO_2 in EOR is found to be negligible because of its cost and comparatively paid less attention by the researchers. Ehtesabi et al. (2014) have revealed that there is no significant change in reduction of IFT between injected fluid and oil in the presence of Titanium dioxide (TiO_2) nanoparticles (15 nm). However, it has influenced surface modification of rocks due to its deposition over the rock surfaces. The minimum IFT reduction generally achieved at lowest pH, however, it was not observed in case of the TiO_2 nanoparticles. It was reported that enhanced oil recovery is due to change in wettability of surface rather than IFT. Hendraningrat et al. (2013) state that the stability of nanofluid is challenging factors, because NPs have tendency to agglomerate due to forces of different natures. Therefore, it is essential to choose proper dispersive medium for preparation of stable nanofluid emulsion. However stability of TiO_2 nanoparticles (106 nm) was noticed to be possessed good stability at higher temperature of 50 °C. Moreover, a considerable reduction in oil viscosity was observed after TiO_2 nanofluids flooding at 50 and 60 °C, whereas no significant reduction in IFT was observed (Ali et al. 2014).

3.2 Wettability

Wettability is the tendency of one fluid to spread on or adhere to on a solid surface in the presence or absence of other immiscible fluids. Wettability can be understood as the interaction between the fluid and solid phases. In a reservoir, the liquid phase can be water or oil, and the solid phase is the rock of the reservoir pores in which contain crude oil. It is one of the most critical variables in enhanced oil recovery and also affects few other reservoir parameters such as capillary pressure, relative permeability, and sweeping efficiency of injected fluids (Almahfood and Bai 2018). The reservoir by wettability can be divided into three types: (i) oil-wet reservoir, (ii) mixed-wet reservoir, and (iii) water-wet reservoir. Production of oil from the oil-wet reservoir is least as compared to other two due to weak sweeping efficiency; however, the recovery of oil from water-wet reservoir is more than that of the mixed-wet reservoir. Hence, modification of wettability is essential for the improved oil recovery process. Wettability evaluation is carried out by contact angle measurement method. Theoretically, the contact angle is found out by Young's equation, i.e.,

$$Y_{lv}\,\mathrm{Cos}\theta_Y = Y_{sv} - Y_{sl}$$

Y_{lv}, Y_{sv}, and Y_{sl} are the interfacial tension of liquid–vapor, solid–vapor, and solid–liquid phases. θ_Y is Young's contact angle. Similarly, ***Telescope-Goniometer*** is used to determine the contact angle of various liquid on the polish surface experimentally. A pictorial representation of wetting nature of the surface is given in Fig. 9.

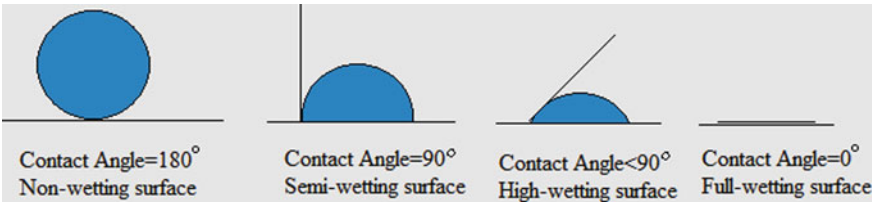

Fig. 9 Wetting characteristics of a droplet on the solid surface

3.2.1 Effect of Silica Nanoparticles

Several studies have been conducted to investigate the surface modification ability of nanoparticles by various researchers. SiO_2 has been found to be the most effective one among experimented. Nanoparticles (SiO_2) can modify the oil-wet surface to water-wet surface and enhances the oil production (Ogolo et al. 2012). Performance of silica nanoparticles in the presence of polymer shows an excellent result in altering the oil-wet surface to active water-wet surface (Maghzi et al. 2013). Joonaki et al. (2014) stated that silica nanoparticles have good ability in wettability alteration and reduction in IFT of two miscible fluids. The above statements support silica nanoparticles to be an active surface modifying agent. Silica nanoparticles can improve surface conditions from oil-wet to water-wet. Yousefvand et al. (2015) have performed wettability tests using water flooding, polymer flooding, and polymer nanosilica. He noticed that oil recovery was 16.63% during 42 min of water flooding. Similarly, oil recovery was 26.32% during continuous polymer flooding for a time period of 64 min. But oil recovery was 35% in the presence of nanoparticles with polymer within 84 min of flooding duration. Yousefvand concluded that drastic increase in oil recovery from 16.63 to 35% was due the surface modification nature of silica nanoparticles.

The surface altering properties of silica nanoparticles (11–14 nm) from oil-wet to water-wet is agreed with the recent result. Contact angle measurement by sessile drop method stated that in the presence of silica nanoparticles in sodium hydroxide alkali flooding enhances oil recovery up to 11%. This result reveals that the contact angle of substrate reduced from 140 to 60–40° and IFT of Na_2CO_3 at different concentrations decreased from 29.8 to 5.903 mN/m in the presence of silica nanoparticles (Elyaderani and Jafari 2019).

3.2.2 Effect of Zinc Oxide Nanoparticles

Adsorption and wettability are both surface phenomena in which substrate molecules interact with surfaces. This interaction of molecules depends on surface free energy available to each surface and the nature of interacting molecules. The amount of energy needed for adsorption by the adsorbate (surfactant, nanoparticles) on the surface of the substrate (rocks) is called adsorption energy. If the adsorption of

energy is more, cluster of atoms likely to get adsorbed on the surface. Adsorption energy is found to be very high for zinc nanoparticles on calcite surface. Hassan et al. (2018) state that on the adsorption of zinc oxide nanoparticles, the wettability of surface changes. It indicates that the zinc oxide nanoparticles have a significant impact in altering the wettability of calcite surface.

3.2.3 Effect of Iron Oxide Nanoparticles

Iron oxide usually exists in three different forms such as ferrous oxide (FeO), ferric oxide (Fe_2O_3), and magnetite (Fe_3O_4). They have attracted extensively due to their magnetic properties and their potential application in many fields. As a consequence of this researchers have tried the fate of iron oxide nanoparticles in the field of EOR. To study the effect of wettability of nanoparticles on the oil–water system, numbers of the experiment have been carried out with iron oxide (Fe_2O_3) (20–35 nm) nanoparticles. Wettability of the oil–water system on the surface of the sandstone rocks was justified by contact angle measurement. It was found that iron oxide nanoparticles have negligible effect in altering the wettability of oil–water system on the reservoir rocks (Joonaki and Ghanaatian 2014). It can be concluded that the role of iron oxide nanoparticles has very less influence on the enhanced oil recovery in terms of wettability alteration.

3.3 Viscosity

It is the properties of a fluid by which fluid offers resistance to the flow. It is the internal friction of moving the fluid. In EOR, the viscosity of the displacing fluid should be more than the displaced fluid. In the case of water flooding, displacing fluid is injected water and displaced fluid is oil. The viscosity of displacing fluid can be increased by the addition of polymer in the base fluid (Kamibayashi et al. 2005). Commonly used polymer is polyacrylamide (PAM). It is a long chain organic polymer soluble in water. It forms a colorless nontoxic, nonhazardous solution with water. In addition to this hydrolyzed polyacrylamide and xanthan gum are also used. Application of such polymer in enhancing oil recovery process is known as *polymer flooding EOR methods.* Viscosity is one of the important rheological properties of the injected fluid which can be evaluated by viscometer or rheometer. However, the potential effect of various nanoparticles on viscosity of crude oil and injected fluid is described below for enhancing oil recovery.

3.3.1 Effect of Silica Nanoparticles

Commonly used nanoparticles in EOR for reduction of viscosity of crude oil are silicon dioxide (SiO_2) for its cost-effective and eco-friendly nature. Viscosity is the

function of temperature. An experimental result for viscosity of injected fluid in the presence of SiO_2 nanoparticles (14 nm) at 26 °C was reported as 1.28 cp in brine medium. However, in the absence of nanoparticles at the same temperature in brine medium was observed as 0.94 cp (Ali et al. 2014). SiO_2 nanoparticles have comparatively good impact in reducing the viscosity of crude oil at different temperatures than other nanoparticles used during investigation of EOR. In presence of silica nanoparticles during polymer flooding, the oil recovery enhances up to 20% than only polymer flooding. The size of the nanoparticles taken in this investigation was between 11 and 13 nm (Yousefvand and Jafari 2015). It has been noticed that the oil recovery percentage was increased due to the increase in viscosity of the injected fluid. Increased in the viscosity of injected fluid accelerate oil displacement and hence consequently oil recovery. This modification in the properties of injected fluid might lead to higher amount of oil recovery (Yousefvand and Jafari 2015).

Sharma and Sangwai (2017) performed number of experiments to investigate the rheological properties of different nanofluids at room temperature (25 °C). Different types of nanofluids were prepared by varying the concentration of SiO_2 nanoparticles in the base fluid, i.e., deionized water containing polymer, polyacrylamide. Compositional details and the nomenclature of various nanofluids they have used during the investigation are listed in Table 2. Their investigation also includes the effects of temperature on the viscosity of various nanofluids and is presented in Table 3.

From Table 2, it has been observed that with increase in the concentration of SiO_2 NPs in the base fluid (deionized water with polymer), viscosity increases (For NP and NSP nanofluid). A plot of viscosity versus concentration of nanoparticles has been drawn to better understand the relation between viscosity and concentration of nanoparticles (Fig. 10a). The reason for increase in the viscosity of nanofluids may be due to the better dispersion of polymer molecules in the presence of nanoparticles. However, size of the nanoparticles plays an important role for enhancement of viscosity of the nanofluids. Increase in the viscosity of injected fluid during EOR may

Table 2 Compositional details and nomenclature of various nanofluids (Sharma and Sangwai 2017)

Nanofluid	SiO_2 (wt%)	SDS (cmc wt%)	PAM (PPM)	Temperature (°C)	Viscosity (Pa.s)
NPs	0.5	0	1000	25	1.77
+Polymer (NP)	1.0				3.49
	1.5				3.99
	2.0				4.24
NPs+	0.5	0.14	1000	25	1.31
Surfactant+	1.0				3.04
Polymer (NSP)	1.5				3.26
	2.0				3.58

Table 3 Effect of temperature on viscosity of various nanofluids (Sharma et al. 2016)

NPs + Polymer (NP)		NPs + Surfactant + Polymer (NSP)		Surfactant + Polymer (SP)		Polymer (P)	
Viscosity (Pa.s)	Temperature (°C)	Viscosity (Pa.s)	Temperature (°C)	Viscosity (Pa.s)	Temperature (°C)	Viscosity (Pa.s)	Temperature (°C)
7.6	30	7.1	30	3.1	30	5.05	30
7.4	50	6.2	50	1.4	50	3.58	50
7.1	70	6.07	70	0.63	70	2.44	70
6.7	90	5.6	90	0.49	90	1.79	90

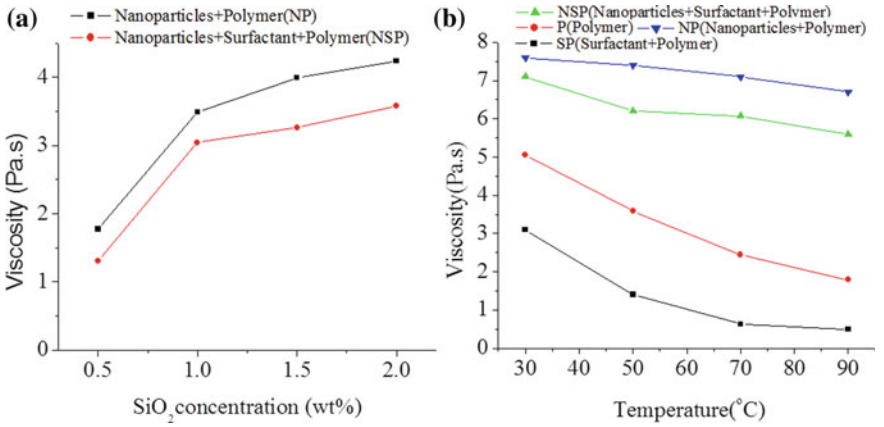

Fig. 10 **a** Variation of viscosity of different nanofluids (NP and NSP) with concentration of SiO_2; **b** Effect of temperature on viscosity of various fluids (P, SP, NP, and NSP)

lead to higher recovery because of higher sweeping efficiency and reduced viscous fingering.

Figure 10b and also Table 3 show that viscosity of the various fluids decreases with increase in temperature. This is because with increase in temperature the cohesive force between the molecules decreases and hence viscosity. However, the effect of temperature on viscosity for nanofluids NP and NSP is relatively less than the conventional P and SP fluids. This indicates that SiO_2 nanoparticles have favorable effect on rheological properties of nanofluids at elevated temperature (Sharma et al. 2016). Thus, from above investigation a conclusion can be drawn that at higher temperature EOR application, nanofluids can perform comparatively better than conventional fluids due their thermal stability. Similarly, a study on heavy oil by Kumar et al. (2018) reveal that the viscosity of heavy crude oil can be reduced by solvent-based Pickering emulsion in which SiO_2 NPs play an important role to stabilize the emulsion.

3.3.2 Effect of Alumina Nanoparticles

Aluminum oxide (Al_2O_3) nanoparticles are the second most popularly used nanoparticles during investigation in the lab scale for enhanced oil recovery. Bayat et al. (2014) studied the influence of Al_2O_3 nanoparticles on viscosity reduction of crude oil at different temperatures from 26 °C to 60 °C through core flooding experiments. They have investigated the rheological property of the crude oil after each flooding. They have reported that viscosity of crude oil decreased to a large extent in the presence of Al_2O_3 nanoparticles at 60 °C and enhanced oil recovery by 4.895%. Ogolo et al. (2012) conducted an experiment to study the viscosity of crude oil in the presence of Al_2O_3 nanoparticles. The nanoparticles Al_2O_3 (40 nm) were dispersed in brine to prepare nanofluids to investigate the effect of nanofluids in reduction of viscosity of the crude oil. They have reported that there was significant reduction in the viscosity of crude oil at 26 °C. Extensive study with various nanoparticles such as Al_2O_3, Fe_2O_3, magnesium oxide (MgO), zinc oxide (ZnO), and tin oxide (SnO) reveals that alumina nanoparticles (40 nm) have tendency to improve oil recovery by reducing the viscosity of the crude oil. Kamal et al. (2017) performed the number of experiment with Al_2O_3, SiO_2, and TiO_2 nanoparticles in brine with 0.3 wt% NaCl for water flooding at 26 °C. The recovery of crude oil was found to be on average of 47.3%. But in the same injection condition in the presence of the above-mentioned nanoparticles oil recovery was increased due to decrease in viscosity of the crude oil. Recoveries of oil in the presence of Al_2O_3, SiO_2, and TiO_2 nanoparticles are reported by authors as 52.6%, 50.9%, and 48.7%, respectively. The decreased viscosity of crude oil helps in reducing the surface tension, increase the permeability of oil and improve the reservoir seepage conditions.

3.3.3 Effect of Nickel Oxide Nanoparticles

Nickel oxide nanoparticles (Ni_2O_3) have been speculated as a good in situ agent in resolving the oil recovery problems. Dispersion medium plays an important role; therefore, it is important to select a good dispersion medium for particular types of dispersed phase during oil recovery operation. Ogolo et al. (2012) experimented four types of dispersion medium, namely, distilled water, brine, ethanol, and diesel. The best result in terms of oil recovery obtained was with ethanol dispersion medium. It was observed that viscosities of injected fluid (NPs + ethanol, NPs + Brine, NPs + distilled water) were much more than the recovered oil. Viscosity of carbon dioxide gas (CO_2) increased when 1 wt% of nickel oxide (NiO) NPs (60 nm) and 2 wt% of polydimethylsiloxane mixed with 97 wt% of CO_2. The above-mentioned injecting fluid was prepared by dispersing NiO nanoparticles into CO_2 prior to injection into the oil reservoir. This process was carried out at minimum miscible pressure (6000 psi) to secure CO_2 miscibility at 120 °C. Oil containing asphaltene recovery percentage increases dramatically by the injection of above prepared fluid up to 70% (Hashemi et al. 2016). Another study by Barkat et al. (2008) reported that NiO NPs enhance the viscosity and thermal conductivity of polymer mixture with increasing

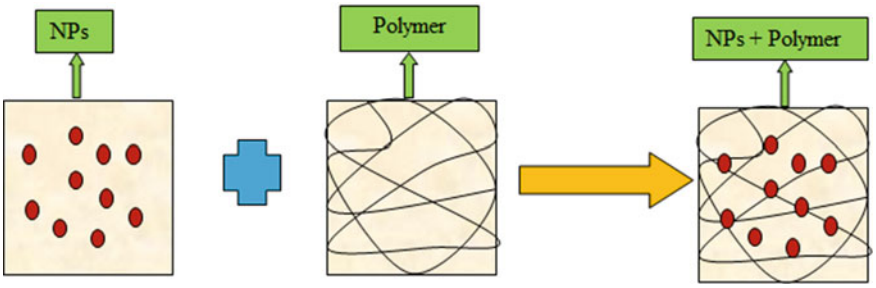

Fig. 11 Schematic diagram describing interaction of NPs with polymer solution

the concentration of nickel oxide nanoparticles. NiO NPs have high tendency to form chemical bond with polymer, resulting high viscosity polymer mixture (Fig. 11).

3.3.4 Effect of Iron Oxide

With unique magnetic and electrical properties, iron oxide NPs have been proposed as nanosensor. However, a few numbers of studies have been observed on the potential use of iron oxide NPs in the field of EOR application. Iron oxide NPs can increase the viscosity of injected fluid (displacing fluid), which leads to higher sweep efficiency. It was reported that magnetic fluid (iron oxide nanofluid) in the presence of surfactant and carrier fluid enhances the viscosity of the displacing fluid. The magnetic fluid is a smart fluid which contains Fe_2O_3 nanoparticles along with base fluid under the application of a magnetic field. The experimental result shows that there is an increase in the viscosity of the base fluid in the presence of a magnetic field. When the magnetic field is removed, fluid behaves as base fluid with reduced viscosity. In this study it was reported that oil recovery can be improved by the application of such kind of smart fluid (Kothari et al. 2010). Ferrofluids (Fe_3O_4) were proposed for magnetic heavy oil recovery by Shekhawat et al. (2016). The magnetic recovery mechanism involves injection of magnetic NPs into the reservoir and pushing the NPs toward the production zone of the reservoir using a repelling magnetic force from downhole tools. Then, inward magnetic forces are applied toward the borehole to attract and recover the magnetic NPs that are already soaked with oil. In this way greater percentage of recovery can be achieved.

Based on the density of oil, the reservoir is divided into two types, namely, light oil reservoir and a heavy oil reservoir. Chemical flooding and polymer flooding are usually adapted to recover the crude oil from light oil reservoir. However, various thermal methods are applied to recover crude oil from heavy oil reservoir. Some of the heavy oil reservoir, trial of chemical flooding has been taken into consideration for EOR study.

In field scale, most common methods used for heavy oil production is thermal enhanced oil recovery. In situ combustion is one of the rapidly applicable methods

for enhanced oil recovery. In this method, fire is ignited in the subsurface with a fire fed by continuous supply through the injection well. Finally, fire moves toward the production well from the injection well. With the generation of huge heat in the reservoir higher hydrocarbon compound decomposes to produce smaller ones which result in increase in mobility due to mixing the vapor of lighter hydrocarbon with the reservoir fluid and hence increases fluid flow.

4 Thermal Methods for Enhanced Oil Recovery

Some popular thermal methods have been adopted for heavy oil reservoirs for oil production in which heat energy is introduced into the formation containing highly viscous crude oil. These methods are divided into two types: (a) steam injection methods; (b) in situ combustion methods. Steam injection is most common method used for shallow heavy oil. Some of the examples of such reservoirs are in the San Joaquin Valley of California or those that comprise the oil sands of Alberta, Canada. In steam injection methods, steam is injected into the formation through the injection well and is driven toward the oil to physically displace it. Steam floods require continuity in the formation to allow steam to drive oil toward the production well. As steam carry huge amount of heat along with it, the complex hydrocarbon molecule of reservoir fluid decomposes producing numbers of lower hydrocarbons. Lowering the viscosity of the reservoir fluid is due to mixing the vapor of lower hydrocarbon with the reservoir fluid. The decreased viscosity helps to reduce the interfacial tension, increase the permeability of oil and improves the reservoir seepage conditions. Steam injection is usually more environmental friendly than other EOR methods. The steam itself does not pose a great threat since it just condenses to water, which causes no pollution.

Similarly, during in situ combustion process, significant amount of heat is generated in the reservoir leading to breaking of complex molecular compounds. In situ combustion is basically injection of an oxidizing gas (air or oxygen-enriched air) to generate heat by burning a portion of resident oil. Most of the oil is driven toward the producers by a combination of the gas, steam, and water. This process is also called fire flooding to describe the movement of a burning front (forward or reverse) inside the reservoir. During the process, oil-wet surface of the rocks changes into water-wet and viscosity of the oil reduced drastically. The decrease in viscosity of the oil increases the probability of higher oil production. Thermally enhanced oil recovery method is the best technique for unlocking the heavy oil formation (Sahar et al. 2018).

The result of recent experiments (Sahar et al. 2018) reported that the application of iron oxide (Fe_2O_3) nanoparticles (2 wt%) with distilled water as a dispersion medium on heavy oil reservoir has decreased the viscosity of the oil and increased the oil recovery. The results also revealed that heavy oil recovery with application of iron oxide nanofluid also known as magnetic fluid was achieved up to 68.41%. The investigation report revealed that in the presence of Fe_2O_3 NPs (30 nm), oil

mobility increases due to reduction in oil viscosity. With the reduction in viscosity of the reservoir fluid, swept efficiency of oil increased (Sahar et al. 2018). This result indicates that Fe_2O_3 nanoparticles have good influenced over the reduction of viscosity of heavy oil reservoir fluids.

5 Microbial Method

This is the enhanced oil recovery method in which microbes are used for better production of the oil from existing dead well. Under this method, suitable microbes are introduced into oil wells along with water or biodegradable polymer to produce nontoxic by-products which help in oil recovery. This may include oily substances or gases that may help in extracting oil out of the well. The released material may help to mobilize the oil and facilitate oil flow by reducing oil viscosity or altering wettability. In Table 4, some bio-product along with their functions is described.

Some microbes release slimy substances known as exopolysaccharides to protect themselves from drying out. This substance helps bacteria to plug the pores seen on the surface of the rock. This may allow the oil to move through the rock surfaces more easily. Blocking of high permeable oil zone by exopolymeric substance and allowing the water to flow through low permeable zone of oil reservoir is known as selective plugging. This facilitates smooth movement of water through low permeable zone leading to increase oil recovery. Microorganisms produce oily substances called surfactants which help in altering oil-wet rock surface to water-wet. As they are naturally produced by biological microorganisms, they are referred to as biosurfactants. Biosurfactants act like slippery detergents, helping the oil move more freely away from rocks and crevices so that it may travel more easily out of the well. This method is still in developing stage as significant field-scale application is not observed or may have applied rarely. If this became successful, the crude oil productions costs would be reduced to a large extent. This method may become a

Table 4 Bio-Products of microbial degradation and their functions (Lazar et al. 2007)

S. No	Bio-product	Function of bio-product
11	CH_4, CO_2: gas	Reduce oil viscosity and improve fluid flow
2	Biosurfactants: slippery solid substance	The slippery substance that reduces interfacial tension alter wettability
3	Bio-polymers: solid substance	Improve the viscosity of injected water in water flooding and displaces reservoir fluids. This result in enhanced oil recovery
4	Biomass: microbial cells	Can plug high permeability zones Help in partial degradation of complex C–C bond
5	Lower density sour gas: CO_2	Help in the reduction of viscosity

more attractive alternative to replace traditional chemical methods of improved oil recovery. A new concept for plugging is developed by biomineralization to form calcite cement layer in carbonate formations (Sheehy 1991). This concept relates to microbacteria generated from the indigenous reservoir through nutrient manipulation. Field-scale application on this concept needs to improve technically. From this literature studies, we can say that there is a lot of scopes to research in this field. An experiment was conducted in the laboratory to see the effect of silica nanoparticles with biosurfactant on interfacial tension. To view the influence, three different types of solutions were prepared, namely, distilled water-nanosilica, distilled water-biosurfactant, and distilled water-nanosilica with biosurfactant (Khademolhosseini et al. 2015). The oil recovery for the individual sample is reported as 19%, 29%, and 52%, respectively. This indicates oil recovery is highly influenced by the presence of silica nanoparticles with biosurfactant.

6 Gas Injection Method

Gas injection is a type of secondary or tertiary oil recovery method in which miscible gas is injected into the crude oil reservoirs. Gas injection method is adopted for a medium pressure reservoir. Miscible gases such as hydrocarbon carbon (methane) and non-hydrocarbon gases (nitrogen or carbon dioxide) injection into the reservoir help in maintaining partially or completely the reservoir pressure. In addition to balancing the reservoir pressure, soluble gases in the oil result in swelling of oil and increase the oil mobility which expand oil recovery. Gas injection methods are mostly applicable to the oil reservoir unsaturated with hydrocarbon gas for effective result. Recovery efficiencies increase with continued gas injection, but the rate of recovery diminishes after gas breakthrough occurs as the gas–oil ratio increases. Non-hydrocarbon gases can also be used provided they should not have any contribution in imparting corrosion and should be separable easily.

The most successful immiscible gas injection projects are the vertical gravity drainage projects in which gas is injected into the crestal primary or secondary gas cap, with the oil wells producing from as far downdip as possible to maximize this distance from the gas cap both vertically and laterally. The pictorial view of the gas injection process is represented in Fig. 12.

Gas injections well are potentially used to inject gas (miscible-CO_2 or immiscible-N_2) into the reservoir to push the oil to a producing well. A case study can be discussed to better understanding the process. Bender and Akin (2017) mentioned that a field-scale study was conducted for few years to know the production ability of pure carbon dioxide (CO_2) and flue gas ($CO_2 + N_2 + SOx + NOx$). It was found that the production rate of CO_2 was more than flue gas due to its solubility over the same period. According to the authors, pressurizing the reservoir with flue gas injection followed by pure CO_2 injection may improve the production and can make the process more economical. For heavy oil reservoir gas injection process is applied rarely. However, this is one of the best methods in which CO_2 and flue gases can be

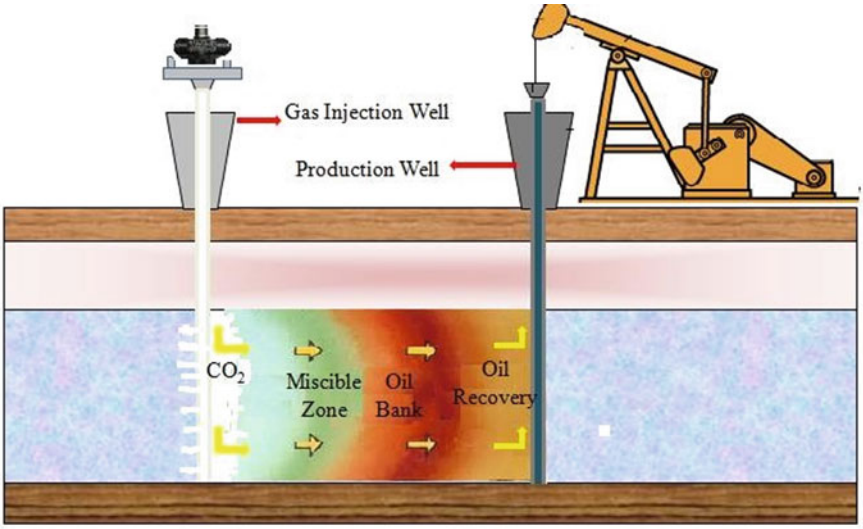

Fig. 12 Pictorial view of a gas injection well and production well

used for oil production and simultaneously can be protected the environment from those unwanted gases. Miscible gas injection increases the overall displacement efficiency, minimizes residual oil saturation, promotes low IFT, and increases oil production significantly.

Nanowater with alternative gas injection (NWAG) is one of the most recent novel methods that have been tested for oil recovery in lab scale. Moradi et al. (2015) claimed that NWAG (silica nanoparticles dispersed in water gives nanofluid) enhances the oil recovery from 54.7 to 79.3% compared to the traditional water alternative gas (WAG) injection methods. The nanoparticles within the size range of 11–14 nm have ability to recover more oil than the nanoparticles with size range 30–40 nm. It was reported that mixture of Ni_2O_3 nanoparticles (100 nm, 1 wt%) and PDMS (Polydimethylsiloxane, 2 wt%) dispersed in CO_2 dispersion medium to investigate the asphalting recovery. The oil recovery factor obtained was 78.57% Hashemi et al. (2016). Hence, this method can be considered as one of the feasible potential crude oil recovery processes for oil-wet carbonated reservoir.

7 Field Application of Nanoparticles

Application of nanoparticles in the real oilfields is still under decision. Nevertheless, minimal field applications are available that reflect satisfactory results in crude oil production. Environment feasibility and cost of nanoparticles are the two most important factors that stand against application of nanoparticles in field scales. But it

is expected that in near future nanotechnology may play vital role in oil and gas industries. This is because of expansion of nanotechnology in every field as a success tool which enhances curiosity among the researchers of oil and gas industries. Bera and Belhja (2016) state that an offshore well of china suffers from production loss due to fine migration. Polymer cross-link nanoparticles whose surface treated with proppant (solid material typically sand designed to induce hydraulic fracture open) were used and oil production was recovered. The recovery was because of surface-modified nanoparticles which carry fine migrant into the fracture during fluid flow.

Another field study which was carried out in Arab-D carbonated reservoir of giant Ghawar of Saudi Arabia. The objective of the field study was to observe the recover percentage of A-dot nanoparticles (special design hairy carbon-based fluorescent nanoparticles for this field application) during the production which is most challenging one. During the production 5 kg of A-dot nanoparticles in 255bbl of injection water was employed per batch. The bottom-hole temperature of 90 °C and pressure less than 1500 psi signify the reservoir condition. When the production resumed, 84 samples were collected within a period of 2 days to investigate the concentration of nanoparticles in each sample at different levels of production. The samples have undergone several tests (SEM, TEM, and AFM) to find out the concentration of A-dot nanoparticles. It was concluded that A-dot nanoparticles were stable even if harsh condition of reservoir and 82–86% of used nanoparticles could be recovered. This was one of the successful field trials in terms of recovery of nanoparticles ever observed (Mazen et al. 2011).

The common reason for formation damage is due to fine migration that plugged the pore near the wellbore which decelerate the production capacity of the well. A wellbore located in Gulf of Mexico encountered with similar problem. The reservoir temperature was about 160 °F and pay zone measured depth of 15,760–15,860 ft. During about 14 month of production period, production declined from 7,500 to 2,200 barrel of oil per day and gas from 6000 MCF to 2000MCF (MCF sands for thousand cubic feet). A frac-packing treatment was carried out to get rid of the problem. Proppant surface coated with nanoparticles at loading of 1 lb per 1000 lb of proppant were used. The flow of fine migrant was restricted due to adsorption on surface-treated proppant particles and the production was brought back (Huang et al. 2010).

8 Limitation of Nanoparticles in EOR

Nanoparticles are prepared through various complex processes which have been discussed earlier. As the production cost of NPs is quite expensive, therefore application of NPs in field scale is still questionable. Keeping in the view of cost as an important factor most of the researchers have used SiO_2 nanoparticles during the investigation (Kamal et al. 2017). In addition to the above-discussed factor stability of nanoparticles in dispersion is most challenging one which needs to be addressed. However, oil–water–surfactant emulsion better stabilized in presence of silica nanoparticles

was reported in literature. Investigation result proved that oppositely charge NPs and surfactant system, i.e., anionic surfactant with cationic NPs or cationic surfactant with anionic NPs provide comparatively good stabilization (Danial et al. 2018). It is also noticed that nanoparticles-based stabilized emulsion can sustain even in the harsh reservoir condition. But there is no field application observed so far based on the researcher investigation result; hence, a concrete statement cannot be given at this time.

Another most important concern is safety which needs to be addressed. Nanoparticles are injected into reservoir or wellbore along with drilling fluid, completion fluid, water flooding, or EOR fluid. Thus, during the operation field worker need to have preventive measures or else these tiny nanoparticles may enter into the lungs through respiration and block the lungs pore and cause many more health problems in human beings. There is no proper technology so far developed to recover the NPs from the base fluid once after used. If the base fluid is thrown on to the earth's surface without recovering nanoparticles, then they may enter into the living body and interact with cells because of their mobility nature. This interaction of nanoparticles with cells may damage the body tissue causing other problems as well. Due to the large surface area, nanoparticles absorb quantitatively more body fluid onto their surface when they encounter with macromolecules. This may affect the regulatory mechanisms of enzymes and other proteins. Research has shown that buckminsterfullerene, a spherical fullerene molecule with formula C60 can cause brain damage in fish (Karkare 2015). Therefore, the above-discussed issue should be addressed before the field-scale application of nanoparticles in EOR.

9 Conclusion

It has been observed that different types of nanoparticles have been used in enhanced oil recovery investigations by various researchers. Nanoparticles used in enhanced oil recovery to investigate the effect of particular nanoparticles in wettability alteration; viscosity enhancement and IFT reduction are found to be encouraging for oilfield application. Use of nanoparticles with displacing fluid decreases the interfacial tension, increases the rheological properties; alters wettability from oil-wet to more water-wet. The trial of silica nanoparticles is considered by many researchers for EOR application. It has been found that even though there is a little variation in the silica nanoparticles size, a good agreement in crude oil recovery is observed. Stability of nanoparticles in the dispersed phase is one of the challenging factors which have to be addressed by the researchers. Numbers of articles have been published by various researches, but no field application is carried out so far based on different nanoparticles. Hence, it is essential to make the process more feasible for field-scale applications. As the cost of nanoparticles is very high, researchers should pay more attention to low-cost nanoparticles for EOR application. The recovery procedures of nanoparticles need more investigations. The nanoparticles are dispersed in the air

medium and can quickly enter into lung leading to lung diseases. Therefore, adequate handling and disposal methods should be proposed.

References

Ali M, Riyaz K, Ali M, Mohammad HG (2014) The impact of silica nanoparticles on the performance of polymer solution in the presence of salts in polymer flooding for heavy oil recovery. Fuel 123:123–132

Almahfood M, Bai B (2018) The synergistic effects of nanoparticle-surfactant nanofluids in EOR applications. J Pet Sci Eng 171:196–210

Barakat NA, Omran AENM, Aryal S, Sheikh, FA, Kang HK, Kim HY (2008) Production of beads like hollow nickel oxide nanoparticles using colloidal-gel electrospinning methodology. J Mater Sci 43: 860–864

Bayat AE, Junin R, Samsuri A, Piroozian A, Hokmabadi M (2014) Impact of metal oxide nanoparticles on enhanced oil recovery from limestone media at several temperatures. Energy Fuels 28:6255–6266

Bender S, Akin S (2017) Flue gas injection for EOR and sequestration: a case study. J Pet Sci Eng 157:1033–1045

Bera A, Belhaj H (2016) Application of nanotechnology by means of nanoparticles and nanodispersions in oil recovery—a comprehensive review. J Nat Gas Sci Eng 34:1284–1309

BP statistical review of world energy, 67th ed, June 2018

Ceriotti RG (2014) Carbon-based nanoparticles: synthesis, characterization, and applications. Diss Rice Univ 1–220

Chou SI, Shah DO (1981) The optimal salinity concept for oil displacement by oil—external micro emulsions and graded salinity slugs. J Can Pet Technol 20:83–91

Christian P, Vonderkammer F, Baalousha M, Hofmann T (2008) Nanoparticles: structure, properties, preparation and behavior in environmental media. Ecotoxicology 326–346

Danial A, Apostolos K, Steven LB (2018) Nanoparticles stabilized oil in water emulsions: a critical review. J Pet Sci Eng 163:217–242

Data source 2016 of IEA

Davis ME, Chen Z, Shin DM (2008) Nanoparticles therapeutics: an emerging treatment modality for cancer. Nat Rev Drug Discov 7:771–782

Ealias AM, Saravanakumar MP (2017) A review on the classification, characterization, synthesis of nanoparticles and their application. In: 14th ICSET, IOP conference series, Mater Sci Eng 263:1–14

Ehtesabi H, Ahadian MM, Taghikhani V (2014) Investigation of diffusion and deposition of TiO_2 nanoparticles in sandstone rocks for EOR application. In: 76th EAGE conference and exhibition, 16 June 2014

Elyaderani SMG, Jafari A (2019) Microfluidics experimental study in porous media applied for nanosilica/alkaline flooding. J Pet Sci Eng 173:1289–1303

Hashemi SI, Fazelabdolabadi B, Moradi S, Rashidi AM, Shahrabadi A, Bagherzadeh H (2016) On the application of NiO nanoparticles to mitigate in situ asphaltene deposition in carbonate porous matrix. Appl Nanosci 6:71–81

Hassan S, Baig MK, Yahya N, Khodapanah L, Sabet M, Demiral BMR, Burda M (2018) Synthesis of ZnO nanoparticles for oil-water interfacial tension reduction in enhanced oil recovery. Appl Phys A 124–128

Hendraningrat L, Li S, Torsæter O (2013) A core flood investigation of nanofluid enhanced oil recovery. J Pet Sci Eng 111:128–138

Hirasaki G, Miller CA, Puerto M (2011) Recent advances in surfactant EOR. SPE J 889–907

Hisatomi T, Kubota J, Domen K (2014) Recent advances in semiconductors for photo catalytic and photo electrochemical water splitting. Chem Soc Rev 43:7520–7535

Huang TT, Evans BA, Crews JB, Belcher CK, Hughes B (2010) Field case study on formation fines control with nanoparticles in offshore wells. In: SPE annual technical conference and exhibition held in Florence, Italy, 19–22 September 2010 (SPE-135088)

Ibrahim K., Khalid S, Idrees K (2017) Nanoparticles: properties, applications, and toxicities. Arabian J Chem 1–24

Joonaki E, Ghanaatian S (2014) The application of nanofluids for enhanced oil recovery: effects on interfacial tension and core-flooding process. Pet Sci Technol 32:2599–2607

Kamal MS, Adewunmi AA, Sultan AS, Al-Hamad MF, Mehmood U (2017) Review article: recent advances in nanoparticles enhanced oil recovery: rheology, interfacial tension, oil recovery, and wettability alteration. J Nanomater 1–15

Kamibayashi M, Ogura H, Otsubo Y (2005) Viscosity behavior of silica suspensions flocculated by associating polymers. J Colloid Interface Sci 290:592–597

Kammler HK, Madler L, Pratsinis SE (2001) Flame synthesis of nanoparticles. Chem Eng Technol 24:583–596

Karkare M (2015) Nanotechnology: fundamentals and applications. I. K. International Publishing House, New Delhi

Khademolhosseini R, Jafari A, Shabani MH (2015) Enhanced oil recovery using polymer/nanosilica. In: 5th international Biennial conference on ultrafine grained and nanostructures materials, UFGNSM15, Procedia Mater Sci 11:171–175

Kiani S, Zadeh MM, Khodabakhshi S, Rashidi A, Moghadasi J (2016) Newly prepared nano gamma alumina and its application in enhanced oil recovery: an approach to low-salinity water flooding. Energy Fuels 30:3791–3797

Kothari N, Raina B, Chandak KB, Iyer V, Mahajan HP (2010) Application of ferrofluids for enhanced surfactant flooding in IOR. In: SPE EUROPEC/EAGE annual conference and exhibition, Barcelona, Spain 14–17 June 2010 (SPE-131272-MS)

Krumrine PH, Falcone JS, Campbell TC (1982) Surfactant flooding 1: the effect of alkaline additives on 1FT, surfactant adsorption, and recovery efficiency. In: SPE oil field and geothermal chemistry symposium, Standford, CA, 28–30 May 1982 (SPE8998)

Kumar G, Kakati A, Mani E, Sangwai JS (2018) Nanoparticles stabilized solvent—based emulsion for enhanced heavy oil recovery. In: SPE heavy oil technical conference held in Calgary, Alberta, Canada, 13–14 March 2018 (SPE-189774-MS)

Kumar S, Panigrahi P, Saw RK, Mandal A (2016) Interfacial interaction of cationic surfactants and its effect on wettability alteration of oil-wet carbonate rock. Energy Fuels 30:2846–2857

Lazar I, Petrisor IG, Yen TF (2007) Microbially enhanced oil recovery (MEOR). Pet Sci Technol 25:1353–1366

Mabena LF, Sinha RS, Mhlanga SD, Coville NJ (2011) Nitrogen-doped carbon nanotubes as a metal catalyst support. Appl Nanosci 1:67–77

Maghzi A, Mohebbi A, Kharrat R, Ghazanfari MH (2013) An experimental investigation of silica nanoparticles effect on the rheological behavior of polyacrylamide solution to enhance heavy oil recovery. Pet Sci Technol 31:500–508

Mazen YK, Harunar R, Emmanuel PG (2011) Industry first field trial of reservoir nanoagents. In: SPE Middle East oil and gas show and conference held in Mnama, Bahrain, 25–28 September 2011 (SPE-142592-MS)

Mody VV, Siwale R, Singh A, Mody HR (2010) Introduction to metallic nanoparticles. J Pharm Bioallied Sci 2:282–289

Mohammadi S, Harvey A, Boodhoo KVK (2014) Synthesis of TiO_2 nanoparticles in a spinning disc reactor. Chem Eng J 258:171–184

Moradi B, Pourafshary P, Jalali F, Mohammadi M, Emadi MA (2015) Experimental study of water-based nanofluid alternating gas injections a novel enhanced oil-recovery method in oil-wet carbonate reservoirs. J Nat Gas Sci Eng 27:64–73

Negin C, Ali S, Xie Q (2017) Most common surfactants employed in chemically enhanced oil recovery. Petroleum 3:197–211

Ogolo NA, Olafuyi OA, Onyekonwu MO (2012) Enhanced oil recovery using nanoparticles. In: SPE Saudi Arabia section technical symposium and exhibition, Al-Khobar, Saudi Arabia, 8–11 April 2012 (SPE-160847-MS)

Sahar A, Mohammad RE, Mohammad N, Emad R (2018) Effect of Fe_2O_3 and WO_3 nanoparticles on steam injection recovery. Energy Source, Part A 40:251–258

Sarit KD, Stephen USC, Wenhua Y, Pradeep T (2007) Nanofluids science and technology. Wiley, 1–389

Sharma T, Iglauer S, Sangwai JS (2016) Silica nanofluids in oilfields polymer polyacrylamide: interfacial properties, wettability alteration and application for chemical enhanced oil recovery. Ind Eng Chem Res 55:12387–12397

Sharma T, Sangwai JS (2017) Silica nanofluids in polyacrylamide with and without surfactant: viscosity, surface tension, and interfacial tension with liquid paraffin. J Pet Sci Eng 152:575–585

Sharma V, Rao LJ (2014) An overview of chemical composition, bioactivity and processing of leaves of Cinnamomum tamala. Crit Rev Food Sci Nutr 54:433–448

Sheehy AJ (1991) Microbial physiology and enhancement of oil recovery—recent advances. In: Donaldson EC (ed) Development in Petroleum Science, 31. Elsevier, Amsterdam, pp 37–44

Shekhawat DS, Aggarwal A, Agarwal S, Imtiaz M (2016) Magnetic recovery—injecting newly designed magnetic fracturing fluid with applied magnetic field for EOR. In SPE Asia Pacific hydraulic fracturing conference, Beijing, China, 24–26 August 2016 (SPE-181853-MS)

Shin WK, Cho J, Kannan AG, Lee YS, Kim DW (2016) Cross-linked composite gel polymer electrolyte using mesoporous methacrylate-functionalized SiO_2 nanoparticles for lithium-ion polymer batteries. Sci Rep 6:1–10

Suleimanov BA, Ismailov FS, Veliyev EF (2011) Nanofluid for enhanced oil recovery. J Pet Sci Eng 78:431–437

Thomas S, Harshita BSP, Mishra P, Talegaonkar S (2015) Ceramic nanoparticles: fabrication methods and applications in drug delivery. Curr Pharm Des 21:6165–6188

U.S. Department of energy (2011) Enhanced oil recovery. Washington, DC

Xu K, Zhu P (2016) A microfluidic investigation of the synergetic effect of nanoparticles and surfactants in micro emulsion based EOR. In: SPE improve oil recovery conference held in Tulsa, Oklahoma, USA, 11–13 April 2016 (SPE-179691-MS)

Yousefvand H, Jafari A (2015) Enhanced oil recovery using polymer/nanosilica. In: 5th international biennial conference on ultrafine grained and nanostructures materials, UFGNSM15 Procedia Mater Sci 11:565–570

Versatile 1-D Nanostructures for Green Energy Conversion and Storage Devices

R. R. Deshmukh, A. S. Kalekar, S. R. Khaladkar and O. C. Maurya

Abstract Increasing population and living standards demands high energy provisions; but considering pollution issues and depleting fossil fuel reservoirs, the fulfillment of the energy demands through eco-friendly/green renewable energy technologies have become an urgent need. Among all renewable energy systems, photovoltaic solar cells (PSC) with energy storage systems (ESS) such as batteries or supercapacitors have attracted great attention as the next generation of energy suppliers. However, the efficiency of PSC and ESS inherently depends on the electrode material's properties, like structure, size, shape, charge transport properties, active surface area, and so on. Owing to maximum active surface area, high surface to volume ratio, fast charge transport, efficient light harvesting, and simplistic eco-friendly growth, the one-dimensional (1-D) nanostructures has become a promising solution to the fabrication of efficient PSC and ESS. Here in this chapter we have discussed simple, cost-effective and environmentally benign growth of 1-D nanostructures and their efficient application in PSC and ESS. This chapter brings you updated literature survey on green synthesis of 1-D nanostructures applied in PSC and ESS.

Keywords 1D nanostructures · Solar cells · Batteries · Supercapacitors

1 Introduction

Continuously increasing world population and improving living standards are placing huge demand of energy. It has been speculated that the world energy demand will reach 612 quadrillions Btu (~649 × 10^{18} J or 33 GW years) in 2020 (Ganguly et al. 2014). Current energy consumption scenario (Fig. 1a) depicts that nearly 70% of energy demand is fulfilled from fossil fuels that include oil, coal, and natural gas, which has become our main energy source for human activity. Such a situation will put us in major problem in future, because fossil fuels are non-renewable and are depleting. Moreover, global warming, air pollution, environmental degradation, ozone layer depletion, and ecological devastation are some of the major concerns

R. R. Deshmukh (✉) · A. S. Kalekar · S. R. Khaladkar · O. C. Maurya
Department of Physics, Institute of Chemical Technology, Matunga, Mumbai 400019, India
e-mail: rr.deshmukh@ictmumbai.edu.in

L. Ledwani and J. S. Sangwai (eds.), *Nanotechnology for Energy and Environmental Engineering*, Green Energy and Technology,
https://doi.org/10.1007/978-3-030-33774-2_14

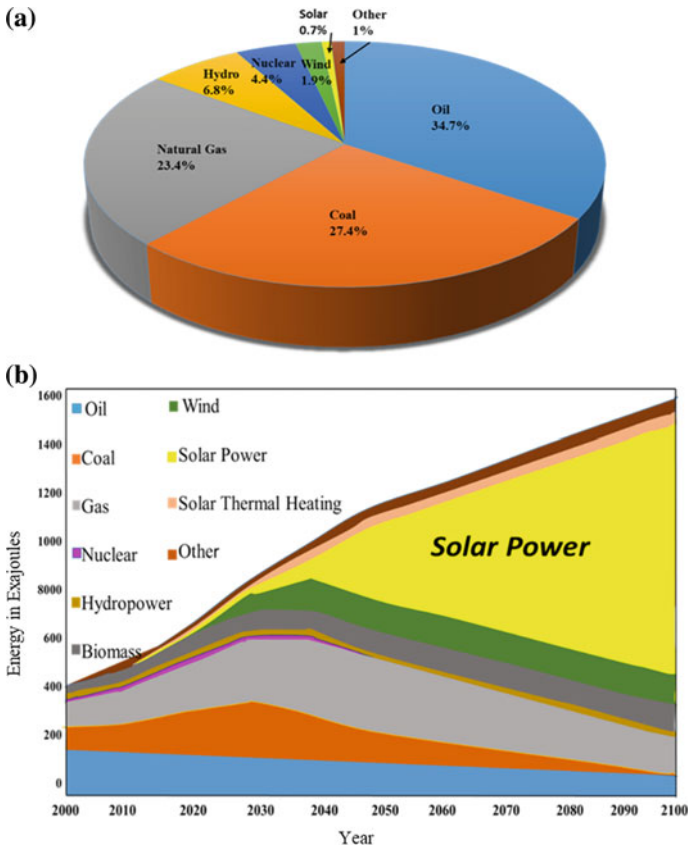

Fig. 1 **a** Recent world primary energy consumption (British Petroleum 2018). **b** Source-wise projected share of annual global energy production [73]

associated with the fossil fuels. Thus, development of green energy technologies based on renewable energy resources has become urgent need of globe for sustainable progress of human being.

In the pursuit of green and efficient renewable energy harvesters, various energy technologies have been discovered by scientists. These various technologies include hydro energy, tidal energy, wind energy, geothermal energy, and solar energy. Among all these renewable energy resources, hydroelectric and wind energy heavily dominate the renewable energy sectors which are about 6.8 and 1.9%, respectively, of total yearly energy consumption, as seen from Fig. 1a. The problem associated with the wind energy is very high cost of installation and maintenance, fluctuation of winds over a period of time, and some sort of noise pollution (Eric Rosenbloom 2006), whereas expensive costs and huge environmental impact are certain disadvantages to use hydroelectric energy. Thus the best alternative is to use solar energy which includes photovoltaic solar cells (PSC) and efficient energy storage systems (ESS)

as future generation energy sources. It is very clear from Fig. 1 that currently solar energy accounts just about 1% of the total energy consumption which is quite low. But from Fig. 1b, we see that the demand for solar energy will increase exponentially and it will surpass all other sources of energy to be the most prominent alternative energy source by the end of this century. What do you think is responsible for such a large-scale growth in solar energy sector? The primary reason for the same lies in the fact that current annual world energy consumption is nearly 1.6×10^5 TW, while in one hour the earth receives 1.73×10^5 TWh of energy from the sun (Goswami and Besarati 2013).

Thus, the earth receives more energy from the sun in a single hour than the whole of humanity consumes in an entire year. With advent in technologies, low-cost solar cell fabrication, one-time investment, government incentives and greater awareness, world is trying to shift toward solar energy. Studying the end use distribution of PSC generated energy, it is found that after generation storage of energy is the second important issue; in view to resolve it, intense research work is required for the development of efficient energy storage devices like rechargeable and high-capacity batteries and supercapacitors. Therefore, energy conversion, as well as energy storage research, is at the focal point of current research activities.

The fabrication of efficient energy generation and storage devices cannot be completed without the use of nanomaterials. As the recent studies in various disciplines such as biology, chemistry or physical sciences, and technologies have shown that when particles approach their nanoscales, they show completely different properties as compared to their bulk material. For example, gold which we see yellow appears red or purple in nanoscale. In nanoparticles, quantum effects dominate the behavior and properties of particles. Secondly, "tunability" of properties can be done, that is, one can fine-tune the properties of material of interest by changing the size and shape at nanoscale. The key importance of making nanostructures is they have far large surface areas as compared to similar bulk material. To be more precise, consider an example of solid cube with sides of 1 cm; its surface area is of 6 cm^2. If the same cube is filled with 1 nm-sized cubes, they cover an effective area of about 600,000 cm^2, which is about one-third size of a football field. This key property of having a very large surface area in small volume, that is, high surface to volume ratio of nanomaterials boosts the performance of devices (Thaxton et al. 2009). Recent research shows that along with size, the shape of nanostructure also plays a crucial role in modifying electrical, magnetic, optical and mechanical properties of material (Kamble et al. 2016). The nanomaterials in energy conversion and storage devices perform photovoltaic interactions as well as the chemical reactions at the surfaces/interfaces, so the surface energy, specific surface area, charge transportation, light harvesting and surface chemistry play a very important role. To grab all these properties in nanomaterials, the one-dimensional (1-D) nanostructure is the best option; hence the 1-D nanomaterials have stimulated an increasing interest in research and industries of PSC and ESS. Various 1-D nanostructures like nanofibers, nanorods, nanowires, nanobelts, nanotubes, hierarchical nanostructures and so on, as shown in Fig. 2, seem to be grown by different techniques. Such 1-D nanostructures

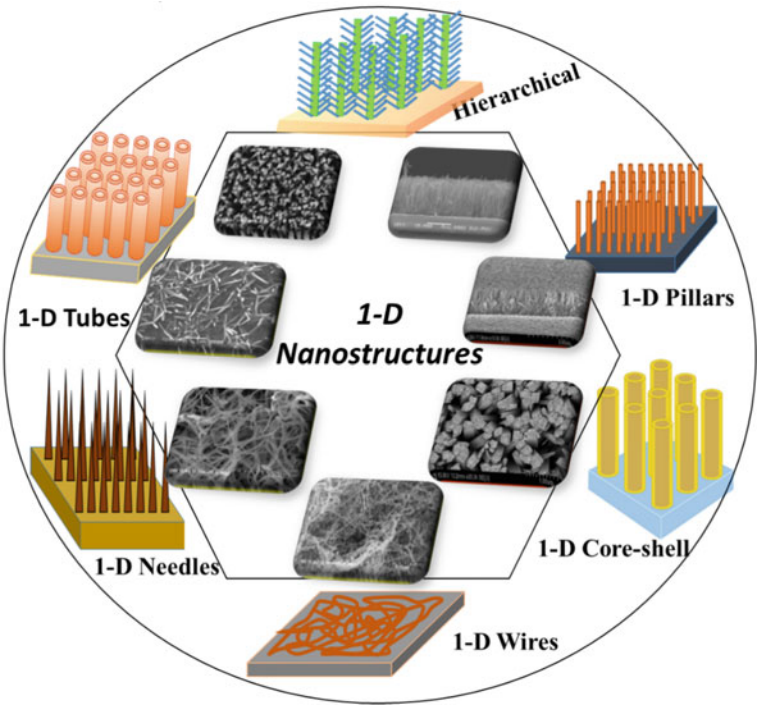

Fig. 2 Different 1-D nanostructures applicable in energy conversion and storage devices

assure increased surface reaction sites, efficient light harvesting and charge transportation, owing to their large length to diameter ratio, that is, aspect ratio (Han et al. 2011). Hence the 1-D nanomaterials have a profound impact in the development of nanoelectronics, photonics, nanoenergy devices, and so on. Although so many methods have been developed to fabricate 1-D nanomaterials, the development of practical, simple, high-yield and low-cost method is still of a great challenge. This chapter comes with an updated literature survey and a brief discussion about the growth and application of 1-D nanomaterials in PSC and ESS.

2 Growth of 1-D Nanomaterials

Various techniques are used for 1-D nanomaterials growth including physical as well as chemical techniques. Though physical techniques give more ordered nanostructures, the need of high temperature and vacuum makes it costly and unsuitable for large-scale production. Whereas with fine optimization of growth conditions one can achieve finely tuned 1-D nanostructures using cost-effective, green and scalable chemical techniques, particularly hydrothermal, chemical reduction, chemical bath

deposition and so on (Tiwari et al. 2012). Chemical techniques can give scalable products and through proper selection of precursors and some optimizations one can adopt completely green synthesis route. One-dimensional nanomaterials can normally be synthesized either by top-down or bottom-up approach and both of them have their own set of advantages and disadvantages. Both these approaches are discussed in detail below.

2.1 Top-Down Approach

In this method, a bulk material is taken and then broken down into finer pieces by chemical or mechanical energy known as physico-chemical etching of bulk crystals to nanodimensions using masks. Thus, it is a technique which retains the bulk order at highly reduced scales with structures that are also sometimes termed as "self-determined". If the mask is used conventionally, then it is termed as photolithography while the other process is called as e-beam lithography or imprint lithography if the mask is not used directly (Ganguly et al. 2014). This process is not cheap and is not suitable for large-scale production.

One of the chemical methods in the top-down approach is metal-assisted chemical etching. Metal-assisted chemical etching is a technique which is mainly used for fabricating silicon and germanium nanowires. The silicon and germanium is etched by using hydrogen peroxide and highly hazardous hydrogen fluoride in the presence of noble metals such as platinum, silver, gold and so on. The etching mechanism is dependent on various factors which are the etchant, illumination, noble metal used, doping type and the concentration of the substrate taken (Huang et al. 2011). As this method includes hazardous enchants and expensive metals, the method is inconvenient to use and less popular. The difference in top-down and bottom-up approach can be easily understood from Fig. 3.

2.2 Bottom-up Approach

In this method the material is synthesized via chemical reactions in such a way that the atoms or molecules aggregate into clusters which allow the precursor particles to grow in size, and it known as nucleation. The nucleation process generates clusters like "seeds" which further generate the long range order needed for crystallization. Thus, in this technique, self-assembly of crystalline order takes from disordered vapor (which may be atoms, molecules or ions), solid or liquid phase through least machine or human interference (Ganguly et al. 2014). Typical examples are quantum dot formation during epitaxial growth and formation of nanoparticles from colloidal dispersion. The process is less expensive and large amount of nanomaterials can be synthesized easily as compared to top-down approach. It can be classified mainly into two types.

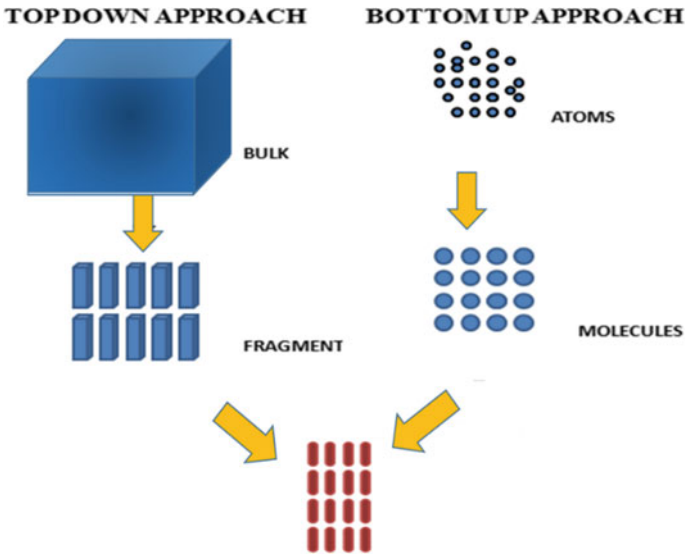

Fig. 3 Top-down and bottom-up growth mechanism of 1-D nanostructures

2.2.1 Catalyst-Assisted Approach

In this approach the metal catalyst eutectic temperature reduces the symmetry of the seed by introducing a liquid–solid interface. When the super saturation of the catalyst takes place with the source, it leads to the precipitation of source in the crystalline form which further grows in an anisotropic manner to generate nanowires (NW) (Wu 2002). This is popularly known as vapor–liquid–solid (VLS) strategy. On increasing the size of the catalyst particle, the diameter of the resultant nanowire can be increased.

2.2.2 Catalyst-Free Approach

The bottom-up approach can also be done even without using the metal catalyst. One-dimensional nanowire growth can be achieved due to the intrinsic anisotropic property of a solid crystal where the crystallizations are preferred along a certain crystal axis. Examples include low-pressure chemical vapor deposition growth of germanium and silicon nanowires on silicon (110) and (100) substrates, respectively (Kim et al. 2009). It is also found that gallium nitride also shows anisotropic growth (Schlager et al. 2006). The most common method in the catalyst-free approach is the vapor–solid (VS) method where the source vapor dissociates at higher temperature and undergoes a chemical reaction in the gas phase and condenses on a substrate kept at lower temperatures (Duay et al. 2013; Duong et al. 2014). In the case of growth of nanowires and nanorods, mostly molecular beam epitaxy (MBE) or plasma-assisted

molecular beam epitaxy process (PAMBE) are used. The method requires an ultra-high vacuum of the order of 10^{-8} torr and low deposition rate, which is approximately 10 nm/min that minimizes the lattice mismatch (epitaxy) between the growing crystal and the substrate. Ultra-pure solid sources, such as gallium (Ga) or indium (In), are heated in a Knudsen effusion cell where they sublimate and the beam of evaporated atoms reach the substrate without any gas-phase reaction. On the substrate, kept at controlled temperatures, the beams may react with each other and condense to form 1-D nanostructures of high crystallinity. Such pure and strain-free materials are required for applications such as LASERS and light-emitting diodes (LEDs) (Chen et al. 2011; Krishnapriya 2017; Lu et al. 2013). Also, the variety of pure semiconductor 1-D nanostructures can be grown by various low-cost chemical techniques (Kamble et al. 2014, 2015a, b; Patil 2017).

The top-down and bottom-up approaches of growth are followed, both in physical and chemical synthesis techniques. Physical technique includes: (1) evaporation technique, (2) sputtering technique, (3) lithography processes, (4) hot and cold processes, (5) spray pyrolysis, (6) inert gas-phase condensation technique, (7) pulsed laser ablation. While chemical techniques include: (1) lyotropic liquid crystal technique, (2) electrochemical deposition, (3) electroless deposition, (4) hydrothermal and solvothermal techniques, (5) sol–gel technique, (6) chemical vapor deposition, (7) chemical bath deposition (CBD), (8) successive ionic layer adsorption and reaction (SILAR), and so on.

Both the physical and chemical techniques have their own advantages and limitations. But chemical methods are preferred and have an important role in developing large-scale 1-D nanostructures which can be attributed to the following properties of chemical techniques: (1) good chemical homogeneity as it offers mixing at the molecular level and (2) its versatility in designing and synthesizing new materials which can be further refined into the final end products (Tiwari et al. 2012).

3 1-D Nanostructures for Photovoltaic Solar Cells (PSC)

The basic phenomenon in PSC includes the excitation of electrons in semiconductor to higher energy level due to incident photons, and these photo-excited electrons and their positive counterparts (holes) are able to generate an electrical current in an external circuit. However, an asymmetry in the electronic system is required to separate these positive and negative charges. Bringing two different (e.g. p- and n-type) semiconducting materials into contact with each other can cause this. Also the device concepts like Schottky diodes or sandwich of a low-doped semiconductor in between two different metal electrodes, and photo-electrochemical device are some of the other possibilities. Depending on the device concept and material used for separation of photo-generated charge carriers there are different types/generations of solar cells like silicon solar cells which comes in first generation, thin film solar cells from second generation, from third generation dye-sensitized solar cells (DSSC), quantum dot sensitized solar cell (QDSSC), polymer heterojunction solar cell, and

newly emerged fourth generation that includes highly efficient Perovskite solar cells and so on. Among all these types of solar cells the third- and fourth-generation solar cells has great potential to overcome Shockley Queisser limit; hence the development of new generation solar cells based on high surface area nanostructures has become research focal point of all scientists. To get high surface area and efficient charge transportation in the same nanostructure, the 1-D nanostructures, like nanoribbons, nanorods, nanoneedles, nanowires, nanotubes, hierarchical 1-D nanoarchitectures and so on, are the best option. As shown in Fig. 4a, the large surface area of 1-D nanorods (shown in green color) provides maximum surface sites for loading of light absorbers/sensitizers (shown in red-colored particles), like dye molecules, quantum dots and so on. So one can modulate the loading of absorbers in wide range.

Also the 1-D nanostructures especially vertically aligned nanorods with proper geometrical configuration facilitate the collection of free charge carriers in the exciton separation step; also their physical dimensions are similar to the carrier diffusion length, as shown in Fig. 4b. This figure gives impression of minimization of charge recombination losses in 1-D structures owing to less grain boundaries. The particles

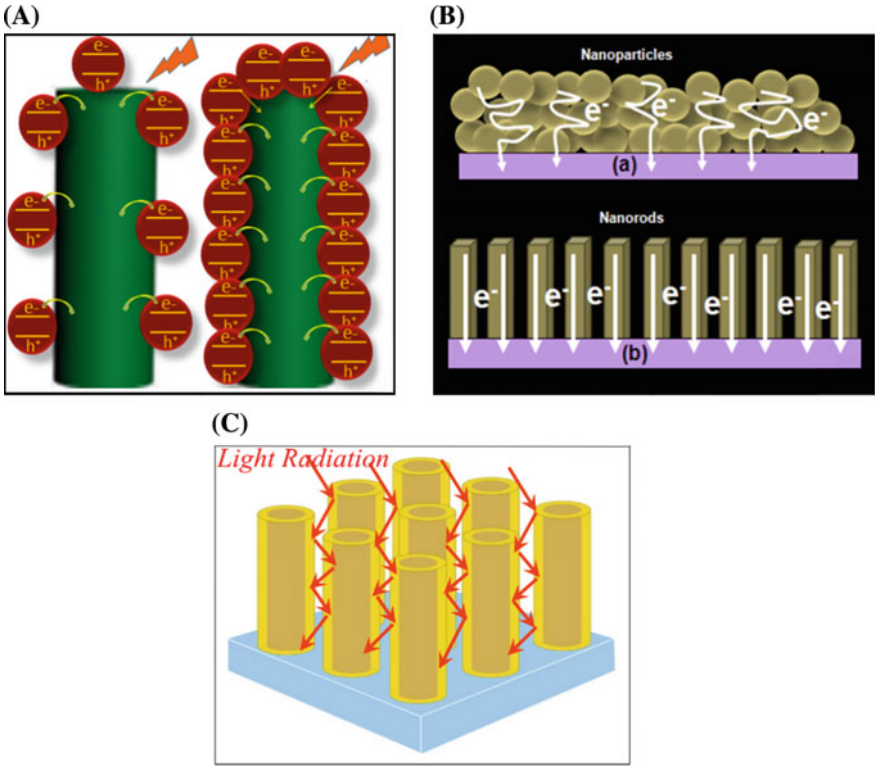

Fig. 4 Benefits of 1-D structures in PSC **A** 1-D nanorod (Green) sensitized with visible light absorbers (Red), **B** comparison of charge transport through nanoparticles and 1-D nanostructures, **C** diffused internal scattering of light radiation through inter-rod spacing

like structures suffer from large charge carrier recombination losses as the charge carrier has to cross many grain boundaries. When light falls on 1-D nanostructured arrays, it undergoes diffuse scattering as shown in Fig. 4c, which reduces the reflection losses and boosts the light harvesting.

To manifest all these beneficial properties of 1-D nanostructures in PSC, scientists have developed various 1-D nanostructures and have successfully applied in various types of solar cells. Corresponding literature survey is given in Table 1.

The 1-D nanostructures, like nanoribbons, nanorods, nanobelts, and so on, of ZnO, TiO_2, CdO, CdSe, and so on have proven to be beneficial for solar cells because they easily provide large surface to volume ratios, facile surface functionalization, high aspect ratios, and superior stabilities owing to perfect crystallinities (Kamble et al. 2014). Considering all the benefits mentioned above, we have synthesized 1-D nanostructures of various materials, like ZnO, TiO_2, CdSe, CdO, CdO–ZnO composite and so on, by cost-effective and green chemical route. The synthesis of nanostructures is often carried out with environmentally hazardous and toxic chemicals, like olylamine, dodecanthiol, octadecene, hydrazene hydrate and so on. Here we have synthesized 1-D nanostructures of various materials by simple, non-vacuum, low temperature and scalable green chemical route.

The ZnO nanorods are synthesized by hydrothermal technique at 90 °C. We have studied the effect of hydroxide anion generating agents like hexamine and ammonia. Earlier it was believed that hexamine plays a key role in 1-D growth of ZnO, but through our work we have shown that with the use of ammonia also one can grow 1-D ZnO nanostructures with high aspect ratio and shorter reaction time as compared to hexamine (Kamble et al. 2014). Figure 5a depicts the uniform growth of high aspect ratio ZnO nanorods array with rod diameter in range 20–60 nm and length in few micrometers. The cross-sectional image in Fig. 5b and very high intensity XRD peak of (002) plane (Fig. 5c) gives an idea of large aspect ratio of synthesized ZnO nanorod arrays.

Synthesized ZnO nanorod arrays are successfully applied in photo-electrochemical solar cells. We also have fabricated 1-D core/shell nanostructures of ZnO–CdS for fabrication of semiconductor sensitized solar cell (SSSC) (Kamble et al. 2015a, b). The ZnO–CdS core/shell structure based on 1-D ZnO facilitates the maximum light harvesting and reduced recombination losses; all the details of synthesis and solar cell performance are given in our research articles (Kamble et al. 2015a, b).

Considering the remarkable physico-chemical properties of 1-D TiO_2, such as high optical transmittance in the visible–IR spectral range, high chemical stability, mechanical resistance, efficient electron transporter and self-cleaning property, 1-D TiO_2 is widely used in various applications like perovskite solar cells, DSSC, QDSSC, photocatalysis, sensors, self-cleaning materials, Li-ion battery and so on (Bian et al. 2014; Giannuzzi et al. 2014; Liu et al. 2008; Mali et al. 2017).

Various techniques found to be used for the synthesis of 1-D TiO_2, like electrochemical anodization, AAO template-assisted deposition, CVD, sol–gel and so on. Among all these techniques, the precise control over size and shape can be achieved through hydrothermal technique. Not only the TiO_2 nanorods but also the

Table 1 Literature survey on solar cell electrodes of different 1-D nanostructures of various materials and their performance

Types of solar cells	Different 1-D nanostructures	1-D nanostructured materials	Solar power conversion efficiency (%)	Ref. no.
Thin film solar cell	Nanorods	$Cu_2In_2ZnS_5$	6.1	Liu et al. (2013)
		GO-ZnO	~2.5	Ameen et al. (2012)
		Indium tin oxide (ITO) nanorods and $CuInS_2$ (CIS)	1.01	Cho et al. (2012)
	Hierarchical structures (nanorods with microspheres)	$Cu_2Zn_{1.5}Sn_{1.2}S_{4.4}$ (FTO/TiO_2/CdS/CZTS/Au)	1.45	Varadharajaperumal et al. (2017)
	Nanotubes	DWNTs-on-Si	>1	Wei et al. (2007)
	Core/shell nanowires	ZnO/TiO_2	2.3	Parize et al. (2017)
DSSC	Nanowires	N719 dye with 0.7% Au@TiO_2	10.2	Choi et al. (2012)
		N719 dye with 0.7% Au@SiO_2	9.8	Choi et al. (2012)
	Nanorods	TiO_2-MWCNT composite	2.4	Sadhu and Poddar (2014)
	Nanotubes	TiO_2	3.33	Wang et al. (2013)
	Hierarchical structure of 1-D materials	5 mol% CO_2 + ion-doped ZnO	4.36	Krishnapriya (2017)
QDSSC	Aligned carbon nanotube	VACNT/CdS	1.1	Li et al. (2013)
	Nanotubes	CNT@rGO@MoCuSe	8.28	Gopi et al. (2018)
	Nanowires	Combine CdSe ZnO	0.4	Leschkies et al. (2007)
	Hierarchical	CuS	4.32	Wang et al. (2014a, b, c)
	Core/shell	CdS/Cu_2S	>6	Ghosh et al. (2018)
Perovskite solar cell	Nanowire	$CH_3NH_3PbI_3$	14.71	Im et al. (2015)
	Nanotubes	TiO_2@$MAPbI_3$_xClx	13.07	Zhu et al. (2019)
	Core/shell	ZnO@ZnTe@CdT@$CH_3NH_3PbI_3$	0.43	Jang et al. (2016)
	Hierarchical	TiO_2@$MAPbI_3$_xClx	17.55	Zhu et al. (2019)
Polymer	Nanorods	Ag and Au	8.67	Lu et al. (2013)
	Nanowires	Ag	2.5	Yang et al. (2011)
	Nanotubes	CNTs	~0.2	Borchert et al. (2012)
	Hierarchical	PTB7 or hieno[3,4-b]thiophene and benzodithiophene	7.4	Chen et al. (2011)

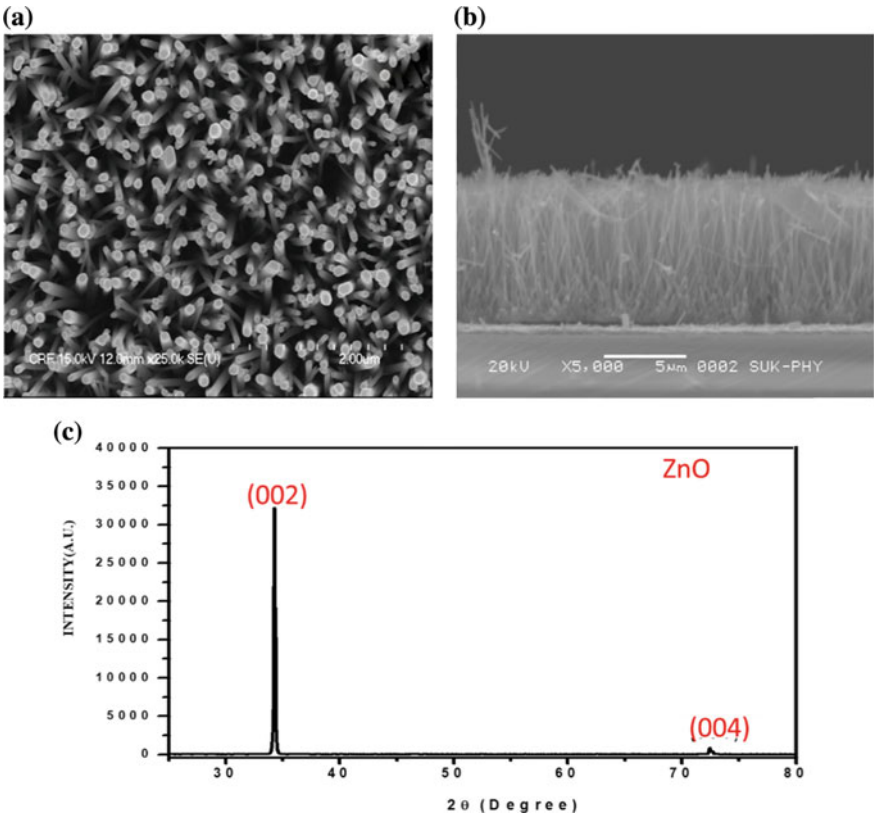

Fig. 5 ZnO nanorod's **a** top surface SEM image, **b** cross-section SEM image, **c** XRD pattern

1-D nanotubes, 1-D hierarchical nanostructures and so on can also be prepared with hydrothermal technique with precise size control (Mai et al. 2013).

Here, we have used simple Teflon-lined autoclave as shown in Fig. 6a for the synthesis of TiO_2 nanorod array. The two-hour reaction conducted at 120 °C resulted in the formation of uniform nanorod array as shown in Fig. 6b, c. Further, the conversion from TiO_2 nanorod to nanotube can be carried out by simple hydrothermal treatment, that is, through hydrothermally chemical etching procedure this transformation raises the surface area of materials by many folds (Mali et al. 2017).

Various metal hydroxides, like $Cd(OH)_2$, $Cu(OH)_2$, $Mg(OH)_2$, $Ni(OH)_2$, are used as potential templates or precursors for the synthesis of corresponding metal oxides, sulfides and selenides (Lu et al. 2013, 2014). Among these different metal hydroxides, $Cd(OH)_2$ is efficient and versatile precursor for the subsequent growth of efficient visible light absorbers such as CdS, CdTe and CdSe through reaction with appropriate compounds. Here, we have synthesized ultra-long nanowires of $Cd(OH)_2$ on glass substrate at room temperature by template-free, one-step, seedless chemical bath deposition technique (Kamble et al. 2011a, b). In such a simple method, controlled

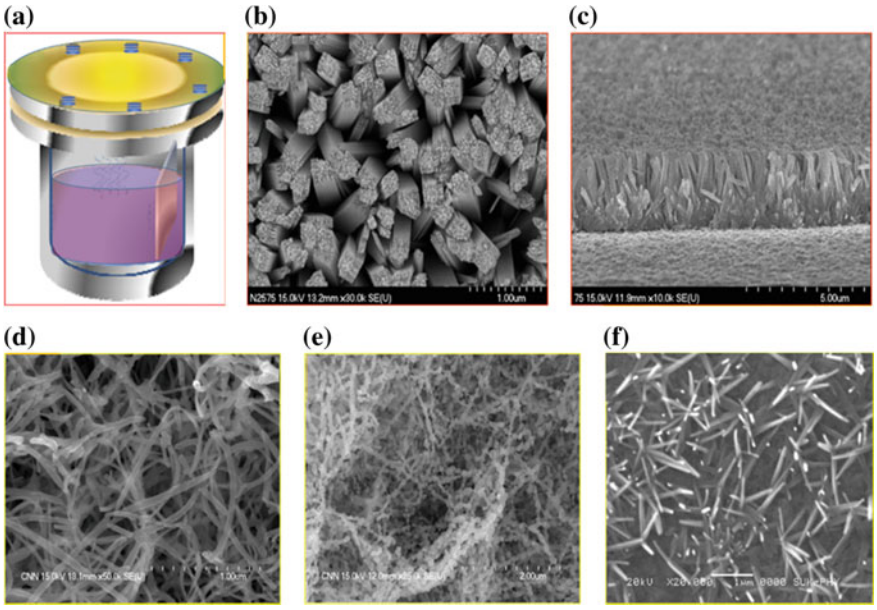

Fig. 6 **a** Schematic of hydrothermal unit used for TiO_2 nanorod growth, and SEM images of **b** TiO_2 nanorods surface, **c** cross-section of TiO_2 nanorods, **d** CdO nanowires, **e** CdO–ZnO composite-beaded nanowires and **f** CdSe nanorods

chemical growth of material takes place when ionic products exceed the solubility products. These $Cd(OH)_2$ nanowires can be easily converted to CdO through heat treatment in air. Figure 6d shows the SEM image of CdO nanowires with diameter in the range of 40–50 nm and of ultra-high length. The synthesis procedure, structural properties, surface adsorptivity and other properties are discussed in detail in our earlier report (Kamble et al. 2011a, b). These smooth and ultra-long nanowires are transferred into 1-D beaded nanowire structure on making composite with ZnO, as shown in Fig. 6e. These wires can also act as efficient template for the synthesis of photoactive materials. Also, we have carried out direct growth of photoactive CdSe nanosticks by one-step electrochemical growth, as shown in Fig. 6f. CdSe is one of the efficient visible light-absorbing photoactive material. We have successfully synthesized high surface area nanostructures of CdSe (Kamble et al. 2017).

4 One-Dimensional Nanostructures for Energy Storage

Various materials and their different nanostructures are used in the fabrication of electrodes for energy storage devices, which has high-end properties like energy density, power density and cycling performance. Among the various nanostructures used for ESS electrodes, the 1-D nanostructures having shorter bi-continuous ion and electron

transport pathways validate the advantage of high-rate performance. Moreover, their larger surface area makes redox active material easily accessible to electrolyte, and their smaller size boosts the capacity of obliging the volume changes, accompanying with electrochemical reactions as it facilitates the stress relaxation. Hence the 1-D nanostructures effectively upsurge the power density, energy density and cycling performance (Chen 2018). The schematic representation of supercapacitor and battery is shown in Fig. 7.

The surface area of 1-D nanostructures can be further amplified by making them hollow and porous, so various 1-D porous nanomaterials have been used in commercialized supercapacitors as the capacitance is directly proportional to the total surface area of electrode material, and the nanopores are anticipated to achieve high specific surface area (Wei 2017). One-dimensional nanostructures of different materials like carbon, silicon, metal oxides and conducting polymers are explored for ESS (Jeevanandam et al. 2018). The 1-D nanomaterials can be categorized into two major types: one is homostructure and the other is heterostructure. One-dimensional homostructures are only one component singular structure, such as nanowires, nanorods and nanotubes, and heterostructures usually consist of more than one component (Chen et al. 2007). Here we are discussing the different 1-D structures which have been successfully implemented as electrode materials for supercapacitors and batteries with the latest literature survey on the same, as given in Tables 2 and 3.

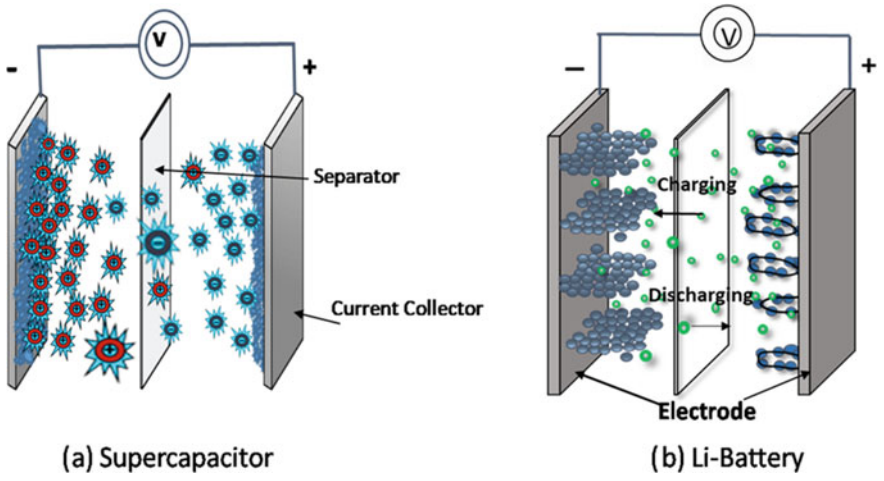

Fig. 7 Basic structures of **a** supercapacitor and **b** Li battery

Table 2 Survey on battery electrodes of different 1-D nanostructures of various materials and their performance

S. no.	1-D nanostructures	Electrode materials	Reversible capacity (mAh^{-1} g^{-1})	Synthesis method	Ref. no.
1	Nanorod/nanopillar	Si-NRs	1038	MR	Chen et al. (2018)
		SnO_2	580	HT	Liu et al. (2009)
		TiO_2	31.44	HT	Zhang et al. (2015)
		Al-doped $LiMn_2O_4$/$LiMn_2O_4$	NA	HT	Yang et al. (2009)
2	Nanowire (NW)	Si-NSi-NWs	3124	VLS	Chan (2008)
		Hybrid nanostructural VO_2	1000	HT	Mai et al. (2013)
		Porous Si-NWs	2000	DE	Ge et al. (2012)
		Li_2MnO_3	1279	HT	Wang et al. (2014)
3	Nanotube (NT)	MWCNTs	950	CVD	Wang et al. (2006)
		SWCNTs	700	CVD	Shimoda et al. (2002)
		Si-NTs	2700	HT@CVD	Song et al. (2010)
		TiO_2	182	EA	Liu et al. (2008)
4	Core/shell	α-Fe_2O_3@ $Li_4Ti_5O_{12}$	249.3	HT	Chen et al. (2014)
		Ti@Si	1125	HT	Meng and Deng (2015)
5	Hierarchically	Ni/NiO/MnO_x/Carbon	1360	ES	Bhaway et al. (2016)
		NH_4VO_3	390	HT@ ES	Mai et al. (2010)

4.1 Nanowires for ESS

One-dimensional nanowires have been studied as energy storage electrode materials due to large surface area to store charges and an efficient pathway to transport charges. Silicon-NWs (Si-NWs) on stainless steel substrate exhibited a very high initial discharge capacity (3124 mAh g^{-1}) and reasonable coulombic efficiency (73%)

Table 3 Literature survey on supercapacitor electrodes of different 1-D nanostructures of various materials and their performance

S. no.	1-D nanostructure	Electrode materials	Specific capacitance F g^{-1}	Synthesis method	Ref. no.
1	Nanorods/nanopillars	CNTs	NA	HT	Duong et al. (2014)
		Fe_2O_3	64.5	HT	Lu et al. (2014)
		MnO_2	302	ED	Yuan et al. (2012)
		PAN	3407	ED	Peng et al. (2011)
2	Nanowires	Co_3O_4	754	HT	Xia et al. (2012)
		PANI	950	EP	Wang et al. (2014)
		$NiCo_2O_4$	1118.6	–	Zhang et al. (2012)
		Si-NWs	13	HWCVP	Soam (2017)
3	Nanotubes	CNTs	80	CVD	Futaba et al. (2006)
		MnO_2	320	ED	Xia (2010)
		PEDOT	132	EP	Liu et al. (2008)
		TiO_2	49.9	EA	Endut et al. (2013)
4	Core/shell	PANI/CNTs	310	–	de Riccardis et al. (2012)
		CuO@AuPd@MnO_2	1400	ED	Yu and Thomas (2014)
		MnO_2/PEDOT	240	ED	Liu and Sang (2008)
		Fe_3O_4@Fe_2O_3	1206	ED	Tang et al. (2015)
5	Hierarchical	$NiCo_2O_4$@MnO_2	1471.4	HT	Yu et al. (2012)
		$M(OH)_2$/MnO_2	298	HT	Duay et al. (2013)
		NHCNs	210.1	HT@C	Zhang et al. (2014)
		$NiCo_2O_4$	2876	HT	Yedluri and Kim (2019)

* *ES* Electrospinning, *DE* Direct etching, *MR* Magnesiothermic reduction, *HT* Hydrothermal, *VLS* Vapor–liquid–solid, *ED* Electrodeposition. *EP* Electrochemical polymerization, *HWCVP* Hotwire chemical vapor process, *CVD* Chemical vapor deposition, *EA* Electrochemical anodization, *C* carbonization

while the constant discharge capacity of over 3000 mAh g^{-1} was retained from the second to the tenth cycle (Chan 2008). Porous-doped Si-NWs produced by direct etching of boron-doped silicon wafers show large pore size and high porosity that can retain its structure after lithium ion intercalation while having low stress, and which gives high capacity and long cycle retention. The capacity remained stable above 1100, 1600 and 2000 mAh/g at current rates of 18, 4 and 2 A/g, respectively, even after 250 cycles (Ge et al. 2012). Nanoscroll buffered hybrid nanostructural (HNS) VO_2 composed of nanobelts and nanowires exhibited long-life performance with capacity retention over 82% after 1,000 cycles at ~9 C (1,000 mA g^{-1}), and high rate up to ~20 C (2,000 mAh g^{-1}) (Mai et al. 2013). Similarly, Li_2MnO_3 nanowire anode material for Li batteries had the reversible capacity that can reach 1279 mAh g^{-1} at a current density of 0.5 mAh g^{-1} after 500 cycles, more than pure MnO_2 nanowires (Wang et al. 2014).

In case of supercapacitors, it was reported that single-crystalline Co_3O_4 nanowire array on a nickel and single-crystalline $NiCo_2O_4$ nanoneedle arrays on conductive substrates (such as Ni foam and Ti) had a high specific capacitance of 599 F/g and 1118.6 F g^{-1} respectively (Xia et al. 2012; Zhang et al. 2012). Vertically aligned PANI nanowire arrays have great potential applications in electrode materials of supercapacitor. The specific capacitance can keep high value 950 F g^{-1} even at the large current density 40 A g^{-1}. By using different electrolytes like LiTFSI, $HClO_4$ aqueous solution, and nonsolvent electrolyte EMITFSI ionic liquids, the capacitive behavior of PANI nanowire arrays were also investigated. They show a quite stable capacitance in ionic liquids during the cyclic life test, which may guide to the finding of a suitable electrolyte for their future applications (Wang et al. 2014).

4.2 Nanorods for ESS

The nanorods are similar to nanowires except the fact that the height is restricted in case of nanorods. Therefore, nanorods/nanopillars surface area ratio is limited compared to nanowires/nanofibers; but the neighboring structure of the individual nanorod/nanopillar significantly lowers chances of collapse making them more accessible to the electrolyte, which increases the ionic conductivity.

Mesoporous silicon nanorods and SnO_2 nanorod arrays were prepared using MWCNTs template and flexible metallic substrates (Fe–Co–Ni alloy and Ni foil) respectively. The silicon nanorods showed a reversible capacity as high as 1038 mAh g^{-1} after 170 cycles while SnO_2 nanorod had 580 mAh g^{-1} after 100 cycles (Liu et al. 2009). Using electron-cyclotron-resonance CVD process, free-standing Si nanorods are prepared on a copper substrate which shows capacity of 2911 mAh g^{-1} and a coulombic efficiency of 95% during the first discharge with capacity retention of 84% after 25 cycles. Also, using electron-cyclotron-resonance plasma-enhanced CVD method, bundles of Si nanorods were fabricated which had discharge capacity of 2990 mAh g^{-1} with a coulombic efficiency of 92% (Chen et al. 2018). TiO_2 nanorod film when used as Li-ion battery electrode had initial reversible discharge

capacity 31.44 mAh g^{-1} with a current density of 30 mAh g^{-1} (Zhang et al. 2015). In case of $LiMn_2O_4$ and Al-doped $LiMn_2O_4$ nanorods, synthesized by a two-step method that combines hydrothermal synthesis of β-MnO_2 nanorods and a solid state reaction to convert them to $LiMn_2O_4$ nanorods retains 96% of capacity after 100 cycles (Yang et al. 2009).

As for supercapacitor application, Fe_2O_3 nanorod hydrothermally synthesized in an aqueous solution containing sodium nitrate, ferric chloride, and hydrogen chloride and heated at high temp in N_2 and air, separately resulted in oxygen-deficient Fe_2O_3 nanorods and pristine Fe_2O_3 nanorods. Specific capacitance of oxygen-deficient Fe_2O_3 (64.5 F g^{-1}) was found to be more than pristine Fe_2O_3 nanorods (Lu et al. 2014). Thomas et al. has reported a facile method i.e. spin on nanoimprinting (SNAP) to synthesize highly ordered carbon nanopillars (shown in Fig. 8) as supercapacitor electrodes that achieved an energy density of ~9.4 × 10^{-4} Wh/cm^3 and power density of 1.48 W/cm^3 (Duong et al. 2014). Another material i.e. solid-state supercapacitor based MnO_2 nanorod by simple synthesis and electrodeposited method on carbon cloth had specific capacitance 320 F g^{-1} while PAN nanorods prepared using

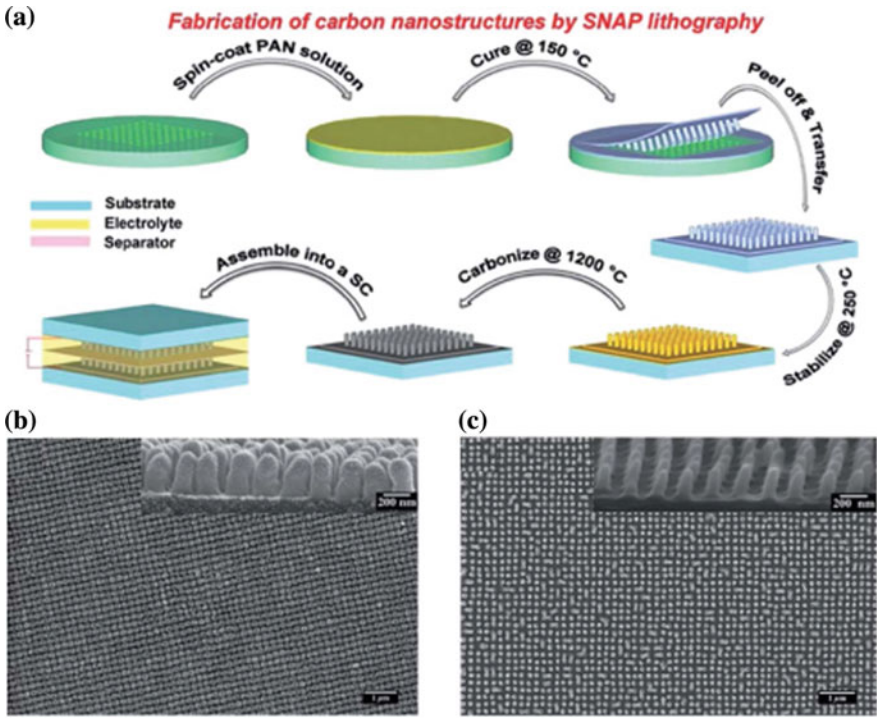

Fig. 8 **a** Schematic of synthesis of carbon nanostructures by SNAP method, **b** the top view and side view (inset) SEM images of polymer nanopillars, **c** the top view and side view (inset) SEM images of carbon nanopillars. Reprinted with permission from (Duong et al. 2014). Copyright (2019) Wiley Online Library

a template with nanoholes on indium tin oxide (ITO) coated substrate gives ultrahigh specific capacitance value of 3407 F g^{-1} (Yuan et al. 2012).

4.3 Nanotubes for ESS

When nanowires are made hollow, this makes both inner and outer surface areas available for energy conversion or storage mechanism; making surface area almost two folds more effective. Thus, nanotube has been widely used electrode material due to their large surface area to store charges and an efficient pathway to transport charges in the tubular nanostructures. They can be of carbon like CNT or of metal oxides like TiO_2, MnO_2 etc. Nanotubes can be randomly distributed or aligned properly in arrays like honeycomb structures.

One dimensional CNTs with significant length-to-diameter ratio, in which carbon atoms are arranged as a hexagonal lattice with each carbon atom surrounded by three nearest neighboring atoms, to form a special covalent sp^2 carbon bonding. In addition, CNTs possess unique size-/surface-dependent properties useful for efficient energy storage (Ganguly et al. 2014). High-purity vertically aligned multiwalled carbon nanotubes (MWCNTs) gave a high reversible lithium storage capacity of 950 mAh/g in lithium-ion cells (Wang et al. 2006). By opening or cutting the CNTs, the capacity can be further increased. SWNTs are prepared by using strong acid to open the tubes and reducing their length to obtain a reversible capacity of about 700 mAh g^{-1} (Shimoda et al. 2002). TiO_2 nanotubes in Li-ion batteries, exhibited an overall capacitance of 182 mAh g^{-1} at a charge/discharge rate of 80 mAh g^{-1} (Liu et al. 2008).

By using electrochemical deposition techniques, Xia et al. synthesized free-standing MnO_2 nanotube arrays on a Pt substrate. They showed that the MnO_2 nanotube array electrode had good capacitive behavior than MnO_2 nanowire array electrode. The MnO_2 nanotube arrays showed a specific capacitance of 320 F g^{-1}, which is high as compared to the MnO_2 nanowire array electrode (Xia 2010). Poly (3, 4-ethylenedioxythiophene) (PEDOT) nanotubes electrode based supercapacitor gave a high power density of 25 kW kg^{-1} at energy density (5.6 Wh kg^{-1}) maintained at 80% (Liu et al. 2008). The TiO_2 nanotubes prepared by anodization for different durations induced porosity which had an impact on the capacitance value as 18.3 μF/cm^2, 19.3 μF/cm^2, 27.7 μF/cm^2 and 49.9 μF/cm^2 for 10 s, 30 s, 600 s, and 1800 s, respectively (Endut et al. 2013).

4.4 Core-Shell Structures for ESS

One dimensional nanostructured current collector core can provide a support for active sites, forming a core-shell 1-D nano material. The fabrication of core–shell nanostructures of the same or different materials provides stable nanostructured

anodes. It is similar to the nanorod or nanotube but coated with thin shell of another efficient material.

Core–shell nanorod arrays of Ti@Si on Ti foil via hydrothermal method and carbon-free core–shell α-iron oxide (α-Fe_2O_3) @ spinel lithium titanate ($Li_4Ti_5O_{12}$, LTO via facile hydrothermal process when used as electrodes of Li ion battery demonstrated reversible capacity of 1125 mAh g^{-1} and 249.3 mAh g^{-1} respectively (Chen et al. 2014; Meng and Deng 2015).

Yu and Thomas have reported CuO@AuPd@MnO_2 core shell NWs as electrode for supercapacitor. It can drop the surface energy of the active material, reduce the aggregation possibility and relive the electrode electrolyte side reaction. It gives good results and show specific capacitance ~1400 F/g @ 5 mV/s (Yu and Thomas 2014). PANI/CNTs combine the large pseudocapacitance of the conducting polymers with the fast charging/discharging double-layer capacitance with CNTs and give specific capacitance ~260 F/g @ 50 mV/s (de Riccardis et al. 2012). In another process, MnO_2/PEDOT coaxial nanowires synthesized by a one-step co-electrodeposition method in a porous alumina template showed specific capacitance values of MnO_2 films of 190–240 F/g (Liu and Sang 2008). Also, hierarchical heterostructure comprising Fe_3O_4@Fe_2O_3 core/shell nanorod arrays (NRAs) exhibited a high capacitive performance, compared to the bare Fe_2O_3 and Fe_3O_4 NRAs electrodes and delivered specific capacitance 1206 F/cm^3 with a mass loading of 1.25 mg/cm^2 (Tang et al. 2015).

4.5 Hierarchical Nanostructures for ESS

In this type of structures, pseudocapacitive and electric double-layered capacitor (EDLC) materials are combined, leading to an enhancement in charge storage, as both charge storage mechanisms (EDLC and pseudo-capacitive) reinforced in the same structure. The combinations can be carried out for different materials and different 1-D nanostructures (like 1-D branched heterostructures) by easy methods.

Electronically conductive and interconnected porous metal oxide fiber composites (Ni/NiO/MnO_x/carbon nanofiber) offer several advantages over isolated nanowire and nanotube-based Li-ion battery electrode. It has the highest discharge capacity of 1360 mAh g^{-1} after 200 cycles on the basis of active material for the mesoporous Ni66–Mn33/C fiber anode and also exhibits good cycling stability and low impedance (238 Ω) (Bhaway et al. 2016). In another process, using low-cost NH_4VO_3 as the starting materials, a cost-saving method was developed to synthesize ultra-long hierarchical vanadium oxide nanowires constructed from attached vanadium oxide nanorods for lithium-ion batteries cathode electrode. The NH_4VO_3 nanorods growth on the surface of electrospun NH_4VO_3/PVA composite nanowires exhibited a high performance for lithium-ion batteries, which delivered high discharge capacity of 390 mAh/g and improved cycling stability (Mai et al. 2010).

Lee Yu and co-workers constructed hierarchical $NiCo_2O_4$@MnO_2 core/shell heterostructured NW array for supercapacitor electrode on nickel foam and delivered

high specific capacitance of 1.66 F cm^{-2} even at 20 mA cm^{-2} (Yu et al. 2012). Another experiment reported hierarchical $M(OH)_2/MnO_2$ nanofibrils/nanowire array, where a layer of MnO_2 nanofibrils was fabricated on the surface of the individual MnO_2 nanowire. Using aqueous electrolyte, material shows high specific capacitance of 174 F/g at 250 mV/s and 298 F/g at 50 mV/s and maintained 85.2% of its capacitance after 1000 cycles (Duay et al. 2013). Hierarchical mesoporous spinel $NiCo_2O_4$ nanowires made via facile hydrothermal method delivered a high specific capacitance of 2876 F g^{-1} at a current density of 1 A g^{-1} and retained 84.7% after 500 cycles (Yedluri and Kim 2019). In another case, a new class of hierarchical 1-D nano-doped porous carbon nanowhiskers on CNFs was prepared through the polymerization of aniline on the CNFs and then annealing the nanocomposite in the N_2 atmosphere at high temperature. When used as supercapacitor electrode, NHCNs and KOH-activated NHCNs carbonized at 750 °C show the optimal specific capacitances of 210.1 and 254.3 F g^{-1}, respectively. This result shows that NHCNs are a very promising electrode.

Yu and Thomas have reported CuO@AuPd@MnO_2 core/shell NWs-based hierarchical electrode (shown in Fig. 9) for supercapacitor with improved performance.

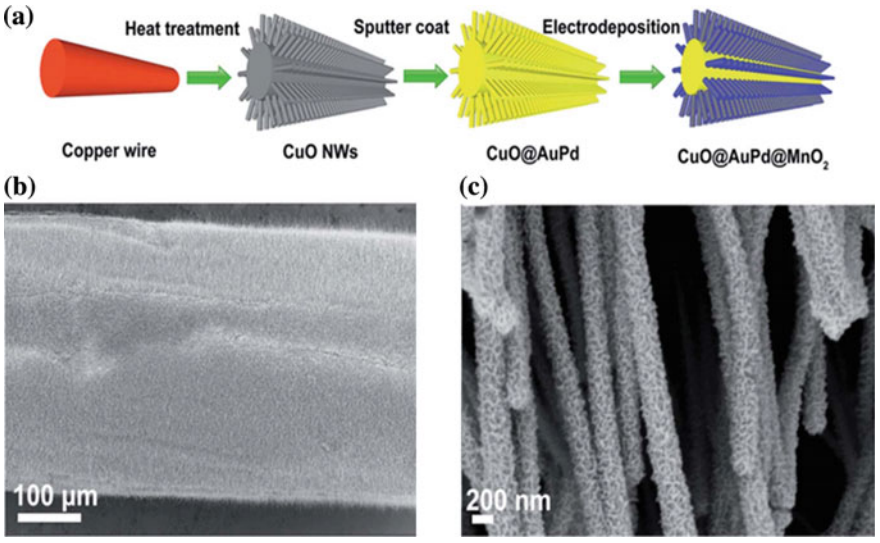

Fig. 9 **a** Schematic illustration of the CuO@AuPd@MnO_2 NWs fabrication process, **b**, **c** SEM images of CuO@AuPd@MnO_2NWs hierarchical structures. Reprinted with permission from (Yang et al. 2009). Copyright (2019) Wiley Online Library

5 Conclusion

The book takes you through the details about the recent development of various 1-D nanostructures that have potential use in PSC and ESS. One-dimensional nanostructures can be architectured into hierarchical and hybrid nanostructures with different additional materials to improve the light absorbance and charge storage capacity. The latest progress in synthesis techniques and versatile nature of 1-D nanomaterials potentially gave us new opportunities for current and future research for material scientists. The future progress has also opened the doors for understanding how composition, morphology and size along with the chemical conditions affect the efficiency of such nanostructures. From the literature survey on efficiencies of different 1-D nanomaterials, we come to the conclusion that still much work has to be done to enhance the efficiency and to develop optimized energy storage devices. The final goal is to achieve faster charging, higher energy storage capacity and higher cyclic stability of such materials. The other challenges include the production cost, synthesis scale, environmental issues and safety problems associated with it. Also, we require more knowledge to understand about the physical and chemical properties of 1-D nanostructures to exploit their properties for magnetic, optical and electric-based applications. In addition to this, the development of 1-D-based nanomaterials will help us to improve our older technologies paving way for further research that will benefit industries as well as society.

References

Ameen S et al (2012) Vertically aligned ZnO nanorods on hot filament chemical vapor deposition grown graphene oxide thin film substrate: solar energy conversion. ACS Appl Mater Interfaces (American Chemical Society) 4(8):4405–4412. https://doi.org/10.1021/am301064j

Bhaway SM et al (2016) Hierarchical electrospun and cooperatively assembled nanoporous Ni/NiO/MnOx/Carbon nanofiber composites for lithium ion battery anodes. ACS Appl Mater Interfaces 8(30):19484–19493. https://doi.org/10.1021/acsami.6b05592

Bian J et al (2014) Carbon dot loading and TiO_2 nanorod length dependence of photoelectrochemical properties in carbon dot/TiO_2 nanorod array nanocomposites. ACS Appl Mater Interfaces 6(7):4883–4890. https://doi.org/10.1021/am4059183

Borchert H et al (2012) Vertically oriented carbon nanostructures and their application potential for polymer-based solar cells. J Phys Chem C 116(1):412–419. https://doi.org/10.1021/jp2095592

British Petroleum (2018) 67th edition Contents is one of the most widely respected, Statistical review of world energy. https://www.bp.com/content/dam/bp/en/corporate/pdf/energy-economics/statistical-review/bp-stats-review-2018-full-report.pdf. Accessed 14 May 2019

Chan CK et al (2008) High-performance lithium battery anodes using silicon nanowires. Nature Nanotechnol 3(1):31–5. https://doi.org/10.1038/nnano.2007.411

Chen C et al (2018) One-dimensional nanomaterials for energy storage. J Phys D Appl Phys (IOP Publishing) 51(11). https://doi.org/10.1088/1361-6463/aaa98d

Chen J, Wiley BJ, Xia Y (2007) One-dimensional nanostructures of metals: large-scale synthesis and some potential applications. Langmuir 23(8):4120–4129. https://doi.org/10.1021/la063193y

Chen M et al (2014) Fabrication of core-shell α-Fe_2O_3@ $Li_4Ti_5O_{12}$ composite and its application in the lithium ion batteries. ACS Appl Mater Interfaces 6(6):4514–4523. https://doi.org/10.1021/am500294m

Chen Q et al (2018) Selflating synthesis of silicon nanorods from natural sepiolite for high-performance lithium-ion battery anodes. J Mater Chem A (Royal Society of Chemistry) 6(15):6356–6362. https://doi.org/10.1039/c8ta00587g

Chen W et al (2011) Hierarchical nanomorphologies promote exciton dissociation in polymer/fullerene bulk heterojunction solar cells. Nano Lett (American Chemical Society) 11(9):3707–3713. https://doi.org/10.1021/nl201715q

Cho JW et al (2012) Bulk heterojunction formation between indium tin oxide nanorods and CuInS2 nanoparticles for inorganic thin film solar cell applications. ACS Appl Mater Interfaces (American Chemical Society) 4(2):849–853. https://doi.org/10.1021/am201524z

Choi H, Chen WT, Kamat PV (2012) Know thy nano neighbor. plasmonic versus electron charging effects of metal nanoparticles in dye-sensitized solar cells. ACS Nano 6(5):4418–4427. https://doi.org/10.1021/nn301137r

Goswami DY, Besarati SM (2013) World Energy Council 2013 World energy resources: solar, pp 1–28. http://www.worldenergy.org/wp-content/uploads/2013/10/WER_2013_8_Solar_revised.pdf

Duay J et al (2013) Self-limiting electrodeposition of hierarchical MnO_2 and $M(OH)_2/MnO_2$ nanofibril/nanowires: Mechanism and supercapacitor properties. ACS Nano 7(2):1200–1214. https://doi.org/10.1021/nn3056077

Duong B et al (2014) High throughput printing of nanostructured carbon electrodes for supercapacitors. Adv Mater Interfaces 1(1):1–5. https://doi.org/10.1002/admi.201300014

Endut Z, Hamdi M, Basirun WJ (2013) An investigation on formation and electrochemical capacitance of anodized titania nanotubes. Appl Surf Sci (Elsevier B.V.) 280:962–966. https://doi.org/10.1016/j.apsusc.2013.05.118

Eric Rosenbloom (2006) A problem with wind power [AWEO.org]. http://www.aweo.org/problemwithwind.html

Futaba DN et al (2006) Shape-engineerable and highly densely packed single-walled carbon nanotubes and their application as super-capacitor electrodes. Nat Mater 5(12):987–994. https://doi.org/10.1038/nmat1782

Ganguly A et al (2014a) Production and storage of energy with one-dimensional semiconductor nanostructures. Crit Rev Solid State Mater Sci 39(2):109–153. https://doi.org/10.1080/10408436.2013.796909

Ganguly A et al (2014b) Production and storage of energy with one-dimensional semiconductor nanostructures. Crit Rev Solid State Mater Sci (Taylor & Francis) 39(2):109–153. https://doi.org/10.1080/10408436.2013.796909

Ge M et al (2012) Porous doped silicon nanowires for lithium ion battery anode with long cycle life. Nano Lett 12(5):2318–2323. https://doi.org/10.1021/nl300206e

Ghosh D et al (2018) Photoactive core-shell nanorods as bifunctional electrodes for boosting the performance of quantum dot sensitized solar cells and photoelectrochemical cells. Chem Mater (American Chemical Society) 30(17):6071–6081. https://doi.org/10.1021/acs.chemmater.8b02504

Giannuzzi R et al (2014) Ultrathin TiO_2 (B) nanorods with superior lithium-ion storage performance. ACS Appl Mater Interfaces 6(3):1933–1943. https://doi.org/10.1021/am4049833

Gopi CVVM et al (2018) CNT@rGO@MoCuSe composite as an efficient counter electrode for quantum dot-sensitized solar cells. ACS Appl Mater Interfaces (American Chemical Society) 10(12):10036–10042. https://doi.org/10.1021/acsami.7b18526

Gujar TP et al (2008) Formation of CdO films from chemically deposited $Cd(OH)_2$ films as a precursor. Appl Surf Sci 254(13):3813–3818. https://doi.org/10.1016/j.apsusc.2007.12.015

Han N, Wang F, Ho JC (2011) One-dimensional nanostructured materials for solar energy harvesting. Nanomater Energy 1(1):4–17. https://doi.org/10.1680/nme.11.00005

Huang Z et al (2011) Metal-assisted chemical etching of silicon: a review. Adv Mater (Germany) 23(2):285–308. https://doi.org/10.1002/adma.201001784

Im JH et al (2015) Nanowire perovskite solar cell. Nano Lett (American Chemical Society) 15(3):2120–2126. https://doi.org/10.1021/acs.nanolett.5b00046

Jang YJ et al (2016) Unbiased sunlight-driven artificial photosynthesis of carbon monoxide from CO_2 Using a ZnTe-based photocathode and a perovskite solar cell in tandem. ACS Nano (American Chemical Society) 10(7):6980–6987. https://doi.org/10.1021/acsnano.6b02965

Jeevanandam J et al (2018) Review on nanoparticles and nanostructured materials: History, sources, toxicity and regulations. Beilstein J Nanotechnol 9(1):1050–1074. https://doi.org/10.3762/bjnano.9.98

Kamble A, Sinha BB et al (2015a) Boosting the performance of ZnO/CdS core-shell nanorod array-based solar cells by ZnS surface treatment. Isr J Chem 55(9):1011–1016. https://doi.org/10.1002/ijch.201400205

Kamble A, Sinha B et al (2015b) Facile linker free growth of CdS nanoshell on 1-D ZnO: solar cell application. Electron Mater Lett 11(2):171–179. https://doi.org/10.1007/s13391-014-4236-x

Kamble A et al (2016) Sulfur ion concentration dependent morphological evolution of CdS thin films and its subsequent effect on photo-electrochemical performance. Phys Chem Chem Phys (Royal Society of Chemistry) 18(40):28024–28032. https://doi.org/10.1039/c6cp00903d

Kamble AS, Pawar RC, Tarwal NL et al (2011) Ethanol sensing properties of chemosynthesized CdO nanowires and nanowalls. Mater Lett (Elsevier B.V.) 65(10):1488–1491. https://doi.org/10.1016/j.matlet.2011.02.049

Kamble AS, Pawar RC, Patil JY et al (2011) From nanowires to cubes of CdO: ethanol gas response. J Alloys Compd (Elsevier B.V.) 509(3):1035–1039. https://doi.org/10.1016/j.jallcom.2010.09.166

Kamble AS et al (2014) Effect of hydroxide anion generating agents on growth and properties of ZnO nanorod arrays. Electrochim Acta (Elsevier Ltd) 149:386–393. https://doi.org/10.1016/j.electacta.2014.10.049

Kamble AS et al (2017) Influence of surfactants on electrochemical growth of CdSe nanostructures and their photoelectrochemical performance. J Solid State Electrochem 21(9):2649–2653. https://doi.org/10.1007/s10008-017-3651-y

Kim BS et al (2009) Catalyst-free growth of single-crystal silicon and germanium nanowires. Nano Lett (American Chemical Society) 9(2):864–869. https://doi.org/10.1021/n1803752w

Krishnapriya R et al (2017) Unveiling the Co^{2+} ion doping-induced hierarchical shape evolution of ZnO: in correlation with magnetic and photovoltaic performance. ACS Sustain Chem Eng (American Chemical Society) 5(11):9981–9992. https://doi.org/10.1021/acssuschemeng.7b01918

Leschkies KS et al (2007) Photosensitization of ZnO nanowires with CdSe quantum dots for photovoltaic devices. Nano Lett (American Chemical Society) 7(6):1793–1798. https://doi.org/10.1021/nl070430o

Li Chen et al (2013) Photovoltaic property of a vertically aligned carbon nanotube hexagonal network assembled with CdS quantum dots. ACS Appl Mater Interfaces 5(15):7400–7404. https://doi.org/10.1021/am401725x

Liu D et al (2008a) TiO_2 nanotube arrays annealed in N_2 for efficient lithium-ion intercalation. J Phys Chem C 112(30):11175–11180. https://doi.org/10.1021/jp801300j

Liu J et al (2009) Direct growth of SnO_2 nanorod array electrodes for lithium-ion batteries. J Mater Chem 19(13):1859–1864. https://doi.org/10.1039/b817036c

Liu R, Cho SI, Lee SB (2008) Poly(3,4-ethylenedioxythiophene) nanotubes as electrode materials for a high-powered supercapacitor. Nanotechnology 19(21). https://doi.org/10.1088/0957-4484/19/21/215710

Liu R, Sang BL (2008) MnO2/poly(3,4-ethylenedioxythiophene) coaxial nanowires by one-step coelectrodeposition for electrochemical energy storage. J Am Chem Soc 130(10):2942–2943. https://doi.org/10.1021/ja7112382

Liu Y et al (2013) Controllable synthesis of $Cu_2In_2ZnS_5$ nano/microcrystals and hierarchical films and applications in dye-sensitized solar cells. J Phys Chem C 117(20):10296–10301. https://doi.org/10.1021/jp401998p

Lu L et al (2013) Cooperative plasmonic effect of Ag and Au nanoparticles on enhancing performance of polymer solar cells. Nano Lett (American Chemical Society) 13(1):59–64. https://doi.org/10.1021/nl3034398

Lu X et al (2014) Oxygen-deficient hematite nanorods as high-performance and novel negative electrodes for flexible asymmetric supercapacitors. Adv Mater 26(19):3148–3155. https://doi.org/10.1002/adma.201305851

Mai L et al (2010) Electrospun ultralong hierarchical vanadium oxide nanowires with high performance for lithium ion batteries. Nano Lett 10(11):4750–4755. https://doi.org/10.1021/nl103343w

Mai L et al (2013) Nanoscroll buffered hybrid nanostructural VO_2 (B) cathodes for high-rate and long-life lithium storage. Adv Mater 25(21):2969–2973. https://doi.org/10.1002/adma.201205185

Mali SS et al (2017) Secondary hydrothermally processed engineered titanium dioxide nanostructures for efficient perovskite solar cells. Energy Technol 5(10):1775–1787. https://doi.org/10.1002/ente.201700030

Meng X, Deng D (2015) Core-shell Ti@Si coaxial nanorod arrays formed directly on current collectors for lithium-ion batteries. ACS Appl Mater Interfaces 7(12):6867–6874. https://doi.org/10.1021/acsami.5b00492

Parize R et al (2017) $ZnO/TiO_2/Sb_2S_3$ core-shell nanowire heterostructure for extremely thin absorber solar cells. J Phys Chem C (American Chemical Society) 121(18):9672–9680. https://doi.org/10.1021/acs.jpcc.7b00178

Patil JV et al (2017) Electrospinning: a versatile technique for making of 1D growth of nanostructured nanofibers and its applications: an experimental approach. Appl Surf Sci (Elsevier B.V.) 423:641–674. https://doi.org/10.1016/j.apsusc.2017.06.116

Peng C, Hu D, Chen GZ (2011) Theoretical specific capacitance based on charge storage mechanisms of conducting polymers: comment on "Vertically oriented arrays of polyaniline nanorods and their super electrochemical properties". Chem Commun 47(14):4105–4107. https://doi.org/10.1039/c1cc10675a

de Riccardis MF et al (2012) Functional characterisations of hybrid nanocomposite films based on polyaniline and carbon nanotubes. Adv Sci Technol 79:81–86. https://doi.org/10.4028/www.scientific.net/ast.79.81

Sadhu S, Poddar P (2014) Template-free fabrication of highly-oriented single-crystalline 1D-rutile TiO_2-MWCNT composite for enhanced photoelectrochemical activity. J Phys Chem C 118(33):19363–19373. https://doi.org/10.1021/jp5023983

Schlager JB et al (2006) Polarization-resolved photoluminescence study of individual GaN nanowires grown by catalyst-free molecular beam epitaxy. Appl Phys Lett (American Institute of Physics) 88(21):213106. https://doi.org/10.1063/1.2206133

Shi SC et al (2005) Growth of single-crystalline wurtzite aluminum nitride nanotips with a self-selective apex angle. Adv Func Mater 15(5):781–786. https://doi.org/10.1002/adfm.200400324

Shimoda H et al (2002) Lithium intercalation into etched single-wall carbon nanotubes. Physica B 323(1–4):133–134. https://doi.org/10.1016/S0921-4526(02)00876-1

Shinde VR et al (2008) A solution chemistry approach for the selective formation of ultralong nanowire bundles of crystalline $Cd(OH)_2$ on substrates. Adv Mater 20(5):1008–1012. https://doi.org/10.1002/adma.200701828

Soam A et al (2017) Fabrication of silicon nanowires based on-chip micro-supercapacitor. Chem Phys Lett (Elsevier B.V.) 678:46–50. https://doi.org/10.1016/j.cplett.2017.04.019

Song T et al (2010) Arrays of sealed silicon nanotubes as anodes for lithium ion batteries. Nano Lett 10(5):1710–1716. https://doi.org/10.1021/nl100086e

Tang X et al (2015) Hierarchical $Fe_3O_4@Fe_2O_3$ core-shell nanorod arrays as high-performance anodes for asymmetric supercapacitors. ACS Appl Mater Interfaces 7(49):27518–27525. https://doi.org/10.1021/acsami.5b09766

Thaxton CS et al (2009) Nanoparticle-based bio-barcode assay redefines "undetectable" PSA and biochemical recurrence after radical prostatectomy. Proc Natl Acad Sci 106(44):18437–18442. https://doi.org/10.1073/pnas.0904719106

Tiwari JN, Tiwari RN, Kim KS (2012) Zero-dimensional, one-dimensional, two-dimensional and three-dimensional nanostructured materials for advanced electrochemical energy devices. Progr Mater Sci (Elsevier Ltd) 57(4):724–803. https://doi.org/10.1016/j.pmatsci.2011.08.003

Varadharajaperumal S et al (2017) Morphology controlled n-type TiO_2 and stoichiometry adjusted p-type Cu_2ZnSnS_4 thin films for photovoltaic applications. Cryst Growth Des (American Chemical Society) 17(10):5154–5162. https://doi.org/10.1021/acs.cgd.7b00632

Wang D et al (2014a) Novel Li_2MnO_3 nanowire anode with internal Li-enrichment for use in a Li-ion battery. Nanoscale 6(14):8124–8129. https://doi.org/10.1039/c4nr01941e

Wang F et al (2014b) One-step electrochemical deposition of hierarchical CuS nanostructures on conductive substrates as robust, high-performance counter electrodes for quantum-dot-sensitized solar cells. J Phys Chem C (American Chemical Society) 118(34):19589–19598. https://doi.org/10.1021/jp505737u

Wang GX et al (2006) Growth and lithium storage properties of vertically aligned carbon nanotubes. Met Mater Int 12(5):413–416. https://doi.org/10.1007/BF03027708

Wang K et al (2014c) Conducting polymer nanowire arrays for high performance supercapacitors. Small 10(1):14–31. https://doi.org/10.1002/smll.201301991

Wang X et al (2013) Electron transport and recombination in photoanode of electrospun TiO_2 nanotubes for dye-sensitized solar cells. J Phys Chem C (American Chemical Society) 117(4):1641–1646. https://doi.org/10.1021/jp311725g

Wei J et al (2007) Double-walled carbon nanotube solar cells. Nano Lett (American Chemical Society) 7(8):2317–2321. https://doi.org/10.1021/nl070961c

Wei Q et al (2017) Porous one-dimensional nanomaterials: design, fabrication and applications in electrochemical energy storage. Adv Mater 29(20). https://doi.org/10.1002/adma.201602300

Windmills for electricity—where generating electricity from the wind isn't a dream! (no date). https://windmillsforelectricity.com/. Accessed 3 May 2019

Wu Y et al (2002) Inorganic semiconductor nanowires: rational growth, assembly, and novel properties. Chemistry (Weinheim an der Bergstrasse, Germany) 8(6):1260–1268. http://www.ncbi.nlm.nih.gov/pubmed/11921209

Xia H et al (2010) MnO_2 nanotube and nanowire arrays by electrochemical deposition for supercapacitors. J Power Sour (Elsevier B.V.) 195(13):4410–4413. https://doi.org/10.1016/j.jpowsour.2010.01.075

Xia XH et al (2012) Freestanding Co_3O_4 nanowire array for high performance supercapacitors. RSC Adv 2(5):1835–1841. https://doi.org/10.1039/c1ra00771h

Yang L et al (2011) Solution-processed flexible polymer solar cells with silver nanowire electrodes. ACS Appl Mater Interfaces (American Chemical Society) 3(10):4075–4084. https://doi.org/10.1021/am2009585

Yang Y et al (2009) Single nanorod devices for battery diagnostics: a case study on $LiMn_2O_4$. Nano Lett (American Chemical Society) 9(12):4109–4114. https://doi.org/10.1021/nl902315u

Yedluri AK, Kim HJ (2019) Enhanced electrochemical performance of nanoplate nickel cobaltite (NiCo2O4) supercapacitor applications. RSC Adv (Royal Society of Chemistry) 9(2):1115–1122. https://doi.org/10.1039/c8ra09081e

Yu L et al (2012) Hierarchical $NiCo_2O_4$ @MnO_2 core–shell heterostructured nanowire arrays on Ni foam as high-performance supercapacitor electrodes. Chem Commun 49(2):137–139. https://doi.org/10.1039/c2cc37117k

Yu Z, Thomas J (2014) Energy storing electrical cables: integrating energy storage and electrical conduction. Adv Mater 26(25):4279–4285. https://doi.org/10.1002/adma.201400440

Yuan L et al (2012) Flexible solid-state supercapacitors based on carbon nanoparticles/MnO_2 nanorods hybrid structure. ACS Nano 6(1):656–661. https://doi.org/10.1021/nn2041279

Zhang GQ et al (2012) Single-crystalline $NiCo_2O_4$ nanoneedle arrays grown on conductive substrates as binder-free electrodes for high-performance supercapacitors. Energy Environ Sci 5(11):9453–9456. https://doi.org/10.1039/c2ee22572g

Zhang J et al (2014) Nitrogen-doped hierarchical porous carbon nanowhisker ensembles on carbon nanofiber for high-performance supercapacitors. ACS Sustain Chem Eng 2(6):1525–1533. https://doi.org/10.1021/sc500221s

Zhang Y et al (2015) An electrochemical investigation of rutile TiO_2 microspheres anchored by nanoneedle clusters for sodium storage. Phys Chem Chem Phys (Royal Society of Chemistry) 17(24):15764–15770. https://doi.org/10.1039/c5cp01227a

Zhu H et al (2019) Perovskite and conjugated polymer wrapped semiconducting carbon nanotube hybrid films for high-performance transistors and phototransistors. ACS Nano (American Chemical Society) 13(4):3971–3981. https://doi.org/10.1021/acsnano.8b07567

Nanoporous Polymeric Membranes for Hydrogen Separation

Rajesh Kumar, Kamakshi, Manoj Kumar and Kamlendra Awasthi

Abstract In today's world, it becomes a necessity to develop an eco-friendly and renewable energy source to overcome the pollution and energy requirement problem. Among all renewable energy sources, hydrogen has been found a more attractive energy carrier due to its high efficiency and cost-effective sustainable energy source. For practical use of H_2 as an energy source, it should be separated from a mixture of gases by using hydrogen-selective membranes. In the present chapter, we have reviewed the membrane-based gas separation process. Furthermore, we have summarized the H_2 gas separation data based on the different membranes and approaches to prepare hydrogen-selective membranes.

1 Introduction

From the last few decades, the membranes-based technology have noteworthy advantage form wastewater treatment for water purification to the high efficiency of the solar cell. In considering the future energy requirement membrane equipment and technology can be a good option because of its eco-friendly nature, low cost, economical processing capabilities, and modification acceptability. To satisfy the energy requirement of the world, fossil fuels are not only insufficient but also very harmful and dangerous for life. In current global energy consumption, it is predicted that it will be double by 2050 (Ockwig and Nenoff 2009). The byproducts of fossil fuels affect the human's life as well as the degrading environment. So, overall air pollution and energy requirement are the two main issues in the present scenario. The current fossil fuel consumption rate directs for clean, eco-friendly, and sustainable fuel.

The availability of renewable energy sources is unlimited and the main advantage is no harmful byproduct (Thomas et al. 2000). Hydrogen is one of the respectable fuel for the coming time and hydrogen fuel cell will provide the unit, which converts

R. Kumar · M. Kumar · K. Awasthi (✉)
Department of Physics, Malaviya National Institute of Technology, Jaipur, Rajasthan, India
e-mail: kawasthi.phy@mnit.ac.in

Kamakshi
Department of Physics, Banasthali Vidyapith, Vanasthali, India

L. Ledwani and J. S. Sangwai (eds.), *Nanotechnology for Energy and Environmental Engineering*, Green Energy and Technology,
https://doi.org/10.1007/978-3-030-33774-2_15

hydrogen into another form of energy (Chen et al. 2011; Dicks 1996; Beltrán Cilleruelo 2016). Compared to other conventional vehicles, hydrogen fuel cell vehicles are more profitable also as there is no toxic gas explosion (Isfahani and Sedaghat 2016). The essential stuff for a fuel cell is pure hydrogen for better efficiency and lifetime. Many methodologies have been followed by the researcher for the improvement of selectivity of hydrogen over other gases and impurities (Yilanci et al. 2009). But separation/purification by selective transport with the help of polymeric membranes is one of the fastest growing branches (Castel and Favre 2018). In the reference of the original polymeric membrane, composite membranes are always beneficial in the goal of selectivity and permeability alteration. Because in the composite membranes, many parameters can be tuned like concentration, size, shape, distribution of filler material, etc.

2 Why Hydrogen as a Future Fuel

To overcome the problems of air pollution by the fossil fuel and energy requirement, our energy dependence on renewable energy sources should be high. However, besides hydrogen energy, the main issue with these energy sources is the energy density and area dependency. In the case of solar energy, per area density of energy is low which is also not possible in the cold states. Similarly, ocean energy is possible only in areas near the ocean but not applicable in the dry states, etc. But the acceptance in the form of hydrogen energy is high because of the hydrogen (H_2) obtainability. H_2 has been widely deliberated as an attractive energy carrier with high efficiency in developing an environmental friendly and cost-effective, sustainable energy system. H_2 has been recognized as an effective and clean energy carrier to alleviate the mounting global energy and environmental crisis and directing toward developing capable H_2 separation technologies.

The unit which is used to convert hydrogen in the other form of energy is called the hydrogen fuel cell. But the primary requirement of the fuel cell is the purified H_2 from the impurities or separated H_2 from other gases. Otherwise, the lifetime and the efficiency of the fuel cell decreases drastically. So, the purity of H_2 is a principal factor to decide the effectiveness of a fuel cell system. The most important advantage with the hydrogen fuel cell has water as a byproduct obtained after the energy generation. Produced water can be used in other useful applications. That's the way the main benefit of using H_2 as an energy carrier is a "green fuel source" which does not harm the ecological system. H_2 energy is not only a clean energy source but it also has the offshoot in the form of water. So the separation/purification of H_2 is the solution for a new renewable energy source and it is also useful for controlling the air pollution. So to use H_2 as an energy source and preserve the environment from global warming, it is necessary to separate or purify H_2 gas from the other gases and impurities.

3 Why Membrane-Based Hydrogen Separation

In order to resolve these problems of the separation, it might be helpful to combine the separation process with membrane technology (Castel and Favre 2018). There are many types of methods, which are used to separate/purify hydrogen gas. Some of them are membrane technology, pressure swing adsorption, chemical absorption, catalytic purification, metal hydride separation, and cryogenic separation, etc. Membrane-based technology for H_2 separation/purification has attracted extensive response due to characteristic benefits over other separation approaches (Pandey and Chauhan 2001; Sridhar et al. 2014). The membrane-based separation process is not only cost-effective but also environmentally friendly as well (Yampolskii 2012; Sanders et al. 2013). Except for membrane technology, all other mentioned methods are not popular and also not cost-effective. Some of the advantages of the membrane-based gas separation are mentioned below:

- Mechanical strength and durability
- Controlled pore shape and size
- Chemical stability
- Thermal stability
- Manufacturing reproducibility
- Space saving
- Low weight
- Flexibility
- Low energy consumption
- Easy to manufacture
- Easy to clean
- High potential of adaptability
- Low capital cost over other conventional separation methods.

Despite several advantages of the membrane-based gas separation, this process suffers from a problem in the form of trade-off connection between selectivity and permeability. So the control over selectivity and permeability of the gases is the main goal for the membrane-based gas separation.

4 Gas Separation Mechanism

In the membrane-based separation process, gas molecules are separated by the difference in permeation rate of gas molecules. Adolph Fick gives the fundamental law's called "Fick's law," and it explains the basic mechanism of the gas diffusion or permeation through the membrane (Denny Kamaruddin and Koros 1997). The gas separation/permeation with the membrane is measured by the two key parameters (1) diffusion coefficient (D) and (2) solubility coefficient (S) (Javaid 2005; Rahimpour 2017). Based on the membrane structure (pores and non-pores)/morphology

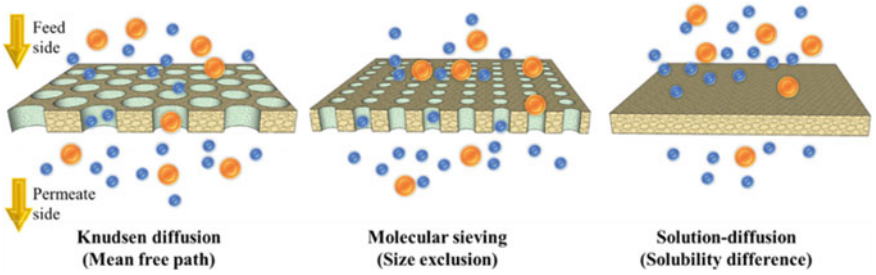

Fig. 1 Schematic representation of the gas permeation models

gas permeation can be explained using three models. Schematic representation of these models is shown in Fig. 1.

As according to Eq. 1, Knudsen number (K_n), which is the fraction of the gas molecule mean free path to the pore size of the membrane, is normally used to distinguish among the three mechanisms.

$$K_n = \frac{\lambda}{d_p} \tag{1}$$

In the equation, d_p is the diameter of the pore and λ is the mean free path of the gas molecules. Mean free path of the gas depends on the pressure (p), temperature (T), and the effective diameter of the gas molecule (dg) as according to the given equation

$$\lambda = \frac{K_B T}{\sqrt{2} p \pi d_g^2} \tag{2}$$

where K_B is the Boltzmann constant.

Based on the porosity of the membrane there are three basic permeation processes: Knudsen diffusion, molecular sieving, and solution diffusion.

4.1 Solution Diffusion

The gas permeation in the case of the dense membrane can be explained by the solution-diffusion model. The solution-diffusion model has been described widely in many articles (Wijmans and Baker 1995; Zito et al. 2017) and books as well (Wijmans and Baker 2006; Ismail et al. 2011). In this model, gas permeation is a cross product of the solubility coefficient (S) and diffusion coefficient (D). The overall equation can be shown as;

$$P = D \times S \tag{3}$$

Both the coefficient D and S depends on the membrane material and the type of gas chosen for permeation. Every material has a different value of diffusion coefficient and solubility coefficient according to the gas type. Also, both the coefficients change with temperature, as the temperature changes the polymer structure and mobility of gas molecules. As mentioned above temperature depends on P, D, and S *which* can be represented by the Arrhenius type equation.

$$P = P_0 \exp\left(\frac{-E_p}{RT}\right) \tag{4}$$

$$S = S_0 \exp\left(\frac{-\Delta H_s}{RT}\right) \tag{5}$$

$$D = D_0 \exp\left(\frac{-E_d}{RT}\right) \tag{6}$$

where P_0, S_0, and D_0 are represented as pre-exponential values for the corresponding equation. R is used for universal gas constant and T for the temperature. E_d, ΔH_s, and E_p are the activation energy for diffusion, heat of solution/sorption, and activation energy for permeation, respectively.

4.2 Molecular Sieving

In terms of gas separation, molecular sieve membranes have been recognized as a very promising applicant for gas separation (Ma et al. 2013; Liu et al. 2019). These molecular sieves are porous solids that contain constrictions of apertures that approach molecular dimensions of diffusing gas molecules. A typical schematic diagram of molecular sieving mechanism for gas–polymer interaction phenomena is shown in Fig. 2.

When pore diameter or opening of the membrane is relatively smaller than the gas molecule, then repulsive force dominates (Zhang et al. 2014). In this case, higher activation energy is required for the permeation. In the same situation, when a gas molecule has suggestively small diameter compared to opening or pore diameter, then it requires a small amount of energy for the permeation. Molecular sieving

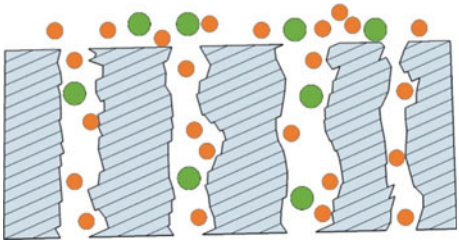

Fig. 2 Typical molecular sieving mechanism for gas–polymer interaction phenomena

Table 1 Gases with their molecular weight, kinetic diameter specific gravity and volume

Gas	State	Molecular weight	Kinetic diameter (Å)	Specific gravity at 70°F (1 atm)	Specific volume (cf/lb)
H_2	Compressed Gas	2.02	2.89	0.0696	192
N_2	Compressed Gas	28.01	3.64	0.967	13.8
He	Compressed Gas	4.003	2.6	0.138	96.7
O_2	Compressed Gas	32.0	3.46	1.105	12.1
CO_2	Liquefied Gas	44.01	3.3	1.52	8.74
C_3H_6	Liquefied Gas	42.08	4.4	1.501	9.05
C_3H_8	Liquefied Gas	44.1	3.96	1.55	8.5
CH_4	Compressed Gas	16.04	3.8	0.555	23.7
CO	Compressed Gas	28.01	3.76	0.97	13.8
Ar	Compressed Gas	39.95	3.4	1.38	9.7

dominates the mechanism for the above-mentioned conditions (Jones and Koros 1994). Overall, pore diameter and gas molecule size is a key element to control the separation performance of such type of membranes. The molecular diameter of the gases and other important properties are listed in Table 1 (Kuwahara et al. 2009).

4.3 Knudsen Diffusion

When the mean free path of the gas molecules is in the order of the pore diameter than the dominating mechanism for the gas permeation is Knudsen diffusion (Liu and Wei 2014). Because the walls of the pore are involved in the mechanism, the walls of the membrane also affect the gas permeability. The general equation for the Knudsen diffusion for the gas is given by Eq. 7.

$$J_{iK} = -D_{iK} \frac{\partial c_i}{\partial x} \tag{7}$$

where D_{iK} is representation for the Knudsen diffusivity. D_{iK} can be calculated by Eq. 8. In this mechanism, the molecules collision with pore walls is more repeated than the collision among molecules. Also, the selectivity of gases is inversely proportional to the square root of the molecular weights.

$$D_{iK} = \frac{d_p}{3}\sqrt{\frac{8RT}{\pi M_i}} \tag{8}$$

where, M_i showing the molecular weights for gas species and d_p is the average pore size of the porous membrane. Generally, Knudsen diffusion is useful during low pressure, because due to the bigger pore diameter the permeation rate in such membrane is high at low pressure. This mechanism is ruled in the zeolites membranes (Zito et al. 2018), CNT-polymer composite membranes (Damle et al. 1994), swift heavy ion irradiated membranes, fiber membranes and the membranes have porous structure across the thickness, etc.

5 Types of Membranes

Commercially, various types of membranes are used for application on hydrogen separation like metal membranes, track-etched membranes, polymer membranes, ceramic membranes, etc. (Jose et al. 2018; Ng et al. 2013).

Because the material of a membrane is the most essential fragment for the better selectivity and permeability of the gas, the selection of the membrane material is very important for the required application.

Based on the properties and approach, the membrane can be classified into many categories. De Falco et al. (2011) has reported the generalized classification of the membrane as shown in Fig. 3.

In the field of gas separation, most of the samples are in the form of mixed matrix membranes (MMMs) (Bakhtiari and Sadeghi 2015; Shimekit et al. 2011), as shown in Fig. 4. In MMMs materials, two phases are present; one is the polymer matrix which acts as a bulk phase and another one is the filler material like zeolite, carbon nanotubes, a different form of metal (nanoparticles, nanorod, nanoflakes, etc.) (Carreon et al. 2016). MMMs is one of the advantageous forms of the samples to overcome this problem, relatively to a pristine polymer or pure filler material. At the

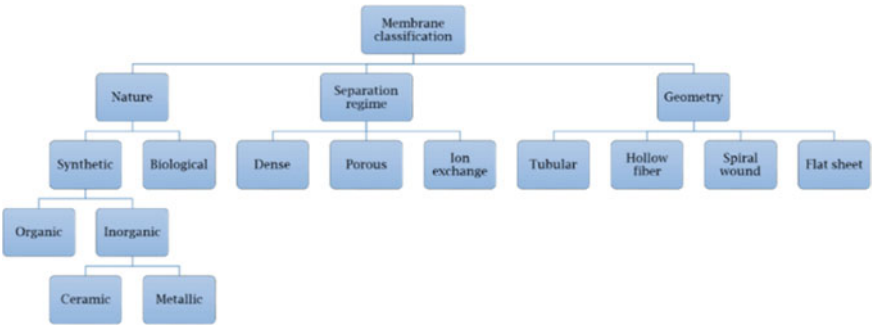

Fig. 3 Generalized classification of the membranes

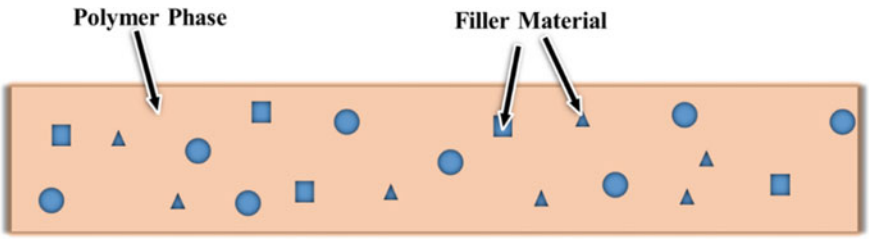

Fig. 4 Schematic representation of Mixed Matrix Membrane (MMMs)

same time, the cost of the MMMs is low compared to the pure material; at the same time, MMMs have high flexibility.

For the hydrogen gas separation, the following membranes are being used by various researchers.

5.1 Composite Membranes

The amazing properties of nanomaterials result in a new class of composite material, which helps to improve the separation properties (Dolan 2010; Dolan et al. 2006). In the composite membranes, it covers metallic alloys (Dolan 2010; Dolan et al. 2006), organic polymers, and inorganic oxides (Lin et al. 2019; Li et al. 2018). Here we will critically compare the diverse composite membrane materials, which are used for H_2 separation/purification in the composite form. The simplest way for the classification of the composite membrane is to categorize them based on the filler material. It can be as follows; pure metals, alloys, oxides, ceramics, zeolites, glasses and carbon products (CNT, graphene, graphene oxide, graphite) (Bespalko et al. 2018; David and Kopac 2011; Malzbender 2016; Thakkar et al. 2018), etc. carbon-based composite membranes have broad area and different approach. So carbon-based membranes will be explained in the next section.

During the selection of composite membranes, some of the targeted key points are like H_2 selectivity, and the permeability should be high. Composite materials' cost should be low. From the commercial point of view, the durability of the sample should be good. The last production/fabrication process cost is not to be expansive. In a broad sense, a composite membrane affects only H_2 molecules for the selectivity. That means only H_2 molecules or other gas molecules (impurities) interact with the composite membrane.

Typically metallic composite membranes are dense membranes, in which a specific metal is used as a filler material. The selectivity of such membranes is high, but the permeability is low. Metal can be used in different forms of structures such as; nanoparticles, nanorods, nanotubes, nanoframes, ribbons, etc. the most suitable and reliable metal for H_2 is Palladium (Pd). Because Pd has high diffusivities or solubility for the hydrogen, and has excellent thermal stability (Gao et al. 2004; Paglieri and

Way 2002). Platinum (Pt) is one more metal which is used as a spare filler material for palladium (Patel and Acharya 2018). Both Pt and Pd also used with Ni, Ag, Au, and Cu as alloy metals in composite membranes. The performance, fundamental concept, and mechanism for the metallic membranes for gas separation have been explained by many researchers (Moss et al. 1998; Ward and Dao 1999).

Due to some of the limitations with the metallic membranes, silica composite membranes are an alternative approach for H_2 separation application. Compared to metallic membranes; silica membranes are easy to fabricate, have controllable filler porosity, and low cost of production. Silica has pores network matrix in which the approximate diameter of the pore is 0.5 nm. Such small pores can control permeation of the small gas molecules such as H_2, CO_2, He, CO, O_2, and N_2. Such type of composite membranes is not 100% selective for an individual component (Ghasemzadeh et al. 2017; Nwogu et al. 2016). The separation of gas mixtures is centered on a competitive process of different molecules moving in the micropores network (Verweij 2003). Commonly two types of synthesis methods are used for silica-based composite membranes; chemical vapor deposition (CVD) and sol–gel method (Khatib and Oyama 2013). In a comparison of both methods, sol–gel provides good permeability as well as selectivity. While the problem with the sol–gel method is reproducibility of the samples which can be achieved by CVD method by the controlled condition of deposition.

For the last few years, zeolite membranes have achieved considerable attention in the field of gas separation (Kosinov et al. 2016; Wee et al. 2008). Zeolite membranes have controlled pore shape and size with the enhanced properties of mechanical, thermal, and chemical stability. Such types of membranes have a long lifetime and can be used multiple times. The optimized thickness of the zeolite membranes is the key parameter for the selectivity and permeability data. Zeolites have uniform and molecular-sized pores with crystalline inorganic nature. Most of the zeolites are made with the TO_2 unit, where T represents a tetrahedral framework atom (Si, Al, B, Ge, etc.) (Koohsaryan and Anbia 2016).

The long lifetime, stability at high temperature, and the ability of the regeneration makes these membranes a competitive candidate for H_2 separation/purification application.

5.2 Carbon-Based Membranes

In the comparison with other materials, the composite material of carbon with polymer has been the center of demand due to their unique properties and technological usage, especially for gas separation application (Haider et al. 2018; Hamm et al. 2017; Ismail and David 2001). Carbon-based polymer composites such as carbon nanotubes (CNTs), graphite, graphene, graphene oxide (GO) have been reported widely.

Since the discovery of carbon nanotubes (CNTs) by Iijima (Tersoff and Ruoff 1994; Iijima and Ichihashi 1993; Iijima 1991), it has made supreme impacts on nanotechnology and nanoscience in the reference of electrical, thermal, and mechanical properties of the materials (Tersoff and Ruoff 1994; Kholmanov et al. 2015). Mostly CNTs are categorized in the single wall carbon nanotubes (SWCNTs), double wall carbon nanotubes (DWCNTs) and multiwall carbon nanotubes (MWCNTs). The arc discharge is one of the oldest and worthy techniques to produce the CNTs. According to the physical and chemical properties of CNTs, these have a potential application in the gas separation. There is a large variation in the ratio of length and diameter of the CNTs. Many types of CNTs composites are used for gas separation applications. Structure and orientation of CNTs are key parameters for the conductivity as well as the permeability and selectivity of the gases. In the field of hydrogen separation, many researchers used the aligned orientation of CNTs to improve the selectivity of gases (Swain et al. 2017; Babu et al. 2013). It is expected that the alignment of CNTs in polymer matrix provides more number of channels and dissolution opportunities in comparison to randomly distributed MWCNTs. Also, the separation application is based on the functionalization of the CNTs (Sanip et al. 2011; Ma et al. 2010). Functionalization of the CNTs is useful for the attachment of gas-sensitive nanomaterials which helps to enhance the selectivity of a specific gas. Based on the diameter of the CNT in the composite membrane permeation, the gases can be combined as an effect of solution diffusion and molecular sieving model. These features make CNTs highly useful in reinforcement nano filter, probes, energy storage, gas filters, bio applications, and various electronic and thermal devices.

Graphene also has a great opportunity for membrane-based gas separation applications because of critical thickness, chemical stability, flexibility, and mechanical strength. Molecular Dynamic (MD) simulation and Density Functional Theory (DFT) calculation shows that the graphene-based membranes are one of the good choices for the H_2 separation application (Tao et al. 2014; Wei et al. 2018). H_2 has a significant difference in its kinetic diameter (2.9 Å for H_2) compared with other gases molecules (3.64 Å for N_2, 3.8 Å for CH_4 and 3.76 Å for CO, etc.) (Robeson 1991). DFT calculation explained that the pore size in graphene is nearly the molecular diameter of H_2. So there are many possibilities that H_2 molecule will separate from other gas molecules. Because H_2 is a candidate having nearly equal pore size and other gas molecules will block due to bigger kinetic diameter. The approach with graphene polymer composite membrane can enhance the H_2 selectivity over other gases multiple times. However, the drawback is that due to smaller pore size the permeability decreases.

Functionalized graphene (graphene oxide) can be used with a polymer matrix to reduce the lower permeability problem (Sun and Li 2018). GO can also be utilized as a unique material for gas separation applications. Functionalization of the graphene can enhance the H_2 attachment probabilities. Separation mechanism for the GO composite membranes follows the molecular sieving as explained in the previous part. Nanoparticles, nanowires, and other nanostructures can interact with the GO lay and helpful to expand the gaps (Ebrahimi et al. 2016; Wang et al. 2017; Zhang et al. 2019). This explanation offers fast permeation of the gas molecules through the

channels. Such an approach is useful for the high permeability with high selectivity of H_2.

5.3 Track-Etched Membranes

Now these days, track-etched membranes are a new class of the gas separation/purification applications. Track-etched polymeric membranes have received considerable attention in gas separation applications due to tunable pore shape and size due to chemical etching and choice of the ion (Chakarvarti 2009; Gómez Álvarez-Arenas et al. 2009; Sudowe et al. 1999; Yamazaki et al. 1996). Swift Heavy Ion (SHI) irradiation process is used to create the tracks, and subsequently, the tracks are converted into nanopores by selective chemical etching. Basically the ions beam having the heavy energy in the range of 100 MeV were bombarded on the membranes.

Due to heavy energy, this ion passed throughout the membrane, and local damaged zones (latent tracks) were created along the ion path. In detail, the passing ion interacts with the loosely bound electrons of the polymer and transfers its energy to them. Such electrons of the polymer gradually transfer this energy in the outward direction of the ion path. Due to this phenomena, a cylindrical zone is created, which is called the latent tracks.

These tracks can be converted into the pores by the chemical etching. The schematic representation of the followed process is shown in Fig. 5.

Type of the ion and its energy affects the damaged area of the membrane matrix, which is a responsible factor for the pore size. But the chemical etching process is responsible for the pore shape and size (Apel et al. 2006). To control the pore size, chemical etching time needs to be optimized, and the shape of the pore depends on

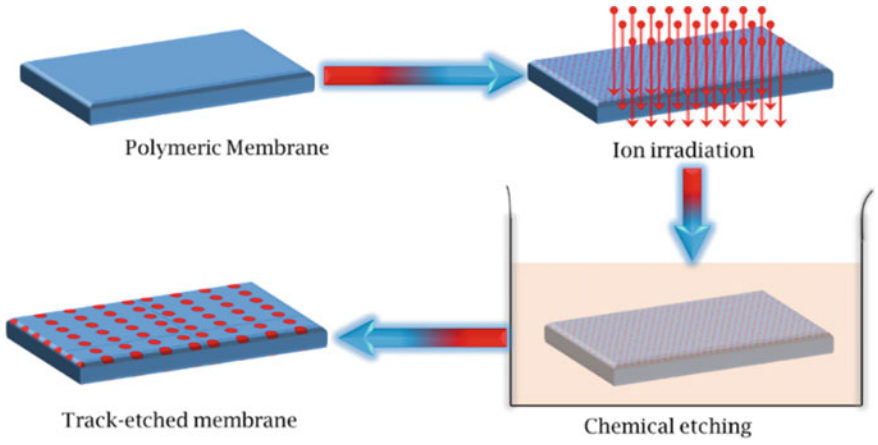

Fig. 5 Swift Heavy Ion (SHI) irradiation and track creation process

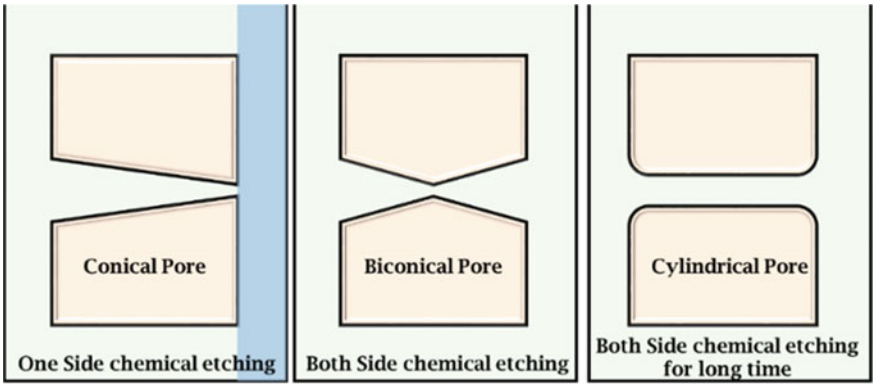

Fig. 6 A schematic representation for track-etched nanochannels with different shapes with the type of chemical etching

the one or both side etching. One side chemical etching generates the conical shape of the pore. Both side chemical etching leads to the double conical/biconical shape, and later it's converted into the cylindrical shape as shown in Fig. 6.

The main advantage of such membranes is that we can control pore shape, size, length, and distribution. So, based on the application, we can obtain the required pores. The most natural example of such track-etched nanochannels is living human skin. Human skin can selectivity permeate water and ions in the form of sweat, not the blood cells.

Separation and selectivity of the gases also depend on the interaction of the gas within the pore wall and the surface of the membranes. These track-etched membranes can modify them after or before the irradiation process. These modified membranes have more benefit than the pristine form of these membranes.

5.4 Block Copolymer-Based Composite Membrane

There are some potential advantages for block copolymers (BCPs) as filtration membranes, such as varied nanoscale morphology. Block copolymer membranes offer the opportunity to produce such type of membranes by using their self-assemble nature. Due to their self-assembled nature, regular structures can be obtained, which lead to high pore density on the nanoscale dimension. But the large-scale fabrication of block copolymer membranes is quite tough and costly too. To overcome this problem, a straightforward way is casting of a block copolymer solution onto a substrate (composite membrane). This substrate can be dense or porous; it depends on the requirement.

For the block copolymer composite membranes, the polymer solution was cast on the substrate and the prepared polymer film has to be removed from the substrate after

drying. This procedure may be quite simple when the removed film is mechanically stable that can be used as a self-supported membrane, but it turns very difficult for the thin film which needs mechanical stabilization. It is tedious when a block copolymer thin film is transferred from a dense substrate to the porous material, and on a large scale, it can hardly perform. So, to provide more stabilization, this film is transferred onto the porous substrate (Basyooni et al. 2017; Beard et al. 2014; Kim et al. 2001; Phillip et al. 2010; Sirelkhatim et al. 2015; Zhang et al. 2016).

In a block copolymer, mechanism of synthesis is independent, and it is formed by joining two or more chemically distinct polymers which are bonded by a covalent bond. Phase behavior of the block copolymer strongly depends on the selected composition, block copolymer structure, degree of polymerization, and the interaction parameter between the fragment–fragment (van Zoelen and ten Brinke 2009). In a block copolymer, shapes of the isolated domains are produced by the volume fraction of minority block (f). The regular shape and uniform spaced nanodomains occur when minority blocks are segregated from the majority block (Segalman 2005).

An effort is done for gas permeability application by depositing the block copolymer nanotemplates on the highly porous track-etched membrane so that the upper layer can help in improving selectivity and lower have high selectivity. Kamakshi et al. (2017) have used porous PET membranes having different pore sizes (0.1–0.2 μm) which are taken as mechanical support, and then a layer of the block copolymer (PS-b-P4VP) with the additive (HABA) is casted on this porous PET support. After solvent annealing, the additive is removed from PET coated BC membranes to recover porosity again. It was demonstrated that the gas permeability for both gases changes drastically and shows a remarkable change after the coating of block copolymer nanotemplates. Thus, the upper layer of block copolymer nanotemplates influences the permeability and reduces the gas permeability of H_2 and CO_2 through the composite membrane. The schematic diagram for such a composite membrane is presented in Fig. 7.

Bonder et al. (2000) found an application of block copolymers in the exclusion of CO_2 from mixtures with H_2, and PEBA block has been identified to be responsible for high selectivity. They also examined the permeability of H_2, N_2, and CO_2 in block copolymers and CO_2 permeability is directly correlated with PE block composition. Permeability increases with increasing the amount of polyether. Selectivity for CO_2/H_2 was found 9.8 whereas for CO_2/N_2 it was found 56. Kim et al. (2001) have demonstrated the PE block of the block copolymer is responsible for the higher permeability and perm-selectivity of polarizable gases. High permeability and high selectivity achieved with PE BAX copolymer. Obtained results show the selectivity for CO_2/N_2 was 61 whereas SO_2/N_2 was 500. Lindemann et al. (2014) prepared conjugated microporous polymer membranes via layer by layer approach on sacrificial substrates and found with gas permeability measurements that these membranes show high selectivity.

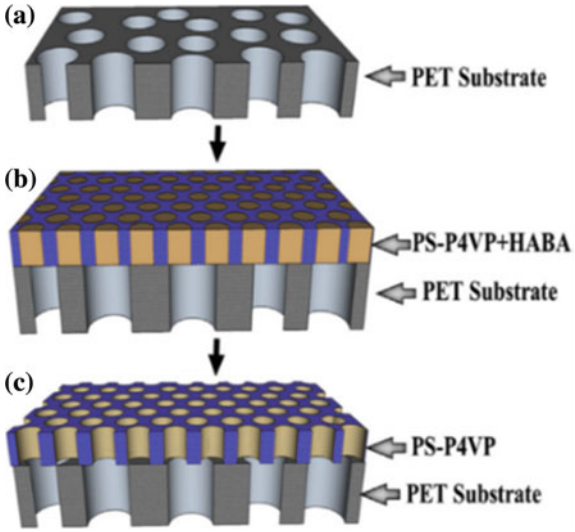

Fig. 7 Schematic for composite membrane generation: **a** PET porous membrane. **b** Block copolymer additive coated on PET. **c** Block copolymer coated PET after removal of the additive (*Reprinted from Publication* Hydrogen gas separation with controlled selectivity **via** efficient and cost-effective block copolymer coated PET membranes, *International Journal of Hydrogen Energy (2017), Volume 42, Issue 31, Pages 16186–16194, Copyright 2017, with permission from Elsevier*)

5.5 Functionalized Porous Membranes

Functionalization is the advanced technique by which surface properties of the required material can be altered. There are so many activating functional groups for improving hemocompatibility of the material surface. Some of them are of hydroxy group (–OH), carboxyl group (–COOH), amine group ($–NH_2$), thiol group (–SH), sulfonic acid ($–SO_3H$), amide group ($–CONH_2$), etc. (Sadilov et al. 2019; Jue and Lively 2015). After treating with these functional groups, modified surface is relatively more stable, which can be utilized for the physical and chemical properties of the surface. The functionalized membrane with proper activating groups can extend the application ranging from selective and tunable permeation and separation (Baker and Lokhandwala 2008; Du et al. 2012).

McCool and DeSisto 2005 have made an effort by functionalizing the silica membrane with an amino group by using three different synthesis procedures. And find that procedure with a maximum loading of the amino group has the highest permeation of CO_2. An effort has been made by Urch et al. (2006), by depositing functionalized calcium phosphate ($Ca_3(PO_4)_2$) nanoparticles on track-etched PET membrane and found that there was no particle adsorption on the un-functionalized surface while functionalized surface binds the nanoparticle. Palladium nanotubes have deposited into the pores of the track-etched polycarbonate (PC) membrane by electroless plating technique by Yu et al. (2005). It was observed that nanotubes having high surface area due to their granular surface which shows high sensitivity and the small detection limit for hydrogen sensing.

Shi et al. (2006) observed the binding of palladium toward the pore and surface with the increasing time by an electroless process. The porous stainless steel is used as

a substrate, and there are many pores of size ranging from 0.2 to 10 μm, Pd nanoparticles were used for depositing on the substrate. These membranes also expended for purification due to their higher permeability and selectivity, chemical compatibility for gas separation. Such types of membranes prepared in a composite form containing Pd in a different form for example nanoparticle, alloy, etc. These nanocomposite membranes provide high hydrogen perm-selectivity (David and Kopac 2011; Hatlevik et al. 2010).

PET porous membranes were modified with the carboxylic group and an amino group. After the functionalization, these membranes are dipped in palladium nanoparticle solution at a different time. High binding of Pd nanoparticles is achieved in the aminated functionalized membrane in comparison with carboxylic as well as un-functionalized PET membranes. Figure 8 represents the schematic palladium nanoparticles interaction with the functionalized membranes. It is an effective way to which permeability and selectivity both can be modified. Higher selectivity was founded in highly attached Pd nanoparticle membrane. For H_2/N_2 as well as H_2/CO_2.

Hence functionalization of the membrane's surface, pore walls, and deposition of nanostructures is a proficient procedure for gas separation (Weng et al. 2009; de Lannoy et al. 2013). Such types of membranes could frequently be used for gas separation and purification engineering applications. By introducing gas-sensitive nanomaterials on the surface and pore walls of modified membranes, it can be made beneficial for separation applications.

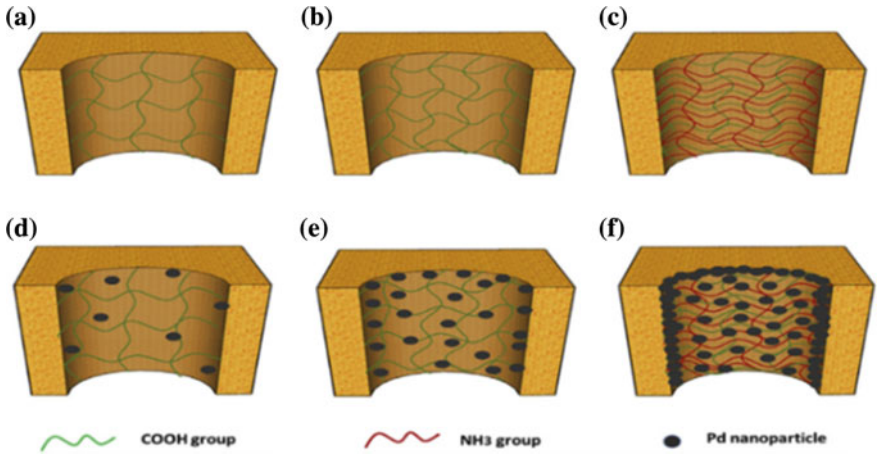

Fig. 8 Schematic diagram of **a** Pristine porous PET membrane. **b** Carboxylated porous PET membrane. **c** Aminated porous PET membrane. **d** Pd binded pristine porous PET membrane. **e** Pd binded in carboxylated porous PET membrane. **f** Pd binded in aminated pore (*Reprinted from Publication Palladium nanoparticle binding in functionalized track-etched PET membrane for hydrogen gas separation, International Journal of Hydrogen Energy (2017), Volume 42, Issue 25, Pages 16186–16194, Copyright 2017, with permission from Elsevier*)

6 Hydrogen Separation by Using Membranes

Due to the fact that, the H_2 molecule has the smallest kinetic diameter the selection of H_2 over other gases is easy. Since H_2 molecule has the biggest diffusion coefficient, permeability and selectivity of H_2 can be tuned. In this section, we will go through some of the articles in which the researcher attempted a different type of sample and method to reach higher H_2 permeability and selectivity.

Because Pd is one of the best absorbent materials for hydrogen, but also expensive compared to other metals. So researchers are also searching for the alternative to replace Pd by alloys. Liu et al. (2018) fabricated alloy of $Nb_{35}Mo_5Ti_{30}Ni_{30}$ as an alternative of Pd for hydrogen purification/separation application. They presented the theoretical calculation by DFT for the optimization of the combination of the alloy. Experimental data indicate that $Nb_{35}Mo_5Ti_{30}Ni_{30}$ membrane shows remarkable H_2 separation and can be a replacement of palladium metal.

In the same direction of the Pd membrane, Cheng et al. (2002) compared the H_2 permeation from the commercial Towngas (49% H_2, 28.5% CH_4, 19.5% CO_2 and 3% CO) by using alumina, zeolite, Pd, and Pd–Ag alloy membranes. Their results show that alumina and the zeolite are not suitable options for the H_2 separation from the Towngas. Whereas Pd and Pd–Ag membranes show great results for H_2 separation from Towngas to achieve high purity of H_2, the purification efficiency is further increased by the addition of silver, due to larger lattice spacing in the resulting alloy material. Some of the previous review articles for H_2 separation by Pd and Pd alloys are described significantly (Hatlevik et al. 2010; Cheng et al. 2002).

Beside Pd and its alloys, Chen et al. (2018) used a Pt layer over the surface of the $La_{5.5}W_{0.45}Nb_{0.15}Mo_{0.4}O_{11.25-\delta}$ membrane for the reflection effect on H_2 permeation. With a combination of 50% H_2—50%, He at 1000 °C achieved permeation flux of H_2 is 0.483 mL/min cm^2 from both sides. This permeation rate is twice the uncoated $La_{5.5}W_{0.45}Nb_{0.15}Mo_{0.4}O_{11.25-\delta}$ membrane, which indicates that the Pt layer exhibits a positive effect on the H_2 selectivity. This enhancement is due to H_2 dissociation/combination on the Pt layer. Fasolin et al. (2018) fabricated a vanadium-based multilayer structure ($Pd/V_{93}Pd_7/Pd$) having thickness of <7 μm onto porous alumina. Results show that these membranes have high H_2 selective flux up to 0.26 mol m^{-2} s^{-1} at 375 °C.

Since the discovery of CNT by Iijima in 1991, CNTs have come to the forefront of nanostructured materials and research interest has grown exponentially. Extensive work has been done to characterize CNTs including their exceptional mechanical, thermal, and electrical characteristics. CNTs are also known to show extremely high aspect ratios of their length and diameter. Many of the researchers observed some of the respectable results in the field of H_2 separation/purification. Vijay et al. and his group are doing a wide-ranging study on the CNT-polymer nanocomposite for the hydrogen gas separation (Kumar et al. 2011; Sharma et al. 2009, 2010; Sharma and Vijay 2012). Their results show that the alignment and uniform distribution of the CNTs is beneficial to enhance the H_2 permeability as well as the selectivity.

Li et al. (2017) fabricated a hybrid membrane of C/CNT for the gas permeability of H_2, CO_2, O_2, N_2, and CH_4. In this work, authors used CNTs in the form of single-walled carbon nanotubes (SWCNTs) and multiwalled carbon nanotubes (MWCNTs) individually in the membranes. Their results show that MWCNTs incorporated Carbon membrane exhibit higher permeability but lower selectivity than SWCNTs embedded Carbon membrane. Further, acid treatment of the MWCNTs helps to open the blocked ends which can help to enhance the selectivity. There are many review articles published for the composite polymeric membranes for the hydrogen separation. Some of them are Perovskite-based (Hashim et al. 2018), graphene-based (Song et al. 2018), dense metal membrane-based (Al-Mufachi et al. 2015), silica-based membranes (Khatib and Oyama 2013) and non-Pd BCC alloy-based membranes (Dolan 2010).

7 Conclusion

In this chapter, we have discussed the gas separation of engineered porous polymeric membranes by different methods for the fabrication of gas-selective membranes. Membrane-based gas separation has the trade-off relation between the permeability and selectivity. To overcome this issue, the engineering of pore channels by functionalization with a suitable group and depositing the gas-sensitive nanomaterials could be one possible way. Composite membranes with block copolymer nanotemplates also affect the permeability of a specific gas as well as selectivity. Carbon-based dense membranes are also useful to alter the gas permeability and selectivity of the polymeric membranes.

References

1. Al-Mufachi NA, Rees NV, Steinberger-Wilkens R (2015) Hydrogen selective membranes: a review of palladium-based dense metal membranes. Renew Sustain Energy Rev 47:540–551. https://doi.org/10.1016/j.rser.2015.03.026
2. Apel PY, Blonskaya IV, Dmitriev SN et al (2006) Structure of polycarbonate track-etch membranes: origin of the "paradoxical" pore shape. J Memb Sci 282:393–400. https://doi.org/10.1016/j.memsci.2006.05.045
3. Babu DJ, Lange M, Cherkashinin G et al (2013) Gas adsorption studies of CO_2 and N_2 in spatially aligned double-walled carbon nanotube arrays. Carbon NY 61:616–623. https://doi.org/10.1016/j.carbon.2013.05.045
4. Baker RW, Lokhandwala K (2008) Natural gas processing with membranes: an overview. Ind Eng Chem Res 47:2109–2121
5. Bakhtiari O, Sadeghi N (2015) Mixed matrix membranes' gas separation performance prediction using an analytical model. Chem Eng Res Des 93:710–719. https://doi.org/10.1016/j.cherd.2014.06.013
6. Basyooni MA, Shaban M, El Sayed AM (2017) Enhanced gas sensing properties of spin-coated Na-doped ZnO nanostructured films. Sci Rep 7:41716
7. Beard MC, Luther JM, Nozik AJ (2014) The promise and challenge of nanostructured solar cells. Nat Nanotechnol 9:951

8. Bespalko Y, Sadykov V, Eremeev N et al (2018) Synthesis of tungstates/Ni0.5Cu0.5O nanocomposite materials for hydrogen separation cermet membranes. Compos Struct 202:1263–1274. https://doi.org/10.1016/j.compstruct.2018.06.004
9. Bondar VI, Freeman BD, Pinnau I (2000) Gas transport properties of poly (ether-b-amide) segmented block copolymers. J Polym Sci Part B Polym Phys 38:2051–2062
10. Carreon M, Dahe G, Feng J, Venna SR (2016) Mixed matrix membranes for gas separation applications. In: Membranes for gas separations. World Scientific, pp 1–57
11. Castel C, Favre E (2018) Membrane separations and energy efficiency. J Memb Sci 548:345–357. https://doi.org/10.1016/j.memsci.2017.11.035
12. Chakarvarti SK (2009) Track-etch membranes enabled nano-/microtechnology: a review. Radiat Meas 44:1085–1092. https://doi.org/10.1016/j.radmeas.2009.10.028
13. Chen Y-H, Chen C-Y, Lee S-C (2011) Technology forecasting and patent strategy of hydrogen energy and fuel cell technologies. Int J Hydrog Energy 36:6957–6969. https://doi.org/10.1016/J.IJHYDENE.2011.03.063
14. Chen Y, Wei Y, Zhuang L et al (2018) Effect of Pt layer on the hydrogen permeation property of La5.5W0.45Nb0.15Mo0.4O11.25-Δmembrane. J Memb Sci 552:61–67. https://doi.org/10.1016/j.memsci.2018.01.068
15. Cheng YS, Peña MA, Fierro JL et al (2002) Performance of alumina, zeolite, palladium, Pd-Ag alloy membranes for hydrogen separation from towngas mixture. J Memb Sci 204:329–340. https://doi.org/10.1016/S0376-7388(02)00059-5
16. Damle AS, Gangwal SK, Venkataraman VK (1994) Carbon membranes for gas separation: developmental studies. Gas Sep Purif 8:137–147. https://doi.org/10.1016/0950-4214(94)80024-3
17. David E, Kopac J (2011) Devlopment of palladium/ceramic membranes for hydrogen separation. Int J Hydrog Energy 36:4498–4506. https://doi.org/10.1016/j.ijhydene.2010.12.032
18. De Falco M, Salladini A, Palo E, Iaquaniello G (2011) Reformer and membrane modules (RMM) for methane conversion powered by a nuclear reactor. In: Nuclear power-deployment, operation and sustainability. InTech
19. de Lannoy C-F, Soyer E, Wiesner MR (2013) Optimizing carbon nanotube-reinforced polysulfone ultrafiltration membranes through carboxylic acid functionalization. J Memb Sci 447:395–402
20. Denny Kamaruddin H, Koros WJ (1997) Some observations about the application of Fick's first law for membrane separation of multicomponent mixtures. J Memb Sci 135:147–159. https://doi.org/10.1016/S0376-7388(97)00142-7
21. Dicks AL (1996) Hydrogen generation from natural gas for the fuel cell systems of tomorrow. J Power Sources 61:113–124. https://doi.org/10.1016/S0378-7753(96)02347-6
22. Dolan MD (2010) Non-Pd BCC alloy membranes for industrial hydrogen separation. J Memb Sci 362:12–28. https://doi.org/10.1016/j.memsci.2010.06.068
23. Dolan MD, Dave NC, Ilyushechkin AY et al (2006) Composition and operation of hydrogen-selective amorphous alloy membranes. J Memb Sci 285:30–55. https://doi.org/10.1016/j.memsci.2006.09.014
24. Du N, Park HB, Dal-Cin MM, Guiver MD (2012) Advances in high permeability polymeric membrane materials for CO_2 separations. Energy Environ Sci 5:7306–7322
25. Ebrahimi S, Mollaiy-Berneti S, Asadi H et al (2016) PVA/PES-amine-functional graphene oxide mixed matrix membranes for CO_2/CH_4 separation: experimental and modeling. Chem Eng Res Des 109:647–656. https://doi.org/10.1016/j.cherd.2016.03.009
26. Fasolin S, Barison S, Boldrini S et al (2018) Hydrogen separation by thin vanadium-based multi-layered membranes. Int J Hydrog Energy 43:3235–3243. https://doi.org/10.1016/j.ijhydene.2017.12.148
27. Gallucci F, Fernandez E, Corengia P, van Sint AM (2013) Recent advances on membranes and membrane reactors for hydrogen production. Chem Eng Sci 92:40–66
28. Gao H, Lin YS, Li Y, Zhang B (2004) Chemical stability and its improvement of palladium-based metallic membranes. Ind Eng Chem Res 43:6920–6930

29. Ghasemzadeh K, Sadati Tilebon SM, Basile A (2017) Chapter 10—Silica membranes application for hydrogen separation. In: Basile A, Ghasemzadeh K (eds) Current trends and future developments on (bio-) membranes. Elsevier, pp 243–264
30. Gómez Álvarez-Arenas TE, Apel PY, Orelovitch OL, Muñoz M (2009) New ultrasonic technique for the study of the pore shape of track-etched pores in polymer films. Radiat Meas 44:1114–1118. https://doi.org/10.1016/j.radmeas.2009.09.002
31. Haider S, Lindbråthen A, Lie JA, Hägg M-B (2018) Regenerated cellulose based carbon membranes for CO_2 separation: durability and aging under miscellaneous environments. J Ind Eng Chem. https://doi.org/10.1016/j.jiec.2018.10.037
32. Hamm JBS, Ambrosi A, Griebeler JG et al (2017) Recent advances in the development of supported carbon membranes for gas separation. Int J Hydrog Energy 42:24830–24845. https://doi.org/10.1016/J.IJHYDENE.2017.08.071
33. Hashim SS, Somalu MR, Loh KS et al (2018) Perovskite-based proton conducting membranes for hydrogen separation: a review. Int J Hydrog Energy 43:15281–15305. https://doi.org/10.1016/j.ijhydene.2018.06.045
34. Hatlevik Ø, Gade SK, Keeling MK et al (2010) Palladium and palladium alloy membranes for hydrogen separation and production: history, fabrication strategies, and current performance. Sep Purif Technol 73:59–64
35. Iijima S (1991) Helical microtubules of graphitic carbon. Nature 354:56
36. Iijima S, Ichihashi T (1993) Single-shell carbon nanotubes of 1-nm diameter. Nature 363:603
37. Isfahani SNR, Sedaghat A (2016) A hybrid micro gas turbine and solid state fuel cell power plant with hydrogen production and CO_2 capture. Int J Hydrog Energy 41:9490–9499. https://doi.org/10.1016/j.ijhydene.2016.04.065
38. Ismail AF, David LIB (2001) A review on the latest development of carbon membranes for gas separation. J Memb Sci 193:1–18. https://doi.org/10.1016/S0376-7388(01)00510-5
39. Ismail AF, Rana D, Matsuura T, Foley HC (2011) Carbon-based membranes for separation processes, pp 17–27. https://doi.org/10.1007/978-0-387-78991-0
40. Javaid A (2005) Membranes for solubility-based gas separation applications. Chem Eng J 112:219–226. https://doi.org/10.1016/j.cej.2005.07.010
41. Jones CW, Koros WJ (1994) Carbon molecular sieve gas separation membranes-I. Preparation and characterization based on polyimide precursors. Carbon NY 32:1419–1425. https://doi.org/10.1016/0008-6223(94)90135-X
42. Jose AJ, Kappen J, Alagar M (2018) 2—Polymeric membranes: classification, preparation, structure physiochemical, and transport mechanisms. In: Thomas S, Balakrishnan P, Sreekala MS (eds) Fundamental biomaterials: polymers. Woodhead Publishing Series in Biomaterials. Woodhead Publishing, pp 21–35
43. Jue ML, Lively RP (2015) Targeted gas separations through polymer membrane functionalization. React Funct Polym 86:88–110. https://doi.org/10.1016/j.reactfunctpolym.2014.09.002
44. Khatib SJ, Oyama ST (2013) Silica membranes for hydrogen separation prepared by chemical vapor deposition (CVD). Sep Purif Technol 111:20–42. https://doi.org/10.1016/j.seppur.2013.03.032
45. Kholmanov I, Kim J, Ou E et al (2015) Continuous carbon nanotube-ultrathin graphite hybrid foams for increased thermal conductivity and suppressed subcooling in composite phase change materials. ACS Nano 9:11699–11707. https://doi.org/10.1021/acsnano.5b02917
46. Kim JH, Ha SY, Lee YM (2001) Gas permeation of poly (amide-6-b-ethylene oxide) copolymer. J Memb Sci 190:179–193
47. Koohsaryan E, Anbia M (2016) Nanosized and hierarchical zeolites: a short review. Chin J Catal 37:447–467. https://doi.org/10.1016/S1872-2067(15)61038-5
48. Kosinov N, Gascon J, Kapteijn F, Hensen EJM (2016) Recent developments in zeolite membranes for gas separation. J Memb Sci 499:65–79. https://doi.org/10.1016/j.memsci.2015.10.049
49. Kumar R, Saraswat VK, Kumar M et al (2017) Hydrogen gas separation with controlled selectivity via efficient and cost effective block copolymer coated PET membranes. Int J Hydrog Energy. https://doi.org/10.1016/j.ijhydene.2017.06.113

50. Kumar S, Srivastava S, Agrawal S et al (2011) Effect of electric field alignment of MWCNT in PMMA matrix for hydrogen gas purification. AIP Conf Proc 1349:1061–1062. https://doi.org/10.1063/1.3606228
51. Kuwahara Y, Morita M, Nagami T, et al (2009) Functionalization of a polymer using nanoparticles immobilized in supercritical carbon dioxide. Jpn J Appl Phys 48:06FF13
52. Li B, Wen H-M, Yu Y et al (2018) Nanospace within metal–organic frameworks for gas storage and separation. Mater Today Nano 2:21–49. https://doi.org/10.1016/j.mtnano.2018.09.003
53. Li L, Song C, Jiang D, Wang T (2017) Preparation and enhanced gas separation performance of carbon/carbon nanotubes (C/CNTs) hybrid membranes. Sep Purif Technol 188:73–80. https://doi.org/10.1016/j.seppur.2017.07.019
54. Lin R-B, Xiang S, Xing H et al (2019) Exploration of porous metal–organic frameworks for gas separation and purification. Coord Chem Rev 378:87–103. https://doi.org/10.1016/j.ccr.2017.09.027
55. Lindemann P, Tsotsalas M, Shishatskiy S et al (2014) Preparation of freestanding conjugated microporous polymer nanomembranes for gas separation. Chem Mater 26:7189–7193
56. Liu D, Li X, Geng H et al (2018) Development of Nb35Mo5Ti30Ni30alloy membrane for hydrogen separation applications. J Memb Sci 553:171–179. https://doi.org/10.1016/j.memsci.2018.02.052
57. Liu J, Wei J (2014) Knudsen diffusion in channels and networks. Chem Eng Sci 111:1–14. https://doi.org/10.1016/j.ces.2014.01.014
58. Liu Q, Gupta KM, Xu Q et al (2019) Gas permeation through double-layer graphene oxide membranes: the role of interlayer distance and pore offset. Sep Purif Technol 209:419–425. https://doi.org/10.1016/j.seppur.2018.07.044
59. Ma P-C, Siddiqui NA, Marom G, Kim J-K (2010) Dispersion and functionalization of carbon nanotubes for polymer-based nanocomposites: a review. Compos Part A Appl Sci Manuf 41:1345–1367. https://doi.org/10.1016/j.compositesa.2010.07.003
60. Ma X, Swaidan R, Teng B et al (2013) Carbon molecular sieve gas separation membranes based on an intrinsically microporous polyimide precursor. Carbon NY 62:88–96. https://doi.org/10.1016/j.carbon.2013.05.057
61. Malzbender J (2016) Mechanical aspects of ceramic membrane materials. Ceram Int 42:7899–7911. https://doi.org/10.1016/j.ceramint.2016.02.136
62. McCool BA, DeSisto WJ (2005) Amino-functionalized silica membranes for enhanced carbon dioxide permeation. Adv Funct Mater 15:1635–1640
63. Moss TS, Peachey NM, Snow RC, Dye RC (1998) Multilayer metal membranes for hydrogen separation. Int J Hydrog Energy 23:99–106. https://doi.org/10.1016/S0360-3199(97)00030-X
64. Ng LY, Mohammad AW, Leo CP, Hilal N (2013) Polymeric membranes incorporated with metal/metal oxide nanoparticles: a comprehensive review. Desalination 308:15–33. https://doi.org/10.1016/j.desal.2010.11.033
65. Nwogu NC, Anyanwu EE, Gobina E (2016) An initial investigation of a nano-composite silica ceramic membrane for hydrogen gas separation and purification. Int J Hydrog Energy 41:8228–8235. https://doi.org/10.1016/j.ijhydene.2015.11.162
66. Ockwig NW, Nenoff TM (2009) Membranes for hydrogen separation. Chem Rev 110:2573–2574. https://doi.org/10.1021/cr078108l
67. Paglieri SN, Way JD (2002) Innovations in palladium membrane research. Sep Purif Methods 31:1–169. https://doi.org/10.1081/SPM-120006115
68. Pandey P, Chauhan RS (2001) Membranes for gas separation. Progr Polym Sci 26:853–893. https://doi.org/10.1016/S0079-6700(01)00009-0
69. Patel AK, Acharya NK (2018) Metal coated and nanofiller doped polycarbonate membrane for hydrogen transport. Int J Hydrog Energy 43:21675–21682. https://doi.org/10.1016/j.ijhydene.2018.03.205
70. Phillip WA, O'Neill B, Rodwogin M et al (2010) Self-assembled block copolymer thin films as water filtration membranes. ACS Appl Mater Interfaces 2:847–853
71. Álvarez-Fernández R, Beltrán Cilleruelo F, IVM (2016) A new approach to battery powered electric vehicles: a hydrogen fuel-cell range extender system. Int J Hydrog Energy 41:4808–4819

72. Rahimpour MR, Samimi F, Babapoor A et al (2017) Palladium membranes applications in reaction systems for hydrogen separation and purification: a review. Chem Eng Process Process Intensif 121:24–49. https://doi.org/10.1016/j.cep.2017.07.021
73. Robeson LM (1991) Correlation of separation factor versus permeability for polymeric membranes. J Memb Sci 62:165–185. https://doi.org/10.1016/0376-7388(91)80060-J
74. Sadilov IS, Petukhov DI, Eliseev AA (2019) Enhancing gas separation efficiency by surface functionalization of nanoporous membranes. Sep Purif Technol. https://doi.org/10.1016/j.seppur.2019.03.078
75. Sadykov VA, Krasnov AV, Fedorova YE et al (2018) Novel nanocomposite materials for oxygen and hydrogen separation membranes. Int J Hydrog Energy. https://doi.org/10.1016/j.ijhydene.2018.02.182
76. Sanders DF, Smith ZP, Guo R et al (2013) Energy-efficient polymeric gas separation membranes for a sustainable future: a review. Polymer (Guildf) 54:4729–4761. https://doi.org/10.1016/J.POLYMER.2013.05.075
77. Sanip SM, Ismail AF, Goh PS et al (2011) Gas separation properties of functionalized carbon nanotubes mixed matrix membranes. Sep Purif Technol 78:208–213. https://doi.org/10.1016/J.SEPPUR.2011.02.003
78. Segalman RA (2005) Patterning with block copolymer thin films. Mater Sci Eng R Rep 48:191–226. https://doi.org/10.1016/j.mser.2004.12.003
79. Sharma A, Kumar S, Tripathi B et al (2009) Aligned CNT/Polymer nanocomposite membranes for hydrogen separation. Int J Hydrog Energy 34:3977–3982. https://doi.org/10.1016/J.IJHYDENE.2009.02.068
80. Sharma A, Tripathi B, Vijay YK (2010) Dramatic Improvement in properties of magnetically aligned CNT/polymer nanocomposites. J Memb Sci 361:89–95. https://doi.org/10.1016/j.memsci.2010.06.005
81. Sharma A, Vijay YK (2012) Effect of electric field variation in alignment of SWNT/PC nanocomposites. Int J Hydrog Energy 37:3945–3948. https://doi.org/10.1016/j.ijhydene.2011.03.166
82. Shi Z, Wu S, Szpunar JA, Roshd M (2006) An observation of palladium membrane formation on a porous stainless steel substrate by electroless deposition. J Memb Sci 280:705–711
83. Shimekit B, Mukhtar H, Murugesan T (2011) Prediction of the relative permeability of gases in mixed matrix membranes. J Memb Sci 373:152–159. https://doi.org/10.1016/j.memsci.2011.02.038
84. Sirelkhatim A, Mahmud S, Seeni A et al (2015) Review on zinc oxide nanoparticles: antibacterial activity and toxicity mechanism. Nano-Micro Lett 7:219–242
85. Song N, Gao X, Ma Z et al (2018) A review of graphene-based separation membrane: materials, characteristics, preparation and applications. Desalination 437:59–72. https://doi.org/10.1016/J.DESAL.2018.02.024
86. Sridhar S, Bee S, Bhargava SK (2014) Membrane-based gas separation : principle, applications and future potential. 1–25
87. Sudowe R, Vater W, Ensinger W et al (1999) Basic research on nuclear track microfilters for gas separation. Radiat Meas 31:691–696. https://doi.org/10.1016/S1350-4487(99)00179-1
88. Sun M, Li J (2018) Graphene oxide membranes: functional structures, preparation and environmental applications. Nano Today 20:121–137. https://doi.org/10.1016/j.nantod.2018.04.007
89. Swain SS, Unnikrishnan L, Mohanty S, Nayak SK (2017) Carbon nanotubes as potential candidate for separation of H_2CO_2 gas pairs. Int J Hydrog Energy 42:29283–29299. https://doi.org/10.1016/j.ijhydene.2017.09.152
90. Tao Y, Xue Q, Liu Z et al (2014) Tunable hydrogen separation in porous graphene membrane: first-principle and molecular dynamic simulation. ACS Appl Mater Interfaces 6:8048–8058. https://doi.org/10.1021/am4058887
91. Tersoff J, Ruoff RS (1994) Structural properties of a carbon-nanotube crystal. Phys Rev Lett 73:676–679. https://doi.org/10.1103/physrevlett.73.676

92. Thakkar H, Lawson S, Rownaghi AA, Rezaei F (2018) Development of 3D-printed polymer-zeolite composite monoliths for gas separation. Chem Eng J 348:109–116. https://doi.org/10.1016/j.cej.2018.04.178
93. Thomas C, James BD, Lomax FD, Kuhn IF (2000) Fuel options for the fuel cell vehicle: hydrogen, methanol or gasoline? Int J Hydrog Energy 25:551–567. https://doi.org/10.1016/S0360-3199(99)00064-6
94. Urch H, Geismann C, Ulbricht M, Epple M (2006) Deposition of functionalized calcium phosphate nanoparticles on functionalized polymer surfaces. Mater und Werkstofftechnik Entwicklung, Fert Prüfung, Eig und Anwendungen Tech Werkstoffe 37:422–425
95. van Zoelen W, ten Brinke G (2009) Thin films of complexed block copolymers. Soft Matter 5:1568–1582
96. Verweij H (2003) Ceramic membranes: morphology and transport. J Mater Sci 38:4677–4695
97. Wang M, Wang Z, Zhao S et al (2017) Recent advances on mixed matrix membranes for CO_2 separation. Chin J Chem Eng 25:1581–1597. https://doi.org/10.1016/j.cjche.2017.07.006
98. Wang Y, Yang Q, Zhong C, Li J (2017) Theoretical investigation of gas separation in functionalized nanoporous graphene membranes. Appl Surf Sci 407:532–539. https://doi.org/10.1016/j.apsusc.2017.02.253
99. Ward TL, Dao T (1999) Model of hydrogen permeation behavior in palladium membranes. J Memb Sci 153:211–231
100. Wee S-L, Tye C-T, Bhatia S (2008) Membrane separation process—pervaporation through zeolite membrane. Sep Purif Technol 63:500–516. https://doi.org/10.1016/j.seppur.2008.07.010
101. Wei S, Zhou S, Wu Z et al (2018) Mechanistic insights into porous graphene membranes for helium separation and hydrogen purification. Appl Surf Sci 441:631–638. https://doi.org/10.1016/j.apsusc.2018.02.111
102. Weng T-H, Tseng H-H, Wey M-Y (2009) Preparation and characterization of multi-walled carbon nanotube/PBNPI nanocomposite membrane for H_2/CH_4 separation. Int J Hydrog Energy 34:8707–8715
103. Wijmans JG, Baker RW (1995) The solution-diffusion model: a review. J Memb Sci 107:1–21. https://doi.org/10.1016/0376-7388(95)00102-I
104. Wijmans JGH, Baker RW (2006) The solution-diffusion model: a unified approach to membrane permeation. Materials science of membranes for gas and vapor separation. Wiley, Chichester, UK, pp 159–189
105. Yamazaki IM, Paterson R, Geraldo LP (1996) A new generation of track etched membranes for microfiltration and ultrafiltration. Part I: Preparation and characterisation. J Memb Sci 118:239–245. https://doi.org/10.1016/0376-7388(96)00098-1
106. Yampolskii Y (2012) Polymeric gas separation membranes. Macromolecules 45:3298–3311. https://doi.org/10.1021/ma300213b
107. Yilanci A, Dincer I, Ozturk HK (2009) A review on solar-hydrogen/fuel cell hybrid energy systems for stationary applications. Prog Energy Combust Sci 35:231–244. https://doi.org/10.1016/J.PECS.2008.07.004
108. Yu S, Welp U, Hua LZ et al (2005) Fabrication of palladium nanotubes and their application in hydrogen sensing. Chem Mater 17:3445–3450. https://doi.org/10.1021/cm048191i
109. Zhang J, Liu X, Neri G, Pinna N (2016) Nanostructured materials for room-temperature gas sensors. Adv Mater 28:795–831
110. Zhang J, Xin Q, Li X et al (2019) Mixed matrix membranes comprising aminosilane-functionalized graphene oxide for enhanced CO_2 separation. J Memb Sci 570–571:343–354. https://doi.org/10.1016/j.memsci.2018.10.075
111. Zhang W, Gaggl M, Gluth GJG, Behrendt F (2014) Gas separation using porous cement membrane. J Environ Sci 26:140–146. https://doi.org/10.1016/S1001-0742(13)60389-7
112. Zito PF, Caravella A, Brunetti A et al (2017) Knudsen and surface diffusion competing for gas permeation inside silicalite membranes. J Memb Sci 523:456–469
113. Zito PF, Caravella A, Brunetti A et al (2018) Discrimination among gas translation, surface and Knudsen diffusion in permeation through zeolite membranes. J Memb Sci 564:166–173. https://doi.org/10.1016/j.memsci.2018.07.023

Functionalized Nano-porous Silicon Surfaces for Energy Storage Application

Pushpendra Kumar

Abstract Energy storage has been of a topic of curiosity since long for a persistent human activity. Storing power from several intermittent sources has been a great interest of scientific community and grows as the renewable energy industry begins to generate a larger fraction of overall energy consumption. Several renewable sources of energy exist, e.g., wind energy, solar energy, bioenergy, etc., but the problem is to store this energy and again reuse it when needed. For that an electrode is required that has high-energy storage capacity. The electrode that has a very large surface area, long durability, and high conductivity is prerequisite. Electrochemically prepared porous silicon where the physical properties, e.g., pore diameter, porosity, and pore length can be controlled by etching parameter and the functionalized nanostructured surfaces of porous silicon, might be the key material to develop high-energy storage electrodes.

Keywords Porous silicon · Renewable energy · Functionalized nanostructured surfaces · Electrochemical etching

1 Introduction

Climate change is one of the major challenges that the international community is facing at present. However, there is no immediate solution to the problem. But it can only be solved through efficient materials and scientific knowledge. Most of the scientists agree that the climate change is due to greenhouse gases. The gases that contribute to the greenhouse effect are N_2O, CO_2, CH_4, water. One of the important sources for generating these greenhouse gases is the burning of fossil fuels like coal and oil. An alternative source of renewable energy that includes solar energy, wind energy, hydropower, geothermal energy, and biomass energy is required to avoid the use of fossil fuels. The power generation systems such as solar and wind have limitations due to their intermittency and the fact that maximum production periods do not correspond to the times of highest demand. This limits the practicality of solar

P. Kumar (✉)
Department of Physics, Manipal University Jaipur, Jaipur 303007, Rajasthan, India
e-mail: pushpendra.kumar@jaipur.manipal.edu

L. Ledwani and J. S. Sangwai (eds.), *Nanotechnology for Energy and Environmental Engineering*, Green Energy and Technology,
https://doi.org/10.1007/978-3-030-33774-2_16

and wind power in areas without backup of grid connections. Therefore, the capacity to store converted solar and wind energy is an urgent requirement of renewable energy.

As the electrical energy has to be used immediately, therefore, it is difficult to match electrical energy demand with the intermittent source of renewable energy without cheap storage. At present the researcher is working on two main concepts to address this problem. The first is based upon photocatalytic processes where the solar energy is directly converted into storable fuels. In the second concept the batteries are used to store energy. A lot of research efforts are being made by researchers across the world to develop an capable electrode materials to store energy. For that a high-energy storage capacity electrode is needed. Electrode designs that have a very large surface area, highly conducting, and long durability are required. Modified nanostructured surface of nanostructured materials might be few of the key materials to develop high-energy storage electrode. There have been wide ranges of porous material, e.g., metal-organic frameworks (MOFs) (Furukawa et al. 2013), mesoporous materials (Schuth and Schmidt 2002), and electrochemically etched porous semiconductors (Foll et al. 2006) where fine control over physical properties of porous materials is achieved utilizing controlled techniques, such as directing molecular building blocks into porous structures for MOFs.

One-dimensional nanostructured materials are promising building blocks for next generation photovoltaic, optoelectronic, batteries and photonic devices due to their dimensional dependence physical, optical, and electronic properties. Silicon is a high density material compared to carbon materials, therefore the silicon-based batteries have higher volumetric energy density and can easily be integrated on chip with silicon devices, which would make the silicon battery electrode potential candidates for energy storage applications. Further the porous matrix offers high volumetric storage characteristics that are required for transportation applications and mobile technology (Gogotsi and Simon 2011). This underlines a structural advantage of controllable porous materials and one-dimensional nanostructured materials, such as nanoporous silicon (PS), since the chemical and electrochemical etch process that forms the active material structure dictates the volumetric energy storage properties and enables this metric to be easily assessed and controlled (Gaur et al. 2013; Granitzer and Rumpf 2010). However, PS suffers from high reactivity due to its relatively high resistance resulting in poor stability and low power density. Coating of graphene on PS has been possible solution to increase the stability by reducing the resistance of PS (Desplobain et al. 2007; Min-Gi et al. 2016; Oakes et al. 2013), but even for coated electrodes the performance has still been many orders of magnitudes lower that of carbon-based batteries. This has been attributed to the fact that the power density is finally controlled by the resistance of the complex Si nanostructure and, therefore, in addition to the stability the coating also has to provide high conductivity. Graphene coating on PS is an alternative to provide very large surface area, stability as well as high conductivity.

The physical properties, e.g., the lateral width, randomness, length scale, and chemical functionality of PS host matrix can easily be controlled and graphene coating protects the PS from electrochemical degradation with the electrolyte, resulting in

increased energy density compare to uncoated samples. This chapter detailed about the synthesis and characterization of PS and how the functionalization of PS can enhance the overall properties that are required to store energy efficiently.

2 Synthesis of Porous Silicon with Different Pore Diameter

A material that has a small hole in it through which water, liquid, vapors, and gas can be passed and provide large surface to volume ratio in the order of 500 m^2/cm^3 called porous materials. Porous silicon (PS) which has accidentally discovered while Uhlir Jr. and Ingeborg Uhlir in 1956 at the Bell labs in U.S. were developing a technique for polishing and shaping the surface of silicon and germanium (Ulhir 1956; Zhang 2004). During that process under several conditions they observed thick black, brown, and red film on the surface of the materials. But at that time, the finding was described as porous silicon and only published in Bell lab's technical notes. The scientific community was not interested in porous silicon despite the discovery of porous silicon in 1956 till Leigh Canham published an experimental result in 1990 on photoluminescence appearance in PS (Canham 1990). Since the discovery of photoluminescence in PS, it has triggered large-scale investigation for its use in technological applications. Several methods have been used to prepare the PS that include electrochemical etching, stain etching, and hydrothermal etching (Abramof et al. 2006; Liua and Wang 2005; Smith and Collins 1992) which allows to vary physical and chemical properties of PS as per the technical and scientific demands. The physical properties, e.g., specific surface area, porosity, pore diameter, and pore orientation of PS can be varied by changing etching parameters such as current density, type of doping, level of doping, or crystallographic orientation of the silicon wafers used (Herino et al. 1987). The well-defined PS morphology is ranged from microporous with pore size <10 nm and branchy mesoporous silicon with pore size 10–50 nm to the classical macroporous silicon of pore size 50–20 μm.

2.1 Pore Formation in Silicon

Several methods can be used to synthesis porous silicon as discussed in the introduction part. However, in this chapter the electrochemical etching of Si in aqueous HF solution was discussed. The holes are prerequisite to create pores in Si. The pores in Silicon form during anodic polarization in aqueous HF solution, depending on applied potential between electrode, doping level in Si wafer and HF concentration. Several mechanism for pore formation have been discussed in the literature (Smith and Collins 1992; Zhang 2004). The pore formation in Si is the results of inhomogeneous dissolution of the Si surface in HF-based electrolyte due to competing reactions lead to silicon oxide formation followed by dissolution of the oxide by HF. The overall process during pore formation in Si can be expressed by following

equations:

$$\mathrm{Si} + 2\mathrm{HF} + 2h^{+} \rightarrow \mathrm{SiF_2} + 2\mathrm{H^{+}}, \quad (1)$$

$$\mathrm{SiF_2} + 4\mathrm{HF} \rightarrow \mathrm{H_2} + \mathrm{H_2SiF_6} \quad (2)$$

The etching rate is determined by the holes (h^{+}) accumulation in the adjacent regions of the HF electrolyte and Si atoms.

The electrochemical cell used for making porous silicon is given in Fig. 1. The polymer such as Teflon is highly acidic resistant material and used to make electrochemical etching cell. A conducting and HF-resistant material such as platinum is generally taken as a cathode in the cell. The Si wafer acts as the anode and placed on metal disk and sealed through an O-ring so that only front side of Si is exposed to electrolyte. Using this cell the pores are formed on the surface of Si wafer exposed to HF, including the cleaved edges. The simplicity and homogeneously anodization of Si surface is an advantage of the geometry of this cell.

When a Si wafer with high resistivity (i.e., more than a few mΩ/cm) is used, a high dose implantation on the back surface of the wafer is required to increase the electrical contact between the wafer and the metal disk.

HF diluted in deionized water was used as an electrolyte to form PS. However, due to the hydrophobic character of the clean Si surface, the purely aqueous HF solutions did not infiltrate in the pores of PS. To increase the wettability, the ethanol is usually added to the aqueous solution. Ethanol not only increases the wettability but also help for the lateral homogeneity of the PS layer in depth and remove bubbles form due to

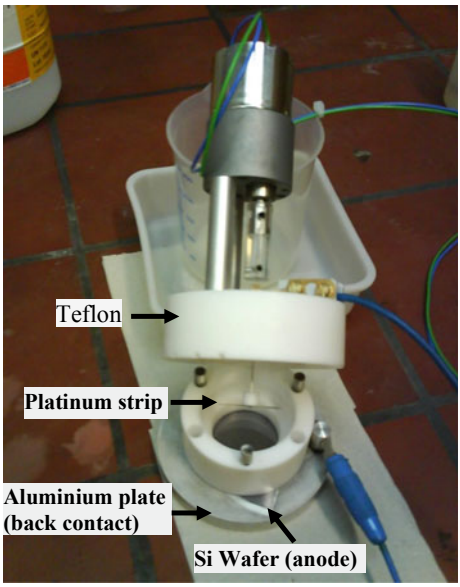

Fig. 1 Photograph of electrochemical cell to produce PS

hydrogen evolution on the surface of Si. Due to these reasons the concentration ration of HF and ethanol or other surfactant is very important to vary the physical properties of PS. Another factor in deciding the physical properties of PS is potentially applied between the electrodes. Generally it is preferable to work with constant current because it allows better control of physical properties and reproducibility of the PS layer.

2.2 Change in Physical Properties of Porous Silicon

Several mechanisms have been proposed to explain the porous silicon formation. In most the mechanism basic need is as follows: The holes are prerequisite for pore formation in Si substrate and the Si wafer must be anodically biased. This corresponds to reverse biasing for n-type doped silicon and forward biasing for p-type doped silicon. For semi-insulating p-type doped and n-type doped silicon, light must be supplied to have enough holes in the substrate. Optimized current density below the critical value must be used. The holes are used up during the etching of silicon in first two conditions. Enough holes are available at the pore tips, where, the dissolution occurs as schematically shown in Fig. 2. Depending on the orientation of Si wafer, the etching of porous silicon continues in depth that follows the anodic current paths inside silicon. No more electrochemical etching takes place once a porous silicon layer is formed but a slow chemical reaction starts, due to the permanence in HF. The reaction is limited by mass transfer to the solution when the third condition of critical current is not satisfied resulting the piling up of holes at the silicon-HF interface and electropolishing take place. For all the three conditions stated above

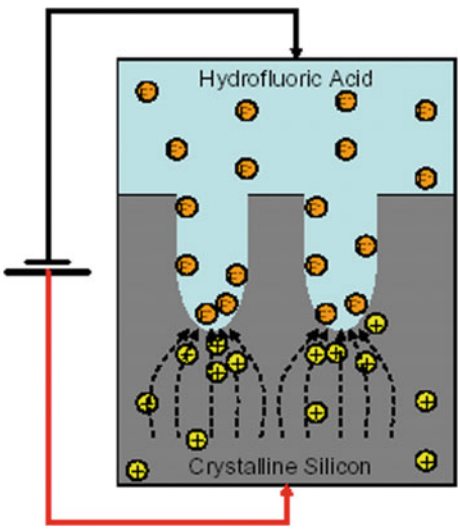

Fig. 2 Schematic of PS formation. Etching occurs only at the pore tips where the holes (h^+) are focused by the electric field

the holes play the main role: in fact, porous silicon formation is a self-regulated mechanism, with hole depletion as the controlling agent. The dissolution reaction initiates at defects on the surface of silicon, the pores are formed and their walls are eroded until they are emptied of the holes. This formation process passivates them from further attack, and the reaction proceeds at the pore tip only. The overall etching process is self-adjusting and the physical properties of porous silicon, i.e., shape, diameter of pores, the porosity, and the thickness of the formed porous layer is given by the electrochemical parameters only. The physical properties of PS can be varied with extreme control by changing of the electrochemical etching parameters, e.g., current density, substrate doping level and type or HF concentration (Kumar and Huber 2007; Kumar 2011). In addition, when the feature size of the pores of PS is less than a few nanometers, various quantum-size effects occur, which make PS even more fascinating. Many theories on the PS formation mechanisms have been reported since its discovery. In the Fig. 3 it is shown that by changing the HF concentration in etching solution the pore diameter and porosity of PS can be varied that results in the different color of PS. In Fig. 3, SEM images, the color observation and photoluminescence spectroscopy measurements for three different samples were shown. From the figure it is clear that with increase in ethanol to HF concentration by keeping other parameters constant the pore diameter and porosity is increased. As Si is indirect bandgap material and does not show any PL therefore is limited in many of the technology. However, PS shows the PL properties as shown in Fig. 3 and open up several optical applications. With increase in pore diameter in the PS sample the distance between two pores is decreased results in the decrease of Si crystalline size. When the size of Si crystallites among the pore reduces less than the bohr's exciton radius, i.e., 4.9 nm for Si, several quantum effect starts to occur and that resulted in the photoluminescence appearance in PS. The physical properties of PS are determined by two large groups of factors, the first group of factors includes doping type and level and potential that affect carrier density on the surface of a pore bottom and second group of factors includes HF concentration and current density that affect only the dissemination of the reactions. In this chapter, the effect of HF concentration on physical properties by keeping other parameters constant as shown in Fig. 3 was discussed. Si surface is hydrophobic in nature, therefore ethanol is usually added to aqueous etching solution to increase the wettability of the PS surface. Ethanol is very important for the lateral homogeneity of the PS layer in depth because ethanoic solution infiltrates the pores, while pure aqueous HF solution does not. Further during the etching the hydrogen evolution in bubbles form takes place and stick on the Si surface in pure aqueous solutions whereas they are easily removed if ethanol is present. With increase of HF concentration in etching electrolyte, the pore diameter and porosity of PS decreases that can be understood as follows: both the pore diameter and wall thickness for highly doped *p*-type Si, are largely determined by the thickness of the space-charge layer formed at the interface of electrolyte and Si. Thus, in general, the thickness of the space-charge layer has the same order of magnitude as pore diameter. The wall thickness is generally less than twice the space-charge layer thickness. The wall region is depleted of carriers and is thus not conductive due to the overlapping of two space-charge regions entering

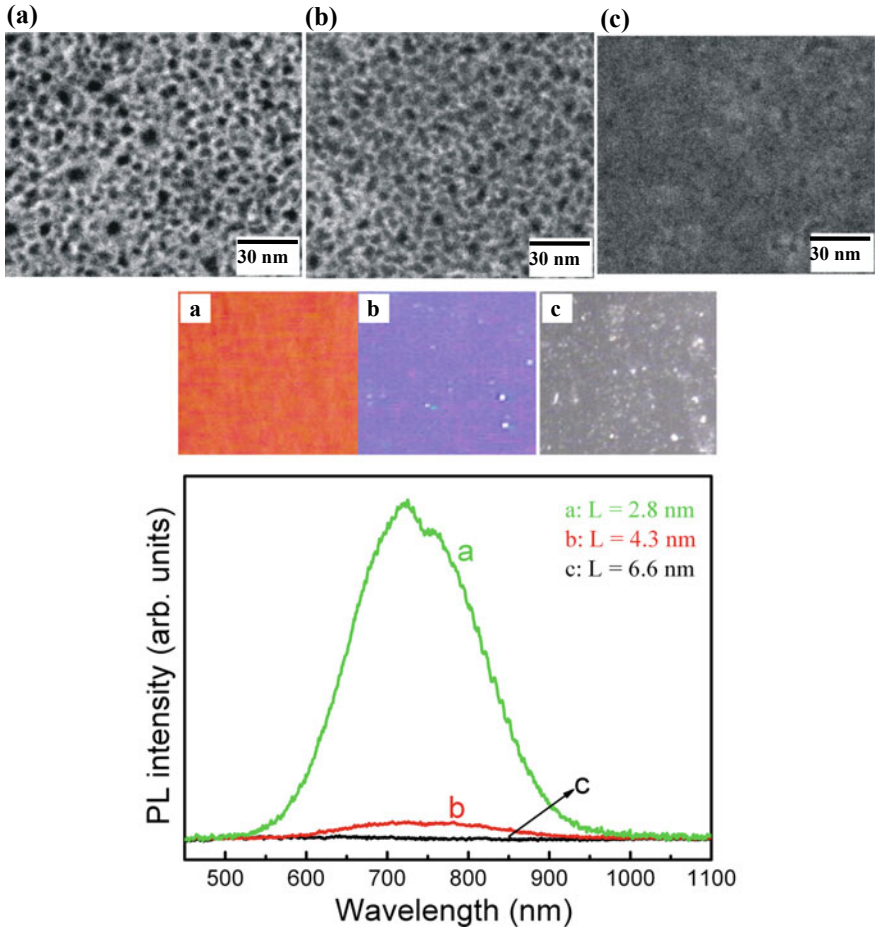

Fig. 3 FESEM image, visual images and PL spectra (L is Si crystallize size between two pores) of samples prepared in different concentration of etching solution for HF:Ethanol **a** 3:7 **b** 4:6 **c** 6:4

at neighboring pores. The walls are not depleted of carriers if the wall thickness is larger than twice the space-charge layer thickness and dissolution can still occur to form new pores on the walls. With controlled space-charge layer thickness to form PS, the actual wall thickness is determined by the relative dissolution rates between the pore tip (i_t) and the edge of a pore bottom (i_b). If i_t is comparable to i_b, significant dissolution occurs at the edge of the pore bottom before the pore tip propagates far away resulting in a thin wall or the annihilation of walls. On the other hand, The relatively thick walls and small pore can be generated, if i_b is very small compared to i_t, the pore tip propagates relatively fast before much dissolution occurred on the edge of the pore bottom, where dissolution is virtually stopped due to lack of carriers. In *p*-Si by increasing the HF concentration the thickness of the space-charge

layer reduces and the pore tip current density increases results in smaller pores and thicker walls. On the other hand, polishing of silicon in aqueous HF solution is known to be preceded by silicon oxide formation. The oxide is then dissolved by HF through formation of a fluoride complex in the solution. With increasing HF concentration in etching electrolyte the dissolution rate of silicon oxide increases that in turn increases the critical current density at which the surface is covered by oxide. As a result, walls become thicker and the pores become smaller with increasing HF concentration (Kumar 2009; Michler et al. 2000; Zhang 2004).

3 Energy Storage Devices

An energy storage device is a device that is used to store electric energy when needed and releasing it when required. High-power and high-energy storage devices is a long-standing goal of material scientist that is source of portable energy for transportation to reduce the reliance on fossil fuels. To encounter the problem of global warming due to the use of fossil fuels, the energy storage device technology in fields such as renewable energy generation and hybrid automobile systems is an emerging field of research. Energy can be stored in a range of ways depending upon the intentional use with each method having its advantages and disadvantages. Batteries, fuel cells, and supercapacitors have been used and studied since long to store electrical energy. The need to develop energy storage devices to store energy from sustainable and renewable energy sources is leading society to develop energy from sources that are not continuously available, such as the wind and sun. Several types of energy storage devices are available with different properties given in Table 1. Energy generated from renewable sources has to be converted and stored by highly efficient and eco-friendly ways for sustainable economic growth and environment protection. Rechargeable batteries and supercapacitor storage devices are the most common means of storing energy.

However, there are a number of tasks that need to be addressed in order to improve their performance and to make them economically viable. Therefore, electrochemical devices that can deliver high energy density are increasingly important. As renewable energy sources become increasingly predominant the need for high-power storage and high energy-density devices with long durability is greater than ever. The development of suitable materials for these devices originates with a complete understanding of the complex processes that govern energy storage and conversion spanning several orders of magnitude in time and length scales. Figure 4 shows the Ragone plot of the energy storage and power handling capacity of some different storage techniques.

Table 1 Type of energy storage devices with analysis

Type of energy	Power density (kW/m^3)	Energy density (kWh/m)	Electrical efficiency (%)	Life-time	Typical range	Response time	Backup time
Mechanical							
a. Pumped hydroelectric storage, PHS	$f(h_1 \sim h_2)$	3–6 Wh/L	75–80	~50 years	Up to 2.1 GW	1–2 mins	Days
b. Compressed air energy storage, CAES	360 MW	2–6 Wh/L	60–80	<50 years	25–350 MW	1–2 mins	Hours
c. Flywheel energy storage	>707–1767	>282–424	90–95	10–20 years	In kW	~1–2 mins	~mins
Thermal							
Molten salt	200	40–110 kWh/ton	~90	30+ years	~200 MW	Seconds	Hours
Chemical							
a. Fuel cell	Up to 30 kW	300–600 Wh/kg	40–60	1–2 years	Up to 30 kW	Seconds	Days
b. Synthetic natural gas		1200 kWh/Nm^3	50–60	–	Up to 100 MW	–	–
Electrochemical							
Battery energy storage system, BESS	>106–7067	>70–247	~90	3–6 years	100–20 MW	Seconds	Hours
Electrical							
a. Supercapacitor	>176, 678	>53	~90	10–20 years	1–250 kW	Milliseconds	Seconds
b. Superconducting magnetic energy storage	>530	>7	~95	~30 years	1–100 MW	Milliseconds	Seconds

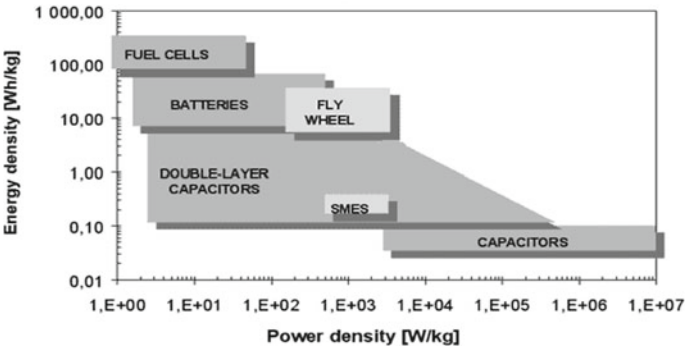

Fig. 4 The Ragone plot shows the energy storage and power handling capacity of some alternative storage techniques. Taken for representation from https://www.mpoweruk.com/alternatives.htm

3.1 Battery

A battery consists of two or more electric cells joined together and these cells convert chemical energy to electrical energy. The cells consist of negative and positive electrodes combined by an electrolyte. In battery, the DC electricity is generated by the chemical reaction between the electrodes and the electrolyte. In the case of rechargeable or secondary batteries, by reversing the current the chemical reaction can also be reversed and the battery returned to a charged state. Large number of materials and electrolytes were studied and that have been combined to form a battery. However, relatively only a small number of combinations has been developed as marketable rechargeable electric batteries appropriate for use in vehicles. Several types of batteries that include nickel cadmium, lead acid, nickel iron, nickel metal hydride, lithium polymer and lithium-ion, sodium metal chloride, sodium sulphur, and others have been designed to meet required duration, specific power, and energy density.

Battery store energy through changes in their internal chemistry and understanding of battery chemistry is required for their performance, maintenance and their limited life, self-discharge, and reduce efficiency at higher current. When a battery discharge through a load, the internal battery chemistry undergoes a change. To recharge a battery, the chemical changes are reversed, and energy is again stored in the battery. A specific amount of energy can be stored in the battery depending on the specification of battery. A lot of research is going on to improve the basic parameters of batteries that are reviewed briefly here.

3.1.1 Cell and Battery Voltage

In order to have desired net voltage, a number of cells are connected in series to form a battery. Voltage across the terminal is given as

$$V = E - IR \tag{3}$$

where E is the fixed voltage, I is current flowing in the circuit and R is the internal resistance.

3.1.2 Battery Capacity

The energy stored in a battery called the battery capacity and measured either in ampere-hours (Ahr) or Watt-hours (Wh), kilowatt-hours (kWh).

3.1.3 Energy Stored

The energy stored in the battery depends on the charge stored and its voltage.

Energy in Whr = V × Ahr.

3.1.4 Specific Energy

Specific energy is the amount of electrical energy stored per unit mass and has units of $Wh\ kg^{-1}$.

3.1.5 Energy Density

Energy density is the amount of electrical energy stored in a given system per unit volume. It normally has units of $Wh\ m^{-3}$.

3.1.6 Specific Power

Specific power is the amount of power obtained per kilogram of battery. It is a highly variable and rather anomalous quantity, since the power given out by the battery depends more on the load connected to it than the battery itself.

3.1.7 Power Density

Power density is the maximum power per unit volume and measures how quickly the battery can deliver energy. Its units are W/kg or W/m^3.

Reasonable price, high energy density, fast charging and discharging capability, safety, and good durability are the key characteristics of an optimal battery. The energy density of a battery can be varied by three factors: (1) by having a large chemical potential difference between the two electrodes; (2) by making the volume

or mass of the reactants per exchanged electron as small as possible; (3) electrolyte should not be consumed in the chemistry of the battery. The Lithium-ion batteries are widely used due to their high energy density in mobile technology and are considered to be one of the best choices as a power source for vehicles. However, an effort is being made to increase the capacity of lithium-ion batteries by replacing the traditional graphite as the anode material with the use of silicon (Si). Silicon has a theoretical specific capacity of ~4200 mAh/g for lithium compare to traditional graphite that has specific capacity of ~370 mAh/g. Even when taking into account the volumetric expansion, simply by changing the graphitic anode by silicon, it has been estimated that the cell energy density could be improved by 10–30% (Bogart et al. 2014; Obrovac and Chevrier 2014). Silicon is commonly used in anodes today and can hold 10 times more lithium ions than the graphite. But Si expands its volume three times when completely lithiated. The swelling and shrinking on repeated cycle causes silicon to quickly break down. To overcome these problems of stability due to volumetric expansion, a functionalized mesoporous silicon is being used as an anode material. It is reported that the pores between the Si material help to provide the space for volumetric expansion results in better stability. Therefore an optimized pore size of porous silicon has been studied for stability of battery electrode (Ikonen et al. 2017).

3.2 Supercapacitor

Capacitors are devices in which two conducting plates are separated by an insulator and a supercapacitors are capacitors, which can store large quantities of electricity. Energy storage capacity per unit volume or mass of supercapacitor is 10–100 times more than electrolytic capacitors. They can be charged and discharged much quicker than batteries, and have many more charging and discharging life cycles than rechargeable batteries. The electric energy in capacitors is stored by accumulating positive and negative charges often on parallel plates separated by an insulating dielectric while batteries store electricity using electrochemical potential. Capacitors have traditionally been used to provide very short bursts of energy usually less than one second. The charge storage capacity of the capacitor is limited and is usually much larger and heavier than a battery of equivalent power. Supercapacitors have been projected as a potential replacement for traditional batteries due to rises in storage capacity. Capacitors are potential candidates for energy storage for regenerative breaking due to its quick charge and discharge capacity. The capacitor storage capacity is decided by the surface area of its two charged plates. The higher surface area of plates has larger capacitance. The surface area of capacitor plate can be increased by the use of nanostructured surfaces results in the increase in charge capacity of capacitor. The energy stored in a capacitor is given by the following equation

$$E = \frac{1}{2} C V^2 \tag{4}$$

where E is the energy stored in Joules and V the voltage between the plate. The stored energy in the capacitor can be increased by increasing the voltage stored on the capacitor or the capacitance C. The capacitance C of a capacitor is given by the equation:

$$C = \varepsilon \frac{A}{d} \tag{5}$$

where C is the capacitance in Farads, ε is the permittivity of the material between the plates, d is the separation between the plates and A is the area of plate. The small separation between the plates is the key to modern supercapacitors. The capacitance arises from the formation of the double layer of electrolytic ions on the surface of electrode. Due to high surface areas of 10,00,000 m^2kg^{-1}, and a capacitance of 4,000 F they can be fitted into a container of the size of a beer can. However, the problem with these capacitor is that the voltage across it can be very low, between 1 and 3 V as is clear from Eq. 4 that limits the energy density of the capacitor. Several capacitors have to be connected in series to store charge at a reasonable voltage. This not only adds cost but also brings other problems too. Energy storage capacity is still very less in supercapacitor and a lot of research is being done to increase the energy density (Gupta et al. 2011).

4 Functionalized Nano-porous Silicon

The active materials are required for future energy storage challenges to store energy produced from low-cost sources for consumer-level electronics applications or grid-scale applications. The 2nd most abundant element on the earth is Silicon and has been material with revolutionary impact on the solar industries and electronics (Palestino et al. 2007). Silicon is a high-density material than carbon materials, therefore, the silicon-based capacitors have higher volumetric energy density and can easily integrated on chip with silicon devices that would make the Si capacitors potential candidates for technological applications. Further the porous matrix offers high volumetric storage characteristics that are required for transportation applications and mobile technology. However, doped silicon suffers from the immense reactivity of surface-bound silicon atoms with electrolytes that hinders electrochemical stability and surface traps that obstruct conductivity (Michler et al. 2000; Pelton et al. 2002). Si has been used widely as anode materials in metal-ion batteries due to its surface reactivity with electrolyte that helps charge to store through intercalation reactions, but has hindered producing silicon-based materials for stable double-layer charge storage (Santori et al. 2001; Yuan et al. 2002). Only few investigation of Si materials in electrochemical environments have been reported till now. In which the specific capacitances in device configurations have been reported orders of magnitude lower (5 mF/g) than carbon materials for on-chip micro-supercapacitors and a strong dependence of the equivalent series resistance (ESR) on the surface characteristics of the

silicon (Desplobain et al. 2007; Thissandier et al. 2012; Thissandier et al. 2013). Carbon-based nanostructured materials have been used for supercapacitor applications along with the development of new architectures of meso-and nanoporous materials because of their inherent good electrical conductivity and electrochemical stability (Jha et al. 2012; Zhu et al. 2012). However, volumetric performance is often ignored due to inhomogeneity in sample thickness despite the industrial importance of volumetric storage characteristics when assessing performance for technological applications (Gogotsi and Simon 2011). This highlights a structural benefit of controllable porous materials, such as porous silicon that is formed by electrochemical etching process and the porous active material that can be varied by etching condition can decide the volumetric energy storage properties. PS has been a material of interest due to its high energy density and easy synthesis. However, due to high resistance and high reactivity of PS it results in low power density and poor stability. Coating of thin layer of materials on PS has been possible solution to increase the stability and lessen the resistance (Oakes et al. 2013; Rowlands et al. 1999), but even for coated electrodes the performance has still been many orders of magnitudes lower that of carbon-based supercapacitors. However, the resistance of the complex Si nanostructure has limited the power density, therefore, in addition to the stability the coating also needs to provide high conductivity. Graphene coating on PS is an alternative to provide both stability as well as high conductivity. Graphene a 2 D material has shown a wide range of properties that includes strength, elasticity, mechanical stiffness, electrical and thermal conductivity, it is chemically inert, impermeable to gases, optically active and flexible. Graphene, being a highly inert material can act as a corrosion barrier against most gases, water, and oxygen diffusion.

Functionalization of porous silicon surface with graphene was done by Oakes et al. for stable and high-performance electrochemical supercapacitor. In this study highly doped (0.01–0.02 Ω cm) Si wafer has been used to make porous silicon in HF-based electrolyte using electrochemical etching. As shown in Fig. 3 by changing etching conditions that include HF concentration in electrolyte, etching current density, etching time, type and doping level of Si, the physical properties of PS can be varied. An optimized PS of 75% porosity and 4 μm thick sample has been used for graphene coating to check its stability and energy storage capacity. For graphene coating, the PS sample has been treated with C_2H_2/H_2/Ar gas mixtures over a temperature ramp from 650 to 850 °C for 20 min. With this treatment mono or few layer graphene has been coated on PS surface. The coating of graphene on PS has enhanced conductivity as well as provides a stable electrode–electrolyte interface that is critical to attain good energy storage characteristics. With the same porous structure, graphene-coated PS devices compared to pristine PS has leaded much greater charge storage capacity as illustrated in Fig. 5a. FESEM images of pristine PS and graphene-coated PS shown in Fig. 5b and c respectively revealed nanoscale structure provides high surface areas that enable this material architecture for electrochemical supercapacitor electrodes reported by Oakes et al. in scientific reports (Oakes et al. 2013). They have shown that the graphene-coated PS has outstanding electrochemical properties compared to uncoated PS in every measure and by using electrochemical device testing data, a

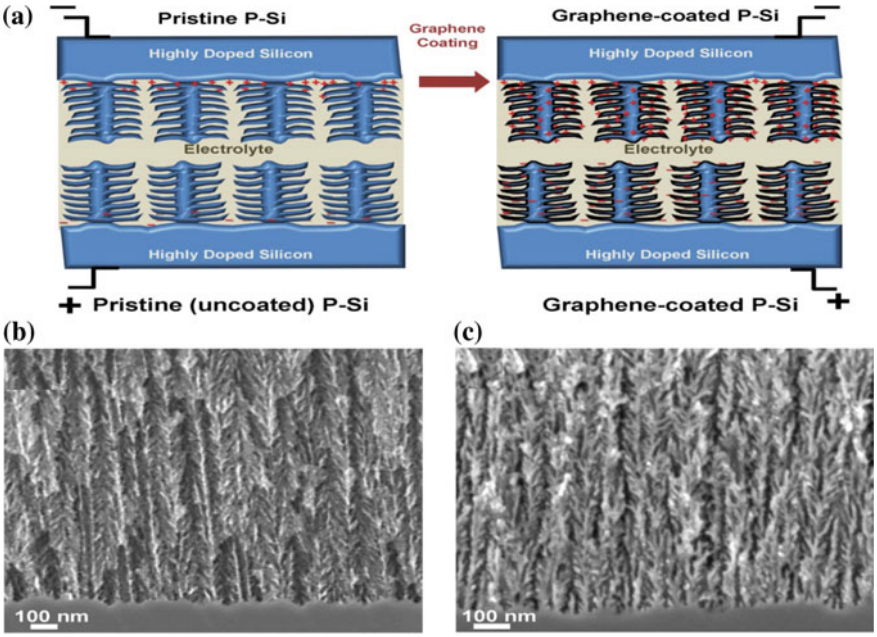

Fig. 5 Graphene coating on porous silicon. **a** Scheme of the effect of coating *p*-Si on the capacitive charge storage properties. SEM cross-sectional images of porous silicon showing the interface between the etched porous silicon and the silicon wafer for the case of **b** uncoated, pristine porous silicon and **c** graphene coated porous silicon

Ragone plot was constructed to show the energy–power characteristics of this device that include specific and volumetric energy storage capacity shown in Fig. 6a and b respectively. The graphene-coated PS has shown ~50X lesser resistance than fresh

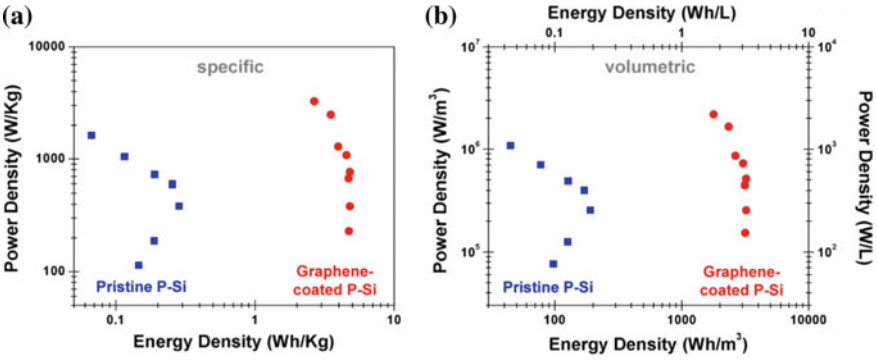

Fig. 6 Specific and volumetric Ragone plots for coated and pristine porous silicon Ragone analysis for pristine, uncoated *p*-Si (blue, squares) and graphene-coated *p*-Si (red, circles) in the framework of both **a** specific and **b** volumetric energy storage characteristics

PS, attributable to the presence of surface traps in fresh *p*-Si that reverse doping effects. Graphene coating on PS has improved ~30X electrolyte–electrode interface charge transfer resistance, ~15X Warburg diffusion resistance ~2X electrochemical window, ~10–40X in both specific energy density and volumetric shown in Fig. 6 and considerably enhanced long-term cycling characteristics with less than 1% change in capacitance over 3500 cycles.

5 Conclusion

The energy storage devices can play a vital role in storing renewable energy for technology applications in several fields. Different type of energy storage systems with their characteristic parameter were reviewed. The silicon, due to its high theoretical specific capacity of ~4200 mAh/g and second most abundant element on the planet, has been explored for energy storage devices. The PS that further provide large surface area for electrode was discussed in detail. The surface of PS is highly reactive with electrolyte and has high resistance. The coating of graphene on PS has enhanced conductivity as well as provides a stable electrode–electrolyte interface that is critical to attain decent energy storage characteristics. The PS with optimized physical properties that include porosity, thickness, and morphology can provide the potential toward integration of efficient energy storage into existent silicon-based technology platforms in diverse technologies such as sensors, electronics, and solar devices.

References

Abramof PG, Beloto AF, Ueta AY, Ferreira NG (2006) X-ray investigation of nanostructured stain-etched porous silicon. J Appl Phys 99:024304

Bogart TD et al (2014) Lithium ion battery peformance of silicon nanowires with carbon skin. ACS Nano 8:915–922

Canham LT (1990) Silicon quantum wire array fabrication by electrochemical and chemical dissolution of wafers. Appl Phys Lett 57:1046

Desplobain S, Gautier G, Semai J, Ventura L, Roy M (2007) Investigations on porous silicon as electrode material in electrochemical capacitors. Phys Status Solidi C 4:2180–2184

Dian J, Konečný M, Broncová G, Kronďák M, Matolínová I (2013) Electrochemical fabrication and characterization of porous silicon/polypyrrole composites and chemical sensing of organic vapors. Int J Electrochem Sci 8:1559–1572

Foll H, Carstensen J, Frey S (2006) Porous and nanoporous semiconductors and emerging applications. J Nanomater 2006:91635

Furukawa H, Cordova KE, O'Keeffe M, Yaghi OM (2013) The chemistry and applications of metal-organic frameworks. Science 341:1–974

Gaur G, Koktysh DS, Weiss SM (2013) Immobilization of quantum dots in nanostructured porous silicon films: characterizations and signal amplification for dual-mode optical biosensing. Adv Funct Mater 23:3712

Gogotsi Y, Simon P (2011) True performance metrics in electrochemical energy storage. Science 334:917–918
Granitzer P, Rumpf K (2010) Porous silicon-a versatile host material. Materials 3:943–998
Gupta R et al (2011) Application of energy storage devices in power systems. Int J Eng Sci Technol 3:289–297
Herino R, Bomchil G, Barla K, Bertrand C, Ginoux JL (1987) Porosity and pore size distributions of porous silicon layers. J Electrochem Soc 134, 1994
Ikonen T et al (2017) Electrochemically anodized porous silicon: towards simple and affordable anode material for Li-ion batteries. Sci Rep 7:1–8
Min-Gi J et al (2016) Nitrogen-doped carbon coated porous silicon as high performance anode material for lithium-ion batteries. Electrochim Acta 209:299–307
Jha N, Ramesh P, Bekyarova E, Itkis ME, Haddon RC (2012) High energy density supercapacitor based on a hybrid carbon nanotube-reduced graphite oxide architecture. Adv Energy Mater 2:438–444
Kumar P, Huber P (2007) Effect of etching parameter on pore size and porosity of electrochemically formed nanoporous silicon. J Nanomater, Article ID 89718, 4 p
Kumar P (2011) Effect of silicon crystal size on photoluminescence appearance in porous silicon. ISRN Nanotechnol, Article ID 163168, 6 p
Kumar P et al (2009) Effect of HF concentration on physical and electronic properties of electrochemically formed nano-porous silicon. J Nanomater, Article ID 728957, 7 p
Liua H, Wang ZL (2005) Etching silicon wafer without hydrofluoric acid. Appl Phys Lett 87:261913
Michler P et al (2000) A quantum dot single-photon turnstile device. Science 290:2282
Oakes L et al (2013) Surface engineered porous silicon for stable, high performance electrochemical supercapacitors. Sci Rep 3:3020
Obrovac MN, Chevrier VL (2014) Alloy negative electrodes for li-ion batteries. Chem Rev 114:11444–11502
Palestino AG et al (2007) Fluorescence tuning of confined molecules in porous silicon mirrors. Appl Phys Lett 91:121909
Pelton M et al (2002) Efficient source of single photons: a single quantum dot in a micropost microcavity. Phys Rev Lett 89:233602
Rowlands SE, Latham RJ, Schlindwein WS (1999) Supercapacitor devices using porous silicon electrodes. Ionics 5:144–149
Santori C et al (2001) Triggered single photons from a quantum dot. Phys Rev Lett 86:1502
Schuth F, Schmidt W (2002) Microporous and mesoporous materials. Adv Mater 14:629
Smith RL, Collins SD (1992) Porous silicon formation mechanisms. J Appl Phys 71, RI
Thissandier F et al (2012) Highly doped silicon nanowires based electrodes for microelectrochemical capacitor applications. Electrochem Commun 25:109–111
Thissandier F, Pauc N, Brousse T, Gentile P, Sadki S (2013) Micro-ultracapacitors with highly doped silicon nanowires electrodes. Nanoscale Res Lett 8:1–5
Ulhir A (1956) Electrolytic shaping of germanium and silicon. Bell Syst Tech J 35:333
Yuan Z et al (2002) Electrically driven single-photon source. Science 295:102
Zhang XG (2004) Morphology and formation mechanisms of porous silicon. J Electrochem Soc 151:C69–C80
Zhu Y et al (2012) A seamless three-dimensional carbon nanotube graphene hybrid material. Nat, Commun, p 3
Zhu J et al (2014) The application of graphene in lithium ion battery electrode materials. Springer Plus 3:585

Optimization of $MAPbI_3$ Film Using Response Surface Methodology for Enhancement in Photovoltaic Performance

Nitu Kumari, Sanjaykumar R. Patel and Jignasa V. Gohel

Abstract In the present study, optimization of process parameters for the deposition of methylamine lead iodide ($CH_3NH_3PbI_3$ or $MAPbI_3$) film is focus upon using parametric study and response surface methodology (RSM), respectively. The independent parameters to be optimized are PbI_2:CH_3NH_3I ratio (1:2–1:4); spin speed (2000–3000 rpm); and annealing temperature (60–100 °C). The dependent parameter considered in this study is power conversion efficiency (PCE) of perovskite solar cell (PSC) fabricated using $MAPbI_3$ layer. The value of the device efficiency at parametric optimum condition was 7.30%. Furthermore, to achieve specific optimum condition, RSM was applied to estimate the impact of deposition parameters on device efficiency. The predicted value of the PCE of PSC at optimum condition using RSM was 8.52%. The improvement of 16.7% in efficiency of the device can be clearly observed after the application of RSM.

Keywords $MAPbI_3$ perovskite · Response surface methodology · Spin coating · Perovskite solar cell · Power conversion efficiency

1 Introduction

Low cost and excellent performance of solar cells based on $MAPbI_3$/$FAPbI_3$ make it a significant breakthrough in the field of photovoltaic (Lina et al. 2019). The major role of the perovskite layer is to absorb photons and generation of electron–hole pairs in solar cells (Zhang et al. 2019). The PCE of PSC has been quickly enhanced with the improvement of film qualities, and modification in device structure (Kumari et al. 2018). Miyasaka et al. 2009 have synthesized first organometal halide ($MAPbI_3$) solar cell and achieved PCE of 3.9% (Kojima et al. 2009). After that, through careful strategy and using new material designs for PSC (Noh et al. 2019; Xie et al. 2019; Wang et al. 2018), PSCs have reached certified PCE up to 23.2% (Jeon et al. 2018). The PCE of PSCs depends on the quality of each and every layer associated with the

N. Kumari · S. R. Patel · J. V. Gohel (✉)
Department of Chemical Engineering, Sardar Vallabhbhai National Institute of Technology, Surat 395007, Gujarat, India
e-mail: sjn@ched.svnit.ac.in

L. Ledwani and J. S. Sangwai (eds.), *Nanotechnology for Energy and Environmental Engineering*, Green Energy and Technology,
https://doi.org/10.1007/978-3-030-33774-2_17

device and the recombination of charges on the surface is one of the major reasons to reduce PCE of PSC (Yang et al. 2019; Seo et al. 2019). The surface charge recombination is significantly reduced by using uniform, dense, and smooth perovskite layer in PSC as it increases the concentration of charges (Kumari et al. 2018). The highly efficient devices usually utilize TiO_2 layer (n-type), spiro-OMeTAD (p-type), and a metal back contact to form n-i-p PSC (Chen et al. 2019). Despite these advances, PSCs have not still become commercialized due to device stability, poor film morphology, low PCE (Rehman et al. 2019; Lee et al. 2015). Spin coating technique is one of the most common and cost-effective methods to prepare and control the morphology of perovskites light absorber layer. The major independent parameters associated with spin coating technology that helps to improve the quality of $MAPbX_3$ films are the precursor ratio (PbX_2:MAX), spinning speed, and annealing temperature. Xie et al. (2016) and Zhang et al. (2017) have studied the effect of precursor ratio whereas Dualeh et al. (2014) have reported the effect of annealing temperature detail. The simultaneous effect of all these parameters is yet to be reported. So, a study on the effect major deposition parameters on the device efficiency is focused in this paper.

RSM is a cost-effective and dominant optimization technique used to get a relation between process parameters (independent variables) and responses (dependent variables). RSM has gained recognition because it reduces the workload as well as production cost by optimizing the process parameters (Biira et al. 2017). RSM utilizes mathematical and statistical techniques that make it more efficient than the other conventional optimization techniques (Jambo et al. 2019). Up to now, there was no detailed improvement inquire about that utilized RSM programming to optimize the processing parameters of spin coater during the synthesis of $MAPbI_3$ film for the application in PSCs. Therefore, the purpose of this study is the synthesis of $MAPbI_3$ films by optimizing the deposition parameters of spin coater using Box–Behnken design (BBD) (3^3) response surface designs. The prepared and optimized $MAPbI_3$ films were applied in PSCs fabrication to enhance device efficiency. Previously optimized ZnO (Kumari et al. 2017, 2018) and TiO_2 (Kumari et al. 2018) films were used as bilayer electron transport layer during device fabrication in this study. The range of precursor ratio (PbI_2:MAI), spin speed, annealing temperature were kept as (1:2–1:4), (2000–3000 rpm), and (60–100 °C), respectively, to evaluate their effect on PCE of PSC.

2 Materials and Methodology

2.1 Material

All chemicals are obtained from Sigma-Aldrich except if expressed and utilized without further purification.

2.2 Methodology

2.2.1 Deposition of TiO_2/ZnO Bilayer

TiO_2/ZnO bilayer was coated upon fluorine-doped tin oxide (FTO) substrate as indicated by the technique announced in our past investigation (Kumari et al. 2018) to make electron transport bilayer.

2.2.2 Deposition of $MAPbI_3$ Films Using Spin Coating Technology

$MAPbI_3$ thin films have been prepared by one-step spin coating method using PbI_2 and MAI. Precursor solution was made by dissolving PbI_2 and MAI in the mixture of GBL and DMSO. Then it was spin-coated on pre-coated FTO/TiO_2/ZnO substrate to prepare $MAPbI_3$ film. During spinning, some amount of toluene is dripped on the substrate to make intermediate phase by removing residual DMSO and GBL. The influence of various control parameters has been studied in detail to find optimum conditions. During deposition of $MAPbI_3$ films using parametric study, it was observed that the PCE of device using 1:1 ratio of PbI_2 and MAI was not high. Therefore, this combination is not considered for further study. The ratio of PbI_2 and MAI (1:2–1:4), spin speed (2000–3000 rpm), and annealing temperature (60–100 °C) were varied.

2.3 Perovskite Solar Cell Fabrication

Every one of the layers with the exception of $MAPBI_3$ layer was coated upon FTO substrate as indicated by the technique specified in our beforehand announced paper (Kumari et al. 2018) and the $MAPBI_3$ layer was coated by the strategy made in the Sect. 2.2.2. The device structure can be found in Fig. 1.

2.4 Characterization

All the characterizations were finished utilizing the same techniques from announced in our past investigation (Kumari et al. 2018).

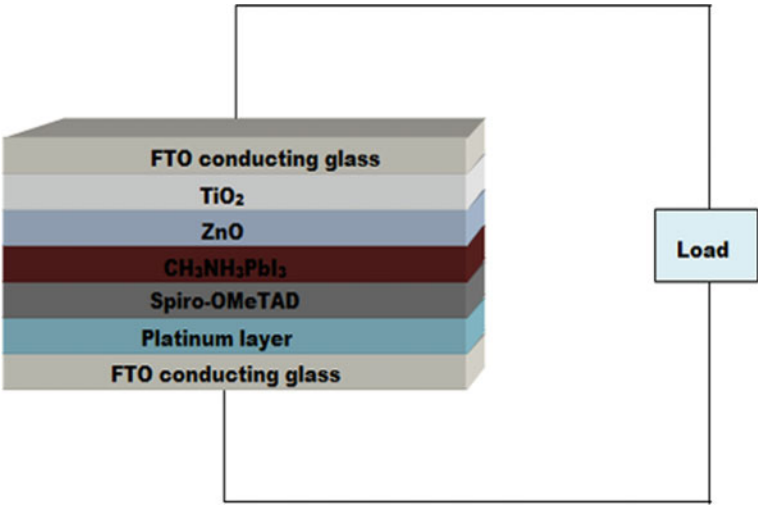

Fig. 1 Device structure of PSC

3 Results and Discussion

3.1 Optimization of $MAPbI_3$ Using the Parametric Study

3.1.1 Effect of Precursor Ratio

To see the impact of the forerunner proportion on the device efficiency, it was differed from 1:2 to 1:4 keeping spin speed (2000 rpm) and annealing temperature (100 °C) steady. The XRD image of deposited $MAPbI_3$ films at different forerunner proportions is appeared in Fig. 2. The diffraction peaks of $MAPbI_3$ film were gotten at 12.62°, 14.34°, 28.42°, and 32.06° relating to the planes (001), (110), (220), and (310), respectively. This confirms the conversion of PbI_2 into $MAPbI_3$. Figure 2 demonstrates that with the expansion in forerunner proportion from 1:4 to 1:2, the impurity peaks of PbI_2 getting smaller in the XRD pattern. A similar type of result was observed by Xie et al. (2016). This might be attributed to the presence of fewer amounts of MAI.

Additionally, to support our findings, further elemental analysis (see Table 1) and optical properties (Fig. 3) of prepared $MAPbI_3$ films got at three distinctive forerunner proportions were inspected. From Table 1, it is clear that percentage compositions of the carbon and nitrogen increase with the decrease in the precursor ratios. This may be attributed to the increase of the MAI content in the precursor solution. From Fig. 3, it is clear that the bandgap of $MAPbI_3$ (~1.63 eV) and the light assimilation capacity of $MAPbI_3$ layer prepared at 1:3 precursor ratio was observed to be maximum. Further, the films obtained at 1:4, 1:3, and 1:2 precursor ratios were used in device preparation (named D_1, D_2, and D_3, respectively). The efficiency of

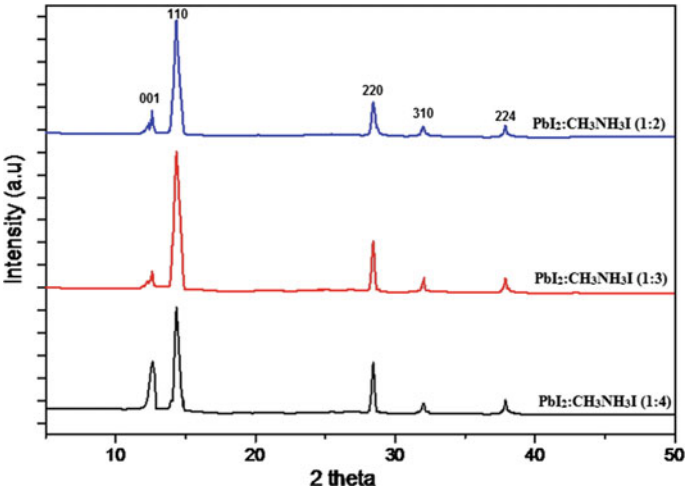

Fig. 2 XRD spectra of prepared $MAPbI_3$ films at different precursor ratios

Table 1 Elemental composition in $MAPbI_3$ films at different precursor ratios

PbI_2:MAI ratio	1:2	1:3	1:4
C	11.19	20.96	26.40
N	5.73	6.82	7.76
I	36.13	23.08	9.38
Pb	19.68	11.23	6.75
Amorphous C	25.84	37.29	48.24
Metallic Pb	1.43	0.62	1.47

PSC prepared using $MAPbI_3$ at 1:3 was found to be higher among all three devices (see Table 2 and Fig. 4) and therefore, 1:3 precursor ratio was considered as optimum for further study.

3.1.2 Effect of Annealing Temperature

To see the impact of annealing temperature on the device efficiency, it is varied from 60 to 100 °C keeping spin speed (2000 rpm) and forerunner ratio (1:3) constant. The significant diffraction peaks of unadulterated $MAPbI_3$ film were gotten at 14.34°, 28.42°, and 32.06° relating to the planes (110), (220), and (310), respectively (see Fig. 5). Figure 5 demonstrates that expansion in the annealing temperature from 60 to 100 °C leads to higher transformation of PbI_2 into $MAPbI_3$ because of better crystallization. This outcome is in good agreement with the outcome revealed by Dualeh et al. (2014). It is confirmed by three dimensional AFM images of $MAPbI_3$ films at various annealing temperatures as shown in Fig. 6. The optical properties of

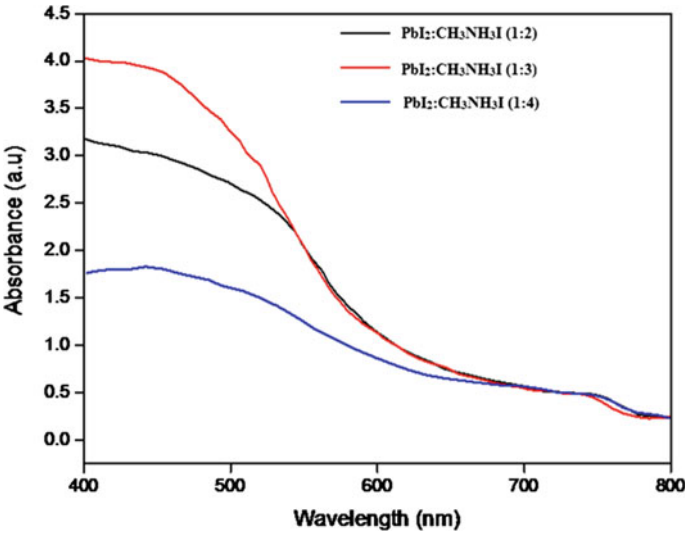

Fig. 3 Absorption spectra of prepared $MAPbI_3$ films at different precursor ratios

Table 2 Experimental data (PCE of PSC) obtained at various processing conditions

Sr. No.	Parameters			Responses			
	Speed (rpm)	Temp (°C)	Ratio (PbI_2:CH_3NH_3I)	Jsc (mA cm^{-2})	Voc (V)	FF (%)	PCE (%)
D_1	2000	100	1:2	8.87 ± 0.17	0.64 ± 0.01	57 ± 0.04	5.67 ± 0.11
D_2	2000	100	1:3	16.89 ± 0.19	0.72 ± 0.03	60 ± 0.05	7.30 ± 0.07
D_3	2000	100	1:4	11.12 ± 0.20	0.71 ± 0.04	62 ± 0.02	6.20 ± 0.09
D_4	2000	60	1:3	11.00 ± 0.15	0.64 ± 0.03	56 ± 0.03	5.41 ± 0.11
D_5	2000	80	1:3	15.54 ± 0.23	0.70 ± 0.02	60 ± 0.04	7.03 ± 0.12
D_6	2500	100	1:3	15.16 ± 0.25	0.71 ± 0.02	66 ± 0.03	6.65 ± 0.10
D_7	3000	100	1:3	15.81 ± 0.26	0.69 ± 0.04	63 ± 0.02	6.82 ± 0.09

$MAPbI_3$ films prepared at various annealing temperatures are shown in Fig. 7. From Fig. 7, it is clear that the light absorption ability (of $MAPbI_3$ film) is observed to be maximum, when prepared at 100 °C annealing temperature. At 60 °C, the absorption is very low that also predicts incomplete conversion of PbI_2 into $MAPbI_3$. Further, the $MAPbI_3$ films acquired at various annealing temperature were connected in PSC creation (D1, D4, and D5, separately). The PCE of the device achieved at 100 °C annealing temperature was watched higher than different devices (see Table 2 and Fig. 4) and in this manner, 100 °C annealing temperature is considered as optimum for further examination.

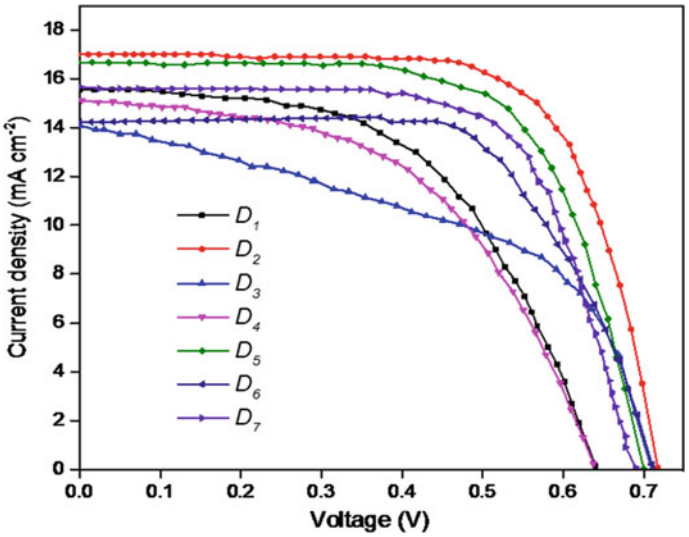

Fig. 4 J–V curve of PSC fabricated at different parametric conditions

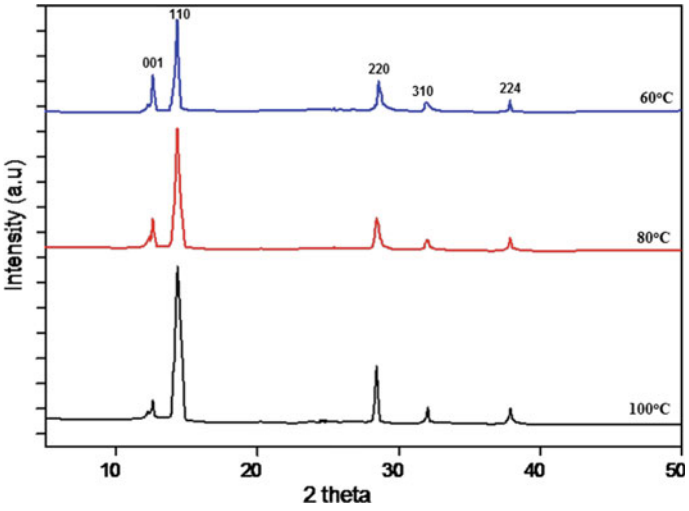

Fig. 5 XRD spectra of prepared $MAPbI_3$ films at different annealing temperatures

3.1.3 Effect of Spin Speed (rpm)

To see the impact of spin speed on the efficiency, annealing temperature (100 °C), and forerunner proportion (1:3) were kept steady and spin speed was varied from 2000 rpm to 3000 rpm. Figure 8 demonstrates the XRD image of $MAPbI_3$ film at different rotating speed. The real diffraction peaks of unadulterated $MAPbI_3$ film

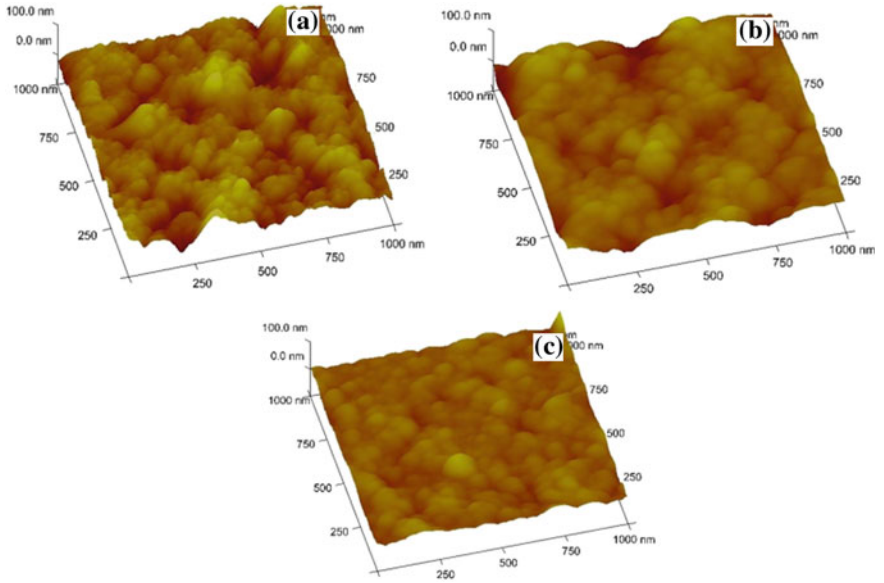

Fig. 6 AFM image of prepared $MAPbI_3$ films at different annealing temperatures

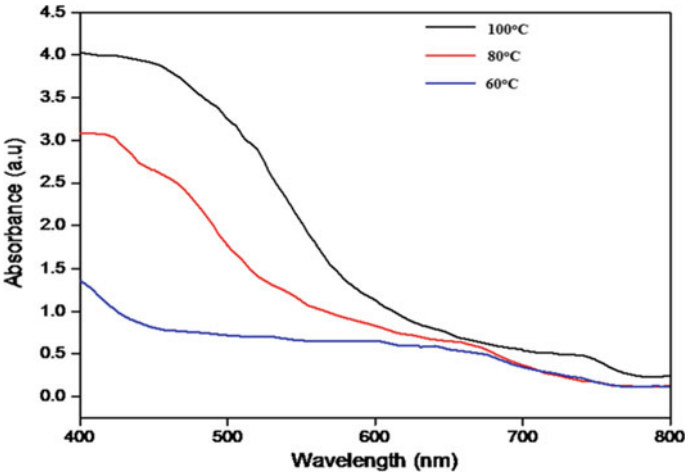

Fig. 7 Absorption spectra of prepared $MAPbI_3$ films at different substrate temperatures

were acquired at 14.34°, 28.42°, and 32.06° comparing to the planes (110), (220), and (310), respectively. The structural properties of $MAPbI_3$ films at different spin speed remains almost unchanged as can be seen from Fig. 8. Therefore, further analysis was not done at different spin speeds. The PCE of the device acquired at

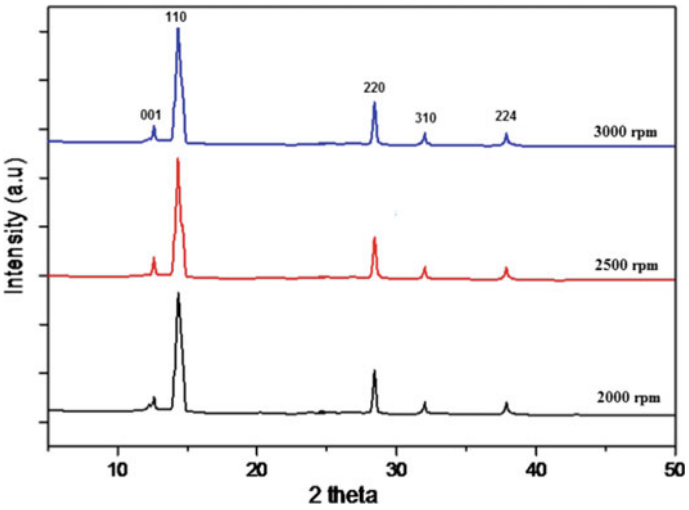

Fig. 8 XRD spectra of prepared $MAPbI_3$ films at different spin speeds

2000 rpm was marginally more among each of the three devices (see Table 1 and Fig. 4, D_1, D_6–D_7). Thus, 2000 rpm spin speed was considered as the optimum.

In this manner, the optimum condition utilizing parametric investigation was seen as an arrangement of forerunner proportion (1:3), substrate temperature (100 °C), and spin speed (2000 rpm).

3.2 Optimization of $MAPbI_3$ Using the Response Surface Methodology

3.2.1 Experimental Design

The experimental design was developed using three-level three-factor BBD model by RSM techniques to see the impact of the deposition process on the PCE of the device. The PCE of PSC achieved by (at 1:1 ratio of PbI_2 and MAI) was not high (Kumari et al. 2019). So a higher ratio (1:2–1:4); was considered in this study. PSCs made at spin speed below 2000 rpm has not given good results so, higher speed (2000–3000 rpm) is considered in this study. PbI_2 to MAI ratio, spin speed and the annealing temperature have been considered as free factors. The annealing temperature was changed from 60 to 100 °C.

The autonomous parameters and their levels of the BBD are appeared in Table 3. The predicted responses were computed by the technique detailed in our past examination (Kumari et al. 2019) and the formed BBD is illustrated in Table 4. To see the significance of models, ANOVA and f-test were performed by the technique made

Table 3 Independent variable and levels used for response surface design

Independent variables	Symbols	Low level (−1)	Medium level (0)	High level (+1)
PbI_2:MAI ratio	X_1	1:2	1:3	1:4
Rotational speed (rpm)	X_2	2000	2500	3000
Annealing temperature (°C)	X_3	60	80	100

Table 4 Experimental data for three-level, three-factor surface response design with coded values of variables

Experimental run	Factors			Response
	X_1 (ratio)	X_2 (rpm)	X_3 (°C)	Y (%)
1	2	2500	100	7.39
2	2	2500	60	5.41
3	3	2000	100	7.41
4	2	2000	80	5.29
5	4	2500	60	4.19
6	3	2000	60	5.59
7	3	3000	60	4.89
8	3	2500	80	7.37
9	4	3000	80	3.69
10	3	2500	80	7.34
11	4	2000	80	4.29
12	3	2500	80	7.31
13	4	2500	100	6.39
14	2	3000	80	4.71
15	3	2500	80	7.36
16	3	3000	100	7.09
17	3	2500	80	7.32

Y: Power conversion efficiency (%) of PSC

reference to in our past investigation (Kumari et al. 2019). What's more, the fitted outcomes are appeared in Table 5. From Table 5, plainly the p-estimation of the quadratic model is under 0.0001. In this way, a quadratic model was considered for further investigation.

Table 5 Adequacy of the model tested

Sequential model sum of squares					
Source	SS	MS	f-value	p-value	Remark
Mean	624.5	624.54			
2FI	0.048	0.0161	0.008	0.9988	
Quadratic	18.31	6.1035	3051.7	<0.0001	Suggested
Cubic	0.011	0.0038	5.846	0.0605	Aliased
Residual	0.002	0.0006			
Total	654.1	38.480			
Model summary statistics					
Source	R^2	Adj. R^2	Pred.R^2	PRESS	Remark
2FI	0.3816	0.0105	−1.070	61.35	
Quadratic	0.9995	0.9989	0.993	0.18	Suggested
Cubic	0.9999	0.9996		+	Aliased

SS: sum of square; MS: mean square
Note +, Case(s) with leverage of 1.0000: PRESS statistic not defined

3.2.2 Second-Order Polynomial Model Building and Statistical Analysis

The last quadratic model got from exploratory information for device efficiency in coded form is appeared in Eq. 1. The ANOVA and f-test of the model represented by Eq. 1 is appeared in Table 6.

From Table 6, plainly the p-value of the quadratic model is under 0.0001. Therefore, the model represented by Eq. 1 is highly significant. The significance of the model is also confirmed by the f-value (1645.34). The f-value of the lack of fit is 5.85 which show the non-significance of lack of fit. Nonsignificant lack of fit of the model depicts that the model condition was adequate for foreseeing the efficiency of PSC. The effects of the film ($MAPbI_3$) deposition parameters on efficiency were investigated. According to Table 6, X_1, X_2, X_3, X_1^2, X_2^2, X_3^2, X_1X_3, and X_2X_3 are significant models for the efficiency of PSC. The experimental data and predicted data of the PCE of PSC are correlated and it is observed that they are in good agreement with each other as can be seen in Fig. 9.

$$\text{Efficiency}\,(\%) = 7.34 - 0.53X_1 - 0.28X_2 + 1.03X_3 - 1.62X_1^2 - 1.22X_2^2 + 0.13X_3^2 - 0.005X_1X_2 + 0.055X_1X_3 + 0.095X_2X_3 \quad (1)$$

Table 6 Analysis of variance (ANOVA) for the fitted quadratic polynomial model

Sources	RC	f-value	p-value	
Model	7.34	1645.34	<0.0001	Significant
X_1	−0.53	1123.60	<0.0001	
X_2	−0.27	302.50	<0.0001	
X_3	1.02	4202.50	<0.0001	
X_1^2	−0.005	5542.12	<0.0001	
X_2^2	0.055	3146.33	<0.0001	
X_3^2	0.095	34.22	0.0006	
X_1X_2	−1.62	0.050	0.8294	
X_1X_3	−1.22	6.05	0.0435	
X_2X_3	0.12	18.05	0.0038	
Lack of fit	–	5.85	0.0605	Not significant
R^2	0.9995			
Adj. R^2	0.9989			
Pred. R^2	0.9937			

RC: regression coefficient

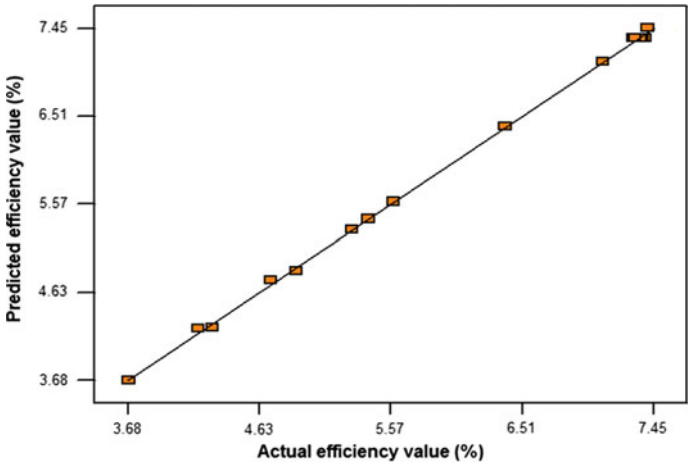

Fig. 9 Scatter diagrams of predicted response versus actual response for Efficiency of PSC

3.2.3 Impact of Process Variables

The interaction of inputs is shown by three dimensional response surface plots (see Fig. 10). Figure 10 shows that the efficiency of device increases when precursor ratio increases from 1:2 to 1:3. A similar type of result is obtained when spin speed increases from 2000 to 2500 rpm, whereas with an increase in spin speed after

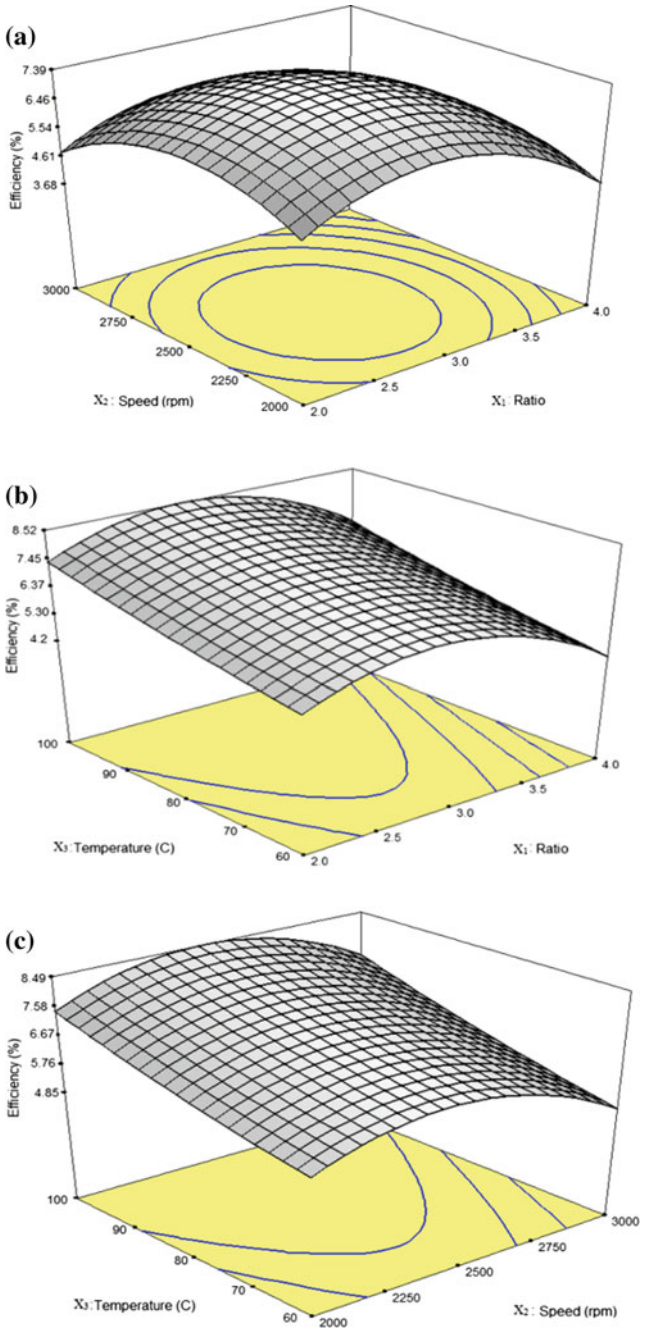

Fig. 10 Three-dimensional (3D) response surface and contour plot for efficiency of PSC and effect of **a** ratio of PbI_2 and CH_3NH_3I (X_1) and spin speed (X_2); X_3 (annealing temperature) = 80 °C, **b** ratio of PbI_2 and CH_3NH_3I (X_1) and annealing temperature (X_3); X_2 = 2500 rpm, and **c** spin speed (X_2) and annealing temperature (X_3); X_1 = 3.00

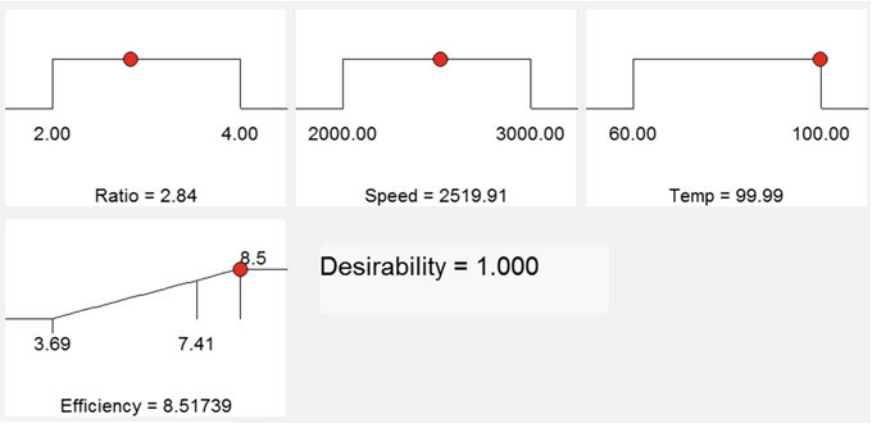

Fig. 11 Ramp graph of desirability function for power conversion efficiency of PSC

2500 rpm, the device efficiency decreases. However, the device efficiency increases with increasing the annealing temperature. From Fig. 10, it is also clear that the efficiency of PSC is maximum at the parameters having a combination of 1:2.8 (the ratio of PbI_2:MAI), 2520 rpm (spinning speed) and 100 °C (annealing temperature). Therefore, this condition was supposed to be an optimum condition.

Further, to justify the optimum condition, desirability of model given by Eq. 1 is checked by the RSM and the slope chart of attractive quality capacity of the model is appeared in Fig. 11. From Fig. 11, obviously the attractive quality of the model at ideal condition is 1.000 and the estimation of PCE of PSC at this condition anticipated by the model was 8.52%. To check the exactness of the model, the analysis was performed at optimum condition and the exploratory estimation of PCE of PSC was found as 8.39% for device efficiency (see Fig. 12). The distinction among anticipated and test esteems was less which affirms the legitimacy of the anticipated model.

3.3 Optical and Electrochemical Analysis of PSC

To support our discoveries, facilitate optical property of PSC was analyzed utilizing UV-visible spectroscopy and photo-luminescence (PL) spectroscopy (Nagane et al. 2014) as illustrated in Fig. 13. From PL examination, a sharp pinnacle is seen at 767 nm. The absorption and PL information are plotted in a similar chart to demonstrate that the observed emission at 767 nm has a tendency to match with the band edge of the perovskite data (728 nm) (see Fig. 13), which infers the nearness of not very many deformity states in the band hole. Additionally, electrochemical impedance spectroscopy measurement (Kim et al. 2013) is employed to analyze the electrochemical property of PSC and also to justify the PCE enhancement at optimum condition, as illustrated in Fig. 14. The EIS of PSCs were performed in dark under a

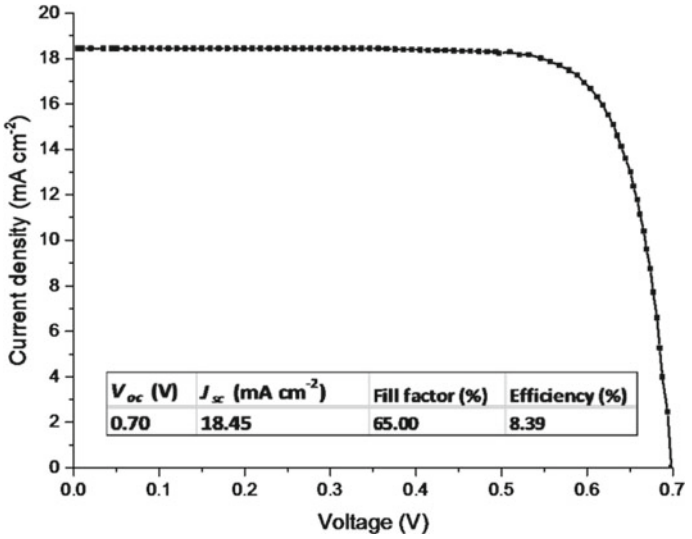

Fig. 12 Current density–voltage (J–V) curve of PSC prepared at optimum condition (inset: data obtained from the graph)

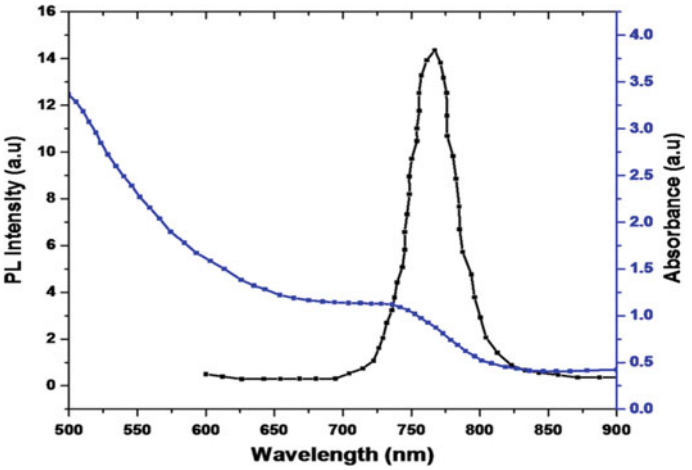

Fig. 13 Absorption and PL-spectra of $MAPbI_3$ film at optimum condition

bias voltage of 0.8 V. From Fig. 14, it is clear that the nature of Nyquist plots for all devices are semicircle in nature. In the equivalent circuit, R_{CT} represents the recombination charge transfer resistance of the cell and *R-CPE* is the resistance-constant phase model. The value of R_S and R_{CT} are 57.74 Ω and 750.79 Ω, respectively, as obtained from Fig. 14.

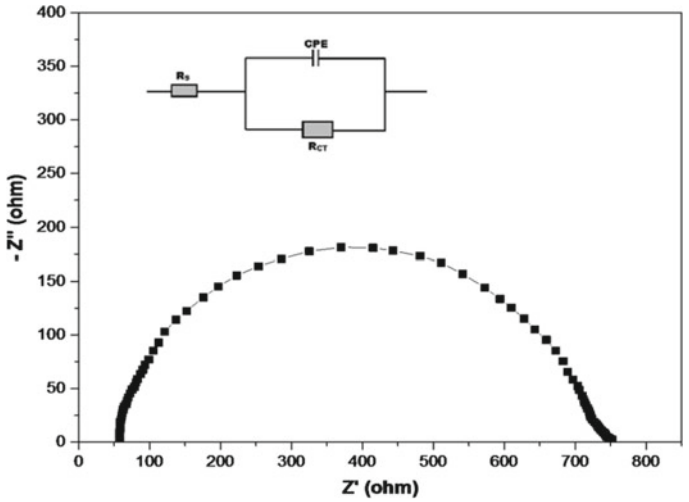

Fig. 14 Nyquist plot (inset: equivalent circuit) of PSC at optimum condition

4 Conclusion

In the present investigation, process parameters for the deposition of $MAPbI_3$ film were optimized utilizing parametric examination and in addition utilizing RSM. The process parameters to be optimized were PbI_2:CH_3NH_3I proportion (1:2–1:4), spin speed (2000–3000 rpm), and annealing temperature (60–100 °C). The parametric investigation has proposed the ideal condition as an arrangement of forerunner proportion (1:2), spin speed (2000 rpm), and annealing temperature (100 °C). After optimizing the deposition parameters, prepared $MAPbI_3$ film was effectively connected in PSC manufacture and the device efficiency at this ideal condition was 7.30%. Besides, to accomplish particular ideal condition, RSM was connected to assess the impact of deposition parameters on the device efficiency. The ideal optimum conditions recommended by RSM was the arrangement of 1:2.8 (the proportion of PbI_2:MAI), 2520 rpm (spinning speed) and 100 °C (annealing temperature). The estimation of the efficiency of PSC anticipated by the model at optimum condition was 8.52% with the desirability quality of 1.000. If there should arise an occurrence of RSM, efficiency was improved up to 8.52% (16.7% improvement) contrasted with 7.30% utilizing parametric investigation. To check the model precision, the test was performed at optimum condition. The exploratory estimation of PCE of PSC at optimum condition was found as 8.39%. The test esteems affirm the legitimacy of the anticipated model.

This research did not receive any specific grant from funding agencies in the public, commercial, or not-for-profit sectors.

References

Biira S, Crouse PL, Bissett H, Alawad BAB, Hlatshwayo TT, Nel JT, Malherbe JB (2017) Optimisation of the synthesis of ZrC coatings in a radio frequency induction-heating chemical vapour deposition system using response surface methodology. Thin Solid Films 624:61–69

Chen Y, Wu W, Ma R, Wang C (2019) Perovskites fabricated with volatile anti-solvents for more efficient solar cells. J Mol Struct 1175:632–637

Dualeh N, Tetreault T, Moehl P, Ga MK, Nazeeruddin M (2014) Gratzel, effect of annealing temperature on film morphology of organic-inorganic hybrid pervoskite solid-state solar cells. Adv Funct Mater 24:3250–3258

Jambo SA, Abdulla R, Marbawi H, Gansau JA (2019) Response surface optimization of bioethanol production from third generation feedstock - eucheuma cottonii. Renew Energy 132:1–10

Jeon NJ, Na H, Jung EH, Yang TY, Lee YG, Kim G, Shin HW, Seok S, Lee J, Seo J (2018) A fluorene-terminated hole-transporting material for highly efficient and stable perovskite solar cells. Nat Energy 3:682–689

Kumari N, Patel SR, Gohel JV (2018a) Enhanced stability and efficiency of Sn containing perovskite solar cell with $SnCl_2$ and SnI_2 precursors. J Mater Sci: Mater Electron 29:18144–18150

Kojima A, Teshima K, Shirai Y, Miyasaka T (2009) Organometal halide perovskites as visible-light sensitizers for photovoltaic. JACS Commun 131:6050–6051

Kumari N, Patel SR, Gohel JV (2018b) Current progress and future prospective of perovskite solar cells: a comprehensive review. Rev Adv Mater Sci 53:161–186

Kim HS, Mora-Sero I, Gonzalez-Pedro V, Francisco FS, Emilio JJP, Park NG, Bisquert J (2013) Mechanism of carrier accumulation in perovskite thin-absorber solar cells. Nat Commun 4:1–7

Kumari N, Gohel JV, Patel SR (2017) Multi-response optimization of ZnO thin films using Grey-Taguchi technique and development of a model using ANN. Optik 144:422–435

Kumari N, Patel SR, Gohel JV (2018c) Optical and structural properties of ZnO thin films prepared by spray pyrolysis for enhanced efficiency perovskite solar cell application. Opt Quant Electron 50:180–201

Kumari N, Gohel JV, Patel SR (2018d) Optimization of TiO_2/ZnO bilayer electron transport layer to enhance efficiency of perovskite solar cell. Mater Sci Semicond Process 75:149–156

Kumari N, Patel SR, Gohel JV (2019) Superior efficiency achievement for FAPbI3-perovskite thin film solar cell by optimization with response surface methodology technique and partial replacement of Pb by Sn. Optik 176:262–277

Lina L, Jianga L, Li P, Fan B, Qiu Y, Yan F (2019) Simulation of optimum band structure of HTM-free perovskite solar cells based on ZnO electron transporting layer. Mater Sci Semicond Process 90:1–6

Lee K, Hsiung S, Wang K, Chang CM, Cheng HM, Kei CC, Tseng ZL, Wu CG (2015) Thickness effects of ZnO thin film on the performance of tri-iodide perovskite absorber based photovoltaics. Sol Energy 120:117–122

Nagane S, Bansode U, Game O, Chhatre S, Ogale SB (2014) CH3NH3PbI(3–x)(BF4)x: molecular ion substituted hybrid perovskite. Chem Commun 50:9741–9744

Noh MFM, Arzaee NA, Safaei J, Mohamed NA, Kim HP, Yusoff ARM, Jang J, Teridi MAM (2019) Eliminating oxygen vacancies in SnO2 films via aerosol-assisted chemical vapour deposition for perovskite solar cells and photoelectrochemical cells. J Alloy Compd 773:997–1008

Rehman F, Mahmood K, Khalid A, Zafar MS, Hameed M (2019) Solution-processed barium hydroxide modified boron-doped ZnO bilayer electron transporting materials: toward stable perovskite solar cells with high efficiency of over 20.5%. J Colloid Interface Sci 535:353–362

Seo YH, Bang SM, Lim B, Na SI (2019) Efficient planar perovskite solar cells with a conjugated random terpolymer as a novel hole-transporting material. Dyes Pigm 160:930–935

Wang H, Zeng W, Xia R (2018) Antisolvent diethyl ether as additive to enhance the performance of perovskite solar cells. Thin Solid Films 663:9–13

Xie H, Liu X, Lyu L, Niu D, Wang Q, Huang J, Gao Y (2016) Effects of precursor ratios and annealing on electronic structure and surface composition of $CH_3NH_3PbI_3$ perovskite films. J Phys Chem C 120:215–220

Xie H, Yin X, Liu J, Guo Y, Chen P, Que W, Wang G, Gao B (2019) Low temperature solution-derived TiO2-SnO2 bilayered electron transport layer for high performance perovskite solar cells. Appl Surf Sci 454:700–707

Yang L, Wang X, Mai X, Wang T, Wang C, Li X, Murugadoss V, Shao Q, Angaiah S, Guo Z (2019) constructing efficient mixed-ion perovskite solar cells based on TiO2 nanorod array. J Colloid Interface Sci 534:459–468

Zhang ZL, Men BQ, Liu YF, Gao HP, Mao YL (2017) Effects of precursor solution composition on the performance and I-V hysteresis of perovskite solar cells based on $CH_3NH_3PbI_{3-x}Cl_x$. Nanoscale Res Lett 12:4–11

Zhang W, Zhang X, Wu T, Sun W, Wu J, Lan Z (2019) Interface engineering with NiO nanocrystals for highly efficient and stable planar perovskite solar cells. Electrochim Acta 293:211–219

Application of Nanotechnology in Diagnosis and Therapeutics

R. Mankamna Kumari, Ritu Goswami and Surendra Nimesh

Abstract The rapid advances in nanotechnology have paved way toward a sustainable path by providing innovative solutions with the issues related to ecosystem as well as human health. In terms of human healthcare and therapy, nanoparticles are expected to contribute to drug delivery and regenerative medicine with its ability to target the source of disease with increased efficiency and minimal side effects. Thus by miniaturizing the drug delivery systems, treatment of several diseases can be made possible. Nanomedicine offers several advantages, such as protection of the payload from degradation in both in vitro and in vivo milieu, facilitation of controlled release of entrapped drugs, prolonged therapeutic effect, and enhancement of targeted delivery along with diminished side effects. Nanotechnology has proved to address some of the problems related to diagnostics, therapeutics, and biomedical aspects. Accordingly, this chapter mainly emphasizes on the evolution of nanoparticles to meet the challenges relevant to healthcare system.

Keywords Polymeric nanoparticles · Inorganic nanoparticles · Therapeutics and diagnostics

1 Introduction

In the last few decades, nanotechnology has gained vast attention owing to its unique and beneficial properties. Nanoparticles (NPs) are colloidal particles within the range of 10–100 nm, with preferential size range of 200 nm for nanomedical applications (Biswas et al. 2014). With the increasing complexity in the treatment of serious ailments, there has been a tremendous advancement to address incurable diseases. However, most of the medications developed so far come with severe side effects that can outweigh the benefits of the drug (Liebler and Guengerich 2005). By applying nanotechnology, efficient drug delivery systems could be developed. Efficiency of nano-drug delivery systems largely depends on the size and charge of the particles.

R. Mankamna Kumari · R. Goswami · S. Nimesh (✉)
Department of Biotechnology, School of Life Sciences, Central University of Rajasthan, Ajmer 305817, Rajasthan, India
e-mail: surendranimesh@curaj.ac.in

L. Ledwani and J. S. Sangwai (eds.), *Nanotechnology for Energy and Environmental Engineering*, Green Energy and Technology,
https://doi.org/10.1007/978-3-030-33774-2_18

The small size and large surface area provide enhanced bioavailability and increased ability to cross the blood-brain barrier and pulmonary system (Kohane 2007). In addition, the new formulation can give a new life to those drugs in the market that are unmarketable due to their low solubility and bioavailability along with toxicity and other side effects. Currently, NPs for drug delivery are synthesized using synthetic or natural polymers besides inorganic materials, as they can be easily customized and targeted to the specific site along with increased bioavailability and controlled release of the drug in the physiological system (Onoue et al. 2014). The targeted approach of drug delivery is mainly achieved by either active or passive route. Passive delivery of drugs is achieved by the small size of NPs and enhanced permeability retention effect owing to high vascularization and permeability of solid tumors (Boylan et al. 2012; Harris et al. 2001). In case of active targeting, ligand grafted NPs are used for its specific binding to cancer cells (Fig. 1). In addition to drug molecules, various nucleic acids have also been explored, such as plasmid DNA, oligonucleotides, miRNA, and siRNA. The limiting factor for the direct delivery of nucleic acids is its high negative charge (Elsabahy et al. 2011; Gao et al. 2011; Guo et al. 2010). Thus, to overcome this barrier, cationic lipids and polymers are employed for the delivery of nucleic acids owing to their high biocompatibility and biodegradability (Bhavsar et al. 2012; Xiong et al. 2011).

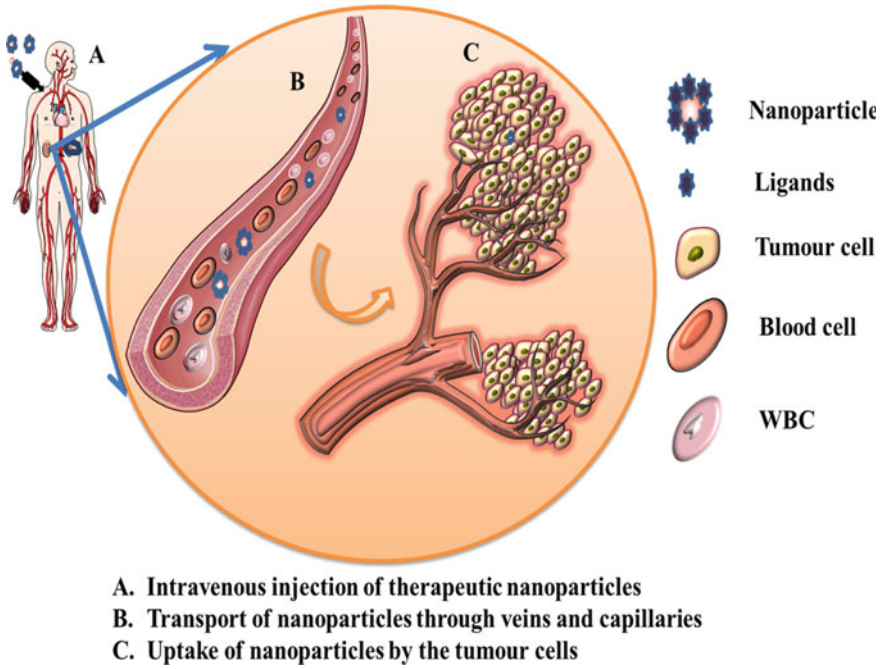

Fig. 1 Represents the uptake of ligand conjugated nanoparticles by the targeted tumor cells

The synthesis approach for polymeric NPs differs from that of inorganic NPs. Several methods are implied for the polymeric nanoparticle synthesis, such as, emulsification, solvent evaporation (Pankhurst et al. 2003; Yoneki et al. 2015), nanoprecipitation (Crucho and Barros 2015; Tang et al. 2015; Yaméogo 2014), supercritical antisolvent (Kalani and Yunus 2012; Zhao et al. 2014) and salt precipitation method (Song et al. 2008). Among these methods, emulsification and solvent evaporation method are the first to synthesize polymeric particles. These NPs are administered via three main routes: oral uptake, direct injection, and inhalation. Upon entering into the systemic circulation, the NPs interact with the proteins before getting distributed to various organs. The lymphatic system works to eliminate foreign particles in the systemic circulation. After filtration process, the fluid containing NPs can be recognized as a foreign material and further engulfed by the macrophage system, thereby clearing from the physiological system. This major drawback in the distribution of NPs could be influenced by controlling size and surface properties of the particles. In general, the efficiency of NPs is enhanced by modulating their surfaces using biocompatible materials such as Polyethylene glycol (PEG) and coating with polymers such as poloxamers and poloxamines. This significantly reduces toxicity and other issues such as opsonisation and promotes internalization by the cell (Fig. 2) (Masood et al. 2013; Shah et al. 2010).

The current chapter summarizes the characteristics of nano-drug formulations along with its several applications in diagnostics as well as therapeutics. Among

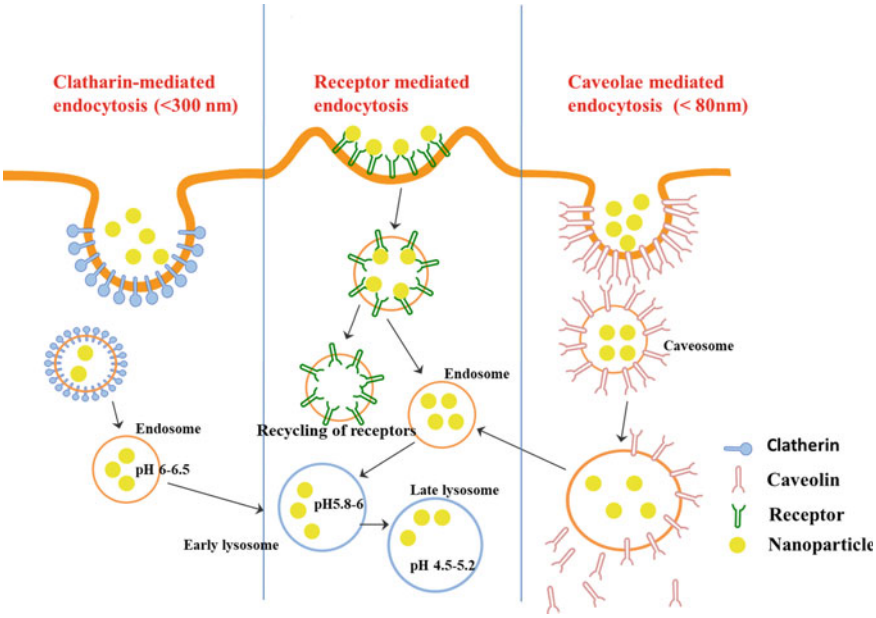

Fig. 2 Different pathways for uptake of nanoparticles by the cell

plethora of polymers and inorganic metals available for synthesis of NPs, polyhydroxyalkanoates (PHA), poly-lactide-co-glycolide (PLGA) and cyclodextrins are widely used for NPs development. On the other hand, silver, gold, carbon nanotubes, and quantum dots are widely investigated in the field of inorganic nanoparticle synthesis for therapeutic process. However, there are certain challenges faced during NPs development, regarding characterization, safety, and manufacturability. The drugs would be ineffective if it degrades within NPs or not released in a controlled manner; this might also lead to toxicity as well as non-specificity. Thus, a complete understanding of size, formulation, composition, toxicity, reactivity, and biodegradability is required to bring nanoformulations to bring it to the clinical level.

2 Characteristics of NPs for Drug Delivery

As discussed earlier, the cellular uptake and pharmacokinetics of the NPs depends mainly on several characteristics of NPs such as size, shape, surface charge, drug loading, and release.

2.1 Effect of Size on Drug Delivery

The size of NPs dictates the toxicity, targetability, and distribution of the drugs (Fig. 3). It has been reported that NPs of size around 100 nm can exhibit 2.5-fold greater uptake than NPs of size range of 1 μm and sixfold greater uptake than 10 μm (Desai et al. 1997). As discussed previously, the major obstacles in drug delivery are rapid clearance of NPs from circulatory system by mononuclear phagocyte system and reticuloendothelial system, which can be prevented by tuning the size of NPs. Also, the size of the NPs has known to influence the cellular uptake by the cells by changing enthalpic and entropic properties that affect the adhesion properties of the cellular receptors and NPs (Elias et al. 2013). Other studies also showed size-dependent uptake. Zhang et al. synthesized ligand coated NPs of size 50 nm that exhibited efficient uptake. Similarly, mesoporous silica NPs developed in the range of 50 nm showed highest uptake by the cells. Also, gold NPs at a size range of 50 nm showed highest uptake in the SKBR-3 cells (Jiang et al. 2008b; Lu et al. 2009; Zhang et al. 2009). Also, endocytosis requires membrane-wrapping process, which becomes feasible with decreased size of particles. Thus, NPs carrying small number of ligands on the surface can easily bind to the receptors. It is to be noted that enthalpic limit for most of the spherical NPs is supposed to be around 30 nm, which indicates that NPs of size less than this will not drive membrane-wrapping process to permit endocytosis to occur effectively (Albanese et al. 2012; Yuan et al. 2010; Zhang et al. 2009). Contrastingly, it was observed that gold NPs coated with Herceptin of size range between 2 and 100 nm showed good cellular uptake in relative to non-coated NPs. Besides size of the NPs, other factors affecting the receptor mediated uptake of NPs

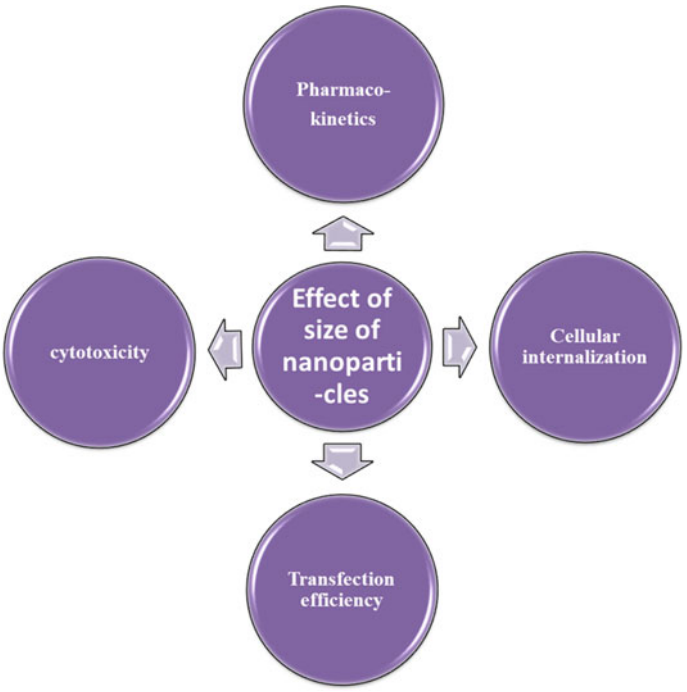

Fig. 3 Represents effect of size on biological properties

are the presence of endosomes and multivesicular bodies. Large NPs drive the process of membrane-wrapping by binding to many receptors. However, the efficiency of NP uptake is lowered due to larger size (>60 nm) resulting in receptor shortage due to increase in entropic penalty. Thus, ligand coated NPs of size between 30 and 60 nm can bind to numerous receptors, thereby enhancing the membrane-wrapping process. However, the optimal diameter of NPs can vary between applications. In addition to this, from most of the studies it has been seen that the maximum uptake of NPs has been in the range of 10–60 nm regardless of its core material or surface charge (Jiang et al. 2008b; Yuan et al. 2010; Zhang et al. 2009).

2.2 Effect of Shape of NPs on Drug Delivery

Besides size of the NPs, shape also plays a crucial role in biological functions (Fig. 4). Though most of the NPs are usually spherical in shape, several nanofabrication methods are capable of synthesizing different shapes of NPs with unique properties (Huang et al. 2006). In one of the studies, it was revealed that the shape of the particles could have a profound effect on the biological properties, such as the filomicelles that are flexible and filamentous micelles built of block copolymer amphiphiles,

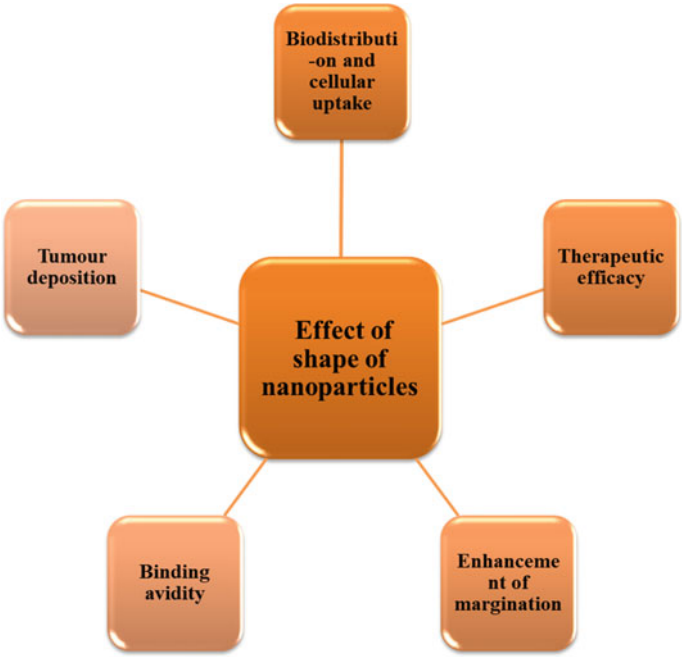

Fig. 4 Represents effect of shape on biological properties and therapeutics

analogous to filovirus and also proplatelets that break up into smaller platelets in blood stream. Thus, long flexibility and length may contribute to long circulation with optimal length up to 8 μm. Also paclitaxel loaded filomicelles showed higher penetration in the tumor stroma that lead to tumor shrinkage and cell apoptosis. Muzykantov's group also studied the effect of disk-shaped carriers toward intercellular adhesion molecules and found longer half-lives (Christian et al. 2009; Geng et al. 2007; Muro et al. 2008; Yoo et al. 2011). Similarly, in another study Decuzzi and Ferrari's group investigated the effect of silicon-based particles within diameter 700–3 μm with quasi-hemispherical, cylindrical, and discoidal shapes. From the studies it was observed that discoidal particles accumulated more efficiently in most of the organs which could be attributed to its higher rotational inertia and surface of contact (Decuzzi et al. 2010). In addition to this, other studies have demonstrated profound effects of shape on phagocytosis as well. Mitragotri's group showed the effect of poly-styrene particles of different sizes and shapes on alveolar macrophages. They found that the cells attached on the major axis of elliptical disk were internalized efficiently within 3 min while cells that were attached to the flat side of disk did not internalize the particle. It was discerned that the tangent angles of the point of attachment of the particles determined its uptake, validated by computational approaches (Champion and Mitragotri 2006; Lamprecht et al. 1999; Yang and Ma 2010). Rod-shaped particles such as pegylated gold nanorods have reduced clearance with longer circulation time in relative to spherical particles. In this support,

nanorods synthesized by self-assembly of amphiphilic dendritic polymer-drug conjugate showed greater circulation with longer blood clearance kinetics, high-cellular uptake as well as higher accumulation (Arnida et al. 2011; Zhou et al. 2013). There are also evidences indicating cylindrical-shaped NPs in contributing to higher circulation times and accumulation in the targeted tissue. For instance, in one of the published study cylindrical silica NPs were found to get deposited in the liver than the discoidal silica particles. Similarly amine-modified mesoporous silica nanorods displayed predominant accumulation in the lungs that the equivalent nanospheres (Dalhaimer et al. 2003, 2004; Geng et al. 2007).

2.3 Effect of Surface Charge

Zeta potential (ZP) is a scientific term for electrokinetic potential that expresses the potential difference between the dispersion medium and fluid that is sticking over the surface of the dispersed particles in the colloidal suspension (Kutscher et al. 2010). This is basically measured by two techniques: microelectrophoresis, which is based on capturing the images of particles moving around, and the other one is electrophoretic light scattering, that is, based on dynamic light scattering (Kedar et al. 2010; Van Butsele et al. 2009). As discussed in the earlier sections, size and shape of the NPs play a critical role in drug delivery. However, it has been observed that negatively charged particles get easily opsonized and cleared by reticuloendothelial system, mainly mediated by liver and spleen. Thus, variation in the surface charge of the NPs can potentially aid in binding to the tissues (Chen et al. 2010; Patil et al. 2007; Reis et al. 2006). Cellular surfaces are rich in negatively charged proteoglycans that play a part in cellular proliferation, migration, and motility. Thus, NPs with higher positive surface charge could show enhanced uptake by the cell. A study conducted by Patil et al. showed enhanced uptake of cerium oxide NPs, which had ZP of −43 mV (Bernfield et al. 1999; Mislick and Baldeschwieler 1996). Whereas particles with less negative or positive charge did not show efficient uptake by the cells. The uptake was highly pronounced due to electrostatic interactions. Interestingly, in another study it was observed that NPs with lesser surface charge also showed uptake by adsorption of negatively charged molecules on the cationic sites in the form of clusters. However, surface modification of NPs can alter the behavior of cellular uptake, as in case of histidine substituted amino group of glycol chitosan self-assembled NPs. Due to strong cationic nature of histidine at acidic pH, it is capable of interacting with the endosomal membrane and its destabilization. Accordingly, the delivery of drugs becomes convenient in case of cancer cells as well. Cancer cell surfaces are usually negatively charged and acid-outside plasma pH gradients. This mediates stronger interactions between cationic NPs and tumor tissues responsible for increased tumor accumulation. This strategy is known as passive targeting or enhanced permeability retention effect (EPR), where particle size along with the surface charge and stability of the particles are known to contribute to the tumor accumulation (Park 2006; Staples et al. 2006). In similar to drug delivery through parenteral route, drug delivery

through skin also follows the same principle. Cationic compounds can easily penetrate through the skin as the skin carries negative surface charge due to the presence of phosphotidylcholine and carbohydrates. Thus, nanoemulsions with phytosphingosine were able to effectively deliver fludrocortisones' acetate and flumethasone through the porcine skin than those of negatively charged ones (Chang et al. 2006; Hoeller et al. 2009; Staples et al. 2006).

3 Polymeric Nanoparticles and Its Role in Therapeutics and Diagnostics

3.1 Chitosan

Chitosan is a heteropolymer made of N-acetyl glucosamine and D-glucosamine subunits which is derived from naturally available polymer, chitin by N-deacetylation process (Kumar 2000). This is an extensively studied polymer that is water-soluble in nature, along with high biocompatibility, biodegradability, hydrophilicity, and other protective properties (Gazori et al. 2009). Besides, numerous other polymers have been implemented for the purpose of drug delivery. However, insoluble polymers used for nanoformulation make use of organic solvents; heat and high shear force that could possibly affect the inherent properties of drugs or therapeutic molecules. Every polymer depending on its constituents exhibits specific physicochemical properties such as charge, lipophilicity, solubility, and particle size (Dobrovolskaia and McNeil 2007; Fischer and Chan 2007; Gazori et al. 2009). Henceforth, the physicochemical factors can potentially affect the pharmacological property as well as the biocompatibility of the polymer. To overcome the biocompatibility issues, surface modification of the NPs with hydrophilic polymers is one of the strategies to prevent opsonisation by improving the surface properties of the NPs in the physiological milieu (Naahidi et al. 2013). Further, several chitosan derivatives were developed such as trimethyl chitosan (Chen et al. 2008a), thiolated chitosan, chitosan esters and conjugates to improve the pharmaceutical efficiency of the polymer (Bernkop-Schnürch et al. 2003) and have been implemented for mucosal, anticancer, and antimicrobial delivery. Chitosan, with its mucoadhesive property has been implemented for the intranasal delivery of drugs such as olanzapine and didanosine to increase its systemic bioavailability (Al-Ghananeem et al. 2010; Baltzley et al. 2014). It is well known that the current anticancer drugs have marked its promising benefits in cancer therapeutics. However, these drugs also pose deleterious side effects. Chitosan NPs were widely studied to deliver several anticancer drugs including methotrexate, curcumin, doxorubicin, and docetaxel. It was observed that chitosan NPs were able to release 50% of methotrexate loaded within 48 h. Doxorubicin loaded NPs were able to release the drug into the cell in its active form. Also, the toxicity of docetaxel was significantly reduced in relative to free drug, with reduction in tumor volume of mice (Anitha et al. 2012; Hwang et al. 2008; Janes et al. 2001; Yang et al. 2008). Further,

antimicrobial drugs such as rifampicin, amphotericin B, and amoxicillin have been extensively utilized for controlled and sustained release of drug to the targeted site and increasing the patient compliance in infectious diseases (Dube et al. 2014; Jain et al. 2014; Lin et al. 2013). Chitosan, nontoxic, low eye irritation, sustained release, mucoadhesive, in situ gelling, transfection, and permeation enhancing properties aid its application in ocular delivery of drugs such as indomethacin and pilocarpine. It was observed that the drug level significantly increased in the anterior segment of the eye and vitreous in relative to indomethacin eye drops. Pilocarpine formulations showed increased sustained release and therapeutic efficacy (Calvo et al. 1996, 1997; Kao et al. 2006; Lin et al. 2007).

3.2 Poly (Lactic-co-Glycolic Acid)

PLGA is a copolymer of lactic acid and glycolic acid, which is currently considered as the best biomaterial for drug delivery. The poly-lactic acid and poly-glycolic acid are basically synthesized in a fixed ratio (Makadia and Siegel 2011). It is synthesized by ring-opening copolymerization of monomers, lactic acid, and glycolic acid via ester linkages. PLGA are present in various forms, depending on the ratio of lactide and glycolide (PLGA (50:50) and PLGA (75:25)). Consequently, the ratio of monomers affects the properties of the polymer. Low molecular weight of the polymer with high-glycolide content display more hydrophilicity, amorphous nature, and less deterioration time. This can be attributed to the hydrophic nature of glycolide. In contrast, polymer with high-lactide content shows more hydrophocity and higher deterioration rate due to less water absorption (Danhier et al. 2012; Prokop and Davidson 2008; Schliecker et al. 2003). Further, physical properties such as molecular weight, polydispersity index, $T_{g,}$ and degree of crystallinity have a profound effect on swelling behavior, biodegradation rate, and mechanical strength of the polymer (Siegel et al. 2006). The unique properties have allowed the polymer application in drug delivery owing to its controlled drug release from weeks to months. The hydrolysed products: lactic acid and glycolic acid are further metabolized into CO_2 and H_2O via Krebs cycle. Thus, PLGA is a widely explored polymer for the purpose of drug delivery (Acharya and Sahoo 2011).

In order to serve as a drug delivery vehicle, the polymeric NPs are required to persist in systemic circulation for a prolonged duration. However, clearance of NPs through reticuloendothelial system (RES) remains to be one of the most challenging problems in the development of drug delivery system (Danhier et al. 2012; Kumari et al. 2010). The clearance of NPs is mainly mediated by binding of opsonin proteins in the blood serum, where the particles are engulfed by phagocytosis. Thus, despite all the beneficial properties, PLGA NPs are prone to renal clearance (Jain et al. 2011). To overcome this trouble, the NPs are subjected to surface modification using hydrophilic molecules to prevent rapid clearance from the body (Jeong et al. 2001). Hydrophilic polymeric nanoparticles have longer retention time in comparison to hydrophobic molecules. Therefore, PLGA were derivatized using hydrophilic

polymers and ionic surfactants such as polyethylene glycol (PEG) and polysorbate 20, 40, 60, and 80, respectively.

Cancer cells, unlike the normal cells have the ability to over-proliferate and over-express cell surface receptors. Utilizing this property of overexpression of the cell surface receptors NPs decorated with ligands could be implemented for the delivery of therapeutic molecules. The receptors mediate the uptake of the molecules via receptor mediated endocytosis (Jain et al. 2011). This phenomenon is known as active targeting. Although, the modified nanoformulations have improved targetability and bioavailability, it is still a challenge to get sufficient amount of NPs around the target region. There are several ligands that are employed for targeted delivery, such as folic acid, transferrin, and biotin, including different polysaccharides and peptides. For example, folate receptors are highly expressed in breast, ovarian, lung, uterine, head and neck cancer. For this purpose, folic acid is used, which has 30 times more affinity than any other folate derivatives. The particles are then taken up by the cell by receptor-mediated endocytosis (Narayanan et al. 2010; Zhao et al. 2008). Similarly, transferrin receptors are overexpressed in glioblastoma which makes them an attractive target for the use of transferrin as ligand molecules. It was noted that transferrin was highly expressed during malignancy due to higher requirement of DNA synthesis for the proliferation of cells (Tortorella and Karagiannis 2014).

Besides its role in cancer therapeutics, PLGA nanoparticles are also implemented for the treatment of other diseases including inflammatory diseases, neurodegenerative and infectious diseases. Gastrointestinal tract (GI) is known to be a complex organ performing diverse functions such as digestion, absorption, and excretion. One of the commonly prevailing diseases, inflammatory bowel disease (IBD) severely affects any part of the GI tract causing improper functioning. The commonly used drugs for its treatment are 5-aminosalicylic acid (5-ASA) or Mesalamine and immunosuppressive agents. However, the cure of the nanoparticles depends mainly on the intensity of the disease and gives symptomatic relief. The disadvantages were overcome by using nanoparticles via rectal administration. This showed higher bioavailability and treatment efficacy (IBD). In another study, fluoromethalone loaded PLGA NPs were developed for the treatment of inflammatory disease of eye. The formulation showed ocular tolerance, anti-inflammatory efficacy and bioavailability. Further, it showed greater penetration toward vitreous and higher anti-inflammatory effects (Gonzalez-Pizarro et al. 2018).

Another group of diseases include neurodegenerative diseases characterized by persistent loss of neuronal activity, which includes Alzheimers (AD) and Parkinsons disease (PD). The prevalence of the disease has increased exponentially in the last years. Their pathogenesis is mainly characterized by accumulation and aggregation of proteins along with alterations and disturbances in tissue homeostasis (Farlow 2001; Kabanov and Gendelman 2007; Sahni et al. 2011; Tosi 2011). FDA approved drugs: galantamine hydrobromide and memantine (MEM) are commonly prescribed according to the degree and intensity of the disease. However, these formulations lack efficacy. Galantamine loaded polymeric nanoparticles were synthesized to overcome the disadvantages and were found to have less cytotoxicity at therapeutic dosage. Similarly, in another study, MEM-PEG-PLGA NPs were synthesized against brain

cell lines (bEnd.3 and astrocytes). The nanoformulation was tested both *in vitro* and *in vivo*. Results showed reduced β-amyloid plaques and inflammation of AD (Sánchez-López et al. 2018). With the increasing use of phytochemicals, curcumin was also utilized for the treatment of AD (Fan et al. 2018).

3.3 Polyethylenimine

Polyethylenimine is a polycationic molecule, that occur in the form of branched (with primary, secondary, and tertiary amines) or linear isomers (lPEI). The polymer has emerged as a favorable vector for the delivery of nucleic acids (NA) at low cost. Branched PEI (bPEI) was first introduced in the year 1995. It soon flourished as a promising vector for transfection studies using oligonucleotides (Bandyopadhyay et al. 1999), plasmids (Liu et al. 2009), and ribozymes (Aigner et al. 2002). bPEI and lPEI behave differently in terms of DNA compactability (Boussif et al. 1995), nuclear uptake (Brunner et al. 2000, 2002), and biological performance (Wightman et al. 2001). For example BPEI forms a stable and smaller sized NPs with more transfectability, whereas lPEI forms NPs of size near micrometer range with more tendency to form aggregation (Goula et al. 1998; Wightman et al. 2001). However, lPEI is known to be less toxic that was seen to exhibit tenfold higher expression of luciferase activity upon nasal instillation in mice (Grosse et al. 2008). The difference in the behavior of bPEI and lPEI could be attributed to the polyplex preparation, administration routes, and other conditions. In addition, nanocomplexes could be delivered by utilizing targeting ligands as discussed in the earlier sections. In one of the studies, hyaluronic acid (HA)-PEI (HA-PEI) conjugate was used for the delivery of siRNA complexes to B16F1 cells expressing hyaluronan receptor-1 (LYVE-1). This showed higher luciferase activity in relative to non-LYVE-1 expressing cell lines (Jiang et al. 2008a). PEGylation of PEI NPs also proved to be beneficial with reduced drawbacks. Unmodified PEI NPs carrying NA shows less efficacy *in vivo* conditions. This could be attributed to its interaction with serum proteins such as albumin, fibrinogen, IgD, IgM, apolipoproeins, and components of compliment system (Ahn et al. 2002; Nguyen et al. 2000; Plank et al. 1996; Tang et al. 2003). The polyplexes get cleared by reticuloendothelial system. Thereby, reducing its plasma circulation life. PEGylation subsequently increased the solubility, blood circulation time, and decreased aggregation as well as macrophage capture (Kichler et al. 2002; Sung et al. 2003; Vonarbourg et al. 2006). Furthermore, PEG could be conjugated to specific ligands to improve its cellular uptake and targetability. In one of the studies, Chen et al. synthesized galactose-PEG-bPEI copolymers that exhibited 4.5–11.6 fold increase in the transfection efficiency in A549 cell line and in mice, respectively, in relative to conventional bPEI/DNA complexes (Chen et al. 2008b). Peptide conjugated PEG-PEI NPs are also being used as a targeting ligand. Kleeman et al. synthesized peptide-conjugated bPEI (25KDa) via hetero-bifunctional PEG spacer (Kleemann et al. 2005). Overall, it was observed that acid-labile linkages of ligand and PEG displayed enhanced improvement of PEGylated vectors. In addition to

PEGylation several other modifications and substitutions of PEI have been investigated. PLGA incorporated PEI NPs not only showed better *in vivo* transfection but also proved to be a suitable vector for DNA vaccination (Bivas-Benita et al. 2009; Chumakova et al. 2008). In a recent study, lPEI was substituted by hydroxyethyl with a degree of substitution varying from 15% to 45%. It was observed that even after the loss of ionizable amines, there was a subsequent increase in pH-independent solubility and buffering capacity. Further, it reduced erythrocyte aggregation, hemolytic potential, in vitro cytotoxicity, and efficient mRNA knockdown (Patil et al. 2018). Multidrug resistance is another common trouble faced in the field of cancer therapeutics. This phenomenon is mediated by the overexpression of P-glycoproteins (P-gp) that plays an important role in resistance to chemotherapy. This plasma membrane glycoprotein causes efflux of major chemotherapeutic drugs such as vinblastine, doxorubin, and paclitaxel (Perez 2009; Riordan et al. 1985; Wind and Holen 2011). P-gp inhibitors are commonly employed to circumvent the problem; however, they are associated with certain side effects such as toxicity, off target distribution and other pharmacokinetic interactions. In a study, phospholipid modified PLGA NPs carrying siRNA against P-gp was introduced in breast cancer. First, DOPE-PEI nanocarriers with PEG coating was introduced in breast tumor model that showed 8% injected dose accumulation in the tumor owing to its property of enhanced permeability retention effect (EPR). In the second experiment, DOPE-PEI/siRNA along with Doxorubicin showed decreased tumor volume by threefold versus control with specific P-gp downregulation (Essex et al. 2015). In a similar type of study, siRNA was targeted against Multidrug resistance-associated protein 1 (MRP1) via PEI capped porous silica NPs. The nanoformulation showed optimized release profile and proved to be biocompatible, better cellular uptake, and effective knockdown of MRP1. With these, there was a profound decrease in the reduction of glioblastoma multifome (GBM) proliferation. The formulation also displayed positive result in mice with significant 82% reduction in the protein level 48 h post injection. In addition, there was no histopathological signs of acute damage in the organs (Tong et al. 2018). The miRNAs also have a role in cancer. To inhibit its activity, short seed-directed LNA oligonucleotides (12- or 14-mer antiseeds) were introduced for miRNA inhibition. It was observed that miRNA against miR-17-5p and miR-20a downregulated the expression of p21 expression than any other miRNA hairpin inhibitors (Thomas et al. 2012).

3.4 Dendrimers

Dendrimers are polymers possessing a core connected to polymer branches, where different molecules are conjugated at its terminals. It is inherently hydrophilic that makes it a good candidate for the delivery of therapeutic molecules including hydrophobic drugs. The small size of polymer (<15 nm) further makes it a suitable candidate for its delivery into tumour through EPR effect. Polyamidoamine

(PAMAM) is the most vividly used dendrimer that is highly biocompatible and water-soluble. In one of the studies, it was reported that hydrophobic molecules can be easily attached at the terminal ends or entrapped in the middle of the polymer. Further, in another study it was found that in the presence of dendrimers, the water insoluble aceclofenac was able to easily solubilize upon increasing the pH of the solution. This was attributed to the fact that the terminal groups of dendrimers reacted with the carboxyl group of aceclofenac (Patel et al. 2011). Similarly different drugs are being used for its delivery *in vitro* for the treatment of several diseases including inflammatory disease, cancer, and infectious diseases. Inflammatory diseases such as arthritis, acute lung inflammation, and retinal degeneration are widely investigated fields. Folate (FA) and methotrexate (MTX) conjugated dendrimer (G5-FA-MTX) were used in a study to ameliorate collagen-induced arthritis in a rat model. The cellular uptake was mediated by receptor-mediated endocytosis and there was significant decrease in the ankle swelling, paw volume, cartilage damage, and bone resorption (Thomas et al. 2011). Similarly, in another study azabisphosphonate (ABP)-capped dendrimer was used for the treatment of rheumatoid arthritis in a mice model. The outcome showed positive results characterized by normal synovial membranes, reduced inflammatory cytokines, and absence of cartilage destruction as well as erosion. The study showed promising role of dendrimers in rheumatoid arthritis (Hayder et al. 2011). Another group of disease described in the earlier sections is cancer. Dendrimers have also been investigated for the delivery of anticancer agents such as cisplatin and doxorubicin. The dendrimer-platinate (Pt) conjugate showed selective accumulation in the tumor tissue via EPR effect with a 50-fold increase in the area under the curve in relative to free cisplatin. Also, the dendrimer-Pt showed less toxicity (Malik et al. 1999). A commonly used anticancer drug such as doxorubicin was also formulated with dendrimer. PEGylated polylysine dendrimers with 50% surface conjugation of doxorubicin through acid-labile 4-hydrazinosulfonyl benzoic acid linker showed efficient antitumor efficacy in walker 256 rat tumor model and human MDA-MB231 xenograft in mice. A direct comparison was made with liposomal formulation that showed reduction in the tumor proliferation >75% in the doses ranging between 2 and 10 mg/Kg with a better tolerance in both the rats (Kaminskas et al. 2012). Infectious diseases such as those induced by *E. coli* and HIV are also investigated for its treatment using dendrimer. The study showed the in vivo antimicrobial efficacy of PAMAM dendrimers and its mechanism. It was observed that upon cervical administration generation-4 neutral dendrimer (G(4)-PAMAM-OH) showed considerable effect on the *E.coli* induced uterine infection in Guinea pig model with chorioamnionitis. The collection of amniotic fluid after treatment showed decrease in the number of E.coli. The possible antibacterial mechanism proposed was its ability to bind to the polyanionic lipopolysaccharide or formation of hydrogen bonds with the O-antigens of E.coli. Further, third mechanism could be its ability to chelate divalent ions in outer cell membrane. It is to be noted that this was the first study showing G(4)-PAMAM-OH dendrimer as an antibacterial agent (Wang et al. 2010). Similarly, SPL7013 Gel (VivaGel(®)), a microbicide was developed for prevention of HIV and HSV. The study showed potential antiviral activity with vaginal administration of

3% SPL7013 gel in healthy women. Also, the antiviral activity was tested in the presence of seminal plasma (Price et al. 2011).

4 Inorganic Nanoparticles in Therapeutics and Diagnostics

4.1 Gold Nanoparticles

The nobel metal NPs are the most notable types of nanoparticle among all. Among the available nobel metal NPs, gold NPs (AuNPs) are an important component for the biomedical applications. To enhance the biological activity and targetability of NPs, AuNPs are readily conjugated with antibodies or oligonucleotides for the detection of target biomolecules. The transportation of therapeutic agents to the cells by using AuNPs is a critical approach in biomedical treatment. Therapeutics can be transported into the cells either by active or passive ways. The passive way of transportation relies on the enhanced permeability and retention (EPR) effect where the gold NPs accumulate in the tumor due to the irregular vasculature (Huang et al. 2007). The active way involves specificity and selectivity for the target analyte by explicitly designed surface functional ligands. Many therapeutic applications have been developed including photothermal therapy, genetic regulation, and drug treatment by using AuNPs for effective targeting and delivery. AuNPs have been found attractive for the formation of transfection agents in gene therapy for the cure of cancer and genetic disorders, where the RNA-AuNPs conjugates used knockdown expression gene in various gene therapies.

Gold NPs are also availed for the drug encapsulation through hydrophobic or hydrophilic pockets generated by the monolayer of polymers such as polyethylene glycol (PEG). Recently, Burda et al. used PEG-coated AuNPs for the encapsulation of cancer treatment drug. The PEG coating provides the amphiphilic environment for capturing hydrophobic silicon phthalocynanin (PC), photo dynamic therapy drug. The results showed that the releasing of drug was through passive accumulation and the PC 4-AuNPs conjugates delivered drugs quickly and penetrated deep inside the tumors within hours. Also, AuNPs are used in clinical diagnosis of cancer, Alzheimer, HIV, hepatitis B, and tuberculosis (Wilson 2008).

Besides, AuNPs are also used for metabolic disorders such as Diabetes mellitus (type-I). It is a metabolic disorder that features high blood sugar levels over a prolonged time period. It is caused by the destruction of insulin secreting beta cells of the pancreatic islets of Langerhans affecting over 0.3% of the world's population every year. Gold NPs are used as potent carriers for the transmucosal insulin delivery. In normal human beings, pancreatic insulin is released as a process of burst in the first phase, followed by the gradual increasing release of insulin for several hours. In the postprandial hyperglycemia (PPHG), there is a loss of insulin secretion in this first phase, which leads to reduced suppression of hepatic glucose production causing higher glucose levels in the blood. So, one is required to provide this initial

phase to treat PPHG (Joshi et al. 2006). Current dosage of insulin comprises four subcutaneous injections per day, which only reduce the serum glucose levels. This therapeutic regimen fails to deliver the insulin in physiological pattern. Insulin is injected from outside in proper dosage. Oral administration of insulin is a challenge due to gastric enzymes which are potent to degrade the insulin. AuNPs are biocompatible and nontoxic in nature hence insulin is loaded on the gold NPs. This gives a sustained release of insulin in the body and helps in the treatment of PPHG.

AuNPs are used as the labels in diagnostics and detection. They are extensively used in the lateral flow devices and immunoassays. Lateral flow devices are very popular among the user stem because of its low cost manufacturing and simplicity that allows nonspecialized users to perform complicated tests easily. It is formed of white porous membrane striped with a line of antibodies or antigen and interfaced with antibodies conjugated with labels which are generally of gold nanoparticles that is used for the detection of low molecular weight targets (Wilson 2008). AuNP have a tremendous use in "bio-barcode assay". This ultrasensitive assay is vigorously used for detecting target proteins and nucleic acids. The principle of "Bio-barcode assay" utilizes conjugated gold NPs with two barcodes oligonucleotides and target specific antibodies and magnetic micro-nanoparticles functionalized with monoclonal antibodies. A large amount of barcode oligonucleotides are released upon detection of target molecule. It provides identification and quantification of the target molecules. Prostate-specific antigen (PSA) can be detected by this method with the detection limit of 330 fg/ml given by Mirkin et al. (Wilson 2008).

There is a passive role of AuNPs in the imaging and detection but it has an active role in sensing. It is preferentially used in the optical sensors. The surface Plasmon resonance of the gold NPs is greatly helpful in optical sensors. There is a dramatic influence of inter-AuNPs distance on the Plasmon resonance, when this distance is reduced to less than the AuNPs diameter; it is the important factor in the sensor application of the AuNPs. The biological analyte linked with AuNPs results in the color change that makes the basis of the sensing. This principle is pioneered by Leuvering. Its sensitivity has been improved by using hyper-Rayleigh scattering, a differential light-scattering spectroscopy (DLSS) (Boisselier and Astruc 2009). These are extensively utilized in electrochemical biosensors. In electrochemical bioassays, AuNPs are used to connect the enzymes to the electrode surfaces. They mediate electrochemical reactions as the redox catalyst and helps in amplification of recognition signals for biological processes. A wire of gold NPs is formed which connects the electrode and the reaction center in the enzyme. The conducting tunnel of AuNPs serves in electron transferring. Thus, the NPs attached to enzymes, for example, glucose oxidase acts as the nanoelectrodes so that the turnover rate of electrons transferred can reach to 5000 which is seven times higher turnover rate of electron transfer from the active site of glucose oxidase to oxygen (Boisselier and Astruc 2009). Example for immunosensor is hepatitis B surface antigen determination kit. It carries multilayer films of negatively charged AuNPs/positively charged tris(2,2́-bipyridyl)cobalt(III) assembled on platinum electrode surface covered with a layer of plasma-polymerized Nafion film. DNA electrochemical sensing contains AuNPs modified with thiol-functionalized oligonucleotides submitted to hybridization of the target DNA sequence. The basic

concept of this assay relies on the release of AuNPs by oxidative metal dissolution and indirect determination of the HBr solubilized Au(III) ions by anodic stripping voltammetry. HBr/Br_2 is highly toxic in nature. So to avoid it, direct electrochemical detection tags were developed (Boisselier and Astruc 2009).

Furthermore, AuNPs are implemented as new contrasting agents for magnetic resonance imaging (MRI). Here AuNPs work as the templating carriers for the gadolinium chelates that are currently used in the clinical diagnosis. The sensitivity of MRI is increased by using the AuNPs along with iron oxide. The gold shell of the particle provides the optical properties and the core of iron oxide will give magnetism (Boisselier and Astruc 2009). In addition, these particles possess an excellent property of fluorescence. This behavior of gold nanoparticle is vitally used in the fluorescence correlation spectroscopy (FCS) and fluorescence microscopy. The fluorescence of AuNPs carries the eminent behavior of anti-photobleaching under strong light illumination. It gives a new cell imaging method. The cells are stained with AuNPs and illuminated under strong light. The florescence of AuNPs on the cell membrane and inside the cell is collected for the cell imaging.

Forensic researchers are making continuous efforts for enhancing the methods for detecting finger prints. Saunders introduced the use of AuNPs in detection of fingerprint and later Schnetz and Margots improved the idea. The colloidal of AuNPs of low pH is used for getting fingerprint present on the substrate. It acts by the mechanism of electrostatic attraction as when the substrate with fingerprint is immersed in the colloidal gold, the particles start bounding to print and later the bound particles are enhanced by catalytic deposition of metallic silver (Wilson 2008).

4.2 Silver Nanopartcles

The widespread use of silver NPs in various fields, including medical, food, health care, and industrial purposes are due to their unique chemical and physical properties. Silver NPs have capability of cellular imaging in vivo. It is widely investigated in studying inflammation, tumors, immune response, and the effect of stem cells. The contrast agents are conjugated or encapsulated to NPs by modifying the surface and bioconjugation of NPs. Due to its stronger and sharper Plasmon resonance, Ag plays an important role in imaging. Earlier nanosilver along with vanadium oxide were used for enhancement of battery performance in next generation active implantable medical devices (Etheridge et al. 2013; Zhang et al. 2016).

Recently silver-based biosensors are designed for the clinical detention of serum P53 in head and neck squamous cell carcinomas. This can easily locate the cancer cells and can absorb the light and destroy the targeted cancer cells selectively by photothermal therapy. Silver NPs have potential usage in cancer diagnostics and treatments. It can cause apoptosis in the cancer cells. Asharani et al. studied human lung cells IMR-90 and brain cancer cells U251 (AshaRani et al. 2008; Zhang et al. 2016). They observed that there were cytosolic proteins attached on the surface of the silver NPs and this may influence the function of intracellular factors which are

involved in certain gene expression and functioning of pro inflammatory cytokines. Autophagy is another anti-cancer mechanism followed by AgNPs. It causes critical cellular damage by NPs and elevated autophagy promotes cell death (Zhang et al. 2016).

Silver NPs are frequently used in antiseptic creams due to its wound healing properties. It also shows a broad biocidial activity against the microorganisms by disrupting their unicellular membrane thus disrupting their enzymatic activities. The antimicrobial activity of AgNPs is very beneficial. They act on bacteria by forming pits in the cellular membrane of the microorganism. This causes structural changes and increases membrane permeability and cell death. Another proposed mechanism of cell death is the formation of free radicals by the silver NPs. The electron spin resonance spectroscopy studies suggest that free radicals formed by the AgNPs have the ability to damage the cell membrane and make it porous which ultimately leads to death of bacteria (Zhang et al. 2016).

The biosynthesized silver NPs are also utilized for the localization of drug molecules inside the cell. They are identified by bright red florescence. Nano silver helps in bioimaging because of its plasmonic properties. It replaces the fluorescent dyes and do not undergo photobleaching. The plasmonic nature of nanosilver can also be used to destroy the unwanted cells (Zhang et al. 2016).

Nowadays, clinical diagnostics strongly rely on the identification of biomarker proteins for disease characterization. The antigens and antibodies are used for molecular recognition in protein biosensening. The metal NPs helps in enhancing the signals in protein detection schemes (Zhang et al. 2016). It is beneficial using the nanostructures in drug delivery systems. Silver NPs are efficient in gastrointestinal delivery of the anti-inflammation drugs.

Another promising advantage of silver NPs in the area of therapeutics is in formation of silver-impregnated catheters. Central venous catheters (CVCs) are regularly used in the hospitals. It has potential infective complications especially, catheters-related bloodstream infections. So to avoid these types of infections antibiotic-impregnated catheters were used. But the problem with antibiotic-impregnated catheters was that it can eventually lead to bacterial resistance. Now a new generation of silver-impregnated catheters has replaced the antibiotic ones. It is based on the use of inorganic silver powder, on which silver ions are bonded with an inert ceramic zeolite. In the comparative studies between silver-impregnated catheters and other catheters it was observed that there were lower bloodstream infections in case of silver-impregnated catheters. There was significantly lower colonization rate in the silver-impregnated CVCs (Wong and Liu 2010). The tip colonization of coagulase negative staphylococci was also less in them. Hence all these properties of these catheters made them used increasingly in the medical field. Ventricular drainage catheters are used in the intensive care patients of acute occlusive hydrocephalus. But the complication with this is the bacterial colonization due to external cerebrospinal fluid (CSF) drainage, resulting in ventriculomeningitis and encephalitis. The silver-impregnated ventricular catheters were the important finding for the neurological and neurosurgical patients requiring external CSF drainage. The scientists observed that the CSF cultures performed at least three times a week showed 25%

more positive cultures in the control groups compared to 0% in the treatment group using silver catheters. Now it is extensively used in the treatment of diseases (Wong and Liu 2010).

Arthritic disease is very common in population. The major symptom of this disease is joint pain and swelling. The treatment for many types of arthritis involves artificial joint replacements.

There is a high risk of bacterial infection in the bone cements such as polymethylmetacrylate when inserted into the human body. Hence, an increasing number of joint infections with multi resistance bacteria are very problematic. Nanosilver came as a boon to overcome this problem. Bone cements loaded with nanosilver have shown high antibacterial activity against multiple strains such as methicilin-resistance staphylococcus aureus (MRSA) and also it does not show any cytotoxicity to osteoblasts grown in vitro. Nanosilver is also used in joint inserts. Earlier the joint inserts were made up of ultra-high molecular weight polyethylene (UHMWPE). The major drawback with longevity of UHMWPE is wear and containment of debris generation, which can activate the macrophages that cause inflammation and eventual failure of the inserts in the joints. Incorporation of silver NPs demonstrated both physical and chemical stabilization of the polymer surface layer toward friction oxidation and degradation. Hence, the use of nanosilver greatly reduces the debris formation and at the same time enhances the biocompatibility and antimicrobial activity of UHMWPE (Wong and Liu 2010).

There is a wide use of surgical mesh in bridging large wounds as well as reinforcements to tissue repair. However, being foreign material for the human body they do carry a risk of infection. It has been observed through data collected that one million nosocomial infections are seen each year in the patients with prosthetic implanted materials. The recent studies showed that silver NPs polypropylene mesh have significant advantages over the regularly used surgical mesh. The silver nanoparticle polypropylene has remarkable bactericidal efficacy against *S. aureus*. Another notable property of silver nanoparticle is that they can diffuse off the mesh and have sustained activity (Wong and Liu 2010).

4.3 Carbon Nanotubes

Carbon NPs (CNTs) are the cylindrical nanostructure of carbon's allotrophes. These cylindrical carbon nanostructures have unique electrical and optical properties which are very beneficial in nanotechnology and other medical technologies. These basically consist of carbon atoms arranged in a series of condensed benzene rings rolled up into the tubular structure. They own extraordinary thermal conductivity and mechanical properties. There are different types of carbon nanotubes single, double, triple, and multi-walled.

Carbon nanotubes have immense role in diagnostics and therapeutics. It is used in various biomedical applications. Absence of acute toxicity, rapid renal clearance,

and relatively long circulation time also makes carbon nanotubes an attractive diagnostic and therapeutic nanodevices. The existing anticancer drugs are potent small molecules, but they are restricted in terms of efficiency as they are toxic systemically and have a narrow therapeutic window. Drug resistance and limited cellular entry are another major limitation of the cancer drugs. Carbon nanotubes have shown great results in cancer drug delivery system (Panchapakesan et al. 2005). It is capable of crossing the biological barriers independently of the cell type they interact with and the functional groups at their surface. It provides large surface areas for the multiple attachments of the targeting drug which is very advantageous over the existing delivery vectors. Carbon nanotubes conjugates such as CNT-methotrexate developed by Pastorin et al. (linked them with covalent linkages), are efficient in drug delivery. The nature of covalent bonds between CNT and small molecules affects the efficiency of the drug. Scientists have explored that non-covalent multi-walled carbon nanotubes (MWNTs) are also efficient for the cancer drug delivery. In a study it was observed that at certain mass ratio of drug and MWNTs have capability of killing human breast cancer cells (Ali-Boucetta et al. 2008). The functionalized CNTs are also used as the nucleic acids delivery vectors. The selective targeting to the tumor cells can also be possible through nanoscale CNTs. The soluble nanoscale CNTs are modified by attaching specific antibodies on the surface. These antibodies help in targeting the tumor cells (Panchapakesan et al. 2005).

Carbon nanotubes exhibits great potential in enhancing the antitumor immunotherapies. Cancer cells have various properties. They easily escape the body's immune response system and develop resistance against it. Antitumor immunotherapies are implied for the cancer treatment that can become more efficient (Meng et al. 2008). There are various antitumor immunotherapies that involve tumor cell vaccines made of inactivated cancer cells, dendritic cells that have been exposed to tumor antigens or cytokines that modulates the immune functions. Here, the remarkable property of CNTs is by using it as transporters for bioactive molecules. The CNTs conjugated with tumor cell lysate proteins show enhancement of specific antitumor immune response (Meng et al. 2008).

Single-wall carbon nanotube (SWCNT) are potent therapeutic nanobomb agents for killing breast cancer cells (Panchapakesan et al. 2005). The working phenomenon of nanobombs is the thermal-energy-confinement in SWCNT bundles and subsequent vapourization of liquids between SWCNT in bundles that creates pressure followed by eventual explosion. This system works in a host of different liquids such as alcohols, deionized water, and phosphate buffered saline system. The cancer cells can be completely explored by using potent nanobombs. These SWCNT are hydrated in sheets and co-localized in the cancer cells. This method causes minimum collateral damage to the neighboring cells. The optimal thermal transitions in SWCNT are the creators of nanobombs (Panchapakesan et al. 2005). The cause of explosion in the nanobombs is hydration of SWCNT and exposure to light that causes the thermal energy to heat the water molecules which in turn creates pressure inside the SWCNT bundles. This method is highly effective against cancer cells (Panchapakesan et al. 2005).

Photoacoustic imaging is used in the biomedical field for imaging the biological tissues by using non-ionizing laser pulses (De La Zerda et al. 2008). It provides higher spatial resolution and allows deeper tissues to be imaged compared to the most optical bio-imaging techniques. There are many diseases which do not show natural photoacoustic agents especially in the early stages. So in these cases it becomes a necessity to administer some photoacoustic agents from outside for better imaging. There are a number of photoacoustic agents available. However, they do not exhibit proper targeting to a diseased site in living subjects (De La Zerda et al. 2008). Single-walled carbon nanotubes conjugated with cyclic Arg-Gly-Asp (RGD) peptides are the potent contrasting agent for photoacoustic imaging of tumors. Mice bearing tumors were injected intravenously with these modified targeted carbon nanotubes showed photoacousting signals to be eight times better than mice injected with non-targeted nanotubes (De La Zerda et al. 2008). The results were cross checked ex vivo by using Raman spectroscopy. Hence, the photoacoustic imaging of targeted single-walled carbon nanotubes can be used in non-invasive cancer imaging and monitoring of nanotherapeutics in living subjects.

Carbon nanotubes are good at biosensing. It provides specific sensing of wide variety of biological species. It performs sensing operation without the use of any labels or complex reaction schemes. Single-walled carbon nanotubes provide optical detection of DNA conformational polymorphism (Heller et al. 2006). There is a synthetic approach which uses cell free synthesis on to SWCNT for the production of label free protein microarray capable of single protein detection (Ahn et al. 2011). These are used for detection of single molecules as well.

4.4 Quantum Dots

Quantum dots (QDs) are tiny semiconductors that are few nanometers in size. They show wide electronic and optical properties which differ from the LED particles. These quantum dots when excited by electricity or light, emits light at the frequencies that can precisely be tuned by changing the dot's size, shape material, enabling myriad application.

Quantum dots are one of the most vital and fascinating nanomaterial among several metallic NPs that are involved in biomedical application. They have been focused on potential applications in cancer diagnosis and therapy. These are frequently used in bioimaging of living cells and tissues as bio probes or labels (Onoshima et al. 2015) and incorporated in various biological assays for reversible detection and quantification of biomolecules. These assays are based on distance-dependent fluorescence resonance energy transfer (FRET) and multiplexed bioanalysis with multiple colors. It is further utilized in immunoassays, molecular diagnosis, clinical analysis, and cellular analysis (Onoshima et al. 2015).

QDs help in biological imaging and cellular studies but the toxic nature of cadmium is the major concern. The recent advancement developed the cadmium-free quantum dots. This made easy in vitro and in vivo bio-imaging studies. The cellular

uptake studies can be modulated by size, shape, and surface functionalization. The multicolor quantum dots are efficient in stem cell bio imaging. QD-based FRET probes are developed that includes QDs-conjugated hybridization probes for preliminary screening of siRNA sequences. The unique photophysical properties of QDs are used in ultra-sensitive nanosensors (single QDs) (Onoshima et al. 2015).

Quantum dots have very high efficiency for sensitive detection of cancer biomarkers such as breast cancer, ovarian cancer, and prostate cancer. The two tumor biomarkers, alpha-fetoprotein, carcinoembryonic antigen in human serum, were detected by Quantum dot-based nanosensors. Nucleic acids are effective tumor markers. QDs show very useful detection of nucleic acids, especially in a multiplexed format. The target sequences can be detected simultaneously by using FRET assay that uses immobilized QDs as donors. A single quantum dot-based nanosensors have been developed for specific miRNA detection. There are various ways for miRNA detection, but there are problems such as low sensitivity and less specificity. Single-QD-based nanosensor was fabricated to overcome these problems. They have been utilized as imaging probes, especially in cancer research for the recognition of the special cell types and tissues in the clinical settings. QD probes such as ABC tri-block copolymer coated QDs have been developed for imaging prostrate cancer. Glioma cells can be detected by using QDs nanoprobes. These cells overexpress extracellular matrix glycoproteins, tenascin-C. Tenascin-C have the key role in tissue remodeling and invasion of glioblastoma into surrounding brain tissue. A single-stranded aptamer for targeting QDs to tenascin-C (Onoshima et al. 2015).

The prominent fluorescence properties of QDs are used in Fluorescent imaging (FI) helps in detecting the transplanted stem cells in vivo. This provides higher sensitivity in comparison to other imaging modalities. Thus, "stem cell labeling technology using QDs" and "in vivo fluorescent imaging technology for visualizing transplanted stem cells labeled with QDs" are vitally used for analyzing the transplanted stem cells (Onoshima et al. 2015).

4.5 Iron Oxide NPS

In recent years, the medicine and biology have progressed a lot in pharmaceutical domain. Metal NPs have advanced application in biomedical field. Iron NPs have most developed applications in resonance imaging and biosensors. The super paramagnetic iron oxides (SPIONs) have been extensively used in the cancer imaging and therapy. They have immense qualities and controllable properties such as size, shape, magnetism, crystallinity, and flexibility. The multifunctional SPIONs with fluorescence are used for targeting ligands, drugs, etc.

MRI is most widely used medical diagnostic techniques. It is difficult to differentiate between normal and abnormal tissues, therefore some specific exogenous contrast agents are required to increase the contrast and obtain higher resolution and sensitivity. SPIONs are the best contrasting agent used in the MR imaging techniques. They work as MR imaging probes by (i) Magnetism: when external magnetic field is

applied, the super paramagnetic SPIONs show high magnetism and it becomes zero in the absence of external magnetic field. They give the negative contrast as dark in appearance by enhancing T_2/T_2^* relaxivity of water protons for MRI. Here, the core of NPs is of SPIONs. (ii) Well developed surface coating and functionality: the magnetic NPs are coated with targeting ligands such as proteins, peptides, antibodies, polymers, carbohydrates, aptamers, DNA, RNA, oligosaccharides to improve the target—specific delivery (Yen et al. 2013).

Iron oxide NPs have potential application in the field of neurooncology and other CNS inflammatory conditions. Ultra small superparamagnetic iron oxide NPs (USPIONs) are utilized in the imaging of central nervous system tumors. The actual mechanism of accumulation of USPIONs in the cells is not known but it is believed that this might be due to its prolong circulation time and uptake by the inflammatory cells within and around the tumor. For CNS tumor imaging, the evaluation of low concentrations of iron oxide NPs transversing the blood-brain barrier (BBB) is done by T_1 weighted scans. But the imaging is also dependent on the MRI acquisition including the magnetic field strength (Weinstein et al. 2010).

5 Conclusion

Nanomedicine has already laid its strong impact on different areas of diagnostics and therapeutics as discussed in the aforementioned sections. Though a large number of nanomedicines have advanced into preclinical and clinical trials, there has been only 20 nanoparticle therapeutics currently in clinical use. However, this shows its ability to improve the therapeutic index of drugs. Further, other nanomedicines already in the preclinical phase would come to the market in near future. With persistent and continues research, nanotechnology would soon have a tremendous impact on health sector.

References

Acharya S, Sahoo SK (2011) PLGA nanoparticles containing various anticancer agents and tumour delivery by EPR effect. Adv Drug Deliv Rev 63:170–183

Ahn C-H, Chae SY, Bae YH, Kim SW (2002) Biodegradable poly (ethylenimine) for plasmid DNA delivery. J Control Release 80:273–282

Ahn J-H et al (2011) Label-free, single protein detection on a near-infrared fluorescent single-walled carbon nanotube/protein microarray fabricated by cell-free synthesis. Nano Lett 11:2743–2752

Aigner A, Fischer D, Merdan T, Brus C, Kissel T, Czubayko F (2002) Delivery of unmodified bioactive ribozymes by an RNA-stabilizing polyethylenimine (LMW-PEI) efficiently down-regulates gene expression. Gene Ther 9:1700

Al-Ghananeem AM, Saeed H, Florence R, Yokel RA, Malkawi AH (2010) Intranasal drug delivery of didanosine-loaded chitosan nanoparticles for brain targeting; an attractive route against infections caused by AIDS viruses. J Drug Target 18:381–388

Albanese A, Tang PS, Chan WC (2012) The effect of nanoparticle size, shape, and surface chemistry on biological systems. Annu Rev Biomed Eng 14:1–16

Ali-Boucetta H, Al-Jamal KT, McCarthy D, Prato M, Bianco A, Kostarelos K (2008) Multiwalled carbon nanotube–doxorubicin supramolecular complexes for cancer therapeutics. Chem Commun 459–461

Anitha A, Maya S, Deepa N, Chennazhi K, Nair S, Jayakumar R (2012) Curcumin-loaded N, O-carboxymethyl chitosan nanoparticles for cancer drug delivery. J Biomater Sci Polym Ed 23:1381–1400

Arnida M, Ray A, Peterson C, Ghandehari H (2011) Geometry and surface characteristics of gold nanoparticles influence their biodistribution and uptake by macrophages. Eur J Pharm Biopharm 77:417

AshaRani P, Low Kah Mun G, Hande MP, Valiyaveettil S (2008) Cytotoxicity and genotoxicity of silver nanoparticles in human cells. ACS Nano 3:279–290

Baltzley S, Mohammad A, Malkawi AH, Al-Ghananeem AM (2014) Intranasal drug delivery of olanzapine-loaded chitosan nanoparticles. AAPS PharmSciTech 15:1598–1602

Bandyopadhyay P, Ma X, Linehan-Stieers C, Kren BT, Steer CJ (1999) Nucleotide exchange in genomic DNA of rat hepatocytes using RNA/DNA oligonucleotides Targeted delivery of liposomes and polyethyleneimine to the asialoglycoprotein receptor. J Biol Chem 274:10163–10172

Bernfield M, Götte M, Park PW, Reizes O, Fitzgerald ML, Lincecum J, Zako M (1999) Functions of cell surface heparan sulfate proteoglycans. Annu Rev Biochem 68:729–777

Bernkop-Schnürch A, Kast C, Guggi D (2003) Permeation enhancing polymers in oral delivery of hydrophilic macromolecules: thiomer/GSH systems. J Control Release 93:95–103

Bhavsar D, Subramanian K, Sethuraman S, Maheswari Krishnan U (2012) Translational siRNA therapeutics using liposomal carriers: prospects & challenges. Curr Gene Ther 12:315–332

Biswas AK, Islam MR, Choudhury ZS, Mostafa A, Kadir MF (2014) Nanotechnology based approaches in cancer therapeutics. Adv Nat Sci: Nanosci Nanotechnol 5:043001

Bivas-Benita M et al (2009) Pulmonary delivery of DNA encoding Mycobacterium tuberculosis latency antigen Rv1733c associated to PLGA–PEI nanoparticles enhances T cell responses in a DNA prime/protein boost vaccination regimen in mice. Vaccine 27:4010–4017

Boisselier E, Astruc D (2009) Gold nanoparticles in nanomedicine: preparations, imaging, diagnostics, therapies and toxicity. Chem Soc Rev 38:1759–1782

Boussif O, Lezoualc'h F, Zanta MA, Mergny MD, Scherman D, Demeneix B, Behr J-P (1995) A versatile vector for gene and oligonucleotide transfer into cells in culture and in vivo: polyethylenimine. Proc Natl Acad Sci 92:7297–7301

Boylan NJ, Suk JS, Lai SK, Jelinek R, Boyle MP, Cooper MJ, Hanes J (2012) Highly compacted DNA nanoparticles with low MW PEG coatings: in vitro, ex vivo and in vivo evaluation. J Control Release 157:72–79

Brunner S, Fürtbauer E, Sauer T, Kursa M, Wagner E (2002) Overcoming the nuclear barrier: cell cycle independent nonviral gene transfer with linear polyethylenimine or electroporation. Mol Ther 5:80–86

Brunner S, Sauer T, Carotta Sea, Cotten M, Saltik M, Wagner E 2000 Cell cycle dependence of gene transfer by lipoplex, polyplex and recombinant adenovirus. Gene Ther 7:401

Calvo P, Alonso MJ, Vila-Jato JL, Robinson JR (1996) Improved ocular bioavailability of indomethacin by novel ocular drug carriers. J Pharm Pharmacol 48:1147–1152

Calvo P, Vila-Jato JL, Alonso MaJ (1997) Evaluation of cationic polymer-coated nanocapsules as ocular drug carriers. Int J Pharm 153:41–50

Champion JA, Mitragotri S (2006) Role of target geometry in phagocytosis. Proc Natl Acad Sci 103:4930–4934

Chang JH et al (2006) Characterization and formation of phospholipid nanoemulsion coatings on Mg-modified sericite surface. J Ind Eng Chem 12:635–638

Chen C-C, Tsai T-H, Huang Z-R, Fang J-Y (2010) Effects of lipophilic emulsifiers on the oral administration of lovastatin from nanostructured lipid carriers: physicochemical characterization and pharmacokinetics. Eur J Pharm Biopharm 74:474–482

Chen F, Zhang Z-R, Yuan F, Qin X, Wang M, Huang Y (2008a) In vitro and in vivo study of N-trimethyl chitosan nanoparticles for oral protein delivery. Int J Pharm 349:226–233
Chen J et al (2008b) Galactose-poly (ethylene glycol)-polyethylenimine for improved lung gene transfer. Biochem Biophys Res Commun 375:378–383
Christian DA, Cai S, Garbuzenko OB, Harada T, Zajac AL, Minko T, Discher DE (2009) Flexible filaments for in vivo imaging and delivery: persistent circulation of filomicelles opens the dosage window for sustained tumor shrinkage. Mol Pharm 6:1343–1352
Chumakova OV et al (2008) Composition of PLGA and PEI/DNA nanoparticles improves ultrasound-mediated gene delivery in solid tumors in vivo. Cancer Lett 261:215–225
Crucho CI, Barros MT (2015) Formulation of functionalized PLGA polymeric nanoparticles for targeted drug delivery. Polymer 68:41–46
Dalhaimer P, Bates FS, Discher DE (2003) Single molecule visualization of stable, stiffness-tunable, flow-conforming worm micelles. Macromolecules 36:6873–6877
Dalhaimer P, Bermudez H, Discher D (2004) Biopolymer mimicry with polymeric worm-like micelles: MW-scaled flexibility, locked-in curvature, and coexisting microphases. In: Abstracts of papers of the American chemical society, 2004. Amer chemical soc 1155 16th St, NW, Washington, DC 20036 USA, pp U543–U544
Danhier F, Ansorena E, Silva JM, Coco R, Le Breton A, Préat V (2012) PLGA-based nanoparticles: an overview of biomedical applications. J Control Release 161:505–522
De La Zerda A et al (2008) Carbon nanotubes as photoacoustic molecular imaging agents in living mice. Nat Nanotechnol 3:557
Decuzzi P, Godin B, Tanaka T, Lee S-Y, Chiappini C, Liu X, Ferrari M (2010) Size and shape effects in the biodistribution of intravascularly injected particles. J Control Release 141:320–327
Desai MP, Labhasetwar V, Walter E, Levy RJ, Amidon GL (1997) The mechanism of uptake of biodegradable microparticles in Caco-2 cells is size dependent. Pharm Res 14:1568–1573
Dobrovolskaia MA, McNeil SE (2007) Immunological properties of engineered nanomaterials. Nat Nanotechnol 2:469
Dube A, Reynolds JL, Law W-C, Maponga CC, Prasad PN, Morse GD (2014) Multimodal nanoparticles that provide immunomodulation and intracellular drug delivery for infectious diseases. Nanomed Nanotechnol Biol Med 10:831–838
Elias DR, Poloukhtine A, Popik V, Tsourkas A (2013) Effect of ligand density, receptor density, and nanoparticle size on cell targeting. Nanomedicine: Nanotechnol Biol Med 9:194–201
Elsabahy M, Nazarali A, Foldvari M (2011) Non-viral nucleic acid delivery: key challenges and future directions. Curr Drug Deliv 8:235–244
Essex S, Navarro G, Sabhachandani P, Chordia A, Trivedi M, Movassaghian S, Torchilin VP (2015) Phospholipid-modified PEI-based nanocarriers for in vivo siRNA therapeutics against multidrug-resistant tumors. Gene Ther 22:257
Etheridge ML, Campbell SA, Erdman AG, Haynes CL, Wolf SM, McCullough J (2013) The big picture on small medicine: the state of nanomedicine products approved for use or in clinical trials. Nanomedicine: Nanotechnol Biol Med 9:1
Fan S et al (2018) Curcumin-loaded PLGA-PEG nanoparticles conjugated with B6 peptide for potential use in Alzheimer's disease. Drug Deliv 25:1091–1102
Farlow MR (2001) Pharmacokinetic profiles of current therapies for Alzheimer's disease: implications for switching to galantamine. Clin Ther 23:A13–A24
Fischer HC, Chan WC (2007) Nanotoxicity: the growing need for in vivo study. Curr Opin Biotechnol 18:565–571
Gao Y, Liu X-L, Li X-R (2011) Research progress on siRNA delivery with nonviral carriers. Int J Nanomed 6:1017
Gazori T, Khoshayand MR, Azizi E, Yazdizade P, Nomani A, Haririan I (2009) Evaluation of Alginate/Chitosan nanoparticles as antisense delivery vector: formulation, optimization and in vitro characterization. Carbohydr Polym 77:599–606
Geng Y, Dalhaimer P, Cai S, Tsai R, Tewari M, Minko T, Discher DE (2007) Shape effects of filaments versus spherical particles in flow and drug delivery. Nat Nanotechnol 2:249

Gonzalez-Pizarro R, Silva-Abreu M, Calpena AC, Egea MA, Espina M, García ML (2018) Development of fluorometholone-loaded PLGA nanoparticles for treatment of inflammatory disorders of anterior and posterior segments of the eye. Int J Pharm 547:338–346

Goula D, Remy J, Erbacher P, Wasowicz M, Levi G, Abdallah B, Demeneix B (1998) Size, diffusibility and transfection performance of linear PEI/DNA complexes in the mouse central nervous system. Gene Ther 5:712

Grosse S et al (2008) In vivo gene delivery in the mouse lung with lactosylated polyethylenimine, questioning the relevance of in vitro experiments. J Control Release 132:105–112

Guo J, Fisher KA, Darcy R, Cryan JF, O'Driscoll C (2010) Therapeutic targeting in the silent era: advances in non-viral siRNA delivery. Mol BioSyst 6:1143–1161

Harris JM, Martin NE, Modi M (2001) Pegylation. Clin Pharmacokinet 40:539–551

Hayder M et al (2011) A phosphorus-based dendrimer targets inflammation and osteoclastogenesis in experimental arthritis. Sci Transl Med 3:81ra35–81ra35

Heller DA, Jeng ES, Yeung T-K, Martinez BM, Moll AE, Gastala JB, Strano MS (2006) Optical detection of DNA conformational polymorphism on single-walled carbon nanotubes. Science 311:508–511

Hoeller S, Sperger A, Valenta C (2009) Lecithin based nanoemulsions: a comparative study of the influence of non-ionic surfactants and the cationic phytosphingosine on physicochemical behaviour and skin permeation. Int J Pharm 370:181–186

Huang X, El-Sayed IH, Qian W, El-Sayed MA (2006) Cancer cell imaging and photothermal therapy in the near-infrared region by using gold nanorods. J Am Chem Soc 128:2115–2120

Huang X, Jain PK, El-Sayed IH, El-Sayed MA (2007) Gold nanoparticles: interesting optical properties and recent applications in cancer diagnostics and therapy

Hwang H-Y, Kim I-S, Kwon IC, Kim Y-H (2008) Tumor targetability and antitumor effect of docetaxel-loaded hydrophobically modified glycol chitosan nanoparticles. J Control Release 128:23–31

Jain AK, Das M, Swarnakar NK, Jain S (2011) Engineered PLGA nanoparticles: an emerging delivery tool in cancer therapeutics. Crit Rev Ther Drug Carrier Syst 28:1–45

Jain V, Gupta A, Pawar VK, Asthana S, Jaiswal AK, Dube A, Chourasia MK (2014) Chitosan-assisted immunotherapy for intervention of experimental leishmaniasis via amphotericin B-loaded solid lipid nanoparticles. Appl Biochem Biotechnol 174:1309–1330

Janes KA, Fresneau MP, Marazuela A, Fabra A, Alonso MaJ (2001) Chitosan nanoparticles as delivery systems for doxorubicin. J Control Release 73:255–267

Jeong YI, Cho CS, Kim SH, Ko KS, Kim SI, Shim YH, Nah JW (2001) Preparation of poly (DL-lactide-co-glycolide) nanoparticles without surfactant. J Appl Polym Sci 80:2228–2236

Jiang G et al. (2008a) Hyaluronic acid–polyethyleneimine conjugate for target specific intracellular delivery of siRNA. Biopolym: Orig Res Biomol 89:635–642

Jiang W, Kim BY, Rutka JT, Chan WC (2008b) Nanoparticle-mediated cellular response is size-dependent. Nat Nanotechnol 3:145

Joshi HM, Bhumkar DR, Joshi K, Pokharkar V, Sastry M (2006) Gold nanoparticles as carriers for efficient transmucosal insulin delivery. Langmuir 22:300–305

Kabanov A, Gendelman HE (2007) Nanomedicine in the diagnosis and therapy of neurodegenerative disorders. Prog Polym Sci 32:1054–1082

Kalani M, Yunus R (2012) Effect of supercritical fluid density on nanoencapsulated drug particle size using the supercritical antisolvent method. Int J Nanomed 7:2165–2172

Kaminskas LM et al (2012) Doxorubicin-conjugated PEGylated dendrimers show similar tumoricidal activity but lower systemic toxicity when compared to PEGylated liposome and solution formulations in mouse and rat tumor models. Mol Pharm 9:422–432

Kao HJ, Lo YL, Lin HR, Yu SP (2006) Characterization of pilocarpine-loaded chitosan/Carbopol nanoparticles. J Pharm Pharmacol 58:179–186

Kedar U, Phutane P, Shidhaye S, Kadam V (2010) Advances in polymeric micelles for drug delivery and tumor targeting. Nanomed Nanotechnol Biol Med 6:714–729

Kichler A, Chillon M, Leborgne C, Danos O, Frisch B (2002) Intranasal gene delivery with a polyethylenimine–PEG conjugate. J Control Release 81:379–388
Kleemann E et al (2005) Nano-carriers for DNA delivery to the lung based upon a TAT-derived peptide covalently coupled to PEG–PEI. J Control Release 109:299–316
Kohane DS (2007) Microparticles and nanoparticles for drug delivery. Biotechnol Bioeng 96:203–209
Kumar MNR (2000) A review of chitin and chitosan applications. React Funct Polym 46:1–27
Kumari A, Yadav SK, Yadav SC (2010) Biodegradable polymeric nanoparticles based drug delivery systems. Colloids Surf B: Biointerfaces 75:1–18
Kutscher HL et al (2010) Enhanced passive pulmonary targeting and retention of PEGylated rigid microparticles in rats. Int J Pharm 402:64–71
Lamprecht A, Ubrich N, Pérez MH, Lehr C-M, Hoffman M, Maincent P (1999) Biodegradable monodispersed nanoparticles prepared by pressure homogenization-emulsification International. J Pharm 184:97–105
Liebler DC, Guengerich FP (2005) Elucidating mechanisms of drug-induced toxicity. Nat Rev Drug Discov 4:410–420
Lin H-R, Yu S-P, Kuo C-J, Kao H-J, Lo Y-L, Lin Y-J (2007) Pilocarpine-loaded chitosan-PAA nanosuspension for ophthalmic delivery. J Biomater Sci Polym Ed 18:205–221
Lin Y-H, Tsai S-C, Lai C-H, Lee C-H, He ZS, Tseng G-C (2013) Genipin-cross-linked fucose–chitosan/heparin nanoparticles for the eradication of Helicobacter pylori. Biomaterials 34:4466–4479
Liu Y, Nguyen J, Steele T, Merkel O, Kissel T (2009) A new synthesis method and degradation of hyper-branched polyethylenimine grafted polycaprolactone block mono-methoxyl poly (ethylene glycol) copolymers (hy-PEI-g-PCL-b-mPEG) as potential DNA delivery vectors. Polymer 50:3895–3904
Lu F, Wu SH, Hung Y, Mou CY (2009) Size effect on cell uptake in well-suspended, uniform mesoporous silica nanoparticles. Small 5:1408–1413
Makadia HK, Siegel SJ (2011) Poly lactic-co-glycolic acid (PLGA) as biodegradable controlled drug delivery carrier. Polymers 3:1377–1397
Malik N, Evagorou EG, Duncan R (1999) Dendrimer-platinate: a novel approach to cancer chemotherapy. Anti-Cancer Drugs 10:767–776
Masood F, Chen P, Yasin T, Fatima N, Hasan F, Hameed A (2013) Encapsulation of Ellipticine in poly-(3-hydroxybutyrate-co-3-hydroxyvalerate) based nanoparticles and its in vitro application. Mater Sci Eng C 33:1054–1060
Meng J et al (2008) Carbon nanotubes conjugated to tumor lysate protein enhance the efficacy of an antitumor immunotherapy. Small 4:1364–1370
Mislick KA, Baldeschwieler JD (1996) Evidence for the role of proteoglycans in cation-mediated gene transfer. Proc Natl Acad Sci 93:12349–12354
Muro S et al (2008) Control of endothelial targeting and intracellular delivery of therapeutic enzymes by modulating the size and shape of ICAM-1-targeted carriers. Mol Ther 16:1450–1458
Naahidi S, Jafari M, Edalat F, Raymond K, Khademhosseini A, Chen P (2013) Biocompatibility of engineered nanoparticles for drug delivery. J Control Release 166:182–194
Narayanan S, Binulal N, Mony U, Manzoor K, Nair S, Menon D (2010) Folate targeted polymeric 'green' nanotherapy for cancer. Nanotechnology 21:285107
Nguyen H et al (2000) Evaluation of polyether-polyethyleneimine graft copolymers as gene transfer agents. Gene Ther 7:126–138
Onoshima D, Yukawa H, Baba Y (2015) Multifunctional quantum dots-based cancer diagnostics and stem cell therapeutics for regenerative medicine. Adv Drug Deliv Rev 95:2–14
Onoue S, Yamada S, Chan H-K (2014) Nanodrugs: pharmacokinetics and safety. Int J Nanomed 9:1025–1032
Panchapakesan B, Lu S, Sivakumar K, Taker K, Cesarone G, Wickstrom E (2005) Single-wall carbon nanotube nanobomb agents for killing breast cancer cells. NanoBiotechnology 1:133–139

Pankhurst QA, Connolly J, Jones S, Dobson J (2003) Applications of magnetic nanoparticles in biomedicine. J Phys D Appl Phys 36:R167
Park JS et al (2006) N-acetyl histidine-conjugated glycol chitosan self-assembled nanoparticles for intracytoplasmic delivery of drugs: endocytosis, exocytosis and drug release. J Control Release 115:37–45
Patel J, Garala K, Basu B, Raval M, Dharamsi A (2011) Solubility of aceclofenac in polyamidoamine dendrimer solutions. Int J Pharm Investig 1:135–138
Patil S, Lalani R, Bhatt P, Vhora I, Patel V, Patel H, Misra A (2018) Hydroxyethyl substituted linear polyethylenimine for safe and efficient delivery of siRNA therapeutics RSC. Advances 8:35461–35473
Patil S, Sandberg A, Heckert E, Self W, Seal S (2007) Protein adsorption and cellular uptake of cerium oxide nanoparticles as a function of zeta potential. Biomaterials 28:4600–4607
Perez EA (2009) Impact, mechanisms, and novel chemotherapy strategies for overcoming resistance to anthracyclines and taxanes in metastatic breast cancer. Breast Cancer Res Treat 114:195
Plank C, Mechtler K, Szoka FC Jr, Wagner E (1996) Activation of the complement system by synthetic DNA complexes: a potential barrier for intravenous gene delivery. Hum Gene Ther 7:1437–1446
Price CF et al (2011) SPL7013 Gel (VivaGel®) retains potent HIV-1 and HSV-2 inhibitory activity following vaginal administration in humans. PLoS One 6:e24095
Prokop A, Davidson JM (2008) Nanovehicular intracellular delivery systems. J Pharm Sci 97:3518–3590
Reis CP, Neufeld RJ, Ribeiro AJ, Veiga F (2006) Nanoencapsulation I. Methods for preparation of drug-loaded polymeric nanoparticles. Nanomed Nanotechnol Biol Med 2:8–21
Riordan JR, Deuchars K, Kartner N, Alon N, Trent J, Ling V (1985) Amplification of P-glycoprotein genes in multidrug-resistant mammalian cell lines. Nature 316:817–819
Sahni JK, Doggui S, Ali J, Baboota S, Dao L, Ramassamy C (2011) Neurotherapeutic applications of nanoparticles in Alzheimer's disease. J Control Release 152:208–231
Sánchez-López E et al (2018) Memantine loaded PLGA PEGylated nanoparticles for Alzheimer's disease: in vitro and in vivo characterization. J Nanobiotechnol 16:32
Schliecker G, Schmidt C, Fuchs S, Kissel T (2003) Characterization of a homologous series of D, L-lactic acid oligomers; a mechanistic study on the degradation kinetics in vitro. Biomaterials 24:3835–3844
Shah M, Naseer MI, Choi MH, Kim MO, Yoon SC (2010) Amphiphilic PHA–mPEG copolymeric nanocontainers for drug delivery: preparation, characterization and in vitro evaluation. Int J Pharm 400:165–175
Siegel SJ, Kahn JB, Metzger K, Winey KI, Werner K, Dan N (2006) Effect of drug type on the degradation rate of PLGA matrices. Eur J Pharm Biopharm 64:287–293
Song X et al (2008) PLGA nanoparticles simultaneously loaded with vincristine sulfate and verapamil hydrochloride: systematic study of particle size and drug entrapment efficiency. Int J Pharm 350:320–329
Staples M, Daniel K, Cima MJ, Langer R (2006) Application of micro-and nano-electromechanical devices to drug delivery. Pharm Res 23:847–863
Sung S-J, Min SH, Cho KY, Lee S, Min Y-J, Yeom YI, Park J-K (2003) Effect of polyethylene glycol on gene delivery of polyethylenimine. Biol Pharm Bull 26:492–500
Tang G et al (2003) Polyethylene glycol modified polyethylenimine for improved CNS gene transfer: effects of PEGylation extent. Biomaterials 24:2351–2362
Tang X, Liang Y, Feng X, Zhang R, Jin X, Sun L (2015) Co-delivery of docetaxel and Poloxamer 235 by PLGA–TPGS nanoparticles for breast cancer treatment. Mater Sci Eng C 49:348–355
Thomas M et al (2012) PEI-complexed LNA antiseeds as miRNA inhibitors. RNA Biol 9:1088–1098
Thomas TP, Goonewardena SN, Majoros IJ, Kotlyar A, Cao Z, Leroueil PR, Baker JR Jr (2011) Folate-targeted nanoparticles show efficacy in the treatment of inflammatory arthritis. Arthritis Rheum 63:2671–2680

Tong WY et al (2018) Delivery of siRNA in vitro and in vivo using PEI-capped porous silicon nanoparticles to silence MRP1 and inhibit proliferation in glioblastoma. J Nanobiotechnol 16:38
Tortorella S, Karagiannis TC (2014) Transferrin receptor-mediated endocytosis: a useful target for cancer therapy. J Membr Biol 247:291–307
Tosi G et al (2011) Investigation on mechanisms of glycopeptide nanoparticles for drug delivery across the blood–brain barrier. Nanomedicine 6:423–436
Van Butsele K et al (2009) Synthesis and pH-dependent micellization of diblock copolymer mixtures. J Colloid Interface Sci 329:235–243
Vonarbourg A, Passirani C, Saulnier P, Benoit J-P (2006) Parameters influencing the stealthiness of colloidal drug delivery systems. Biomaterials 27:4356–4373
Wang B et al (2010) Inhibition of bacterial growth and intramniotic infection in a guinea pig model of chorioamnionitis using PAMAM dendrimers. Int J Pharm 395:298–308
Weinstein JS et al (2010) Superparamagnetic iron oxide nanoparticles: diagnostic magnetic resonance imaging and potential therapeutic applications in neurooncology and central nervous system inflammatory pathologies, a review. J Cereb Blood Flow Metab 30:15–35
Wightman L, Kircheis R, Rössler V, Carotta S, Ruzicka R, Kursa M, Wagner E (2001) Different behavior of branched and linear polyethylenimine for gene delivery in vitro and in vivo. J Gene Med 3:362–372
Wilson R (2008) The use of gold nanoparticles in diagnostics and detection. Chem Soc Rev 37:2028–2045
Wind N, Holen I (2011) Multidrug resistance in breast cancer: from in vitro models to clinical studies. Int J Breast Cancer, Article ID 967419
Wong KK, Liu X (2010) Silver nanoparticles—the real "silver bullet" in clinical medicine? MedChemComm 1:125–131
Xiong F, Mi Z, Gu N (2011) Cationic liposomes as gene delivery system: transfection efficiency and new application. Die Pharm-An Int J Pharm Sci 66:158–164
Yaméogo JB et al (2014) Self-assembled biotransesterified cyclodextrins as potential Artemisinin nanocarriers. II: In vitro behavior toward the immune system and in vivo biodistribution assessment of unloaded nanoparticles. Eur J Pharm Biopharm 88:683–694
Yang K, Ma Y-Q (2010) Computer simulation of the translocation of nanoparticles with different shapes across a lipid bilayer. Nat Nanotechnol 5:579–583
Yang X, Zhang Q, Wang Y, Chen H, Zhang H, Gao F, Liu L (2008) Self-aggregated nanoparticles from methoxy poly (ethylene glycol)-modified chitosan: synthesis; characterization; aggregation and methotrexate release in vitro. Colloids Surf B: Biointerfaces 61:125–131
Yen SK, Padmanabhan P, Selvan ST (2013) Multifunctional iron oxide nanoparticles for diagnostics, therapy and macromolecule delivery. Theranostics 3:986–1003
Yoneki N et al (2015) One-pot facile preparation of PEG-modified PLGA nanoparticles: effects of PEG and PLGA on release properties of the particles. Colloids Surf A 469:66–72
Yoo J-W, Irvine DJ, Discher DE, Mitragotri S (2011) Bio-inspired, bioengineered and biomimetic drug delivery carriers. Nat Rev Drug Discov 10:521–535
Yuan H, Li J, Bao G, Zhang S (2010) Variable nanoparticle-cell adhesion strength regulates cellular uptake. Phys Rev Lett 105:138101
Zhang S, Li J, Lykotrafitis G, Bao G, Suresh S (2009) Size-dependent endocytosis of nanoparticles. Adv Mater 21:419–424
Zhang X-F, Liu Z-G, Shen W, Gurunathan S (2016) Silver nanoparticles: synthesis, characterization, properties, applications, and therapeutic approaches. Int J Mol Sci 17:1534
Zhao X, Li H, Lee RJ (2008) Targeted drug delivery via folate receptors. Expert Opin Drug Deliv 5:309–319
Zhao Z, Li Y, Zhang Y, Chen A-Z, Li G, Zhang J, Xie M-B (2014) Development of silk fibroin modified poly (l-lactide)–poly (ethylene glycol)–poly (l-lactide) nanoparticles in supercritical CO2. Powder Technol 268:118–125
Zhou Z et al (2013) Linear-dendritic drug conjugates forming long-circulating nanorods for cancer-drug delivery. Biomaterials 34:5722–5735

Designing Novel Photocatalysts for Disinfection of Multidrug-Resistant Waterborne Bacteria

Sourav Das, Ananyo Jyoti Misra, A. P. Habeeb Rahman, Aradhana Basu, Amrita Mishra, Ashok J. Tamhankar, Cecilia Stålsby Lundborg and Suraj K. Tripathy

Abstract Water is the main source of sustaining life. It is an indispensable need for flora and fauna alike. However, water is often contaminated by multidrug-resistant bacteria and various other contaminants. Disinfection methods like ozonation and chlorination fail to curtail these menace, often generating harmful by-products in this process. Photocatalysis, a subsidiary of advanced oxidation processes might have an important role to play in water decontamination. They are effective, do not generate by-products, and provide complete inactivation against these MDR strains and pollutants. The already existing photocatalysts like Titanium Dioxide and Zinc Oxide are being depleted to their core. So, newer and novel photocatalysts need to be developed with a more proficient, eco-friendly and biocompatible approach. This discussion aims to have a closer look at the existing disinfection techniques and the emerging players in the field of photocatalysis.

Keywords Multidrug-resistant bacteria · Photocatalysis · Core-shell nanocomposites · Graphene oxide · Graphitic carbon nitride

Abbreviations

PCD	Photocatalytic Disinfection
NC	Nanocomposites
MDR	Multidrug-resistant
ARG	Antibiotic-resistance genes

S. Das · A. J. Misra · A. P. Habeeb Rahman · S. K. Tripathy (✉)
School of Chemical Technology, Kalinga Institute of Industrial Technology (KIIT), Bhubaneswar, India
e-mail: suraj.tripathy@kiitbiotech.ac.in

S. Das · A. J. Misra · A. P. Habeeb Rahman · A. Basu · A. Mishra · A. J. Tamhankar · S. K. Tripathy
School of Biotechnology, Kalinga Institute of Industrial Technology (KIIT), Bhubaneswar, India

A. J. Tamhankar · C. S. Lundborg
Department of Public Health Sciences, Karolinska Institute, Stockholm, Sweden

L. Ledwani and J. S. Sangwai (eds.), *Nanotechnology for Energy and Environmental Engineering*, Green Energy and Technology,
https://doi.org/10.1007/978-3-030-33774-2_19

GO	Graphene Oxide
SODIS	Solar Disinfection
LED	Light Emitting Diode
DNA	Deoxyribonucleic Acid
ROS	Reactive Oxygen Species
VB	Valence Bond
CB	Conduction Band
RNA	Ribonucleic Acid
UV	Ultra Violet

1 Introduction

1.1 Current Scenario of Waste Water and Multidrug-resistant Waterborne Bacteria

Abundance of ground and surface water is the uniqueness of planet Earth in the solar system. Origin of life and its sustainable evolution is hence possible, but unfortunately, it is a matter of concern that scarcity of consumable grade water is an age-long problem (Malato et al. 2009; Schwarzenbach et al. 2010). In view of growing population and the need for freshwater trends, it can be forecasted that about a third of the world's population would be affected by illness and poverty due to global problem of water scarcity by the year 2025 (Shannon et al. 2010). The majority of water present in and on earth is infected with microorganisms and persistent organic pollutants (POP). In India, areas with adequate water supplies struggle for its sustainable management while others struggle with the scarcity of pure drinking water (Ashbolt 2004; Viessman et al. 1998). Underlying this disparity in water availability is the key to waterborne diseases. In the last 5 years, waterborne and diarrheal diseases like cholera, gastroenteritis, and diarrhea have killed more than ten thousand people in India, victimizing mostly infants. Disease-causing aquatic bacteria such as coliform *Escherichia coli (E. coli), Vibrio cholerae (V. cholerae), Shigella flexneri (S. flexneri),* and *Salmonella typhi (S. typhi)* are reported to cause explosive outbreaks and rapid transmission of waterborne diseases over huge geographic spans, specifically Asia, Africa, and South America, developing pandemics (Yang et al. 2012). The major reasons for these outbreaks are overpopulation, unsafe hygiene and sanitation, limited fresh and drinking water sources, and tropical climatic conditions (Greer et al. 2008; Levy et al. 2016). This situation worsens more where the wastewater is contaminated with multidrug-resistant (MDR) microorganisms (Delgado-Gardea et al. 2016). Water contamination also occurs due to insufficient and unskilled management of resources as well as informal discharge of sewage into the water sources. Wastewater treatment plants (WWTPs) were employed to dispose of this waterborne

bacteria but they were suspected to be one of the foremost hotspots and anthropogenic sources for release of antibiotics, MDR bacteria, and antibiotic-resistant genes (ARG) into the environment (Barancheshme and Munir 2018). In countries with low per capita income, where hospital wastewater is treated along with municipal effluent or discharged without any treatment, the situation becomes more critical. Specifically, MDR bacteria that carry ARGs, often contaminate the community water sources; transferring their resistance to harmless nonpathogenic bacteria; ultimately posing a severe public health threat (Lien et al. 2017).

Antibiotic usage has tremendously increased in the past decade for clinical applications, agriculture and the food industry, and aquaculture. Partially metabolized, unprescribed, overused, and incomplete used antibiotics were reported as the major reasons behind the development of MDR microorganisms (Prestinaci et al. 2015). The presence of antibiotic residues in varying concentrations in aquatic bodies like river, lake, and pond ecosystems has been well-documented (Diwan et al. 2010). The "Indian Ganges", along with its auxiliary tributaries, supplies water to over 500 million individuals. Thus contamination of even one water source could affect the livelihood of millions of people categorically. Antibiotics are reported to be present in rivers and other aquatic bodies at concentrations that could not only modify the ecological dynamics of the environment but also give rise to antibiotic-resistant bacteria (ARB) and ARGs (Barancheshme and Munir 2018). Exposure of commensals like *E. coli and Staphylococcus aureus* (*S. aureus*) to antibiotics increases the carriage level of ARGs. This might then be transferred to other bacteria to develop their more virulent variants like Methicillin-resistant *S. aureus* (MRSA) and Vancomycin-resistant *S. aureus* (VRSA), Extended-spectrum beta-lactamases (ESBL) producing *E. coli* (Barancheshme and Munir 2018). These MDR organisms and ARGs are constantly emerging and dispersing worldwide, thus threatening the therapeutic potential of antibiotics against the treatment of infectious diseases resulting in increasing mortality (Prestinaci et al. 2015). This has become such a serious concern for global public health that in 2015 the World Health Organization (WHO) reported a document on the global surveillance of antimicrobial resistance (World Health Organization 2014). Thus, it necessitates the "one health approach" to attain most ideal health conditions for mankind, animals, and environment (Ryu et al. 2017). This may have better emphasis on development of global public health and nullify the global burden caused by MDR microorganisms.

Additionally harmful organics, chiefly industrial wastes such as organic dyes, pharmaceuticals more specifically antibiotics, polychlorinated pesticides, polycyclic aromatic hydrocarbons polychlorinated dibenzodioxins, dibenzofurans, and biphenyls pose serious threats through biomagnification and deterioration of public health has turned out to be a matter of concern for global environmental legislatives and scientists (Qing Li et al. 2006).

1.2 Problems, Consequence Associated, and Disease Caused

The late twentieth century has witnessed a rapid increase in the number of microbe related infections. Unrequited exploitation of antimicrobial drugs and antibiotics in treatments ultimately led to the advent of resistance among most of the microorganisms (Malato et al. 2009). MDR is defined as the non-susceptibility of a particular microorganism against a set of common drugs which once had detrimental effects on the survivability of the microbe (Barancheshme and Munir 2018). As per the WHO, these resistant microorganisms specifically belonging to bacteria, fungi, viruses, and parasites lead to ineffective treatment offered by these antibiotics, resulting in doggedness and spreading of such deadly infections and infectious diseases. *Escherichia coli* is considered one of the common fecal coliforms that contaminate drinking water. It has been the prime indicator of fecal contamination in water quality monitoring for many decades (WHO 2004). With tropical and monsoon climatic conditions in India, these coliforms with uttermost rate of incidence may be washed into hospital water, creeks, rivers, streams, lakes, or groundwater. Where they come in contact with other *E. coli* with significant reservoir of genes coding for MDR and thus propagates the resistance leading to waterborne deadly infections. Other bacteria which squad this phenomenon includes species from *Klebsiella, Salmonella enterica subsp. Enterica Serovar Typhi, Salmonella enterica subsp. Enterica Serovar Paratyphi*, *Shigella spp., Vibrio cholerae, Acinetobacter sp., Clostridium spp.,* and *Bacillus anthracis, Legionella, Burkholderia* . Methicillin-resistant staphylococcus has also been found in different WWTP effluents (WHO 2004).

Although these phenomena of drug-resistance are natural, behemoth rise in the number of immune-compromised states specifically due to HIV-infection, HSV and Hepatitis-B infections, TB Infection, diabetes, brutal burns, and organ transplantation brands the human body an unforced target for nosocomial infectious diseases, and promotes further spread of MDR. According to the WHO report, greater rates of resistance against antibiotics as cephalosporin and fluoroquinolones in *Escherichia coli associated with coliform-based infections*, against cephalosporin and carbapenems in *Klebsiella pneumoniae* associated to pneumonia, against methicillin in *Staphylococcus aureus* associated to skin borne diseases, against penicillin in *Streptococcus pneumoniae*, against fluoroquinolones in *Nontyphoidal Salmonella*, against fluoroquinolones in *Shigella* species associated with dysentery, against cephalosporin in *Neisseria gonorrhoeae* associated to gonorrhoeae, and against rifampicin in *Mycobacterium tuberculosis* associated to tuberculosis, and against isoniazid and fluoroquinolone in urinary tract infections, pneumonia, bloodstream and other nosocomial infections. In case of fungal strains, a lesser number of drugs have been identified till today. Unfortunately some species of fungus belonging to genus (Ventola 2015) *Aspergillus, Cryptococcus, Candida, Scopulariopsis, Pseudallescheria,* and *Trichospron* have been reported to have developed resistance polyene macrolides (amphotericin B), azole derivatives (ketoconazole, fluconazole, itraconazole, and voriconazole), nucleic acid synthesis inhibitors (flucytosine), and glucan synthase inhibitors (echinocandins) (Fernández-Silva et al. 2013). Long-lasting drug exposure

and uncontrollable viral duplication result in the introduction of a range of resistant strains and diligence of infections despite therapy. Likewise the impact could also be observed in higher group of microorganisms belonging to parasites. *Plasmodia, Leishmania, Entamoeba, Trichomonas vaginalis, schistosomes,* and *Toxoplasma gondii* were found to have extensive resistance or tolerance against chloroquine, pyrimethamine, artemisinin, pentavalent antimonials, miltefosine, paromomycin, and amphotericin B and atovaquone and sulfadiazine (Labro 2012). Malaria and Amoebiasis parasite *Plasmodium falciparum* and *Entamoeba* spp, respectively, along with schistosomiasis have also been reported to be prone for MDR infections (Tanwar et al. 2014) instigating afore most public health threat in many tropical and subtropical countries.

Antimicrobial drugs have been used throughout the world for decades. Clinical surveillance in Africa, America, Eastern mediterranean region, Europe, South-East Asia, and Western pacific region has revealed that many infectious microorganisms have evolved over the past few decades and an alarming rise among the antibiotic-resistant species have been observed. Not only bacteria but almost all the competent infecting organisms like bacteria, fungi, viruses, and parasites have employed high levels of MDR with superior morbidity and mortality and thus got the status of "superbugs" (Nagarajan et al. 2018; Parida et al. 2015). TB, pneumonia, deadly virus like HIV and influenza, malaria, hepatitis, yeast infections accompanied with other lethal ailments are the chief causes of deaths in the contemporary times, demonstrating MDR as a fervent worldwide menace to public health. The likelihoods of regulating tuberculosis have lessened due to resistance of (Tanwar et al. 2014), occasioning in substitution of ancient ineffective drugs by novel drugs that radically increased the health care expenses, worsening the situation of economically challenged citizens.

1.3 Current Scenario of Water and Existing Solutions for Water Disinfection

Escalating world population, industrialization, and droughts have increased the demand for clean water sources worldwide. With a climbing demand, innumerable practical approaches and solutions have been implemented like rainwater harvesting, increasing catchment volumes, etc. for better yield of freshwater resources (Rahman et al. 2014). It is anticipated that billions of people worldwide will have scarce access to sterile water supply, and countless beings will be victimized by severe waterborne diseases and infections due to improper release of micropollutants and sewage in natural aquatic bodies (Malato et al. 2009). With regards to this deterioration of clean water and potential shortage, advancements in affordable and highly efficient water treatment technologies for wastewater treatment (WWT) are desirable. Few smarter approaches like possible onsite reuse of rural wastewater or the treated municipal wastewater from WWTPs for agricultural and industrial applications (Bradley et al. 2002; Lapena et al. 1995) have been proposed. Wastewater reuse and recycling are

generally associated with the presence of dissolved refractory organic components, suspended solids and fecal coliforms that are both annoying and expensive to get rid of (Viessman et al. 1998). Universal water treatment technologies like adsorption or coagulation simply concentrate the pollutants, transferring them to other harmful chemical forms, face problems for complete elimination and decontamination (Padmanabhan et al. 2006). Conventional methods like membrane filtration technologies, sedimentation, and chemical treatment involve greater operating costs and produce lethal secondary pollutants into the aquatic ecosystem (Gaya and Abdullah 2008). These unnecessary secondary pollutants are apprehensive worldwide due to the growing environmental consciousness and legislatures. Thus remedies include chemical treatment methods like chlorination and ozonation and other treatment like UV light has been most commonly and widely used disinfection process.

1.3.1 Chlorination

Chlorination is one of the most universally used practises for disinfection owing its economical factors. It is used in the final step of WWTP which involves addition of gaseous chlorine (Cl_2), calcium, or sodium hypochlorite ($Ca(OCl)_2$)/(NaOCl), to water which ultimately acts in disinfection of waterborne pathogens with the generation of hypochlorous acid (HOCl). The mechanism of action generally involves oxidation of bacterial germ cells, and cell membranes, along with inhibition of enzyme activity. Regrettably, chlorination has been scarce for effective inactivation of viral pathogens (Kitajima et al. 2010). He reported the presence of *enteroviruses* in nearly 58% of the samples and adenoviruses in nearly all samples collected from six different WWTP after chlorination process. Since 1970s the effect of chlorination MDR bacteria has been studied. More recently, Huang et al. showed that the though inactivation rates of MDR bacteria (namely, chloramphenicol-, rifampicin-, tetracycline-resistant bacteria) stayed comparatively high with respect to other heterotrophs but the fraction of MDR increased numerously after chlorination (Huang et al. 2013). This includes increased resistance toward of *E. coli* tetracycline antibiotics, whose inactivation rates with Cl_2 (1.5 mg/L) have been lesser in comparison to the sensitive ones. This may lead to selectivity of resistant strains in drinking and wastewater. Studies performed by Munir et al. from five WWTPs in Michigan (USA), reports no significant involvement of this technique to MDR and ARG reduction. Consequently, the mechanism of how chlorine action toward MDR and ARG assortment in wastewater is greatly unidentified and further insights into this research is required (Munir et al. 2011).

1.3.2 Ozonation

Ozonation is a typical process used for oxidative disinfection of water and polluted waters. Ozone effectually incapacitates survivors of chlorination process, i.e., protozoans like *Cryptosporidium* and *Giardia* (Rennecker et al. 1999; Von Gunten 2003).

But the dosage at which it is performed results in the creation of unsolicited disinfection by-products like bromates from bromide which has been proven a potential human carcinogen (Agus et al. 2009). Lower dosage may not efficiently inactivate cysts, spores, and viruses (Cho et al. 2003), other factors like contact time, the target microorganisms and characteristics of the wastewater matrix also play an important part. Interesting observations were reported by Selma et al. (2007), where 1.6 and 2.2 mg L^{-1} of initial ozone doses result 3.7 and 5.6 log reduction of 10^8 CFU $mL^{-1}$of *S. sonnei,* respectively. Consequences of ozonation on MDR bacteria have been scarcely addressed Oncu et al. (2011) did a comparative investigation on chlorination, ozonation, and feebly applied heterogeneous photocatalytic process for disinfection of MDR microorganisms. Chlorination had no impact on the plasmid DNA structure, whereas ozonation at concentrations 1–4.42 mg L^{-1} and treatment time 1 min and photocatalysis lead to conformational changes in them, which showed direct correlation with oxidant doses. Investigations by Lee et al. (2013) stated 3-log reduction in chlortetracycline-resistant bacteria from livestock wastewater within 10 min (Öncü et al. 2011).

1.3.3 UV Irradiation

UV radiation is the most globally used disinfection treatment as far as surface, water and food-based sterilization are concerned. UV-C (250–280 nm) radiation has the most detrimental effect on the genetic material (DNA and RNA) of microorganisms. It results in the inhibition of the replication machinery and reproducibility if the doses applied are lethal. The UV dose is the main factor to specify by what means it will be used for decontamination of wastewater. It is described as the product of the average UV intensity in mW cm^{-2} and the average exposure time in seconds(s).

UV irradiation might fail in the inactivation of MDR and ARG lessening in wastewater under commonly applied doses of 30 mJ cm^{-2}. However, UV dosages somewhat near or equal to 50 mJ cm^{-2}, inactivation of the MDR could be achieved. But according to them, UV radiation increased the MDR selectivity and ARG lessening (Guo et al. 2013); in particular, this treatment could reduce the percentage of erythromycin-resistant bacteria, augmented that of tetracycline-resistant bacteria, and ARG concentrations. Thus as per the references in literature, damaging of ARGs requires substantially high UV doses of 200–400 mJ cm^{-2} in contrast to that required for 4–5 log reduction of MDR (McKinney and Pruden 2012).

UV disinfection effect had been assessed at large-scale setups for effluents to observe in-significant reduction of MDR and ARGs [tet(G) or tet(Q)] (McKinney and Pruden 2012) and found almost equivalent to chlorination process as per the statistical student t-test ($p > 0.05$). The investigators highlight that even though it was indecisive to reach an apparent conclusion, UV irradiation mediated disinfection to decrease loads of some tetR gene and their respective diversity is still under question. In a further large-scale study report by Francy et al. (2012) adenovirus was detected in the UV-treated effluent in between 25 and 36%. Though these detection percentages

were superior than reports from post-chlorination disinfection in another WWTP where survivability of adenovirus was 75%.

Therefore, UV Irradiation and chlorination might be ineffective in producing considerable effect over MDR and ARG in wastewater, with unclear reasons. Although evidence of a selection process for MDR and ARG produced by these treatments are probable, but this is not a conclusive fact; it typically depends on the antibiotic, mechanism of resistance achieved and the bacteria.

1.4 Wastewater Disinfection by Nonconventional Process like Heterogenous Photocatalysis

Above mentioned inadequacies in conventional water treatment process have led to the rapid development in AOPs as an inventive water treatment method. The AOPs involve in situ generations of ROS like OH•, H_2O_2, and $O_2•^-$. These ROS were reported as the chief arsenal for photocatalysis of refractory organic molecules and disinfection of microorganisms (Esplugas et al. 2002). Among these AOPs, heterogeneous photocatalysis employing semiconductor metal oxide catalysts mainly TiO_2, ZnO, Fe_2O_3, CdS, GaP, and ZnS has confirmed its competence in mineralization of a wide range of refractory and POPs into readily less harmful intermediates, and their eventual mineralization into harmless carbon dioxide and water. Among the semiconductor metal oxide photocatalysts, TiO_2, and ZnO have received tremendous attention owing to their UV light and visible light-mediated activation properties, respectively. Both of them were reported to have high thermal, chemical, and mechanical stability making them ideal candidates for photocatalytic treatment applications (Chong et al. 2010).

Heterogeneous photocatalysis possesses certain important features that promote its applicability in water treatment; they are (1) operation under ambient pressure and temperature and, (2) total mineralization of refractory and persistent organics minus generating secondary pollutants, and (3) low operational costs. The ROS produced as a result of the photo-induced charge separation on semiconductor metal oxide surface has been well-documented for microbial disinfection and POP mineralization without generating secondary pollutants. Being so, versatile semiconductor metal oxide photocatalysts possess some technical challenges. This may include post-reaction separability of the semiconductor photocatalyst after water treatment, which is pausing their practicality as an industrial process. The fine particle size of semiconductor metal oxides, together with their large surface area and surface energy creates a resilient inclination for catalyst agglomeration during application. This is vastly adverse in terms of particles size maintenance, decreasing surface area, and its reusability. Further technical confrontations involve designing catalysts which will be active for a wider spectrum of light, keeping in mind the photoperiods of 12 h sunlight and 12 h dark for real-time photocatalytic applications (Chong et al.

2010). Moreover, understanding the technical rationale behind the common reactor geometry, design, kinetics, and operational parameters is necessary for process optimization.

1.4.1 Mechanism of Heterogenous Photocatalysis

Mechanism of heterogenous photocatalysis depends on the chemistry of photophysics and photochemistry employing metal oxide semiconductors as catalytic agents which has been long reported in literature (Matsunaga et al. 1985). Semiconductors like TiO_2 and ZnO are generally used as photocatalysts owing to their potential to induce reduction and oxidation-based reactions on their surface, which is exclusively due to the discrete lone electron property in its outermost orbital. When photonic energy, i.e., λμ of greater than or equal to the bandgap energy of metal oxide semiconductor is illumined onto its surface, the lone electron (e^-) from the valence band (VB) of semiconductor will be photoexcited to the empty conduction band (CB) within femtoseconds leaving behind hole (h^+) in the VB of the semiconductor. This e^-/h^+ pair (charge carriers) gets transferred to the photocatalyst surface and participates in the reduction and oxidation reactions. High amount of ROS is produced in the system through the series of reactions mentioned in Figs. 1 and 2 OH•, $O_2•^-$, $HO_2^•$ (hydroperoxyl), are the key arsenal ROS responsible for photocatalytic activity. It is recognized that OH• (from oxidation of water by h^+ in the VB) is primarily responsible for this PCD of POPs and disinfection of bacteria (Malato et al. 2009). Additionally, other ROS like $O_2•^-$ (from reduction of Oxygen in the CB) and H_2O_2 also play a crucial part in photocatalytic oxidation (Regmi et al. 2018). The following set of reactions describes the molecular mechanisms for stepwise generation of ROS in a photocatalyst.

O_2 is highly electronegative in nature and has been reported as one of the best electron scavengers, in absence of an actual electron scavenger during the photocatalytic process; the faster electron–hole recombination takes place with concurrent

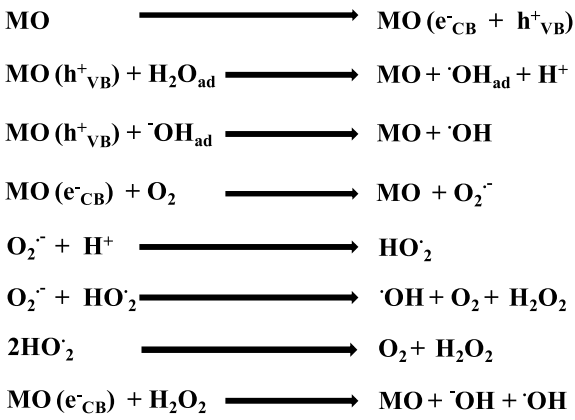

Fig. 1 Where MO stands for metal oxide that may be TiO_2 and ZnO etc. [Reprinted with Permission from Das et al. (2018). Copyright 2018 MDPI UNDER Creative Commons Attribution License. (CC BY 4.0).]

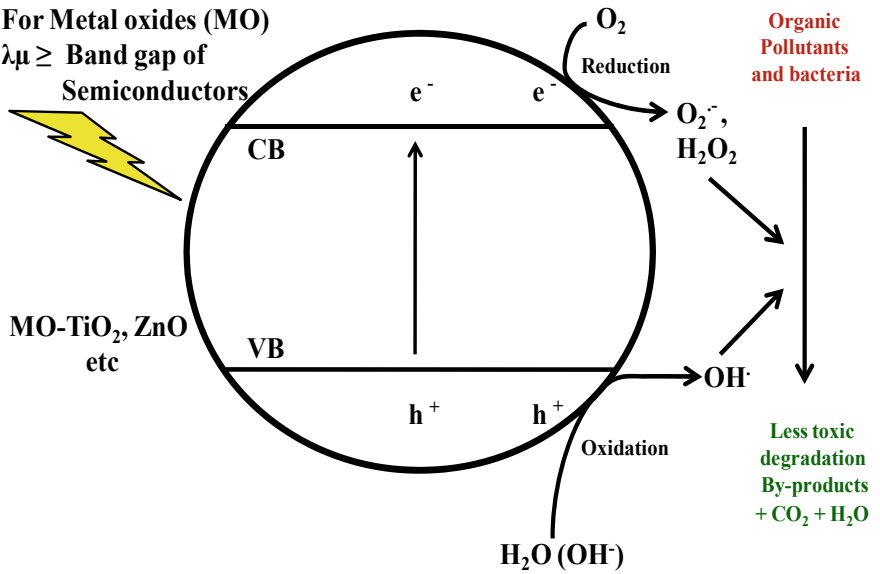

Fig. 2 Schematic representation of semiconductor metal oxide-mediated photocatalysis and the possible redox reactions involved that lead to the generation of different ROS ($OH^{\bullet}$, $O2^{\bullet -}$, H_2O_2) and subsequent degradation and disinfection of organic pollutants and bacteria (Das et al. 2017). [Reprinted with Permission from (Das et al. 2017). Copyright 2017 Springer Nature Publishing Company UNDER Creative Commons Attribution License. (CC BY 4.0).]

dissipation of heat. Thus, prolonging this recombination time is reported as one of the key rationales behind successful execution of photocatalysis (Chong et al. 2010). Figure 1 shows how presence of oxygen in the form of dissolved oxygen (DO) in the photocatalytic system, delays the recombination of electron–hole pair, allowing the formation of $O_2^{\bullet -}$. This further can be protonated to form the $HO_2^{\bullet}$ and subsequently into H_2O_2 on further reaction with $O_2^{\bullet -}$ (Scheme-1). $HO_2^{\bullet}$ previously has been reported to own scavenging property and therefore its presence in the system can further prolong the electron–hole recombination time (Chong et al. 2010).

All these reactive species in the photocatalytic system have been generated through the presence of both DO and water molecules. Many literature state their importance, and futility of photocatalysis without them. The generation of such effective ROS has been the key behind breaking down of various refractory organic molecules within their main chemical chain, and killing of bacteria in the water matrices by targeting their molecular machinery. The resulting nontoxic by-products/intermediates are further converted to carbon dioxide and water as the final products of photocatalytic process (Regmi et al. 2018).

Mass transfer or adsorption of organic molecules on the photocatalyst surface or the mass transfer of nanosized photocatalyst on the bacteria surface has been reported as the rate-determining step of photocatalysis. For an efficient photocatalysis reaction to occur, the target and the photocatalyst must be in close proximity to each other. It is

mainly because the ROS generating on the photocatalyst surface lose their affectivity on diffusing away from the catalyst surface. Similarly, desorption of the degraded molecules from the catalyst surface are also rate determining if the concentration of the organics in the system is high, and the photocatalytic reaction has to run for longer intervals for complete degradation of organic targets (Chong et al. 2010).

In case of microorganisms, their surface interaction with the photocatalyst (TiO_2 and ZnO) in PCD is crucial for enhancing the rate of inactivation. When the ROS generated during photocatalysis comes in close proximity with the microorganisms, bacterial membrane will be the primary target for ROS attack (Maness et al. 1999). ROS could break open even the strongest of covalent bonds (C–C, C–H, C–N, C–O, and H–O) present in biomolecules such as lipids, carbohydrates, nucleic acid, and proteins. The lipopolysaccharide layer and proteins will be oxidized by the photo-induced ROS and subsequent loss in respiratory activity. Peroxidation of lipids generates aldehydes in the system called malondialdehyde (MDA) and hydroxynonenal (4-HNE), which serve as the initial biomarkers for photocatalytic oxidation or PCD (Maness et al. 1999), (Joshi et al. 2011). This is followed by compromisation of bacterial membrane permeability and consequent leakage of cytoplasmic contents, specifically potassium (K^+) ions and cellular biomolecules like proteins and DNA from the bacterial cells as shown in Fig. 3 (Das et al. 2017; Misra et al. 2018). Oxida-

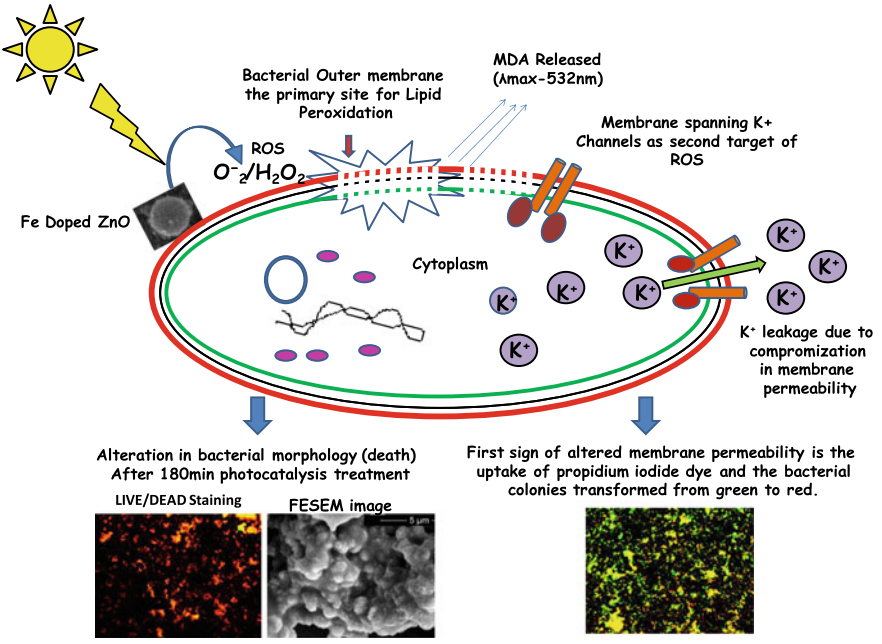

Fig. 3 Schematic view of a hypothesized mechanism for solar-PCD of MDR *E. coli* in presence of Fe Doped ZnO NCs (Das et al. 2017). [Reprinted with Permission from Das et al. (2017). Copyright 2017 Springer Nature Publishing Company UNDER Creative Commons Attribution License. (CC BY 4.0).]

tive stress may also result in change in membrane fatty acid components in bacteria and their corresponding membrane fluidity, which are studied using Fourier transmission infrared spectroscopy (FTIR) and analysis of Fatty acid methyl esters (FAME) (Kiwi and Nadtochenko 2005; Misra et al. 2018). The development of oxidative stress and its impact on the bacterial cell membrane can be observed using Transmission electron microscopy (TEM), Field emission scanning electron microscopy (FESEM) and advanced atomic force microscopy (AFM) or attenuated total reflection Fourier transform infrared spectroscopy (ATR-FTIR) (Choi et al. 2016; Kiwi and Nadtochenko 2005; Longo and Kasas 2014). After membrane, bacterial intracellular components like nucleic acids and proteins are primary targets for ROS attack. The damage in protein and nucleic acids could be studied using Sodium Dodecyl Sulfate Poly Acrylamide Gel Electrophoresis (SDS-PAGE) and Agarose Gel Electrophoresis respectively (Carré et al. 2014; Misra et al. 2018). The rate of photocatalyst adsorption on bacterial surface and the ultimate photocatalytic inactivation shows positive correlation to the ROS generation and bactericidal effect of semiconductor metal oxide-based photocatalysts. These interactions could be the rate-determining step in bacterial PCD (Das et al. 2017).

2 Innovation in Photocatalyst Technology

TiO_2 electrode had been used first in 1972 (Fujishima and Honda 1972) for water splitting applications. Since then researchers have been synthesizing TiO_2 of different sizes, characteristics, and physical and chemical properties to be exploited for numerous photocatalytic applications (Fujishima and Honda 1972; Kondo et al. 2008; Wang et al. 1998). Nanosized TiO_2 with its light opaque properties in comparison to its bulkier form was reported to have a superior oxidation competency (Siddiquey et al. 2008). Still problems regarding their morphology, particle size, and vulnerability in harsh chemical environment, remain the biggest challenge for large-scale photocatalytic applications and post-reaction separability (Byrne et al. 1998). However, the most important drawback of TiO_2 photocatalysis is mismatching between its bandgap energy and the sunlight spectra. The TiO_2 bandgap overlap only with the UV (320–400 nm) ranges, as a consequence of which it can only take benefit of less than 5% of the solar spectrum reaching the earth's surface, and thus its less likely to be used for real-time photocatalytic applications for sustainable development (Chong et al. 2010). This has intensely influenced research in photocatalyst development, to make better usage of the visible spectrum. In this perspective, the feasibility of using ZnO and CdS photocatalysts has been re-evaluated with respect to recent advances in nanotechnology. ZnO, possessing a wide bandgap energy of 3.37 eV and hefty exciton binding energy up to 60 meV, has gained high consideration in the past decade because of its ease of synthesis and exceptional optical, photovolatic, photocatalytic, high photochemically active and biocompatible properties (Chong et al. 2010). In contrast, the immobilization of the photocatalysts in inert substrate or matrices drastically reduces the active site of catalyst and will

decrease the mass transfer phenomena. This further creates more problems in photocatalytic operations due to reduced light penetration and reduced photocatalyst activation. Integrating photocatalysis with membrane technologies or membrane filtration like TiO_2/Al_2O_3 composite, TiO_2 supported on polymeric and metal and ceramic membranes (Kim et al. 2003) or polymeric membranes containing TiO_2 particles entrapped in the assembly process (Artale et al. 2001) has somewhat solved the issue of catalyst reusing. Still problems regarding membrane fouling, blockage, regeneration and backwashing, low photocatalytic potential and time-dependent loss of photocatalyst layer over time persist. Thus developing photocatalysts with high settling potential and lesser chances of deterioration under harsh chemical surroundings are the need of this era. The current section technically provides solutions to the challenges that prevent the application of TiO_2 and ZnO in slurry based photocatalytic system (Chong et al. 2010).

2.1 Doping of Photocatalysts for PCD of Microbes

Ion doping of TiO_2 and ZnO, both metallic and nonmetallic, has shown immense potential in achieving visible light photocatalysis. The dopant usually generates impurity in the semiconductor narrowing their bandgap and broadening their capability to capture the most abundant solar spectrum. With respect to PCD, nitrogen (N) has been reported as the most potential dopant (Fujishima et al. 2008; Rizzo et al. 2014) reported the effect of N-doped TiO_2 on the PCD of MDR *E. coli* strain obtained from a WWTP showing higher disinfection rates as compared to undoped TiO_2. Mesoporous, N-doped TiO_2 thin films exhibited visible light-driven PCD against both Gram-positive and Gram-negative bacteria like *Bacillus amyloliquefaciens* and *Pseudomonas aeruginosa,* respectively (Mamane et al. 2014; Soni et al. 2013). Other nonmetallic dopants like Sulfur (S) have been reported in few literature. Sol–gel mediated synthesis of S-Doped TiO_2 has been reported to have strong visible light disinfection ability against *Micrococcus lylae*in lesser time in comparison to its undoped variant (Yu et al. 2005).

Transition metal like iron (Fe) has been effectively used as a dopant for ZnO, for visible light PCD of MDR *E. coli* with/without any further reactivation as depicted in Figs. 3 and 4 (Das et al. 2017). Generally, the effectiveness of the dopant relies on its electronegativity and the difference between dopant and ionic radius of Zinc (Zn). Thus, Fe being chemically stable and existing in two possible oxidation states, Fe^{2+} (Ionic radii 0.78 Å) and Fe^{3+} (ionic radii 0.64 Å) close to Zn^{2+} (ionic radii 0.74 Å), can easily pierce into Zn lattice without distressing the crystal structure of ZnO. This results in more charge carriers to improve its conductivity and photocatalytic potency (Kafle et al. 2016). Increasing Fe concentration as dopant showed that the optical bandgap gradually diminished (Kafle et al. 2016). Also noble metals like silver (Ag) when used as dopants convert the n-type ZnO semiconductors into p-type, enhancing their optoelectronic potential and photocatalytic ability. Adhikari

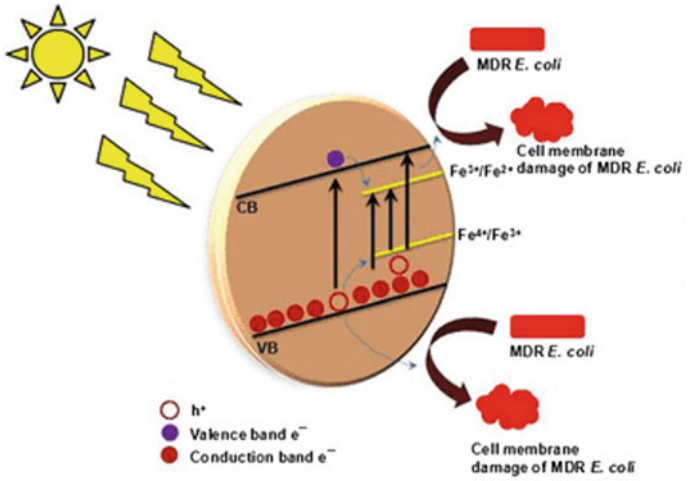

Fig. 4 Schematic representation of charge separation in Fe Doped ZnO NCs, presence of Fe^{3+} ion as a dopant delays the electron–hole recombination, allowing more generation of ROS and subsequent disinfection of waterborne microorganisms (Das et al. 2017). [Reprinted with Permission from Das et al. (2017). Copyright 2017 Springer Nature Publishing Company UNDER Creative Commons Attribution License. (CC BY 4.0)]

et al. (2015) have reported the effective visible light PCD of *E. coli* in comparison to ZnO alone (Adhikari et al. 2015).

Besides the single elemental doping, multiple elemental co-doping has been promising for further enhancing the photocatalytic activity of semiconductors. The visible light photocatalytic activity of the Er–Al co-doped ZnO was inspected for degradation of methyl orange (MO) (Ong et al. 2015). Er–Al co-doped ZnO showed highly enhanced photocatalytic activity in comparison to pristine ZnO. Moreover, Feilizadeh et al. (2015) reported an almost complete bacterial disinfection within 45 min of visible light irradiation by using Fe (Feilizadeh et al. 2015), Cd-co-doped TiO_2. Feilizadeh et al. (2015) found co-doping of B and Ni to have outstanding photocatalytic activity against *E. coli* under visible light irradiation. In fact, it is interesting to observe that the bacterial cells were inactivated by diffusing ROS even when they are not in direct contact with the photocatalyst.

2.2 *Core-Shell Nanocomposites for PCD of Microbes*

Vast progress in the field of nanotechnology motivated the synthesis of the refined nanostructures which possess tremendous optical, mechanical, chemical and electrical properties. Since 1990, researchers shifted their focus on synthesizing concentric multilayer semiconductor NPs with a transition of noble metal core to improve their optical property, these modified nanostructures are better termed core-shell

NCs. These two-component organization of NCs, have attracted tremendous interests in contrast to the conventional one-component systems. Core-Shell NCs possess improvised characteristics due to their multifunctional magnetic, chemical and optical properties, higher stability in harsh environmental conditions and high surface area (Das et al. 2015; Tripathy et al. 2013). Owing to the above factors, core–shell NCs have found more recognition in the field of chemical sensors, electro-optics, enhanced drug delivery, immobilization of enzyme, catalysis, and photocatalysis.

It has been discussed earlier that lower quantum efficiency of photocatalytic systems resulting from the faster electron–hole recombination in semiconductor and the unproductive use of visible light for semiconductors of wider bandgap are the two critical challenges obstructing the usage of photocatalysis for real-time applications (Chong et al. 2010). Thus, tuning the physical and chemical properties of the photocatalyst is of greater interest for the real-world applications for creation of sustainable environment and meeting the increasing demands of energy. Photocatalyst doping has been a technique of choice for this purpose. Moreover, optimization of the shape, structure, topology and minor defects of the photocatalysts has significantly influenced their prospective for photocatalytic applications. Semiconductor-based core–shell NCs, which involve integration of improved composition and structural features, have been promising for photocatalytic applications (Liu et al. 2012). Core-Shell NCs generally avoid the usage of strong chemical oxidants and have been considered 'green' as far as the process of synthesis is concerned. Their variants include metal–semiconductor (Au@ZnO, Ag@ZnO, Ag@TiO_2) semiconductor–semiconductor (CdS-TiO_2, TiO_2@ZnO), semiconductor–shell (graphene and SiO_2) (Liu et al. 2012).

Metal-cored–semiconductor shell NCs are the mostly studied photocatalysts in the field of transformation of organic refractory organics into less toxic by-products and intermediates due to their robust structural properties. The metallic core in the core-shell NCs possessing low Fermi energy level can serve as an electron pool during photoactivation, prolonging the existence of charge carriers, and thus possibly increasing the overall photocatalytic efficiency of the NCs Fig. 5 (Das et al. 2015). Moreover, their useful construction can not only increase the stability of core metallic NP from aggregation but also defend them against undesirable corrosion or leaching during practical application. Their flawless three-dimensional architecture also facilitates the proper interfacial charge transfer between metallic core and semiconductor shell. These exceptional merits profoundly linked with the metal-core–semiconductor shell NCs promise their immense prospective as a novel alternative to novel light-harvesting photocatalysts for real-life heterogenous photocatalytic applications (Liu et al. 2012).

Semiconductor–Semiconductor Core–Shell photocatalysts is a successful approach for improvising the photocatalytic performance of a semiconductor system. This technology involves coupling two semiconductor particles with diverse energy or bandgap levels to accomplish effectual charge separation and subsequent generation of ROS (Chong et al. 2010). In such coupled systems, on photoactivation, the photo-generated electrons gather at the lower lying CB of one semiconductor while subsequently accumulating the h^+ at the VB of the other semiconductor. Liu

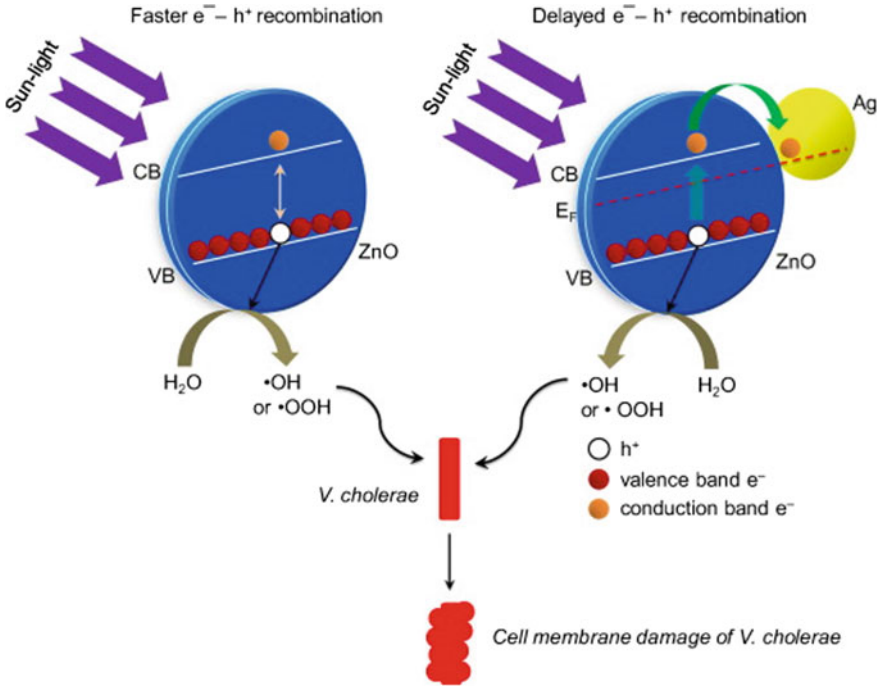

Fig. 5 Schematic representation of sunlight assisted PCD of *V. cholera* in presence of ZnO NPs and Ag@ZnO core–shell NCs. Presence of Ag core allows delayed electron–hole recombination Das et al. (2015). [Reprinted with Permission from Das et al. (2015), vide license number 4533041191524. Copyright Elsevier Publishing Company, 2015]

et al. (2012) reported faster charge partition (picosecond) from laser flash photolysis study of the CdS–TiO_2 suggesting one of their biggest advantages. Thus, their exploration for environmental remediation, organic transformation, and water splitting application is the need of this era.

Liu et al. (2012) reported M@TiO_2 (M = Au, Pd, Pt) core–shell NCs created via hydrothermal method. On exploring their performance for visible light-mediated PCD of rhodamine B, tunable photoreactivity of the as-synthesized NCs were displayed. Incorporation of a noble metal in the core promotes an enhancement in electron trapping, improving the life of electron–hole pairs, and enhances the visible light photocatalytic performance of TiO_2 as well (Hirakawa and Kamat 2005). However, under UV light ($\lambda = 365 \pm 15$ nm), the photocatalytic performance was lower in comparison to its bare TiO_2 variant, which may be due to lesser light absorption in UV region and improper electron–hole separation. Yang et al. (2015) reported some interesting phenomena based on the shell thickness in a core–shell NCs, in Au@CdS. The rate constant for electron-transfer was found to be improved with increasing thickness of the shell. This may be probably attributed to lesser definite

electron–hole interaction of thicker CdS shell, facilitating a greater magnitude in involvement of photoexcited electrons during the charge separation.

Photocatalytic applications involve decontamination of an extensive range of organic refractory pollutants. This also involves various microbes like waterborne bacteria and fungus. Das et al. (2015) for the first time, reported the utilization of colloidally-synthesized (chemically precipitated) Ag@ZnO Core-shell NCs for the complete PCD of *V. Cholerae* in 90 min. Reports of the efficient PCD of *E. coli* and *S. aureus* were reported displayed by the same group using sonochemically synthesized Ag@ZnO core-shell NCs (Das et al. 2018). In both the cases, the structural integrity of the core-shell NCs were found to be properly maintained during and post-reaction as confirmed from the Atomic Absorption Spectroscopy studies (AAS) or Microwave plasma atomic emission spectroscopy (MP-AES). Moreover, application of these NCs in real water conditions and reusability has also set a benchmark for their real-time application to get rid of waterborne bacteria. Though core-shell NCs were reported as suitable photocatalysts (Das et al. 2017), their potentials as antimicrobial agents have been convincing too. Das et al. (2016) reported for the first time biologically synthesized Ag@ZnO core-shell NCs for complete inactivation of *Candida krusei* fungus without the involvement of any light (Das et al. 2016). Thus, tuning the structural properties of these semiconductors may help these core-shell NCs as potential antimicrobial agents against both water and skin borne pathogens.

2.3 Clay-Based Nanocomposites for Photocatalytic Disinfection of Microbes

Clays are naturally occurring layered plates of aluminosilicates stacked or mound together. Their broad classification includes as montmorillonite-smectite, kaolinite, illite, and chlorite types. Clays might be also be grouped as phyllosilicates that fit into three standard groups: montmorillonite, illite, and kaolinite. Phyllosilicates are two-dimensional arrays of silicon–oxygen tetrahedral and two-dimensional arrays of aluminum or magnesium–oxygen–hydroxyl octahedral. Montmorillonite-layered silicates and illite have 2:1 layered configuration whereas and kaolinite has 1:1 layered configuration. The physicochemical characteristics differ but are principally eminent for their hydrous alumina-silicates contents. Clays generally have intersected silicates sheet joint with a second sheet-like alignment of metal atoms, oxygen, and hydroxyl ions (Bergaya and Lagaly 2006; Weaver and Pollard 2011). The fundamental configuration units are divided into silica sheets and brucite or gibbsite sheets (Miranda-Trevino and Coles 2003). The 1:1 configuration type consists of one tetrahedral sheet and one octahedral sheet; (Miranda-Trevino and Coles 2003; Yaya et al. 2012). Octahedron consists of two planes of hydroxyl ions amidst which a plane of magnesium or aluminum ions is situated that is usually synchronized by hydroxyl sheets octahedrally. These octahedrons called octahedral sheets are also

arranged in a hexagonal pattern. The 2:1 configuration type comprises of two silica tetrahedral sheets amidst which lies an octahedral sheet. This includes the most abundant clay minerals mica and smectite groups. The serpentine and mica group is further subdivided by the criteria of dioctahedral and trioctahedral type (Weaver and Pollard 2011).

They possess adsorbing antimicrobial as well as medicinal properties and have been explored since long. They serve as a mineral remedy for diarrhea, dysentery, tapeworm, hookworm, wounds, and abscesses (Otto and Haydel 2013). With excellent adsorption ability, they have been employed for mitigating bacteria in wastewater treatment plants (Hrenovic et al. 2009) and also applications in bioremediation of other different contaminants (Muter 2014). Their general application could be observed in home-based water purification or purifying systems where they serve the purpose for an excellent adsorbent for heavy metals, chemical contaminants, and bacteria. Clay minerals have an added advantage over other adsorbents via their relative abundance in nature, hydro-plasticity, economical aspects, and environmental affability while usage. Moreover, their large specific surface area, porosity, surface charge, and functional groups are added advantage toward being a good adsorbent (Yuan et al. 2015). Few problems associated with them for large-scale disinfection applications involve their poorer recovery rate from aqueous solution. However, engineering or modifying their surfaces or crystal lattice with metal oxides or NPs does improve their expediency, particularly in disinfection of water.

PCD process using bare ZnO NPs may illustrate few limiting factors like stubborn aggregation, alteration of the surface characteristics or crystal growth, and reduced quantum effects that eventually will lessen its catalytic proficiency and can frontier its commercial utilization. Nonetheless, retrieval of the small-sized nano-photocatalyst subsequently after water treatment would prove as a technical hindrance and henceforth own ambiguity on particle reusability (Chong et al. 2010). To address such confines, it is proposed to use clay-based matrices for immobilization of nano-photocatalyst particles (Praneeth and Paria 2017). Among these, Kaolinite clay has been extensively accepted as a cosmetic material that has antimicrobial and healing properties, establishing itself as a harmless candidate for treating water.

Misra et al. modified kaolinite with ZnO using a simple coprecipitation method and successfully employed it for visible light PCD of a MDR *Enterobacter sp.* which is a coliform bacterium possessing potential threats of waterborne nosocomial infections. To our astonishment, only 150 mg/L of the designed clay-based photocatalyst was sufficient enough to cause 7-log reduction of bacteria within 120 min (Misra et al. 2018). Moreover, when the reusability and recoverability of the catalyst were measured, it was found to be photocatalytically efficient for three subsequent cycles. Earlier Chong et al. (2011) reported the PCD performance of the TiO_2–Kaolinite catalyst synthesized using simple two-step sol–gel method against a sewage-isolated *Escherichia coli sp*. (ATCC 11775). Normal *E. coli* is a common model organism to quantify the efficacy of treatment. Thus using environmental or sewage isolates demonstrate how PCD could behave in case of robust environmental isolates. Under the illumination of UV-A light, a 5-log bacterial reduction was achieved in 70 min at the best operation conditions of 6 g/L TiO_2–K loading, pH 4.0 and 7.5 L/min

aeration rate. Interesting observations were made, that TiO_2–Kaolinite photocatalyst was operable under a wider pH range up to 7.0 in contrast to other conventional photocatalysts. However, a very low PCD rate was achieved at pH 10.0, which is related due to variation in surface charge or PZC (TiO_2–Kaolinite) that weakens the bacteria catalyst interaction.

The use of clay-based photocatalytic nanocomposite is not only restricted to water-based disinfection process. Their applications have been extended to food packaging materials as well. In the late 1980s, Toyota research group reported pronounced improvements in nylon-6 (N6)/montmorillonite (MMT) nanocomposite for their thermal, gas barrier, and mechanical properties. Nanosized clays confer several benefits over conventional micro-sized clays in polymer matrix. This laid the foundation for polymer/clay nanocomposites in various industrial packaging applications. These systems prolong the food shelf life via curbing of humidity, oxygen, ethylene, aroma, or unfamiliar flavors interacting with the food. Most importantly, the presence of clay restricts the growth of foodborne contaminating bacteria and fungus. Bodaghi et al. (2014) reported about low-density polyethylene (LDPE) nanocomposite films with two types of NPs, TiO_2 (3 wt%) and Closite 20A (3 and 5 wt%), synthesized using a melt blow extrusion method (Bodaghi et al. 2013). These NCs showed more mechanical reinforcement, increased gas barrier than their conventional counterparts. Moreover, in 8 Watts UV lamp, tremendous photocatalytic inactivation of *Pseudomonas spp.* and *Rhodotorula mucilaginosa* and degradation of ethylene was achieved in presence of these LDPE-based nanocomposite film that consisted of two kinds of NPs. This might find its application in fresh horticultural product packaging as antimicrobial materials with reformed barrier properties.

Other than photocatalysis, clay founds huge application in antimicrobials. Pyrophyllite, a hydrous aluminosilicate clay mineral achieved 94% disinfection of *E. coli* in solution even while bicarbonates were situated (Kang et al. 2013). Blended Bentonite–polymer composites were also used as antimicrobials. Their blends with sand, zeolite, vermicompost, and charcoal in the form of a filter could intensify their actions and help removal of coliform bacteria from water samples, thus acting as a great source of decontamination in rural areas where resources are limited. Intercalated Montmorillonite, Vermiculite, Palygorskite, and Kaolin with quaternary phosphonium salt and their antibacterial properties were successfully reported against *E. coli ATCC 25922* and *Staphylococci aureus ATCC 6538*. This antimicrobial activity depends on the amount of phosphonium surfactant released, the surface charge and particle size of the adsorbents or organo-clay minerals. According to Wu et al. (2011) increasing the release of phosphonium surfactant, increasing zeta potential (positive charges) and then narrow particle size distribution of the organo-clay adsorbent boosts its antimicrobial proficiency.

2.4 Graphene-Based Nanocomposites

Graphene possesses a plane monolayered two-dimensional (2D) arrangement of carbon atoms in the form of a honeycomb. They are the major building blocks for 0D fullerenes, 1D carbon nanotubes, and 3D graphite. Graphene acquires a high thermal conductivity, electrical properties (π-conjugation), mobile charge carriers at room temperature, and exceptionally high theoretical specific surface area (2600 m^2/g). This had resulted in their exploitation as photocatalyst support for enhanced photocatalytic activity. The ground-breaking reports by Kamat et al., where they created graphene oxide (GO)-TiO_2 nanocrystalline composites demonstrated for the first time the feasibility of using graphene in photocatalytic nanocomposites, inspiring intensive research on their development of next-generation photocatalysts (Williams et al. 2008). Graphene alone possesses antimicrobial activity owing to its which is physicochemical properties related to size, morphology, and surface functional groups. Reports by Akhavan et al. suggested antibacterial action of graphene nanosheets against *E. coli* as well. According to them, the bacterial inactivation in this case is due to a "suicidal mechanism". Normal GO was capable of proliferating the bacterial growth until it was found that components of the bacteria reduce the GO to generate bactericidal and hence suicidal molecules (Akhavan and Ghaderi 2012; Williams et al. 2008). In another study by the group, biocompatible antioxidant melatonin was used for reduction of GO. The bacteria captured within the aggregated GO nanosheets were biologically detached from their surroundings and subsequently killed. Also, if required, photothermal therapy using near-infrared irradiation at 808 nm, could also kill the bacteria. Since the GO does not serve detrimental until reduced, they are applied as an encapsulating material for transport of preferred microorganisms, surface sterilizing agents, and smart-coat technologies for inactivation of microorganisms (McGuinness et al. 2016).

Salient application of graphene in accelerating photocatalytic disinfection is in the form of hybrid nanocomposites with conventional photocatalysts like TiO_2 and ZnO. This could be done by the direct embedding of the semiconductors on the GO surface or crystal lattice. As per Cao et al., graphene/TiO_2 NCs photocatalysts displayed better visible light absorption and also superior photocatalytic inactivation toward *E. coli* when irradiated under visible light, where pure TiO_2 actions were reported negligible (McGuinness et al. 2016). The visible light PCD of these reduced GO/TiO_2 has not been restricted to common Gram-negative organisms, but has also been reported against MDR *E. coli.* As per Prasad et al., it took 120 min for complete disinfection of *E. coli* with detrimental loss to the bacterial genetic component and antibiotic resistance (Prasad et al. 2017). Sun and coworkers constructed GO–TiO_2–Ag NCs with GO sheets (2D) with TiO_2 nanorods (1D) and Ag quantum dots(0D) using a facile two-phase method. These GO–TiO_2–Ag NCs displayed tremendous intrinsic disinfection and biocidal properties against *E. coli* cells. This may be attributed to easy transfer of photo-generated electrons from TiO_2 to GO sheets (Liu et al. 2013). Since the work function of surface-deposited Ag NPs has a Fermi level lower than that of GO the photo-generated electrons might further be transferred from GO to

Ag NPs resulting in delayed electron–hole recombination and better photocatalytic yield. This has been confirmed by other studies too. ZnO has been once considered as the most appropriate alternative for $TiO_2$and photocatalytic applications. Sulphonated GO with ZnO nanorods along with Ag could have greater photocatalytic inactivation activity toward *E. coli* cells than their two-component counterparts like of SGO–ZnO, and ZnO–Ag. Also CdS is recognized as an excellent photocatalyst under visible light. Thus, efforts were use them in graphene-based composites were accomplished by a novel two-phase mixing method. Their visible light PCD performance was evaluated against Gram-negative *E. coli* and Gram-positive *B. subtilis*. The composite was reported to achieve 100% disinfection of *E. coli* and about 90% of *B. subtilis* in 20 and 10 min, respectively (Zhao et al. 2013). This efficiency is better than their lone counterparts, i.e., CdS and GO individually. The much detrimental action on Gram-positive bacteria is attributed to the lack of additional outer membrane in them unlike Gram-negative bacteria, which usually can protect the inner peptidoglycan layer from reactive oxygen species-mediated peroxidation (Ong et al. 2015). On another instance, reduced graphene oxide (RGO)-modified with Bi_2MoO_6 nanoplates using hydrothermal treatment possess superior uniformity and ordered orientation of their active lattice (Ong et al. 2015). They were reported to have better visible light PCD against *E. coli*, i.e., nearly 5-log reduction in 3 h, where Bi_2MoO_6 failed in even 4 h with just 2-log reduction. The better PCD efficiency with oxide (RGO)-modified with Bi_2MoO_6 was attributed to effective charge transfer from Bi_2MoO_6 to graphene (Zhang et al. 2013).

2.5 Nonmetallic Materials Graphitic Carbon Nitride

Polymeric graphitic carbon nitride (g-C_3N_4) has been the major source of photocatalytic attraction in the modern era (Ong et al. 2016). The presence of heptazine ring structure and a great degree of condensation serves advantages related to good physicochemical stability, attractive electronic structure with a bandgap of 2.7 eV, making it sunlight or visible light responsive (Wang et al. 2015). With the ease of preparation involving thermal polycondensation of the less expensive N-rich precursors, like cyanamide (Lei et al. 2015), urea (Lei et al. 2015), thiourea (Lei et al. 2015), melamine (Shan et al. 2016), and dicyandiamide, they can be suitable candidates in water splitting and PCD of harmful coliform waterborne and MDR bacteria.

The photocatalytic efficiency of such materials for the disinfection of *E.coli* was first reported by Huang et al. They reported that the mesoporous form of g-C_3N_4 with surface area nearly equal to 230 m^2/g, resulted complete disinfection of the *E. coli K-12* in presence of sunlight in less than 4 h time (Huang et al. 2014).

Pure g-C_3N_4 endures inadequacy as a suitable photocatalyst due to faster recombination of electron–hole pairs, lesser specific surface area, and lower visible light utilization (Zhang et al. 2012). Thus, researchers are focussing on layering the bulk g-C_3N_4 into nanosheets for better photocatalytic activity. Evidences from Zhao et al. (2014), where a 0.5 nm thick single layer g-C_3N_4 nanosheets using thermal etching

and ultrasonic exfoliation was created, showed visible light-driven photocatalytic inactivation of *E. coli* nearly 7-log reduction within 4 h, unlike their bulk counterparts. This enhancement of photocatalytic efficiency might be credited to the low charge transfer resistance and slower electron–hole recombination.

2.6 Magnetically Separable Photocatalysts for Better Reusability

Iron oxide and some minerals possess the magnetically separable properties might be a good photocatalyst absorbing at visible spectrum of light. In contrast to universally used TiO_2 and ZnO, which mainly absorbs at UV spectrum corresponding to just 5% of the solar spectrum due to its wide bandgap of 3.2 eV. Fe_2O_3 on the other hand have a bandgap of 2.2 eV (Akhavan and Azimirad 2009) and thus is an exciting n-type semiconductor suitable for photocatalysis under visible light spectrum. This better photocatalytic can be attributed to eventual creation of electron–hole pairs via the narrow bandgap illumination. Many variety of Iron (III) oxides have been anticipated like α-Fe_2O_3,γ-Fe_2O_3, α-FeOOH, β-FeOOH, and γ-FeOOH, to degrade organic pollutants and disinfection of bacteria (Zhong et al. 2017). Moreover, these materials work in both liquid and gaseous phase, possess good post-reaction separability, easy to synthesize, high quantum-yield and kinetics, and efficiency, improved surface area and surface charge transfer (Bandara et al. 1997). These iron oxide NCs are evocative for new ways for successful manipulation of photocatalytic properties of iron oxide toward a benign and useful substance in wastewater treatment.

Magnetic iron oxide NC scan be formulated into composites based on TiO_2 or ZnO and other magnetic nanostructures/minerals with enhanced photocatalytic properties. Configuration is based on a magnetic core coated with a titania nanoshell (Iron oxide Core@TiO_2/ZnO), which has been reported. Other group includes a magnetic core, an interlayer of mesoporous SiO_2 and titania or ZnO outer shell (Core@Coating@TiO_2/ZnO). Reports regarding composites with surface decoration using various dopants (Ag/Au/N) have also been explored (Core@(Coating)@TiO_2-doped). Huang et al. reported the utility of Ag/AgBr@$CoFe_2O_4$ composites (250 mg/L) as good antibacterial agents against *E. coli* under visible light (Huang et al. 2017). This is based on the Z-scheme pathway for photocatalytic mechanism. In another report by Ma et al., Fe_3O_4–TiO_2 Nanosheets synthesized using lamellar reverse micelles and solvothermal technique was found to have photocatalytic antibacterial effect on both *E. coli* and *S. aureus* at very less concentration (Ma et al. 2015). The synthesized photocatalysts were found to be efficient even after five repeated cycles. According to them, this happens as a result of H_2O_2 generation by the NCs, which substantially damages the bacterial membrane and deteriorates the whole bacteria structure. The antibacterial effects of iron oxide NCs are not restricted to photocatalysis only. Pairing radiofrequency with magnetic Fe_3O_4@SiO_2–NH_2 core–shell NPs may serve as an alternative physical technique for disinfection of

MDR bacteria. According to the reports by Chaurasia et al., this may serve beneficial in combating biofilm producing bacteria and killing of MDR *S. Aureus* and uropathogenic *E. coli* in less than 30 min (Chaurasia et al. 2016).

However, in spite all the efforts, magnetically separable iron oxide visible light active photocatalysts find limited application, owing to their lessened photocatalytic activity and reduced stability at times (Beydoun et al. 2000). Therefore, seeking out and utilizing the naturally existing magnetic minerals might be a preferred method to attend this crisis. Studying or mining out the photocatalytic properties of natural magnetic sphalerite (NMS) is greatly needed for assessing its application in bacterial disinfection.

Since its discovery from a lead–zinc mine in China, NMS had been directly utilized for visible light bacterial inactivation (Xia et al. 2013). Xia et al. reported that with 6 h irradiation of fluorescent light, they could irreversibly inactivate both Gram-positive *S. aureus* and Gram-negative *E. coli* without. The inactivation or cell damage involves substantial membrane damage and other cellular components as verified by TEM. Point of contact plays a very crucial role in this inactivation, which initiates the damage from the cellular membrane. Interestingly, the primary ROS involved in this study was not like the usual •OH or H_2O_2, but with superoxide radical ($\bullet O_2^-$). If we get into more insights of this study, a five cycle repeated run revealed admirable NMS devoid of a substantial loss in photocatalytic and magnetic property. Although AAS results confirmed a minute ion of heavy metal leaching into the system, i.e., Zn^{2+} (0.17 ppm) and Fe^{2+} (0.032 ppm) when suspended in bacterial cell solution for 8 h. Fortunately, other metal impurities were untraceable and the control experiments do not show toxicity toward cells due to metal ion leakage. In another report by Peng et al., NMS was used as the photocatalyst against *E. coli*, which could be separable and reused using magnetic field (Peng et al. 2017). Results confirmed with irradiation Blue LED light complete disinfection of 1.5×10^5 cfu/mL of *E. coli* could be achieved within 120 min for the first three cycles. However, the PCD efficiency started to decline in the fourth run, while in the fifth run just 3.3-log and 3.5-log reduction could be achieved with blue LED and sunlight respectively. The stability and run dependent loss in photocatalytic properties of NMS might be blockage of the photocatalyst active sites due to the adsorption of the degraded bacterial compounds, reducing the probability of light absorption and charge separation for ROS generation. Their results also showed validation of the process with other Gram-positive bacteria like *S. aureus*, *Microbacterium barkeri*, and *Bacillus subtilis*.

Enthused by the good photocatalytic performance of NMS against bacterial pathogens, the assortment and improvement of efficient alternative materials more of this kind are immediately needed for lost-cost environmental or water remediation. However, the problems of ion leaching and narrow activity might restrict their diverse applications (Xia et al. 2013). Thus, thermally altering them might be a viable option to address the crisis. Thermal treatment can repair the crystal lattice defects, improve their degree of crystallinity and size (Luan et al. 2014), alter the mineral phase (Aramendía et al. 2008), and possibly help in better remediation of waterborne bacteria.

With this regards natural magnetic mineral pyrrhotite photocatalyst was explored and tailored by thermal treatment (Aramendía et al. 2008). Natural pyrrhotite always occurred with impurities corresponding to mineral phases like pyrite (FeS_2), a semiconductor mineral. A pure pyrrhotite sample is a mixture of phases of pyrrhotite-6 T ($Fe_{1-x}S$, PDF 29-0725)and pyrite (FeS_2, PDF 42-1340). A broad absorption band in the range of 300–800 nm could be observed in case of pyrrhotite, a sign of being active in both UV and visible light ranges.

The photocatalytic activity of treated pyrrhotite was assessed by photocatalytic inactivation of *E. coli* K-12 under visible light. With the best activity conferred by the pyrrhotite calcined at 600°C, where the PCD rate was nearly three times higher than that of untreated pyrrhotite. The X-ray diffraction spectra specified the mineral phase of calcined pyrrhotite was altered to mixed crystallite phases of hematite-pyrite (Fe_2O_3–FeS_2) composite. So, the escalation in PCD performance could be attributed to the formation of Z-scheme photocatalysis system composed of hematite and pyrite which guarantees better electron–hole separation efficiency and the bactericidal efficiency (Wang et al. 2008).

3 Challenges Associated with Photocatalysis

Throughout the entire lesson, we have been talking about the utility of photocatalytic reaction in various forms of bactericidal and photocatalytic efficiency. The advantages generally include (Saravanan et al. 2017).

(i) Photocatalysis is a renewable alternative for the energy and cost-intensive conventional treatment methods (adsorption on activated carbon and synthetic resins, ultrafiltration, reverse osmosis, chemical coagulants, ion-exchange methods, and membranes), with remediation efficiency throughout the day time in presence of just sunlight and atmospheric oxygen and water.
(ii) Photocatalysis transfer the pollutants from one phase to nontoxic by-products and secondary wastes unlike conventional treatment measures.
(iii) The photocatalytic process can be applied to various kinds of hazardous organic, inorganic, and microbial contaminants present in waste water matrix.
(iv) It is a reaction that requires mild conditions, lesser time, and chemical input.
(v) Its versatility can be useful for hydrogen generation, gaseous and aqueous phase treatments as well for solid-phase treatments moderately.

The limitation of photocatalysis relies on its interfacial charge separation and charge transfer and delayed recombination of the charge carriers in the form of electron and holes. These are the key factors controlling the photocatalytic efficiency.

Despite a steady development in the use of photocatalyst technologies in recent years, some primary scientific questions must be answered before it can be widely applied and its considerable benefits can be properly exploited.

As per the challenges are concerned, light availability and applicability in multiple geographical locations seem to be the greatest challenge. Proficient photocatalytic

materials found in the literature are metal oxides such as TiO_2, ZnO, and CeO_2. When compared with other metal oxides, titanium dioxide (3.32 eV) is considered better and also a hopeful candidate for the photocatalytic devastation of organic pollutants due to its high quantum efficiency, high stability in aqueous media, and nontoxic in nature (Konstantinou and Albanis 2004; Nakata and Fujishima 2012; Schneider et al. 2014). ZnO and CeO_2 which have a similar bandgap of about 3.32 eV are sometimes preferred over TiO_2 for the degradation of organic pollutants due to its high adsorption properties (Choi et al. 2016; Saravanan et al. 2017; Zhang et al. 2009). Unfortunately, both TiO_2 and ZnO which are highly evaluated for UV photocatalysis are inactive under visible light due to their wide bandgaps. Resulting their inapplicability in spite of a readily available source of visible light (almost 46%) in the form of solar irradiation. Thus, designing the catalyst with lower bandgap is the need of this era, requiring high throughput engineering skills and mineral and oxide processing knowledge for achieving higher catalytic efficiency with these materials, particularly under visible light.

Technical challenges in photocatalyst also persist while modifying them for visible light activation. When a light absorber is hybridized or merged with an additional semiconductor/cocatalyst/or mineral/metal oxide, some of the naturally existing active sites on the light absorber would be blocked by the hybrid components due the coverage of the hybrid materials being extreme. For example, Zhang et al. (2015) customized Ag/$BiVO_4$with 4 wt% of Ag loading to find a diminished photocatalytic activity than the one with lower Ag loading. Another technical challenge of hybridized photocatalyst is reduced light absorption due to the hybrid material shielding phenomenon. This is mainly observed in materials like carbon nanotubes (Ong et al. 2013) graphene, (Ong et al. 2015) and NiSx, (Yin et al. 2014). Thus, engineering them with skills is mostly entertained. Recently, the development of optically transparent guest materials like $Co(OH)_2$/Co_3O_4,[86g] NiO_x, (Morales-Guio et al. 2015) and $NiFeO_x$ with the expectation to reduce undesired light shielding. These materials have proven their worth to be used in photocatalysis. Hybrid materials also possess risk of faster electron–hole recombination for a wide variety of causes owing to structural defects and energetic. Wu et al. (2017) reported that photoactive octahedral Cu_2O became inactive after adding ZnO due to unfavorable band alignment at the interface between ZnO (101) and Cu_2O (111). Thus, the hybrid material engineering has to be judiciously done to abate misalliances that might led to the creation of charge traps for momentous recombination (Morales-Guio et al. 2015).

Geographical conditions of a place along with its latitude and longitude coordinates are one of the major challenges faced with photocatalysis technology. Since the availability of sunlight is utmost near the equatorial region with good amount of the sunlight flux in the countries locating between tropic of cancer and capricorn. Photocatalysis has been widely used in many parts of the world with a savior role in pathogen infested geographical locations of Asia, Africa, and South America. But its applications are limited in Scandinavian countries where rays of sunlight are inadequate. Though the technology could be implemented with artificial light sources, but problems associated with process economy will be the biggest of questions arising.

4 Catalyst Poisoning and Long Term Effect on Human Health, Animal Health and Agriculture

Nanomaterials are extensively being used in the field of medicine and drug delivery for consumer products and money-making that leads to greater exposure direct and indirect in humans (Pattan and Kaul 2014). They are often intentionally coated with biomolecules like protein, DNA and monoclonal antibodies to target human cells (Lewinski et al. 2008; Nalwa 2014). The new physicochemical properties of these formulations may begin new means of damage and toxicological effects due to their disparaging interactions with biological systems and the environment (Ray et al. 2009; Yan et al. 2016). Albeit not as much studied than human health, apprehension regarding environmental impacts specifically with ecotoxicology, environmental chemistry, behavior, and fate are areas of limelight (Zhu et al. 2008). Nanomaterials might possibly pose a threat to the environment through directly effecting invertebrates, microorganisms, aquatic organisms and other species, their interaction with other pollutants might alter into toxic by-products which are more bioavailable, altering the dynamics of nonliving environmental bodies like the carbon, nitrogen, phosphorus, and sulfur cycle (Dhawan and Sharma 2010). Thus, understanding this phenomenon is a decisive phase for the accountable advance of nanotechnology and to attain full advantage of its applications. As nanotechnology establishes its worth, questions are being provoked concerning whether the nanoformulations will be hazardous to the environment and to the health of humans as a whole and whether the processing will generate new hazards when released into waste streams, and agriculture runoffs. Infact, nanomaterials may have significant, unidentified, threats that might be of threat to the workers in research, industries and laboratory, cleaners in disposal and waste facilities (Iavicoli et al. 2014) with major areas of exposure through dermal, respiratory, and gastrointestinal tracts.

In humans, inhalable nanomaterials that have a particle size more than 2.5 μm have a propensity to deposit in the nose and throat whereas NPs lesser than 2.5 μm size can locate their way to the upper airways (Alfaro-Moreno et al. 2007). Owing to their small size, they might possibly pass into the bloodstream through the lungs and eventually taken up by cells and other organs like liver, spleen, kidney, and heart (Sturm 2015). Anatase TiO_2 metal oxide when modified to fibrous structure of greater than 15 μm was toxic enough to initiate an inflammatory response by alveolar macrophages owing to their non-compatible biocompatibility (Hamilton et al. 2009). Further, the size, i.e., 1 nm, shape, and charge of nanomaterials are the foremost feature that facilitates their uptake across the gills or gastrointestinal tract of aquatic and terrestrial organisms (Batley et al. 2012). Wang and their group reported that photoactivated cerium-doped TiO_2 induces apoptosis in Bel 7402 human hepatoma cells (Wang et al. 2007). NPs like ZnO and sunscreen TiO_2 can also induce oxidative damage to DNA as studied in vitro with human fibroblast cells (Braydich-Stolle et al. 2009; Dunford et al. 1997), demonstrated that 100% anatase NPs, in spite of their big size, induces necrosis and cell membrane leakage, without the generation of ROS in contrast to the apoptotic rutile NPs that generate ROS. Thus, it appears that size

and crystal structure might have a function in NPs mediated cytotoxicity. Lucarelli et al. (2004) with their in vitro studies reported SiO_2 and cobalt (Co) NPs to be significantly pro-inflammatory in human marrow monocytes (Vale et al. 2016).

The outcome of nanomaterials in the aquatic environment might be influenced by different factors and processes, such as particle size and charge, aggregation and disaggregation, diffusion, intra interaction between NPs and natural water organic, inorganic components, transformation by-products, biotic and abiotic degradation and photosensitivity (Vale et al. 2016). Currently, nanomaterials are highly suggested for the application of wastewater treatment due to their extraordinary properties. Misra et al. (2018) reported clay-based ZnO NCs for photocatalytic disinfection of MDR microorganisms. The NCs were reported biocompatible against HCT-116 cell lines at an effective concentration of 200 mg/L, it is shown that about 74% of the cells survive. The effect of toxicity was also studied on Zebra Fish Model, to have a better overview of the animal model, where they were reported to be effective, at a concentration of about 150 mg/L, without creating any visible changes in the intestinal linings of the fish, signifying its use in the selective disinfection of MDR species without having post threats of aquatic toxicity (Misra et al. 2018). The reduced toxicity of ZnO based NCs on plant species was also reported by Rahman et al. (2018) where PCD treated water was found to have supportive effects on the germination of *Zea mays* (Misra et al. 2018).

Thus, engineering green NCs has been portrayed as the advancement of clean technologies to lessen possible environmental and human health risks. Also these compatible nanomaterials should promote the replacement of existing toxic nano products with novel formulations that are more environmentally friendly throughout their life cycle and use (Hutchison 2008).

5 Future Perspectives and Practical Applicability of Photocatalyst Technology

Practical demonstrations of water disinfection using TiO_2 and ZnO mediated photocatalysis using immobilized systems can be found in literature galore and possess a big challenge. Current scenario of development of photocatalytic WWT processes dictates that their potential usage at pilot plant scale is still under investigation. Some pilot plants have been created to obtain probable data in terms of efficiency of treatment, volume-specific site area requirements, power consumption, chemical costs, and post-process emissions. The heterogeneous photocatalysis and photo-Fenton plants from pilot plants of Instituto Nacional de Engenharia, Technologia Industrial e Inovacao, Portugal (INETI) and Plataforma Solar de Almeria, Spain (PSA) have delivered most of these data for technical evaluation and further modifications. Both these units have installed compound parabolic collectors with an aperture of 4.16 m^2 to harvest the maximum of sunlight and utilize it for PCD applications in batch

mode. More upgradations in the systems and technology could be made by integrating ideas from experts in process chemistry, environmental biology, mechanical and civil engineering (Chong et al. 2010).

In perspective of the Indian subcontinent, putting on such large treatment plants will be a very hectic task as far as the legislative and economy are concerned. The above description might seem very lucrative in addressing one of the key problems of India, namely, the problem of wastewater treatment. However, there are many operational challenges that still need to be met, while setting up any treatment plants. Moreover, the geographical variations of India are a challenge in itself. From the vast Himalayas that cover the Northern Regions of India to the South Indian Peninsula, each region is a challenge in itself. To overcome this topographical challenge and to provide a smooth channel of technology transfer from the bench to the field, a point of care disinfection device can be proposed. The synthesized biocompatible, inert, nontoxic, and widely accepted modified clay-based NCs would be used in developing a potable point of use water purification device particularly for remote areas, where setting up of water treatment plants is itself a technical confront. The device will not require external energy other than readily available sunlight sources and will totally be based on the synthesized photocatalyst immobilized on the surface of an adsorbent matrixlike commercially available sponges. This may be suggested as a modification of SODIS mechanism which has saved thousands of life in African nations (Sciacca et al. 2010). Adsorbent system, when put inside containers along with water containing bacteria, minor organic, and heavy metal contaminants and exposed to the sunlight, may lead to remediation of the contaminants based on photocatalysis and adsorption mechanism. Thus, allowing the residents to directly drink the water after the 3–4 h treatment. A lot of research is currently into action to find better advancements to this technology in the form of natural agents and membranes. It might need engineering, polymer engineering, chemist, clinicians, and statistical minds for better development. This indigenously proposed technology can indeed help to curtail the menace spread by drinking polluted water. The technique if implemented could indeed provide a low-cost solution to a rising problem in a developing country like India, where capital is always a limiting factor. The economics of production are good enough and the time required for technology transfer is also less, making the goal of this process well achievable.

6 Conclusion

In terms of creating a sustainable environment and public health, proper research and development are needed for designing biocompatible and less expensive photocatalyst for large-scale implications. Although photocatalyst like TiO_2 and ZnO have been employed in Spain and Portugal for real-time applications, the “cost factor” emerges as the biggest challenge. Thus, we are in uttermost need for tracking or mining of naturally occurring substances that could be explored for PCD applications. With this regards clay-based photocatalyst, naturally available minerals, and

iron oxide NCs are gaining much attention due to their robust properties relative to biocompatibility, catalytic efficiency, stability, post-reaction separability. One such catalyst based on clay has been successfully used in PCD of *Enterobacter sp.* by our group. The clay-based photocatalyst was found to have much better biocompatibility and possess no ecotoxic effects when threats of animal cytotoxicity and aquatic toxicity are concerned.

The proposed technology can be one of the cost-effective and technically robust methods to control enteric microbial pathogens including MDRs. This might prevent the nation from outbreaks of cholera and other diarrheagenic diseases and serve beneficial for improving the quality of life in both urban and economically backward rural areas. Moreover the proposed technology can be easily translated for on-field application in the form of a device with proper validation using real hospital and municipal wastewater system for complete disinfection of MDRs and other waterborne bacteria. The proposed technology can equally contribute toward generation of potable water for consumption which finally leads to the overall national development (Chong et al. 2010).

References

Adhikari S, Banerjee A, Eswar NK, Sarkar D, Madras G (2015) Photocatalytic inactivation of E. coli by ZnO–Ag nanoparticles under solar radiation. RSC Adv 5(63):51067–51077

Agus E, Voutchkov N, Sedlak DL (2009) Disinfection by-products and their potential impact on the quality of water produced by desalination systems: a literature review. Desalination 237(1–3):214–237

Akhavan O, Azimirad R (2009) Photocatalytic property of Fe_2O_3 nanograin chains coated by TiO_2 nanolayer in visible light irradiation. Appl Catal A 369(1–2):77–82

Akhavan O, Ghaderi E (2012) Escherichia coli bacteria reduce graphene oxide to bactericidal graphene in a self-limiting manner. Carbon 50(5):1853–1860

Alfaro-Moreno E, Nawrot TS, Nemmar A, Nemery B (2007) Particulate matter in the environment: pulmonary and cardiovascular effects. Curr Opin Pulm Med 13(2):98–106

Aramendía M, Borau V, Colmenares J, Marinas A, Marinas J, Navío J, Urbano F (2008) Modification of the photocatalytic activity of Pd/TiO2 and Zn/TiO2 systems through different oxidative and reductive calcination treatments. Appl Catal B 80(1–2):88–97

Artale MA, Augugliaro V, Drioli E, Golemme G, Grande C, Loddo V, Molinari R, Palmisano L, Schiavello M (2001) Preparation and characterisation of membranes with entrapped TiO_2 and preliminary photocatalytic tests. Annali di chimica 91(3–4):127–136

Ashbolt NJ (2004) Microbial contamination of drinking water and disease outcomes in developing regions. Toxicology 198(1–3):229–238

Bandara J, Pulgarin C, Peringer P, Kiwi J (1997) Chemical (photo-activated) coupled biological homogeneous degradation of p-nitro-o-toluene-sulfonic acid in a flow reactor. J Photochem Photobiol A Chem 111(1–3):253–263

Barancheshme F, Munir M (2018) Strategies to combat antibiotic resistance in the wastewater treatment plants. Front Microbiol 8:2603

Batley GE, Kirby JK, McLaughlin MJ (2012) Fate and risks of nanomaterials in aquatic and terrestrial environments. Acc Chem Res 46(3):854–862

Bergaya F, Lagaly G (2006) General introduction: clays, clay minerals, and clay science. Dev Clay Sci 1:1–18

Beydoun D, Amal R, Low GK-C, McEvoy S (2000) Novel photocatalyst: titania-coated magnetite. Activity and photodissolution. J Phys Chem B 104(18):4387–4396

Bodaghi H, Mostofi Y, Oromiehie A, Zamani Z, Ghanbarzadeh B, Costa C, Conte A, Del Nobile MA (2013) Evaluation of the photocatalytic antimicrobial effects of a TiO_2 nanocomposite food packaging film by in vitro and in vivo tests. LWT-Food Sci Technol 50(2):702–706

Bradley BR, Daigger GT, Rubin R, Tchobanoglous G (2002) Evaluation of onsite wastewater treatment technologies using sustainable development criteria. Clean Technol Environ Policy 4(2):87–99

Braydich-Stolle LK, Schaeublin NM, Murdock RC, Jiang J, Biswas P, Schlager JJ, Hussain SM (2009) Crystal structure mediates mode of cell death in TiO_2 nanotoxicity. J Nanopart Res 11(6):1361–1374

Byrne J, Eggins B, Brown N, McKinney B, Rouse M (1998) Immobilisation of TiO_2 powder for the treatment of polluted water. Appl Catal B 17(1–2):25–36

Carré G, Hamon E, Ennahar S, Estner M, Lett M-C, Horvatovich P, Gies J-P, Keller V, Keller N, Andre P (2014) TiO_2 photocatalysis damages lipids and proteins in Escherichia coli. Appl Environ Microbiol 80(8):2573–2581

Chaurasia AK, Thorat ND, Tandon A, Kim J-H, Park SH, Kim KK (2016) Coupling of radiofrequency with magnetic nanoparticles treatment as an alternative physical antibacterial strategy against multiple drug resistant bacteria. Sci Rep 6:33662

Cho M, Chung H, Yoon J (2003) Quantitative evaluation of the synergistic sequential inactivation of Bacillus subtilis spores with ozone followed by chlorine. Environ Sci Technol 37(10):2134–2138

Choi YI, Lee S, Kim SK, Kim Y-I, Cho DW, Khan MM, Sohn Y (2016) Fabrication of ZnO, ZnS, Ag–ZnS, and Au–ZnS microspheres for photocatalytic activities, CO oxidation and 2-hydroxyterephthalic acid synthesis. J Alloy Compd 675:46–56

Chong MN, Jin B, Chow CW, Saint C (2010) Recent developments in photocatalytic water treatment technology: a review. Water Res 44(10):2997–3027

Chong MN, Jin B, Saint CP (2011) Bacterial inactivation kinetics of a photo-disinfection system using novel titania-impregnated kaolinite photocatalyst. Chem Eng J 171(1):16–23

Das S, Ghosh S, Misra A, Tamhankar A, Mishra A, Lundborg C, Tripathy S (2018b) Sunlight assisted photocatalytic degradation of ciprofloxacin in water using Fe doped ZnO nanoparticles for potential public health applications. Int J Environ Res Public Health 15:2440

Das B, Khan MI, Jayabalan R, Behera SK, Yun S-I, Tripathy SK, Mishra A (2016) Understanding the antifungal mechanism of Ag@ ZnO core-shell nanocomposites against Candida krusei. Sci Rep 6:36403

Das S, Ghosh S, Misra A, Tamhankar A, Mishra A, Lundborg C, Tripathy S (2018) Sunlight assisted photocatalytic degradation of ciprofloxacin in water using Fe doped ZnO nanoparticles for potential public health applications. Int J Environ Res Public Health 15(11):2440

Das S, Sinha S, Das B, Jayabalan R, Suar M, Mishra A, Tamhankar AJ, Lundborg CS, Tripathy SK (2017) Disinfection of multidrug resistant Escherichia coli by solar-photocatalysis using Fe-doped ZnO nanoparticles. Sci Rep 7(1):104

Das S, Sinha S, Suar M, Yun S-I, Mishra A, Tripathy SK (2015) Solar-photocatalytic disinfection of Vibrio cholerae by using Ag@ ZnO core–shell structure nanocomposites. J Photochem Photobiol B 142:68–76

Delgado-Gardea M, Tamez-Guerra P, Gomez-Flores R, Zavala-Díaz de la Serna F, Eroza-de la Vega G, Nevárez-Moorillón G, Pérez-Recoder M, Sánchez-Ramírez B, González-Horta M, Infante-Ramírez R (2016) Multidrug-resistant bacteria isolated from surface water in Bassaseachic Falls National Park, Mexico. Int J Environ Res Public Health 13(6):597

Dhawan A, Sharma V (2010) Toxicity assessment of nanomaterials: methods and challenges. Anal Bioanal Chem 398(2):589–605

Diwan V, Tamhankar AJ, Khandal RK, Sen S, Aggarwal M, Marothi Y, Iyer RV, Sundblad-Tonderski K, Stålsby-Lundborg C (2010) Antibiotics and antibiotic-resistant bacteria in waters associated with a hospital in Ujjain, India. BMC Public Health 10(1):414

Dunford R, Salinaro A, Cai L, Serpone N, Horikoshi S, Hidaka H, Knowland J (1997) Chemical oxidation and DNA damage catalysed by inorganic sunscreen ingredients. FEBS Lett 418(1–2):87–90

Feilizadeh M, Mul G, Vossoughi M (2015) E. coli inactivation by visible light irradiation using a Fe–Cd/TiO_2 photocatalyst: statistical analysis and optimization of operating parameters. Appl Catal B Environ 168:441–447

Fernández Silva FV. Evaluation of virulence and new experimental therapeutic strategies for emerging and uncommon medically important fungal pathogens, Universitat Rovira i Virgili

Fernández-Silva F, Capilla J, Mayayo E, Sutton DA, Hernández P, Guarro J (2013) Evaluation of the efficacies of Amphotericin B, Posaconazole, Voriconazole, and Anidulafungin in a murine disseminated infection by the emerging opportunistic Fungus Sarocladium (Acremonium). Antimicrob Agents Chem 57(12):6265–6269

Francy DS, Stelzer EA, Bushon RN, Brady AM, Williston AG, Riddell KR, Borchardt MA, Spencer SK, Gellner TM (2012) Comparative effectiveness of membrane bioreactors, conventional secondary treatment, and chlorine and UV disinfection to remove microorganisms from municipal wastewaters. Water Res 46(13):4164–4178

Fujishima A, Honda K (1972) Electrochemical photolysis of water at a semiconductor electrode. Nature 238(5358):37

Fujishima A, Zhang X, Tryk DA (2008) TiO_2 photocatalysis and related surface phenomena. Surf Sci Rep 63(12):515–582

Gaya UI, Abdullah AH (2008) Heterogeneous photocatalytic degradation of organic contaminants over titanium dioxide: a review of fundamentals, progress and problems. J Photochem Photobiol C 9(1):1–12

Greer A, Ng V, Fisman D (2008) Climate change and infectious diseases in North America: the road ahead. CMAJ 178(6):715–722

Guo M-T, Yuan Q-B, Yang J (2013) Ultraviolet reduction of erythromycin and tetracycline resistant heterotrophic bacteria and their resistance genes in municipal wastewater. Chemosphere 93(11):2864–2868

Hamilton RF, Wu N, Porter D, Buford M, Wolfarth M, Holian A (2009) Particle length-dependent titanium dioxide nanomaterials toxicity and bioactivity. Part Fibre Toxicol 6(1):35

Hirakawa T, Kamat PV (2005) Charge separation and catalytic activity of Ag@ TiO_2 core—shell composite clusters under UV—irradiation. J Am Chem Soc 127(11):3928–3934

Hrenovic J, Ivankovic T, Tibljas D (2009) The effect of mineral carrier composition on phosphate-accumulating bacteria immobilization. J Hazard Mater 166(2–3):1377–1382

Huang J-J, Hu H-Y, Wu Y-H, Wei B, Lu Y (2013) Effect of chlorination and ultraviolet disinfection on tetA-mediated tetracycline resistance of Escherichia coli. Chemosphere 90(8):2247–2253

Huang J, Ho W, Wang X (2014) Metal-free disinfection effects induced by graphitic carbon nitride polymers under visible light illumination. Chem Commun 50(33):4338–4340

Huang S, Xu Y, Xie M, Liu Q, Xu H, Zhao Y, He M, Li H (2017) A Z-scheme magnetic recyclable Ag/AgBr@ $CoFe_2O_4$ photocatalyst with enhanced photocatalytic performance for pollutant and bacterial elimination. RSC Adv 7(49):30845–30854

Huang Y-Y, Choi H, Kushida Y, Bhayana B, Wang Y, Hamblin MR (2016) Broad-spectrum antimicrobial effects of photocatalysis using titanium dioxide nanoparticles are strongly potentiated by addition of potassium iodide. Antimicrob Agents Chemother 60(9):5445–5453

Hutchison JE (2008) Greener nanoscience: a proactive approach to advancing applications and reducing implications of nanotechnology. ACS Publications

Iavicoli I, Leso V, Ricciardi W, Hodson LL, Hoover MD (2014) Opportunities and challenges of nanotechnology in the green economy. Environ Health 13(1):78

Joshi SG, Cooper M, Yost A, Paff M, Ercan UK, Fridman G, Friedman G, Fridman A, Brooks AD (2011) Nonthermal dielectric-barrier discharge plasma-induced inactivation involves oxidative DNA damage and membrane lipid peroxidation in Escherichia coli. Antimicrob Agents Chemother 55(3):1053–1062

Kafle B, Acharya S, Thapa S, Poudel S (2016) Structural and optical properties of Fe-doped ZnO transparent thin films. Ceram Int 42(1):1133–1139

Kang J-K, Lee C-G, Park J-A, Kim S-B, Choi N-C, Park S-J (2013) Adhesion of bacteria to pyrophyllite clay in aqueous solution. Environ Technol 34(6):703–710

Kim SH, Kwak S-Y, Sohn B-H, Park TH (2003) Design of TiO_2 nanoparticle self-assembled aromatic polyamide thin-film-composite (TFC) membrane as an approach to solve biofouling problem. J Membr Sci 211(1):157–165

Kitajima M, Tohya Y, Matsubara K, Haramoto E, Utagawa E, Katayama H (2010) Chlorine inactivation of human norovirus, murine norovirus and poliovirus in drinking water. Lett Appl Microbiol 51(1):119–121

Kiwi J, Nadtochenko V (2005) Evidence for the mechanism of photocatalytic degradation of the bacterial wall membrane at the TiO_2 interface by ATR-FTIR and laser kinetic spectroscopy. Langmuir 21(10):4631–4641

Kondo Y, Yoshikawa H, Awaga K, Murayama M, Mori T, Sunada K, Bandow S, Iijima S (2008) Preparation, photocatalytic activities, and dye-sensitized solar-cell performance of submicron-scale TiO_2 hollow spheres. Langmuir 24(2):547–550

Konstantinou IK, Albanis TA (2004) TiO_2-assisted photocatalytic degradation of azo dyes in aqueous solution: kinetic and mechanistic investigations: a review. Appl Catal B 49(1):1–14

Labro M-T (2012) Immunomodulatory effects of antimicrobial agents. Part II: antiparasitic and antifungal agents. Expert Rev Anti-infect Ther 10(3):341–357

Lapena L, Cerezo M, Garcia-Augustin P (1995) Possible reuse of treated municipal wastewater for Citrus spp. plant irrigation. Bull Environ Contam Toxicol 55(5):697–703

Lei J, Chen Y, Shen F, Wang L, Liu Y, Zhang J (2015) Surface modification of TiO_2 with g-C_3N_4 for enhanced UV and visible photocatalytic activity. J Alloy Compd 631:328–334

Levy K, Woster AP, Goldstein RS, Carlton EJ (2016) Untangling the impacts of climate change on waterborne diseases: a systematic review of relationships between diarrheal diseases and temperature, rainfall, flooding, and drought. Environ Sci Technol 50(10):4905–4922

Lewinski N, Colvin V, Drezek R (2008) Cytotoxicity of nanoparticles. Small 4(1):26–49

Li J, Shao B, Shen J, Wang S, Wu Y (2013) Occurrence of chloramphenicol-resistance genes as environmental pollutants from swine feedlots. Environ Sci Technol 47(6):2892–2897

Lien L, Lan P, Chuc N, Hoa N, Nhung P, Thoa N, Diwan V, Tamhankar A, Stålsby Lundborg C (2017) Antibiotic resistance and antibiotic resistance genes in Escherichia coli isolates from hospital wastewater in Vietnam. Int J Environ Res Public Health 14(7):699

Liu J, Zhang Y, Lu L, Wu G, Chen W (2012) Self-regenerated solar-driven photocatalytic water-splitting by urea derived graphitic carbon nitride with platinum nanoparticles. Chem Commun 48(70):8826–8828

Liu L, Bai H, Liu J, Sun DD (2013) Multifunctional graphene oxide-TiO_2-Ag nanocomposites for high performance water disinfection and decontamination under solar irradiation. J Hazard Mater 261:214–223

Longo G, Kasas S (2014) Effects of antibacterial agents and drugs monitored by atomic force microscopy. Wiley Interdiscip Rev Nanomed Nanobiotechnol 6(3):230–244

Luan Y, Jing L, Wu J, Xie M, Feng Y (2014) Long-lived photogenerated charge carriers of 0 0 1-facet-exposed TiO_2 with enhanced thermal stability as an efficient photocatalyst. Appl Catal B 147:29–34

Ma S, Zhan S, Jia Y, Zhou Q (2015) Superior antibacterial activity of Fe_3O_4–TiO_2 nanosheets under solar light. ACS Appl Mater Interfaces 7(39):21875–21883

Malato S, Fernández-Ibáñez P, Maldonado MI, Blanco J, Gernjak W (2009) Decontamination and disinfection of water by solar photocatalysis: recent overview and trends. Catal Today 147(1):1–59

Mamane H, Horovitz I, Lozzi L, Di Camillo D, Avisar D (2014) The role of physical and operational parameters in photocatalysis by N-doped TiO_2 sol–gel thin films. Chem Eng J 257:159–169

Matsunaga T, Tomoda R, Nakajima T, Wake H (1985) Photoelectrochemical sterilization of microbial cells by semiconductor powders. FEMS Microbiol Lett 29(1–2):211–214

McGuinness NB, John H, Kavitha MK, Banerjee S, Dionysiou DD, Pillai SC (2016) Self-cleaning photocatalytic activity: materials and applications. Photocatalysis 204–235
McKinney CW, Pruden A (2012) Ultraviolet disinfection of antibiotic resistant bacteria and their antibiotic resistance genes in water and wastewater. Environ Sci Technol 46(24):13393–13400
Miranda-Trevino JC, Coles CA (2003) Kaolinite properties, structure and influence of metal retention on pH. Appl Clay Sci 23(1–4):133–139
Misra AJ, Das S, Rahman AH, Das B, Jayabalan R, Behera SK, Suar M, Tamhankar AJ, Mishra A, Lundborg CS (2018) Doped ZnO nanoparticles impregnated on Kaolinite (Clay): a reusable nanocomposite for photocatalytic disinfection of multidrug resistant Enterobacter sp. under visible light. J Colloid Interface Sci 530:610–623
Morales-Guio CG, Mayer MT, Yella A, Tilley SD, Grätzel M, Hu X (2015) An optically transparent iron nickel oxide catalyst for solar water splitting. J Am Chem Soc 137(31):9927–9936
Munir M, Wong K, Xagoraraki I (2011) Release of antibiotic resistant bacteria and genes in the effluent and biosolids of five wastewater utilities in Michigan. Water Res 45(2):681–693
Muter O (2014) Assessment of bioremediation strategies for explosives-contaminated sites. Biological remediation of explosive residues. Springer, pp 113–148
Nagarajan K, Marimuthu SK, Palanisamy S, Subbiah L (2018) Peptide therapeutics versus superbugs: highlight on current research and advancements. Int J Pept Res Ther 24(1):19–33
Nakata K, Fujishima A (2012) TiO_2 photocatalysis: design and applications. J Photochem Photobiol C 13(3):169–189
Nalwa HS (2014) A special issue on reviews in nanomedicine, drug delivery and vaccine development. J Biomed Nanotechnol 10(9):1635–1640
Öncü NB, Menceloğlu YZ, Balcıoğlu IA (2011) Comparison of the effectiveness of chlorine, ozone, and photocatalytic disinfection in reducing the risk of antibiotic resistance pollution. J Adv Oxid Technol 14(2):196–203
Ong W-J, Gui MM, Chai S-P, Mohamed AR (2013) Direct growth of carbon nanotubes on Ni/TiO_2 as next generation catalysts for photoreduction of CO_2 to methane by water under visible light irradiation. RSC Adv 3(14):4505–4509
Ong W-J, Tan L-L, Chai S-P, Yong S-T, Mohamed AR (2015) Surface charge modification via protonation of graphitic carbon nitride (g-C_3N_4) for electrostatic self-assembly construction of 2D/2D reduced graphene oxide (rGO)/g-C_3N_4 nanostructures toward enhanced photocatalytic reduction of carbon dioxide to methane. Nano Energy 13:757–770
Ong W-J, Tan L-L, Ng YH, Yong S-T, Chai S-P (2016) Graphitic carbon nitride (g-C_3N_4)-based photocatalysts for artificial photosynthesis and environmental remediation: are we a step closer to achieving sustainability? Chem Rev 116(12):7159–7329
Organization WH (2004) Guidelines for drinking-water quality. World Health Organization
Organization WH (2014) Antimicrobial resistance: global report on surveillance. World Health Organization
Otto CC, Haydel SE (2013) Exchangeable ions are responsible for the in vitro antibacterial properties of natural clay mixtures. PLoS ONE 8(5):e64068
Padmanabhan P, Sreekumar K, Thiyagarajan T, Satpute R, Bhanumurthy K, Sengupta P, Dey G, Warrier K (2006) Nano-crystalline titanium dioxide formed by reactive plasma synthesis. Vacuum 80(11–12):1252–1255
Parida S, Axelsson-Robertson R, Rao M, Singh N, Master I, Lutckii A, Keshavjee S, Andersson J, Zumla A, Maeurer M (2015) Totally drug-resistant tuberculosis and adjunct therapies. J Intern Med 277(4):388–405
Pattan G, Kaul G (2014) Health hazards associated with nanomaterials. Toxicol Ind Health 30(6):499–519
Peng X, Ng TW, Huang G, Wang W, An T, Wong PK (2017) Bacterial disinfection in a sunlight/visible-light-driven photocatalytic reactor by recyclable natural magnetic sphalerite. Chemosphere 166:521–527
Praneeth N, Paria S. Clay-semiconductor nanocomposites for photocatalytic applications. In: Clay minerals: properties, occurrence and uses

Praneeth N, Paria S (2017) Clay-semiconductor nanocomposites for photocatalytic applications. Clay Miner Prop Occur Uses 144–184

Prasad K, Lekshmi G, Ostrikov K, Lussini V, Blinco J, Mohandas M, Vasilev K, Bottle S, Bazaka K, Ostrikov K (2017) Synergic bactericidal effects of reduced graphene oxide and silver nanoparticles against Gram-positive and Gram-negative bacteria. Sci Rep 7(1):1591

Prestinaci F, Pezzotti P, Pantosti A (2015) Antimicrobial resistance: a global multifaceted phenomenon. Pathog Global Health 109(7): 309–318

Qing Li Q, Loganath A, Seng Chong Y, Tan J, Philip Obbard J (2006) Persistent organic pollutants and adverse health effects in humans. J Toxicol Environ Health Part A 69(21):1987–2005

Rahman AH, Misra AJ, Das S, Das B, Jayabalan R, Suar M, Mishra A, Tamhankar AJ, Lundborg CS, Tripathy SK (2018) Mechanistic insight into the disinfection of Salmonella sp. by sun-light assisted sonophotocatalysis using doped ZnO nanoparticles. Chem Eng J 336:476–488

Rahman S, Khan M, Akib S, Din NBC, Biswas S, Shirazi S (2014) Sustainability of rainwater harvesting system in terms of water quality. Sci World J 2014

Ray PC, Yu H, Fu PP (2009) Toxicity and environmental risks of nanomaterials: challenges and future needs. J Environ Sci Health Part C 27(1):1–35

Regmi C, Joshi B, Ray SK, Gyawali G, Pandey RP (2018a) Understanding mechanism of photocatalytic microbial decontamination of environmental wastewater. Front Chem 6:33

Regmi YN, Mann JK, McBride JR, Tao J, Barnes CE, Labbé N, Chmely SC (2018b) Catalytic transfer hydrogenolysis of organosolv lignin using B-containing FeNi alloyed catalysts. Catal Today 302:190–195

Rennecker JL, Mariñas BJ, Owens JH, Rice EW (1999) Inactivation of Cryptosporidium parvum oocysts with ozone. Water Res 33(11):2481–2488

Rizzo L, Sannino D, Vaiano V, Sacco O, Scarpa A, Pietrogiacomi D (2014) Effect of solar simulated N-doped TiO_2 photocatalysis on the inactivation and antibiotic resistance of an E. coli strain in biologically treated urban wastewater. Appl Catal B 144:369–378

Ryu S, Kim BI, Lim J-S, Tan CS, Chun BC (2017) One Health perspectives on emerging public health threats. J Prev Med Public Health 50(6):411

Saravanan R, Gracia F, Stephen A (2017) Basic principles, mechanism, and challenges of photocatalysis. In: Nanocomposites for visible light-induced photocatalysis. Springer, pp 19–40

Schneider J, Matsuoka M, Takeuchi M, Zhang J, Horiuchi Y, Anpo M, Bahnemann DW (2014) Understanding TiO_2 photocatalysis: mechanisms and materials. Chem Rev 114(19):9919–9986

Schwarzenbach RP, Egli T, Hofstetter TB, Von Gunten U, Wehrli B (2010) Global water pollution and human health. Annu Rev Environ Resour 35:109–136

Sciacca F, Rengifo-Herrera JA, Wéthé J, Pulgarin C (2010) Dramatic enhancement of solar disinfection (SODIS) of wild Salmonella sp. in PET bottles by H_2O_2 addition on natural water of Burkina Faso containing dissolved iron. Chemosphere 78(9):1186–1191

Selma MV, Beltrán D, Allende A, Chacón-Vera E, Gil MI (2007) Elimination by ozone of Shigella sonnei in shredded lettuce and water. Food Microbiol 24(5):492–499

Shan W, Hu Y, Bai Z, Zheng M, Wei C (2016) In situ preparation of g-C_3N_4/bismuth-based oxide nanocomposites with enhanced photocatalytic activity. Appl Catal B 188:1–12

Shannon MA, Bohn PW, Elimelech M, Georgiadis JG, Marinas BJ, Mayes AM (2010) Science and technology for water purification in the coming decades. Nanosci Technol Collec Rev Nat J (World Scientific) 337–346

Siddiquey IA, Furusawa T, Sato M, Honda K, Suzuki N (2008) Control of the photocatalytic activity of TiO_2 nanoparticles by silica coating with polydiethoxysiloxane. Dyes Pigm 76(3):754–759

Soni S, Dave G, Henderson M, Gibaud A (2013) Visible light induced cell damage of Gram positive bacteria by N-doped TiO_2 mesoporous thin films. Thin Solid Films 531:559–565

Sturm R (2015) A computer model for the simulation of nanoparticle deposition in the alveolar structures of the human lungs. Ann Transl Med 3(19)

Tanwar J, Das S, Fatima Z, Hameed S (2014) Multidrug resistance: an emerging crisis. Interdiscip Perspect Infect Dis 2014

Tripathy SK, Mishra A, Jha SK, Wahab R, Al-Khedhairy AA (2013) Synthesis of thermally stable monodispersed Au@ SnO_2 core–shell structure nanoparticles by a sonochemical technique for detection and degradation of acetaldehyde. Anal Methods 5(6):1456–1462

Vale G, Mehennaoui K, Cambier S, Libralato G, Jomini S, Domingos RF (2016) Manufactured nanoparticles in the aquatic environment-biochemical responses on freshwater organisms: a critical overview. Aquat Toxicol 170:162–174

Ventola CL (2015) The antibiotic resistance crisis: part 1: causes and threats. Pharm Ther 40(4):277

Viessman W, Hammer MJ, Perez EM, Chadik PA (1998) Water supply and pollution control

Von Gunten U (2003) Ozonation of drinking water: Part II. Disinfection and by-product formation in presence of bromide, iodide or chlorine. Water Res 37(7):1469–1487

Wang K, Li Q, Liu B, Cheng B, Ho W, Yu J (2015) Sulfur-doped g-C_3N_4 with enhanced photocatalytic CO_2-reduction performance. Appl Catal B 176:44–52

Wang L, Mao J, Zhang G-H, Tu M-J (2007) Nano-cerium-element-doped titanium dioxide induces apoptosis of Bel 7402 human hepatoma cells in the presence of visible light. World J Gastroenterol WJG 13(29):4011

Wang L, Pan Y, Li J, Qin H (2008) Magnetic properties related to thermal treatment of pyrite. Sci China Ser D Earth Sci 51(8):1144–1153

Wang R, Hashimoto K, Fujishima A, Chikuni M, Kojima E, Kitamura A, Shimohigoshi M, Watanabe T (1998) Photogeneration of highly amphiphilic TiO_2 surfaces. Adv Mater 10(2):135–138

Weaver CE, Pollard LD (2011) The chemistry of clay minerals. Elsevier

Williams G, Seger B, Kamat PV (2008) TiO_2-graphene nanocomposites. UV-assisted photocatalytic reduction of graphene oxide. ACS nano 2(7):1487–1491

Xia D, Ng TW, An T, Li G, Li Y, Yip HY, Zhao H, Lu A, Wong P-K (2013) A recyclable mineral catalyst for visible-light-driven photocatalytic inactivation of bacteria: natural magnetic sphalerite. Environ Sci Technol 47(19):11166–11173

Yan L, Feng M, Liu J, Wang L, Wang Z (2016) Antioxidant defenses and histological changes in Carassius auratus after combined exposure to zinc and three multi-walled carbon nanotubes. Ecotoxicol Environ Saf 125:61–71

Yang K, LeJeune J, Alsdorf D, Lu B, Shum C, Liang S (2012) Global distribution of outbreaks of water-associated infectious diseases. PLoS Negl Trop Dis 6(2):e1483

Yaya A, Agyei-Tuffour B, Dodoo-Arhin D, Nyankson E, Annan E, Konadu D, Sinayobye E, Baryeh E, Ewels C (2012) Layered nanomaterials-a review. Global J Eng Des Technol 2:32–41

Yin L, Yuan Y-P, Cao S-W, Zhang Z, Xue C (2014) Enhanced visible-light-driven photocatalytic hydrogen generation over gC_3N_4 through loading the noble metal-free NiS_2 cocatalyst. RSC Adv 4(12):6127–6132

Yu JC, Ho W, Yu J, Yip H, Wong PK, Zhao J (2005) Efficient visible-light-induced photocatalytic disinfection on sulfur-doped nanocrystalline titania. Environ Sci Technol 39(4):1175–1179

Yuan P, Tan D, Annabi-Bergaya F (2015) Properties and applications of halloysite nanotubes: recent research advances and future prospects. Appl Clay Sci 112:75–93

Zhang L, Yang H, Xie X, Zhang F, Li L (2009) Preparation and photocatalytic activity of hollow ZnSe microspheres via Ostwald ripening. J Alloy Compd 473(1–2):65–70

Zhang N, Liu S, Xu Y-J (2012) Recent progress on metal core@ semiconductor shell nanocomposites as a promising type of photocatalyst. Nanoscale 4(7):2227–2238

Zhang X, Dong S, Zhou X, Yan L, Chen G, Dong S, Zhou D (2015) A facile one-pot synthesis of Er–Al co-doped ZnO nanoparticles with enhanced photocatalytic performance under visible light. Mater Lett 143:312–314

Zhang Y, Zhu Y, Yu J, Yang D, Ng TW, Wong PK, Jimmy CY (2013) Enhanced photocatalytic water disinfection properties of Bi_2MoO_6–RGO nanocomposites under visible light irradiation. Nanoscale 5(14):6307–6310

Zhao H, Yu H, Quan X, Chen S, Zhang Y, Zhao H, Wang H (2014) Fabrication of atomic single layer graphitic-C_3N_4 and its high performance of photocatalytic disinfection under visible light irradiation. Appl Catal B 152:46–50

Zhao J, Deng B, Lv M, Li J, Zhang Y, Jiang H, Peng C, Li J, Shi J, Huang Q (2013) Graphene oxide-based antibacterial cotton fabrics. Adv Healthc Mater 2(9):1259–1266

Zhong D, Ma W, Jiang X, Yuan Y, Yuan Y, Wang Z, Fang T, Huang W (2017) Transformation rules and degradation of CAHs by Fentonlike oxidation in growth ring of water distribution network-A review. In: IOP conference series: earth and environmental science. IOP Publishing

Zhu X, Zhu L, Duan Z, Qi R, Li Y, Lang Y (2008) Comparative toxicity of several metal oxide nanoparticle aqueous suspensions to Zebrafish (Danio rerio) early developmental stage. J Environ Sci Health Part A 43(3):278–284

Magnetic Nanoparticles: Green and Environment Friendly Catalyst for Organic Transformations

Suman Swami and Rahul Shrivastava

Abstract Catalysis by nanoparticles seems an attractive and sustainable alternative of conventional catalyst systems in organic transformations because of their small size and larger reactive surface to volume ratio with higher potential for selectivity. Among the nanocatalysts, magnetic nanoparticles or magnetic core–shell nanoparticles have gained a significant place due to their paramagnetic nature facilitates the separation of catalyst through the use of an external magnet which makes the recovery of the catalyst easier and prevents loss of catalyst associated with conventional filtration or centrifugation methods. The possibility of reusability and milder reaction conditions are additional advantages of nanoparticle catalyzed organic transformations.

1 Introduction

Catalysis is an essential tool in modern science and technology as they meet the demands of the development of eco-compatible and sustainable chemical processes which minimize the energy requirements, use and generation of hazardous reagents and solvents (Govan and Gun'ko 2014). An important demand for a suitable catalyst is their recovery and reusability at the industrial scale, homogenous catalysts demonstrated their superiority in terms of activity and selectivity but majority of industrial catalysts remain heterogeneous because of the simplicity of the latter in tenure of recovery (Hudson 2014). However, in this context nanoparticles seems to be an attractive and sustainable alternative option in term of high activity, selectivity, and improved recyclability possibilities. Among nanoparticles magnetic nanoparticles or core–shell functionalized magnetic nanoparticles have received important place since these MNPs displayed different applications in various domains such as magnetic resonance imaging, data storage, drug delivery, biomedicine, and bioelectrochemical sensing (Mornet 2006; Hyeon 2003; Blanco-Canosa 2014; Delehanty et al. 2009). Besides these important applications, the paramagnetic nature of magnetic nanoparticle simplifies the separation and recovery task and prevents loss of

S. Swami · R. Shrivastava (✉)
Department of Chemistry, Manipal University Jaipur, Jaipur 303007, Rajasthan, India

L. Ledwani and J. S. Sangwai (eds.), *Nanotechnology for Energy and Environmental Engineering*, Green Energy and Technology,
https://doi.org/10.1007/978-3-030-33774-2_20

catalyst which is generally associated with conventional filtrations and centrifugation methods (Swami et al. 2016).

During the past decade, the application of magnetic nanoparticles (MNPs) in organic transformation like synthesis of amino nitriles (Kassaee et al. 2011), dibenzo xanthene derivative (Amoozadeh et al. 2018), friedlander quinoline reaction (Rezayati 2016), oxidations of sulfides and oxidative coupling of thiols (Mahyari and Shaabani 2014), suzuki coupling reactions (Taher 2009), regioselective azidolysis of epoxides (Sajjadifar 2014), knovengel reaction (Zhang and Xia 2009), hydrogenation of alkynes (Abu-Reziq 2007), bignelli synthesis (Safari and Zarnegar 2014), epoxidation of alkenes (Kooti and Afshari 2012), etc., rapidly evolved to further simplify the recovery and reusability of the catalyst with advantages of high product yield, lesser reaction time, and mild reaction conditions. MNps were classified in various classes according to nature of the magnetic core utilized for the same purpose. Among oxides, iron oxides (Fe_2O_3 and Fe_3O_4) has found wide application in organic transformations. The use of metal ferrites (MFe_2O_4, M = Cu, Co, Zn, Mn) generated by partial substitution of iron by a second metal inside the crystal lattice of Fe_3O_4, allow the extension of their catalytic scope, while the iron component continues to enable magnetic recovery (Hudson 2013). For example $CoFe_2O_4$ a magnetic nanoparticle immobilized diamine-*N*-sulfamic acid ($CoFe_2O_4$@SiO_2-DASA) was synthesized by using chemical co-precipitation method and utilized for the amide synthesis via Ritter reaction. Reusability of catalyst was evaluated, after completion of reaction catalyst was recovered by applying strong external magnet followed by washing with ethyl acetate and dried in vacuum (Zhao 2014) (Scheme 1). Similarly magnetic $CoFe_2O_4$ nanoparticles were also used as a catalyst for the oxidation of various alkene in the presence of *tert*-butylhyroperoxide (Kooti and Afshari 2012) (Scheme 2).

Polyphosphoric acid supported on silica-coated $Ni_{0.5}Zn_{0.5}Fe_2O_4$ nanoparticles for their catalytic application in 5-cyano-1,4-dihydropyrano[2,3-c]pyrazole synthesis. 5-cyano-1,4-dihydropyrano[2,3-c]pyrazole was obtained by the four-component condensation of hydrazine hydrate, ethyl 3-oxoproponoate, aromatic aldehyde, and malononitrile in presence of $Ni_{0.5}Zn_{0.5}Fe_2O_4$@SiO_2-PPA as heterogeneous catalyst. $Ni_{0.5}Zn_{0.5}Fe_2O_4$@SiO_2-PPA could be recycled after a very simple work up and

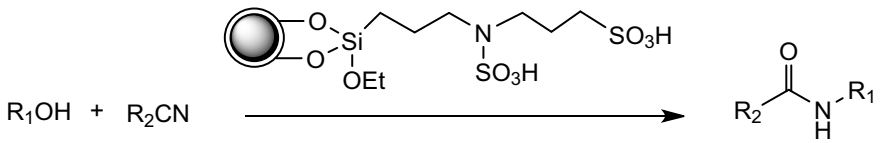

R_1 = $PhCH_2$, 2-$MeC_6H_4CH_2$, 4-$MeC_6H_4CH_2$, Ph_3C
R_2= CH_3, C_6H_5, 4-FC_6H_4, 4-BrC_6H_4, 4-ClC_6H_4, Ph_2CH

Scheme 1 Synthesis of Amide using $CoFe_2O_4$@SiO_2-DASA catalyst (Ritter reaction)

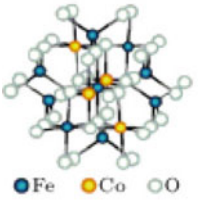

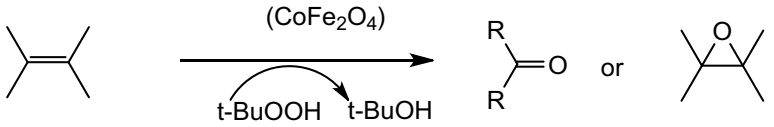

Scheme 2 Oxidation of Alkene using $CoFe_2O_4$ MNPs catalyst

reused at least for six runs without appreciable reduction on its catalytic activity (Moeinpour and Khojastehnezhad 2017) (Scheme 3).

Silane ligand could be achieved as shown in Scheme 4. These synthesized silane ligand was utilized for functionalization of iron oxide magnetic nanoparticles (Scheme 5). These synthesized Lys-Chol-Magnetic NPs were used for condensation of benzaldehyde with malononitrile or ethyl cyanoacetate at room temperature as depicted in Scheme 6. In the above condensation reaction, NH_2 group of amino acid extracts the proton from the methylene group of ethyl cyanoacetate or malononitrile to form the corresponding carbanion. Next, the resulting carbanion attacks on the

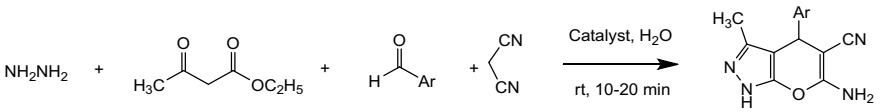

Scheme 3 $Ni_{0.5}Zn_{0.5}Fe_2O_4$@SiO_2-PPA catalyzed the synthesis of pyranopyrazoles

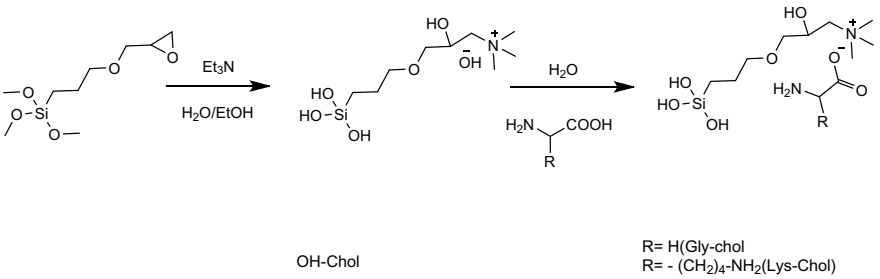

Scheme 4 Synthesis of silane ligands containing choline amino acid ionic liquid

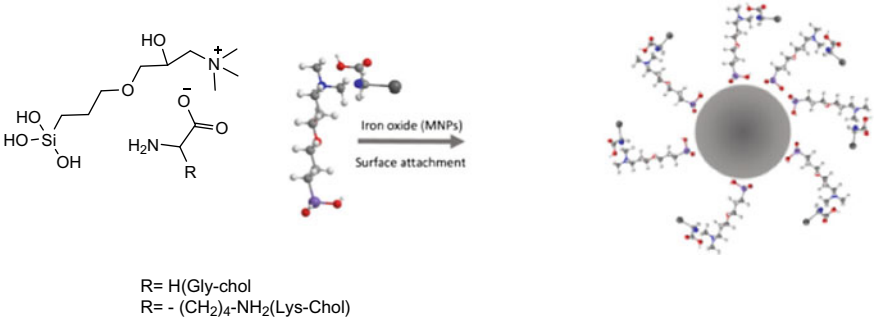

Scheme 5 Silanization of iron oxide magnetic nanoparticles

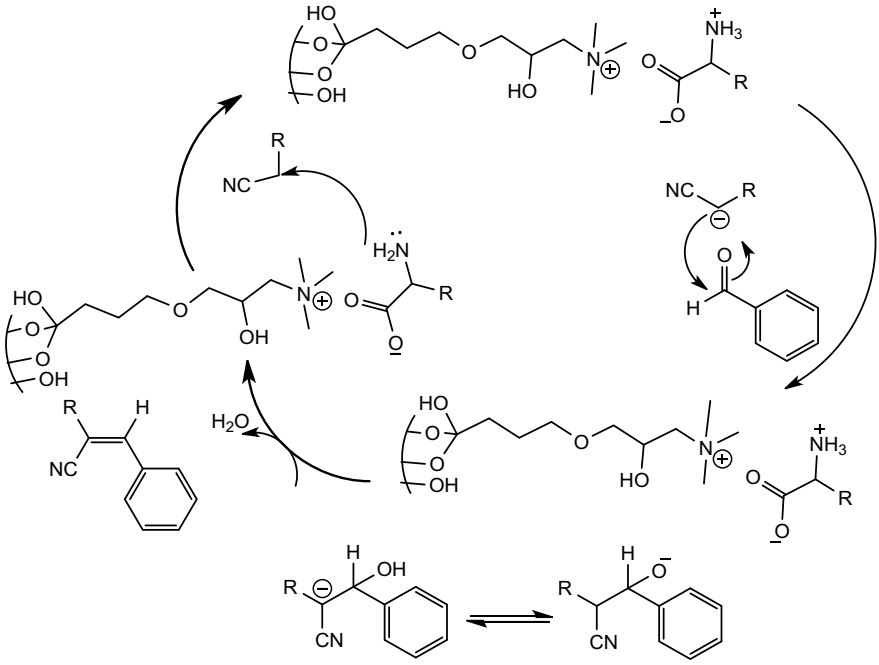

Scheme 6 Proposed ion-pair mechanism for the Knovengel condensation reaction using Lys-Chol-MNPs and Gly-Chol-MNPs catalyst

carbonyl group of the benzaldehyde to yield an enol species, which finally offered the desired product via capturing the proton of the catalyst (del Hierro et al. 2018).

Similarly, a silver supported γ-Fe_2O_3@HAp-Ag magnetic nanoparticle catalyst was prepared for coumarin synthesis. These MNps used as magnetically recyclable

heterogeneous catalysts for the synthesis of coumarin derivatives by one-pot condensation of various phenols with ethyl acetoacetate under solvent and halogen-free conditions. A proposed mechanism for 7-hydroxy-4-methyl-2H-chromen-2-one synthesis from the reaction of ethyl acetoacetate with resorcinol using γ-Fe_2O_3@HAp-Ag NPs was depicted in Scheme 7 (Abbasi 2017).

Another case of Fe_3O_4 nanoparticles is functionalized with calix[4]arene proline moiety (Calix-Pro-MN) which is used as recyclable organocatalyst in asymmetric aldol condensation of cyclohexanone and aromatic aldehydes as depicted in Scheme 8 (Akceylan 2015).

Another magnetic nanoparticles Fe_3O_4@SiO_2GMSI-VBI were prepared via three step synthetic protocol as depicted in Scheme 9. In the first step Fe_3O_4 Nps were synthesized via chemical co-precipitation of $FeCl_2$ and $FeCl_3$ and then these Nps were coated with TEOS via Stober method. In second step, commercially available GMSI was reacted with VBI in dry THF to yield GMSI-VBI ligand. Finally Fe_3O_4@SiO_2GMSI-VBI MNPs obtain by refluxing suspended mixture of GMSI-VBI and Fe_3O_4@SiO_2 in dry THF. The synthesized Fe_3O_4@SiO_2GMSI-VBI MNps has prominent advantage compare to other catalysts used for 2,3-dihydroquinazolin-4(1H)-ones synthesis like shorter reaction time, low catalyst loading, and readily recovered using external magnet and reused without any treatment with efficient catalytic activity (Azizi et al. 2017).

A class of magnetic silver nanoparticles were supported over Al_2O_3 cores and Fe_2O_3 shells were prepared successfully as depicted in Scheme 10. Synthesized Ag-Al_2O_3@Fe_2O_3 magnetic nanoparticles used as a catalyst in synthesis of 1,2,3-triazole and acylation of benzyl alcohol. Mesoporous Ag-Al_2O_3@Fe_2O_3 shows high catalytic efficiency for synthesis of 1,4-disubstituted 1,2,3-triazole in aqueous medium and

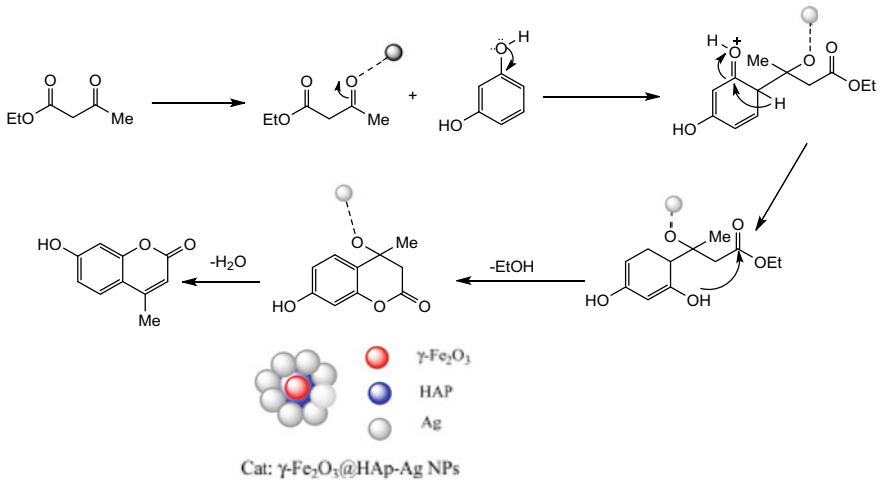

Scheme 7 Proposed mechanism for one-pot synthesis of 7-hydroxy-4-methyl-2H-chromen-2-one promoted by γ-Fe_2O_3@HAp-Ag NPs

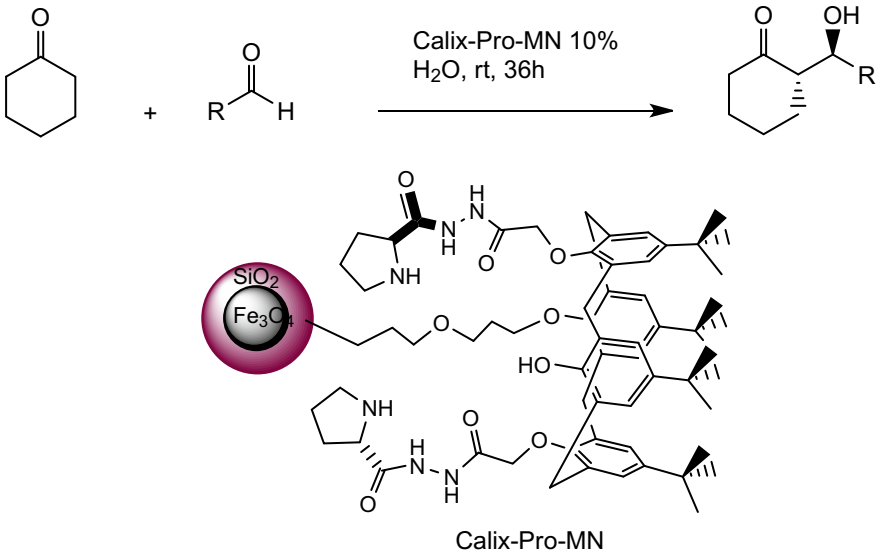

Scheme 8 Fe_3O_4 nanoparticles are functionalized with calix[4]arene proline moiety

acylation of benzyl alcohol under solvent-free condition (Basu 2017) (Schemes 11 and 12).

$Fe_3O_4@SiO_2$ NPs were synthesized by surface modification of Fe_3O_4 NPs. The surface modification was carried out by the hydrolysis of tetraethylorthosilicate in presence of ammonia as shown in Scheme 13, $Fe_3O_4@SiO_2$ consist of Fe_3O_4 magnetic core and outer shell of SiO_2. 1,4-dihydropyridine derivatives were obtain via one-pot multicomponent condensation of 4-hydroxycoumarine or dimedone, aldehydes and ammonium acetate using $Fe_3O_4@SiO_2$ as reusable heterogeneous catalyst. A plausible mechanism for the synthesis of 1,4-dihydropyridines is shown in Scheme 14. Initially MNPs bind at carbonyl oxygen atom which increases the carbonyl activity and makes α-H highly acidic. Thereby this highly acidic α-H facilitates the enolization and nucleophilic attack to the aromatic aldehydes for Knovengel product formation. This Knovengel product further reacted in Michael manner with another C-H activated molecule to furnish an intermediate, this intermediate offered target product via ammonia induced cyclization (Dam et al. 2014).

An iron oxide modification, Cu-doped $CoFe_2O_4$ magnetic nanoparticles were synthesized and used in carbon–nitrogen cross-coupling reaction. The Cu-doped $CoFe_2O_4$ synthesis was achieved in four synthetic steps, first step involves synthesis of cobalt ferrire magnetic, thereafter in next step cobalt ferrite Nps are functionalized with amine groups. In third step amino propyl silica composite was treated with furfural and finally furfural grafted amine functionalized cobalt ferrite Nps were doped with copper by using copper acetate in acetone at room temperature for 24 h as shown in Scheme 15. The synthesized $CoFe_2O_4@SiO_2$-NH_2-furfural-$Cu(OAc)_2$

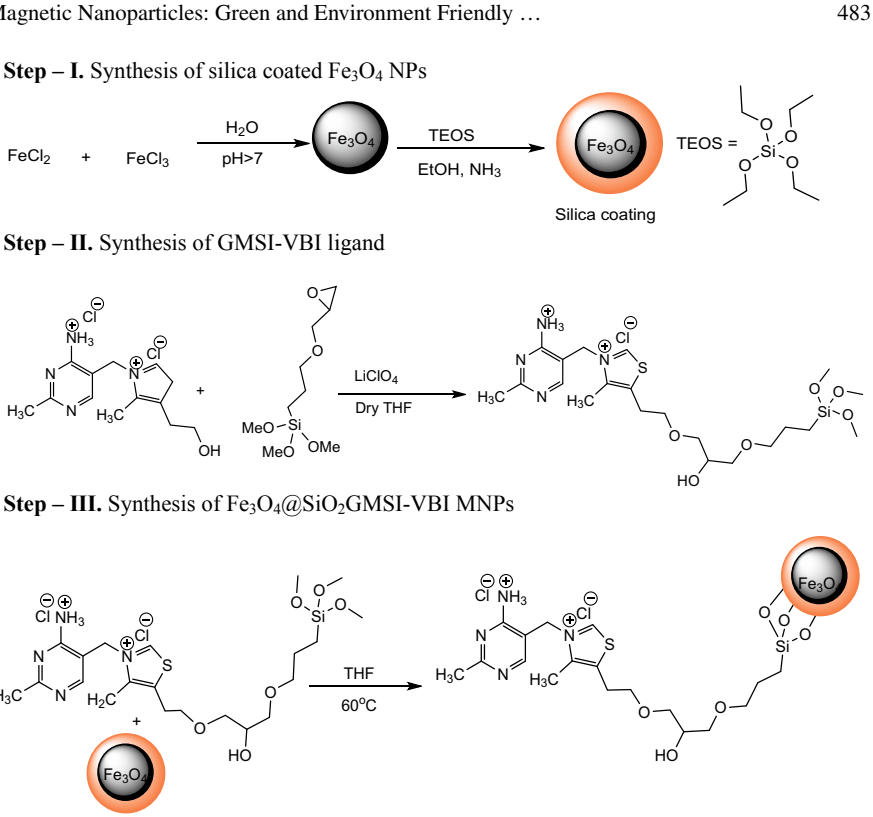

Scheme 9 Synthetic route of Fe_3O_4@SiO_2GMSI-VBI MNPs synthesis

successfully used in Chan-Lam type cross-coupling of benzamide with boronic acid (Dutta and Phukan 2018).

$CuFe_2O_4$ magnetic nanoparticles also used as catalysts for the synthesis of 1,2,4,5-tetrasubstituted imidazoles via four-component condensation of 1,2-diketone with an aldehyde, propargylamine and ammonium acetate in aqueous medium. The catalytic activity of $CuFe_2O_4$ proceeds via the diamine intermediate formation, which is formed by the activation of aldehyde carbonyl group by $CuFe_2O_4$ magnetic nanoparticles, thereafter condensation of diamine with 1,2-diketone followed by dehydration and then rearrangement through the imino intermediate yielded the target product as depicted in Scheme 16 (Ali and Abu-Dief 2015).

A copper supported $CuCl_2/Fe_3O_4$-TEDETA magnetic nanoparticles prepared for catalytic application in the synthesis of 2,3-dihydroquinazolin-4(1H)-ones derivatives. The $CuCl_2/Fe_3O_4$-TEDETA MNps were prepared by using four-step synthetic protocol as depicted in Scheme 17. In the first step Fe_3O_4 MNPs were prepared by co-precipitation of Fe^{2+} and Fe^{3+} using NH_3 solution, then in second step the 3-aminopropyltriethoxysilane added was adsorbed onto the surface of the Fe_3O_4 nanoparticles and form coordination bond with hydroxyl group,

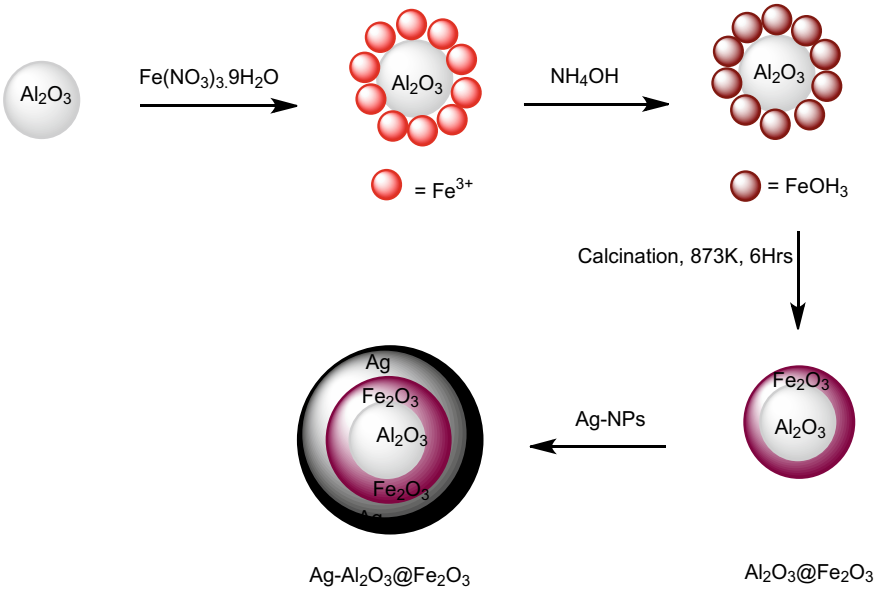

Scheme 10 Synthesis of mesoporous Ag-Al_2O_3@Fe_2O_3 core–shell nanocatalyst

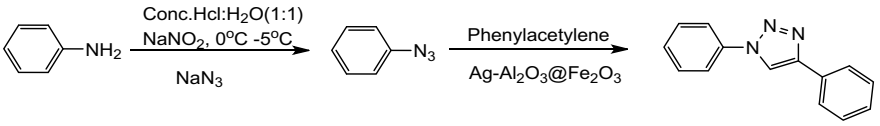

Scheme 11 One–pot synthesis of 1,4-diphenyl-1H-1,2,3-triazole

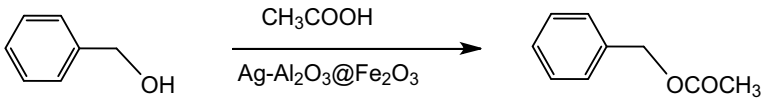

Scheme 12 Acylation of benzyl alcohol

thereafter the obtained amino-coated Fe_3O_4 nanoparticles were reacted with acryloyl chloride led to acryloxy groups-functionalized magnetic Fe_3O_4 nanoparticles. These acryloxyl groups-functionalized magnetic Fe_3O_4 nanoparticles reacted with tetraethyldiethylenetriamine to get Fe_3O_4-TEDETA Nps. Finally, the complexes $CuCl_2$/Fe_3O_4-TEDETA were prepared by the reactions of copper(II) chloride with the individual ligands MNO-TEDETA ethanol. These synthesized $CuCl_2$/Fe_3O_4-TEDETA used as catalyst in condensation of 1-aminobenzamide with aldehyde to afford the corresponding 2,3-dihydroquinazolin-4(1H)-one derivatives in excellent yield at reflux conditions (Ghorbani-Choghamarani and Norouzi 2014).

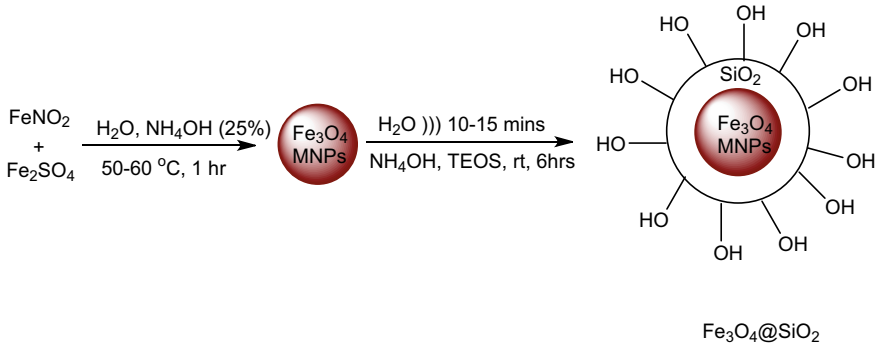

Scheme 13 Synthesis of Fe_3O_4@SiO_2 magnetic nanoparticles

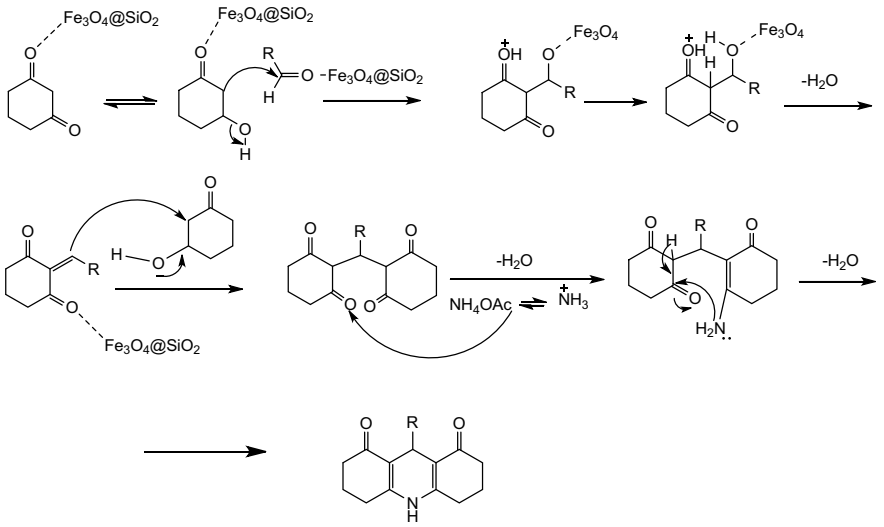

Scheme 14 Plausible mechanism for the synthesis of 1,4-dihydropyridines derivatives

In another example, 2-hydroxyethylammonium sulphonate immobilized on γ-Fe_2O_3 nanoparticles for the preparation of Fe_2O_3-2HEAS magnetic nanoparticles as depicted in Scheme 18. Initially, in the first step γ-Fe_2O_3 obtain by chemical co-precipitation of ferrous and ferric in alkali solution, thereafter γ-Fe_2O_3 enrich with the hydroxyl groups using ammonium hydroxide and finally 2-hydroxyethylammonium sulphonate immobilized on γ-Fe_2O_3 by using ethanolamine precursor. These Fe_2O_3-2HEAS used for the synthesis of 2-amino-3,5-dicarbonitrite-6-thio-pyridines from aliphatic aldehydes or thiols (Sobhani and Honarmand 2013).

Fe_3O_4 magnetic nanoparticles lead an organic transformation 5,5-disubstituted hydantoin from multicomponent reactions of carbonyl compounds, potassium cyanide, and ammonium carbonate in solvent-free conditions. Fe_3O_4 MNPs works

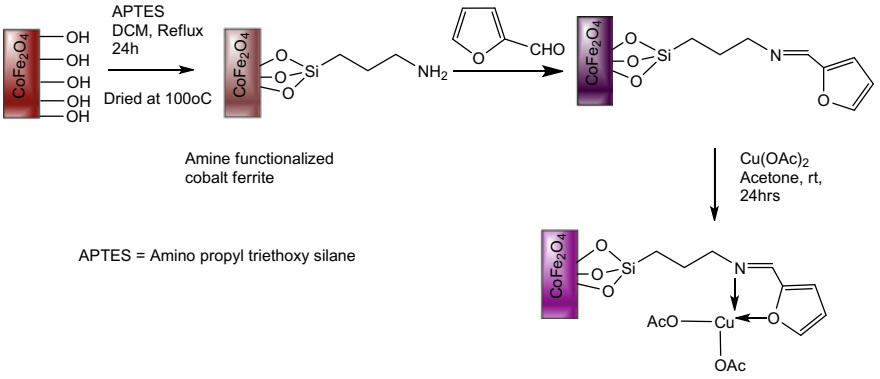

Scheme 15 Synthesis of $CoFe_2O_4$@SiO_2-NH_2-Furfural-$Cu(OAc)_2$

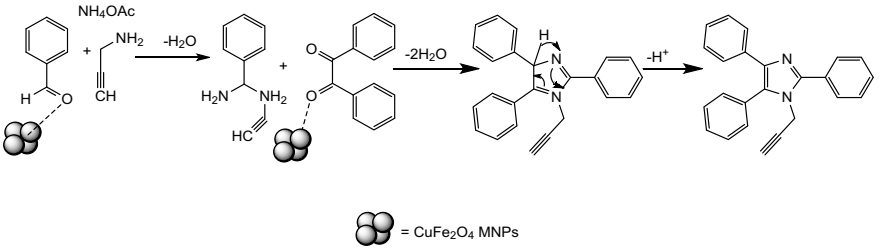

Scheme 16 Plausible mechanism for the formation of substituted propynyl-1H-imidazoles

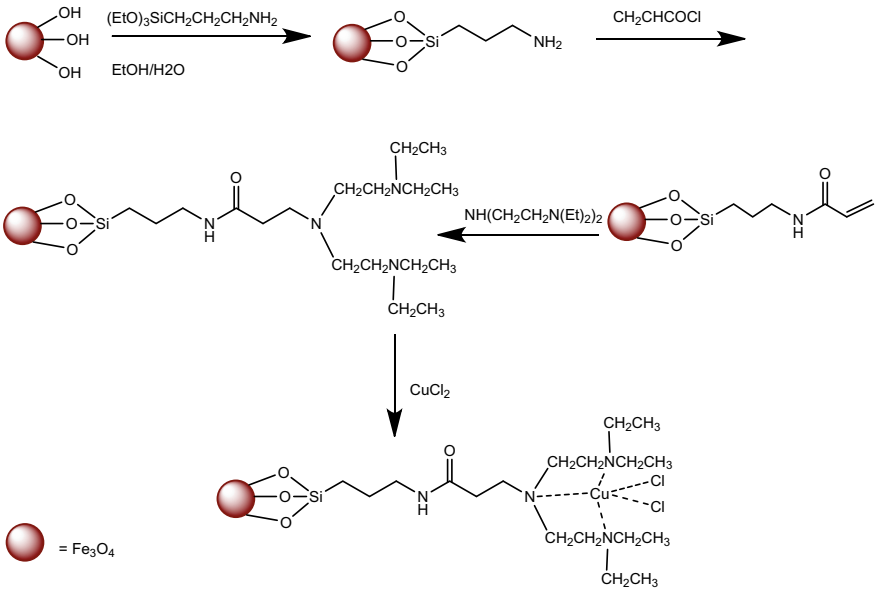

Scheme 17 Synthesis of $CuCl_2/Fe_3O_4$-TEDETA

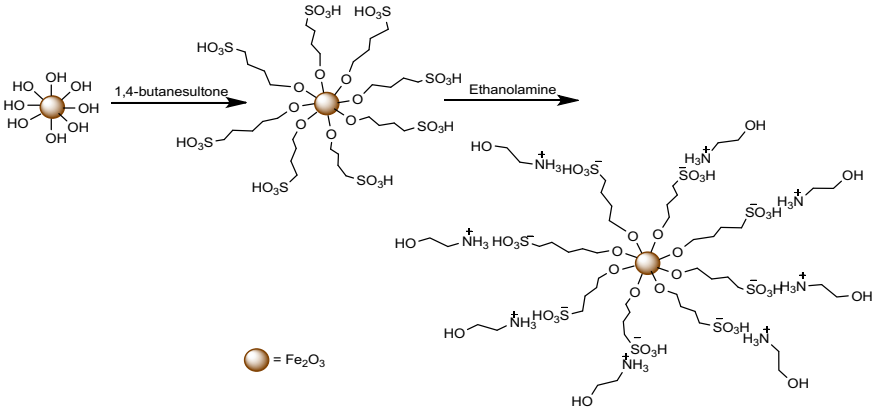

Scheme 18 Synthesis of Fe_2O_3-2HEAS

as reusable heterogeneous catalyst in this transformation (Safari and Javadian 2013) (Scheme 19).

Similarly, Fe_3O_4 magnetic nanoparticles also employed as catalyst in the synthesis of 1,4-dihydropyridine and polyhydroquinoline derivatives as shown in Scheme 20. A proposed mechanism also depicted in Scheme 21 for the catalytic activity of Fe_3O_4 MNPs in polyhydroquninolines synthesis. Basically it involves knovengel condensation of aldehydes and active methylene compounds and subsequently Michael type

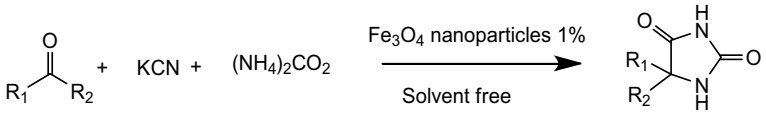

Scheme 19 Synthesis of hydantoin derivatives by using magnetic Fe_3O_4 nanoparticles under solvent-free conditions

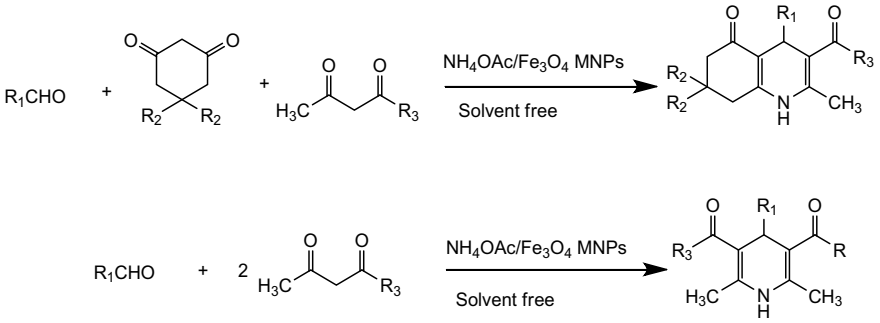

Scheme 20 Synthesis of polyhyrdoquinolines

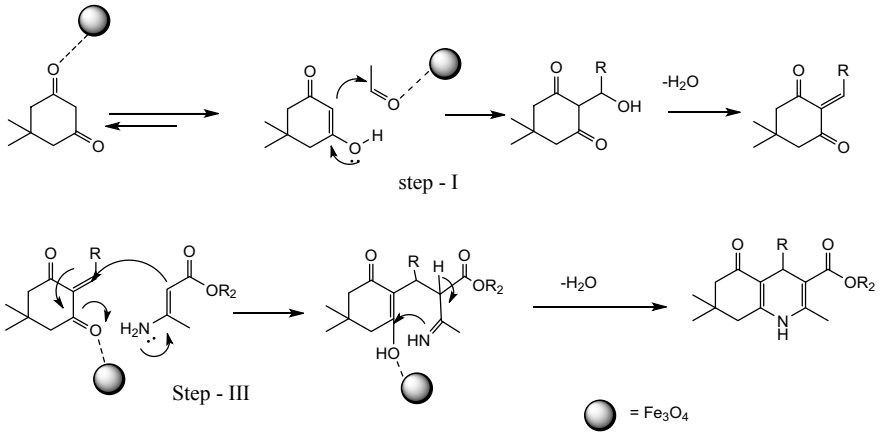

Scheme 21 Plausible mechanism for polyhyrdoquinolines synthesis

addition of intermediated formed as shown in Scheme 21. The role of catalyst comes in steps 1 where it catalyzes the Knoevenagel type coupling of aldehydes with active methylene compounds and in steps 3 where it catalyzes the Michael type addition of intermediates to give product (Nasr-Esfahani 2014).

In continuation of magnetic nanoparticle catalyze organic transformation, a sulfonic acid-functionalized silica-coated $CuFe_2O_4$ magnetic nanoparticles ($CuFe_2O_4$@SiO_2-SO_3H) employed for 2-pyrazole-3-amino-imidazo-fused polyheterocycles synthesis. $CuFe_2O_4$@SiO_2-SO_3H Nps were prepared by adopting a multistep reaction procedure as shown in Scheme 22. Firstly, $CuFe_2O_4$ nanoparticles were prepared via chemical co-precipitation of $Cu(CH_3COO)_2 \cdot H_2O$ and $FeCl_3 \cdot 6H_2O$ in alkali medium. Thereafter silica coating was achieved using sol-gel process with TEOS in ammonium medium. Finally, silica-coated magnetic $CuFe_2O_4$@SiO_2 were functionalized with chlorosulfonic acid which yielded $CuFe_2O_4$@SiO_2-SO_3H magnetic Nps. Resulting $CuFe_2O_4$@SiO_2-SO_3H serve as reusable catalyst for the 2-pyrazole-3-amino-imidazo[1,2-a]pyridine derivative synthesis via four-component

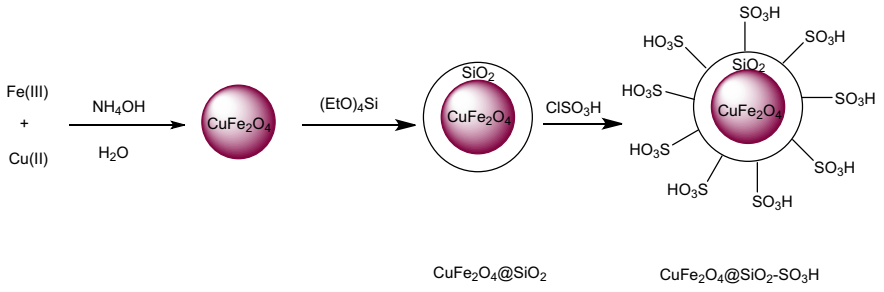

Scheme 22 Synthesis of sulfonic acid-functionalized silica-coated $CuFe_2O_4$ magnetic nanoparticles ($CuFe_2O_4$@SiO_2-SO_3H)

condensation reaction of 2-aminoazine, alkyl-4-formyl-1-substituted phenyl-1H-pyrazole-3-carboxylate and isocyanides in ethanol (Swami et al. 2016) (Scheme 23).

Similarly, a carbon nanotube supported $CoFe_2O_4$/CNT-Cu magnetic nanoparticles were used in 3-nitro-2-arylimidazo [1,2-a]pyridines synthesis. $CoFe_2O_4$/CNT-Cu Nps offer a reusable catalytic activity for 3-nitro-2-arylimidazo [1,2-a]pyridines synthesis via a three-component reaction of 2-aminopyridines, aldehydes, and nitromethane in PEG 400 under aerobic conditions as shown in Scheme 24 (Zhang 2016).

Another example of ferrite magnetic nanoparticle in organic transformation is $CuFe_2O_4$ Nps, these Nps are magnetically recoverable and reusable catalyst for the synthesis of 5-substituted 1H-tetrazoles. A variety of aryl nitriles undergoes 2 + 3 cycloaddition in the presence of $CuFe_2O_4$ magnetic Nps as shown in Scheme 25, $CuFe_2O_4$ provides mild reaction condition, excellent yield, and reusability around five-times without losing catalytic efficiency (Sreedhar et al. 2011).

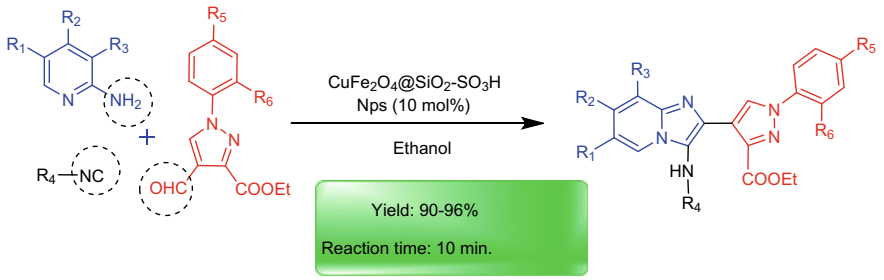

Scheme 23 Synthesis of 2-pyrazole-3-amino-imidazo[1,2-a]pyridine derivative in presence of $CuFe_2O_4$@SiO_2-SO_3H magnetic nanoparticles

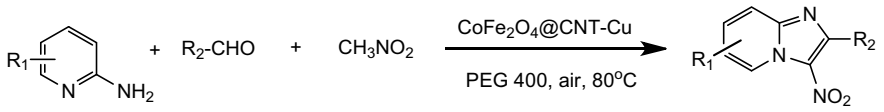

Scheme 24 Synthesis of 3-nitro-2-arylimidazo [1,2-a]pyridines catalyzed by $CoFe_2O_4$/CNT-Cu Nps

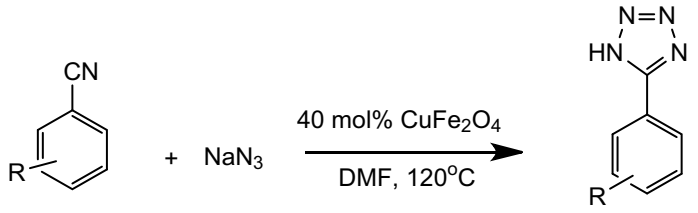

Scheme 25 Synthesis of 5-substituted 1H-tetrazoles using $CuFe_2O_4$ Nps

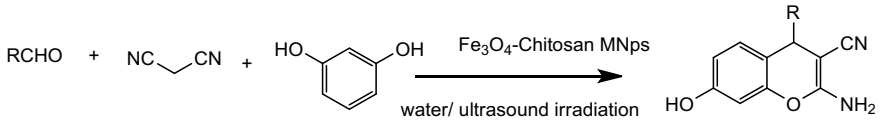

Scheme 26 One-pot synthesis of 2-amino-4H-chromenes catalyzed by Fe_3O_4-chitosan magnetic Nps at 50 °C under ultrasound irradiation

Similarly, a ferrite magnetic Fe_3O_4-Chitosan nanocatlyst used for synthesis of 2-amino-4H-chromones derivatives. These magnetic nanoparticles allow synthesis of 2-amino-4H-chromones derivatives under ultrasound irradiation in shorter time with excellent yield. A plausible mechanism for the formation of 2-amino-4H-chromenes is also depicted in Scheme 27, in which free hydroxyl groups on the surface of chitosan of Fe_3O_4-Chitosan nanocatlyst play a significant role in increasing electrophilic character of the aldehyde so that carbonyl group of aldehyde could activate for Knovengel condensation with malononitrile. Thereafter resulting intermediate which is formed through Knovengel condensation of aldehyde and malononitrile, further via Michael addition to form an intermediate (transition sate). This intermediate proceeds through cyclization to yield target 2-amino-4H-chromones derivatives (Safari and Javadian 2015) (Scheme 26).

In the connection of magnetic nanocatalyzed organic transformation, a magnetic core–shell Fe_3O_4@SiO_2-Au/Cu nanoparticles were prepared for the catalytic performance in Ullmann coupling reaction of bromamine acid. As depicted in Scheme 28, initially the surface of silica-coated Fe_3O_4@SiO_2 was first function-

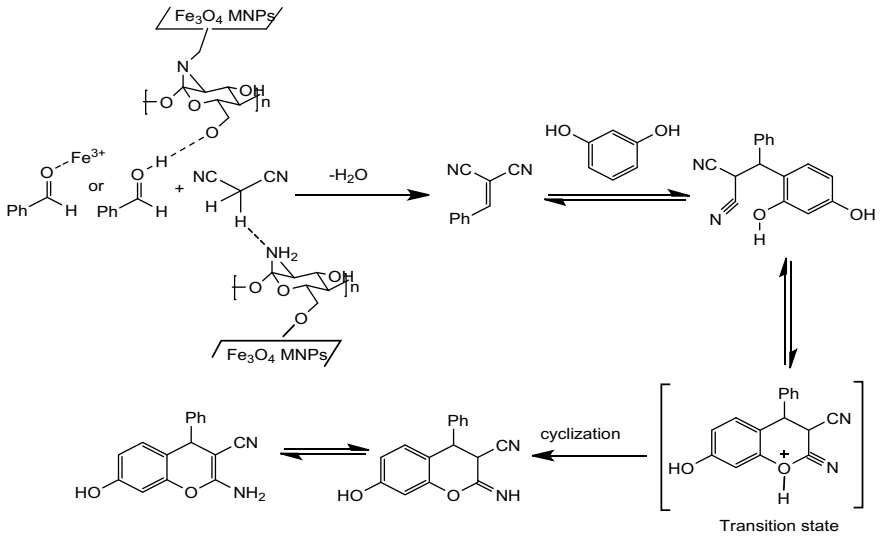

Scheme 27 Plausible mechanism for Fe_3O_4-Chitosan catalyzed one-pot synthesis of 2-amino-4H-chromenes

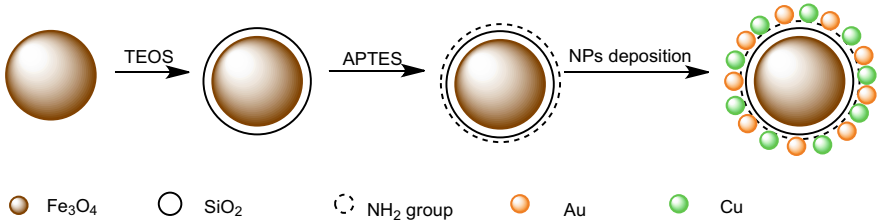

Scheme 28 Stepwise synthesis/fabrication of Fe_3O_4@SiO_2-Au/Cl Nps

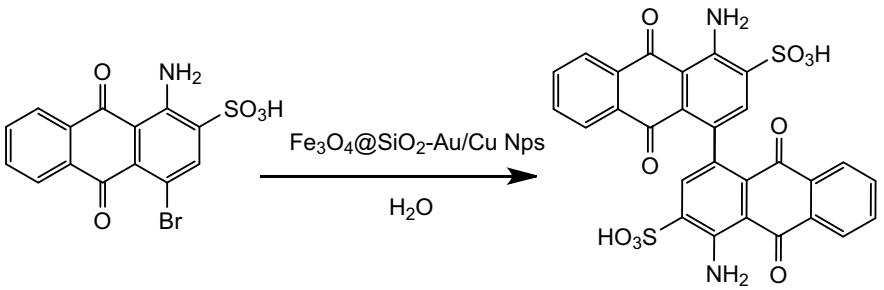

Scheme 29 The Ullmann coupling reaction of bromamine acid

alized with amino groups using 3-aminopropyltriethoxysilane, thereafter Au and Cu Nps were separately synthesized by direct reduction method using HAuCl4 and $CuSO_4$ as precursors, trisodium citrate dehydrate as the capping agent and $NaBH_4$ as the reducing agent. The sequential adsorption of Au and Cu Nps on Fe_3O_4@SiO_2 gave the Fe_3O_4@SiO_2-Au/Cu nanoparticles. The good dispersion of Au/Cu Nps on Fe_3O_4@SiO_2 surface provides high catalytic efficiency for the synthesis of 4,4′-diamino-1,1′dianthraquinonyl-3,3′-disulfonic acid from bromamine acid as shown in Scheme 29 (Gao 2018).

2 Conclusion(s)

In this chapter, we discussed the catalytic advantage of magnetic nanoparticle over the homogeneous catalyst in organic synthesis due to their simplicity of the latter in tenure of recovery. We also discussed synthesis of various magnetic or magnetic core–shell nanoparticles by different approaches and their uses as catalyst in different organic transformations with advantages of easy separation, milder reaction conditions, and reusability.

Acknowledgements R. S. acknowledge Manipal University Jaipur for seed money grant. S. S. acknowledges MUJ for teaching assistantship.

References

Govan J, Gun'ko YK (2014) Recent advances in the application of magnetic nanoparticles as a support for homogeneous catalysts. Nanomaterials 4(2):222–241

Hudson R (2014) Bare magnetic nanoparticles: sustainable synthesis and applications in catalytic organic transformations. Green Chem 16(10):4493–4505

Mornet S (2006) Magnetic nanoparticle design for medical applications. Prog Solid State Chem 34(2–4):237–247

Hyeon T (2003) Chemical synthesis of magnetic nanoparticles. Chem Commun 8:927–934

Blanco-Canosa JB (2014) Recent progress in the bioconjugation of quantum dots. Coord Chem Rev 263:101–137

Delehanty JB, Mattoussi H, Medintz IL (2009) Delivering quantum dots into cells: strategies, progress and remaining issues. Anal Bioanal Chem 393(4):1091–1105

Swami S, Agarwala A, Shrivastava R (2016) Sulfonic acid functionalized silica-coated $CuFe_2O_4$ core–shell nanoparticles: an efficient and magnetically separable heterogeneous catalyst for the synthesis of 2-pyrazole-3-amino-imidazo-fused polyheterocycles. New J Chem 40(11):9788–9794

Kassaee M, Masrouri H, Movahedi F (2011) Sulfamic acid-functionalized magnetic Fe_3O_4 nanoparticles as an efficient and reusable catalyst for one-pot synthesis of α-amino nitriles in water. Appl Catal A 395(1–2):28–33

Amoozadeh A, Hosseininya SF, Rahmani S (2018) Nano titania-supported sulfonic acid (n-TSA) as an efficient, inexpensive, and reusable catalyst for one-pot synthesis of 1, 8-dioxo-octahydroxanthene and tetrahydrobenzo [b] pyran derivatives. Res Chem Intermed 44(2):991–1011

Rezayati S (2016) Imidazole-functionalized magnetic Fe_3O_4 nanoparticles: an efficient, green, recyclable catalyst for one-pot Friedländer quinoline synthesis. Res Chem Intermed 42(6):5887–5898

Mahyari M, Shaabani A (2014) Graphene oxide-iron phthalocyanine catalyzed aerobic oxidation of alcohols. Appl Catal A 469:524–531

Taher A (2009) Highly active and magnetically recoverable Pd-NHC catalyst immobilized on Fe_3O_4 nanoparticle-ionic liquid matrix for Suzuki reaction in water. Synlett 15:2477–2482

Sajjadifar S (2014) Ni^{2+} supported on hydroxyapatite-core–shell γ-Fe_2O_3 nanoparticles: a novel, highly efficient and reusable lewis acid catalyst for the regioselective azidolysis of epoxides in water. J Iran Chem Soc 11(2):335–340

Zhang Y, Xia C (2009) Magnetic hydroxyapatite-encapsulated γ-Fe_2O_3 nanoparticles functionalized with basic ionic liquids for aqueous Knoevenagel condensation. Appl Catal A 366(1):141–147

Abu-Reziq R (2007) Platinum nanoparticles supported on ionic liquid-modified magnetic nanoparticles: selective hydrogenation catalysts. Adv Synth Catal 349(13):2145–2150

Safari J, Zarnegar Z (2014) Brønsted acidic ionic liquid based magnetic nanoparticles: a new promoter for the Biginelli synthesis of 3, 4-dihydropyrimidin-2 (1H)-ones/thiones. New J Chem 38(1):358–365

Kooti M, Afshari M (2012a) Phosphotungstic acid supported on magnetic nanoparticles as an efficient reusable catalyst for epoxidation of alkenes. Mater Res Bull 47(11):3473–3478

Hudson R (2013) Copper ferrite ($CuFe_2O_4$) nanoparticles. Synlett 24(10):1309–1310

Zhao X-N (2014) Magnetic $CoFe_2O_4$ nanoparticle immobilized N-propyl diethylenetriamine sulfamic acid as an efficient and recyclable catalyst for the synthesis of amides via the Ritter reaction. Appl Catal A 482:258–265

Kooti M, Afshari M (2012b) Magnetic cobalt ferrite nanoparticles as an efficient catalyst for oxidation of alkenes. Sci Iran 19(6):1991–1995

Moeinpour F, Khojastehnezhad A (2017) Polyphosphoric acid supported on $Ni_{0.5}Zn_{0.5}Fe_2O_4$ nanoparticles as a magnetically-recoverable green catalyst for the synthesis of pyranopyrazoles. Arab J Chem 10:3468–3474

del Hierro I, Pérez Y, Fajardo M (2018) Silanization of Iron Oxide Magnetic Nanoparticles with ionic liquids based on amino acids and its application as heterogeneous catalysts for Knoevenagel condensation reactions. Mol Catal 450:112–120

Abbasi Z (2017) Preparation of a novel, efficient, and recyclable magnetic catalyst, γ-Fe_2O_3@HAp-Ag nanoparticles, and a solvent-and halogen-free protocol for the synthesis of coumarin derivatives. Chin Chem Lett 28(1):75–82

Akceylan E (2015) Calixarene-proline functionalized iron oxide magnetite nanoparticles (Calix-Pro-MN): an efficient recyclable organocatalyst for asymmetric aldol reaction in water. Appl Catal A 499:205–212

Azizi N, Abbasi F, Abdoli-Senejani M (2017) Thiamine immobilized on silane-functionalized magnetic nanoparticles for catalytic synthesis of 2, 3-dihydroquinazolin-4 (1H)-ones in water. Mater Chem Phys 196:118–125

Basu P (2017) Silver nanoparticles supported over Al_2O_3@Fe_2O_3 core–shell nanoparticles as an efficient catalyst for one-pot synthesis of 1, 2, 3-triazoles and acylation of benzyl alcohol. Molecular Catalysis 439:31–40

Dam B, Nandi S, Pal AK (2014) An efficient 'on-water'synthesis of 1, 4-dihydropyridines using Fe_3O_4@SiO_2 nanoparticles as a reusable catalyst. Tetrahedron Lett 55(38):5236–5240

Dutta MM, Phukan P (2018) Cu-doped $CoFe_2O_4$ nanoparticles as magnetically recoverable catalyst for CN cross-coupling reaction. Catal Commun 109:38–42

Ali MAEAA, Abu-Dief AM (2015) $CuFe_2O_4$ nanoparticles: an efficient heterogeneous magnetically separable catalyst for synthesis of some novel propynyl-1H-imidazoles derivatives. Tetrahedron 71(17):2579–2584

Ghorbani-Choghamarani A, Norouzi M (2014) Synthesis of copper (II)-supported magnetic nanoparticle and study of its catalytic activity for the synthesis of 2, 3-dihydroquinazolin-4 (1H)-ones. J Mol Catal A Chem 395:172–179

Sobhani S, Honarmand M (2013) Ionic liquid immobilized on γ-Fe_2O_3 nanoparticles: a new magnetically recyclable heterogeneous catalyst for one-pot three-component synthesis of 2-amino-3, 5-dicarbonitrile-6-thio-pyridines. Appl Catal A 467:456–462

Safari J, Javadian L (2013) Supplementary material: a one-pot synthesis of 5, 5-disubstituted hydantoin derivatives using magnetic Fe_3O_4 nanoparticles as a reusable heterogeneous catalyst. Comptes Rendus Chimie 16(12):1165–1171

Nasr-Esfahani M (2014) Magnetic Fe_3O_4 nanoparticles: efficient and recoverable nanocatalyst for the synthesis of polyhydroquinolines and Hantzsch 1, 4-dihydropyridines under solvent-free conditions. J Mol Catal A Chem 382:99–105

Zhang M (2016) Magnetic carbon nanotube supported Cu ($CoFe_2O_4$/CNT-Cu) catalyst: a sustainable catalyst for the synthesis of 3-nitro-2-arylimidazo [1, 2-a] pyridines. Catal Commun 78:26–32

Sreedhar B, Kumar AS, Yada D (2011) $CuFe_2O_4$ nanoparticles: a magnetically recoverable and reusable catalyst for the synthesis of 5-substituted 1H-tetrazoles. Tetrahedron Lett 52(28):3565–3569

Safari J, Javadian L (2015) Ultrasound assisted the green synthesis of 2-amino-4H-chromene derivatives catalyzed by Fe_3O_4-functionalized nanoparticles with chitosan as a novel and reusable magnetic catalyst. Ultrason Sonochem 22:341–348

Gao A (2018) Synthesis of Fe_3O_4@SiO_2-Au/Cu magnetic nanoparticles and its efficient catalytic performance for the Ullmann coupling reaction of bromamine acid. Chin Chem Lett 29(8):1301–1304

A Comprehensive Characterization of Stress Relaxed ZnO Thin Film at Wafer Level

Priyanka Joshi, Jitendra Singh, V. K. Jain and Jamil Akhtar

Abstract The chapter goes onto explore the impact of sputtering parameters on structural, optical, and mechanical properties of reactive magnetron sputtered ZnO thin film. Stress relaxed and room temperature deposited ZnO film is highly desirable from fabrication aspects. Oxygen partial pressure is varied from 30 to 60% and *c*-axis oriented ZnO (002) thin films are prepared at room temperature. The stress varies in -0.06×10^9 to -2.27×10^9 dyne/cm^2 range, and compressive in nature. A detailed characterization of ZnO sputtered film is carried out in order to correlate the mechanical, structural, and optical properties of thin film. A theoretical model has been proposed to understand the consequences of oxygen-induced stress in ZnO thin films. It is established that nearly stress-free, single-phase, and highly *c*-axis oriented ZnO thin film can be deposited using a unique combination of sputter parameters.

Keywords Zinc oxide · Characterization · Stress · Sputtering · Oxygen partial pressure

1 Introduction

Zinc Oxide (ZnO) is a versatile material and exhibits semiconducting, optical and piezoelectric properties (Ozgur et al. 2005) Micro-electro-mechanical systems (MEMS) based devices require ZnO thin films as a functional layer for sensing and actuation applications. ZnO can be integrated into variety of devices such as acoustic resonators, sensors, optical waveguides and microwave filters (Wang and Song 2006; Joshi et al. 2018, 2019). Stress relaxed and room temperature deposited ZnO film is highly desirable from fabrication aspects (Baraki et al. 2014; Fu et al. 2010; Gardeniers et al. 1998). Further, ZnO is a green material and compatible to semiconductor

P. Joshi (✉) · J. Singh · J. Akhtar
Smart Sensors Area, CSIR-Central Electronics Engineering Research Institute, Pilani 333031, Rajasthan, India
e-mail: piyujsh@gmail.com

P. Joshi · V. K. Jain
College of Engineering and Technology, Mody University, Lakshmangarh 332311, Rajasthan, India

L. Ledwani and J. S. Sangwai (eds.), *Nanotechnology for Energy and Environmental Engineering*, Green Energy and Technology,
https://doi.org/10.1007/978-3-030-33774-2_21

manufacturing process. Sensing and actuation properties of ZnO thin film strongly depend on the crystalline structure of ZnO film. Menon et al. (2011) deposited ZnO films on silicon and glass substrate and discussed origin of stress. The crystalline structure depends on growth parameters such as sputter pressure, ambient temperature, gas flow rate, and target substrate distance, etc. (Menon et al. 2008; Singh et al. 2007). Over the past decades, ZnO thin film and its different properties have been researched extensively. Singh et al. (2015) directly measured the stress of ZnO film by curvature method and correlated with the ZnO optical properties. Ondo-Ndong et al. (2003) prepared the ZnO films using metallic zinc target and effect of process parameters on film properties was analyzed. Rao et al. (2009) investigated the effect of stress on optical band gap of ZnO and the thin films were prepared by spray pyrolysis method. Ashrafi et al. (2004) deposited epitaxial ZnO layers on 6H-SiC substrates and analyzed strain relaxation effect on exciton resonance. Epilayers of GaN on Si (111), 6H-SiC (0001) and c-plane sapphire were grown by Zhao et al. (2003) and stress effect on optical properties was studied. Maniv et al. (1982) reported that the sputtering pressure and incidence angle affect the reactive ZnO layers. Nucleation and growth of AlN thin films were investigated and influence of process parameters was explored (Engelmark et al. 2000; Iborra et al. 2004). Loebl (2003) investigated AlN *c*-axis orientation effect on Electromechanical coupling coefficient. With optimal sputter deposition parameters stress-free ZnO thin film was obtained (Drese and Wuttig 2005; Krupanidhi and Sayer 1984). Jou et al. (1992) used sputter pressure 17 mTorr and Ar oxygen ratio 1:1 for stress-free ZnO thin films. Though, residual stress also affects the optical properties of ZnO thin films (Ghosh et al. 2004; Shan et al. 1996). The Band gap of ZnO film shows red/blue shift with increasing compressive/tensile biaxial stress. Li et al. (2007) estimated tensile stress in ZnO films deposited on quartz by X-ray diffraction technique and a blue shift was observed in optical band gap with increasing tensile stress. Mohanty et al. (2009) investigated the thickness-dependent stress in ZnO films on Si/SiO_2 and found compressive stress $\sim -2.0 \times 10^{10}$ dynes/cm^2 in ~1 μm thick films. It is very useful to investigate the change in lattice constants with residual stress. Ping et al. (2012) reported that lattice constant(c) has linear relation with compressive stress. Rieger et al. (1996) explored the influence of biaxial compressive stress on optical band gap and lattice constant of GaN thin film. With increasing biaxial compressive stress, band gap (blue shift) as well as lattice constant increases.

Further, stress relaxed ZnO thin film shows enhanced performance and resulting devices are highly reliable and reproducible (Ashrafi et al. 2004; Maniv et al. 1982; Trodahl et al. 2006). Device yield and long term reliability can be improved by stress engineering. In-plane stress primarily produced in ZnO thin films caused by the conditions imposed by underlying substrate and ambient conditions. Large in-plane stress develops in ZnO thin films due to intrinsic or extrinsic effects (Ondo-Ndong et al. 2003; Rao et al. 2009). Usually, MEMS devices consist of metal, dielectric, and functional multilayers. Consequently, to avoid multilayer's inter-diffusion, ZnO processing temperature must be low (Mass et al. 2003). Sharp, clean, and crack-free interfaces are highly desirable for long term reliability of MEMS devices. Further, when MEMS devices are exposed to high ambient temperature, there is a possibility

to develop cracks or fracture in multilayer stack due to the thermal coefficient of expansion (TCE) mismatch. Therefore, an industrial process is required to deposit the ZnO thin film at room temperature (Iborra et al. 2004; Engelmark et al. 2000). Usually, thin-film stress is estimated by X-ray diffraction technique (Conchon et al. 2010) and this process is only applicable to crystalline films. X-ray diffraction is an indirect method and only provides local information about a small area of a sample. Nevertheless, wafer curvature method is a direct measurement technique and provides overall information about the measuring wafer. The resulting information is more precise and based on bow of the wafer. Moreover, the wafer curvature method is also applicable to amorphous thin films.

Although the effect of sputter partial pressure has been performed earlier (Menon et al. 2011; Singh et al. 2015) however, the influence of oxygen partial pressure on as-deposited ZnO thin film's structural, optical, and mechanical properties has never been investigated in detail. In the present work, we report on the role of oxygen partial pressure (R_{O2}) and stress measurement of ZnO thin film using the wafer curvature method. By analysis, it was found that stress variation depends on the oxygen partial pressure. At low R_{O2}, oxygen defects are prominent and responsible for in-plane residual stress. Experimentation has been carried out to obtain minimal stress ZnO film, which is highly desirable for the fabrication of ZnO based MEMS devices.

2 Experimental Procedure

Single crystal Si (100) wafers were cleaned by a standard semiconductor cleaning process. Wafers were boiled in organic solvents such as trichloroethylene, acetone, and methanol and followed by rinsing with deionized (DI) water. Organic residues were removed in piranha (H_2SO_4:$H_2O_2 = 5$:1) solution. After Piranha dip, thin layer of oxide was grown over the Si surface and it was removed in 2% HF solution and then wafers were rinsed with DI water. Dried wafers were loaded in oxidation furnace for ~1 μm thick thermal silicon oxide (SiO_2) growth. The SiO_2 layer works as an isolation layer between underlying Si substrate and ZnO film. Reactive magnetron sputtering system was used for the growth of ZnO film. The base vacuum of sputtering chamber was achieved at $\sim 2 \times 10^{-6}$ Torr. The oxygen partial pressure ratio (R_{O2}) is defined as $R_{O2} = P_{O2}/(P_{O2} + P_{Ar}) \times 100\%$, where P_{Ar} and P_{O2} are argon and oxygen partial pressure, respectively. This ratio was varied in 30–60% range by controlling $Ar + O_2$ gas flow.

The ZnO film thickness was ~0.8 μm and retained the same in all the samples. The industrial sputtering process was established up to 6-in. diameter wafer and optimal processing parameters are listed in Table 1. Stress was measured using dual laser switching technology. Crystalline structure and surface morphology of ZnO thin film were investigated by Bruker X-ray diffractometer (XRD) and atomic force microscopy (AFM). To measure the optical band gap, ZnO film was deposited on SiO_2/glass substrate and transmittance spectra was recorded using high sensitivity 3600 UV-VIS-NIR Spectrophotometer (wavelength range 200–1100 nm). Raman

Table 1 Sputtering parameters for ZnO thin film deposition

Sputter target	6″ diameter metallic Zinc (purity 99.99%)
Substrate	Si/SiO_2 (1 μm)
Target to substrate distance	11 cm
RF power (13.56 MHz)	400 W
Sputtering gas	$Ar + O_2$ (varying)
Deposition rate	0.81–0.86 Å/s
Sputtering pressure	20 mTorr
Substrate temperature	Room temperature

spectroscopy was used for vibrational phonon studies. Fourier transform infrared spectroscopy (FTIR) spectra of ZnO samples were measured using Tensor 37 FTIR spectrometer in 300–4000 cm^{-1} range.

3 Results and Discussion

In-plane ZnO film stress was measured using the wafer curvature method. Initially, SiO_2/Si bare wafer was scanned and wafer curvature (R) was measured as shown in Fig. 1a. Subsequently, ZnO film was deposited by varying oxygen partial pressure (R_{O2}) and stress mapping profiles are shown in Fig. 1b–e. The oxygen partial pressure (R_{O2}) was varied in 30–60% range. In all the cases ZnO film thickness was similar ~0.8 μm, to rule out the effect of film thickness on film stress. It is clearly noted that there is a change in wafer curvature due to the deposition of ZnO thin film. Film stress (σ_f) is given by Stoney's equation (Stoney 1909; Kunj and Sreenivas 2016) as follows:

$$\sigma_f = \frac{E_s D_s^2}{6(1-\nu_s)} \cdot \frac{1}{d_f} \cdot \frac{1}{R} \tag{1}$$

where E_s is substrate's Young's modulus, ν_s is substrate's Poisson ratio, D_s is substrate's thickness, d_f is the thickness of film and R is radius of curvature. Experimentally, stress was found in -0.06×10^9 to -2.27×10^9 dyne/cm^2 range and compressive in nature. The maximum stress was obtained for $R_{O2} = 30\%$ deposited films. The mechanical properties of reactive magnetron sputtered films are very sensitive to deposition conditions. At lower oxygen pressure, ZnO films are metallic in nature due to the deficiency of oxygen content. With the increase of R_{O2}, more oxygen content is available to react with sputtered zinc and it results in stress relaxed films. With increase in $R_{O2} \geq 40\%$, stress is minimized and indicates growth of stress relaxed film. Usually, at lower oxygen partial pressure ($R_{O2} = 30\%$), ZnO films are oxygen-deficient and results in higher compressive stress. Conversely, when ZnO films are grown at higher oxygen flow rates, i.e., R_{O2} ~ 50 and 60%, deposition rates

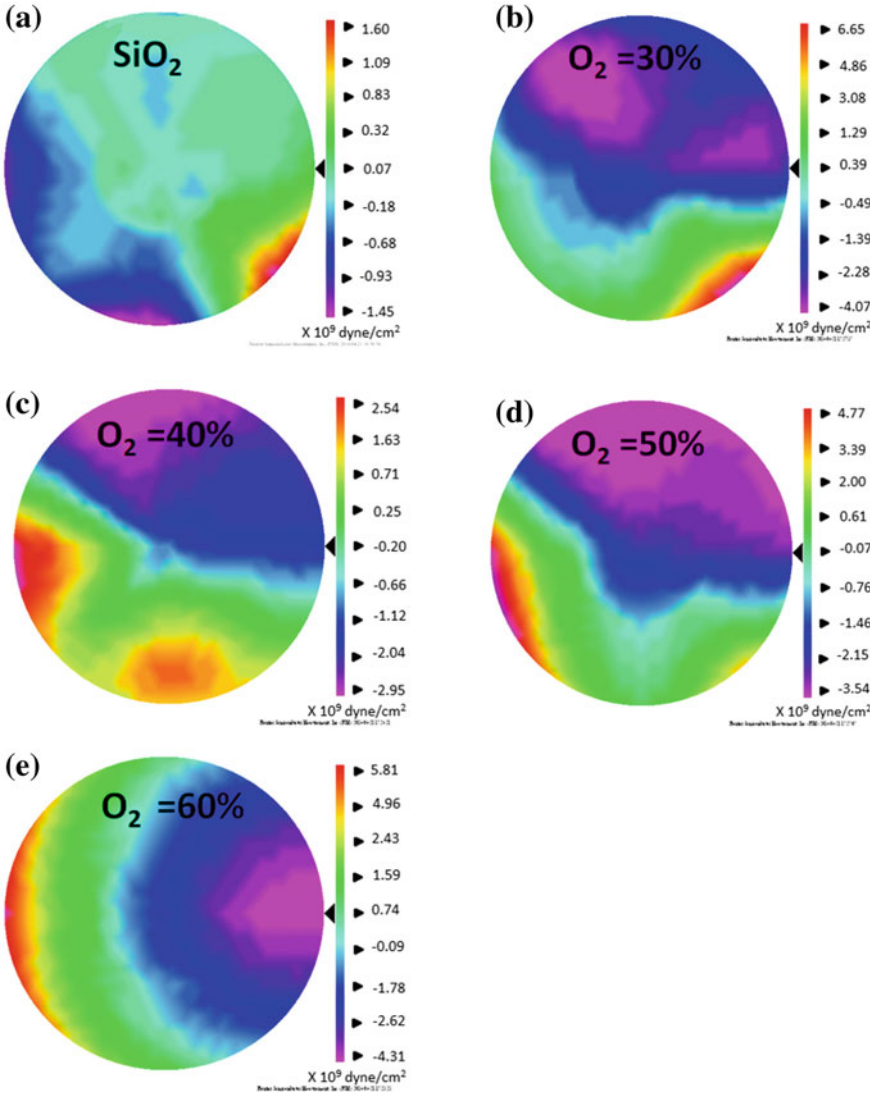

Fig. 1 **a–e** Film stress mapping profile of ZnO thin film for varying oxygen content

are reduced as well as stoichiometry of ZnO thin films is not balanced which again causes in-plane stress. Therefore, optimal process conditions are desired for good quality stress relaxed ZnO thin films. As discussed, wafer curvature changes with R_{O2} according to Eq. (1) and Fig. 2 shows the accumulated wafer curvature due to SiO_2 and ZnO layer depositions. The SiO_2 film showed nearly similar compressive stress ($\sim -1.6 \times 10^9$ dyne/cm^2) in all the wafers. Successively, ZnO layers (~0.8 μm) were grown and accumulated curvature is shown in Fig. 2. It is found that 30% R_{O2}

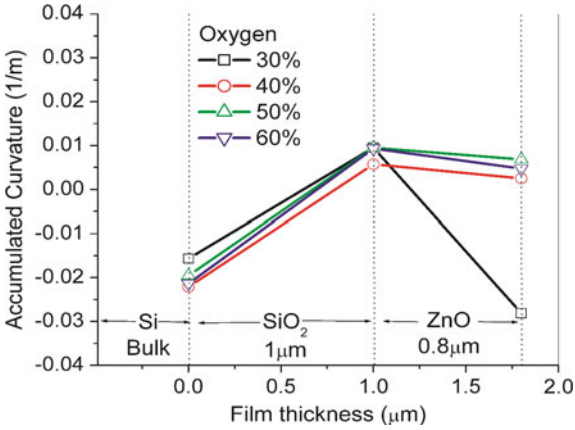

Fig. 2 Accumulated curvature variation of bilayer deposition ZnO/SiO_2 over Si Substrate

film has shown large change in curvature due to the high compressive stress in ZnO film.

Figure 3 depicts the X-ray diffraction result of ZnO thin film with varying oxygen partial pressure. The effect of sputter pressure has already been established (Singh et al. 2015) and same was maintained in all the cases. In diffraction pattern, only strong peak corresponding to ZnO (002) was observed, which indicates that ZnO films are highly *c*-axis oriented and having wurtzite crystal structure. It is known that surface free energy is minimal in wurtzite structure and therefore, ZnO films are grown along the *c*-axis direction. For $R_{O2} = 30\%$, XRD 2θ peak was found at 34.49°, indicates that grown film is under compressive stress, which is also consistent with the film stress measurement result. The ZnO film deposited at $R_{O2} = 30\%$, shows lower c ~ 5.194 Å values, compared to bulk ZnO (c ~ 5.20 Å).

So, the ratio of *c*/*a* ~ 1.6 is no longer maintained and shrinks along the *c*-axis direction (Kunj and Sreenivas 2016). As a consequence, the lattice parameter in the

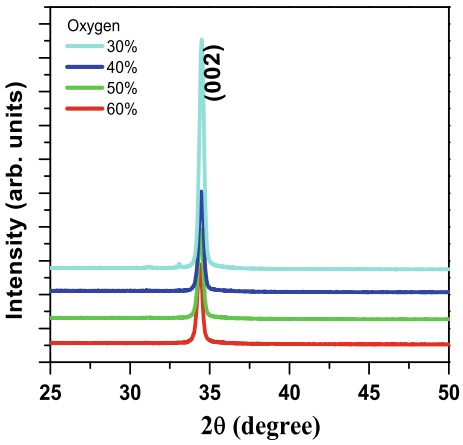

Fig. 3 X-ray diffraction profile of ZnO thin film prepared at varying oxygen flow (30–60%)

basal plane is expanded to maintain the unit cell volume. This distortion in the unit cell results in higher stress (-2.27×10^9 dyne/cm^2). This is probably due to the extensive bombardment of energetic particles on the film surface at higher sputter rate and excessive presence of metallic Zn in ZnO thin film. At higher $R_{O2} = 40\%$, XRD 2θ peak is shifted to lower 2θ angle and stress relaxed films were obtained. With further increasing oxygen flow from 40 to 60%, ZnO thin film shows increase in stress (-0.41 dyne/cm^2) due to the presence of excessive oxygen. At higher $R_{O2} >$ 40%, XRD (002) peaks show shift towards lower 2θ angles (34.46°–34.38°), which again indicates in-plane stress.

Surface morphologies were investigated by using an atomic force microscope (AFM) and 2D Figures (1 μm × 1 μm) are shown in Fig. 4. It is clearly noticed that films are smooth and surface roughness reduces from 5.33 to 4.61 nm with increase in oxygen partial pressure. The grain size was measured using image analysis software and it tunes with the oxygen content. The uniform grains of small size (~66.6 nm) were obtained for film deposited at $R_{O2} = 30\%$. As R_{O2} increased to 40%, grain size was also increased (~95.5 nm) and shows circular, uniform distribution of grains, which indicates that the oxygen flow has major effect on micro-structure properties. Further increase in oxygen flow (50 and 60%), shows more uniform distribution of

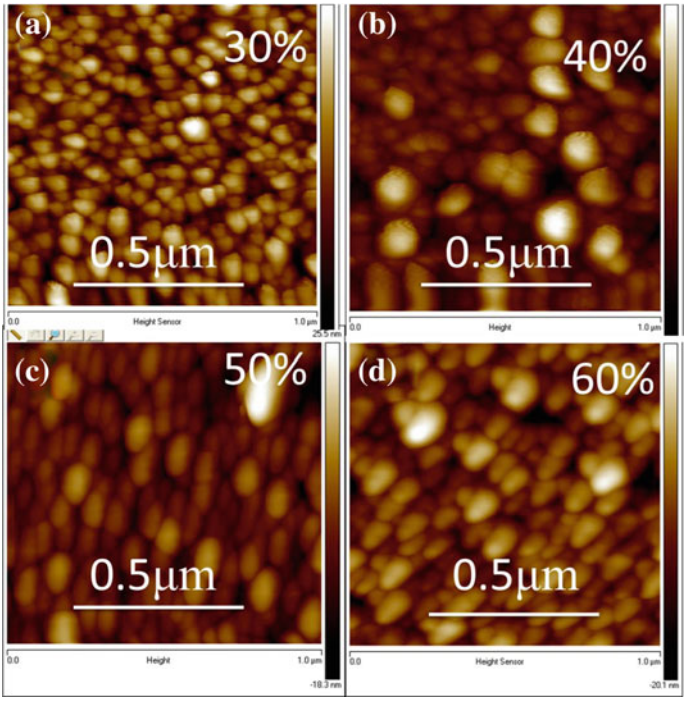

Fig. 4 **a–d** AFM images (1 × 1 μm^2) of magnetron sputtered ZnO thin films at different oxygen partial pressure

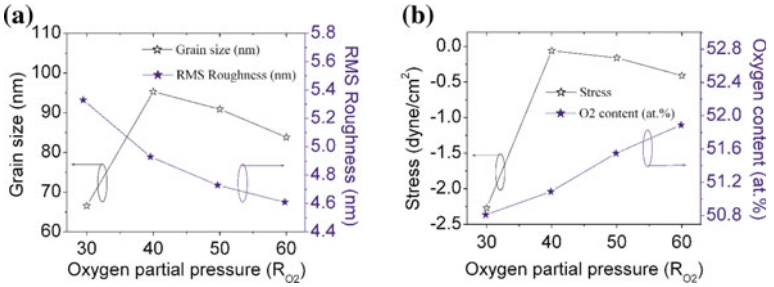

Fig. 5 Variation of **a** grain size and RMS roughness with oxygen partial pressure, **b** stress and oxygen content (at.%) with oxygen partial pressure

grains due to the reduced growth rate at higher oxygen flow. Therefore, grain size and surface roughness are strongly dependent on the partial flow of oxygen gas (Menon et al. 2011; Singh et al. 2007, 2015).

Figure 5a shows the variation in grain size and RMS roughness decreases with increasing oxygen partial pressure. For oxygen flow up to 40%, the grain size was increased due to the grain growth mechanism. Further, increase in R_{O2} i.e. >40%, should be noted that higher oxygen flow does not allow for the growth of large grain particles. The RMS roughness of ZnO thin film decreases with increasing oxygen partial pressure due to the slower growth rate.

Figure 5b shows the stress variation with oxygen content. As discussed, low oxygen content (30%) films have the highest compressive stress. As the oxygen content was increased, ZnO films become nearly stress relaxed as shown in Fig. 5b and with further increasing the oxygen flow (>40%), stoichiometry of ZnO is no longer maintained and induces small in-plane stress. The oxygen content in ZnO films was measured using energy dispersive X-ray (EDX) measurement and it was found that oxygen content in ZnO thin films is increased with the oxygen partial pressure indicates that more oxygen is incorporated in the ZnO crystal structure.

Further, ZnO thin film stoichiometry was indirectly evaluated by observing the UV-VIS-IR transmittance spectra. Figure 6a–b shows UV-Visible transmittance spectra and plot of $(\alpha h\upsilon)^2$ with photon energy $(h\upsilon)$ for band gap measurement of ZnO thin films prepared at various oxygen flow. All the samples revealed good optical transmittance in the visible range. It was noticed that the transmittance keeps on increasing with the increase in oxygen partial pressure.

ZnO film, being a direct band gap semiconductor has an absorption coefficient α (cm^{-1}), which obeys the following relation for high photon energies (Tauc et al. 1966; El Zawawi and Abd Alla 1999):

$$(\alpha)^2 = \beta(h\nu - E_g) \tag{2}$$

where β is energy independent constant, h is Plank's constant, E_g is optical band gap and ν is the frequency of the incident photon. The absorption coefficient (α) is determined from the transmittance spectra and related to the photon energy as given

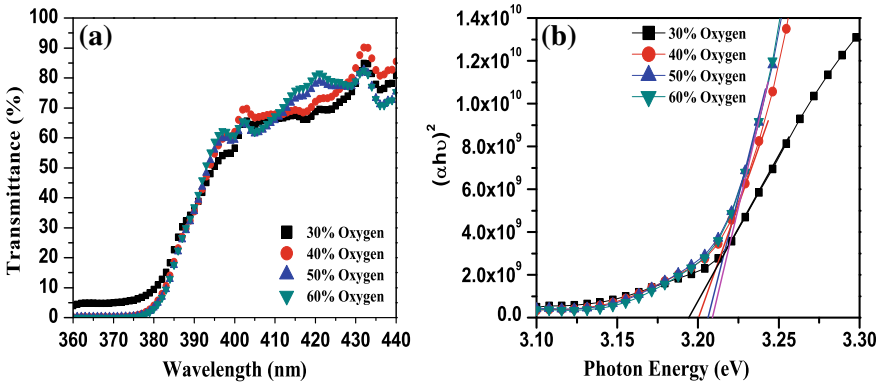

Fig. 6 **a** UV-Visible transmittance spectra, **b** plot of $(\alpha h\upsilon)^2$ versus photon energy $(h\upsilon)$ for band gap measurement of ZnO

by

$$\alpha = \frac{1}{d}\ln\frac{1}{T} \tag{3}$$

where d and T are thickness and transmittance of ZnO thin film, respectively. We assume that the absorption coefficient is correlated with the direct band gap of the wurtzite structure. By extrapolating the straight line portion at zero absorption coefficient of $(\alpha h\upsilon)^2$ versus photon energy $(h\upsilon)$ gives information about the band gap energy (E_g) (Zhou et al. 2012; Orikasa et al. 2008). The oxygen flow is responsible for tuning in band gap of ZnO films. In fact, there is a change in film stress due to oxygen flow. With the increase in oxygen flow, the fundamental absorption edge is shifted towards the shorter wavelength and band gap (E_g) is increased. In the case of 30% R_{O2}, ZnO film exhibits lower transmittance which may be due to the presence of oxygen vacancies. Here, defect-related electronic states may be originated in the band gap and which can be associated with the oxygen vacancies and Zn interstitials. The band gap of ZnO thin film is increased from 3.19 to 3.21 eV with increasing oxygen partial pressure (Wang et al. 2016). The comparative study of ZnO film in-plane stress, 2θ peak position, 2θ—FWHM, band gap (E_g), RMS roughness and FTIR—FWHM are shown in Table 2.

Zinc oxide is a wurtzite hexagonal crystalline structure and related to C_{6v}^4 space-group symmetry. According to group theory, phonon modes exist for $2E_2$, $2E_1$, $2A_1$, and $2B_1$ symmetries. Here, as observed deposited ZnO film is highly c-axis oriented. The B_1 symmetry mode shows Raman and FTIR response. The non-polar modes E_2 (high) and E_2 (low) show only Raman response. E_2 (high) mode is associated with the vibration of oxygen sublattice and E_2 (low) is related to the vibration of Zn sublattice. The other modes E_1 and E_1 are polar modes and composed of longitudinal optical (LO) and transverse optical (TO) phonon modes, where A_1 phonon vibration

Table 2 Experimentally measured and estimated ZnO thin film parameters

$R_{O2} = P_{O2}/(P_{O2} + P_{Ar}) \times 100\%$	Stress $\times 10^9$ (dyne/cm^2)	XRD 2θ (degree)	XRD 2θ FWHM (degree)	Band gap (eV)	RMS roughness (nm)	FTIR FWHM (cm^{-1})
30	−2.27	34.49	0.3589	3.192	5.33	20.3
40	−0.06	34.42	0.3607	3.2	4.93	19.4
50	−0.16	34.40	0.37	3.203	4.73	18.3
60	−0.41	34.38	0.3798	3.203	4.61	13.0

is parallel to polar (c-axis) and E_1 is perpendicular (Karthikeyan et al. 2016; Arguello et al. 1969; McCluskey and Jokela 2009).

Figure 7 shows the Raman spectra of ZnO thin films for various oxygen flows. It can be seen that E_2 (high) and E_1 (low) modes corresponding to ZnO thin film are present in the figure and some Raman peaks are also there which correspond to Si substrate. The intense sharp peak at 437 cm^{-1} and a very weak peak at around 585 cm^{-1} are observed for all the samples and assigned to the ZnO E_2 (high) mode and E_1 (LO) mode, respectively (Agarwal et al. 2006; Damen et al. 1966). At all the oxygen contents, ZnO thin film exhibited a dispersed E_1 (LO) peak with low intensity. In addition, no frequency shift was observed in E_1 (LO) Raman peak with increasing oxygen partial pressure. It is believed that the appearance of E_1 (LO) mode in the Raman scattering is associated with the presence of oxygen vacancies and interstitial zinc and their complexes. According to reports, the E_2 (high) mode is associated with the characteristic band of ZnO wurtzite structure and demonstrates that the films have c-axis preferred orientation. With increasing oxygen flow (30–60%), there is lower frequency shift observed for E_2 (high) phonon mode.

It is reported that the E_2 (high) peak had a close relationship with the intrinsic stress in ZnO thin film (Menon et al. 2008; Singh et al. 2007, 2015). Additionally, if tensile stress occurs in the film, the E_2 (high) peak shifts towards the lower frequencies and

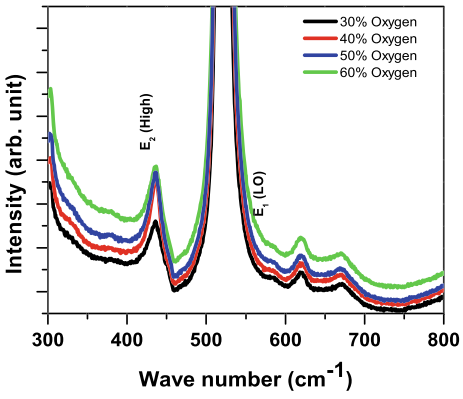

Fig. 7 Raman spectra of ZnO films under varying oxygen content (30–60%)

if compressive stress in the films exists, it shifts to higher frequencies compared to the bulk value of ZnO E_2 (high) mode (437 cm^{-1}) (Damen et al. 1966; Zhang et al. 2003). Therefore, the Raman result is supported by the X-ray diffraction measurement results where stress was confirmed by crystal structure.

The FTIR spectra of ZnO samples were measured in the range of 300–1600 cm^{-1} and shown in Fig. 8. The spectrum shows several peaks corresponding to sample layers in all the four cases. For $R_{O2} = 30$–60% oxygen in the chamber, the existence of distinct characteristic absorption peaks are observed at ~413 cm^{-1} and ~461 cm^{-1} due to the ZnO stretching vibrations (Yang et al. 2009; Ivanova et al. 2010). The peak at ~609 cm^{-1} is due to the existence of local vibrations of the substituted carbon in the Si crystal lattice (Singh et al. 2007). The sharpest IR peak at ~1093 cm^{-1} is attributed to the stretching frequency of Si-O bond. From the result, it is evident that sample with 60% oxygen content has the highest absorbance. It is noticed that the position of 609 cm^{-1} and 810 cm^{-1} remain almost the same when R_{O2} in the process chamber increases from 30 to 60%. With the increase of R_{O2}, the position of IR peaks for ZnO stretching vibrations is also changed. It can be seen that ZnO stretching bond splits into two peaks positioned at ~413 and ~461 cm^{-1} (Sun et al. 1999; Laidani et al. 1993). FWHM of FTIR peak is found to be decreased from 20.3 to 13 cm^{-1} with increasing the oxygen flow. This also indicates that ZnO film crystallinity is improved with the oxygen flow and the analysis is supported by XRD result.

For acquiring better understanding, stress generation mechanism has been explained with the effect of oxygen partial pressure. Figure 9a–c illustrates the effect of oxygen partial pressure on hexagonal wurtzite ZnO. The substrate bonding structure in presence of (a) low R_{O2} (<40%), (b) moderate R_{O2} (~40%) and (c) high R_{O2} (>40%) are shown in Fig. 9. Commonly, stress is generated between deposited thin film and substrate due to the crystalline imperfection like dislocations, point defects, and grain boundaries. For ZnO thin films, presence of excessive Zn or O atoms may inhibit Zn and O proper stoichiometry which further interrupts the crystalline

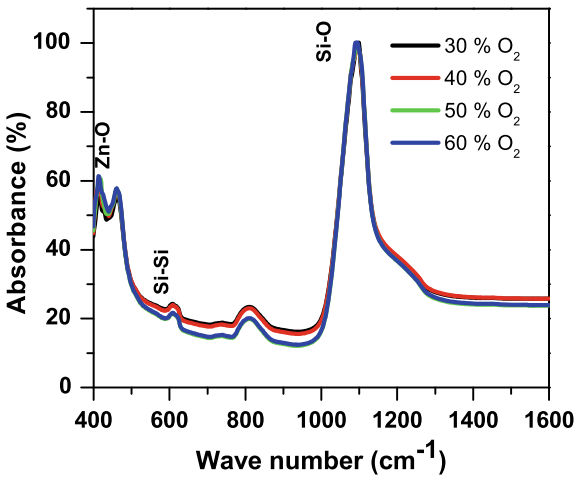

Fig. 8 FTIR spectra of ZnO thin films under varying oxygen content (30–60%)

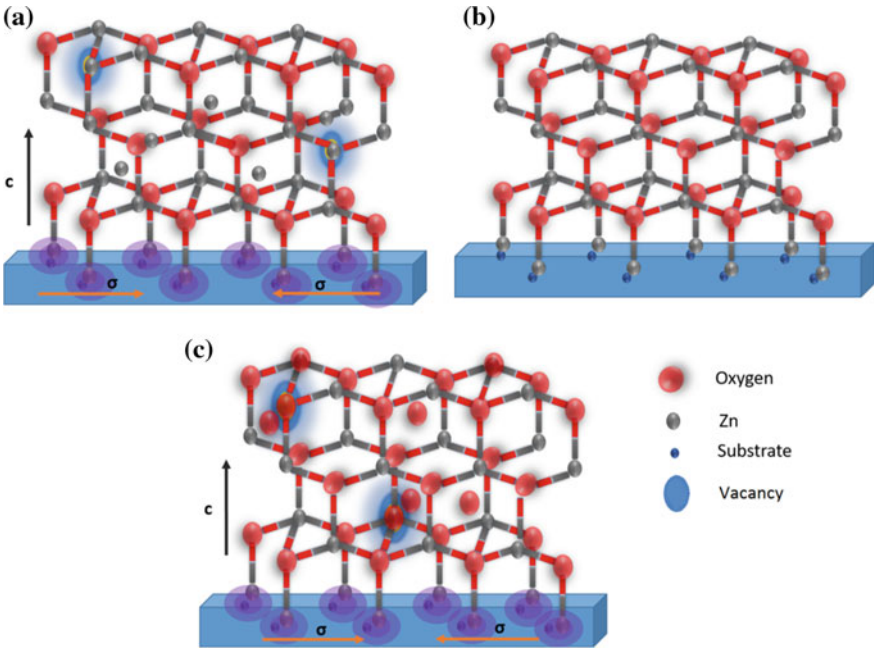

Fig. 9 **a**–**c** Effect of oxygen partial pressure on hexagonal wurtzite ZnO with substrate bonding structure in presence of **a** low, **b** moderate and **c** high oxygen contents

growth of ZnO lattice. Therefore, change in crystal lattice parameters generates in-plane stress between ZnO and substrate atoms. Figure 9b represents ZnO crystalline stress relaxed growth in presence of moderate oxygen partial pressure (~40%). This moderate oxygen pressure provides perfect hexagonal wurtzite growth and proper Zn/O stoichiometry. At higher oxygen partial pressure (>40%), excessive oxygen might be incorporated in the ZnO lattice and distort the crystal structures as shown in Fig. 9c.

All polycrystalline single-phase ZnO films have shown oxygen partial pressure dependent physical properties and require precise control of processing parameters to obtain high-quality ZnO thin films.

4 Conclusion

Stress relaxed and highly *c*-axis oriented single-phase ZnO thin film was deposited at room temperature using reactive sputtering process. The crystalline structure and mechanical stress of vacuum-deposited films are very sensitive to deposition conditions. The oxygen flow in the chamber (30–60%) was varied to tune the physical properties. It was found that stress varies in -0.06×10^9 dyne/cm^2 to -2.27×10^9

dyne/cm^2 range as a function of oxygen partial pressure. The residual stress strongly depends on the processing parameters and nearly stress-free films are obtained using a unique combination of sputter parameters. The mechanical, structural, and optical properties are correlated. Low-stress ZnO piezoelectric films are highly desirable for MEMS device applications.

Acknowledgements Authors are thankful to Director CSIR-CEERI Pilani for continuous support and encouragement. This research work was supported by the 12th Plan network project PSC-0102 (*R*-Nano). Mr. Arvind Kumar Singh and Mr. Prateek Kothari helped to maintain ZnO sputtering machine.

References

Agarwal DC, Chauhan RS, Amit Kumar D, Kabiraj F, Singh SA, Khan DK, Avasthi JC, Pivin M, Kumar JG, Satyam PV (2006) Synthesis and characterization of ZnO thin film grown by electron beam evaporation. J Appl Phys 99:123105

Arguello CA, Rousseau DL, Porto SPS (1969) First-order Raman effect in wurtzite-type crystals. Phys Rev 181:1351

Ashrafi ABMA, Binh NT, Zhang BP, Segawa Y (2004) Strain relaxation and its effect in exciton resonance energies of epitaxial ZnO layers grown on 6H-SiC substrates. Appl Phys Lett 84:2814

Baraki R, Novak N, Frömling T, Granzow T, Rödel J (2014) Bulk ZnO as piezotronic pressure sensor. App Phys Lett 105:111604

Conchon F, Renault PO, Goudeau P, Le Bourhis E, Sondergard E, Barthel E, Grachev S, Gouardes E, Rondeau V, Gy R, Lazzari R, Jupille J, Brun N (2010) X-ray diffraction analysis of thermally-induced stress relaxation in ZnO films deposited by magnetron sputtering on (100) Si substrates. Thin Sol Films 518:5237

Damen TC, Porto PS, Tell B (1966) Raman effect in zinc oxide. Phy Review 142:570

Drese RJ, Wuttig M (2005) Stress evolution during growth in direct-current-sputtered zinc oxide films at various oxygen flows. J Appl Phys 98:073514

El Zawawi LK, Abd Alla RA (1999) Electrical and optical phototransformation properties in As doped Se thin films. Thin Sol Films 339:314

Engelmark F, Fucntes G, Katardjiev IV, Harsta A, Smithand U, Berg S (2000). Synthesis of highly oriented piezoelectric AlN films by reactive sputter deposition. J Vac Sci Technol A 18:1609

Fu YQ, Luo JK, Du XY, Flewitt AJ, Li Y, Markx GH, Walton AJ, Milne WI (2010) Recent developments on ZnO films for acoustic wave based bio-sensing and microfluidic applications: a review. Sens Actuators B 143:606

Gardeniers JGE, Rittersma ZM, Burger GJ (1998) Preferred orientation and piezoelectricity in sputtered ZnO films. J Appl Phys 83:7844

Ghosh R, Basak D, Fujihara S (2004) Effect of substrate-induced strain on the structural, electrical, and optical properties of polycrystalline ZnO thin films. J Appl Phys 96:2689

Iborra E, Olivares J, Clement M, Vergara J, Sanz-Hervas A, Sangrador J (2004) Piezoelectric properties and residual stress of sputtered AlN thin films for MEMS applications. Sens Actuators A 115:501

Ivanova T, Harizanova A, Koutzarova T, Vertruyen B (2010) Study of ZnO sol–gel films: effect of annealing. Mater Lett 64:1147

Joshi P, Singh J, Sharma R, Jain VK, Akhtar J (2018) A facile approach to fabricate ZnO thin film based micro-cantilevers. Microelectron Eng 187–188:50–57

Joshi P, Kumar S, Jain VK, Akhtar J, Singh J (2019) Distributed MEMS mass-sensor based on piezoelectric resonant micro-cantilevers. J Microelectromech Syst. https://doi.org/10.1109/JMEMS.2019.2908879

Jou JH, Han M-Y, Cheng D-J (1992) Substrate dependent internal stress in sputtered zinc oxide thin films. J Appl Phys 71:4333

Karthikeyan B, Pandiyarajan T, Mangalaraj RV (2016) Enhanced blue light emission in transparent ZnO: PVA nanocomposite free standing polymer films. Spectrochim Acta A 152:485

Krupanidhi SB, Sayer M (1984) Position and pressure effects in RF magnetron reactive sputter deposition of piezoelectric zinc oxide. J Appl Phys 56:3308

Kunj S, Sreenivas K (2016) Residual stress and defect content in magnetron sputtered ZnO films grown on unheated glass substrates. Curr Appl Phys 16:748

Laidani N, Capelletti R, Elena M, Guzman L, Mariotto G, Miotello A, Ossi PM (1993) Spectroscopic characterization of thermally treated carbon-rich Si1–xCx films. Thin Sol Films 223:114

Li YF, Yao B, Lu YM, Cong CX, Zhang ZZ, Gai YQ, Zheng CJ, Li BH, Wei ZP, Shen DZ, Fan XW, Xiao L, Xu SC, Liu Y (2007) Characterization of biaxial stress and its effect on optical properties of ZnO thin films. Appl Phys Lett 91:021915

Loebl HP, Klee M, Metzmacher C, Brand W, Milsom R, Lok P (2003) Piezoelectric thin AlN films for bulk acoustic wave (BAW) resonators. Mat Chem Phys 79:143

Maniv S, Westwood WD, Colombini E (1982) Pressure and angle of incidence effects in reactive planar magnetron sputtered ZnO layers. J Vac Sci Technol 20:162

Mass J, Bhattacharya P, Katiyar RS (2003) Effect of high substrate temperature on Al-doped ZnO thin films grown by pulsed laser deposition. Mater Sci Eng B 103:9

McCluskey MD, Jokela SJ (2009) Defects in ZnO. J Appl Phys 106:071101

Menon R, Sreenivas K, Gupta V (2008) Influence of stress on the structural and dielectric properties of RF magnetron sputtered zinc oxide thin film. J Appl Phys 103:094903

Menon R, Gupta V, Tan HH, Sreenivas K, Jagadish C (2011) Origin of stress in radio frequency magnetron sputtered zinc oxide thin films. J Appl Phys 109:064905

Mohanty BC, Jo YH, Yeon DH, Choi IJ, Choa YS (2009) Stress-induced anomalous shift of optical band gap in ZnO: Al thin films. Appl Phys Lett 95:062103

Ondo-Ndong R, Ferblantier G, Kalfioui MA, Boyer A, Foucaran A (2003) Properties of RF magnetron sputtered zinc oxide thin films. J Cryst Growth 255:130

Orikasa Y, Hayashi N, Muranaka S (2008) Effects of oxygen gas pressure on structural, electrical, and thermoelectric properties of (ZnO)3In2O3 thin films deposited by RF magnetron sputtering. J Appl Phys 103:113703

Ozgur U, Alivov YI, Liu C, Teke A, Reshchikov MA, Dogan S, Avrutin V, Cho SJ, Morkoç H (2005) A comprehensive review of ZnO materials and devices. J Appl Phys 98:041301

Ping Y, Pei L, Li-Qiang Z, Xiao-Liang W, Huan W, Xi-Fu S, Fang-Wei X (2012) Uniaxial stress influence on lattice, band gap and optical properties of n-type ZnO: first-principles calculations. Chin Phys B 21:016803

Rao TP, Kumar MCS, Angayarkanni SA, Ashok M (2009) Effect of stress on optical band gap of ZnO thin films with substrate temperature by spray pyrolysis. J Alloy Comp 485:413

Rieger W, Metzger T, Angerer H, Dimitrov R, Ambacher O, Stutzmann M (1996) Influence of substrate-induced biaxial compressive stress on the optical properties of thin GaN films. Appl Phys Lett 68:970

Shan W, Hauenstein RJ, Fischer AJ, Song JJ, Perry WG, Bremser MD, Davis RF, Goldenberg B (1996) Strain effects on excitonic transitions in GaN: deformation potentials. Phys Rev B 54:13460

Singh P, Kumar A, Deepak DK (2007b) Growth and characterization of ZnO nanocrystalline thin films and nanopowder via low-cost ultrasonic spray pyrolysis. J Cryst Growth 306:303

Singh R, Kumar M, Chandra S (2007a) Growth and characterization of high resistivity C-axis oriented ZnO films on different substrates by RF magnetron sputtering for MEMS applications. J Mater Sci 42:4675

Singh Jitendra, Ranwa Sapana, Akhtar Jamil, Kumar Mahesh (2015) Growth of residual stress-free ZnO films on SiO_2/Si substrate at room temperature for MEMS devices. AIP Adv 5:067140
Stoney GG (1909) The tension of metallic films deposited by electrolysis. Proc R Soc London Ser A 82:172
Sun Y, Miyasato T, Wigmore JK (1999) Characterization of excess carbon in cubic SiC films by infrared absorption. J Appl Phys 85:3377
Tauc J, Grigo Rovici R, Vancu A (1966) Optical properties and electronic structure of amorphous germanium. Physica Status Sol (b) 15:627
Trodahl HJ, Martin F, Muralt P, Setter N (2006) Raman spectroscopy of sputtered AlN films: E2(high) biaxial strain dependence. Appl Phys Lett 89:061905
Wang ZL, Song J (2006) Piezoelectric nanogenerators based on zinc oxide nanowire arrays. Science 312:242
Wang BB, Shaob RW, Huangc X, Zheng K, Zhu K, Cheng QJ (2016) Structure and photoluminescence properties of graphene nanoflakes grown on zinc oxide films by hot filament chemical vapor deposition. Diam Relat Mater 64:42
Yang Z, Ye Z, Xu Z, Zhao BH (2009) Effect of the morphology on the optical properties of ZnO nanostructured. Physica E 42:116
Zhang Y, Jia H, Wang R, Chen C, Luo X, Yua D (2003) Low-temperature growth and Raman scattering study of vertically aligned ZnO nanowires on Si substrate. Appl Phys Lett 83:4631
Zhao DG, Xu SJ, Xie MH, Tong SY (2003) Stress and its effect on optical properties of GaN epilayers grown on Si(111), 6H-SiC(0001), and c-plane sapphire. Appl Phys Lett 83:677
Zhou B, Rogachev AV, Liu Z, Piliptsou DG, Ji H, Jiang X (2012) Effects of oxygen/argon ratio and annealing on structural and optical properties of ZnO thin films. Appl Surf Sci 258:5759

Microstructurally Engineered Ceramics for Environmental Applications

Pradip Sekhar Das, Shruti Kakkar and Anoop Kumar Mukhopadhyay

Abstract This chapter focusses on how the microstructurally engineered ceramics can be successfully used for environmental applications, e.g., in development of materials that can be used for treatment of industrial wastewater. Industrial wastewater comes from mainly iron and steel industries, textile, and leather industries, as well as paper and pulp industries. Other contributors to this scenario are non-ferrous metals, chemicals, mining, petrochemicals, and refineries. Microelectronics as well as the pharmaceutical industries also contribute. It is well known that industrial wastewater contains toxic ions and dyes. When such contents cross the permissible limit it may become an issue of major environmental concern. The present work demonstrates that by using the microstructurally designed, phase pure $Mg(OH)_2$ nanoplatelets 99.99% adsorption of the toxic Cu(II) ion can be achieved. Further, it is shown that phase pure micro-dumbbell shaped three dimensional, self-assembly of $Mg(OH)_2$ nanoplatelets can degrade MB dye with 98% efficacy. The mechanisms behind such extraordinary capabilities of engineered nanoceramics are discussed. The implications of such developments for futuristic industrial wastewater treatment is also focused on.

Keywords Ceramic · Industrial · Magnesium hydroxide · Toxic · Ion · Dye · Nanoplatelet · Wastewater

P. S. Das · A. K. Mukhopadhyay (✉)
Advanced Mechanical and Materials Characterization Division (AMMCD), CSIR-Central Glass and Ceramic Research Institute, Kolkata 700032, India
e-mail: anoopkumar.mukhopadhyay@jaipur.manipal.edu

P. S. Das
Fuel Cell and Battery Division, CSIR-Central Glass and Ceramic Research Institute, Kolkata 700032, India

S. Kakkar
Department of Chemistry, Faculty of Science, School of Basic Sciences, Manipal University Jaipur, 303007, Rajasthan, India

A. K. Mukhopadhyay
Department of Physics, Faculty of Science, School of Basic Sciences, Manipal University Jaipur, 303007, Rajasthan, India

L. Ledwani and J. S. Sangwai (eds.), *Nanotechnology for Energy and Environmental Engineering*, Green Energy and Technology,
https://doi.org/10.1007/978-3-030-33774-2_22

1 Introduction

Wastewaters are conventional effluents from industrial activities. These wastewaters often contain toxic ions and dyes. There is a high possibility that toxic agents in the wastewater are beyond the limit that can be permitted. In such cases people exposed to such situation may get endangered. This danger can be reduced by using the microstructurally designed nanoceramics and grapheme oxides (Ruíz-Baltazara et al. 2019; Zhao et al. 2011). Considering the scientific, technological, and societal impact of this issue a brief literature survey is conducted. The literature survey (Chen and Song 2013; Heidari-Chaleshtori and Nezamzadeh-Ejhieh 2015; Hua et al. 2012; Jiang et al. 2015; Khan et al. 2014; Kuwahara et al. 2013; Li et al. 2014; Liu et al. 2013, 2015; Ma et al. 2015; Ray et al. 2015; Shaw et al. 2016; Simeonidis et al. 2016; Speed et al. 2015; Wang et al. 2015; Wu et al. 2014; Zhang et al. 2013, 2015; Zhou et al. 2015) on removal of toxic metals and ions is provided in Table 1. Similarly, the literature survey (Abdal-hay et al. 2015; Abdullah et al. 2016; Bhunia and Jana 2014; Bumajdad and Madkour 2014; DePuccio et al. 2015; Houas et al. 2001; He et al. 2016; Lin et al. 2012; Zhang et al. 2014) on the toxic dye, e.g., Methylene Blue (MB) removal by photocatalytic degradation is presented in Table 2. A glimpse of some most recent reports on both toxic metal removal and dye degradation (Cao et al. 2012; Das et al. 2017, 2018; Liu et al. 2015; Yang et al. 2016) is given in Table 3.

In terms of toxic components, the literature survey (Table 1) identifies a few facts. It is evident that many toxic ions, e.g., Zn(II), Cu(II), Pb(II), Ni(II), Cr(VI), Hg(II), etc. (Liu et al. 2015; Ma et al. 2015; Khan et al. 2014; Li et al. 2014; Kuwahara et al. 2013; Speed et al. 2015; Jiang et al. 2015; Simeonidis et al. 2016; Zhou et al. 2015; Heidari-Chaleshtori and Nezamzadeh-Ejhieh 2015; Zhang et al. 2013; Chen and Song 2013; Liu et al. 2013; Wu et al. 2014; Ray et al. 2015; Zhang et al. 2015; Wang et al. 2015; Hua et al. 2012; Shaw et al. 2016) *are currently in focus*. However, most of the reported work (Table 1) *focusses on Cu(II) highlighting thereby that the problems are yet to be resolved*. The wide variety of adsorbents used (Table 1) include nanoparticles (NPs) (Liu et al. 2015; Simeonidis et al. 2016; Ray et al. 2015), nanocomposites (NCs) (Ma et al. 2015; Khan et al. 2014; Jiang et al. 2015; Zhou et al. 2015), hybrid adsorbents (HA) (Zhang et al. 2013), modified LDH (m-LDH) (Heidari-Chaleshtori and Nezamzadeh-Ejhieh 2015), recyclable core–shell nanocomposites (RCSNCs) (Zhang et al. 2015), designed core–shell nanocomposites (DCNCS) (Shaw et al. 2016) and many others (Li et al. 2014; Kuwahara et al. 2013; Speed et al. 2015; Heidari-Chaleshtori and Nezamzadeh-Ejhieh 2015; Liu et al. 2013; Hua et al. 2012). There is only *one instance where $Mg(OH)_2$ nanoflakes (NFLs) are used to remove Cr(VI)* (Wang et al. 2015).

Similarly, most of the reported work (Table 2) concentrates on photocatalytic degradation of MB (Abdullah et al. 2016; DePuccio et al. 2015; Abdal-hay et al. 2015; Shaw et al. 2016; Lin et al. 2012; Zhang et al. 2014; Houas et al. 2001; Bumajdad and Madkour 2014) thereby emphasizing the unresolved issues related to the removal of this toxic dye. Relatively lesser focus is on photocatalytic degradation of Phenol, Bisphenol A, Atrazine (Bhunia and Jana 2014), and Salicylic Acid as well

Table 1 Literature survey on toxic metal removal

Toxic metal removal		
Adsorbent	Ion/metal removal by adsorption	References
Magnetite NPs	Ar(III)	Liu et al. (2015)
$CoFe_2O_4$-GO NCs	Pb(II)	Ma et al. (2015)
PANI–SnSiP NCs	Pb(II), Hg(II), Co(II) (selectivity)	Khan et al. (2014)
nZVI	Cu(II)	Li et al. (2014)
Calcium silicate hydrate (CSH)	Al, Mg, Fe, Ti, Mn	Kuwahara et al. (2013), Speed et al. (2015)
(GO)/β-FeOOH NCs	Cu(II)	Jiang et al. (2015)
Inorganic nanoparticles (NPs)	Toxic metals	Simeonidis et al. (2016)
Recyclable graphene/Fe_3O_4 NCs	Fe (III), Cu(II), Cd(II), etc.	Zhou et al. (2015)
Aspartic acid modified nano clinoptilolite	Zn(II), Cu(II), Pb(II), Ni(II) etc	Heidari-Chaleshtori and Nezamzadeh-Ejhieh (2015)
Hybrid adsorbents (HA)	Cu(II)	Zhang et al. (2013)
Zn_4Al–CTA–LDH (m-LDH)	Cr(VI), Cu(II)	Chen and Song (2013)
APS modified chrysotile	Cu(II)	Liu et al. (2013)
Biogenic oyster shells (BOS)	Cu(II)	Wu et al. (2014)
Nano Cu_2S (Porous) NPs	Hg(II) and Pb(II)	Ray et al. (2015)
Recyclable RCSNCs ($Mg(OH)_2$ shell-Ni core)	Zn(II), Cd(II), Cu(II), Kaolin	Zhang et al. (2015)
$Mg(OH)_2$ NFLs	Cr(VI)	Wang et al. (2015)
Nanosized Metal Oxides	Toxic metals	Hua et al. (2012)
DCSNCs (Porous NFL ZnO shell-Zeolite core)	Pb(II), MB	Shaw et al. (2016)

as Rhodamine B (He et al. 2016). Most of the photocatalytic agents are various types of NCs (Abdullah et al. 2016; Bhunia and Jana 2014; DePuccio et al. 2015; Abdalhay et al. 2015; Lin et al. 2012; Zhang et al. 2014). The rest of the photocatalytic agents are either NPs (Houas et al. 2001; He et al. 2016) or modified NPs (Bumajdad and Madkour 2014).

Most recent work (Table 3) indicates that only scarcely $Mg(OH)_2$ NPs (Liu et al. 2015) and nanoflowers (NFs) (Cao et al. 2012; Yang et al. 2016) are used for removal of Pb(II), Cd(II) while a singular work (Das et al. 2017) attempts removal of Cu(II) by nanoplatelet (NPL) of $Mg(OH)_2$. Similarly, there is another attempt (Das et al. 2018) that uses 3D self-assembled $Mg(OH)_2$ nanoplatelet assembly to degrade MB dye by photocatalysis. Therefore, the objective of the present work is to use the optimally designed microstructure of $Mg(OH)_2$ for dual purpose of removal of Cu(II) ions and degradation of MB dye.

Table 2 Literature survey on toxic dye degradation

Toxic dye degradation		
Photocatalytic agent	Toxic dye removal by photocatalytic degradation	Reference
ZnO/Ag_2O NCs, nylon-ZnO/Ag_2O hybrid NCs	MB	Abdullah et al. (2016)
rGO–Ag NCs	Phenol, bisphenol A, atrazine	Bhunia and Jana (2014)
Au–WO_3, Au–SiO_2–WO_3 NCs	MB	DePuccio et al. (2015)
PVAc–TiO_2 NCs	MB	Abdal-hay et al. (2015)
PANI/TiO_2 NCs	MO	Lin et al. (2012)
MnO_2 nanoflakes-modified diatomite NCs	MB etc	Zhang et al. (2014)
TiO_2	MB	Houas et al. (2001)
nano ZnO, nano ZnS	Salicylic acid and rhodamine B	He et al. (2016)
Au, Pt, Pd, Ag etc. NPs modified TiO_2	MB etc	Bumajdad and Madkour (2014)

Table 3 Most recent reports on toxic metal removal and dye degradation

Most recent work on toxic metal and dye removal		
Adsorbent material	Removed ion/dye	Reference
$Mg(OH)_2$ NPs	Pb(II)	Liu et al. (2015)
$Mg(OH)_2$ NFs	Pb(II)	Cao et al. (2012)
MgO NFs	Pb(II), Cd(II)	Yang et al. (2016)
$Mg(OH)_2$ NPL	Cu(II)	Das et al. (2017)
3D self-assembled $Mg(OH)_2$ NPA	MB	Das et al. (2018)

2 Materials and Methods

The synthesis of the designed nano $Mg(OH)_2$ powders are already reported (Das et al. 2017, 2018) and hence will not be repeated here for the sake of brevity. Here we shall use MHNPL to designate magnesium hydroxide nanoplatelets and CAMHNPL to designate Cu(II) ion adsorbed MHNPL. Similarly, DMHNPLA stands for 3-D designed magnesium hydroxide nano-platelet assembly.

The physical structure was determined by recording the X-ray diffraction (XRD) patterns before and after Cu(II) absorption. The microstructure was observed by field emission scanning electron microscopy (FESEM), energy dispersive X-ray analysis (EDAX), and transmission electron microscopy (TEM) techniques. Further, microstructural details were recorded by high resolution transmission electron

microscopy (HRTEM) technique and selected area diffraction (SAED) pattern analysis. The surface area was evaluated by the BET method. The surface states were identified by the fourier transformed infrared (FTIR) technique using KBr as an internal reference standard (Das et al. 2017). Further, the X-ray photoelectron spectroscopy (XPS) technique was also used to identify the surface oxidation states. Both the initial concentration, C(I) of the Cu(II) solutions, e.g., S1 (~80 mg L^{-1}), S2 (~95 mg L^{-1}), S3 (~100 mg L^{-1}), S4 (~140 mg L^{-1}), and S5 (~920 mg L^{-1}) and the corresponding *MHNPL samples* treated final solution concentrations, C(F); were determined by the inductively coupled plasma atomic emission spectroscopy (ICP-AES) technique (Das et al. 2017). For MB dye degradation efficacy examination, the DMHNPLA was synthesized in a similar manner as described in (Das et al. 2017) but with a specialized sonication technique (Das et al. 2018) to make the structure more porous. The characterization techniques were almost similar to those reported earlier (Das et al. 2017). In addition, the direct bandgap (E_g) energy values were evaluated by using the diffuse reflectance measurements from the UV-Vis spectra (Das et al. 2018). Thus, for both control MB dye solution and *DMHNPLA samples treated* MB dye solutions (volume −50 cc, concentration −4.6 mg L^{-1}) the optical properties in the range 200–800 nm were recorded by the calibrated UV-Vis technique (Das et al. 2018). Prior to addition of about 10 mg $Mg(OH)_2$ powders the MB dye solutions were preserved in dark (Das et al. 2018). Following the addition, the solutions were exposed for 60, 90, 120, 150, and 180 min to direct sunlight. Further details of both synthesis and characterizations are reported by us elsewhere (Das et al. 2017, 2018).

3 Results and Discussions

3.1 MHNPL Nano-Adsorbent

3.1.1 XRD Studies

A comparison of the XRD patterns of MHNPL (Fig. 1a) and CAMHNPL (Fig. 1b), respectively, confirms that pure hexagonal brucite phase (ICSD Code: 31053) occurs in MHNPL and that it adsorbs Cu(II) ions in its structure. The monoclinic copper nitrate hydroxide $[Cu_2(NO_3)(OH)_3]$ (ICSD Code: 31353) is, therefore, present as a minor phase in Fig. 1b.

3.1.2 Pore Size and Surface Area

Based on N_2 adsorption and desorption data and BET measurement data published elsewhere (Das et al. 2017, 2018), the characteristic pore size details along with the data on isotherm type and BET surface area are given in Table 4. These data match with those from the literature (Yu et al. 2004). Further, MHNPL samples have

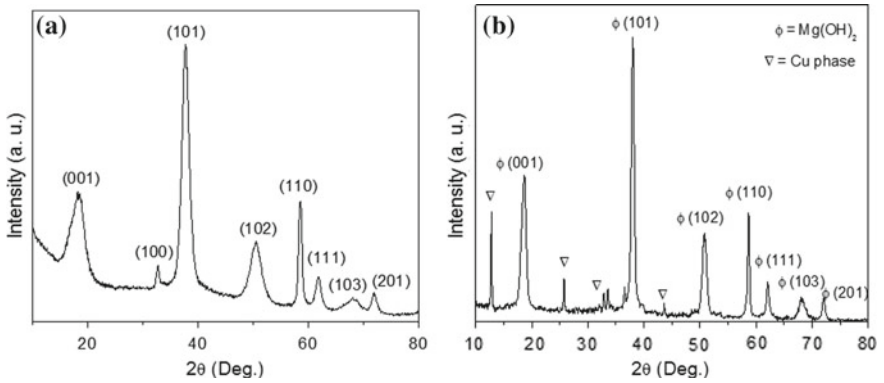

Fig. 1 The XRD patterns of **a** MHNPL and **b** CAMHNPL samples (Reprinted with permission from Das et al. (2017))

Table 4 Pore size and surface area of MHNPL and DMHNPLA samples

Sample	Isotherm type	Nature of porosity	Pore geometry	Pore size range (nm)	Average pore size (nm)	Surface area (m^2 g^{-1})	Ref. No.
MHNPL	H3 type hysteresis loop	Mesoporous	Slit	~1–5	4.2[a]	273	Das et al. (2017)
DMHNPLA	H3 type hysteresis loop	Mesoporous	Slit	~3–9	6	342	Das et al. (2018)

[a]Occasional random large pore size 30–36 nm (Das et al. 2017)

surface area two and half times that reported (Liu et al. 2011) in literature. On further optimization of microstructure (Das et al. 2018) the surface area of the DMHNPLA samples is raised to as high as, e.g., 342 m^2 g^{-1}. Thus, the enhancement in surface area should give rise to much more effective active sites for adsorption (Das et al. 2017) as well as initiation of photocatalytic activities (Das et al. 2018).

3.1.3 Microstructural Studies by TEM

The TEM photomicrograph given in Fig. 2a confirms the hexagonal nanoplatelet structure formation with interconnected porosity. The sample has (101) orientation as confirmed by HRTEM, Fig. 2b and the SAED pattern shown as the inset. The d values estimated for the (101) and (102) planes from SAED pattern corroborate well with those obtained from Fig. 1a [*ca. 0.238 nm versus 0.236 nm for (101) plane and 0.180 nm versus 0.182 nm for (102) plane*].

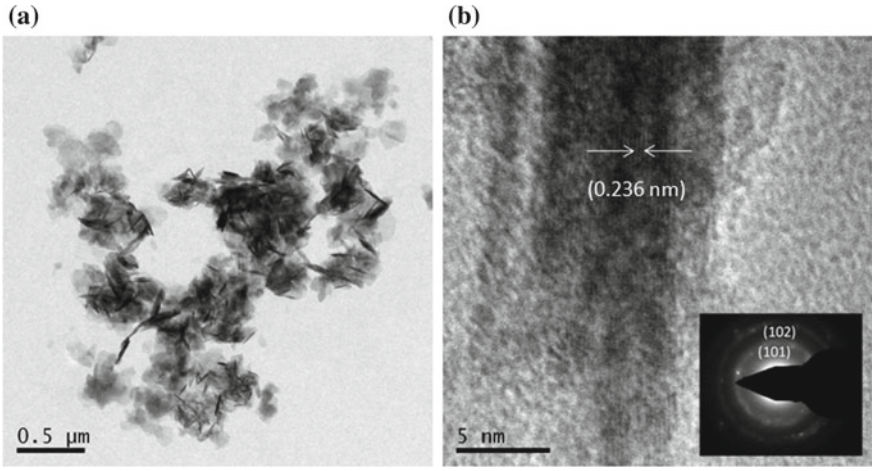

Fig. 2 TEM photomicrographs of **a** Hexagonal MHNPLs **b** HRTEM of (101) plane (*Inset* Corresponding SAED pattern. Reprinted with permission from Das et al. (2017))

3.1.4 Microstructural Studies by FESEM

Further confirmation of the porous microstructure in MHNPL and CAMHNPL samples come from FESEM photomicrographs presented in Fig. 3a and b, respectively (Das et al. 2017). The inset of Fig. 3b shows the corresponding nanoplatelet powders agglomerated together (Das et al. 2017). These evidences also confirm the presence of a highly porous structure. The corresponding EDX data (Fig. 4) collected from spot 1 shown as inset of Fig. 4 confirm the presence of Cu in the CAMHNPL powder. Here, signals of Al and Si come from the glass substrate used to hold the drop casted CAMHNPL samples (Das et al. 2017).

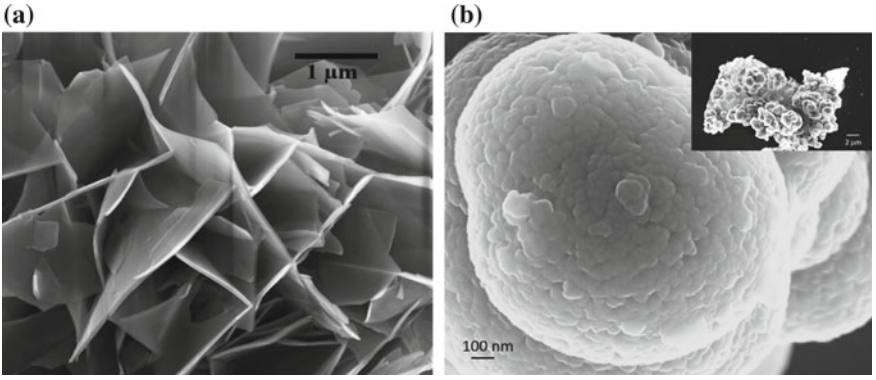

Fig. 3 FESEM photomicrographs of **a** MHNPL and **b** CAMHNPL samples (*Inset* Corresponding nanoplatelet powder. Reprinted with permission from Das et al. (2017))

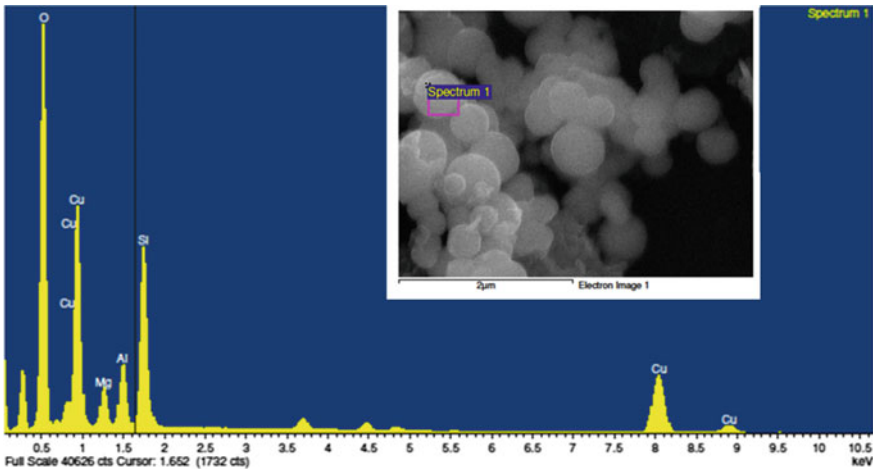

Fig. 4 EDAX spectra of CAMHNPL samples (*Inset* Spot from where EDAX spectra is taken)

3.1.5 ICP-AES Studies

The initial concentration C(I) of Cu(II) in untreated Cu(II) solution each of 1 L volume and final concentrations C(F) of all the 100 mg MHNPL 20 min treated Cu(II) 1 L solutions (i.e., S1, S2, S3, S4, and S5) are shown in Fig. 5a and its inset, respectively. The corresponding Cu(II) ion removal efficacies of MHNPL for the solutions S1, S2, S3, S4, and S5 are shown in Fig. 5b.

The ICP-AES derived (Das et al. 2017) results presented in Fig. 5a, b confirm that the Cu(II) ion removal efficacies of the MHNPL samples are 99.67, 99.83, 99.99, 99.84, and 99.76% respectively, for the solutions S1, S2, S3, S4, and S5. Thus, the MHNPL samples synthesized in the present work exhibit the most consistent Cu(II) ion adsorption efficiency of more than 99%. The efficiency ranges from, e.g., 99.67

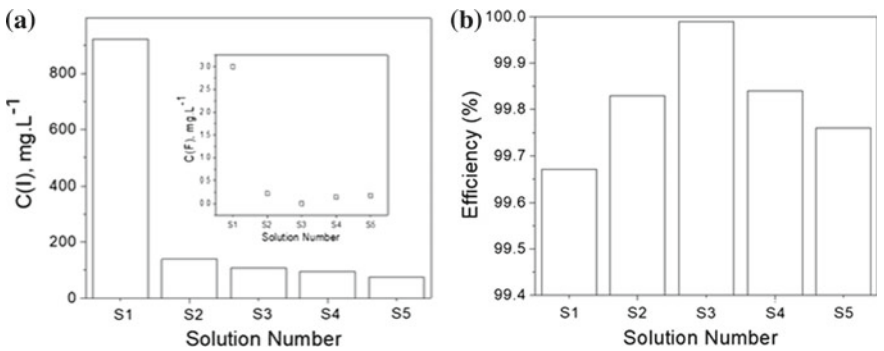

Fig. 5 Cu (II) ion removal efficacies of MHNPL samples as a function of solution number **a** Variation of C(I) and C(F) (*Inset*) and **b** Efficiency (%)

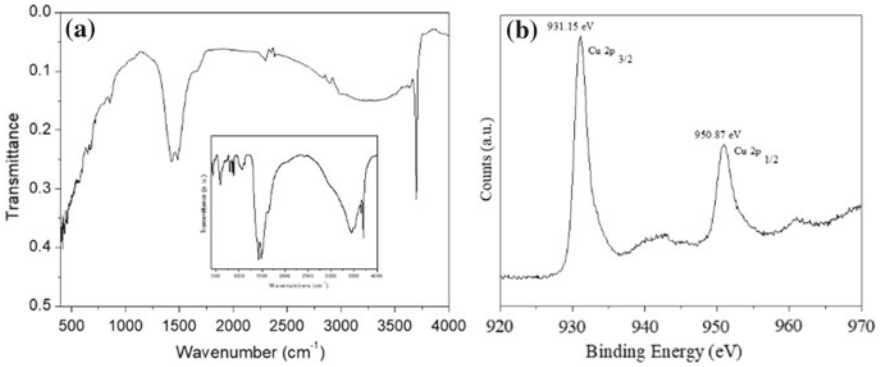

Fig. 6 Surface characteristics of the CAMHNPL samples **a** FTIR spectra (*Inset* FTIR spectra of MHNPL samples) and **b** XPS spectra (Reprinted with permission from Das et al. (2017))

to 99.99%. These results (Das et al. 2017) ensure further that the average efficiency is almost as high as 100%, e.g., (99.81 ± 0.11)%.

3.1.6 FTIR and XPS Studies

For the CAMHNPL samples, the confirmatory evidence of Cu absorption comes from the extra two peaks at ~1433 and ~1490 cm^{-1} (Fig. 6a) which are absent in the FTIR spectra of the MHNPL samples shown as inset of Fig. 6a. Cu-OH moiety has OH bands (Liu et al. 2011). The first extra peak is linked to that. Similarly, the second extra peak springs up due to occurrence of NO_3^- (Wolf and Feldmann 2010). The Cu $2p_{3/2}$ and Cu $2p_{1/2}$ peaks in the XPS spectra of the CAMHNPL samples (Fig. 6b) further confirm that Cu is definitely adsorbed and it exists in divalent state (Chen and Song 2013; Das et al. 2017).

3.1.7 How the MHNPL Samples Work as a Nano-Adsorbent

The MHNPL has a self-supported, highly porous microstructure with an average pore size of about 4 nm (Table 4; Figs. 2, 3). Thus, the microstructure provides many active sites. Hence, Mg(II) ions leach out from such active sites. Occupying only a small fraction of the active sites, a monolayer of Cu(II) ions are at first adsorbed on the MHNPLs by an *ion exchange* mechanism, Fig. 4 (Das et al. 2017). Further *Cu(II) ions adsorb on these nuclei of nascent Cu(II) ions* through the ion exchange mechanism to ultimately form $Cu_2(NO_3)(OH)_3$ *as a step that dictates the rate of adsorptions*, Figs. 1b, 6a, b. The average adsorption efficiency of as high as ~99.81% (Das et al. 2017) is thus achieved through numerous localized repetition of these unit steps, Fig. 5a. The statistical randomness in the availability of active sites and the

Cu(II) ion concentrations dictates the relative variations in efficacies as a function of solution number, Fig. 5b.

3.2 DMHNPLA for MB Dye Degradation

3.2.1 Synthesis of DMHNPLA Samples

The details of the synthesis procedure for DHNPLA are already reported (Das et al. 2018). The synthesis procedure is almost similar to that of MHNPL (Das et al. 2017). However, with an aim to create more uniform and relatively narrower pore size distribution as well as interconnected pores, $Mg(NO_3)_2$ solution of pH about 6.4 is kept under a sonication bath. Now NaOH solution of pH ~ 12.8 is added dropwise at an average rate of about 0.14 $cc.s^{-1}$ to the $Mg(NO_3)_2$ solution under ambient laboratory condition (i.e., 30 °C). Next, by following the procedural steps as detailed in (Das et al. 2017, 2018); the sample powders are obtained as a three dimensional (3D) self-assembly of MHNPL structures. These are designated as DMHNPLA which stands for 3-D designed magnesium hydroxide nano-platelet assembly, as mentioned above.

3.2.2 Phase Purity and Surface Area Studies

The phase purity of the DMHNPLA samples is confirmed from the XRD pattern reported earlier by us (Das et al. 2018). Based on Scherrer's equation and single profile Rietveld analysis (Das et al. 2018) the variations in crystallite sizes and corresponding lattice strain as a function of the Miller indices of the various crystallographic planes are shown in Fig. 7. The crystallite sizes range from ~3 to 13 nm with an average of about 8 nm while most of the strains range from about 0.5 to 5.85% (Fig. 7) with an

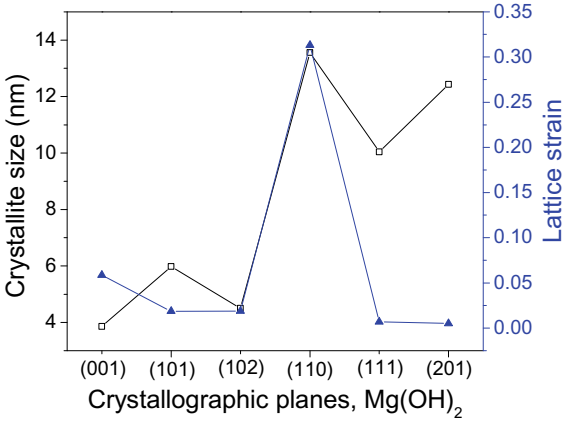

Fig. 7 Variations of crystallite size and lattice strains among the various crystallographic planes of the DMHNPLA samples

average of about 2.16%. The (110) plane exhibits exceptionally high strain of about 31.30% and is, therefore, excluded in estimating the average magnitude of strain. As mentioned earlier in Table 4, the DMHNPLA samples have surface area much higher than that reported (Liu et al. 2011) in literature. It happens due to large pore volume with narrow size distribution of pores with an average size of only about 6 nm, Table 4 (Das et al. 2018).

3.2.3 Microstructural Studies

Figure 8 shows a typical illustrative FESEM photomicrograph of the three-dimensionally self-assembled nanopowders which exhibit a *connected micro dumb-bell* like microstructure. The average length and width of individual micro dumb-bells are ~9 and ~1.9 μm, respectively (*Inset* Fig. 8). The photomicrograph (Fig. 8) confirms the presence of *beautiful flower-bud like microstructure comprised of self-assembled particles of* ~100–200 nm *size*.

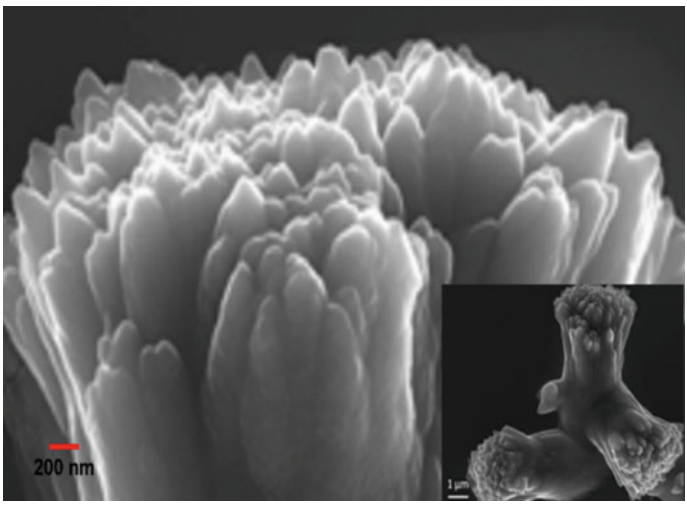

Fig. 8 FESEM photomicrograph of the micro dumbbells in the DMHNPLA samples (*Inset* The three dimensional self-assembly of the micro dumbbells. Reprinted with permission from Das et al. (2018))

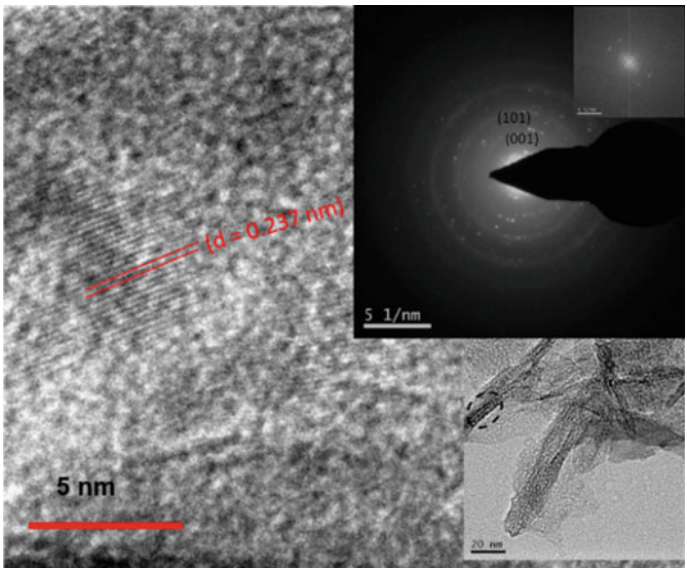

Fig. 9 Lattice fringe of (101) plane obtained by HRTEM (*Insets* Bottom Right—The porous microstructure, Top Right: The corresponding SAED pattern, Topmost Right: The Corresponding FFT pattern. Reprinted with permission from Das et al. (2018))

The HRTEM image (Fig. 9) exhibits the lattice fringe of ~0.237 nm that corresponds to the (101) plane as mentioned in sub-Sect. 3.2.2. The microstructure in the bottom right side inset exhibits the average pore size of ~5 nm. These are channel pores. From the SAED pattern shown as the top right inset, the d-spacings are ~0.238 nm for the (101) plane and ~0.180 nm for the (102) plane. These data corroborate nicely with those from the XRD pattern. The FFT pattern shown as the topmost right-hand side inset in Fig. 9 confirms further the presence of the (101) plane. The corresponding typical representative EDAX data published elsewhere (Das et al. 2018) confirm that the ratio of Mg: O by wt% is about 58.73% whereas stoichiometry wise it should be ~74.98% (Li et al. 2013). So, the DMHNPLA samples have deficiency of magnesium and excess of oxygen.

3.2.4 The Direct Bandgap (E_g) Evaluation

As reported elsewhere by us (Das et al. 2018) and also based on the literature report (Bai et al. 2016) the (E_g) values of DMHNPLA samples are estimated as 5.08 and 3.76 eV (Fig. 10). These data match with those reported for nanosheets and 2D structures of $Mg(OH)_2$ (Suslu et al. 2016; Kim et al. 2000). But this match may be incidental. It is opined (Sun et al. 2017; Wang et al. 2014) that in nanopowders the crystalline phase and amorphous phase may coexist. When it happens, it affects the

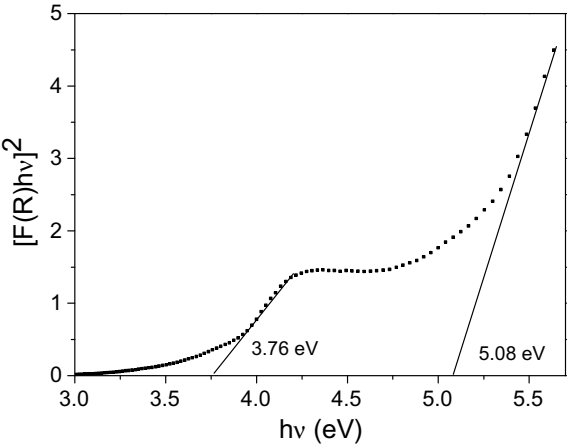

Fig. 10 The plot of $[F(R)](h\nu)^2$ versus $(h\nu)$ for the DMHNPLA samples. Reprinted with permission from Das et al. (2018)

sub-bandgap. A similar situation prevails in the present DMHNPLA samples (Figs. 1 and 9). Another factor that may affect E_g (Fig. 10) is crystallite size (Lu et al. 2015).

3.2.5 The Dye Degradation Efficacy

Figure 11a–c presents the absorption spectrum on MB dye degradation efficacy of the present three dimensional DMHNPLA samples. The peaks representing MB dye occur at 292 and 663 nm in Fig. 11a but are absent in Fig. 11b which shows the data for DMHNPLA treated MB dye solution exposed to direct sunlight for 60, 90, 1220, 150, and 180 min. Further confirmation of their absence is provided by the exploded view presented in Fig. 11c for the region 660–670 nm. The amount of degradation is more at higher exposure time (Fig. 11b). In fact at 60 min exposure to direct sunlight the degradation efficacy of three dimensional DMHNPLA samples is more than 98%, which is much higher than those reported in literature (Abdullah et al. 2016; Bhunia and Jana 2014; DePuccio et al. 2015; Abdal-hay et al. 2015).

The photocatalytic efficacy becomes sensitive to the intensity of light used when a solar simulator is used as a light source (Shaw et al. 2016; Shanmugam et al. 2015). However, the same is immaterial here. The reason is that all the photocatalytic experiments are conducted in the presence of *only direct sunlight exposure*. Since the photocatalytic degradation efficacy of the DMHNPLA samples is significant for the cationic MB dye; it deserves an explanation.

The experimental results (Figs. 7, 8, 9, 10, 11; Table 4) suggest that there are few factors that may simultaneously contribute (Das et al. 2018). These are, viz., (a) mesoporous microstructure, (b) 6 nm average pore size, (c) small pore size distribution, (d) high pore volume, (e) very high surface area, (f) large value of E_g and (g) the –OH bonding vibrations. It is suggested that an optimum synergistic contribution of aforesaid factors possibly leads to high efficacy of the DMHNPLA samples. Thus, the reactive, negatively charged surface of the photocatalyst (Das et al. 2018) gets

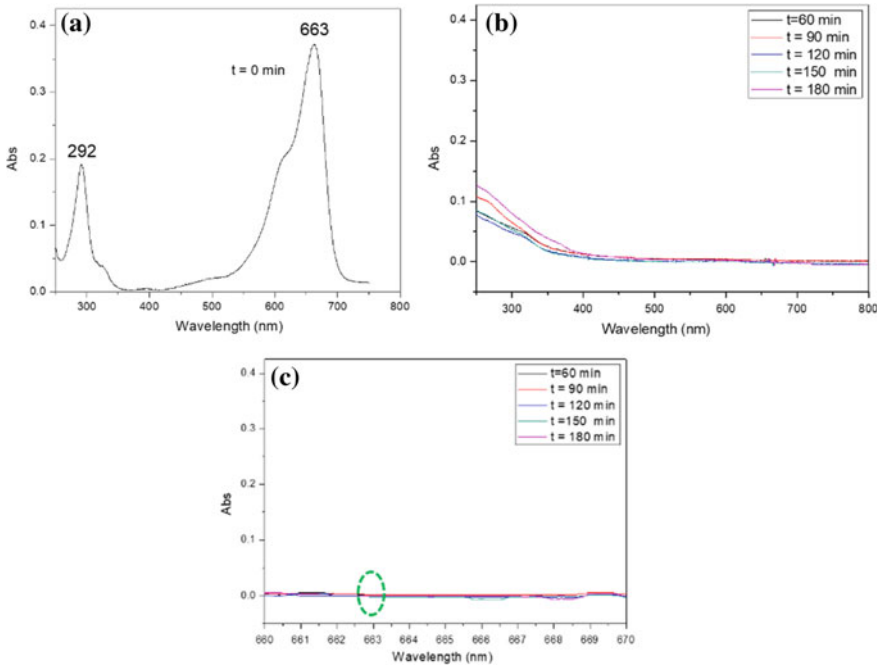

Fig. 11 UV-Vis absorption spectra of MB solution **a** Control solution, **b** after exposure to direct sunlight for different times in presence of the DMHNPLA samples, **c** exploded view of the region 660–670 nm from Fig. 11b. (Reprinted with permission from Das et al. (2018))

the dye adsorbed on the surface. Further, the surface also has higher redox potential for both electrons as well as hole. When incident sunlight provides energy $>E_g$, the electrons are excited. These photo-excited electrons can and do jump into conduction band. As the photo-excited electrons move over to the conduction band, the corresponding positively charged holes remain in the DMHNPLA sample surface (Xu et al. 2014). It is most likely that the *free hydroxyl radical generated by these holes, degrade the cationic MB dye* (Das et al. 2018). The contact with *water has no effect on crystal facets of brucite* $Mg(OH)_2$ (Ou et al. 2014). Therefore, through direct sunlight-induced photocatalytic activity the phase pure DMHNPLA samples can be used to *degrade MB dye in industrial wastewater*. Thus, for *futuristic applications in treatment of industrial wastewater both MHNPL and DMHNPLA samples exhibit good promise*.

4 Conclusion

The MHNPL samples show the *efficiency as high as 99.99% for the removal of Cu(II) ions* through adsorption. It occurs most likely by an *ion-exchange mechanism*. The DMHNPLA samples *exhibit 98% efficacy for degradation of MB dye*. This occurs *due to direct sunlight-induced photocatalytic activity that aids in generation of free hydroxyl radicals which degrade the cationic MB dye*. These facts show that *microstructurally designed nanoceramic hydroxides, e.g., $Mg(OH)_2$* can be successfully used for futuristic *environmental applications,* e.g., treatment of industrial wastewater containing toxic ions and dyes.

Acknowledgements Two of the authors (PSD and AKM) are grateful to Dr. K. Muraleedharan, Director, CSIR-Central Glass and Ceramic Research Institute (CGCRI), Kolkata for his kind permission to publish this paper. The corresponding author (AKM) also acknowledges the kind permissions received from Dr. G. K. Prabhu, President, Manipal University Jaipur, Jaipur 303007, Rajasthan, India and Prof N. N. Sharma, Pro-President, Manipal University Jaipur, Jaipur 303007, Rajasthan, India to publish this work. The authors appreciate the infrastructural supports received from all colleagues of the Advanced Mechanical and Materials Characterization Division (AMMCD), Advanced Materials Characterization Unit (AMCU) and Materials Characterization and Instrumentation Division (MCID) at CSIR-CGCRI.

References

Abdal-hay A, Hamdy Makhlouf AS, Khalil KA (2015) Novel, facile, single-step technique of polymer/TiO_2 nanofiber composites membrane for photodegradation of methylene blue. ACS Appl Mater Interfaces 7(24):13329–13341

Abdullah H, Kuo DH, Kuo YR, Yu FA, Cheng KB (2016) Facile synthesis and recyclability of thin nylon film-supported n-type ZnO/p-type Ag_2O nano composite for visible light photocatalytic degradation of organic dye. J Phys Chem C 120(13):7144–7154

Bai X, Wei J, Tian B, Liu Y, Reiss T, Guiblin N, Gemeiner P, Dkhil B, Infante IC (2016) Size effect on optical and photocatalytic properties in $BiFeO_3$ nanoparticles. J Phys Chem C 120(7):3595–3601

Bhunia SK, Jana NR (2014) Reduced graphene oxide-silver nanoparticle composite as visible light photocatalyst for degradation of colorless endocrine disruptors. ACS Appl Mater Interfaces 6(22):20085–20092

Bumajdad A, Madkour M (2014) Understanding the superior photocatalytic activity of noble metals modified titania under UV and visible light irradiation. Phys Chem Chem Phys 16(16):7146–7158

Cao CY, Qu J, Wei F, Liu H, Song WG (2012) Superb adsorption capacity and mechanism of flowerlike magnesium oxide nanostructures for lead and cadmium ions. ACS Appl Mater Interfaces 4(8):4283–4287

Chen Y, Song YF (2013) Highly selective and efficient removal of Cr(VI) and Cu(II) by the chromotropic acid-intercalated Zn–Al layered double hydroxides. Ind Eng Chem Res 52(12):4436–4442

Das PS (2018) Green synthesis of ultrafine ceramic powders for advanced applications. Ph.D. dissertation, Jadavpur University, Kolkata, India, 2 Feb

Das PS, Bakuli S, Samanta A, Mandal AK, Ghosh J, Dey A, Mukhopadhyay AK (2017) Very high Cu(II) adsorption efficacy of designed nano-platelet $Mg(OH)_2$ assembly. Mater Res Express 4(2):025025

Das PS, Das S, Ghosh J, Mukhopadhyay AK (2018) Unique microstructure of 3D self-assembled $Mg(OH)_2$ nanoparticles for methylene blue degradation in presence of direct sun light. Trans Indian Ceram Soc 77(4):226–234

DePuccio DP, Botella P, O'Rourke B, Landry CC (2015) Degradation of methylene blue using porous WO_3, SiO_2–WO_3, and their Au-loaded analogs: adsorption and photocatalytic studies. ACS Appl Mater Interfaces 7(3):1987–1996

Heidari-Chaleshtori M, Nezamzadeh-Ejhieh A (2015) Clinoptilolite nano-particles modified with aspartic acid for removal of Cu(II) from aqueous solutions: isotherms and kinetic aspects. New J Chem 39(12):9396–9406

He W, Jia H, Cai J, Han X, Zheng Z, Wamer WG, Yin JJ (2016) Production of reactive oxygen species and electrons from photoexcited ZnO and ZnS nanoparticles: a comparative study for unraveling their distinct photocatalytic activities. J Phys Chem C 120(6):3187–3195

Houas A, Lachheb H, Ksibi M, Elaloui E, Guillard C, Herrmann JM (2001) Photocatalytic degradation pathway of methylene blue in water. Appl Catal B 31(2):145–157

Hua M, Zhang S, Pan B, Zhang W, Lv L, Zhang Q (2012) Heavy metal removal from water/wastewater by nanosized metal oxides: a review. J Hazard Mater 211:317–331

Jiang T, Yan L, Zhang L, Li Y, Zhao Q, Yin H (2015) Fabrication of a novel graphene oxide/β-FeOOH composite and its adsorption behavior for copper ions from aqueous solution. Dalton Trans 44(22):10448–10456

Khan MA, Ahmad A, Umar K, Nabi SA (2014) Synthesis, characterization, and biological applications of nanocomposites for the removal of heavy metals and dyes. Ind Eng Chem Res 54(1):76–82

Kim E, Jiang ZT, No K (2000) Measurement and calculation of optical band gap of chromium aluminum oxide films. Jpn J Appl Phys 39(8R):4820

Kuwahara Y, Tamagawa S, Fujitani T, Yamashita H (2013) A novel conversion process for waste slag: synthesis of calcium silicate hydrate from blast furnace slag and its application as a versatile adsorbent for water purification. J Mater Chem A 1(24):7199–7210

Lin Y, Li D, Hu J, Xiao G, Wang J, Li W, Fu X (2012) Highly efficient photocatalytic degradation of organic pollutants by PANI-modified TiO_2 composite. J Phys Chem C 116(9):5764–5772

Liu W, Huang F, Wang Y, Zou T, Zheng J, Lin Z (2011) Recycling $Mg(OH)_2$ nanoadsorbent during treating the low concentration of CrVI. Environ Sci Technol 45(5):1955–1961

Liu K, Zhu B, Feng Q, Wang Q, Duan T, Ou L, Zhang G, Lu Y (2013) Adsorption of Cu(II) ions from aqueous solutions on modified chrysotile: thermodynamic and kinetic studies. Appl Clay Sci 80:38–45

Liu CH, Chuang YH, Chen TY, Tian Y, Li H, Wang MK, Zhang W (2015a) Mechanism of arsenic adsorption on magnetite nanoparticles from water: thermodynamic and spectroscopic studies. Environ Sci Technol 49(13):7726–7734

Liu M, Wang Y, Chen L, Zhang Y, Lin Z (2015b) $Mg(OH)_2$ supported nanoscale zero valent iron enhancing the removal of Pb(II) from aqueous solution. ACS Appl Mater Interfaces 7(15):7961–7969

Li C, Zhuang Z, Huang F, Wu Z, Hong Y, Lin Z (2013) Recycling rare earth elements from industrial wastewater with flowerlike nano-$Mg(OH)_2$. ACS Appl Mater Interfaces 5(19):9719–9725

Li S, Wang W, Yan W, Zhang WX (2014) Nanoscale zero-valent iron (nZVI) for the treatment of concentrated Cu(II) wastewater: a field demonstration. Environ Sci Process Impacts 16(3):524–533

Lu Y, Liu X, Qiu K, Cheng J, Wang W, Yan H, Tang C, Kim JK, Luo Y (2015) Facile synthesis of graphene-like copper oxide nanofilms with enhanced electrochemical and photocatalytic properties in energy and environmental applications. ACS Appl Mater Interfaces 7(18):9682–9690

Ma S, Zhan S, Jia Y, Zhou Q (2015) Highly efficient antibacterial and Pb(II) removal effects of Ag-$CoFe_2O_4$-GO nanocomposite. ACS Appl Mater Interfaces 7(19):10576–10586

Ou X, Li J, Lin Z (2014) Dynamic behavior of interfacial water on $Mg(OH)_2$ (001) surface: a molecular dynamics simulation work. J Phys Chem C 118(51):29887–29895

Ray C, Sarkar S, Dutta S, Roy A, Sahoo R, Negishi Y, Pal T (2015) Evolution of tubular copper sulfide nanostructures from copper(I)–metal organic precursor: a superior platform for the removal of Hg(II) and Pb(II) ions. RSC Adv 5(16):12446–12453

Ruíz-Baltazara AJ, Reyes-López SY, Mondragón-Sánchez ML et al (2019) Eco-friendly synthesis of Fe_3O_4 nanoparticles: evaluation of their catalytic activity in methylene blue degradation by kinetic adsorption models. Results Phys 12:989–995

Shanmugam M, Alsalme A, Alghamdi A, Jayavel R (2015) Enhanced photocatalytic performance of the graphene-V_2O_5 nanocomposite in the degradation of methylene blue dye under direct sunlight. ACS Appl Mater Interfaces 7(27):14905–14911

Shaw R, Sharma R, Tiwari S, Tiwari SK (2016) Surface engineered zeolite: an active interface for rapid adsorption and degradation of toxic contaminants in water. ACS Appl Mater Interfaces 8(19):12520–12527

Simeonidis K, Mourdikoudis S, Kaprara E, Mitrakas M, Polavarapu L (2016) Inorganic engineered nanoparticles in drinking water treatment: a critical review. Environ Sci Water Res Technol 2(1):43–70

Speed D, Westerhoff P, Sierra-Alvarez R, Draper R, Pantano P, Aravamudhan S, Chen KL, Hristovski K, Herckes P, Bi X, Yang Y (2015) Physical, chemical, and in vitro toxicological characterization of nanoparticles in chemical mechanical planarization suspensions used in the semiconductor industry: towards environmental health and safety assessments. Environ Sci Nano 2(3):227–244

Sun H, Xiao J, Zhu S, Hu Y, Feng G, Zhuang J, Zhao L (2017) Crystallinity and sub-band gap absorption of femtosecond-laser hyperdoped silicon formed in different N-containing gas mixtures. Materials 10(4):351

Suslu A, Wu K, Sahin H, Chen B, Yang S, Cai H, Aoki T, Horzum S, Kang J, Peeters FM, Tongay S (2016) Sci Rep 6:20525

Wang D, Huang JF, Yin LX, Cao LY, Ouyang HB, Li JY, Hao W (2014) Photocatalytic activity of hexagonal prism $Sm(OH)_3$ nanocrystallites for decomposition of rhodamine B. Mater Lett 116:393–395

Wang Z, Li C, Mu Y, Lin Z, Yi A, Zhang Q, Yan B (2015) Nanoadduct relieves: alleviation of developmental toxicity of Cr(VI) due to its spontaneous adsorption to $Mg(OH)_2$ nanoflakes. J Hazard Mater 287:296–305

Wolf S, Feldmann C (2010) $Cu_2X(OH)_3$ ($X = Cl^-$, $NO_3{}^-$): synthesis of nanoparticles and its application for room temperature deposition/printing of conductive copper thin-films. J Mater Chem 20(36):7694–7699

Wu Q, Chen J, Clark M, Yu Y (2014) Adsorption of copper to different biogenic oyster shell structures. Appl Surf Sci 311:264–272

Xu C, Rangaiah GP, Zhao XS (2014) Photocatalytic degradation of methylene blue by titanium dioxide: experimental and modeling study. Ind Eng Chem Res 53(38):14641–14649

Yang S, Huang P, Peng L, Cao C, Zhu Y, Wei F, Sun Y, Song W (2016) Hierarchical flowerlike magnesium oxide hollow spheres with extremely high surface area for adsorption and catalysis. J Mater Chem A 4(2):400–406

Yu JC, Xu A, Zhang L, Song R, Wu L (2004) Synthesis and characterization of porous magnesium hydroxide and oxide nanoplates. J Phys Chem B 108(1):64–70

Zhang Y, Wang X, Liu J, Wu L (2013) Removal of copper (Cu^{2+}) from water using novel hybrid adsorbents: kinetics and isotherms. J Chem Eng Data 58(5):1141–1150

Zhang YX, Hao XD, Li F, Diao ZP, Guo ZY, Li J (2014) pH-dependent degradation of methylene blue via rational-designed MnO_2 nanosheet-decorated diatomites. Ind Eng Chem Res 53(17):6966–6977

Zhang M, Song W, Chen Q, Miao B, He W (2015) One-pot synthesis of magnetic Ni@$Mg(OH)_2$ core–shell nanocomposites as a recyclable removal agent for heavy metals. ACS Appl Mater Interfaces 7(3):1533–1540

Zhao G, Li J, Ren X, Chen C, Wang X (2011) Few-layered graphene oxide nanosheets as superior sorbents for heavy metal ion pollution management. Environ Sci Technol 45(24):10454–10462

Zhou G, Xu X, Zhu W, Feng B, Hu J (2015) Dispersedly embedded loading of Fe_3O_4 nanoparticles into graphene nanosheets for highly efficient and recyclable removal of heavy metal ions. New J Chem 39(9):7355–7362

Eco-friendly Surface Modification and Nanofinishing of Textile Polymers to Enhance Functionalisation

Mumal Singh, Mona Vajpayee and Lalita Ledwani

Abstract The chapter gives brief information about the application of non-thermal atmospheric pressure plasma and nanotechnology in the fields of textiles. Four types of atmospheric pressure plasma are used for surface modification of textiles, namely, corona discharge, atmospheric pressure plasma jet (APPJ), atmospheric pressure glow discharge (APGD) and dielectric barrier discharge (DBD). Cold plasma or non-thermal plasma is considered superior to other conventional modification techniques as it can modify the polymeric surface without altering the bulk properties of the material. The chapter also provides a brief idea about the classification, synthesis and application of nanoparticles existing in different forms. The application of nano-sized particles on textile materials confers unexpected properties different from those of the bulk material. Together with plasma technology, nanoparticle-coated fabrics can enhance the overall wear, comfort and care of the fabric. This chapter reviews the recent studies involving modification and characterisation of textile highlighting plasma and nano-pretreatment. This chapter also attempts to give an overview of the literature on treatment of textiles categorising them on the basis of different functional properties like antimicrobial, UV resistance, easy care, dye adsorption and flame-retardant finishes that could be achieved by the application of metal and metal oxide nanoparticles and enhanced by plasma pretreatment.

Keywords Non-thermal plasma · Textiles · Surface modification · Nanoparticles · Antimicrobial · UV protection · Dyeing

1 Introduction

Textiles have been an essential part of human history and can be seen everywhere in modern society as well. Textiles can be divided into two main categories according to their applications; one is traditional textiles that are used in fashion clothing and apparels, and other is technical textiles (Schwarz and Kovačević 2017). Technical textiles are used in diverse applications ranging from automobiles (in car interiors),

M. Singh · M. Vajpayee · L. Ledwani (✉)
Department of Chemistry, School of Basic Science, Manipal University Jaipur, Rajasthan, India
e-mail: lalita.ledwani@jaipur.manipal.edu

L. Ledwani and J. S. Sangwai (eds.), *Nanotechnology for Energy and Environmental Engineering*, Green Energy and Technology,
https://doi.org/10.1007/978-3-030-33774-2_23

agriculture (used for crop protection), civil engineering (as reinforcement textile for roads), medical and hygiene (bandages, surgical gowns and sutures), protective clothing (firefighter clothes), sportswear, defence (bulletproof jackets), packaging, etc. Looking at the broad spectrum of applications for which textiles are being used, it is necessary to manufacture textiles with specifically designed surface properties like wettability, increased adhesion, dyeability and softness (John and Anandjiwala 2009; Wei et al. 2009). It is essential to understand that often natural or fabricated polymer surfaces do not have the same compositions as the bulk phase. This difference in surface properties can result from chemical reactions of surface molecules (like oxidation or sulphonation), microbial attack, adherence of environmental contaminants like (dirt or soil) and low surface energy of molecular groups. Sometimes, physical defects like scratches or abrasion can also lead to defunctionalisation of textile for a particular application. Therefore, surface modification of textile surface is not only preferable but also essential whether it may be merely to clean the surface or modify it chemically or physically to alter the interactions with substrate and generate result as per our requirement (Hoffman 1996).

Surface modification is the process of modifying material surface either by physical, chemical or biological methods to impart certain features which distinguish it from the untreated one. Over the years, various surface modification techniques have been employed for the alternation of textile surface properties which can be broadly divided into physical, chemical, biological and mechanical methods (Fig. 1). The physical processes involve treatment with active gases or radiations which can be achieved by (a) deposition of molecules from active gases used during plasma treatment or flame spray treatment, (b) etching or oxidation of fabric surface with highly accelerated ions generated during ion bean treatments, radiofrequency plasma discharge and gamma-ray treatments, and (c) cross-linking of surface molecules initiated by free radical formation during UV treatment, corona discharge, etc. The chemical surface treatment methods generally use wet chemical treatments for surface modification along with disinfection to remove microbes or soil and contaminants using any or all four described methods: (a) dipping/coating/spraying of polymer solution or surfactant, (b) desorption of surface-active compounds from bulk to surface, (c) chemical treatment to modify fabric surface by various processes like oxidation, sulphonation, chlorination, etc., and (d) chemical bonding of molecules like PEG or sulphonating agents to fabric surface. Sometimes, surface modification has to be performed by both physical and chemical methods jointly; it is called physicochemical methods. Mechanical means of surface modification involve roughening which make the surface rough or porous and micromanipulation, i.e. using AFM probes and scanning tunnelling microscopy. Biological processes of surface modification are also used in case of biomedical applications by applying four different ways (a) physical adsorption of biomolecules like peptides, proteins, ligands, etc., (b) physical adsorption along with cross-linking of these biomolecules like enzyme attachment to fabric surface, (c) chemical attachment of biomolecules to surface molecules and (d) multiplication of cells and growth to convergence (Hoffman 1996; Jaganathan 2015).

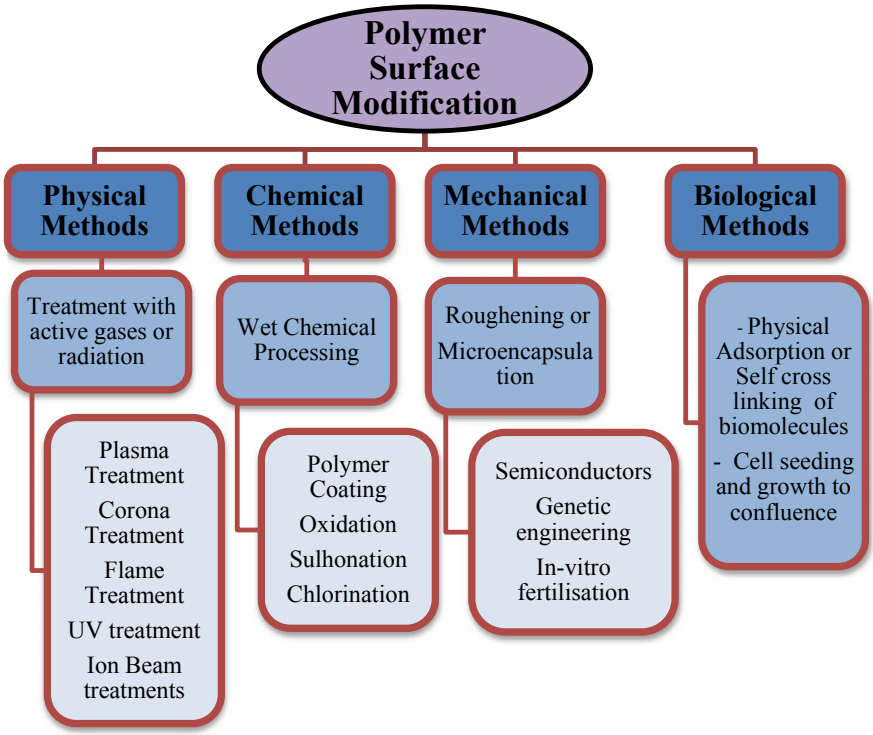

Fig. 1 Schematic representation of various surface modification methods with few examples

Wet chemical processing is the conventional technique used for surface finishing of textiles. Chemical treatments although provide a wide array of reagents to treat fabric but it requires rigorous process control and a lot of hazardous chemicals. The wastewater generated from these treatments has a deteriorative effect on the environment and along with human health as well (Gorjanc et al. 2013). Biological methods of surface treatment, though, do not generate hazardous wastes but they require a lot of time and patience to achieve optimum working conditions. Thus, among various methods of surface modification, the physical techniques offer significant precedence over all the other. The first and foremost benefit of physical processes is that they provide more precise modification of the top layer of fabric surface without affecting the bulk properties and without the need for harsh chemical roughening agents. These are relatively simpler, cost-effective and environmentally safe as compared to the others (Ozdemir et al. 1999). Physical methods of surface modification specifically atmospheric pressure plasma systems have revolutionised textile processing technology from the late 1990s. Both R&D organisations and industries have been carrying out extensive research in the fields of non-thermal plasma to enhance the surface properties of textile polymers and bring out functionalised fabrics to the market. Any type of fibre can be modified by plasma to change or enhance one or more of the following

properties like wetting, adhesion, dye absorption and dye fastness, antistatic property, desizing, water or oil repellency, biocompatibility, anti-felting and shrinkage, UV resistance and so forth (Rezaei 2016). Atmospheric pressure plasma technology is a cheap, clean and dry technology which uses less energy and generates no toxic waste; thus, it is widely favoured and accepted for fabric processing.

Nanotechnology is another revolutionary technique which is interdisciplinary and finds critical applications in all fields of science like chemistry, physics and material science. Large varieties of metals have been used to synthesise nanoparticles like gold, silver, palladium, platinum, zinc, titanium and copper. Nanoparticle application on textile materials could lead to drastic changes in the surface properties of the fabric. The silver nanoparticle has been used for imparting antimicrobial finish to fabrics. Zinc oxide nanoparticles provide UV blocking feature to fabrics, whereas nano-titania is used for imparting hydrophobicity and self-cleaning properties. Nano-based chemical finishes are also being used at the manufacturing level to enhance bonding of chemicals to fabric surface which incorporates functionalities like wrinkle resistance, hydrophilicity and stain resistance in fabrics (Nema and Jhala 2015).

2 Non-thermal Atmospheric Pressure Plasma

2.1 Plasma

The fourth state of matter, popularly known as plasma, consists of a large number of different species such as electrons, positive and negative ions, free radicals, gas atoms and molecules in the ground or any higher state (Nehra 2008). Classically, plasma can be considered as quasineutral species made of an equal number of positive and negative ions but due to long-ranged Coulomb's forces of attraction, the individual behaviour of particles is lost and the entire plasma act in a collective way. Approximately, 99% matter of the universe is made of plasma. The temperature of the natural plasma is very high, ranging from several tens to hundred thousand kelvins (Nema and Jhala 2015).

2.2 Classification of Plasma

Typically, plasma can be classified as thermal (hot) and non-thermal (cold) plasma based on temperature. In thermal plasma, all the species composing plasma are in thermal equilibrium with a temperature of the order of thousands of kelvin. Thermal plasma exists in solar corona, lightening, and hence cannot be used for treating any material. The non-thermal plasma, on the other hand, is maintained at room temperature; although, here, the smaller sized electrons are at a higher temperature, the other larger reactive species remain at room temperature. Thus, cold plasma

is most suitable for surface modification of textiles as during plasma processing of textiles minimal thermal degradation of the fabric takes place. In non-thermal plasma, continuous loss of energy takes place whether through radiation or conduction or various interactions within the plasma species, therefore, for constant processing of the sample, power has to be supplied continuously from an external source usually using an electrical discharge. These electrical discharges are provided either at low pressure in vacuum chambers or at atmospheric pressure.

Low-pressure plasma technology has been spearheaded by the microelectronics industry and material technology. Low-pressure plasma systems generally operate in vacuum conditions at a pressure between 1–100 Pa and near ambient temperature. The system is usually pumped down, and only necessary plasma gases like neon, argon, helium, nitrogen and oxygen are then pumped into the large vacuum chambers. Low-pressure plasma systems have been adopted for textile processing, but the requirement for airtight enclosures makes them highly expensive and time-consuming. Therefore, recently the focus has been on developing more accessible and easy processing techniques and hence came atmospheric pressure plasma systems (Mather 2009). The atmospheric pressure plasma are generated at high pressure of approximately 1 atm. These systems are remarkably better than low-pressure system since do not require the presence of vacuum conditions, and they also possess increased reactive chemical species with higher selectivity along with low gas temperature (Nehra 2008).

2.3 Types of the Non-thermal Atmospheric Pressure Plasma System

The economic viability and ease of operation at 1 atm pressure have led to the development of a variety of atmospheric pressure plasma sources for various scientific and industrial applications (Table 1).

The following four discharges can obtain atmospheric pressure plasma discharge.

2.3.1 Corona Discharge

Corona discharge is the most primitive type of plasma treatment. The system requirement for this kind of discharges consists of two electrodes of opposite charges and a high voltage supply. The inhomogeneous electrode arrangement is the characteristic of Corona discharge where one electrode is highly curved like a pointed needle or wire, and the other one is planar or flat. The discharge is created when current flows from the strong curvature electrode kept at a higher potential into a neutral fluid which is usually air and ionises the nearby area. Furthermore, the corona developed in high field region discharges to area of lower potential and passes to the planar electrode. Coronas can be either positive or negative depending on the polarity of

Table 1 Properties of plasma generated by different atmospheric pressure plasma setups (Nehra 2008; Nema and Jhala 2015)

Parameters	Corona discharge	APPJ	APGD	DBD
Type of electrode	Sharp pointed electrode	Two small, concentric electrodes	Capacitively coupled parallel plate electrodes	Parallel plates covered with dielectric material
Power supply	Pulsed DC	RF with low power in the range of 100–150 V	RF in MHZ range with a low voltage around 200 V	RF to microwave, AC power up to 20 kV
Breakdown voltage (kV)	10–50	0.05–0.2	0.2–0.8	5–25
Plasma density (cm^{-3})	10^9–10^{13}	10^{11}–10^{12}	10^5–10^{13}	10^{12}–10^{15}
Temperature (K)	Room	300–600	400	Average gas temp (300)
Gas	Air	Helium, Neon, Argon or other noble gas	Helium	Air or noble gases or a mixture of gases

the electrode. If the curved electrode is connected to the positive terminal of power supply, it is a positive corona, and if it is connected to the negative terminal of power supply, it is negative corona. Corona treatment has several commercial applications like water purification, photocopying machine, printers and powder coating; however, their weak and inhomogeneous nature and restricted area of application have limited their application in textile processing (Mather 2009; Nehra 2008; Nema and Jhala 2015).

2.3.2 Atmospheric Pressure Plasma Jet

Atmospheric pressure plasma jet (APPJ) is a small, torch-like, non-thermal plasma producing device which operates on radiofrequency (RF) power. It consists of a two-electrode setup where the outer cylindrical electrode is grounded, and the inner central electrode is pointed like a jet. These electrodes are supplied with a mixture of gas consisting of helium, oxygen, argon or other noble gases. On applying RF power, the plasma discharge is ignited feeding continuously on a mixture of gases and produces a high-velocity stream of chemically reactive species which on passing through the central electrode exits through its nozzle. The key features of APPJ are that it produces stable and homogenous discharge and operates without any dielectric cover on the electrodes. APPJ technology is used in a large number of applications like sterilisation of surgical and dental equipment, etching of metals and polymers, deposition of SiO_2

and TiO_2 by plasma-assisted chemical vapour deposition technique, graffiti removal, removal of paint and many more (Nehra 2008; Nema and Jhala 2015).

2.3.3 Atmospheric Pressure Glow Discharge

An atmospheric pressure glow discharge (APGD) is generated at a low voltage and very high frequency, i.e. radiofrequency across parallel plate electrode setup which is separated from each other by a few millimetres. The plasma-forming gas used is usually helium since helium has a very low breakdown voltage and longer transition time which help in extending the micro-discharge points on the insulating electrode. The APGD is beneficial for material processing due to its capability for homogenous treatment and stability of discharge, as it operates on a lower voltage than other atmospheric pressure discharges. Moreover, the electrodes are not covered by any dielectric material. The use of helium as the discharge gas limits its commercial applicability in textile processing since it is costly and difficult to recover (Mather 2009; Nema and Jhala 2015).

2.3.4 Dielectric Barrier Discharge

A dielectric barrier discharge (DBD), also called as silent discharge, is produced between two parallel electrodes where at least one of the electrodes is covered with an insulating dielectric barrier. These discharge operate at atmospheric pressure, typically in the range of 0.1–1 atm. A high AC voltage with an amplitude of the order of 1–100 kV and frequency from a few kHz to MHz (corresponding to lower RF—microwave range) is applied to the setup. A dielectric layer made of glass, quartz, ceramic or polymer material, placed between the two metal electrodes, is the characteristic of DBDs. The inter-electrode distance varies from a few mm to a few cms depending on the processing requirement (Bogaerts et al. 2002). When the DBD is powered with a high AC voltage, gases breakdown between the parallel plates in filamentary mode, i.e. the discharge is constituted by a large number of individual tiny breakdown filaments distributed uniformly over the entire dielectric layer, referred to as micro-discharges or streamers. The use of dielectric as an insulating layer has few advantages; firstly, it enables a continuous flow of current by avoiding glow to arc transition and secondly, it creates random streamers by electron accumulation on the electrode surface to ensure homogenous treatment of any surface (Nema and Jhala 2015). DBD discharge differs from a classical discharge significantly, as in classical discharge the electrodes are not covered with any dielectric layer; hence, they come in direct contact with highly activated chemical species and thus causes electrode etching and corrosion which is not the case in a DBD. Another major point of difference is that DBD cannot be operated with a DC voltage due to the presence of capacitive coupling which require an alternating current with time-lapse to drive the displacement current (Nehra 2008). The dielectric barrier discharge has become an important tool for surface modification of textiles at atmospheric pressure.

The surface modification helps in altering various properties to improve wettability, dyeability, stain removal and sterilisation. DBD techniques are the need of the hour as it is a green technology which does not generate any wastewater or harmful chemical.

2.4 Advantages of Plasma Treatment

Plasma technology for pretreatment and finishing of textiles has become an important industrial process. It offers numerous advantages:

- Gas plasma technology follows the principles of Green technology as it offers a clean, dry and zero waste alternative to conventional processes.
- Modification by plasma is highly surface-specific as they do not affect the bulk properties and only the top layer is altered.
- Non-thermal plasma is particularly useful for textile processing as most of the textile material is heat sensitive and atmospheric pressure plasma can activate surface reactions without excessive thermal degradation of the substrate.
- The modified layer formed is relatively uniform and cover the whole and large surface area.
- By using a variety of gases, different functional groups can be incorporated on the fabric surface depending on the type of functionality to be introduced on the fabric like wettability, adhesion, printability, hydrophobicity and hydrophilicity (Morent et al. 2008).

2.5 Plasma–Substrate Interaction

When a fabric is exposed with plasma, various surface reactions occur leading to change in properties of the exposed surface. The activated chemical species present in plasma discharge like electrons, ions, excited molecules, neutral atoms interact and generate other active species. Figure 2 depicts the process of substrate interaction with plasma. Reactions of gas plasma with the substrate produce four processes.

2.5.1 Cleaning and Etching

Organic contaminants such as oils and waxes are removed from the substrate surface in the presence of oxygen plasma. Energetic oxygen species react with the surface contaminants such as oligomers, antioxidants, anti-blocking agents and undergo hydrogen abstraction with free radical formation along with chain scissions until the molecular weight is significantly low to boil away in the form of water and carbon dioxide mainly during processing (Chan et al. 1996). Ultraviolet light generated in

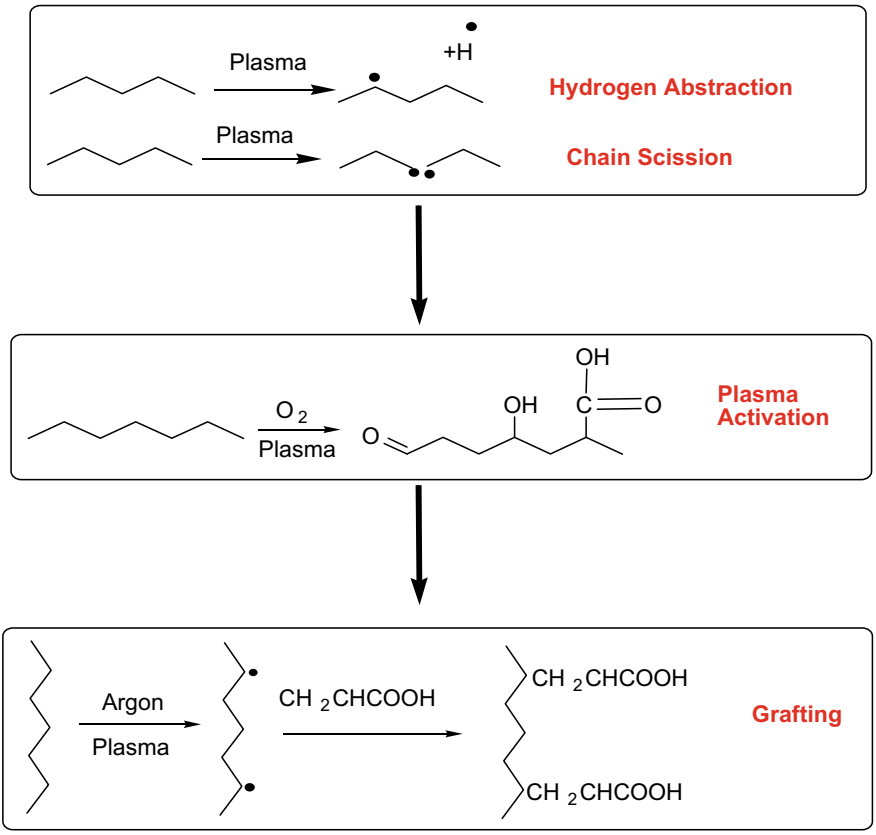

Fig. 2 Figure depicting the process of substrate interaction with plasma

the plasma also helps in breaking the bonds of silicones and other surface contaminants. Plasma etching increases the roughness of the surface on a microscopic level, thereby increasing surface area and making the material easily wettable.

2.5.2 Activation of the Surface

Post etching and cleaning of the substrate, when the material is treated with gases like oxygen, ammonia or any other gas that does not contain carbon, the reactive radicals or ions generated in plasma bind to the substrate surface. Etching primarily results in creating a surface highly active to different binding agents resulting in the incorporation of functional groups such as hydroxyl, carboxylic and amino acids. Plasma activation results in enhanced efficiency of the substrate during printing, varnishing or glueing as it may confer improved wettability, biocompatibility, adhesion and other surface properties.

2.5.3 Grafting

In the grafting process, argon is used as the plasma-forming gas, and active plasma species are created. These active species interact with the substrate surface and produce free radicals. When a monomer capable of forming covalent bonds with the free radicals is introduced into the chamber, it reacts with the active plasma species and gets grafted. Some classic examples of monomers used for grafting are acrylic acid or allyl alcohol or allylamine.

2.5.4 Deposition or Plasma Polymerization

The deposition of polymer in the form of a thin film on a plasma-activated surface via polymerisation of an organic monomer like CH_4 and CCl_4 is referred to as plasma polymerisation. A complex monomer gas is introduced in the chamber to initiate the process which is ionised by colliding plasma species. The monomer molecule thus undergoes fragmentation in smaller species like ions, free radicals, metastable and ultimately react with each other to combine or gets condensed and polymerised on the substrate. The advantage of plasma polymerisation is that it creates cross-linked polymers on the top layer with no repeat units (Nema and Jhala 2015; Sparavigna 2008).

3 Nanotechnology

The revolutionary lecture titled 'There is Plenty of Room at the Bottom', given by Nobel laureate, physicist Richard Feynman on December 29, 1959, opened a new door of experimentation to then-existing scientific methods and technologies. In that lecture, he advocated that atoms can be manipulated at the nanoscale level, but it was in 1980 that his visions were materialised into a new branch of science called nanotechnology supported by years of substantiated research efforts. Nanotechnology is a branch of science that deals with particles within the dimensions of 100 nm which can include nanoparticles, nanorods and nanotubes, nanowires, nanocages, nanocrystals, nanofiber, thin films and all the other particles which fall under the specified range (Vigneshwaran 2009). Broadly, a material can be considered as a nanomaterial if it possesses properties different from the bulk form of the same chemical constituent. The characteristics of nanoparticles which make them such a sought after materials are as follows:

- They have small size but an extensive surface area and most of the interacting atoms reside in the surface layer; thus the interparticle distance is minimal.
- They have a smaller energy band gap compared to bulk particles.
- They can have an amorphous or crystalline nature.
- Their surface is used as a carrier for liquid or gaseous agents.

- These are non-toxic due to they are nanosize, as, by a rule, toxicity decreases when particle size increases (Mishra 2014).

Further, the mechanical and thermal properties of nanomaterials depend on several features like particles size, pores and their distribution, impurity percentage, method and duration of their application, the method used for their production, pH and temperature conditions (Joshi and Bhattacharyya 2011). Nanoparticles due to their small size, large surface area and exceptional surface properties have shown great potential for a wide variety of applications may it be drug delivery, biosensors, food technology, antimicrobial coatings, quantum science, lasers or textile finishing technology (Dhand et al. 2015).

3.1 Classification of Nanoparticles

See Fig. 3.

3.1.1 Organic Nanoparticles

Liposomes, micelles and dendrimers are some of the few examples of organic nanoparticles. These nanomaterials are biodegradable and non-toxic. They are mostly either nanospheres or nanocapsules in shape and are sensitive to electrochemical and thermal degradation just like polymers. The organic nanoparticles find best applications in drug delivery and biomedical application where the required chemical is carried to its receptor without any toxic effects to the body due to their organic nature.

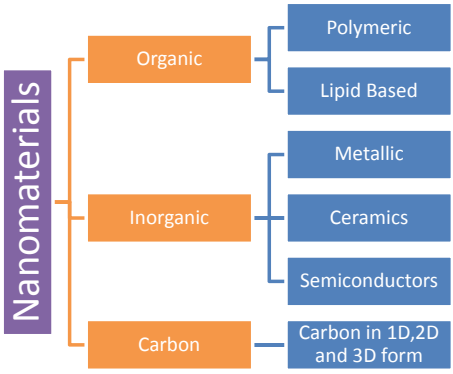

Fig. 3 Schematic classification of nanomaterials on the basis of their physical and chemical properties

3.1.2 Inorganic Nanoparticles

A. **Metal Nanoparticles**
Nanoparticles made of metal and metal oxides except carbon are considered as inorganic. A large number of metals have been used for the synthesis of nanomaterials like aluminium (Al), cadmium (Cd), cobalt (Co), copper (Cu), gold (Au), iron (Fe), lead (Pb), silver (Ag) and zinc (Zn). The well-known localised surface plasmon resonance (LSPR) characteristics provide these NPs unique optical and electrical properties. Furthermore, surface characteristics like high surface area-to-volume ratio, surface charge due to presence of metal ions, crystalline or amorphous nature and reactivity to environmental factors such as heat, light and moisture provides extensive usage of these materials in numerous applications.

B. **Ceramic Nanoparticles**
Inorganic, non-metallic, heat-resistant nanoparticles are generally called as ceramic nanoparticles because they possess properties just like macroscopic ceramics materials. They are present in amorphous, dense, polycrystalline and hollow forms and hence offer unique features like being dielectric, ferroelectric, superconductive, electro-optical and magnetoresistive to name a few. They have high utilisation in applications like catalysis, photodegradation of dye and photocatalysis.

C. **Semiconductor**
A semiconductor is a material which possesses properties of both metal and non-metals as here metals of group 2–6 are doped in the carbon backbone. This amalgam enhances the efficiency of semiconductor nanoparticles, and they show significant alternation in their properties due to wide band gaps. These particles find extensive usage in the microelectronics industry, photo-optics and electronic devices.

3.1.3 Carbon

The nanoparticles made exclusively of carbon are considered as carbon-based nanoparticles. All these are allotropes of carbon and can be divided into five categories depending on the dimensions of these particles—3-D Fullerene, 2-D Graphene, 1-D Carbon nanotubes, Carbon nanofiber and Carbon black. These particles have created noteworthy commercial hold due to their electrical conductivity and high strength. Due to their unique chemical characteristic and physical structure, they are used as nanocomposites, efficient gas adsorbents for environmental remediation, and due to their easy penetration to cell cytoplasm, they are used in drug delivery and peptide delivery (Bhatia 2016; Ealias and Saravanakumar 2017; Khan et al. 2017).

3.2 *Synthesis of Nanoparticles*

For the practical applications of nanoparticles, some conditions are required to be met like ensuring uniform and desired particle size by overcoming their immense surface energy, preventing agglomeration of particles establishing uniform morphology, chemical composition, microstructure and crystallinity (Vigneshwaran 2009).

Two primary methodologies (Fig. 4) are used for the fabrication of nanostructures which can be broadly named as **bottom-up approach** where we work by assembling atoms and molecules to synthesise nanoparticles of diverse shape and size like those used in sol–gel processing, chemical vapour deposition, laser pyrolysis, etc. and the other is **top-down approach** which involves working from bigger to smaller objects and it is extensively used in photolithography, electron beam treatment, plasma etching, etc.

The three methods of nanoparticle synthesis, i.e. Physical, Chemical and Biological (Fig. 5), work on either of the two above-mentioned methodologies. Nanoparticle synthesis by physical techniques employs the use of high energy radiation, thermal or electrical energy, mechanical pressure for material etching, melting or evaporation. These methods possess the minimum risk of contamination as they are free of any solvent system. The chemical methods of nanoparticles synthesis have the drawback of utilising toxic chemicals and the generation of harmful and non-biodegradable by-products. Biological methods of nanostructures follow the principle of green chemistry; hence, they are the demand of current time. They are environmentally safe, clean, non-hazardous, and cost- and energy-efficient. Microorganisms like bacteria, fungi and algae can survive in severe conditions such as the high temperature of the solvent bath and high concentration of metal ions. Plant-mediated synthesis incorporates medicinal values of these plant in synthesised structures which are being used in enhancing antibacterial properties of various materials like textiles, polymers, medical devices, etc. (Dhand et al. 2015; Shamim 2018).

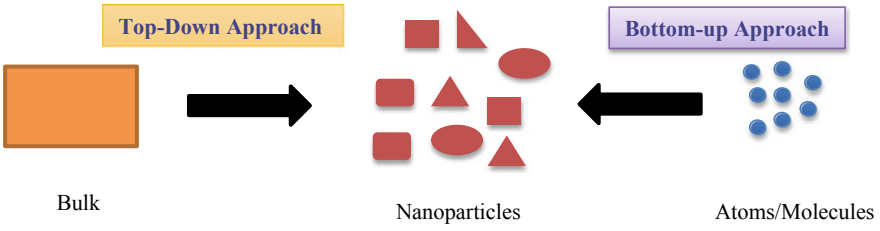

Fig. 4 Schematic representation of top-down and bottom-up approaches of nanostructure synthesis

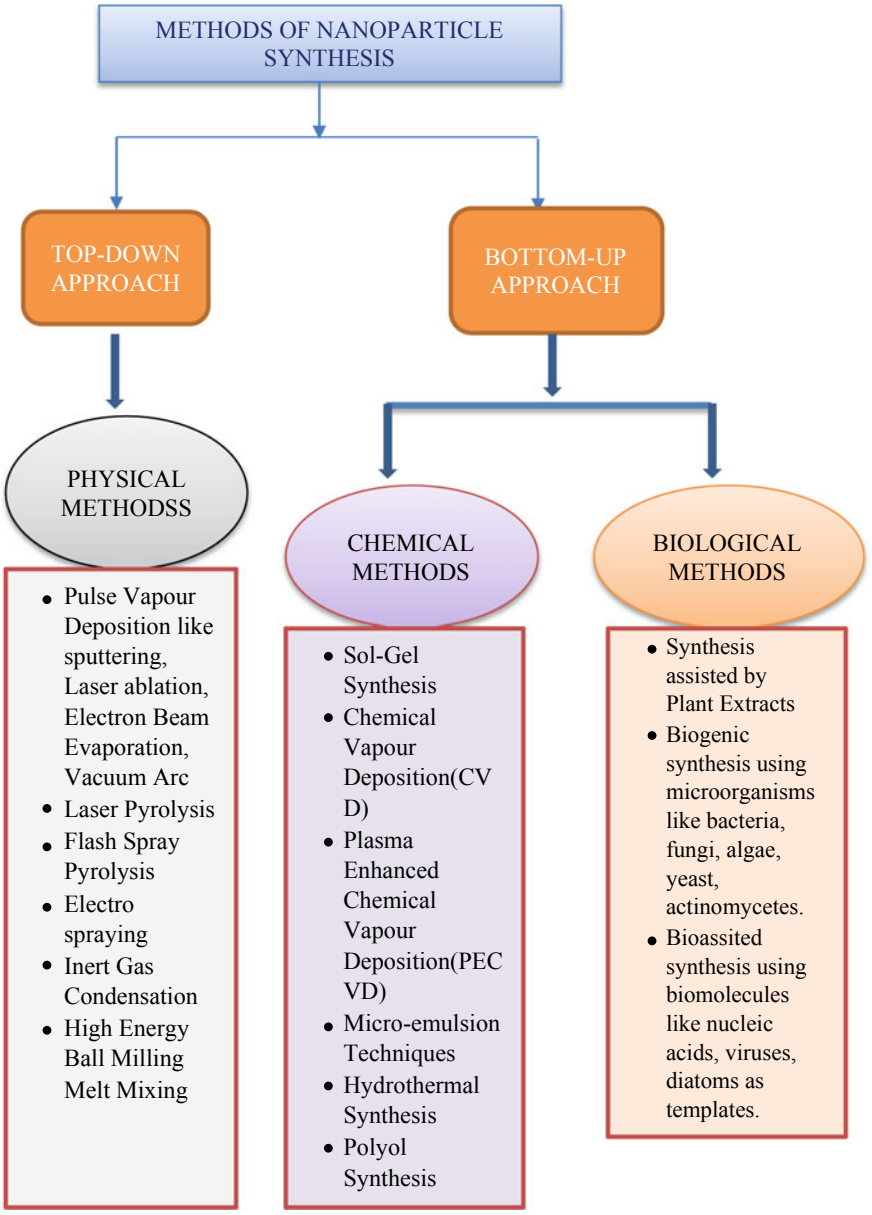

Fig. 5 Flowchart depicting an overview of different methods of nanoparticle synthesis

3.3 *Application of Nanoparticles in Textile Surface Modification*

Nanoparticles have multifaceted applications in the textile industry (Fig. 6) whether they may be used as nanosols or nanoemulsions or directly sprayed on the substrate. Nanoparticles enhance textile finishing making it more even, exhaustive and precise. They have favourably removed the micron-sized particles used for finishing to produce high performance or functional textiles since they have a larger surface area, thereby more efficiency than larger sized particles. Nano-functionality modifies clothes at nano-level making them stain and dirt resistant, thus saving time and money for laundering. Nanofinishes allow excellent breathability and flow which reduces the chances of allergies and dermatitis in sensitive skin people. The microscopic protective clothing on textiles as a result of nanofinishing provides the fabric with various characteristics like heat-resistant, antibacterial, oil-water resistant, wrinkle resistance, UV protection and improvement in dyeability. They do not affect the colour and brightness of the fabric. Nano-processed fabrics are ecologically safe, garments stay bright and fresh and are more durable than non-processed fabrics. Nanotechnology is being used exhaustively to varied disciplines, industries and materials along with fashion and textiles to bring imaginative, exciting and novel properties to

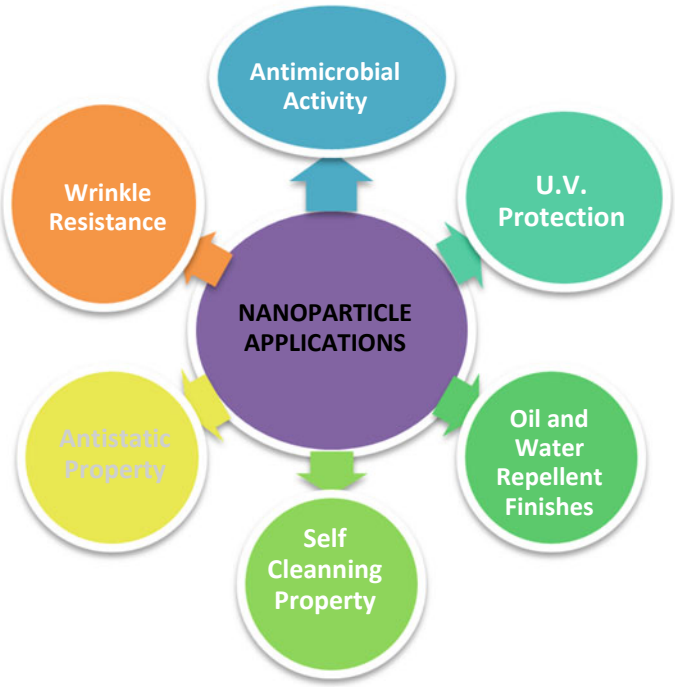

Fig. 6 Some areas where nanoparticles are being used for textiles surface modification

fabrics. Innovation in nano-processing has led to the development of materials which range from scent producing, colour changing and lightweight bulletproof materials to textiles with displays (Joshi and Bhattacharyya 2011; Mishra 2014; Rezaei 2016).

With an overview of widespread applications of nanoparticles in the field of surface modification of materials, it is vital to understand the mechanism of adhesion of these particles on the substrate. The attachment of nanostructures onto the substrate can be physical or chemical. The physical adhesion occurs mostly due to van der Waals forces or electrostatic forces of attraction between interacting particles while the chemical adhesion of particles is an outcome of ionic, covalent, metallic and hydrogen bonds. Apart from physical and chemical adhesion, nanoparticles also get attached due to mechanical interlocking with the substrate surface wherein they penetrate deep into certain parts of the substrate like pores, hole or crevices formed as a result of surface etching or surface roughness effects. The first consequence of plasma or corona treatment of the fabric is etching or surface cleaning which leads to an increase in surface roughness and ultimately leads to improved adhesion of nanostructures on the fabric surface (Gorjanc et al. 2013).

4 Recent Studies on Modification of Textiles by Plasma and Nanoparticles

In recent times, the use of plasma technology for physicochemical surface modification of textiles has become a fascinating and efficient technique for enhancement or replacement of conventional wet chemical processing. This approach furnishes a unique opportunity to modify the surface properties without interfering with the bulk material to suit the particular end use. With the low cost of operation, rapid processing and high efficiency, it is an environmentally friendly technique which is aimed at saving energy and water consumption by textile industries.

4.1 Antimicrobial Finish

Demand for antimicrobial textiles has been on an upsurge in recent years due to public awareness of potential threats and infections (Gorjanc et al. 2010). Generation of antimicrobial textiles is a necessity for health and hygiene industry along with prominent importance to sports, military, bedding, childcare and underclothes. Medical textiles such as surgical masks, caps, gowns and bio-implants all need to possess high antimicrobial efficiency and biodegradability. To render a fabric antimicrobial, a lot of chemical approaches are used like the use of chemicals like N-halamine, quaternary ammonium salts, nanoparticles of zinc and silver, chitosan nanocomposites and coating with chemicals to provide oil-repellent finishes (Ilić et al. 2009; Primc 2016). In particular, silver in its ground state (as AgNPs) shows strong bactericidal effects

and strong antimicrobial effects in its ionic state (Ag^+) (Deng et al. 2015). Zinc oxide (ZnO) nanoparticles possess excellent photocatalytic activity, superior UV blocking capacity, as well as antifungal and antibacterial properties (Rezaei 2016). ZnO is an inexpensive and abundant material. The use of nanoparticles has been done extensively to enhance the antimicrobial activity of textile materials as their size is similar to that of most biological molecules. Therefore, they can easily penetrate the organic matrix and can be used for in vivo and in vitro medical research. Metallic oxides or metals in ionic states are toxic to bacteria even at low concentrations. The various mechanisms responsible for the action have been proposed. Binding to intracellular proteins and inactivating the bacteria or damage to microbial cell wall due to reactive oxygen species are some of the reported effects of metal nanoparticles (Shahidi 2018). However, their immobilisation on textile material is a challenge which can be overcome by pretreatment of fabric by plasma, and many studies have reported favourable results (Airoudj et al. 2014).

Cellulose is the most prevalent natural biopolymer on this planet, assimilating many important properties like bioavailability, biodegradability and biocompatibility. Cotton is the natural fibre which is composed of 95% cellulose. It is the primary source of sustainable clothing material with the highest demand due to being comfortable to wear and easy to maintain. Natural cellulose materials are easily attacked by microbes like bacteria and fungi due to their moisture-retaining ability and presence of organic materials in their skeletal framework (Gorjanc et al. 2010).

Gorjanc et al. studied the effect of plasma treatment on the adhesion of silver nanoparticles on cotton fabric and antimicrobial effect of silver nanoparticles on plasma-treated and plasma-untreated fabrics against *E. coli* and *P. aeruginosa* bacteria. They treated cotton fabric in CF_4 gas created in an RF plasma system for 10 s. SEM images showed that untreated cotton had a smoother surface, whereas the plasma-treated surface appeared non-structured due to etching by F and O radicals which led to a dramatic increase in surface roughness and hence to higher adsorption of silver nanoparticles. Plasma treatment effect could sustain up to ten washing cycles as the quantity of silver on plasma-treated and washed samples did not show much variation in the tests. The antimicrobial efficacy of silver nanoparticles was also proved with reasonable reduction of more than 77 and 68% in *P. aeruginosa* and *E. coli,* respectively, in plasma-treated and silver nanoparticle-loaded samples (Gorjanc et al. 2010, 2013). Shahidi and Ghoranneviss deposited a nanolayer of silver ions on cotton fabric using a DC magnetron sputtering system. A silver anode and cathode were used, and samples placed on anode were sputtered with metal particles on both sides. The cotton fabric kept on anode were functionalised with low-pressure plasma for different exposure times (10, 150, 300 s) and different gas pressures (0.002, 0.05, 0.08 Torr) divided into nine runs with a combination of treatment time and gas pressure. The changes in surface topology with rough and etched surface and deposited silver nanoparticles are visible in SEM images plasma-treated cotton samples. The highest amount of deposited silver was 1.018% for run 6 which was at 0.05 Torr gas pressure and 300 s of treatment time which reduced to 0.998% after ten washing cycles. This shows that the durability of silver ions is maintained even after repeated laundering. The bacterial counting test showed a 100% reduction of bacteria, *E. coli*

and *S. aureus*, from 300 s treatment but just 10 s treatment gave 96 and 98% bacterial reduction for the bacteria, respectively, and that results were maintained even after ten cycles of washing (Shahidi and Ghoranneviss 2016).

Grafting of textiles has also been used to achieve surface modification for enhancing the antimicrobial efficiency of the fabric. Airoudj et al. reported a solvent-free, dry-plasma polymerisation method for firmly anchoring silver nanoparticles on cotton fabrics to achieve antibacterial property. Plasma polymer functionalised cotton was obtained by coating a thin film of maleic anhydride powdered vapours along with air plasma onto the fabric for 2, 8 and 30 min time interval. The anhydride groups were then hydrolysed into carboxylic acids by dipping the fabrics in water. These charged acidic groups were meant to help in better adhesion of silver ions through electrostatic interactions. Then, the maleic acid-plasma polymerised substrate was dipped in an aqueous solution of silver ions which reduced and coalesced into nanoparticles in an $NaBH_4$ solution. The formation and adhesion of nanoparticles were confirmed by TEM images which showed uniformly distributed spherical-shaped nanoparticles with an average size of 8 nm. The loading of silver ions was also confirmed by surface plasmon resonance (SPR) band of AgNPs in the UV–Vis region with a maximum at 415 nm. The UV–Visible absorbance spectra depicted a decrease in optical density by varying the plasma duty cycle with maximum intensity for 2 min treatment and minimum for 30 min. Antibacterial activity of treated samples which was evaluated by two methods, i.e. agar-plate and epifluorescence studies, both reported no or less growth of bacteria in AgNPs and plasma polymerised samples. The bactericidal effect was explained as a consequence of the leaching of antibacterial silver ions from the attached nanoparticles into the plasma polymerised samples. The durability of silver ions on the plasma polymerised sample was checked by subjecting them to three washing cycles in a hot water bath. The results depicted no change in colour (yellow due to the presence of silver ions) of the samples along with no change in UV–Vis absorbance spectra indicating that silver particles are quite strongly linked to the fabric (Airoudj et al. 2014). In another study (Haji et al. 2013), researches enhanced the antimicrobial activity of cotton fabric by using radiofrequency (13.56 MHz) low-pressure oxygen plasma pretreatment for 5 min along with grafting of acrylic acid monomer to activate the surface for better attachment of silver particles on the substrate. The activated cotton fabric samples were immersed in $AgNO_3$ solution and after that in $NaBH_4$ solution to reduce the adsorbed Ag^+ ions into $Ag^{\cdot}$ radicals. A colour change in the fabric from white to brownish yellow indicated synthesis and attachment of silver nanoparticles which was also confirmed by SEM analysis as the plasma polymerised and AgNP-loaded surface appeared rough and etched as compared to untreated. Cotton fabric surface consists of an overall negative charge due to the presence of carboxyl and hydroxyl group in the polymer chain. Pretreatment with oxygen plasma and acrylic acid helped in enhancing the negative charge along with increasing the roughness of the surface by plasma etching. The silver ions carrying a positive charge (Ag^+) get incorporated to the surface due to strong electrostatic interactions and gets strongly bonded to the active sites created as a result of plasma etching and acrylic acid grafting. The absorbed silver ions were converted to silver atoms and coalesce to generate nanoparticles in the presence of reducing

agent $NaBH_4$. The proposed mechanism of silver ion adsorption and reduction to nanoparticles is as follows:

$$\begin{aligned} \text{Cotton - } XH &\longrightarrow \text{Cotton - } X^- \quad (\text{XH} = \text{OH, COOH}) \\ \text{Cotton - } X^- + \text{Ag}^+ &\longrightarrow \text{Cotton - } X^-\text{Ag}^+ \\ \text{Cotton - } X^-\left(\text{nAg}^+\right) + \text{NaBH}_4 &\longrightarrow \text{Cotton - } X(\text{Ag})_\text{n} \end{aligned}$$

The acrylic acid grafted and silver ion-loaded samples gave an active zone of inhibition against test organisms *E. coli* and *S. aureus* as compared to untreated samples indicating better loading efficiency as a result of plasma treatment. The same plasma setup was used by researchers to enhance the antimicrobial activity of acrylic acid grafted wool fibre using silver nanoparticles and Berberine natural dye as two different kinds of antibacterial agents. From the SEM images, it was clearly evident of nanosilver loading on the fabric surface which was attributed due to increased surface roughness after plasma treatment, the formation of active surface groups and removal of surface lipids layers. Compared to untreated fabrics, Berberine dyed plasma pretreated samples showed better dye absorption and good fastness to light, washing and rubbing along with an excellent antibacterial activity to *E. coli* and *S. aureus* bacteria. Berberine which is an N containing quaternary ammonium compound causes bacterial lysis by destroying the negatively charged cell membrane with denaturing of protein and ultimately disrupting cell structure. In order to replace metal mordant like alum due to toxic nature, the plasma pretreated samples were grafted with β-cyclodextrin prior to dyeing with Berberine. The said samples showed an increase in weight gain due to increased dye attachment along with 99.9% bacterial reduction as compared to untreated dyed sample (48.1%) (Haji 2015).

Shahidi et al. studied the enhancement of antimicrobial characteristic in cotton fabric by functionalizing it first with plasma and then with ZnO nanoparticles. Pre functionalisation of the material was done using low-pressure DC magnetron plasma sputtering device using air for 5 min. ZnO nanoparticles were then *in situ* synthesised by sonochemical method at room temperature on both untreated and plasma-treated fabrics. FESEM analysis of the samples reported the presence of spherical nanoparticles within the size range of 20–90 nm along with the generation of porous and rough areas on the plasma-treated surface which is supposed to enhance the absorption of solvents like ZnO nanoparticles and increase hydrophilicity. XRD analysis of the treated samples also confirmed the presence of nanoparticles by giving peaks corresponding to the spherical type of ZnO. The FTIR study of the samples also showed an overlap of –OH and –NH functional groups in the region of 3400 cm^{-1} which arise due to the reaction between the active plasma species and fabric surface atoms. The antibacterial studies performed using colony count method concluded that the untreated fabric does not have any antibacterial properties, whereas the ZnO plasma-treated samples demonstrated strong antibacterial efficiency. The difference in the bactericidal property was explained to be due to the chemical interactions between peroxide radicals of air plasma and membrane proteins as well as the lipid bilayer

of bacteria which ultimately lead to breaking of membrane and killing of the organism. The percentage reduction of bacteria for plasma-treated and ZnO nanoparticle deposited cotton fabric was 100% compared to untreated and ZnO nanoparticle-coated samples, and antimicrobial property sustained even after 30 washing cycles with no visible growth of bacteria (Shahidi 2018).

There has been a rigorous attempt in the field of textile engineering to improve the characteristics of synthetic fibres to imitate natural ones. Synthetic fabrics although have various advantages like low prices, more strength and elasticity but they lack basic properties essential for a clothing application like hydrophilicity, dye adhesion and capillary action. Plasma treatment thus is used to modify the surface of the fibres and keeping bulk properties intact. Although low-pressure RF plasma sources provide greater stability and uniformity, they are much difficult to handle than corona discharges and dielectric barrier discharges due to complex handling of vacuum systems (Ilić et al. 2009; Radetić et al. 2008; Rezaei 2016).

A study was carried out by Rezaei et al. to optimise the percent nano-adhesion of ZnO nanoparticles on nylon fabric after corona treatment to improve antibacterial resistance and dyeing properties. It was easily illustrated from the results that wettability of the fabric increased with increasing the power and numbers of passages which can be attributed to an increase in surface area of the sample along with imbibing various hydrophilic functional groups like COOH or OH. The SEM investigation showed corona treatment helped in etching the surface as well as creating holes which makes any particles to adhere to the surface easily like dyes or nanoparticles. Corona pretreated fabric when imbued with nano-zinc filled the empty holes and stuck to the surface. The antibacterial results showed a 96% reduction for *S. aureus* and 100% reduction for *E. coli* (Rezaei 2016).

Radetic et al. studied the possibility of using a corona treatment on polyamide and polyester fabrics to facilitate the loading of silver nanoparticles on the activated surface. Despite wide applications of these synthetic fabrics like polyester (PES) and polyamide (PA), their hydrophobic nature and low surface energy act as a barrier between the surface and different coatings. However, corona treatment and plasma treatment can act as a means of overcoming this difficulty due to enabling oxidation of fibre surface and formation of new functional groups like COOH or OH. The hydrophilicity induced by corona treatment gave a sharp decrease in the contact angle of a water droplet from 86° to 56° for polyester, while a small decrease was observed in polyamide fabric from 83° to 76°. SEM studies also showed that corona treatment roughened the surface with an increased and uniform surface area. Corona induced morphological changes in the form of fibre etching as a consequence of the severe bombardment of ions and energetic particles. SEM analysis clearly indicated a remarkable increase in number and uniformity of attached colloidal AgNPs on untreated and silver-loaded fabrics. The increase in hydrophilicity, as well as chemical and physical changes on the fabric surface, influences the binding ability of water-based colloidal silver nanoparticles. The XPS spectra also showed a considerable increase in O/C ration. C18 spectra result clearly indicated a significant increase in the content of C = O and O–C = O groups on PES surface, whereas the C–N and C–O groups were almost doubled in PA fabric with a visible decrease in

C–C and C–H groups confirming the chain scission induced by plasma particles and further oxidation of the carboxylate groups. Corona treatment leads to an increasing amount of silver on PES and PA fabric although PES fabric contained higher amount due to more number of carboxyl groups and benzene ring in their skeleton confirmed by surface-enhanced Raman spectroscopy of the strong interaction between AgNPs and benzene ring. The bacterial reduction test showed maximum reduction by silver-loaded polyamide fabric with 99% reduction than polyester for both the bacteria, i.e. *S. aureus* and *E. coli*. Improved antibacterial resistance can be attributed to enhanced surface roughness and hydrophilicity which made silver nanoparticles to easily adhere to the fabric and in turn to bacteria to finally degrade them. The antibacterial effect was almost not altered after washing in both the silver-loaded fabrics indicating outstanding laundering durability (Radetić et al. 2008). Radetic and Ilic also studied the antifungal effect on silver-coated, dyed and undyed corona-treated fabrics against a most common fungus responsible for itching skin infections, i.e. *Candida albicans* using disperse dyes. Antifungal tests showed more percent fungal reduction in corona-treated PA fabric but after 5 washing the % reduction was more in PES fabric which is in the direct effect of higher adsorption of silver nanoparticles. The fungal reduction of dyed untreated and corona-treated PES fabric loaded with AgNPs was more than in undyed samples which could be due to the presence of amino groups in the dye structure which is known to obstruct the fungal growth by cell membrane lysis (Ilić et al. 2009).

Deng et al. studied a novel method for incorporating silver nanoparticles on nonwoven polyethylene terephthalate (PET) fabric for preparation of antibacterial textiles by double-layer plasma deposition of silicon films. A plasma jet generated in a mixture of N_2 and O_2 gas along with tetradimethyldisiloxane (TMDSO) as the organosilicon precursor was used for deposition (Fig. 7).

The nanosilver PET fabrics were prepared in a three-step procedure: First by depositing a layer of an organosilicon thin film called a reservation layer, using atmospheric pressure plasma system, then immersing the fabric in AgNPs and finally coating the second layer of organosilicon to act as a barrier layer to prevent removal of attached nanoparticles (Fig. 8).

The nanoparticles were coated at four different concentrations, i.e. 1, 2, 5 and 10 mg/ml. The SEM images depicted a smooth and uniformly incorporated AgNPs on the PET surface. All sliver-treated fabrics showed activity against the chosen microbes but the fabric treated with 5 mg/ml sample showed maximum bacterial reduction with reduction rates corresponding to 99 and 100% for *S. aureus* and *E. coli*. The Gram-positive bacterium, *S. aureus,* consists of peptidoglycan in the cell

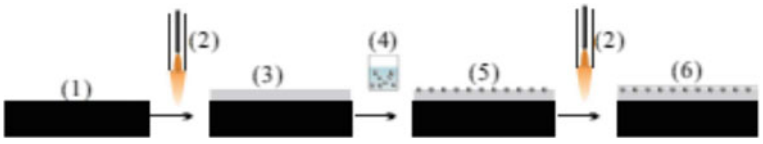

Fig. 7 Diagrammatic representation of surface modification of the substrate (Deng et al. 2015)

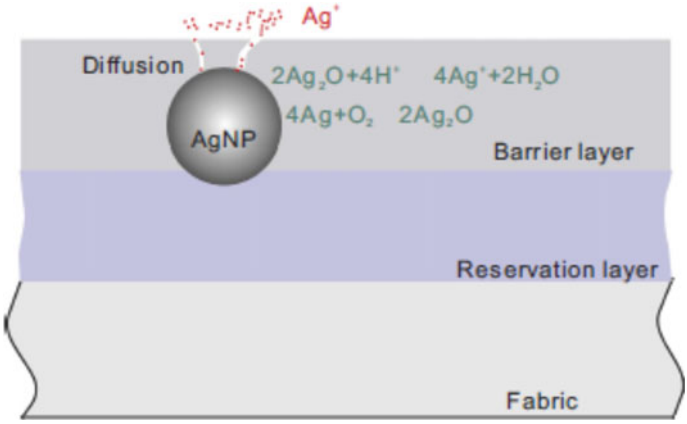

Fig. 8 Schematic representation of silver ions generation and diffusion from the barrier layer to liquid medium (Deng et al. 2015)

wall which provides them higher cell protection against penetration of antibiotics in their cytoplasm since it is much thicker than Gram-negative bacteria, *E. coli* (Deng et al. 2014, 2015). They also studied the antifungal and antibacterial effect of organosilicon plasma deposition on PET fabric against common pathogenic bacteria like *P. aeruginosa*, *S. aureus* and a fungus *C. albicans* causing serious skin infections. Both the bacteria are resistant to a great number of antimicrobial agents and are the most common source of infection in hospitalised patients. The XPS and SEM results demonstrated equal concentrations of elements on both the top and bottom surfaces indicating plasma penetrated into the structure of the fabric and both the sides can be treated simultaneously. The antimicrobial tests revealed that sample with 10 nm barrier layer showed more microbial reduction (90% in case of *S. aureus* and *C. albicans* and 80% in the case of *P. aeruginosa*) than those with 50 nm layer. The washing fastness also revealed that silver concentration showed greater fluctuations in samples without barrier layer, whereas the samples coated with barrier layer have almost negligible fluctuations for all washing cycles. The results were thus explained as the barrier layer led to effective immobilisation of silver in the matrix along with stability which sustained even after 10 washing (Deng et al. 2015). Kumar et al. modified the surface of polyethylene terephthalate by grafting plasma polymerised acrylic acid monomer to study the antibacterial activity of fabric with silver nanoparticles. The qualitative and quantitative results depicted a strong bacterial reduction (more than 99%) against *E. coli* and *S. aureus* by plasma-modified fabric compared to untreated one (Kumar 2013).

4.2 UV Treatment

With the growing environmental concern for the degradation of the ozone layer and global warming, awareness has been created for protection against harmful UV rays, one of the most prominent risk factors for the development of skin cancer. Fabrics are the easiest and convenient UV protection source, but they do not completely block the harmful UV rays. To determine the UV protection strength of the fabric, UV protection factor (UPF) is commonly used. UPF allows an evaluation of UV protection provided by textiles concerning the spectral composition of sunlight and human skin sensitivities. The higher the value of UPF, the more is the UV blocking capacity of the fabric. According to ASTM standards, range of UPF rating given to fabrics is as follows (Shahidi and Ghoranneviss 2016):

UPF rating	Protection quality	%UV radiation blocked
15–24	Good UV protection	93–95
25–39	Very good UV protection	96–97
40–50+	Excellent UV protection	97.5–98+

The UPF values of textiles can be increased by treating them with metal nanoparticles like ZnO; however, excessive use of nanoparticles can lead to ecological problems as they are easily washed off and contaminate the water bodies. Physical adhesion of nanoparticles to the fabric surface can be enhanced by pretreatment of fabric with plasma (Gorjanc et al. 2014) (Fig. 9).

Shahidi and Ghoranneviss deposited nanolayer of silver on cotton fabric using a DC magnetron sputter device. They studied the UV blocking capacity of the treated and untreated fabrics using UV transmittance study and UPF estimation. The UV

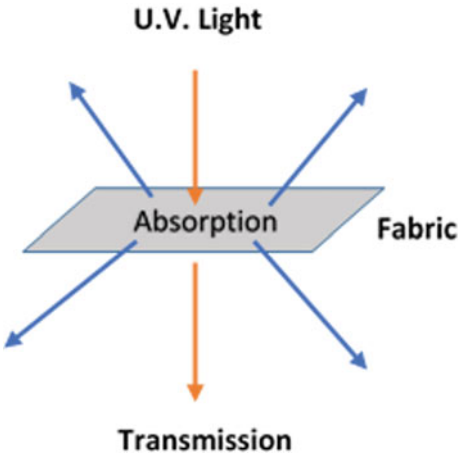

Fig. 9 Schematic representation of UV light affecting the fabric

transmittance of plasma-treated and silver-sputtered fabrics increased gradually from less than 4% in the UV-B region for run 1 and grew to a minimum of 0.2% for a run 6 compared to 7–10% transmittance of untreated samples indicating that the resistance of an untreated fabric to UV rays was weak. UPF values increased to 264.34 for the silver-sputtered cotton fabric in run 6 that was 300 s and 0.005 gas pressure compared to 11.71 of untreated. These results indicate that untreated cotton had a high UV transmittance and low UPF, while the sputtered fabrics had a high UPF and low UV transmittance which increased with plasma treatment time. These results present plasma and nanoparticles as a promising technology for developing UV protection textiles (Shahidi and Ghoranneviss 2016). In one of the studies, scientists treated cotton samples in low-pressure inductively coupled radiofrequency plasma system for 10, 20 and 30 s to increase their adsorptive properties. Plasma-treated samples were functionalised with 3% ZnO nanoparticles for enhancing UV protection properties of the fabric. The XPS survey spectra depicted a higher O/C ratio along with increased C–O bonds and decreased C–C bonds due to the incorporation of oxygen-containing functional groups on the cellulosic surface. SEM images also clearly showed the increasing percentage of ZnO nanoparticles on the plasma-treated surface with even distribution and no agglomerates after more prolonged plasma treatment. Zinc oxide nanoparticles functionalised cotton fabric showed excellent UV protection with a UPF value of 33.63, but it increased twofold in case of 30 s plasma-treated sample which proved that more prolonged plasma treatment increased the content of ZnO nanoparticles on the fibres. The durability of plasma and nanoparticle treatment was assessed in 10 washing cycles. After one wash, UPF value were not changed extensively, but after ten wash there was a significant decrease in UPF values although the values remained highest for 30 s plasma-treated samples (Jazbec et al. 2015). CF_4 plasma has also been used to increase the adhesion of ZnO nanoparticles and in turn, generate good UV protective properties on cotton fabrics. Gorjanc et al. treated cotton fabrics in weakly ionised gaseous plasma created in a mixture of CF_4 and H_2O gas with an electrodeless RF discharge for a treatment time of 10, 20 and 30 s. The researchers claimed that although CF_4 gas is typically associated with hydrophobicity when used in combination with oxygen it increases the polymer etch rates. To confirm the hypothesis that treatment with moist CF_4 plasma gives better etch results, a series of characterisation studies were carried out. Optical emission spectroscopy (OES) study reveals that the intensity of CO molecular bands was much lower for CF_4 plasma-treated sample compared to H_2O plasma-treated sample indicating that better etching and oxidation was achieved in the earlier plasma gas. SEM images showed a smooth exterior of untreated fibrils compared to rough topography of 30 s plasma-treated cotton fibres. SEM images of H_2O plasma-treated sample also showed morphological changes but the etching effect was less pronounced than CF_4 plasma-treated fibres. The XPS spectra of 30 s plasma-treated sample detected the measurable amount of F along with a decreased O/C ratio, whereas all the other samples were free of it suggesting of its hydrophobic nature. Wettability and absorptivity measurements performed on untreated and CF_4 plasma-treated cotton samples also backed the XPS results as the 30 s CF_4 plasma-treated samples displayed hydrophobic character with

zero capillary rise of water and 186 s of wet-out time compared to 61 mm capillary rise and 0 s wet-out time of 10 s plasma-treated samples. To analyse the effect of ZnO adhesion on fabric after plasma treatment SEM, UPF and ICP-M analyses were carried out. SEM analyses indicated that difference in zinc nanoparticles distribution. Untreated samples had unevenly distributed nanoparticles where the 10 s plasma-treated samples were covered with a larger quantity of non-agglomerated nanoparticles which was just opposite to 30 s plasma-treated sample as unevenly agglomerated nanoparticles were present on the fibre surface. The UPF results and ICP-MS analyses authenticated SEM analysis. The sample that was treated for 10 s CF_4 plasma contained the highest quantity of Zn with highest UPF value (58.89), whereas the untreated fabric had the lowest amount of zinc and minimum UPF value (33.63). The amount of zinc and UPF values of H_2O plasma-treated samples were lower than 10 and 20 s CF_4 plasma-treated samples. These results clearly prove that plasma treatment increases the adsorption of ZnO nanoparticles on cotton but only up to 10 s treatment time. Smaller nanoparticles offer more protection against harmful UV radiation than larger particles; hence, although increased surface roughness of 30 s plasma-treated samples had enhanced nanoparticles adhesion but still had the lowest UPF value as the particles were agglomerated. The whiteness index of cotton was enhanced after ZnO binding but decreased by long exposure to plasma treatment even after ZnO nanoparticle functionalisation. The wash fastness of ZnO functionalised samples was not at par as the UPF values decreased dramatically after washing but since no binders were used to stabilise nanoparticles upon the surface the obtained results were expected (Gorjanc et al. 2014).

4.3 Self-cleaning

Self-cleaning has been observed in plants like lotus as an important property. SEM images of lotus leaf surface have shown a number of micro- to nanostructures which do not allow particles to adhere and roll off water droplets from the surface picking long dust particles to keep the leaf surface clean and dry even in swampy areas. The technical expression of this basic idea has been patented by the trade name Lotus effect® for such type of superhydrophobic self-cleaning products (Vigneshwaran 2009).

Application of crystalline TiO_2 as photocatalyst has increased tremendously over the period of time due to the large surface area and better diffusibility of nanoparticles than macro-sized one. Commercially, nano-TiO_2 find widespread applicability in water purification, air purification, disinfection but their usage in the textile surface modification is still in early stages. With plasma pretreatment, a variety of negatively charged functional groups like C–O, C = O, –COH, –COOH were introduced on the fabric surface by the reaction between active O species of air and plasma-activated carbon functional groups of textiles which helped in better bondability of Ti^{+4} ion of TiO_2. To develop the self-cleaning functionality of fabrics, Bozzi et al. activated cotton, polyester, wool–polyamide with radiofrequency (RF) plasma (13.6 MHz,

100 W) and microwave (MW) plasma (2450 MHz, 600 W). Post-plasma treatment 100 °C temperature was sufficient to attach TiO_2 to the fabric in contrast to the conventional high temperature of 500 °C used for coating of glass and silica. The degradation of organic stains like coffee, wine or grease on textiles activated by plasma and TTIP or $TiCl_4$ colloidal TiO_2 was accompanied with the release of CO_2. In case of cotton, a 60 min RF plasma-treated bleached cotton showed the maximum CO_2 evolution (2000 μl) and a mercerised cotton showed the maximum amount of CO_2 for just 15 s MW plasma treatment for wine stain after 24 h suntest light irradiation. MW plasma treatment was accompanied by heat so it increased the contact between cotton tissue and TiO_2 nanoparticle surface, thus increasing dispersion rate on the fabric with little treatment time. No CO_2 was observed in any of the fabric in the absence of TiO_2 or absence of any stain. In case of pretreated polyester and wool–polyamide samples, self-cleaning action was enhanced in 30 min RF plasma-treated sample coated with colloidal TiO_2 as a basic layer followed by another coating of Degussa P-25 nanoparticles. The action of nanoparticles was clearly visible with partial discolouration induced by light and a generous amount of CO_2 gas evolved. A TiO_2 coating with 150–220 nm thickens was observed in TEM micrograph for cotton samples and 20–25 nm for synthetic fabric. XRD spectra showed peaks for rutile form of TiO_2 nanoparticle along with some amorphous TiO_2. The mechanism of self-cleaning was explained by a photochemical reaction where coffee or wine pigments would inject an electron in TiO_2 conduction band to generate highly active O– radicals (Airoudj et al. 2014), or the excited pigment will react with photo-induced holes which will react with carboxylic acids through Kolbe-type reaction to generate CO_2 (Bhatia 2016). The active O– species further generate oxidative radicals like $HO_2^{\cdot}$–, $OH^{\cdot}$, $RO^{\cdot}$, $RO_2^{\cdot}$ which will eventually degrade the textile stains (Bozzi et al. 2005).

$$e_{cb}^{-} + O_2 \longrightarrow O_2^{-} \tag{1}$$

$$RCOO^{-} + h_{vb^+} \longrightarrow R^{\bullet} + CO_2 \tag{2}$$

4.4 Dye Adsorption Enhancement

Plasma treatment has been highly successful in etching the hydrophobic layer in natural polymers. Etching of the surface improves dye and fibre interaction thereby more dye particles get attached to the treated substrate and penetrate into the bulk. Plasma pretreatment of any textile thus is effective in enhancing dyeing rate, dye bath exhaustion and provide more homogenised dyeing (Morent et al. 2008). Rezaei et al. showed that corona treatment was helpful in increasing the attachment of nano-zinc on nylon fabric surface which was visible with SEM studies. The pretreated sample was dyed with acidic dye. The K/S results demonstrated that with increasing

Table 2 K/S values of untreated and plasma-treated dyed samples (UT—untreated, PT—plasma-treated, US—untreated and silver-loaded samples, PS—plasma-treated silver-loaded sample)

Sample	K/S	λ_{max}
UT	0.8573	550
PT	0.8292	550
US	0.0762	360
PS	0.1528	360

power and treatment time, dye absorption decreases due to increase in nanoparticle adsorption As corona method enhanced porosity of the fabric the number of adhered nanoparticles increased and thus decreased the adsorption of dye particles due to less free space which was clearly visible from K/S values with maximum value of the untreated dyed sample without nanoparticle. The reflectance values in UV range showed that with increasing power and time the reflectance values increased which can be used to interpret that due to nano-ZnO ability to absorb high energy beans in UV region means that with nano-treatment UV blocking fabric can be produced (Rezaei 2016).

Gorjanc et al. studied the difference in dye adsorption using a reactive dye Cibacron Deep Red S-B. The K/S values of untreated and plasma-treated dyed fabrics did not show much difference, whereas the K/S values of CF_4 plasma processed and silver nanoparticle-loaded samples increased by 50% compared to untreated silver-loaded samples (Table 2) (Gorjanc et al. 2013).

4.5 Mechanical Strength

Low-pressure radiofrequency oxygen plasma discharge was applied on ZnO nanoparticle functionalised cotton fabric to check the mechanical strength of the samples. The breaking strength and breaking elongation analysis explained that the untreated sample had the lowest value of breaking strength and elongation, while the 30 s treated sample had the highest mechanical strength. The SEM analysis of more prolonged plasma-treated cotton samples depicted more grooved and etched surface. In the images, it is visible that upper individual microfibrils were stripped and separated and intertwined with fibres at the surface, increasing interyarn and interfiber friction, thereby enhancing the breaking strength of the textile fabric (Jazbec et al. 2015).

4.6 Moisture Absorption

Synthetic fibres like polyamide and polyester have an upper hand in consumer usage due to their high modulus strength, stiffness, wrinkle resistance and cheaper value but

they possess poor absorption property which limits their application in the apparel sector. A study was carried out to check the influence of atmospheric pressure plasma on silicon nanoemulsions softener on polyester fibre, and it was observed that plasma treatment escalated the recovery angles. Plasma processing increases the roughness of the surface which captures more air and water from atmosphere leading to better moisture absorption and it also generates more polar groups which thereby improves the hydrophilicity of the sample. Thus, the application of plasma before softener coating increased the penetration of nanoemulsions to the depth hence reduced friction of fibres and as a result ability of the fabric to recover from deformation improved. The nanoemulsions silicone softer is hydrophobic in nature. The results indicated a decrease in moisture regain for plasma pretreated and silicone-coated fabric compared to only nanoemulsions coated fabric. It can be clearly explained as a result of an increase of hydrophilicity of plasma-treated fabric which facilitated better adhesion and spreading of nanoemulsions ultimately reducing the moisture absorption by the surface (Joshi and Bhattacharyya 2011; Parvinzadeh and Ebrahimi 2011).

4.7 Flame-Retardant Textiles

Surface modification by plasma treatment can be significant in synthesising nanoporous structures. Coating by plasma method is considered more durable than spraying methods since the molecules are chemically bonded to the treated substrate. Functional textiles are the new demand in recent times in the textile industry and the demand for flame-retardant textiles is particularly in firefighter clothes, upholstery, military garments and work clothing. Raslan et al. studied the effect of dielectric barrier discharge (DBD) plasma treatment after the deposition of fire-resistant aluminium oxide (Al_2O_3) nanopowder on polyester fabric to measure the flame-retardant capability of the treated fabric. SEM images showed a clear deposition of Al_2O_3 nanoparticles in the cracks and pores resulted from plasma treatment on the fibre surface. The thermogravimetric analysis (TGA) values exhibited an increase in the start of degradation temperature from 291.58 °C of untreated sample to 320.96 °C of nanocoated and plasma-modified sample. Furthermore, the flame retardancy test results completely correlated with TGA analysis and showed an increase in burning time from 39 s for untreated samples to 50 s for plasma-treated sample and at the same time a decrease in burning rate from 230 mm/min to 180 mm/min for the sample samples. These results indicated that the thermal stability of the fabric increased after nanocoating followed by plasma surface modification (Raslan et al. 2011).

5 Conclusion and Future Trend

In recent times, the use of plasma technology for physicochemical surface modification of textiles has become a fascinating and efficient technique for enhancement or

replacement of conventional wet chemical processing. The properties of the selected material can be modified using different plasma gas and changing the treatment parameters like time, voltage and power. Apart from plasma technology, nanotechnology also makes for a promising tool to modify and enhance the characteristics of fabrics. Nanoparticles have a smaller size and large surface area which makes this method a suitable method for tailoring a wide range of surface properties which are much difficult by conventional methods. Apart from the properties mentioned in Sect. 4 like antimicrobial, UV protection, stain removal, better dye adsorption, a plasma pretreated and nanoparticle-coated polymers can advance anti-felting, antistatic, electrical conductivity and abrasion resistance properties. It also strengthens the mechanical durability of fabric by increasing fabric roughness and optical reflectivity which is crucial for developing photocatalytic applications. Though these technologies have so much to offer, the industrial scale-up of pretreated textiles is still in the research stage and has been rather slow in delivering clothing to customers to be worn on a daily basis. One of the few prominent reasons for this holdback is the durability of treatments whether it may be plasma or nanoparticles and also the need to use different types of reactors and gases varying with different samples. But on a positive note, an increasing integration among the researchers, textile technologists and designers can be seen to overcome the challenge of industrialisation of plasma-treated clothes. It is to be expected that if fully utilised, these technologies can be used in different branches of the industries to develop much more durable and special trait-oriented fabric for biomedical, health care and military and also develop smart and intelligent textiles.

References

Airoudj A, Ploux L, Roucoules V (2014) Effect of plasma duty cycle on silver nanoparticles loading of cotton fabrics for durable antibacterial properties. J Appl Polym Sci 132(1):1–9. https://doi.org/10.1002/app.41279

Bhatia S (2016) Natural polymer drug delivery systems. Springer international publishing, Cham, Switzerland. https://doi.org/10.1007/978-3-319-41129-3

Bogaerts A et al (2002) Gas discharge plasmas and their applications. Spectrochim Acta—Part B AtIc Spectrosc 57(4):609–658. https://doi.org/10.1016/S0584-8547(01)00406-2

Bozzi A et al (2005a) Self-cleaning of modified cotton textiles by TiO2 at low temperatures under daylight irradiation. J Photochem Photobiol A 174(2):156–164. https://doi.org/10.1016/j.jphotochem.2005.03.019

Bozzi A, Yuranova T, Kiwi J (2005b) Self-cleaning of wool-polyamide and polyester textiles by TiO_2-rutile modification under daylight irradiation at ambient temperature. J Photochem Photobiol, A 172(1):27–34. https://doi.org/10.1016/j.jphotochem.2004.11.010

Chan CM, Ko TM, Hiraoka H (1996) Polymer surface modification by plasmas and photons. Surf Sci Rep 24(1–2):1–54. https://doi.org/10.1016/0167-5729(96)80003-3

Deng X et al (2014) Engineering of composite organosilicon thin films with embedded silver nanoparticles via atmospheric pressure plasma process for antibacterial activity. Plasma Process Polym 11(10):921–930. https://doi.org/10.1002/ppap.201400042

Deng X, Nikiforov A et al (2015b) Antibacterial activity of nano-silver non-woven fabric prepared by atmospheric pressure plasma deposition. Mater Lett 149:95–99. https://doi.org/10.1016/j.matlet.2015.02.112

Deng X, Yu Nikiforov A et al (2015a) Antimicrobial nano-silver non-woven polyethylene terephthalate fabric via an atmospheric pressure plasma deposition process. Sci Rep 5:1–10. https://doi.org/10.1038/srep10138

Dhand C et al (2015) Methods and strategies for the synthesis of diverse nanoparticles and their applications: a comprehensive overview. RSC Advances R Soc Chem 5(127):105003–105037. https://doi.org/10.1039/c5ra19388e

Ealias AM, Saravanakumar MP (2017) A review on the classification, characterisation, synthesis of nanoparticles and their application. IOP Conf Ser Mater Sci Eng 263(3). https://doi.org/10.1088/1757-899x/263/3/032019

Gorjanc M et al (2010) CF_4 plasma and silver functionalized cotton. Text Res J 80(20):2204–2213. https://doi.org/10.1177/0040517510376268

Gorjanc M et al (2014) Creating cellulose fibres with excellent UV protective properties using moist CF_4 plasma and ZnO nanoparticles. Cellulose 21(4):3007–3021. https://doi.org/10.1007/s10570-014-0284-5

Gorjanc M et al (2013) Multifunctional textiles—modification by plasma, dyeing and nanoparticles. In: Eco-friendly textile dyeing and finishing, pp 3–32. https://doi.org/10.5772/53376

Haji A, Qavamnia SS, Barani H (2013) In situ synthesis of silver nanoparticles onto cotton fibres modified with plasma treatment and acrylic acid grafting. Micro Nano Lett 8(6):315–318. https://doi.org/10.1049/mnl.2013.0157

Haji A et al (2015) Application of plasma technology for improved attachment of natural and nano-sized antibacterial agents to textile fibers. In: International conference on medical textiles and healthcare products. At Lodz, Poland, pp. 34–40

Hoffman AS (1996) Surface modification of polymers: physical, chemical, mechanical and biological methods. Macromol Symp 101:443–454. https://doi.org/10.1002/masy.19961010150

Ilić V et al (2009) Antifungal efficiency of corona pretreated polyester and polyamide fabrics loaded with Ag nanoparticles. J Mater Sci 44(15):3983–3990. https://doi.org/10.1007/s10853-009-3547-z

Jaganathan SK et al (2015) Review: radiation-induced surface modification of polymers for biomaterial application. J Mater Sci 2007–2018. https://doi.org/10.1007/s10853-014-8718-x

Jazbec K et al (2015) Functionalization of cellulose fibres with oxygen plasma and ZnO nanoparticles for achieving UV protective properties. J Nanomater 2015:1–9. https://doi.org/10.1155/2015/346739

John MJ, Anandjiwala RD (2009) Surface modification and preparation techniques for textile materials. In: Surface modification of textiles, pp 1–25. https://doi.org/10.1533/9781845696689.1

Joshi M, Bhattacharyya A (2011) Nanotechnology—a new route to high-performance functional textiles. Text Prog 43(3):155–233. https://doi.org/10.1080/00405167.2011.570027

Khan I, Saeed K, Khan I (2017) Nanoparticles: Properties, applications and toxicities. Arab J Chem The Authors. https://doi.org/10.1016/j.arabjc.2017.05.011

Kumar V et al (2013) Development of silver nanoparticle loaded antibacterial polymer mesh using plasma polymerization process. J Biomed Mater Res—Part A, 101 A(4), 1121–1132. https://doi.org/10.1002/jbm.a.34419

Mather RR (2009) Surface modification of textiles by plasma treatments. In: Surface modification of textiles, Woodhead Publishing Limited, pp 296–317. https://doi.org/10.1533/9781845696689.296

Mishra R et al (2014) The production, characterization and applications of nanoparticles in the textile industry. Text Prog (Taylor & Francis) 46(2):133–226. https://doi.org/10.1080/00405167.2014.964474

Morent R et al (2008) Non-thermal plasma treatment of textiles. Surf Coat Technol 202(14):3427–3449. https://doi.org/10.1016/j.surfcoat.2007.12.027

Nehra V (2008) Atmospheric non-thermal plasma sources. Int J 2(2):53–68. http://en.scientificcommons.org/redirect/55380120/2/Atmospheric+Non+Thermal+Plasma+Sources

Nema SK, Jhala PB (2015) Plasma technologies for textile and apparel, 1st edn. Woodhead Publishing India Pvt. Ltd. https://doi.org/10.1201/b18244

Ozdemir M, Yurteri CU, Sadikoglu H (1999) Physical polymer surface modification methods and applications in food packaging polymers. Crit Rev Food Sci Nutr 39(August 2014):457–477. https://doi.org/10.1080/10408699991279240

Parvinzadeh M, Ebrahimi I (2011) Atmospheric air-plasma treatment of polyester fibre to improve the performance of nanoemulsion silicone. Appl Surf Sci Elsevier B.V. 257(9):4062–4068. https://doi.org/10.1016/j.apsusc.2010.11.175

Primc G et al (2016) Biodegradability of oxygen-plasma treated cellulose textile functionalized with ZnO nanoparticles as antibacterial treatment. J Phys D Appl Phys 49(32). https://doi.org/10.1088/0022-3727/49/32/324002

Radetić M et al (2008) Antibacterial effect of silver nanoparticles deposited on corona-treated polyester and polyamide fabrics. Polym Adv Technol 19(12):1816–1821. https://doi.org/10.1002/pat.1205

Raslan WM et al (2011) Ultraviolet protection, flame retardancy and antibacterial properties of treated polyester fabric using plasma-nano technology. Mater Sci Appl 02(10):1432–1442. https://doi.org/10.4236/msa.2011.210194

Rezaei F et al (2016) Improvement properties of nylon fabric by corona pre-treatment and nano coating. J Text Inst (Taylor & Francis) 107(10):1223–1231. https://doi.org/10.1080/00405000.2015.1100394

Schwarz I, Kovačević S (2017) Textile application: from need to imagination. In: Textiles for advanced applications, InTech, pp 3–28. https://doi.org/10.5772/intechopen.68376

Shahidi S, Ghoranneviss M (2016) Plasma sputtering for fabrication of antibacterial and ultraviolet protective fabric. Cloth Text Res J 34(1):37–47. https://doi.org/10.1177/0887302X15594455

Shahidi S et al (2018) In situ synthesis of ZnO Nanoparticles on plasma treated cotton fabric utilizing durable antibacterial activity. J Nat Fibers (Taylor & Francis) 15(5):639–647. https://doi.org/10.1080/15440478.2017.1349714

Shamim A et al (2018) Synthesis of metallic nanoparticles by physical, chemical and biological methods and their characterization. http://uow.edu.pk/ORIC/Publications/4thMDSRIC-296.pdf. Accessed: 16 Apr 2019

Sparavigna A (2008) Plasma treatment advantages for textiles. *eprint* arXiv:0801.3727, p 16. https://doi.org/10.5772/53376

Vigneshwaran N (2009) Modification of textile surfaces using nanoparticles. In: Surface modification of textiles, Woodhead Publishing Limited, pp 164–184. https://doi.org/10.1533/9781845696689.164

Wei Q, Huang F, Cai Y (2009) Textile surface characterization methods. In: Surface Modification of Textiles, pp 26–57. https://doi.org/10.1533/9781845696689.26

Removal of Ni(II) and Zn(II) from Aqueous Media Using Algae-Sodium Bentonite Nanocomposite

Tanveer Rasool and Waris Baba

Abstract The composite made by mixing dead *Spirogyra* algal biomass with nano-bentonite clay, was used to study the adsorption of Ni(II) and Zn(II) as a function of pH, contact time, adsorbent dosage and initial ion concentration. An average crystal size of the composite synthesized was found to be 34.11 nm. The optimum temperature for maximum adsorption was found at 328 and 313 K for Ni(II) and Zn(II), respectively, in the pH range of 5–6. The results were achieved for the absorbent dosage between 0.1–0.3 gms per 100 ml of the solution. A decreasing trend was observed for adsorption capacity by the composite with maximum value at 0.1 gm dosage for both the metal ions. In contrary, an increasing trend in adsorption was observed in the concentration range while changing the metal ion concentration from 25 to 150 mg/l. Within the range of optimized parameters calculated, the maximum percentage recovery was found to be 108.67 mg/g (81%) and 100.78 mg/g (77%) for Ni(II) and Zn(II), respectively. Langmuir adsorption isotherm and pseudo second order models were best fit for equilibrium data, highlighting the potential of Algae-bentonite composite as possible feed stock for adsorption of heavy metals from aqueous media.

Keywords Nano composite · Adsorption · Algae · Optimization

1 Introduction

The rapid rise in the industrialization and urbanization have coupled itself with the serious environmental pollution causing serious threat to humanity at large. Heavy metals present in effluents and chemicals from industries above a certain permissible limit are known for their high toxicity and serious public health issues (Freitas et al. 2008). Some of the common heavy metals reported are mercury, lead, arsenic, cobalt, chromium, nickel, zinc, manganese, selenium, antimony etc. (Ngah et al. 2011). Their biological accumulation brings out many chronic issues and have a direct impact on

T. Rasool (✉) · W. Baba
Department of Chemical Engineering, National Institute of Technology Srinagar, Srinagar 190006, Jammu & Kashmir, India
e-mail: tanveer@nitsri.net

L. Ledwani and J. S. Sangwai (eds.), *Nanotechnology for Energy and Environmental Engineering*, Green Energy and Technology,
https://doi.org/10.1007/978-3-030-33774-2_24

chemical, neurological and physical impact on humans (Mehta and Gaur 2014). Unlike organic pollutants which are biodegradable, heavy metals pose a serious challenge for their removal or remediation from effluents and wastewaters. The focus of this study are two heavy metals Zn(II) and Ni(II), which owe their origin mostly from automobile, petroleum, pulp and paper, steel, organic and inorganic chemical, fertilizer, mining, metal electroplating and steel power plants (Mali et al. 2014; Srivastava et al. 2007). The permissible concentration limit set by World Health Organization (W.H.O) for nickel discharge is 0.5 mg/l for surface water and 0.05 mg/l in drinking water while that for zinc, it is 5 mg/l and 0.05 mg/l, respectively (WHO 2004).

Adsorption has been potentially proven as one of the non destructive and efficient methods for removal of heavy metals from effluents and waste water (Mali et al. 2014). The recent trend in the removal of heavy metals through adsorption has been the application of various biomass and clay based composites and these composites have proven both effective, efficient and eco-friendly in nature (Mali et al. 2014; Ngah et al. 2011; Rashid et al. 2016). Biomasses based on algae, fungi, bacteria, seaweeds and other aquatic and terrestrial plankton have been often used for the removal of heavy metals based on adsorption (Elangovan et al. 2008). On the other hand investigations on clays such as monti-morillonites, kiolinites, esmectities for adsorption have shown promising tendencies and efficiencies for removal of heavy metals from wastes due to their diverse and dynamic characteristics primarily the overall negative charge on its surface which facilitates the removal of positively charged metal ions along with physical and chemical stabilities and high superficial area. Bentonite composed of monti-morillonites contains swelling clays along with MgO, Fe_2O_3, Na_2O, SiO_2, Al_2O_3, and K_2O and its composites with various biomasses have emerged as promising and excellent agents for removing heavy metals from waste water (Rashid et al. 2016). In view of promising adsorption characteristics shown by both the dead algal biomass and bentonite, a nanocomposite of algae-sodium bentonite (ABC) was synthesized and evaluated for the removal of Ni(II) and Zn(II) from aqueous media.

2 Materials and Methodology

Analytical grade sodium-bentonite (Sigma Aldrich) was used for synthesis of composite bioadsorbent. Besides analytical grade nickel nitrate, zinc nitrate, sodium hydroxide, hydrochloric acid, sodium chloride, calcium chloride, iron chloride were used. Deionized water (ASTM Type-II, Rions India) with total chlorides less than 3 ppm, was used for all the experimental procedures. The samples of algae were collected from popular Dal Lake in Srinagar of Jammu & Kashmir (India). The samples were collected using standard procedure and strains were identified using inverted microscopy and identified as *Spirogyra* species. The microscopic view of the algal strain is presented in Fig. 1.

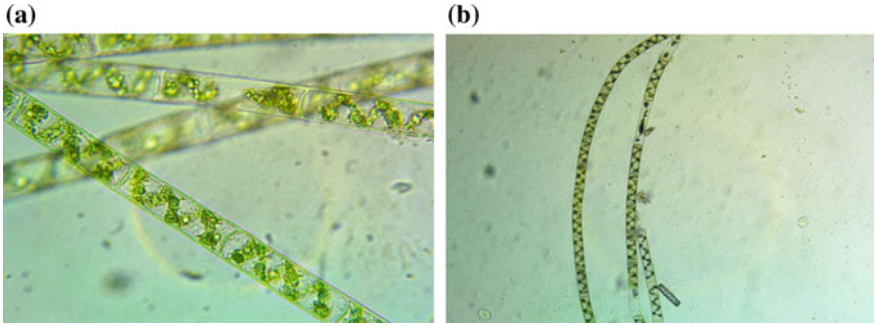

Fig. 1 Microscopic view of *Spirogyra* species of algae

2.1 Pre-treatment of Algal Biomass and Composite Preparation

Algal mass obtained was thoroughly washed with deionized water. The washed samples of algae were first sun dried for a full day followed by oven drying at 105 °C for 8 h to ensure the algal mass is dried completely. The dried algae were manually ground to obtain powdered algae. The Na-bentonite and powdered algal biomass were mixed in a ratio of 1:2 in a total mixture weight of 100 gm using deionized water. The solution was mixed using a magnetic stirrer for 4 h. After mixing properly, the oven drying of mixture was done at 75 °C for about 7 h. The composite was again ground manually using a mortar and a pastel. The composite was again dried in an oven at 105 °C till weight remained constant. The Algae Bentonite Composite (ABC) thus obtained was pretreated with salt solutions of NaCl followed by KCl. For each run, salt solutions of 5% by weight were mixed with the ABC and agitated for 1 h at 130 rpm. Thorough filtering and washing of ABC was done with deionized water followed by oven drying at 65 ± 5 °C for 6 h and used for batch adsorption experiments (Rashid et al. 2016). Ni(II) and Zn(II) stock solution of 500 mg/l were prepared and diluted to required concentrations for each batch experiment. Atomic Absorption Spectroscopy (ASS-Perkin Elmer Analyst 800) was used for determining concentrations of metal ions.

2.2 Adsorption Studies

Stock solutions of Zn(II) and Ni(II) ions were prepared by dissolving the respective amounts of $Zn(NO_3)_2.6H_2O$ and $Ni(NO_3)_2.6H_2O$ in ultra-pure deionized water. Working solutions were prepared from stock using dilution method. The variation of parameters like pH, dosage of adsorbent, time of contact, initial concentration of metal ions in aqueous solution and temperature were observed. pH of the working solutions was adjusted using 0.1 M NaOH and 0.1 M HCl. The batch experiments

were performed in 250 ml Erlenmeyer flasks and shaking was done in an orbital shaking incubator at 125 rpm. The pH, contact time, dosage of adsorbent, initial concentration of metal ions, and temperature were studied in the range of 2–6, 10–120 min 100–300 mg, 50–200 mg/L, and 303.15–333.15° K, respectively. The adsorption capacity and percentage recovery were calculated using Eqs. 1 and 2, respectively.

$$q_e = \frac{\left[\left(C_i - C_f\right)\frac{V}{1000}\right]}{m} \tag{1}$$

$$R\% = \left[\frac{\left(C_i - C_f\right)}{C_i}\right] \times 100 \tag{2}$$

where, C_i and C_f are the initial and final concentrations of metal ions present in solution (mg/l), q_e is adsorption capacity, $R\%$ is recovery percentage, V is the volume of the working solution (ml) and m is the adsorbent dosage (gm).

3 Results and Discussion

3.1 Adsorbent Characterization

ABC characterization was conducted using FTIR, SEM and XRD Analysis. The infra-red (IR) spectra of the samples were recorded by using Agilent Technologies Cary 630 FTIR spectrophotometer. The spectra recording were done in the transmission band mode in the range varying from 750–4500 nm. FTIR analysis of the composite shows that a large number of peaks are obtained which specifies many functional groups. Thus, a large number of sites are available for the metal ions to adsorb. The main functional groups identified are carboxylic groups at 1622 cm^{-1}(–C = O) with ligand atom O has a strong affinity for metal ions. At 1584 cm^{-1}, peak corresponds to an amine group ($–NH_2$) with N as a ligand atom. At 1511 cm^{-1}, alkanes are present. A peak at 1341 cm^{-1}, corresponds to have strong nitro groups. The strong phenyl groups are there at 734 cm^{-1}. Other than these ether groups (C–O), alkenes, ketones and aldehydes are also present. All these groups have good affinity to adsorb the heavy metal ions which paves the way for efficient adsorption (Abbas et al. 2014). Scanning Electron Microscopy (FE-SEM 3600-Japan) images of deal algal biomass and algae bentonite composite were used to study the morphology of the composite. The image of ABC shows clear cracks on its surface and seems more porous than lone algal biomass. The crystal size of the composite and its constituents was determined using X-Ray Diffraction (SmartLab 3KW, Rigaku Corporation Japan). The average crystal grain size of the algal powder, bentonite and the ABC was found in the ranges of 45.2 nm, 57.9 nm and 34.11 nm, respectively. The SEM images and the diffraction pattern of the composite are presented in Figs. 2 and 3, respectively.

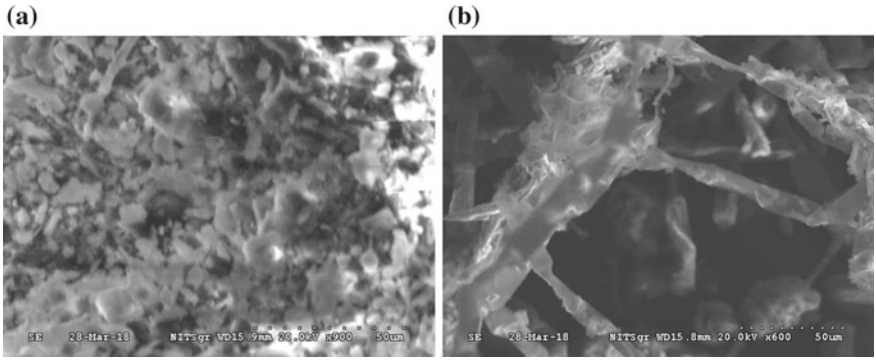

Fig. 2 SEM image of **a** dead algal biomass **b** ABC

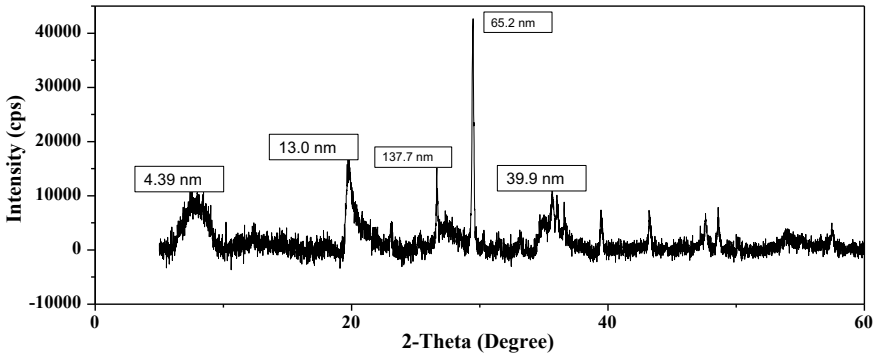

Fig. 3 Diffraction pattern of the ABC

3.2 Effect of Initial pH

The effect of pH on Zn(II) and Ni(II) is shown in Fig. 4. The maximum adsorption for Zn(II) was observed at pH of 5 while for Ni(II) it was found to fall around the pH 6. The adsorption of Zn(II) was slightly lower than that of Ni(II). The variation in the adsorption of both Zn(II) and Ni(II) at different pH values onto ABC may be attributed to the variation of charges on the surface of adsorbent at different pH values due to different solute speciation, adsorbent surface and degree of ionization (Fan et al. 2012). It was observed that the adsorption of metals at extreme basic and acidic conditions was low. For metal binding functional groups play an important role and pH significantly effects the functional groups by protonation/deprotonation which causes varying forces of attraction between sorbate and metal ions (Ullah et al. 2013). At low pH adsorption is not favoured due to competition of metal ions with H^+ ions. As the pH increases, the ligands carrying negative charge increase facilitating the better binding of positively charged species (Rashid et al. 2016). The adsorption of both the metals is found to be maximum at pH of about 5–6. Further it may be

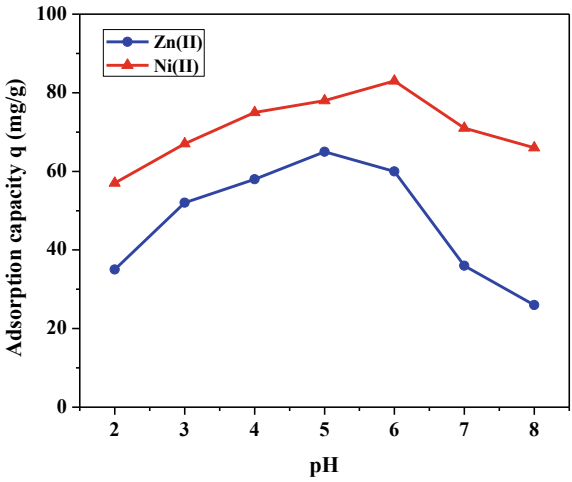

Fig. 4 Effect of initial pH on adsorption capacity Zn(II) and Ni(II) on ABC

explained by relating the effect of pH to the competition between the metal ions and the hydronium ions onto the working sites of ABC surface. At lower pH of solution, functional groups get easily protonated due to their association with hydronium ions (H_3O^+) resulting in the overall positive charge of the surface. Thus, this phenomenon results in the low uptake of metals at low pH which can be attributed to the repulsive forces by the composite surface. As the pH increases more functional groups like carboxylic, amino groups, phosphate groups get exposed which easily facilitate the binding of metal ions. Again at much higher pH the adsorption of both the metals began to drop. This happens due to the OH^- species of the solution, which compete with anion species of divalent Zn(II) and Ni(II) and result in the adsorption of metal ions.

3.3 Effect of Adsorbent Dosage

The sorption of Zn(II) and Ni(II) on ABC was studied by varying the dosage 0.1 to 0.3 g per 100 ml of solution. The respective results are depicted in Fig. 5. The results reveal that with an increase in the adsorbent dosage, the adsorption capacity of the ABC decreases. At the same time the recovery percentage also decreased at higher dosage for both the metal ions. The maximum adsorption for both the ions was obtained at 0.1 g of adsorbent dosage. Due to fixed total amount of Zn(II) and Ni(II) ions available for removal, ion adsorption per mass of adsorbent (adsorption capacity, q) decreased at higher dosage. The study is in order with some previous findings (Fourest and Roux 1992; Gong et al. 2005). Moreover, at higher adsorbent dosage removal efficiency becomes stable showing a low sorption rate increment per increment of algae bentonite added. The adsorption capacity of Zn(II) and Ni(II) declined from 69.79 mg/g to 18.64 mg/g and from 85.32 mg/g to 21 mg/g respectively.

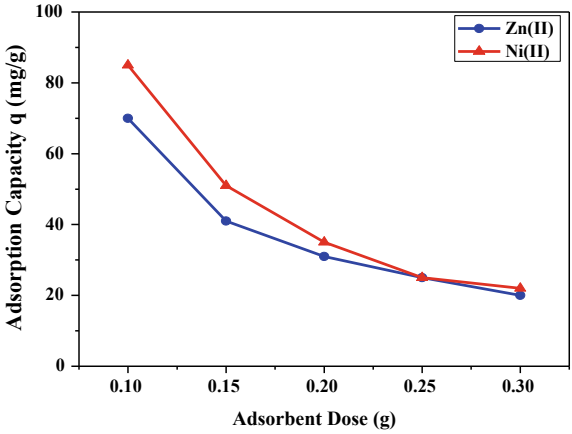

Fig. 5 Effect of adsorbent mass on adsorption capacity of ABC

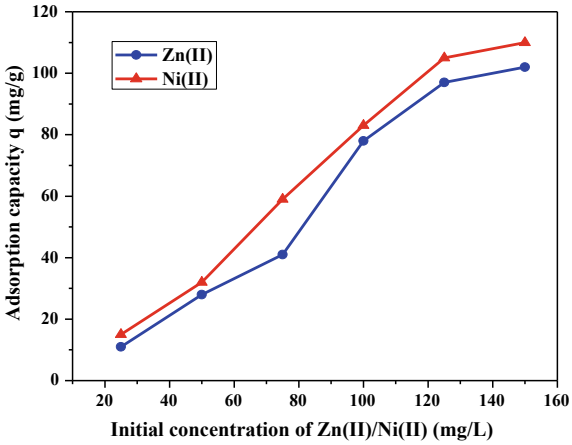

Fig. 6 Effect of initial concentration on adsorption capacity of ABC

The maximum removal efficiency for Zn(II) was at 69.79% while that for Ni(II), it is on higher side at 86%.

3.4 Effect of Initial Ion Concentration

As a well-known fact, that only certain amount of adsorbate can adsorb on the surface of a given mass of adsorbent. As such, the initial ion concentration of metals plays a vital role in the overall efficiency of the process of adsorption. In the present case, the initial ion concentrations of both the metals under study, were varied from 25 to 150 mg/l to evaluate this effect. The results of which are depicted in Fig. 6. At lower concentrations, less metal ions were available for both the solutions, therefore

the behavior of adsorption seems to be independent of initial concentration of metal ions. It can be seen that higher percentage of both the metal ions were removed at lower concentrations. In previous studies, similar adsorption capacity behavior at lower metal ions concentration have been observed and reported (Gong et al. 2005; Manzoor et al. 2013; Ullah et al. 2013). But the amount of Zn(II) and Ni(II) metal ions adsorbed per unit mass of adsorbent improved with increase in metal ion initial concentrations in both the cases. For Zn(II), the maximum adsorption capacity came out to be 100.78 mg/g and for Ni(II), it was found to be 108.67 mg/g. At higher concentrations the available sites might be occupied while as at lower concentrations more binding sites were available for the metal ions to be adsorbed. At low concentrations the binding sites of the algae bentonite composite remained unsaturated. The findings reiterate that initial metal ion concentration plays a vital role in the process of adsorption and therefore the optimization of initial metal ion concentration is necessary for an efficient adsorption process. The maximum removal efficiencies for Zn(II) and Ni(II), however, were found to be 77% and 82%, respectively.

3.5 Effect of Contact Time

The rate of adsorption being an characteristic parameter in the design of batch reactors, the effect of contact time was evaluated for the exchange of adsorbate from the solution on the adsorbent. The effect of contact time for the adsorption of Zn(II) and Ni(II) metal ions on to the ABC was analyzed for 129 min with initial ion concentration of 100 mg/l for both Zn(II) and Ni(II) ions at 303.15 K. The adsorbent dosage was taken as 1 g/l for both Zn(II) and Ni(II) metal ions. A 100 ml metal ion solution was used, so 100 mg of adsorbent was used for adsorption of Zn(II) and Ni(II) ions, respectively. The pH of the solution was fixed at an optimum values of 5 for Zn(II) and 6 for Ni(II), respectively. The uptake of both the Zn(II) and Ni(II) species was fast at an initial stage of contact time but became slower towards the equilibrium as indicated from the curves presented in Fig. 7. This is due to the fact that during the initial stage of adsorption, vacant sorption active sites available for attachment were large in number. The equilibrium was reached in 50 min for Zn(II) and that for Ni(II), it was attained in about 60 min. The adsorption capacities of ABC at equilibrium was found to be 64.87 mg/g for Zinc and that for nickel, it was on the higher side than that of Zn(II), at 87.2 mg/g. Thus it seems that that the process of adsorption had followed a two step process, faster initial regime and a slower second regime. As contact time was further increased the adsorption capacities didn't increase any further. This behavior of faster first phase and slower second phase can be explained by the fact that initially active sites were readily available on the adsorbent surface while as during the second phase, the exhaustion of vacant sites leads to the slower adsorption rate. The behavior is in complete agreement with some earlier studies on various adsorbent materials (Marandi 2011; Safa and Bhatti 2011).

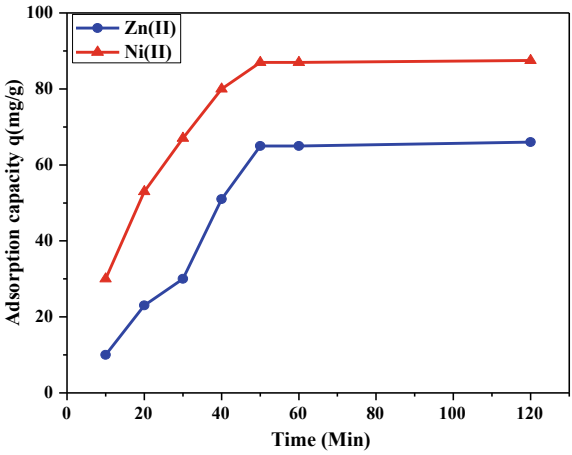

Fig. 7 Effect of contact time on adsorption capacity of ABC

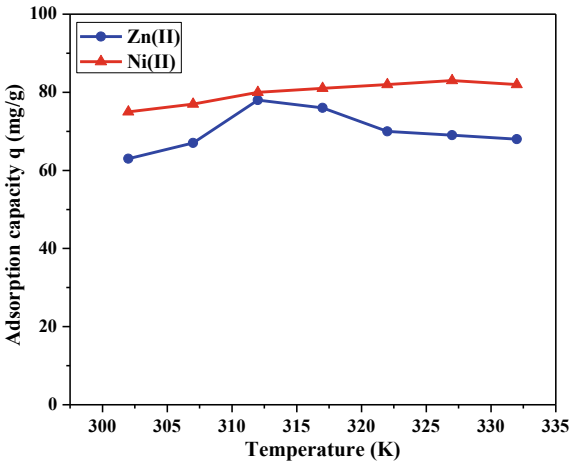

Fig. 8 Effect of temperature on adsorption capacity of algae bentonite composite

3.6 Effect of Temperature

For both the metal ions, the effect of temperature on adsorption for the present study was carried out for the range 303.15–333.15 K. As temperature was varied in the given range the adsorption capacities increased as represented in Fig. 8 for both Zn(II) and Ni(II) metal ions. For Zn(II), the adsorption capacity of ABC increased up to a certain amount at 313.15 K and the further elevation in temperature showed a dip in adsorption capacity. A similar regime was shown by Ni(II) where after 328.15 K, the capacity began to show a minor decrease. The lower adsorption at higher temperatures might be attributed to the weakening of working attractive forces between the adsorbate and adsorbent (Ho et al. 2005). Thus positive adsorption was shown by the composite at moderate temperature. At elevated temperatures the active

sites might be damaged which might be the reason for the decrease in adsorption capacity. Also according to an adsorption theory by increasing the temperature the adsorption may decrease because the ions previously adsorbed may begin to desorb due to elevating temperatures (Ho et al. 2005).

3.7 Equilibrium Isotherm Modeling

The experimental equilibrium data was subjected to different isotherms to get a deeper insight of the process of adsorption onto the ABC. The equilibrium data was tested by using Langmuir (1918), Freundlich (1906) and Harkins-Jura isotherms (1944). In order to optimize the adsorption process, the understanding of the forces governing the interaction between the ions and adsorbent is necessary.

Langmuir adsorption model assumes that only specific homogenous sites on the surface of an adsorbent are responsible for adsorption and intermolecular forces depend directly on the distance from the adsorbent surface and may show a rapid decrease with the movement of adsorbate away from adsorbent surface. Further the model assumes that the surface on which adsorption takes place is homogenous in structure and the sites available for adsorption are all identical in terms of energy. The Freundlich isotherm is an empirical isotherm used to describe the heterogeneity of system. The Harkins-Jura isotherms isotherm is employed for multilayer adsorption. Heterogeneous pore distribution accounts for the multilayer adsorption. The details of adsorption and kinetic models and the parameters used is compiled in Table 1.

Langmuir adsorption Isotherm can be expressed in the form of a dimensionless constant separation factor (R_s), expressed as:

$$R_s = \frac{1}{1 + K_b C_o}$$

where C_o is the maximum initial metal ion concentration (mg/l) and K_b(l/mg) is the Langmuir constant. R_s provides information about the adsorption behavior as irreversible ($R_s = 0$); linear ($R_s = 1$); favorable ($0 < R_s < 1$) and unfavorable ($R_s > 1$) (Rashid et al. 2016; Kilic et al. 2013). The calculated isotherm parameters for the adsorption of Zn(II) and Ni(II) using Langmuir, Freundlinch and Harkins-Jura models are given in Table 2.

The analysis of results from the Table 2 shows that overall Langmuir adsorption isotherm is a best fit for the experimental data of both Zn(II) and Ni(II) ions as compared to other isotherms. Freundlich isotherm model indicates the heterogeneity of the surface and simultaneously supports the adsorption of the metal ions on to the adsorbent. Freundlich isotherm also suggests that chemisorption is governing the adsorption process over physiorption. This indicates both physiorption and chemisorption are playing their role in the process of adsorption for removing the metal ions from aqueous solutions. Besides, it is not restricted to the monolayer as in

Table 1 Models and their parameters

Models (adsorption and kinetic)	Governing equations	Parameters
Langmuir model	$q_e = \frac{q_{\max} K_b C_e}{1+K_b C_e}$	q_e(mg/g): An amount of ions adsorbed at equilibrium per unit mass of adsorbent. $q_{\max}$(mg/g): Maximum adsorption capacity K_b(1/mg): Langmuir adsorption constant
Freundlich model	$q_t = K_F C_e^{\frac{1}{n}}$	K_F: Freundlich adsorption constant n: The empirical parameter indicating adsorption favorability
Harkins-Jura model	$\frac{1}{q_e^2} = \frac{B}{A} - \frac{1}{A}\log C_e$	A, B: Harkins Jura adsorption constants
Pseudo-First order	$q_t = q_e\left[1 - \exp(-K_1 t)\right]$	q_t(mg/g): Adsorption capacity at time t q_e(mg/g): Adsorption capacity at equilibrium K_1(1/min): Rate constant of Pseudo first order adsorption t(min): Time of contact
Pseudo-Second order	$q_t = \frac{q_e^2 K_2 t}{1+t K_2 q_e}$	q_t(mg/g): Adsorption capacity at time t K_2(g/mg min): Rate constant of Pseudo Second order adsorption
Intra-Particle diffusion model	$q_t = K_{id}\, t^2 + I$	q_t(mg/g): Adsorption capacity at time t $K_{id}\left(\text{mg/g min}^2\right)$: Intra particle diffusion rate constant I: Intercept representing boundary layer thickness

Table 2 Isotherm parameters for Zn(II) and Ni(II) adsorption onto the ABC

Models	Parameters	Metal ions Zn(II) Ni(II)	
Langmuir	$q_{\max}\left(\text{mg}/\text{g}\right)$	125	142.85
	$K_b\left(\text{L}/\text{g}\right)$	0.25	0.028
	R^2	0.9633	0.9707
Freundlich	K_F	7.4	9.7
	n	1.82	1.859
	R^2	0.9234	0.95
Harkins-Jura	A	714	970.87
	B	1.992	1.893
	R^2	0.701	0.723

Table 3 Comparison of adsorption capacities of various biomass adsorbent materials

Adsorbent material	Metal	Operating conditions				
		pH	q_e (mg/L)	Adsorbent dose (g/L)	Concentration (mg/L)	References
Penicillium digitatum	Zn(II)	5.5	9.7	7.0	25	Galun et al. (1987)
Rhizopus arrhizus	Zn(II)	6–7	13.5	3.0	10–600	Fourest and Roux (1992)
Botrytis cinerea	Zn(II)	5–6	12.9	0.1	100	Tunaliand and Akar (2006)
Spirogyra **(ABC)**	Zn(II)	5	101	0.1	150	**Present Study**
Sea Weeds	Ni(II)	4.5	20.63	4.5	100	Vijayaraghavan et al. (2005)
Almond Shell	Ni(II)	7.0	22.22	7.0	100	Kilic et al. (2013)
Spirogyra **(ABC)**	Ni(II)	6	108	0.1	150	**Present Study**

case of Langmuir isotherm but the R^2 values obtained in case of Langmuir isotherm model were more than that of Freundlich model.

The R^2 values for Harkins-Jura model are on much lower side which indicates that it is an inadequate model to define and represent the adsorption process of Zn(II) and Ni(II) onto the composite.

The adsorption capacity of ABC has been compared with some earlier studies and the comparison is presented in Table 3. The results of the present experimental study is in line with the reported studies and highlights the potential of ABC as an efficient feedstock for adsorption of heavy metals.

3.8 Kinetic Modeling

The kinetic modeling of adsorption process is an essential tool in the design of adsorption experiments and optimization of the operating conditions for running of full scale batch processes. The kinetic study was performed in order to evaluate the various kinetic parameters and to understand the mechanism of adsorption of Zn(II) and Ni(II) metal ions onto the ABC. The experimentally generated data was subjected to Pseudo-first order, pseudo-second order and intra-particle diffusion models (Table 1) and the calculated values of variables are depicted in Table 4.

It was observed that the Pseudo-Second order model showed the highest correlation coefficient (0.99) for both Zn(II) and Ni(II) metal ions. This signifies that the adsorption follows the Pseudo-Second order reaction and the mechanism for adsorption is based on chemisorption process.

Table 4 Kinetic parameters for Zn(II) and Ni(II) adsorption onto the ABC

Kinetic model	Metal	Parameters		
Pseudo-First-order		$K_1(\text{min}^{-1})$	q_e(mg/g)	R^2
	Zn(II)	0.055	55.795	0.601
	Ni(II)	0.068	55.99	0.719
Pseudo-Second-order		$K_2 \times 10^3$(g/mg min)	q_e(mg/g)	R^2
	Zn(II)	3.589	50.787	0.994
	Ni(II)	2.924	67.613	0.997
Intra-Particle diffusion		K_{id}(mg/g min^2)	I	R^2
	Zn(II)	7.877	6.642	0.714
	Ni(II)	7.263	25.412	0.609

3.9 Thermodynamic Parameter Evaluation

In order to comprehend the feasibility of process of adsorption and to understand its nature, thermodynamic study plays a critical role in highlighting its dependence on temperature. As such, various thermodynamic parameters like Gibbs free energy (ΔG°), change in standard enthalpy (ΔH°) and standard entropy (ΔS°) are estimated using classical Vant Hoff's equation relating (ΔG°, kJ/mol) to the linear adsorption diffusion coefficient $\left(K_D = q_e / C_e, \text{l/g}\right)$ of the adsorption process following Eq. 3.

$$\Delta G^\circ = -RT \ \ln K_D \tag{3}$$

where R, is the gas constant (8.314 kJ/mol K). ΔG° is also related to the entropy change ΔS°(kJ/ mol K) and the enthalpy change ΔH°(kJ/mol) at absolute temperature $T(K)$ following Eq. 4

$$\Delta G^\circ = \Delta H^\circ - T\Delta S^\circ \tag{4}$$

Equations 3 and 4 together lead to following equation.

$$\ln K_D = \frac{\Delta H^\circ}{R} - \frac{\Delta S^\circ}{RT} \tag{5}$$

Using Eq. 5, ΔH° and ΔS° are obtained from the slope and intercept of the plot between $\ln K_D$ and $1/T$ (Kilic et al. 2013). The thermodynamic results calculated for both the Zn(II) and Ni(II) onto the ABC are shown in Table 5.

It was observed with the increase in temperature the adsorption process increases for both the metals indicating that the process of adsorption onto the adsorbent composite was endothermic in nature. The ΔG° was found to be negative indicating

Table 5 Thermodynamic parameters for Zn(II) and Ni(II) adsorption onto the ABC

Temperature (K)	Zn(II)			Ni(II)		
	ΔG° (kJ/mol)	ΔH° (kJ/mol)	ΔS° (kJ/mol K)	ΔG° (kJ/mol)	ΔH° (kJ/mol)	ΔS° (kJ/mol)
303.15	−0.306	23.786	0.078	−0.877	26.222	0.0886
308.15	−1.072	–	–	−1.799	–	–
313.15	−1.316	–	–	−2.275	–	–
318.15	−1.448	–	–	−2.297	–	–
323.15	−1.946	–	–	−2.640	–	–
328.15	−2.044			−2.933	–	–

the spontaneity of the process. The ΔS° values indicate the increase in the randomness of the process of adsorbing the metals onto the adsorbent composite (Galun et al. 1987). Generally, ΔG° values ranging from 0 to −20 kJ/mol corresponds to physisorption, whereas value of ΔG° ranging from −80 to −400 kJ/mol is the indication of chemisorption (Wu et al. 2013). Therefore, the Ni(II) and Zn(II) adsorption on algae bentonite composite is endothermic, spontaneous and combination of physisorption and chemisorption in nature.

4 Conclusions

A locally available algal biomass and Na-Bentonite was used to prepare a composite which was in turn used for the adsorption of Zn(II) and Ni(II) ions from aqueous media. The optimum conditions for the adsorption were evaluated and it was found that Langmuir Isotherm Model is best fitted to equilibrium data of the adsorption of Zn(II) and Ni(II) ions onto the synthesized composite while as the kinetics were found to follow Pseudo-second order kinetic model. The calculated values of ΔG°, ΔH° and ΔS° indicate a spontaneous, endothermic and chemically favoured adsorption process. The adsorption efficiency of the composite revealed promising results as an effective material for removal of heavy metals from industrial effluents and waste water. Besides, the easy availability and low cost of both the algal biomass and clays account for the favorable economics of the process.

References

Abbas SH, Ismail I, Mostafa TM, Sulaymon AH (2014) Biosorption of heavy metals: a review. J Chem Sci Technol 3(4):74–102

Elangovan R, Philip L, Chandraraj K (2008) Biosorption of chromium species by aquatic weeds: kinetics and mechanism studies. J Hazard Mater 152:100–112. https://doi.org/10.1016/j.jhazmat.2007.06.067

Fan L, Luo C, Li X, Lu F, Qiu H, Sun M (2012) Fabrication of novel magnetic chitosan grafted with graphene oxide to enhance adsorption properties for methyl blue. J Hazard Mater 215:272–279. https://doi.org/10.1016/j.jhazmat.2012.02.068

Fourest E, Roux JC (1992) Heavy metal biosorption by fungal mycelial by-products: mechanisms and influence of pH. J Appl Microbiol Biotechnol 37:399–403

Freitas OMM, Martins RJE, Delerue-Matos CM, Boaventura RA (2008) Removal of Cd, Zn and Pb from aqueous solution by brown marine macroalgae: kinetic modeling. J Hazard Mater 153:493–501. https://doi.org/10.1016/j.jhazmat.2007.08.081

Freundlich HMF (1906) Uber die adsorption in losungen. J Phys Chem 57:385–470

Galun M, Galun E, Siegel B, Keller P, Lehr H, Siegel S (1987) Removal of metal ions from aqueous solutions by penicillium biomass: kinetic and uptake parameters. J Water Air Soil Pollut 33:359–371

Gong R, Ding Y, Liu H, Chen Q, Liu Z (2005) Lead biosorption and desorption by intact and pretreated spirulina maxima biomass. J Chemosphere 58:125–130. https://doi.org/10.1016/j.chemosphere.2004.08.055

Harkins WD, Jura G (1944) Surfaces of solids. XII. an absolute method for the determination of the area of a finely divided crystalline solid. J Am Chem Soc 66(8):1362–1366. https://doi.org/10.1021/ja01236a047

Ho YS, Chiu WT, Wang CC (2005) Regression analysis for the sorption isotherms of basic dyes on sugarcane dust. J Bioresour Technol 96:1285–1291. https://doi.org/10.1016/j.biortech.2004.10.021

Kilic M, Kibiyik C, Cepeliogullar O, Putun AE (2013) Adsorption of heavy metal ions from aqueous solutions by biochar, a by-product of pyrolysis. J Appl Surf Sci 283:856–862. https://doi.org/10.1016/j.apsusc.2013.07.033

Langmuir I (1918) The adsorption of gases on plane surfaces of glass, mica and platinum. J Am Chem Soc 40:1361–1403. https://doi.org/10.1021/ja02242a004

Mali A, Pandit V, Majumder DR (2014) Biosorption and desorption of zinc and nickel from wastewater by using dead fungal biomass of aspergillus flavus. J Tech Res Appl 2:42–46

Manzoor Q, Nadeem R, Iqbal M, Saeed R, Ansari TM (2013) Organic acids pretreatment effect on Rosa bourboniaphyto-biomass for removal of Pb(II) and Cu(II) from aqueous media. J Bioresour Technol 132:446–452. https://doi.org/10.1016/j.biortech.2013.01.156

Marandi R (2011) Biosorption of hexavalent chromium from aqueous solution bydead fungal biomass of Phanerochaetechrysosporium: batch and fixed bedstudies. J Can Chem Eng Technol 2:8–22

Mehta SK, Gaur JP (2014) Concurrent sorption of Ni_2^+ and Cu_2^+ by chlorella vulgaris from a binary metal solution. J Appl Microbiol Biotechnol 55:379–382

Ngah WW, Teong L, Hanafiah M (2011) Adsorption of dyes and heavy metal ions by chitosan composites: a review. J Carbohydr Polym 83:1446–1456. https://doi.org/10.1016/j.carbpol.2010.11.004

Rashid A, Bhattia HN, Iqbal M, Noreen S (2016) Fungal biomass composite with bentonite efficiency for nickel and zinc adsorption: a mechanistic study. J Ecol Eng 91:459–471. https://doi.org/10.1016/j.ecoleng.2016.03.014

Safa Y, Bhatti HN (2011) Kinetic and thermodynamic modeling for the removal of direct red-31 and direct orange-26 dyes from aqueous solutions by ricehusk. J Desalination 272:313–322. https://www.doi.org/10.1016/j.desal.2011.01.040

Sari A, Tuzen M, Uluozlu OD, Soylak M (2007) Biosorption of Pb(II) and Ni(II) from aqueous solution by lichen (Cladoniafurcata) biomass. J Biochem Eng 37:151–158. https://doi.org/10.1016/j.bej.2007.04.007

Srivastava VC, Mall IO, Mishra IM (2007) Adsorption thermodynamics and isosteric heat of adsorption of toxic metal ions onto bagasse fly ash (BFA) and rice husk ash (RHA). Chem Eng J 132:267–278. http://doi.org/10.1016/j.cej.2007.01.007

Tunali S, Akar T (2006) Zn(II) biosorption properties of botrytis cinerea biomass. J Hazard Mater 131:137–145. https://doi.org/10.1016/j.jhazmat.2005.09.024

Ullah I, Nadeem R, Iqbal M, Manzoor Q (2013) Biosorption of chromium onto native and immobilized sugarcane bagasse waste biomass. J Ecol Eng 60:99–107. https://www.doi.org/10.1016%2Fj.ecoleng.2013.07.028

Vijayaraghavan K, Jegan J, Palanivelu K, Velan M (2005) Biosorption of cobalt(II) and nickel(II) by seaweeds: batch and column studies. J Sep Purif Technol 44:53–59. http://dx.doi.org/10.1016%2Fj.seppur.2004.12.003

WHO (2004) Guidelines for drinking-water quality, vol 1, World Health Organization, p 459

Wu Y, Luo H, Wang H, Wang C, Zhang J, Zhang Z (2013) Adsorption of hexavalent chromium from aqueous solutions by graphene modified with cetyl trimethyl ammonium bromide. J Colloid Interface Sci 394:183–191. https://doi.org/10.1016/j.jcis.2012.11.049

Nucleic Acid Based Nanoconstructs for Environmental Analysis in Atypical Contexts

Aditi Singhal, Kriti Kapil, Ankit Dodla, Sanjay Kumar and Bhaskar Datta

Abstract The use of biomolecules toward environmental analysis provides impressive advantages in terms of selectivity and efficiency. Proteins have served as the classical choice of biomolecules in this regard partly due to their natural function as strong and specific binding agents. Nevertheless, biomolecules are usually considered unsuitable for large-scale environmental applications due to their fragility and cost. In this chapter, we first examine the emergence of nucleic acid based nanotechnology in the context of environmental analysis. Notably, the development of nucleic acid aptamers, aptazymes, and nano-architectures has facilitated application as both a receptor in biosensors as well as versatile scaffolds for engineering functional constructs. Further, we present a proof-of-concept of nucleic acid based nanoconstructs as a reusable adsorbing agent. We have developed nucleic acid three-way junction-based matrices that are capable of retrieval and reuse of a commonly used staining agent. Immobilization of the nucleic acid architectures on magnetic nanoparticles enables their reuse across samples. Inherent sophistication of biomolecules in general and nucleic acid based constructs, in particular, supports their deployment in specialized applications at a smaller scale pertinent to individual human activity. The perspective presented in this chapter is expected to encourage environmental engineering in distinctive and atypical contexts.

Keywords Nucleic acids · Three-way junction · Magnetic nanoparticles · Dye adsorption · Environmental analysis

A. Singhal · A. Dodla · S. Kumar · B. Datta
Department of Biological Engineering, Indian Institute of Technology Gandhinagar, Gandhinagar, Gujarat, India

K. Kapil · B. Datta (✉)
Department of Chemistry, Indian Institute of Technology Gandhinagar, Gandhinagar, Gujarat, India
e-mail: bdatta@iitgn.ac.in

L. Ledwani and J. S. Sangwai (eds.), *Nanotechnology for Energy and Environmental Engineering*, Green Energy and Technology,
https://doi.org/10.1007/978-3-030-33774-2_25

1 Introduction

Two main types of biomolecular receptors have been used for environmental analysis: antibodies and enzymes. The use of enzymes in biosensor applications predates the use of antibodies. Sophistication in analytical techniques has enabled the production of many enzymes at suitable purity for research and biotechnological applications (Homaei et al. 2013). Traditional industrial application of enzymes has involved food processing such as cheese making, beer brewing, and wine making (Gurung et al. 2013). This emphasis is not surprising considering the critical role of enzymes in metabolic processes. Modern advances in protein engineering have led to the establishment of customized enzymes for novel applications. Certain characteristics of enzymes have played an important role in imagining and applying them in a biosensory context. Enzymes introduce an attractive element of selectivity and ability to amplify the response to a substrate by way of catalytic transformation (Fig. 1). Enzyme-based biosensors are useful for the clinical identification and quantification of key metabolites.

While the affinity and catalytic performance of enzymes are attractive, their stringent operating conditions, especially in terms of temperature and pH, can serve as constraints for widespread use. Nevertheless, the distinctive properties of enzymes

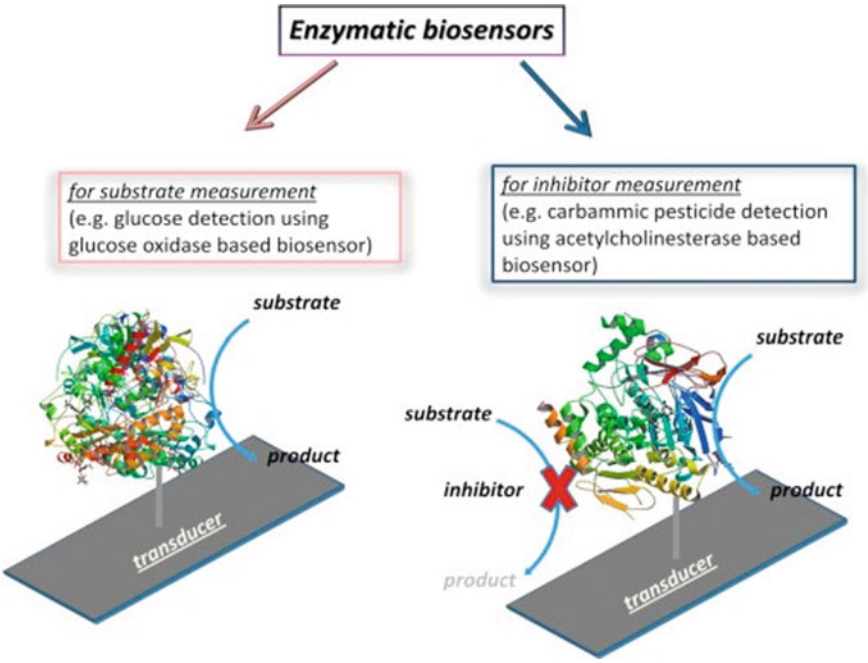

Fig. 1 Scheme of the biosensor for substrate and inhibitor detection; reproduced with permission from Amine et al. (2016)

have been the cornerstone of industries including pharmaceutical, chemical manufacturing, bio-fuel production and solid waste or water treatment (Li et al. 2012). Enzymes have found use in two broad aspects of environmental analysis, namely, detection of specific analytes and small-scale remediation.

Research has sought to develop suitable bio- and macromolecules that can address the operational constraints of enzymes. DNAzymes and aptazymes are examples of such artificially engineered moieties. DNAzymes are synthetic analogues of ribozymes and are DNA molecules that are capable of catalyzing nucleic acid hydrolysis. They have emerged as robust catalysts in their own right and have been adapted for biosensor applications based on their ability to incorporate nucleic acid secondary structures that act as receptors for specific analytes. DNAzyme based biosensors for the detection of toxic metals such as Hg^{2+}, (Li et al. 2009) Pb^{2+} (Li and Lu 2000; Shen et al. 2008) and Cu^{2+} (Liu and Lu 2007a, b) have been reported. Advances in transducing nucleic acid interactions through colorimetry, fluorescence, and electrochemical means have been useful in such biosensor development (Zhang et al. 2011). Apart from use as biosensors, enzymes have been comprehensively examined towards environmental remediation. Parathion hydrolase is one example of an enzyme that has been used for detoxification of water both in free (Munnecke and Hsieh 1976) and in the immobilized form (Munnecke 1977). Phenol oxidases have been suggested for the removal of xenobiotics from water. Similarly, horseradish peroxidase has been successfully used to dephenolize coal-conversion wastewaters. The enzyme is also effective in removing chlorophenols, chloroanilines, benzidines, and diphenylanilines (Klibanov et al. 1983).

The use of biomolecules such as enzymes, antibodies or DNAzymes in biosensors for environmental analysis faces a stiff test in terms of robustness and stability under field testing conditions. Immobilization of the biomolecules on solid supports is a prominent strategy for addressing these challenges (van de Velde et al. 2002). The immobilized form of enzymes mimics their natural mode in living cells in many cases considering their placement and attachment to membranes, organelle structures or the cellular cytoskeleton. The solid supports seek to stabilize the enzymes while rendering superior mass transfer of analytes thereby contributing to enhanced robustness and catalytic performance of the overall construct (Datta et al. 2013). Immobilized biomolecular systems enable greater sophistication in the design of biosensors thereby helping with their each of use. Enzyme immobilization can also facilitate enhanced environmental remediation activity. For example, immobilization of cyanate hydratase on magnetic multi-walled carbon nanotubes has been used for the simultaneous removal of heavy metal and cyanate in wastewater samples (Ranjan et al. 2019). An example of sophistication in immobilized enzyme-based approaches is the adoption of enzyme cascade reactions. Immobilization of enzymes constituting cascade reactions leads to improved efficiency in the transfer of intermediates from one step to the next akin to the behavior of complex multi-enzyme complexes underlying several metabolic processes (Schmitt and An 2017). A plethora of strategies have been devised for the physical and chemical immobilization of biomolecules on solid supports. In particular, the conjugation of enzymes is often associated with structural alterations that result in the creation of a distinctive microenvironment of

the biomolecule as compared to the bulk solution (Mohamad et al. 2015). Physical methods for immobilization include entrapment, adsorption, and microencapsulation. Chemical strategies cover various ways of covalently linking well-defined functional groups and include the use of affinity ligands such as biotin-streptavidin. Compared to their free forms, immobilized enzymes are usually more stable and easier to handle (Homaei et al. 2013). Further, the corresponding reaction products can be separated easily and is of special relevance to the food and pharmaceutical industries (Kirk et al. 2002). Nevertheless, the structural disruption of biomolecules due to immobilization poses a substantial challenge. For example, irreversible deactivation of enzymes upon covalent immobilization renders both the enzymes and often-costly support unusable. Similarly, non-covalent attachment of biomolecules is fraught with leaching in aqueous media. Cross-linking in gel matrix or carrier can result in a reduction in activity due to misfolding. Further, the preparation of cross-linked enzyme aggregates necessitates the crystallization of enzymes, which is a laborious and unpredictable process (Sheldon and van Pelt 2013). Site-specific conjugation approaches have witnessed significant advances in recent years. The sophisticated application of organic chemistry and molecular biology has enabled the anchoring of enzymes and antibodies on various supports thereby expanding the scope of protein microarrays, biosensors and flow reactor systems (Wallace and Balskus 2014). In this context, nucleic acid based scaffolds and conjugation approaches have occupied a distinctive niche. The predictable and programmable self-assembly characteristics of DNA and RNA have been exploited for the design and construction of complex nanostructures that facilitate the detailed spatial organization of attached moieties (Zhang et al. 2014).

Nucleic acid scaffolds have been used for organizing enzyme cascade reactions. Double-stranded DNA templates result in only modest improvements in enzyme performance (Muller and Niemeyer 2008; Niemeyer et al. 2002). Small DNA nanostructures have been more effective in this regard and several novel designs including double-crossover tiles (Fu et al. 2014) and three-point star DNA (Rothemund 2006) are noteworthy (Fig. 2). Scaffolded DNA origami templates have provided a unique opportunity for precise spatial anchoring of biomolecules. 3D DNA origami templates have been deployed for eliciting superior enzyme cascade efficiencies when compared to freely diffusing enzymes in solution (Fu et al. 2012). The semi-confined character of rectangular origami systems has been partially implicated in such improved enzyme efficiency along with the stabilizing effect of the origami. Other strategies for enzyme immobilization on nucleic acid scaffolds include the use of nucleic acid binding protein domains (Nakata et al. 2015) and aptamer binding interactions (Hasegawa et al. 2016).

Developments in the nucleic acid based scaffolding and conjugation of biomolecules should be juxtaposed with the advances in DNA-based biosensors. For example, electrochemical DNA (E-DNA) sensors have gained traction and have been used to detect the presence of hazardous substances such as drugs and heavy metal ions (Lubin and Plaxco 2010). E-DNA sensors rely on the ability of the constituent nucleic acid to make contact with an electrode generating detectable Faradaic current in response to a specific analyte (Lubin and Plaxco 2010). Nucleic acid secondary

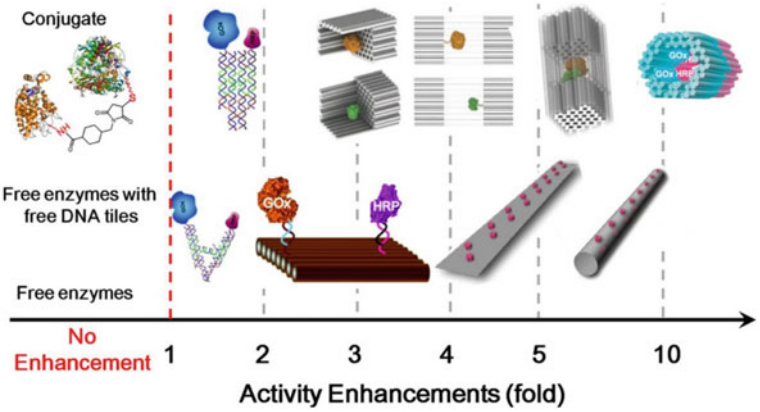

Fig. 2 Reported comparison of activity enhancements of various DNA scaffolded enzyme systems; reproduced with permission from Zhang and Hess (2017)

structures such as quadruplexes and architectures such as three-way junction (TWJ) have been incorporated in the design of DNA receptors (Chilka et al. 2018). Other signal transduction methods such as fluorescence and electroluminescence have been used in conjunction with the nucleic acid receptor systems. For example, an electroluminescence sensor for Pb^{2+} was based on the conformational change of DNA in the presence of the target (Hai et al. 2013). Similarly, TWJ-based triple biosensors have been developed for the detection of three different analytes depending on the stimulus received (Fig. 3) (Zhang et al. 2015).

The discourse surrounding the use of biomolecules in environmental analysis is punctuated by the constraints of the scale of application. Sophisticated biomolecular constructs are arguably more attractive at a smaller scale of application and in unorthodox contexts. For example, the analysis and remediation of specific chemical substances deployed in laboratory-scale research and development are often overlooked albeit such analysis may proffer several benefits. In this work, we use DNA-based nanoconstructs to separate a dye that is commonly used for molecular biology work. Our attempt serves to provide proof-of-concept of the use of immobilized biomolecules for adsorption and release of specific substances at a scale that is relevant in terms of human activity.

Dyes and pigments are traditionally considered as coloring agents, especially for textiles. The revolutionary changes in biotechnology and molecular biology over the past half-century have been facilitated by the development of dyes that can be used for staining and visualization of biomolecules. Notably, while the amount of these dyes used in clinical and research context is not substantial, they are usually extremely toxic and can serve as environmental hazards. Further, these dyes are expensive and would benefit from entrapment and reuse. SYBR Gold is an example of a cyanine dye with impressive nucleic acid fluorescence imaging capability (Tuma et al. 1999). In fact, it has been used as a substitute for the more widely known ethidium bromide, which is now discouraged due to its carcinogenicity. In this work, we have designed

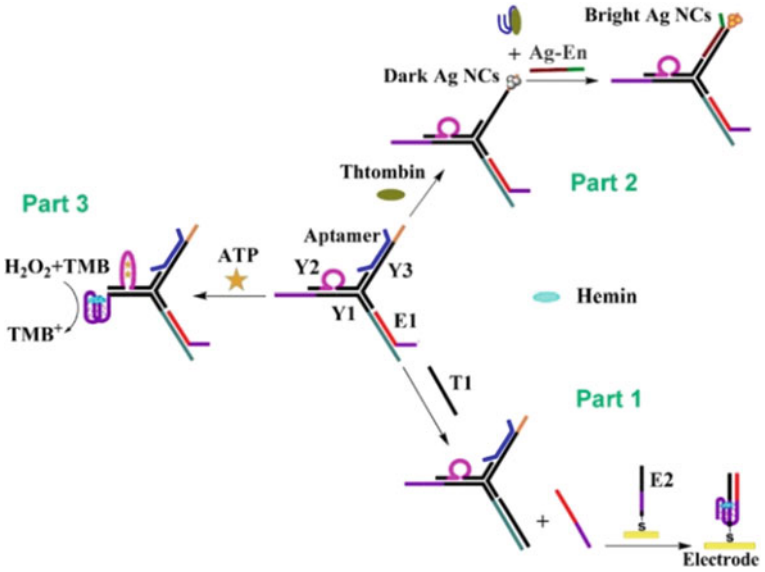

Fig. 3 Schematic Illustration of the TWJs-based sensing platform used for the DNA, Thrombin, and ATP analysis, respectively; reproduced with permission from Lubin and Plaxco (2010)

DNA-based nanobio-constructs that are effective for dye adsorption, retrieval, and reuse.

2 Materials and Methods

5′-amino or 5′-biotin labeled oligonucleotides were purchased from IDT (Bangalore, India). Unmodified oligonucleotides were purchased from Sigma (Bangalore, India). Stock solutions were prepared in Tris-EDTA (pH 7.5) buffer. Stock solutions (~100 μM) and 260/280 ratio of the stock were calculated using Thermo Scientific Nanodrop 2000c and stored at −20 °C for further use. Mili-Q water was used for all preparations. Nucleic acid sequences used in the work are as follows:

Name	Oligonucleotide sequence	Modification
A1N	GGTGAGGTGGCGAGAGCGACGATCCATGCC	NH_2
S2N	GGCATGGATCGTCGCAGAGTTGACCTGACC	NH_2
S3N	GGTCAGGTCAACTCTTCTCGCCACCTCACC	NH_2
B1S2-10	GGCATGGATC	Biotin
B1S3-10	GGTCAGGTCA	Biotin

(continued)

(continued)

Name	Oligonucleotide sequence	Modification
S2-20	GTCGCAGAGTTGACCTGACC	
S3-20	ACTCTTCTCGCCACCTCACC	
S1	GGTGAGGTGGCGAGAGCGACGATCCATGCC	
S2	GGCATGGATCGTCGCAGAGTTGACCTGACC	
S3	GGTCAGGTCAACTCTTCTCGCCACCTCACC	
ss1	CAGATCCGAGGAATCTG	
ss1c	CAGATTCCTCGGATCTG	
ss2	ACATGAAATTAAATACATGT	
ss2c	ACATGTATTTAATTTCATGT	

Nanobio-Construct Design

Our nanobio-construct comprises a three-way junction with biotinylation at different locations to enable attachment with avidin. The constituent components include the following:

A. **Three-Way Junction (3WJ)** comprising constituents as shown below

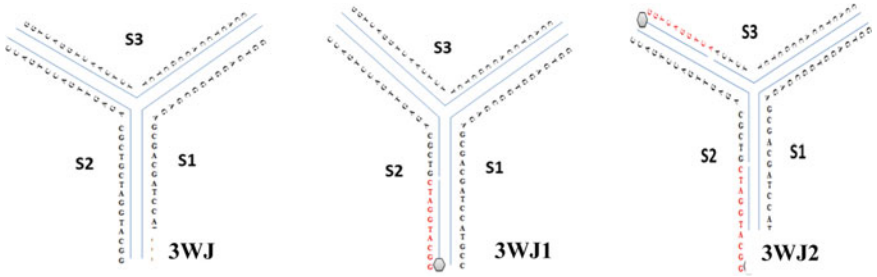

B. **Biotinylated Three-Way Junctions**

- **3WJ1** one arm bearing shorter sequence modified with biotin.
- **3WJ2** two arms bearing shorter sequences modified with biotin groups.

The three-way junctions (3WJs) were prepared by incubating the appropriate DNA strands in a 10 mM Tris-Cl (pH 7.5) buffer containing, 1 mM EDTA and 1 M NaCl. The concentration of DNA was 2 μM of each strand. The mixture was heated for a brief period (at ~95 °C) and slowly cooled to room temperature. Based on the above architectures, two types of nanoconstructs were constructed. These were borne from 3WJ1 and 3WJ2 by the addition of avidin.

M3WJ1: Matrix 3WJ1 (M3WJ1) was prepared by incubating of avidin with biotinylated 3WJ1 in a 1:3 stoichiometry at room temperature for 30 min in a 10 mM Tris-Cl (pH 7.5) buffer containing, 1 mM EDTA, and 1 M NaCl.

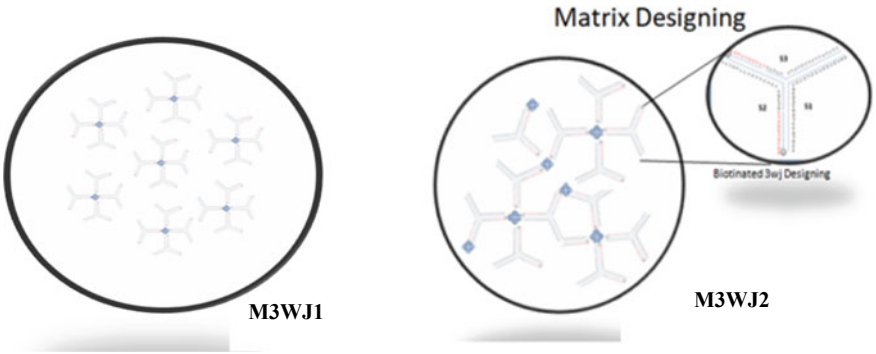

M3WJ2: Matrix 3WJ2 (M3WJ2) was prepared by incubating avidin with biotinylated 3WJ1 in 1.25:1 μM stoichiometry at room temperature for 30 min in a 10 mM Tris-Cl (pH 7.5) buffer containing, 1 mM EDTA, and 1 M NaCl.

Magnetic Nanoparticle Synthesis: The reported wet-chemical approach was used to synthesize magnetic nanoparticles (Park et al. 2011). Briefly, 0.25 M Ferrous Chloride was dissolved and homogenized in 50 ml mili-Q water followed by titration with 1 M KOH solution with continuous stirring and adjustment of pH to 9.0. The titrated solution was placed at room temperature for precipitation over a period of 2 h. Black precipitate hence formed was decanted using a magnet, washed with water and ethanol to remove impurities and kept overnight in a vacuum oven to dry (Park et al. 2011).

Surface Modification of MNPs: The surface of magnetic nanoparticles was modified with APTES and glutaraldehyde for the covalent attachment of oligonucleotides as per reported procedures (Kumar et al. 2016). Briefly, 10% APTES in methanol was added to the prepared iron oxide nanoparticles and the sample was sonicated for 5–10 min, until it was entirely homogenized. The resulting solution was kept for overnight vortex at 800 rpm. APTES-modified MNP was decanted and washed three times with methanol and left to dry in the desiccator (Park et al. 2011). 10 mg of MNP-APTES was dissolved in 8 ml of 8% of glutaraldehyde followed by 5-min sonication. After a 1-h vortex at room temperature and centrifugation at 10,000 rpm the particles, were decanted and washed twice with water. This step introduces an active-COOH group on MNP-APTES. Oligonucleotide immobilization on surface-modified MNPs having active-COOH groups which covalently bound to the NH_2-modified oligonucleotides. 25 μl of 100 μM DNA was added to 5 mg MNP-APTES-GLU. The resulting solution (2 mL) was vortexed overnight at room temperature and 850 rpm. After decanting, the supernatant was collected and the concentration of free DNA was determined. The precipitate was washed twice with water followed and the total volume was made up to 1.5 ml with TE buffer. For cross-linking avidin was added to the above complex thereby obtained.

Dye Adsorption: 5x of SYBR Gold was incubated with nanobio-construct for 20–30 min at room temperature. The supernatant was collected via centrifugation at

13,000–13,500 rpm for 20–30 min at room temperature followed by measurement of absorbance. Magnetic decantation for 5 min at room temperature was performed by using a strong bar magnet. 100 μl of each sample was loaded in a clear 96 well plate. The absorbance of supernatant corresponds to the absorbance of free dye in solution and a decrease in absorbance in the presence of nanobio-construct is an indication of retention by the construct.

Dye Desorption: After the adsorption of dye via nanobio-construct, the latter was decanted out from the solution by use of magnetic bars. The construct was washed twice with water and then incubated in desorption buffer (300 mM sodium acetate, pH 5.2 with 200 mM NaCl) for 25–30 min at 4 °C at very low rpm. The supernatant containing only dye was collected via nanobio-construct magnetic decantation and the concentration of dye in supernatant equating dye desorption was calculated.

3 Results and Discussion

3.1 Development and Characterisation of Nanobio-Constructs

The formation of secondary structure elements of DNA used in current work was characterized by electrophoretic mobility shift assay (EMSA). Higher molecular weight species are correlated with lower mobility and are attributed to three-way (3WJ) junction formation. As shown in Fig. 4, lanes c and d represent the formation

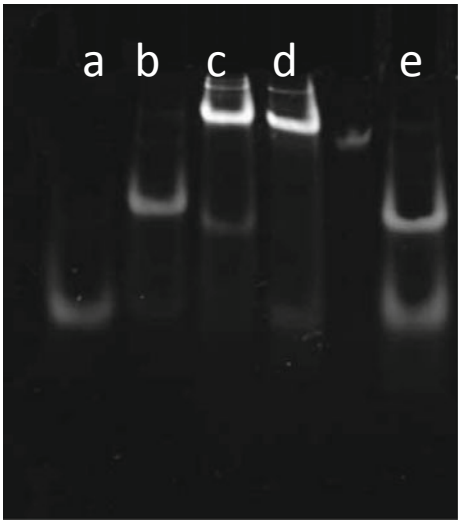

Fig. 4 Gel electrophoretic (20% SDS PAGE) analysis of various DNA constructs. Lanes contain 2 μM sample of **a** SSDNA, **b** DSDNA, **c** 3WJ1, **d** 3WJ2, **e** components of 3WJ2, respectively

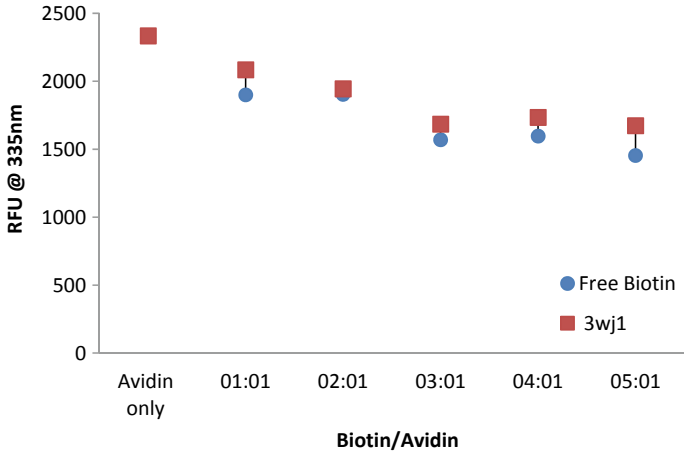

Fig. 5 Titration of Avidin into free biotin, and one ARM Biotinylated 3WJ1 monitored by fluorescence spectroscopy; $\lambda_{exc} = 280$ nm, $\lambda_{em} = 335$ nm

of three-way junctions in comparison to lane e which represents single-stranded and double-stranded constituents of the three-way junction.

The fluorescence of avidin can be used to verify differences in its state of complexation (Hytonen 2017). Free avidin exhibits emission in the range of 330–335 nm and upon binding to biotin, the emission is shifted to 320 nm (Hirsch et al. 2002). We observed a shift in fluorescence indicating complexation of avidin to a biotinylated three-way junction (3WJ1). The fluorescence of avidin can also be used to evaluate the extent of biotinylation. Upon the introduction of the free or biotinylated three-way junction, the fluorescence intensity of avidin decreased and was attenuated beyond a specific ratio of biotin/avidin (of 3:1) (Fig. 5). This attenuation is indicative of saturation of the avidin binding sites.

Various concentrations of 3WJ1 samples were incubated with 1 μM avidin at room temperature for a minimum of half hour and the resulting binding of molecules was assessed by EMSA. Gel electrophoretic analysis (10% PAGE) on 5 samples of 3WJ1+avidin in the 3WJ1:avidin ratios (a) 1:1, (b) 2:1, (c) 3:1, (d) 4:1 and (e) 5:1, was performed. Mobility shift was strongly affected by complexation (Fig. 6). In the presence of avidin, biotinylated 3WJ1 formed a network corresponding to high molecular weight species. Beyond threshold amounts of avidin, (lanes d and e), higher mobility bands were observed which are attributed to unbounded 3WJ1. Notably, lane c where 3WJ1: avidin ratio is 3:1 shows the sharpest band with the least amount of unbound sequences.

Similarly, EMSA on 3WJ2 was performed to assess the formation of three-way junctions by the corresponding complexes. Lanes a–e (Fig. 7) represent 3WJ2 incubated with various concentrations of avidin while lane f contains ssDNA. In the absence of avidin, there was no formation of a three-way junction. The addition of avidin resulted in the formation of a significantly slower moving complex. In lane

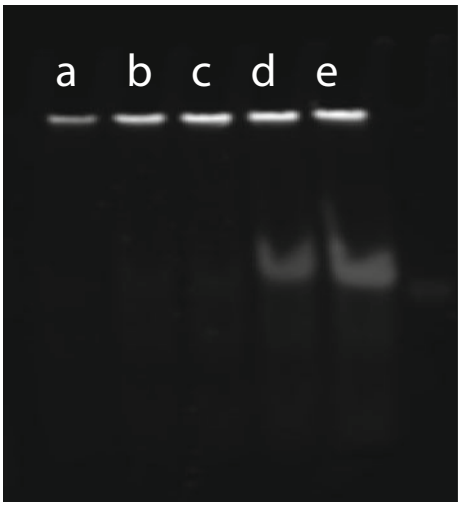

Fig. 6 EMSA of Biotinylated-3WJ1 in presence of variable amounts of Avidin

Fig. 7 EMSA of Biotinylated-3WJ2 in presence of variable amounts of Avidin

d a sharp band was observed with less unbound sequences. This ratio indicates the most suitable combination toward the formation of a matrix by 3WJ2. At higher concentrations of avidin, no significant changes were observed.

SEM analysis of the nanoconstructs revealed distinctive morphologies in each case. The magnetic nanoparticles with APTES and Glutaraldehyde conjugation displayed similar spherical morphologies albeit with slightly different size ranges (Fig. 8a, b); 32–37 nm for MNP-APTES and 38–48 nm for MNP-APTES-GLU. The increase in the network from amino-functionalized nucleic acid three-way junctions

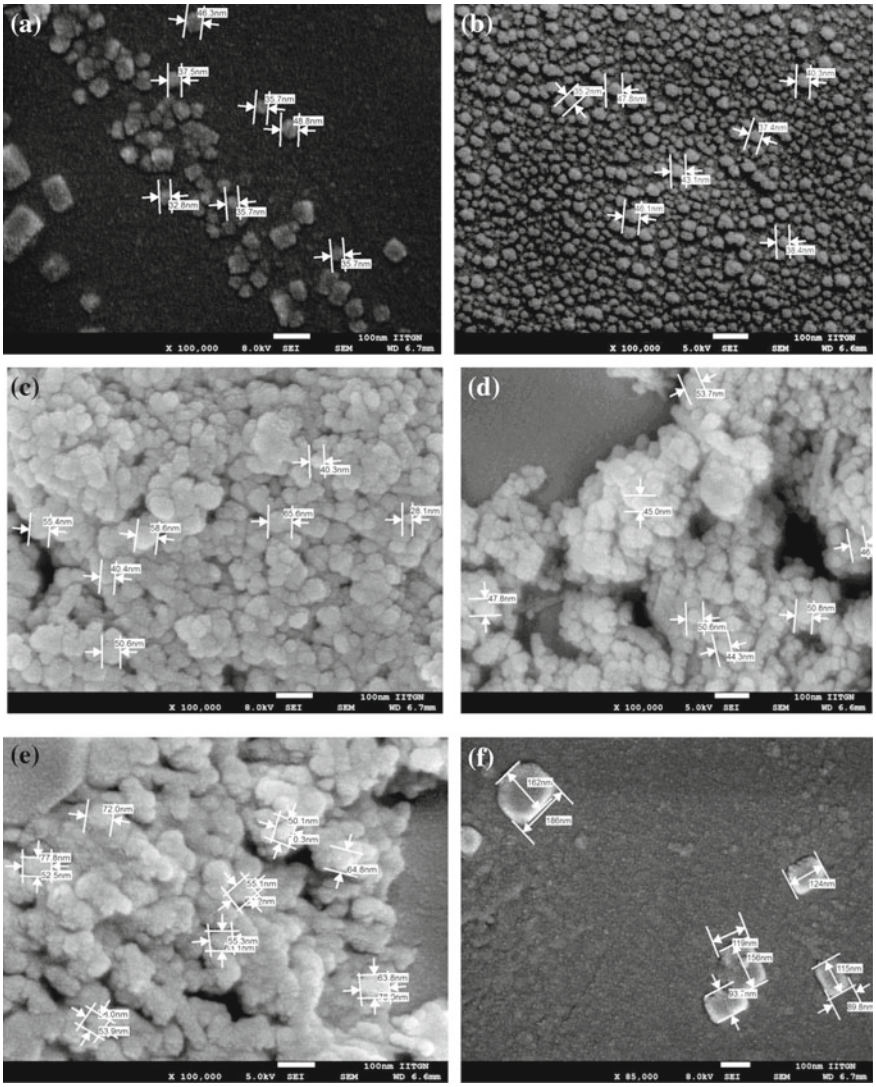

Fig. 8 SEM of various nucleic acid-nanoparticle constructs; **a** MNP-APTES, **b** MNP-APTES-GLU, **c** MNP-APTES-N3, **d** MNP-APTES-TWJ1, **e** MNP-APTES-TWJ1-AVIDIN and **f** MNP-APTES-TWJ2-AVIDIN (5 kV, 100,000 magnification)

(MNP-APTES-TWJ1) (Fig. 8d) to AVIDIN-conjugated matrix (Fig. 8e) manifested in greater particle sizes (from 45–54 nm to 55–80 nm) and change in morphology (spherical to cubical). The more complex network accomplished via MTWJ2 is evident from the wider size range of 100–190 nm for the MNP-APTES-TWJ2-AVIDIN (Fig. 8f).

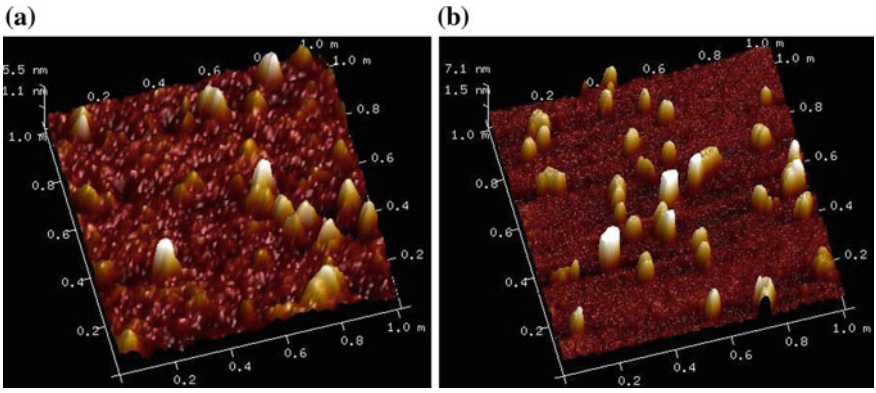

Fig. 9 3D-AFM of **a** MNP-APTES-GLU and **b** 3WJ1 attached on MNP

The morphology of constructs was further assessed by AFM. Attachment of the three-way junctions to MNPs resulted in a sharper distribution of topologies as compared to MNPs that only had the conjugating linker on them (Fig. 9). MNPs with immobilized three-way junctions are expected to produce a narrower dispersion of particles as compared to bare or linker-attached nanoparticles considering the propensity of the latter to agglomerate in a stochastic manner. Reasonably uniform topologies of 3WJ1 attached to MNPs were also indicative of satisfactory efficiency of conjugation being performed.

FTIR analysis of the constructs was performed to ascertain characteristic conjugations. The peaks at 550 cm^{-1} attributed to stretching vibration of Fe–O bond and 3350 cm^{-1} corresponding to OH stretch together emphasize the successful formation of MNPs (Fig. 10) (Niemirowicz et al. 2015). In the case of MNP-APTES, in addition to the Fe–O and OH stretches, band at 1640 cm^{-1} band is attributed to N–H bend. Also, 1070 cm^{-1} is due to asymmetric stretching of Si–O–Si, 950 cm^{-1} for Si–OH and 1508 cm^{-1} for CH_2 (Fig. 10).

In the case of MNP-APTES-Glu, the 1645 cm^{-1} peak is assigned for N–H bend. Further, bands at 1090 cm^{-1} for asymmetric stretching of Si–O–R, 1010 cm^{-1} for Si–O and 2775 cm^{-1} corresponding to C–H complete the characteristic peaks.

For the constructs containing DNA three-way junctions, bands at 1640 cm^{-1}, 1570 cm^{-1} and 1540 cm^{-1} are attributed to C=O, C=N, C=C stretching and N-H bending of nucleotides, respectively (Camacho et al. 2017). Further, 1211 cm^{-1}, 1121 cm^{-1}, 1280 cm^{-1} belong to the asymmetric stretch of PO^{2-}, symmetric of PO^{2-} and P–O–C backbone, respectively (Najafabadi et al. 2015). Immobilization of 3WJ was confirmed by the presence of peaks corresponding to bases and phosphate backbone of DNA.

XRD was used to assess differences in the crystal lattice structure of various constructs. Observable diffraction peaks (2θ) at (30.37), (35.78), (43.32), (53.66), (57.4) and (63.11) correspond to (220), (311), (400), (422), (511), (400) respectively as shown in Fig. 11 (JPCDS card, file No. 77–1545). These peaks are characteristic

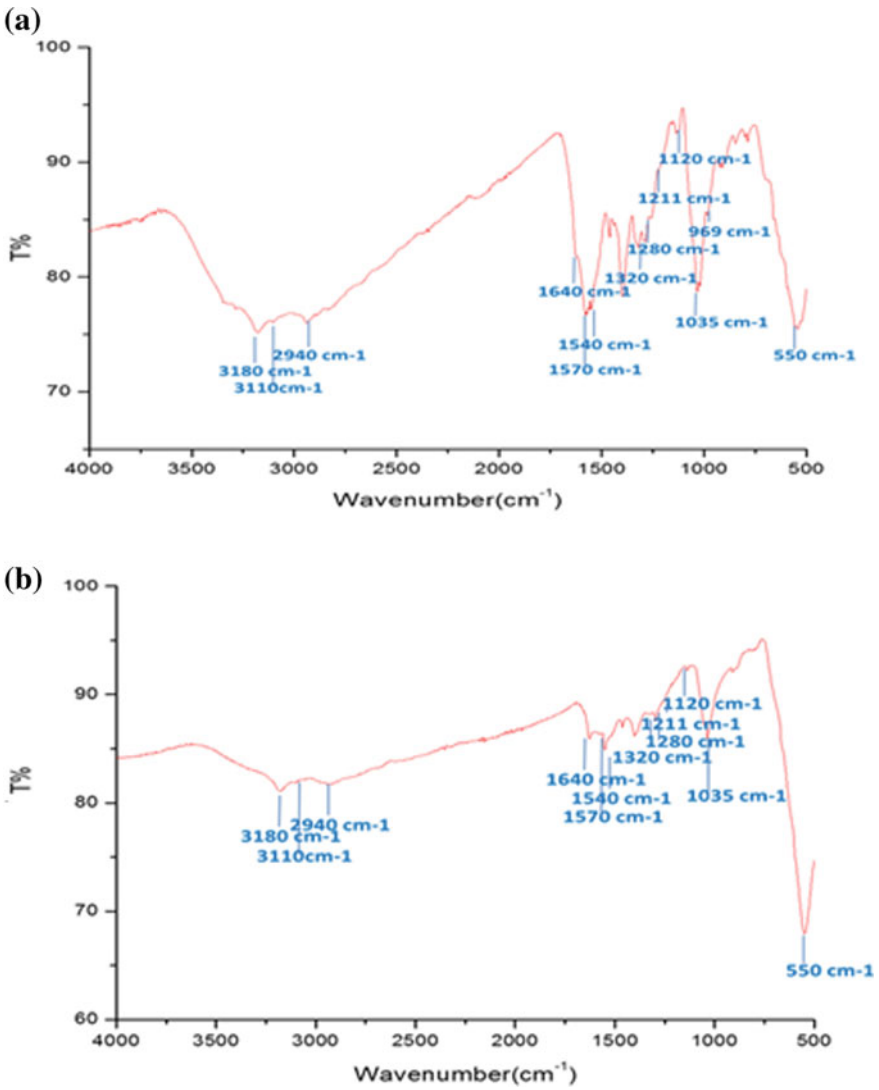

Fig. 10 FT-IR spectra of **a** MNP-3WJ with amino-functionalized termini and **b** MNP-3WJ with biotinylated DNA

for Fe_3O_4 and confirm the formation of MNPs (Unsoy et al. 2012). The highest peak at 35.78 and a very weak peak at 53.66 is obtained in every sample. Additionally, even on the attachment of linker and 3WJ all peaks are still present which implies no changes in the behavior of MNPs upon attachment of nucleic acid three-way junctions.

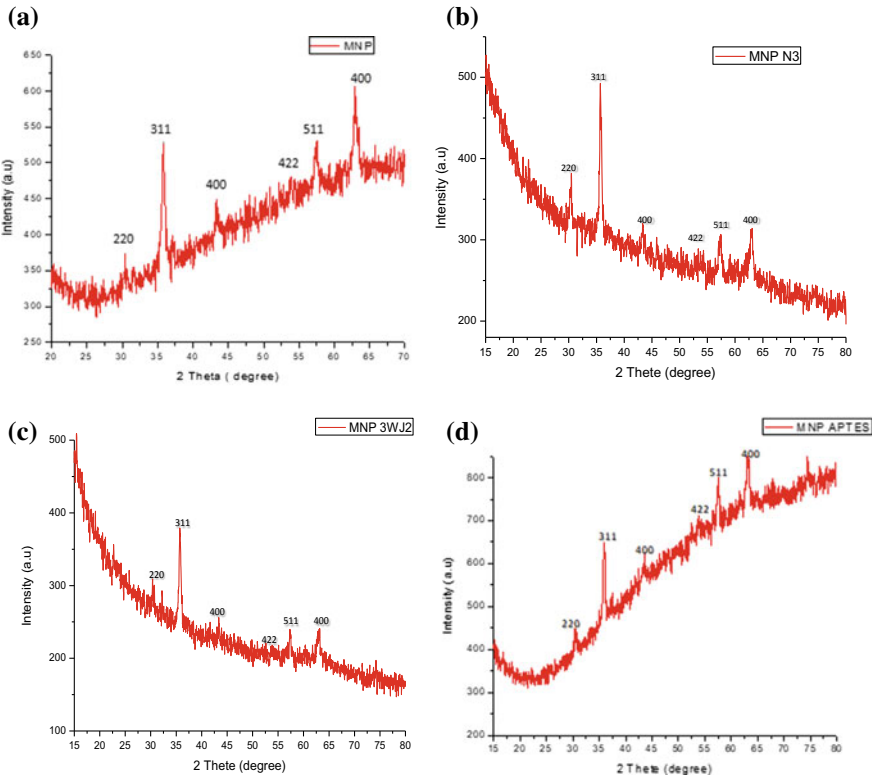

Fig. 11 XRD patterns of **a** MNP, **b** APTES-MNP, **c** MNP-Biotinylated 3WJ, **d** 3WJ with amino-functionalization immobilized on MNP

3.2 Dye Adsorption and Desorption Studies

We have used SYBR Gold for our current work. SYBR Gold binds with nucleic acids SYBR Gold binds to the nucleic acid via intercalation mode and displays an absorption maximum at 485 nm (Zipper et al. 2004). The wavelength maxima is red shifted upon binding to DNA possibly due to a decrease in $\pi-\pi^*$ electron transition. On increasing concentration of DNA from 1x to 100x, the spectrum shifted toward higher wavelength which clearly indicates the binding of SYBR Gold to dsDNA (*data not shown*).

Various bare and MNP-immobilized nucleic acids were tested for their ability to adsorb SYBR Gold. Dye adsorption to dsDNA was 20.24% (at 100x of DNA) and was improved to 26.11% upon attachment of the DNA to MNP (Fig. 12).

We tested our nucleic acid three-way junction-based constructs for dye retention and retrieval. The nucleic acid samples were incubated with avidin for 2 h at room temperature. Subsequently, the complexes were incubated with 5x SYBR Gold for 30 min at room temperature at low rpm. This was followed by centrifugation to

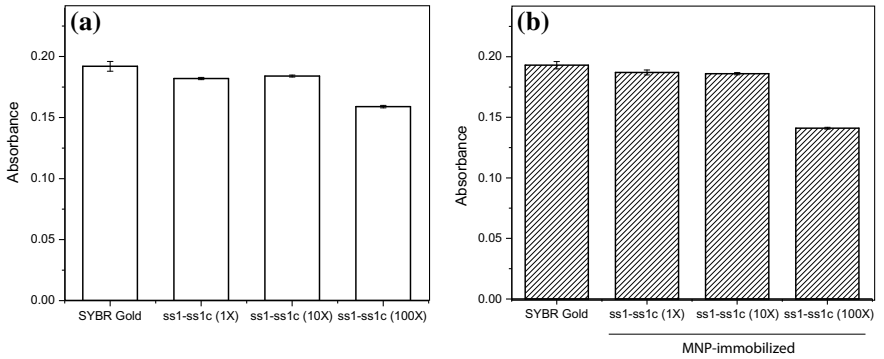

Fig. 12 SYBR Gold absorbance in presence of **a** bare and **b** MNP-immobilized dsDNA

separate out complexes from the buffer. Measurement of absorbance was performed on the supernatant post-magnetic separation. Based on the absorbances measured, retention of the dye was estimated at 39.4% on (M3WJ1) and 51.8% dye via a large matrix structure (M3WJ2) was retrieved (Fig. 13).

Finally, we tested MNP-immobilized matrix three-way junctions (M3WJ1 and M3WJ2) for their (i) ability to retrieve SYBR Gold, (ii) capability for reuse and (iii) dye desorption from the matrix constructs (Fig. 14). Samples were prepared by the incubation of nucleic acids with avidin at least for 1 h at room temperature. The MNP-M3WJ1 and MNP-3WJ2 constructs displayed superior ability towards adsorption of SYBR Gold as compared to the simpler nucleic acid-MNP constructs. Notably, 43.23% and 52.47% of dye retrieval were observed with MNP-3WJ1 and MNP-3WJ2, respectively.

Repeat use of the nanobio-constructs on a fresh batch of dye solutions resulted in a very similar level of dye retention; 42.57% and 52.04% for MNP-3WJ1 and MNP-3WJ2, respectively. Notably, 99.4% of dye desorption was affected for MNP-3WJ1 and 99.6% for MNP-3WJ2 during first use. The total dye desorption decreased

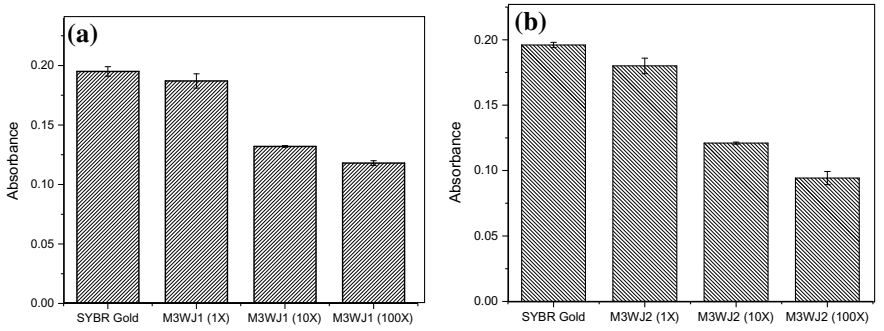

Fig. 13 SYBR Gold adsorption by **a** M3WJ1 and **b** M3WJ2

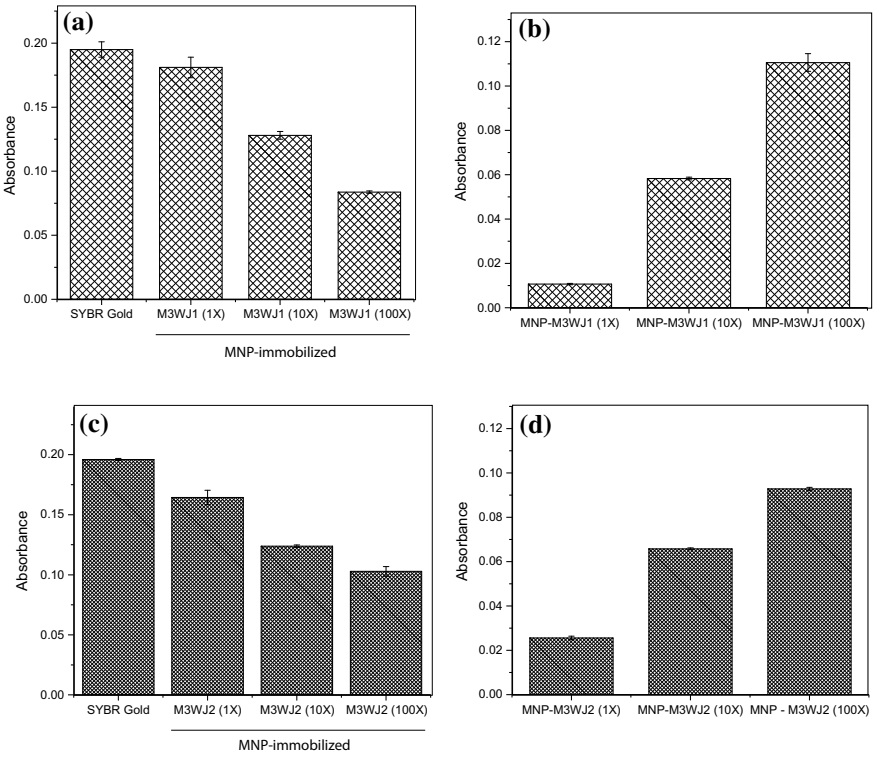

Fig. 14 SYBR gold adsorption on **a** MNP-M3WJ1, **c** MNP-M3WJ2 and desorption from **b** MNP-M3WJ1, **d** MNP-M3WJ2

slightly to 97.5% and 98.4% during the second use of the MNP-3WJ1 and MNP-3WJ2, respectively (*data not shown*). Overall, both constructs are extremely potent in terms of their ability to retrieve and release SYBR Gold dissolved in solution. MNP-3WJ2 is somewhat superior based on the adsorption and desorption efficiency during use and reuse.

4 Conclusion

The confluence of nanomaterials and biological macromolecules has enabled expanded paradigms of environmental analysis and remediation. The bulk of work in this context has been within an analytical or bio-sensory framework. This is not surprising considering the sophistication in the function of biomolecules and constraints in terms of scale-up of operations. Nevertheless, a unique set of applications of such biomolecule-nanomaterial constructs can be envisaged if one were to reimagine the environment to include the immediate proximity of human activity. Processes and

products being used at the human scale could provide unmatched opportunities for nanobio-constructs. In this chapter, we have examined the context of the application of nucleic acid-based nanoconstructs in terms of orthodox environmental analysis. Further, we provide proof-of-concept of novel nucleic acid-based nanoconstructs toward adsorption and reuse of a clinically relevant dye. The work provides perspective to the use of nucleic acid (or other biomolecule-based) nanoconstructs for environmental analysis in atypical contexts.

Acknowledgements The authors are grateful to the Ministry of Human Resource and Development (MHRD), Govt. of India for financial support of this work through IMPRINT grant no. 6349.

References

Amine A, Arduini F, Moscone D, Palleschi G (2016) Recent advances in biosensors based on enzyme inhibition. Biosens Bioelectron 76:180–194

Camacho AS, Martin-Garcia I, Contreras-Celedon C, Chacon-Garcial L, Alonso F (2017) DNA-supported palladium nanoparticles as a reusable catalyst for the copper- and ligand-free Sonogashira reaction. Catal Sci Technol 7:2262–2273

Chilka P, Reddy PR, Datta B (2018) Dimeric carbocyanine dye and nucleic acid aptamer mediated detection of food borne toxin. Indian J Chem 57B:281–286

Datta S, Rene CL, Sriramulu RYR (2013) Enzyme immobilization: an overview on techniques and support materials. Biotech 3:1–9

Fu J, Liu M, Liu Y, Woodbury NW, Yan H (2012) Interenzyme substrate diffusion for an enzyme cascade organized on spatially addressable DNA nanostructures. J Am Chem Soc 134:5516–5519

Fu J, Yang YR, Johnson-Buck A, Liu M, Liu Y, Walter NG, Woodbury NW, Yan H (2014) Multi-enzyme complexes on DNA scaffolds capable of substrate channeling with an artificial swinging arm. Nat Nanotechnol 9:531–536

Gurung N, Ray S, Bose S, Rai V (2013) A broader view: microbial enzymes and their relevance in industries, medicine and beyond. Biomed Res Int 329121

Hai H, Yang F, Li J (2013) Electrochemiluminescence sensor using quantum dots based on a G-quadruplex aptamer for the detection of Pb^{2+}. RSC Adv 3:13144–13148

Hasegawa H, Savory N, Abe K, Ikebukuro K (2016) Methods for improving aptamer binding affinity. Molecules 21:421

Hirsch JD, Eslamizar L, Filanoski BJ, Lalekzadeh N, Haugland RP, Beecham JM, Haugland RP (2002) Easily reversible desthiobiotin binding to streptavidin, avidin, and other biotin-binding proteins: uses for protein labeling, detection, and isolation. Anal Biochem 308:343–357

Homaei AA, Sariri R, Vianello F, Stevanato R (2013) Enzyme immobilization: an update. J Chem Biol 6:185–205

Hytonen VP (2017) Optimized streptavidin for fluorescent labeling of biotinylated targets. Cell Chem Biol 24:921–922

Kirk O, Borchert TV, Fuglsang CC (2002) Industrial enzyme applications. Curr Opin Biotechnol 13:345–351

Klibanov AM, Tu TM, Scott KP (1983) Peroxidase-catalyzed removal of phenols from coal-conversion waste waters. Science 221:259–261

Kumar S, Sharma P, Ratrey P, Datta B (2016) Reusable nanobiocatalysts for the efficient extraction of pigments from orange peel. J Food Sci Technol 53:3013–3019

Li J, Lu Y (2000) A highly sensitive and selective catalytic DNA biosensor for lead ions. J Am Chem Soc 122:10466–10467

Li S, Yang X, Yang S, Zhu M, Wang X (2012) Technology prospecting on enzymes: application, marketing and engineering. Comput Struct Biotechnol J 2:e201209017

Li T, Dong S, Wang E (2009) Label-free colorimetric detection of aqueous mercury ion (Hg^{2+}) using Hg^{2+}-modulated G-quadruplex-based DNAzymes. Anal Chem 81:2144–2149

Liu J, Lu Y (2007a) Colorimetric Cu^{2+} detection with a ligation DNAzyme and nanoparticles. Chem Comm 46:4872–4874

Liu J, Lu Y (2007b) A DNAzyme catalytic beacon sensor for paramagnetic Cu^{2+} ions in aqueous solution with high sensitivity and selectivity. J Am Chem Soc 129:9838–9839

Lubin AA, Plaxco KW (2010) Folding-based electrochemical biosensors: the case for responsive nucleic acid architectures. Acc Chem Res 43:496–505

Mohamad NR, Marzuki NHC, Buang NA, Huyop F, Wahab RA (2015) An overview of technologies for immobilization of enzymes and surface analysis techniques for immobilized enzymes. Biotechnol Biotechnol Equip 29:205–220

Muller J, Niemeyer CM (2008) DNA-directed assembly of artificial multienzyme complexes. Biochem Biophys Res Commun 377:62–67

Munnecke DM (1977) Properties of an immobilized pesticide-hydrolyzing enzyme. Appl Environ Microbiol 33:503–507

Munnecke DM, Hsieh DP (1976) Pathways of microbial metabolism of parathion. Appl Environ Microbiol 31:63–69

Najafabadi ME, Khayamian T, Hashemian Z (2015) Aptamer-conjugated magnetic nanoparticles for extraction of adenosine from urine followed by electrospray ion mobility spectrometry. J Pharm Biomed Anal 107:244–250

Nakata E, Dinh H, Ngo TA, Saimura M, Morii T (2015) A modular zinc finger adaptor accelerates the covalent linkage of proteins at specific locations on DNA nanoscaffolds. Chem Comm 51:1016–1019

Niemeyer CM, Koehler J, Wuerdemann C (2002) DNA-directed assembly of bienzymic complexes from in vivo biotinylated NAD(P)H:FMN oxidoreductase and luciferase. ChemBioChem 3:242–245

Niemirowicz K, Surel U, Wilczewska AZ, Mystkowska J, Piktel E, Gu X, Namiot Z, Kulakowska A, Savage PB, Bucki R (2015) Bactericidal activity and biocompatibility of ceragenin-coated magnetic nanoparticles. J Nanobiotechnol 13:32

Park HJ, McConnell JT, Boddhi S, Kipper MJ, Johnson PA (2011) Synthesis and characterization of enzyme-magnetic nanoparticle complexes: effect of size on activity and recovery. Colloids Surf B Biointerfaces 83:198–203

Ranjan B, Pillai S, Permaul K, Singh S (2019) Simultaneous removal of heavy metals and cyanate in a wastewater sample using immobilized cyanate hydratase on magnetic-multiwall carbon nanotubes. J Hazard Mater 363:73–80

Rothemund PWK (2006) Folding DNA to create nanoscale shapes and patterns. Nature 440:297–302

Schmitt DL, An S (2017) Spatial organization of metabolic enzyme complexes in cells. Biochemistry 56:3184–3196

Sheldon RA, van Pelt S (2013) Enzyme immobilisation in biocatalysis: why, what and how. Chem Soc Rev 42:6223–6235

Shen L, Chen Z, Li Y, He S, Xie S, Xu X, Liang Z, Meng X, Li Q, Zhu Z, Li M, Le XC, Shao Y (2008) Electrochemical DNAzyme sensor for lead based on amplification of DNA-Au Bio-Bar codes. Anal Chem 80:6323–6328

Tuma RS, Beaudet MP, Jin X, Jones LJ, Cheung C-Y, Yue S, Singer VL (1999) Characterization of SYBR gold nucleic acid gel stain: a dye optimized for use with 300 nm ultraviolet transilluminators. Anal Biochem 268:278–288

Unsoy G, Yalcin S, Khodadust R, Gunduz G, Gunduz U (2012) Synthesis, optimization and characterization of chitosan-coated iron oxide nanoparticles produced for biomedical applications. J Nanopart Res 14:964

van de Velde F, Lourenco ND, Pinheiro HM, Bakker M (2002) Carrageenan: a food-grade and biocompatible support for immobilization techniques. Adv Synth Catal 344:815–835

Wallace S, Balskus EP (2014) Opportunities for merging chemical and biological synthesis. Curr Opin Biotechnol 30:1–8

Zhang F, Nangreave J, Liu Y, Yan H (2014) Structural DNA nanotechnology: state of the art and future perspective. J Am Chem Soc 136:11198–11211

Zhang L, Guo S, Zhu J, Zhou Z, Li T, Li J, Dong S, Wang E (2015) Engineering DNA three-way junction with multifunctional moieties: sensing platform for bioanalysis. Anal Chem 87:11295–11300

Zhang X-B, Kong R-M, Lu Y (2011) Metal ion sensors based on DNAzymes and related DNA molecules. Ann Rev Anal Chem 4:105–128

Zhang Y, Hess H (2017) Toward rational design of high-efficiency enzyme cascades. ACS Catal 7:6018–6027

Zipper H, Brunner H, Bernhagen J, Vitzthum F (2004) Investigations on DNA intercalation and surface binding by SYBR Green I, its structure determination and methodological implications. Nucl Acids Res 32:e103